
SECTION TWO

CHAPTER 8

Ignition of Liquid Fuels

A. Murty Kanury

Introduction

This chapter introduces the topic of liquid fuel ignition in air. A qualitative description of the physical and chemical steps leading to ignition makes possible a systematic identification of the factors of concern. Different measures of liquid fuel ignitability are defined, and a comprehensive collection of data is presented. Simple mechanistic models are formulated for the piloted ignition (i.e., flash point) of liquids as well as for the autoignition of vapor and air mixtures. The results of these models are employed to highlight (1) the manner in which physics and chemistry play a complicated role to culminate in ignition, (2) the resultant dependency of the measurements on the specific apparatus test method, and (3) a number of dependencies of the measured ignition temperature on experimental conditions. These predicted dependencies are found to be consistent with the trends in reported data.

Liquid combustibles are ever-present in the context of mobile and stationary power plants as well as in an innumerable array of industrial processes. A variety of physical forms in which they arise can be identified. Dip tanks of paints or solvents, sprays, spills from a storage tank, flowing or creeping films, and pools in open pits are but a few examples. In almost all situations, air is in contact, or readily comes into contact, with the fuel to make the associated fire hazard obvious. The following questions arise in relation to fire safety in these situations:

1. Under what circumstances is ignition possible?
2. Under the conditions of possible ignition, what is the external impulse required to produce ignition within a given time? Alternately stated, given a set of conditions under which ignition is possible, how long an exposure is required to produce ignition?

The first of these questions is addressed here along with some cursory observations on the second question.

Ignition is defined as the onset or initiation of combustion, usually flaming. As such, ignition is indicated by the oxidation reaction attaining a rapidly increasing rate. The rapidity often makes the ignition phenomenon an abrupt event. In practice, ignition is noted by the appearance of a flame, by a significant increase in oxidative energy release, or by a corresponding large rise in temperature.

Three sets of conditions have to be fulfilled to ignite a condensed-phase material. First, sufficient quantities of combustible vapors and gases have to be emanated as a result of preheating the solid or liquid. Second, these vapors and gases have to be mixed with the oxidant in the gas phase. Third, the mixture has to be either at a high enough temperature to induce self-accelerative oxidation (i.e., *spontaneous* or *autoignition*) or to be provided with a pilot source (e.g., a small ignitor flame, a heated wire, or an electric spark) to locally heat a minimum quantity of the mixture to a temperature approaching the adiabatic flame temperature (i.e., *piloted* or *forced ignition*). These three sets of conditions enable a systematic enumeration of the factors influencing the ignition process.

Vaporization: A Contrast between Liquid and Solid Combustibles

All condensed-phase materials release vapors and gases in response to heating. As related to the first of the three steps mentioned above, this response is dramatically different between solids and liquids.

Liquids generally* vaporize in the sense of a thermodynamic phase change in which the chemical structure of vapor remains the same as that of liquid. Such a vaporization is usually a surface mass transfer phenomenon,

Dr. A. Murty Kanury is professor of mechanical engineering at Oregon State University. His professional activities are centered around teaching thermal science and research in fire and combustion.

*Some high molecular weight liquids are exceptional in that they exhibit a chemical breakdown in response to heating.

although intense (and internal) heating may produce bubbles within the liquid. In contrast, heating of solids generally* results in complicated destructive distillation (also known as thermochemical degradation or *pyrolysis*) to yield a complex combustible mixture of gases and vapors. Known also as pyrolyzate, this mixture is produced *within* the solid at a rate dependent upon the local instantaneous density and temperature. The pyrolysis process, thus, is volumetric and chemical rather than superficial and physical.

Pyrolysis of most solids leaves a carbon-rich porous residue, known as char, behind. Vaporization of most common liquids, in contrast, leaves no residue behind.

Upon heating a liquid body, internal convective currents develop with an intensity dependent on the heating rate, viscosity, surface tension, gravity, and geometry of the body. The heating of a solid, by definition, does not invoke the same sort of bulk flows. There does arise, however, an internal convection process associated with the outflow of the pyrolyzates through the partially or totally degraded porous solid. The temperature distribution within a liquid body can be made artificially uniform by mixing with a stirrer; the same is not possible within a solid body.

The ease with which vapors can be produced by heating a liquid is known as its volatility. A liquid is said to be highly volatile if its vapor pressure at a given temperature is high (i.e., its boiling point at a given pressure is low), and its *latent heat* (i.e., enthalpy of vaporization) is low.

Mixing of Vapors with Air

The vapors emanating from the surface of a heated liquid mix with the ambient gas, which is usually air at normal pressure. This mixing is dependent on such factors as whether the air is quiescent or in motion, whether the liquid reservoir is closed or open, the geometry relative to the gravity vector, the temperature of the liquid surface relative to the ambient, the molecular weight of the vapors relative to that of air, and the height and nature of the lip of the vessel containing the liquid.

Ignition of the Mixture

The mixture thus formed has to be rich enough in combustible content to be over the so-called *lean limit of flammability* to make a propagable flame possible from a localized pilot source. The location and nature of the pilot is of obvious importance. Generally, when ignition is possible, the flame would simply flash through the mixture, consume the combustibles in its sweep, and then go out. Only if the vaporization is copious enough, due to a higher bulk temperature of the liquid, does the flame become self-sustained. These flashing and self-sustainment concepts are central to the liquid fuel ignition process.

If the gaseous mixture temperature is sufficiently high, ignition may occur even without a pilot source. This is known as auto- or spontaneous ignition.

*Some solids, such as waxes, are exceptional in that they melt and vaporize in the manner of a simple liquid. Some other exceptional solids, such as camphor and sulfur, sublime to a gas phase.

Figure 2-8.1, the rudiments of which were first formulated by Zabetakis,¹ indicates the essence of the previous descriptions. Part (a) of Figure 2-8.1, familiar from elementary thermodynamics, exhibits the exponential dependency of equilibrium vapor pressure on the liquid temperature. The normal melting and boiling point temperatures are also shown in this figure. Part (b) shows that as the temperature is gradually raised, the vapor pressure of the combustible liquid gradually rises to yield, at a limit temperature, T_L , a lean limit mixture capable of supporting a propagable flame. At a higher temperature, the partial pressure may become too high and make the mixture too rich to support a flame. Furthermore, at relatively high temperatures exceeding T_a , ignition can occur even in the absence of a pilot source. As indicated, the lean and rich limits, as well as the autoignition limits, are generally temperature dependent. Part (c) shows that the features of ignition of a pyrolyzing combustible solid are similar to those of a combustible liquid, except for the fact that the pyrolyzates are evolved due to degradation over a range of temperatures.

Some Experimental Techniques and Definitions

Piloted ignition data are mostly measured in a number of American Society for Testing and Materials (ASTM) tests.² These tests involve either an open-cup (e.g., ASTM D1310 open-cup test or D92 Cleveland Test) or a closed-cup test (e.g., ASTM D56 Tag Closed Tester and D93 Pensky-Martens test) to hold the fuel to a prescribed level. This cup is then heated either directly by a prescribed, Bunsen-type laboratory flame, or indirectly by a water (or water and glycol mixture) bath. There are similar international tests under a variety of names, including Engler and Haass, Danish open, Tagliabue, Elliot, Luchaire, Treumann, Albrecht, Abel, Saybolt, and Parish, among others.

Mullins³ presents a comprehensive review of a variety of methods by which the spontaneous ignition temperature, T_a , of combustible liquids is experimentally determined. A number of variations, in which the reaction vessel is a crucible, flask, furnace, bomb, or a compression device, are employed to precisely control the experimental conditions, to observe whether or not ignition will occur, and to measure the time to ignition (i.e., the ignition delay). Flow methods, as well as heating of the liquid by hot surfaces, are also frequently employed. The ASTM test standard D2155 holds the liquid in a flask, which is heated in a furnace to determine the autoignition temperature and ignition delay.

The finer details of these tests are not materially relevant to the scope of this chapter. Zabetakis¹ and the ASTM standards² do an excellent job of giving these details. It is important, however, to define certain measures of the volatility and ignitability of liquid fuels as obtained from these experimental techniques.

The *bubble point* ($R : 1$) of a liquid fuel⁴ is the temperature at which equilibrium exists between the wholly condensed fuel and an infinitesimal quantity of its vapor mixed with air in the ratio of $1 : R$. When R is zero, the bubble point is the same as the normal boiling point.

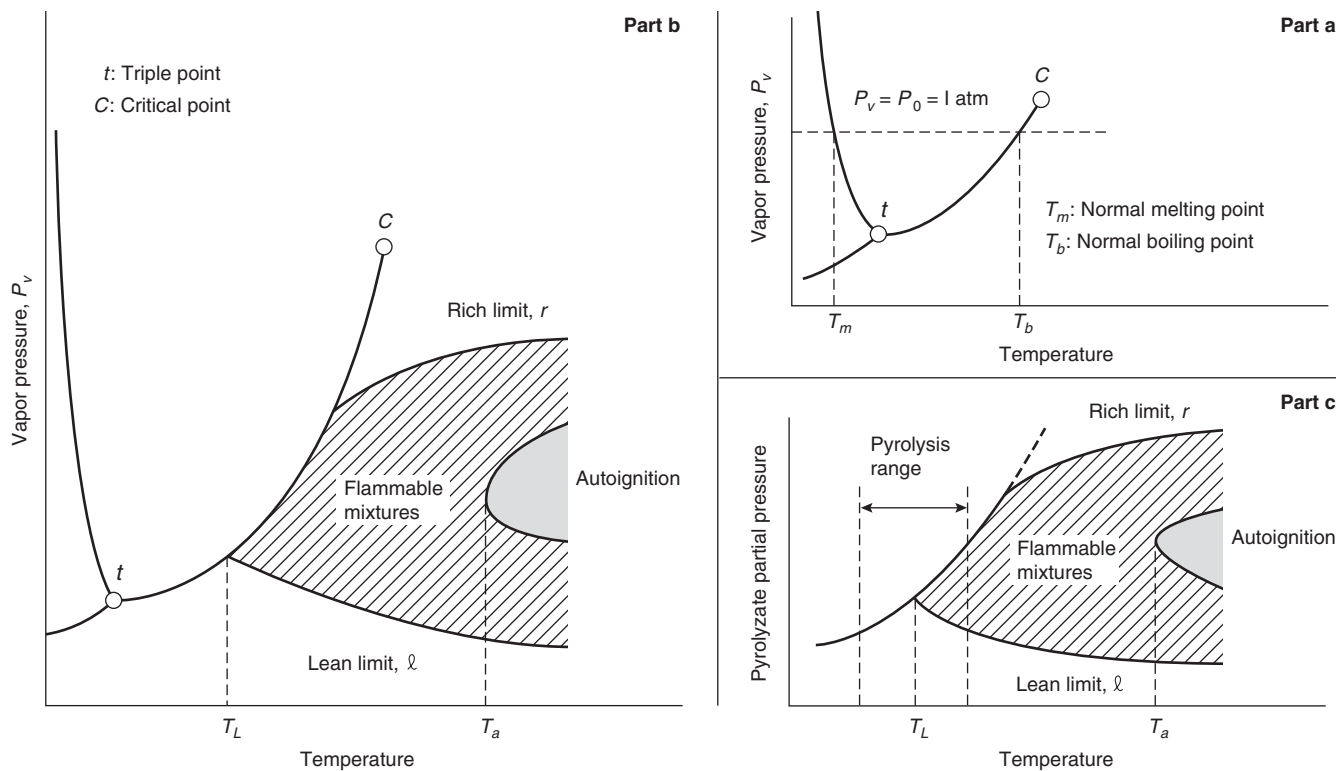


Figure 2-8.1. Phase-change diagram for: (a) an inert liquid; (b) a combustible liquid; and (c) a combustible solid.

The *flash point* of a liquid fuel is its temperature (presumed to be uniform) at which the vapor and air mixture lying just above its vaporizing surface is capable of supporting a momentarily flashing propagation of a flame when prompted by a quick sweep of a small gas flame pilot near the surface. It is expected that the flash point is somehow related to the minimum temperature, T_L , for piloted ignition indicated in Figure 2-8.1(b).

The *fire point* of a liquid fuel is very similar in definition to the flash point, except that the flame does not merely flash and cease but must also be self-sustained, so as to continue burning the liquid.

The *autoignition temperature*, T_a , of a vapor (or gas) and air mixture is the minimum temperature at which the mixture is self-igniting.

Another property relevant in interpreting the significance of flash point is the *lean limit of flammability*, defined as the lowest *volume* percentage of fuel vapor (or gas) in the mixture with air (or oxygen) that will support propagation of a flame away from a pilot ignition source.

Example Data

The most extensive flash point and fire point data sources are the *International Critical Tables*⁵ and the *Loss Prevention Handbook*.⁶ Tables 2-8.1, 2-8.2, and 2-8.3 are excerpted from these two sources to note the typical values and to make several important observations.

Table 2-8.1 shows the flash points of a number of liquids in air measured by various test methods to indicate that the measurements depend quite strongly upon the

apparatus employed. Although, as expected, the closed-cup tests (e.g., Pensky-Martens) produce flashing at a lower temperature than the open-cup tests (e.g., Cleveland). Other differences are neither small nor systematic.

Table 2-8.2 gives open- and closed-cup flash and fire points for a number of real-world combustibles of varying specific gravity. Two points are noteworthy: the fire point consistently exceeds the flash point by about 20 to 40°C, and heavier fuels tend to have higher flash points. Recalling that a higher flash point implies a lower saturation pressure and, hence, a lower volatility, this second observation is reasonable.

Table 2-8.3, adapted from *ICT*,⁵ shows the closed-cup flash points as well as the minimum autoignition temperatures for a number of real liquids. The decrease in T_a due to high pressure is noteworthy.

Table 2-8.4, is a comprehensive collection of the flash points, lean limits, and autoignition temperatures for a host of liquid fuels in air at a nominal pressure of 1 atm. A number of other properties, useful in the following section, are also included. Besides serving as a practical reference dictionary, Table 2-8.4 also indicates a number of trends that are often vague or weak. Most of these trends are conceptually unsubstantiated to date. For example, in a given family of fuels, an increase in fuel molecular weight generally (but not always) indicates (1) a marked increase in the normal boiling point T_b^o , (2) a slight decrease in the normal enthalpy of vaporization h_{fg}^o , (3) an apparent increase in the flash point T_F^o , (4) a modest and erratic decrease in the lean limit ℓ , and (5) a noticeable decrease in the minimum temperature for autoignition, T_a .

Table 2-8.1 Flash Points of Several Combustible Liquids Measured by Several Different Tests in Air

	Flash Point (°C) as Measured in						
	Abel	Tagliabue	Elliot	Pensky-Martens	Cleveland	Luchaire	Open Cup
Naphtha	34.4	39.4	36.4	40.6	46.1	50.0	
Kerosene	52.8	54.4	53.3	57.2	60.0	58.9	
Petrolite	61.1	59.4	60.0	65.6	68.3	62.2	
Gas oil				90.6	93.3	92.2	
300 oil				123.9	129.4	130.0	
Straw oil				157.2	162.8	161.1	
Engine oil				221.1	226.7	221.1	
Heavy oil				265.6	293.3	265.5	
Mexican crude				19.0			35.0
Petrol				26.5			33.5
Tar oil				87.0			92.5

Source: Excerpted from the *International Critical Tables*⁵

Theory and Discussion

Theoretical models are required in order to substantiate and understand these and other trends that may lie buried in elaborate data. The mechanisms culminating in the global effects of flashing and autoignition also elicit the way in which the measured properties depend on the apparatus used and the testing procedure followed. However, the physics and chemistry involved in open- or closed-cup flash point and autoignition testers is much too complicated, with numerous interacting thermodynamic, fluid mechanical, heat and mass transport, and chemical kinetic processes. Complete mathematical models capable of predicting the outcome of a specific test do not exist and are nearly impossible. Simple syntheses of the essential physical and chemical processes of the tests, are not only possible but enlightening.

Flash Point and Lean Flammability Limit

In principle, the problem involves transient analysis of heat and mass transfer with oxidative reactions in the gas phase lying above the liquid surface. In cup tests, the boundaries of the three-dimensional space of interest are the vaporizing liquid surface at the bottom, the open or closed top, and the side walls, which are probably cylindrical and therefore impervious to mass but conductive to heat. (The flash points and autoignition temperatures measured in cups or flasks whose walls are highly conductive are known to be higher.) If the cup were open, airflow and drafts in the room would be expected to alter the heat and mass transport processes of concern, and hence, the measurement. A closed cup minimizes these alterations by allowing air to stealthily leak into the region of interest.

Table 2-8.2 Flash and Fire Points of Some Hydrocarbon Liquids in Air

Liquid	Flash Point (°C)	Fire Point (°C)	Specific Gravity
Fuel oil ^a	133	164	0.921
Crude ^a	125	155	0.923
Light fuel ^a	187	220	0.900
Black oil ^a	144	172	0.928
Refined oil ^a	122	135	0.904
Texas solar oil ^a	92	97	0.862
Shale oil ^a	130	150	0.862
Gas oil ^a	90	109	1.067
Neutral oils ^a	135	163	0.843
	216	252	0.878
Paraffin oils ^a	163	193	0.870
	216	254	0.912
Paraffin oil ^b	98	112	0.916
Naphthalene base oil ^a	196	227	0.937
Diesel fuel ^b			
Russia	53–138	78–180	0.876–0.950
N. America	82–166	103–200	0.865–0.950
India	92–150	120–174	0.890–0.950
Tar oil for diesels ^b			
Coke oven	90–135	108–166	1.14–1.18
Water gas	34–91	50–155	0.97–1.13
Oil gas	18–69	20–89	1.05–1.07
Coal tar oil	66–121	84–160	1.00–1.11

^a = Open cup^b = Pensky closed cupSource: Extracted from the *International Critical Tables*⁵**Table 2-8.3 Autoignition Temperatures at Two Pressures and Closed-Cup Flash Points for a Number of Liquid Fuels in Air**

Fuel	Flash Point (K)	Autoignition Temp. T_a (K)	
		$P^\circ = 1 \text{ atm}$	$P^\circ = 33 \text{ atm}$
Sperm oil	509	581	413
Lard oil	513	546	417
Castor oil	536	598	426
Glycerine	—	685	478
Kerosene	328	528	448
Spindle oil	467	521	451
Turbine oils	—	—	526–564
Compressor oil, A	—	582	461
Compressor oil, B	469	546	460
Compressor oil, C	489	559	430

Source: Adapted from the *International Critical Tables*⁵

Table 2-8.4 (Continued)

Fuel	Formula	Weight (kg/kmol)	T_b° (K)	h_{fg}° (kJ/kg)	h_c (MJ/kg)	T_k° (K)		Fl. Limits by Vol.		T_a° (K)	h_{fg}°/RT_b°
						Closed	Open	Lean	Rich		
<i>Carbonyls:</i>											
Formaldehyde	CH ₂ O	30	370	826	18.7	366	—	0.070	0.73	703	8.05
37% in H ₂ O	—	—	370 ^a	826 ^a	—	327	366	0.070 ^a	—	697	8.05
Acetaldehyde	C ₂ H ₄ O	44	294	570	25.1	235	—	0.040	0.570	477	10.26
Allyl alcohol	C ₃ H ₆ O	58	368	684	31.9	294	297	0.025	0.180	651	12.93
<i>i</i> -Butyraldehyde	C ₄ H ₈ O	72	334	444 ^a	33.8	233	249	0.025	—	503	11.51
Crotonaldehyde	C ₄ H ₆ O	70	375	490 ^a	34.8	286	—	0.021	0.155	505	11.00
Diethyl Acetaldehyde	C ₄ H ₁₂ O	76	391	500 ^a	—	294	—	—	—	—	11.70
Ethyl Hexaldehyde	C ₈ H ₁₆ O	128	436	325 ^a	39.4	—	325	—	—	—	11.48
Paraldehyde	C ₆ H ₁₂ O ₃	132	397	328	—	290	309	0.013	—	511	13.11
Salicyl aldehyde	C ₇ H ₆ O ₂	122	469s	396	—	351	—	—	—	—	12.39
Benzaldehyde	C ₇ H ₆ O	106	452	362	—	337	347	—	—	465	10.21
<i>Ketones:</i>											
Acetone	C ₃ H ₆ O	58	329	521	29.1	255	264	0.026	0.128	738	11.05
2-Butanone	C ₄ H ₈ O	72	353	443	33.8	271	274	0.018	0.095	677	10.87
Diethyl ketone	C ₅ H ₁₀ O	86	374	380	33.7	—	286	—	—	723	10.51
Methyl <i>i</i> -Butyl ketone	C ₆ H ₁₂ O	100	389	345 ^a	35.2	296	297	0.014	0.076	806	10.66
Dipropyl ketone	C ₇ H ₁₄ O	114	417	317	38.6	—	—	—	—	806	10.42
Methyl <i>n</i> -Propyl ketone	C ₅ H ₁₀ O	86	375	376 ^a	33.7	280	289	0.015	0.082	613	10.37
Methyl vinyl ketone	C ₄ H ₆ O	70	354	440 ^a	—	266 ^a	—	—	—	—	10.46
<i>Acids:</i>											
Formic acid	CH ₂ O ₂	46	374	502	5.7	342	—	—	—	813	7.42
Acetic acid	C ₂ H ₄ O ₂	60	391	405	14.6	313	330	0.054	—	737	7.48
Benzoic acid	C ₇ H ₆ O ₂	122	523s	270 ^a	24.4	394	—	—	—	843	7.58
<i>Miscellany:</i>											
Camphor	C ₁₀ H ₁₆ O	152	477s	265 ^a	38.8	339	366	0.006	0.035	739	10.16
Carbon disulfide	CS ₂	76	320s	—	13.6	303	—	0.013	0.500	398	—
<i>m</i> -Creosol	C ₇ H ₈ O	108	476	—	34.6	359	—	0.011	—	832	—
<i>o</i> -Creosol	—	464	—	34.1	354	—	0.013	—	872	—	
<i>p</i> -Creosol	—	475	—	34.1	359	—	0.010	—	832	—	
Furan	C ₄ H ₄ O	68	304	399	—	238	—	0.023	0.143	—	10.73
Pyridine	C ₅ H ₅ N	79	387	449	35.0	293	—	0.018	0.124	755	11.02
Aniline	C ₆ H ₇ N	93	456	434	36.5	349	364	0.013	—	890	10.64
Acetal	C ₆ H ₁₄ O ₂	118	376	277	31.8	252	—	0.016	0.104	503	10.46
<i>p</i> -Cymene	C ₁₀ H ₁₄	134	449	283	43.9	320	336	0.007	0.056	709	10.16
<i>o</i> -Dichloro Benzene	C ₆ H ₄ Cl ₂	146	453	—	19.3	339	347	0.022	0.092	921	—
1.1-Dichloro Ethylene	C ₂ H ₂ Cl ₂	96	310	—	—	—	263	0.056	0.114	733	—
1.2-Dichloro Ethylene	—	334	—	—	—	279	—	0.097	0.128	—	—
Monochloro Benzene	C ₆ H ₅ Cl	112	405	—	—	305	311	0.018	—	947	—
Resorcinol	C ₆ H ₆ O ₂	110	549	—	26.0	400	—	0.014	—	881	—
Ethylformate	C ₃ H ₆ O ₂	74	327	—	22.5	253	261	0.027	0.164	728	—
EthylAcetate	C ₄ H ₈ O ₂	88	350	—	25.9	269	272	0.022	0.114	700	—
Methyl Propionate	C ₄ H ₈ O ₃	104	353	—	22.2	271	—	0.024	0.130	742	—
Acrolein	C ₃ H ₄ O	56	326	—	29.1	—	247	0.028	0.310	508	—
Acrylonitrile	C ₃ H ₃ N	53	350	—	24.5	—	273	0.030	0.170	754	—
<i>n</i> -Amyl Acetate	C ₇ H ₁₄ O ₂	130	422	—	33.5	297	300	0.011	0.075	633	—
1-Amyl Acetate	—	416	—	—	298	311	0.010	0.075	652	—	
1,3-Butadiene	C ₄ H ₆	54	269	—	—	197	—	0.020	0.115	693	—
<i>n</i> -Butyl Acetate	C ₆ H ₁₂ O ₂	116	400	—	30.0	295	305	0.014	0.076	694	—
<i>n</i> -Butyl Ether	C ₈ H ₁₈ O	130	414	—	39.7	298	311	0.015	—	467	—
Dimethyl Ether	C ₂ H ₆ O	46	249	—	31.6	232	—	0.034	0.267	623	—
Divinyl Ether	C ₄ H ₄ O	70	312	—	—	243 ^a	—	0.017	0.270	633	—
Diethyl Ether	C ₄ H ₁₀ O	74	308	—	37.4	228	—	0.019	0.365	433	—
Gasoline ~	—	—	306	—	44.1	228	—	0.014	0.068	644 ^a	—
Naptha ~	—	—	450	—	—	314	—	0.008	0.050	519	—
Petroleum Ether	—	—	351	—	—	255	—	0.014	0.059	561	—

^aEstimate; ~ approximate line; — unavailable; R = \bar{R}/M ; $\bar{R} = 8.314 \text{ kJ/kmol K}$.

If the vapor were to be released at a constant rate at the hot liquid surface, beginning with time, t , equal to zero, it would transiently diffuse in the vertical direction, leading to a concentration profile* with the highest vapor concentration at the fuel surface and the least at the mouth of the cup. In the initial stages, the concentration everywhere is too low to support a flame. As time progresses, however, the temperature of the gas mixture near the surface rises beyond the minimum temperature limit T_L . (See Figure 2-8.1.) Equally important, the vapor concentration also increases to, and beyond, the lean limit. Later still, the thickness of the mixture layer that is beyond the lean limit increases due to diffusion. (If a pilot source were presented to this layer, a propagable flame could be generated. Thus, it is evident that the location and time at which a pilot is introduced are important in a test seeking the conditions of a propagable flame.) With continued time, the mixture at the surface becomes much too fuel-rich (oxygen-poor) to permit generation of a propagable flame with a pilot source. After longer periods of time, the spatial belt containing mixtures between the lean and rich limits broadens and propagates away from the surface.

This description of transient diffusion of vapor issued at a constant rate at the surface also holds, qualitatively, to a situation of a temporally variable vapor release rate, as in a typical flash point test.

As pointed out by Burgoyne and Williams-Leir⁹ and Kanury,¹⁰ the vapor release boundary condition is quite crucial in the flash point phenomenon. For a flame to flash over the surface of liquid fuel when presented with an ignition source, the vapor and air mixture (at the location and instant of the ignition source) has to contain sufficient fuel to be above the lean limit of flammability, ℓ . The partial pressure of the vapor in the mixture at the liquid surface is approximately equal to the saturation pressure, P_{vs} , of the fuel at the surface temperature, T . The error associated with the assumption of thermodynamic equilibrium (at the surface across which mass transfer occurs at a nonnegligible rate) is known to be quite small. The $P_v(T)$ relation is given by the integrated form of the well-known¹¹ Clausius-Clapeyron equation of state[†]

$$\frac{P_{vs}}{P^\circ} = \exp \left[\left(\frac{h_{fg}^\circ}{RT^\circ} \right) \left(1 - \frac{T^\circ}{T_s} \right) \right] \quad (1)$$

*The steady-state, one-dimensional diffusion version of this problem is known as the *Stefan problem* and can be found in Bird, Stewart, and Lightfoot.¹²

[†]With its genesis in the Maxwell relation $(\partial P / \partial T)_v = (\partial s / \partial v)_T$, Equation 1 arises from the facts: (1) equilibrium evaporation is a reversible process of constant pressure and temperature; (2) the heat addition in a constant temperature reversible process is equal to $T\Delta s$; and (3) the constant pressure heat addition is equal to Δh ; and the assumptions: (1) the enthalpy change associated with the change of phase from saturated liquid to saturated vapor is independent of temperature so that $\Delta h = h_{fg}^\circ$, a constant; (2) the vapor volume far exceeds the liquid volume; and (3) the vapor behaves nearly as an ideal gas. The basic constraint of equilibrium, of course, is the equality of Gibbs' free energy of the saturated liquid and that of the saturated vapor.

where T° and P° are reference temperature and pressure. The subscript s denotes the surface. When T° is equal to the normal boiling point temperature, T_b° , of the liquid, the reference vapor pressure, P° , will become equal to the atmospheric total pressure. Equation 1 is generally written in the form $\ln P_{vs} = -\alpha/T_s + \beta$, where $\alpha \equiv h_{fg}^\circ/R$ and $\beta \equiv \ln P^\circ + \alpha/T^\circ$ are constants of the liquid. The CRC Handbook of Physics and Chemistry⁷ gives extensive $P_v(T)$ tabulations for hundreds of liquids.

For many nonpolar liquids, the molar specific entropy of vaporization is found to be a universal constant, a consequence of the observed invariance of the ratio of normal boiling point to the critical temperature, so that

$$\frac{h_{fg}^\circ}{RT_b^\circ} \approx \text{a constant} = 10.18$$

Known as *Trotton's rule*,¹³ this powerful relation enables one to estimate the normal enthalpy of vaporization h_{fg}° from a knowledge of the normal boiling point T_b° and the liquid molecular^{*} weight, M . The last column of Table 2-8.4 indicates the validity of Trotton's rule; in general, Trotton's constant is larger than 10.18 for alcohols and smaller for acids.

Due to noninfinite diffusion effects, the molar (or volume) fraction, $X_v = P_v/P^\circ$, of fuel vapor at stations away from the surface will be smaller than that at the surface, given by Equation 1. The solution of the diffusion equation, with Equation 1 serving as one of the boundary conditions, gives the following distribution. With y denoting the distance in the gas phase from, and normal to, the surface and t denoting time, let $g(y, t)$ be a distribution solution such that

$$\frac{P_v(y, t)}{P^\circ} = g(y, t) \frac{P_{vs}}{P^\circ} \quad (2)$$

The function $g(y, t)$ is dimensionless and smaller than unity in magnitude.

Suppose that a large enough pilot source is introduced at a height, y_p , and time, t_p . Recalling the definition of the lean limit, ℓ , the flame would then flash if the local instantaneous mole fraction, $P_v(y_p, t_p)/P^\circ$, is even marginally in excess of the lean limit, ℓ . Thus, the flash point and the lean limit are related by

$$g(y_p, t_p) \exp \left[\left(\frac{h_{fg}^\circ}{RT^\circ} \right) \left(1 - \frac{T^\circ}{T_F} \right) \right] \geq \ell \quad (3)$$

Taking the total pressure to be 1 atm, $T^\circ = T_b^\circ$, the normal boiling point. We denote the flash point in 1 atm air by T_F° . The inequality sign in this equation is quite close to an equality. Noting that g and ℓ are smaller than unity, Equation 2 can be rewritten as

$$\ln \left(\frac{1}{\ell} \right) \approx \left(\frac{h_{fg}^\circ}{RT_b^\circ} \right) \left(\frac{T_b^\circ}{T_F^\circ} - 1 \right) + \ln \frac{1}{g(y_p, t_p)} \quad (4)$$

^{*}Recall that the gas constant R is related to the universal gas constant $\bar{R} = 8.314 \text{ (kJ/kmol K)}$ through the molecular weight $M \text{ (kg/kmol)}$ by $R = \bar{R}/M \text{ (kJ/kg K)}$.

The following comments can be made of Equation 4:

1. The lean limit of flammability, ℓ , as listed in the literature and in Table 2-8.4, is itself an apparatus-dependent property. The most notable factor influencing it is gravity (causing buoyancy in the limit mixtures and inhomogeneity of the fuel-air mixture). The approximate equality sign in Equation 4 is meant to highlight this point.
2. Most of the flash point data seldom point out explicitly that they have been determined in air and nominally at 1 atm total pressure.
3. If the ambient total pressure, P° , is higher than 1 atm, the flash point is expected to be higher also. A plot of $\ln P^\circ$ versus $1/T_F^\circ$ is known to be a straight line, apparently parallel to the boiling point line for the same liquid. Thus, correction for the flash point dependency on pressure can be made the same way as for the boiling point dependency. Leslie and Geniesse refer in *ICT*⁵ (p. 161) to a method by which the flash point is calculated as the temperature at which the liquid's vapor pressure is equal to P°/kN , where P° is the total pressure, N is the number of moles of oxygen stoichiometrically required for complete combustion of 1 mole of the liquid, and k is an apparatus constant of about 8. The stoichiometry ratio, N , apparently is introduced through the lean limit, ℓ .
4. The question of the dependency of lean limit on whether the ambient gas is normal air or pure oxygen is a complicated one. If the oxygen/fuel ratio at the lean limit is assumed to be the same for both cases, then ℓ is expected to be numerically larger in pure oxygen than in air. Lewis and von Elbe⁸ report a few values to confirm this expectation. A consensus exists in combustion literature that the percent of fuel in the limit mixtures is, more or less, independent of the presence of nitrogen. This, too, leads to a larger value of ℓ in pure oxygen than in air. Both these arguments, coupled with Equation 4, lead to the conclusion that the flash point of a liquid will be higher (and closer to the boiling point) in pure oxygen than in air.

This conclusion is, however, contrary to common sense. Ignition is expected to occur more easily in the absence of the impeding inert nitrogen. Experience indicates that in pure oxygen atmospheres, the minimum ignition energies of combustible mixtures are lower, quenching distances are smaller, and flame temperatures and speeds are larger. Based on this experience, it is logical to surmise that the chemical kinetics of oxidation and thermochemistry underlying the concept of the lean limit are far more complex than mere mass conservation. The paper of Mullins¹⁴ on combustion in vitiated air and the tome of Lewis and von Elbe⁸ serve well as starting points for a much-needed research investigation into this important unresolved issue of limit mixtures.

5. When the cup is closed, the escape of the fuel vapor to the environment is prevented or minimized. Appearing as the second boundary condition in the diffusion equation, this results in a higher value of $g(y, t)$ at any location and time. For a given lean limit, Trouton's constant, and normal boiling point, Equation 4 indi-

cates that the observed flash point will be lower than if the cup were open.

6. The effects of the cup being open and the air being in a state of motion due to gravity or due to disturbance are in the direction of increasing the observed flash point, all due to reduced $g(y, t)$.
7. Burgoyne and Williams-Leir⁹ assume the dispersion function $g(y_p, t_p)$ to be unity to use a variant form of Equation 4 to predict the flash point from given ℓ , h_{fg}° , and T_b° .
8. Such a use of Equation 4 as a predictive tool is probably premature for several reasons. First, the transient convective-diffusion process underlying the g -function has a crucial role to play in determining T_F° . Second, even if one works out the solution to obtain $g(y, t)$, the flash point experiments do not clearly stipulate the $y = y_p$ and $t = t_p$ values; that is, they do not state the time and location at which the pilot is introduced. Thus, the estimates of $g(y_p, t_p)$ require subjective judgments. Last, as discussed in item 4, the lean limit, ℓ , is still an empirical extrinsic parameter whose dependence on fundamental properties of the system is not quantitatively known.

Notwithstanding these reasons, by merely noting that the last term in Equation 4 is always positive, one concludes that

$$\ln\left(\frac{1}{\ell}\right) \geq \left(\frac{h_{fg}^\circ}{RT_b^\circ}\right)\left(\frac{T_b^\circ}{T_F^\circ} - 1\right)$$

A plot of $\ln(1/\ell)$ on the y -axis and $(T_b^\circ/T_F^\circ - 1)$ on the x -axis should then yield all experimental points lying above a straight line of slope $(h_{fg}^\circ/RT_b^\circ) \approx 10.18$ and intercept zero. Figure 2-8.2 shows most of the data of Table 2-8.4 thus plotted. It is obvious that the hypothesis underlying Equation 4 bears merit. The general trend of data (especially for each family of fuels) indicates that Trouton's constant (or a like one) holds to describe the slope. The intercept, expected to be zero if diffusional effects are absent, indicates that $g(y_p, t_p)$ lies in the approximate range of 0.07 to 0.25, substantially smaller than unity, indicating the need for consideration of diffusion.

9. All through this discussion energy conservation has not been considered, although it may be important.

Autoignition Temperature

Whereas the piloted ignition in flash point tests involves a localized initiation of the flame and observation to see if it would propagate away from the ignitor, the autoignition is a self-induced initiation of the flame in a relatively larger volume of the reacting gases. As such, the autoignition is perhaps amenable to an easier description than the forced ignition. At the outset, it should be noted that the autoignition process pertains to the vapor (or gas) and air mixture, irrespective of the source of the vapor or gas. Figure 2-8.1, part (b), indicates that by the time the autoignition process becomes evident, the liquid fuel will be vaporizing vigorously and even boiling.

Consider the oxidation reaction in a vessel of known geometry. The initial temperature and mixture composition

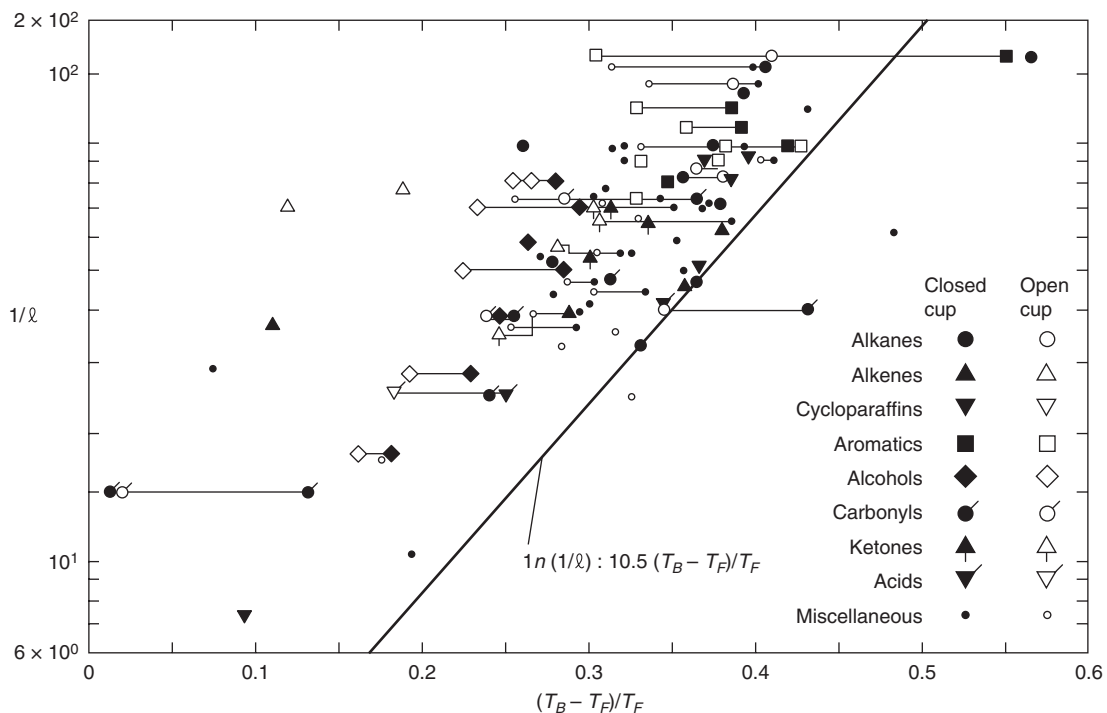


Figure 2-8.2. A relation between the lean limit, flash point, and boiling point.¹⁰

are usually known. The mechanism of heat exchange between the reactive medium and the vessel walls constitutes the most important of the boundary conditions. Although the oxidation mechanism is probably composed of a complex set of elementary reaction steps, a global rate law for the fuel consumption rate generally suffices.

$$-\dot{W}_A''' = k_0 Y_A^n Y_B^m \exp\left(\frac{-E}{RT}\right) \quad (5)$$

The quantity on the left side of Equation 5 is fuel consumption rate in kg/m³.s. The empirical kinetic constants k_0 , n , m , and E are, respectively, the collision factor, orders with respect to the fuel (A) and oxygen (B), and activation energy (kJ/kmol). In principle, then, the equations of conservation of mass, momentum, energy, and species can be solved to obtain the transient fields of velocity, temperature, and composition. According to thermal theory,^{15,16} ignition is inferred to have occurred at the instant when the temperature (usually, in the middle of the reactor) increases rapidly. Known as *thermal runaway*, this event also marks the onset of a rapid decrease in the reactant mass fractions, Y_A and Y_B . If the reactant consumption in the preignition period is ignored, then the autoignition is called a *thermal explosion*.

Solutions are available in the literature for this problem, with and without reactant depletion, for a number of geometries of the reactant mass and of boundary conditions. When the reactant depletion is ignored, the species equations become unnecessary. The convective mixing in gaseous mixtures is usually taken into account by defining an effective, augmented, thermal conductivity so as to obviate the momentum conservation and reduce the problem to one involving merely transient, reactive con-

duction. By considering the effective conductivity to be large (due to good mixing) and the heat loss from the reacting mixture to the vessel boundaries to be by convection, Semenov¹⁵ solves the resultant transient, uniform reaction problem to predict thermal runaway conditions as

$$\frac{E(T_a - T_w)}{RT_w^2} = 1 \quad (6)$$

$$Da_0 \equiv \frac{[h_c V(-\dot{W}_A''')_0]}{[hS(T_a - T_w)]} \geq 1/e$$

where

T_a = (critical) temperature of the reactive mass at the instant of explosion (see Figure 2-8.1)

T_w = vessel wall temperature

h_c = enthalpy of combustion (kJ/kg fuel)

h = heat transfer coefficient between the mixture and the walls (kW/m² K)

V/S = volume-to-surface ratio of the reactive mass

$(-\dot{W}_A''')_0$ = reaction rate given by Equation 5 at the initial conditions $T = T_0$, $Y_A = Y_{A0}$, and $Y_B = T_{B0}$

e = Naperian constant

Two points are immediately notable from Equation 6. First, the critical temperature T_a is quite close to T_w , since RT_w^2/E is, generally, quite small. Thus, $T_a \approx T_w$. Second, due to the mixture being well mixed, the precise geometry of the reacting body is irrelevant; its V to S ratio suffices; $V/S = a/(j + 1)$, where $j = 0, 1$, and 2 , respectively, for an infinite plane slab geometry of thickness, $2a$, for an

infinitely long cylinder of diameter, $2a$, and a sphere of diameter, $2a$. Other implications of Equation 6 will be discussed later.

Frank-Kamenetskii¹⁶ solves the problem by assuming that the effective conductivity, K , is small and seeks the conditions under which steady-state solutions are impossible. Thermal runaway is found to occur pursuant to the following critical conditions:

$$\frac{E(T_a - T_w)}{\bar{R}T_w^2} \quad j = 0 \quad j = 1 \quad j = 2 \\ 1.20 \quad 1.37 \quad 1.60 \quad (7)$$

$$Da_\infty \equiv \frac{a^3 h_c k_0 Y_{A0}^n Y_{B0}^m \exp(-E/\bar{R}T_w)}{a^2 K(T_a - T_w)/a} \quad 0.88 \quad 2.00 \quad 3.32$$

This solution, as does Equation 6, indicates that $(T_a - T_w) \approx \bar{R}T_w^2/E$ is small. Vessels with a geometry resulting in a larger surface-to-volume ratio (e.g., a sphere) exhibit a larger critical temperature, T_a .

The nondimensional parameters Da_0 and Da_∞ of Equations 6 and 7, respectively, are known as Damköhler numbers. A Damköhler number is the ratio of the characteristic rate of energy release due to chemical reaction to that of physical dissipation (by convection in the Semenov problem and by conduction in the Frank-Kamenetskii problem).

The Semenov problem corresponds to the zero Biot number limit, while the Frank-Kamenetskii problem deals with the infinite Biot number situation. The finite Biot number problem has been solved by Thomas¹⁷ and Kanury and Gandhi.¹⁸ (An excellent review of this subject is presented by Gray and Lee.¹⁹) Equations 6 and 7 can be seen to be in mutual agreement if one notes that the heat transfer coefficient, h , is linearly proportional to the ratio of gas conductivity, K , to the vessel half-size, a .

Even more importantly, the pressure dependency of the collision factor is given by

$$k_0 \equiv k'_0 M_A^{(1-n)} M_B^{-m} \left(\frac{PM}{\bar{R}T} \right)^{(n+m)} \quad (8)$$

where

k'_0 = function only of the molecular collisional nature of species A and B

M_A and M_B = molecular weights, respectively, of the fuel (A) and oxygen (B)

M = mean molecular weight of the mixture

P = total pressure of the reacting mixture

The Damköhler number, Da_∞ , from the criterion for explosion given by Equation 7 can then be recast to the form

$$Da_\infty \equiv \left(\frac{k'_0 \bar{R} M_B^{-m} M^{(n+m)} Y_{A0}^n Y_{B0}^m}{E^{(1+n+m)}} \right) \left(\frac{a^2 h_c P^{(n+m)} M_A^{1-n}}{K} f(T_a) \right) \quad (9)$$

where $f(T_a) \equiv [\exp(-E/\bar{R}T_a)]/(\bar{R}T_a/E)^4$. If the initial mixture composition (Y_{A0} , Y_{B0}) is kept fixed, the first bracketed quantity of Equation 9 is, more or less, a constant. For typical hydrocarbons reacting with air, $n \approx 0.5$,

$m \approx 1.5$, and $E/\bar{R} \approx 15,000$ K. The function $f(T_a)$ monotonically increases with $(\bar{R}T_a/E)$, as indicated in Figure 2-8.3. The second bracketed term of Equation 9 and the explosion criterion constant of Equation 7 thus give the influence of a , h_c , P , M_A , and K on the minimum temperature for autoignition, T_a . Specifically, it is clear that the autoignition temperature is lower if the vessel size is larger, heat of combustion is larger, pressure is higher, fuel molecular weight is larger, or the mixture conductivity is smaller. This predicted pressure dependency is in excellent quantitative agreement with the data in Table 2-8.3. The influence of molecular weight appears corroborated by the data in Table 2-8.4. Not so evident from Table 2-8.4 is the effect of the heat of combustion, mainly due to the relatively minor variance of h_c within a family of fuels.

Ignition Delay

The discussion so far has centered on the threshold conditions below which ignition is not possible (i.e., question 1 of the Introduction). So far as the flash point and fire point are concerned, a more detailed analysis is required to go further. Concerning autoignition, however, a few further steps can be taken related to question 2 of the Introduction. First, note that the critical temperature T_a from Equations 6, 7, and 9 and Table 2-8.4 is the minimum temperature of the mixture that can produce autoignition, but marginally. This marginality implies that time to ignition at T_a is infinite. Any temperature greater than T_a will result in ignition within a finite time. The larger the temperature, the sooner the ignition.

Furthermore, as indicated in Figure 2-8.1, there exist upper and lower composition limits to autoignition at any $T > T_a$. The most quickly ignitable mixture at any T

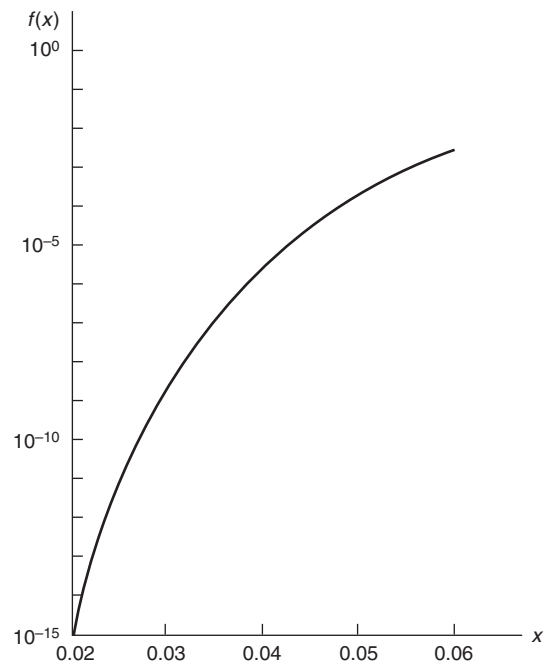


Figure 2-8.3. The monotonic nature of $f(x) = [\exp(-1/x)]/x^4$.

will perhaps be near stoichiometric in composition. Thus, energy balance on the reacting mixture leads to the approximate ignition delay, t_i , of

$$t_i \approx \frac{(pC_p)(T - T_0)}{h_c(-W''')_{\text{ref}}} \quad (10)$$

where (pC_p) is mixture volumetric heat capacity ($\text{kJ}/\text{m}^3 \text{K}$), T_0 is initial temperature of the mixture, and the reaction rate is estimated at the reference conditions of 0 for the Semenov (Biot number = 0) problem and w for the Frank-Kamenetskii (Biot number = ∞) problem. This rate also accounts for the mixture composition Y_{A0} and Y_{B0} . The Arrhenius dependency of the reaction rate on temperature makes the ignition delay, t_i , proportional to $\exp(-E/\bar{R}T_{\text{ref}})$. Thus, measurement of t_i at various T_{ref} values leads to determination of the activation energy, E . In the light of Equation 8, t_i will be approximately proportional to the inverse of the mixture pressure and to the square root of the molecular weight of the fuel. Since Da_0 and Da_{∞} are about unity, the denominator of Equation 10 is proportional to $K(T - T_w)/a^2$ so that ignition delay is longer for higher conductivity mixtures, if all else is kept fixed.

If the consumption of reactants in the preignition reactions is significant, the problem becomes more difficult. The outcome, however, is that reactant consumption makes the limit temperature, T_a , somewhat higher than the estimates from Equations 6, 7, and 9, and the ignition delay is longer than that given by Equation 10.

Concluding Remarks

The concepts of piloted ignition of liquid fuels and the spontaneous ignition of their vapors mixed with air are examined in this chapter. Starting with a physical description of the ignition process and definitions, a number of experimental techniques were alluded to, and typical data were presented. The empirical trends were shown to be consistent with the predictions based on simple mechanistic models.

Although the flash point concept is useful in rating the volatility and ease of ignition of a variety of liquid combustibles, it must be noted that many practical situations involve heating of the liquid by a heat flux imposed on the evaporating surface. The heating process itself might then become a major topic of study to estimate the liquid surface temperature before examining whether this temperature is above or below the flash point at a given instant.

Nomenclature

a	vessel half-size (m)
C_p	specific heat ($\text{kJ}/\text{kg}\cdot\text{K}$)
Da_0	Semenov's Damköhler number
Da_{∞}	Frank-Kamenetskii's Damköhler number
E	activation energy (kJ/kmol)
e	Naperian constant
g	dispersion function
h	heat transfer coefficient ($\text{W}/\text{m}^2\cdot\text{K}$)
h_c	enthalpy of combustion (kJ/kg)
h_{fg}^o	enthalpy of vaporization (kJ/kg)
j	geometry index
K	mixture thermal conductivity ($\text{W}/\text{m}\cdot\text{K}$)
k	apparatus constant
k_0	collision factor ($\text{kg}/\text{m}^3\cdot\text{s}$)
k'_0	collision parameter
ℓ	lean limit of flammability
M	molecular weight (unsubscripted for the mixture) (kg/kmol)
m	a reaction order
N	Stoichiometric molar O_2 /fuel ratio
n	reaction order
P	pressure (atm)
P°	total pressure (atm)
P_v	vapor pressure (atm)
R	gas constant ($\text{kJ}/\text{kg}\cdot\text{K}$)
\bar{R}	universal gas constant ($\text{kJ}/\text{kmol K}$)
S	surface area (m^2)
s	specific entropy ($\text{kJ}/\text{kg K}$)
T	temperature (K)
T_a	the least autoignition temperature (K)
T_b°	normal boiling point (K)
T_F°	flash point in air at 1 atm (K)
t	time (s)
V	volume (m^3)
v	specific volume (m^3/kg)
\dot{W}'''	reaction rate ($\text{kg}/\text{m}^3 \text{s}$)
Y	mass fraction
y	distance into gas phase from, and normal to, the vaporizing surface (m)

Greek

α	property constant (K)
β	property constant
ρ	density (kg/m^3)

Subscripts

A	fuel
a	autoignition
B	oxygen
b	boiling point
c	combustion
F	flash point
i	ignition
0	initial
p	pilot
s	liquid surface
v	vapor
w	vessel wall surface

References Cited

1. M.G. Zabetakis, *Bulletin No. 627*, U.S. Bureau of Mines, Pittsburgh, PA (1965).
2. ASTM, *Standard, Vol. 17, 20, and 22*, American Society for Testing and Materials, Philadelphia (1972).
3. B.P. Mullins, *Spontaneous Ignition of Liquid Fuels*, Butterworths, London (1955).
4. B.P. Mullins, in *Combustion Researches and Reviews*, Butterworths, London (1957).
5. *International Critical Tables of Numerical Data, Physics, Chemistry, and Technology*, McGraw-Hill, New York (1927).
6. Factory Mutual Research Corp., *Factory Mutual Handbook of Loss Prevention*, McGraw-Hill, New York (1967).
7. CRC *Handbook of Physics and Chemistry*, Chemical Rubber Co., Cleveland (1973).
8. B. Lewis and G. von Elbe, *Combustion, Flames and Explosions of Gases*, 3rd ed., Academic, New York (1987).
9. J.H. Burgoyne and G. Williams-Leir, *Fuel*, 28-7, p. 145 (1949).
10. A.M. Kanury, *Comb. Sci. and Tech.*, 31, p. 297 (1983).
11. W.C. Reynolds and H.C. Perkins, *Engineering Thermodynamics*, McGraw-Hill, New York (1977).
12. R.B. Bird, W.E. Stewart, and E.N. Lightfoot, *Transport Phenomena*, Wiley, New York (1960).
13. F. Daniels and R.A. Alberty, *Physical Chemistry*, Wiley, New York (1967).
14. B.P. Mullins, in *Selected Combustion Problems*, Butterworths, London (1954).
15. N. Semenov, *Chemical Kinetics and Chain Reactions*, Oxford, London (1935).
16. D.A. Frank-Kamenetskii, *Diffusion and Heat Exchange in Chemical Kinetics*, Princeton University, Princeton (1955).
17. P.H. Thomas, *Trans. Faraday Soc.*, 54, 421, p. 60 (1958).
18. A.M. Kanury and P.D. Gandhi, *Theory of Spontaneous Heating and Thermal Ignition: A Review*, unpublished manuscript (1989).
19. P. Gray and P.R. Lee, in *Oxidation and Combustion Reviews*, Elsevier, Amsterdam (1967).

SECTION TWO

CHAPTER 9

Smoldering Combustion

T. J. Ohlemiller

Introduction

Smoldering is a slow, low-temperature, flameless form of combustion, sustained by the heat evolved when oxygen directly attacks the surface of a condensed-phase fuel. Smoldering constitutes a serious fire hazard for two reasons. First, it typically yields a substantially higher conversion of a fuel to toxic compounds than does flaming (though this occurs more slowly). Second, smoldering provides a pathway to flaming that can be initiated by heat sources much too weak to directly produce a flame.

The term *smoldering* is sometimes inappropriately used to describe a non-flaming response of condensed-phase organic materials to an external heat flux. Any organic material, when subjected to a sufficient heat flux, will degrade, gasify, and give off smoke. There usually is little or no oxidation involved in this gasification process, and thus it is endothermic. This process is more appropriately referred to as forced pyrolysis, not smoldering.

A burning cigarette is a familiar example of true smoldering combustion. It is also one of the most common initiators of smoldering in other materials, especially upholstery and bedding.¹ A cigarette also has several characteristics common to most materials that smolder. The finely divided fuel particles provide a large surface area per unit mass of fuel, which facilitates the surface attack by oxygen. The permeable nature of the aggregate of fuel particles permits oxygen transport to the reaction site by diffusion and convection. At the same time, such particle aggregates typically form fairly effective thermal insulators that help slow heat losses, permitting sustained combustion despite low heat release rates.

The physical factors that favor smoldering must be complemented by chemical factors as well. Like virtually

all other cellulosic materials, tobacco in a cigarette, when degraded thermally, forms a char. A char is not a well-defined material, but typically it is considerably richer in carbon content than the original fuel; its surface area per unit mass is also enhanced. This char has a rather high heat of oxidation and is susceptible to rapid oxygen attack at moderate temperatures (≥ 670 K). The attack of oxygen (to form mainly carbon monoxide and carbon dioxide) is facilitated not only by the enhanced surface area but also by alkali metal impurities (present in virtually all cellulosic materials derived from plants) which catalyze the oxidation process.² Char oxidation is the principal heat source in most self-sustained smolder propagation processes; the potential for smoldering combustion thus exists with any material that forms a significant amount of char during thermal decomposition. (Char oxidation is not always the only heat source and it may not be involved at all in some cases of smolder initiation.)³

Various quantitative combinations of these physical and chemical factors can produce a material that will undergo sustained smoldering in some conditions. The enormous range of factors results in materials that will only smolder when formed into fuel aggregates many meters across, at one extreme, to materials that smolder when formed into aggregates only a few tens of microns across. Unfortunately, a theory that allows for the calculation of materials and conditions that are conducive to smoldering has been developed only for certain types of smolder initiation. (See Section 2, Chapter 10.) Conditions sufficient to yield smolder initiation, especially near an external heat source, are not necessarily sufficient to assure self-sustained smolder spread away from the initiation region. The potential transition of the smolder process into flaming combustion is even less correlated with factors determining smolder initiation.

This chapter is restricted to consideration of post-initiation behavior of smoldering. There are several models of smoldering combustion in the literature, but they are mostly numerical in nature, and do not shed much light on the practical aspects of the problem. Smolder

Dr. T. J. Ohlemiller is a member of the research staff of the National Institute of Standards and Technology, Building and Fire Research Laboratory. He has investigated a variety of solid fuel combustion problems, specializing in smoldering and the flammability of solid fuels.

modeling has been reviewed by Ohlemiller,⁴ but the reader should be aware that there has been substantial activity since that review. Readers wishing to pursue the literature on modeling of one-dimensional smolder propagation should refer to References 5–16. Two-dimensional propagation models can be found in References 17–20. Distinctive features peculiar to one- and two-dimensional smolder propagation modes are described later. Lacking any definitive theoretical description, this chapter is largely restricted to examining typical experimentally determined behavior. In this overview of smoldering, an attempt is made to convey some of the qualitative interplay of processes that determines overall behavior, together with specific experimental results.

Self-Sustained Smolder Propagation

The smolder initiation process is dominated by the kinetics of the oxidation of the solid. Subsequent propagation of smolder is controlled to a large degree, however, by the rate of oxygen transport to the reaction zone. The control via transport rate occurs because the heat evolved during smolder initiation raises the local temperature and thus the local reaction rate, until all of the neighboring oxygen is consumed. Subsequently, the reaction continues to consume oxygen as fast as it reaches the reaction zone, yielding a very low oxygen level locally, which limits the reaction rate.

The subsequent evolution of the smoldering zone away from the initiation region is heavily influenced by oxygen supply conditions. If initiation occurs deep within a layer of fine particles (sawdust, coal dust), for example, it will slowly work its way to the nearest free surface at a rate dictated by oxygen diffusion through the particle layer. (The more coarse and loosely packed the particles, the greater the influence of buoyant flow through the fuel leading to predominant upward spread.) When the smolder zone reaches the free surface region, it will spread more rapidly over this region in response to local convective and diffusive oxygen supply conditions. As will be seen, when smolder spread over the surface region of a fuel layer is forced by airflow, its response also depends on heat transfer considerations.

In examining self-sustained smolder propagation and its response to oxygen supply conditions, dimensionality is important. It is necessary to distinguish one-dimensional from multi-dimensional configurations. Further, it is necessary to discern whether the smolder zone is spreading in the same or opposite direction as the net movement of oxygen.

One-Dimensional Smolder Spread

One-dimensional smolder spread is an idealized situation that is sometimes approximated in real fires. For example, the spread outward or upward from deep in a layer of fuel particles approaches this one-dimensional limit when oxygen diffusion dominates convection and any curvature of the reaction front is small compared to the reaction zone thickness. In practice, this curvature requirement would likely be met by spread about 0.10 to

0.20 m away from the ignition source. One-dimensional smolder can be characterized by the direction of smolder propagation relative to the direction of oxygen flow—forward and reverse propagation.

Reverse propagation: When oxygen diffuses to the reaction zone from the outer surface of the fuel layer, through the unburned fuel and toward the reaction front, it is moving opposite to the direction of smolder propagation. Such a case of relative movement is called reverse smolder.

Palmer²¹ examined this diffusive reverse smolder case using layers of wood sawdust of various depths. The configuration was only roughly one-dimensional. Some of his results are shown in Figure 2-9.1. Note that the time scale is in hours. The time to smolder up through a layer 1-m deep is about two weeks, a surprisingly long time. Palmer

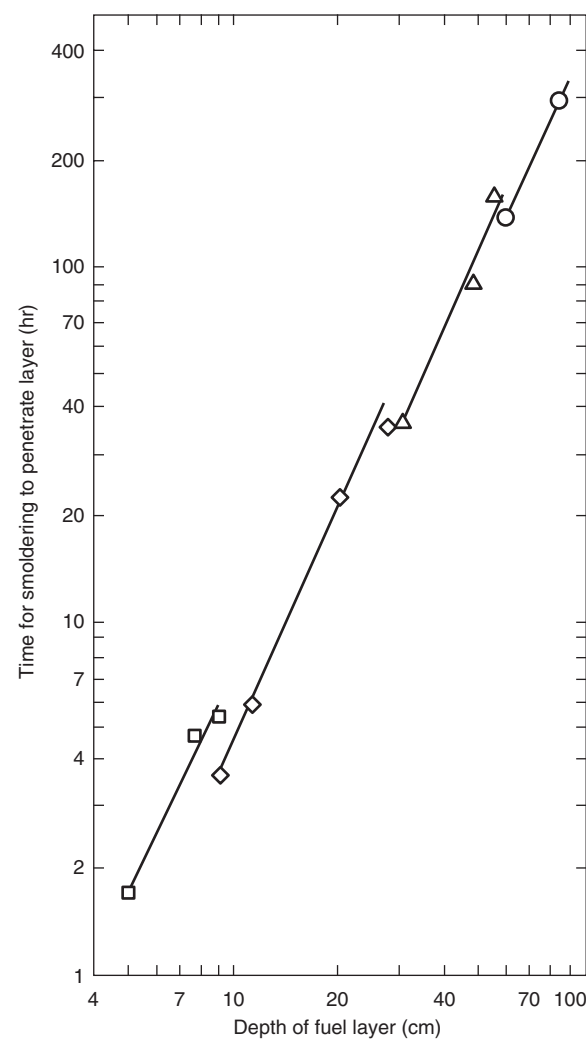


Figure 2-9.1. Smoldering upward from bottom within thick layers of mixed wood sawdust.²¹ Squares: initiating layer 0.025 m deep, 0.3-m square box; diamonds: initiating layer 0.052 m deep, 0.3-m square box; triangles: initiating layer 0.052 m deep, 0.6-m square box; circles: initiating layer 0.052 m deep, 0.9-m square box.

noted that in this configuration the smoldering process gave little hint of its presence until it was close to the surface of the fuel layer.

The slope in Figure 2-9.1 indicates that the time for smolder to penetrate a fuel layer in this mode is nearly proportional to the square of the layer depth.²¹ Palmer showed that a second power dependence on layer depth would be expected if it is assumed that the smolder reaction zone propagation velocity is proportional to the one-dimensional diffusion rate of oxygen from the surroundings, through the unburned fuel, to the reaction zone. This results in

$$t_L = AL^2 \quad (1)$$

where t_L is the time for the smolder zone to penetrate the layer of thickness, L ; and A is a constant that can, at present, only be determined by experimental measurement of at least one layer thickness.

This relation and Figure 2-9.1 imply that a 10-m fuel layer, such as might be encountered in a landfill or coal mine tailing pile, would require more than four years for smolder penetration. Such a deep layer is unlikely to be uniform in practice and the smolder front movement would be dominated by buoyant convective flow in regions of lesser flow resistance. However, this does illustrate how very slow some smolder processes can be.

A well-insulated reaction zone is a key factor in the existence of stable, self-sustaining smolder at such extremely low rates. The heat loss rate cannot exceed the heat generation rate. In this case, the same factor that is slowing the oxygen supply rate, and therefore the heat generation rate (i.e., the thick layer of wood particles over the reaction zone) is also slowing the heat loss rate.

In the previous example, the smolder propagation process is inherently unsteady because of the time-dependent oxygen supply process. If oxygen is instead continually supplied by a forced convective flow *through* the fuel layer, nearly steady propagation occurs. Such a configuration is encountered in some incinerators and coal burners but rarely in a smoldering fire. This configuration has been examined experimentally^{8,9,22} and modeled,^{5,6,8-12} and is a relatively well-understood smolder mode with underlying mechanisms qualitatively similar to the transient case just discussed.

In this mode of reverse smolder propagation, oxygen surrounds the fuel particles as they are heated by the advancing smolder reaction zone. Thermal degradation of some fuels in the presence of oxygen is exothermic. This exothermic degradation is particularly true of cellulosic materials and this heat can be sufficient to drive the smolder wave without any char oxidation.²² In flexible polyurethane foams, the presence of oxygen during degradation plays another key role. Without oxygen many foams do not form any char,²³ although char oxidation is a necessary source of heat for these materials. In the reverse smolder mode, the net oxidation rate and net heat release rate are again directly proportional to the oxygen supply rate. The smolder zone spreads to adjacent material as fast as this generated heat can be transferred and radiated to it. An increased oxygen supply rate causes a greater rate of heat release and increased peak

temperature in the reaction zone which, in turn, increases the heat transfer rate to adjacent fuel, thus accelerating the smolder spread rate. This sequence implies that the smolder reaction zone may well move through a layer of fuel without fully consuming the solid at any point. This unconsumed material, in fact, acts like an insulator for the reaction zone, increasing its stability. On the other hand, Dosanjh et al.,⁶ point out that this mode of smolder propagation can achieve a steady-state only if, as a minimum, the energy released is sufficient to heat the incoming air supply; otherwise it will extinguish.

Figure 2-9.2 shows measured reverse smolder velocities for several types of fuel as a function of airflow velocity through the fuel bed. The bulk densities of the fuel bed are all low but typical for these types of materials. Note that the airflow velocity range is also quite low, although higher flows are sufficient to move the fuel particles in the bed (i.e., an upward flow higher than approximately 0.01 to 0.02 m/s would fluidize the fuel bed).

Despite the considerable variation in the chemical nature of these fuels, the smolder velocity is always of order 10^{-4} m/s. For the same air supply rate, the smolder velocities do not vary much more than a factor of 2. This is consistent with the idea that the oxygen supply rate, not reaction kinetics, dominates the propagation process. (If the oxidizer flow rate is forced upward sufficiently in circumstances where bed fluidization is prevented, the smolder velocity begins to drop as cooling effects dominate. See Reference 8 for an example.) The differences with fuel nature that do exist mainly appear to reflect variations in available heat and effective thermal conductivity.

Only limited information is available on toxic gas production from this mode of smoldering. The molar percentage of carbon monoxide in the evolved gases has been examined for two of the fuels in Figure 2-9.2. For the flexible polyurethane foam, the carbon monoxide was 6 to 7 mole percent for an air velocity of 1.5×10^{-3} m/s. The flow rate dependency was not examined.²³ For the cellulosic insulation material,²⁴ the carbon monoxide mole fraction varied from about 10 to 22 percent from the lowest to the highest air flow velocity in Figure 2-9.2. The mass flux of carbon monoxide from such a smoldering process (grams of CO/m² of smolder front/second) then is estimated as follows:

$$Y_{CO}(\dot{m}_{air} + \dot{m}_{GS}) \quad (2)$$

or

$$Y_{CO}[\rho_{air} v_{air} + (1 - \phi)\Delta\rho_s v_s] \quad (3)$$

Here Y_{CO} is the mass fraction of carbon monoxide in the evolved product gases (approximately equal to the mole fraction); \dot{m}_{air} is the mass flux of air entering the smolder zone; \dot{m}_{GS} is the mass flux of gaseous material evolved from the solid fuel; ρ_{air} is the density of the air at the point where its velocity, v_{air} , is measured; ϕ is the initial void fraction of the fuel bed; $\Delta\rho_s$ is the change in density of the fuel bed (for reverse smolder, typically 65 to 95 percent of the original mass is gasified); and v_s is the smolder front velocity.

Limited information is also available on the aerosol emitted by a reverse smolder source.²⁵ This is pertinent to

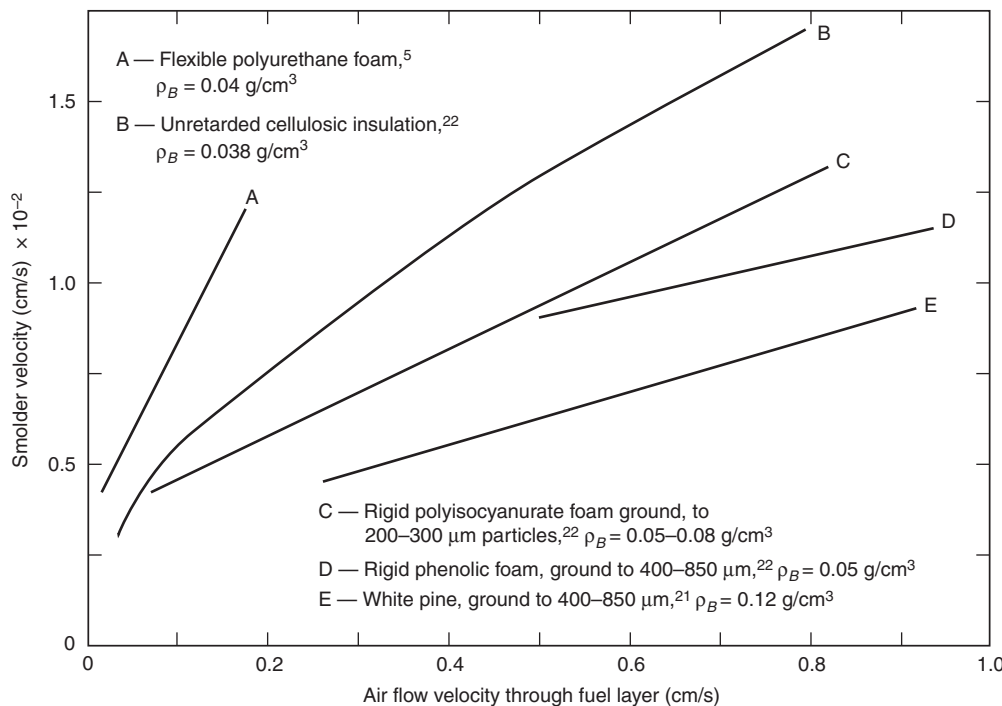


Figure 2-9.2. Smolder velocity versus airflow velocity into reaction zone for nearly one-dimensional reverse smolder. ρ_B is bulk density.

detection of a smoldering fire. The source studied was essentially identical to that used to obtain the data for curve B in Figure 2-9.2. The fuel again was an unretarded cellulosic insulation. The mass mean particle size of the aerosol was 2 to 3 μm ; this is about 5 times larger than cigarette smoke, and 50 to 200 times larger than the sooty particulate produced by flaming combustion. This large size explains the relatively poor sensitivity of ionization smoke detectors to realistic smolder sources. The residual solid left in the smolder wave and the original fuel both were found to be effective filters for this aerosol. This finding helps explain the observation by Palmer²¹ that smoldering in a thick layer of fuel was not detectable until it neared the surface exposed to the ambient atmosphere.

The rate of heat release for this mode of smolder can be estimated from the total mass flux of products and their heat content (gas temperature typically 670 to 970 K). The result is a few kW/m^2 of smolder front. This translates to a few hundredths of a kW for a reverse smolder source 0.1 to 0.15 m in diameter. The strength of the heat source has a bearing on the behavior of the buoyant plume. (See Section 2, Chapter 1.) Sources as weak as those considered here generate plumes that may not reach the ceiling of a room.²⁶

Forward propagation: The second limiting case of one-dimensional smolder propagation is called forward smolder. In this case the oxygen flow is in the same direction as the movement of the smolder front. The most familiar example (though not one-dimensional) of forward propagation is a cigarette during a draw. This limiting case is

encountered in some industrial combustion processes but is unlikely to be found in its pure, one-dimensional form in a fire context (some elements of this mode are encountered in realistic cases, however). An approximate model of this process (in one dimension) has been presented by Dosanjh and Pagni.⁷ They point out that this smolder mode will die out if the heat generated by char oxidation is insufficient to drive the drying and fuel pyrolysis reactions that precede char formation in the reaction zone. Other modeling studies of forward smolder propagation can be found in References 13–16. It is shown in Reference 14 that one-dimensional forward smolder is, in principle, capable of four differing modes of propagation depending on the oxygen concentration and supply rate. Two of these are limited by oxygen supply rate and two by reaction kinetics. Further experimental studies of forward smolder propagation through polyurethane foam can be found in References 27–28. A transient study of the requirements for the initiation of this smolder rate in polyurethane foam can be found in Reference 29.

Some characteristics of forward propagation are briefly mentioned here to describe the major effects that reversing the direction of oxygen flow can have on smolder propagation characteristics.

Forward and reverse smolder propagation have been compared experimentally.^{22,24} The fuel was an unretarded cellulosic insulation. Forward smolder through this same fuel at the same air supply rate is about ten times slower than reverse smolder. The carbon monoxide mole fraction is independent of air supply rate and is about 0.09. Forward smolder also allows for more complete combustion

of the fuel. These and other differences between the two smolder modes can be explained in terms of the differing wave structures.²²

An interesting aspect of a propagating, one-dimensional smolder wave is that the counterflowing materials (gas and solid, as viewed from the moving smolder front) form a system that retains the reaction heat and preheats the reactants with that heat.¹³ This effect implies that the internal peak temperature can rise above the adiabatic reaction temperature. In Reference 16 an expression is given for limiting temperature in the reaction wave for the case in which there is only a single, net exothermic reaction. Whether this feature of forward smolder plays a role in the potential for transition into flaming has not been explored.

Frandsen³⁰ investigated the downward propagation of smoldering in horizontal layers of peat as a model fuel for the complex duff layer found on the floor of a forest. No external flow was imposed. This is essentially a diffusion-driven forward smolder process forced to be one-dimensional in this study; it normally is multidimensional in character. The influence of both moisture and inorganic diluents on the limits of smolder propagation was measured. At extremes, it was found that this cellulosic fuel will just smolder when it contains 50 percent water by weight and no inorganic diluents. When dry, it will just smolder when the mix contains 80 percent inorganic diluents. These results should be roughly indicative of the limits for other cellulosic fuels in the absence of a cross-flow over the fuel layer.

Multi-Dimensional Smolder Spread

Factors such as ignition source geometry, fuel geometry, and the strong influence of buoyant flow on oxygen supply usually interact to assure that a smolder reaction zone has significant gradients of temperature and species in two or three dimensions. The number of possible configurations becomes virtually limitless. The practical configurations that have been studied are few and they are usually two-dimensional; they do shed some light on most cases likely to be of practical interest.

Horizontal fuel layer: The configuration that has been studied most extensively is two-dimensional smolder propagation in a uniform horizontal layer of particles or fibers. Ohlemiller examined the structure of the smolder zone³¹ in a thick (0.18-m) horizontal layer of cellulosic insulation in the absence of any forced airflow over the fuel layer. In these conditions, the flow induced by the buoyant plume rising above the smolder zone assures a constant supply of oxygen to the space above the layer. Oxygen penetrates the layer largely by diffusion.

If such a layer is ignited uniformly on one end, the smolder reaction zone soon evolves into a new shape dictated by oxygen supply rates.³¹ The uppermost elements of the reaction zone, being closest to the free surface, and hence, ambient air, spread away from the ignition source the fastest. Successively deeper elements spread in the same direction but more slowly. The result is a smolder reaction zone that (viewed in vertical cross section) slopes upward from the bottom of the layer to the top, in the direction of movement. The steady-state length of this in-

clined smolder front is roughly twice the depth of the original fuel layer. This inclined reaction zone is several centimeters thick, and across this thickness there is a smooth transition from unburned fuel to ash. On the ash side (the free surface adjacent to air) oxygen diffuses down and inward in the same direction as the smolder front is moving and attacks the charred fuel; this is analogous to forward smolder discussed earlier. On the unburned fuel side of the inclined smolder front, oxygen diffuses in from the region ahead of the front to react with the fuel as it is thermally degraded by heat conducted from the char oxidation region. Oxygen here is moving opposite to the direction of smolder propagation, so this aspect of the overall reaction zone is analogous to reverse smolder. Remember that in cellulosic materials, this oxidative/thermal degradation is exothermic. Thus the two-dimensional horizontal smolder zone incorporates features of both forward and reverse smolder and is driven forward by the combined heat release from char oxidation and oxidative/thermal degradation.

The participation of oxidative/thermal degradation in driving the smolder process requires that oxygen have free access to the thermal degradation region. For a low-permeability fuel such as solid wood, this is not the case. Even though solid wood has basically the same reaction chemistry as cellulosic insulation (which consists mostly of wood fibers) and smolders with a qualitatively similar inclined reaction zone, it must be driven solely by char oxidation.

The low permeability and corresponding high density of solid wood has another consequence with regard to smolder. The self-insulating quality of the reaction zone is much less than with a low-density layer of fuel particles or fibers. A single layer of wood will not sustain smolder unless it is subjected to an additional heat input of about 10 kW/m^2 .³⁶ This heat could come from some external radiant source or from another piece of smoldering wood that has an adequate radiative view factor with respect to the first piece.

In view of the strong role of oxygen supply rate in shaping the smolder process in a horizontal fuel layer, it is not surprising that smolder also accelerates in response to an increased oxygen supply rate produced by an airflow over the top of the smoldering layer. As with the one-dimensional propagation situation, two possibilities again exist: the airflow can travel in the same direction as the smolder front (again called forward smolder) or in the opposite direction (reverse smolder). Note, however, that now the actual fluxes of oxygen *within* the smoldering fuel bed may go in various directions. They are no longer constrained to being parallel to the smolder wave movement, as in the one-dimensional cases.

Palmer²¹ examined both of the flow direction possibilities for relatively thin horizontal layers (3×10^{-3} to $5.7 \times 10^{-2} \text{ m}$) of various cellulosic particles (cork, pine, beech, grass). Figure 2-9.3 shows some typical results. Note that the smolder velocities are less than or equal to those in Figure 2-9.2, despite the much higher air velocities. This is probably due to differing rates of actual oxygen delivery to the reaction zone, and to the fact that the near-surface region, which receives the best oxygen supply, is also subjected to the highest heat losses.

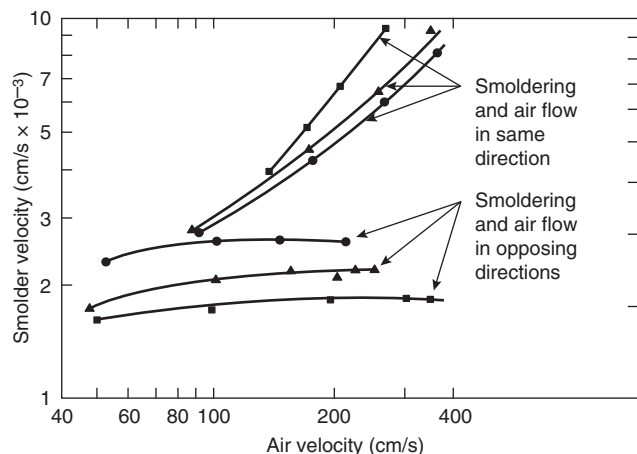


Figure 2-9.3. Dependence of smolder propagation rate through horizontal layers of beech sawdust on air velocity over top of layer.²¹ Circles: 120 μm mean particle size; triangles: 190 μm mean particle size; squares: 480 μm mean particle size.

The influence of two factors, fuel particle size and relative direction of airflow and smolder propagation is shown in Figure 2-9.3. Particle size has a relatively weak effect on smolder velocity but its effect depends on whether the smolder configuration is forward or reverse. The configuration itself (i.e., the relative direction of airflow and smolder propagation) has a much greater effect.

Ohlemiller³⁷ obtained comparable smolder velocities and dependence on configuration for 0.10- to 0.11-m thick layers of cellulosic insulation. It was found that the configuration dependence cannot be explained solely on the basis of oxygen supply rates. The mass transfer rate to the surface of the fuel bed was measured for forward and reverse configurations. It differed by only 20 to 30 percent (these differences were caused by changes in the bed shape due to shrinkage during smolder). It was pointed out that the observed dependence on relative direction of the airflow was consistent with there being a prominent role for convective heat transfer along the top surface of the fuel layer. This dependence occurs only if part of the smolder wave, that is, the region near the leading edge, is kinetically limited (and therefore highly temperature sensitive) rather than oxygen supply rate limited. This phenomenon explains the qualitative impact of both relative airflow direction and combustion retardants on smolder velocity. It also explains why forward smolder is faster than reverse smolder in the horizontal layer configuration, whereas the opposite was true for one-dimensional propagation. The role played by fuel particle size may be implicit in this view, but a quantitative model is not yet available.

In contrast to the monotonic enhancement of forward smolder velocity with increased airflow rate found by Palmer and by Ohlemiller, Sato and Seg³⁸ observed more complex behavior with thin (0.004 to 0.01-m) layers of a cellulosic mixture. Smolder velocity increased up to freestream air velocities of about 3 m/s and then re-

mained constant to the highest air velocity examined (6 m/s). This plateau correlated with erratic behavior at the leading edge of the smolder reaction zone involving both periodic extinctions and mechanical disruptions. These authors also examined the thermal structure of their forced smolder waves. The results were qualitatively similar to those of Ohlemiller for buoyant smolder,³¹ but the peak temperatures were appreciably higher due to the enhanced oxygen supply rates.

There is a minimum thickness below which a horizontal fuel layer will not undergo self-sustained smolder propagation. As the thickness of a fuel layer decreases, its surface-to-volume ratio increases (inversely with thickness to the first power). The ratio of the rate of heat loss to the rate of heat generation also varies in this manner so that ultimately the losses are overwhelming and extinction occurs. The exact thickness will depend on factors such as bulk density, fuel type and particle size, rate of oxygen supply, and so forth, influencing the heat generation per unit volume at a given thickness. The same considerations apply to other thin layers of fuel such as fabrics on upholstery and sheets of paper, wood, or particle board. Palmer²¹ found that the minimum depth for sustained smolder in still air increased linearly with particle size for beech, pine and cork. For cork this dependence ceased above 2 mm, apparently because more complete oxidation of the char stabilized the process in the layers of larger particles. For very small particles, (<100 μm), the minimum depth dropped as low as 1 mm for cork dust, while 0.01 m was typical of small particles of beech or pine sawdust. Ohlemiller and Rogers³⁹ found the minimum depth in still air for an unretarded cellulosic insulation to be 0.035 m; a heavy loading of the smolder retardant boric acid roughly doubled this value. Since the insulation has a very small effective particle size and essentially the same chemistry as Palmer's sawdusts, most of the difference in minimum depth (for the unretarded material) probably lies in the bulk density, which is about four to five times less for the insulation compared to the sawdusts (40 kg/m³ versus 180 kg/m³). Palmer found that the minimum depth dropped rapidly with increased airflow over the sawdust layers, in keeping with the idea that a greater rate of heat release per unit volume stabilizes the smolder process.

Beever^{32,40} has addressed a problem at the opposite extreme of layer thickness, that of underground fires in land fills, peat deposits, and mine tailings. These tend to be smoldering fires in roughly horizontal layers where the principal mode of oxygen access is from the top surface. Beever³² studied this process on a laboratory scale using mixtures of fine sawdust or charcoal with an inert diluent, that is, diatomaceous earth, in a trough that was insulated on the sides and bottom but open to quiescent air on the top. The trough was 0.13 m by 0.38 m in cross section and 0.14 m deep. A deeper trough was used in separate experiments in which pure layers of the inert diluent were placed atop the combustible layer. Local ignition near the top of a layer yielded steady propagation over a limited depth at rates that varied only weakly with inert content. However, while 25 percent fuel content yielded smolder spread, 10 percent fuel content did not. (Frandsen³⁰ diluted peat moss and Douglas Fir duff with

powdered silica in his downward smolder propagation studies. He found sustained smolder in dry material at up to 80 percent inorganic loading, but the allowable inorganic level decreased strongly as moisture level was increased.) The depth to which Beever's spreading smolder zone reached increased with the cross-sectional dimensions of the fuel bed. Material below this depth, having been heated and partially decomposed by the smoldering zone above, could itself subsequently propagate a second wave moving in the opposite direction. It was pointed out that such behavior can make it possible for a landfill or similar fire to spread under a barrier intended to stop it. Similarly, inert covering layers may simply slow but not stop such fires. The true key to stopping a smoldering fire is getting the heat out of the fuel, but this can prove to be extraordinarily difficult. Oxygen removal is insufficient unless it is sustained until the fuel cools to a point where oxygen readmission will not cause reignition. For a landfill fire, the cooling period can be impractically large.

The duff layer on a forest floor was mentioned previously. This porous layer of decaying organic material is frequently ignited to smoldering by the passage of a forest fire. Smoldering in this layer is highly spatially irregular in extent. In addition to posing a threat of reignition of a flaming fire, this smoldering also has broad implications about the viability of dormant seeds and forest regeneration. This subject is reviewed in Reference 41.

Smolder propagation data on a few other fuels (including some that are inorganic) in horizontal layers can be found.⁴² Unfortunately, no data are currently available on the yield of evolved products of horizontal layer smolder. For crude estimates on cellulosic materials the previous results for reverse smolder are adequate, but they should be applied here with caution.

The propagation of smoldering through a porous, horizontal fuel layer has been modeled numerically to a limited extent.¹⁷ The predicted smolder wave shape was in qualitative agreement with experiment. The effects of variations in the reaction rate parameters on this wave structure and on the smolder propagation velocity were examined.

Other fuel configurations: Data on a few other multidimensional smolder configurations are summarized in Table 2-9.1. Again there is little more information available than the rate of smolder propagation. An exception to this is the smoldering cigarette, which has been extensively studied,⁴³⁻⁴⁵ albeit usually in a manner most pertinent to its peculiar mode of cyclically forced air supply. The cigarette smolder propagation process has also been numerically modeled one-¹³ and two-dimensionally.^{17,18} (Other two-dimensional and numerical smolder propagation models can be found in References 19 and 20.)

All the materials in Table 2-9.1 are fairly porous. As noted previously, solid wood, a low-porosity fuel, also smolders, given a configuration that limits heat losses.^{36,52,53}

Ohlemiller^{52,53} examined smolder spread along the interior surface of a three-sided channel constructed of either white pine or red oak. A controlled flow of air was introduced at one end of the channel; the products evolved from the other end were monitored as was the rate of smolder spread. For both types of wood, stable smolder

was observed for only a narrow range of inlet air velocities, 0.05 to 0.20 m/s. (From limited data this appeared true for both forward and reverse smolder.) Below this range the smolder process extinguished and above it flaming eventually erupted. Both of these limits, but particularly the lower limit, are probably dependent on the specific conditions of the tests. Carbon monoxide typically comprised 2 to 3 percent of the gases leaving the channel or about 10 to 15 percent of the gases leaving the surface of the wood. The rate of heat release during smoldering was estimated from the oxygen consumption rate, correcting for carbon monoxide. This rate ranged from about 0.5 to 2 kW or roughly 10 to 30 kW/m², based on the approximate area visibly glowing.

The last type of smolder configuration referenced in Table 2-9.1 is quite pertinent to the scenario that makes smoldering a major contributor to residential fire deaths, that is, upholstery and bedding fires initiated by cigarettes. This is frequently a composite problem, with the smoldering tendency of both the fabric and the substrate (polyurethane foam, cotton batting) pertinent to the overall smolder behavior of the combined assembly.⁵⁴ Ortiz-Molina et al. have shown that the combination of a cellulosic fabric plus a polyurethane foam can smolder over a substantially wider range of conditions than can the foam alone.⁵⁵ The fabric smolder process supplies added heat to the foam smolder zone while simultaneously competing for oxygen. The full complexity of this interaction is yet to be explored. A considerable amount of empirical data on the tendency of cigarettes to initiate this type of smolder is available.^{49,56-63} The factors influencing the smolder tendency of upholstery fabrics have been examined as well.⁶⁴⁻⁶⁹

The life hazard posed by smoldering bedding or upholstery within a closed room has been studied to some extent.⁷⁰⁻⁷² Data have been presented⁷⁰ on the buildup of carbon monoxide (near the ceiling) in a 2.4-m room on a side due to cigarette-initiated smolder in a cotton mattress. The smolder front was reported to spread radially at a rate of 6.3×10^{-5} m/s independent of the size of the smoldering area. In two out of five tests the smolder process underwent a transition to flaming combustion after 65 to 80 minutes, which is close to the time at which total carbon monoxide exposure was estimated to be lethal. Similar data are reported⁷¹ for a greater variety of bedding and upholstery materials; these were ignited by cigarettes (and by flaming sources) in a room $4.3 \times 3.6 \times 2.4$ m. Carbon monoxide and several other gases were sampled at three locations. Flaming developed from smoldering in several of the tests; this usually required 2 to 3 hours of smoldering first. Again, the total exposure to carbon monoxide from the smolder smoke approached or exceeded lethal levels. Lethal conditions due to carbon monoxide were reached in much shorter times in some cases.

All available data on the hazards of smoldering in a closed room were evaluated.⁷² It was concluded that the probability of a lethal carbon monoxide dose and of transition to flaming are comparable for a period from 1 to 2½ hours after cigarette initiation of smoldering. A model is presented for buildup of carbon monoxide due to a smoldering fire;⁷² the results generally show reasonable

Table 2-9.1 Data on Multi-Dimensional Smolder in Various Fuels

Fuel	Fuel/Smolder Configuration	Air Supply Condition/Rate	Smolder Velocity (cm/sec)	Maximum Temp. (°C)	Reference	Comment
Pressed fiber insulation board, 0.23–0.29 g/cc	1.3 cm thick, horizontal strips, width large compared to thickness	Natural convection/diffusion	$1.3\text{--}2.2 \cdot 10^{-3}$	NA	21	Smolder velocity increased ≈ 50% for strips with width ≈ thickness
Pressed fiber insulation board, 0.23–0.29 g/cc	1.3 cm × 1.3 cm strips varied angle to vertical	Natural convection/diffusion	$2.7\text{--}4.7 \cdot 10^{-3}$	NA	21	Smolder velocity highest for upward spread; lowest for horizontal spread
Pressed fiber insulation board, 0.23–0.29 g/cc	1.3 cm × 5 cm strips forward smolder	Forced flow, 20 to 1500 cm/s	$3.5 \cdot 10^{-3}$ cm/s (20 cm/s air) $13.0 \cdot 10^{-3}$ cm/s (1400 cm/s air)	770°C (200 cm/s) 790°C (900 cm/s)	21	Some samples extinguished due to air cooling at air velocity > 1450 cm/s
Pressed fiber insulation board, 0.23–0.29 g/cc	1.3 cm × 5 cm strips reverse smolder	Forced flow, 80–700 cm/s	$2.8\text{--}3.5 \cdot 10^{-3}$ cm/s	NA	21	Extinguishment indicated above 900 cm/s
Pressed fiber-board (pine or aspen) 0.24 g/cc	1.3 cm × 30 cm sheets, horizontal, forward smolder	Forced flow, 10–18 cm/s	$0.7 \cdot 10^{-3}$ cm/s	NA	46	
Cardboard	Vertical rolled cardboard cylinder, downward propagation, varied dia. 0.19–0.38 cm	Natural convection, diffusion	$5.0\text{--}8.4 \cdot 10^{-3}$ cm/s	NA	47	Small dia. ≈ 2 × faster than large dia.; ambient temp. effect measured
Shredded tobacco	0.8 cm dia. cigarette, horizontal, in open air	Natural convection, diffusion	$3.0\text{--}5.0 \cdot 10^{-3}$ cm/s	820°C	48	
Cellulose fabric + 3% NaCl	Double fabric layer, 0.2 cm thick, horizontal, forward smolder	Forced flow, ≈ 10 cm/s	$\approx 1.0 \cdot 10^{-2}$ cm/s	770°C	49	Smolder behavior dependent on alkali metal content
Cellulosic fabric on substrates	Various weight fabrics horizontal on fiberglass, PU foam, cotton batting	Natural convection, diffusion	$\approx 3.0\text{--}75 \cdot 10^{-3}$ cm/s dependent on substrate and fabric	Reported values suspiciously low	50, 51	Smolder fastest on inert fiberglass substrate

agreement with experiment, though some of the input parameters must be forced slightly.

In contrast to the above result, a more recent study of the fire risks associated with upholstered furniture implied that the toxic exposure from a smoldering chair in an average house was rarely fatal; transition to flaming brought with it death due to thermal causes.⁷³ The methodology was indirect, and involved using the Hazard I smoke movement and tenability models in a reasonably successful effort to reproduce national fire statistics for upholstery fires. There are not as yet sufficient data on the toxicity hazards of smoldering upholstery materials to definitively resolve this issue.

A relatively common practical problem in smolder extinguishment occurs in grain silos.⁷⁴ Here the smoldering must be completely extinguished before emptying the silo, to avoid the possibility of a dust explosion. The practical problems are considerable due to the tendency of

any extinguishing agent to follow higher permeability channels and thereby miss significant smolder zones. In Reference 74 a number of extinguishing agents were tested in small-scale tests. Gaseous CO₂, fed from the bottom, was found to be the most effective.

Transition to Flaming

The transition process from smolder to flaming in the above bedding and upholstery fires is essentially spontaneous. At room conditions both smoldering and flaming are possible in many such systems. Sato and Sega³³ explored the domain of overlapping smolder and flaming potential for cellulosic materials and noted a hysteresis in the spontaneous transition between these two combustion modes. The mechanism of such a spontaneous transition has not been investigated in detail. It has been suggested on the basis of small mock-up studies that a

chimneylike effect develops in the crevice between the horizontal and vertical cushions of a smoldering chair.⁶² The enhanced air supply presumably accelerates local char oxidation, heating the char to the point where it can ignite pyrolysis gases. Such a mechanism is plausible but it has not been demonstrated to be operable in real upholstery or bedding, where the chimney effect may not develop so readily.

Transition to flaming (fast exothermic gas-phase reactions) requires both a mixture of gases and air that are within their flammability limits and a sufficient heat source to ignite this mixture. Furthermore, these two requirements must be realized at the same locus in space and at the same time. Any factor that either enhances the net rate of heat generation or decreases the net rate of heat loss will move the smoldering material toward flaming ignition by increasing both local temperature and rate of pyrolysis gas generation. Such factors include an enhanced oxygen supply, an increase in scale (which usually implies lesser surface heat losses per unit volume of smoldering material), or an increasingly concave smolder front geometry, which reduces radiative losses to the surroundings and enhances gaseous fuel concentration buildup. All of these factors may be operating simultaneously in the case of upholstery and bedding smolder. Sequential photos of smolder initiation, growth, and transition to flaming in an upholstered chair appear consistent with this idea.^{62,75}

A further factor in this and in other systems involving cellulosic materials is secondary char oxidation. This process is quite similar to the afterglow seen in cellulosic chars left by flaming combustion. Intense, high-temperature (probably greater than 1070 K) reaction fronts propagate intermittently in seemingly random directions through the fibrous low-density char left by the main lower temperature smolder front. In charred fabrics, these glowing fronts can sometimes progress in a stable manner along the charred residue of a single fiber, despite very high heat losses per unit volume of fuel. Such a process requires the catalytic action of alkali metals that are frequently found naturally in cellulosics or left there during manufacture.^{63-65,69,76} While in a very hot smolder front the size of a single fiber is unlikely to be sufficiently energetic to ignite flammable gases, the larger fronts (10^{-3} to 10^{-2} m in scale) may well be. An analogous process has been found to cause occasional flaming ignition of smoldering, unretarded cellulosic insulation.³¹

Babrauskas and Krasny⁷⁷ surveyed the available literature data on the buoyant smolder in upholstered chairs and beds. They found that about two-thirds of the tested items underwent a transition into flaming combustion. The reported times for this to occur varied from 22 min to 306 min after the initiation of the smoldering process.

The transition from smolder to flaming can also be induced, for example, by a forced increase in oxygen supply rate to the smolder reaction zone.^{21,23,33,34,78} This effect was first studied quantitatively by Palmer²¹ for airflow over horizontal layers of wood sawdust. This process, of course, is familiar to anyone who has started a camp fire from tinder and sparks. Transition to flaming was noted by Palmer only for airflow in the same direction as smol-

der propagation (forward smolder). Depending on the material, the transition occurred at airflow velocities from about 0.9 to 1.7 m/s. For these materials, flaming did not develop when the mean particle size was less than 1 mm. Ohlemiller^{37,78} did obtain transition to flaming in layers of fibrous insulation materials of very small diameter (~25 μm) but again only with forward smolder. This result occurred at air velocities of about 2 m/s for unretarded insulation. Leisch³⁴ utilized ignition sources placed midway along the length of grain and wood particle fuel layers so that forward and reverse smolder zones were simultaneously obtained. Flaming was noted at 4 m/s air velocity only after the smoldering process produced a substantial depression or cavity in the surface of the fuel layer.

Ohlemiller^{37,78} explained the weak response and lack of flaming transition in reverse smolder on the basis of heat transfer effects influencing the leading edge of the smolder reaction zone. These heat transfer effects intensify the smolder in the leading edge region for forward smolder. In the case of cellulosic insulation, the intensification leads to random development of small (a few cm) cavities near the leading edge which act as flame initiation regions and flame holders.

Ohlemiller⁷⁸ also found that both boric acid (a smolder retardant) and borax (a flame retardant) could each eliminate the transition to flaming when the retarded cellulosic insulation was the only fuel. However, the effectiveness of the acid and borax was substantially reduced if the smoldering fuel abutted unretarded wood (as it typically does in residential housing). Heat transferred from the smolder zone readily ignited the wood. Palmer⁷⁹ noted similarly that layers of fine dust that would not themselves undergo transition to flaming readily ignited adjacent flammable materials.

Smoldering solid wood undergoes a transition to flaming readily in a configuration that minimizes heat losses.^{52,53} It was inferred that the limiting variable in the transition is the surface temperature of the smoldering wood, with the transition occurring when that temperature reached about 950 to 1000 K.

The transition from two-dimensional, forced flow smolder propagation, to flaming in polyurethane foam was investigated by Tse, et al.^{80,81} The configuration involved a contained slab of foam with forced air across its outer surface. No fabric was involved. Smoldering ignition was on the upstream end so this was two-dimensional forward smolder propagation. A unique ultrasonic technique was used to follow the density distribution of the foam during the tests along with schlieren imaging of the gas flow near the foam surface. It was inferred that the transition to flaming in this system occurred not at the foam/air interface, but rather within the depth of the char left by the smolder front. Continued reactions there opened holes which allowed the onset of vigorous gas phase reactions. This is not greatly dissimilar to the mechanism found for the onset of flaming in a horizontal layer of cellulosic insulation subjected to an air flow over its top surface.³⁷ In a study of smoke explosions in a reduced-scale enclosure containing a smoldering wood crib, the transition from smoldering to flaming was hypothesized as the trigger of this explosion.⁸² The evidence was indirect and not entirely unambiguous.

Conclusion

Smoldering is a branch of solid fuel combustion quite distinct in many aspects from flaming, but equally diverse and complex. Unfortunately it has not been studied nearly to the same extent as flaming. This is quite apparent in the lack of quantitative guidelines that can be provided here for estimating the behavior of realistic smolder propagation processes, smolder detection, toxic gas production, and the transition to flaming. The experimental data provided can be readily used for closely analogous situations. They must be used cautiously for dissimilar conditions. The reader should always bear in mind the strong role that the oxygen supply rate has on the smolder process. The other very important factor is the relative direction of movement of oxygen supply and smolder propagation. This can be somewhat obscure in many realistic configurations. The actual chemical nature of the fuel is relatively secondary, at least with regard to smolder rate. It may be important for toxic gas production rates, but the data here are quite limited.

References Cited

1. K. Rohr, "U.S. Home Product Report, 1992–1996: Forms and Types of Materials First Ignited in Fires," National Fire Protection Association, Quincy, MA (1999).
2. R. McCarter, "Smoldering Combustion of Cotton and Rayon," *J. Cons. Prod. Flamm.*, 4, p. 346 (1977).
3. P. Bowes, *Self-Heating: Evaluating and Controlling the Hazards*, Elsevier, New York, Chap. 7 (1984).
4. T. Ohlemiller, "Modeling of Smoldering Combustion Propagation," *Prog. in Energy and Comb. Sci.*, 11, p. 277 (1985).
5. T. Ohlemiller, J. Bellan, and F. Rogers, "A Model of Smoldering Combustion Applied to Flexible Polyurethane Foams," *Comb. and Flame*, 36, p. 197 (1979).
6. S. Dosanjh, P. Pagni, and C. Fernandez-Pello, "Forced Cocurrent Smoldering Combustion," *Comb. and Flame*, 68, p. 131 (1987).
7. S. Dosanjh, and P. Pagni, *Proc. of the 1987 ASME/JSME Thermal Engineering Joint Conference—Volume 1*, (P. Marto and I. Tanasawa, eds.) American Society of Mechanical Engineers, New York (1987).
8. M. Fatehi and M. Kaviani, "Adiabatic Reverse Combustion in a Packed Bed," *Comb. Flame*, 116, pp. 1–17 (1994).
9. D. Walther, C. Fernandez-Pello, and D. Urban, "Space Shuttle Based Microgravity Smoldering Combustion Experiments," *Comb. Flame*, 116, pp. 398–414 (1999).
10. A. Aldushin, B. Matkowsky, and D. Schult, "Downward Buoyant Filtration Combustion," *Comb. Flame*, 107, pp. 151–175 (1996).
11. S. Leach, J. Ellzey, and O. Ezekoye, "A Numerical Study of Reverse Smoldering," *Comb. Sci. Tech.*, 130, p. 247 (1997).
12. C. Fernandez-Pello, B. Matkowsky, D. Schult, and V. Volpert, "Propagation and Extinction of Forced Opposed Flow Smolder Waves," *Comb. Flame*, 101, pp. 461–470 (1995).
13. M. Summerfield, T. Ohlemiller, and H. Sandusky, "A Thermophysical Mathematical Model of Steady-Draw Smoking and Predictions of Overall Cigarette Behavior," *Comb. Flame*, 33, pp. 263–279 (1978).
14. C. Fernandez-Pello, B. Matkowsky, D. Schult, and V. Volpert, "Forced Forward Smolder Combustion," *Comb. Flame*, 104, pp. 1–26 (1996).
15. J. Buckmaster and D. Lozinski, "An Elementary Discussion of Forward Smoldering," *Comb. Flame*, 104, pp. 300–310 (1996).
16. A. Aldushin, L. Rumanov, and B. Matkowsky, "Maximal Energy Accumulation in a Superadiabatic Filtration Combustion Wave," *Comb. Flame*, 118, pp. 76–90 (1999).
17. M. Muramatsu, "Studies on the Transport Phenomena in Naturally Smoldering Cigarettes," *Japan Tobacco Monopoly Research Report No. 123* (1981).
18. H. Mitler and G. Walton, "Modeling the Ignition of Soft Furnishings by a Cigarette," *Report SP 852*, National Institute of Standards and Technology, Gaithersburg, MD (1993).
19. M. Moallemi, H. Zhang, and S. Kumar, "Numerical Modeling of Two-Dimensional Smoldering Processes," *Comb. Flame*, 95, pp. 170–182 (1993).
20. C. DiBlasi, "Mechanisms of Two-Dimensional Smoldering Propagation through Packed Fuel Beds," *Comb. Sci. Tech.*, 106, pp. 103–124 (1995).
21. K. Palmer, "Smoldering Combustion in Dusts and Fibrous Materials," *Comb. and Flame*, 1, p. 129 (1957).
22. T. Ohlemiller and D. Lucca, "An Experimental Comparison of Forward and Reverse Smolder Propagation in Permeable Fuel Beds," *Comb. and Flame*, 54, p. 131 (1983).
23. F. Rogers and T. Ohlemiller, "Smolder Characteristics of Flexible Polyurethane Foams," *J. Fire Flamm.*, 11, p. 32 (1980).
24. D. Lucca, *An Investigation of Co-Current and Counter-Current Smoldering Combustion in Particulated Fuel Beds*, M.S.E. Thesis, Princeton University, Princeton (1979).
25. G. Mulholland and T. Ohlemiller, "Aerosol Characterization of a Smoldering Source," *Aero. Sci. and Tech.*, 1, p. 59 (1982).
26. H. Hotta, Y. Oka, and O. Sugawa, "Interaction between Hot Layer and Updraft from a Smoldering Source. Part 1. An Experimental Approach," *Fire Sci. and Technol.*, 7, p. 17 (1987).
27. J. Torero and C. Fernandez-Pello, "Upward Smolder of Polyurethane Foam," *Fire Safety J.*, 24, pp. 35–52 (1995).
28. J. Torero and C. Fernandez-Pello, "Forward Smolder of Polyurethane Foam in a Forced Air Flow," *Comb. Flame*, 106, pp. 89–109 (1996).
29. R. Anthineni and C. Fernandez-Pello, "A Study of Forward Smolder Ignition of Polyurethane Foam," *Proceedings 27th Symposium (International) on Combustion*, Vol. 2, Combustion Institute, Pittsburgh, PA, pp. 2683–2690 (1998).
30. W. Frandsen, "The Influence of Moisture and Mineral Soil Content on the Combustion Limits of Smoldering Forest Duff," *Can. J. For. Res.*, 17, p. 1540 (1987).
31. T. Ohlemiller, "Smoldering Combustion Propagation through a Permeable Horizontal Fuel Layer," *Comb. and Flame*, 81, p. 341 (1990).
32. P. Beever, "Initiation and Propagation of Smouldering Reactions," Ph.D. Dissertation, University of Leeds, (1986).
33. K. Sato and S. Segu, "The Mode of Burning Zone Spread along Cylindrical Cellulosic Material," *J. Fire Sci.*, 3, p. 26 (1985).
34. S. Leisch, *Smoldering Combustion in Horizontal Dust Layers*, Ph.D. Dissertation, University of Michigan, Ann Arbor (1983).
35. J. Jones, T. Goh, and M. Dijanovic, "Smouldering and Flaming Combustion in Packed Beds of Casuarina Needles," *J. Fire Sciences*, 12, pp. 442–451 (1994).
36. T. Ohlemiller, unpublished test results.
37. T. Ohlemiller, "Forced Smolder Propagation and the Transition to Flaming in Cellulosic Insulation," *Comb. and Flame*, 81, p. 354 (1990).
38. K. Sato and S. Segu, *Fire Safety Science—Proceedings of the Second International Symposium*, Hemisphere Publishing Corp., New York, p. 87 (1989).

39. T. Ohlemiller and F. Rogers, "Cellulosic Insulation Material II. Effect of Additives on Some Smolder Characteristics," *Comb. Sci. and Tech.*, 24, p. 139 (1980).
40. P. Beever, "Subterranean Fires in the UK—the Problem," *Paper IP 3/89*, Building Research Establishment (1989).
41. E. Johnson and K. Miyanishi (eds.), *Forest Fires: Behavior and Ecological Effects*, Academic Press, New York (2000).
42. L. Cohen and N. Luft, "Combustion of Dust Layers in Still Air," *Fuel*, 34, p. 154 (1955).
43. R. Baker, "Temperature Distribution inside a Burning Cigarette," *Nature*, 247, p. 405 (1974).
44. R. Baker and K. Kilburn, "The Distribution of Gases within the Combustion Coal of a Cigarette," *Beitrage zur Tabakforschung*, 7, p. 79 (1973).
45. R. Baker, *Beitrage zur Tabakforschung*, 11, p. 1 (1981).
46. J. Brenden and E. Schaffer, "Wavefront Velocity in Smoldering Fiberboard," *Research Paper FPL 367*, U.S. Forest Products Laboratory (1980).
47. T. Kinbara, H. Endo, and S. Sega, *Proceedings 11th Symposium (International) on Combustion*, Combustion Institute, Pittsburgh, PA, p. 525 (1967).
48. A. Egerton, K. Gugan, and F. Weinberg, "The Mechanism of Smouldering in Cigarettes," *Comb. Flame*, 7, p. 63 (1963).
49. R. Gann, R. Harris, J. Krasny, R. Levine, H. Mitler, and T. Ohlemiller, "The Effect of Cigarette Characteristics on the Ignition of Soft Furnishings," *Technical Note 1241*, National Bureau of Standards, Gaithersburg, MD (1988).
50. D. Donaldson and D. Yeadon, "Smolder Characteristics of Cotton Upholstery Fabrics," *Textile Res. J.*, March, p. 196 (1981).
51. D. Donaldson and D. Yeadon, "Smoldering Phenomena Associated with Cotton," *Textile Res. J.*, March, p. 160, (1983).
52. T. Ohlemiller and W. Shaub, "Products of Wood Smolder and Their Relation to Wood-Burning Stoves," *NBSIR 88-3767*, National Bureau of Standards, Washington, DC (1988).
53. T. Ohlemiller, *Fire Safety Science—Proceedings of the Third International Symposium*, Elsevier, New York, p. 565 (1991).
54. G. Tesoro and T-Y. Toong, *Smoldering in Cotton Upholstery Fabrics and Fabric/Cushioning Assemblies*, Massachusetts Institute of Technology, Cambridge (1981).
55. M. Ortiz-Molina, T-Y. Toong, N. Moussa, and G. Tesoro, *17th Symposium (International) on Combustion*, Combustion Institute, Pittsburgh, PA (1979).
56. G. Damant, "A Survey of Upholstery Fabrics and Their Flammability Characteristics," *J. Cons. Prod. Flamm.*, 2, p. 2 (1975).
57. G. Damant, "Cigarette Induced Smoldering of Uncovered Flexible Polyurethane Foams," *J. Cons. Prod. Flamm.*, 2, p. 140 (1975).
58. G. Damant, "Home Furnishings Fire Retardant Requirements: The California Experience," *J. Cons. Prod. Flamm.*, 6, p. 95 (1979).
59. K. Palmer and W. Taylor, "Fire Hazards of Plastics in Furniture and Furnishings: Ignition Studies," *J. Cons. Prod. Flamm.*, 1, p. 186 (1974).
60. J. Loftus, *NBSIR 78-1438*, National Bureau of Standards, Washington, DC (1978).
61. J. Krasny, "Cigarette Ignition of Soft Furnishings—A Literature Review with Commentary," *NBSIR 86-3509*, National Bureau of Standards, Washington, DC (1986).
62. R. Salig, *Smoldering Behavior of Upholstered Polyurethane Cushioning and Its Relevance to Home Furnishings Fires*, Master's Thesis, Massachusetts Institute of Technology, Cambridge (1981).
63. A. Ihrig, A. Rhyne, V. Norman, and A. Spears, "Factors Involved in the Ignition of Cellulosic Upholstery Fabrics by Cigarettes," *J. Fire Sci.*, 4, p. 237 (1986).
64. K. Yeh, Z. Song, J. Reznichenko, and K. Jang, "Alkali Metal Ions and Their Effects on Smoldering of Cotton Upholstery Fabric—A Literature Review," *J. Fire Sciences*, 11, pp. 351–367 (1993).
65. A. Ihrig and S. Smith, "The Role of Alkaline Earth Metal Ions in Cellulosic Smoldering," *J. Fire Sciences*, 12, pp. 357–375 (1994).
66. L. Lewis, M. Morton, V. Norman, A. Ihrig, and A. Rhyne, "The Effects of Upholstery Fabric Properties on Fabric Ignitabilities by Smoldering Cigarettes," *J. Fire Sciences*, 13, pp. 445–471 (1995).
67. D. Kellogg, B. Waymack, D. McRae, and R. McGuire, "Smolder Rates of Thin Cellulosic Materials," *J. Fire Sciences*, 15, pp. 390–403 (1997).
68. A. Dyakanov and D. Grider, "Smolder of Cellulosic Fabrics. I. Development of a Framework," *J. Fire Sciences*, 16, pp. 297–322 (1998).
69. A. Dyakanov and D. Grider, "Smolder of Cellulosic Fabrics. II. Alkali and Inner Oxygen as Variables," *J. Fire Sciences*, 17, pp. 71–85 (1999).
70. K. Sumi and G. Williams-Leir, *Research Paper No. 402*, National Research Council, Ottawa (1969).
71. C. Hafer and C. Yuill, *Characterization of Bedding and Upholstery Fires*, Southwest Research Institute, San Antonio (1970).
72. J. Quintiere, M. Birky, F. McDonald, and G. Smith, "An Analysis of Smoldering Fires in a Closed Compartment and Their Hazard due to Carbon Monoxide," *Fire and Matls.*, 6, p. 99 (1982).
73. W. Stiefel, R. Bukowski, J. Hall, and F. Clarke, "Fire Risk Assessment Method: Case Study 1, Upholstered Furniture in Residences," *NISTIR 90-4243*, National Institute of Standards and Technology, Gaithersburg, MD (1990).
74. M. Tuomisaari, D. Baroudi, and R. Latva, "Extinguishing Smouldering Fires in Silos," *Publication 339*, VTT Technical Research Centre of Finland, Espoo, Finland (1998).
75. R. Ogle and J. Schumacher, "Fire Patterns on Upholstered Furniture. Smoldering Versus Flaming Combustion," *Fire Technol.*, 34, pp. 247–265 (1998).
76. R. McCarter, "Smoldering Combustion of Cotton and Rayon," *J. Cons. Prod. Flamm.*, 4, p. 346 (1977).
77. V. Babrauskas and J. Krasny, "Upholstered Furniture Transition from Smoldering to Flaming," *J. Forensic Sci.*, Nov., pp. 1029–1031 (1997).
78. T. Ohlemiller, *NBSIR 85-3212*, National Bureau of Standards, Washington, DC (1985).
79. K. Palmer, *Dust Explosions and Fires*, Chapman and Hall, London (1973).
80. S. Tse, C. Fernandez-Pello, and K. Miyasaka, *Proceedings 26th Symposium (International) on Combustion*, Combustion Institute, Pittsburgh, PA, pp. 1505–1513 (1996).
81. S. Tse, C. Fernandez-Pello, and K. Miyasaka, *Proceedings Eighth International Symposium on Transport Phenom. in Combustion*, Francis & Taylor, Washington, DC, pp. 689–700 (1995).
82. B. Sutherland, "Smoke Explosions," *Fire Engineering Research Report 99/15*, University of Canterbury, Christchurch, New Zealand (1998).

CHAPTER 10

Spontaneous Combustion and Self-Heating

Brian Gray

Introduction

The term *spontaneous combustion* will be used here to refer to the general phenomenon of an unstable (usually oxidizable) material reacting with the evolution of heat, which to a considerable extent is retained inside the material itself by virtue of either poor thermal conductivity of the material or its container. Under some circumstances this process can lead to flaming combustion and overt fire in which case it is properly called *spontaneous ignition* and is regarded here as a special case of spontaneous combustion. This phenomenon has been responsible for significant losses of life and enormous losses of property.

Fire loss statistics from many sources show that spontaneous ignition is quoted as the cause in a much greater proportion of cases with multimillion-dollar losses than in smaller fires. Of course one should also note that the proportion of results having an unknown cause follows a similar trend, probably due to the greater degree of destruction and hence lost evidence in larger fires. In other circumstances, clearly delineated from the former, only relatively mild self-heating occurs. This occurrence may be referred to as *self-heating, spontaneous combustion*, or by research scientists as *subcritical* behavior. By the same token, spontaneous ignition would be referred to as *super-critical* behavior. The well-defined boundary between the two types of behavior is referred to as the *critical condition* and it plays an absolutely central role, both conceptually and pedagogically. It can crudely but pictorially be thought of as a watershed.

The critical condition is actually a whole set of combinations of parameters that affect the behavior. The most important of these are the ambient (surrounding) temper-

ature, and the size and shape of the body of material involved. Thus for a given body of a particular material we would normally talk about the *critical ambient temperature* (CAT). If we were dealing with a situation where the size of the body was always fixed by commercial practice, for instance, this term would be the normal statement of the critical condition. However, in the case of storage of a variable amount of material in a constant temperature environment, one would talk about the *critical size* or the *critical diameter* of the body for a given fixed temperature. The CAT is the most commonly used and stated critical condition.

For both fire prevention and fire cause investigation, it is essential to be able to identify the critical condition if spontaneous ignition is a possibility either before or after the event. It is also important to be aware of other possible factors operating in particular cases, such as solar irradiation in outdoor storage and preheating if recently manufactured or processed goods are involved. In cases such as hot laundry; hot new chipboard; hot, oily, porous food products (instant noodles, fried fish scraps); bagasse* the temperature of the material itself is a most important parameter affecting criticality in addition to the usual ones. In such cases we have to deal with and determine a critical stacking temperature (CST), which refers to the temperature of the material itself, not the ambient temperature. The CST is dependent on the CAT and the size of the body so such cases are a degree more complicated than the traditional ones involving, usually, agricultural materials stacked at ambient temperature. In addition, in such cases with preheated materials, the time to ignition (defined precisely later) is usually very much shorter than it is where the material is stacked at ambient temperature.

Since the basic processes competing with each other in spontaneous combustion are heat generation by chem-

Emeritus Professor Brian Gray has published extensively on spontaneous combustion and ignition of gases and solids, gas ignition, flame propagation, and related topics for many years. He now runs a combustion consulting company in Sydney, Australia, and was Professor of chemistry at Macquarie University, Sydney, from 1976 to 1998.

*Bagasse is the remainder of sugar cane after the extraction of sugar. It is cellulosic in nature and usually contains 50 percent water.

ical reaction and heat loss to the surroundings mainly by conduction, it is easy to see qualitatively why both a larger body and higher ambient temperature will favor ignition rather than subcritical behavior as they both decrease the rate of heat loss. Generally the temperature profile across the body itself is roughly parabolic in shape, with a peak at the center. Most chemical reaction rates increase almost exponentially with temperature whereas heat loss processes such as conduction increase only linearly. Thus the center of the body where the temperature is highest is the region where ignition, or *thermal runaway*, will commence if it is going to take place at all. Many bodies that have undergone spontaneous ignition show this telltale signature of charring or complete destruction to ash in the center while retaining almost pristine appearance on the outside, sometimes presenting rather dangerous situations for fire fighters in large-scale examples such as bagasse, woodchip, or peat piles. Similarly, the deep-seated nature of the burning started by spontaneous ignition can be difficult to extinguish completely, often reigniting days after apparent extinction.

The purpose of this article is to expound the detailed nature of the situations described above in a manner that approaches the relevant principles and minimizes mathematical formulation as far as is reasonable. The subject will involve relevance to fire cause and fire investigation and as such will refer mainly to solid systems. Many of the basic principles used were actually clarified by experimental work on gaseous systems; such systems still play a central role in current research on this topic, particularly ones where the chemical kinetics are simple and well understood in their own right.

A closely related aspect to be discussed here is the subject of *runaway reaction*, or *thermal runaway*. In the past two decades this topic has developed a literature of its own¹ and threatened to lose contact with the extensive literature on spontaneous combustion. These two terms, which can be taken as synonymous, are applied to supercritical conditions as defined above but only in the context of a chemical reactor. The reactor may be of batch, semibatch, or continuous flow type, but it will almost invariably be well stirred either mechanically or by deliberate turbulent mixing. Therein lies the attraction of such studies from a pedagogical point of view since the main difficulties in mathematical modeling of solid spontaneous combustion arising from spatial temperature variation and gradually decreasing concentration of reacting material are not present. Thus a mathematical theory describing such processes exactly serves as a first approximation, and a tractable one at that, to the more complex topic of solid spontaneous combustion. In addition, the difficult and messy "corrections" to the simplest possible theories due to Semenov² and Frank-Kamenetskii³ are often impossible to apply in practical situations due to the dearth of data and/or their numerical uncertainties.

In addition, in the rare event that precise input data are available and detailed chemical kinetics are known, it is now entirely feasible for particular cases to invoke directly numerical integration of the relevant equations without use of the empirical and semiempirical curve fits involved in the classical corrections to the simplest theories. At the time of writing, average laptop computers

were quite capable of such calculations for all but the most irregularly shaped bodies where finite element methods need to be invoked and custom written.

Accordingly we will spend some time here expounding the simplest possible theory (Semenov), which contains all the essential concepts for the understanding of criticality, the tangency between heat release and heat loss curves, and the existence (or otherwise) of stable and unstable steady states. We then move on briefly to the application of such ideas to more complex chemistry and the idea of thermal runaway in continuous stirred tank reactors (CSTR).

We then discuss the Frank-Kamenetskii version of thermal explosion theory, which considers temperature gradients within the self-heating body (thereby generalizing Semenov) and often gives better agreement with experiment for solid bodies with low thermal conductivity. For this reason it is much used in fire investigations, particularly when it is necessary to predict the CAT for a large-scale industrial body from small-scale laboratory tests. However this type of extrapolation requires great care in its application to all but the simplest chemistry.

We then present some ways in which corrections can be made to the predictions of the Frank-Kamenetskii theory occurring under conditions where some of its assumptions are not too accurate. This occurs when the heat of reaction is relatively small and/or when the resistance to heat flow in the boundary of the body (or container wall) is relatively large compared to that inside the body itself (case of small Biot number). Corrections are also necessary when more than one chemical reaction generates heat and when oxygen diffusion into the interior of the body is rate limiting.

All these factors are difficult to handle quantitatively, but fortunately none of them really alter the *qualitative* conceptual nature of what is going on. It is important in gaining an understanding of spontaneous combustion *not* to be confused by these corrections although in certain cases they can be quite large.

We will then move on to discuss experimental testing methods, both on a laboratory and a larger scale where possible. A large array of calorimetric methods can be used to obtain relevant information, but not all of them, particularly differential scanning calorimetry (DSC) and differential thermal analysis (DTA), can give other than very general information. Nevertheless such methods have their purpose when material of unknown origin and composition is involved. Sometimes one needs to know whether the unknown is capable of exothermic reaction at all as postulation of spontaneous ignition because a fire cause looks rather silly in its absence (this happens!).

A characteristic of fires where spontaneous ignition is suspected as the cause is that they often occur on premises that have been closed up or unoccupied for a significant period of time. A question of very great interest in such a context is, What is the time scale expected for a body of a given size in a given ambient temperature to reach ignition, that is, the appearance of overt flame? As one would expect, by application of Murphy's law, this question is very difficult to answer with confidence except in the simplest cases. The time to ignition is a parameter that is not only extremely sensitive to many factors,

which are often unknown, but also extremely sensitive to the degree of supercriticality, that is, how far the body is from the watershed. Not only does it depend on how far the body is from the watershed, but it depends sensitively on the direction as well. In other words, the term *degree of supercriticality* needs to be refined before any idea of time to ignition can be properly formulated.

A number of investigations of this problem have been carried out, and it is essential to recognize that most of the earlier ones addressed the question of time to ignition for the initial temperature of the body equal to the ambient temperature—such as would be the case in the building of a haystack. Hot, stacked material requires totally different considerations for the evaluation of times to ignition, and classical formulae cannot be used in such situations. Such bodies can ignite in times that may be an order of magnitude shorter than predicted by uncritically using classical formulae.

In the penultimate section of this article, we move on to discuss the actual fire where spontaneous ignition has been the cause, or suspected cause, of the fire. We discuss factors that would be either positive or negative indicators of spontaneous ignition, and also the appropriate examination of the aftermath of the fire for pointers as to whether or not spontaneous ignition was the cause. We then proceed to illustrate all the above with a number of case histories, some of them common and illustrative of the basic principles expounded here, others of a novel nature involving quite subtle and detailed investigations that nevertheless can give very definite results.

The Literature

There is a large and varied literature on this topic ranging from sophisticated mathematical theory to technical measurements on industrial and agricultural products. It is scattered over a very wide range of journals, magazines, and disciplines. The most comprehensive publication is probably the book written by Bowes,⁴ *Self-Heating: Evaluating and Controlling the Hazards*. This book was published in 1984 and contains references to work published up to 1981, so at the present time it is in need of updating. However, it is the most useful reference available for those working, or commencing work, in the field, either from an academic or technical viewpoint.

Although much of the understanding of spontaneous combustion has come from the basic study of gas phase reactions, where it is generally referred to as *autoignition*, this article will be limited to spontaneous combustion of solid materials generally. Many advances have been made in the field of gaseous autoignition over the last decade or so, stemming from accurate and detailed kinetic measurements and considerable advances in computing power. The critical condition for gaseous systems is a very complex locus in the parameter space characterized by ambient temperature (as for solids), pressure, and composition. Many organic materials, such as hydrocarbons, exhibit more than one autoignition temperature and many also exhibit the phenomenon of igniting on *decreasing* ambient temperature. Many older tabulations of autoignition temperatures do not recognize these peculiarities and should

be used with great caution. A detailed description of the reasons for such complexities and their importance in a hazard context is given by Griffiths and Gray⁵ in the twenty-fourth Loss Prevention Symposium of the American Institute of Chemical Engineers (1990). A comprehensive list of references up to 1990 can be found in this article.

Reference to liquid reactions and related spontaneous ignitions and thermal instabilities will be given later in this article in the section on spatially homogeneous, or “well-stirred,” systems. Otherwise references will be given at points throughout this text resulting in a reasonably complete bibliography.

The Concept of Criticality

During the last two decades the concept of criticality, which has been present in the thermal context for many years,⁶ has been recognized as a branch of bifurcation theory,⁷ an area of nonlinear applied mathematics that has grown rapidly and proven to be extremely powerful in solving nonlinear problems. In our case the nonlinearity comes from the temperature dependence of the chemical reaction (and therefore heat production) rate. The Arrhenius form for this for a single reaction is $Ze^{-E/RT}$ where E is the activation energy and R is the universal gas constant. T is the absolute temperature, of course. At temperatures rather less than E/R (which can typically be 10,000 K or more), the Arrhenius function is very convex; that is, it curves upward rather rapidly with temperature. In contrast, the rate of heat loss from a reacting body is generally only a linear function of temperature, for example, conduction. Although radiation losses are nonlinear functions of temperature, they are much more weakly nonlinear than the Arrhenius function and also generally rather small at the low temperatures involved in solid spontaneous combustion even though they are important in flame extinction. Typical heat generation and heat loss loci are shown in Figure 2-10.1.

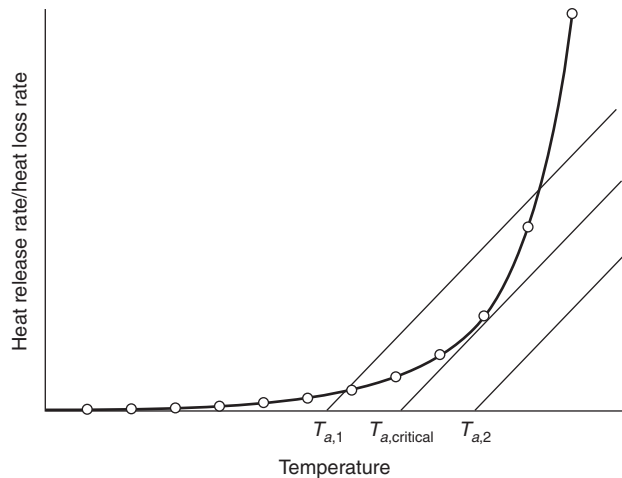


Figure 2-10.1. Typical Arrhenius heat-release and loss curves.

The low temperature range of the Arrhenius curve is seen here to be rather convex and rapidly increasing with temperature. The three straight lines represent the rate of heat loss from a body of fixed given size at various ambient temperatures $T_{a,1}$, $T_{a,critical}$, and $T_{a,2}$.

At $T_{a,1}$ it can be seen that the heat production and loss curves intersect at two points. At $T_{a,2}$ they do not intersect at all and at $T_{a,critical}$ they intersect at only one point and, in fact, touch tangentially.

Since intersections represent conditions where heat production and loss balance exactly, we expect them to represent some sort of "equilibrium" or stationary point where the temperature of the body remains constant in time. It is important to remember that they do not represent equilibrium in any thermodynamic sense.

In the region of the lower intersection at $T_{a,1}$ it can be seen from the diagram that the temperature of the body will increase up to the balance point from below as heat release is greater than heat loss in this region. On the other hand, just above this balance point the temperature of the body will move down to it since the heat release is lower than the heat loss in this region. Thus the lower balance point occurring at ambient temperature $T_{a,1}$ is recognized as a *stable* balance, or stationary point. Small perturbations from it will be nullified and the body in this region will tend to stay at the balance point. Note that the temperature of the balance point is not $T_{a,1}$ but slightly above it, usually by 5–20°C. It represents subcritical self-heating and can cause loss of the material, but not by overt ignition or fire. It can appear as degradation or discoloration of many materials, making them useless for their required purpose. For example woodchips degraded in this way are not suitable for paper or cardboard production, and dried milk powder when discolored is unacceptable.

The second balance point at the ambient temperature $T_{a,1}$ can be seen by a similar simple analysis to be *unstable* in the sense that in the temperature region just below it, the heat production is *lower* than the heat loss, so the temperature tends to drop. In the temperature region just above it, the converse is true, so the body temperature tends to rise and leave the balance point. The latter acts as a watershed between two totally distinct types of behavior, that is, the temperature of the body dropping to the lower balance point or running away to the right of the diagram and much higher temperatures, representing ignition.

Here the temperature at the higher balance point would actually be the CST or *critical stacking temperature* for this particular body when stored at ambient temperature $T_{a,1}$. We can immediately see that if the ambient temperature is increased, that is, the straight line is moved to the right with fixed slope (which is determined by the size and shape of the body as we shall see later), the CST will decrease, a physically reasonable and intuitive result.

Thus this oversimplified but extremely useful model gives a simple understanding of what Bowes refers to as *thermal ignition* of the second kind, that is, what is probably better referred to as the *hot stacking problem*, a much more descriptive term. Not only that, but it also gives us a qualitatively correct picture of the more common or "normal" type of thermal ignition when the body self-heats from ambient to ignition without any preheating. At $T_{a,1}$ if we very slowly increase the ambient temperature after the

steady state has been reached, we can see that the now "quasi-steady state" will also slowly increase until at $T_{a,critical}$ the quasi-steady state and the CST merge at the point of tangency. Beyond this ambient temperature there is no balance point, and in this temperature region the heat-release curve is now *always above the loss line* and therefore the temperature can only increase. Subsequent ignition will then occur. It will occur after some delay since the rate of temperature increase in this simple model is proportional to the imbalance between heat production and loss (i.e., the vertical distance between the two curves). This is initially quite small, increasing as the temperature rises. In this observation lie the seeds of the calculation of the *ignition delay* or *time to ignition* (*tti*) to be examined later.

Even more insights can be obtained from this simple type of reasoning. As we shall see later, the slope of the heat loss line is dependent on the surface area/volume ratio of the body in question. Thus for a body of given shape, the surface/volume ratio increases as the body gets smaller and decreases as the body gets larger. In Figure 2-10.2 we can see the effect of increasing the size of a body at a fixed ambient temperature. For this fixed ambient temperature we can speak of subcritical, critical, and supercritical sizes for the body, depending on whether any balance points exist.

Thus for a body with characteristic dimension r_{sub} we see the existence of both a CST and a balance point. For a larger body with dimension r_{super} we see that neither exist and we expect temperature rise to ignition. The critical condition, in this case expressed as a radius or body dimension, is given again by the tangency condition. This critical condition of course is identical with that obtained by thinking of quasi-static variation of the ambient temperature as well. The critical radius for a given ambient temperature will be identical with the CAT for a body of that same radius. How we describe it is simply a matter of where we are coming from.

Of course we do not usually continuously vary the size of a body, but we *do* often stack bodies together, for ex-

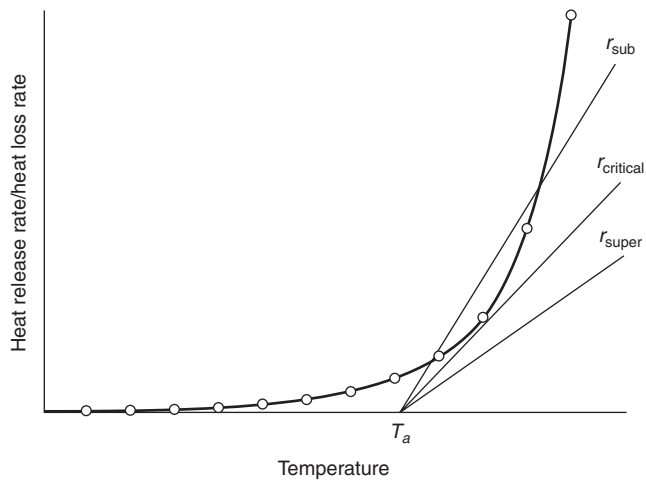


Figure 2-10.2. Disappearance of balance points with body size increase.

ample, bales of cotton, bales of hay, and so forth, and allow larger than normal quantities to accumulate, for example, coal stockpiles. Even from the point of view of this very rudimentary theory, it is obvious that the CAT of two bales in contact will be considerably less than that for a single bale. Thus tests of the CATs of single bodies that are going to be stacked in groups either for transport or storage are useless unless a theory is available enabling calculation of the dependence of CAT on body size. The theory allowing this is thus extremely useful in relating practical tests on small bodies to be applied to storage of large numbers of them (with certain caveats to be discussed later).

To conclude this section it remains to show a convenient method of representing the behavior of the stable balance point and the unstable CST as a control parameter is varied (i.e., the ambient temperature or size of the body). This method enables a quick and convenient representation of the discussion given above on a single diagram (a bifurcation diagram) and also gives us a useful link to the mathematical developments of bifurcation theory.

Figure 2-10.3 shows what happens to the balance point temperature and the CST when T_a is varied continuously from below its critical value to above it. This takes place at constant body size. In this case the ambient temperature is known as the bifurcation parameter. We should note that even at very low ambient temperatures, the CST tends to a finite limit. In fact it becomes very insensitive to the ambient temperature, and no matter how cold the ambient temperature, there is no corresponding rise in the CST. Storing hot products in a cold warehouse does not help the problem much!

Conversely Figure 2-10.4 shows how the CST rises indefinitely as the size of the body decreases at fixed ambient temperature. Regardless of ambient temperature it does pay to keep hot stored bodies small! Figure 2-10.4 also shows how for sizes above the critical dimension there is no alternative but ignition. Of course the critical dimension depends on the ambient temperature, and as the latter goes down the critical dimension goes up. It is sometimes very useful to draw a critical dimension ver-

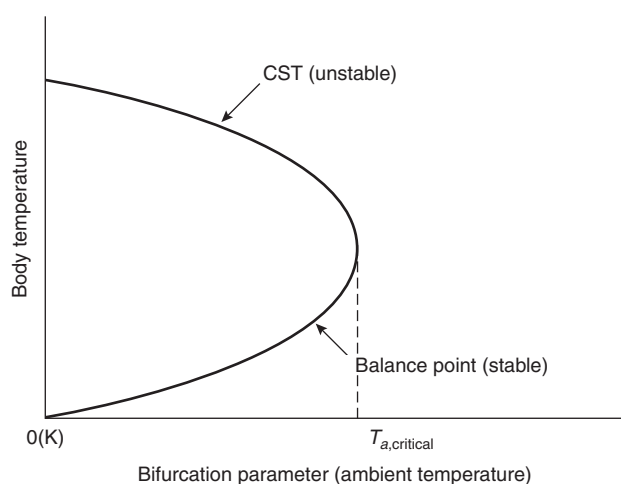


Figure 2-10.3. Variation of CST and stable subcritical temperature with ambient temperature, fixed body size.

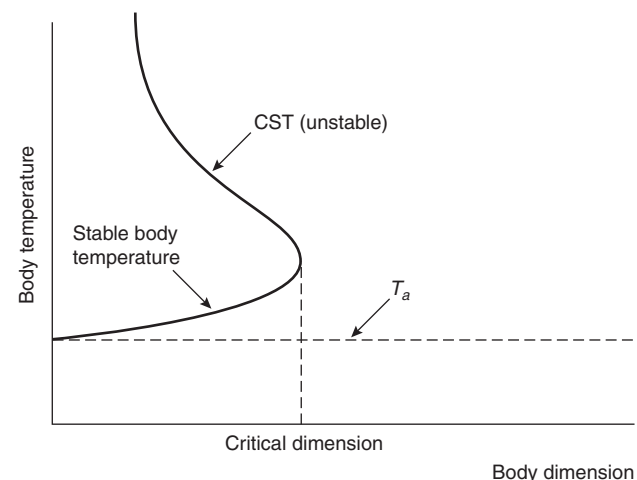


Figure 2-10.4. Variation of CST and stable subcritical temperature with body dimension, fixed ambient temperature.

sus critical ambient temperature graph, and we will see how to do this later.

The whole discussion above assumes that we are dealing with a given material so that the thermal and chemical properties do not vary. The effects of varying thermal conductivity, heat-transfer coefficients, and density on the critical condition are also important but only when comparing different materials. The dependence of the critical condition on these properties will be enunciated in a later section.

One final point needs to be mentioned here. The Arrhenius function does actually level out to an asymptote at very high temperatures, which are off the scale in Figures 2-10.1 and 2-10.2. Thus, theoretically there is another balance point at very high temperature, but in fact this point is not physically significant as it usually occurs at many thousands of degrees, well beyond the region where the assumptions of the model are valid. It also gives rise to a high temperature branch of the curves in Figures 2-10.3 and 2-10.4, which is disjoint from the curves shown. Again it can be ignored from the point of view of low-temperature spontaneous ignition.

The Semenov (Well-Stirred) Theory of Thermal Ignition

The Semenov Theory represents the simplest mathematical formulation of the ideas presented above in qualitative form. As such it is a valuable introduction to quantitative aspects of spontaneous ignition without introducing the technical difficulties associated with more elaborate forms of theory where spatial variations of temperature and reaction rate within the body are considered. The assumptions for this theory follow.

1. **The temperature within the reacting body is spatially uniform:** A spatially uniform temperature implies either that the material of the body is well stirred (i.e., it would

have to be liquid or gas) or the resistance to heat flow within the body is so low compared to that within the container or boundary that it can all be assumed to be concentrated within the boundary. The latter results in a temperature discontinuity at the boundary of the material and is a good approximation in deliberately stirred fluids.⁸

It is not a good approximation for materials of vegetable origin where thermal conductivities of materials such as cellulose are low and of the order of 0.05 W/mK. Nevertheless, even for such materials semiquantitative conclusions can be drawn from this theory if the spatially averaged temperature of the body is used.

2. The heat generation is assumed to be due to a single chemical reaction of simple integral order: This assumption is often a reasonably good approximation, particularly when a "lumped" or empirically determined rate law has been measured independently. It does not mean that the chemical reaction taking place is only a single step reaction. In fact this empirical approximation works quite well in many cases that are not single step reactions.

3. Both the heat of reaction and activation energy are assumed to be sufficiently large to support ignition behavior: The reasons for these assumptions will become clearer later, but it is intuitively obvious that if there is zero heat of reaction, ignition cannot occur. Likewise with zero activation energy (acceleration of reaction rate with temperature increase), ignition cannot occur either.

With these assumptions we can write down two equations that determine the temperature and fuel concentration as functions of time (but uniform in space). These are simply the conservation of energy and the kinetic rate law respectively. They are

$$C_v \rho V \frac{dT}{dt} = VQf(c)e^{-E/RT} - S\chi(T - T_a) \quad (1)$$

$$\frac{dc}{dt} = -f(c)e^{-E/RT} \quad (2)$$

where

C_v = heat capacity at constant volume

ρ = density

V = volume

T = temperature of the reacting material (in K)

T_a = ambient temperature of the surroundings (assumed constant in time)

Q = heat of reaction per unit concentration of fuel

$f(c)$ = kinetic rate law

c = concentration of fuel

E = activation energy of the reaction

R = universal gas constant

S = surface area of the interface across which heat is lost to the surroundings

χ = heat transfer coefficient

The independent variable is time.

The first term on the right side of Equation 1 represents the rate of heat generation by the self-heating reaction. The second term represents the heat lost to the surroundings. The left side represents the difference between these two. Equation 2 simply expresses the fact that as the reaction proceeds, the concentration c decreases as the fuel is used up. The commonest and simplest form for $f(c)$ is Zc where Z is known as the preexponential factor, a constant. This case is known as a first-order reaction. These two terms are shown graphically in Figure 2-10.1 for any particular value of c .

Despite their apparent simplicity these two equations are not soluble by classical methods, so we cannot write down their solution. Nevertheless, we can in fact write down the critical condition exactly (and other important quantities) using bifurcation theory. We will illustrate this for the simplest possible case only, remembering that it can also be done for more realistic and complicated cases as well as within the confines of the Semenov theory.

First we write Equations 1 and 2 in dimensionless form (see nomenclature for details):

$$\frac{du}{d\tau} = ve^{-1/u} - \ell(u - u_a) \quad (3)$$

$$\frac{dv}{d\tau} = \varepsilon ve^{-1/u} \quad (4)$$

where u and v are dimensionless temperature and fuel concentration, respectively, and ε is a dimensionless version of the ratio C_v/Q ; that is, it is a measure of the amount of fuel decomposition required to produce a temperature rise of 1°C. τ is a dimensionless time and ℓ is a dimensionless heat transfer coefficient.

The most frequently used version of this theory, without fuel consumption, corresponds to taking the limit $\varepsilon \rightarrow 0$, thus maintaining v at its initial value v_0 . We have only a single equation to deal with now, that is,

$$\frac{du}{d\tau} = v_0 e^{-1/u} - \ell(u - u_a) \quad (5)$$

Even this much-simplified equation is not analytically soluble. However, it relates exactly to Figure 2-10.1 and can be used to calculate the critical condition readily. We first note that the balance points in Figure 2-10.1 must satisfy the equation

$$v_0 e^{-1/u_s} - \ell(u_s - u_a) = 0 \quad (6)$$

For subcritical values of the ambient temperature, this equation will have three solutions for a given set of parameter values, v_0 , u_a , and ℓ . From Figure 2-10.1 it can be seen that at the critical condition ($T_{a,\text{critical}}$ corresponding to $u_{a,\text{cr}}$) not only do the two terms of Equation 6 balance, but their slopes also balance at this condition. Mathematically this means that their differential coefficients with respect to temperature must also be equal, that is,

$$\left[\frac{\partial(v_0 e^{-1/u})}{\partial u} \right]_{u=u_s} = \frac{v_0 e^{-1/u_s}}{u_s^2} = \ell \quad (7)$$

The critical value of u_s is then obtained by solving Equations 6 and 7 simultaneously, which interestingly can be done in closed form simply by eliminating the exponential, leaving a quadratic equation:

$$u_{s,\text{cr}}^2 - u_{s,\text{cr}} + u_{a,\text{cr}} = 0 \quad (8)$$

From our definition of $u = RT/E$ and the general knowledge that $R/E \approx 0.0001$ for most combustion reactions, we can see that at normal ambient temperatures for ignition we will have $u_{a,\text{cr}} \approx 0.02$, or in any case $u_{a,\text{cr}} \ll 1$. Using the standard formula for the solution of a quadratic equation and expanding the radical occurring, we can derive

$$u_{s,\text{cr}} = u_{a,\text{cr}} + u_{a,\text{cr}}^2 + \dots \quad (9)$$

which is the lower of the two roots (the upper one is unphysical).

If we substitute this back into either Equation 6 or 7, we get a relationship between the parameters of the problem *which holds at criticality only*. Thus if we use Equation 6, we obtain, after some rearrangement,

$$\ell_{\text{cr}} = \frac{v_0 e^{-1/u_{a,\text{cr}}(1+u_{a,\text{cr}})}}{u_{a,\text{cr}}^2 (1 + u_{a,\text{cr}})^2} \quad (10)$$

We can interpret this equation in a number of ways. Since ℓ_{cr} involves the size of the body as the only physically variable parameter, and v_0 is proportional to the bulk density of the material, we can take this equation to give us the critical size body for a given ambient temperature and bulk density. $u_{a,\text{cr}}$ is the only parameter here that cannot easily be made the argument of the equation.

Converting Equation 9 into dimensional form quickly gives us the relationship:

$$T_{s,\text{cr}} - T_{a,\text{cr}} \equiv \Delta T_{\text{cr}} \equiv \frac{RT_{a,\text{critical}}^2}{E} \quad (11)$$

at the critical condition. ΔT_{cr} would typically be 20–30°C for ambient temperatures around 30–40°C. Not surprisingly, it is independent of the body shape, being dependent only on the total surface area through which heat is lost. Nevertheless, even this oversimplified result can be very useful in an emergency situation. If E is not known, it is a useful rule of thumb (especially for agricultural cellulosic materials) that self-heating of more than 30°C above ambient, that is, typically a body temperature of more than 60–70°C, represents imminent spontaneous ignition whereas an internal body temperature of 35–40°C represents subcritical heating that is unlikely to run away but quite likely to lead to degradation of the material.

Two further points need to be made before leaving this simplified model. First, in order that Equation 8 has real roots, it is necessary to require that

$$E \geq 4RT_{a,\text{critical}} \quad (12)$$

Physically this means that the chemical heat generation rate is sufficiently accelerative to produce the phenomenon of criticality. If it is not satisfied, there is only a single

stable balance point for all conditions and no abrupt change in behavior can occur.

Second, if we examine Equation 10, the critical condition, we should note that where the concentration v_0 appears, in the case of gases we would normally convert this to pressure. Thus in this case Equation 10 gives a relationship between ambient temperature and pressure at the critical condition. This relationship is the familiar explosion limit curve extensively used in the study of gaseous explosions.

Inclusion of Fuel Consumption

If we do not make the assumption $\epsilon \rightarrow 0$ in Equation 4, the clear distinction between subcritical and supercritical behavior no longer exists. We can no longer define the critical condition as the disappearance of two balance points. Equations 3 and 4 possess only a single balance point, $u = u_a$, and $c = 0$ for all possible parameter values, and this refers to the equilibrium state when all fuel has been exhausted and nothing is happening—clearly a condition of no interest. For the definition of criticality in such a case, it is helpful to examine the *experimental* or *phenomenological* definition. The experimentalist determines the critical condition by performing various tests at differing ambient temperatures (we will outline the details of test procedure in a later section) and by measuring the temperature/time history at the center of the sample. They will plot the maximum temperature attained against ambient temperature and will find there is a steep increase in slope over a narrow region of ambient temperature. The result is illustrated in Figure 2-10.5.

The distinction between points 1 and 2 is very clear both in terms of the maximum temperature attained and the physical condition of the material itself after the test is finished. Typically, at point 2 the material is hardly different visually from the initial condition, whereas at point 1 there is usually no more than a small amount of ash remaining. The temperature attained at point 1 is often of

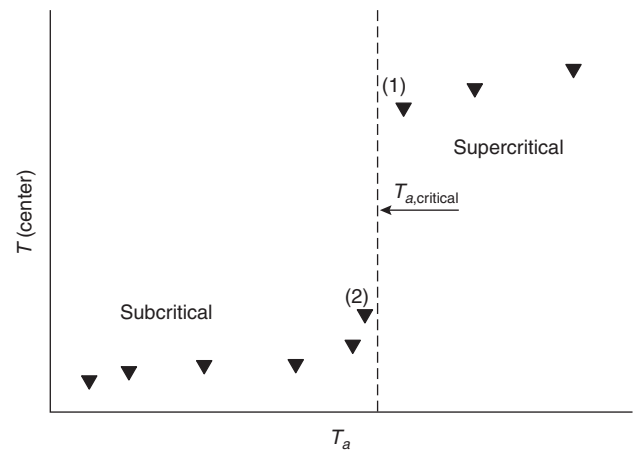


Figure 2-10.5. Typical experimental results for criticality tests.

the order of hundreds of degrees above ambient compared with probably 30 degrees above ambient at point 2.

It is impossible to get points between 1 and 2 experimentally without wasting a great deal of time due to the extreme sensitivity in this region, so the convention is to define the CAT as the arithmetic mean of $T_{a,\ell}$ and $T_{a,2}$. With good equipment these will only be 3 or 4 degrees apart at the most.

From the point of view of theoretical calculation of the CAT in this case, we note that the points in Figure 2-10.5 can be joined by a smooth curve with a very steep region around an inflection point. It has been shown⁹ that this definition of the CAT, when fuel consumption is significant, leads to a relation between the usual parameters, and this relation passes over smoothly to the one derived from the tangency condition as $\epsilon \rightarrow 0$. For $\epsilon \approx 0.05$ or less, which is the case for most practically important materials, the corrections arising from fuel consumption are not usually significant. This result is especially the case in fire investigations where a posteriori numerical knowledge of parameter values is rather limited, and this correction (and others) is not justified.

Extensive discussion of earlier work on the fuel consumption correction is given in Bowes's book.⁴ Many empirical and semiempirical corrections were devised based on approximated integration of Equations 3 and 4. These corrections will not be discussed here since the advent of powerful PC and laptop computational capabilities has rendered them irrelevant. Equations 3 and 4 can be integrated with great speed and precision if accurate parameter values are available. Even so, it is necessary to have a definition of criticality when a computed or experimental version of Figure 2-10.5 has been obtained. With the definition given in Reference 9, allied with numerical integration, the problem can be regarded as solved for all practical purposes.

Extension to Complex Chemistry and CSTRs

Complex Chemistry

Other than elementary gas phase reactions, very few examples of chemical change occur via a single step as assumed above. As already remarked, the simple theory is more useful than might be expected because many complex chemical reactions behave as if they were a single step, over limited temperature ranges. This is usually because a single step does dominate the heat production rate, for example, when two reactions occur in parallel. If the activation energies are rather different, they will each in turn dominate the heat generation in two different temperature ranges and in each of these ranges the simple theory will hold. Of course, it will not hold in the changeover region.

Another case where the simple theory can hold unexpectedly is when a number of reactions are in series and one is particularly slow. The slow reaction will determine the overall heat generation rate and its parameters will dominate the critical condition. If none of the above conditions hold, it is still possible to derive a generalization of the theory that is conceptually very closely related. It is

possible to prove¹⁰ that if the heat release rate is defined as the sum of the heat release rates of all reactions taking place in the system, then the critical condition can be defined as the tangency of this quantity with the heat loss line. Thus a diagram like Figure 2-10.1 can be drawn and the same constructions used, provided the total heat release curve for all the reactions is used.

The heat release curve in this case can have a complex shape, and thus *more than one* critical condition can occur. This state of affairs is extremely important in the ignition of most organic vapors, particularly hydrocarbons⁵ where some critical conditions occur on *decreasing* the ambient temperature. Also in the ignition of some commonly occurring solids, particularly when wet, more than one heat-generating reaction can be important, for example, in the spontaneous ignition of moist bagasse.¹¹ In this case there are two critical conditions, one where a jump from virtually no self-heating to self-heating of $\sim 35^\circ\text{C}$ occurs, and a second critical condition where this intermediate state jumps to full-fledged ignition. Modeling of such situations is possible but beyond the scope of this chapter; however, similar behavior is likely to occur in other moist cellulosic materials, including hay, chipboard, and so forth.

At this stage it is worth pointing out that for bagasse at least, microbial "heat production" is not a factor in these phenomena. Although natural bagasse contains large numbers of microorganisms, sterilization by various methods *does not affect heat production or self-heating* at all, as measured by Dixon¹² and predicted on the basis of bacterial microcalorimetric data by Gray.¹³ Similar work on hay is under way.

CSTRs and Thermal Runaway

Strangely, this topic has become uncoupled from work on spontaneous ignition over recent years even though the basic principles and mathematical methods used are similar. It is a huge problem in the chemical process industry and receives much attention. For example, in 1998 the Joint Research Centre of the European Commission, Institute for Systems Informatics and Safety, produced a book describing the proceedings of a European Union seminar held in Frankfurt in 1994 that managed to avoid almost completely any reference to the fundamentals of the problem or related material. *Risk analysis* appears to have replaced fundamental scientific understanding in some aspects of this problem.

We will confine ourselves here to writing down the basic equations governing a single exothermic chemical reaction taking place in a CSTR (continuously stirred tank reactor) to exhibit their similarity to the equation describing a spontaneously ignitable material, that is, Equations 3 and 4.

The appropriate equations for this case are in fact 3 and 4 with terms representing inflow and outflow of reactants and products, that is,

$$V\rho C_v \frac{dT}{dt} = QVf(c)e^{-E/RT} - S\chi(T - T_a) - FC_v\rho(T - T_f) \quad (13)$$

$$V \frac{dc}{dt} = -Vf(c)e^{-E/RT} + F(c_f - c) \quad (14)$$

F is a volumetric flow rate and the subscript f refers to feed values. These equations can be cast in dimensionless form also. Here we simply note that they possess steady-state (balance point) solutions without making any approximations at all (such as neglect of fuel consumption) and Figure 2-10.1 can be applied directly in slightly modified form. The critical condition referred to earlier occurs here also, but it can now be stated in terms of the CAT or a critical feed temperature or, indeed, a critical flow rate.

A critical size also occurs and is particularly prominent in CSTR considerations where "scaleup" from prototype size to commercially viable size has resulted in exceeding the critical condition. Some references to scaleup are given in Reference 1, and there are many more in the chemical engineering literature and the study of self-heating in catalyst particles. See Aris¹⁴ for an excellent discussion of this area.

The Frank-Kamenetskii Theory of Criticality

In its original form the Frank-Kamenetskii theory included a more realistic model of heat transfer within the reacting solid, that is, by incorporating the heat conduction law of Fourier. This law allows a calculation of the variation of temperature within the self-heating body itself and allows comparison of measured and calculated self-heating to take place. However, it sacrifices the simple description of time-dependent behavior given by the Semenov model because such considerations involve the solution of partial differential equations. This is now much faster than even a few years ago, in terms of numerical computation, and improving day by day. Nevertheless, such numerical solutions do not lend themselves to simple interpretation even with the use of rapidly developing file visualization techniques. Construction of appropriate meshes for finite element computation, necessary for practically occurring three-dimensional shapes, is also far from trivial.

As a result, the Frank-Kamenetskii theory is still mainly used for interpretation of testing experiments on self-heating and subsequent evaluation of parameters for individual systems. This is a viable proposition for materials with sufficiently large heats of reaction and activation energies. In such cases we shall see that the stationary (in time) conditions assumed in the Frank-Kamenetskii theory are indeed well approximated for the duration of typical tests in practical cases. In its original form this theory also neglects fuel consumption, as does the Semenov theory, with similar consequences. With these assumptions the equation describing the theory is

$$\kappa \nabla^2 T + Qf(c_0)e^{-E/RT} = 0 \quad (15)$$

with the boundary condition $T = T_a$ on the wall(s) of the body. T_a is the ambient temperature of the surroundings. This boundary condition assumes instantaneous transfer of heat from the surface of the body to the surrounding medium (usually air). When this is not approximately correct, very important consequences follow, as we shall see in a later section on the interaction of self-heating bod-

ies with each other. In this formulation the shape of the body and its size both enter the mathematical formulation through the boundary condition only.

As usual, Equation 15 is not analytically soluble. However, by using an approximation to the Arrhenius function (Frank-Kamenetskii¹⁵), the modified equation can be solved analytically for a one-dimensional infinite slab of material. This same approximation was later shown to be analytically soluble for an infinite cylinder by Chambre.¹⁵

With this approximation, Equation 15 takes the form:

$$\nabla^2 \theta + \delta e^\theta = 0 \quad (16)$$

with $\theta = 0$ on the boundary. θ is a dimensionless temperature defined by

$$\theta = \frac{E(T - T_a)}{RT_a^2} \quad (17)$$

that is, it is a measure of the temperature excess within the body at various points. The dimensionless parameter δ is defined by Equation 18:

$$\delta = \frac{QEr^2 f(c_0) e^{-E/RT_a}}{\kappa RT_a^2} \quad (18)$$

where the symbols are already defined apart from r , which is usually one-half of the smallest dimension of the body, that is, the radius of a cylinder, the radius of a sphere, or the half-width of a slab. Mathematical treatment of Equation 16, whether it is exactly soluble or not, indicates that a solution satisfying the boundary conditions exists only when $\delta \leq \delta_{\text{critical}}$ where δ_{critical} is some number depending on the shape of the body only. For an infinite slab of material $\delta_{\text{critical}} = 0.878$ and for an infinite cylinder it has the value 2.000. For other shape bodies the critical value has to be obtained either numerically or by semiempirical methods outlined in some detail by Bowes.⁴ For convenience, a few of the values are listed in Table 2-10.1.

The tabulation of figures for infinite slab or infinite square rod is useful in so far as they are often rather good approximations for real bodies, provided one or more of their dimensions are much larger than the others. Thus for the rectangular box, if we take $r = l = 1$, $m = 10$, we get

Table 2-10.1 Values of δ_{critical} for Various Geometries

Geometry	Dimensions	δ_{critical}
Infinite plane slab	Width $2r$	0.878
Rectangular box	Sides $2l, 2r, 2m$; $r < l, m$	0.873 $(1 + r^2/l^2 + r^2/m^2)$
Cube	Side $2r$	2.52
Infinite cylinder	Radius r	2.00
Equicylinder	Height $2r$, radius r	2.76
Sphere	Radius r	3.32
Infinite square rod	Side $2r$	1.700

$\delta_{\text{critical}} = 1.75$ compared to 1.700 for the infinite square rod. If we now look at Equation 18 for the particular case of a cube as an example, we get

$$\frac{QEf(c_0)r^2e^{-E/RT_{a,\text{critical}}}}{\kappa RT_{a,\text{critical}}^2} = 2.52 \quad (19)$$

at the critical condition. We have a number of choices as to interpretation of this equation depending on which parameter can be made the argument. If r is chosen as the argument, then the equation would be interpreted as giving a critical size for the body at a fixed ambient temperature T_a . Since c_0 depends on the density of the material, Equation 19 could be rearranged to give a critical density for that particular size body at ambient temperature T_a . What is not possible is isolation of T_a as the argument of the equation, and this is often the most easily varied parameter in a typical test oven.

This complex dependence of the critical condition on T_a is dealt with by rearranging Equation 18 and taking natural logarithms as follows:

$$\ln \left[\frac{\delta_{\text{critical}} T_{a,\text{critical}}^2}{r^2} \right] = \ln \left[\frac{QEf(c_0)}{R\kappa} \right] - \frac{E}{RT_{a,\text{critical}}} \quad (20)$$

from which it can be seen that a plot of $\ln(T_{a,\text{critical}}^2/r^2)$ against $1/T_{a,\text{critical}}$ will be a straight line with slope $-E/R$ and intercept $\ln[QEf(c_0)/\kappa R \delta_{\text{critical}}]$. The traditional and recommended test protocol for spontaneous ignitions makes explicit use of this logarithmic form of the critical condition. Not only does it yield the activation energy from the slope, but the occurrence of a straight line plot assures us that the assumption of an Arrhenius temperature dependence for the heat-generating reaction is correct over the temperature range investigated.

Equation 20 can also be regarded as a scaling law, in principle enabling the prediction of CATs for large-scale bodies from measured CATs for much smaller laboratory-sized samples. However, as we shall see, it is necessary to ensure that the same chemical kinetics applies over the whole temperature range involved. Finally if it becomes necessary to estimate the CAT for a complex shape, not included in Table 2-10.1, an excellent and comprehensive discussion of approximation methods is given by Boddington, Gray, and Harvey.¹⁶

Experimental Testing Methods

Experimental testing methods are traditionally based on the scaling relationship (Equation 20). Appropriate containers (usually stainless steel gauze baskets) of various dimensions are used, being limited only by the size and heating capability of an accurately thermostatted oven, which must also have a spatially homogeneous ambient-temperature distribution ($\pm 1^\circ\text{C}$ is recommended). The gauze containers may be any convenient shape, equicylindrical or cubic being preferred due to ease of construction. The gauze does not restrict oxygen ingress through the boundary, nor does it restrict egress of carbon dioxide and other product gases during combustion. If the air inside the oven is sufficiently turbulent, usually the boundary conditions of the Frank-Kamenetskii theory will hold quite well.

The boundary condition is easier to satisfy when the thermal conductivity of the material inside the gauze baskets is relatively low, as it is with many agricultural materials containing cellulose ($\kappa \sim 0.05 \text{ W/mK}$). The efficacy of the boundary condition is determined by the heat transfer rate from the gauze to the oven air relative to the conduction rate within the material itself. This ratio ($\chi r/\kappa$) is known as the Biot number, and the larger it gets, the more accurate the Frank-Kamenetskii boundary condition ($T = T_a$) becomes. In practice a Biot number greater than 30 is effectively infinite as the CAT becomes extremely insensitive to it. We will return to this topic in a later section where the dependence of the critical condition on the Biot number is outlined.

The test procedure involves starting with the smallest basket and a trial oven temperature. The sample is equipped with one or more fine thermocouples placed at the center of the sample and, if desired, at various places along a radius if a spatial profile is wanted (this is generally not necessary). The sample is placed in the pre-heated oven and the center temperature followed as a function of time. If the oven temperature is well below the CAT, the sample will simply approach the oven temperature asymptotically. If it is slightly below, but getting close, it will cross above the oven (ambient) temperature and attain a maximum of the order of 1–30°C above ambient before declining. This oven temperature represents the subcritical condition.

The sample is discarded and replaced with a fresh, similar one. If the previous run was subcritical, the oven temperature will be increased usually by 20°C or less depending on the experience of the operator. The run is then repeated. If it is still subcritical, the procedure is again repeated until a supercritical oven temperature is attained. The arithmetic mean of the lowest supercritical temperature and the highest subcritical temperature is taken as the first estimate of the CAT. The uncertainty may be quite large at this stage, so the process is usually continued by testing at the estimated CAT. The process is repeated, halving the difference between highest subcritical and lowest supercritical temperatures each time until the desired errors are obtained. Typical temperature/time plots showing the critical separation are shown in Figure 2-10.6.

This reaction is an exothermic decomposition evolving oxygen. From these measurements one would conclude that the CAT was $55.2 \pm 1.34^\circ\text{C}$. For greater accuracy the next test would be run at an ambient temperature of 55.2°C . After at least four or five such sets of runs have been carried out in differently sized containers, giving four or five CATs at various radii, then the next step is to construct the Frank-Kamenetskii plot of the scaling Equation 20. A typical plot is shown in Figure 2-10.7.

This plot shows a range of CATs for cylinders ranging in radius from 0.191 m down to 0.026 m, the larger radii corresponding to commercial containers. From the slope of this line, E/R can be read off directly and from the intercept; so can the dimensionless group occurring in the scaling equation. Sometimes components of this group may be known from independent measurements, for example, Q from calorimetry, κ from direct measurement, or $f(c_0)$ from kinetic measurements, in which case all the parameters can be obtained.

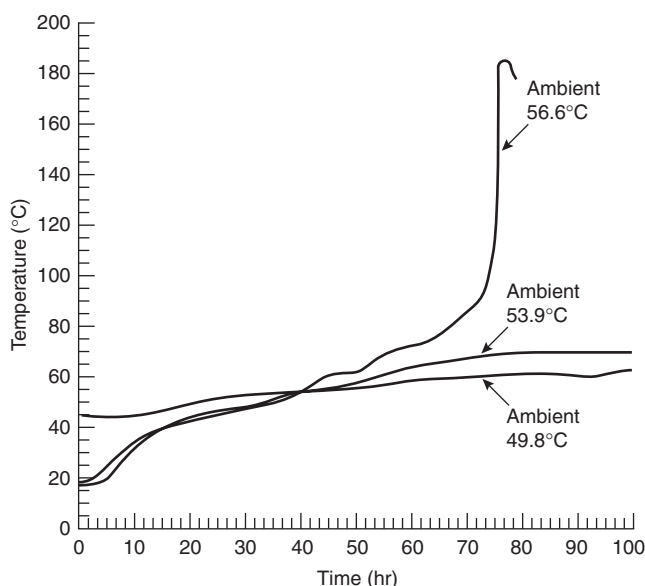


Figure 2-10.6. Two subcritical and one supercritical center temperature/time traces for a 0.175-m-radius equicylinder of hydrated calcium hypochlorite.¹⁷

Special Cases Requiring Correction

The Presence of Water

When water is present in spontaneously combustible material, special considerations apply. First it is necessary to note that endothermic evaporation would be expected to partly offset some of the heat generation by the exothermic reactions taking place. While this expectation is true, it is often the case that at the high oven temperatures used in testing small samples, the low activation energy for evaporation (~ 40 kJ/mol) leads to rapid evaporation before the exothermic process has got fully under way. Many spontaneous combustion reactions

have activation energies around 100 kJ/mol, particularly the group of reactions of cellulosic materials.

As a result, the high temperature CATs reflect the properties of the dry material, in particular the thermal conductivity. Consequently, extrapolations to temperatures well below 100°C will be questionable for this reason alone. In the lower temperature range the heat transfer will be significantly affected by the presence of water and its transport from the hotter to the cooler regions of the body by evaporation, diffusion, and condensation.

Many cellulosic materials are known to exhibit a "wet reaction"^{19,20} in addition to the dry exothermic reaction. This reaction involves liquid water as a reactant and further complicates the picture as far as high-temperature testing is concerned. Simultaneous evaporation, diffusion, condensation, and reaction involving water have been modeled recently in connection with bagasse,^{21,22} using an experimentally measured rate law for the wet reaction²³ giving results that are in good agreement with measured results for commercial-size piles of this material (minimum dimension 5–10 m).

The detailed nature of the wet reaction with a rate maximum around the 50–60°C mark has led to false identification with microbial activity. In bagasse at least it has been shown^{24,25} that microbial activity does not contribute to self-heating to any significant degree. Piles sterilized by various methods showed self-heating rates indistinguishable from those of nonsterile piles. Microbial counts were carried out in all cases and large decreases did not affect the self-heating rates. It would be rather surprising if similar results were not obtained from tests on hay and straw where microbiological activity (but not necessarily heating) are known to occur, and it is surprising that such tests have not yet been carried out.

Parallel Reactions

If more than one exothermic reaction can take place in the material, and these reactions have rather different activation energies, then each will dominate in its own temperature range. Thus the higher activation energy reaction will cut in at higher temperatures and be insignificant at lower temperatures when the low activation energy reaction will dominate the heat generation. The wider the divergence in activation energies, the sharper the discontinuity in slope, that is, the narrower the temperature range over which both will contribute. Hydrated calcium hypochlorite shows a clear example of this, and it is reflected in a sharp break in the slope of the Frank-Kamenetskii plot where the changeover occurs. Figure 2-10.8 shows this plot. The low temperature activation energy for this system is about 48 kJ/mol while that of the higher temperature reaction is around 125 kJ/mol, the transition temperature being around 120°C.¹⁷ Extrapolation of the high temperature line in this case gives CATs for large commercial-size containers that are seriously in error; that is, they are predicted to be much higher than they actually are. In the general case of two reactions with different activation energies, this will always be the case as the high activation energy is "frozen out" at low temperatures and the low activation energy reaction is "swamped" at higher temperatures.

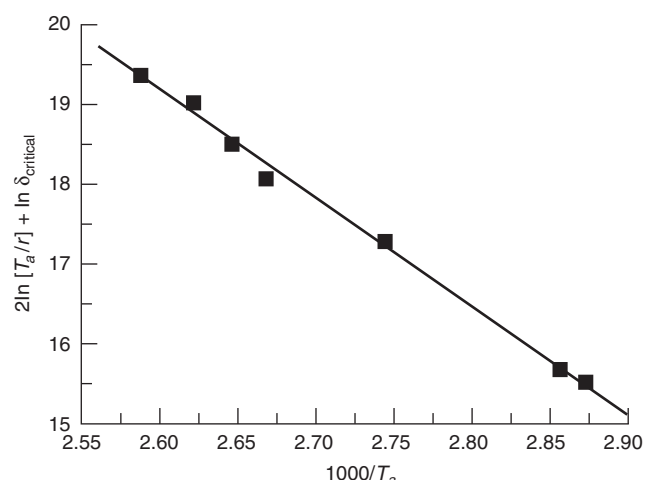


Figure 2-10.7. Typical Frank-Kamenetskii plot for anhydrous calcium hypochlorite from Uehara et al.¹⁸

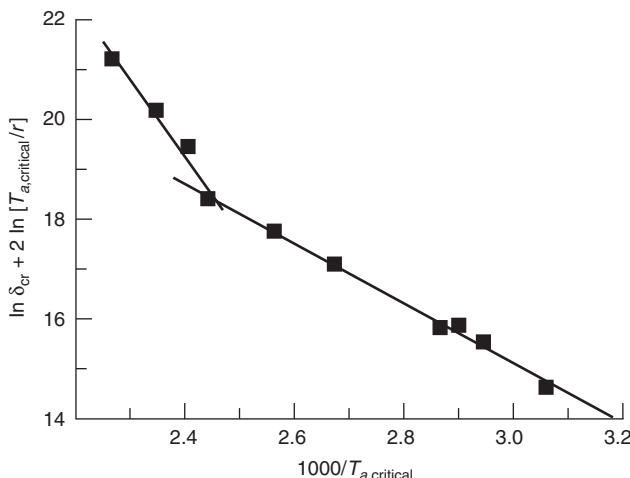


Figure 2-10.8. Frank-Kamenetskii plot for hydrated calcium hypochlorite with reaction mechanism change.

Other examples of mechanism change are known and discussed by Bowes.⁴ In such cases accurate predictions of CATs can still be made within each temperature range. This type of example emphasizes the need for tests covering as wide a range of temperatures as possible. Recent methods put forward as viable alternatives to the standard method, for example, Jones²⁶ and Chen,²⁷ are restricted to either measurement at a single temperature or over a limited temperature range and can give dangerously flawed results. Empirical tests such as the Mackey test²⁸ and the crossover test²⁹ are not reliable and cannot be properly related to the basic principles of spontaneous ignition theory.

Finite Biot Number

The Biot number is defined as

$$Bi = \frac{\chi r}{\kappa} \quad (21)$$

where

χ = surface heat-transfer coefficient

r = smallest physical dimension of the body

κ = thermal conductivity of the material

It is the dimensionless measure of the ratio of the resistance to heat transfer within the body to that from the surface to the surroundings. Thus the Semenov theory is often referred to as *zero Biot number* and the Frank-Kamenetskii theory as *infinite Biot number*. They are both special cases of a more general (and more exact) formulation, as was originally pointed out by Thomas.^{30,31}

In general the boundary condition at the edge of a self-heating body has the form of a *continuity condition*, which refers to the energy flux across the boundary. It states that the energy flux within the body (given by

Fourier's law) and the energy flux from the body surface to the surrounding air must be equal, that is,

$$\kappa \frac{dT}{dn} = \chi(T - T_a) \quad (22)$$

In dimensionless form this becomes

$$\frac{du}{dn} = Bi(u - u_a) \quad (23)$$

This boundary condition does not hold if there exist any heat sources on the boundary of the body itself, as can occur when there is incidence of radiation or when there is heat generated by friction during pulverization of materials capable of self-heating. Such cases (in the shape of an infinite cylinder) have been treated and the modified critical condition obtained.^{32,33}

The values of the critical parameter δ quoted for the Frank-Kamenetskii theory are all for the limiting case $Bi \rightarrow \infty$, and both Thomas and Barzykin have given semi-empirical functions exhibiting the dependence of $\delta_{critical}$ on Bi , which are detailed in the book by Bowes. As the Biot number decreases, so does $\delta_{critical}$ and hence so does the CAT, all compared with the standard Frank-Kamenetskii theory. For Biot numbers >30 , the correction is rather small but is significant for smaller values. Typical heat transfer coefficients from smooth solid surfaces to rapidly stirred air (in a test oven for example) are of the order of 20 W/m²·K, and thermal conductivities of typical cellulosic materials (such as sawdust) are around 0.05 W/m·K, giving a ratio of 400/m. Clearly for laboratory-size test bodies ($r \sim 0.1$ m), the Biot number is rather large.

For this reason a significant amount of work has simply assumed a sufficiently large Biot number without investigation of its actual numerical value. Sometimes the assumption is not justified, particularly where inorganic materials are involved, as their thermal conductivities can be quite large. For example, typical, inorganic salt thermal conductivities lie in the range of 0.2–3.0 W/m·K, giving for the ratio (χ/κ) a value of 7–100/m. Clearly for test bodies with $r \sim 0.1$ m, the Biot number will be only 0.7–10. The effect of the small Biot number on $\delta_{critical}$ is to reduce it by a factor ranging from 0.21 to 0.83, respectively. Clearly for such materials, the more general boundary condition suggested by Thomas must be used, and it is good practice for all but the most strongly insulating materials to estimate the thermal conductivity (particularly in the presence of water) independently of the standard testing regime.

A further important feature of self-heating bodies with finite Biot number is that their CATs will be sensitive to the heat-transfer coefficient from their surface to the surrounding air. Thus the value of the CAT obtained may well be test-oven sensitive and be strongly influenced by air movement. For example, it has been shown for hydrated calcium hypochlorite¹⁷ that in stirred air in a typical test oven the CAT is 60°C for a 0.175-m-radius container, but in still air the CAT is 55°C.

This observation raises serious questions about the value of empirical testing methods such as the SADT test for shipping self-heating materials³⁴ that determines

criticality-related parameters under vaguely defined conditions of forced airflow in a test oven. The results are then used to determine "safe" conditions for shipping such materials in *still air* inside, for example, a shipping container. Almost invariably many self-heating bodies are stacked inside the same still air inside a container, and they will interact with each other to a very significant extent if the transfer of heat through the container wall is not very rapid. In practice such transfer is rather slow, involving two successive air/metal transfers. As a result the self-heating bodies collectively heat the air inside the container and produce a "cooperative CAT," which can be tens of degrees lower than the CAT of a single body. The Semenov-type theory for this collective ignition has been formulated by Gray.³⁵ A more accurate version, where the individual bodies are assumed to obey the general boundary condition put forward by Thomas, has also been formulated (in preparation). The predictions of this theory have been compared to the experimental CAT for 18 14-kg equicylinders packed in a rectangular steel box with good agreement.³⁶ The CAT was reduced from 62.5°C for a single keg in still air to 54°C for 18 kegs in still air.

Times to Ignition (Induction Periods)

The terms *times to ignition* and *induction periods* tend to be used synonymously. Here we will abbreviate to *tti*. This represents the most difficult area of spontaneous combustion in so far as prediction is concerned. There are three principal reasons for this:

1. The theoretical treatment is much more difficult than that of criticality itself.
2. The actual definition has been greatly confused from case to case.
3. The *tti*, however defined, can be extremely sensitive to quantities that have hardly any effect on the position of the critical condition.

Theoretical Treatment

We refer the reader to Bowes⁴ for discussion of earlier treatments. For illustrative purposes we will initially follow Bowes and define *tti* from Equation 5 by integration from ambient temperature to some value u_1 , say,

$$\tau_i = \int_{u_a}^{u_1} [v_0 e^{-1/u} - \ell(u - u_a)]^{-1} du \quad (24)$$

The equation is of course in dimensionless form. Our present interest is the implicit use of u_a as the lower limit; that is, it is the time for the sample to go from ambient temperature to some predetermined arbitrary figure, possibly the maximum temperature attained (it turns out that the integral is not sensitive to this limit, provided it is sufficiently high).

While the maximum temperature attained is a meaningful figure for laboratory tests under some circumstances, it does not always correspond to practical large-scale circumstances. For example, it requires recording the time taken for the center of the sample to heat up

in a test oven to ambient temperature and using this as the reference time for *tti*. Unfortunately, when the center has reached this point, other parts of the body have often attained rather higher temperatures,³⁷ and the subsequent *tti* will be reduced compared to a large-scale body that may well have been built at ambient temperature and be quite uniform initially. Extrapolations of such laboratory tests will not then be reliable since the initial condition will not be appropriate.

The *tti* for the hot stacking problem is qualitatively different from that in which the body is formed uniformly at ambient temperature. Generally this time is *much shorter* than the *tti* for the more common case of initially ambient temperature throughout the body. The reasons have been given, with a comparison of the two cases, by Gray and Merkin.³⁸ Similar considerations apply when part of the body is at a high temperature (hot spot) and this case has been discussed in detail by Thomas.³⁹

With the ready availability of powerful and fast numerical techniques, it is now feasible to integrate routinely the time-dependent heat conduction equation for this problem, which is probably the best solution. Zinn and Mader⁴⁰ were early participants in this effort, and more recently Gray, Little, and Wake³⁷ have noted that such numerical results can be usefully used to predict a very good lower bound to the *tti*. These results are desirable as they err on the side of safety.

Very close to criticality, perturbation treatments have been formulated,⁴¹⁻⁴⁵ but these are mainly of theoretical interest. At the critical condition the *tti* becomes infinite, and close to this condition it is extremely sensitive to the degree of criticality, so unless this is known accurately (hardly ever the case), use of such formulae is not advised.

In addition to the difficulties discussed above, which apply even when only a single simple reaction is assumed, there are others that are largely chemically kinetic. It has long been known that chain reactions, whether branching or not, can exhibit very long induction periods followed by very rapid onset of (sometimes non-explosive) reaction. Many exothermic, spontaneous ignition reactions do possess some chain characteristics even though these do not manifest themselves once the reaction is well underway. Thus it is feasible for complex chain mechanisms to determine the details of the *tti* but not be at all important in determining the critical condition where gross heat balance considerations are crucial. In many cases this leads to extremely irreproducible *ttis* without similar variation of CATs or other properties. In case this list of difficulties leads to an overly pessimistic view of the topic of *tti*, there are some things which can generally be relied on as far as the practical situation of fire investigation is concerned.

Very crudely speaking, notwithstanding the above discussion, the larger the body, the longer the *tti* will usually be. Thus a fire thought to have been caused by spontaneous ignition of a pile of linseed oil-contaminated rags contained in a wastepaper basket will usually appear within a few hours of the rags being placed there. On the other hand, a fire resulting from spontaneous ignition of thousands of metric tons of woodchips would only occur after some months of assembly, assuming the pile was

assembled at ambient temperature. For such bodies it is generally true that the *tti* increases with size in this manner. Accordingly haystacks tend to ignite (if they are supercritical) after a few weeks and coal stockpiles after a few months. However the *tti* can decrease dramatically if the body is very far beyond the CAT.

For hot stacked bodies on the other hand, times are generally much shorter and not particularly sensitive to the ambient temperature. Thus stacks of freshly manufactured chipboard with a volume of a few cubic meters can ignite much more quickly, that is, hours rather than days, than a similarly sized body self-heating from ambient. Beyond these general comments one has to treat each separate case on its merits with a careful eye for exceptions to any general rules. For example, the presence of any catalytic material, such as rusty metal (a common contaminant of many materials), can dramatically decrease the *tti*. This indicates the presence of free-radical or chain reactions and is fairly common, although the CATs and CSTs are only slightly affected.

In summary, in fire cause investigation, where spontaneous ignition is suspected, it is wise to be circumspect about time factors without a thorough investigation and detailed knowledge of the initial conditions likely to have existed when the body was put in place. Even the traditional linseed-oil rag example can be thrown out of the normal pattern by the presence of mineral turpentine, a very common diluent for oil-based stains. The evaporation of this from the rags can greatly prolong the *tti* by virtue of the consequent cooling effect and also the exclusion of air by the vapor. Depending on the circumstances, these factors could add two or three days to a *tti* that would normally be no more than a few hours.

Investigation of Cause of Possible Spontaneous Ignition Fires

From the investigative point of view it is well to list the practical factors which enhance the possibility of spontaneous ignition as a possible fire cause.

The size of the body of material: The larger the size of the body of material, the greater the likelihood of spontaneous ignition. By *size of the body* we mean the parts that are in thermal contact. A large pile of cotton bales with aisles through it would not necessarily be a large body in the thermal sense used here. This classification would be true even if (as often happens), once ignited, fire could spread easily from one section to the next.

High ambient temperatures: Since the air around the body in question has to act as a heat sink, the higher the ambient temperature, the more inefficient is the air as a coolant. Also, direct placement underneath a metal roof or adjacent to a northwest- (southern hemisphere) or southeast- (northern hemisphere) facing wall is a positive factor.

Thermal insulation: Sometimes spontaneously ignitable materials are stored in chemical warehouses or else-

where packed against inert solids that prevent free airflow over the surface, thus reducing heat losses. This effect is evidenced by the appearance of maximum charring or self-heating that is off center and closer to the insulated side of the body. It also results in a reduced CAT.

Fibrous nature and porosity of material: Fibrous or porous materials allow greater access of air than otherwise (solid wood is not subject to spontaneous ignition at normal ambient temperatures, but woodchips and sawdust certainly are!). The concept that packing such porous materials by compression will increase the CAT by oxygen exclusion is badly flawed. This procedure increases the density (thus *lowering* the CAT) and has virtually no effect on the availability of oxygen. During the preflame development, the oxygen requirement is very low; by the time overt flame is observed, there are usually broad channels of destroyed material (chimneys) that will allow ready access.

Pure cotton in a test oven with a nitrogen atmosphere has been shown to undergo spontaneous ignition but with a longer induction period than in the presence of air.⁴⁶ This could be due to adsorbed oxygen on the cellulose fibers or due to exothermic decomposition of the cellulose in the absence of air.⁴⁷

Otherwise "harmless" materials (i.e., liquids with very high flashpoints) can undergo spontaneous ignition at temperatures more than a hundred degrees below either their flashpoints or their so-called autoignition temperatures. The familiar drying oils (flashpoints around 230°C) spread on cotton afford such an example, igniting sometimes at room temperature under the appropriate conditions. In bulk such oils pose little threat of fire causation.

Similarly, hydraulic fluids, specifically designed for nonflammability and with extremely high flashpoints, can undergo spontaneous ignition if allowed to leak onto thermal lagging, such as mineral wool, fiberglass, and so forth, which are characterized by having particularly high surface area. Practical cases of this and experimental tests have been reported by Britton,⁴⁸ with particular reference to ethylene oxide fires. More recently a modeling project has been carried out^{49,50} based on adaptation of the Semenov theory of ignition to a porous solid that was wetted with combustible liquid.

Temperature of stacking: The factor of temperature of stacking is simple—the hotter the worse! The main question is, How hot? The CST (critical stacking temperature) is only weakly dependent on the ambient temperature at low ambient temperatures, but it is sensitive to the size of the hot body. This situation arises with freshly manufactured products such as foodstuffs (milk powder, flour, instant noodles, fried batter, etc.), synthetic materials such as chipboard, cotton bales straight from the ginning process, bagasse straight from the sugar mill, fresh laundry (usually in commercial quantities), and so on.

To evaluate the CST requires full testing to obtain the parameters for the material (such as E , Q , κ , etc.) and then application of one of the methods in the literature for its calculation. Thomas⁵⁹ has given a method for hot spots of material, and Gray and Scott⁵¹ have given a generaliza-

tion of this, removing the approximation to the Arrhenius function made by Thomas. A simpler method of calculation of the CST has been given by Gray and Wake.⁵² It uses a spatially averaged temperature in the Arrhenius function and then obtains exact results for this simplified problem.

Length of time undisturbed: Material that has been in place for longer than usual is reason to suspect spontaneous ignition as a fire cause. Many industrial procedures involve the temporary storage of materials that are *normally* above their CAT but that are not left undisturbed for a period longer than or equal to their *tti*. Thus under normal circumstances fire does not occur even though the *tti* is regularly exceeded. If processes are slowed down for some reason, or storage is prolonged due to vacation, fire can occur even though no other parameters have been changed.

The Aftermath

There are very often characteristic signs of spontaneous ignition even after it has been the cause of a very large fire. Internal charring and ash is very characteristic in cellulose materials. Combustion starts in the well-insulated internal areas of the body, and warm or hot combustion products rise by convection through the path of least resistance (which is not always vertically upward) forming a "chimney" of discolored and partially combusted material. Since large bodies of material are rarely uniform in density or porosity, there can be more than one chimney formed and this is the norm. The occurrence of multiple chimneys and consequent discovery of more than one heavily charred or ashed area inside the body has led to erroneous charges of arson on the basis of the myth that more than one fire seat means the fire was deliberately lit. When a chimney reaches the edge of the body, smoke first becomes visible, then ingress of air causes flame. The latter may engulf more flammable materials in the building, and the whole structure can be destroyed while the spontaneously combustible material may well be chugging away slowly throughout most of its volume. This can even be the case after the fire has been extinguished. The result is then plenty of evidence as to the cause and origin of the fire. The author has measured temperatures as high as 200°C in buried, spontaneously ignited material more than two weeks after the extinction of the fire!

The internal burning of large piles or stacks of material can cause mechanical instability, and often the body collapses inward in the later stages of ignition. This inward collapse can cause some confusion in excavations, which should always be carried out if spontaneous ignition is suspected along with photographic and thermocouple temperature probe records at all stages.

It should be emphasized that the occurrence of significant amounts of unconsumed, spontaneously ignitable material does not mean that spontaneous ignition was not the cause of the fire. Frequently, oily rags are recovered almost intact from the bottom of waste bins that have been

the seat of very large fires. The lower rags tend to be protected from incineration by a layer of char and also by lack of oxygen in the lower reaches of the bin.

Case Histories and Examples

Cottonseed Meal—Living Dangerously

A transit warehouse temporarily storing cottonseed meal to a depth of about 3 m burned down and was completely destroyed. The length and breadth of the building were much larger than the depth of the meal so the relevant physical dimension (for substitution into the formula for δ_{critical}) was 3 m. Spontaneous ignition was suspected because of the known presence of unsaturated fatty acids prone to this. Standard CAT tests for small laboratory samples were carried out, and the extrapolation to lifesize was expected to be reasonably accurate since only small amounts of water were present and wet reaction was not suspected.

The body of meal in the warehouse turned out to be supercritical for the average ambient temperature in the area. The unusual factor in this particular case was the fact that the meal had been left undisturbed for much longer than usual due to a transport strike. It remained in place for longer than the *tti* although under normal circumstances it would have been moved on to customers well before significant self-heating could take place.

In this case an enlightened management installed underfloor ducting to produce a high-pressure air blast capable of rearranging the meal substantially from time to time. A similar solution has long been practiced for coal stockpiles, although in that case the disturbance is usually caused by a front-end loader.

Flaming Instant Noodles

Some years ago an instant noodle factory burned down soon after new management had taken over. New management was not satisfied with the throughput of the production line and wanted higher productivity. The latter was dependent on the speed of a single conveyer belt that conveyed the raw noodles through a hot oil bath, then under a number of powerful fans to remove excess oil and cool the cooked noodles for packing and palleting. Increasing the speed of the conveyer certainly increased the throughput in proportion, but the smaller length of time the noodles spent in the hot oil resulted in incomplete cooking. Thus the oil-bath temperature was increased substantially to compensate for this and again produce fully cooked noodles. However, the faster moving belt was now conveying cooked noodles to the packing area in a shorter time than before and they were also coming out of the fryer hotter than before. The result was that they were packed and palleted at a significantly higher temperature than under previous management.

Although the scientific and technological literature contained no reference to spontaneous ignition of noodles, their porous and oily nature indicated a possibility that this could occur. The suspicion was confirmed by

laboratory tests obtaining the CAT for a particular size noodle block. On this basis a full series of tests was carried out, and the parameters for the noodles obtained from the Frank-Kamenetskii plot in the usual way. With these parameters available it was possible to calculate the CST for a pallet full of noodle packages as these were shrink wrapped onto the pallets and completely encased in plastic, that is, the whole pallet full of noodles was in fact the body in question. The calculated CSTs (for a range of feasible ambient temperatures) turned out all to lie above the temperatures reached with the old process parameters but well below the temperatures reached with the new high-productivity parameters. The "bean counters" managed to achieve a productivity of zero until the factory was rebuilt.

Bagasse Storage—Some Complex Chemistry

The sugar industry in Australia wished to use bagasse containing the usual 50 percent moisture as a biomass for cogeneration of electricity as large excess tonnages are produced biannually. Removal of moisture increases the calorific (and hence monetary) value of the material as a fuel, provided it can be removed at no energy cost. At the same time it has been known for some time that large piles of bagasse are prone to spontaneous ignition and self-heating with consequent loss of value and also considerable pollution from the combustion products. An obviously desirable aim would be to create piles of bagasse that are not large enough to be supercritical but nevertheless large enough to self-heat significantly and hence drive off some of the moisture at no cost. Thus one would turn a dangerous energy release into a benefit. Clearly the balance would have to be just right. Consequently, a major research project was undertaken, both experimental and theoretical.

Application of the standard laboratory test methods to bagasse⁵² results in a prediction of critical dimension for a pile at ambient temperature 30°C, which is an order of magnitude greater than the observed value. This is now known to be due to the fact that laboratory test CATs are above 100°C and simply drive off the moisture before the self-heating can get underway. The extrapolated results are therefore only good predictors for dry piles of material. In practice the water content of bagasse is close to 50 percent on a dry-weight basis, and this has recently been shown to be instrumental in partaking in a heat-producing reaction in addition to the one predominating in the dry material at higher temperatures.^{19,20} This wet reaction has been characterized in isothermal calorimetric measurements over the temperature range 30°C to 90°C, and in this range the high-activation-energy dry reaction is almost completely shut down by the negative exponential in the Arrhenius function.

The wet reaction does not follow an Arrhenius temperature dependence at all, rather having a maximum rate at about 55–60°C. It also has a sharp, almost discontinuous dependence on water concentration, cutting out completely below 20 percent moisture. These characteristics are probably responsible for its occurrence being mistaken for microbiological activity. Inclusion of such complex chemistry in a generalization of the Frank-Kamenetskii

theory for distributed temperatures, as well as the evaporation, condensation, and diffusive movement of water vapor through the pile, results in probably the most complex modeling yet of ignition phenomena.

Nevertheless this model describes quantitatively the behavior of real bagasse piles and answers the questions that led to its creation, that is, How does one choose a pile size in order to maximize the water removal without losing the pile to spontaneous ignition? The modeling is described in a number of publications (e.g., see Reference 11) and shows that present-day computing power coupled with appropriate knowledge of physical parameters enables quantitative or at worst semiquantitative modeling of spontaneous ignition situations with input of realistic chemistry and transport processes. Such developments have also taken place in the modeling of realistic chemistry in gas phase ignition of hydrocarbons and related organic materials dating back to the early work at the Shell Research Laboratories by Quinn et al.⁵³ and pursued by a number of workers, including Westbrook et al.⁵⁴

It seems that we are not far from a situation where the simplified theories that have been useful tools for so long (with their empirical corrections) will be superseded by more detailed calculation of required properties such as CATs and CSTs. Nevertheless, the simplified theories will never lose their pedagogical value and will remain a firm conceptual foundation for more sophisticated models.

Milk Powder—A Numerical Example

The following example was given by Beever.⁵⁵ In a milk-drying plant air entering the spray dryer was heated to 200°C, and it was thought that surfaces in the region of the inlet may also reach this temperature. Any collection of powder on hot surfaces could cause spontaneous ignition, that would not only spoil the product but act as a source of ignition for a dust explosion. These have occurred in milk-drying plants with devastating consequences. Further down the dryer where there was deemed to be a greater likelihood of powder accumulation, surface temperatures of 80°C occurred. Three laboratory basket sizes were tested with half side-lengths of 0.025, 0.0375, and 0.050 m. The CATs of these were 171°C, 156°C, and 141.5°C, respectively. For a cube we can substitute the value 2.52 for δ_{critical} in Equation 20:

$$\ln \left(\frac{\delta_{\text{critical}} T_{a,\text{critical}}^2}{r^2} \right) = 41.85 - \frac{9497}{T_{a,\text{critical}}}$$

We can make r the argument of this equation and then substitute for $T_{a,\text{critical}}$ as required. If we require the critical temperature for a layer of material, we would use the value for δ_{critical} appropriate to an infinite slab, that is, 0.88. For such a flat layer with ambient temperature on each side of 200°C, a critical thickness of 0.017 m is obtained. For the cooler regions of the dryer at 80°C, a critical thickness of 0.4 m is obtained. It was decided that these critical thicknesses were sufficiently realistic to require regular cleaning inside the dryer to remove buildup. This problem is actually more complicated than indicated here since the critical parameters are rather sen-

sitive to moisture content, the critical thickness increasing significantly with moisture content, which can be up to 4 percent.⁵⁶

Nomenclature

C_v	heat capacity at constant volume per unit mass (J/K·mol)
c	concentration (mol/m ³)
c_f	feed concentration in CSTR (mol/m ³)
CAT	critical ambient temperature (K)
CST	critical stacking temperature (K)
E	activation energy (J/mol)
F	feed rate in CSTR (m ³ /s)
$f(c)$	chemical reaction rate (mol/m ³ ·s)
Q	heat of reaction (J/mol)
R	universal gas constant (J/mol·K)
r	characteristic radius
S	surface area (m ²)
T	temperature (K)
T_a	ambient temperature (K)
$T_{a,critical}$	critical ambient temperature (CAT) (K)
T_f	feed temperature in CSTR (K)
tti	time to ignition(s)
u	dimensionless temperature (RT/E)
u_a	dimensionless ambient temperature
V	volume of self-heating body (m ³)
v	dimensionless concentration (c/c_0)
δ	Frank-Kamenetskii parameter
θ	Frank-Kamenetskii dimensionless temperature
ρ	bulk density (mol/m ³)
κ	thermal conductivity (W/m·K)
χ	heat-transfer coefficient (W/m ² ·K)
ε	inverse dimensionless heat of reaction
τ	dimensionless time
ℓ	dimensionless heat transfer coefficient
Bi	Biot number ($\chi r/\kappa$)
$\partial(\cdot)/\partial n$	differential coefficient in a direction normal to the boundary of the body

References Cited

1. *Safety and Runaway Reactions*, Institute for Systems Informatics and Safety, Joint Research Centre European Commission, EUR 17723 EN (1998).
2. N.N. Semenov, *Z. Phys. Chem.*, 48, p. 571 (1928).
3. D.A. Frank-Kamenetskii, *Diffusion and Heat Transfer in Chemical Kinetics*, Plenum, New York (1969).
4. P.C. Bowes, *Self-Heating: Evaluating and Controlling the Hazards*, HMSO, London (1984).
5. J.F. Griffiths and B.F. Gray, *Twenty-Fourth Loss Prevention Symposium*, American Institute of Chemical Engineers, San Diego (1990).
6. J. Taffanel and M. Le Floch, *Compt. Rendus*, 156, p. 1544; 157, p. 469 (1913).
7. G.C. Wake, J.B. Burnell, J.G. Graham-Eagle, and B.F. Gray, 25–37, *Reaction Diffusion Equations*, (K.J. Brown and A.A. Lacey, eds.) Oxford, UK (1990).
8. J.F. Griffiths and J.A. Barnard, *Flame and Combustion*, Blackie, Glasgow, Scotland (1995).
9. B.F. Gray, *Combustion and Flame*, 24, p. 43 (1975).
10. B.F. Gray, *Transactions Faraday Society*, 65, p. 1603 (1969).
11. C. Macaskill, M.J. Sexton, and B.F. Gray, *J. Aust. Math. Soc.*, Series B (2001).
12. T. Dixon, *Proc. Aust. Sugar Cane Tech.*, 53 (1988).
13. B.F. Gray, unpublished.
14. R. Aris, *The Mathematical Theory of Diffusion and Reaction in Permeable Catalysts*, Oxford (1975).
15. P.L. Chambre, *J. Chem. Phys.*, 20, p. 1795 (1952).
16. T. Boddington, P. Gray, and I Harvey, *Phil. Trans. Roy. Soc.*, A270, p. 467 (1971).
17. B.F. Gray and B. Halliburton, *Fire Safety Journal* 35, pp. 223–241 (2000).
18. Y. Uehara, H. Uematsu, and Y. Saito, *Combustion and Flame*, 32, p. 85 (1978).
19. I.K. Walker, W.J. Harrison, and F.H. Jackson, *NZ J. Science*, 21, p. 487 (1978).
20. R.A. Sisson, A. Swift, G.C. Wake, and B.F. Gray, *IMA J. Applied Math.*, 50, p. 285 (1993).
21. R.A. Sisson, A. Swift, G.C. Wake, and B.F. Gray, *IMA J. Applied Math.*, 49, p. 273 (1992).
22. B.F. Gray and G.C. Wake, *Combustion and Flame*, 79, p. 2 (1990).
23. B. Halliburton, Ph.D. Dissertation, Macquarie University, Sydney, Australia (in press).
24. T. Dixon and N. Ashbolt, Sugar Research Institute, Mackay, Queensland, Australia, (1985).
25. B.F. Gray and B. Halliburton, *J. Chem. Tech. Biotech.* (in press) (2000).
26. J.C. Jones, *J. Loss Prevention in the Process Industries*, 12, p. 331 (1999).
27. X.D. Chen and L.V. Chong, *Trans. I. Chem. E.*, 76B, p. 90 (1998).
28. Mackey, W., *J. Soc. Chem. Ind.*, 15, p. 90 (1896).
29. N. Kirov, CSIRO Technical Note, Chatswood, Australia (1954).
30. P.H. Thomas, *Transactions Faraday Society*, 54, p. 60 (1958).
31. P.H. Thomas, *Transactions Faraday Society*, 56, p. 833 (1960).
32. B.F. Gray and G.C. Wake, *Combustion and Flame*, 55, p. 23, (1984).
33. B.F. Gray, A. Gomez, and G.C. Wake, *Combustion and Flame*, 61, p. 177 (1985).
34. "Transport of Dangerous Goods," *Manual of Tests and Criteria*, 2nd ed., United Nations, New York (1995).
35. B.F. Gray, *J. Aust. Math. Soc.*, Series B (in press) (2001).
36. B.F. Gray and B. Halliburton, *Fire Safety Science* (in preparation).
37. B.F. Gray, S.G. Little, and G.C. Wake, *24th International Combustion Symposium*, Combustion Institute, Pittsburgh, PA (1992).
38. B.F. Gray and J.H. Merkin, *Math. Engng. Ind.*, 4, p. 13 (1993).
39. P.H. Thomas, *Combustion and Flame*, 21, p. 99 (1973).
40. J. Zinn and L. Mader, *US J. App. Physics*, 31, p. 323 (1960).
41. T. Boddington, C. Feng, and P. Gray, *J. Chem. Soc. Faraday Trans. 2*, 79, p. 1299 (1983).
42. T. Boddington, C. Feng, and P. Gray, *J. Chem. Soc. Faraday Trans. 2*, 80, p. 1155 (1984).
43. T. Boddington, C. Feng, and P. Gray, *Proc. Roy. Soc.*, A385, p. 289 (1983).

44. T. Boddington, C. Feng, and P. Gray, *Proc. Roy. Soc.*, A391, p. 269 (1984).
45. B.F. Gray and J.H. Merkin, *J. Chem. Soc. Faraday Trans. 2*, 86, p. 597 (1990).
46. S.G. Little, "Spontaneous Ignition Studies," Masters Thesis, Macquarie University, Sydney, Australia (1991).
47. Y.I. Rubtsov, A.I. Kazakov, L.P. Andrienko, and S.B. Manelis, *Comb. Exp. and Shock*, 29, p. 710 (1993).
48. L.G. Britton, *Twenty-Fourth Loss Prevention Symposium*, American Institute of Chemical Engineers, San Diego (1990).
49. A.C. McIntosh and B.F. Gray, *Comb. Sci. and Technology*, 113, p. 503 (1996).
50. A.C. McIntosh, B.F. Gray, and G.C. Wake, *Proc. Roy. Soc.*, A453, p. 281 (1997).
51. B.F. Gray and S.K. Scott, *Comb. and Flame*, 61, p. 227 (1985).
52. B.F. Gray, J.F. Griffiths, and S.M. Hasko, *J. Chem. Tech. and Biotech.*, 34A, p. 453 (1984).
53. M.P. Halstead, A. Prothero, and C.P. Quinn, *Comb. and Flame*, 20, p. 211 (1973).
54. C.K. Westbrook, J. Warnatz, and W.J. Pitz, *22nd Symposium (International) on Combustion*, Combustion Institute, Pittsburgh, PA (1988).
55. P.F. Beever, "Self Heating and Spontaneous Combustion," in *SFPE Handbook of Fire Protection Engineering*, 2nd ed. (P.J. di-Nenno et al., eds.), pp. 2-180-2-189 (1988).
56. C.M. Rivers, "Numerical Studies in Spontaneous Ignition," Master's Thesis, Massey University, Palmerston North, New Zealand (1994).

CHAPTER 11

Flaming Ignition of Solid Fuels

A. Murty Kanury

Introduction

This chapter concerns flaming ignition of solid combustibles that are heated by either thermal radiation or convection. Different kinds of ignitions encountered in practice are defined. The existing empirical knowledge is highlighted by describing Martin's map of spontaneous ignition of radiantly heated cellulosic solids. The various physical and chemical processes that culminate in ignition of a heated solid are identified through a qualitative description and a simplified mathematical model. The typical assumptions underlying a theoretical model are systematically enumerated to point out the complexities involved in the ignition problem.

A number of existing criteria for ignition are examined. Limiting case models are demonstrated to increase understanding of the ignition process. Analysis of the solid-conduction-controlled case, for example, leads to a prediction of the main features of Martin's map. A thumbnail sketch of the gas phase problem, in another limit, confirms the observed influences of the gas phase properties on ignition. Finally, a brief summary is given of the comprehensive analysis of Gandhi. Many existing fragments of knowledge on the ignition problem can now be synthesized into a coherent quantitative description.

The Process of Ignition

A number of aspects of unwanted combustion, in which an understanding of the ignition process is required, can be readily enumerated.

1. An obvious first step in all fire prevention strategies is the ignition-hardening of materials of construction, finishings, and furnishings.

2. Fire spread over combustibles is often viewed as a process of continuous ignition of the successively upstream material.
3. Room fire flashover is believed by many to be a process in which the contents of the room experience a nearly simultaneous ignition.
4. The jump of a forest fire across a firebreak is generally viewed to be a radiant ignition process.
5. Fire growth over noncontiguous surfaces in arrays of combustibles, such as buildings in a city, involves radiant heating to ignition.

Most of the natural and synthetic organic (and some inorganic) solids in air will become ignited in response to an externally imposed heating source. The subtleties of the ignition process—the definition and delineation of different sorts of ignitions, and the qualitative and quantitative understanding of the influence of various physical and chemical factors on ignition—are not always familiar. Kanury¹ and Steward² have presented comprehensive reviews of this subject. The global objective of this chapter is to develop a concise description of the ignition process to achieve enough familiarity with the concepts involved, existing literature and implications of this knowledge in such real-world problems as enumerated above.

Ignition of a heated combustible body marks a stage beyond which the associated fuel/oxidant system is capable of supporting a sustained exothermic reaction. It is necessary to clarify this definition to develop a qualitative picture of the technical problem addressed here and to define the scope of this chapter.

The heated body (i.e., the target) is taken here to be a piece of a cellulosic solid (e.g., wood, paper, cloth, etc.). The concepts are generally adaptable³ to synthetic solids (e.g., the numerous modern polymers popularly known as *plastics*) as well. The physical and chemical characteristics of the body are assumed to be known. Thermophysical (conductivity, density, specific heat, etc.) and geometrical (dimensions, shape, and configuration) properties are

Dr. A. Murty Kanury is professor of mechanical engineering at Oregon State University. His professional activities are centered around teaching thermal science and research in fire and combustion.

physical. The intrinsic thermochemical properties (e.g., pyrolysis kinetics and energetics) are chemical.

Heating is presumed to be externally imposed. It can be radiative (as from a heat lamp, a bank of electrically heated incandescent tungsten filaments, a gas-fired radiant panel, or a nearby flame) and/or convective (as from a hot gas flowing about the body). These two modes of heating will be considered individually to note certain commonalities and differences, although many practical situations involve simultaneous convective and radiative heating.

When a porous reactive solid body is kept immersed in an ambient medium, a runaway self-heating may become possible if the rate of internal reactive energy release exceeds the rate of energy loss from the body to the ambient medium. This sort of self-heating is known to arise in connection with contaminated sawdust, oily shop rags, grain silos, and certain unstable solid propellant storages. The energy loss mechanism is generally conductive and convective. While an enhanced convective transport tends to increase the energy loss rate, it also increases the oxygen mass transfer to the surface and the net effect is quite complex. This type of self-heating problem is addressed in Section 2, Chapter 10.

Smoldering, a familiar fire phenomenon, is defined as a relatively low temperature combustion process within a porous fuel bed. Its inception usually involves a localized ignition source (such as an overheated electrical conductor or a steam pipe) within the fuel bed. The fuel bed porosity plays an important role in smoldering. A highly porous solid (1) implies finely divided, thermally thin fuel elements that are more easily heated conductively, and (2) offers an effective diffusion of the oxidant gas into the interior of the bed. Furthermore, high porosity makes the overall thermal conductivity of a solid quite low and, hence, ignition is easier. Once smoldering ignition begins, the smolder combustion wave propagates into the fresh fuel at a rate governed by thermal conduction in the porous solid and oxidant gas diffusion. It is possible for convection to intrude into this propagation process. The intensity with which this occurs is dependent upon such factors as the porosity itself; if the bounding surfaces are sealed or unsealed; and the direction of propagation relative to the sealed surfaces and to the gravity vector. Under certain suitable conditions, a smolder may suddenly flare into flame. The ignition and propagation of the smoldering combustion and its transition to flaming are addressed in Section 2, Chapter 9.

The combustible may be supplied to the reaction system in a gaseous, liquid, or solid state. It is solids we are concerned with here. All cellulosic and some synthetic solids undergo thermal degradation to yield char and fuel gases. Some other synthetic solids, known as thermoplastics, melt, depolymerize and decompose to yield fuel vapors. Some depolymerization reactions proceed in a manner remarkably similar to the simple physical vaporization of pure liquids.

Because the focus here is on gas phase ignition of charring type solids, there arises a possibility of surface ignition of the char. This type of an ignition marks the inception of glowing combustion of the carbonaceous solid (such as that encountered in carbon and charcoal com-

bustion). The glowing ignition problem is not covered in this chapter.

As an event, ignition occurs at a certain pronounced instant in the history of the exposure. The time to ignition in a given situation depends upon three broadly grouped factors: (1) the degradative thermal response of the solid to yield the combustible gases, (2) the mixing of these gases with the oxidant gas (generally the oxygen of the normal air), and (3) the induction of the temperature- and composition-dependent rate of the combustion reaction to a sufficiently high level to be measurable and self-supporting. Sustainment of the reaction implies that the reaction can self-perpetuate even if the external heating is removed, and can even self-accelerate to grow in space or in intensity at a fixed size. An *exothermic reaction* refers to the combustive oxidation reaction itself. This reaction is called smoldering if it is situated within the subsurface layers of the solid, glowing if at the solid-gas interface, and flaming if in the gas phase.

Ignition in the absence of a pilot source is known as spontaneous, or autoignition. Ignition in the presence of a pilot source (such as a small flame, a heated wire, or an electric spark) in the reactive fuel/air mixture flow is called piloted, or forced ignition. A pilot source is not meant to heat the solid to generate the fuel gases nor to enhance the mixing of the fuel gases with air, but to locally induce the combustion reaction which would propagate into the mixture.

Finally, a distinction should be made between transient and persistent ignitions. Ignition can be produced with a minimum required heating, but the flame would not sustain itself if the external heating is removed. This is transient ignition, akin to the flash point phenomenon in liquid fuel ignition. Substantially longer heating is required to make a flame that would self-sustain, self-perpetuate, or persist even after the external heating is removed. This distinction becomes clearer in the next section of this chapter.

Conduction-Controlled Spontaneous Ignition of Cellulose Due to Radiant Heating—Martin's Map

The large number of experiments on spontaneous ignition of radiantly heated cellulosic solids (insulated back face) has been synthesized by Martin.⁴ (See Figure 2-11.1.) The x -axis is the quantity $i_0\ell/K_s$ where i_0 is the exposure irradiance, ℓ is the target thickness and K_s is the target solid conductivity. Martin calls this quantity normalized irradiance, and its units are those of temperature (K). The y -axis, termed normalized exposure, is $i_0 t / \rho_s C_s \ell$ (where t is exposure time and $\rho_s C_s$ is the volumetric heat capacity of the solid); its units are K.

This ignition map shown in Figure 2-11.1 can be delineated into four distinct regions. The lowermost boundary indicates the minimum exposure intensity and time required to produce ignition. When intensity is low and exposure is long, glowing ignition of a thermally thin body is accomplished. In the upper left region of the map, the thickness of the target specimen is noted to be of

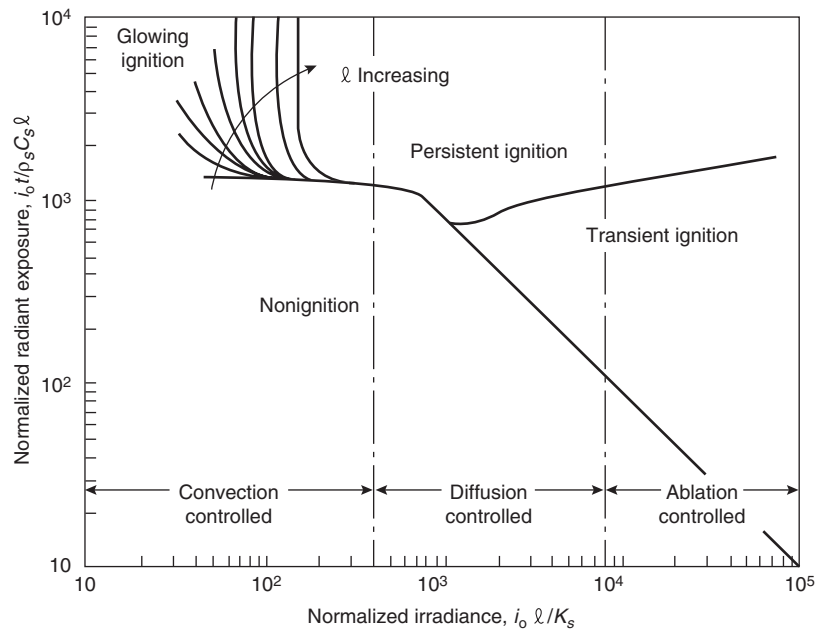


Figure 2-11.1. Ignition behavior of cellulose, showing areas controlled by convective cooling, diffusion of heat into the solid, and ablation of the exposed surface. Martin's map.⁴

consequence—the thinner the specimen, the quicker the ignition. Furthermore, these thin bodies ignite not to yield a flame but to yield glowing combustion of the solid residue. The pyrolyzates not only are limited in quantity but are also released at a rate and time unsuitable for flame evolution.

The middle right region of the map deals with heating of thick targets with moderately high exposure intensities. Flaming ignition will occur within a moderate exposure time but will not persist to yield a self-supporting flame, presumably due to excessive conductive drain of energy into the thick solid and inadequate production of the pyrolyzates. At even higher exposure intensities, the surface is found to experience ablation without ignition.

For the ignition of thick bodies to persist into a flame, significantly longer exposures are required which are nearly independent of the exposure intensity. Martin considered many tests, which led him to draw the boundary line between the transient and persistent ignition regions. The persistence of flames is expected to depend on a purely physical cause such as the sustained evolution of pyrolyzates due to attainment of a certain minimum relaxed temperature by the entire body. Further discussion of Martin's work is presented later in this chapter.

A Qualitative Description

The initial uniform temperature of a vertical cellulosic slab (of known dimensions standing in a quiescent atmosphere of normal air) is perhaps the same as the temperature of the ambient air. (See Figure 2-11.2.) Orientation, geometry, the kind of solid, and the composition and motion of the atmosphere are chosen to consolidate a pic-

ture of the physical and chemical processes leading to ignition. The concept elicited in this qualitative description can be adapted, in principle, to other situations.

The front face of the solid is exposed to a radiant flux from time $t = 0$. In reality, this flux is generally unsteady in the period of exposure, nonuniform over the target surface, and composed of a spectrum of wavelengths. However, it is assumed that the incident flux is steady and uniform, and that the target surface is a diffuse, gray absorber/emitter. Furthermore, the incident flux is radiative

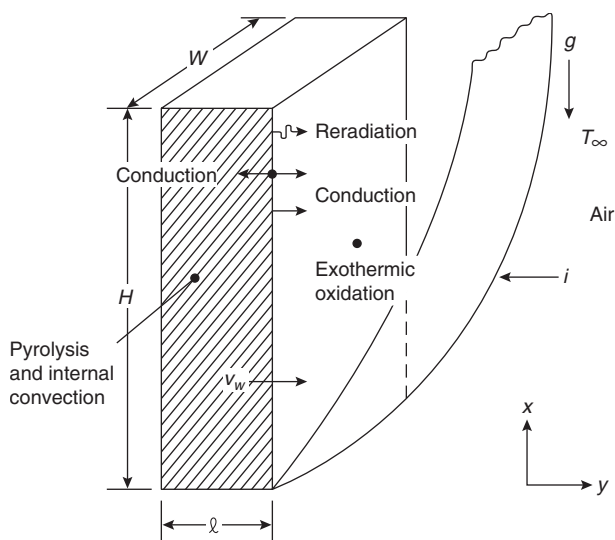


Figure 2-11.2. Schematic representation of the component processes.

alone; the back face of the solid and its edges are taken to be impervious to both heat and mass flows.

Once the exposure is triggered, the interior of the solid is heated by transient conduction. The now hotter surface commences to reradiate energy to the surroundings. Energy is also imparted by the hot surface by transient conduction to the infinite, initially quiescent, adjacent, ambient gas. This heated gas soon responds to buoyancy and forms a transient natural convective boundary layer.

The incident radiant energy is thus partitioned into three components: conduction into the interior of the solid, reradiation to the surroundings, and natural convection to the adjacent gas. All these three components are transient. The energy conducted into the solid initially raises the solid temperature within a progressively thickening "conductive penetration layer." Any free moisture in the solid will be driven away from a layer when it attains a temperature of approximately 100°C. While most of the water vapor released in this manner flows out of the solid, some vapor may migrate towards the cooler interior to augment the heat flux by both convection and condensation. Subsequent evaporation will not only introduce a distinct heat sink but also physically and chemically modify the original solid, which is yet to experience pyrolysis.

There would soon ensue an instant at which layers of the solid near its surface would become sufficiently hot to undergo pyrolysis, leaving a carbonaceous residue (char) behind. With continued heating, progressively deeper layers of the solid become pyrolyzed so that the release of the gas mixture is distributed in space and time. The gas mixture, thus originating at different rates at different depths and time, flows predominantly out through the porous char. This flow introduces an outwardly convective heat flux in the char. The outward flux opposes the inward conductive flux and tends to retard the heating.

Integration of the pyrolysis rate over the thickness of the entire solid yields the total pyrolyzate mass flux issuing at the solid surface into the gas phase. This transpiration tends to thicken the instantaneous boundary layer. The boundary layer flow is generally expected to be laminar since the target size is usually small. This flow will cause mixing of the pyrolyzates with the ambient air.

If the pyrolyzates are either absent or inert, the boundary layer continues to receive heat from the bounding hot solid surface by conduction. The gas temperature profile will then be a monotonically decreasing function of the distance normal to the surface into the gas. If the pyrolyzates are combustible, however, oxidative energy release alters the boundary layer temperature profile to such an extent as to exhibit a temperature maximum in the gas phase at some finite distance from the surface. This nonmonotonic gas temperature profile, at later times, indicates a gas phase conductive heat flux to, rather than from, the solid surface. As the oxidation reaction develops in the boundary layer, the nature of the temperature profile is drastically changed. Spontaneous ignition can be presumed to have occurred in the reactive boundary layer at the instant when the sign of the gas temperature gradient at the surface is reversed. This time to ignition obviously depends upon factors governing the surface temperature, pyrolyzate transpiration rate and

composition, air induction rate into the boundary layer, mixing of air and pyrolysis gases and gas-phase reactions.

This qualitative description applies to spontaneous ignition in the boundary layer, which is defined as a situation where the boundary layer mixture is not only within the flammability limits of composition but also at such a thermal condition that it can react on its own in an accelerating manner and lead to a flame. This description can also be extended to piloted ignition, that is, ignition in the presence of an ignition source such as a small flame, an electrical filament or spark, or an incandescent particle. A boundary layer mixture within the flammability limits of composition is a sufficient condition for piloted ignition. The required energetic strength of the ignition source is a function of several thermochemical and physical properties of the mixture in addition to its composition and temperature. Generally, the pilot source is so small that its contribution to heating and pyrolyzing the solid can be ignored. Changes brought by the pilot source in the boundary layer of the chemical environment can also be ignored. It is customary to consider the ignition source as a localized initiator of the combustion reaction whereupon the reaction wave propagates into the mixture. The ignition theory of premixed gases, however, dictates that the pilot source cannot be infinitely small. The source must exceed the approximate characteristic quenching distance of the ignited mixture.

Mixing of the transpired pyrolyzates with the induced air is a necessary condition for ignition. Turbulence in the boundary layer is obviously desirable to produce this mixing. Spontaneous ignition sometimes occurs in the wake of the target with the (so initiated) flame propagating down into the boundary layer. While mixing the fuel gases and air is a prerequisite for ignition, mixing may also result in thermal dilution (i.e., lowering of the mean boundary layer temperature) which is contrary to the requirements of spontaneous ignition.

The possibility also exists that the pyrolyzate plus air mixture in the boundary layer can selectively attenuate the incoming radiant beam so that the irradiance actually experienced by the exposed surface is substantially less than the level calibrated without the absorbing gas. This phenomenon has implications yet to be understood. First, attenuation is expected to retard the rate of heating and pyrolysis of the solid, and consequently to delay the attainment of an ignitable boundary layer mixture. Second, the attenuation in the boundary layer is expected to become significant only after vigorous pyrolysis of the solid is established to furnish the boundary layer with the attenuating species. Third, the attenuation and absorption is expected to raise the local temperature in the reactive boundary layer to accelerate the oxidation reaction leading to ignition. Finally, this attenuation is expected to occur selectively in certain distinct wavelength regions and hence to depend on the emission characteristics of the radiation source.

It is evident from the present qualitative description of flaming ignition that the total problem is complex and involves difficult features such as: (1) unsteady development of physical and chemical processes, (2) conjugate coupling of the solid and gas phases, (3) chemical kinetics and the associated strong nonlinearities of pyrolysis in the

solid phase and oxidation in the gas phase, (4) moving boundaries, (5) coupling of conservation equations, (6) strongly variable properties. When the lack of well-established input databases for the transport, thermodynamic (and thermochemical), and reaction kinetic properties is superimposed on this complexity, it is imminently clear that all attempts to solve the problem theoretically and apply the predictions to experimental data are prone to extensive approximation. Some of these attempts will be described in a subsequent section of this chapter.

Conservation Equations

In this section, the preceding qualitative description is cast into a mathematical form to identify the assumptions involved. For example, consider a vertical slab of a solid fuel of thickness, ℓ , height, H , and width, W , standing in a quiescent air atmosphere. The solid will occupy $0 \leq y \leq \ell$ and the gas phase, $\ell \leq y < \infty$. (See Figure 2-11.2.) For time $t \geq 0$, the front face $y = \ell$ of the solid is exposed to an irradiance, i . While a part, i_0 , of this flux is absorbed by the solid, the rest of the irradiance is reflected. The absorbed flux is partially conducted into the solid, partially reradiated by the surface to the surroundings, and the rest of the flux is imparted by gaseous conduction to the gaseous boundary layer. These three processes are highly transient. The heated solid undergoes transient pyrolysis, and the pyrolyzates flow out of the solid to mix with air in the boundary layer. At the instant when the mixture composition and temperature are suitable, flaming ignition will occur in the boundary layer. This section of the chapter will describe the estimation of this time to ignition.

A number of simplifying assumptions make the problem formulation easier. The initial temperature of the solid is usually uniform and equal to the temperature of the ambient air. The back face, $y = 0$, as well as all edges of the solid slab, are assumed to be impervious to both heat and mass. The solid surface is taken to be grey and diffuse with uniform radiosity. The imposed irradiance is considered to be constant with respect to time, and uniform over the entire exposed surface. The transient gas boundary layer problem is simpler to deal with in two dimensions, that is, $W \gg \ell$ and H . The transient solid conduction problem is taken to be one-dimensional in the direction of y . The solid is taken here to be initially dry. Absorption of radiation is taken to occur only at the solid surface and not in the layers beneath the surface; that is, diathermancy of the solid is taken to be zero. The char and virgin solid properties are considered to be different but independent of temperature.

A single-step Arrhenius rate law with reaction order equal to unity is generally sufficient to describe the pyrolysis kinetics. The pyrolyzates are viewed to flow through the char with no resistance. Thermal equilibrium between the pyrolyzates and the porous matrix is assumed. Secondary chemical transformation of the pyrolyzates flowing through the char is negligible, as is migration of the pyrolyzates into the cooler interior of the solid.

The air, pyrolyzates, and products of oxidation are taken to behave as radiatively nonparticipating ideal gases. The gas phase density is considered to be constant

in all respects except in producing the buoyancy force (in other words, the Boussinesq approximation is made). Boundary layer approximations are made for the transient free convective gas flow in the vicinity of the heated surface. All gas properties are taken in this discussion to be constants, independent of both the temperature and composition. (This appears to be an overly crude approximation but leads to reasonable results.) Viscous dissipation in the boundary layer is ignored. Cross-diffusion effects in the gas phase are assumed to be absent.

The gas phase oxidation reaction is assumed to follow a simple, single step, second order, Arrhenius rate law. (Since the pyrolyzate composition is known to vary not only with time but also with the heating conditions and precise chemical constituency of the target solid, any further sophistication of these kinetics appears to be unwarranted at present.) Simple stoichiometry relates the sources and sinks of energy, fuel pyrolyzate, oxygen, and the products.

The conservation equations describing this problem follow. For the solid phase, the continuity and energy equations suffice, while the momentum equation is obviated by the assumption of no resistance to flow. Thus,

$$\frac{\partial \rho_s}{\partial t} + \frac{\partial \dot{m}_p''}{\partial y} = 0 \quad (1)$$

$$\begin{aligned} \frac{\partial}{\partial t}(\rho_s C_s T_s) + \frac{\partial}{\partial y}(\dot{m}_p'' C_p T_s) \\ = \frac{\partial}{\partial y}\left(K_s \frac{\partial T_s}{\partial y}\right) + \dot{q}_p''' \end{aligned} \quad (2)$$

where

s = solid

p = pyrolyzate gas mixture

ρ = density

\dot{m}'' = mass flux

C = specific heat

T = temperature

K = thermal conductivity

t = time

y = depth normal to the exposed surface

Equation 1 says that the local spatial gradient of the pyrolyzate mass flux \dot{m}_p'' is equal in magnitude to the local and instantaneous rate of pyrolysis. The terms in the energy equation represent the unsteady energy accumulation rate, internal convective excess flux, conductive excess flux, and the pyrolysis sink, respectively. The constitutive equations for this part of the problem are given by the pyrolysis rate equation and the definition of the energy sink.

$$-\frac{\partial \rho_s}{\partial t} = Z_s(\rho_s - \rho_c) \exp\left(\frac{-E_s}{RT_s}\right) \quad (3)$$

$$\dot{q}_p''' = h_p \left(-\frac{\partial \rho_s}{\partial t} \right) \quad (4)$$

Here ρ_s is the instantaneous, local solid density while ρ_c is the ultimate char density, Z_s is the pre-exponential factor, E_s is the activation energy of the pyrolysis reaction, and h_p is the pyrolysis enthalpy of reaction. The boundary and initial conditions will be discussed later in the chapter.

Let v and u denote the gas velocity components in the normal (y) and longitudinal (x) directions, respectively. With the enumerated assumptions the gas phase mass, momentum, energy, and species conservation equations then take the following forms:

$$\frac{\partial u}{\partial x} + \frac{\partial v}{\partial y} = 0 \quad (5)$$

$$\frac{\partial u}{\partial t} + u \frac{\partial u}{\partial x} + v \frac{\partial u}{\partial y} = v_g \frac{\partial^2 u}{\partial y^2} + \frac{(\rho_\infty - \rho_g)}{\rho_g} g \quad (6)$$

$$\frac{\partial P}{\partial y} = 0 \quad (6a)$$

$$\frac{\partial T_g}{\partial t} + u \frac{\partial T_g}{\partial x} + v \frac{\partial T_g}{\partial y} = a_g \frac{\partial^2 T_g}{\partial y^2} + \frac{\dot{q}_g'''}{\rho_g C_g} \quad (7)$$

$$\frac{\partial Y_i}{\partial t} + u \frac{\partial Y_i}{\partial x} + v \frac{\partial Y_i}{\partial y} = D_{ig} \frac{\partial^2 Y_i}{\partial y^2} + \frac{\dot{m}_i'''}{\rho_g} \quad (8)$$

Here, subscript g is the gas mixture, ∞ the ambient conditions, and v, a, D_{ig} are momentum, heat and species- i -mass diffusivities, respectively; P is pressure, Y_i is the i th species mass fraction with $i = F$ for the fuel pyrolyzate gas (O for oxygen, P for product and I for the inert). The respective volumetric source-sink strength due to the oxidation reaction is \dot{m}_i''' . The corresponding energy source strength is \dot{q}_g''' . While the energy and species equations indicate a balance between the unsteady accumulation, convection, diffusion and reaction rates, Equation 6 shows that momentum is conserved under the balance of accelerative, inertial, viscous, and buoyant forces. The constitutive relations to complement Equations 5 through 8 are

$$\sum Y_i = 1 \quad (9)$$

$$P = \rho_g (\bar{R}/M_g) T_g \quad (10)$$

$$\dot{m}_F''' = -Z_{gF} \rho_g^2 Y_F Y_O \exp(-E_g/\bar{R}T_g) \quad (11)$$

$$-\dot{m}_F'''/f = -\dot{m}_O'''/1 = +\dot{m}_P'''/(1+f) = +\dot{q}_g'''/fh_c \quad (12)$$

$$\dot{m}_I''' = 0 \quad (12a)$$

where

Z_{gF} = pre-exponential factor

E_g = activation energy

f = fuel pyrolyzate to oxygen stoichiometric mass ratio

h_c = enthalpy of oxidation

Besides the fact that all the edges of the solid are sealed for both mass and heat, the initial and boundary conditions are quite straightforward. In the solid $0 \leq y \leq \ell$,

$0 \leq x \leq H$; for $t < 0$, $T_s = T_{s0}$ ($= T_\infty$) and $\rho_s = \rho_{s0}$, both uniform in space. At the back face of the solid $y = 0$, at all times $t \geq 0$, $\partial T_s / \partial y = 0$ as well as $\dot{m}_p''' = 0$. In the gas, at $t < 0$, $\ell \leq y < \infty$, all x , and at $t \geq 0$, as $y \rightarrow \infty$, for all x , $u = v = 0$, $T_g = T_\infty$, $Y_F = Y_P = 0$ and $Y_O = Y_{O\infty}$.

The boundary conditions at the gas-solid interface ($y = \ell$, subscript w) play an important role in the physics of the problem. To avoid slip for the momentum equation, $u = 0$. The time-dependent normal transpiration velocity $v = v_w(t)$ is given by the transpiration mass flux of pyrolyzates $\dot{m}_{pw}''(t)$ [given by integration of the pyrolysis rate over the entire solid (Equation 1)] divided by the local gas density. The species balance at the interface indicates that the flux of species i arriving from within the solid is carried away into the gas phase by combined convection and diffusion. This balance, known as the Dankwert boundary condition, is given by

$$\dot{m}_{pw}'' Y_{iR} = \rho_g v_w Y_{iw} + (-\rho_g D_{ig} \partial Y_i / \partial y)_w \quad (13)$$

where Y_{ik} is the mass fraction of species i in the pyrolyzate mixture prior to any dilution with air. The energy interface condition states that the absorbed irradiance, i_0 , is conducted into the solid and the gas or reradiated.

The problem is now fully formulated. Relaxation of any of the simplifying assumptions can be done by appropriately reworking the model equations. The intention here is to present the skeletal model which can reasonably easily be adapted to suit special needs. The solution is straightforward in principle, although implementation is not. The transience, conjugate nature, the radiation non-linearity, and the presence of the Arrhenius exponential prevent these coupled equations from possessing similarity solutions. It is possible to obtain some approximate solutions which are useful in understanding the ignition process.

Ignition Criteria

Based upon experimental observations and intuition, attempts to identify the instant of ignition have led to the development of a number of criteria for ignition. The experiments of Bamford⁵ with wood suggest that ignition can be expected when the pyrolyzate outflow rate reaches $2.5 \times 10^{-4} \text{ g/cm}^2\text{s}$. Martin,⁴ Akita,⁶ and others^{7,8} advocate that the event of ignition can be described simply by the attainment of a critical temperature of the exposed surface. Martin⁴ postulates that persistent ignition is possible only when the entire solid attains an average temperature that exceeds a critical value. All these criteria presumably have something to do with the ease of heating the solid to cause sufficiently intense combustible gas generation by pyrolysis, and with the thermal conditions of the boundary layer conducive to flame inception. Experimental evidence developed by Alvares⁹ suggests that the surface temperature and the pyrolyzate efflux rate at ignition are not constants but depend upon the exposure flux and other factors.

Deveral and Lai¹⁰ showed theoretically that for solids that undergo ignition through gas-phase exother-

mic oxidation reactions, a reversal in the sign of the boundary layer gas temperature gradient at the solid-gas interface was a definite indication of ignition. Consistent with some experimental data for premixed gases ignited by a heated wire,¹¹ the transition of the gas-phase boundary layer to flaming justifies the gradient reversal criterion. Employing high-speed motion picture photography, Simms⁷ observed that the flame is indeed initiated in the relatively well-mixed wake of the finite height vertical target, and that this flame quickly propagates down into the boundary layer, altering the nature of the gas temperature distribution so as to reverse the gradient at the interface. Sauer's correlations¹² on thick slabs of wood showed that a certain minimum char depth was required before ignition could occur. The method of estimating the instantaneous char thickness, however, is experimentally subjective and analytically difficult.

Intuition suggests that a rapid rise of gas temperature is a sure sign of ignition. Since this abrupt rise is due to the oxidation reaction, the phenomenon of ignition should be associated somehow with the reaction rate in the gas boundary layer. In pursuing this line of thought, Kashiwagi¹³ suggested that ignition occurs when the reaction rate in the boundary layer exceeds an arbitrary value of approximately 10^{-5} g/cm³s. This type of criterion is consistent with ideas employed in solid propellant ignition studies,¹⁴ in which a surface reaction rate greater than a prescribed critical value is taken to ensure ignition of the exothermic surface reactions.

The ignition criteria utilized by various investigators can thus be summarized:

1. $T_{sw} \geq T_1^*$ —critical surface temperature (Simms, Martin)
2. $\bar{T}_s \geq T_2^*$ —critical average solid temperature (Simms, Martin)
3. $\dot{m}_{pw}'' \geq R_t^*$ —critical pyrolyzate mass flux rate (Bamford)
4. $\delta_c \geq \delta_c^*$ —critical char depth (Sauer)
5. $\partial T_g / \partial t \geq R_3^*$ —critical local gas temperature increase rate
6. $\int_0^\infty (\text{Reaction rate}) \geq R_4^*$ —critical total reaction rate in the boundary layer (Kashiwagi)
7. $(\partial T_g / \partial y)_{y=0} = 0$ —gas temperature gradient reversal at the solid-gas interface (Deverall and Lai)

Kashiwagi demonstrated that if arbitrary but "reasonable" values were selected for the critical condition, the ignition delay was not sensitive to any particular ignition criterion employed. This is fully expected, for each of Numbers 1 through 6 above indicates a feature of the incipient flame and none excludes or contradicts another. Number 7 is a trivial, although powerful, indicator of the arrival of the flame.

If it is accepted that flaming ignition is merely the onset of significant gas oxidation reactions in the boundary layer, then it is evident that Numbers 5 through 7 would not only necessarily but also sufficiently address the ignition process mechanistically by accounting for the gas oxidation reaction as well as its prerequisite, namely, the solid decomposition rate. The question of which of

these three criteria is more desirable may be answered if the sequence of events that lead to ignition is followed qualitatively.

The previous section on conduction-controlled spontaneous ignition indicates that the transiently heated solid conducts heat to the gas phase in the early stages of ignition. As the solid pyrolyzes, oxidation reactions begin in the gas phase. The reaction rate at any time is a function of distance normal to the slab surface. The composition distribution dictates that the reaction rate be zero at the edge of the boundary layer, and maximum somewhere within it. Therefore, a shift in the temperature profile occurs such that the deviation from the inert temperature profile at any point in the boundary layer reflects the oxidation reaction rate at that point. If the exothermic gas reactions persist, the gradient at the wall will eventually become zero. Beyond that point the solid begins to receive energy from the hotter gas, and the pyrolysis and gas oxidation rates increase until flaming occurs. Upon flaming, the gas temperature increases from the solid surface to the flame and then decreases from the flame to the ambient. Hence, attainment of a zero gradient of gas temperature at the wall is not only an important event leading to ignition but also a necessary indicator of the evolution of the flame. It must be recognized, however, that the gas temperature gradient reversal criterion is conservative in that it estimates the time to ignition equal to or less than the actual measured time.

Employing an integral solution approach, Gandhi¹⁵ solves the ignition model of the preceding section of this chapter, paying full attention to simultaneous developments in both the solid and gas phases. A comparison^{15,16} is made of the ignition criteria one, three, and six in the framework of criterion seven to note that the surface temperature, pyrolyzate efflux rate, and the total extent of gas phase reaction at ignition will all strongly depend upon such factors as the exposure intensity, target height and thickness, reradiant loss, and the chemical kinetics of both the pyrolysis and oxidation reactions. Alvares' experiments⁹ are thus explained with the conclusion that the critical temperature, pyrolyzate efflux, and gas reaction criteria are not generally acceptable, although they are valid in narrowly defined circumstances.

Solid Conduction-Controlled Ignition

The complex problem of heterogeneous ignition has been tackled by various investigators to identify two limiting cases. When the intensity of exposure is relatively low and the pyrolyzate production is relatively slow, the time to ignition is found to be 10^{-1} second or longer and mainly governed by characteristics of the solid phase thermal response. Higher heating rates, higher fuel volatility, and low gas pressures are found to result in a short time to ignition (of the order of 10^{-2} second or shorter) and are mainly governed by the gas phase phenomena.

In the solid phase-controlled limit, the solid is approximated to be inert. Its ignition is presumed to occur when the exposed surface attains a prescribed critical temperature, a property of the substance. As discussed in

the preceding section of this chapter, this criterion is simple although limited in the range of validity.

Let the inert slab of thickness, ℓ , conductivity, K_s , density, ρ_s , specific heat, C_s , and initial uniform temperature, T_{s0} , experience heating at the front face $y = \ell$ by a calibrated constant uniform absorbed irradiance, i_o , while the back face $y = 0$ is insulated. (The solution will later be extended to ignition by convective heating.) As heating occurs, the front face is permitted to lose heat to the surroundings at T_∞ by convection. The convection loss coefficient, h , is assumed to be constant and uniform; the reradiative loss is ignored.

The solid phase continuity equation (Equation 1), the pyrolysis terms in the solid energy conservation (Equation 2), the gas-phase species conservation (Equation 3), and the energy source term (Equation 7) all become unnecessary. The gas phase continuity and the momentum and energy equations also become unnecessary because their combined outcome is embodied in the prescribed heat loss transfer coefficient, h . The interface boundary condition is simplified by ignoring the reradiative loss term and setting the gas conduction flux equal to the convective loss flux, $h(T_{sw} - T_\infty)$. The resulting simple one-dimensional transient conduction problem has a well-known closed-form solution. Adapted from Carslaw and Jaeger¹⁷ the solution is

$$\frac{T_s - T_{s0}}{(i_o/h) + T_\infty - T_{s0}} = 1 - \sum_{n=1}^{\infty} \frac{2\text{Bi} \sec(a_n) \cos(a_n y / \ell)}{\text{Bi}(\text{Bi} + 1) + a_n^2} \exp\left(\frac{-a_n^2 a_s t}{\ell^2}\right) \quad (14)$$

where $\text{Bi} \equiv h\ell/K_s$ is the Biot number, indicating the characteristic ratio of convective and conductive fluxes. The constants a_n , $n = 1, 2, \dots, \infty$, are the positive roots of $a \tan(a) = \text{Bi}$; the first six of these roots are presented in Table 2-11.1. It is important to note that Equation 14 is applicable to (1) heating by irradiation in conjunction with surface heat loss by convection to the surrounding gas at T_∞ (which may be equal to the initial temperature of the solid, T_{s0}), (2) heating (or cooling) by convection alone (i_o is set equal to zero and T_∞ equal to the hot ambient gas temperature), and (3) heating by combined radiation and convection. The limiting form of Equation 14 when $h \rightarrow 0$ (i.e., radiant heating without the convective loss) is avail-

able explicitly as given in the final section of this chapter along with the versions of Equation 14 corresponding to thermally thin and semi-infinitely thick bodies.

Integration of Equation 14 over the space $0 \leq y \leq \ell$ leads to the determination of the average temperature, \bar{T}_s , of the solid at any point in time. The result¹⁷ is

$$\frac{\bar{T}_s - T_{s0}}{(i_o/h) + T_\infty - T_{s0}} = 1 - \sum_{n=1}^{\infty} \frac{2(\text{Bi}/a_n)^2}{\text{Bi}(\text{Bi} + 1) + a_n^2} \exp\left(\frac{-a_n^2 a_s t}{\ell^2}\right) \quad (15)$$

Other inert transient conduction solutions involving two- and three-dimensional effects, a variety of geometries, and boundary conditions can be found in a number of treatises. Equations 14 and 15 are sufficient for the present purposes.

Equations 14 and 15 are shown plotted in Figure 2-11.3, taking $T_\infty = T_{s0}$. The solid curves show the surface temperature while the dashed curves indicate the mean temperature. The coordinates used in this figure are related to those obvious from

$$x\text{-coordinate: } \frac{i_o \ell}{K_s(T_s - T_{s0})} \equiv \frac{\text{Bi}}{(T_s - T_{s0}) / [(i_o/h) + T_\infty - T_{s0}]} \quad (16)$$

$$y\text{-coordinate: } \frac{i_o a_s t}{K_s(T_s - T_{s0}) \ell} \equiv \frac{a_s t}{\ell^2} \cdot x\text{-coordinate} \quad (17)$$

The x -coordinate is the intensity of radiant exposure normalized with the instantaneous characteristic conduction flux. The y -coordinate has the meaning of the radiant fluence, $i_o t$, nondimensionalized with the appropriate instantaneous conduction quantities. A quick comparison of Figures 2-11.1 and 2-11.3 points to the reasons underlying the choice of presenting Equations 14 and 15 in these coordinates. The following observations can be made from Figure 2-11.3.

The surface temperature is shown in Figure 2-11.3 for six different convective loss Biot numbers. The effect of convective heat loss is most pronounced when the specimen thickness is small, intensity of irradiance is low, and duration of exposure is long (i.e., in the top left region of the graph). The thin body limit solution is given by Equation 22 which shows the reason, in that convective loss

Table 2-11.1 The First Six Roots¹⁷ of the Transcendental Equation $a \tan a = \text{Bi}$

Bi	a_1	a_2	a_3	a_4	a_5	a_6	a_n
0	0	3.1416	6.2832	9.4248	12.5664	15.7080	$(n-1)\pi$
10^{-3}	0.0316	3.1419	6.2833	9.4249	12.5665	15.7080	
10^{-2}	0.0998	3.1448	6.2848	9.4258	12.5672	15.7086	
10^{-1}	0.3111	3.1731	6.2991	9.4354	12.5743	15.7143	
10^0	0.8603	3.4256	6.4373	9.5293	12.6453	15.7713	
10^1	1.4289	4.3058	7.2281	10.2003	13.2142	16.2594	
10^2	1.5552	4.6658	7.7764	10.8871	13.9981	17.1093	
∞	1.5708	4.7124	7.8540	10.9956	14.1372	17.2788	$(n-1/2)\pi$

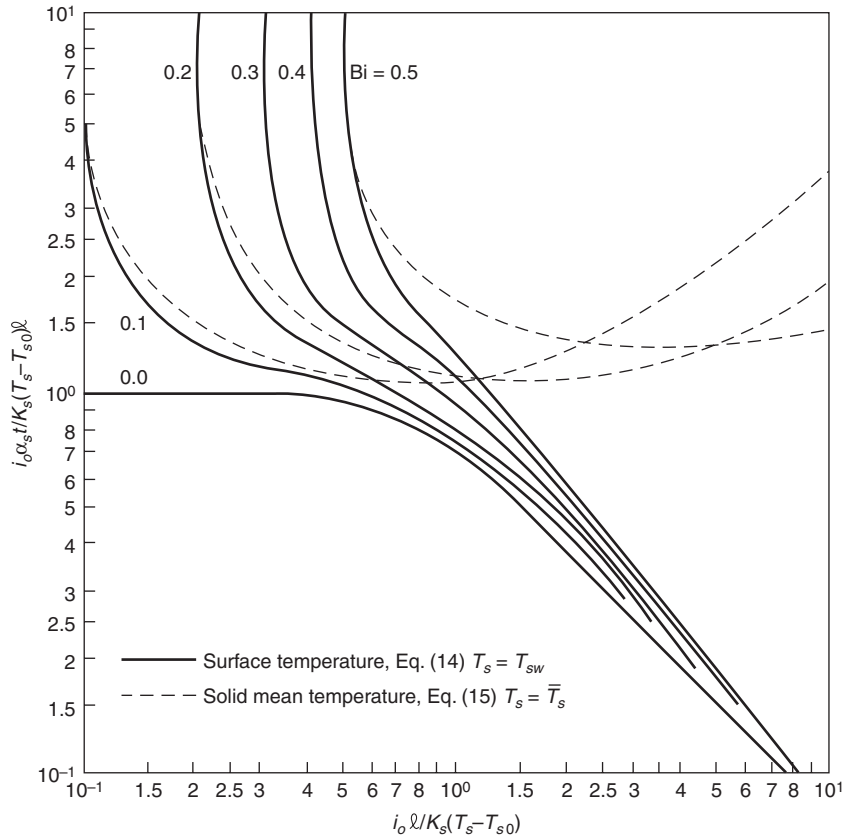


Figure 2-11.3. Surface and solid mean temperature histories for a slab heated by radiation and cooled by convective loss. Solid lines: surface temperature, Equation 14, $T_s = T_{sw}$. Dashed lines: solid mean temperature, Equation 15, $T_s = \bar{T}_s$. Numbers on curves are values of Bi .

plays an equally prominent role with the radiant heating of the solid.

As the slab thickens (i.e., in the lower right region of the graph), the convective loss exerts a less significant effect, compared to the effect of conduction, on the surface temperature history. In this thick regime, the semi-infinite solid solution without surface heat loss given by Equation 25 results in a surface temperature history of

$$\frac{i_o \alpha_s t}{K_s (T_s - T_{s0}) \ell} = \frac{\pi/4}{i_o \ell / [K_s (T_s - T_{s0})]} \quad (16)$$

where the length, ℓ , is used to depict this limiting solution on the same plane as the thin and finitely thick slab solutions. The $Bi = 0$ line of Figure 2-11.3 in the lower right region is, in fact, Equation 16 indicating a slope of -1 .

Expectedly, the mean temperature of a heated solid is always lower than its surface temperature. When the solid is thin, internal gradients become negligible, and the mean and surface temperatures are equal and relatively low. Convective loss obviously makes the surface temperature always lower than it is without losses. This is not always true, however, for the mean temperature. A complex compromise between the exposure irradiance and the his-

tories of conductive drain and convective loss results in a minimum in the exhibited mean temperature curves.

Consider now the premise that spontaneous ignition of a radiantly heated organic solid is primarily a consequence of heat conduction in the solid and convective loss to the gas phase, and that all other physical and chemical processes occur promptly without exerting any resistance. Additionally, the symptom of the incipient ignition is the attainment of a prescribed critical temperature at the exposed surface. Then, setting $T_{sw} = T_{sw}^*$ the solid curves of Figure 2-11.3 should give the time to ignition $t = t^*$. It may be postulated further that persistent flaming of thick bodies will occur only when the mean temperature of the body becomes sufficiently high to promise a continuous pyrolysis at an adequately high rate. Then the mean temperature curves of Figure 2-11.3 are expected to indicate the minimum required exposure for persistent flaming. With this framework of an ignition criterion, a remarkable similarity between Figures 2-11.1 and 2-11.3 can be recognized. This similarity perhaps endorses the prescribed critical temperature criterion for ignition and the cumulative outcome of the numerous assumptions underlying the development of Figure 2-11.3. The limitations of this success will be discussed later in this chapter.

There is a particular physical meaning of the coordinates chosen for Figure 2-11.3. As mentioned earlier, the x -coordinate, $i_o \ell / K_s (T_s - T_{s0})$, is a ratio of the imposed flux, i_o , to the instantaneous characteristic conductive flux, $K_s (T_s - T_{s0}) / \ell$. The x -coordinate can also be viewed as a ratio of the physical thickness, ℓ , to the thermal length characteristic, $K_s (T_s - T_{s0}) / i_o$, which is approximately the depth to which the thermal wave would penetrate into the solid in the time taken by the surface to raise its temperature from T_{s0} to T_s . If the ratio $i_o \ell / K_s (T_s - T_{s0}) \ll 1$, the solid may be considered thermally thin. On the other hand, if this ratio is much greater than unity, either because the solid is in fact physically thick or because the thermal length is small, then the body behaves as thermally thick. Large temperature gradients then exist near the exposed surface, and the relatively well-insulated interior of the solid results in the surface temperature being much higher than the average temperature.

The y -axis, $i_o a_s t / K_s (T_s - T_{s0}) \ell = i_o t / \rho_s C_s \ell (T_s - T_{s0})$, can also be viewed in different ways. It can be seen as a ratio of total energy incident on a unit area within the time, t (known as the *fluence*), to the characteristic enthalpy rise of the mass lying within this area. It is equally interesting to view the y -axis as a ratio of the elapsed time, t , to the heating time $\rho_s C_s \ell (T_s - T_{s0}) / i_o$ taken by the flux, i_o , to raise the temperature of the involved solid mass from T_{s0} to T_s . The y -axis is also recognizable as the product of the x -axis and the traditional Fourier modulus, $a_s t / \ell^2$. It is thus clear that when the intensity and duration of exposure are low, ignition of the solid is impossible.

Where possible, ignition can be one of three kinds

1. Thin bodies exposed to low intensity ignite, but only after a long exposure. The convective losses and the specimen thickness have a strong effect on this thin body ignition. In fact, experiments indicate that these thin bodies yield their small pyrolyzate content to the gas phase rather abruptly at a high rate. This happens so quickly that the gas phase thermal and mixture conditions are mutually out of phase to exclude the development of a flame. By the time the surface reaches a sufficiently high temperature, the solid is already converted to char. This char experiences the observed thin body glowing ignition. Martin's experiments confirm the strong influence of the specimen thickness on this glowing ignition. While this description is valid for isolated single thin fuel elements, it should not imply that beds of shredded paper and clouds of minute fuel particles will fail to flame. Such beds or clouds will have to be considered to be the global fuel element with low conductivity and large thickness, belonging at moderate to high values of the x -axis of Figure 2-11.3. Consideration of the volumetric absorption of radiation may become crucial in such a scenario.
2. Ignition occurs at moderate values of the exposure and fluence parameters, yielding only a transient flame. If the externally controlled exposure were then interrupted, the flame would cease, presumably due to large conductive and convective losses and inadequately established pyrolyzate production.
3. At moderate values of exposure intensity and long exposure time, the flaming will persist even if the exter-

nal irradiance is cut off. The longer exposure will raise the entire solid to a sufficient temperature, at which sustained production of the pyrolyzate is possible. Martin's experiments confirm that the effect of specimen thickness on this persistent flaming ignition is relatively weak.

Figures 2-11.1 and 2-11.3 also show that as the irradiant intensity is gradually reduced, a threshold (a lower limit of i_o) is approached below which ignition is impossible even with infinitely long exposure. While both the theory based on prescribed critical temperature criterion and the related experiments appear to adequately predict the nature of and time to ignition, they do not address the ignition threshold. A scrutiny of the gas phase reaction dynamics is required to gain an understanding of this issue. In fact, sufficient evidence exists⁹ to indicate that the ignition temperature increases with decreasing irradiance.

This is not the first time the essence of Figure 2-11.1 has been developed by inert conduction theory. Kanury¹ and Steward² independently obtained plots similar to Figure 2-11.3. The present Figure 2-11.3 is special because it is based on a single equation (Equation 14) rather than a patching of several solutions.

Martin's collection of experimental data, when examined in the perspective of Figure 2-11.3, indicate that for spontaneous ignition of radiantly heated thick cellulose, the critical surface temperature is in the vicinity of 900 K. These findings are in keeping with the measurements of Alvares⁹ and Akita.⁶ A comparison of the presently predicted and Martin's experimental results for persistent ignition leads to an estimation of the required mean solid temperature to be between 800 and 1200 K. Using physical reasoning, this temperature should be near, and slightly above, the temperature at which cellulose would pyrolyze profusely. Pyrolysis literature indicates this to be about 600 K. The present overestimation may be a consequence of the ignored reradiative heat loss from the surface.

Koohyar¹⁸ demonstrates that the present concepts are valid also for a variety of woods exposed to radiation from flames, provided corrections are made for the surface absorptivity differences. Koohyar¹⁸ and Wesson¹⁹ demonstrate that the ignition of radiantly heated wood in the presence of a small pilot flame in the reactive boundary layer also obeys the essence of the inert conduction theory. The critical surface temperature for this situation is about 600 K, near the pyrolysis temperature. This is consistent with the conclusions reached earlier by Akita.⁶ It thus appears that two conditions have to be met for spontaneous ignition: first, heating has to be sufficiently intense and long to produce sufficient pyrolyzates, which would result in a boundary layer mixture of fuel content exceeding the lean limit of flammability; and second, the boundary layer has to become sufficiently hot enough to support significant oxidation reaction. For piloted ignition, the first condition is adequate.

Hallman³ demonstrates that the inert conduction theory can be used to predict piloted ignition time for a variety of synthetic materials (i.e., plastics) as well. Smith²⁰ experimentally found that edges and corners of pieces of pine blocks exposed to irradiation from a quartz lamp ignite sooner but require a higher surface temperature than

that required for surface ignition. Multidimensional conduction and the effect of orientation on the reactive boundary layer characteristics are the two most relevant factors here.

Equations 14 and 15 indicate that if i_o is replaced by $h(T_\infty - T_{s0})$, Figure 2-11.3 can describe ignition by convective heating²¹ as well. The x - and y -coordinates then are

$$\text{Bi} \cdot \frac{T_\infty - T_{s0}}{T_s - T_{s0}} \quad \text{and} \quad \text{Bi} \cdot \frac{T_\infty - T_{s0}}{T_s - T_{s0}} \cdot \frac{a_s t}{\ell^2}$$

respectively, with the same physical meaning as before. Several points should be noted

1. The Biot number stands to represent the convective losses in radiant ignition. In convective ignition, however, it stands to represent the heating itself.
2. In practice, convective heating generally occurs as a result of flowing hot flame gases adjacent to the target surface. These gases are either devoid of, or diminished in, the oxygen content. Such a heating may produce pyrolytic damage to the target without ever producing ignition and flame. If the oxygen content of these heating gases is sufficiently high, potential ignition may be piloted by the hot gas flame itself. To avoid these real-world complexities, application of Figure 2-11.3 to convective heating should be made only when the convective heat source is hot air.
3. It may seem desirable to sort out the framework of the ignition map such that the heating Biot number is removed from the coordinates and made to appear only as a parameter in the curves. If this occurs, however, all the physical interpretations must be revised as well. (No substantial improvement in understanding seems to be gained.)
4. Akita's⁶ experiments indicate that spontaneous and piloted ignition temperatures¹ of convectively heated wood are about 765 and 725 K, respectively.

Role of the Gas Phase Processes

Alvares and Martin²² reported experiments in which cellulose was radiantly and spontaneously ignited in an atmosphere of oxygen-enriched air at high pressures. Eliciting a number of interesting gas phase processes that influence heterogeneous ignition, this work indicates that the time to ignition is dramatically reduced by an increase in the ambient oxygen mass fraction and/or ambient gas pressure, and by a reduction in its thermal conductivity. The surface temperature at ignition is also found to substantially decrease with an increase in the oxygen content and in the pressure of the ambient gas. A simple analysis can be made to predict these observations and attempt to develop an understanding of the activity in the gas phase.

Consider a situation in which attention is focused only on the gas phase. Assume, accordingly, that the solid phase problem furnishes to the boundary layer a pyrolyzate content corresponding to a mass fraction of Y_F and the ambient gas furnishes oxygen such that its mass fraction is Y_O . Let the solid surface at $T_g = T_{sw}$ and the edge of the boundary layer at $T_g = T_\infty < T_{sw}$ constitute two large parallel plates separated by a distance, δ . Assume

further that the reactive fluid mixture in this layer is stagnant so that energy transfer from the hot to cold boundary occurs only by conduction. Additionally, let the problem be steady state. Then, all equations become irrelevant, except for Equation 7, simplified. This simplification is

$$K_g \frac{d^2 T_g}{d\hat{y}^2} + h_c \left[Z_{gF} \rho_g^2 Y_F Y_O \exp\left(\frac{-E_g}{RT_g}\right) \right] = 0 \quad (17)$$

with the boundary conditions: $\hat{y} = 0$, $T_g = T_{sw}$ and $\hat{y} = \delta$, $T_g = T_\infty$. Recall that the square-bracketed term in this equation is the volumetric fuel consumption rate due to oxidation, whose kinetics are taken to exhibit an order of unity with respect to both the pyrolyzate fuel and the oxygen.

For an inert gas mixture with constant conductivity, steady-state conduction would occur across the gas layer with a linear temperature profile. On the other hand, if the mixture is reactive in a strongly temperature dependent way, the energy source prevalent in the proximity of the hot wall will locally reduce the temperature gradient. The stronger this energy source becomes, the greater is this gradient reduction. In fact, if the source is strong and T_{sw} is sufficiently high, the gradient near the hot wall will even be reversed in sign, signifying that heat would flow from the reacting gas to the hot wall as well as to the cold wall. Ignition is thus conceivably accomplished when T_{sw} is just high enough to result in a zero temperature gradient at the hot wall. This critical T_{sw} will depend upon the kinetics and energetics of the exothermic reaction and the gas thermal conductivity. To determine the critical T_{sw} , the energy conservation problem of Equation 17 must be solved, in which the preignition reactant consumption is ignored and the mixture conductivity is assumed constant. Upon defining

$$\theta = \frac{E_g (T_{sw} - T_g)}{\bar{R} T_{sw}^2} \quad \eta = \frac{\hat{y}}{\delta}$$

and

$$D = \frac{E_g \delta^2 h_c \rho_g^2 Z_{gF} Y_F Y_O \exp(-E_g/\bar{R}T_{sw})}{\bar{R} T_{sw}^2 K_g}$$

Equation 17 reduces to $d^2\theta/d\eta^2 - D \exp(-\theta) = 0$ with the boundary conditions $\theta(0) = 0$ and $\theta(1) = \theta_\infty$. Integration of this equation is quite straightforward, although somewhat tedious. One integration gives

$$\frac{d\theta}{d\eta} = \sqrt{[4C_1^2 - 2D \exp(-\theta)]} \quad (18)$$

relating local temperature to its gradient. With one additional integration and application of the boundary conditions, $\theta = \theta(\eta; D, \theta_\infty)$ can be found and the conditions of $D = D^*(\theta_\infty)$ surrounding the ignition indicated by the zero temperature gradient at the hot wall can be deduced.

There is a simple approximation by which this ignition result can be obtained relatively easily. The temperature profile of a marginally igniting system is given by Equation 18 in which the constant, C_1 , is evaluated by setting θ and $d\theta/d\eta$ equal to zero at $\eta = 0$. Thus, for the

temperature profile in the system at ignition, $4C_1^2 = 2D$, so that $d\theta/d\eta = \{2D[1 - \exp(-\theta)]\}^{1/2}$. Change in this gradient at ignition from zero to a nearly constant value of $\{2D[1 - \exp(-\theta_\infty)]\}^{1/2} \approx (2D)^{1/2}$ occurs within a remarkably small distance from the hot wall. If one assumes that the linearity of the temperature profile holds in the entire range $0 \leq \xi \leq 1$, the gradient is noted to be equal to θ_∞ . Thus, ignition by the hot surface is expected if $(2D)^{1/2} \geq \theta_\infty$; that is, if

$$D \geq \frac{\theta_\infty^2}{2}$$

Written in physical terms, ignition would occur if

$$\frac{2\delta^2 \bar{R}T_{sw}^2 h_c \rho_g^2 Z_g Y_F Y_O \exp(-E_g/\bar{R}T_{sw})}{K_g E_g (T_{sw} - T_\infty)^2} \geq 1 \quad (19)$$

If T_∞ is small, the hot wall temperature appears only in the Arrhenius term. Therefore, it is easy to see that a small gas layer thickness requires a higher T_{sw} to produce ignition.

If the reactive gas were to be flowing over a hot plate, Equation 19 can be adapted by viewing δ , the boundary layer thickness, as the average thermal boundary layer thickness and the ratio (K_g/δ) as the average heat transfer coefficient, h . Inasmuch as both the boundary layer thickness and the heat transfer coefficient depend upon the flow dynamics and the nature of the fluid, ordinary heat transfer results may be incorporated into Equation 19. With $\delta = H/\text{Nu}$ where H is the flow characteristic length and Nu is the average Nusselt number (which depends on the Grashof or Reynolds number of the flow and the Prandtl number of the fluid), ignition occurs if

$$\frac{2H^2 \bar{R}T_{sw}^2 h_c \rho_g^2 Z_g Y_F Y_O \exp(-E_g/\bar{R}T_{sw})}{\text{Nu}^2 K_g E_g (T_{sw} - T_\infty)^2} \geq 1 \quad (20)$$

If all else is kept fixed, longer hot plates are capable of producing ignition with lower wall temperatures. Faster moving gas streams are not as likely to be ignited by the same T_{sw} hot plate as are the slower moving ones. This ignition-retarding effect of flow speed is more pronounced for laminar flows than for turbulent flows. (This deduction is, of course, based on the fact that $\text{Nu} \propto \text{Re}^b$, where $b \approx 1/2$ for laminar flow and $b \approx 1/5$ for turbulent flow.) Note also that Equation 20 can be adapted to hold for combustible gas flows over a variety of geometries.

Equations 19 and 20 are entirely consistent with the observations of Alvares and Martin.²² As the surface temperature, T_{sw} , develops slowly due to the solid phase conductive response to heating, the gas phase responds quickly. It is eminently clear from Equations 19 and 20 that taller targets in a slow-moving, poorly conducting, low viscosity, high pressure, oxygen-enriched ambient gas will ignite sooner at a lower surface temperature. Although the present analysis is only approximate, it powerfully depicts how gas phase oxidation reactions are induced by the composition and thermal conditions.

Gandhi¹⁵ solved the comprehensive set of the conservation equations, accounting for the full unsteady, reactive, conjugate heat and mass transfer problem with reradiant heat loss at the surface of the target, which is vertical and subjected to external irradiance. An integral technique is employed to obtain the characteristics of

the transiently developing, reactive, natural convective boundary layer averaged over the target height. The gas temperature gradient reversal at the gas-solid interface is used as the criterion for spontaneous ignition. This solution yielded valuable information on the ignition criterion as discussed previously. Additionally, it is possible to predict such radiant spontaneous ignition phenomena as the time to ignition and ignition thresholds.

Figure 2-11.4 indicates Gandhi's predicted influence of exposure irradiance and the target thickness on the time to ignition for fixed values of the plate height, H , and kinetics of oxidation and pyrolysis. The general characteristics of Figures 2-11.1 and 2-11.3 obviously appear to be captured. (Recall that the surface reradiant energy loss has been ignored in deducing Figure 2-11.3.) Typical agreement of the predictions with measurements is shown in Figure 2-11.5. Further details of this predictive model are available.^{15,16,23}

Most importantly, Gandhi predicts the lower limit exposure flux below which ignition of a given solid in a given situation is impossible. These limiting conditions, known as ignition thresholds, are difficult to measure experimentally. The threshold minimum flux is found to depend on the slab height and thickness, gas and solid phase reaction kinetics, and reradiant loss as well as the heat of combustion of the pyrolyzates. One typical prediction is indicated in Figure 2-11.6, where the threshold flux is plotted as dependent on the heat of combustion and the slab height for given reradiant loss and kinetics. Ignition will not occur in the area lying below the curve, while it will occur elsewhere. Taller targets will experience ignition even if the pyrolyzate is less combustible; for a fixed heat of combustion of the pyrolyzates, taller targets exhibit a lower threshold flux. The minima in these curves indicate that when the heat of combustion is very low, ignition is impossible irrespective of the exposure flux level. At enthalpies of combustion that are close to but slightly larger than the limiting value (which depends on the target height), two roots of the threshold flux exist between which ignition is possible. These are

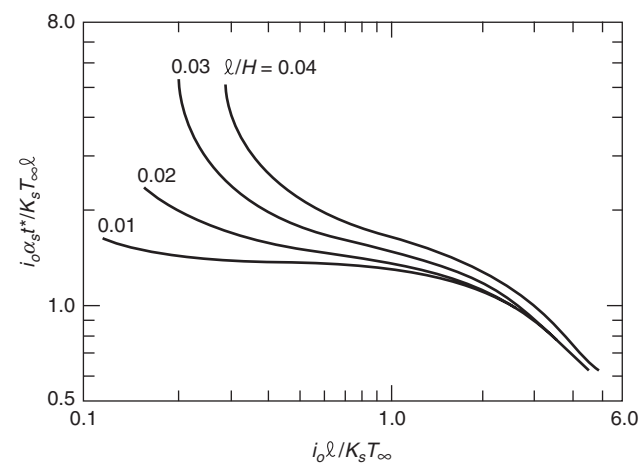


Figure 2-11.4. *Influence of slab thickness on time of ignition.* $gH^3/v_g^2 = 10^6$; $E_g/\bar{R}T_\infty = 30$; $Z_g F \rho_g \ell^2/a_s = 10^8$; $E_s/\bar{R}T_\infty = 50$; $Z_s \ell^2/a_s = 10^7$.

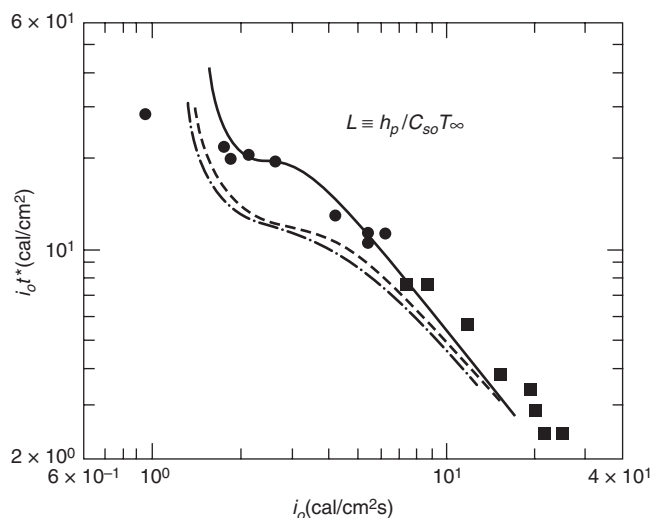


Figure 2-11.5. Comparison with Martin's data for cellulose. ■ and ●: data²⁴ solid line: theory¹⁵ ($L = -1$); dashed line: theory¹⁵ ($L = 1$); dash-dotted line: theory¹⁵ ($C_p = 0$).

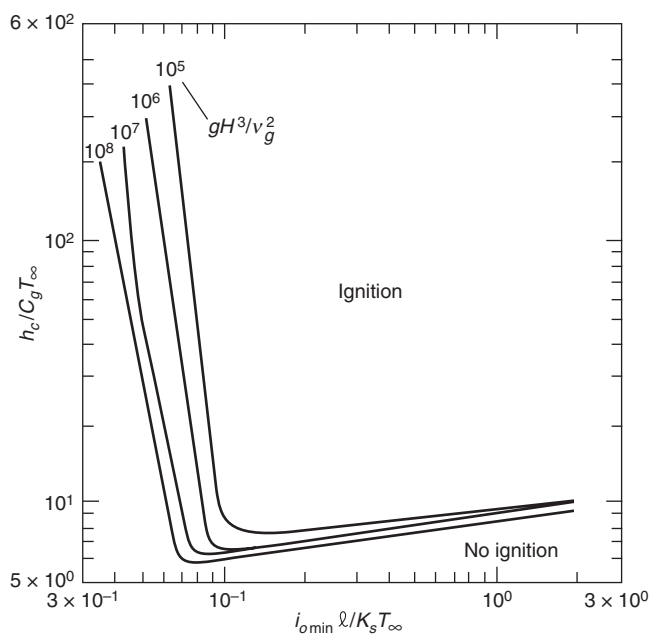


Figure 2-11.6. Influence of slab height on threshold flux. $E_s/\bar{R}T_\infty = 50$. $E_g/\bar{R}T_\infty = 30$. $\sigma \varepsilon_{sw} T_\infty^3 \ell/K_s = 10^{-3}$.

important findings and must be further studied for use in fire safety. While Figure 2-11.6 is presented here only as an example of Gandhi's predictions, much similar information is available.¹⁵

Some Practical Issues

The understanding of the ignition process developed earlier in this chapter is useful in a number of practical fire safety problems, including those cited in the Introduction. These problems fall broadly into two groups: those pertaining to the very initiation of the fire, and those pertaining to the spatial (or temporal) growth of fire in combustible ensembles. A number of questions arise in attempts to assess the ignition hazard on the basis of the existing simple viewpoints. These questions point out the need for care and for a comprehensive model of ignition through which the assessment can be made with some confidence.

The possibility of ignition of an object under a given set of conditions is presently judged by evaluating whether or not the exposed surface would attain a critical ignition temperature, T^* , construed as a property (albeit, extrinsic) of the material. T^* for transient ignition of a broad range of natural and synthetic organic solids is taken to be approximately as follows: for spontaneous ignition, 600°C for radiant exposure and 500°C for convective exposure; for piloted ignition, 300 to 410°C for radiant exposure and 450°C for convective exposure. Note that these are approximate values, mostly deduced from experiments on small vertical specimens. Measurements of this temperature on ignition of horizontal surfaces are also available in the recent literature.

Persistent ignition would require heating of the solid, over a minimum thickness near its exposed surface, to a

mean temperature in excess of the material's characteristic pyrolysis temperature to ensure continued pyrolysis. This would presumably mean higher surface temperatures than those just cited. It is noteworthy in this context that in spite of significant physical and chemical differences in structure and composition, most organic solids undergo pyrolysis in a rather narrow temperature range of $325 \pm 50^\circ\text{C}$.

It is also important to note here that the size of the specimen and its orientation are expected to exert an influence on T^* by altering the convective patterns and rates of heat loss and gas mixing. The mechanisms involved in this influence are not straightforward. Reduction of heat loss from the surface of a radiantly heated solid will obviously tend to increase its heating and pyrolysis. It is, therefore, expected to result in a hastened ignition. This expectation, however, is not always valid since the gas phase ignition requires mixing of the pyrolyzates with air and heating of the mixture so as to induce the preignition oxidation reaction. These mixing and heating processes of the gas phase require a certain optimal boundary layer flow. Thus, while mixing and heating of the boundary layer gases is a condition required for ignition, excessive mixing will dilute the reactant mixture and deprive the solid from its energy demand for sustained production of pyrolyzate.

These ideas are also important from another practical viewpoint. Traditional strategies to delay or prevent ignition involve a physical and/or chemical alteration of the materials. One goal of such an alteration is usually to make the pyrolysis difficult, for example, by increasing the associated activation energy or endothermicity. If the heating were convective, however, an easy pyrolysis with

an increased rate may be more desirable, for then the copious production of the pyrolyzate is expected to retard the convective heating rate by thickening the boundary layer.

Another material alteration that can delay or prevent ignition (irrespective of the radiative or convective heating mode) is to chemically tamper with the composition of the pyrolyzate mixture, rendering it abundant in such inert species as water vapor and carbon dioxide. Means of accomplishing this can be found in organic chemistry, wherein even trace quantities of certain additives are known to profoundly alter both the rate of production and composition of the pyrolyzate. However, complications arise due to the dependency of the action of these additives on the rate of heating of the sample.

The differences between spontaneous and piloted ignitions, and between radiant and convective heating to ignition, should be noted here. Spontaneous ignition requires (1) sufficient heating of the solid to produce enough pyrolyzates continuously, (2) mixing of these pyrolyzates with air to produce a mixture above the lean limit, and (3) heating of this boundary layer mixture to a temperature sufficiently high to result in a thermochemical runaway to the state of flame. Requirement 3 is not necessary for piloted ignition, wherein an external ignition energy source is available to initiate the flame. If the heating were by irradiation of the specimen, the exposed surface of the solid would be at the highest temperature, invoking a transient natural convective boundary layer in which the induced air mixes with the effluent pyrolyzates. If forced blowing of air over a radiantly heated solid surface were involved, the surface then would be cooled more intensely than due to natural convection. This would likely diminish the pyrolysis rate within the solid while enhancing the mixing in the boundary layer and its heating. The resultant ignition behavior would be rather complicated.

If the heating were by convection, drastic differences would arise, depending upon the nature of the convecting hot gas. Heating by hot air is conducive to quick ignition. Heating by hot (nonflaming) combustion gases can result in copious pyrolysis, but ignition in the mixing layer is thwarted by the poor oxygen content. If the convective heating were by hot flames, the flames themselves would become extended in space due to the added pyrolyzate fuel. In these circumstances, the very idea of ignition becomes vague.

The multitude of complexities and ambiguities involved in assessing the ignition hazard of a practical situation, even with the simple critical surface temperature criterion, is obvious. Care is therefore required in drawing quick conclusions from current simplified practices. The surface temperature at ignition is not a cause but an effect, and as such, depends on the conditions of an experiment (so, also, are most of the other known ignition criteria). A comprehensive quantitative model of physical chemistry of ignition, such as that presented by Gandhi for spontaneous ignition of radiantly heated vertical cellulosic solids, seems to be needed for piloted radiant ignition, for (spontaneous and piloted) ignition due to convective heating, and for a number of specimen orientations.

A Practical Illustration

Great advances have been made in understanding the fundamental mechanisms involved in flaming ignition of radiantly and/or convectively heated solids—natural as well as synthetic—with and without the presence of a pilot source. The current practice of ignition hazard assessment employs such simplified concepts as a prescribed critical ignition temperature of the solid. This practice is prone to ambiguities and difficulties. Physico-chemical models of ignition are available and can be used to examine the ignition process in a broader and more complete perspective. Quantitative assessment of the conditions that differentiate between possible and impossible ignition is now feasible from these models. The time to ignition and energy required for ignition can be estimated with reasonable accuracy. The present understanding can be refined by relaxing most of the assumptions enumerated in the section of this chapter on conservation equations; but the degree of and the need for the necessary refinement must first be addressed.

To illustrate the practical utility of Figure 2-11.3, consider a firwood target 1 cm thick and 2 cm in height initially at 300 K in normal air, also at 300 K. Will spontaneous ignition occur if this target is exposed to an absorbed radiant flux of 2 W/cm^2 continuously for 1000 seconds? Will the ignition, if possible, be transient or sustained?

Approximate answers to such questions can be given using Figure 2-11.3. First, the conductivity, specific heat, density, and diffusivity of fir, respectively, are found to be $0.17 \text{ W/m}\cdot\text{K}$, $2500 \text{ J/kg}\cdot\text{K}$, 600 kg/m^3 , and $11.3 \times 10^{-8} \text{ m}^2/\text{s}$. From convection literature, the heat transfer coefficient, h , is estimated to be about $15 \text{ W/m}^2\cdot\text{K}$. Then the Biot number and x , y -coordinates for Figure 2-11.3 are calculated with the given exposure flux and duration.

$$\text{Bi} \equiv \frac{h\ell}{K_s} \approx \frac{15(\text{W/m}^2\text{K})1(\text{cm})}{0.17(\text{W/mK})} \approx 0.88$$

$$x = \frac{i_0\ell}{K_s(T^* - T_0)} \approx \frac{2(\text{W/cm}^2)1(\text{cm})}{0.17(\text{W/mK})(873 - 300)(\text{K})} \approx 2.05$$

$$y = \frac{i_0 a_s t}{K_s(T^* - T_0)\ell} \approx \frac{2(\text{W/cm}^2)11.3 \times 10^{-8}(\text{m}^2/\text{s})1000(\text{s})}{0.17(\text{W/mK})573(\text{K})1(\text{cm})} \\ \approx 2.32$$

The critical temperature $T^* = 873 \text{ K}$ comes from the summary in the previous section and corresponds to spontaneous ignition due to radiant heating. Entering these values of Bi, x , and y on Figure 2-11.3, sustained spontaneous ignition is concluded to be possible with the given exposure and duration. If the exposure duration were shorter, say 400 seconds, the y -coordinate would be 0.93, indicating that the ignition would be transient. With even shorter exposure (less than 260 seconds), y will be less than approximately 0.6 and ignition would not occur.

Repeating the example but with a thinner target of thickness $\ell = 0.1 \text{ cm}$, and keeping all else unchanged, the Bi, x , and y coordinates are estimated to be 0.088, 0.205, and 23.2, respectively. Sustained spontaneous ignition is obviously ensured on this thin body. With 400 seconds of exposure, $y \approx 9.28$, sustained ignition continues to be possible. The minimum exposure required of this thin body

to produce ignition is 40 seconds, which is substantially shorter than the exposure of 260 seconds needed for transient ignition of the thicker body considered above.

If a pilot source were available, the appropriately lower critical temperature from the previous section of this chapter would enable similar estimates to be made of whether ignition would occur with a given exposure duration, whether the possible ignition would be transient or sustained, and of the minimum required exposures.

If convective heating from a hot gas flow at a temperature T_∞ were involved rather than radiant heating, the x - and y -coordinates of Figure 2-11.3 would be estimated by the definitions given at the end of the section of this chapter on solid conduction-controlled ignition. Throughout this example it should be remembered that Figure 2-11.3 has been developed on the basis of a greatly simplified view of the ignition process. The very concept of the prescribed critical temperature involves an oversimplification and limited validity. Detailed models, such as those underlying Figures 2-11.4 through 2-11.6, are more reliable, although considerably more difficult to apply.

Mathematical analyses lead to a predictive capability which is limited only by the accuracy and detail of such input data as the pyrolysis and combustion kinetic and thermodynamic properties, values of transport properties and their variability with temperature and composition, and so forth. Many real-world complexities exist: (1) materials are often encountered in practice as composites with glues, stitches, and bonds; (2) practical geometries of targets are seldom simple; (3) aging and durability of a solid alter its physical and chemical characteristics; (4) surfaces are almost always multicolored; and so forth. An adherence to fixed sets of physical and chemical properties or to voluminous dictionaries of property values under different circumstances may not be wise for use in a predictive model. It may be more prudent to seek only a fundamental conceptual or mechanistic understanding of a phenomenon such as flaming ignition from a mathematical model.

Even more importantly, mathematical models suggest useful ways of correlating the experimental measurements. Meaningful correlations lead one to maximize the value of limited experiments, generalize the observations, and to postulate, interpret, and exploit the basic mechanisms of chemistry and physics.

Conclusion

A qualitative, comprehensive map of flaming ignition has been developed in the work presented here. The nature of the problem and the component processes are well identified, and the global physicochemical behavior appears to be clear. Employing this understanding, it must be possible to draw some conclusions on the effects of such nonidealities as the edges and corners that reflect in three-dimensional conduction and in complicated boundary layer flows, surface roughness and color in conjunction with the nature of the radiation source, convective heating by vitiated hot gases, leakage of energy and mass through the backface and edges, and others.

Explicit Forms of Equation 14 for Some Limiting Cases

1. *Explicit form of Equation 14 as convective losses tend to zero:* The transcendental equation becomes $\sin a = 0$ so that $a_n = n\pi$, $n = 1, 2, \dots, \infty$. This solution¹⁷ is given as

$$\frac{K_s(T_s - T_{s0})}{i_o \ell} = \frac{\alpha_s t}{\ell^2} + \frac{y^2}{2\ell^2} - \frac{1}{6} - \sum_{n=1}^{\infty} \frac{2(-1)^n}{\pi^2 n^2} \cos\left(\frac{n\pi y}{\ell}\right) \exp\left(-\frac{n^2 \pi^2 \alpha_s t}{\ell^2}\right) \quad (21)$$

2. *Thermally thin slab:* If the solid were either physically so thin and/or so highly conductive that the temperature gradients within the solid are promptly relaxed by the rapid conduction, then the solid temperature is a function of time alone. The energy equation for this case is obtainable by integrating Equation 2 as $\rho_s C_s (V/S) dT_s/dt = i_o - h(T_s - T_\infty)$ along with the initial condition $T_s = T_{s0}$ at time $t = 0$. The ratio (V/S) is the solid volume over its surface area, equal to the thickness, ℓ , for a slab. The solution is easily obtained:

$$\frac{T_s - T_{s0}}{(i_o/h) + T_\infty - T_{s0}} = 1 - \exp\left(-\frac{hSt}{\rho_s C_s V}\right) \quad (22)$$

which in fact is a limiting form of Equation 14. In the further limit $h \rightarrow 0$, as in Item (1) above, Equation 22 reduces to

$$\frac{\rho_s C_s V (T_s - T_{s0})}{i_o St} = 1 \quad (23)$$

- for pure radiant heating of a thin body without any convective loss.
3. *Semi-infinite slab:* If the slab were physically so thick and/or so poor a conductor that the back face does not realize the effect of thermal exposure at the front face within the time period of interest, the slab then can be considered as a semi-infinite solid. A high front face exposure flux and a low conductivity will tend to make even a physically thin sheet of a slab behave as though it is thermally infinitely thick. With radiant heating and convective loss at the only face, we know that $y' = 0$ (with y' measured into the interior from the surface), and the temperature-time-space distribution corresponds to the small time limit of Equation 14. This solution is given explicitly as

$$\frac{T_s - T_{s0}}{(i_o/h) + T_\infty - T_{s0}} = \operatorname{erfc}\left(\frac{y'}{2\sqrt{\alpha_s t}}\right) - \left[\operatorname{erfc}\left(\frac{y'}{2\sqrt{\alpha_s t}} + \frac{h\sqrt{\alpha_s t}}{K_s}\right) \exp\left(\frac{hy'}{K_s} + \frac{h^2 \alpha_s t}{K_s^2}\right) \right] \quad (24)$$

(The manner in which the unavailability of a physical reference length, ℓ , is handled can be observed from Equation 24.) Heating by radiation alone without any

Table 2-11.2 The Error Function and Its Derivative

ϕ	$\text{erf}\phi$	$\text{erfc}\phi = 1 - \text{erf}\phi$	$\frac{d}{d\phi} \text{erf}\phi = (2/\sqrt{\pi}) \exp(-\phi^2)$
0	0	1.0	1.1284
0.05	0.05637	0.9436	1.1256
0.1	0.1125	0.8875	1.1172
0.2	0.2227	0.7773	1.0841
0.3	0.3286	0.6714	1.0313
0.4	0.4282	0.5716	0.9615
0.5	0.5205	0.4795	0.8788
0.6	0.6039	0.3961	0.7872
0.7	0.6778	0.3222	0.6913
0.8	0.7421	0.2579	0.5950
0.9	0.7969	0.2031	0.5020
1.0	0.8427	0.1573	0.4151
1.5	0.9661	0.0339	0.3568
2.0	0.9953	0.00468	0.0827
2.5	0.9996	0.00041	0.0109
3.0	0.99998	0.00002	0.0008

convective loss calls for the limit of Equation 24 as $h \rightarrow 0$. This limit solution¹⁷ is given to be

$$\frac{K_s(T_s - T_{s0})}{2i_o\sqrt{a_s t}} = \frac{1}{\sqrt{\pi}} \exp\left(-\frac{y'^2}{4a_s t}\right) - \left(\frac{y'}{2\sqrt{a_s t}}\right) \text{erfc}\left(\frac{y'}{2\sqrt{a_s t}}\right) \quad (25)$$

where erfc is the complementary error function. This and other related functions are tabulated in Table 2-11.2.

Nomenclature

a_n	constants, $n = 1, 2, \dots, \infty$
b	index
Bi	Biot number
C	specific heat (kJ/Kg·K)
D	Damköhler number
D_{ig}	species i mass diffusivity through the gas mixture (m ² /s)
E	activation energy (kJ/kmol)
f	fuel pyrolyzate/oxygen stoichiometric mass ratio (kg F/kg O)
g	standard acceleration of gravity (m/s ²)
H	height of the solid target slab (m)
h	heat transfer coefficient (W/m ² ·K)
h_c	enthalpy of combustion of fuel pyrolyzate (kJ/kg)
h_p	enthalpy of pyrolysis (kJ/kg)
i	incoming exposure irradiance (W/m ²)
i_o	absorbed exposure irradiance (W/m ²)

K	thermal conductivity (W/m·K)
ℓ	thickness of the solid target slab (m)
M	molar mass (kg/kmol)
\dot{m}''	mass flux (kg/m ² ·s)
\dot{m}_i'''	species i source-sink strength (kg/m ³ ·s)
Nu	Nusselt number
P	pressure (Pa)
\dot{q}'''	energy source-sink strength (W/m ³)
Re	Reynolds number
\bar{R}	universal gas constant (kJ/kmol·K)
S	surface area (m ²)
T	temperature (K)
\bar{T}_s	mean temperature of the solid (K)
t	time (s)
u	x-directional velocity component (m/s)
V	volume (m ³)
v	y-directional velocity component (m/s)
W	width of the solid target slab (m)
x	coordinate along the surface (m)
γ_i	species i mass fraction
y	coordinate normal to the surface (m)
\hat{y}	($y - \ell$) (m)
y'	($\ell - y$) (m)
Z	pre-exponential (or collision) factor (1/s for solid pyrolysis, and m ³ /kg·s for gas oxidation)

Greek Symbols

α	thermal diffusivity (m ² /s)
δ	reactive boundary layer thickness (m)
ε_s	solid surface emissivity
η	nondimensional y
θ	nondimensional temperature
ν	kinematic viscosity (m ² /s)
ρ	density (kg/m ³)

Subscripts

c	char
F	fuel pyrolyzate
g	gas
I	inert
O	oxygen
0	initial
P	products
p	pyrolysis or fuel pyrolyzate
R	reservoir
s	solid
w	interface
∞	ambient

Superscript

*	ignition
---	----------

References Cited

1. A.M. Kanury, *Fire Res. Abst. and Rev.*, 14, p. 24 (1971).
2. F.R. Steward, in *Heat Transfer in Fires*, Scripta, Washington, DC, p. 379 (1974).
3. J.R. Hallman, J.R. Welker, and C.M. Sliepcevich, "Ignition of Polymers," *Proceedings of 30th Annual Conference*, Soc. Plastics Engineers, p. 283 (1972).
4. S.B. Martin, "Diffusion-Controlled Ignition of Cellulosic Materials by Intense Radiant Energy," *10th Symposium (International) on Combustion*, Combustion Institute, Pittsburgh, PA, p. 877 (1965).
5. C.H. Bamford, J. Crank and D.H. Malan, *Proc. Cambridge Phil. Soc.*, 42, p. 166 (1946).
6. K. Akita, *Report Fire Res. Inst.*, Tokyo, 9 (1959).
7. D.L. Simms, *Comb. and Flame*, 4, p. 293 (1960).
8. C.C. Ndibizu and P. Durbetaki, *Fire Res.*, 1, p. 281 (1977-78).
9. N.J. Alvares, *Tech. Report 735*, U.S.N.R.D.L., San Francisco (1964).
10. L.I. Deverall and W. Lai, *Comb. and Flame*, 13, p. 8 (1969).
11. G. Adomeit, "Ignition of Gases at Hot Surfaces Under Non-steady State Conditions," *10th Symposium (International) on Combustion*, Combustion Institute, Pittsburgh, PA, p. 237 (1965).
12. F.M. Sauer, *Interim Technical Report AFSWP-868*, U.S. Department of Agriculture/Forest Service, Berkeley, CA (1956).
13. T. Kashiwagi, *Comb. Sci. and Tech.*, 8, p. 225 (1974).
14. E.W. Price, H.H. Bradely, Jr., and G.L. Dehority, *AIAA J.*, 4, p. 1153 (1966).
15. P.D. Gandhi, "Spontaneous Ignition of Organic Solids by Radiant Heating in Air," Ph.D. dissertation, University of Notre Dame, Notre Dame, IN (1984).
16. P.D. Gandhi and A.M. Kanury, *Comb. Sci. and Tech.*, 50, p. 233 (1986).
17. H.S. Carslaw and J.C. Jaeger, *Conduction of Heat in Solids*, Oxford University, London (1959).
18. A.N. Koohyar, J.R. Welker, and C.M. Sliepcevich, *Fire Tech.*, 4, p. 284 (1968).
19. H.R. Wesson, J.R. Welker, and C.M. Sliepcevich, *Comb. and Flame*, 16, p. 303 (1971).
20. W.K. Smith, *Ignition of Edges and Corners of Wood*, WAM Paper No. 72-WA/HT-20, ASME, New York (1972).
21. W.D. Weatherford and D.M. Sheppard, "Basic Studies of the Mechanics of Ignition of Cellulosic Materials," *10th Symposium (International) on Combustion*, Combustion Institute, Pittsburgh, PA, p. 897 (1965).
22. N.J. Alvares and S.B. Martin, "Mechanism of Ignition of Thermally Irradiated Cellulose," *13th Symposium (International) on Combustion*, Combustion Institute, Pittsburgh, PA, p. 905 (1971).
23. P.D. Gandhi and A.M. Kanury, in *Dynamics of Reactive Systems, Part I: Flames and Configurations*, AIAA, New York, p. 208 (1986).
24. S.B. Martin and N.J. Alvares, *Tech. Report 1007*, U.S.N.R.D.L., San Francisco (1968).

SECTION TWO

CHAPTER 12

Surface Flame Spread

James G. Quintiere

Introduction

This chapter covers both opposed flow and wind-aided flame spread over solids. Approximate formulas are developed using simple assumptions in order to illustrate the role of the relevant physical and chemical variables. The relationship between these approximate formulas and more exact results and data is discussed. Although an extensive review is not presented, an attempt is made to illustrate the extent of knowledge and opportunities for application. Flame spread over liquid fuels, in the forest, and in microgravity is also briefly discussed.

This chapter has been entitled "Surface Flame Spread" to ensure its distinction from flame propagation in premixed fuel and air systems. In the context here, flame spread applies to the phenomenon of a moving flame in close proximity to the source of its fuel originating from a condensed phase, (i.e., solid or liquid). As in the premixed case, the flame propagates in the gas phase, with its front associated with the lower flammability limit mixture. The fuel in the mixture is the vaporized condensed-phase fuel. The vaporization process is caused by heat transfer from the advancing flame itself and is necessary to sustain the spreading flame. Thus, two advancing fronts are present (1) the flame in the gas phase, and (2) the evaporation or pyrolysis region in the condensed phase. The former is easily perceived by the casual observer, while the evaporation front is actually a measure of the surface flame spread for the condensed phase. This front is not easily measured, but its rate of movement is defined as the *flame spread velocity*. These processes are illustrated in Figures 2-12.1 and 2-12.5.

In natural fires, it is the flame-spread process that is critical to the fire's destiny. This applies whether the fire is

an urban conflagration or is the first growth after ignition of a room's draperies. The process of growth is unstable, with the time for flame spread competing with the time for burning. If the spread time is small compared to the burn time, fire growth is likely to accelerate. Conversely, fire growth could decelerate and stop if the spread time is large compared to the burn time.

An example might illustrate the significance of flame spread in fire growth. Consider the ignition of an upholstered chair over a region 6 cm in diameter. Typical unenhanced spread rates are of the order of magnitude 1 mm/s, so in one minute the pyrolyzing region would be 18 cm in diameter, since the front would have grown 6 cm. This is nearly a tenfold increase in the pyrolyzing region, and, for sufficient fuel (long burn time), the increased rate of energy release will provide enhanced heat transfer to increase the flame spread rate. The fire growth is manifested by the size of the evaporation region over the condensed phase, and the rate of movement of its boundary is the flame spread velocity. Thus, surface flame spread plays a significant role in natural fire growth.

Premixed flame propagation can also occur in natural fires, provided that, in the gas phase, fuel and air are within their flammable limits over an extended region. This might result from a combustible gas leak, or could also arise under sufficient heating or restrictive ventilation conditions during the development of a fire in a confined space. In such cases, a sufficient energy source would initiate the propagation of flames in the gas phase at velocities of the order of magnitude 1 m/s compared to 1 mm/s associated with representative surface spread velocities. These values suggest the plausible limits of flame propagation in natural fires, but it is the lower end of the scale that governs the early development of fires on solid and liquid fuels. Subsequently, the nature and controlling variables can be described for such flame spread over solids and liquids. Table 2-12.1 gives the relative rates of flame spread for several fire phenomena, including horizontal surface spread and gas phase phenomena.

Dr. James G. Quintiere is the John L. Bryan Professor in the Department of Fire Protection Engineering at the University of Maryland, College Park. His research has focused on fire growth and flame spread.

**Table 2-12.1 Relative Flame Spread Rates
(order of magnitude)**

Phenomenon	Rate (cm/s)
Smoldering	10^{-3} to 10^{-2}
Lateral or downward spread on thick solids	$\sim 10^{-1}$
Upward spread on thick solids	1 to 10^2
Horizontal spread on liquids	1 to 10^2
Forest and urban fire spread	1 to 10^2
Pre-mixed flame speeds	
Laminar deflagration	10 to 10^2
Detonation	$\sim 3 \times 10^5$

Background

In recent years, research has focused on methods applying fundamental aspects of flame spread to real problems. Fundamental theory has provided a foundation for application, and formulas have been developed for practical use. However, these formulas are still limited by the lack of material data and phenomenological information about the fire conditions. For solid materials, the development of the cone calorimeter¹ and the lateral ignition and flame spread (LIFT)² tests has provided a basis for the needed material data. Attempts have been made to include configuration effects on flame spread, such as fire spread in vertical corners and ceilings. These attempts have not led to fully established methods, but have shown promise in replacing old flammability indices with more meaningful measures of flammability.

It is not possible to describe completely in a brief chapter all the research on flame spread. Hence, comprehensive reviews should be sought elsewhere. Recent reviews include Quintiere³ on wall fire spread, and Hirano⁴ on fundamental studies. A good source of material property data for wood species and products can be found from Janssens study.⁵ Other noteworthy recent reviews on flame spread can also be found in the literature. For example, Fernandez-Pello and Hirano⁶ give a detailed review of progress in flame spread over solids. Current knowledge on flame spread over liquid fuels is brought into focus by a critical review conducted by Glassman and Dryer.⁷ For a more tutorial discussion, one might read the presentation by Drysdale⁸ in the book, *An Introduction to Fire Dynamics*.

An excellent review and tutorial on flame spread was presented by Williams⁹ in 1976. It organized the subject in terms of the nature of the fuel's configuration and the mechanisms controlling flame spread. Its clarity in describing these mechanisms in simple terms is valuable reading for any serious student of flame spread. It describes each type of flame spread by physical arguments and expressions based upon the "fundamental equation of flame spread." That equation considers the net energy (heat) transferred (per unit area per unit time), \dot{q}'' , ahead of the advancing flame to heat the medium from its initial temperature, T_s , to its ignition temperature, T_{ig} . This energy is equated to the change in enthalpy (per unit area

per unit time) that the medium experiences for an observer on the moving flame front. For steady conditions

$$\rho V \Delta h = \dot{q}'' \quad (1)$$

where

ρ = density of the medium

V = spread rate

Δh = change in enthalpy per unit mass of medium in going from T_s to T_{ig}

The concept of an ignition temperature here represents the solid or liquid surface temperature that would cause sufficient production of fuel in the gas phase to sustain piloted ignition. For liquid fuels, this temperature is called the firepoint, and for solids it would depend on the kinetics of thermal degradation. Usually, it is assumed that the condensed phase is heated to the ignition temperature as a constant-property homogeneous medium; therefore, we can write

$$\Delta h = c(T_{ig} - T_s) \quad (2)$$

where c is the specific heat of the solid or liquid. Thus, a conceptual formulation has been established for the flame spread speed, V . It is interesting to observe that, for a given flame heat flux, V will increase as the fuel density decreases, and will increase without bound as T_s approaches T_{ig} . Thus, low-density solids could pose a potential flame-spread hazard; and, as T_s ahead of the advancing flame is increased by far-field convective and radiative effects of the fire, the spread will accelerate.

Flame Spread over Solids

In this section, some theoretical aspects will be sketched to illustrate the nature of flame spread on solids. In general, flame spread can occur in the presence of an ambient wind, such that the spread is upwind (opposed flow flame spread) or downwind (wind-aided flame spread). The wind might be due to external causes, which could be meteorological in nature, or due to a fire-induced (natural convection) flow created by the spreading flame or an associated fire. These two categories will be treated subsequently. Also, flame spread on solids will depend on geometrical orientation, that is, vertical or horizontal, facing upward or downward. All of these factors will affect the heat transfer (\dot{q}'') indicated in Equation 1. Indeed, the complex problem of computing \dot{q}'' from first principles has limited our ability to predict flame spread. Thus, issues of heat transfer pertaining to laminar and turbulent flow and flame radiation all play a role. Ultimately, chemical kinetic factors that control flame temperature, and indeed the survival of the flame itself, come into play. Hence, only the form of simple theoretical expressions will be derived. For more details and for the inclusion of other variables, specific references should be examined.

Opposed Flow Spread

Following the concept of using an energy conservation principle to describe flame spread (i.e., Equation 1), some simple analyses will be described. Although these analyses will be heuristic, their final results will be consistent with more formal analyses found in the literature. First, opposed flow spread will be considered for a solid whose thickness is sufficiently small so that the temperature is uniform across its thickness. In all cases, the spread rate is assumed steady and the reference frame is fixed to the pyrolysis front, that is, the position where the solid (surface) temperature is T_{ig} . This is illustrated in Figure 2-12.1.

Thermally thin case: For this *thermally thin case* of physical thickness, δ , and no heat loss from the bottom face, the energy equation for the control volume is developed. The control volume has been selected to extend from the region at the onset of pyrolysis, T_{ig} , to the region unaffected by the energy transported into the solid from the flame. This region is a distance Δ from the pyrolysis region to the position of initial solid temperature, T_s . The heat flux from the flame, \dot{q}'' , will be assumed constant over Δ . It follows that for the solid moving steadily through the flame-fixed control volume at the flame spread speed, V ,

$$\rho c \delta (T_{ig} - T_s) V = \dot{q}'' \Delta \quad (3)$$

Equation 3 is a more complete version of Equation 1, with the length scales δ and Δ explicitly included. The net forward flame heat flux characterized as conduction in the gas phase suggests

$$\dot{q}'' \approx k_g \left(\frac{T_f - T_r}{\Delta} \right) \quad (4)$$

where

k_g = gas phase conductivity

T_f = flame temperature

T_r = reference temperature for the solid—either T_{ig} or T_s would suffice

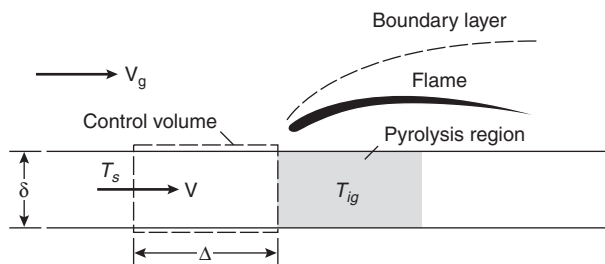


Figure 2-12.1. Energy conservation analysis in opposed flow spread.

Combining Equations 3 and 4 yields an expression nearly identical to that more formally derived by deRis¹⁰ for thermally thin solids

$$V = \frac{\sqrt{2}k_g(T_f - T_s)}{\rho c \delta (T_{ig} - T_s)} \quad (5)$$

The flame temperature, T_f , here should ideally be taken as that due to adiabatic stoichiometric combustion but, in general, could be thought of as less due to heat losses and chemical kinetic effects. Under these ideal theoretical considerations, it can be shown¹¹ that

$$T_f - T_{ig} = \frac{(T_\infty - T_{ig}) + (Y_{ox,\infty}/rc_g)(\Delta H - L)}{1 - Y_{ox,\infty}/r} \quad (6)$$

where

ΔH = heat of combustion of the solid fuel

L = heat of gasification

T_∞ = gas phase ambient temperature

$Y_{ox,\infty}$ = gas phase ambient oxygen concentration

r = stoichiometric mass ratio of oxygen to fuel

c_g = specific heat of the gas phase

Because ΔH and $Y_{ox,\infty}/r$ are relatively large, and $\Delta H_{ox} = \Delta H/r$ is nearly a constant for most hydrocarbons (13 kJ/g), Equation 6 suggests that

$$T_f - T_{ig} \sim Y_{ox,\infty} \Delta H_{ox}/c_g \quad (7)$$

Thus, the flame temperature for many solids is primarily only sensitive to the ambient oxygen concentration. This fact suggests that flame spread over a ceiling in a room would be reduced as the oxygen near the ceiling was reduced. Substitution of Equation 7 into 5, essentially yields the results of Magee and McAlevy;¹² however, they considered pressure effects as well. Incidentally, their early work in flame spread¹² contains extensive data on factors affecting flame spread.

Up to now, no mention of the opposed flow speed, V_g , has been made, and the flame spread velocity appears to be independent of it. Independence is only the case as long as chemical effects are unimportant. Chemical kinetic effects become important when the time for chemical reactions to be completed in the flame (t_{chem}) becomes long compared to the fluid flow transit time (t_{flow}) through the flame. If the flow is too fast, chemical reaction would be incomplete. The Damköhler number (D) is a parameter used to express these effects and may be represented as Equation 8

$$D \sim \frac{t_{flow}}{t_{chem}} \sim \frac{1}{V_g^2} \quad (8)$$

As a consequence, the flame heat transfer or theoretical flame temperature in Equation 5 is then modified by some function of D . The dependence of D measured spread rates over thin paper sheets has been correlated by Fernandez-Pello et al.¹³ in forced flow conditions and by Altenkirch et al.¹¹ under buoyant flow downward spread

conditions. A recent theoretical analysis by Wichman¹⁴ offers some explanation for these correlations. Each investigator defined a slightly different Damköhler number and selected different chemical kinetic property data. But in qualitative terms, Figure 2-12.2 represents the results given, with the measured spread velocity normalized with the ideal theoretical velocity Equation 5 plotted against D . The results show that the flame spread decreases with D , and therefore decreases as the opposed flow velocity is increased for the thermally thin solid.

For flame-induced flows in pure natural convection, the ambient flow velocity is characteristically given as¹¹

$$(V_g)_{\text{natural convection}} \sim \left(\frac{v_g g \Delta H Y_{ox,\infty}}{c_g r T_\infty} \right)^{1/3} \quad (9)$$

where v_g is the gas phase kinematic viscosity. But since $\Delta H/r = \Delta H_{ox}$, approximately constant at 13 kJ/g, V_g induced by buoyancy is primarily a function of $Y_{ox,\infty}$ to the 1/3 power.

In summary, for thermally thin solids, the flame spread speed under an opposed flow velocity, V_g , with an ambient oxygen concentration, $Y_{ox,\infty}$, is from Equation 5

$$V = V_{\text{ideal}} f(D) \quad (10)$$

where V_{ideal} is given by Equation 5 and the general behavior of $f(D)$ is shown in Figure 2-12.2. At some critical value of D , no further flame spread is possible and extinction occurs. For a given material, D depends on V_g and $Y_{ox,\infty}$, and, from Equation 7 the theoretical flame temperature depends only on $Y_{ox,\infty}$. Therefore, from Equations 5 and 10, the general form of the relationship in opposed flow flame spread on thin materials is

$$V = \frac{\phi(V_g, Y_{ox,\infty}, \text{material properties})}{\rho c \delta (T_{ig} - T_s)} \quad (11)$$

where the function ϕ depends on such factors as the gas velocity, the local oxygen concentration, and the properties of the material. For common combustible solids, it has been reasoned¹⁰ that the above analysis holds for $\delta \leq 1$ mm, approximately. In particular, Fernandez-Pello and Hirano⁶ concluded that for polymethyl methacrylate (PMMA), downward flame spread could be considered thermally thin for $\delta < 2$ mm and thermally thick for $\delta > 2$ cm. In between, the solid would have a nonuniform but finite temperature rise throughout flame spread.

Except for items like paper, garments, or draperies, most solids in practice will behave as thermally thick under flame spread conditions. It might appear, for engineering purposes, to regard solids with $\delta > 1$ mm as thermally thick. Up to a thickness of 1 to 2 cm, flame spread could depend on thickness and on the substrate material adjacent to the solid. Based on these factors, it is apparent that the thermally thick case is more significant, and it will be derived below.

Thermally thick case: The analysis based on Figure 2-12.1 still applies, except that for the *thermally thick case*, δ must be considered as the thermal penetration

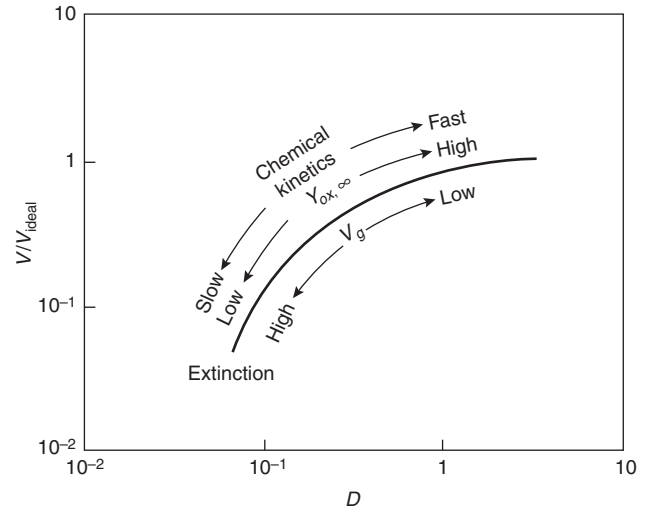


Figure 2-12.2. Qualitative dependence of opposed flow flame speed with Damköhler number, D .

depth, which depends on time. From heat conduction theory, it can be reasoned that

$$\delta \approx \sqrt{\frac{k}{\rho c} t} \quad (12)$$

where t is the time for the flame's pyrolysis front to traverse the heating length, Δ , of the control volume in Figure 2-12.1

$$t = \frac{\Delta}{V} \quad (13)$$

Substitution of Equations 12 and 13 into Equation 3 yields

$$V = \frac{(\dot{q}'')^2 \Delta}{k \rho c (T_{ig} - T_s)^2} \quad (14)$$

The length scale, Δ , depends on the nature of the forward heat transfer. In opposed flow spread, when forward conduction in the gas phase is the dominant mode of heat transfer, it can be reasoned that forward conduction must be balanced with convection, that is,

$$\rho c V_g \frac{\partial T}{\partial x} \sim k \frac{\partial^2 T}{\partial x^2}$$

in the gas phase.

As a consequence,

$$\Delta \sim \left(\frac{k}{\rho c} \right)_g / V_g \quad (15)$$

and, on combining with Equations 4 and 14 yields

$$V = \frac{V_g (k \rho c)_g (T_f - T_{ig})^2}{k \rho c (T_{ig} - T_s)^2} \quad (16)$$

as the flame speed for the thermally thick case—identical to the formally derived by deRis.¹⁰ This expression should

be termed the *ideal value*, with T_f given by its adiabatic stoichiometric value. With this viewpoint, the chemical kinetic effects enter through the Damköhler number, as in the thin case, with the actual velocity given as

$$\frac{V}{V_{\text{ideal}}} = F(D) \quad (17)$$

Figure 2-12.2 applies, as well. But, for the thick case, because the “ideal” flame speed (Equation 16) depends on the opposed velocity, V_g , directly as well as through the Damköhler number, D , the actual flame spread speed may either increase or decrease with V_g , depending on $Y_{\text{ox},\infty}$. Fernandez-Pello et al.¹³ show for PMMA that V is insensitive to V_g for $V_g \leq 30 \text{ cm/s}$ at normal ambient oxygen levels ($Y_{\text{ox},\infty} = 0.233$) and decreases as V_g is increased. These results are sketched in Figure 2-12.3. At higher-than-normal oxygen levels for air, the dependence of V on V_g is more complicated. Thus, the Damköhler number dependence is required to fully understand the effect of V_g on V for thick fuels. One consolation, at least for PMMA, is that under normal fire conditions (e.g., downward spread on a wall), the buoyancy-induced flow speed is roughly 30 cm/s. For this air speed or less, V is primarily dependent on $Y_{\text{ox},\infty}$ only.

In previous studies, the opposed flow has been laminar. The effects of turbulence have been investigated by Zhou and Fernandez-Pello¹⁵ who found that the spread

rate decreased in air flows as the opposed turbulent intensity increased for thin paper, but had a maximum for thick PMMA at approximately 0.5 m/s.

A complete numerical simulation, including the effects of solid- and gas-phase kinetics, has been attempted by Di Blasi et al.¹⁶ with qualitative success. Such models will provide useful insight into the fundamental mechanisms, provided these effects can be computationally resolved.

A practical test procedure has been developed by Quintiere and Harkleroad¹⁷ that allows one to determine the essential parameters needed to describe opposed-flow flame spread on thick materials burning in air under natural convection conditions. As done for the thin case in Equation 11, Equation 17 is rewritten as follows:

$$V = \frac{\Phi}{kpc(T_{ig} - T_s)^2} \quad (18)$$

where Φ depends on V_g and $Y_{\text{ox},\infty}$, in general, for a given material. By measuring the flame spread laterally on a vertical sample exposed to an external radiant heat flux, the parameters Φ , kpc , and T_{ig} are deduced by analysis. A wide range of tests indicated that T_{ig} ranged from 280°C for PMMA to 570°C for the paper on gypsum wallboard. The parameter, Φ , for these conditions in air ranged from about 1 to 15 (kW)²/m³. Also, a critical surface temperature was determined below which continued spread was not possible ($T_{s,\min}$). Table 2-12.2 illustrates these deduced parameters for a range of materials. Results obtained in this lateral mode were shown to be similar to downward spread, except for materials with excessive melting and dripping,¹⁷ and were shown to be similar to axisymmetric spread from a small (pool) fire on a horizontal surface.¹⁸ Other data for wood products are given by Janssens.⁵

In these analyses, the ignition temperature has been assumed constant for each material, and its name implies a relationship between ignition and flame spread. It is interesting to illustrate this relationship by showing the behavior of spread velocity and time to ignite as a function of radiant heating. Consider downward or lateral spread on a vertical surface at various levels of irradiation, \dot{q}_e'' . For each \dot{q}_e'' the surface is allowed to heat to a steady temperature, T_s , before flame spread is initiated. Thus, there is a unique T_s for a given \dot{q}_e'' . Consider, also, piloted ignition of this same material under sufficiently high values of \dot{q}_e'' . Such experiments have been done for a wide range of materials¹⁷ and the results all have the same characteristics. These trends are shown for a 1.27-cm-thick Douglas fir particleboard in Figure 2-12.4. It might be termed a “flamability diagram” for the material, since it shows at a glance its ease of ignition and its propensity for spread. Moreover, the minimum irradiance for ignition, $\dot{q}_e''(T_{ig})$, marks a critical condition for spread; and T_{ig} can be inferred from a knowledge of $\dot{q}_e''(T_s)$. This procedure has been adopted in the standard test known as LIFT (lateral ignition and flamespread test).²

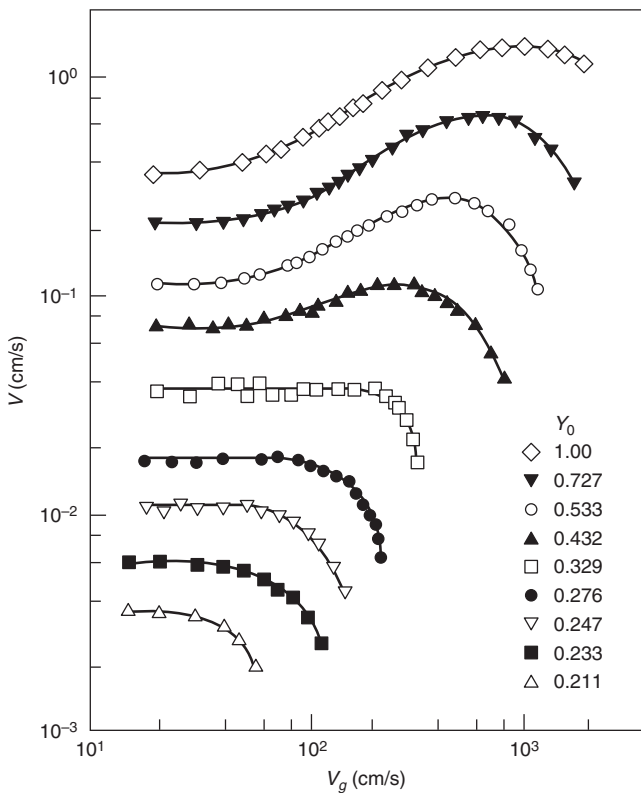


Figure 2-12.3. Effect of opposed velocity and oxygen concentration of flame spread speed for thick PMMA. (Taken from Fernandez-Pello et al.)¹³

Wind-Aided Spread

Flame spread in the same direction as the ambient flow is much different from opposed flow spread. This classification of spread could result from an external wind

Table 2-12.2 Effective Flame Spread Properties (based on experimental correlations¹⁷)

Material	T_{ig} (°C)	kpc (kW ² s/m ⁴ K ²)	Φ (kW ² /m ³)	$T_{s,min}$ (°C)	Φ/kpc (mK ² /s)
PMMA polycast (1.59 mm)	278	0.73	5.4	120	8
Polyurethane (S353M)	280	—	—	105	82
Hardboard (6.35 mm)	298	1.87	4.5	170	2
Carpet (acrylic)	300	0.42	9.9	165	24
Fiberboard, low density (S119M)	330	—	—	90	42
Fiber insulation board	355	0.46	2.2	210	5
Hardboard (3.175 mm)	365	0.88	10.9	40	12
Hardboard (S159M)	372	—	—	80	18
PMMA type g (1.27 cm)	378	1.02	14.4	90	14
Asphalt shingle	378	0.70	5.3	140	8
Douglas fir particle board (1.27 cm)	382	0.94	12.7	210	14
Wood panel (S178M)	385	—	—	155	43
Plywood, plain (1.27 cm)	390	0.54	12.9	120	24
Chipboard (S118M)	390	—	—	180	11
Plywood, plain (0.635 cm)	390	0.46	7.4	170	16
Foam, flexible (2.54 cm)	390	0.32	11.7	120	37
GRP (2.24 mm)	390	0.32	9.9	80	31
Mineral wool, textile paper (S160M)	400	—	—	105	34
Hardboard (gloss paint) (3.4 mm)	400	1.22	3.5	320	3
Hardboard (nitrocellulose paint)	400	0.79	9.8	180	12
GRP (1.14 mm)	400	0.72	4.2	365	6
Particle board (1.27 cm stock)	412	0.93	4.2	275	5
Gypsum board, Wallpaper (S142M)	412	0.57	0.79	240	1
Carpet (nylon/wool blend)	412	0.68	11.1	265	16
Carpet #2 (wool, untreated)	435	0.25	7.3	335	30
Foam, rigid (2.54 cm)	435	0.03	4.0	215	141
Polyisocyanurate (5.08 cm)	445	0.02	4.9	275	201
Fiberglass shingle	445	0.50	9.0	415	18
Carpet #2 (wool, treated)	455	0.24	0.8	365	4
Carpet #1 (wool, stock)	465	0.11	1.8	450	17
Aircraft panel epoxy Fiberite	505	0.24	a	505	a
Gypsum board, FR (1.27 cm)	510	0.40	9.2	300	23
Polycarbonate (1.52 mm)	528	1.16	14.7	455	13
Gypsum board, (common) (1.27 mm)	565	0.45	14.4	425	32
Plywood, FR (1.27 cm)	620	0.76	a	620	a
Polystyrene (5.08 cm)	630	0.38	a	630	a

Values are only significant to two places.

^aFlame spread was not measureable.

or the buoyancy-induced flow as a flame spreads up a wall or under a ceiling. Wind-aided spread can be acceleratory and, therefore, appears more rapid than opposed flow spread. Despite their distinct differences, the previous simplified analyses can still be used to explain wind-aided spread.

The illustration in Figure 2-12.1 can be used here with the control volume of interest selected downstream of the pyrolysis zone. This is shown in Figure 2-12.5, where the length of the control volume, Δ , is selected to span the heat transfer from the adjacent flame and hot combustion products in the boundary layer. Here, Δ is of the order of the flame length and could be in the range of 0.1 to 10 m as compared to Δ in opposed flow flame spread in the range of 1 to 3 mm. The control volume is fixed to the leading edge of the pyrolysis zone where the temperature has achieved the ignition temperature, T_{ig} . A distance Δ away, the solid is still at its initial temperature, T_s , and

moves through the control volume at the flame spread speed V . An energy balance applied to this control volume will lead to the same equations as developed in the opposed flow analyses, but with a different interpretation for the terms \dot{q}'' and Δ . From Equations 3 and 14, those results are given as follows for the thermally thin case:

$$V = \frac{dx_p}{dt} = \frac{\dot{q}''\Delta}{\rho c\delta(T_{ig} - T_s)} \quad (19)$$

and for the thermally thick case:

$$V = \frac{dx_p}{dt} = \frac{(\dot{q}'')^2\Delta}{kpc(T_{ig} - T_s)^2} \quad (20)$$

These results should be taken as qualitatively illustrative, especially since \dot{q}'' has been assumed constant over Δ . Actually the heat flux distribution will vary, in general, with

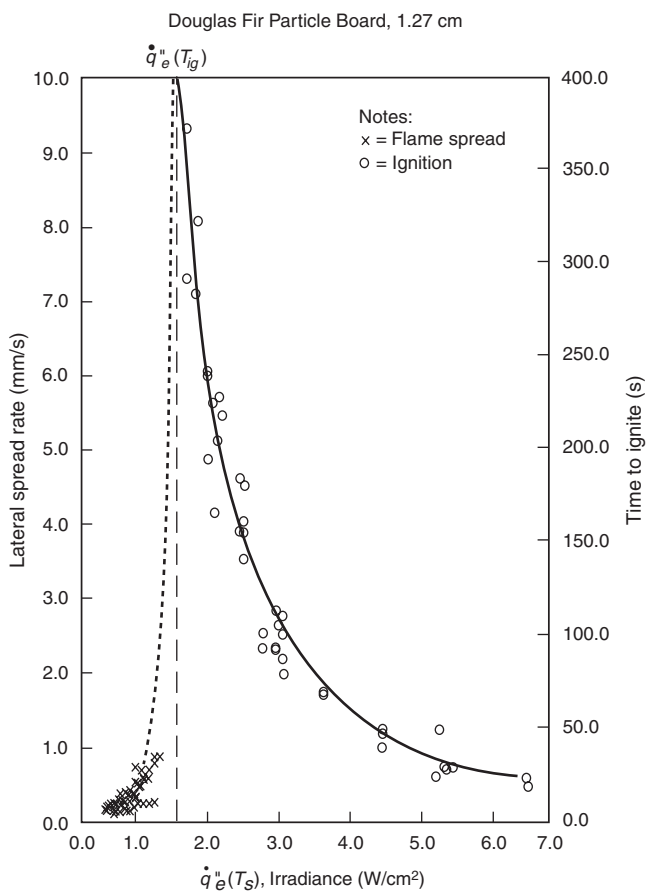


Figure 2-12.4. Relationship between piloted ignition and flame spread velocity.¹⁷

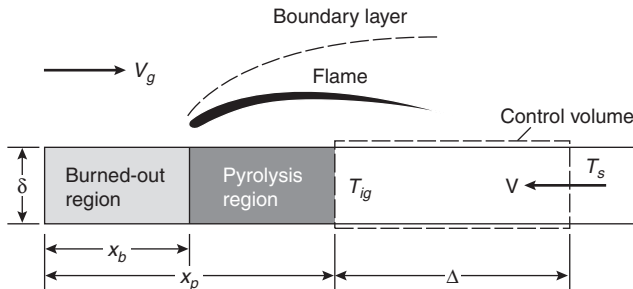


Figure 2-12.5. Energy conservation in wind-aided flame spread.

the downstream coordinate (x) in accordance with the convective boundary layer and flame radiative characteristics. Also, Δ would be intimately related to the nature of the heat flux distribution.

Alternatively, Equations 19 and 20 can be written as

$$V = \frac{dx_p}{dt} = \frac{x_f - x_p}{\tau} \quad (21)$$

where τ is an ignition time associated with the flame heat flux. Wichman and Agrawal¹⁹ more carefully show the

basis of this formulation for wind-aided spread. Here, x_f is the flame length measured from $x = 0$, and the flame heat flux is assumed constant over this region Δ . Saito et al.²⁰ use this formulation to examine upward (or, in general, wind-aided) spread. From the definition of x_p ,

$$x_p = x_p(0) + \int_0^t V(s)ds \quad (22)$$

It is postulated that x_f is directly related to energy released per unit width, \dot{Q}' , so that

$$x_f - x_b = K[\dot{Q}']^n \quad (23a)$$

where

$$\dot{Q}' = \int_{x_b}^{x_p} \dot{Q}''(\xi)d\xi \quad (23b)$$

with \dot{Q}'' the energy release per unit area. It should be noted that the cone calorimeter¹ can potentially provide data to derive \dot{Q}'' . However, this depends on the heat flux appropriate to the flame spread configuration, not necessarily on the cone test irradiance. For example, for upward spread on a flat wall and under turbulent conditions, $K = 0.067 \text{ m}^{5/3} \cdot \text{kW}^{-2/3}$ and $n = 2/3$.²¹ It can be shown²⁰ that

$$\dot{Q}' = x_p(0)\dot{Q}''(t) + \int_0^t \dot{Q}''(t-s)V(s)ds \quad (24)$$

for the case of $x_b = 0$. Substituting Equations 22 through 24 yields an integral equation for V . This formulation gives a framework for solving particular wind-aided spread problems, provided that the flame heat flux and flame length can be expressed for that configuration. Also, material data are needed to express τ and \dot{Q}'' . Variations on this formulation have been applied successfully to predict upward turbulent flame spread.²²⁻²⁵

Fundamental studies have given us some limited results. A simpler result for V can be derived. The heat flux, \dot{q}'' , could be reasoned to depend on the flame temperature, T_f , (Equation 7) and on the boundary layer thickness. The extent of heating, Δ , is related to flame length, and this has been shown to depend on the energy release rate to some power n (e.g., n is believed to be $1/2$ to 1 in upward turbulent spread). Since the energy release rate depends on the extent of the pyrolyzing region, $(x_p - x_b)$, then it suggests that

$$V = \frac{dx_p}{dt} \propto (x_p - x_b)^n \quad (25)$$

provided \dot{q}'' is not sensitive to position. Thus, depending on n and the relationships governing burnout (i.e., $x_b(t)$), the flame speed can accelerate to a limit or without bound if $n > 0$. Markstein and deRis²⁶ found for thin textiles that n varied from 0.5 to 0.7 , with $x_p - x_b$ approaching an asymptotic steady-state limit after some time. The nature of their experiments was upward turbulent burning conditions. Under laminar upward spread, Fernandez-Pello²⁷ derived $n = 3/4$ for the thermally thin case, $n = 1/2$ for the thermally thick case, and $x_b \equiv 0$. Orloff et al.²⁸

found that upward turbulent spread on thick PMMA followed Equation 25, with $n = 0.964$ and $x_b \equiv 0$. After spread extended over approximately 1 m of the PMMA, the speed was measured at roughly 0.5 cm/s. Note, for $n = 1$ and $x_b = 0$, the speed grows exponentially in time. This growth marks the potential hazard of wind-aided spread. It should be clear that the outcome depends on flame length, which is controlled by configuration and flow conditions, and on burnout, which is controlled by the material.

There are several notable wind-aided studies. Atreya and Mekki²⁹ have studied laminar flame spread on a ceiling-mounted sample. Di Blasi et al.³⁰ mathematically modelled this spread problem, including unsteady and kinetic effects. They found that the spread speed reaches steady state at a given flow velocity, and also kinetic effects were only important at extinction. A turbulent flow study by Zhou and Fernandez-Pello³¹ for ceiling- and floor-mounted PMMA (0.3 m in length) found flow speeds of 0.25 to 4.5 m/s with turbulent intensities 1 percent to 15 percent. They also found that the spread rate is steady at a given flow, but increases with flow speed. For their range of flow conditions, they found that Equation 20 agrees with a numerical coefficient of $1.4(4/\pi)$. At larger scales, radiation and buoyancy effects become important, especially for floor-mounted materials. Studies by Apte et al.³² for 2.4-m-long PMMA and by Perzak and Lazzara³³ for 9.8-m-long PMMA at flow speeds of 0.8 to 3.8 m/s show higher spread rates due to flame radiation effects. They measure rates of 1 to 6 cm/s, compared to approximately 0.01 to 0.3 cm/s for smaller samples.³¹

The ASTM E84 Steiner tunnel test is the primary flammability test used in the United States. It represents a complex form of wind-aided spread on a ceiling-mounted material in a duct under forced flow conditions. Although that test is not capable of measuring x_p (nor x_b), a recent correlation showed its sensitivity to energy release rate.³⁴ It was found that tunnel ratings were low and insensitive to energy release rate per unit area, \dot{Q}'' , for values less than approximately 70 kW/m^2 and highly sensitive and increasing above that value. In other words, some critical energy release rate appears to be required to permit sustained spread. It is likely that the ASTM E-84 Steiner tunnel test can be successfully modelled using Equation 20, provided tunnel relationships are developed for \dot{q}'' and Δ .

For upward turbulent flame spread on a vertical surface, it has been found that the flame heat flux ahead of the pyrolysis zone is approximately 25 kW/m^2 for moderate fires ($x_f < 1.4 \text{ m}$), and approximately independent of material. This is shown in Figure 2-12.6 where the sketched region represents the data of Quintiere et al.^{3,35} It also displays the laminar and turbulent results of Ahmed and Faeth³⁶ without radiation effects, the large-scale PMMA results of Orloff et al.³⁷ and power-law correlations of the data by Hasemi.³⁸ It is seen that both laminar and large fires can exceed 25 kW/m^2 . More recent data by Kulkarni et al.²⁴ generally confirm this heat flux distribution, with some exceptions, possibly due to measurement difficulties for melting materials. Figure 2-12.7 shows results of a study by Ito and Kashiwagi³⁹ using interferometry to examine the temperature distributions at the leading edge of spreading flames on PMMA at orientations

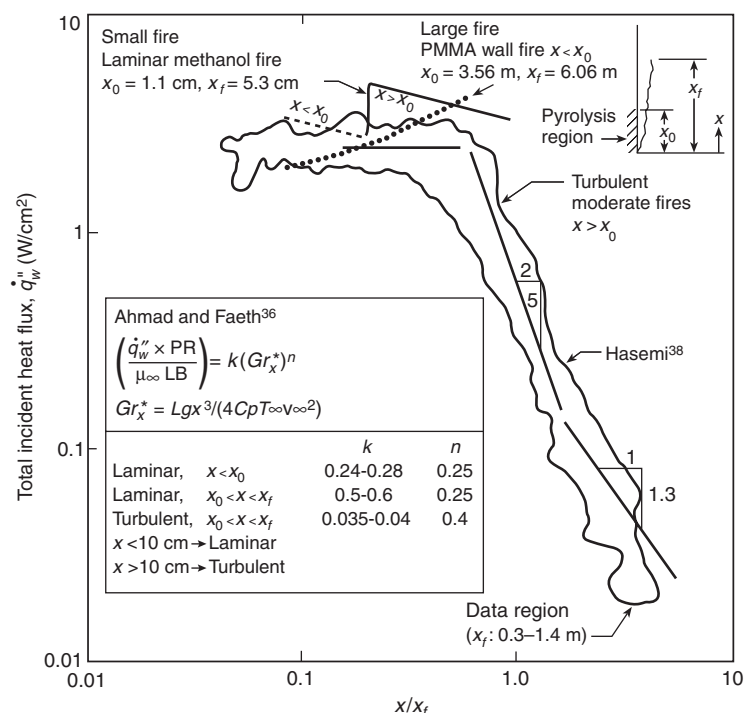


Figure 2-12.6. Wall flame incident heat flux for materials,³⁵ for laminar flames,³⁶ and for a large PMMA wall fire.³⁷

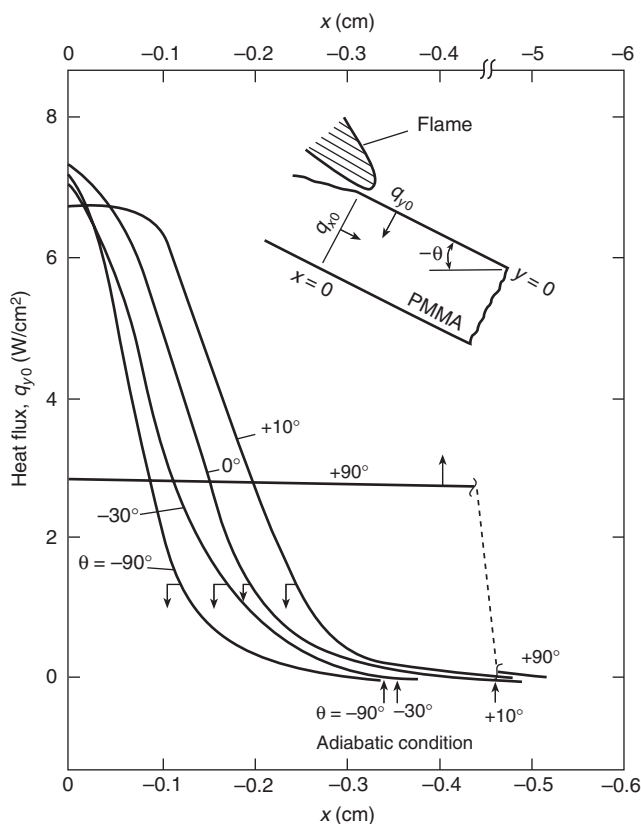


Figure 2-12.7. Distributions of normal heat flux at the surface along the distance ahead of the vaporization front, from Ito and Kashiwagi.³⁹

ranging from +90 degrees (upward vertical) to -90 degrees (downward vertical). Note the constant heat flux of approximately 25 kW/m² for upward spread, and a maximum of 70 kW/m² for downward spread. A notable orientation effect was found in the London King's Cross fire involving spread up a wooden escalator. The sidewalls of the escalator caused the flames to "hug" the steps.⁴⁰

The room-corner test has been developed as a realistic testing protocol for the flammability of interior finish materials. Several investigators have had good success at predicting the results of this configuration using data from the cone calorimeter test and the flame spread equations discussed above.⁴¹⁻⁴⁵ It appears that accurate simulation models for fire growth can be developed using the flame spread theories outlined here along with relevant data.

Flame Spread over Liquids

Flame spread over horizontal pools of liquid fuels differs from flame spread over solids, due to convective flows within the liquid that enhance spread. Also, whereas solid decomposition is more complex, involving kinetically driven pyrolysis, the liquid fuel evaporates under thermodynamic principles. The liquid temperature, T_s , controls the rate of spread relative to a critical (ignition) temperature that corresponds to that necessary to

produce a lean flammability limit over the fuel surface. This temperature is usually referred to as the flash point for liquid fuels, and several methods exist for its measurement. Glassman and Dryer⁷ discuss the implications of its measurement and its relationship to mechanisms associated with flame spread on liquids.

The convective phenomenon generated in the liquid is due to surface tension effects. The surface tension increases inversely with temperature and, thus, can pull the flame toward the unheated liquid. This is illustrated in Figure 2-12.8 for a thin liquid layer, δ . Under steady conditions, the viscous forces on the control volume are balanced by the surface tension forces. Thus, the shear stress, τ , at the bottom surface equals the surface tension gradient ($d\sigma/dx$) along the free surface

$$\tau = \frac{d\sigma}{dx} = \left(\frac{d\sigma}{dT} \right) \left(\frac{\partial T}{\partial x} \right) \quad (26)$$

For a thin liquid layer, the surface tension effect results in nearly a Couette flow (constant shear) over the layer thickness, δ . Hence, it can be approximated that

$$\tau = \left(\mu \frac{\partial u}{\partial y} \right)_{y=0} \approx \mu \frac{V}{\delta} \quad (27)$$

where μ is the liquid viscosity. By further approximating the surface tension gradient as a difference over length Δ , the flame speed can be estimated as

$$V = \frac{[\sigma(T_s) - \sigma(T_{ig})]\delta}{\mu\Delta} \quad (28)$$

provided $\sigma(T)$, the surface tension, is known as a function of temperature for the liquid, and Δ can be estimated for the conditions of spread. Also, δ , as in the thermally thick case for solids, is only the physical liquid depth for pools less than about 1 mm, and, therefore, must be reinterpreted for pools of larger depth.⁹ For example, one might estimate δ as

$$\sqrt{\left(\frac{\mu}{\rho} \right) \left(\frac{\Delta}{V} \right)}$$

for the deep-pool case.

Typical flame spread characteristics over a liquid fuel are sketched in Figure 2-12.9 for liquid methanol from the data of Akita.⁴⁶ Below the flash point, $T_s < T_{ig} \approx 11^\circ\text{C}$, the spread is governed by transport phenomena within

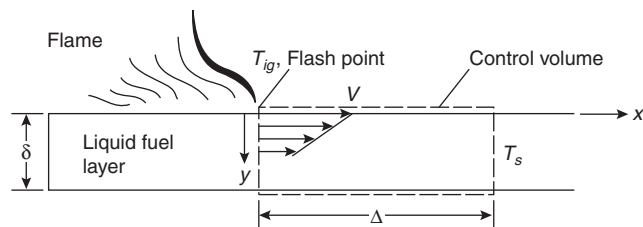


Figure 2-12.8. Enhanced flame spread speed in liquids due to surface-tension induced flow.

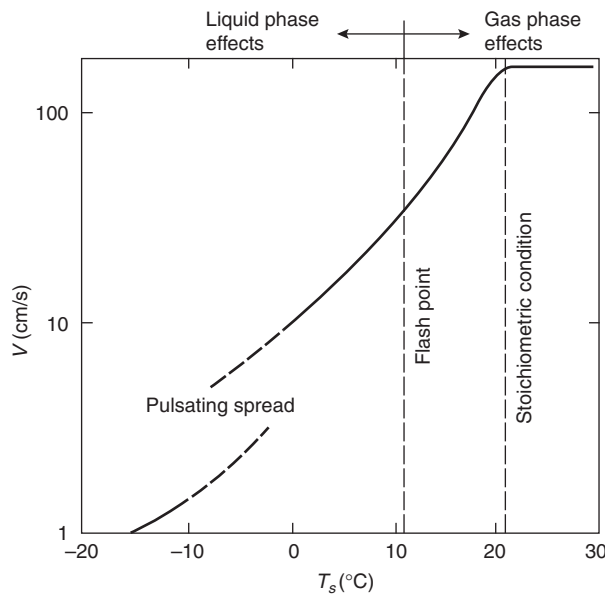


Figure 2-12.9. Results sketched for flame spread over liquid methanol, based on Akita.³

the liquid fuel. For initial liquid bulk temperatures above the flash point, a flammable mixture always exists everywhere above the surface so that propagation is governed by gas phase effects. Above a liquid temperature, which corresponds to stoichiometric conditions above the surface, the flame speed remains constant and usually above the normal premixed laminar flame speed. A recent study by Ito et al.⁴⁷ used holographic interferometry to examine the liquid phase for subflash point liquid bulk temperatures. They examined the pulsating region depicted in Figure 2-12.9 and the adjacent uniform region of spread just below the flashpoint. They found that both a surface tension flow and a gravity-induced circulation flow in the liquid below the flame are present; both appear to contribute to flame spread rate in the uniform region. See Section 2, Chapter 15, for additional information on liquid flame spread.

Flame Spread in Forests

Flame spread in a forest has many characteristics related to fuel type and configuration, terrain, wind conditions, and humidity. Much research has been done, and no effort here will be made to describe that work. In recent years, based on its research, the Forest Service of the U.S. Department of Agriculture has implemented practical methods for estimating flame spread in forests under a variety of field conditions.⁴⁸

Rothermel⁴⁹ presents a thorough review of the theory and models available for forest fire danger rating and behavior prediction. He also discusses a computer model (BEHAVE) that is based on the instructional format previously presented.⁴⁸

Flame spread in a forest depends on radiant heat transfer and convective heating due to wind or the slope

of the terrain. In most cases, the porous brush along the floor of the forest is involved, but for severe fires the crowns of the trees also, or exclusively, become involved. In addition, wind currents can transport large embers (fire brands) great distances from the fire to start spot fires at other locations. Breaks in the fuel array can be used to control the spread, but the size of a break sufficient to interrupt the fire will depend on the size of the fire and its heat transfer characteristics. Albini⁵⁰ gives an excellent discussion of forest fire phenomena in conceptual terms. Many of these cases have been addressed, and the Forest Service and others have developed analytical models and data for their treatment.

An approximate formula applicable to wildland fires, wood cribs, and urban conflagration is given by Thomas⁵¹ as

$$V\rho_b = k(1 + V_\infty)$$

where

ρ_b is the bulk density of the fuel (kg/m^3)

V is the wind speed (concurrent) (m/s)

$k = 0.07$ for wildland fires (kg/m^3)

0.05 for wood cribs

0.046 for the Great Fire of London ($V = 4.5 \text{ m}/\text{s}$)

Figure 2-12.10 shows the results for urban fires in Japan in relationship to this approximate formula.

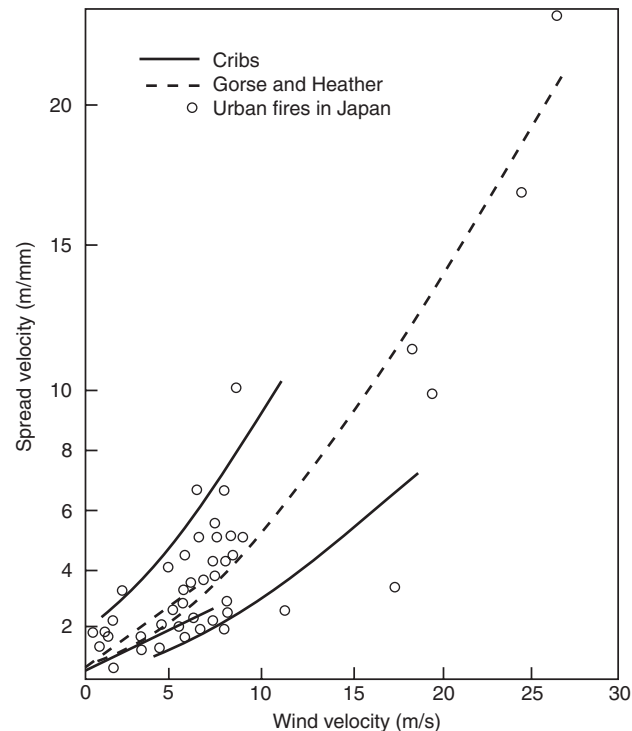


Figure 2-14.10. Comparison of rates of fire spread for urban and wildland fires as a function of wind speed.⁵¹

Flame Spread in Microgravity

Because of an increased activity in space, flame spread research has been conducted under microgravity conditions. Research has been done in drop towers and in the space shuttle Discovery, as reported by Bhattacharjee and Altenkirch.⁵² They examined flame spread over filter paper at 50 percent oxygen in nitrogen in a quiescent atmosphere. The spread rate was measured at 0.44 cm/s compared to a predicted value of 0.42 cm/s. Opposed flow theory applies, but the inclusion of gas-phase radiation was an essential mechanism. A study of flame spread over liquid fuels was conducted by Miller and Ross.⁵³ They found similar results between microgravity and 1-g conditions, except that opposed flow appears to lower the limiting oxygen concentration at extinction for microgravity. Forced-flow wind-aided flame spread would not be expected to be significantly affected by gravity.

Concluding Remarks

This chapter has provided some insight into the nature of fire spread over materials for the practicing engineer. In general, flame spread depends on the heat transfer processes at the flame front. These transport processes depend not only on the fuel, but also the fuel's configuration and orientation, and on ambient environment conditions. Thus, estimates of flame spread require complex analysis and specific material data. The current state of knowledge does provide limited formulas and material data to make some estimates. In this chapter, the full scope of flame spread phenomena has not been addressed. For example, flame spread in enclosures, mines, ducts, and buildings presents an entirely new complex array of conditions. Thus, flame spread on materials must be evaluated in the context of their use, and appropriate data must be made available for proper assessments of materials.

Nomenclature

c	specific heat
δ	fuel thickness
D	Damköhler number, Equation 8
Δh	enthalpy change
ΔH	heat of combustion
ΔH_{ox}	$\Delta H/r$
k	conductivity
μ	viscosity
ρ	density
Φ	numerator in Equation 18
ϕ	numerator in Equation 11
\dot{q}''	heat flux
Q	energy release
r	reference
r	stoichiometric mass ratio oxygen/fuel
t	time
T	temperature
V	spread velocity
V_g	gas velocity

x, y	coordinates
Y	mass fraction
Δ	length of flame heating
ν	kinematic viscosity, μ/ρ
σ	surface tension

Superscripts

.	per unit time
,	per unit length
"	per unit area

Subscripts

b	burnout
f	flame
g	gas phase
i	ignition
ox	oxygen
p	pyrolysis
r	reference
s	surface
∞	ambient

References Cited

- ASTM E1354-90, *Standard Test Method for Heat and Visible Smoke Release Rates for Materials and Products Using an Oxygen Consumption Calorimeter*, American Society for Testing and Materials, West Conshohocken, PA (1990).
- ASTM E1321-90, *Standard Method for Determining Material Ignition and Flame Spread Properties*, American Society for Testing and Materials, West Conshohocken, PA (1990).
- J.G. Quintiere, "Application of Flame Spread Theory to Predict Material Performance," *Journal of Research of the National Bureau of Standards*, 93, 1, pp. 61–70 (1988).
- T. Hirano, "Physical Aspects of Combustion in Fires," in *Proceedings 3rd International Symposium*, (G. Cox and B. Langford, eds.), Elsevier Applied Science, New York, pp. 27–44 (1991).
- M.L. Janssens, "Fundamental Thermophysical Characteristics of Wood and Their Role in Enclosure Fire Growth," National Forest Product Assoc., Washington, DC, p. 492 (Sept. 1991).
- A.C. Fernandez-Pello and T. Hirano, *Comb. Sci. and Tech.*, 32, p. 1 (1983).
- I. Glassman and F.L. Dryer, *F. Safety J.*, 3, p. 123 (1980).
- D.D. Drysdale, *An Introduction to Fire Dynamics*, 2nd ed., John Wiley and Sons, New York (2000).
- F.A. Williams, "Mechanisms of Fire Spread (Invited Review)," in *16th Symposium (International) on Combustion*, Combustion Institute, Pittsburgh, PA, pp. 1281–1294 (1976).
- J.N. de Ris, "Spread of a Laminar Diffusion Flame," in *12th Symposium (International) on Combustion*, Combustion Institute, Pittsburgh, PA, pp. 241–252 (1969).
- R.A. Altenkirch, R. Eichhorn, and P.C. Shang, *Comb. and Flame*, 37, p. 71 (1980).
- R.S. Magee and R.F. McAlevy III, *J. Fire and Flamm.*, 2, p. 271 (1971).
- A.C. Fernandez-Pello, S.R. Ray, and I. Glassman, in *18th Symposium (International) on Combustion*, Pittsburgh, PA (1981).
- I.S. Wichman, *Comb. Sci. and Tech.*, 40, p. 223 (1984).

15. L. Zhou, A.C. Fernandez-Pello, and R. Cheng, "Flame Spread in an Opposed Turbulent Flow," *Journal Combustion and Flame*, 81, 1, pp. 40–495 (July 1990).
16. C. DiBlasi, G. Continillo, S. Crescitelli, and G. Russo, "Numerical Simulation of Opposed Flow Flame Spread Over a Thermally Thick Solid Fuel," *Journal Combustion Science and Technology*, 54, 1-6, pp. 25–36 (1987).
17. J.G. Quintiere and M. Harkleroad, in *Fire Safety Science and Engineering*, American Society for Testing and Materials, West Conshohocken, PA (1985).
18. A. Atreya, C. Carpentier, and M. Harkleroad, in *Fire Safety Science, Proceedings of the First International Symposium on Fire Safety Science*, Hemisphere, New York (1984).
19. I.S. Wichman and S. Agrawal, "Wind-Aided Flame Spread Over Thick Solids," *Journal Combustion and Flame*, 83, 1-2, pp. 127–145 (1991).
20. K. Saito, J.G. Quintiere, and F.A. Williams, "Upward Turbulent Flame Spread," in *Fire Safety Science, Proceedings, 1st International Symposium*, Hemisphere Publishing Corp., New York, (C.E. Grant and P.J. Pagni, eds.), pp. 75–86 (1986).
21. K.-M. Tu and J.G. Quintiere, "Wall Flame Heights with External Radiation," *Fire Technol.*, 27 (3) pp. 195–203 (1991).
22. Y. Hasemi, M. Yoshida, A. Nohara, and T. Nakabayashi, "Unsteady-State Upward Flame Spreading Velocity along Vertical Combustible Solid and Influence of External Radiation on the Flame Spread," in *Fire Safety Science, Proceedings, 3rd International Symposium*, Elsevier Applied Science, New York, (G. Cox and B. Langford, eds.) pp. 197–206 (1991).
23. M.M. Delichatsios, M.K. Mathews, and M.A. Delichatsios, "Upward Fire Spread and Growth Simulation," in *Fire Safety Science, Proceedings, 3rd International Symposium*, Elsevier Appl. Science, New York, (G. Cox and B. Langford, eds.), pp. 207–216 (1991).
24. A.K. Kulkarni, C.I. Kim, and C.H. Kuo, "Turbulent Upward Flame Spread for Burning Vertical Walls Made of Finite Thickness," *NIST-GCR-91-597*, National Institute of Standards and Technology, Gaithersburg, MD (May 1991).
25. D. Baroudi and M. Kokkala, "Analysis of Upward Flame Spread," Project 5 of the EUREFIC Fire Research Program, VTT-Technical Research Center of Finland, Espoo Report, VTT Publications, 89, p. 50 (Feb. 1992).
26. G.H. Markstein and J. deRis, "Upward Fire Spread Over Textiles," in *14th Symposium (International) on Combustion*, Combustion Institute, Pittsburgh, PA, pp. 1085–1097 (1973).
27. A.C. Fernandez-Pello, *Comb. and Flame*, 31, p. 135 (1978).
28. L. Orloff, J. deRis, and G.H. Markstein, "Upward Turbulent Fire Spread and Burning of Fuel Surfaces," in *15th Symposium (International) on Combustion*, Combustion Institute, Pittsburgh, PA, pp. 183–192 (1975).
29. A. Atreya and K. Mekki, "Heat Transfer During Wind-Aided Flame Spread on a Ceiling-Mounted Sample," in *24th Symposium (International) on Combustion*, Combustion Institute, Pittsburgh, PA, pp. 1677–1684 (1992).
30. C. DiBlasi, S. Crescitelli, and G. Russo, "Near-Limit Flame Spread Over Thick Fuels in a Concurrent Forced Flow," *Journal Combustion and Flame*, 72, 2, pp. 205–212 (1988).
31. L. Zhou and A.C. Fernandez-Pello, "Turbulent, Concurrent, Ceiling Flame Spread: The Effect of Buoyancy," *Journal Combustion and Flame*, 92, 1-2, pp. 45–59 (1993).
32. V.B. Apte, R.W. Bilger, A.R. Green, and J.G. Quintiere, "Wind-Aided Turbulent Flame Spread and Burning Over Large-Scale Horizontal PMMA Surfaces," *Journal Combustion and Flame*, 85, 1-2, pp. 169–184 (1991).
33. F.J. Perzak and C.P. Lazzara, "Flame Spread Over Horizontal Surfaces of Polymethylmethacrylate," in *24th Symposium (International) on Combustion*, Combustion Institute, Pittsburgh, PA, pp. 1661–1668 (1992).
34. J. Quintiere, *Fire and Matls.*, 9, p. 65 (1985).
35. J.G. Quintiere, M.F. Harkleroad, and Y. Hasemi, "Wall Flames and Implications for Upward Flame Spread, Final Report," *Proceedings, Journal Combustion, Science and Technology*, 48, 3 & 4, pp. 191–222 (1986).
36. T. Ahmad and G.M. Faeth, in *17th Symposium (International) on Combustion*, Combustion Institute, Pittsburgh, PA, pp. 1149–1160 (1979).
37. L. Orloff, A.T. Modak, and R.L. Alpert, in *16th Symposium (International) on Combustion*, Combustion Institute, Pittsburgh, PA, 1345 (1976).
38. Y. Hasemi, "Thermal Modeling of Upward Wall Flame Spread," in *Proceedings of the 1st International Symposium on Fire Safety Science*, (C.E. Grant and P.J. Pagni, eds.) Hemisphere Publishing Corp., New York, 87 (1985).
39. A. Ito and T. Kashiwagi, "Characterization of Flame Spread Over PMMA Using Holographic Interferometry Sample Orientation Effects," *Proceedings Journal, National Technical Information Services Combustion and Flame*, 71, pp. 189–204 (1988).
40. D.D. Drysdale, A.J.R. Macmillan, and D. Shilitto, "King's Cross Fire: Experimental Verification of the 'Trench Effect,'" *Fire Safety Journal*, 18, 1, pp. 75–82 (1992).
41. ASTM, "Proposed Method for Room Fire Test of Wall and Ceiling Materials and Assemblies," in *ASTM Annual Book of Standards Pt. 18*, American Society for Testing and Materials, West Conshohocken, PA, pp. 1618–38 (1982).
42. B. Karlsson and S.E. Magnusson, "Combustible Wall Lining Materials: Numerical Simulation of Room Fire Growth and the Outline of a Reliability Based Classification Procedure," in *Fire Safety Science, Proc. of the 3rd Int. Symp.*, (G. Cox and B. Langford, eds.), Elsevier Applied Science, London (1991).
43. T.G. Cleary and J.G. Quintiere, "A Framework for Utilizing Fire Property Tests," in *Fire Safety Science, Proceedings of the 3rd International Symposium*, (G. Cox and B. Langford, eds.), Elsevier Applied Science, London (1991).
44. U. Wickström and U. Göransson, "Prediction of Heat Release Rates of Surface Materials in Large-Scale Fire Tests Based on Cone Calorimeter Results," *ASTM J. Testing and Evaluation*, 15(6), pp. 364–370 (1987).
45. J.G. Quintiere, "A Simulation Model for Fire Growth on Materials Subject to a Room-Corner Test," *Fire Safety Journal* 20, pp. 313–339 (1993).
46. K. Akita, in *14th Symposium (International) on Combustion*, Combustion Institute, Pittsburgh, PA, p. 1075 (1975).
47. A. Ito, D. Masuda, and K. Saito, "Study of Flame Spread Over Alcohols Using Holographic Interferometry," *Journal Combustion and Flame*, 83, 3 & 4, pp. 375–389 (1991).
48. R.C. Rothermel, *Gen. Tech. Report INT-143*, Department of Agriculture/Forest Service, Madison, WI (1983).
49. R.C. Rothermel, "Modeling Fire Behavior," in *International Conference on Forest Fire Research*, Coimbra, Portugal (Nov. 1990).
50. F.A. Albini, "Dynamics and Modeling of Vegetation Fires: Observations," in *Fire in the Environment* (P.J. Crutzen and J.G. Goldammer, eds.), John Wiley and Sons, New York, pp. 39–52 (1992).
51. P.H. Thomas, "Rates of Spread for Some Wind-Driven Fires," *Forestry*, XLIV, p. 2 (1971).
52. S. Bhattacharjee and R.A. Altenkirch, "Comparison of Theoretical and Experimental Results in Flame Spread Over Thin Condensed Fuels in a Quiescent, Microgravity Environment," in *24th Symposium (International) on Combustion*, Combustion Institute, Pittsburgh, PA, pp. 1669–1676 (1992).
53. F.S. Miller and H.D. Ross, "Further Observations of Flame Spread over Laboratory-Scale Alcohol Pools," in *24th Symposium (International) on Combustion*, Combustion Institute, Pittsburgh, PA, pp. 1703–1711 (1992).

SECTION TWO

CHAPTER 13

Smoke Production and Properties

George W. Mulholland

Introduction

The term *smoke* is defined in this chapter as the smoke aerosol or condensed phase component of the products of combustion. This differs from the American Society for Testing and Materials (ASTM) definition of smoke, which includes the evolved gases as well. Smoke aerosols vary widely in appearance and structure, from light colored, for droplets produced during smoldering combustion and fuel pyrolysis, to black, for solid, carbonaceous particulate or soot produced during flaming combustion. A large fraction of the radiant energy emitted from a fire results from the blackbody emission from the soot in the flame. The subject of radiant heat transfer is of such importance that it is treated in a separate chapter. This chapter focuses on smoke aerosols outside the combustion zone.

The effects of the smoke produced by a fire depend on the amount of smoke produced and on the properties of the smoke. The following section presents experimental results on smoke emission for a variety of materials. The smoke emission, together with the flow pattern, determines the smoke concentration as smoke moves throughout a building.

The most basic physical property of smoke is the size distribution of its particles. Results on size distribution for various types of smoke and techniques used for measuring particle size are presented in the section "Size Distribution." The section "Smoke Properties" focuses on those properties of greatest concern to the fire protection community: light extinction coefficient of smoke, visibility through smoke, and detectability of smoke. These properties are primarily determined by the smoke concentration and the particle size distribution. References for other

smoke aerosol properties, such as diffusion coefficient and sedimentation velocity, are also provided.

Smoke Production

Smoke emission is one of the basic elements for characterizing a fire environment. The combustion conditions under which smoke is produced—flaming, pyrolysis, and smoldering—affect the amount and character of the smoke. The smoke emission from a flame represents a balance between growth processes in the fuel-rich portion of the flame and burnout with oxygen. While it is not possible at the present time to predict the smoke emission as a function of fuel chemistry and combustion conditions, it is known that an aromatic polymer, such as polystyrene, produces more smoke than hydrocarbons with single carbon-carbon bonds, such as polypropylene. The smoke produced in flaming combustion tends to have a large content of elemental (graphitic) carbon.

Pyrolysis occurs at a fuel surface as a result of an elevated temperature. This may be due to a radiant flux heating the surface. The temperature of a pyrolyzing sample, 600 to 900 K, is much less than the gas phase flame temperature, 1200 to 1700 K. The vapor evolving from the surface may include fuel monomer, partially oxidized products, and polymer chains. As the vapor rises, the low vapor pressure constituents can condense, forming smoke droplets appearing as light-colored smoke.

Smoldering combustion also produces smoke droplets, but in this case the combustion is self-sustaining, whereas pyrolysis requires an external heat source. While most materials can be pyrolyzed, only a few materials, including cellulosic materials (wood, paper, cardboard, etc.) and flexible polyurethane foam, are able to smolder. The temperature during smoldering is typically 600 to 1100 K.

In Table 2-13.1 the smoke conversion factor, ε , is given for a variety of materials commonly found in build-

Dr. George W. Mulholland is head of the Smoke Dynamics Research Group in the Center for Fire Research at the National Bureau of Standards. His research has focused on smoke aerosol phenomena and the development of accurate particle size standards.

Table 2-13.1 Smoke Production for Wood and Plastics

Type	Smoke Conversion Factor, ϵ	Combustion Conditions	Fuel Area, m ²	Reference
Douglas fir	0.03–0.17	Pyrolysis	0.005	1
Douglas fir	< 0.01–0.025	Flaming	0.005	1
Hardboard	0.0004–0.001	Flaming ^a	0.0005	2
Fiberboard	0.005–0.01	Flaming ^a	0.0005	2
Polyvinylchloride	0.03–0.12	Pyrolysis	0.005	3
Polyvinylchloride	0.12	Flaming	0.005	1
Polyurethane (flexible)	0.07–0.15	Pyrolysis	0.005	3
Polyurethane (flexible)	< 0.01–0.035	Flaming	0.005	1
Polyurethane (rigid)	0.06–0.19	Pyrolysis	0.005	1
Polyurethane (rigid)	0.09	Flaming	0.005	1
Polystyrene	0.17 ($m_{O_2} = 0.30$) ^b	Flaming	0.0005	4
Polystyrene	0.15 ($m_{O_2} = 0.23$)	Flaming	0.07	5
Polypropylene	0.12	Pyrolysis	0.005	1
Polypropylene	0.016	Flaming	0.005	1
Polypropylene	0.08 ($m_{O_2} = 0.23$)	Flaming	0.007	5
Polypropylene	0.10 ($m_{O_2} = 0.23$)	Flaming	0.07	5
Polymethylmethacrylate	0.02 ($m_{O_2} = 0.23$)	Flaming	0.07	5
Polyoxymethylene	~0	Flaming	0.007	5
Cellulosic insulation	0.01–0.12	Smoldering	0.02	6

^aSample smoldered for a period of time after the pilot flame was extinguished.

^b m_{O_2} refers to mol fraction of O₂.

ings. The quantity ϵ is defined as the mass of smoke produced/mass of fuel burned.

The references cited in Table 2-13.1 should be consulted regarding the detailed description of the combustion conditions. In many instances,^{1,3} ϵ was measured for a range of radiant fluxes, oxygen concentrations, sample orientations, and ambient temperatures. It is seen in Table 2-13.1 that ϵ has a greater range for flaming combustion, with values in the range 0.001 to 0.17, compared to pyrolysis and smoldering, with values in the range 0.01 to 0.17. The following factors should be taken into account when using this table for smoke emission estimates:

1. Most of the measurements reported in Table 2-13.1 were made on small-scale samples.
2. Most experiments were for free burning at ambient conditions; reduced ventilation can strongly affect the smoke production.
3. In transport, the smoke may coagulate, partially evaporate, and deposit on surfaces through diffusion and sedimentation. Also, additional smoke may be formed through condensation.

Size Distribution

Smoke particle size distribution, together with the amount of smoke produced, primarily determines the properties of the smoke. A widely used representation of the size distribution is the geometric number distribution, $\Delta N/\Delta \log d$, versus $\log d$, where d represents the particle diameter. The quantity ΔN represents the number of particles per cm³, with diameter between $\log d$ and $\log d + \Delta \log d$. As an example, the particle size distribution of

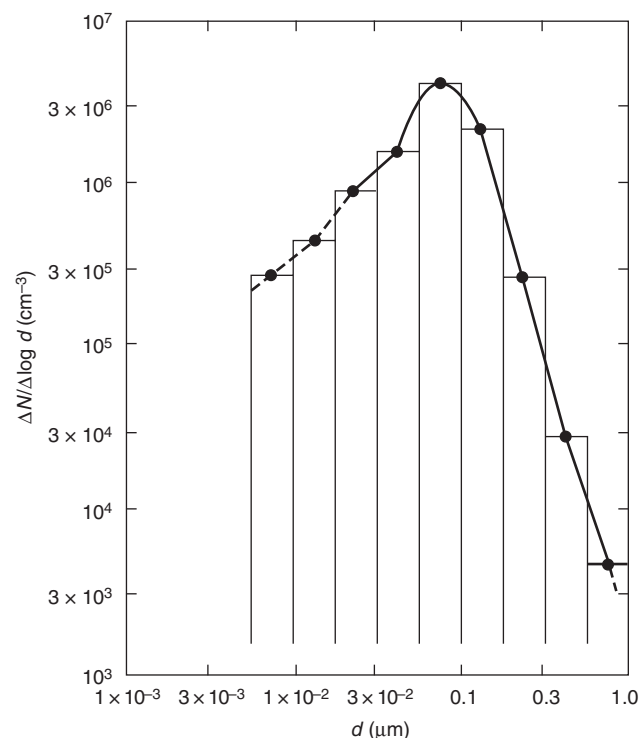


Figure 2-13.1. Size distribution of incense smoke as measured by an electrical aerosol analyzer. There is a large uncertainty in the dashed portion of the curve.

smoke produced by a smoldering incense stick is plotted in Figure 2-13.1, where $\Delta \log d$ for each discrete size range equals 0.25. In this case, the total number concentration for a given size range equals $0.25(\Delta N/\Delta \log d)$. It is seen that the logarithmic scale is necessitated by the wide range in particle size and concentration.

For many applications, the most important characteristics of a size distribution are the average particle size and the width of the distribution. A widely used measure of the average size is the geometric mean number diameter, d_{gn} , defined by

$$\log d_{gn} = \sum_{i=1}^n \frac{N_i \log d_i}{N} \quad (1)$$

where

N = total number concentration

N_i = number concentration in the i th interval

\log is to the base 10

For the size distribution plotted in Figure 2-13.1, $d_{gn} = 0.072 \mu\text{m}$.

The corresponding measure of the width of the size distribution is the geometric standard deviation, σ_g ,

$$\log \sigma_g = \left[\sum_{i=1}^n \frac{(\log d_i - \log d_{gn})^2 N_i}{N} \right]^{1/2} \quad (2)$$

For the size distribution plotted in Figure 2-13.1, $\sigma_g = 1.75$. A perfectly monodisperse distribution would correspond to $\sigma_g = 1$. The parameters d_{gn} and σ_g are useful because actual size distributions are observed to be approximately log-normal, which is the same as a normal or Gaussian distribution, except that $\log d$ is normally distributed instead of d . An important characteristic of the log-normal distribution is that 68.3 percent of the total particles are in the size range $\log d_{gn} \pm \log \sigma_g$; for $d_{gn} = 0.072 \mu\text{m}$ and $\sigma_g = 1.75$, this corresponds to the size range of 0.041 to 0.126 μm .

EXAMPLE 1:

Compute d_{gn} and σ_g for the data given below:

Interval, μm	d_i	N_i, cm^{-3}	$\log d_i$	$N_i \times \log d_i, \text{cm}^{-3}$
0.0056–0.01	0.0078	6×10^4	-2.11	-1.27×10^5
0.010–0.018	0.014	2×10^5	-1.85	-3.7×10^5
0.018–0.032	0.025	4×10^5	-1.60	-6.40×10^5
0.032–0.056	0.044	9×10^4	-1.36	-1.22×10^5
0.056–0.10	0.078	3×10^4	-1.11	-3.33×10^4
0.10–0.18	0.14	1×10^3	-0.85	-0.85×10^3
		7.81×10^5		-1.30×10^6

SOLUTION:

$$d_{gn} = 10^{(-1.30 \times 10^6 / 7.81 \times 10^5)} = 0.022 \mu\text{m}$$

Compute the geometric standard deviation:

N_i	$\log d_i$	$\log d_i - \log d_{gn}$	$N_i(\log d_i - \log d_{gn})^2$
6×10^4	-2.11	-0.45	1.22×10^4
2×10^5	-1.85	-0.19	7.2×10^3
4×10^5	-1.60	0.06	1.4×10^3
9×10^4	-1.36	0.30	8.1×10^3
3×10^4	-1.11	0.55	9.1×10^3
1×10^3	-0.85	0.81	6.5×10^2
7.81×10^5			3.87×10^4

SOLUTION:

$$\sigma_g = 10^{(3.87 \times 10^4 / 7.81 \times 10^5)0.5} = 1.67$$

The size distribution plotted in Figure 2-13.1 is based on electrical mobility analysis of the smoke aerosol. Figures 2-13.2 and 2-13.3 show size distributions of droplet smoke produced by smoldering cellulosic insulation, as measured by an optical particle counter and by two cas-

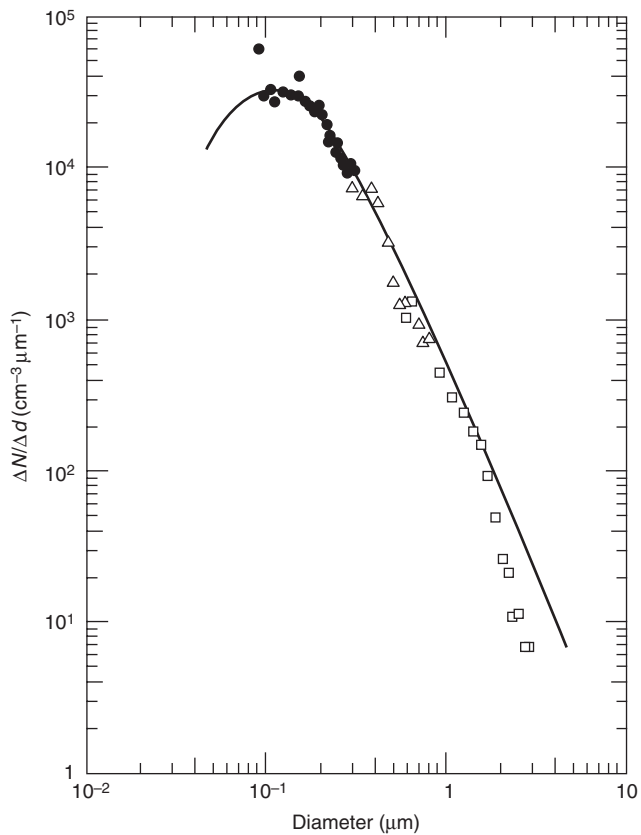


Figure 2-13.2. The number size distribution of smoke generated by smoldering cellulosic insulation as measured by an optical particle counter. The symbols correspond to the particle size range settings of the instrument, and the smooth curve is an exponentially truncated power law distribution fit to the data.

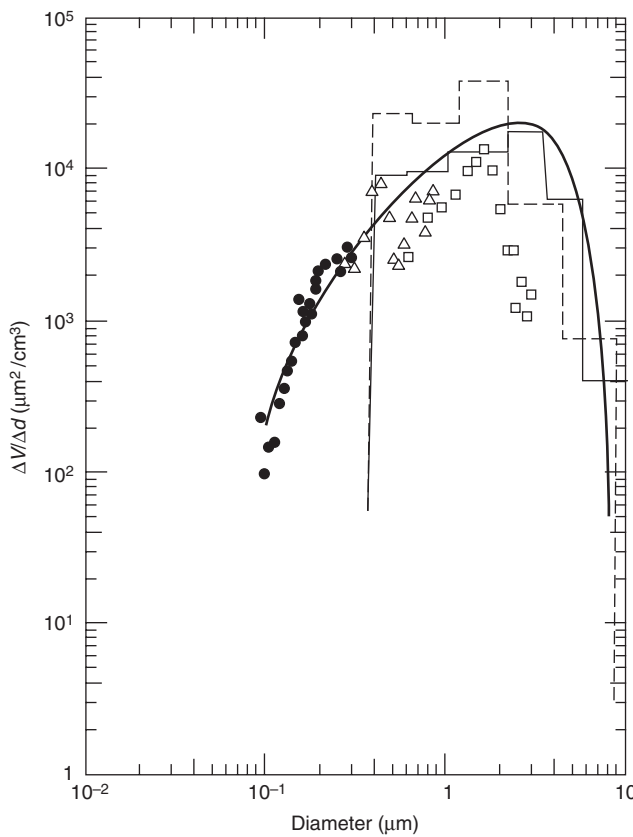


Figure 2-13.3. The volume size distribution of smoke obtained from the optical particle counter, quartz crystal microbalance cascade impactor (dashed histogram), and Andersen impactor (solid histogram). The smooth curve represents the exponentially truncated power law distribution.

cascade impactors.⁶ The smoke volume distribution plotted in Figure 2-13.3 for the optical particle counter is obtained from the number distribution, using the following relation:

$$V_i = N_i \frac{1}{6} \pi d_i^3 \quad (3)$$

For particles sized above 1 μm, impactors provide more reliable information on the smoke volume distribution than optical particle counters. An optical particle counter is the preferred instrument for the number distribution measurement.

To correlate the smoke volume/particle size distribution, the geometric mean volume diameter, d_{gv} , is a convenient measure of average particle size:

$$\log d_{gv} = \frac{\sum_{i=1}^n V_i \log d_i}{V_T} \quad (4)$$

where V_T is the total volume concentration of the smoke aerosol. For a log-normal distribution, there is the follow-

ing relationship between the geometric mean volume diameter, d_{gv} , and the geometric mean number diameter, d_{gn} :

$$\log d_{gv} = \log d_{gn} + 6.9(\log \sigma_g)^2 \quad (5)$$

In the case of smolder smoke, σ_g is above 2.4. This large value of σ_g results in a large difference between d_{gn} and d_{gv} , 0.2 μm versus 2 μm, respectively. Some devices, such as an ionization-type smoke detector, have an output depending primarily on d_{gn} , while others, such as light-scattering-type detectors, have an output depending more on d_{gv} . More than one instrument is necessary for a complete characterization of the smoke size distribution, because it is typically quite wide.

A list of commercially available instruments for measuring smoke aerosol concentration and particle size distribution is given in Table 2-13.2. Smoke measurements pose special problems because of the high concentration, wide particle size range, and sometimes high temperature. In selecting an instrument it is important to make the following considerations:

1. Will the instrument respond to the smoke of interest? For example, the piezoelectric mass monitor does not respond well to soot.
2. Will dilution of the smoke be required?
3. Is the measurement size range of the instrument adequate?
4. Is a mass or number distribution measurement appropriate?
5. What is the particle size resolution needed?
6. Is real-time measurement capability needed?
7. Will the instrument perform at the temperature of the smoke environment?

In Table 2-13.3, average particle size and the width of the size distribution are presented for smoke generated by a variety of materials. The results are most meaningful for smoke droplets produced during pyrolyzing and smoldering combustion. In the case of flaming combustion, complex soot agglomerates are formed as shown in Figure 2-13.4. For soot agglomerates, unlike for spherical smoke droplets, the apparent particle size depends on the measurement technique.

Smoke aerosols are dynamic with respect to their particle size distribution function. Smoke particles or droplets undergoing Brownian motion collide and stick together. The result of this behavior is that, in a fixed volume of smoke-laden gas, the number of particles decreases while the total mass of the aerosol remains unchanged. This process is known as coagulation. The fundamental parameter for describing coagulation is the coagulation coefficient, Γ , the rate constant for the coagulation equation

$$\frac{dN}{dt} = -\Gamma N^2 \quad (6)$$

Γ was found to be about $4 \times 10^{-10} \text{ cm}^3/\text{s}$ for smoke produced from incense sticks and about $1 \times 10^{-9} \text{ cm}^3/\text{s}$ for

Table 2-13.2 Operational Characteristics of Commercially Available Instruments for Smoke Characterization

Instrument Type	Function/Range	Advantage/Limitation for Smoke Measurements
Filter-collection	Mass conc.	Accurate, slow
Piezoelectric mass monitor	Mass conc. $0.01 < d < 5 \mu\text{m}$	Real-time output, but dilution required if $>20 \text{ mg/m}^3$; does not respond well to soot
Tapered element oscillating microbalance	Mass conc. $< 5 \mu\text{m}$	Real time, $0.1\text{--}1000 \text{ mg/m}^3$; replace filter after $3\text{--}100 \text{ mg}$ deposit
Condensation nuclei counter	Number conc. $0.005 < d < 2 \mu\text{m}$	$< 3 \times 10^5 \text{ particles/cm}^3$
Photometer	Scattered light $0.1\text{--}10 \mu\text{m}$	$1.1\text{--}1000 \text{ mg/m}^3$
Nephelometer	Total light scattered	$< 5 \text{ mg/m}^3$
Electrical aerosol analyzer	Size distribution $0.01 < d < 0.3 \mu\text{m}$	$< 5 \times 10^5 \text{ particles/cm}^3$; 2 min/scan
Cascade impactor	Mass size distribution ^a $0.5 < d < 10 \mu\text{m}$	No dilution needed, can be used at high temp., large sample required
Optical particle counter	Number distribution ^b $0.5 < d < 10 \mu\text{m}$	Highest resolution, $< 10^3 \text{ particles/cm}^3$, large dilution

^aLow-pressure impactor extends size range down to $0.05 \mu\text{m}$.^bLaser model extends size range down to $0.1 \mu\text{m}$ and concentration up to $10^4 \text{ particles/cm}^3$.

smoke produced from flaming α -cellulose.⁷ The coagulation process has a more pronounced effect on the number distribution than the mass distribution as small particles collide to form larger particles.

EXAMPLE 2:

Calculate the change in the number concentration over a 5-min time interval for a uniformly distributed smoke, generated from flaming α -cellulose given an initial concentration of $1 \times 10^7 \text{ particles/cm}^3$.

Integrating Equation 6 yields

$$N = \frac{N_0}{1 + \Gamma N_0 t} = \frac{1 \times 10^7}{1 + (10^{-9})(10^7)(300)} = \frac{10^7}{1 + 3}$$

$$N = 2.5 \times 10^6 \text{ particles/cm}^3$$

So in this example, there is a fourfold reduction in number concentration due to coagulation.

The effect of the decrease in number concentration on the size distribution is treated by Mulholland et al.²⁵ A

Table 2-13.3 Particle Size of Smoke from Burning Wood and Plastics

Type	$d_{gm}, \mu\text{m}^a$	$d_{32}, \mu\text{m}^b$	σ_g	Combustion Conditions	Reference
Douglas fir	0.5–0.9	0.75–0.8	2.0	Pyrolysis	1, 3
Douglas fir	0.43	0.47–0.52	2.4	Flaming	1, 3
Polyvinylchloride	0.9–1.4	0.8–1.1	1.8	Pyrolysis	3
Polyvinylchloride	0.4	0.3–0.6	2.2	Flaming	3
Polyurethane (flexible)	0.8–1.8	0.8–1.0	1.8	Pyrolysis	3
Polyurethane (flexible)		0.5–0.7		Flaming	3
Polyurethane (rigid)	0.3–1.2	1.0	2.3	Pyrolysis	3
Polyurethane (rigid)	0.5	0.6	1.9	Flaming	3
Polystyrene		1.4		Pyrolysis	1
Polystyrene		1.3		Flaming	1
Polypropylene		1.6	1.9	Pyrolysis	1
Polypropylene		1.2	1.9	Flaming	1
Polymethylmethacrylate		0.6		Pyrolysis	1
Polymethylmethacrylate		1.2		Flaming	1
Cellulosic insulation	2–3		2.4	Smoldering	6

^a d_{gm} is analogous to d_{gv} but with mass replacing volume in Equation 4. Values of d_{gm} less than about $0.5 \mu\text{m}$ are probably overestimates arising from the minimum size resolution of the impactor at about $0.4 \mu\text{m}$.

^bThe quantity d_{32} is obtained by optical measurements

$$d_{32} = \frac{\sum_{i=1}^{n_i} N_i d_i^3}{\sum_{i=1}^{n_i} N_i d_i^2}$$

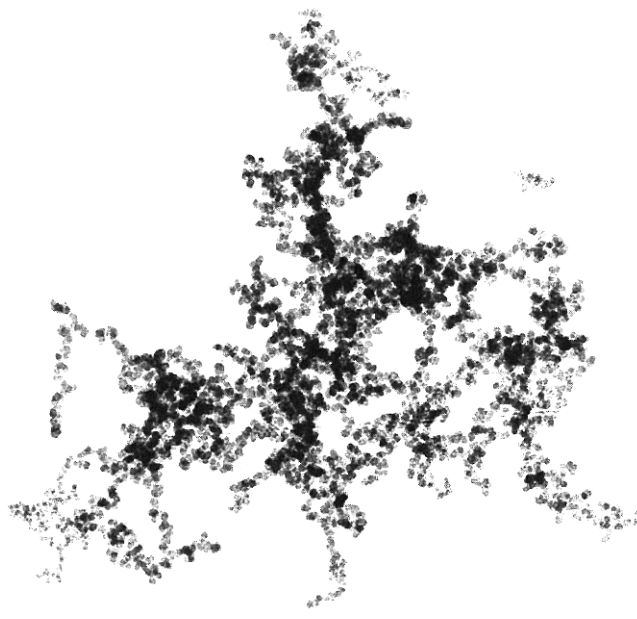


Figure 2-13.4. Transmission electron micrograph of a soot particle. The overall size of the agglomerate is about 6 μm , and the diameter of the individual spherules is about 0.03 μm .

general discussion of coagulation phenomena in aerosols is given by Friedlander.⁸ In addition to coagulation, other smoke-aging processes, including condensation of vapor onto existing particles and evaporation of the volatile component of the smoke, can also take place. There is relatively little information on these processes. Also, smoke particles can be lost to the walls, ceiling, and floor of an enclosure through a variety of processes, including diffusion, sedimentation, and thermophoresis.

Smoke Properties

The smoke properties of primary interest to the fire community are light extinction, visibility, and detection. For completeness, a list of other smoke aerosol properties and references is given in Table 2-13.4.

Table 2-13.4 Smoke Aerosol Properties

Property	Reference
Diffusion coefficient	8
Sedimentation velocity	9
Thermophoretic velocity	10
Aerodynamic diameter	9
Electrical mobility	9
Thermal charging	9
Scattering coefficient	8
Extinction coefficient	8
Condensation/evaporation	8

The most widely measured smoke property is the light extinction coefficient. The physical basis for light extinction measurements is Bouguer's law, which relates the intensity, I_0^λ , of the incident monochromatic light of wavelength λ and the intensity of the light, I_λ , transmitted through the pathlength, L , of the smoke:

$$\frac{I_\lambda}{I_0^\lambda} = e^{-KL} \quad (7)$$

where K is the light extinction coefficient. When Equation 7 is expressed in terms of base 10,

$$\frac{I_\lambda}{I_0^\lambda} = 10^{-DL} \quad (8)$$

The quantity D is defined as the optical density per meter, and $D = K/2.3$.

The extinction coefficient, K , is an extensive property and can be expressed as the product of an extinction coefficient per unit mass, K_m , and mass concentration of the smoke aerosol, m .

$$K = K_m m \quad (9)$$

The specific extinction coefficient, K_m , depends on the size distribution and optical properties of the smoke through the relation

$$K_m = \frac{3}{2\rho m} \int_{d_{\min}}^{d_{\max}} \frac{1}{d} \frac{\Delta m}{\Delta d} Q_{\text{ext}} \left(\frac{d}{\lambda}, n_r \right) \delta d \quad (10)$$

In Equation 10 the symbol $\Delta m/\Delta d$ represents the mass size distribution. The single particle extinction efficiency, Q_{ext} , is a function of the ratio of particle diameter to wavelength of light, d/λ , and of the complex refractive index of the particle, n_r .⁸ The quantity ρ represents the particle density.

Seader and Einhorn¹¹ obtained K_m values of 7.6 m^2/g for smoke produced during flaming combustion of wood and plastics and a value of 4.4 m^2/g for smoke produced during pyrolysis of these materials. The experiments were small scale, utilizing samples of about 50 cm^2 , and the value of K_m represents an integrated result for the entirety of the test. The light source used in the measurements was polychromatic, while Bouguer's law is strictly valid only for monochromatic light. Foster¹² predicted a 22 percent deviation from Bouguer's law over the mass concentration range from 0.06 to 2.8 g/m^3 as a result of using a polychromatic light source with wood smoke. Still, it is useful to use the Seader and Einhorn¹¹ result as a rough guide if more detailed optical data on the smoke of interest is not available.

Mulholland¹³ has described the general design of a light extinction instrument that satisfies Bouguer's law. Two key features are the use of monochromatic light and the elimination of forward scattered light at the detector.

The specific optical density, D_s , is measured in a standard laboratory smoke test¹⁴ for assessing the amount of visible smoke produced in a fire. The dimensionless quantity D_s is defined by

$$D_s = \frac{DV_c}{A} \quad (11)$$

where V_c is the volume of the chamber, and A is the area of the sample. D_s is a convenient quantity to measure if the decomposed area is well defined. Since D_s depends on the sample thickness, the same thickness should be used for relative rating of materials tested. Table 2-13.5 in-

cludes results for D_s based on small-scale experiments with wood and plastics by Gross et al.,¹⁴ Seader and Chien,¹⁵ and Breden and Meisters.¹⁶ Lopez¹⁷ demonstrated a correlation for D_s between small- and large-scale fires with aircraft interior construction materials.

Table 2-13.5 Specific Optical Density and Mass Optical Density for Wood and Plastics

Type (Sample #)	Maximum D_s	D_m (m^2/g) ^a	Combustion Conditions	Sample ^b Thickness (cm)	Reference
Hardboard	6.7×10^1		Flaming	0.6	14
Hardboard	6.0×10^2		Pyrolysis	0.6	14
Plywood	1.1×10^2		Flaming	0.6	14
Plywood	2.9×10^2		Pyrolysis	0.6	14
Polystyrene	$>6.6 \times 10^2$		Flaming	0.6	14
Polystyrene	3.7×10^2		Pyrolysis	0.6	14
Polyvinylchloride	$>6.6 \times 10^2$		Flaming	0.6	14
Polyvinylchloride	3.0×10^2		Pyrolysis	0.6	14
Polyurethane foam	2.0×10^1		Flaming	1.3	14
Polyurethane foam	1.6×10^1		Pyrolysis	1.3	14
Nylon carpet	2.7×10^2		Flaming	0.8	14
Nylon carpet	3.2×10^2		Pyrolysis	0.8	14
Acrylic	1.1×10^2		Flaming	0.6	14
Acrylic	1.6×10^2		Pyrolysis	0.6	14
Plywood	5.3×10^2	0.29	Pyrolysis	0.6	15
Polymethylmethacrylate	7.2×10^2	0.15	Pyrolysis	0.6	15
Polyvinylchloride	1.8×10^2	0.12	Pyrolysis	0.6	15
Polyvinylchloride (with plasticizer)	3.5×10^2	0.64	Pyrolysis	0.6	15
Neoprene	8.8×10^2	0.55	Pyrolysis	0.6	15
Douglas fir	6.2×10^2	0.28	Pyrolysis	0.6	15
Polypropylene	4.0×10^2	0.53	Flaming ^c	0.4	16
Polyethylene	2.9×10^2	0.29	Flaming ^c	0.4	16
Paraffin wax	2.3×10^2	0.23	Flaming ^c	0.4	16
Polystyrene		1.4	Flaming ^c	0.4	16
Styrene		0.96	Flaming ^c	0.4	16
Polyvinylchloride		0.34	Flaming ^c	0.4	16
Polyoxymethylene		~0	Flaming ^c	0.4	16
Polyurethane (7A)	2.1×10^2		Flaming	1.3	17
Polyurethane (7A)	1.5×10^2		Flaming ^d	1.3	17
Wool (8A)	$>5.5 \times 10^2$		Flaming	0.9	17
Wool (8A)	2.2×10^2		Flaming ^d	0.9	17
Acrylic (9B)	5.8×10^1		Flaming	0.14	17
Acrylic (9B)	1.2×10^2		Flaming ^d	0.14	17
Polyurethane (MO1)		0.33	Flaming ^c		18
Polyurethane (MO1)		0.22	Flaming ^e		18
Cotton (MO3)		0.17	Flaming ^c		18
Cotton (MO3)		0.12	Flaming ^e		18
Latex (MO4)		0.65	Flaming ^c		18
Latex (MO4)		0.44	Flaming ^e		18
Neoprene (MO8)		0.40	Flaming ^c		18
Neoprene (MO8)		0.20	Flaming ^e		18
Polystyrene (7)		0.79	Flaming ^c		19
Polystyrene (7)		1.0	Flaming ^f		19
Polystyrene foam (16)		0.79	Flaming ^c		19
Polystyrene foam (16)		0.82	Flaming ^f		19
ABS (18)		0.52	Flaming ^c		19
ABS (18)		0.54	Flaming ^f		19

^aThe value of D_m is computed by Quintiere,²⁰ based on data in Babrauskas.¹⁸

^bSample area is 0.005 m^2 in vertical configuration, unless stated otherwise.

^cSample is in horizontal configuration (0.005 m^2).

^d 0.09 m^2 sample size.

^eThe sample is a mattress.

^fThe sample is a plastic utility table.

If the mass loss of the sample is measured, then the mass optical density, D_m , is the appropriate measure of visible smoke.

$$D_m = \frac{DV_c}{\Delta M} \quad (12)$$

This technique requires an accurate measurement of the mass loss of the sample, ΔM , in addition to a light extinction measurement. Table 2-13.5 includes results for D_m for a variety of materials studied by Seader and Chien,¹⁵ Breeden and Meisters,¹⁶ Babrauskas,¹⁸ and Evans.¹⁹ The results of Babrauskas' study were expressed in terms of D_m by Quintiere.²⁰

In two of the studies,^{18,19} a comparison was made between D_m measured in small-scale tests and D_m measured in large-scale tests. The large-scale tests involved mattresses¹⁸ in one case and plastic utility tables¹⁹ in the other. In these two cases, there appeared to be a qualitative correlation between D_m measured for small- and large-scale tests. Quintiere²⁰ has made an extensive investigation of the correlation between small- and large-scale studies in terms of D_m and D_s and finds that the correlation breaks down as fires become more complex. From his review of the literature, Quintiere²⁰ suggests that heat flux and ventilation conditions can have a major effect on smoke production.

In most cases of practical interest, an important goal is to be able to predict the extinction coefficient based on information regarding D_s or D_m . The extinction coefficient, in turn, is related to visibility through the smoke, as discussed below.

Visibility

Visibility of exit signs, doors, and windows can be of great importance to an individual attempting to survive a fire. To see an object requires a certain level of contrast between the object and its background. For an isolated object surrounded by a uniform, extended background, contrast, C , can be defined as²¹

$$C = \frac{B}{B_0} - 1 \quad (13)$$

where B is the brightness or luminance of the object, and B_0 is the luminance of the background. For daylight conditions, with a black object being viewed against a white background, a value of $C = -0.02$ is often used as the contrast threshold at which an object can be discerned against the background. The visibility of the object, S , is the distance at which the contrast is reduced to -0.02 . Most visibility measurements through smoke have relied on test subjects to determine the distance at which the object was no longer visible rather than the actual measurement of C with a photometer.

Visibility depends on many factors, including the scattering and the absorption coefficient of the smoke, the illumination in the room, whether the sign is light emitting or light reflecting, and the wavelength of the light. Visibility also depends on the individual's visual acuity and on whether the eyes are "dark-" or "light-adapted." Nevertheless, a fair correlation between visibility of test

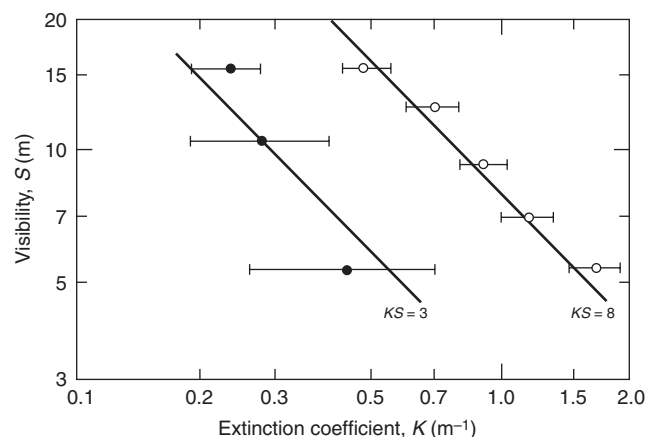


Figure 2-13.5. Visibility versus extinction coefficient for a light-emitting sign (○) and light-reflecting sign (●). The range bars include data for both flame- and smolder-generated smoke and sign illumination levels varying by about a factor of 4.

subjects and the extinction coefficient of the smoke has been obtained in an extensive study by Jin²² as illustrated in Figure 2-13.5. The visibility of light-emitting signs was found to be two to four times greater than light-reflecting signs. The following expressions were found to correlate the data:

$$KS = 8 \quad \text{light-emitting sign} \quad (14)$$

$$KS = 3 \quad \text{light-reflecting sign} \quad (15)$$

The data is based on subjects viewing smoke through glass so that the irritant effect of the smoke was eliminated. Jin and Yamada²³ have studied the visual acuity and eyeblink rate for highly irritant white smoke produced by burning wood cribs. They found that the ratio of visual acuity without goggles to acuity with goggles decreases markedly for smoke extinction coefficient, K , greater than 0.25 m^{-1} .

EXAMPLE 3:

Estimate the visibility of a light-reflecting exit sign in a 6-m square room with a 2.5-m height, as a result of flaming combustion of a 200-g polyurethane foam pillow.

The smoke yield for flexible polyurethane, according to Table 2-13.1, is about 0.03 for flaming combustion. This implies a smoke emission, M_s , given by

$$M_s = (0.03)(200) = 6 \text{ g}$$

The corresponding mass concentration in the room, m , is

$$m = \frac{6}{(6)^2(2.5)} = 0.067 \text{ g/m}^3$$

Taking K_m to be $7.6 \text{ m}^2/\text{g}$ for flaming combustion, one obtains K using Equation 9,

$$K = (7.6)(0.067) = 0.51 \text{ m}^{-1}$$

The visibility is next estimated using Equation 15,

$$S = \frac{3}{K} = \frac{3}{0.51} = 5.9 \text{ m}$$

It is important to point out the approximations made in this analysis.

1. The smoke is confined to the room and is well mixed. Actually the concentration will be higher near the ceiling and decrease abruptly below the flame.
2. The value of 0.03 for the smoke conversion factor, ε , is an estimated value in the upper part of the range (0.01 to 0.035) for generic flexible polyurethane foams measured in small-scale experiments and may not be appropriate for a pillow. In a realistic case, the pillow would probably smolder before flaming, and ε is much larger in the smolder mode.
3. The value of K_m is based on a limited number of small-scale experiments with a polychromatic light source.
4. The range of validity of Equation 15 has not been widely studied.

An alternative method for estimating the visibility is based on using the mass optical density data in Table 2-13.5. The quantity D_m for the pillow is estimated to be 0.22 m²/g based on Babrauskas' results¹⁸ given in Table 2-13.5 for polyurethane (MO1). On rearranging Equation 12, the following result is obtained:

$$D = \frac{D_m \Delta M}{V_c} = \frac{(0.22)(200)}{(6)^2(2.5)} = 0.49 \text{ m}^{-1}$$

The smoke extinction coefficient, K , is 1.12 m⁻¹ or 2.3 times D . Using Equation 15, we obtain $S = 2.7$ m compared to 5.9 m obtained by the first method. In principle, the second method is more reliable, because it is more direct.

Detection

In addition to their utility for estimating visibility, light extinction measurements are also widely used in characterizing smoke detector performance. Underwriters Laboratories' (UL) acceptance testing of smoke detectors²⁴ is based in part on a minimum sensitivity based on optical density per meter, D , of 0.06 (4 percent obscuration per ft for a 5 ft beam length) for gray (cellulosic) smoke and 0.14 (10 percent per ft) for black smoke (kerosene).

The electrical output of a detector, P , from a light-scattering or ionization-type smoke detector can be represented as an integrated product of the size distribution function and the basic response of the detector, $R(d)$.

$$P = \int_{d_{\min}}^{d_{\max}} R(d) \frac{\delta N}{\delta d} \delta d \quad (16)$$

The response functions for two smoke detectors are plotted in Figure 2-13.6. It is seen that the ionization-type smoke detector is more sensitive to smoke particles smaller than about 0.3 μm, and the light-scattering type more sensitive to particles larger than 0.3 μm.

The basic principle of ionization detectors is the interception of gaseous ions by smoke particles, reducing the ion current in the detector until a preset alarm point is

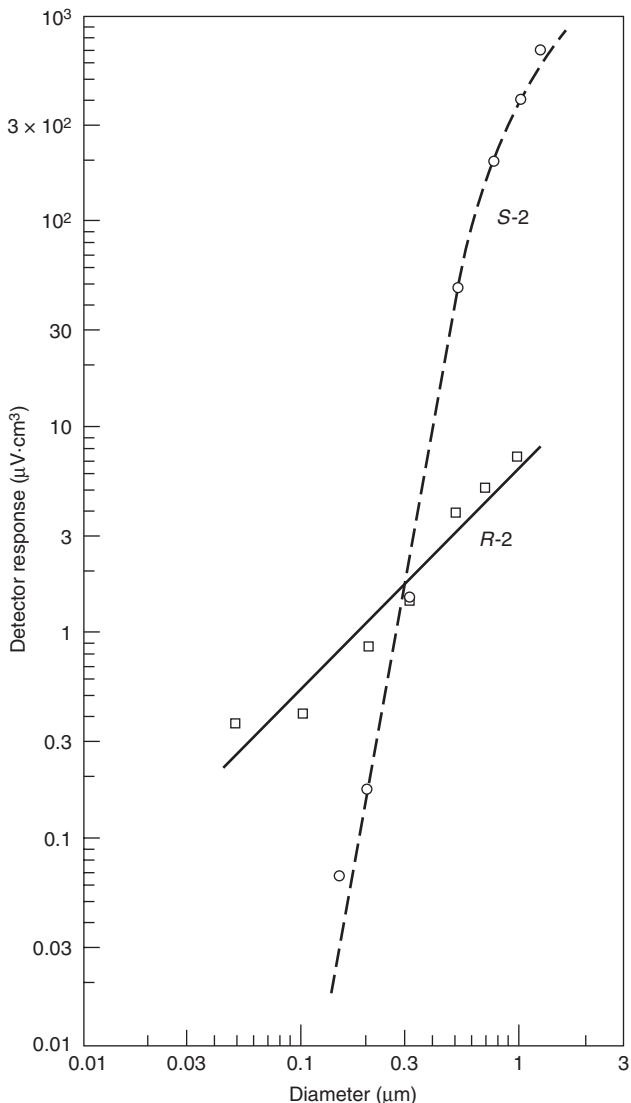


Figure 2-13.6. The detector response function, $R(d)$, is plotted versus particle size for detectors S-2 (light-scattering) and R-2 (ionization).

reached. The detector response function is approximately proportional to the product of the number concentration and particle diameter.^{25,26} For one detector²⁵ the response function is given by

$$R(d) = cd \quad (17)$$

where c has a value of 7 in units of μV per particle concentration per μm (μV cm³/μm). Such detectors tend to be most sensitive to high concentrations of small particles, such as those produced by flaming paper and wood fires, and least sensitive to the low concentration of large smoke droplets produced in smoldering fires.

Light-scattering smoke detectors have a high sensitivity to smoke particles with diameters approximately equal to λ , the wavelength of light, and low sensitivity to

particles much smaller than λ . The response function, $R(d)$, depends on the wavelength of the light source in the smoke detector, the scattering angle, and the scattering volume. For smoke particles with diameter greater than about $0.3 \mu\text{m}$, the output of several light-scattering smoke detectors was found to be approximately proportional to the mass concentration of the smoke.²⁵ Light-scattering detectors complement ionization detectors in that they have high sensitivity to smoldering fires and low sensitivity to low-smoking flaming fires, such as paper and wood fires.

The purpose of smoke detectors is to give the occupants of a room adequate warning to escape a developing fire. The final examples of this chapter illustrate how to utilize all the concepts discussed above to estimate escape time.

EXAMPLE 4:

Suppose the pillow in the preceding example is burning at a steady rate of 50 g/min . How long would it take for an ionization detector with response function given by Equation 17 to alarm? Assume an alarm voltage of 2.5 V above background. How much time would an individual have before the visibility decreased to an unsafe level?

SOLUTION:

First consider a first principle analysis based on the size distribution of the smoke. From Equations 16 and 17,

$$P = c \int_{d_{\min}}^{d_{\max}} d \frac{\delta N}{\delta d} \delta d$$

The following three identities⁹ for the log-normal distribution are needed:

$$\int_0^{\infty} d \frac{\delta N}{\delta d} \delta d = N_0 d_{gn} \exp\left(\frac{1}{2} \ln^2 \sigma_g\right) \quad (\text{I-1})$$

$$\int_0^{\infty} d^3 \frac{\delta N}{\delta d} \delta d = N_0 d_{gn}^3 \exp\left(\frac{9}{2} \ln^2 \sigma_g\right) \quad (\text{I-2})$$

Here N_0 refers to the number concentration. Taking $(\delta N/\delta d)$ to be log-normal and using Equation I-1,

$$P = c N_0 d_{gn} \exp\left(\frac{1}{2} \ln^2 \sigma_g\right)$$

Estimating σ_g to be 2.0 , d_{gn} to be $0.1 \mu\text{m}$ for flexible polyurethane, and c to be $7 \mu\text{V}\cdot\text{cm}^3/\mu\text{m}$, the following expression is obtained for P :

$$P = c N_0 (d_{gn}) \exp\left(\frac{1}{2} \ln \sigma_g^2\right) = 7 N_0 (0.10) \exp\left[\frac{1}{2} (0.69)^2\right]$$

$$P = 0.89 N_0 \mu\text{m}/\text{cm}^3$$

The final task is to estimate N_0 based on the mass generation rate of smoke. In one minute, 50 g of the pillow are consumed and 1.5 g of smoke are produced. This corresponds to a mass concentration, m , given by

$$m = \frac{1.5}{(6)^2 (2.5)} = 0.0167 \text{ g/m}^3 = 1.67 \times 10^{-8} \text{ g/cm}^3$$

The quantity m is the third moment of the size distribution,

$$m = \int_0^{\infty} \frac{1}{6} \pi \rho d^3 \frac{\delta N}{\delta d} \delta d$$

Using Equation I-2,

$$m = \frac{1}{6} \pi \rho N_0 d_{gn}^3 \exp\left(\frac{9}{2} \ln^2 \sigma_g\right)$$

Finally, solving for N_0 ,

$$N_0 = \frac{6m}{\pi \rho d_{gn}^3} \exp\left(-\frac{9}{2} \ln^2 \sigma_g\right)$$

$$= \frac{(6)(1.67 \times 10^{-8})}{(3.14)(2)(1.0 \times 10^{-5})^3} \exp\left[-\frac{9}{2} \ln^2 (2.0)\right]$$

$$N_0 = 1.8 \times 10^6 \text{ particles/cm}^3 \text{ (assuming } \rho = 2 \text{ g/cm}^3\text{)}$$

Substituting in the expression for P ,

$$P = (0.89)(1.8 \times 10^6) = 1.6 \times 10^6 \mu\text{V} = 1.6 \text{ volts}$$

This represents the voltage after 1 min. The estimated time to reach the alarm point, 2.5 V , will be 1.6 min. By the time the entire pillow is consumed in 4 min, the visibility has deteriorated to the point where escape is becoming less likely (visibility 5.9 m , according to Example 3, for a room 6 m across). So the individual's escape time is as follows:

$$\begin{aligned} \text{escape time} &= \text{time to unsafe condition minus time} \\ &\quad \text{to detector alarm} \\ &= 4 - 1.6 = 2.4 \text{ min} \end{aligned}$$

Example 4 is intended to illustrate the complete method for estimating the alarm time of smoke detectors. However, there is not adequate information at this time to implement the method in a realistic manner. Information on the size distribution and on the detector response functions is lacking for smoke agglomerates. The time for the smoke to reach the detector and the time lag for the smoke to enter the sensing zone of the detector are not included in this example, but should be included in a full analysis of the problem.

A simpler method for estimating the alarm time is to calculate the time at which the optical density per meter of the smoke exceeds the value of 0.06 (gray smoke) or 0.14 (black smoke), which correspond to the U.L. minimum sensitivity values. The limitation of this procedure is that a detector set to alarm at a particular optical density for one type of smoke may not respond in the same manner to another with a different size distribution and refractive index.

EXAMPLE 5:

Estimate the alarm time for the conditions given in Example 4, using the simpler method described above.

SOLUTION:

In Example 3, the optical density was estimated to be 0.49 m^{-1} , based on D_m measured for polyurethane. This

value corresponds to the burning of the entire pillow. Assuming a steady smoke generation rate, the alarm time [the time at which the minimum detector sensitivity value is exceeded (0.14 for black smoke)] is estimated to be given by

$$t = \frac{0.14}{0.49} (4) = 1.1 \text{ minutes}$$

This is comparable to the estimated 1.6 minutes in Example 4.

Nomenclature

ε	smoke conversion factor
d	particle diameter (μm)
d_i	midpoint of the i th particle size channel (μm)
d_{gn}	geometric mean number diameter (μm)
d_{gv}	geometric mean volume diameter (μm)
d_{32}	volume surface mean diameter (μm)
σ_g	geometric standard deviation
N	number concentration (particles/ cm^3)
m	mass concentration of smoke (mg/m^3 or g/m^3)
V_T	volume concentration of smoke (cm^3/m^3 or $\mu\text{m}^3/\text{cm}^3$)
$\frac{\Delta N}{\Delta d}$ or $\frac{dN}{dd}$	number size distribution function $\text{cm}^{-3}\cdot\mu\text{m}^{-1}$
$\frac{\Delta N}{\Delta \log d}$ or $\frac{dN}{d \log d}$	geometric number size distribution function (cm^{-3})
$\frac{\Delta m}{\Delta d}$ or $\frac{dm}{dd}$	mass size distribution function ($\text{mg}\cdot\mu\text{m}^{-1}\cdot\text{m}^{-3}$)
Q_{ext}	extinction efficiency
λ	wavelength of light (μm)
n_r	complex refractive index of smoke particles
K	extinction coefficient (m^{-1})
D	optical density per meter (m^{-1})
K_m	specific extinction coefficient (m^2/g)
D_s	specific optical density
D_m	mass optical density (m^2/g)
I_λ	intensity of light at wavelength λ
B	luminance
C	contrast
s	visibility range (m)
L	pathlength
Γ	coagulation coefficient (cm^3/s)
t	time
ΔM	mass loss of sample (g)
P	detector output (V)

$R(d)$	detector size response function ($\mu\text{V cm}^3$)
V_c	volume of chamber (m^3)
A	area of sample (m^2)
M_s	mass of smoke (g)

References Cited

1. C.P. Bankston, B.T. Zinn, R.F. Browner, and E.A. Powell, *Comb. and Flame*, 41, p. 273 (1981).
2. C.J. Hilado and A.M. Machado, *J. Fire and Flamm.*, 9, p. 240 (1978).
3. C.P. Bankston, R.A. Cassanova, E.A. Powell, and B.T. Zinn, *NBS-GCR G8-9000*, National Bureau of Standards, Washington, DC (1978).
4. S.K. Brauman, N. Fishman, A.S. Brolly, and D.L. Chamberlain, *J. Fire and Flamm.*, 6, p. 41 (1976).
5. A. Tewarson, J.L. Lee, and R.F. Pion, *18th Symposium (International) on Combustion*, Pittsburgh, PA (1981).
6. G.W. Mulholland and T.J. Ohlemiller, *Aerosol Sci. and Tech.*, 1, p. 59 (1982).
7. G.W. Mulholland, T.G. Lee, and H.R. Baum, *J. Colloid Interface Sci.*, 62, p. 406 (1977).
8. S.K. Friedlander, *Smoke, Dust and Haze*, John Wiley and Sons, New York (1977).
9. P.C. Reist, *Introduction to Aerosol Science*, Macmillan, New York (1984).
10. T. Waldman and K.H. Schmitt, in *Aerosol Science*, Academic Press, New York (1966).
11. J.D. Seader and I.N. Einhorn, *16th Symposium (International) on Combustion*, Combustion Institute, Pittsburgh, PA (1976).
12. W.W. Foster, *Br. J. App. Phys.*, 10, p. 416 (1959).
13. G.W. Mulholland, *Fire and Mats.*, 6, p. 65 (1982).
14. D. Gross, J.J. Loftus, and A.F. Robertson, *ASTM STP 422*, American Society for Testing and Materials, West Conshohocken, PA (1967).
15. J.D. Seader and W.P. Chien, *J. Fire and Flamm.*, 5, p. 151 (1974).
16. L.H. Breden and M. Meisters, *J. Fire and Flamm.*, 7, p. 234 (1976).
17. E.L. Lopez, *J. Fire and Flamm.*, 6, p. 405 (1975).
18. V. Babrauskas, *J. Fire and Flamm.*, 12, p. 51 (1981).
19. D.D. Evans, *NBSIR 81-2400*, National Bureau of Standards, Washington, DC (1981).
20. J.G. Quintiere, *Fire and Mats.*, 6, p. 145 (1982).
21. E.J. McCartney, *Optics of the Atmosphere*, Wiley and Sons, New York (1976).
22. T. Jin, *J. Fire and Flamm.*, 9, p. 135 (1978).
23. T. Jin and T. Yamada, *Fire Sci. and Tech.*, 5, p. 79 (1985).
24. UL 217, *Standard for Single and Multiple Station Smoke Detectors*, Underwriters Laboratories, Northbrook, IL (1993).
25. G.W. Mulholland and B.Y.H. Liu, *J. Res. NBS*, 85, p. 223 (1979).
26. C. Helsper, H. Fissan, J. Muggli, and A. Scheidweiler, *Fire Tech.*, 14 (1983).

SECTION TWO

CHAPTER 14

Heat Fluxes from Fires to Surfaces

Brian Y. Lattimer

Introduction

The heat transfer from fires to adjacent surfaces is an important consideration in many fire analyses. Some example applications that may require knowledge of the heat transfer from a flame include heating and failure of structural beams, heat transfer through walls and ceilings, and the ignition and flame spread along combustible surfaces.

Flames transfer heat to adjacent surfaces primarily through convection and radiation. Techniques for efficiently modeling the heat transfer from flames are still being developed; however, experimental data and empirical correlations have been generated to predict flame heat transfer for a number of common geometries. This chapter will focus on the data and empirical correlations that have been developed.

Empirical correlations for predicting heat transfer from flames are typically simple to use; however, their use is usually limited to a particular type of fire or the geometry of the surface being heated. The types of fires considered in this chapter include

- Exposure area fires (burning objects)
- Wall and ceiling fires
- Window flames

Exposure area fires are burning objects located adjacent to or near the surface being heated. Wall and ceiling fires are those fires produced by a burning wall or ceiling. Window flames are flames extending outside a compartment containing a fire.

The heat transfer from fires has been characterized for a range of different surface geometries. The geometries included in this chapter are

- Flat vertical wall
- Flat unconfined and confined ceilings
- Parallel flat vertical walls

- Corner walls at 90°
- Corner walls at 90° with a ceiling
- Horizontal I-beams beneath a ceiling

General Topics

The majority of the data reported in this chapter are total heat flux measurements made using water-cooled heat flux gauges. The total incident heat flux to the gauge is comprised of both radiative and convective heat transfer,

$$q''_{inc,m} = q''_{conv} + q''_{rad} \quad (1)$$

where the radiative heat transfer to the gauge can include heating (or heat loss) effects of the environment if the flame is optically thin. Heat flux gauges are typically painted black to produce a high emissivity surface (~ 0.95) over the infrared spectrum. The gauge surface is usually cooled to a temperature ranging from 20–80°C, which can be much lower than the surface temperature of the material of interest. The low surface temperature, T_s , will increase the convective and radiative heat transfer incident on the surface. As a result, the total heat flux measured using water-cooled gauges will be a conservative estimate of the incident heat flux to most surfaces. The measured heat flux can be corrected for the actual heat flux on the surface if the heat transfer coefficient, surface emissive properties, and surface temperature are known.

EXAMPLE 1:

A water-cooled heat flux gauge is mounted onto a flat vertical wall located in a laboratory environment (300 K). The water running through the gauge is at a temperature of 300 K. When a fire with an optically thin flame is placed next to the wall, the heat flux gauge ($\varepsilon = 0.95$) measures the total heat flux to be 30 kW/m². A nearby thermocouple measures the wall material surface ($\varepsilon = 0.88$) temperature to be 600 K, while a second thermocouple measures the flame temperature to be 1300 K. Assuming a heat transfer coefficient to the wall of $h = 0.010 \text{ kW}/(\text{m}\cdot\text{K})$, how much of the measured heat flux is due to radiation?

Dr. Brian Y. Lattimer is a research scientist at Hughes Associates, Inc. His research has focused on species formation and transport in building fires, fire growth inside compartments, flame spread, and heat transfer from flames.

SOLUTION:

An energy balance at the surface of the heat flux gauge can be used to develop an expression for the measured incident heat flux (see Figure 2-14.1). Note that there is no radiation exchange between the heat flux gauge and the lab environment since they are at the same temperature, making the measured heat flux the incident flux on the gauge.

$$q''_{\text{inc},m} = q''_{\text{conv}} + q''_{\text{rad}}$$

Solving for the radiation heat flux,

$$q''_{\text{rad}} = q''_{\text{inc},m} - h(T_g - T_s) - q''_{\text{inc},m}$$

$$q''_{\text{rad}} = 30 - 10 = 20 \text{ kW/m}^2$$

EXAMPLE 2:

For the problem stated in Example 1, what is the actual incident heat flux onto the material?

SOLUTION:

To determine the actual incident heat flux on the material, the reradiation from the surface to the surroundings must be accounted for in the calculations.

$$q''_{\text{inc}} = q''_{\text{conv}} + q''_{\text{rad}} - q''_{rr}$$

or

$$q''_{\text{inc}} = h(T_g - T_s) + q''_{\text{rad}} - \varepsilon\sigma T_s^4$$

Using the radiative heat flux from the flame determined above, the material surface temperature, and the material surface properties, the incident heat flux on the actual material was determined to be

$$q''_{\text{inc}} = 0.010(1300 - 600) + 20 - (0.88)(5.67 \times 10^{-11})(600)^4$$

$$q''_{\text{inc}} = 7.0 + 20 - 6.5 = 20.5 \text{ kW/m}^2$$

Therefore, for this case the incident heat flux onto the surface is approximately 9.5 kW/m² lower than that measured using the water-cooled heat flux gauge.

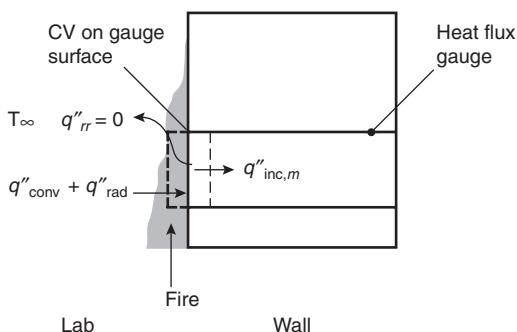


Figure 2-14.1. Energy balance at heat flux gauge surface.

The heat transfer from a flame to an adjacent surface or object has historically been characterized with respect to the flame length. Many of the heat flux correlations developed in the literature are based on flame length data taken in that study. Measured flame lengths can vary depending on the measurement technique, definition, and surrounding geometry. For the studies considered in this chapter, the data was nondimensionalized with either the average (50 percent intermittent) flame length or the flame tip length. Therefore, heat flux correlations should be applied using either the flame length correlation developed in the study or with one that has been demonstrated to predict the flame length in that study.

Exposure Fires

Fires Adjacent to Flat Walls

Heat fluxes from exposure fires adjacent to flat walls have been experimentally studied using propane sand burners and characterized for various burning objects. The experimental study provides a systematic approach of calculating heat fluxes for this geometry.

An extensive experimental study was performed by Back et al.¹ to characterize the heat transfer from a fire to an adjacent wall. In this study, fires were generated using square propane sand burners with edge lengths of 0.28, 0.37, 0.48, 0.57, and 0.70 m. Heat flux fields were measured for fires ranging from 50 to 520 kW.

A plot of the peak heat fluxes measured for each type of fire evaluated is shown in Figure 2-14.2. Peak heat fluxes for the different fires evaluated were determined to be a function of fire heat release rate. This dependence was attributed to the larger fires resulting in thicker boundary layers, which is related to the radiation pathlength. Based on gray-gas radiation theory, the authors found that the following relation adequately represented the data:

$$q''_{\text{peak}} = 200[1 - \exp(-0.09Q^{1/3})] \quad (2)$$

where q''_{peak} is in kW/m² and Q is in kW.

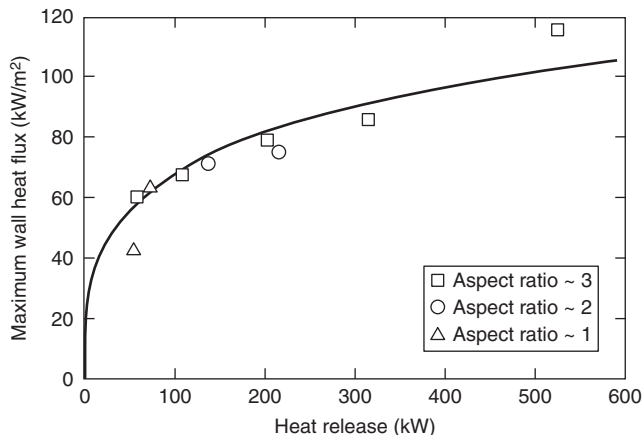


Figure 2-14.2. Peak heat release rates measured in square propane burner fires against a flat wall.¹

These peak heat fluxes were measured in the lower part of the fire ($z/L_f \leq 0.4$) along the centerline, with the flame length taken from Heskstad:²

$$L_f = 0.23Q^{2/5} - 1.02D \quad (3)$$

where L_f and D are in (m) and Q is in (kW)

Above this region, the heat fluxes were measured to decrease with distance above the fire. The heat flux data measured along the centerline is shown in Figure 2-14.3. Lines in this plot are a general correlation of the centerline data:

$$q''_{cl} = q''_{peak} \quad z/L_f \leq 0.4 \quad (4a)$$

$$q''_{cl} = q''_{peak} - \frac{5}{3}(z/L_f - 2/5)(q''_{peak} - 20) \quad 0.4 < z/L_f \leq 1.0 \quad (4b)$$

$$q''_{cl} = 20(z/L_f)^{-5/3} \quad z/L_f > 1.0 \quad (4c)$$

Heat fluxes were measured to decrease with horizontal distance from the centerline, as shown in Figure 2-14.4. The normalized lateral heat flux distribution data shown in Figure 2-14.4 was found to be half-Gaussian in shape over the half-width of the burner. The line in the plots is a fit to the data in Figure 2-14.4(a):

$$q'' = q''_{cl} \exp \left[-\left(\frac{x}{0.5D} \right)^2 \right] \quad \frac{x}{0.5D} \leq 1.0 \quad (5a)$$

$$q'' = 0.38q''_{cl} \left(\frac{x}{0.5D} \right)^{-1.7} \quad \frac{x}{0.5D} > 1.0 \quad (5b)$$

Heat fluxes from burning objects to an adjacent wall have been measured for a variety of items; however, lim-

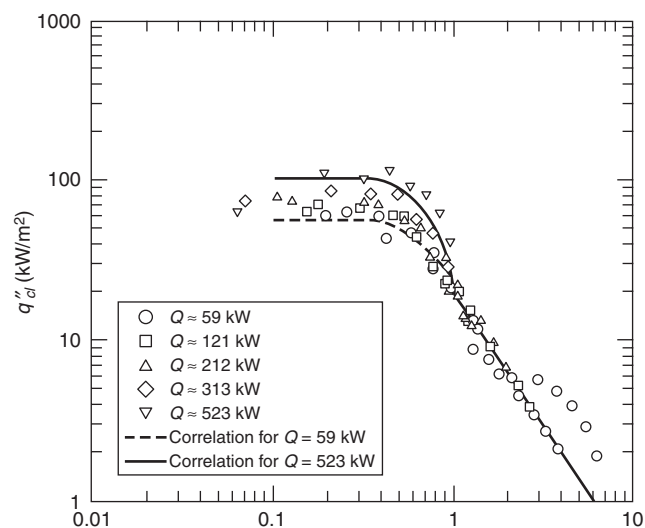


Figure 2-14.3. Vertical heat flux distribution along the centerline of a square propane burner fire adjacent to a flat wall.¹

ited data has been published on this work.^{3,4} Heat fluxes at the rim of wastebasket fires was reported by Gross and Fang.³ At the rim, heat fluxes as high as 50 kW/m² were measured; however, the authors noted that peak heat fluxes for these fires occurred approximately 0.22 m above the rim.

Mizuno and Kawagoe⁴ performed experiments with upholstered chair fires against a flat wall. In these tests, Mizuno and Kawagoe measured heat fluxes to the wall of 40 to 100 kW/m² over the continuous flaming region ($\sim z/L_f < 0.4$). All these tests were performed using foam-padded chairs.

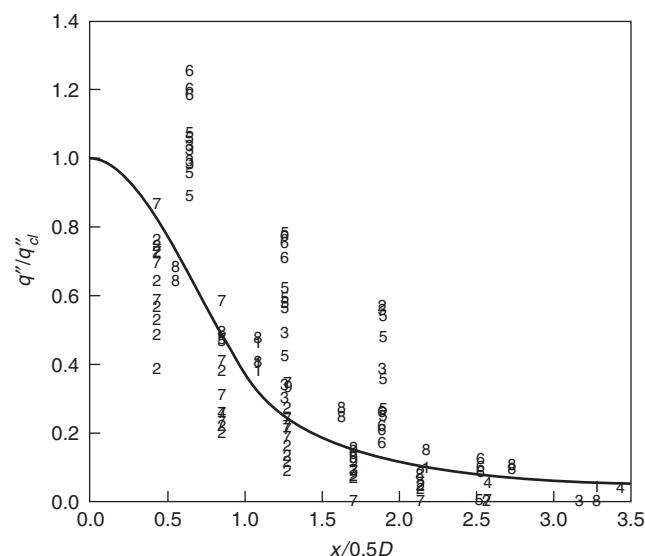
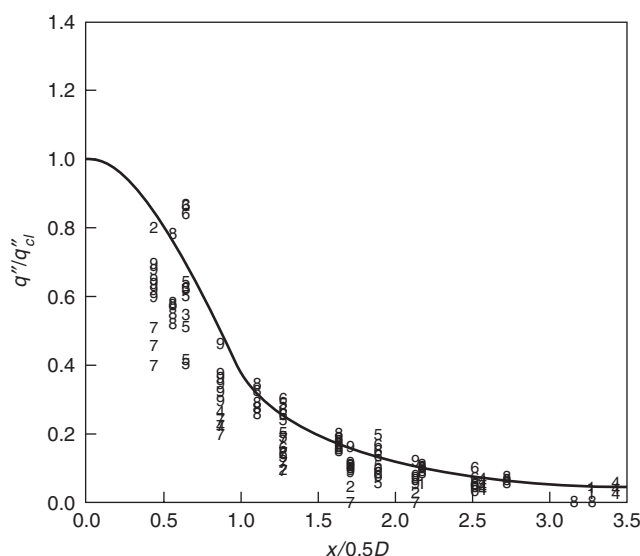


Figure 2-14.4. Lateral heat flux distribution with distance from the centerline of square propane burner fires against a flat wall¹ (a) in the flaming region and (b) in the plume.

Fires in a Corner

Fires in a corner of a room lined with a combustible material have been shown to cause more rapid flame spread and growth to flashover compared to cases with fires in other locations within the room. For these reasons, a significant amount of work has been performed to characterize the heat fluxes produced by corner fires. Heat flux measurements have been performed both in an open environment to quantify the heat flux due to the exposure fire alone and within rooms to measure the heat flux due to the exposure fire and the room environment.

The heat flux from exposure fires have been quantified in several studies performed in an open laboratory environment.⁵⁻¹⁰ All the studies were performed in a non-combustible corner with a ceiling except the study of Kokkala,⁷ which was performed in a noncombustible corner without a ceiling. A comparison of the heat flux fields measured in the study with a ceiling¹⁰ and the study without a ceiling⁷ is shown in Figure 2-14.5. Note that the contour plot of Lattimer et al. is relative to the floor, while the plot of Kokkala is relative to the top of the burner. Lattimer et al. used a burner 0.15 m high.

Up to approximately 1.8 m above the floor, the heat flux distributions are similar. In the case with the ceiling, the ceiling jet and the radiation from the fire flowing along the ceiling was heating the top part of the wall. This resulted in higher heat fluxes further out from the corner along the top part of the wall.

A series of fire tests were performed by Lattimer et al.¹⁰ to develop empirical correlations to estimate heat fluxes from an exposure fire to the walls and ceiling of a corner. Tests were performed using 0.17-, 0.30-, and 0.50-m square propane burners placed directly against the corner. Heat flux fields were measured for fires ranging from 25–300 kW.

Correlations were developed for three regions in the corner: along the height of the walls in the corner, along the top of the walls near the ceiling, and along the ceiling. The region containing the walls in the corner extended from the top of the fire to approximately 1.8 m above the floor, which is approximately the ceiling height minus twice the ceiling jet thickness ($\delta = 0.1H$). Correlations for the top part of the walls, which are heated by the ceiling jet, were developed using data at locations greater than 1.8 m above the floor.

Along the height of the walls in the corner, the peak heat fluxes were typically measured near the base of the fire. The peak heat fluxes along the height of the walls in the corner were measured to be a function of the fire diameter, as shown in Figure 2-14.6. The curve in Figure 2-14.6 is a correlation of the data and is expressed using the following relation:

$$q''_{\text{peak}} = 120[1 - \exp(-4.0D)] \quad (6)$$

The vertical distribution in the maximum heat flux along the walls near the corner is shown in Figure 2-14.7 plotted with the vertical distance normalized with respect to the flame tip,

$$L_{f,\text{tip}}/D = 5.9Q_D^{*1/2} \quad (7)$$

with

$$Q_D^* = \frac{Q}{\rho_\infty C_p T_\infty \sqrt{g D^{5/2}}} \quad (8)$$

Peak heat flux levels were measured in the lower part of the flame ($z/L_{f,\text{tip}} \leq 0.4$), and decreased with distance above $z/L_{f,\text{tip}} = 0.4$. A general correlation to represent this behavior is

$$q''_{\text{max}} = q''_{\text{peak}} \quad z/L_{f,\text{tip}} \leq 0.4 \quad (9a)$$

$$q''_{\text{max}} = q''_{\text{peak}} - 4\left(\frac{z}{L_{f,\text{tip}}} - \frac{2}{5}\right)(q''_{\text{peak}} - 30) \quad 0.4 < z/L_{f,\text{tip}} \leq 0.65 \quad (9b)$$

$$q''_{\text{max}} = 7.2\left(\frac{z}{L_{f,\text{tip}}}\right)^{-10/3} \quad z/L_{f,\text{tip}} \leq 0.65 \quad (9c)$$

This is similar to the form used by Back et al.¹ to correlate heat fluxes from an exposure fire to a wall (see Equations 4a–4c), except the constants are different.

The horizontal distribution in the heat flux along the wall is shown in Figure 2-14.8 to best correlate with actual distance from the corner (in meters).¹⁰ This was attributed to air being entrained in the corner, pushing the fire into the corner. Near the corner the shape is half-Gaussian; however, heat fluxes outside of this decrease more slowly. The trend in the data, which is shown as the line in Figure 2-14.8, can be represented using the following relations:

$$q'' = q''_{\text{max}} \exp[-7.5x^2] \quad x \leq 0.4 \quad (10a)$$

$$q'' = 0.058q''_{\text{max}} x^{-1.8} \quad x > 0.4 \quad (10b)$$

It has not been established whether this correlation holds for fire sources larger than 0.50 m in length on a single side.

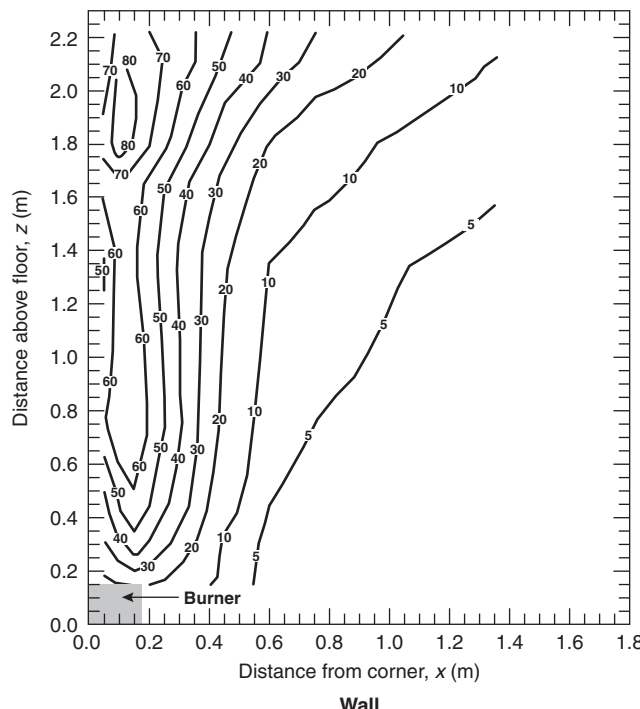
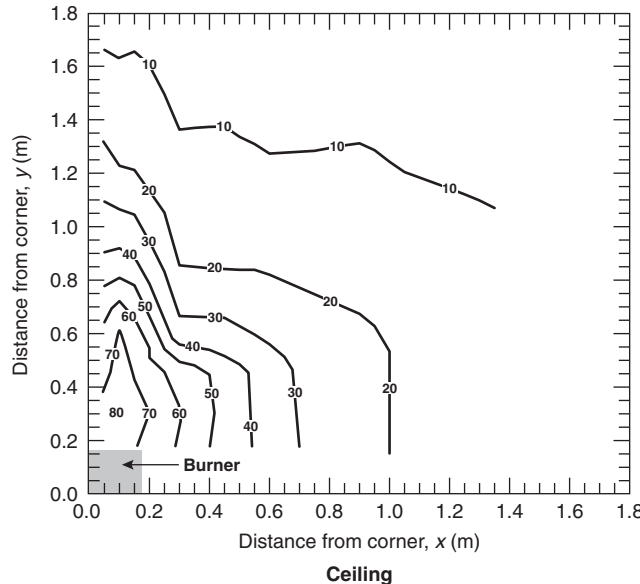
Along the top part of the wall the maximum heat fluxes were measured at locations less than 0.15 m below the ceiling. The maximum heat fluxes are shown in Figure 2-14.9 plotted against the normalized distance along the flame ($x + H)/L_{f,\text{tip}}$, where x is the distance from the corner. These heat fluxes can be estimated using the following relations:

$$q''_{\text{max}} = 120 \quad \left(\frac{x + H}{L_{f,\text{tip}}}\right) \leq 0.52 \quad (11a)$$

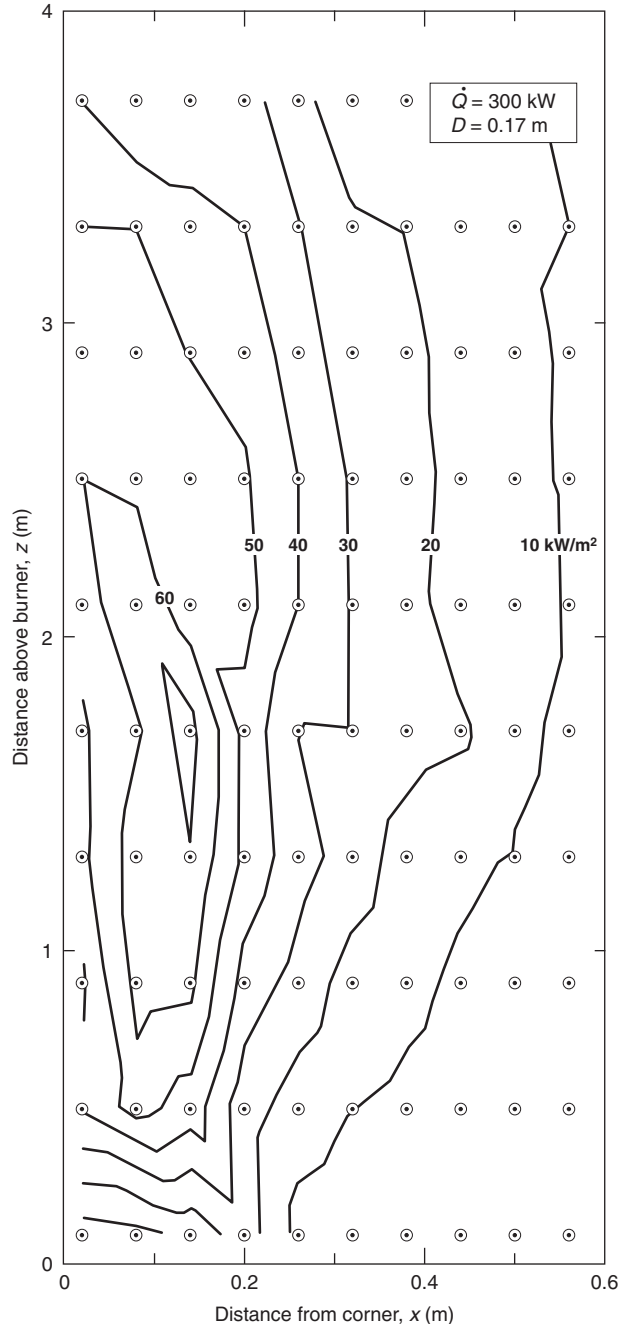
$$q''_{\text{max}} = 13.0\left(\frac{x + H}{L_{f,\text{tip}}}\right)^{-3.5} \quad \left(\frac{x + H}{L_{f,\text{tip}}}\right) > 0.52 \quad (11b)$$

The assumed plateau in the correlation was based upon the maximum heat flux expected from a flame according to Equation 6.

The heat fluxes to the ceiling were determined to be a function of normalized distance along the flame length, $(r + H)/L_{f,\text{tip}}$. All of the ceiling heat flux data taken in the study with a square burner in the corner is shown in Figure 2-14.10. Heat fluxes along the ceiling due to the exposure fire were similar to those measured along the top of



(a)



(b)

Figure 2-14.5. A comparison of the heat flux fields produced in a corner (a) with a ceiling¹⁰ and (b) without a ceiling.⁷ The fire was produced by a 0.17 m square propane burner with a heat release rate of 300 kW. Note that the data of Latimer et al. are plotted relative to the floor and the data of Kokkala are plotted relative to the top of the burner.

the wall. This resulted in similar correlations to estimate the heat flux to the ceiling:

$$q'' = 120 \quad \left(\frac{r + H}{L_{f,tip}} \right) \leq 0.52 \quad (12a)$$

$$q'' = 13.0 \left(\frac{r + H}{L_{f,tip}} \right)^{-3.5} \quad \left(\frac{r + H}{L_{f,tip}} \right) > 0.52 \quad (12b)$$

Again, the assumed plateau in the correlation was based upon the maximum heat flux expected from a flame, according to Equation 6.

Similar levels were measured by Hasemi et al.⁶ with an exposure fire in the corner, simulated burning corner walls, and an exposure fire and simulated burning corner walls in the corner.

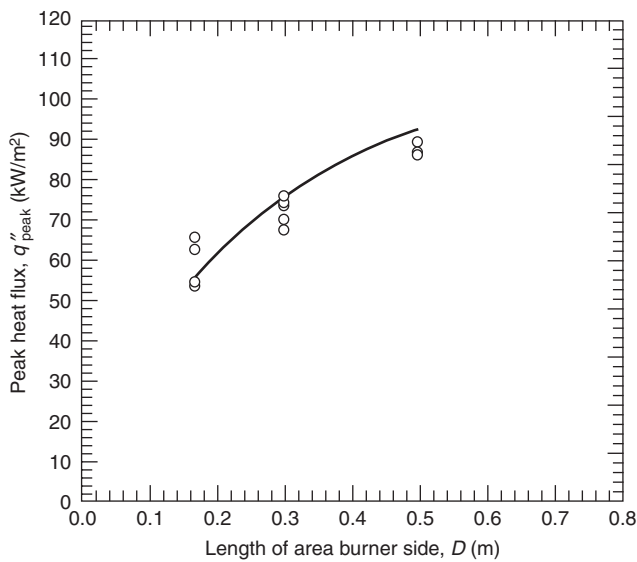


Figure 2-14.6. Peak heat flux along the height of the walls in the corner.¹⁰

Room environment effects: Corner fires are currently used to evaluate fire growth potential of a combustible lining material. As such, several studies have been conducted to characterize the heat flux from an exposure fire inside a room.^{11–14} In these cases, the heat flux to the surface will be due to both the exposure fire and the room environment.

The effect of the room environment on the heat fluxes was clearly demonstrated through the work performed by Dillon¹⁴ in an ISO 9705 room.¹⁵ The incident heat fluxes from the fire were determined by measuring the temperature rise at several locations on an insulated steel

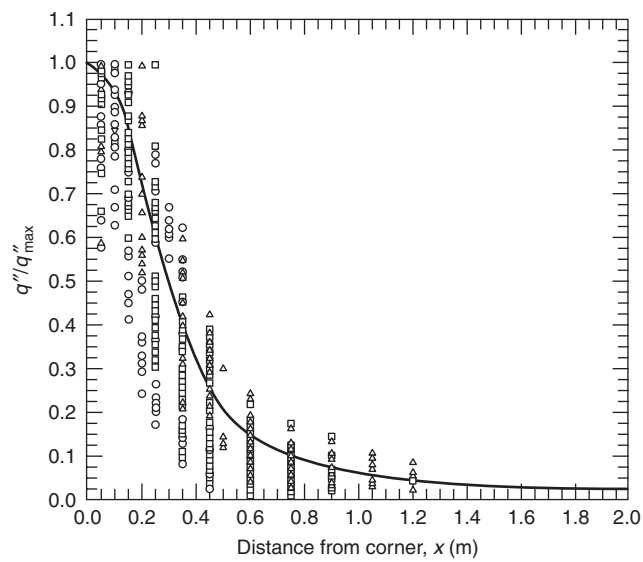


Figure 2-14.8. Lateral distribution in the heat flux along the walls with distance from the corner with square burner sides of 0.17 m (○), 0.30 m (△), 0.30 m (elevated) (▽), and 0.50 m (□) and fire sizes ranging from 50–300 kW.¹⁰

plate. Heat fluxes were calculated using a two-dimensional heat balance on the plate. Heat fluxes included contributions from both the exposure fire and the room environment. Using the surface temperature measurements and initial heat flux measurements after the burner was ignited, the heat fluxes to the hot steel plate were corrected for both reradiation from surfaces in the room and heating by the hot gas layer.

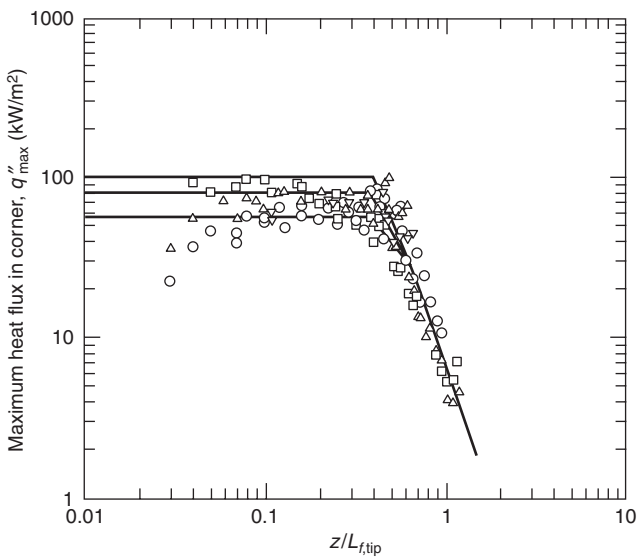


Figure 2-14.7. Maximum heat fluxes to the walls near the corner with square burner sides of 0.17 m (○), 0.30 m (△), 0.30 m (elevated) (▽), and 0.50 m (□) and fire sizes ranging from 50–300 kW.¹⁰

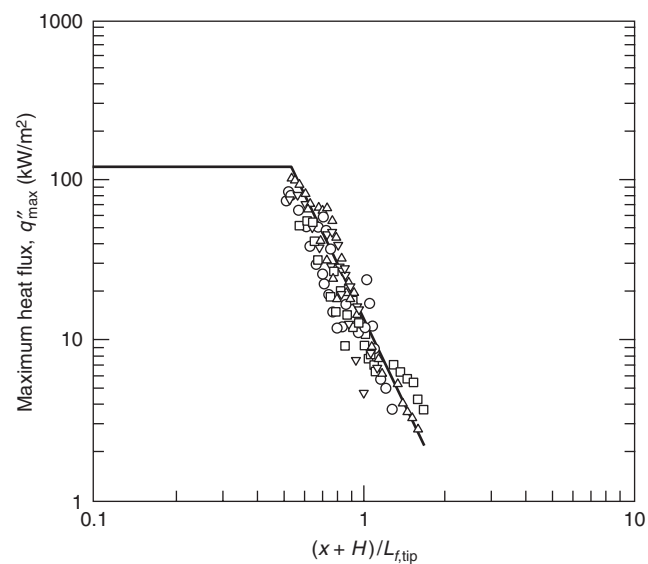


Figure 2-14.9. Maximum heat flux along the top of the walls during a corner fire test with square burner sides of 0.17 m (○), 0.30 m (△), 0.30 m (elevated) (▽), and 0.50 m (□) and fire sizes ranging from 50–300 kW.¹⁰

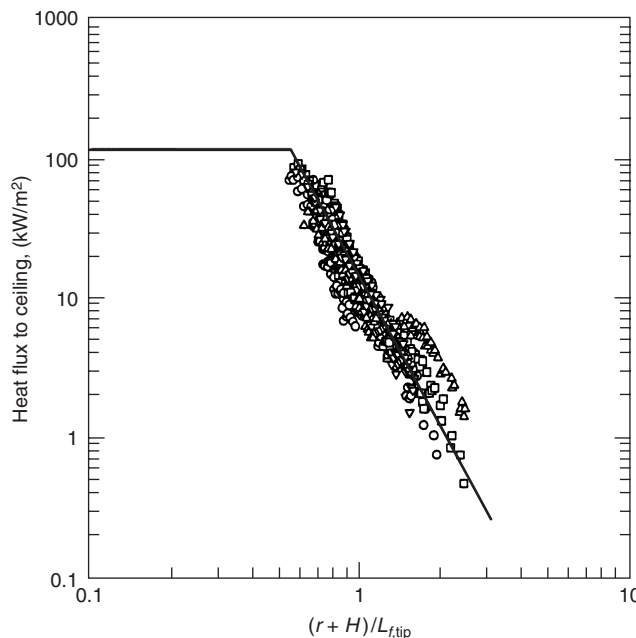


Figure 2-14.10. Heat flux along the ceiling above a fire located in a corner for tests with square burner sides of 0.17 m (○), 0.30 m (△), 0.30 m (elevated) (▽), and 0.50 m (□) and fire sizes ranging from 50–300 kW.¹⁰

The effects of the room environment on the heat fluxes to the corner boundaries is discussed here for the case with a 300-kW fire in the corner, produced using a 0.17-m square burner. The heat fluxes shown in Figure 2-14.11(a) represent the heat flux from the fire only, as measured using a heat flux gauge (i.e., cold surface). Note that the top of the burner is 30 cm above the floor. In general, the heat fluxes in Figure 2-14.11(a) compare well with the total heat flux data shown in Figure 2-14.5(a).

Heat fluxes shown in Figure 2-14.11(b) correspond to heat fluxes due to the fire and the room environment (i.e., hot gas layer and reradiation from walls), as measured using a heat-flux gauge. For this room environment, the heat fluxes including the room environment were higher than the heat fluxes from the exposure fire to a cold wall. The magnitude of the increase depends on the elevation inside the room. Measurements in the lower part of the room showed less of an increase compared with those near the ceiling. Heat fluxes in the upper part of the room increased by as much as 20 kW/m², an increase largely attributed to the hot gas layer that forms inside the room during the fire. For the 300-kW fire inside the ISO 9705 compartment, average gas temperatures in the upper part of the room were measured to be approximately 680 K. Note that the heat flux due to the room environment is dependent on the gas layer temperature, which is dependent on the fire size, room geometry, ventilation, and thermal properties of the boundaries. A room or fire different from that used to produce the data in Figure 2-14.11(b) may result in a different gas layer temperature, which will result in a different heat flux contribution due to the room environment.

Heat fluxes due to the hot layer environment inside a room were measured by Tanaka et al.¹⁶ In tests conducted

in a 3.3-m-wide, 3.3-m-deep, 2.35-m-high room with the propane fire in the center of the room, heat fluxes were measured at different locations on one of the side walls. The average heat flux measured in the upper layer formed inside of the room is shown in Figure 2-14.12 versus the layer temperature for different compartment door widths. The line in the plot represents the black body heat flux using the layer gas temperature, $q'' = \sigma T_{\text{gas}}^4$. As seen in Figure 2-14.12, the black body heat flux using the layer gas temperature provides a reasonable estimate of the incident heat flux to the walls inside a compartment.

Effects of fire standoff distance: Several researchers have investigated the effects of moving the exposure fire away from the corner (i.e., standoff distance).^{5,11,17} As one might expect, moving the fire away from the corner decreases the heat fluxes to the room boundaries. Tests were performed by Williamson et al.¹¹ in a full-scale ISO 9705 room using a 0.30-m-diameter burner. Heat fluxes to the wall were strongly dependent on whether the flame was attached to the corner walls or burned freely near the wall. At a heat release rate of 40 kW, with the burner against the corner walls, the flame was attached to the walls and heat fluxes were measured to be as high as 50 kW/m². When the fire was moved 50 mm from the walls, the flames were observed to be detached from the walls with the highest heat fluxes measured to be approximately 25 kW/m². In tests with a heat release rate of 150 kW, the fire was observed to be attached to the walls and heat fluxes of 40–60 kW/m² were measured at the walls. Additional work needs to be performed to investigate distances at which fires attach to nearby surfaces, such as a flat wall or walls in a corner.

Fires beneath Unconfined Ceilings

There have been several experimental and theoretical studies performed on fires impinging on an unbounded ceiling.^{18–25} Total heat fluxes from fires and fire plumes impinging on the ceiling were measured by Hasemi et al.,¹⁸ You and Faeth,^{20,21} and Kokkala.^{23,24}

Hasemi et al.¹⁸ conducted a series of fire tests using propane gas burners located at different distances beneath a noncombustible ceiling. Fires as large as 400 kW (approximated) were considered in the study. Heat flux gauges were used to measure the incident heat flux along the ceiling at different distances away from the fire centerline, or stagnation point. The measured heat flux at the stagnation point is shown in Figure 2-14.13 to plateau at approximately 90 kW/m². In order to collapse the data, the unconfined flame tip length was normalized with respect to the distance between the ceiling and the fire, H , plus the virtual source location, z' . The virtual source location for this geometry was determined using the following relations:

$$z' = 2.4D(Q_D^{*2/3} - Q_D^{*2/5}) \quad Q_D^* < 1.0 \quad (13a)$$

$$z' = 2.4D(1 - Q_D^{*2/5}) \quad Q_D^* \geq 1.0 \quad (13b)$$

where Q_D^* is defined as in Equation 8, with D being the diameter of the exposure fire, z' is in meters and D is in

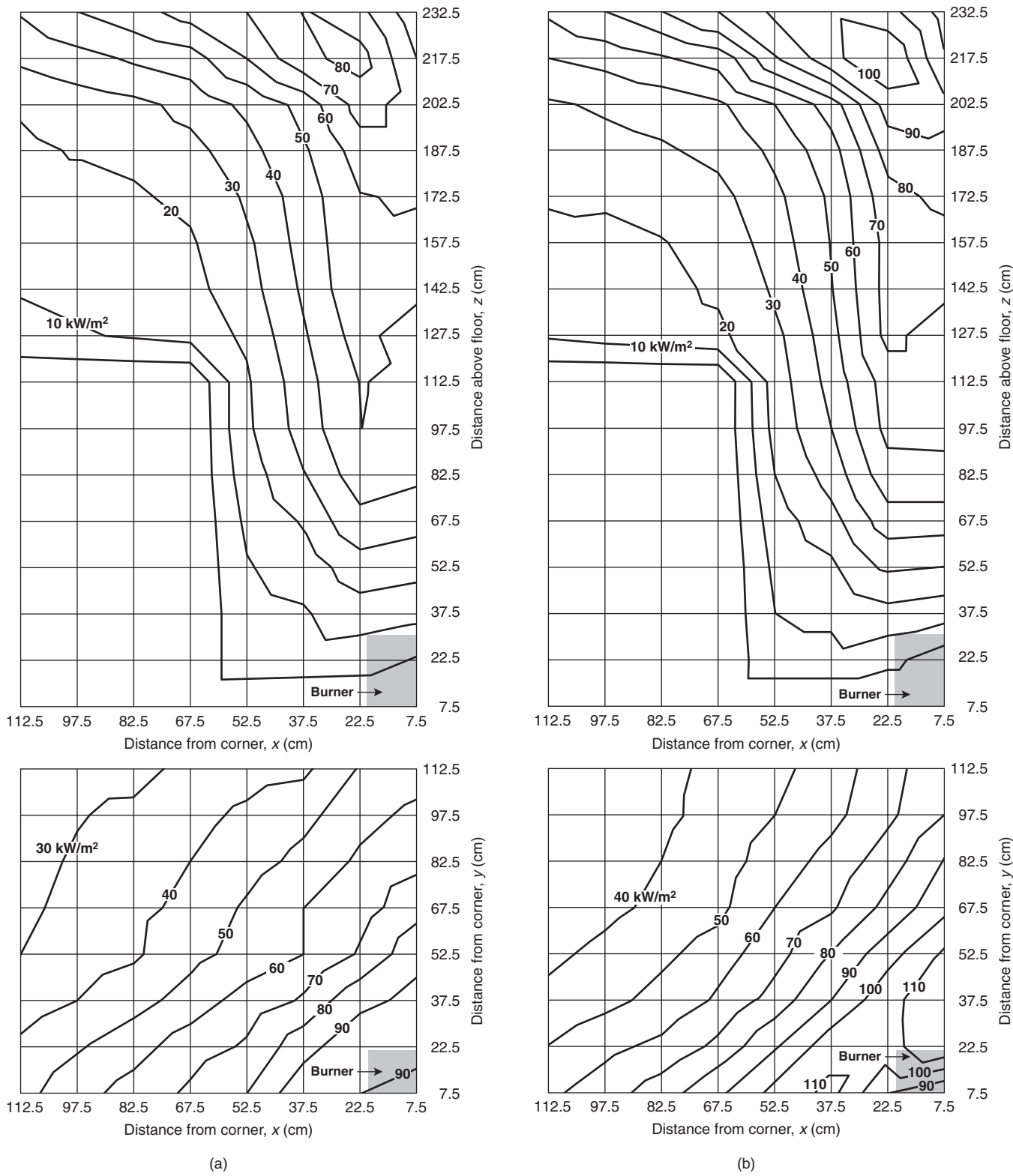


Figure 2-14.11. Heat fluxes to corner boundaries from (a) 300-kW, 0.17-m square propane sand burner exposure fire alone to a cold surface and from (b) the 300-kW exposure fire and the room environment.¹⁴

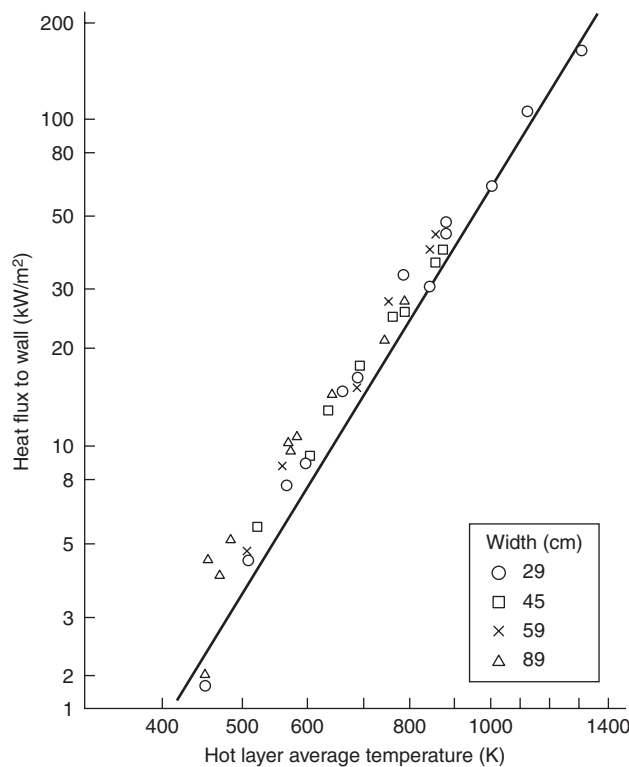


Figure 2-14.12. Heat flux to the walls inside a compartment containing a hot gas layer.¹⁶

meters. The unconfined flame tip length was calculated using $L_f = 3.5Q_D^{*n} \cdot D$, where $n = 2/5$ for $Q_D^* \geq 1.0$ and $n = 2/3$ for $Q_D^* < 1.0$, with L_f and D in meters. The length of the flame, $L_{f,tip}$, in this geometry is defined as the distance between the fire and the ceiling, H , plus the radial extension of the flame out from the center of the fire, L_H . The location of the flame tip in this geometry was found to correlate with Q_H^* , which is defined the same as in Equation 8 except D is replaced by H . The flame tip correlation was determined to be

$$\frac{(L_H + H)}{H} = \frac{L_{f,tip}}{H} = 2.89Q_H^{*1/3} \quad (14)$$

The heat flux was measured to decrease with distance from the fire stagnation point. Figure 2-14.14 contains a plot of the heat flux to the ceiling as a function of location within the flame. The correlation recommended by Wakamatsu²⁶ can be used to predict the heat fluxes:

$$q'' = 518.8e^{-3.7w} \quad (15a)$$

where

$$w = (r + H + z')/(L_H + H + z') \quad (15b)$$

Heat flux measurements with smaller fires (<11 kW) beneath a ceiling were made by Kokkala^{23,24} and You and Faeth.²⁷ Kokkala used natural gas as a fuel and measured heat fluxes to plateau at 60 kW/m² at the stagnation point (see Figure 2-14.15). Due to the small burners used in this study ($D = 0.064$ m), Kokkala's data collapsed without applying a virtual source origin correction. Heat fluxes measured in the natural gas fire tests were lower than those measured by Hasemi et al.,¹⁸ an effect that can partly be attributed to the higher radiation levels from the

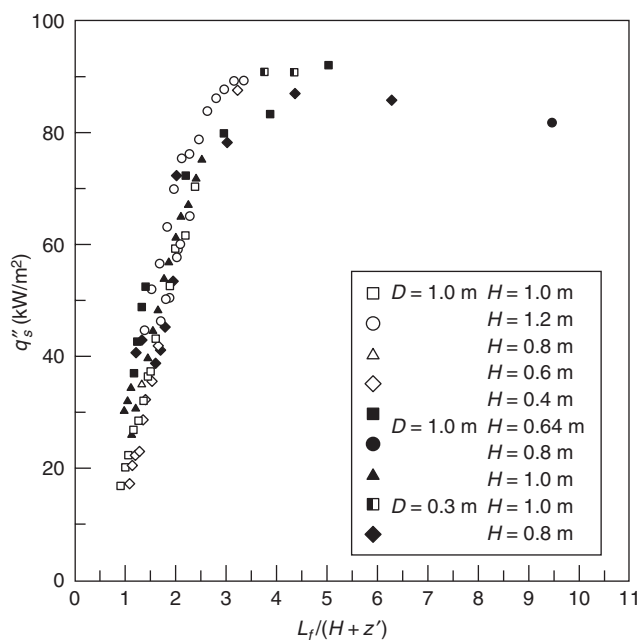


Figure 2-14.13. Stagnation point heat fluxes on an unbounded ceiling with a fire impinging on it.¹⁸

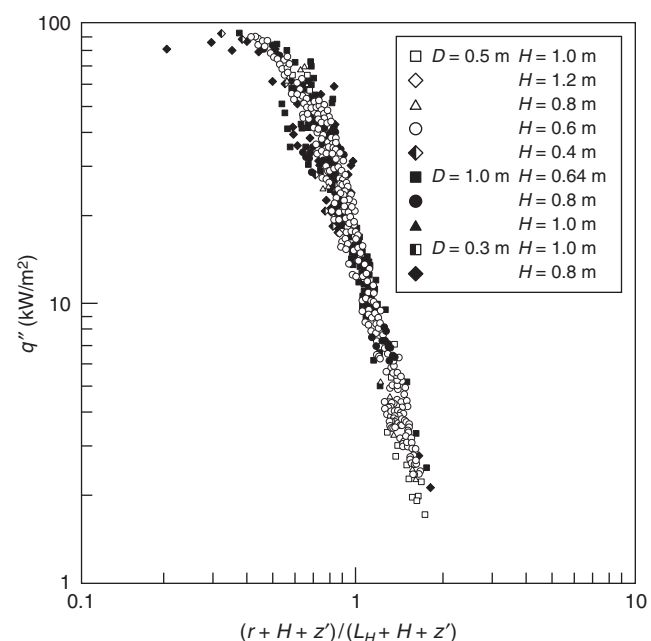


Figure 2-14.14. Heat fluxes to a ceiling due to a propane fire impinging on the surface.¹⁸

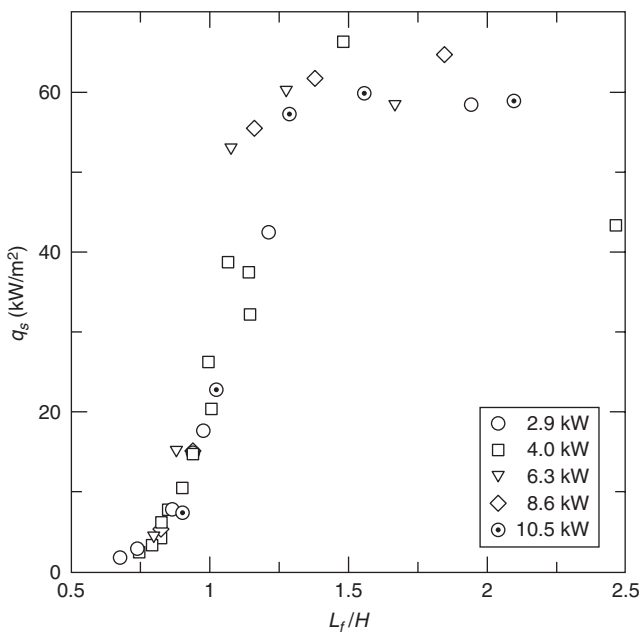


Figure 2-14.15. Heat fluxes at the stagnation point on a ceiling for tests with natural gas fires impinging on the ceiling.²³

propane flames. The heat fluxes measured by Kokkala²³ at different locations from the stagnation point are plotted in Figure 2-14.16. The distribution in the heat flux along the ceiling radially out from the stagnation point was measured to be similar to that measured by Hasemi et al.²⁸ with larger propane gas fires.

Fires in Corridors

There are few reported studies that have measured heat fluxes to the ceiling or walls of a corridor. Hinkley

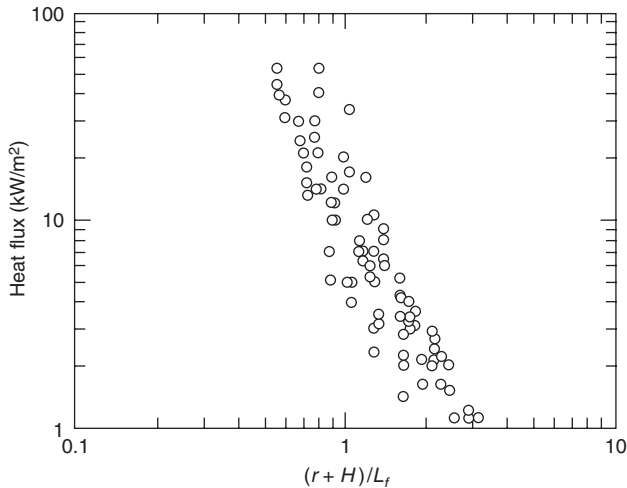


Figure 2-14.16. Heat fluxes to a ceiling due to a natural gas fire impinging on the surface.²³

et al.^{29–31} performed experiments with a town gas burner located at the end of a hallway. In tests with a noncombustible ceiling, tests were performed in a 1.2-m-wide hallway using a range of heat release rates (170–600 kW) with the burner at various distances (0.37–1.20 m) below the ceiling. Heat fluxes were determined through temperature measurements on exposed and unexposed sides of the ceiling material.

The heat fluxes determined in these experiments are provided in Figure 2-14.17, plotted as a function of $(x + x')/L$, where x' is the virtual source and L is the flame length from the virtual source. This plot indicates that heat fluxes as high as 140 kW/m² can exist in these types of scenarios. The increase in the heat flux over the unconfined ceiling data of Hasemi et al.,¹⁸ where peak heat fluxes of approximately 90 kW/m², may be in part due to the thicker layer of flames formed in the corridor. However, due to the method used to develop the heat fluxes, the accuracy of the heat flux data reported by Hinkley et al. is uncertain.^{29,30} Additional work needs to be performed to validate these results. In addition, heat fluxes in corridor geometries may also depend on the width of the corridor since this will affect the flame thickness. No work has been performed to evaluate this, but wider hallways should be expected to begin to provide results closer to the unconfined ceiling data.

Fires beneath I-Beams

Three studies have evaluated the heat flux incident onto an I-beam mounted to a ceiling with an exposure fire impinging upon the beam.^{18,32,33} These studies all measured the heat flux to the four surfaces shown in Figure 2-14.18 on the I-beam: downward face of the lower flange, upward face of the lower flange, the web, and

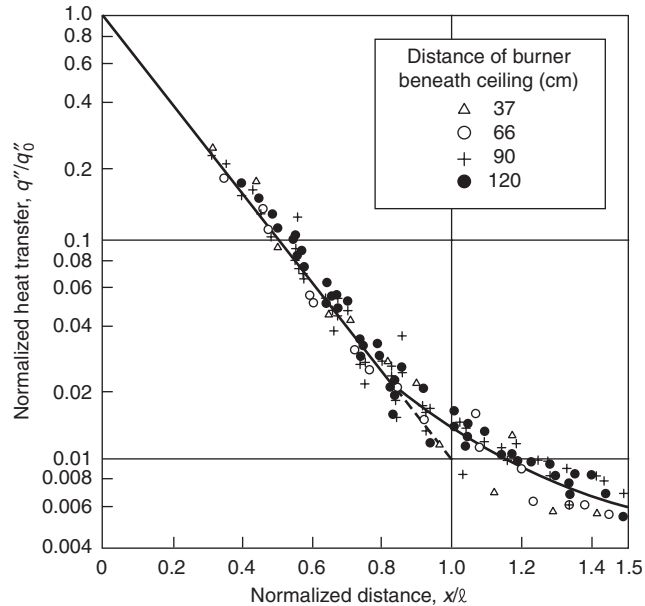


Figure 2-14.17. Heat fluxes to the ceiling in a corridor with an exposure fire at the closed end.³⁰

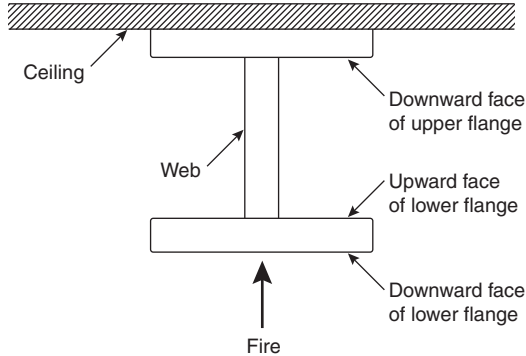


Figure 2-14.18. Location of heat flux measurements on I-beams.

downward face of the upper flange. For each of these surfaces, heat fluxes were measured from the stagnation point of the fire (centerline of the fire) past the location of the flame tip.

The study by Wakamatsu et al.³² provides a framework for determining heat fluxes to different parts of the I-beam. The I-beam evaluated in the study was 3.6 m long, a web 150 mm high and 5 mm thick, and flanges 75 mm wide and 6 mm thick. Tests were performed using fires from 0.5- or 1.0-m propane burners with heat release rates ranging from 100–900 kW. The distance between the fire source and I-beam was also varied.

When the fire impinges on the I-beam, the flame length is different on the lower flange compared to the flame length on the upper flange (see Figure 2-14.19). Flame lengths along the lower flange, L_B , were shorter than those observed near the upper flange, L_C . Heat fluxes along the lower flange were taken to be a function L_B while heat fluxes to other surfaces were related to L_C . Flame lengths were related to the dimensionless Q^* as defined in Equation 8 with D being replaced by the appropriate distance between the fire and the flange,

$$Q_{H_B}^* = \frac{Q}{\rho_\infty C_p T_\infty \sqrt{g} H_B^{5/2}} \quad (16)$$

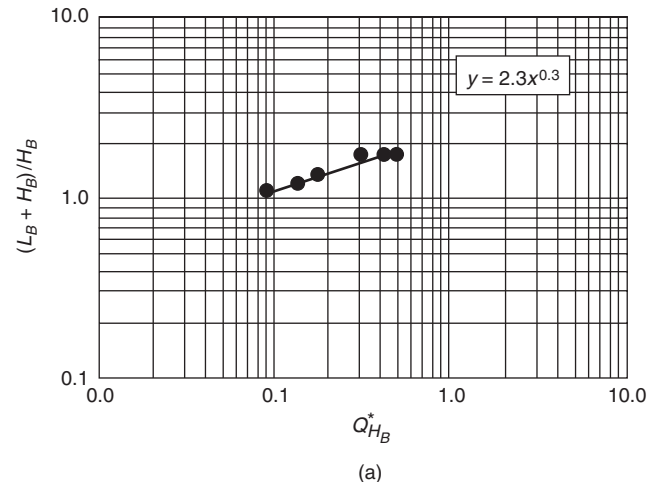
$$Q_{H_C}^* = \frac{Q}{\rho_\infty C_p T_\infty \sqrt{g} H_C^{5/2}} \quad (17)$$

Correlations were developed to predict the flame tip length along the lower and upper flanges:

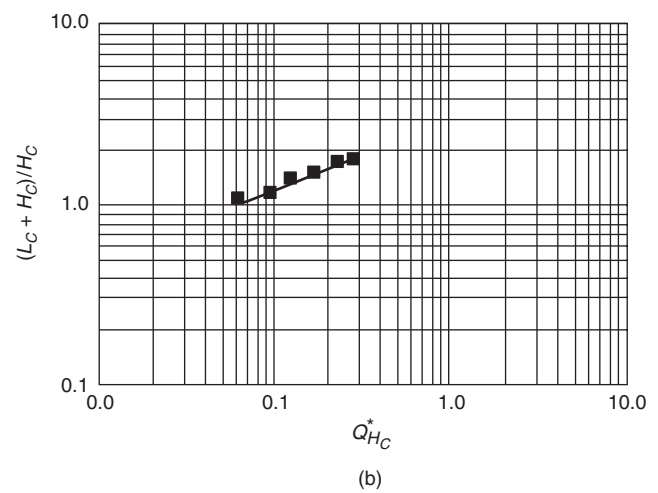
$$\frac{(L_B + H_B)}{H_B} = 2.3 Q_{H_B}^{*0.3} \quad (18a)$$

$$\frac{(L_C + H_C)}{H_C} = 2.9 Q_{H_C}^{*0.4} \quad (18b)$$

The heat flux measured at the stagnation point on the downward face of the lower flange was found to be the same as that measured for a fire beneath a ceiling, see Figure 2-14.20. The location of the virtual origin, z' , was determined using Equation 13. The variation in the heat flux



(a)



(b)

Figure 2-14.19. Flame lengths (a) along the lower flange (Equation 18a) and (b) along the upper flange (Equation 18b) in I-beam tests performed by Wakamatsu et al.³²

along the downward face of the lower flange with horizontal distance r from the stagnation point is shown in Figure 2-14.21. The data appears to fall between the range of the data measured in the unconfined ceiling tests, which are represented by the dashed and solid lines. These heat fluxes were the highest measured on the I-beam assembly and can be estimated using the following correlation:

$$q'' = 518.8 e^{-3.7w} \quad (19a)$$

where

$$w = (r + H_B + z')/(L_B + H_B + z') \quad (19b)$$

The heat fluxes to the upward face of the lower flange and the web are shown in Figures 2-14.22 and 2-14.23 to be lower than those on the downward face of the lower

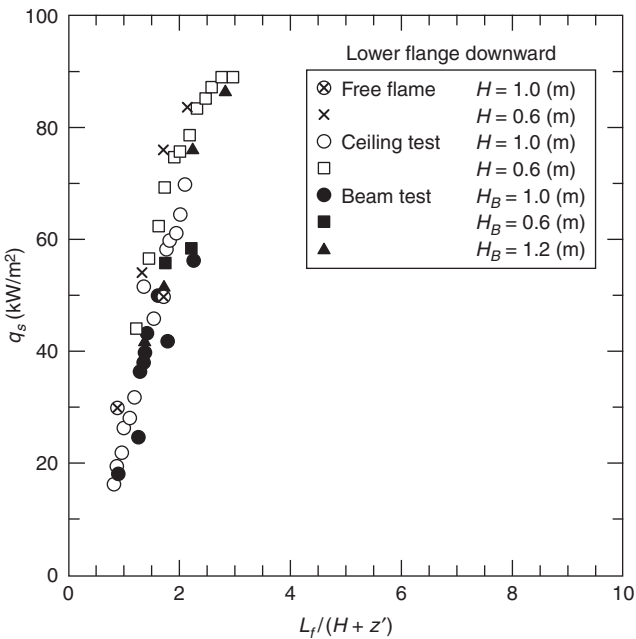


Figure 2-14.20. Heat flux at the stagnation point on the downward face of the lower flange.³²

flange. This was attributed to the lower flange shielding these parts of the I-beam from radiative and convective heat transfer. These data can be represented by the following expression:

$$q'' = 148.1e^{-2.75w} \quad (20a)$$

where

$$w = \frac{(r + H_C + z')}{(L_C + H_C + z')} \quad (20b)$$

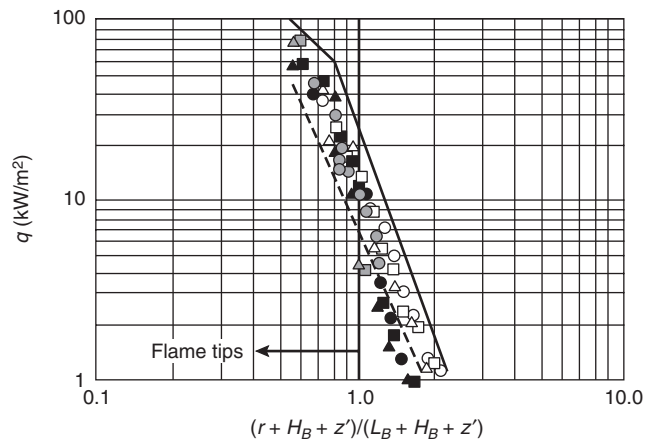


Figure 2-14.21. Heat flux along the downward face of the lower flange.³²

The lowest heat fluxes on the I-beam were measured on the downward facing part of the upper flange. As seen in Figure 2-14.24, heat fluxes to this part of the I-beam are slightly less than those measured on an unconfined ceiling. Heat fluxes to the downward face of the upper flange can be estimated using the following fit to the data:

$$q'' = 100.5e^{-2.85w} \quad (21a)$$

where

$$w = \frac{(r + H_C + z')}{(L_C + H_C + z')} \quad (21b)$$

Myllymaki and Kokkala³³ evaluated the use of the approach and data of Wakamatsu et al.³² to estimate heat fluxes onto I-beams exposed to fires as large as 3.9 MW. They found that for fires over 2.0 MW, the correlations suggested for the upward face of the lower flange, web, and downward face of the upper flange underestimate the heat flux to these areas on the I-beam. For these large fires, the I-beam becomes completely engulfed in fire. As a result, heat fluxes on all parts of the I-beam follow the correlation suggested for the downward face of the lower flange provided in Equation 19. Heat fluxes to the downward face of the lower flange, the upper flange, and the web are shown in Figure 2-14.25, along with the correlations recommended by Wakamatsu.²⁶ The highest heat fluxes measured in the tests performed by Myllymaki and Kokkala³³ were approximately 130 kW/m² and were along the downward face of the upper flange. To predict conditions along the web, Myllymaki and Kokkala³³ normalized the data with respect to the flame length along the center of the web,

$$L_{\text{web}} = H_{\text{web}}(2.9Q_{\text{web}}^{*0.4} - 1)$$

where

$$Q_{\text{web}}^* = \frac{Q}{\rho_{\infty} C_p T_{\infty} \sqrt{g} H_{\text{web}}^{5/2}}$$

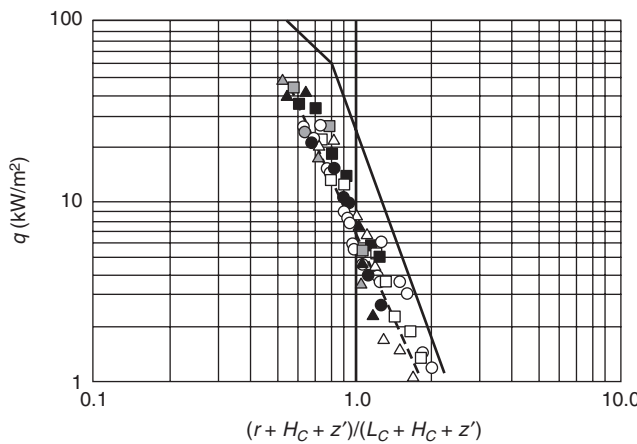


Figure 2-14.22. Heat flux along the upward face of the lower flange (key same as in Figure 2-14.21).³²

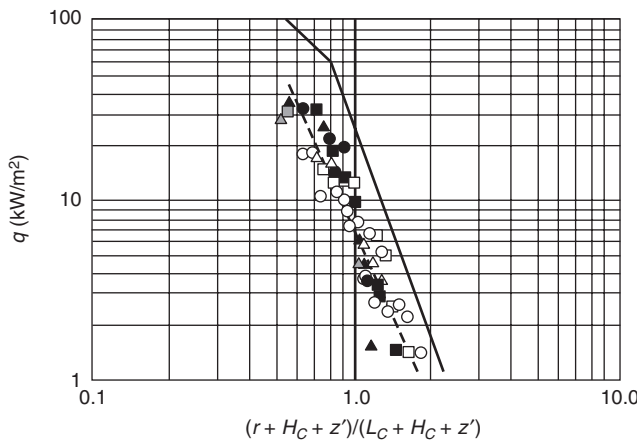


Figure 2-14.23. Heat flux along the web (key same as in Figure 2-14.21).³²

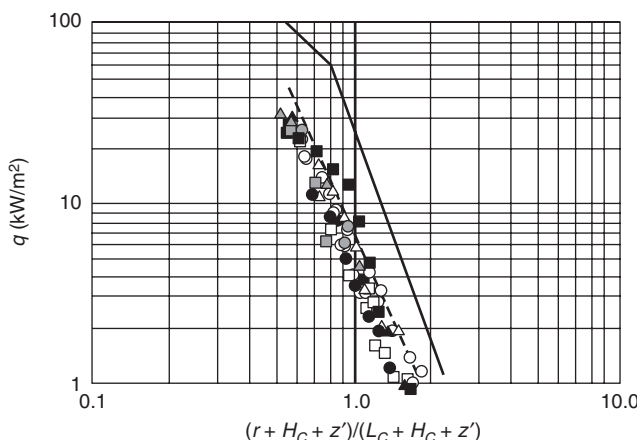


Figure 2-14.24. Heat flux along the downward face of the upper flange (key same as in Figure 2-14.21).³²

Burning Walls and Ceilings

Fires from burning boundaries typically produce thinner flames than those generated by exposure fires. As a result, heat fluxes from burning boundary flames are typically lower than those measured for exposure fires in a similar geometry. As was the case with heat fluxes from exposure fires, heat fluxes from burning boundaries are dependent on the geometry of the burning surfaces.

Wall Fires

Heat fluxes from a burning wall flame back to the surface has been studied fairly extensively. Most of the work in this area has been performed with smaller fires. Though the data indicates that these heat fluxes are dependent both on fire size and smoke production, no reported study has fully characterized this behavior.

Much of the detailed heat flux measurements for fires produced by burning flat surfaces have been done with smaller-scale fires (<100 kW). Through this work, the heat fluxes from flames produced by a variety of different burning materials have been characterized.³⁴⁻³⁷ All these studies were conducted with fires over flat, solid surfaces except the study of Ahmad and Faeth,^{34,35} which was performed using wicks soaked in different alcohols. Ahmad and Faeth performed flat wall fire experiments using a 0.66-m-wide, 0.81-m-high flat wall test apparatus, with the lower part of the wall being an alcohol-soaked wick. Different wick heights and different types of alcohol were included in the study. Data from Quintiere et al.³⁶ was performed using samples 0.28 m by 0.28 m exposed to different external heat fluxes to generate different heat release rate fires from the same sample. Experiments performed by Orloff et al.³⁷ were conducted using a 0.41-m-wide, 1.57-m-high sample of PMMA.

Data from the studies of Ahmad and Faeth^{34,35} and Quintiere et al.³⁶ are shown in Figure 2-14.26. Heat fluxes are approximately 20–30 kW/m² in the lower part of the flame ($z = 0.5L_f$) for a wide range of fuels. Peak heat fluxes measured by Orloff et al.³⁷ (22 kW/m²) were also in this 20–30-kW/m² range. The value of L_f can be determined by using a flame height correlation for a line fire, such as that proposed by Delichatsios:³⁸

$$L_f = 0.052Q'^{2/3} \quad (22)$$

where Q' is the heat release rate per unit length of burning wall (kW/m) and L_f is in (m).

Several empirical correlations have been proposed in the literature³⁹⁻⁴² to predict heat fluxes to walls. All correlations assume a constant heat flux in the lower part of the fire and a power law decay above this. The difference in these correlations is the peak heat flux over the bottom part of the fire and the empirical constants that govern the decay. Similar to that proposed by Hasemi,³⁹ the line in the plot is an average fit to the data:

$$q'' = 25 \quad (z/L_f) \leq 0.5 \quad (23a)$$

$$q'' = 4.4(z/L_f)^{-2.5} \quad (z/L_f) > 0.5 \quad (23b)$$

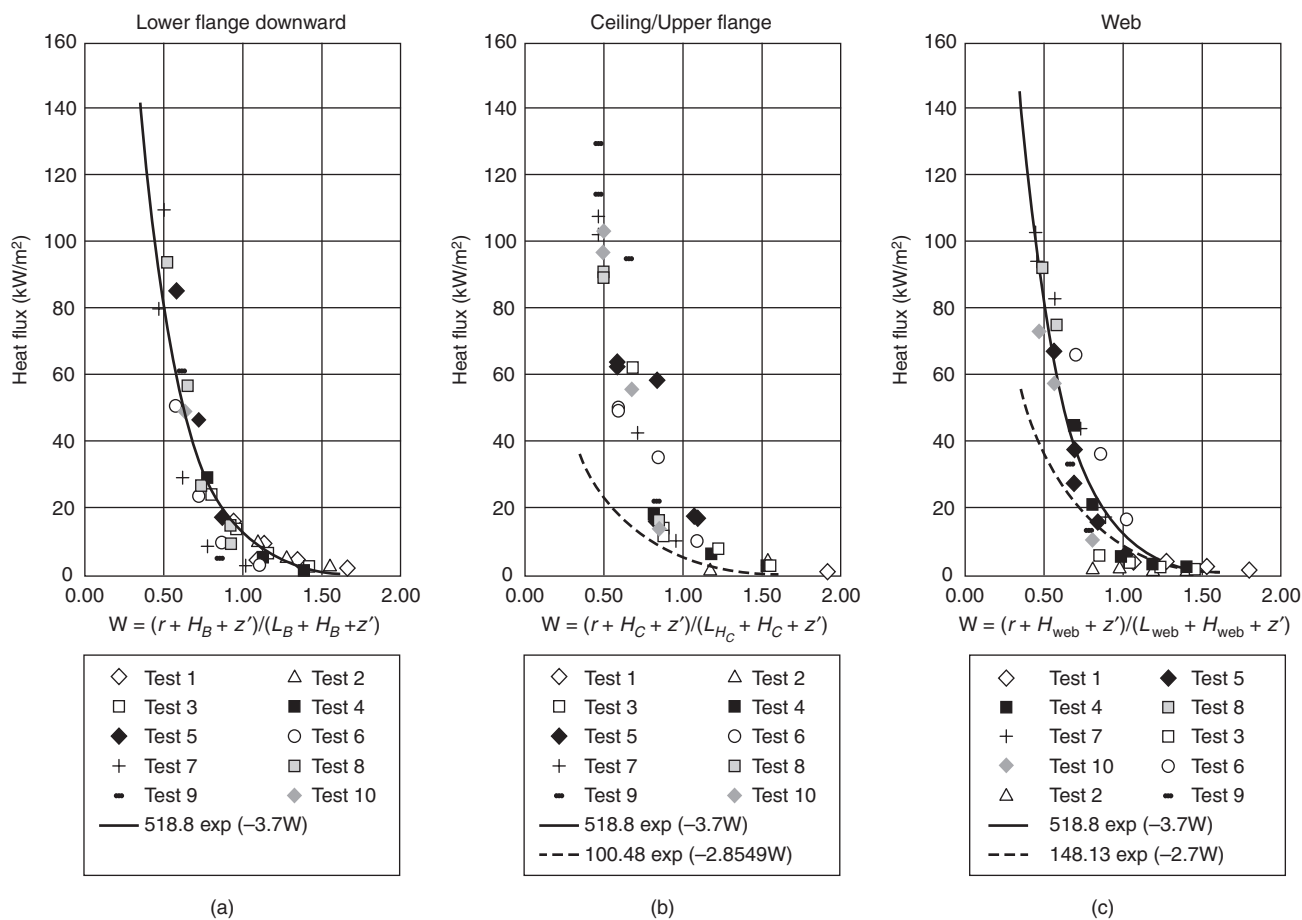


Figure 2-14.25. Heat fluxes measured at the (a) downward face of the lower flange, (b) upper flange, and (c) the web on an I-beam in the study by Myllymaki and Kokkala,³³ with fires as large as 3.9 MW.

A more conservative fit that bounds this data set was developed:

$$q'' = 30 \quad (z/L_f) \leq 0.7 \quad (24a)$$

$$q'' = 12.3(z/L_f)^{-2.5} \quad (z/L_f) > 0.7 \quad (24b)$$

Line burners have been used by some researchers to simulate a fire produced by a burning surface such as a wall. Hasemi^{39,43,44} measured the heat flux from a methane line burner fire to an incombustible wall. In this study, the fire heat release rate per unit length of burner (0.30 m) was varied from 16.7–218.2 kW/m and two different line burner widths (0.037 m and 0.082 m). For the test conditions considered, the heat fluxes along the flame are seen in Figure 2-14.26 to be similar for each test condition. In addition, heat fluxes measured in this study are shown in Figure 2-14.27 to be similar to those shown in Figure 2-14.26. The correlations presented in Equations 23 and 24 adequately bound the data. Line burner experiments using propane as fuel have resulted in higher heat fluxes than those measured with methane as the fuel. In tests using propane with Q' = 83–167 kW/m, Kokkala et

al.⁴⁵ and Lattimer¹⁰ both measured heat fluxes of approximately 45 kW/m² in the lower half of the flame (z = 0.5L_f). Though not shown on the plot, Foley and Drysdale⁴⁶ measured 40–50 kW/m² from propane line burners with Q' = 11.6 and 20.9 kW/m. These data indicate that the radiation from the fire to the surface is dependent on fuel smoke production.

Slightly larger-scale fire tests were performed by Kulkarni et al.^{47,48} In this study, heat flux measurements were made along the lengths of different 0.3-m-wide, 1.2-m-high samples of solid combustibles. Fires were initiated using a line burner at the bottom of the sample, and heat fluxes were continuously measured during the test. Heat fluxes and flame lengths were continuously monitored as the fire spread along the combustible material. These transient heat flux and flame length measurements were averaged over particular time periods and plotted to determine the heat flux at different locations along the flame length.

Figure 2-14.28 provides the heat flux data for the different materials included in the study. Peak heat fluxes measured for the different materials ranged from 25–60 kW/m². Heat fluxes from burning masonite board, card-

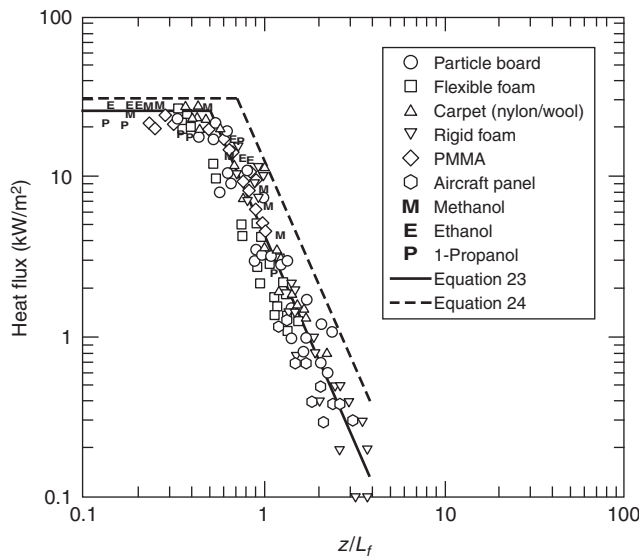


Figure 2-14.26. Heat fluxes from burning flat surfaces for fires less than 100 kW.³⁴⁻³⁶

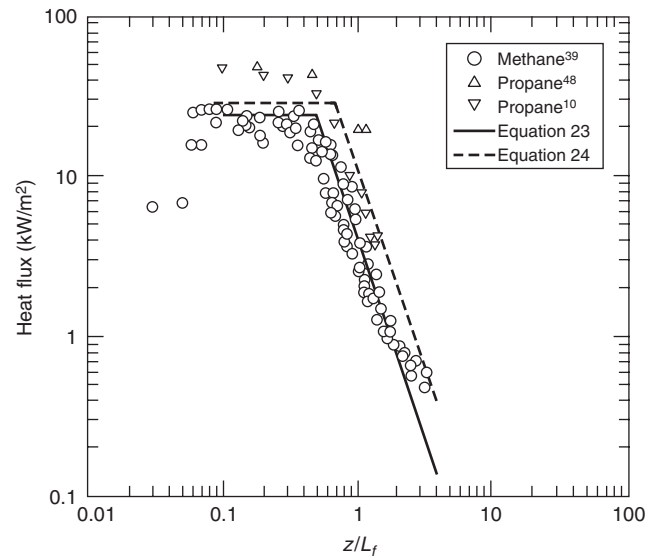


Figure 2-14.27. Heat fluxes from methane line burners against a flat wall.^{10,39,48}

board, and white pine board were in the 20–30-kW/m² range, similar to that measured in experiments by Ahmad and Faeth^{34,35} and Quintiere et al.³⁶ However, fires involving PMMA, polyurethane foam, and velour fabric were all measured to produce heat fluxes greater than 30 kW/m². The PMMA and polyurethane foam had the highest flame lengths of all the materials (~1.75 m), which is comparable to the flame lengths reported by Quintiere et al.³⁶ for similar materials (PMMA and flexible foam). This indicates that the heat release rates for the

PMMA and polyurethane foam is comparable in the two studies. The reason for the differences in the peak heat fluxes (e.g., 30–60 kW/m² in tests by Kulkarni et al.⁴⁸ with PMMA while 20–26 kW/m² in tests by Quintiere et al.³⁶) is not known.

Less detailed heat flux measurements have been reported in the literature for larger fires. Orloff et al.⁴⁹ and Delichatsios³⁸ reported data on heat fluxes from flames produced by a 3.6-m-high burning PMMA wall. Total heat fluxes incident on the PMMA were calculated using theory and mass loss rate data. Heat fluxes are shown in Figure 2-14.29 to increase with height. All the data in this plot were at positions where $z/L_f < 0.5$. This behavior is

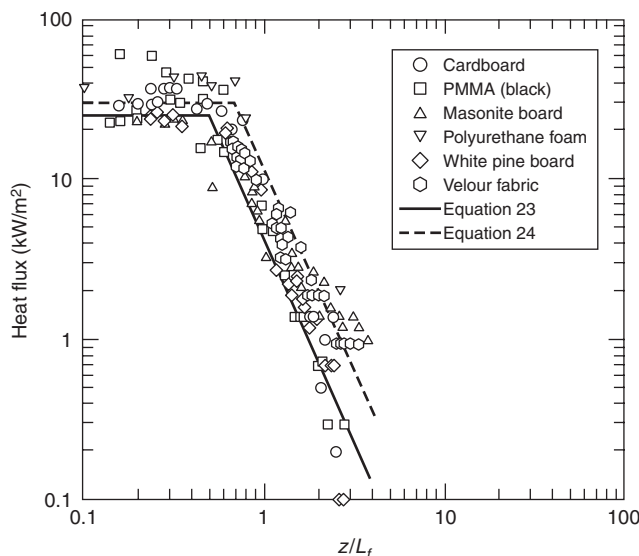


Figure 2-14.28. Heat fluxes for different materials.^{47,48}

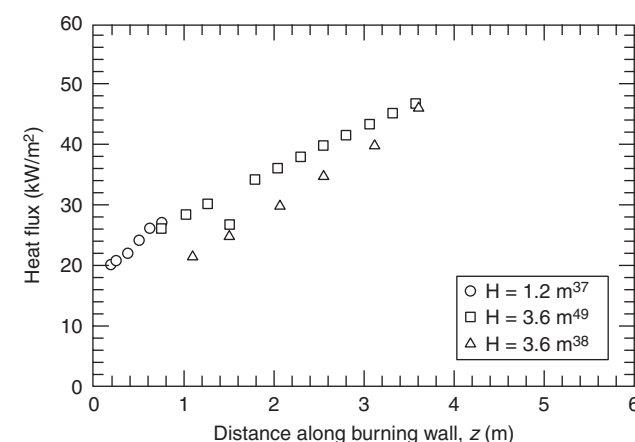


Figure 2-14.29. Heat flux from a PMMA wall flame back to the fuel surface.^{37,38,49}

different than that observed with smaller fires, where heat flux is relatively constant over this region.

Markstein and DeRis⁵⁰ also explored the effects of larger fire size and soot production on the heat flux incident on the burning surface. The apparatus used in the study was 0.38 m wide and 1.98 m high, with the bottom 0.79 m of the wall being a sintered metal gas burner. Heat flux data for methane, ethane, ethylene, and propylene fires were reported. The impact of fire size on the heat flux distribution along the height of the panel is shown in Figure 2-14.30. Similar to the PMMA results, the heat fluxes were measured to increase with height in the test with the higher heat release rate (816 kW/m).

The heat flux from the flame is shown in Figure 2-14.31 to also be a function of fuel smoke production rate. Methane and ethane have low smoke yields (less than 0.013 g/g)⁵¹ and are measured to produce heat fluxes as high as 35–38 kW/m². The smoke yield of ethylene (0.043)⁵¹ is less than that of propylene (0.095), but similar heat fluxes were measured with height along the apparatus. Peak heat fluxes of 59 kW/m² were measured for the largest propylene fire considered in the study.

Heat fluxes were measured in tests on large (2.4-m-high, 0.60-m-wide) plywood walls.⁵² The peak heat fluxes measured in these tests are provided in Table 2-14.1 for various preheat levels. As the heat release rate per unit width increases, the heat flux from the fire to the wall increases. Though heat fluxes are not as high as those measured for a burning PMMA wall, the heat flux is 3–9 kW/m² higher than the 30-kW/m² peak level measured in the smaller-scale tests after the radiant part of the exposure was removed.

Similar experiments were performed by Ohlemiller and Cleary⁵³ on composite panels. The peak heat fluxes measured in this study are provided in Table 2-14.2. Similar to the results of Delichatsios et al.,⁵² heat fluxes were measured to increase with an increase in heat release rate (i.e., increase in external heat flux).

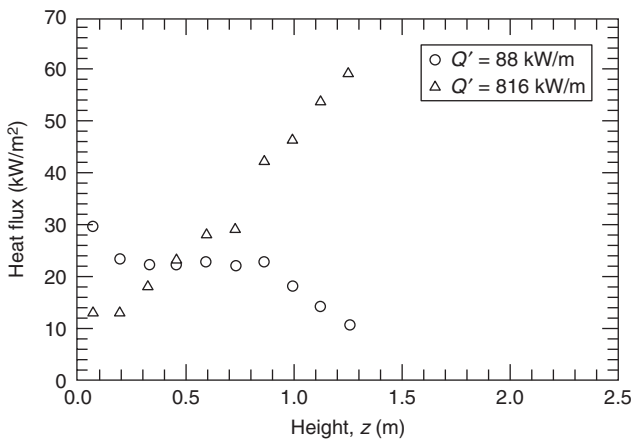


Figure 2-14.30. Heat fluxes along a propylene gas wall fire at different heat release rates per unit width.⁵⁰ Burning wall height was 0.79 m.

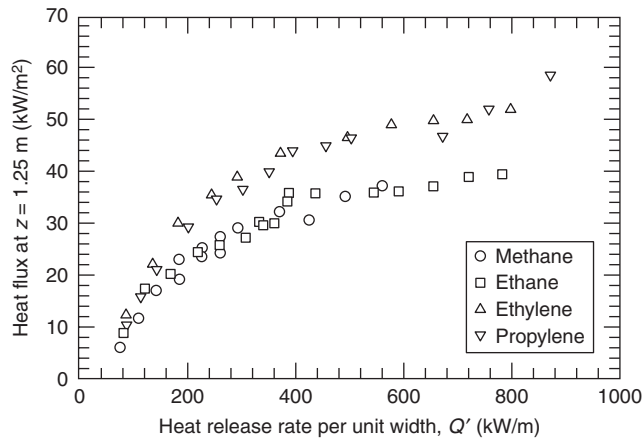


Figure 2-14.31. Heat flux at a height of $z = 1.25$ m for different fire sizes and different fuels.⁵⁰ Burning wall height was 0.79 m.

Data presented in this section demonstrates that both heat release rate and smoke production rate of the fuel can influence the heat flux levels produced by wall flames back onto the burning surface. Larger fires with high smoke production rates can result in heat fluxes to the walls of approximately 60 kW/m². Additional research needs to be performed to better quantify the transition between the smaller-fire experiments and the large-fire results.

Table 2-14.1 Peak Heat Flux from Flames Measured in 2.4 m High, 0.60 m Wide Plywood Wall Experiments⁵² (measurements up to 1.8 m above floor)

Fuel	Radiant Exposure (kW/m ²)	Heat Release Rate per Unit Width Q' (kW/m)	Peak Heat Flux (kW/m ²)
Plywood (finished side exposed)	4.8	175	38
	5.2	197	40
	7	292	45
Plywood (unfinished side exposed)	7.5	217	45
	11	417	50

Table 2-14.2 Heat Fluxes from 1.2 m High, 0.3 m Wide Composite Panel Fires⁵³

Fuel	Radiant Exposure (kW/m ²)	Heat Release Rate per Unit Width Q' (kW/m)	Peak Heat Flux (kW/m ²)
Fire retarded vinyl ester	2.5	N/A	35
	7.5	N/A	48
	11	N/A	52
Polyester	0	N/A	35

Corner Wall Fires

Limited work has been performed to quantify the heat fluxes from burning boundaries in a corner. In general, the heat fluxes produced by burning corner walls are higher than those produced by a wall flame.

Qian et al.^{54,55} measured heat fluxes produced in a corner of burning PMMA walls beneath an incombustible ceiling. In these experiments, a 1.6-m-high corner was lined with 12.7-mm-thick PMMA that was 0.20 m in width. During the tests, the walls were ignited using a torch at the bottom of the corner and were allowed to burn until flames had spread to the top of the walls. The peak heat release rate of the fire was estimated to be 80 kW. Heat fluxes measured during the growing fire are shown in Figure 2-14.32. In the lower half of the flame, heat fluxes were measured to be, on average, 33 kW/m². Above this, heat fluxes were measured to decay similarly to heat fluxes measured for wall fires (see Equations 25 and 26).

A series of experiments were conducted by Hasemi et al.²⁸ using L-shaped, sintered metal burners mounted to the walls of a corner to simulate burning corner walls. Using propane gas as fuel, experiments were conducted using two different burner sizes (0.23 m wide by 0.45 m high, and 0.23 m wide by 0.90 m high) mounted to an open corner of walls with no ceiling. The heat fluxes above the burners in these fires are provided in Figure 2-14.33 for fire heat release rates of 15–60 kW. The line on the plots represents the decay in the heat flux of a wall fire. Peak heat fluxes in the lower part of the flame were measured to range from 28–38 kW/m², and were constant up to approximately half the flame length. Above this, heat fluxes were measured to decay in a manner similar to that determined for burning walls.

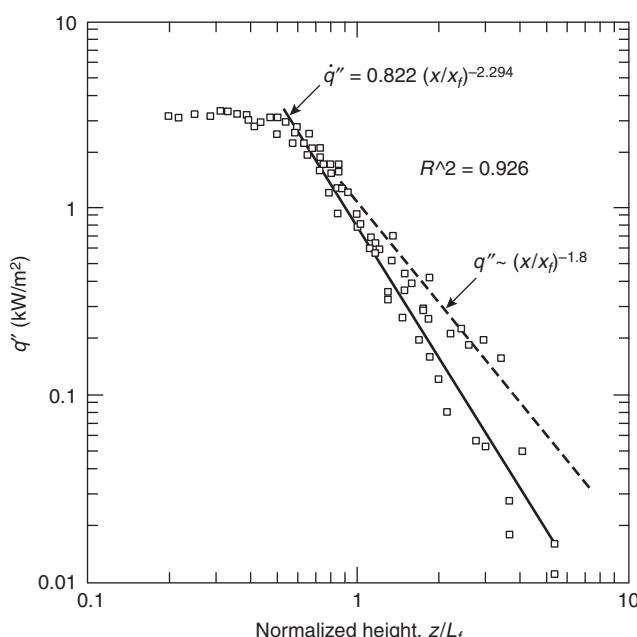


Figure 2-14.32. Heat flux from burning PMMA corner walls (1.6 m high and 0.20 m wide).⁵⁵

Hasemi et al.²⁸ also performed tests in a 1.8-m-high corner with a ceiling. Tests were performed with the top 1.35 m of the corner lined with 0.23-m-wide sintered metal burners and with the top 0.45 m of the corner lined with sintered metal burners. Heat fluxes to the ceiling were measured to be as high as 40 kW/m², while heat fluxes as high as 60 kW/m² were measured along the top of the walls near the ceiling.

Lattimer et al.¹⁰ performed a detailed study using L-shaped propane line burners in the corner. Burners were placed in a 2.4-m-high corner with a ceiling, with all surfaces constructed of noncombustible materials. In this study, heat fluxes were measured for different burner sizes (single side length of 0.17 m, 0.30 m, and 0.50 m) and various heat release rates (50–300 kW).

Similar to the approach used to develop the heat flux correlations for area burners, burning boundary correlations were developed for three regions in the corner: along the height of the walls in the corner, along the top of the walls near the ceiling, and along the ceiling. The region containing the walls in the corner extended from the top of the fire to approximately 1.8 m above the fire. Above 1.8 m was considered to be the region along the top of the wall, or the wall-ceiling interface region.

Heat flux data for these fires was normalized with respect to the flame tip location. The flame tip was the furthest distance at which flaming was visually observed. In cases where the fire impinged and flowed along the ceiling, the flame tip length was taken to be the corner height plus the flame extension along the ceiling. Lattimer et al.¹⁰ developed the following correlation to predict the flame tip of a burning boundary fire:

$$\frac{L_{f,tip}}{d} = 5.9 Q_d^{*1/2} \quad (25)$$

where, dimensionless Q_d^* is

$$Q_d^* = \frac{Q}{\rho_\infty C_p T_\infty \sqrt{g} d^{5/2}} \quad (26)$$

Equations 25 and 26 are similar to those used in predicting flame heights from area burners in a corner except the length scale is d , which is the width of the burning area on the wall or the side of a single L-shaped burner. In the L-shaped line burner tests, d is the length of a single side; however, in a burning corner, d was found to be the average width of the burning on the walls. For fires in a 2.4-m-high corner, the width of the burning 0.90 m above the floor was found to represent the average burning width.¹⁰

The vertical distribution in the maximum heat flux along the walls near the corner is shown in Figure 2-14.34 plotted with the vertical distance normalized with respect to the flame tip. Peak heat fluxes were measured over the initial half of the flame length. Above this, heat fluxes decayed in a fashion similar to that observed for wall fires. The line in the plot represents a fit to the data and are described by the following expressions:

$$q''_{max} = 70 \quad (z/L_f) < 0.5 \quad (27a)$$

$$q''_{max} = 10.0(z/L_f)^{-2.8} \quad (z/L_f) > 0.5 \quad (27b)$$

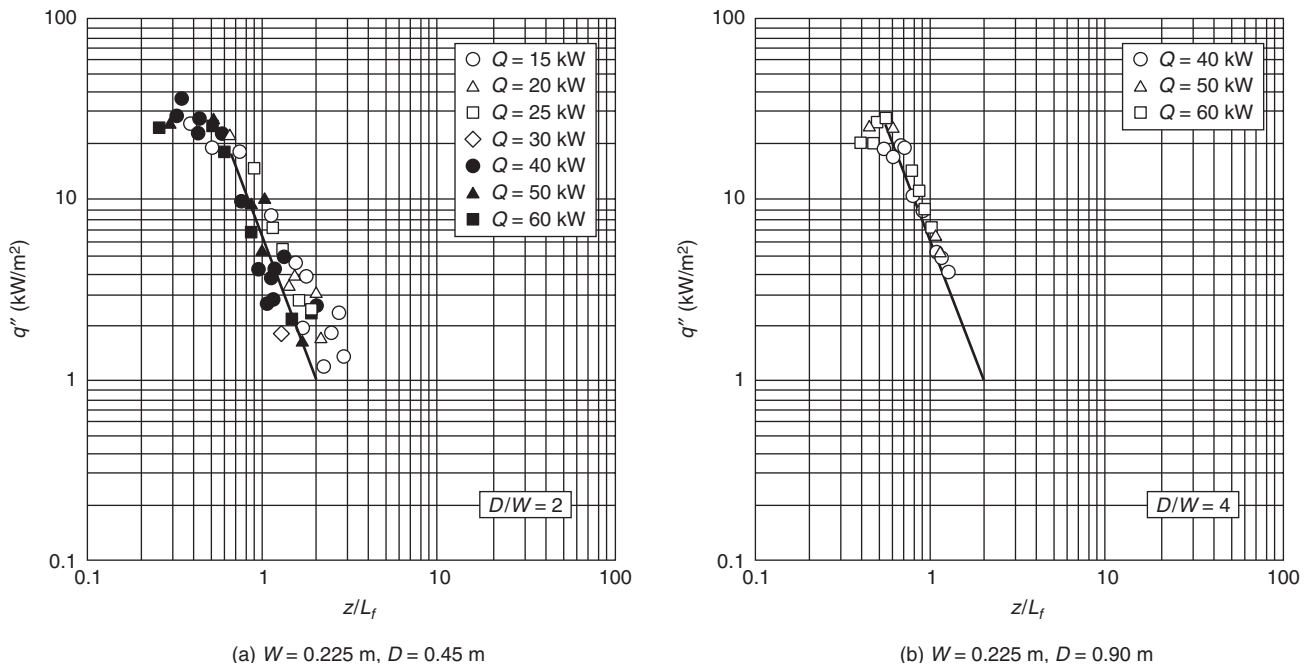


Figure 2-14.33. Heat fluxes to a corner from a simulated burning corner fire using propane as fuel.⁶

Heat fluxes in the decay region ($z/L_f > 0.5$) decrease with dimensionless height raised to the -2.8 power, which is a slightly lower power than the decay for wall fires (-2.5).

Peak heat fluxes in the corner are shown in Figure 2-14.35 to have some dependence on the heat release rate of the fire. The increase in the peak heat flux with increase in fire size was attributed to an increase in radiative pathlength. Assuming the gases to be gray, the following curve fit was developed:

$$q''_{\text{peak}} = 120[1 - \exp(-0.1Q^{1/2})] \quad (28)$$

Based on Equation 28, a more conservative fit to the data in Figure 2-14.34 was developed:

$$q''_{\text{max}} = q''_{\text{peak}} \left(\frac{z}{L_f} \right) \leq 0.5 \quad (29a)$$

$$q''_{\text{max}} = q''_{\text{peak}} - 5 \left(\frac{z}{L_f} - 0.5 \right) (q''_{\text{peak}} - 27) \quad (29b)$$

$$0.5 < \left(\frac{z}{L_f} \right) \leq 0.7 \quad (29b)$$

$$q''_{\text{max}} = 10.0 \left(\frac{z}{L_f} \right)^{-2.8} \quad \left(\frac{z}{L_f} \right) > 0.7 \quad (29c)$$

The maximum heat fluxes along the height of the corner shown in Figures 2-14.34 and 2-14.35 were measured approximately 0.05–0.10 m outside of the corner. Heat fluxes decrease with horizontal distance from the corner. The horizontal heat flux distributions at heights less than 1.8 m below the ceiling are shown in Figure 2-14.36 to be

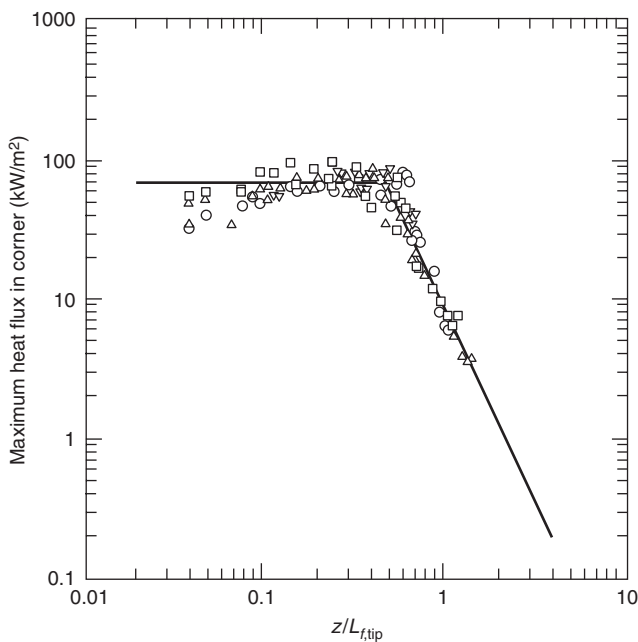


Figure 2-14.34. Heat flux from simulated corner wall fires back to the corner walls at a height less than 1.8 m above the floor. L-shaped line burner with single side lengths of 0.17 m (○), 0.30 m (△), 0.30 m (elevated) (▽), and 0.50 m (□) and fire sizes ranging from 50–300 kW.¹⁰

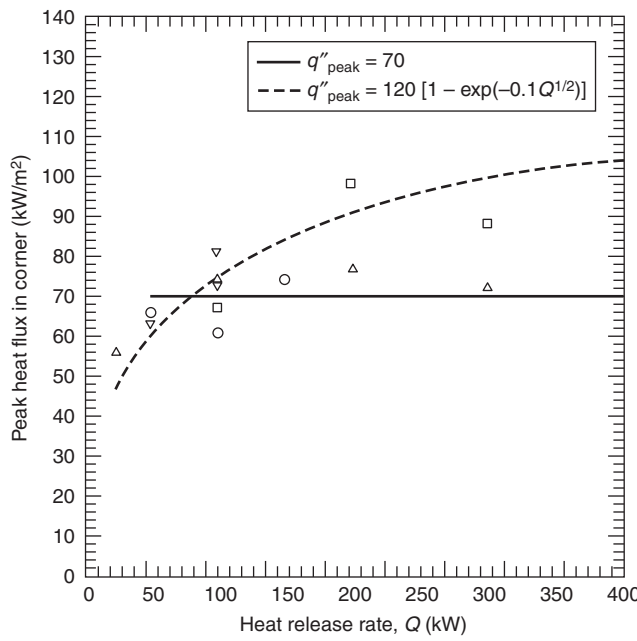


Figure 2-14.35. Peak heat flux to the walls in the corner as a function of wall heat release rate less than 1.8 m above the floor. L-shaped line burner with single side lengths of 0.17 m (\circ), 0.30 m (\triangle), 0.30 m (elevated) (∇), and 0.50 m (\square) and fire sizes ranging from 50–300 kW.¹⁰

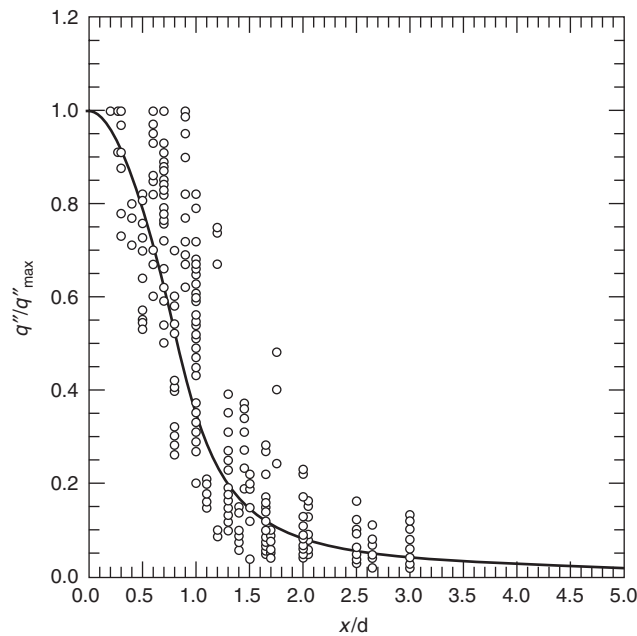


Figure 2-14.36. Horizontal heat flux distribution on the walls out from the corner at a height less than 1.8 m above the floor.¹⁰

half-Gaussian in shape over the flame, but decays slower than predicted by a half-Gaussian curve outside the flaming region. The line in this plot is a fit to the data, which can be represented by the following expressions:

$$\frac{q''}{q''_{\max}} = \exp \left[-1.0 \left(\frac{x}{d} \right)^2 \right] \quad \frac{x}{d} < 1.3 \quad (30a)$$

$$\frac{q''}{q''_{\max}} = 0.30 \left(\frac{x}{d} \right)^{-1.8} \quad \frac{x}{d} \geq 1.3 \quad (30b)$$

Burning boundary beneath a ceiling will form a ceiling jet that will heat the top part of the walls and the ceiling. The maximum heat flux along the top part of the walls is shown in Figure 2-14.37. The line in the plot represents a fit to the data, which can be represented by the following expressions:

$$q''_{\max} = 120 \quad \left(\frac{x+H}{L_{f,tip}} \right) \leq 0.52 \quad (31a)$$

$$q''_{\max} = 13.0 \left(\frac{x+H}{L_{f,tip}} \right)^{-3.5} \quad \left(\frac{x+H}{L_{f,tip}} \right) > 0.52 \quad (31b)$$

The assumed plateau in the correlation is based upon the maximum heat flux expected from a flame in this configuration. This correlation is the same as that determined for area fires in a corner.

The heat flux to the ceiling was correlated to the dimensionless distance away from the burner, $(r+H)/L_{f,tip}$.

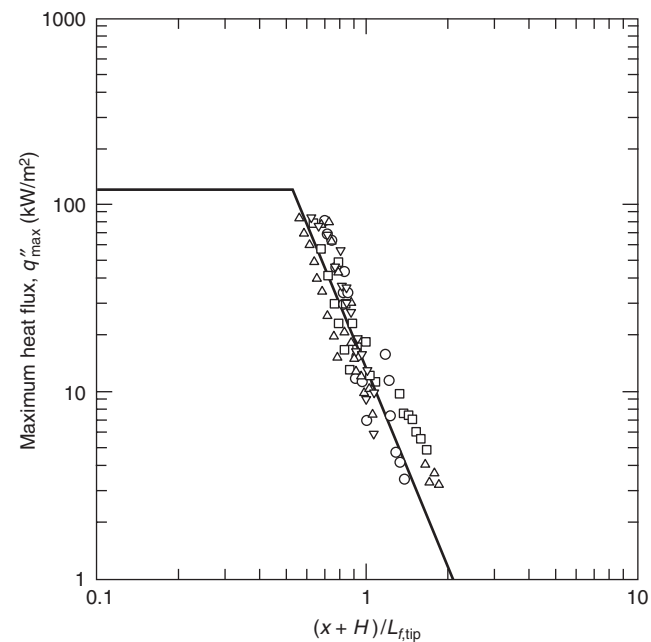


Figure 2-14.37. Maximum heat flux along the top of the walls with a simulated burning boundary fire in the corner. L-shaped line burner with single side lengths of 0.17 m (\circ), 0.30 m (\triangle), 0.30 m (elevated) (∇), and 0.50 m and fire sizes ranging from 50–300 kW (\square).¹⁰

A plot of the heat flux versus this dimensionless parameter is shown in Figure 2-14.38. The line in this plot is a fit to the data, which is represented through the following relations:

$$q'' = 120 \quad \left(\frac{r + H}{L_{f,tip}} \right) \leq 0.52 \quad (32a)$$

$$q'' = 13.0 \left(\frac{r + H}{L_{f,tip}} \right)^{-3.5} \quad \left(\frac{r + H}{L_{f,tip}} \right) > 0.52 \quad (32b)$$

This is the same relation used for the top of the corner walls, except the length scale in the overhead data is r . In addition, this is the same relation determined using the ceiling heat-flux data from tests with an area burner.

Ceiling Fires

Heat fluxes from burning ceilings have been evaluated for both unconfined ceilings and ceilings in a corridor. Due to buoyancy effects, flames from burning ceilings tend to be relatively thin. As a result, peak heat fluxes from burning ceilings range from 20–30 kW/m², which is similar to those measured for small wall fires.

Unconfined ceiling fires: Heat fluxes from unconfined ceiling fires were measured by Hasemi et al.⁵⁶ using different sizes of sintered metal propane gas burners mounted to a 1.8-m square incombustible ceiling. Using two different circular burner sizes ($D = 0.09$ and 0.16 m), heat flux to the ceiling was measured for fire heat release rates of 2.5–38 kW.

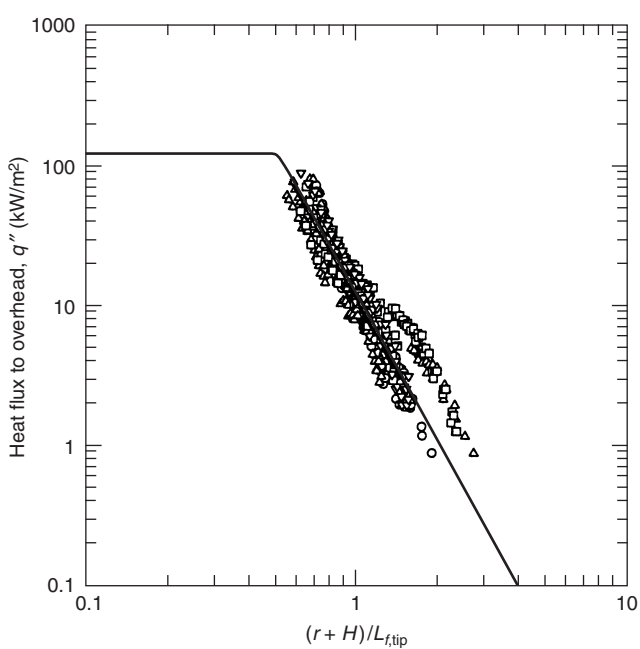


Figure 2-14.38. Heat flux along the ceiling with a simulated burning boundary fire in the corner. L-shaped line burner with single side lengths of 0.17 m (○), 0.30 m (△), 0.30 m (elevated) (▽), and 0.50 m and fire sizes ranging from 50–300 kW (□).¹⁰

The radius of the flame (intermittent) measured using the two burners is shown in Figure 2-14.39 to be slightly dependent on burner size, with the larger burner having a lower radius. However, as the fires become larger, the dependence on burner diameter becomes small. Flame lengths are proportional to the heat release rate raised to the one-half power.

Hasemi et al.⁵⁶ also measured the heat fluxes as a function of distance from the center of the burner. The measured heat fluxes are shown in Figure 2-14.40 to be at peak levels in the first $0.4L_f$ and then decay with distance from the burner. Peak heat fluxes were measured to range from 16–27 kW/m², with the smaller burner producing higher heat fluxes. These peak heat fluxes were similar to those measured for burning ceilings in a corridor (i.e., one-

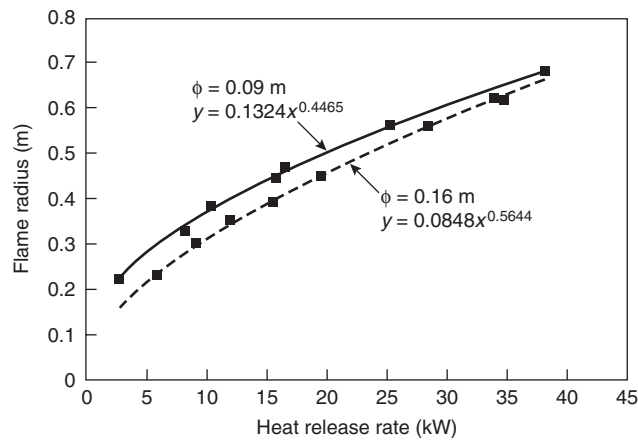


Figure 2-14.39. Flame radius produced by a simulated burning ceiling in an unconfined area.⁵⁶

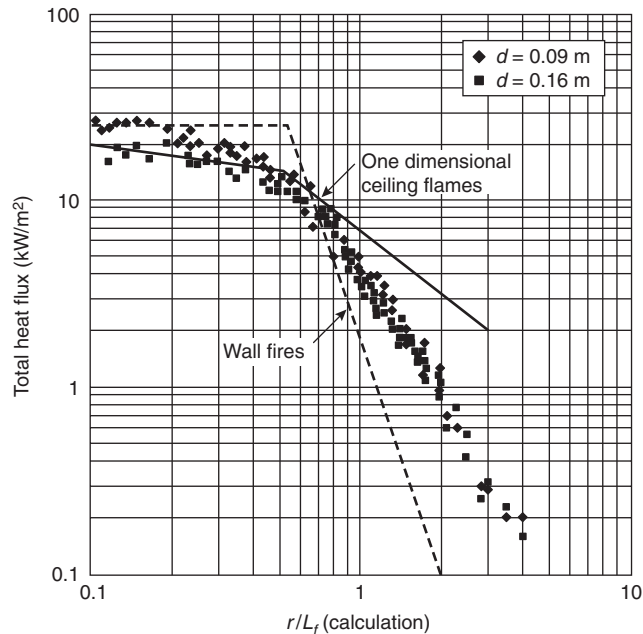


Figure 2-14.40. Heat flux from fires beneath an unconfined ceiling.⁵⁶

dimensional ceiling flames) and for small wall fires. Heat fluxes from the unconfined ceiling fires were measured to decay at a rate between that measured for wall fires and that observed for a burning ceiling in a corridor.

Ceiling fires in a corridor: Heat fluxes from flames produced by burning ceilings in a corridor were investigated by Hasemi et al.²⁸ Tests were performed beneath a 2.73-m-long ceiling with two 0.10-m-high soffits mounted along the length of the ceiling to form a 0.30-m-wide channel. At the closed end of the channel, a 0.30-m-wide, 0.04-m-long porous propane burner was mounted in the ceiling. Heat flux distributions along the corridor were measured for fire heat release rates ranging from 10–50 kW (33–166 kW per meter of corridor width).

The intermittent flame lengths from these fires are seen in Figure 2-14.41 to increase linearly with heat release rate per unit hallway width. A fit to this data produced the following relation to predict flame length due to a burning ceiling in a corridor:

$$L_f = 0.0122Q' \quad (33)$$

The heat fluxes distributions along the center of the corridor are shown in Figure 2-14.42 for the different fires considered in the study. The line in the plot represents a best fit to the methane line burner data of Hasemi.³⁹ Heat fluxes were measured to be constant at approximately 20 kW/m² up to $0.4L_f$. Above this, heat fluxes were measured to decay at a slower rate than that previously measured for wall fires. Heat fluxes along a flame from a burning ceiling in a corridor (not shown in the figure) can be determined using the following expressions:

$$q'' = 20 \quad (x/L_f) \leq 0.4 \quad (34a)$$

$$q'' = 6.36(x/L_f)^{-5/4} \quad (x/L_f) > 0.4 \quad (34b)$$

Burning Parallel Vertical Surfaces

A common configuration encountered when commodities are being stored in rooms or warehouses is par-

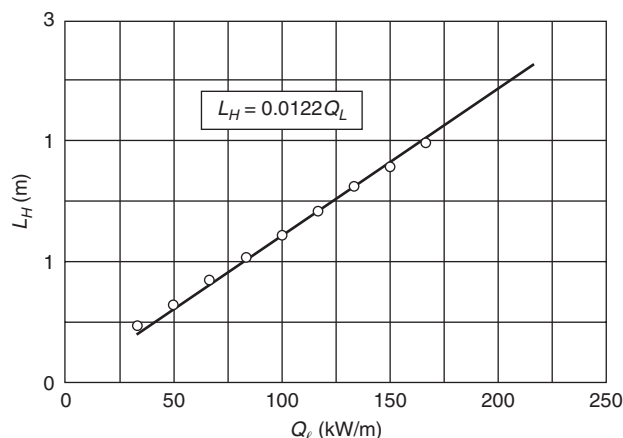


Figure 2-14.41. Flame length produced by a burning ceiling in a corridor.²⁸

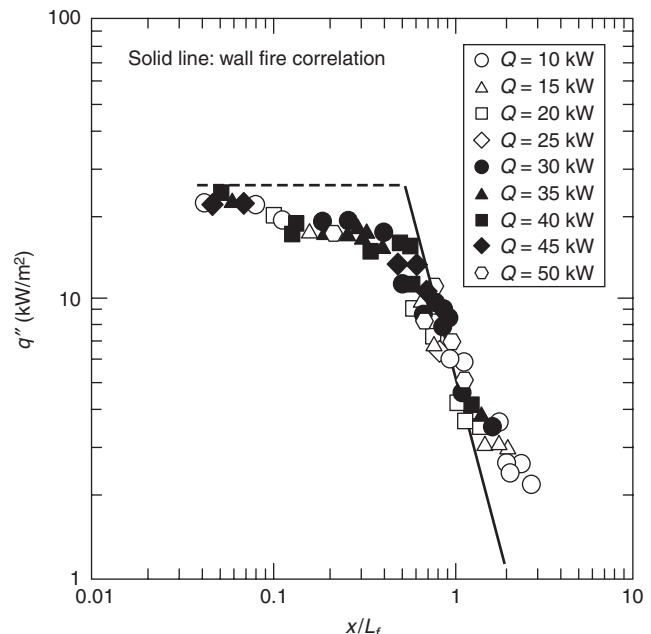


Figure 2-14.42. Heat fluxes to the ceiling of a corridor.²⁸

allel vertical surfaces. As a result, several studies have focused on both experimentally and analytically characterizing this configuration.^{45,57,58} Ingason and DeRis⁵⁹ also performed experiments in a rack storage configuration with a fire between four equally spaced storage towers.

Part of the work by Tamanini^{57,58} investigated the effects of wall spacing on the fuel mass loss rate of combustible parallel vertical walls. Walls were 0.94 m high and 0.460 m wide with the spacing varying from 0.470–0.025 m and no floor at the base of the walls. The average fuel mass loss rate was measured to increase (i.e., the average heat flux to the wall increased) with an increase in spacing until the spacing was less than 0.076 m. At a spacing of 0.038 m or less, the average mass loss rate was less than that measured with no parallel wall. At a spacing of 0.038 m (or wall height divided by spacing of 25 with a fire size of approximately 180 kW), the flames from the two burning surfaces were observed to merge together approximately two-thirds the distance up the walls. Though not evaluated in this study, the presence of a floor may cause the flames to merge together at larger spacings.

Heat fluxes due to a fire between two parallel vertical surfaces were measured by Foley and Drysdale.⁴⁶ The study was performed using two 0.61-m-wide, 0.81-m-high walls separated by a gap of 0.06, 0.10, or 0.14 m. The fire was a 0.60-m-long propane line burner that had either a 11.6-kW/m or a 20.9-kW/m heat release rate per unit length. One of the walls was instrumented with four heat flux gauges that could be moved to measure the heat flux distribution on the walls. Heat fluxes were measured as far as 0.150 m from the centerline of the wall. For the different gap and heat-release rate fires, heat fluxes were measured with the burner against the instrumented wall and with the fire in the center of the gap between the two walls. The effect of air entrainment flow path was also evaluated by performing tests with and without a floor

between the panels. Results were correlated using a/d where the spacing between the walls, a , is divided by the burner length, d , and the dimensionless quantity Q_d^* , as defined in Equation 26, with d being the burner length.

The heat flux distributions measured with the fire against the instrumented wall are shown in Figure 2-14.43. As seen in Figure 2-14.43(a), heat fluxes reached as high as 80 kW/m^2 with an open base (no floor between the walls). Heat fluxes on the panel can be estimated using the following expression:

$$q'' = 67.38 \{z(a/d)^{0.36} / [Q_d^{*2/3} d(y'/d)^{0.38}]\}^{-1.47} \quad (35)$$

where $y' = 0.5d - y$ with y being the horizontal distance from the burner centerline.

With the base of the walls closed (a floor between the walls) and the fire against the instrumented wall, the heat flux data in Figure 2-14.43(b) were seen to be as high as 100 kW/m^2 . Heat fluxes for this case are slightly lower than the open-base case. A similar expression to that in Equation 35 was developed by Foley and Drysdale to predict heat fluxes with the base of the walls closed:

$$q'' = 23.31 \{z(a/d)^{0.905} / [Q_d^{*2/3} d(y'/d)^{2/3}]\}^{-1.2} \quad (36)$$

Heat fluxes were also measured with the fire in the center of the gap between the two walls. In the case with an open base (no floor), the heat fluxes were measured to be 50 percent lower than those measured with the fire against the instrumented wall. As seen in Figure 2-14.44(a), the peak heat flux was measured to be approximately 30 kW/m^2 . This decrease was attributed to the air being drawn up at the base of the walls, preventing the fire from attaching to the instrumented wall. The line in the figure is the best fit to the data, which is given by the following expression:

$$q'' = 22.71 \{z(a/d)^{1.04} / [Q_d^{*2/3} d(y'/d)^{0.806}]\}^{-0.797} \quad (37)$$

The case with the base closed and the fire in the center of the gap resulted in the highest heat fluxes measured in the study. As seen in Figure 2-14.44(b), heat fluxes greater than 100 kW/m^2 were measured in this case. In the tests with the high heat fluxes, the flames were observed to occupy the width of the gap. This behavior was attributed to only allowing air to be entrained into the fire through the sides of the gap. The following expression can be used to estimate the heat flux to the walls for this case:

$$q'' = 23.94 \{z(a/d)^{1.7} / [Q_d^{*2/3} d(y'/d)^{1.34}]\}^{-1.04} \quad (38)$$

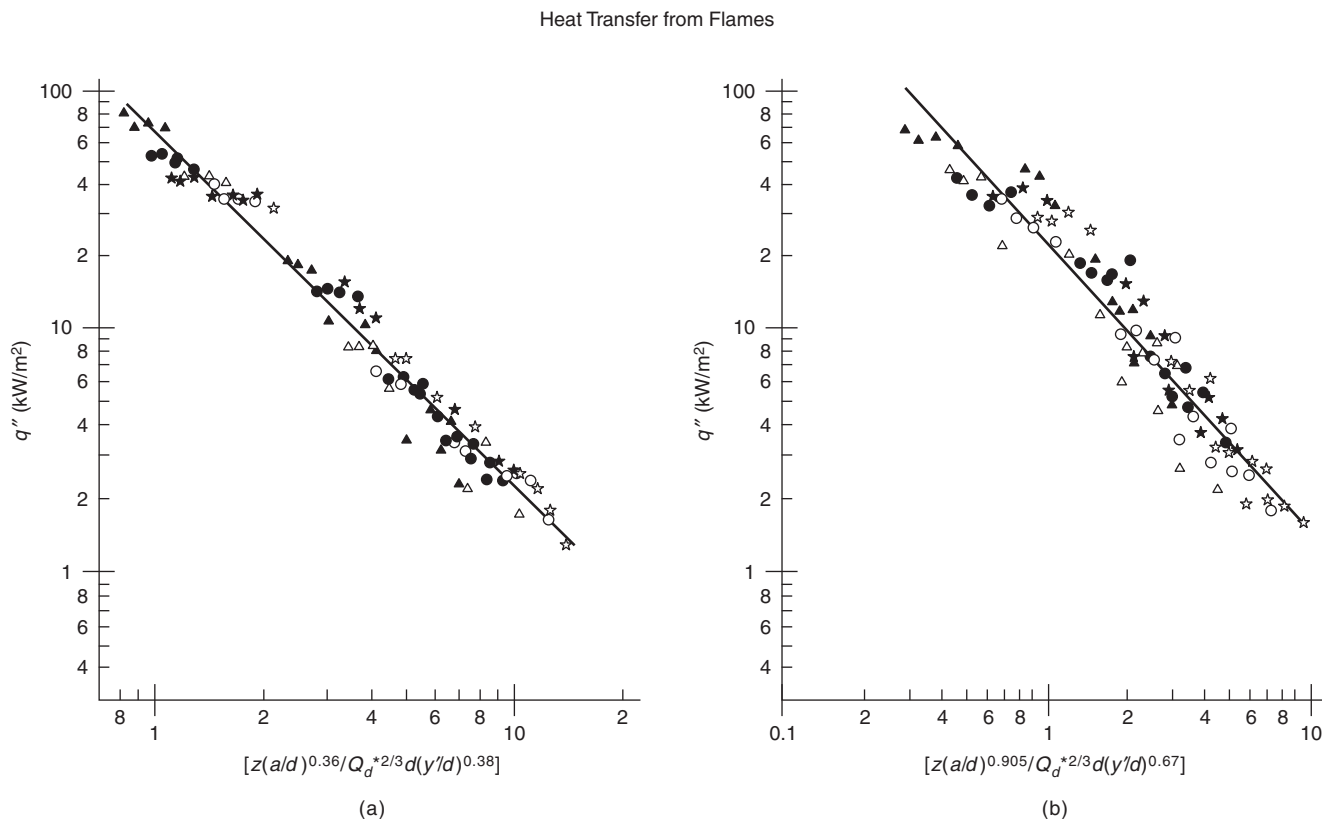


Figure 2-14.43. Heat fluxes measured with the fire against the instrumented wall with (a) an open base (no floor in the gap) and (b) a closed base (a floor in the gap): 0.140-m spacing (\star), 0.10-m spacing (\circ), 0.060-m spacing (\square); open symbols, $Q' = 11.6 \text{ kW/m}$; closed symbols, $Q' = 20.9 \text{ kW/m}$.⁴⁵

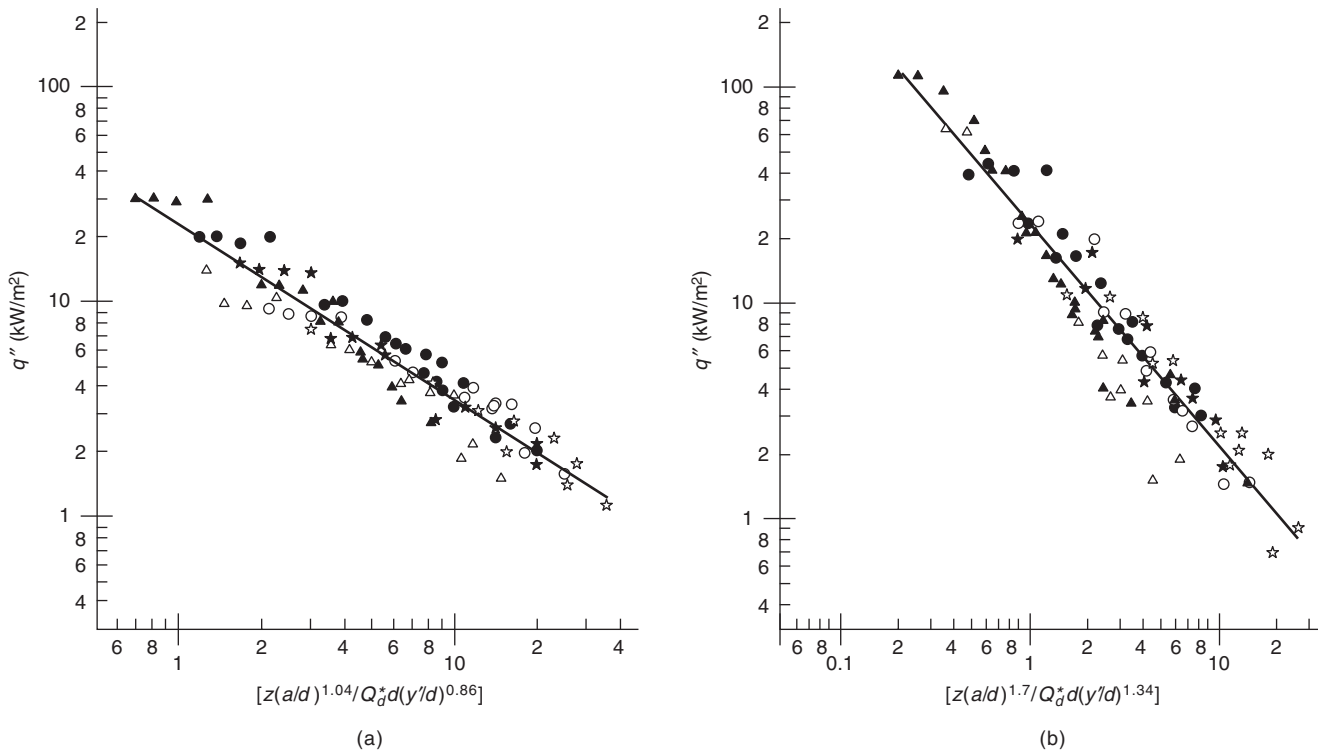


Figure 2-14.44. Heat fluxes measured with the fire in the center of the gap with (a) an open base (no floor in the gap) and (b) a closed base (a floor in the gap): 0.140-m spacing (\star), 0.10-m spacing (\circ), 0.060-m spacing (\triangle); open symbols, $Q' = 11.6 \text{ kW/m}$; closed symbols, $Q' = 20.9 \text{ kW/m}$.⁴⁶

Additional research needs to be performed with this configuration to further validate the results. Larger-scale tests need to be conducted to verify the results of Foley and Drysdale. In addition, the transition from wall fire heat fluxes to gap fire heat fluxes needs to be identified. Heat fluxes produced by area fires between parallel walls also need to be quantified.

Exposure Fires and Burning Walls and Ceilings

A series of tests were performed by Lattimer et al.¹⁰ to investigate the use of steady-state heat flux correlations, developed using burners and noncombustible boundaries, for estimating the heat fluxes in growing fires. Three tests were performed in a 2.4-m-high, 2.0-m-wide open corner lined with a combustible material. A single test was performed on three different lining materials: 12-mm-thick Douglas fir plywood, 12-mm-thick E-glass fire-retarded vinyl ester, and 88-mm-thick sandwich composite (76-mm-thick balsa wood with 6-mm-thick E-glass fire-retarded vinyl ester facings). The initiating fire in the test was a 0.17-m square propane sand burner with a heat release rate of 100 kW for 10 min followed by 300 kW for 10 min, total test time of 20 min. Total heat release during the test was measured by performing oxygen calorimetry on the gases collected in an exhaust hood, and flame

lengths were measured through visual observation. Heat fluxes were measured 0.075 m from the corner along at eight different elevations, 0.15 m below the ceiling along the top of the wall, and along the ceiling on a 45° diagonal out from the corner. Due to mounting the heat flux gauges along the top of the wall too far below the ceiling, no comparison between predicted and measured heat fluxes was done for the region along the top of the wall.

Transient data was averaged every 30 s to generate a reasonable amount of data to compare to the developed correlations. A comparison of the flame length predicted using Equations 7 and 25 and the measured flame length is shown in Figure 2-14.45. The dimensionless length used in this calculation was the width of the burner, D , while the burning had spread laterally less than the width of the burner. When the lateral flame spread 0.9 m above the floor exceeded the burner width, the dimensionless length was taken to be the horizontal flame front location 0.9 m above the floor. The flame front at 0.9 m above the floor was approximately the average flame front on the wall.

Heat fluxes to the walls near the corner are provided in Figure 2-14.46. Measured heat fluxes were slightly higher than values predicted by both the initiating fire correlation and the burning boundary correlation (assuming the heat flux is independent of wall heat release rate). Inspection of the data indicates better agreement between the data and the correlations can be achieved using the initiating fire correlation up to when ignition occurs in the corner. After

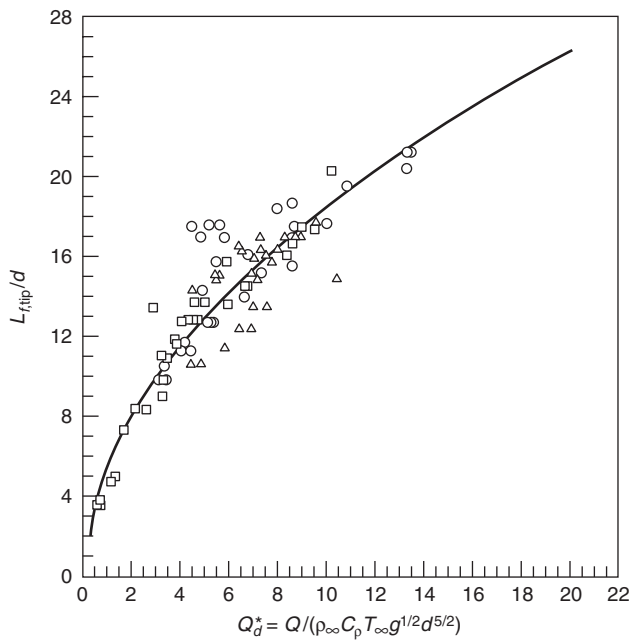


Figure 2-14.45. Flame lengths measured in combustible corner fire tests compared with the flame length correlations developed for initiating and burning boundary fires in Equations 7 and 25: plywood (\square), E-glass FR vinyl ester (\circ), sandwich composite (\triangle).¹⁰

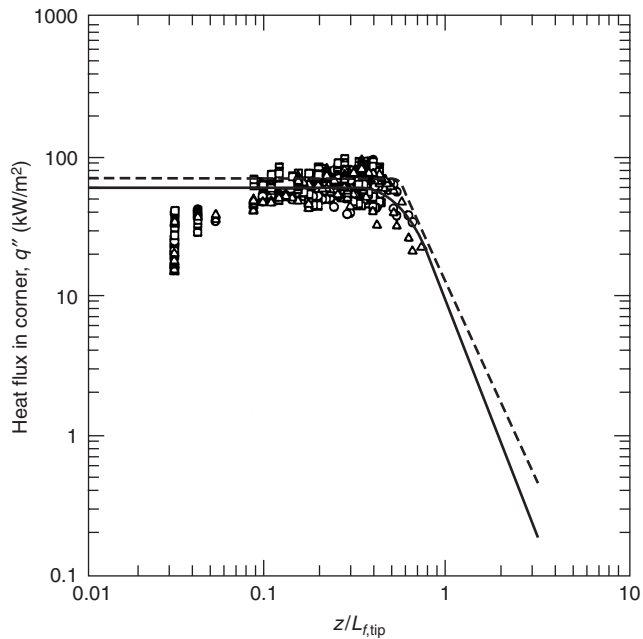


Figure 2-14.46. Heat fluxes along the height of the corner in tests with different combustible boundaries compared with the heat flux predicted using Equation 27 (—) and Equation 9 (---): plywood (\square), E-glass FR vinyl ester (\circ), sandwich composite (\triangle).¹⁰

this, the corner wall heat flux correlations in Equations 28 and 29 can be used to estimate heat fluxes in the corner.

A comparison of the heat fluxes along the ceiling and the heat fluxes predicted using Equation 32 is shown in Figure 2-14.47. In general, heat fluxes are adequately predicted by the correlation, with heat fluxes as high as 130 kW/m² measured during a test. This indicates that Equation 32 can be used to estimate heat fluxes to the ceiling near the corner containing the fire.

Fires from Windows

Fires that have reached flashover conditions typically result in burning outside of the actual burn room. Flames from postflashover fires extending out of a building through a window will buoyantly rise along the exterior of the building. Experiments characterizing the heat fluxes to the wall above the window of a postflashover compartment fire have been performed by Oleszkiewicz,^{60,61} Bullen and Thomas,⁶² and Beitel and Evans.⁶³ In these studies, heat fluxes as high as 200 kW/m² have been measured.

Experiments performed by Oleszkiewicz^{60,61} were conducted using two differently sized full-scale rooms with a wall above the window that extended as much as two stories above the burn room (see Figure 2-14.48). The effects of window size, window aspect ratio, and fire size inside the compartment were evaluated in the study. Heat fluxes from the flames extending outside the burn room for different door sizes and different fire sizes are shown in Figure 2-14.49 and Figure 2-14.50 for propane gas fires.

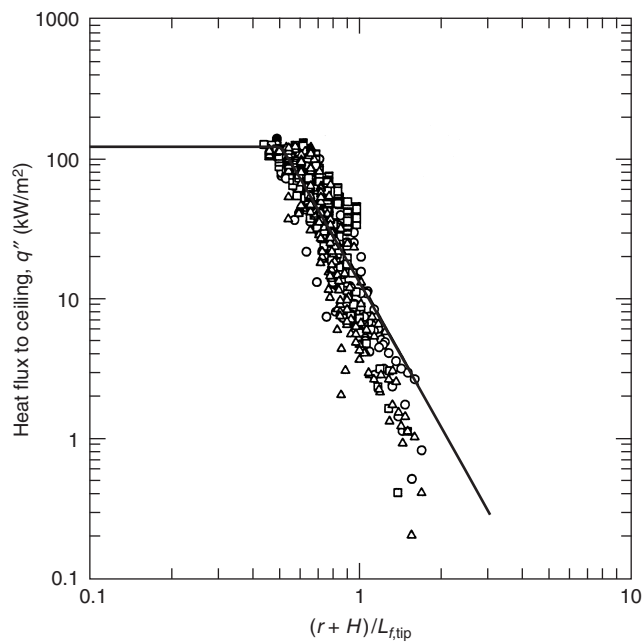


Figure 2-14.47. Heat fluxes to the ceiling during open corner tests with corner lined with a combustible material compared with the heat flux predicted using Equation 32: plywood (\square), E-glass FR vinyl ester (\circ), sandwich composite (\triangle).¹⁰

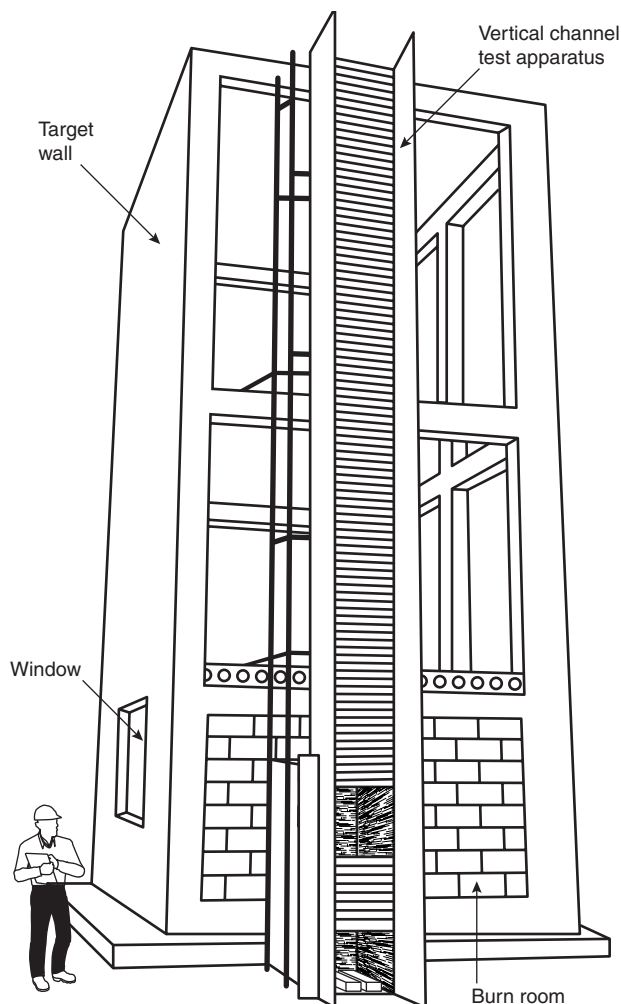


Figure 2-14.48. *Exterior wall fire test facility used by Oleszkiewicz.⁶¹*

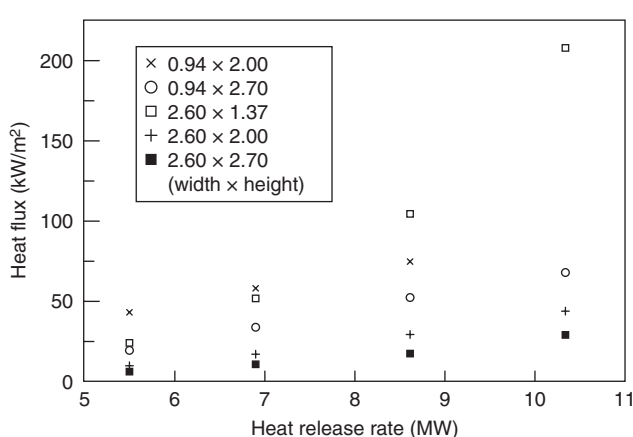


Figure 2-14.49. *Heat fluxes from a window flame 0.5 m above the top of the window for different propane fire sizes inside the compartment.⁶¹*

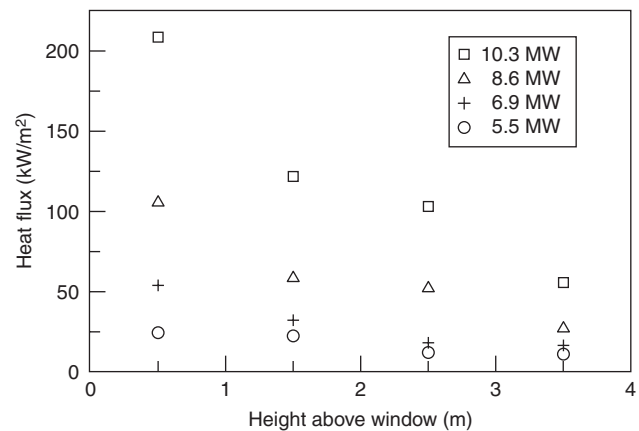


Figure 2-14.50. *Heat fluxes from window flames along the exterior wall above a 2.6-m-wide, 1.37-m-high window.⁶¹*

Note that the heat release rate of the fires stated in Figures 2-14.49 and 2-14.50 is the ideal heat release rate of the compartment fire, which was determined from the gas flow rate and the heat of combustion for propane. Data in Figure 2-14.49 show the effect of fire heat release rate and window size on the heat flux 0.5 m above the window. The distribution in the heat flux along the height of the exterior wall is shown in Figure 2-14.50 for the case with a window 2.6 m wide and 1.37 m high.

Quintiere and Cleary¹³ found that flame lengths for this situation can be estimated using the relation developed by Yokoi.⁶⁴ With L_f being the distance from the bottom of the opening to the average flame height, the heat release rate outside the compartment, Q , and the effective diameter of the window, D , can be used to predict the flame length above the window with the following expression:

$$L_f = 0.0321 \left(\frac{Q}{D} \right)^{2/3} \quad (39a)$$

where

$$D = 2 \sqrt{\frac{H_o W_o}{2\pi}} \quad (39b)$$

Effects of Other Variables

The environment in which a fire is burning can affect the heat flux levels incident on the surface. Studies have been conducted by Atreya and Mekki,⁶⁵ Santo and Tamanini,⁶⁶ Mekki et al.,⁶⁷ and Chao and Fernandez-Pello⁶⁸ to evaluate the impact of oxygen concentration on the heat fluxes transferred by flames to surfaces. In tests with methane fires, Atreya and Mekki⁶⁵ found that flame radiation (and the total heat flux to the surface) was increased by increasing the oxygen concentration.

More important for most problems with fire is the effect of decreasing the oxygen concentration on heat fluxes from the flame. Santo and Tamanini found that decreasing the surrounding oxygen concentration from 20.9 percent to 18.0 percent decreased the radiative flux to an external

target by 40 percent.⁶⁶ This decrease was attributed to a decrease in lower soot concentrations in flames in lower oxygen environments. Chao and Fernandez-Pello⁶⁸ found that this reduction in heat transfer to the surface reduces the flame spread rate along combustible panels.

Nomenclature

a	spacing between parallel walls (m)
C_p	specific heat capacity of air at 300 K [998 kJ/(kg·K)]
d	length of single side on L-shape burner, length of line burner, width of burning area on corner wall (m)
D	length of single side of square burner, diameter (m)
g	acceleration of gravity (9.81 m/s ²)
H	distance between fire and ceiling (m)
H_B	distance between fire and lower flange of I-beam (m)
H_C	distance between fire and upper flange of I-beam (m)
H_o	height of room window (m)
H_{web}	distance between fire and center of web on I-beam (m)
h	convective heat transfer coefficient [kW/(m·K)]
L_B	flame tip length along lower flange of I-beam (m)
L_C	flame tip length along upper flange of I-beam (m)
L_{web}	flame tip length along center of web on I-beam (m)
L_f	average flame length (m)
$L_{f,\text{tip}}$	flame tip length (m)
L_H	flame extension along ceiling away from stagnation point (m)
Q	fire heat release rate (kW)
Q'	fire heat release rate per unit width (kW/m)
Q^*	dimensionless parameter, $Q_D^* = \frac{Q}{\rho_\infty C_p T_\infty \sqrt{g} D^{5/2}}$, with D being length scale
r	distance from corner or stagnation point to measurement location (m)
q''	heat flux (kW/m ²)
T_g	room gas temperature (K)
T_s	material surface temperature (K)
T_∞	ambient temperature (300 K)
W_o	width of room window (m)
w	dimensionless distance along ceiling or I-beam, $w = (r + H_B + z') / (L_B + H_B + z')$
x	horizontal coordinate (m)
y	horizontal coordinate (m)
y'	distance from center of line burner, $y' = 0.5d - y$ (m)
z'	vertical coordinate (m)
z'	virtual source location (m)

Greek

ϵ	material surface emissivity (dimensionless)
ρ_∞	ambient density of air (1.2 kg/m ³)
π	constant (3.14159)
σ	Stefan-Boltzman constant [5.67×10^{-11} kW/(m ² ·K ⁴)]

Subscripts

cl	centerline
conv	convective
d	defined using d as length scale
D	defined using D as length scale
H	defined using H as length scale
B	defined using H_B as length scale
C	defined using H_C as length scale
web	defined using H_{web} as length scale
inc	incident
m	measured
max	max level
net	net
peak	peak
rad	radiative
rr	reradiated

References Cited

1. G. Back, C.L. Beyler, P. DiNenno, and P. Tatem, "Wall Incident Heat Flux Distributions Resulting from an Adjacent Fire," in *Fire Safety Science—Proceedings of the Fourth International Symposium*, International Association of Fire Safety Science, Ottawa, Canada, pp. 241–252 (1994).
2. G. Heskestad, "Luminous Heights of Turbulent Diffusion Flames," *Fire Safety Journal*, 5, pp. 103–108 (1983).
3. D. Gross and J.B. Fang, "The Definition of a Low Intensity Fire," in *NBS Special Publication 361, Volume 1: Performance Concept in Buildings, Proceeding of the Joint RILEM-ASTM-CIB Symposium*, National Bureau of Standards, Washington, DC, pp. 677–686 (1972).
4. T. Mizuno and K. Kawagoe, "Burning Behaviour of Upholstered Chairs, Part 2: Burning Rate of Chairs in Fire Tests," *Fire Science and Technology*, 5, 1, pp. 69–78 (1985).
5. M. Daikoku and K. Saito, "A Study of Thermal Characteristics of Vertical Corner Wall in Room Fire," in *Proceedings of the ASME/JSME Thermal Engineering Joint Conference Book No. H0933C-1995* (L.S. Fletcher and T. Aihara, eds.), Hilton Head, SC, pp. 83–90 (1995).
6. Y. Hasemi, M. Yoshida, S. Takashima, R. Kikuchi, and Y. Yokobayashi, "Flame Length and Flame Heat Transfer Correlations in Corner-Wall and Corner-Wall-Ceiling Configurations," in *Proceedings of INTERFLAM '96*, (Franks and Grayson, eds.), Interscience Communications Ltd., London, pp. 179–188 (1996).
7. M. Kokkala, "Characteristics of a Flame in an Open Corner of Walls," in *Proceedings from INTERFLAM '93*, Interscience Communications Ltd., London, pp. 13–24 (1993).
8. T. Ohlemiller, T. Cleary, and J. Shields, "Effect of Ignition Conditions on Upward Flame Spread on a Composite Material in a Corner Configuration," *Fire Safety Journal*, 31, pp. 331–344 (1998).
9. T.J. Ohlemiller and J.R. Shields, "The Effect of Surface Coatings on Fire Growth over Composite Materials in a Corner Configuration," *Fire Safety Journal*, 32, 2, pp. 173–193 (1999b).
10. B.Y. Lattimer, S.P. Hunt, H. Sorathia, M. Blum, T. Gracik, M. McFarland, A. Lee, and G. Long, "Development of a Model for Predicting Fire Growth in a Combustible Corner," *NSWCCD-TR-64-99/07*, U.S. Navy, West Bethesda, MD (1999).
11. R.B. Williamson, A. Revenaugh, and F.W. Mowrer, "Ignition Sources in Room Fire Tests and Some Implications for Flame

- Spread Evaluation," in *Fire Safety Science—Proceedings of the Third International Symposium*, Elsevier Applied Science, New York, pp. 657–666 (1991).
12. H. Tran and M. Janssens, "Modeling the Burner Source Used in the ASTM Room Fire Test," *Journal of Fire Protection Engineering*, 5, 2, pp. 53–66 (1993).
 13. J.G. Quintiere and T.G. Cleary, "Heat Flux from Flames to Vertical Surfaces," *Fire Technology*, 30, 2, pp. 209–231 (1994).
 14. S.E. Dillon, "Analysis of the ISO 9705 Room/Corner Test: Simulations, Correlations and Heat Flux Measurements," *NIST-GCR-98-756*, U.S. Department of Commerce, National Institute of Standards and Technology, Washington, DC (1998).
 15. International Standards Organization, ISO 9705:1993(E), *International Standard for Fire Tests—Full-Scale Room Test for Surface Products*, International Organization for Standardization (ISO), Geneva, Switzerland (1993).
 16. T. Tanaka, I. Nakaya, and M. Yoshida, "Full Scale Experiments for Determining the Burning Conditions to Be Applied to Toxicity Tests," *Fire Safety Science—Proceedings of the First International Symposium*, Hemisphere Publishing, Gaithersburg, MD, pp. 129–138 (1986).
 17. W. Takashi et al., "Flame and Plume Behavior in and Near a Corner of Walls," in *Fire Safety Science—Proceeding of the Fifth International Symposium* (Y. Hasemi, ed.), International Association for Fire Safety Science, Melbourne, Australia, pp. 261–271 (1997).
 18. Y. Hasemi, S. Yokobayashi, T. Wakamatsu, and A. Ptchelintsev, "Fire Safety of Building Components Exposed to a Localized Fire—Scope and Experiments on Ceiling/Beam System Exposed to a Localized Fire," in *Proceedings from ASIAFLAM*, Kowloon, Hong Kong, pp. 351–361 (1995).
 19. R.L. Alpert, "Convective Heat Transfer in the Impingement Region of a Buoyant Plume," *Transactions of ASME*, 109, pp. 120–124 (1987).
 20. H.Z. You and G.M. Faeth, "Ceiling Heat Transfer during Fire Plume and Fire Impingement," *Fire and Materials*, 3, 3, pp. 140–147 (1979).
 21. H.Z. You and G.M. Faeth, "An Investigation of Fire Impingement on a Horizontal Ceiling," *NBS-GCR-79-188*, U.S. Department of Commerce, Washington, DC (1979).
 22. H.Z. You, "An Investigation of Fire-Plume Impingement on a Horizontal Ceiling 2—Impingement and Ceiling-Jet Regions," *Fire and Materials*, 9, 1, pp. 46–56 (1985).
 23. M. Kokkala, "Heat Transfer to and Ignition of Ceiling by an Impinging Diffusion Flame," *VTT Research Report 586*, Technical Research Centre of Finland, Espoo, Finland (1989).
 24. M. Kokkala, "Experimental Study of Heat Transfer to Ceiling from an Impinging Diffusion Flame," *Fire Safety Science—Proceedings of the Third International Symposium*, Elsevier Applied Science, New York, pp. 261–270 (1991).
 25. L.Y. Cooper, "Heat Transfer from a Buoyant Plume to an Unconfined Ceiling," *ASME Journal of Heat Transfer*, 104, pp. 446–452 (1982).
 26. T. Wakamatsu, personal communication (September, 1999).
 27. H.Z. You and G.M. Faeth, "An Investigation of Fire Impingement on a Horizontal Ceiling," *NBS-GCR-79-188*, U.S. Department of Commerce, Washington, DC (1979).
 28. Y. Hasemi, M. Yoshida, Y. Yokobayashi, and T. Wakamatsu, "Flame Heat Transfer and Concurrent Flame Spread in a Ceiling Fire," in *Fire Safety Science—Proceedings from the Fifth International Symposium* (Y. Hasemi, ed.), International Association for Fire Safety Science, Melbourne, Australia, pp. 379–390 (1997).
 29. P.L. Hinkley, H.G.H. Wraight, and C.R. Theobald, "The Contribution of Flames under Ceilings to Fire Spread in Compartments," *Fire Safety Journal*, 7, pp. 227–242 (1984).
 30. P.L. Hinkley, H.G.H. Wraight, and C.R. Theobald, "The Contribution of Flames under Ceilings to Fire Spread in Compartments, Part I: Incombustible Ceilings," *Fire Research Note No. 712*, Fire Research Stations, Borehamwood, Herts, UK (1968).
 31. P.L. Hinkley, H.G.H. Wraight, and C.R. Theobald, "The Contribution of Flames under Ceilings to Fire Spread in Compartments, Part II: Combustible Ceiling Linings," *Fire Research Note No. 743*, Fire Research Stations, Borehamwood, Herts, UK (1969).
 32. T. Wakamatsu, Y. Hasemi, Y. Yokobayashi, and A.V. Ptchelintsev, "Experimental Study on the Heating Mechanism of a Steel Beam under Ceiling Exposed to a Localized Fire," in *Proceedings from INTERFLAM '96* (Franks and Grayson, eds.), Interscience Communications Ltd., London, pp. 509–518 (1996).
 33. J. Myllymaki and M. Kokkala, "Thermal Exposure to a High Welded I-Beam above a Pool Fire," *First International Workshop on Structures in Fires*, Copenhagen, pp. 211–226 (2000).
 34. T. Ahmad and G.M. Faeth, "Fire Induced Plumes along a Vertical Wall, Part III: The Turbulent Combusting Plume," *NBS Report for Grant No. 5-9020*, U.S. Department of Commerce, Washington, DC (1978).
 35. T. Ahmad and G.M. Faeth, "Turbulent Wall Fires," in *17th Symposium (International) on Combustion*, Combustion Institute, Pittsburgh, PA, pp. 1149–1160 (1979).
 36. J.G. Quintiere, M. Harkelroad, and Y. Hasemi, "Wall Flames and Implications for Upward Flame Spread," *AIAA-85-0456*, American Institute of Aeronautics and Astronautics, Reno, NV (1985).
 37. L. Orloff, J. De Ris, and G.H. Markstein, "Upward Turbulent Fire Spread and Burning of Fuel Surface," in *15th Symposium (International) on Combustion*, Combustion Institute, Pittsburgh, PA, pp. 183–192 (1975).
 38. M.A. Delcatsios, "Flame Heights in Turbulent Wall Fires with Significant Flame Radiation," *Combustion Science and Technology*, 39, pp. 195–214 (1984).
 39. Y. Hasemi, "Experimental Wall Flame Heat Transfer Correlations for the Analysis of Upward Wall Flame Spread," *Fire Science and Technology*, 4, 2, pp. 75–90 (1984).
 40. H. Mitler, "Predicting the Spread Rates on Vertical Surfaces," in *23rd Symposium (International) on Combustion*, Combustion Institute, Pittsburgh, PA, pp. 1715–1721 (1990).
 41. C.L. Beyler, S.P. Hunt, N. Iqbal, and F.W. Williams, "A Computer Model of Upward Flame Spread on Vertical Surfaces," in *Fire Safety Science—Proceedings of the Fifth International Symposium* (Y. Hasemi, ed.), International Association for Fire Safety Science, Melbourne, Australia, pp. 297–308 (1997).
 42. F.W. Williams, C.L. Beyler, S.P. Hunt, and N. Iqbal, "Upward Flame Spread on Vertical Surfaces," *NRL/MR/6180-97-7908*, Navy Technology for Safety and Survivability, Chemistry Division (1997).
 43. Y. Hasemi, "Thermal Modeling of Upward Wall Flame Spread," in *Fire Safety Science—Proceedings of the First International Symposium*, Hemisphere Publishing, Gaithersburg, MD, pp. 87–96 (1986).
 44. Y. Hasemi, "Deterministic Properties of Turbulent Flames and Implications on Fire Growth," *INTERFLAM '88*, John Wiley and Sons, Cambridge, UK, pp. 45–52 (1988).
 45. M. Foley and D.D. Drysdale, "Heat Transfer from Flames between Vertical Parallel Walls," *Fire Safety Journal*, 24, pp. 53–73 (1995).
 46. M. Kokkala, D. Baroudi, and W.J. Parker, "Upward Flame Spread on Wooden Surface Products: Experiments and Numerical Modelling," in *Fire Safety Science—Proceedings of the*

- Fifth International Symposium*, International Association for Fire Safety Science, Melbourne, Australia, pp. 300–320 (1997).
- 47. A.K. Kulkarni, C.I. Kim, and C.H. Kuo, "Heat Flux, Mass Loss Rate and Upward Flame Spread for Burning Vertical Walls," *NIST-GCR-90-584*, U.S. Department of Commerce, Washington, DC 1990.
 - 48. A.K. Kulkarni, C.I. Kim, and C.H. Kuo, "Turbulent Upward Flame Spread for Burning Vertical Walls Made of Finite Thickness," *NIST-GCR-91-597*, U.S. Department of Commerce, Washington, DC (1991).
 - 49. L. Orloff, A.T. Modak, and R.L. Alpert, "Burning of Large-Scale Vertical Surfaces," in *16th Symposium (International) on Combustion*, Combustion Institute, Pittsburgh, PA, pp. 1345–1354 (1977).
 - 50. G.H. Markstein and J. DeRis, "Wall-Fire Radiant Emission, Part 2: Radiation and Heat Transfer from Porous-Metal Wall Burner Flames," in *24th Symposium (International) on Combustion*, Combustion Institute, Pittsburgh, PA, pp. 1747–1752 (1992).
 - 51. Tewarson, "Generation of Heat and Chemical Compounds in Fires," Section 3/Chapter 4, The SFPE Handbook of Fire Protection Engineering, 2nd ed. (P.J.D. Nenno, ed.), NFPA, Quincy, MA, pp. 3-53–3-124 (1995).
 - 52. M.M. Delichatsios, P. Wu, M.A. Delichatsios, G.D. Lougheed, G.P. Crampton, C. Qian, H. Ishida, and K. Saito, "Effect of External Radiant Heat Flux on Upward Flame Spread: Measurements on Plywood and Numerical Predictions," *Fire Safety Science—Proceedings of the Fourth International Symposium*, International Association of Fire Safety Science, pp. 421–432 (1994).
 - 53. T.J. Ohlemiller and T.G. Cleary, "Upward Flame Spread on Composite Materials," *Fire Safety Journal*, 32, pp. 159–172 (1999).
 - 54. C. Qian, H. Ishida, and K. Saito, "Upward Flame Spread along PMMA Vertical Corner Walls, Part II: Mechanism of M Shape Pyrolysis Front Formation," *Combustion and Flame*, 99, pp. 331–338 (1994a).
 - 55. C. Qian and K. Saito, "An Empirical Model for Upward Flame Spread over Vertical Flat and Corner Walls," in *Fire Safety Science—Proceedings from the Fifth International Symposium* (Hasemi, ed.), Melbourne, Australia, pp. 285–296 (1997).
 - 56. Y. Hasemi, M. Yoshida, and R. Takaike, "Flame Length and Flame Heat Transfer Correlations in Ceiling Fires," poster at *Fire Safety Science Sixth International Symposium*, International Association for Fire Safety, Poitiers, France (1999).
 - 57. F. Tamanini, "Calculations and Experiments on the Turbulent Burning of Vertical Walls in Single and Parallel Configurations," *FMRC J. I> OAOE7.BU-2*, FMRC Technical Report, Factory Mutual Research Corporation, Norwood, MA, (1979).
 - 58. F. Tamanini and A.N. Moussa, "Experiments on the Turbulent Burning of Vertical Parallel Walls," *Combustion Science and Technology*, 23, pp. 143–151 (1980).
 - 59. H. Ingason and J. De Ris, "Flame Heat Transfer in Storage Geometries," *Fire Safety Journal*, 31, pp. 39–60 (1998).
 - 60. I. Oleszkiewicz, "Heat Transfer from a Window Fire Plume to a Building Façade," *ASME HTD*, 23, pp. 163–170 (1989).
 - 61. I. Oleszkiewicz, "Fire Exposure to Exterior Walls and Flame Spread on Combustible Cladding," *Fire Technology*, 26, 4, pp. 357–375 (1990).
 - 62. P.H. Thomas and M.L. Bullen, "Compartment Fires with Non-Cellulosic Fuels," in *17th Symposium (International) on Combustion*, Combustion Institute, Pittsburgh, PA, pp. 1139–1148 (1979).
 - 63. J.J. Beitel and W.R. Evans, "Multi-Story Fire Evaluation Program," *SwRI Project 01-6112*, Final Report, Volume 1, Southwest Research Institute, San Antonio, TX, and Society of the Plastics Industry, Inc., New York (1980).
 - 64. S. Yokoi, "Study on the Prevention of Fire Spread Caused by Hot Upward Current," *Report No. 34* Building Research Institute, Tokyo, Japan (1960).
 - 65. A. Atreya and K. Mekki, "Heat Transfer during Wind-Aided Flame Spread on a Ceiling Mounted Sample," in *24th Symposium (International) on Combustion*, Combustion Institute, Pittsburgh, PA, pp. 1677–1684 (1992).
 - 66. G. Santo and F. Tamanini, "Influence of Oxygen Depletion on the Radiative Properties of PMMA Flames," in *18th Symposium (International) on Combustion*, Combustion Institute, Pittsburgh, PA, pp. 619–631 (1981).
 - 67. K. Mekki, A. Atreya, S. Agrawal, and I. Wichman, "Wind-Aided Flame Spread over Charring and Non-Charring Solids: An Experimental Investigation," in *23rd Symposium (International) on Combustion*, Combustion Institute, Pittsburgh, PA, pp. 1701–1707 (1990).
 - 68. Y.H. Chao and A.C. Fernandez-Pello, "Flame Spread in a Viscous Concurrent Flow," *Heat Transfer in Fire and Combustion Systems*, *ASME HTD*, 199, pp. 135–142 (1992).

SECTION TWO

CHAPTER 15

Liquid Fuel Fires

D. T. Gottuk and D. A. White

Introduction

Liquid fuel spill and pool fires represent potential hazards in many applications ranging from accidents at industrial plants, using combustible liquids, to arson fires with flammable fuels. A pool is characterized by a confined body of fuel that typically has a depth greater than 1 cm. A pool can result due to a liquid fuel release that collects in a low spot, such as a trench, or can exist as a result of normal storage of fuels in tanks and containers. A fuel spill is generally associated with thin fuel layers resulting from an unconfined release of fuel. The nature of a spill fire is highly variable, depending on the source of the release, surface features of the substrate (e.g., concrete, ground, water) on which the fuel is released, and the point and time of ignition. The ability to characterize fuel spills and the resulting fires in a consistent and conservative manner is required for many engineering analyses. This chapter provides an overview of the most relevant factors and methodology for evaluating a liquid fuel spill or pool fire in terms of fire growth and size.

The chapter is organized in three major sections corresponding to the three primary steps of evaluating the development of a liquid fuel spill or pool fire: (1) Spill or Pool Size, (2) Fire Growth, and (3) Fire Size. The first section deals with the process of estimating the physical size of any given fuel release or pool of fuel. Both static (fixed quantity of liquid) and continuously flowing spill fires have been considered. Once a liquid fuel spill or pool has occurred, ignition of the fuel will lead to a transient fire growth period. This transient period of a liquid fuel fire is

dictated by the flame spread rate across the surface of the liquid. The second section of the chapter addresses the assessment of fire growth rate by providing an overview of flame spread on liquid fuels. The third section discusses the available data and correlations that can be used to evaluate the size of the fire in terms of heat-release rate and flame height.

The heat release rate of a fire is the primary parameter used in determining the impact of a fire on its surroundings. The impact of a fire is dealt with in other chapters of this handbook. The heat transfer from liquid fuel spill or pool fires is addressed by Beyler.¹

Spill or Pool Size

The first step in analyzing a liquid fuel fire is to characterize the physical dimensions of the fuel spill or pool. The area of the initial body of fuel will correlate to the size of the resulting fire. A confined fuel release or existing open container of fuel will result in a pool fire of a known area. A pool fire represents a body of fuel that is confined by physical boundaries. In other words, the walls of a room or obstructions on a floor will limit a fuel release to a smaller area than the potential unconfined spill area. In almost all cases, a confined fuel release will create a pool that has a greater depth than the depth of an unconfined spill. When fuel is released onto a surface, it will spread laterally based on several factors, including the initial momentum of the fluid, the fluid surface tension, and the features of the substrate onto which it spilled. Some substrate features that need to be considered are porosity of material and surface roughness. Porous materials, such as sand or even some floor coverings like carpet, can result in different spill sizes and different fuel burning rates.

In general, fuel spills can be characterized as either continuously flowing or instantaneous (static). These characterizations are considered with respect to when the spill is ignited. In the case of a continuously flowing spill, ignition has occurred while the fuel is moving away from

Dr. D. T. Gottuk is a senior engineer at Hughes Associates, Inc. He has a Ph.D. in mechanical engineering from Virginia Polytechnic Institute. His research interests lie in fire dynamics and fire detection. D. A. White, P.E., is a senior engineer at the fire science and engineering firm of Hughes Associates, Inc. He has been actively involved in fire hazard analyses for special situations as well as performance-based engineering projects for high-tech industrial facilities.

the source. For a static spill, the fuel nominally spreads to a maximum area and then is ignited, such that the flame spreads across the fuel surface. For a continuously flowing spill fire, the flame may spread across the fuel surface initially, but the flame front is ultimately controlled by the spread of the fuel over the substrate until steady-state burning conditions occur.

The spill area of a continuously flowing spill that is not burning will continue to increase until a physical boundary is reached. A continuous spill that is burning will have a steady-state spill size based on a balance between the volumetric flow rate and the volumetric burning rate of the fuel. This concept is developed later in the section Fire Size.

For a confined pool, the area, A , is dictated by the boundaries, and the pool depth, δ , can be simply calculated based on the volume, V , of liquid:

$$\delta = \frac{V}{A} \quad (1)$$

For an unconfined spill, the area has typically been determined via Equation 1 with an estimate of the fuel depth. There has been little compiled data for establishing appropriate fuel depths or spill areas of various fuels on solid substrates. In the past, engineers have conservatively estimated spill depths based on the minimum depth required to support flame spread (see Fire Growth Rate section). The use of a minimum depth will result in the largest possible spill area that can support a flame, therefore, the largest possible fire.

Literature results along with recently conducted tests provide a basis for estimating spill depths. Figure 2-15.1 shows a plot of spill depths for both noncombustible liquids and combustible fuel spill fires as a function of the amount of liquid released on an unconfined surface. Table 2-15.1 summarizes the details of the data in Figure 2-15.1, with other notable references. The figure shows that JP-8 and JP-4 spill fires occurred with initial spill depths as low as 0.7 mm and 1.0 mm, respectively. It is also interesting to note that both Chambers² and Gottuk et al.³ observed increases in burning fuel spill areas after the liquid spill was ignited. Fires increased the initial fuel spill area by 22 to 89 percent for fuel releases ranging from 2 to 190 l. This increase in area corresponds to a similar decrease in fuel depth, below those reported in Figure 2-15.1. The practical implication of this increase in spill area is that the fires may be substantially larger than would be predicted per the initial fuel spill areas based on Figure 2-15.1. However, the larger area would also result in much shorter burning times before the fuel is consumed. When it is necessary to determine the maximum fire size of an unconfined spill, it is suggested (based on the limited data available) that the area of the fire, A , be equivalent to approximately 155 percent of the initial spill area:

$$A = 1.55A_s \quad (2)$$

The data in Figure 2-15.1 for water and AFFF were obtained by Gottuk et al.³ for unconfined spill experiments in order to provide bounding data for estimating fuel spill depths and areas. The surface tensions of water

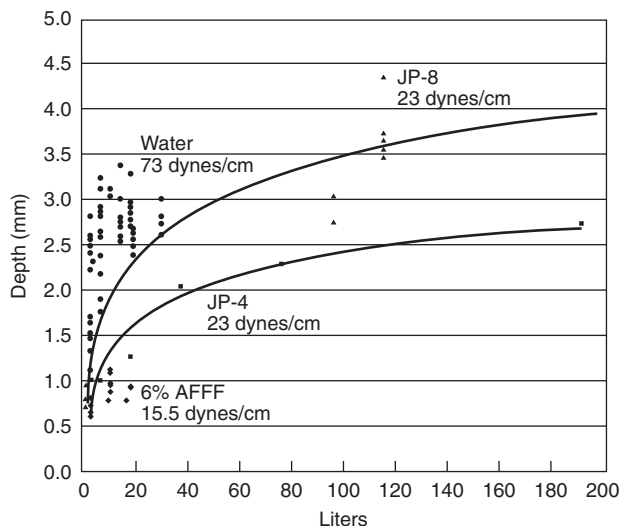


Figure 2-15.1. Liquid spill depths as a function of the amount of liquid released. The lines represent curve fits to the JP-8 and JP-4 data.

and 6 percent AFFF solution bound those of most fuels; water has a surface tension of 73 dynes/cm and the AFFF has a value of approximately 15 to 16 dynes/cm at temperatures of 15 to 32°C.⁴ As can be seen in Figure 2-15.2, the surface tension of different fuels from 10°C to 50°C ranges from 16 to 27 dynes/cm. Though surface tension is not the sole variable dictating spill area, the data in Figure 2-15.1 shows that spill depths for water and solutions of 6 percent AFFF appear to provide bounding values for the available fuel spill fires.

The data of Figure 2-15.1 is presented in an alternate form in Figure 2-15.3, which shows the spill area per unit volume of liquid as a function of the amount of liquid released. Similar to Figure 2-15.1, the data shows quite a bit of variability [0.3 to 1.6 m²/l (12 to 65 ft²/gal)] for small quantities of fluid, particularly ≤ 7.6 l (2 gal). However, with increasing quantities of fluid, the spill area per volume appears to approach a common minimum value of approximately 0.3 m²/l (12 ft²/gal). This minimum value corresponds to the spill depths in Figure 2-15.1 of approximately 2.8 to 4 mm for fuel releases of 95 l (25 gal) or more.

The larger variability of spill depths for releases of ~ 8 l or less is attributed to the greater dependency on multiple variables, such as the initial spill height, surface features, and fluid properties. Though not fully understood, some of these factors are not as prevalent when larger quantities of liquid are spilled. An example of the variability in spill depths is shown in Figure 2-15.4, which presents the same 6 percent AFFF solution and water data of Figure 2-15.1 on an enlarged scale plot. For the water, depths varied for releases at different heights and of different quantities. However, this effect was not observed for releases of the 6 percent AFFF solution. Figure 2-15.4 also shows that similar water spills on vinyl tile floor produced the same spill depths as released on smooth concrete. Modak⁵ reported that for very small spills of various oils (see Table 2-15.1) on steel and epoxy-coated

Table 2-15.1 Summary of Fixed-Quantity, Unconfined Liquid Spill Data

Reference	Fuel	Quantity of Fuel	Spill Depth	Spill Area	Surface
Chambers ²	JP-4	4–189 l (1–50 gal) from 1-ft height	0.7–2 mm after ignition	4–102 m ²	Concrete runway
Gottuk ³	Water	3.8–30 l (1–8 gal)	1.1–3.4 mm	1–11 m ²	Smooth, unfinished concrete and tile floor
Gottuk ³	6% AFFF	3.8–19 l (1–5 gal)	0.6–1.1 mm		Smooth, unfinished concrete
Gottuk ³	JP-8	2–3 l (0.5–0.8 gal)	0.7–1.1 mm	2.1–3.1 m ²	Smooth concrete with polyurethane coating
Hill ²²	JP-8	95–114 L (25–30 gal)	2.8–4.4 mm	26–33 m ²	Smooth, unfinished concrete
Putorti ⁴⁸	Gasoline	0.25–1 l	0.5–0.7 mm	0.4–1.8 m ²	Wood parquet and vinyl tile
Modak ⁵	#2 Fuel oil	0.005–0.030 l	0.22 mm	0.0075–0.0400 m ²	Both epoxy-coated concrete and steel
	Mobil DTE 797 turbine-lubricating oil		0.34 mm		(Spill depths were the same for both surfaces and were independent of the volume of liquid spilled.)
	Pennzoil 30-HD motor oil		0.75		
	Fyrquel 220 hydraulic control oil		0.84		

concrete, the spill areas (and depths) were the same for both substrate materials. However, spill areas were smaller for untreated concrete due to fuel absorption into the substrate surface.

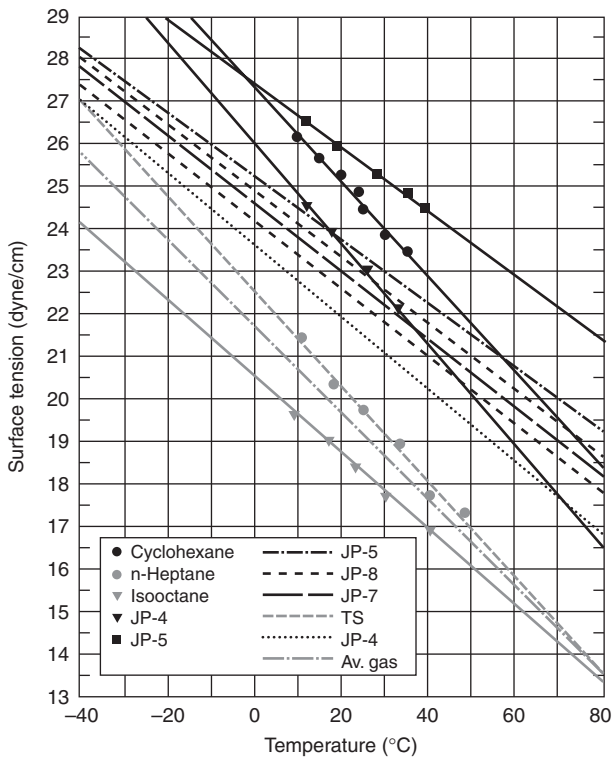


Figure 2-15.2. The effect of temperature on surface tension of hydrocarbon liquids (data taken from References 4 and 48).

Based on the JP-8 spill fire data from Gottuk et al.,³ as well as the bounding spills of 6 percent AFFF solution, the minimum spill depth can be assumed to be 0.7 mm. If an analysis warrants a more accurate assessment for the applicable conditions, the data presented in Figures 2-15.1, 2-15.3, and 2-15.4 can be used to provide guidance.

In summary, spill depths for liquid spill fires can range from 0.7 mm to 4 mm, depending primarily on the initial quantity of fuel released. Based on the data available, the

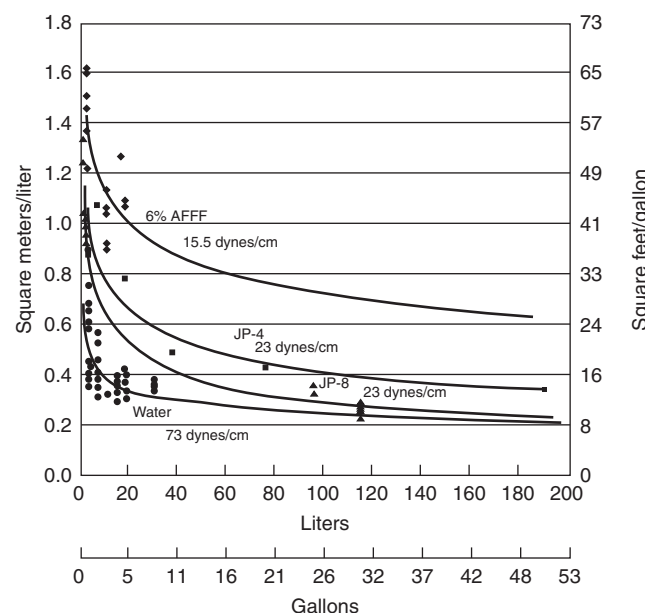


Figure 2-15.3. Spill area per volume of liquid released for the same data presented in Figure 2-15.1.³

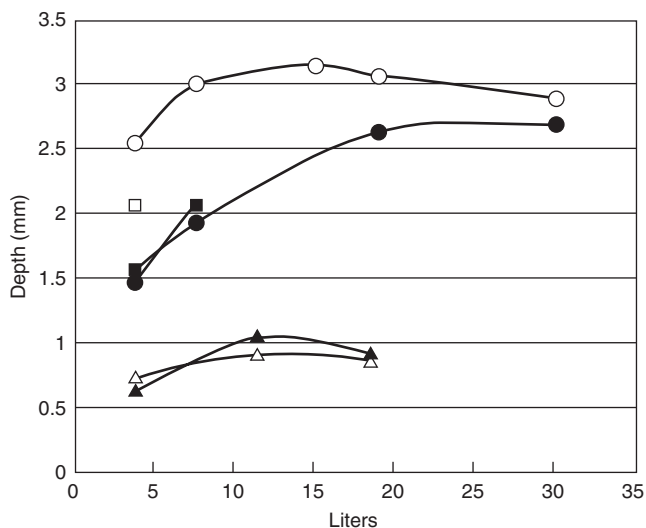


Figure 2-15.4. Spill depths for 6 percent AFFF solution and water releases on smooth concrete and tile floors for various fuel volumes and release heights:³ AFFF on concrete from 0.6 m (Δ), AFFF on concrete from 1.0 m (\blacktriangle), water on concrete from 0.6 m (\circ), water on concrete from 1.0 m (\bullet), water on tile floor from 0.15 m (\square), and water on tile floor from 0.9 m (\blacksquare).

following rules provide conservative minimum depths that will yield the maximum spill area:

$$\text{Spill} < 95 \text{ l (25 gal)} \quad \delta = 0.7 \text{ mm} \quad (3a)$$

$$\text{Spill} > 95 \text{ l (25 gal)} \quad \delta = 2.8 \text{ mm} \quad (3b)$$

Alternatively, the criteria can be stated as the reciprocal of the depth to yield the spill area per volume of fuel:

$$\text{Spill} < 95 \text{ l (25 gal)} \quad A/V = 1.4 \text{ m}^2/\text{l (57 ft}^2/\text{gal)} \quad (4a)$$

$$\text{Spill} \geq 95 \text{ l (25 gal)} \quad A/V = 0.36 \text{ m}^2/\text{l (14.5 ft}^2/\text{gal)} \quad (4b)$$

If a less conservative and potentially more accurate estimate is needed, then Figures 2-15.1, 2-15.3, and 2-15.4 should be used to provide guidance.

Fire Growth Rate

The temperature of the spilled liquid relative to its flash point is the single most important factor in identifying the flame spread rate over the surface of the liquid. The flame spread rate, in turn, determines the heat release rate history of the growing fire. Other factors also affect the flame spread rate, including the depth of the spilled liquid, size of the spill, type of liquid, and the substrate.

Generally, hazard assessments involving flammable, liquid pool fires require a conservative characterization of the fire growth rate history, peak burning rate, and fire duration. The purpose of the hazard assessment often defines that only a subset of these parameters are required.

Peak burning rate and maximum burning duration at the peak burning rate are typically relevant to fire effects such as fire exposure to building elements, ignition of other fuel targets, or general environmental conditions that result from the fire.

The characterization of the spill or pool fire heat release rate history from ignition to peak burning rate (full involvement of pool fuel surface area) is important when dealing with time-related concerns or events. Examples of time-dependent concerns include egress or life safety conditions, activation of detection or suppression systems, spread of fire to other fuel packages, or failure of building elements. Presuming that one is interested in the pool fire heat release rate growth history, this can be defined as the integration of the flame spread rate for the particular geometry in question (e.g., circular for unconfined pools, rectangular for trenches) multiplied by the burning rate per unit surface area for the given liquid. Estimating the flame spread rate over the surface of the flammable/comustible liquid spill becomes critical in characterizing the fire growth history.

The majority of ignited, flammable liquid fuels results in flame spread that can be characterized by one of two major flame spread mechanisms for liquid fuels: liquid phase-controlled flame spread or gas phase-controlled flame spread. Flame spread rates for these two regimes can be grossly benchmarked: 1 to 12 cm/s for liquid phase-controlled flame spread and 130 to 220 cm/s for gas phase-controlled flame spread. A third regime for flammable liquid spills on porous surfaces can be defined where flame spread rates are measured in terms of cm/min. For some hazard analyses, identifying the appropriate flame spread region may sufficiently characterize the flame spread rate in a conservative fashion. The primary driver of the flame spread regime is the temperature of the spilled liquid relative to its flash point.

Basic Theory of Flame Spread on Liquids

Flame spread on liquid fuels has been widely studied in small-scale experiments and theoretical studies.⁶⁻²⁴ The flame spread rates are known to be dependent on fuel temperature and fuel flash point. Below the flash point temperature, the flame spreads by way of surface tension-induced flow of hot fuel ahead of the advancing flame. Above the flash point, the flame spread is by way of gas phase spread, which can be as rapid as 2 m/s. The majority of liquid flame spread studies have been limited to pure fuels, and most of the studies have used alcohol fuels in trays <10 cm wide. The majority of liquid flame spread studies have been focused on pure fuels with heavy emphasis on alcohol fuels in trays less than 10 cm wide. This chapter includes empirical data from nonpure hydrocarbon fuels²⁵ as well as data from large-scale studies.^{26,27}

Flame spread regimes: Several flame spread regimes have been identified in the literature. These flame spread regimes are most notably a function of the liquid temperature. The dependence of flame spread rates on liquid temperature has been studied by a number of investigators.⁶⁻²² The most extensive work has been done with nar-

row pans of alcohol fuels with fuel depths of 2–5 mm. These investigations indicate that the flame spread velocity is a strong function of fuel temperature, even when the fuel temperature is well below the flash point. Figure 2-15.5 shows the extensive work that Akita⁹ conducted using methanol in a 2.6-cm-wide pan. Akita observed a number of different flame spread regimes. Above the flash point, spread was via the gas phase. Below the flash point, he observed regions of uniform, pulsating, and pseudo-uniform spread. The mechanistic explanations for these phenomena below the flash point are not widely agreed upon. A more detailed discussion of flame spread regimes and their mechanisms can be found in the review article by Ross.²⁸

Semilog plots of flame spread rate as a function of liquid temperature have a characteristic shape with three regions: the liquid-controlled region, the gas phase-controlled region, and the asymptotic gas phase-controlled region. The slopes of the curve are different in each of these regions, and these differing slopes serve to define the regions. The transition from liquid to gas phase-controlled burning occurs at a temperature T_{go} ; the transition from gas phase control to asymptotic gas phase spread occurs at a temperature T_{gm} . Figure 2-15.6 graphically portrays these temperatures with respect to flame spread rates. Figure 2-15.6 is intended as a conceptual depiction and the omission of units on the axes is intentional.

Figure 2-15.6 is conceptually the same as a figure first described by Glassman and Dryer.¹⁴ In their paper, they identified the temperature at which gas phase-controlled flame spread begins as the fire point of the liquid; they also identified the temperature at which the maximum flame spread rate occurs as the stoichiometric temperature (the liquid temperature at which the vapor concentration at the surface is stoichiometric). While this interpretation is consistent with the interpretation of data for multicomponent

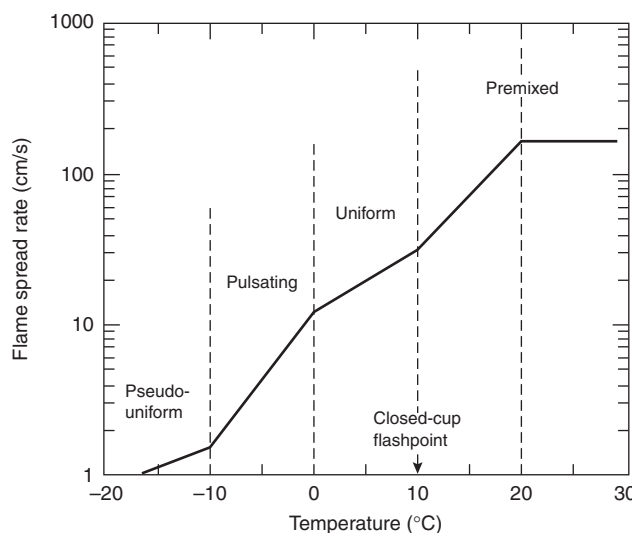


Figure 2-15.5. Flame spread rate on 1-cm-deep methanol as a function of fuel temperature in a 2.6-cm-wide pan.⁹

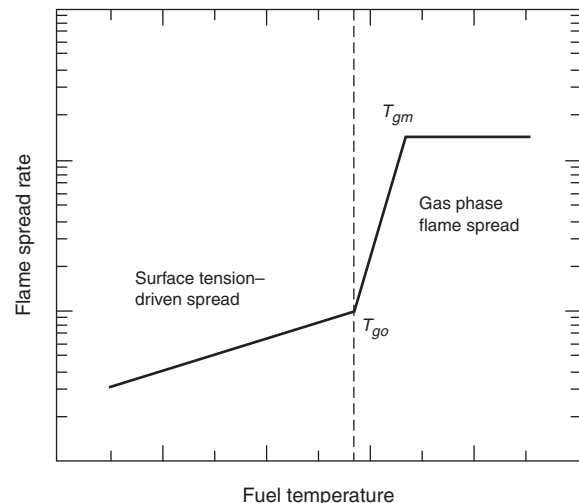


Figure 2-15.6. Graphic representation of the definitions of T_{go} and T_{gm} .

fuels, in light of Glassman and Dryer,¹⁴ it is not practical to define a fire point temperature for a multicomponent fuel. The difficulties are due to the need to model evaporation of many high-volatility components in a multicomponent fuel during the open heating that is required in the determination of a fire point. Determination of the fire point of a multicomponent fuel would require closed-cup heating of a fuel to a test temperature, exposing the liquid surface, and applying an ignition source. If the fire does not continue, the test temperature is below the fire point. Additional temperature tests would be required until the firepoint temperature is bracketed to the desired accuracy. This process is not practical. Similarly, for a multicomponent fuel it is not always practical to define the stoichiometric temperature, since determination of the vapor pressure of each component is, at the least, tedious and often impossible. Thus, while Glassman and Hansel's definitions are not easily generalized to multicomponent fuels, their pure fuel concepts can still provide guidance and motivation for the interpretation of multicomponent, liquid fuel flame spread results.

Pool dimensions: The physical dimensions of a liquid fuel spill or pool influences the flame spread rate, assuming an ignition source is present. The primary factors of importance are pool depth and characteristic width of the pool, as discussed below.

Pool dimensions, including fuel depth, have no effect on the flame spread rate for situations where the flame spread mechanism is considered gas phase-controlled. However, the depth of a flammable liquid does have a significant impact on the flame spread rate for liquid phase-controlled burning. In general, the average flame spread velocity for liquid phase-controlled spread increases with fuel depth. The fuel depth is primarily governed by the type of fuel release, confined versus unconfined.

Scientific study of liquid flame spread can be traced back as far as the 1930s.⁶ Most of the early work was done on relatively small-scale test setups, much of the work having been done with pans only 1–6 cm wide, using alcohol fuels at depths of 2–5 mm.^{7–9} Work by Mackinven, Hansel, and Glassman¹⁰ at Princeton is especially relevant here because it involved extensive experiments with decane, a pure fuel with similar characteristics to aviation fuels and other low-flash point, multicomponent hydrocarbon fuels that are common to fire hazard assessments. These workers documented the effects of pan width and fuel thickness on the observed flame spread rates.¹⁰

Several investigators have performed experiments in order to characterize the impact of fuel depth on liquid-controlled flame spread. Mackinven et al.¹⁰ demonstrated the systematic variation of flame spread rates with fuel depth. They investigated decane fuel depths from 1 mm to 2 cm and found the flame spread rate to increase with fuel depth as shown in Figure 2-15.7. This increase can be attributed to the retarding effect of small fuel depths on liquid recirculation flows that cause flame spread. Calculations by Torrance^{11,12} are in excellent agreement with Mackinven et al.'s experimental data shown in Figure 2-15.7. These calculations indicate that decane flame spread rates increase with pool depth up to 3 cm. Increases in fuel depth beyond this no longer increase the flame spread rate. Of course, fuel depths for unconfined fuel spills will always be far less than 3 cm. Investigations by Mackinven et al.¹⁰ as well as Burgoyne and Roberts^{7,8} indicate that flames do not spread away from the ignition source in liquid pools ≤ 1.5 mm deep. More recent work by Burelbach, Epstein, and Plys³⁰ demonstrated that the limiting fuel thickness for flame spread was 2.0 mm for decane and 2.3 mm for dodecane. Minimum fuel depths for flame spread are for the liquid-controlled spread regime. There is no evidence for fuel depth or pan width effects on gas phase flame spread.^{7,9,13,15,18,20}

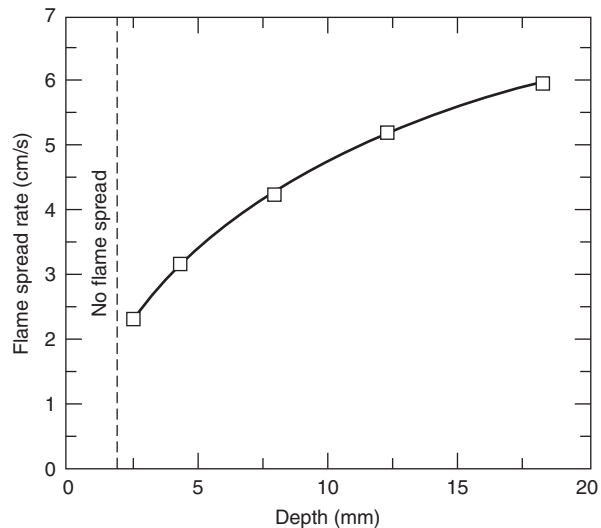


Figure 2-15.7. Flame spread rate on decane as a function of fuel depth.¹⁰

Mackinven et al.¹⁰ found that for pan widths up to 20 cm the flame spread rates on decane are a strong function of pan width. At pan widths from 20 to 80 cm, the maximum width they studied, they observed only slight increases in flame spread rate. Their results are shown in Figure 2-15.8. Both aluminum and glass pan walls were used. While there are small differences between these two wall materials, which may be attributed to heat conduction effects, the major dependence at pan widths < 20 cm is independent of wall material and has been attributed to a momentum reduction associated with viscous drag on the walls. The relative independence of pan width above 20 cm indicates that flame radiation is not a pivotal mechanism in determining liquid phase-controlled flame spread. The results were confirmed by Mackinven et al. by shielding the liquid ahead of the flame from flame radiation during flame spread experiments (20–80-cm-wide pans). They observed modest changes in flame spread rates between the shielded and unshielded experiments.

Temperature effects: The work of Burgoyne and Roberts⁷ showed that at small pan widths the temperature dependence of the flame spread rate is a function of the pan width as shown in Figure 2-15.9. Unfortunately, their work extends only from 2.5- to 6.3-cm widths. The dependence on pan width disappears above 41°C, the flash point of isopentanol. Given the work of Mackinven et al.¹⁰ using varying pan widths (see Figure 2-15.8) with decane 21°C below the closed-cup flash point (44°C) and the work of Burgoyne and Roberts,⁷ the prior work indicates that pan width ceases to have an impact on the temperature dependence of the flame spread rate at pan widths > 20 cm.

Flame spread experiments above the flash point indicate that the flame spread is via the gas phase. The flame spread rate increases rapidly from the flash point to the liquid temperature at which a stoichiometric fuel-air

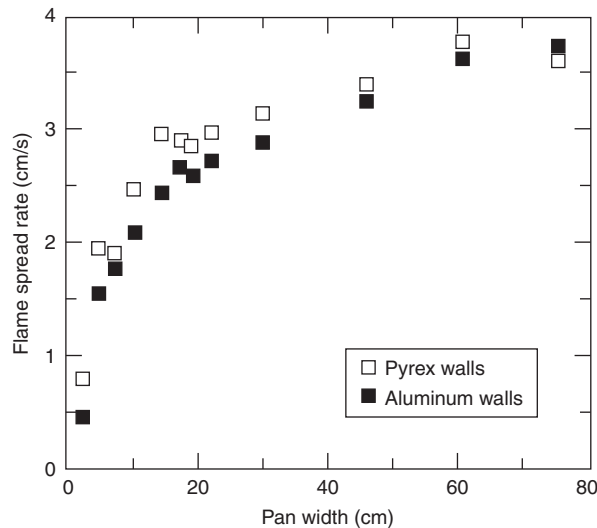


Figure 2-15.8. Flame spread rate on decane as a function of pan width.¹⁰

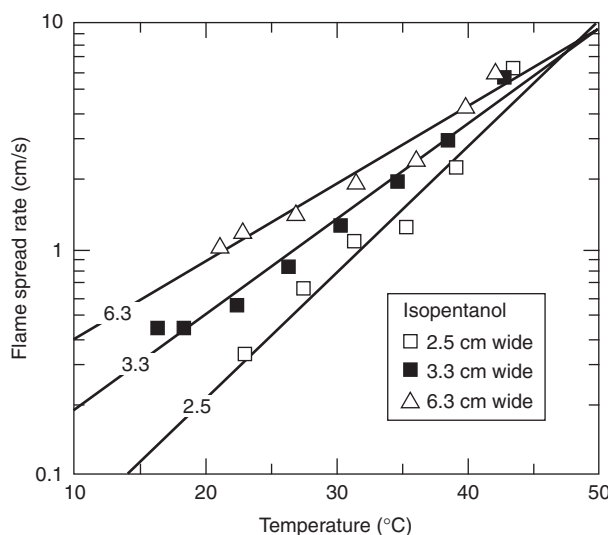


Figure 2-15.9. Effect of pan width on the temperature dependence of flame spread rate on isopentanol.⁷

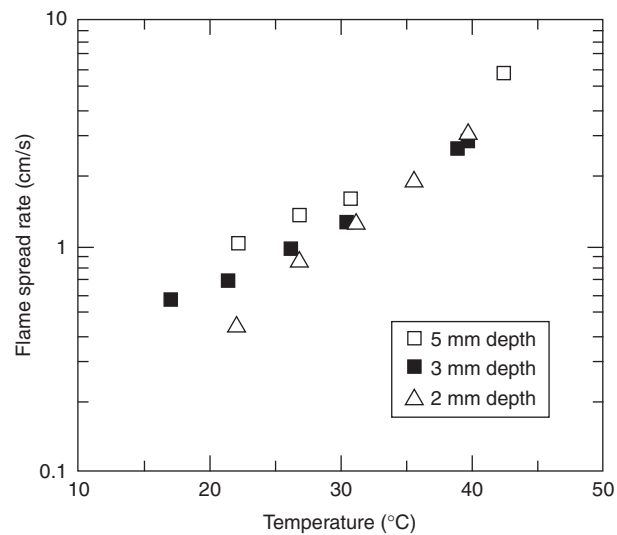


Figure 2-15.10. Effect of fuel depth on the temperature dependence of flame spread rate on isopentanol.⁷

mixture exists above the liquid surface. Above this temperature, the flame spread rate is no longer temperature dependent. The flame spread velocities measured by Burgoyne and Roberts,⁷ Akita,⁹ Nakakuki,¹⁵ and Hirano et al.²⁰ in this temperature region are from 1.3 to 2.2 m/s depending on the fuel. These velocities are similar to flame spread rates measured in stratified fuel-air mixtures found near ceilings of mine tunnels.³¹⁻³³

The work of Burgoyne and Roberts also indicates that the temperature dependence of the flame spread rate is a function of the fuel depth.⁷ They investigated isopentanol at fuel depths of 2 to 5 mm and their results are shown in Figure 2-15.10. Their results indicate that variations in flame spread rate with fuel temperature below the flash point (41°C) are lessened by increasing fuel depth.

Empirical Data

An overview of the experimental results for flame spread velocities follows. The overview includes alcohol fuels, multicomponent hydrocarbon fuels, and blends of multicomponent hydrocarbon fuels. While the bulk of the data is for laboratory-scale pools, there is limited data for large-scale pools of hydrocarbon fuels as well as some data for large-scale spills of jet fuel (hydrocarbon).

White, Beyler, Fulper, and Leonard²⁵ measured flame spread rates for aviation fuels, mixtures of these multicomponent hydrocarbon fuels, as well as 1-pentanol (alcohol). These measurements were made over a range of fuel temperatures in a pan with dimensions of 20 cm in width by 163 cm in length. The results for pure JP-5 and JP-8 are shown in Figures 2-15.11 and 2-15.12. The flame spread rates range from 3 to 140 cm/s over a temperature range of 10–90°C. The solid symbols indicate liquid-controlled flame spread and the open symbols indicate gas phase flame spread. JP-5 is a high-flash point kerosene used by the U.S. Navy that has a specified minimum flash point of 60°C.³⁴ JP-8 is a newer U.S. Air Force

fuel, very similar to commercial Jet A-1, that is a kerosene with a lower specified minimum flash point of 38°C.³⁵ The flame spread rates in the liquid-controlled regime for JP-8 are 0.5 to 2 cm/s greater than for JP-5. At temperatures ~12–20°C above the closed-cup flash point, flame spread rates increase very rapidly to >100 cm/s. The major difference in flame spread characteristics of JP-5 and JP-8 is the temperature at which the flame spread rate rapidly increases: 68°C for JP-5 and 58°C for JP-8.

Figure 2-15.12 shows several data points where the application of the ignition source was systematically var-

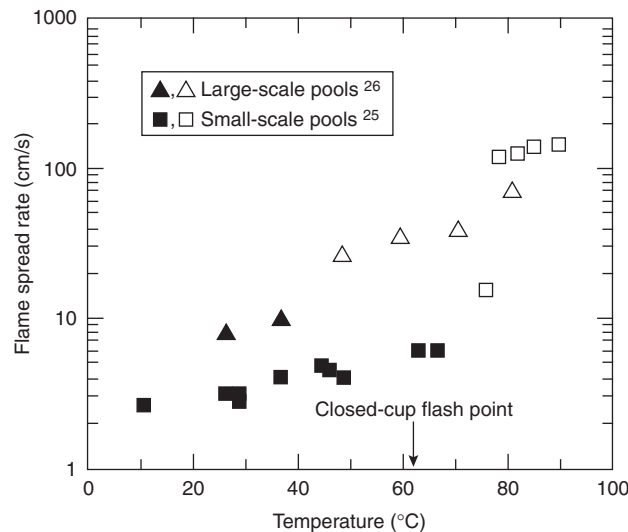


Figure 2-15.11. Flame spread rate for JP-5 as a function of temperature. Solid symbols denote liquid-controlled flame spread and open symbols denote gas phase flame spread for small-scale data only.

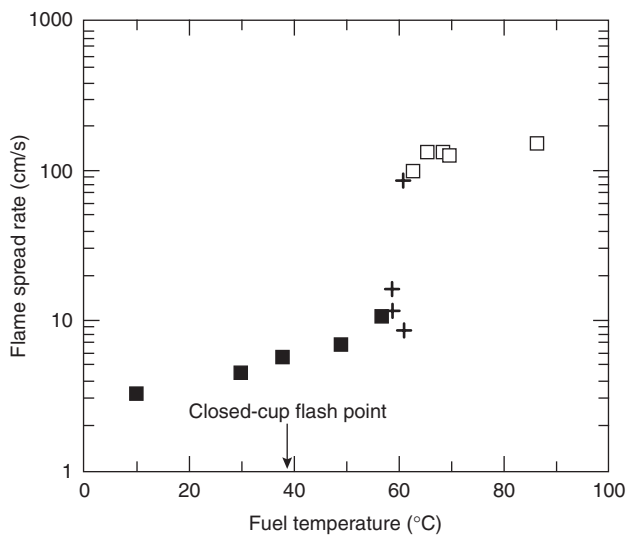


Figure 2-15.12. Flame spread rate for JP-8 as a function of temperature. Solid symbols denote liquid-controlled flame spread and open symbols denote gas phase flame spread; + indicates variable times to ignition of 3, 160, 240, and 460 s. The normal time to ignition is 35 s. Longer ignition times reduce the flame spread rate.²⁵

ied from 3 to 460 s in the most sensitive temperature region (the transition between liquid controlled and gas phase-controlled flame spread). At higher and lower temperatures such ignition delays have little or no effect on the observed flame spread rate. Assuming that the flame spread rate is a function of the liquid temperature relative to the flash point temperature, the results are consistent with an increase in the flash point of $\sim 10^{\circ}\text{C}$ during the 3 to 460 s between fuel discharge and ignition. No systematic study of flash point variations with time for multi-component fuels appears elsewhere in the literature.

The flame spread results for JP-5 and JP-8 indicate that the single most important determinant of flame spread is the initial temperature of the liquid prior to ignition relative to the fuel's flash point. Hillstrom¹³ also observed this correlation and found that plotting the flame spread rate as a function of the temperature difference between the closed-cup flash point, T_{fl} , and the liquid fuel temperature, T_l , correlated data for a number of hydrocarbon fuels. Figure 2-15.13 shows flame spread rate data for pure JP-5, pure JP-8, and mixtures of the two fuels plotted as a function of DT ($T_{fl} - T_l$). In Figure 2-15.13 square symbols represent liquid-controlled flame spread and the X symbols indicate gas phase flame spread. The treatment of the data effectively correlates all of the jet fuel data over a range of DT from -50°C to $+50^{\circ}\text{C}$. This representation of the data clearly shows the importance of DT ($T_{fl} - T_l$) in determining flame spread rate. Figure 2-15.13 also shows excellent consistency in the transition from liquid-controlled flame spread to gas phase spread at $DT = 18^{\circ}\text{C}$.

Leonard et al.²⁶ performed large-scale flame spread experiments as part of an effort to evaluate the fire hazards of mixed jet fuels on aircraft carrier flight decks. The

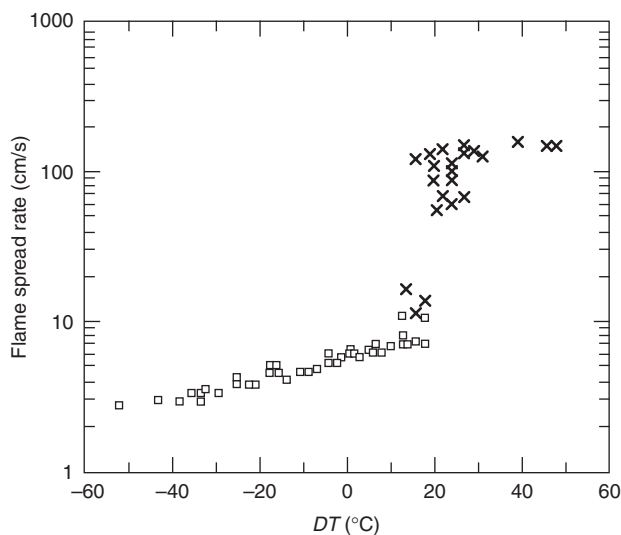


Figure 2-15.13. Flame spread rate for all JP fuels as a function of DT ($T_{fl} - T_l$).²⁵

experiments, which evaluated pure JP-5, pure JP-8, and mixtures of these two jet fuels, were carried out in a large-scale pan measuring 1.52 m in width and 12.2 m in length. The Leonard et al. experiments are the largest pool fire flame spread experiments reported in the literature. The jet fuels were evaluated over a range of temperatures by introducing heated fuel into the large pan, which was also temperature controlled by circulation of water through chambers on the underside of the pan bottom. The results for JP-5 are presented in Figure 2-15.11. The results for JP-8 are illustrated in Figure 2-15.14.

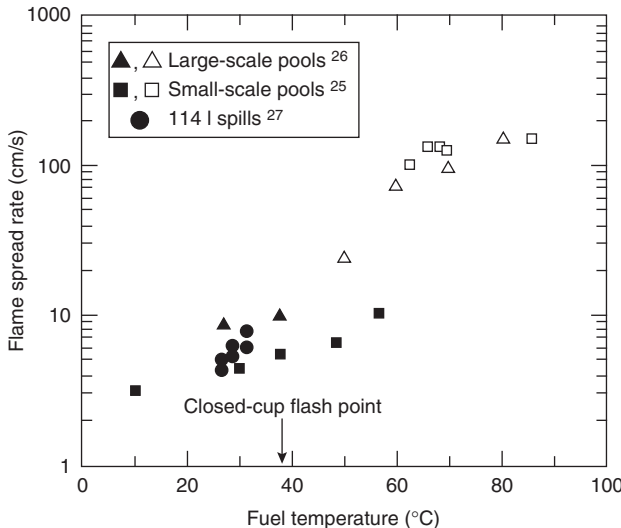


Figure 2-15.14. Flame spread rate for JP-8 as a function of temperature. Solid symbols denote liquid-controlled flame spread and open symbols denote gas phase flame spread.

The large-scale results can easily be compared with the small-scale results in both Figures 2-15.11 and 2-15.14. This comparison yields identical qualitative results. The flame spread rates for the large-scale tests are notably higher for both the JP-5 and JP-8 liquid-controlled flame spread tests. Data for the JP-8 tests indicate that the liquid-controlled flame spread rate is 10 to 11.6 cm/s while that of the JP-5 tests show 8.2 to 10 cm/s in this regime. As with the small-scale tests, there is approximately 1.5- to 1.8-cm/s difference between the two jet fuels, with the JP-8 fuel being slightly faster. The transition to gas phase flame spread appears to occur at a lower temperature for both fuels. Similar gas phase flame spread velocities are obtained between small- and large-scale tests. The disparity between the small-scale and large-scale tests for these two fuels cannot be attributed to a single factor. It is speculated that the difference in flame spread behavior of the two experimental data sets may be due, in part, to width effects and flame radiation effects. Further work is necessary to identify the specific mechanisms responsible for this observed difference.

A recent set of experiments evaluating aircraft hangar fire detection technologies²⁷ included large-scale jet fuel spill fires. Hill, Scheffey, Walker, and Williams²⁷ evaluated alternative fire protection methods for U.S. Air Force aircraft hangars. Their work represents the largest spill fires evaluated in the literature for flame spread. A volume of 114 l (30 gal) of JP-8 was spilled on a concrete pad. While the main focus of this research was fire suppression systems, one important aspect was evaluated: the impact of various suppression systems on the flame spread rate after system activation. The experiments measured the flame spread rate over the large spill area, which covered approximately 30 m² at the time of ignition, both before and after operation of the suppression system. The full free-burn spill size was on the order of 37 m². Time for complete burn-out for the free-burn spill scenario was roughly 2 min. Measured flame spread rates for the JP-8 spills prior to suppression system activation have been identified in Figure 2-15.14. The temperature of the JP-8 fuel was approximately 25°C ± 2°C. These flame spread rates fall close to the data points from the small-scale tests. The Hill et al. data points show a 1.5- to 3.5-cm/s increase over the small-scale data for the liquid-controlled flame spread results. The large-scale spill data show higher flame spread rates in comparison to the small-scale pool experiment data.

Although there are depth issues associated with the comparison of pool experiments to spill experiments, the trend appears to be that larger scale flame spread experiments yield higher flame spread rates for the liquid-controlled flame spread regime with a transition to gas phase spread occurring at a lower temperature than observed in the small-scale pool experiments. While these differences may not be fully explainable, it is important to note that irrespective of the experiment scale, peak flame spread rates for the liquid-controlled flame spread regime is approximately 10 cm/s for JP-5 and 12 cm/s for JP-8. Furthermore, although the transition to gas phase spread seems to occur at a lower temperature, the maximum gas phase flame spread rates are maintained in the 120- to 200-cm/s range for both JP-5 and JP-8. Support for using a maximum flame spread velocity of 10 cm/s for liquid-

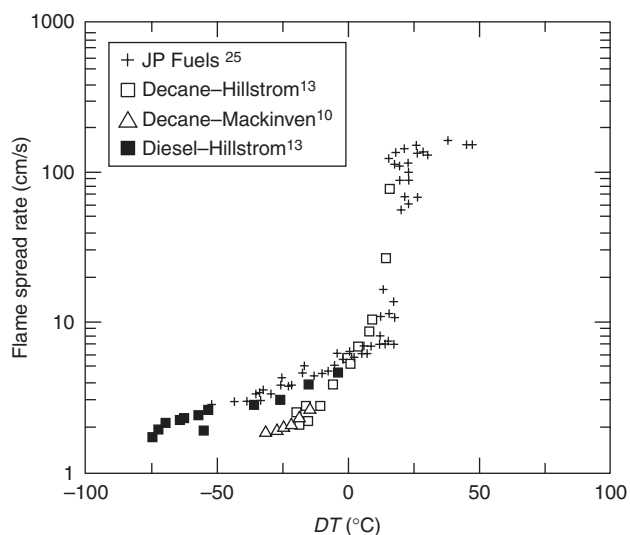


Figure 2-15.15. Comparison of JP fuel data with other hydrocarbon flame spread data from the literature.

controlled flame spread over hydrocarbon fuels can be drawn from Figure 2-15.15. Figure 2-15.15 shows a comparison of the jet fuel data from White et al.²⁵ and other hydrocarbon data from the literature. The results of the jet fuels were consistent with those of Hillstrom¹³ and Mackinven et al.,¹⁰ which show a very modest variation in flame spread rate below the flash point temperature. Figure 2-15.15 shows a comparison between the jet fuel data of White et al.,²⁵ the decane data from Hillstrom,¹³ the diesel fuel data from Hillstrom,¹³ and the decane data from Mackinven et al.¹⁰ The decane results show a rise in the flame spread rate at a smaller value of DT than for the JP fuels. Also, below the closed-cup flash point, the decane shows lower flame spread rates. This variation may be due to the effect of using a water substrate in the decane tests rather than steel as used in the jet fuel work. All the data in Figure 2-15.15 were collected in 20-cm-wide pans.

Empirical data for flame spread over alcohol pools consists of small-scale test data with White et al.²⁵ performing the largest experiments utilizing a 20-cm-wide pan. White et al.²⁵ evaluated 1-pentanol as part of their study. Results from these 1-pentanol flame spread tests are illustrated in Figure 2-15.16. These tests were performed to assess the effect of fuel type on flame spread for an alcohol fuel that had a similar flash point to the jet fuels primarily under study in this specific piece of work. Pentanol was chosen, in part, due to the previous pentanol flame spread work performed by Burgoyne and Roberts.⁷

Liquid-controlled flows were observed at temperatures <52°C. The change from liquid-controlled flame spread to gas phase flame spread occurred at ~4°C above the closed-cup flash point. Figure 2-15.16 illustrates a comparison of the 1-pentanol results from White et al.²⁰ with the alcohol data from Burgoyne and Roberts.² The 1-pentanol results take on the same characteristic dependence on DT, with the Burgoyne and Roberts data showing rapid rise in the flame spread rate at somewhat lower

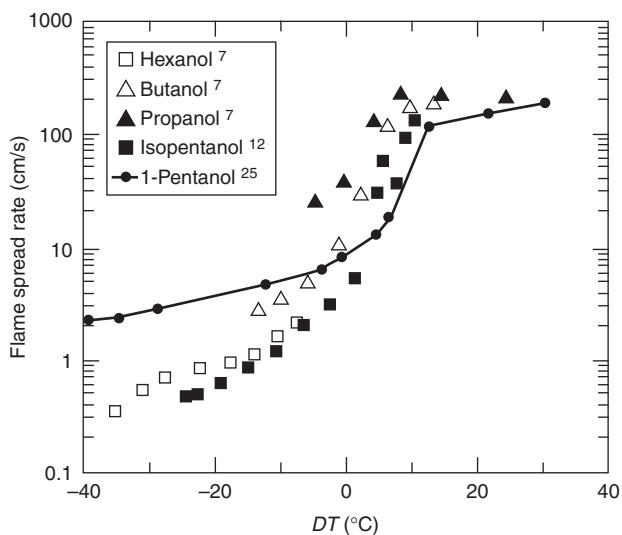


Figure 2-15.16. Comparison of the 1-pentanol data with the alcohol data of Burgoyne and Roberts.⁷

values of DT than the 1-pentanol data. The slope difference between the Burgoyne and Roberts data and the 1-pentanol data for the liquid-controlled flame spread regime can be attributed to the effect of pan width on the temperature dependence of flame spread rate in this regime. It is very interesting to note that the data reflected in Figure 2-15.16 for alcohol flame spread are similar to the hydrocarbon data with respect to the maximum liquid-controlled flame spread rates on the order of 10 cm/s while the gas phase flame spread rates fall between 150 and 200 cm/s.

Table 2-15.2, reproduced from White et al. shows the closed-cup flash point, T_{fl} , the transition from liquid to gas phase-controlled burning, T_{go} , and the transition from gas phase control to asymptotic gas phase spread, T_{gm} , for the small-scale jet fuel data, the 1-pentanol data, and the decane data from Hillstrom.¹³ The difference $T_{go} - T_{fl}$ averages 15°C for the hydrocarbon fuels. The difference $T_{gm} - T_{go}$ averages 6°C and the overall difference $T_{gm} - T_{fl}$ averages 21°C. These results may be expected to represent general properties for small hydrocarbon pools, but should not be used for alcohol fuels.

Glassman and Dryer¹⁴ have pointed out some discrepancies in the measurement of flash points and fire-

points of alcohols versus hydrocarbons, and the relevance of flash points with regard to the hazards of liquid fuels. While each of the standard flash point/fire point testing methods has its own difficulties, it is clear from the work of Glassman and Dryer that none of the standard flash point testing methods correlate with the onset of gas phase flame spread for all fuels. Glassman and Dryer point out major differences between alcohol and hydrocarbon flash points and point to the large quenching diameter for these two classes of fuels. Based on Glassman and Dryer's observations, transition to gas phase flame spread would be expected at temperatures near the closed-cup flash point for alcohol fuels, as observed for the 1-pentanol test results.

However, there are differences in $T_{go} - T_{fl}$ between jet fuels and decane. The more volatile aviation fuels are characterized by $T_{go} - T_{fl} \sim 18^\circ\text{C}$ while decane and JP-5 are characterized by $T_{go} - T_{fl} \sim 12^\circ\text{C}$. This 6°C difference may be due to the loss of light ends from the more volatile hydrocarbon mixtures. This difference is consistent with the variations in the flame spread rate with ignition time delay represented in Figure 2-15.12. White et al. point out that it appears that the actual flash point of the JP-8 may have increased by $\sim 6^\circ\text{C}$ during the discharge and ignition delay period. While this deduction seems reasonable, a more systematic study of this issue is warranted. The important consideration for hazard analyses is that multi-component hydrocarbon fuels can incur a reduction in effective flash point depending on the volatility of the fuel and the time period between the fuel release and ignition. The conservative approach would be to assume instantaneous ignition of the released fuel.

Fuel-soaked beds of porous media (e.g., small beads of glass or metal) have been used in flame spread experiments to simulate a fuel spill onto a porous surface. Flame spread over porous media generally has flame spread rates on the order of 1 to 8 cm/min, which are of similar magnitude to those measured for flame spread over the surface of relatively thick solids. Takeno and Hirano³⁶ have experimentally evaluated several parameters important to characterizing the flame spread rate over porous media soaked with fuel. Figure 2-15.17 represents the results from their study. Table 2-15.3 identifies the conditions of each experiment portrayed in Figure 2-15.17.

These tests used a steel tray 3.5 cm wide and 60 cm long that was filled with either glass or lead beads. Four observations can be made from this data: (1) the flame

Table 2-15.2 Critical Temperatures ($^\circ\text{C}$) for Flame Spread

Fuel	T_{fl}	T_{go}	$(T_{go} - T_{fl})$	T_{gm}	$(T_{gm} - T_{go})$	$(T_{gm} - T_{fl})$
JP-8	39	57	18	62	5	23
25/75 JP-8/5	42	60	18	66	6	24
50/50 JP-8/5	48	65	17	72	7	24
75/25 JP-8/5	54	68	14	74	6	20
JP-5	63	76	13	79	3	16
Decane ⁸	44	56	12	62	6	18
Average 1–6	—	—	15	—	6	21
1-Pentanol	48	52	4	62	10	14

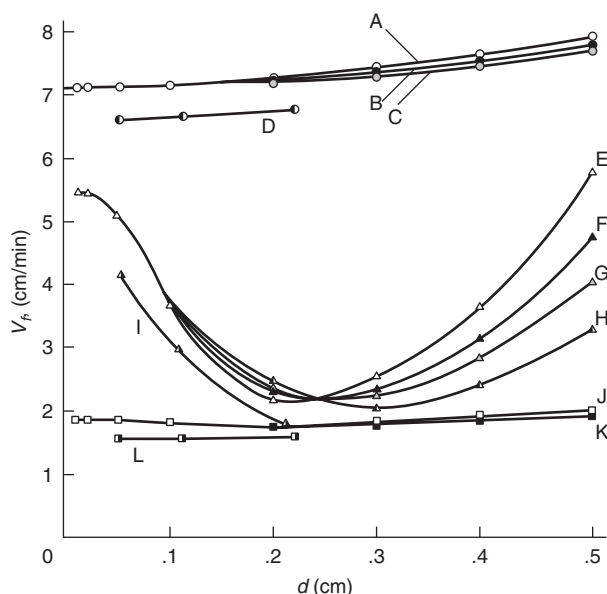


Figure 2-15.17. Variations of flame spread rate with bead diameter.²⁹ Table 2-15.3 lists conditions.⁶²

spread velocity increases slightly as the diameter of the beads, d , increases and there appears to be little dependence on the liquid viscosity (see Figure 2-15.17, conditions A, B, C) for 90 percent by volume of decane and 10 percent hexane; (2) the flame spread for pure decane is a function of the bead diameter and the viscosity (conditions E, F, G, H) where the flame spread velocity decreases with the increase of d for smaller values of d , a minimum flame spread rate occurs at approximately $d = 0.25$ cm, from this point the flame spread velocity increases with d and fuel viscosity effects are more pronounced with flame spread rate decreasing as the viscosity of the fuel increases; (3) for situations where the liquid level is below the top surface of the bead bed (conditions J, K), flame spread velocities are reduced and depend little on bead

diameter or fuel viscosity; (4) when the glass beads are replaced with lead beads (conditions D, I, L), similar variations are observed as with the glass beads; however, the flame spread rates are reduced by approximately 10 percent. In general, the flame spread rates for pure decane ranged from 2 to 6 cm/min while the mixtures of 90 percent decane/10 percent hexane spanned 7 to 8 cm/min.

Ishida³⁷ has also investigated fire growth on fuel-soaked ground with a rectangular pan using central ignition. The shallow square steel tray measured 50 cm × 50 cm × 2 cm deep. The tray was filled with glass beads. Radial flame spread rates were measured for decane fuel over varying bead diameters. Figure 2-15.18 reproduces Ishida's results. Figure 2-15.18 demonstrates that the average flame spread velocity decreases as the bead diameter increases. It is also interesting to note that the flame spread rate accelerates as the fire size increases. The average flame spread rate over the duration from a 2-cm flame diameter to a 30-cm diameter ranges from 6 to 10 cm/min for the bead diameters investigated.

Using Flame Spread Velocities to Characterize the Rate of Involvement of a Pool or Spill

Characterizing the fire growth rate history of a fuel release fire is dependent on describing the time-dependent history of the area involved with fire. The flame spread rate must be placed in context of the fuel release geometry as well as the location of the ignition point. Thus, the geometry of the released fuel and the relative location of the ignition source define the framework for characterizing the area of involvement.

An example for a circular pool of fuel follows. A circular pool with the ignition source in the center yields the most rapid involvement of the entire fuel release. Assuming that uniform spread occurs, a circular fire will develop and the area of the pool involved will be a function of the fire radius:

$$A_{\text{fire}} = \pi r^2 \quad (5)$$

Table 2-15.3 Experimental Conditions of Fuel-Soaked Beds Presented in Figure 2-15.17

	Combustible Liquid	Viscosity μ (cp)	Material of Beads	Initial Liquid Level y_s (cm)	Symbol
A	90% decane + 10% hexane	0.846 (normal)	Glass	0.0	○
B	90% decane + 10% hexane	2.617	Glass	0.0	●
C	90% decane + 10% hexane	4.552	Glass	0.0	●
D	90% decane + 10% hexane	0.846	Lead	0.0	◐
E	Pure decane	0.846	Glass	0.0	△
F	Pure decane	2.617	Glass	0.0	▲
G	Pure decane	4.552	Glass	0.0	▲
H	Pure decane	6.872	Glass	0.0	▲
I	Pure decane	0.846	Lead	0.0	▲
J	Pure decane	0.846	Glass	-0.5	□
K	Pure decane	4.552	Glass	-0.5	■
L	Pure decane	0.846	Lead	-0.5	□

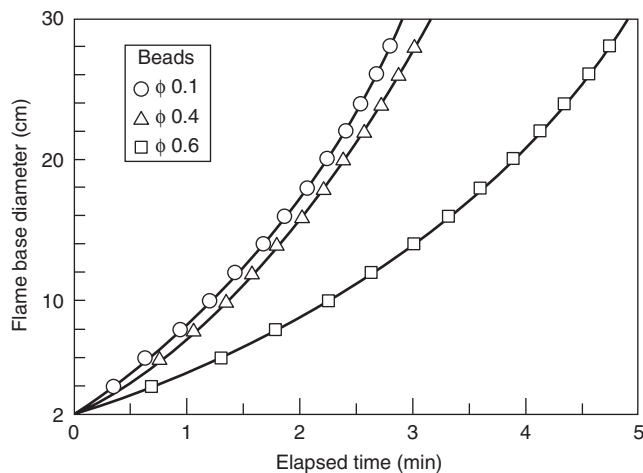


Figure 2-15.18. Diameter of flame pillar base as a function of elapsed time.³⁷

where A_{fire} is the area of the fire in m^2 and r is the radius of the fire in m at any given time, t (s). Assuming a constant flame spread velocity, the radius of the burning area can be defined as

$$r = vt \quad (6)$$

where v is the flame spread velocity in m/s . Substituting Equation 6 into Equation 5:

$$A = \pi v^2 t^2 \quad (7)$$

In this manner, Equation 7 can be used to identify the area of the spill involved at any time subsequent to the ignition. Assuming that the mass burning rate per unit area is at a constant value ($\dot{m}'' = \dot{m}_{\max}''$) and does not change as a function of time, a t^2 fire develops. Of course the time limit is defined when the fire involves the maximum area of the spill and this limit can be defined as follows:

$$t_{A,\max} = \frac{r_{A,\max}}{v} \quad (8)$$

where $t_{A,\max}$ is the time the entire pool surface becomes involved with fire, and $r_{A,\max}$ is the maximum radius of the fuel release.

A similar approach can be applied to a rectangular trench. Assuming an ignition source at one end of the trench, an alternative example can be developed. For the trench geometry the area is defined as

$$A = wl \quad (9)$$

where w is the width of the trench in m and l is the length of the trench involved with fire in m . Assuming w is small compared to l and that the ignition source at one end of the trench spans the width of the trench, and that the flame spread rate is constant, the length of trench involved is

$$l = vt \quad (10)$$

Substituting Equation 10 into Equation 9 yields the time-dependent area of the trench involved:

$$A = wvt \quad (11)$$

In this manner, Equation 11 can be used to identify the area of the trench involved at any time subsequent to the ignition at one end. Assuming that the mass burning rate per unit area is at a constant value ($\dot{m}'' = \dot{m}_{\max}''$) and does not change as a function of time, a t^1 fire develops. Of course the time limit is defined when the fire involves the maximum area of the trench and this limit can be defined as follows:

$$t_{A,\max} = \frac{l_{\max}}{v} \quad (12)$$

where l_{\max} is the maximum length of the trench.

This type of approach can be used for other fuel release configurations and ignition source locations. The heat release rate is then the area of the fuel release involved multiplied by the burning rate per unit area as well as the heat of combustion. This relationship is explained in more detail in the following section.

Fire Size

The fire size is primarily characterized by the heat release rate and the flame height. The heat release rate, \dot{Q} , is calculated as

$$\dot{Q} = \dot{m} \cdot \Delta h_c \quad (13)$$

where \dot{m} is the mass burning rate of the fuel and Δh_c is the fuel heat of combustion. The fuel mass burning rate can be calculated via Equation 14 or 15 as follows:

$$\dot{m} = A \cdot \dot{m}'' \quad (14)$$

where A is the spill fire area and \dot{m}'' is the mass burning rate per unit area ($\text{kg}/\text{m}^2\text{s}$),

$$\dot{m} = A \cdot \dot{y} \cdot \rho \quad (15)$$

where \dot{y} is the fuel burning regression rate (m/s) and ρ is the density of the fuel. The regression rate is the rate at which the fuel surface descends in a vertical direction as it burns; values are often reported in units of mm/min and therefore must be converted to m/s for the above calculations. Both, \dot{m}'' and \dot{y} are empirically based values that are related per Equation 16:

$$\dot{m}'' = \dot{y} \cdot \rho \quad (16)$$

Data in the literature has been presented for both parameters and both are presented below. The most commonly referenced data was developed by Blinov and Khudakov³⁸ for pool fires and presented by Hottel³⁹ as shown in Figure 2-15.19. Figure 2-15.19 shows the regression rate and flame height results for various fuels burning in a broad range of pan sizes, 0.004 to 23 m in diameter. The data indicates that the fuel regression rate is approxi-

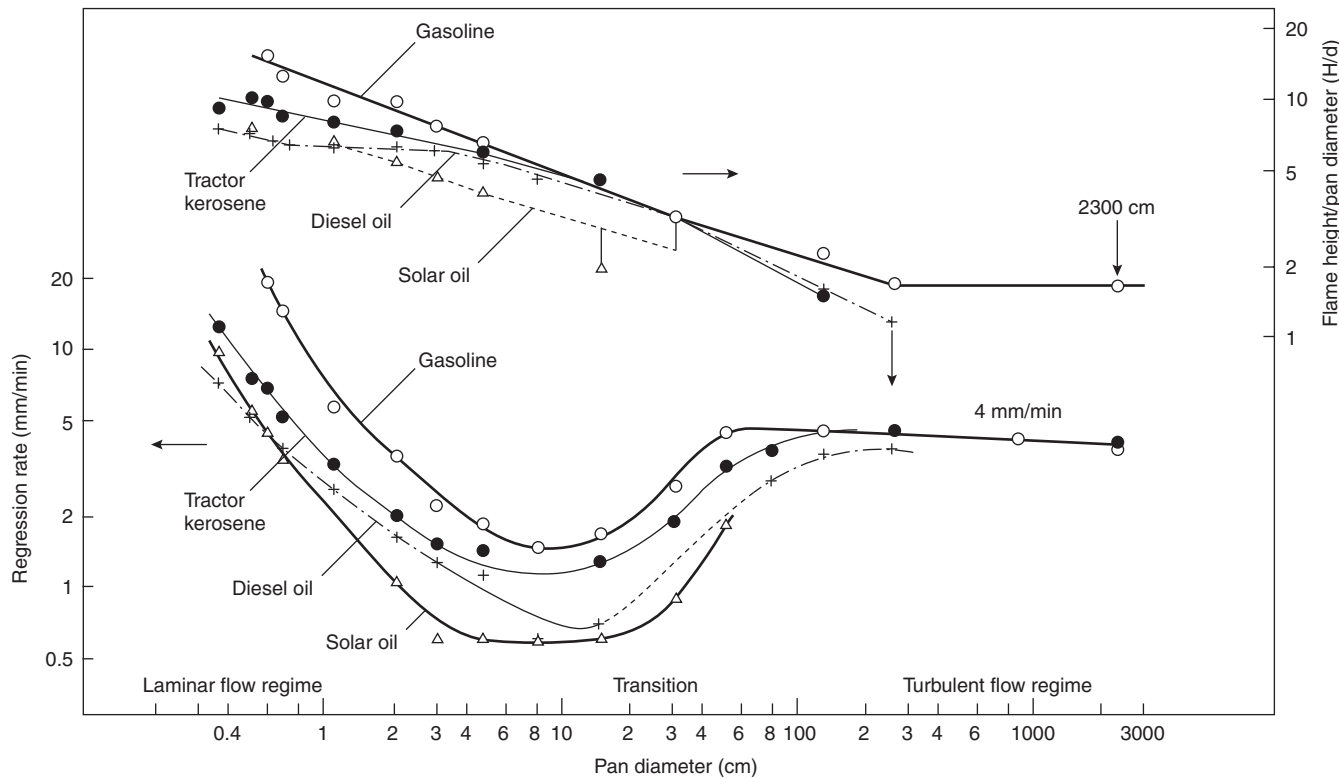


Figure 2-15.19. Regression rate and flame height data for liquid pools from Blinov and Khudiakov.³⁸

mately constant at 4 mm/min for all fuels tested burning as confined pool fires with diameters greater than 1 m. For smaller diameter fires, there is considerable difference in regression rates for the fuels presented. Hottel³⁹ discusses the trends in the burning rate data based on the balance of heat transfer to the fuel.

For fire sizes greater than about 1 m in diameter, the dominant mode of heat transfer to the liquid is via radiation from the plume. For smaller sizes, heat conduction from the pan (walls) or the substrate and convective heat transfer will constitute a larger fraction of the heat transferred to the liquid, thus having a larger effect on the burning rate of the fuel. Hottel,³⁹ Burgess, Strasser, and Grumer,⁴⁰ and Burgess, Grumer, and Wolfhard⁴¹ present detailed discussions on these heat-transfer effects. At larger diameters (typically 1 to 2 m), the burning fuel regression rate tends to level out at a constant maximum value, \dot{y}_{\max} . For these pools in the radiation dominant region, Burgess et al.⁴⁰ with the U.S. Bureau of Mines accurately correlated the maximum regression rates of various single-component, burning fuels (pan fires) based on the thermochemistry of the liquids as follows:

$$\dot{y}_{\max} = 1.27 \times 10^{-6} \frac{\Delta h_c}{\Delta h_{v,\text{sen}}} \quad (\text{m/s}) \quad (17)$$

where Δh_c is the heat of combustion and $\Delta h_{v,\text{sen}}$ is the sensible heat of vaporization, calculated as

$$\Delta h_{v,\text{sen}} = \Delta h_v + \int_{T_0}^{T_b} C_p dt \quad (18)$$

where

Δh_v = heat of vaporization at the boiling point, T_b

C_p = specific heat of the liquid fuel

T_0 = initial temperature of the liquid

The use of the sensible heat of vaporization accounts for the temperature dependence of the regression rate, which will vary appreciably (up to tens of percent) from the value calculated using only Δh_v . As the correlation expressed by Equation 17 suggests, the fuel regression rate is not constant for all fuels at larger diameters as indicated for the limited fuels in Figure 2-15.19. Based on a broad range of hydrocarbon pan fires, Zabetakis and Burgess⁴² fit Equation 17 to the data shown in Figure 2-15.20. The fit is quite good except for the cryogenic fuels, liquefied natural gas and liquefied propane gas. It is noted that the data applies to single-component fuel fires burning in uninitiated air under calm conditions (e.g., no wind).

Further work by the Bureau of Mines researchers, Grumer et al.,⁴³ suggested that the regression rate for blended fuels can be represented by the same correlation (Equation 17) when the heats of combustion and vaporization are presented as shown in Equation 19 for each component of the fuel.

$$\dot{y}_{\max} = 1.27 \times 10^{-6} \left[\frac{\sum_{i=1}^N n_i \Delta h_{c_i}}{\sum_{i=1}^N n_i \Delta h_{v,i} + \sum_{i=1}^N m_i \int_{T_0}^{T_b} C_p(T) dt} \right] \quad (19)$$

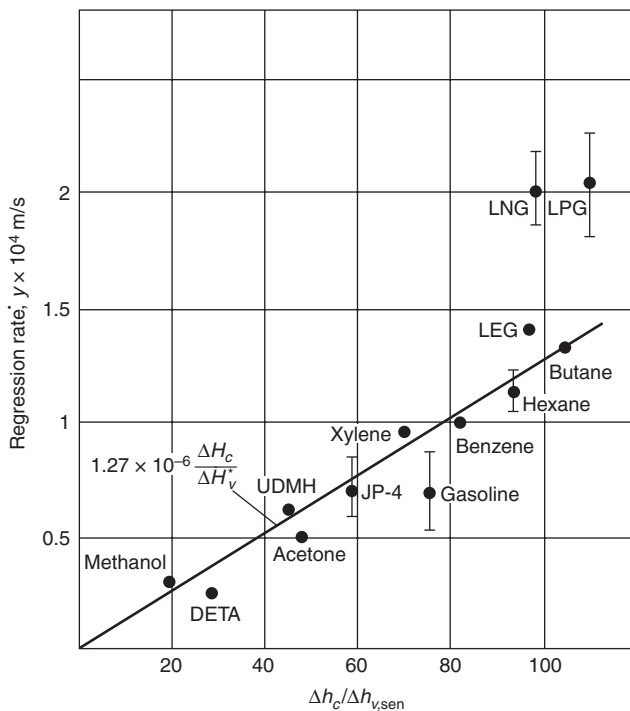


Figure 2-15.20. Burning fuel regression rate plotted versus thermochemical properties of fuels burning as pan fires (taken from Mudan⁵⁶).

where n_i and m_i are the mole fraction composition in the vapor and liquid phases, respectively.

A blended fuel with components of widely varying volatility will not burn at a uniform rate. Initially, the high volatile components will burn, and as time proceeds the burning will become more characteristic of the remaining lower volatile components. For blends, such as gasoline, that have components with similar heats of combustion and heats of vaporization and $n_i \approx m_i$, Equation 19 can be represented by

$$\dot{y}_{\max} = n_1 \dot{y}_1 + n_2 \dot{y}_2 + \dots \quad (20)$$

Equation 20 has been reported to yield good estimates of the regression rate for multicomponent fuel blends.⁴³ Even for blends with widely varying boiling points, Equation 20 provides rough estimates except for the initial and final stages of the fire.

Converting the regression rate data of Figure 2-15.20 via Equation 16 allows the corresponding maximum mass burning rate per unit area, \dot{m}_{\max}'' , to be plotted against the ratio of the heat of combustion to the heat of vaporization (see Figure 2-15.21). The fit to the data is represented by

$$\dot{m}_{\max}'' = 1 \times 10^{-3} \frac{\Delta H_c}{\Delta h_{v, \text{sen}}} = \text{kg/m}^2\text{s} \quad (21)$$

The fit of Equation 21 to the burning rate data is not as good as Equation 17 to the regression rate data. However,

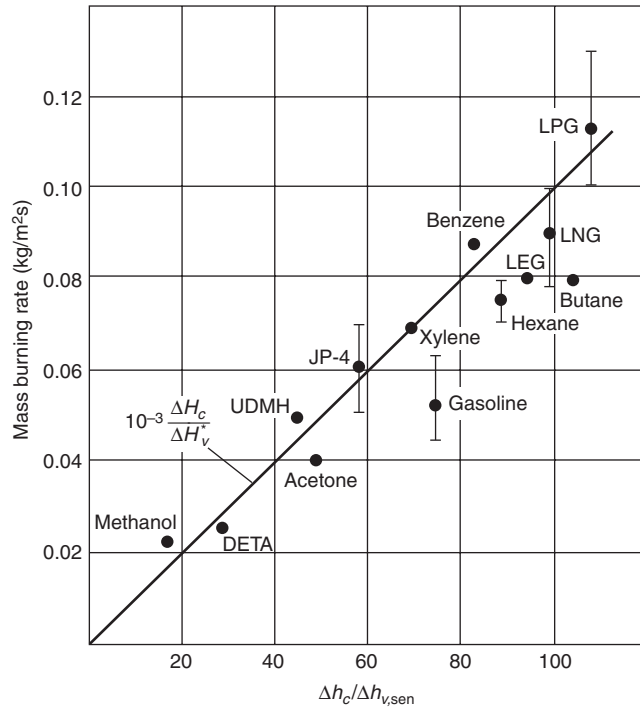


Figure 2-15.21. Mass burning rate per unit area versus the thermochemical property of fuels burning as pan fires (taken from Mudan⁵⁶).

Equation 21 does cover a wider range of fuels, including the liquefied gases.

The regression rate is particularly useful for confined pool fires of significant depth. For many spills, particularly continuously flowing fuels, the more useful quantity is the mass burning rate per unit area. As noted in the previous discussion, the burning rate of pool fires with diameters greater than 0.2 m (see Figure 2-15.19) increases with increasing diameter. Zabetakis and Burgess (1961) developed the following relationship to represent the burning rate per unit area as a function of pool diameter, D :

$$\dot{m}'' = \dot{m}_{\max}'' [1 - \exp(-k\beta D)] \quad (22)$$

where the product $k\beta$ is represented as a single value. k is the extinction coefficient (m^{-1}) and β is the mean-beam-length correction. The maximum burning rate per unit area, \dot{m}_{\max}'' , is also referred to in the literature by Babrauskas⁴⁴ as \dot{m}_{∞}'' , the mass burning rate for an infinite-diameter pool. If a confined pool is not circular, D is equal to the effective diameter, expressed as

$$D = \left(\frac{4A}{\pi} \right)^{1/2} \quad (23)$$

where A is the area of the pool.

Other than the data presented in Figure 2-15.21, the most comprehensive collection of burning rate data has been compiled by Babrauskas⁴⁴ and is presented in Table 3-1.13 in Section 3, Chapter 1. The correlation pre-

sented by Equation 22 agrees extremely well with the experimental data of some fuels, such as gasoline. The greatest disagreement occurs for alcohol fuels for which Babrauskas proposes a set of constant values for different diameter ranges (see *SFPE Handbook*, Section 3, Chapter 1⁴⁵). Due to difficulties in experimentally evaluating the cryogenic fuels, there tends to be more scatter in the data, and thus not as good of a correlation with Equation 22 as seen for other hydrocarbon fuels.

The use of Equation 22 applies to confined pool fires burning in the open, under still-air conditions and in a vessel (e.g., pan or tank) without an excessive lip height.⁴⁴ The burning rate correlations presented have been developed from confined pool fire experiments. There is very limited data available for burning rates of unconfined fuel spill fires. Gottuk et al.⁴⁶ conducted a series of JP-8 and JP-5 fuel spill fires on a smooth polyurethane-coated concrete slab, as used in Navy aircraft hangars. The spill fires consisted of both continuously flowing fuel releases (~0.4, 0.8, and 1.7 lpm) and 1 to 3 l of fixed quantities of fuel that were poured onto the concrete, allowed to spread to nearly a maximum size, and then ignited at the edge of the spill.

The burning rate per unit area data for the unconfined spill fires are presented in Figures 2-15.22 and 2-15.23 for both JP-8 and JP-5, respectively. Figures 2-15.22 and 2-15.23 show the experimentally measured \dot{m}'' for each test versus the measured diameter of the spill fires. Also included for comparison are the curves for burning rate for pool fires as calculated per Equation 22, using the data of Table 3-1.13. A curve for JP-8 does not appear in Figure 2-15.22, due to a lack of experimental pool fire data. How-

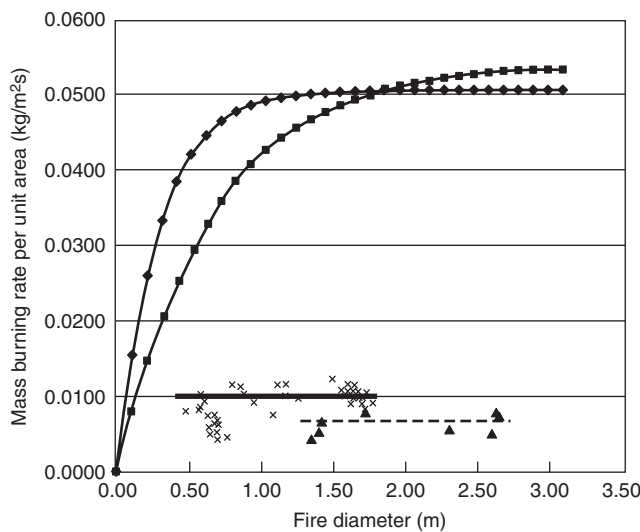


Figure 2-15.22. Mass burning rates for unconfined JP-8 spill fires on concrete⁴⁶: (x) denote 0.4- to 1.7-lpm, continuous spill fires with an average value (—) for diameters >1.5 m; (▲) denote 1- to 3-l fixed-quantity spills with an average value (---) for diameters >1.5 m; the calculated pool fire burning rates per Equation 22 are shown for JP-4 (---◆---) and JP-5 (---■---).

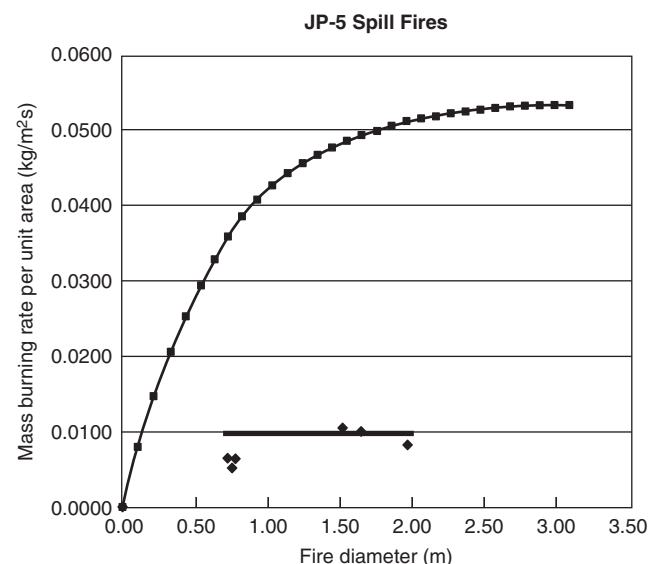


Figure 2-15.23. Mass burning rates for 0.4- to 1.7-lpm, unconfined JP-5 spill fires on concrete (◆).⁴⁶ The average value for diameters >1.5 m is shown as (—); the calculated pool fire burning rate per Equation 22 is shown as (---■---).

ever, it is expected, based on fuel property data, that the burning rate curve for JP-8 is bounded by the curves for JP-4 and JP-5.

The comparison between the spill fire data and the calculated pool fire \dot{m}'' values shows that the unconfined spill fire burning rates are remarkably lower than those for pool fires with the same diameter. For diameters greater than about 1 m, the burning rates for unconfined spill fires are approximately one-fifth of the maximum burning rates of confined pool fires. The results of the spill tests are summarized in Table 2-15.4. The lower burning rate is attributed to greater heat losses from the fuel to the concrete substrate in the spill fires than in the deeper pool fires, which have typically been conducted in pans. The spill fires had fuel depths on the order of 1 mm whereas most pan fire tests have been conducted with fuel depths of 1 to several centimeters. Since concrete has a higher thermal

Table 2-15.4 Unconfined Fuel Spill Burning Rates

Description	Mass Burning Rate per Area (kg/m ² s)	Standard Deviation	Reference
JP-8 1-3-l spills	0.007 ^a	0.0014	46
0.4-1.7-lpm spills	0.010 ^a	0.0009	46
JP-5 0.4-1.7-lpm spills	0.010 ^a	0.0008	46
Gasoline	0.011	—	49

^aRepresents average for fires with diameters greater than 1.5 m

conductivity ($\sim 1.4 \text{ W/mK}$)⁴⁷ than a thick fuel layer ($\sim 0.11 \text{ W/mK}$),⁴⁸ more heat is lost to the substrate, which would otherwise contribute to heating the fuel. In other words, the deep fuel layer of a pool serves as a better insulator to the top fuel surface than does the concrete, resulting in the fuel surface heating up more quickly, and in turn vaporizing and burning at a higher rate.

Figures 2-15.22 and 2-15.23 also show that the spill fire burning rates do not increase significantly over the range of spill sizes evaluated (0.5- to 2.5-m diameter). The data suggest that the use of Equation 22 for the burning rate for spill fires is inappropriate. As illustrated in the figures, it is proposed that the average value for spill diameters greater than 1.5 m be used as the expected burning rate for all diameters.

Putorti et al.⁴⁹ provide burning rates for unconfined gasoline spills on wood parquet, vinyl tile, and various carpets. Consistent with the results for the JP-8 and JP-5 spill fire data noted above,⁴⁶ the burning rates for gasoline on the nonabsorbing materials were found to be one-fifth that of the maximum rate for pool fires. Therefore, based on the limited, fuel spill fire data, it is suggested that burning rates for unconfined liquid fuel spills be estimated as one-fifth of the maximum pool burning rate. The large difference between pool fire and unconfined spill fire burning rates illustrates the need for more experimental work to characterize accurately spill fire sizes, particularly at larger diameters.

As presented in Equations 13 and 14, the heat release rate of an unconfined spill or confined pool fire can be calculated per Equation 24 once the area of the fire is determined and an appropriate mass burning rate per area is identified.

$$\dot{Q} = \dot{m}'' \cdot A \cdot \Delta h_c \quad (24)$$

However, in the case of an unconfined, continuously flowing spill fire, the area is neither known a priori, nor can it be calculated per any fuel depth correlations as with a fixed quantity spill. As fuel flows from a continuous source, the size of the resulting spill will continue to increase indefinitely until a physical boundary is reached or the fuel is ignited and burns. The transient nature of a continuous spill fire is very dependent on the timing of the fuel ignition and the flame spread rate relative to the fuel flow rate and size of the spill at the time of ignition. For example, if a continuously flowing spill is immediately ignited at the source, the fire size will be equal to the spill size if the flame spread rate is faster than the fuel spill spread rate. However, if the fuel spill spread rate is faster than the flame spread rate, the spill will continue to spread out ahead of the flame front.

As discussed below, a continuously flowing spill fire will reach a steady-state burning size, characterized by the equivalent steady-state diameter, D_{ss} . It is possible for a fuel spill to reach a diameter that is larger than D_{ss} before it is ignited. In this case, the flame will spread across the fuel surface to the larger diameter and then the spill fire will reduce in size until D_{ss} is reached. These examples are only several of multiple scenarios that can occur. Currently, complete and accurate models of burning fuel spills do not exist. In order to estimate the transient nature of a continuous fuel spill fire, the engineer must con-

sider the fuel spill rate, the relative time of ignition, and the steady-state burning spill area.

The steady-state burning spill area, A_{ss} , results due to a balance between the volumetric flow rate of the liquid release, \dot{V}_L (m^3/s), and the volumetric burning rate of the fire as described by

$$\dot{V}_L = A_{ss} \cdot \dot{y} = \frac{\pi D_{ss}^2}{4} \dot{y} \quad (25a)$$

or, alternatively in terms of the mass burning rate as

$$\dot{V}_L = A_{ss} \frac{\dot{m}''}{\rho} = \frac{\pi D_{ss}^2 \dot{m}''}{4\rho} \quad (25b)$$

The steady-state size of the spill can be explicitly solved by rearranging Equations 25a and 25b in terms of D_{ss} (m):

$$D_{ss} = \left(\frac{4\dot{V}_L}{\pi \dot{y}} \right)^{1/2} \quad (26a)$$

$$D_{ss} = \left(\frac{4\dot{V}_L \rho}{\pi \cdot \dot{m}''} \right)^{1/2} \quad (26b)$$

The calculation of the spill size per Equation 26 assumes that all fuel is burned from the spill; that is, there are no other losses of fuel from the spill, such as into a porous substrate. As noted by the examples above, D_{ss} does not necessarily correspond to the maximum fire size, but equals the size of the fire once the burning rate becomes constant and equilibrium conditions are reached.

Empirical correlations can also be used to calculate the equivalent diameter of a continuous spill fire. Mansfield and Linley⁵⁰ developed a correlation for the burning spill diameter as a function of fuel flow rate for large release rate fires on concrete. The following correlation was developed for 568- to 2271-lpm (150- to 600-gpm), continuous spill fires of JP-5 ranging in size from 15 to 24 m in diameter:

$$D_{ss} = 134(\dot{V}_L)^{1/2} \quad (27a)$$

$$D_{ss} = 3.5(\dot{V}_L)^{1/2} \quad (27b)$$

where $1 \text{ m}^3/\text{s} = 15,852 \text{ gpm}$.

The tests of Mansfield and Linley⁵⁰ were conducted outside with 2.2- to 12.5-m/s (5- to 28-mph) winds and ambient temperatures ranging from 7 to 32°C. Using Equation 25b with the diameter and spill rate data of Mansfield and Linley,⁵⁰ the mass burning rate per unit area of the large JP-5 continuous spill fires is calculated to be in the range of $0.055 \text{ kg/m}^2 \cdot \text{s}$, which agrees with the pool fire burning rate data reported by Babrauskas⁴⁵ in Table 3-1.13. The data are contrary to the smaller spill fire data of Gottuk et al.⁴⁶ and Putorti.⁴⁹ As a conservative approach to estimating the size of continuous spill fires, it is recommended that pool burning rates, as reported in Table 3-1.13, be used for large fuel release rates ($\sim >10 \text{ lpm}$) and that spill burning rates equal to one-fifth of the pool rates be used for smaller fuel release rates. Until further testing is performed to identify the actual criteria, 10

lpm is suggested since it is slightly larger than the flow rates for which experimental data is available.

As typically conducted in practice, the above discussions have suggested the use of steady-state or peak burning rates for pool fires and for unconfined spill fires. It is also frequently assumed that the peak burning rate occurs throughout the entire duration of the fire. This approach is intended to provide a conservative method for evaluating the largest possible fire given the particular pool or spill. In reality for unconfined spill fires, the peak burning rate will occur over a relatively short period of time. Therefore, a more realistic fire would burn for a longer period of time at a lower, time-averaged heat release rate compared to the assumption that the spill fire burns at the peak burning rate during the entire fire.

Liquid pool fires also demonstrate a similar transient behavior in that although the entire fuel surface may be fully involved, the burning rate per area (or regression rate) will increase over time until the maximum steady-state value is reached.⁴² The transient time period may be tens of seconds to minutes, depending on the type of fuel, the fuel depth, and the bounding materials (e.g., building walls or metal tank). During this transient period, the temperature gradient in the fuel is being established. Once the fuel surface reaches the boiling temperature, the burning rate approaches the steady-state value. If a transient analysis of a fire is required, further consideration must be given to the mass burning rate (or regression rate) that is selected. The use of the maximum value may not be appropriate for the entire burning duration.

Other Factors and Limitations

The spill areas and burning rates of liquid spill or pool fires presented in this chapter have been developed from experimental data of fires on level surfaces. In many applications, fuel spills will occur on inclined and/or cluttered surfaces. Under these conditions, fuel spread will ultimately be dependent on the geometry of the surface, which may lead to pooling of the fuel, channeling, and/or larger wetted areas than would occur on a level surface. Fuel flowing on an inclined surface can result in faster and wider spread of fire. No published studies have evaluated the impact of three-dimensional fuel flow on spill fire burning rates.

This chapter has addressed the burning of liquid fuel fires that occur in the open. Fires occurring in enclosures may exhibit different burning rates as a hot upper layer develops and air becomes restricted. The development of a hot upper layer and hot compartment boundaries can lead to increased burning rates. The burning rates presented in this chapter apply to fuels burning in overventilated conditions. If a liquid fuel fire is burning in vitiated conditions, oxygen entrainment to the fire becomes restricted and the radiant feedback from the fire plume to the fuel can be decreased, resulting in lower burning rates.

Babrauskas⁴⁴ and Zabetakis and Burgess⁴² have reported that burning rates of pool and spill fires both increase and decrease under increased wind speeds. Burgess and Hertzberg⁵¹ reported that wind speeds increased the burning rate for small-diameter fires; however, burning rates never exceeded the maximum burning rate in still air

corresponding to larger diameter fires. High wind speeds can cause fuel to spill out of contained areas or cause unconfined spill fires to move in the direction of the wind. At higher wind speeds, flames can also be blown off.

For pool fires in pans or tanks, the lip height can impact the burning rate of the fuel. There is limited data on this topic and experimental results show both an increase and decrease in the burning rate with larger lip heights.⁴⁴ Much of the experimental data has been for small pan diameters (<1 m) (e.g., Emmons, 1961⁵²).

Flame Height

The flame height of a liquid spill or pool fire can be calculated based on a number of experimental correlations.⁵³ The following correlation developed by Heskstad⁵³ has been shown to be quite robust for different fuels over a wide range of pool fire sizes:

$$L_f = 0.23\dot{Q}^{2/5} - 1.02D \quad (28)$$

where

L_f = the 50 percentile intermittent flame height (m)

\dot{Q} = the heat-release rate (kW)

D = the diameter of the fire (m)

The use of Equation 28 to characterize unconfined spill fire heights was evaluated by Gottuk⁴⁶ for JP-8 and JP-5 spill fires on concrete. The results of the comparison are shown in Figures 2-15.24 and 2-15.25, which present measured intermittent flame heights (50 percentile) and predicted flame height values plotted versus the spill diameter. For comparison, the predicted flame heights of pool fires are also plotted as a curve in each figure. The predicted pool

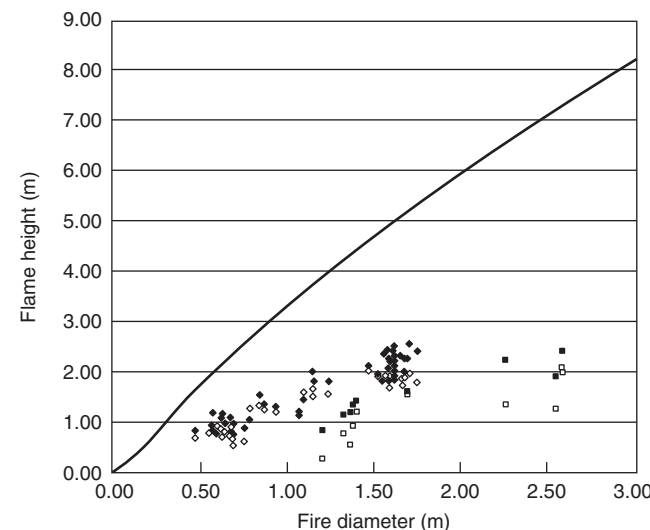


Figure 2-15.24. Comparison of measured and predicted flame heights for unconfined JP-8 spill fires⁴⁶: measured (♦) and predicted (◊) 0.4- to 1.7-lpm, continuously flowing spill fires; measured (■) and predicted (□) 1- to 3-l fixed-quantity spill fires; and predicted pool fires (—).

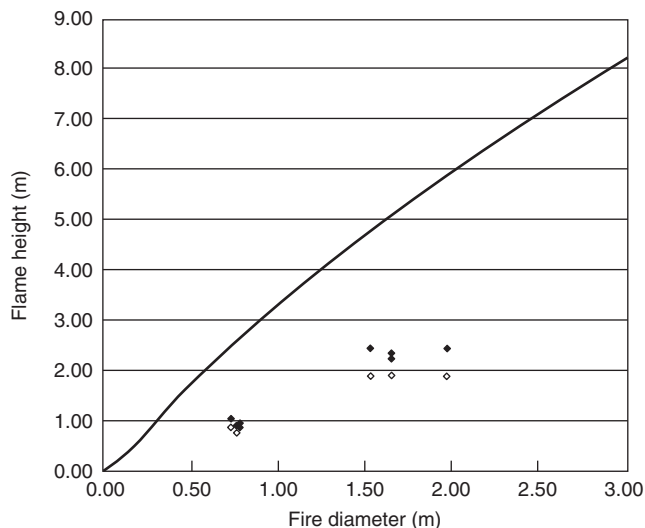


Figure 2-15.25. Comparison of measured and predicted flame heights for unconfined JP-5 spill fires⁴⁶: measured (◆) and predicted (◇) 0.4- to 1.7-lpm, continuously flowing spill fires; and predicted pool fires (—).

fire heights are based on Equation 28 and pool burning rate data of Table 3-1.13. Consistent with the difference in the mass burning rates between spill and pool fires, the spill flame heights are considerably shorter than those for pool fires of the same diameter. Using the Heskstad flame height correlation (Equation 28) with the spill fire data yields predicted heights that are approximately 17 percent low compared to the measured spill fire flame heights. For most engineering applications, the Heskstad flame height correlation (Equation 28) provides satisfactory predictions for both liquid pool and spill fires.

EXAMPLE 1:

A 208-l (55-gal) drum of gasoline is suddenly ruptured during a warehouse accident. The fuel is released quickly across the floor of the warehouse and is ignited when it comes in contact with a piece of faulty equipment. Determine the size of the resulting fire.

SOLUTION:

First the size of the spill is estimated using Equation 4b, assuming that the release occurs instantaneously (i.e., the spill is nearly at its maximum diameter at the time of ignition) and is allowed to spread freely.

$$A_s = (0.36 \text{ m}^2/\text{l})V = (0.36 \text{ m}^2/\text{l})(208 \text{ l}) = 75 \text{ m}^2$$

Per Equation 2, the maximum possible fire size is estimated using a fuel burning area, A , of

$$A = 1.55A_s = 1.55(75 \text{ m}^2) = 116 \text{ m}^2$$

The corresponding diameter of the burning spill is 12.2 m. The heat release rate for the fire is calculated per Equation 24 as

$$\dot{Q} = \dot{m}'' \cdot A \cdot \Delta h_c$$

From Table 3-1.13, the heat of combustion of gasoline is found to be 43.7 MJ/kg, the density is 740 kg/m³, and the maximum mass burning rate per unit area for a pool of gasoline, \dot{m}''_{\max} , is 0.055 kg/m²s. The maximum mass burning rate for the spill fire is estimated to be one-fifth of the maximum pool burning rate, thus yielding 0.011 kg/m²s. The resulting heat release rate is

$$\dot{Q} = (0.011 \text{ kg/m}^2\text{s})(116 \text{ m})(43.7 \text{ MJ/kg}) = 56 \text{ MW}$$

The intermittent flame height is calculated per Equation 28 as

$$\begin{aligned} L_f &= 0.23\dot{Q}^{2/5} - 1.02D \\ &= 0.23(56,000 \text{ kW})^{2/5} - 1.02(12.2 \text{ m}) = 5.8 \text{ m} \end{aligned}$$

If it is assumed that the fuel spill burns at the maximum rate for the duration of the fire, the burn time, t_b , for the fuel spill fire will be only 2 min:

$$t_b = \frac{m_f}{\dot{m}''A} = \frac{V \cdot \rho}{\dot{m}''A} = \frac{0.208 \text{ m}^3 \cdot 740 \text{ kg/m}^3}{0.011 \text{ kg/m}^2\text{s} \cdot 116 \text{ m}^2} = 121 \text{ s}$$

As illustrated in Example 2, the predicted burn time of 2 min is most likely too short. In reality, the fire will last longer due to the fact that the flame takes time to spread across the spill.

EXAMPLE 2:

Consider the situation in Example 1. What is the time required for the entire spill to become involved in the fire? The temperature in the warehouse is 20°C.

SOLUTION:

The most critical step in determining the time for the entire spill to become involved in the fire is to identify both the temperature of the liquid fuel spill and the flash point of the fuel. The flash point of gasoline is indicated to be -45°C as documented in Kanury's⁵⁴ table in the SFPE Handbook, "Selected Ignition, Flammability, and Autoignition Properties of Some Fuels in Air." Assuming that the gasoline is at the same temperature as the warehouse, 20°C, the spill temperature is well above the closed-cup flash point. The elevated temperature indicates that gas phase flame spread will occur if the spill is ignited. A reasonable and generally conservative approximation of the upper, gas phase, flame spread velocity is 200 cm/s.

The problem statement does not specify the location of the ignition source relative to the spill. The most conservative posture would be to assume that the ignition source is in the center of a circular spill. Using Equation 8 for circular spills will define the time for full involvement:

$$t_{A,\max} = \frac{r_{A,\max}}{v}$$

where $r_{A,\max}$ is 6.1 m and v is 2.0 m/s. The time for full involvement becomes

$$t_{A,\max} = \frac{6.1 \text{ m}}{2.0 \text{ m/s}}$$

$$t_{A,\max} = 3 \text{ s}$$

If the ignition source was located at the perimeter of the gasoline spill, it would take approximately 6 s to travel the full 12-m diameter of the pool to involve the spill completely. Irrespective of the ignition location, the time to involve the entire spill is small in the context of most hazard analyses time scales. Therefore, when gas phase flame spread is governing the involvement of a spill or pool of flammable liquid, it is often acceptable to assume instantaneous ignition of the entire fuel surface. This assumption may not be valid for extremely large spills (e.g. tanker spills) or when there are short time-scale concerns.

The difference between gas phase flame spread and liquid-controlled flame spread can be illustrated by assuming that the drum of gasoline in the foregoing example contained diesel fuel. The flash point of diesel fuel ranges from 52–96°C according to NFPA 325.⁵⁵ Since the warehouse is at 20°C, substantially below the flash point of diesel fuel, flame spread would be governed by liquid-controlled mechanisms. A conservative upper bound of the liquid-controlled flame spread in this case would be 10 cm/s. Assuming that the area of the diesel spill was identical to the gasoline spill and that there was a strong enough ignition source present to ignite the spill, a time to full ignition of the spill can be estimated. Assuming that the ignition source was in the center of the spill, Equation 8 would be used again, where the maximum radius of the spill is 6.1 m and the flame spread velocity is 0.1 m/s. The time for full involvement becomes

$$t_{A,\max} = \frac{6.1 \text{ m}}{0.1 \text{ m/s}}$$

$$t_{A,\max} = 61 \text{ s}$$

The conservative estimation of the time for full involvement of the diesel fuel is significantly greater than for the gas phase spread over gasoline.

Nomenclature

A	area (m^2)
A_s	area of spill (m^2)
A_{ss}	steady-state area of continuously flowing burning fuel spill (m^2)
C_p	specific heat of liquid fuel
D	diameter (m)
D_{ss}	steady-state area of diameter of burning fuel spill (m)
DT	$T_{fl} - T_l$
Δh_c	heat of combustion (kJ/kg)
$\Delta h_{v, \text{sen}}$	sensible heat of vaporization (kJ/kg)
k	extinction coefficient (m^{-1})
l	length of a trench involved with fire
l_{\max}	maximum length of trench (m)
L_f	flame height (m)
\dot{m}'	fuel-mass burning rate per unit area ($\text{kg/m}^2\text{s}$)
\dot{m}''_{∞}	fuel-mass burning rate per unit area for infinite size pools ($\text{kg/m}^2\text{s}$)
\dot{m}'_{\max}	maximum fuel-mass burning rate per unit area ($\text{kg/m}^2\text{s}$)

m_i	mole fraction of fuel in liquid phase
n_i	mole fraction of fuel in vapor phase
\dot{Q}	heat release rate (kW)
r	radius of the fire
$r_{A,\max}$	maximum radius of the fire for complete involvement of fuel release
t	time
$t_{A,\max}$	time at which fuel release becomes completely involved
T_b	boiling point temperature of liquid fuel
T_{fl}	closed-cup flash point temperature of fuel
T_{gm}	minimum liquid temperature at which asymptotic gas phase spread occurs
T_{go}	liquid temperature at the transition from liquid to gas phase-controlled burning
T_l	liquid fuel temperature
T_o	initial temperature of liquid fuel
v	flame spread velocity (cm/s)
V	volume (m^3)
\dot{V}_L	volumetric flow rate of liquid fuel (m^3/s)
w	width of a trench (m)
\dot{y}	regression rate (m/s)
\dot{y}_{\max}	maximum regression rate (m/s)

Greek

β	mean-beam-length correction
ρ	density (kg/m^3)
δ	spill depth (m)

References Cited

1. C. Beyler, "Fire Hazard Calculations for Large Open Hydrocarbon Fires," *The SFPE Handbook of Fire Protection Engineering*, NFPA, Quincy, MA, Chapter 3-11 (2002).
2. G.D. Chambers, "Flight Line Extinguisher Evaluation," U.S. Air Force Report DOD-AGFSRS-76-9 (1977).
3. D.T. Gottuk, et al., "Estimating Liquid Fuel Spill Areas," submitted to *Fire Technology* (2001).
4. H.E. Moran, J.C. Burnett, and J.T. Leonard, "Suppression of Fuel Evaporation by Aqueous Filmes of Fluorochemical Surfactant Solutions," *NRL Report 7247*, Naval Research Laboratory, Washington, DC (1971).
5. A.T. Modak, "Ignitability of High-Fire-Point Liquid Spills," *EPRI NP-1731*, Factory Mutual Research Corporation, Norwood, MA (1981).
6. T. Kinbara, *Bull. Inst. Phys. Chem. Res. Japan*, 9, p. 561 (1932).
7. J.H. Burgoyne and A.F. Roberts, "The Spread of Flame across a Liquid Surface, II. Steady-State Conditions," *Proc. Roy. Soc. A*, 308, pp. 55–68 (1968).
8. A.F. Roberts, Ph.D. Thesis, University of London (1959).
9. K. Akita, "Some Problems of Flame Spread along a Liquid Surface," in *14th Symposium (International) on Combustion*, Combustion Institute, Pittsburgh, PA, pp. 1075–1081 (1973).
10. R. Mackinven, J.G. Hansel, and I. Glassman, "Influence of Laboratory Parameters on Flame Spread across Liquid Fuels," *Combustion Science and Technology*, 1, pp. 293–306 (1970).

11. K.E. Torrance, "Subsurface Flows Preceding Flame Spread over a Liquid Fuel," *Combustion Science and Technology*, 3, pp. 133–143 (1971).
12. K.E. Torrance and R.L. Mahajan, "Fire Spread over Liquid Fuels: Liquid Phase Parameters," in *15th Symposium (International) on Combustion*, Combustion Institute, Pittsburgh, PA, pp. 281–287 (1975).
13. W.W. Hillstrom, "Temperature Effects on Flame Spreading over Fuels," *Paper to Eastern Section*, Combustion Institute, Pittsburgh, PA (1975).
14. I. Glassman and F.L. Dryer, "Flame Spreading across Liquid Fuels," *Fire Safety Journal*, 3, pp. 123–128 (1980).
15. A. Nakakuki, "Flame Spread over Solid and Liquid Fuels," *J. Fire & Flammability*, 7, pp. 19–40 (1976).
16. K. Akita and O. Fujiwara, "Pulsating Flame Spread along the Surface of Liquid Fuels," *Combustion and Flame*, 17, pp. 268–269 (1971).
17. H. Ishida, "Flame Spread over Fuel-soaked Ground," *Fire Safety Journal*, 10, pp. 163–171 (1986).
18. H. Ishida, "Flame Spread over Ground Soaked with Highly Volatile Liquid Fuel," *Fire Safety Journal*, 13, pp. 115–123 (1988).
19. W.A. Sirignano and I. Glassman, "Flame Spreading above Liquid Fuels: Surface-Tension-Driven Flows," *Combustion Science and Technology*, 1, pp. 307–312 (1970).
20. T. Hirano, T. Suzuki, I. Mashiko, and N. Tanabe, "Gas Movements in Front of Flames Propagating Across Methanol," *Combustion Science and Technology*, 22, pp. 83–91 (1980).
21. A. Ito, D. Masuda, and K. Saito, "A Study of Flame Spread over Alcohols Using Holographic Interferometry," *Combustion and Flame*, 83, pp. 375–389 (1991).
22. F. Miller and H. Ross, "Further Observations of Flame Spread over Laboratory-Scale Alcohol Pools," *24th Symposium (International) on Combustion*, Combustion Institute, Pittsburgh, PA, pp. 1703–1711 (1992).
23. W.A. Sirignano, "A Critical Discussion of Theories of Flame Spread across Solid and Liquid Fuels," *Combustion Science and Technology*, 6, pp. 95–105 (1972).
24. D.D. Cline and L.N. Koenig, "The Transient Growth of an Unconfined Pool Fire," *Fire Technology*, 19, 3, pp. 149–162 (1983).
25. D. White, C.L. Beyler, C. Fulper, and J. Leonard, "Flame Spread on Aviation Fuels," *Fire Safety Journal*, 28, pp. 1–31 (1997).
26. J.T. Leonard, C.R. Fulper, R. Darwin, G.G. Back, R.E. Burns, and R. Ouelette, "Fire Hazards of Mixed Fuels on the Flight Deck," *Naval Research Laboratory Memorandum Report 6975* (1992).
27. S.A. Hill, J.L. Scheffey, F. Walker, and F.W. Williams, "Tests of Alternative Fire Protection Methods for USAF Hangars," *Naval Research Laboratory Memorandum Report 8337* (1999).
28. H.D. Ross, "Ignition of and Flame Spread Over Laboratory-Scale Pools of Pure Liquid Fuels," *Prog. Energy Combust. Sci.*, 20, pp. 17–63 (1994).
29. I. Glassman and J. Hansel, "Some Thoughts and Experiments on Liquid Fuel Spreading, Steady Burning, and Ignitability in Quiescent Atmospheres," *Fire Research Abstracts and Reviews*, 10, 3, pp. 297–322 (1948).
30. J.P. Burelbach, M. Epstein, and M.G. Plys, "Brief Communication—Initiation of Flame Spreading on Shallow Subflash Fuel Layers," *Combustion and Flame*, 114, 1/2, pp. 280–282 (1998).
31. I. Liebmann, J. Corry, and H.E. Perlee, "Flame Propagation in Layered Methane-Air Systems," *Combustion Science and Technology*, 1, pp. 257–267 (1970).
32. C.C. Feng, S.H. Lam, and I. Glassman, "Flame Propagation through Layered Fuel-Air Mixtures," *Combustion Science and Technology*, 10, pp. 59–71 (1975).
33. H. Phillips, "Flame in a Buoyant Methane Layer," *10th Symposium (International) on Combustion*, Combustion Institute, Pittsburgh, PA, pp. 1277–1283 (1965).
34. Military Specification, "Turbine Fuel, Aviation, Grades JP-4, JP-5, and JP-5/JP-8 ST," *MIL-T-5624N* (1989).
35. Military Specification, "Turbine Fuel, Aviation, Grades JP-8," *MIL-T-83133B*, (1988).
36. K. Takeno and T. Hirano, "Behavior of Combustible Liquid Soaked in Porous Beds during Flame Spread," in *22nd Symposium (International) on Combustion*, Combustion Institute, Pittsburgh, PA, pp. 1223–1230 (1988).
37. H. Ishida, "Initiation of Fire Growth on Fuel-Soaked Ground," *Fire Safety Journal*, 18, pp. 213–230 (1992).
38. V.I. Blinov and G.N. Khudiakov, "Diffusion Burning of Liquids," U.S. Army Translation, *NTIS No. AD296762* (1961).
39. H.C. Hottel, "Certain Laws Governing Diffusive Burning of Liquids," *F. Res. Abs. and Rev.*, 1, p. 41, (1959).
40. D.S. Burgess, A. Strasser, and J. Grumer, "Diffusive Burning of Liquid Fuels in Open Trays," *F. Res. Abs. and Rev.*, 3, p. 177, (1961).
41. D.S. Burgess, J. Grumer, and H.G. Wolfhard, "Burning Rates of Liquid Fuels in Large and Small Open Trays," *Internation Symposium on the Use of Models in Fire Research, Publication 786*, National Academy of Sciences—National Research Council, Washington, DC, pp. 68–75 (1961).
42. M.G. Zabetakis and D.S. Burgess, "Research on Hazards Associated with the Production of and Handling of Liquid Hydrogen," *U.S. Bureau of Mines Report, RI 5705* (1961).
43. J. Grumer, A. Strasser, T.A. Kubala, and D.S. Burgess, "Uncontrolled Diffusive Burning of Some New Liquid Propellants," *Fire Res. Abs. and Rev.*, 3, p. 159 (1961).
44. V. Babrauskas, "Estimating Large Pool Fire Burning Rates," *Fire Tech.*, 19, p. 251 (1983).
45. V. Babrauskas, "Heat Release Rates," *The SFPE Handbook of Fire Protection Engineering*, 3rd edition, NFPA, Quincy, MA (2001).
46. D.T. Gottuk, J. Gott, and F.W. Williams, "Fuel Spill Fire Dynamics," submitted to *Fire Technology* (2001).
47. F.P. Incropera and D.P. DeWitt, *Fundamentals of Heat and Mass Transfer*, 2nd ed., John Wiley and Sons, New York (1985).
48. Coordinating Research Council, *Handbook of Aviation Fuel Properties*, (1983).
49. A.D. Putorti, Jr., J.A. McElroy, and D. Madrzykowski, "Flammable and Combustible Liquid Spill/Burn Patterns," *NIJ Report 604-00*, National Institute of Justice, Washington, DC (2001).
50. J.A. Mansfield and L.J. Linley, "Measurement and Statistical Analysis of Flame Temperatures from Large Fuel Spill Fires," *NWC TP 7061*, Naval Weapons Center, China Lake, CA (1991).
51. D.S. Burgess and M. Hertzberg, "Radiation from Pool Flames," *Heat Transfer in Flames*, Chapter 27, (N.H. Afgan and J.M. Beer, eds) Scripta Book Co., Washington, DC (1974).
52. H.W. Emmons, "Some Observations on Pool Burning," *The Use of Models in Fire Research, Publication 786* NAS-NRC, Washington, DC, pp. 50–67 (1961).
53. G. Hesketh, "Luminous Heights and Turbulent Diffusion Flames," *Fire Safety Journal*, 5, pp. 103–108 (1983).
54. A.M. Kanury, "Ignition of Liquid Fuels," *SFPE Handbook of Fire Protection Engineering*, NFPA, Quincy, MA (1995).
55. NFPA 325, *Guide to Fire Hazard Properties of Flammable Liquids, Gases, and Volatile Solids*, NFPA, Quincy, MA (1994).
56. K.S. Mudan, "Thermal Radiation Hazards from Hydrocarbon Pool Fires," *Prog. Energy Combust. Sci.*, 10, pp. 59–80 (1984).

Section Three

Hazard Calculations

Section 3 Hazard Calculations

Chapter 3-1 Heat Release Rates		Nomenclature	3-187
Introduction	3-1	References Cited	3-187
Definitions	3-1		
Measuring the HRR, Full Scale	3-1		
Measuring the HRR, Bench Scale	3-3		
Measuring the HRR, Intermediate Scale	3-3		
HRR for Real Products	3-10		
Estimating the HRR for General Combustibles	3-32		
Uncertainty of HRR Measurements	3-32		
References Cited	3-34		
Chapter 3-2 Calorimetry			
Introduction	3-38		
Use of Bench-Scale Heat Release Rate Data	3-39		
Techniques for Measuring Heat Release Rate	3-42		
Effects of Bench-Scale Calorimeter Construction Details	3-49		
Survey of Bench-Scale Calorimeters	3-51		
Comparison between Bench-Scale Calorimeters	3-56		
Large-Scale Heat Release Rate Calorimeters	3-57		
Nomenclature	3-59		
References Cited	3-59		
Chapter 3-3 The Cone Calorimeter			
Introduction	3-63		
Summary of Features	3-63		
Sample Testing Specifications	3-72		
Smoke Measurement	3-74		
Calibration Equipment	3-75		
Miscellaneous Details	3-76		
Measurements Taken with the Cone Calorimeter	3-76		
Special Cone Calorimeters	3-78		
References Cited	3-79		
Additional Readings	3-80		
Chapter 3-4 Generation of Heat and Chemical Compounds in Fires			
Introduction	3-82		
Concepts Governing Generation of Heat and Chemical Compounds in Fires	3-83		
Prediction of Fire Properties Using Smoke Point	3-131		
Nonthermal Damage Due to Fire Products	3-133		
Fire Control, Suppression, and Extinguishment	3-143		
Nomenclature	3-156		
References Cited	3-158		
Chapter 3-5 Compartment Fire Modeling			
Introduction	3-162		
Conservation Equations	3-162		
Source Term Submodels	3-165		
Mass and Heat Transport Submodels	3-165		
Embedded Submodels	3-169		
Unresolved Phenomena	3-169		
Selected Reading and Comments	3-169		
Nomenclature	3-169		
References Cited	3-170		
Chapter 3-6 Estimating Temperatures in Compartment Fires			
Introduction	3-171		
Fire Stages	3-171		
Compartment Fire Phenomena	3-172		
Methods for Predicting Preflashover Compartment Fire Temperatures	3-175		
Methods for Predicting Postflashover Compartment Fire Temperatures	3-181		
Predicting Flashover	3-184		
		Chapter 3-7 Zone Computer Fire Models for Enclosures	
		Introduction	3-189
		Enclosure Fire Models	3-189
		Overview of Representative Zone Fire Models	3-190
		References Cited	3-192
		Additional Readings	3-193
		Chapter 3-8 Modeling Enclosure Fires Using CFD	
		Introduction	3-194
		The Principles	3-195
		Boundary Conditions	3-201
		Numerical Solution Method	3-202
		Validation	3-203
		Ensuring Proper Use	3-205
		Some Practical Applications	3-208
		More Advanced Application	3-209
		Software and Hardware Issues	3-211
		Conclusion	3-211
		Appendix: An Exemplification of the Use of CFD for Smoke Control in a Large Atrium Building	3-212
		Nomenclature	3-215
		References Cited	3-216
		Chapter 3-9 Smoke and Heat Venting	
		Introduction	3-219
		Simulating Fire-Generated Environments and the Action of Venting	3-220
		The Physical Basis for Simulating Fire-Venting Phenomena	3-221
		The Minimum Depth of Draft Curtains	3-234
		Required Vent Areas	3-234
		The Design Fire	3-235
		Mechanical Ventilation	3-235
		Designing Systems That Successfully Combine Smoke Vents with Sprinklers	3-236
		Nomenclature	3-240
		References Cited	3-241
		Chapter 3-10 Compartment Fire-Generated Environment and Smoke Filling	
		Fire Safety of Building Designs	3-243
		ASET—A Model for Predicting the Smoke Filling Process in a Room of Fire Origin	3-251
		Available Safe Egress Time from Rooms of Fire Origin—Some Example Calculations	3-255
		A Possible Extension in the Model's Utility	3-257
		Solutions to the Model Equations for a Special Class of Growing Fires	3-260
		Using the $\dot{Q} \sim t^n$ Solution Plots of Figures 3-10.19 and 3-10.20 to Predict Characteristics of Compartment Fire-Generated Environments	3-264
		References Cited	3-266
		Chapter 3-11 Fire Hazard Calculations for Large, Open Hydrocarbon Fires	
		Introduction	3-268
		Hydrocarbon Pool Fires	3-269
		Thermal Radiation Hazards from Liquid Hydrocarbon Pool Fires	3-272
		Thermal Radiation from Jet Flames	3-291
		Thermal Radiation Hazards from Hydrocarbon Jet Flames	3-298
		Unsteady Thermal Radiation Analysis	3-302

Thermal Radiation from Hydrocarbon Fireballs	3-306	Elements of Emergency Movement	3-367
Thermal Radiation Hazards	3-308	Hydraulic Flow Calculations	3-368
Summary	3-310	Impact of Smoke Conditions on Ability to Evacuate	3-372
References Cited	3-311	Evacuation Efficiency Factors	3-375
Chapter 3-12 Behavioral Response to Fire and Smoke		Emergency Movement Models	3-377
Introduction	3-315	Model Selection Factors	3-378
Behavioral Responses of Occupants	3-322	Nomenclature	3-379
Behavior in Hotel Fire Incidents	3-325	References Cited	3-379
Nonadaptive Behavior	3-329		
Occupant Fire Fighting Behavior	3-331	Chapter 3-15 Stochastic Models of Fire Growth	
Occupant Movement through Smoke	3-333	Introduction	3-381
Handicapped or Impaired Occupants	3-335	Basic Features	3-381
Summary	3-339	Markov Model	3-384
References Cited	3-340	Networks	3-389
Chapter 3-13 Movement of People: The Evacuation Timing		Random Walk	3-394
Introduction	3-342	Percolation Process	3-395
Literature Review	3-343	Epidemic Theory	3-396
Crowd Behavior and Management	3-344	Stochastic Differential Equation	3-396
Evacuation Timing	3-347	Other Models	3-400
Evacuation Procedures in Tall Office Buildings	3-355	References Cited	3-400
Occupants with Disabilities	3-359		
Movement in Smoke	3-362	Chapter 3-16 Explosion Protection	
Time-Based Egress Analysis	3-362	Introduction	3-402
Summary	3-364	Flammability, Explosibility, and Inerting	3-402
References Cited	3-364	Closed Vessel Deflagrations	3-406
Chapter 3-14 Emergency Movement		Detonations	3-410
Introduction	3-367	Explosion Venting	3-414

SECTION THREE

CHAPTER 1

Heat Release Rates

Vytenis Babrauskas

Introduction

Calculations of fire behavior in buildings are not possible unless the heat release rate of the fire is known. This chapter on heat release rates provides both theoretical and empirical information. The chapter is organized so that theory and basic effects are considered first, then a compendium of product data is provided, which is arranged in alphabetic order.

Definitions

The essential characteristic that describes quantitatively “How big is the fire?” is the heat release rate (HRR). This is so important that it has been described as the single most important variable in fire hazard.¹ The heat release rate of a burning item is measured in kilowatts (kW). It is the rate at which the combustion reactions produce heat. The term *burning rate* is also often found. This is a less specific term and it may denote either the HRR or the mass loss rate. The latter is measured in units of $\text{kg}\cdot\text{s}^{-1}$. It is best to reserve the term *burning rate* for nonquantitative fire descriptions and to use either HRR or mass loss rate, as appropriate. The relationship of these two quantities can be expressed as

$$\text{HRR} = \Delta h_c \times \text{MLR} \quad (1)$$

where h_c is the effective heat of combustion ($\text{MJ}\cdot\text{kg}^{-1}$) and MLR is the mass loss rate ($\text{kg}\cdot\text{s}^{-1}$). Such an equation implies that HRR and MLR are simply related by a constant. This is not in general true. Figure 3-1.1 shows the results obtained from a test on a 17-mm sample of Western red

cedar. It is clear that the effective heat of combustion is not a constant; it is roughly $12 \text{ MJ}\cdot\text{kg}^{-1}$ for the first part of the test, but increases to around $30 \text{ MJ}\cdot\text{kg}^{-1}$ during the charring period at the end of the test.

In principle, the effective heat of combustion can be determined by theory or by testing. In practice, if the effective heat of combustion is not a constant, then experimental techniques normally involve directly measuring the HRR, rather than using Equation 1.

Measuring the HRR, Full Scale

The simplest case is when full-scale HRR can be directly measured. This can be grouped into two types of techniques: (1) open-burning HRR calorimeters and (2) room fire tests. Open-burning HRR calorimeters were developed in the early 1980s at NIST by Babrauskas and colleagues² and at FMRC by Heskstad.³ The operating principles of these calorimeters are described in Section 3, Chapter 2. Based on this work, a large number of different test standards have been issued. The NORDTEST furniture calorimeter⁷ is shown in Figure 3-1.2. Open-burning HRR measurements are simpler to make since a test room does not need to be constructed. The HRR within a room and under open conditions are, clearly, identical at very low HRR. What happens at higher values of HRR depends on the situation at hand. If the fire is so large that room flashover can be reached (about 1.5–1.75 MW if ventilation is through a single normal-sized door opening), then actual room HRR values postflashover can be drastically different from their open-burning rates. This is due primarily to additional radiant heat flux contribution from the hot gas layer and the hot room surfaces, although ventilation effects can also play a role.

For upholstered chairs, extensive studies have shown that room effects are only at the 20 percent level up to a 1-MW fire.¹⁰ The same study, however, showed that for mattresses, a room presence effect shows up at much lower HRR values. For liquid pools, the HRR is extremely

Dr. Vytenis Babrauskas is the president of Fire Science and Technology, Inc., Issaquah, Washington, a company specializing in fire safety research, fire testing issues, and fire science applications to fire investigations and litigations.

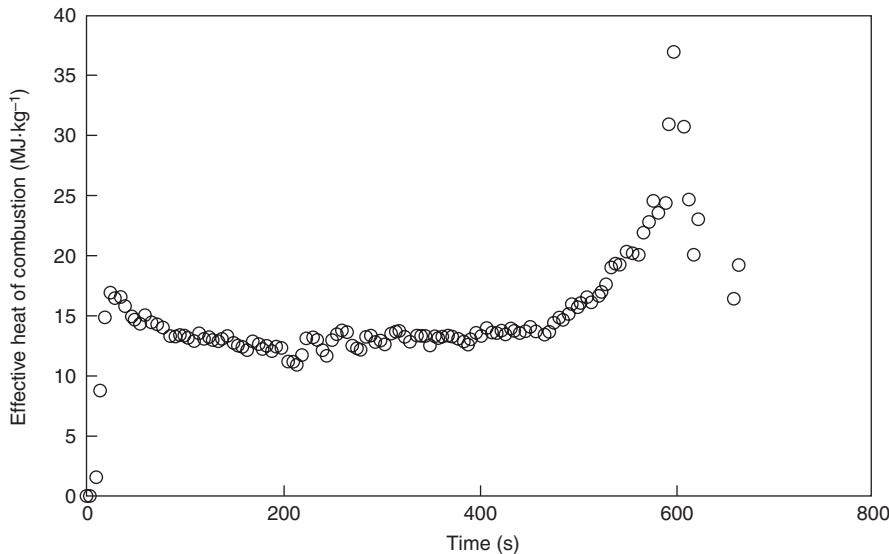


Figure 3-1.1. Effective heat of combustion for 17 mm thick Western red cedar, tested at an irradiance of 65 kW·m⁻².

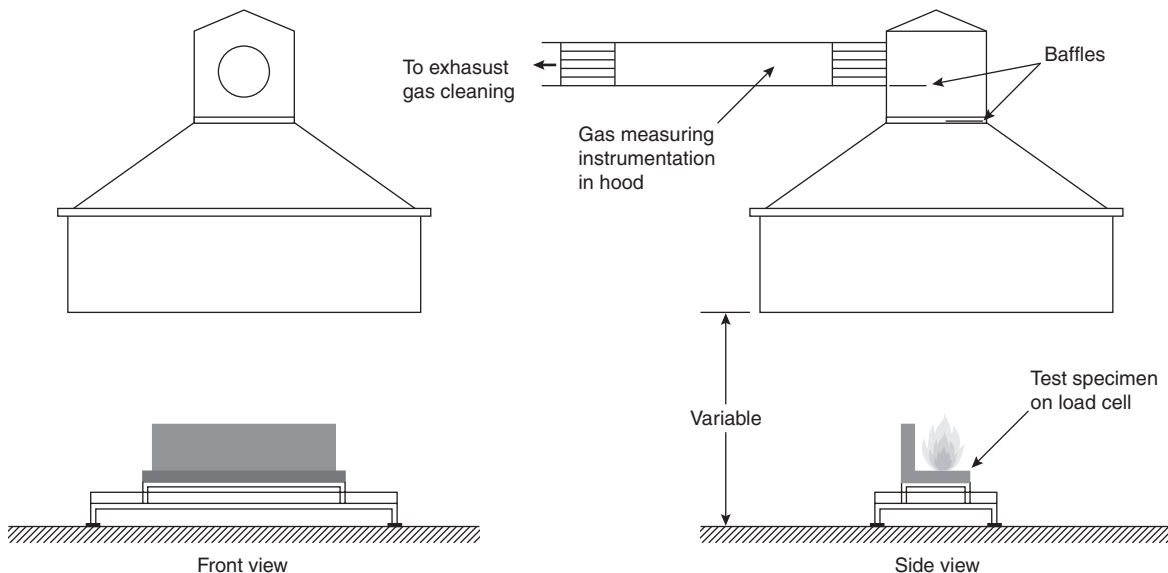


Figure 3-1.2. NORDTEST NT FIRE 032 calorimeter.

strongly affected by the surrounding room.¹¹ For most other commodities, this issue has not been studied. The degree by which the room affects the HRR is largely determined by how “open” the fuel package itself is. A liquid pool on the floor has a view factor of 0 to itself and 1.0 to the room. By contrast, the reason that chairs tend to be little affected by the room is that the chair “sees” its own surfaces to a significant extent, rather than being fully exposed to the room. Some useful error analyses of large open calorimeter measurements have been reported;¹² a

theoretical discussion of the ideal large-scale calorimeter has also been presented.¹³

Room fire tests should be commissioned when room effects are anticipated to be strong, or when a more precise estimate is needed. Apart from cost, there is a drawback to room fire testing. This is because the HRR measured in a room fire cannot be extrapolated to any rooms with larger ventilations. Open-burning HRR data could, by contrast, be applicable to such well-ventilated rooms.

The development of the modern room HRR test took place at several institutions, including Fisher and Williamson at the University of California,¹⁴ Lee at NIST,¹⁵ and Sundström at the Swedish National Testing and Research Institute.¹⁶ Room test standards can be found in NT FIRE 025¹⁷ and ISO 9705¹⁸ and the room test portions of ASTM E1537⁴ and ASTM E1590.⁵ A typical standard room fire test, ISO 9705 is shown in Figure 3-1.3. This test equipment is available for commercial testing in North America, Europe, and other places also.

Measuring the HRR, Bench Scale

To measure the HRR in a bench-scale test is nowadays an easy task. Most commonly, the cone calorimeter¹⁹ developed at NIST by Babrauskas will be used (Figure 3-1.4). These instruments are available at commercial and research laboratories worldwide. The procedures for conducting cone calorimeter tests are described in ASTM E1354²⁰ and ISO 5660.²¹ (See Section 3, Chapter 3.) Other HRR calorimeters, such as the Ohio State University apparatus or the Factory Mutual Research Corporation Flammability Apparatus are also in use at some laboratories. A textbook is available that discusses many of the details of HRR measuring technology.²² Thus, the modeler can assume that if at least enough material is available to run several small samples (100 mm × 100 mm, in the case of the cone calorimeter), an empirical HRR curve can be obtained by running bench-scale tests.

Measuring the HRR, Intermediate Scale

The newest experimental technology for determining the HRR is intermediate-scale calorimetry. Various earlier efforts have been made, but the first instrument to receive standards support is the ICAL, developed at Weyerhaeuser²³ (Figure 3-1.5). It has been standardized as

ASTM E1623.²⁴ This test method accommodates 1.0-m by 1.0-m specimens, which allows for complex or highly nonhomogenous constructions to be tested. However, since the data are still not of full scale, some additional analysis is needed to be able to utilize the test data in fire modeling.

Modeling Implications for Using Full-Scale HRR Data

If access is available to full-scale HRR data, then the task of defining the fire is on a solid basis. Even here, however, there are a number of problems and caveats. Apart from the obvious issue that the available full-scale data must be known to describe the specific fuel source in question (and not some possibly very differently performing similar item), there are some additional concerns. Supposing one finds full-scale test results on one's exact commodity, can the data simply be used unquestioningly? The answer, of course, is no. There are two main issues:

1. The available data may be open-burning calorimetry data. One must then determine whether an enclosure effect needs to be accounted for.
2. The available data may be room fire data, but the test enclosure may not correspond to the room for which modeling is to be done.

The first of these issues was briefly touched on previously. The availability of quantitative guidance is not reassuring. For upholstered chair fires in a room of about the size of the ISO 9705 room, one can estimate a 20 percent augmentation over the open-burn rates when considering fires in the 100- to 1000-kW range. For mattresses, the effect is large and without adequate guidance. For liquid pools, a pool submodel must be specifically present in the fire model used, since no simple approximation is adequate. For wood cribs, there are formulas for guidance,²⁵ although of course wood cribs are hardly a

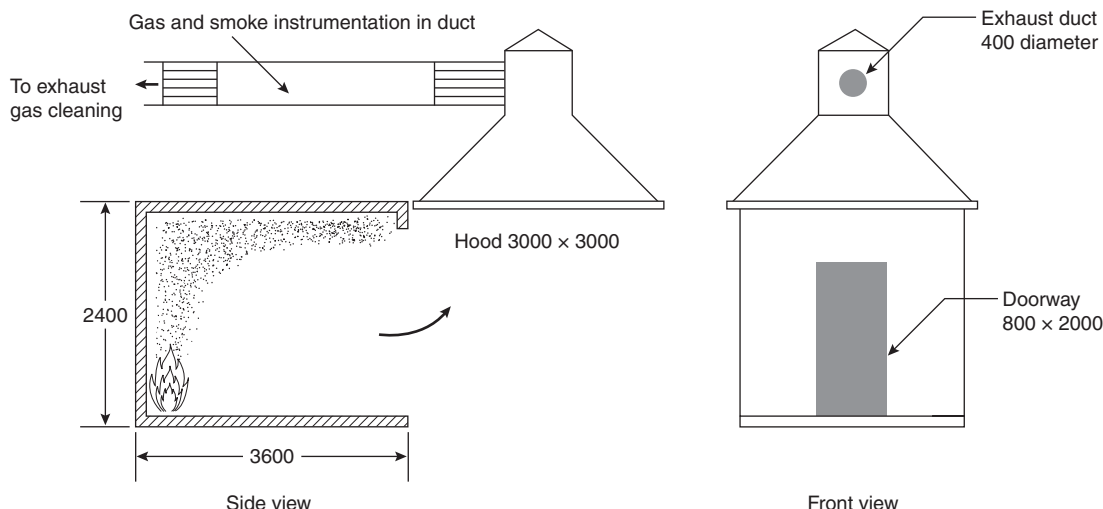


Figure 3-1.3. ISO 9705 room HRR test.

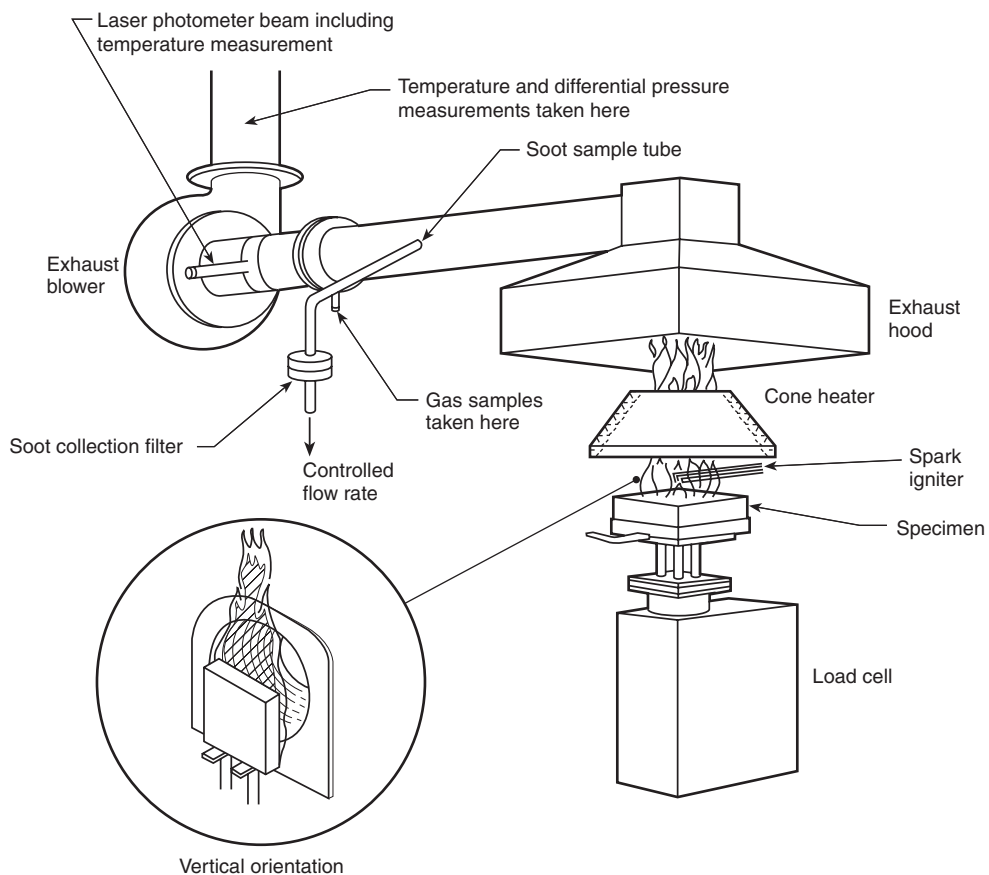


Figure 3-1.4. Bench-scale cone calorimeter.

feature of most real fires. For other combustibles, neither data nor guidance is available.

A very similar problem is faced when the modeler has available full-scale HRR data, but the test was run in a room of different size or ventilation conditions than is the intended application. Only two studies on this topic have been published in the literature. Kokkala and colleagues²⁶ compared some room wall/ceiling linings in a large room to the values obtained in the ISO 9705 room. Also, during the CBUF project some furniture fires were done in rooms of two scales.¹⁰ Neither of these studies looked at this issue comprehensively enough to yield numerical guidance.

Modeling with Bench-Scale HRR Data

If full-scale data on HRR are available, then these are simply used in the fire model. In many cases, however, such data are not available, often due to cost of testing or unavailability of large-size specimens. In such cases, it is desirable to be able to use bench-scale data, denoted as \dot{q}'' and measured in units of $\text{kW}\cdot\text{m}^{-2}$. With the bench-scale HRR, there are two main questions: (1) can it be predicted from some more fundamental measurements? and (2) how can the full-scale HRR be predicted from the bench-scale HRR?

Predicting Bench-Scale HRR from Fundamental Considerations

The former question has been of considerable interest to fire researchers for a number of years now, but practical engineering methods are not yet in hand. The task of predicting from more fundamental measurements is often described as creating a pyrolysis model because the degradation of a material when it is exposed to heat is known as pyrolysis. When a material heats up, degrades, ignites, and burns, complicated physical and chemical phenomena take place.

In addition to a change of phase, there is often flow of moisture, which must be accounted for simultaneously with heat flow. The material may undergo several different types of phase changes during the decomposition process, each accompanied by changes in density and porosity. Bubbles may be created within the bulk of the material and migrate to the surface. These may be accompanied by molten flow ejection at the surface. Oxygen may or may not directly interact with the surface to create a glowing combustion. Chemical reactions are commonly several in number and occur at different temperature regimes.

Finally, the material may undergo large-scale cracking, buckling, or sloughing. Each of these physical phenomena may significantly affect the rate of specimen

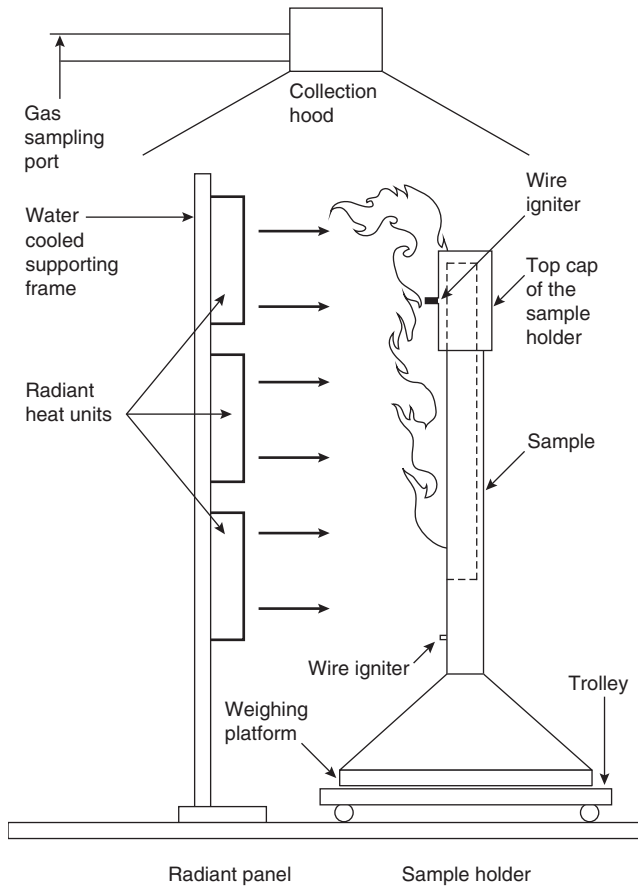


Figure 3-1.5. Intermediate scale ICAL calorimeter.

decomposition. From even this very brief description, it is clear that computing the pyrolysis of a material may be an enormously difficult task. Thus, today, for any fire hazard analysis purposes, HRR is invariably measured, rather than being computed from more fundamental theory.

Readers wishing to look more closely at the type of modeling needed to represent the pyrolysis process can refer to the dissertation of Parker²⁷ as a good example of how charring materials need to be treated. Some half-dozen other dissertations have been written on the same topic. Melting-type materials have proved to be even more interesting as a subject of advanced research. Several hundred papers have been published on various aspects of modeling the pyrolysis behavior of just one common material, poly(methylmethacrylate). References 28–34 can provide an introduction to this research.

Predicting Full-Scale HRR from Bench-Scale Data: Overview

Prediction of full-scale HRR is probably the single most important engineering issue for successfully modeling fires. Schematically, we may write that

$$\dot{q} = \int \dot{q}'' dA \quad (2)$$

This representation does not fully reveal the difficulties involved. More explicitly,

$$\dot{q}(t) = \int \dot{q}''(t, x, y, z) dA(t) \quad (3)$$

This makes more clear that the instantaneous per-unit-area HRR is a function of time and also of the location of the burning element. The instantaneous burning area, $A(t)$, is also a function of time. In addition, while we have not written this explicitly, $\dot{q}''(t)$ depends on the heating boundary conditions to the element. This quantity is usually identified as the *heat flux* or *irradiance* incident upon the element. The latter term is commonly used since, in full-scale fires, heating is dominated by the radiant component.

By examining the nature of $dA(t)$, we can also identify the role of flame spread in characterizing the HRR of full-scale fires. A bench-scale HRR test specimen is usually ignited nearly instantaneously over its entire surface. Full-scale fires, by contrast, nearly always exhibit finite spread rates. The flame spread velocity in a full-scale fire can be identified with the movement of the boundaries of the flame-covered area $dA(t)$. Flame spread may be occurring in several directions over walls, ceilings, floors, and over individual surfaces of discrete commodities burning in a space. Consequently, it can be seen that tracking flame spread and $dA(t)$ is a major undertaking. This task, by its nature, is incompatible with zone-type fire models because it presumes that a mechanism is in place to track very small surface elements. Even the publicly available field models have not yet attempted this task, although some work with proprietary models has been started.³⁵

Our approach will have to be restricted to identifying some of the attempts that have been made to simplify the problem in order to make it tractable for zone modeling. Simplifications are not yet possible for the general case. Instead, we must examine specific combustibles, for which appropriate flame spread representations have been worked out. This is illustrated in a number of discussions in the following sections. Before we do this, however, it is important to examine in more detail some of the variables that influence the HRR.

Predicting Full-Scale HRR from Bench-Scale Data: The Role of Irradiance

Engineering variables such as HRR, ignitability, flame spread, and so on are sometimes viewed as material fire properties. This is a useful view, but it must be kept in mind that such ‘properties’ are not solely defined by the physical/chemical nature of the substance. Instead, they are also determined by the boundary conditions of exposure. Boundary conditions can be divided into two types: (1) intended, and (2) unintended. Intended boundary conditions include irradiance (heat fluxes in room fires are dominated by the radiant component, so irradiance and imposed heat flux are used interchangeably) and thickness. Unintended boundary conditions, sometimes known as *apparatus dependencies*, include such factors as edge effects, perturbations due to nonuniform heating, drafts and uncontrolled air velocities, and so

forth. The latter are usually small if a well-designed test apparatus was used for measuring the response of the specimen.

The most significant intended boundary condition is the heat flux imposed on the specimen. This variable is crucial and no reduced-scale HRR results have meaning without knowing the irradiance. A test apparatus can impose a very wide range of specimen irradiances. For example, the cone calorimeter is capable of irradiances from zero to 100 kW·m⁻². For the user of the data, the crucial question becomes what irradiance to select when requesting a test. There are no simple answers to this, but we summarize here the main conclusions of Babrauskas.³⁶

The major consideration in the selection of the test irradiance must come from a knowledge of heat fluxes associated with real fires. In theory, this could range from zero to an upper value which would be

$$\varepsilon\sigma(T_f^4 - T_o^4)$$

where

ε = emissivity

σ = Stefan-Boltzmann constant (5.67×10^{-11} kW·m⁻²·K⁻⁴)

T_f = flame temperature (K)

T_o = ambient temperature (K)

But the emissivity approaches 1 for larger flames, and the ambient temperature contribution is insignificant, since $T_o \ll T_f$. The adiabatic flame temperature for most organic fuels is approximately 2300 K.³⁷ This would give a maximum irradiance limit of some 1500 kW·m⁻². This limiting value is, of course, nearly 10 times the actual maximum that is found in building fires of normal types. Thus, it is evident that the theoretical bounds to possible heat fluxes do not offer any guidance for testing. Instead, it is necessary to look at experimental data of heat fluxes found in actual building fires. We divide this into several types of building fires to be examined.

Heat fluxes in the vicinity of ignition sources: First, we must be clear by what is meant by *ignition source*. The innate definition of the term does not have limits—a burning building can be the ignition source to its neighboring building, as can a fire bomb. For discussion here, however, ignition sources can be limited to those that are small with respect to a fully developed room fire. Since the latter will be in the range of over 1 MW, the range of fires considered to be ignition sources might be taken as less than approximately 300 kW. A NIST study examined various ignition sources, ranging from 5 kW to over 300 kW.³⁸ The sources included both realistic igniting objects (cigarettes, matches, burning paper lunch bags, etc.) and schematic ones (small gas burners and wood cribs). It was found that, as the power output of the ignition source increased, the peak heat flux generally did not increase. Instead, only the area covered by the peak heat flux progressively increased. For flames ranging from a 0.3-kW Bunsen-type burner to a 50-kW wastebasket, the peak fluxes were remarkably constant at 30–40 kW·m⁻². Thus, for HRR from objects being ignited with a small ignition

source, a test irradiance of 35 kW·m⁻² can be selected. There are some unusual sources having a much higher flux, and these are discussed by Babrauskas.³⁶

For larger burners, such as used in room fire tests, higher heat fluxes may have to be assumed. For porous square-faced gas burners, the wall heat flux was found to depend on the burner face size.³⁹ In some cases, fluxes up to 65–80 kW·m⁻² were noted, although for most cases fluxes of 30–50 kW·m⁻² are considered appropriate.⁴⁰

At the extreme, ignition can occur due to a high velocity jet, such as from a failure on an oil-drilling rig. There, heat fluxes in the vicinity of 150–300 kW·m⁻² have been observed.⁴¹ Such situations, however, are very specialized. For ignitions from small wood cribs or other solid-fuel ignition sources, it can be estimated that the heat flux to adjacent objects is in the same 35-kW·m⁻² range as for small flaming sources. The picture is more complicated, however, for the heat flux from these sources to the object underneath. These heat fluxes may be much higher,³⁶ but they are highly nonuniform and difficult to model.

Heat fluxes in preflashover room fires: After ignition, the combustibles in a room can be considered to be exposed to preflashover conditions. Heat fluxes occurring in preflashover room fires will vary widely. Away from the initial source of fire there will be essentially no heating at all. Near a small initial fire source, heat fluxes of the sort described in the preceding section will be seen. With increasing fire spread and involvement, a hot gas layer will build up below the ceiling. The heat fluxes will be significantly hotter within this layer than in lower spaces. Söderbom⁴² found values typically <45 kW·m⁻² at the center of the ceiling during preflashover fires. The value at the floor level is, of course, always <20 kW·m⁻² prior to flashover, since attaining 20 kW·m⁻² at floor level is one definition of flashover.¹⁵ Since there is surprisingly little general guidance on this point, the user will have to make some assumptions or ad hoc calculations.

Heat fluxes on burning walls: Heat fluxes from burning items of larger types have, in general, not been studied in enough detail to be systematically known. The notable exception is for upward flame spread on vertical surfaces. For this configuration, a number of studies have explored the heat fluxes from the flame to the yet-unignited portion of the surface. Hasemi studied this problem in detail⁴³ and provided correlations. For his experiments, peak values of approximately 25 kW·m⁻² were seen for the region downstream of the ignited area, but before the tip of the flames; beyond the flame tip, fluxes were no longer constant, but dropped off further downstream. Additional similar data have also been presented in a summary form.⁴⁴ Work by Kulkarni and coworkers has enlarged the diversity of material types that have been studied.⁴⁶ The value of 25 kW·m⁻² is seen from these more extensive studies to be the lower bound of where data are clustered—most of the data are in the interval from 25 to 45 kW·m⁻². Thus, a value of 35 kW·m⁻² might better capture the mean behavior.

A 35-kW·m⁻² heat flux, then, can be used to characterize the peak level of heating to a vertical surface ele-

ment from its own upstream flame, just prior to its ignition. This value will need to be increased if the material is so situated as to be in a hot gas layer that is accumulating in the upper reaches of the room. Apart from the data of Söderbom, discussed above, this additional heating has not been studied in detail.

Heat fluxes in postflashover room fires: The maximum temperatures actually seen in postflashover room fires are approximately 1100°C. A perfect black-body radiator at that temperature would produce heat fluxes of approximately 200 kW·m⁻². Actual heat fluxes measured in post-flashover room fires can come close to this value, but are usually somewhat lower. For instance, examining the extensive room burn data of Fang,⁴⁶ one finds the ranges of experimental results shown in Table 3-1-1.

One might reasonably conclude that a heat flux of approximately 150 kW·m⁻² would be needed to properly represent the environment of the postflashover room fire. Today's bench-scale HRR apparatuses, however, can only go to about 100 kW·m⁻² or less. Interestingly, the inability realistically to create the heat fluxes of the postflashover fire has not been seen to be a problem in fire testing. Often, the situation is avoided in its entirety by assuming that the maximum burning rate that will occur within the room is consistent with the available oxygen supply.⁴⁷ Nonetheless, if for more detailed fire modeling the HRR of individual items in the postflashover fire would be required, such high heat-flux values would be required.

The Dependence of the HRR on the Heat Flux

In the simplest case, the relationship of the HRR to the irradiance is very simple, as shown in Figure 3-1-6. Here, we see that the HRR depends in a linear manner on the irradiance. The curve does not pass through the origin due to the existence of flame flux. The total heat flux seen by the specimen can be viewed as comprised of two components: the external irradiance and the flux from its own flame. Only if the flame flux = 0 will the curve pass through the origin. Otherwise, the *x*-axis intercept is equal to (minus) the flame flux.

Flame flux is very difficult to measure experimentally, as decomposing materials tend to foul the instrumentation and invalidate the readings. A value of approximately 35 kW·m⁻² has been reported for the flame flux of PMMA burned in the horizontal orientation in the cone calorimeter.⁴⁸ In another study, estimates of flame flux were made for several plastics burned in a similar manner.⁴⁹ These showed 30, 25, and 14 kW·m⁻², respectively, for nylon,

polyethylene, and polypropylene. The furniture research program CBUF¹⁰ determined that the flame fluxes in the cone calorimeter associated with fabric/foam composites are in the range 20–25 kW·m⁻².

Finally, some data are available⁵⁰ for liquids in containers of similar size as a cone calorimeter specimen holder. Flame fluxes of about 10–15 kW·m⁻² are seen for alcohols and about 15–20 kW·m⁻² for some hydrocarbons (heptane, methylmethacrylate, toluene, styrene). The value appears to depend only slightly on the chemical nature of the fuel. Gore et al.⁵⁰ specifically determined that this value does not increase with increasing fuel-sooting tendencies. All the above data refer specifically to the horizontal specimen orientation. There is very little data for the vertical orientation, although Janssens deduces that for wood products the vertical orientation flame flux is approximately 10–15 kW·m⁻², of which only about 1 kW·m⁻² is due to radiation.⁵¹

With regard to linearity, the following very broad generalization can be made: for many products, over a substantial heat flux range, the HRR is linearly proportional to the heat flux. This generalization, however, will be seen to have only limited utility, since it is rarely known a priori whether it will be obeyed. Furthermore, there is a distinct tendency for most materials and products to deviate from linearity at very high and at very low heat fluxes. This behavior is best illustrated by an example. Some data obtained by Sorathia and coworkers⁵² on advanced composites are shown in Figure 3-1-7. It is clear that the results are somewhat linear, but not precisely so. Some old, but still suggestive, data were obtained in the 1970s by Parker.⁵³ His results for a number of fire-retardant grades of polyurethane foam are shown in Figure 3-1-8. Of the five formulations shown, three show somewhat linear behavior, whereas two clearly do not. For most categories of specimens, however, substantially more linear behavior can be seen.

Predicting Full-Scale HRR from Bench-Scale Data: The Effect of Thickness

The same material may be used in different applications of varying thicknesses. Thickness does affect the HRR response. In general, a thin material will show a

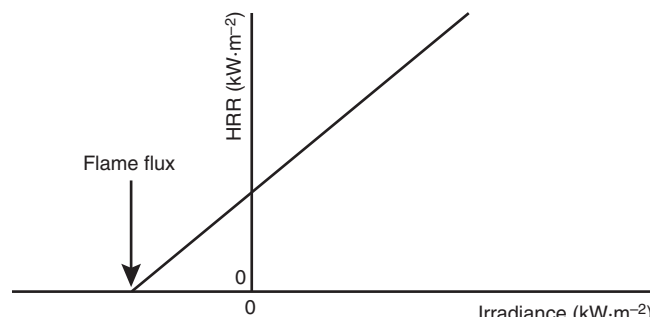


Figure 3-1-6. *The simplest form of HRR dependence on irradiance.*

Table 3-1-1 *Heat Fluxes Measured in Postflashover Room Fires*

	Heat flux (kW·m ⁻²)		
	Ceiling	Walls	Floor
Maximum	106–176	116–229	119–143
Average	68–147	91–194	—

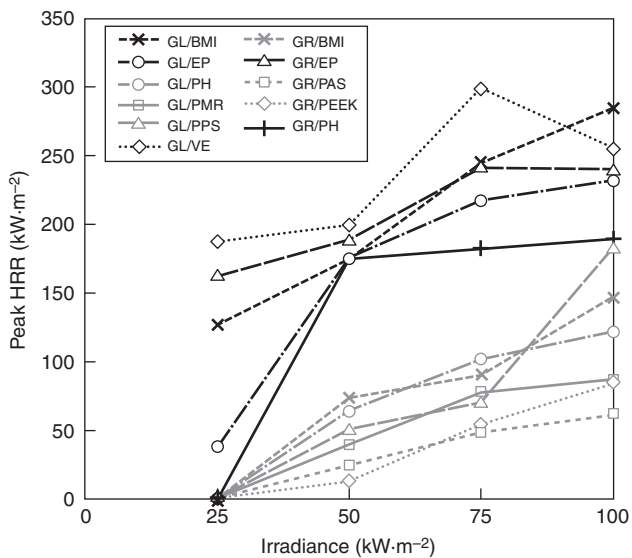


Figure 3-1.7. Response to irradiance of some advanced composite materials. Reinforcements: GL = glass, GR = graphite. Resins: BMI = bismaleimide, EP = epoxy, PAS = polyaryl sulfone, PEEK = poly(ether ether ketone), PH = phenolic, PMR = monomer-reactant polyimide, PPS = polyphenylene sulfide, VE = vinyl ester.

spike of HRR, whereas a thick product will commonly (but not always) show some quasi-steady period of burning. This variable has surprisingly been little explored and not much guidance is available. Perhaps the best illustrative example is due to Paul;⁵⁴ his data for PMMA are shown in Figure 3-1.9. This illustrates that near-steady burning behavior can be seen when the thickness ap-

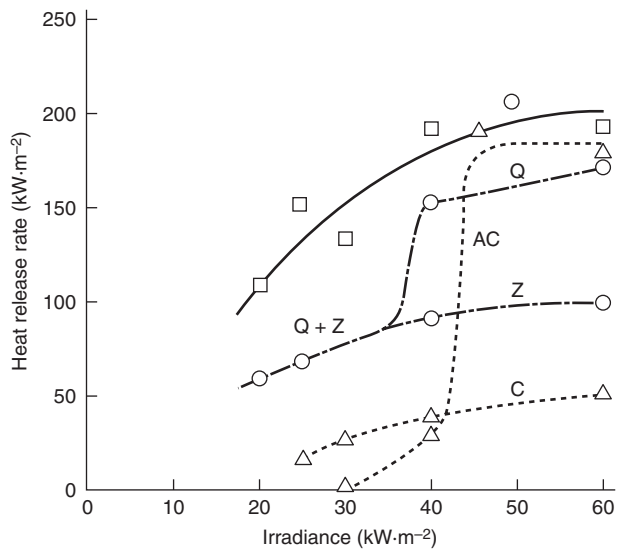


Figure 3-1.8. The results for FR polyurethane foams, as measured in the NBS I calorimeter by Parker.

proaches approximately 20 mm. This is true for many solid materials—thicknesses of this range are required in order to approach steady-burning conditions. A compilation of thickness data for polyethylene,⁵⁵ for example, shows that even 10-mm-thick specimens have not reached steady burning.

For foams, by contrast, no reasonable amount of thickness will normally show steady-state burning. Of special interest are polystyrene (PS) foams. These are normally very low-density foams of about $16 \text{ kg}\cdot\text{m}^{-3}$. When exposed to heat, PS foams tend to collapse their cell struc-

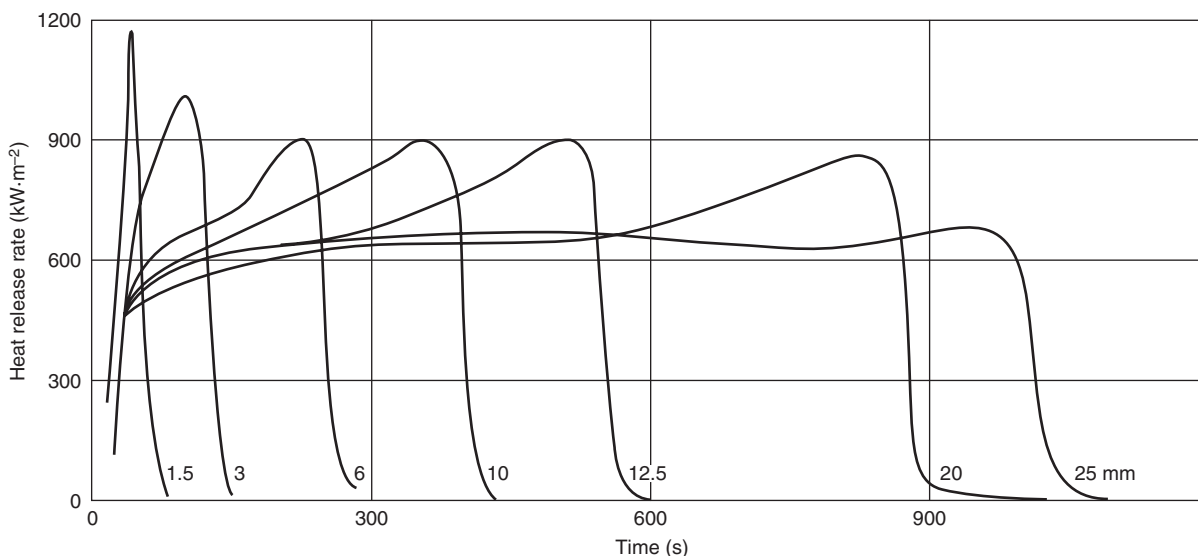


Figure 3-1.9. HRR for PMMA of various thicknesses.

ture and become a thin liquid film. This occurs before ignition takes place. Thus, after ignition, what is burning is a thin coating on whatever was the substrate. This is the reason why the HRR of PS foams tends to be so apparatus dependent that it is hard to discern any intrinsic response of the material at all: its performance is totally dominated by the specimen holder and edge conditions.⁵⁶

Predicting Full-Scale HRR from Bench-Scale Data: The Effect of Orientation

Routine testing in the cone calorimeter is specified by the ASTM standard to be done only in the horizontal orientation. This is because (1) many products show serious testing difficulties (e.g., melting) when tested in the vertical orientation and (2) conversely, the vertical orientation does not provide a better simulation of the burning of vertical objects. This is because there is no direct connection between flame fluxes in a bench-scale test and in a real-scale fire. The actual fluxes occurring in a real-scale fire are determined by many factors, including size of room, thickness of hot gas layer, flame spread occurring over other surfaces, and so forth. None of these are subject to the control of the bench-scale apparatus but, rather, must be specifically modeled.

Orientation effects will also make a difference during the bench-scale testing of specimens. Even though routine testing is done only in the horizontal orientation, a small body of work exists for which both orientations were explored. This is best illustrated by the results of two round robins that were conducted on the cone calorimeter, one under the auspices of ASTM and one under ISO. The data were taken at two irradiances, 25 and 50 kW·m⁻², and the results are briefly summarized in the Appendix to ASTM E1354.²⁰ Such results are especially valuable since the values tabulated are the best estimate and are not subject to the specific errors of any one particular laboratory. A comparison for the peak HRR is shown in Figure 3-1.10, while the comparison for the 180-s average value of HRR is given in Figure 3-1.11. In both cases, the data points plotted represent all the data analyzed within the two round robins for which horizontal and vertical orientation results were obtained on a product.

For the peak HRR, a least-square regression gives that

$$\dot{q}_{pk}''(V) = 0.71\dot{q}_{pk}''(H) \quad (4)$$

while for the 180-s average HRR, the corresponding relation is

$$\dot{q}_{180}''(V) = 0.72\dot{q}_{180}''(H) \quad (5)$$

Both can be adequately approximated by the general relation that

$$\dot{q}''(V) = 0.7\dot{q}''(H) \quad (6)$$

This clearly verifies that the thin, boundary layer-type flames occurring in the vertical orientation provide a lower heat flux than the pool-like flames in the vertical orientation.

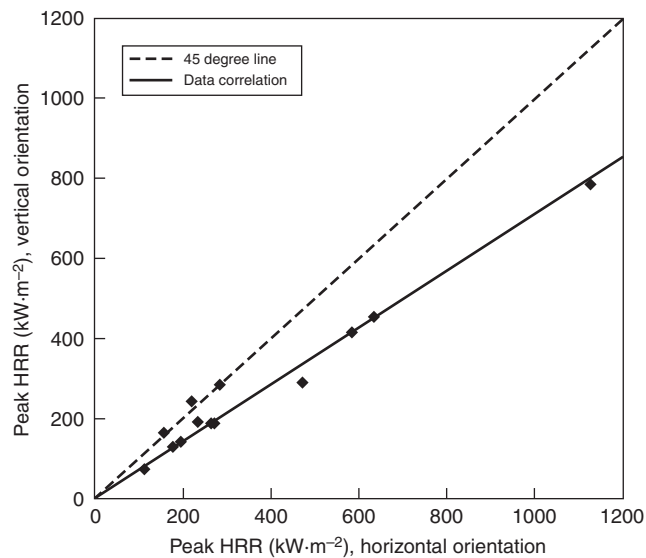


Figure 3-1.10. Orientation effect on the peak HRR, as determined from two cone calorimeter round robins.

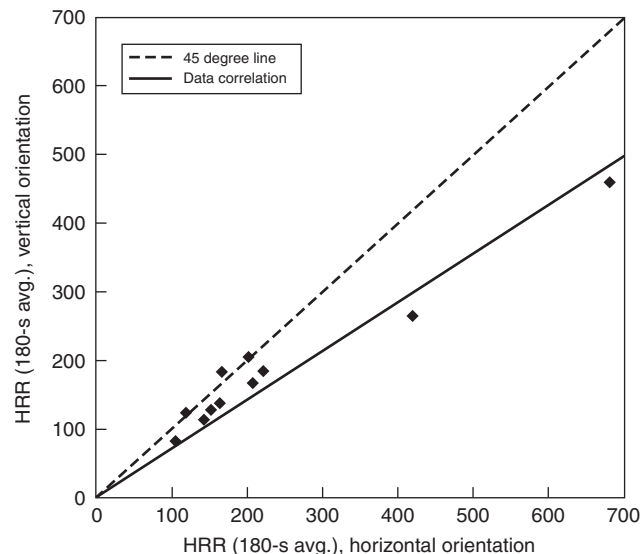


Figure 3-1.11. Orientation effect on the 180-s average HRR, as determined from two cone calorimeter round robins.

Predicting Full-Scale HRR from Bench-Scale Data: Other Controlling Variables

Numerous other variables can, in principle, affect the HRR of specimens. This can include local velocities, scale and intensity of turbulence, and so on. For room fire modeling purposes, such effects can be assumed to be small. Two effects that are often of specific interest, however, are scale and vitiation effects. Scale effects are, in principle, normalized out when the per-unit-area variable is computed. These effects will not be zero, however. One factor

affecting them is the flame flux found in the bench-scale test apparatus. This will have some scale effect.

The studies in this area are not extensive. A study using a custom cone calorimeter with 200-mm × 200-mm specimen size tested horizontally found only a very small-scale effect, when compared to standard cone data.⁵⁷ A comparison between the ICAL and cone calorimeters for a series of wood products showed that systematic differences were surprisingly small, despite the 10× difference in linear dimension of the specimens.⁵⁸ Note, however, that in this case the specimens were tested in the vertical orientation. In such orientation, specimen flames are thin and there is little variation with scale. Of additional guidance is a study by Orloff⁵⁹ in which a vertical 3.56-m-high PMMA slab was burned. The mass loss rate, per unit area, was found to be

$$\dot{m}'' = 5.32 + 3.97x \quad (7)$$

where x is the vertical distance (m). Note that this result implies that there is but little variation for specimens with height <0.5 m, but significant increases for very large specimens.

In the case of objects burning in the horizontal orientation, large pool flames surmount the specimen. The flux from such flames will vary greatly with scale. Guidance provided for estimating burning rates of pools (see below) can be directly applied to this case.

HRR for Real Products

For many objects and commodities, published HRR are not available; thus, laboratory tests will have to be run if an answer is needed. For some commodities, however, exemplar data have been published and are available to the public. The tabulated test data can be very useful as generic representatives of items constructed of these materials, and with this general geometry. Where the analysis is intended to evaluate a specific product, that product should be tested in a suitable calorimeter and the data then used in the analysis. It must be strongly emphasized that in no case should generic database information be used when the purpose of the analysis is to seek regulatory approval for a product or to demonstrate the performance of a specific product in a court of law. In all such cases, actual laboratory testing on the item in question must be done.

In the case of a few product categories, methods are available for estimating large-scale HRR on the basis of bench-scale HRR data. The question then becomes, where can bench-scale HRR data be found? For a few product categories, some data are provided in the sections below. For the user interested in a more comprehensive look at bench-scale HRR data, the textbook *Heat Release in Fires*²² and the cone calorimeter bibliography⁶⁰ are good sources. Also, Section 3, Chapter 4, "Generation of Heat and Chemical Compounds," provides some data on pure chemicals.

For convenience, the sections below are arranged alphabetically by type of product. However, many of the ideas are an offshoot of pioneering studies on pool fires. Thus, it is recommended that the user first read through the section on pools before progressing to other product categories.

Artificial Plants

Some data are shown in Figure 3-1.12.⁶¹

Bookcases, Casegoods, and Storage Units

In most cases, for storage furniture the fire hazard is created by the contents, not by the furniture item itself. An exception is modular storage units made of thermoplastic materials, which tend to burn very vigorously,⁶² but quantitative HRR data have not been published. Storage furniture made of wood or wood covered with thin layers of thermosetting plastic tend to resist ignition unless filled with combustible contents. Some data are illustrated in Figure 3-1.13. The test arrangement for metal

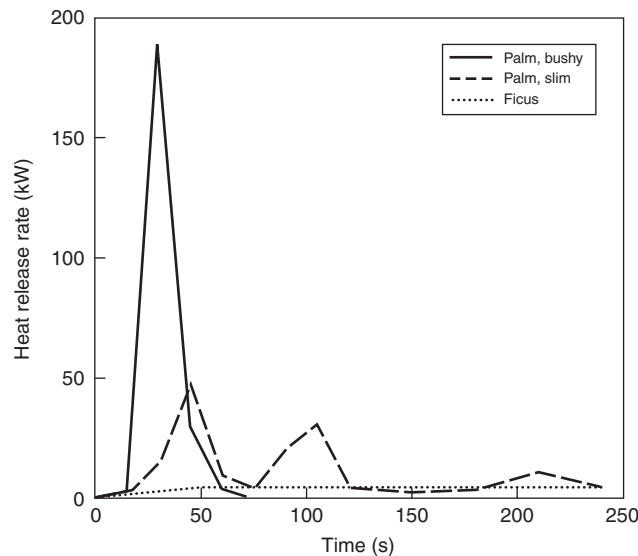


Figure 3-1.12. Artificial plants.

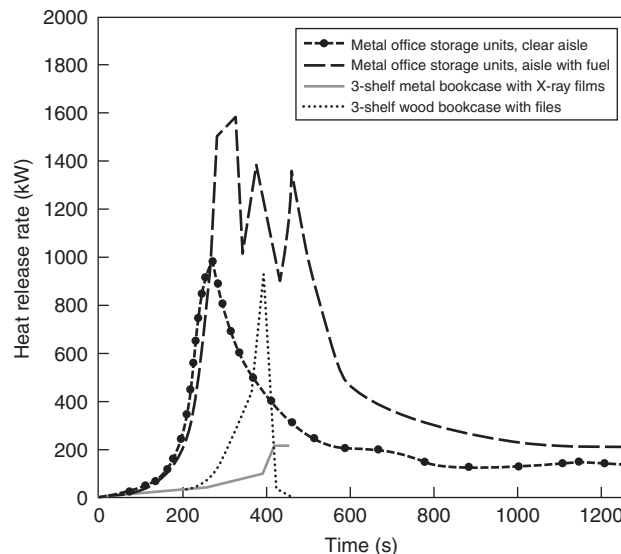


Figure 3-1.13. Storage units.

office storage units¹¹⁰ involved two tiers of shelving with a 0.76-m aisle in between. Each test contained 480 kg of paper fuel load in shelving units totaling 1.67 m² of floor area. For the configuration with fuel in the aisle, only 3 kg was placed in the aisle, but this extra fuel provided a major difference in fire severity. The data on X-ray film shelves and wooden bookcases are from Särdqvist.⁶¹ For storage of paper files, it is known that the arrangement is more important than the quantity of fuel. Especially, storing files in cardboard boxes so that they can exfoliate exacerbates burning. Exfoliation occurs when paper folders are placed parallel, rather than perpendicular, to the front of the shelf. When fire attacks the front, folders progressively fall out and burn in the aisle. While well known, this effect has not been documented with HRR testing.

Cabinets (Electronic, Business Machine, etc.)

A limited amount of testing of business machine cabinets was reported by Babrauskas et al.,⁶³ as shown in Figure 3-1.14. Two series of tests on steel cabinets used for housing nuclear power-plant control electronics were conducted by VTT.^{64,65} These showed HRR peaks of 100–200 kW. The authors also proposed computation formulas for predicting the HRR level that causes internal cabinet flashover and that causes burning to reach a ventilation limit.⁶⁶ Such computations are based on the assumption that air flow occurs only through fixed cabinet openings.

Carpets and Other Floor Coverings

Carpets that are in the room of fire origin are not likely to contribute significantly to fire growth. This has been demonstrated experimentally.⁶⁷ It is also consistent with modeling considerations: the floor area is convectively cooled and normally has the smallest view factor to the hot regions, which tend to be in the upper regions. The

same material may be much more hazardous if installed on wall surfaces, although it must be pointed out that commercial textile wall coverings are normally similar, but not identical, to carpeting.

The hazard from floor coverings arises when an unsuitable product is used in a corridor, especially one that is an escape path. In such situations, very rapid flame spread and high HRR can result due to the fact that the corridor floor covering becomes involved due to a room fire feeding it. Not only carpeting, but solid materials such as linoleum and wood parquet flooring are also subject to becoming fully involved down the length of a corridor. A recent study has quantified this behavior and has also provided a predictive method.⁶⁸ It is shown that floor coverings with a peak HRR of less than 200 kW·m⁻², measured in the cone calorimeter under an irradiance of 25 kW·m⁻² tend not to show accelerating flame spread down a corridor.

Some carpeting materials can present a rapid fire spread hazard when installed on stairs. A residential carpet installed over a stairway has been measured to produce a peak HRR of 3 MW.⁶⁹ The test carpet was 80 percent acrylic and 20 percent nylon; no other types of carpeting were explored.

Chairs, Stackable

Stackable chairs are most commonly used in hotels and banqueting facilities. These chairs typically have metal legs and frame and only a small amount of combustible padding or structural material. Thus, a single chair can be expected to represent negligible hazard. However, when not in active use, they are stored in tall piles and many of these piles may be aggregated together. The hazard of even a single pile of modest height can be notable. Figure 3-1.15 illustrates some typical data on nonupholstered, molded chairs.⁶¹ Figure 3-1.16 illustrates

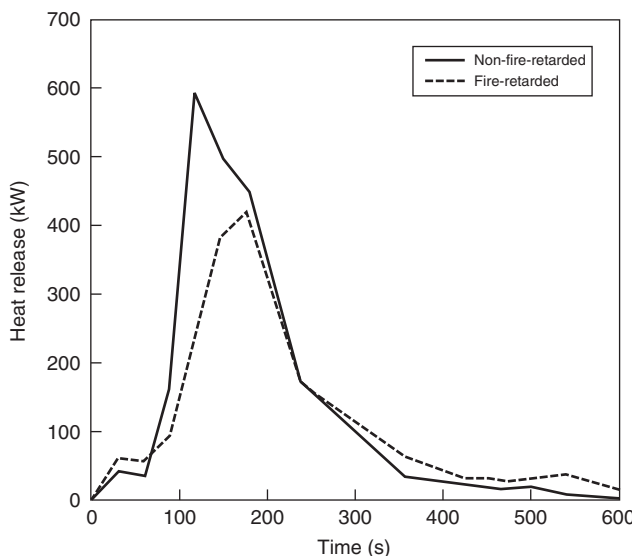


Figure 3-1.14. Business machine cabinets made from polyphenylene oxide plastic.

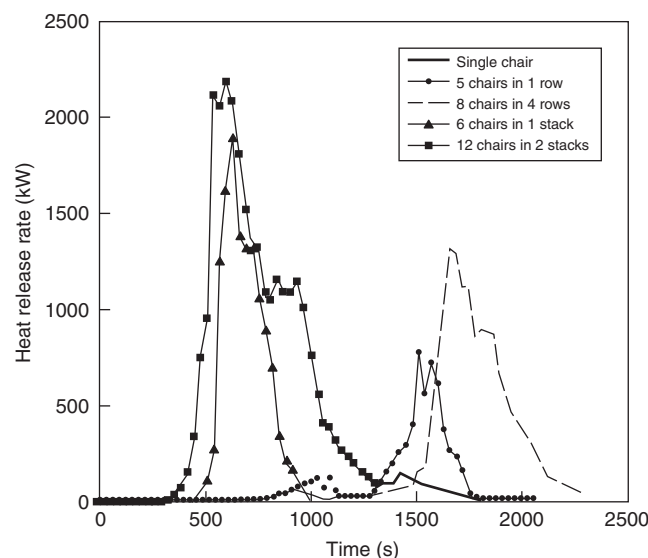


Figure 3-1.15. Stackable chairs, polypropylene with steel frame, no padding.

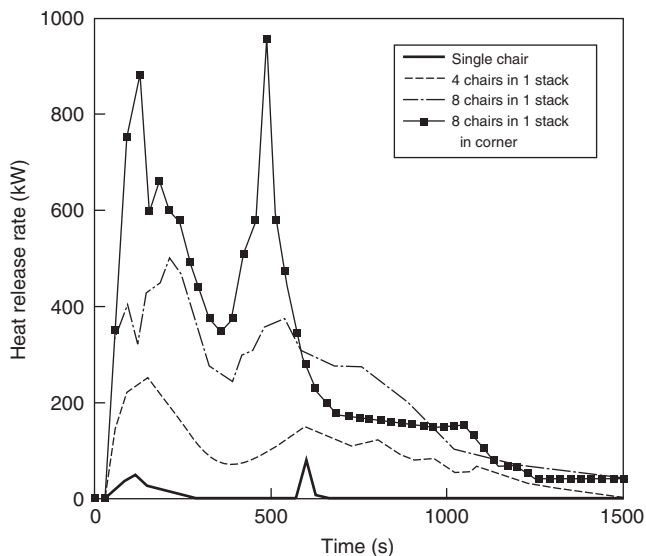


Figure 3-1.16. Metal-frame, upholstered stacking chairs.

some data on lightly upholstered chairs.⁷⁰ For the latter, the effect of radiant augmentation from burning in a corner is also illustrated.

Christmas Trees

Some tests on Christmas trees were reported by VTT⁷¹ and by Damant and Nurbakhsh.⁷² Newer studies, however, indicated that these tests, which examined only a few trees, did not capture the full range of HRR values associated with Christmas trees. The main variables that govern the HRR of Christmas trees are the following:

- Moisture content of the needles
- Mass of the tree
- Species
- Ignition source used

Moisture is the dominant variable and it had not been studied previously. The results of an extensive series of fire tests⁷³ on Douglas fir (*Pseudotsuga menziesii*) trees are shown in Figure 3-1.17, while the HRR of typical tests is illustrated in Figure 3-1.18. The tested trees were about 2.1 m tall, had an average mass of 11 kg, and had been watered according to various watering programs. The average tree was kept for 10 days prior to testing. The relation of the curve fit in Figure 3-1.17 is

$$\dot{q}/\text{mass} = e^{5.84 - 0.017M}$$

where M = moisture of needles (%) and the units of \dot{q}/mass are $\text{kW}\cdot\text{kg}^{-1}$. Moisture is measured on a dry basis, so values can readily exceed 100 percent; also note that it is the needle moisture that governs the burning behavior—trunk moisture is not a relevant variable. To ignite Douglas fir trees with a small flame requires that the moisture content be below 50–60 percent. Otherwise, ignition is still possible if using larger combustible objects. In the work re-

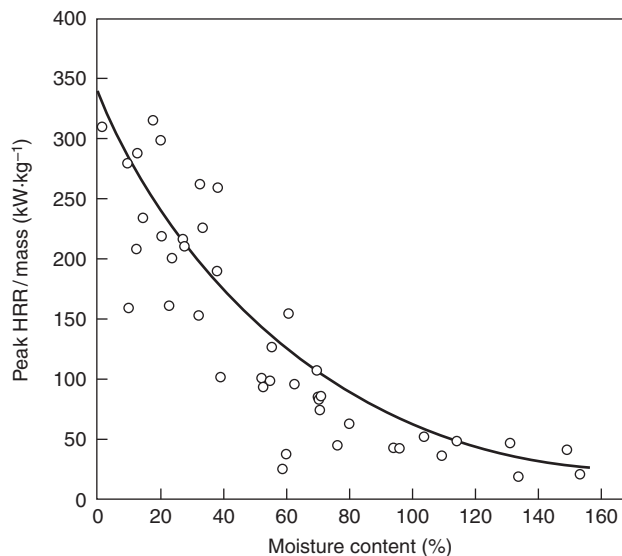


Figure 3-1.17. The peak HRR for Douglas fir Christmas trees, as a function of moisture and mass.

ported, the trees that could not be ignited by a small flame were all ignited by first igniting wrapped gift packages placed under the tree. For design purposes, it should be adequate to assume that the heat-release curve is a triangle. This requires knowing only the peak HRR and the total heat released. To estimate the latter, it was found in the tests that the Christmas trees showed an effective heat of combustion of $13.1 \text{ MJ}\cdot\text{kg}^{-1}$.

Thus, from knowing the mass of the tree and the effective heat of combustion, the total heat release may be

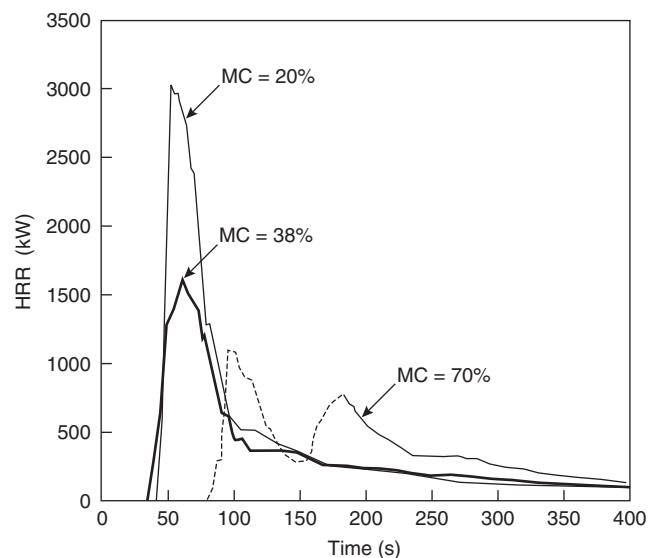


Figure 3-1.18. Typical HRR curves of Douglas fir Christmas trees.

estimated. The needle moisture may not be known for design purposes. It is governed both by the watering program and by the innate biology, for example, the species, of the tree. No model is available at the present time that can predict moisture. However, research indicated that Douglas firs are a notably short-lasting species. The data points shown in Figure 3-1.17, with one exception, represent trees that had been on display for less than 16 days; some were watered carefully and regularly, while others were not. Other species of Christmas trees, such as Noble fir or Fraser fir are considered to be longer lasting, but are less commonly bought.

A smaller test series on Scotch pine trees was reported by Stroup et al.⁷⁴ They examined trees of 2.3–3.1-m height and mass between 9.5 and 20.0 kg; with one exception, the trees were of mass 12.7 kg or greater. Apart from one tree that is not considered here since it was not successfully ignited, the trees were left without water for three weeks in a room at 50 percent relative humidity and 23°C. Ignition was with an electric match to a lower branch of the tree. The Scotch pines were substantially taller and heavier than the Douglas firs, so it is not surprising that higher peak HRR values were attained. The peak HRR values ranged from 1620 to 5170 kW. Normalized per mass, the average was 183 kW·kg⁻¹, with the range being 103–259 kW·kg⁻¹. The moisture of the branches was not recorded, but presumably was <20 percent in all cases. Comparing to the above results, Douglas firs showed about 160–330 kW·kg⁻¹. This would suggest that there is a species effect and that Scotch pines show an HRR/mass ratio ≈ 0.75 of that found for Douglas firs. This conclusion is very tentative, however, since the test programs did not use the same test protocol. Part of the difference might also be attributed to a height effect, since this cannot separately be taken into account.

Clothing Items

Two men's jackets (anoraks) were tested by SP¹⁰ as potential ignition sources. One was a polyester jacket with an outer fabric comprising 65/35 percent cotton/polyester, an inner fabric of 100 percent polyamide, and a filling of 100 percent polyester wadding. Total weight was 739 g. The other was an acrylic jacket with a fabric of nylon/Taslan and a filling of 100 percent acrylic wadding. Total weight was 618 g. The HRR of these jackets are shown in Figure 3-1.19.

Coffee Makers

The HRR of several coffee makers is shown in Figure 3-1.20.⁶¹ The units had total weights of 0.8 to 1.3 kg.

Computer Tapes

A test was conducted on a set of open steel shelves holding 90 computer tapes.⁷⁵ The tapes were 300 mm in diameter and the total mass of 99 kg was distributed on four shelves, two tiers deep. The results are indicated in Figure 3-1.21.

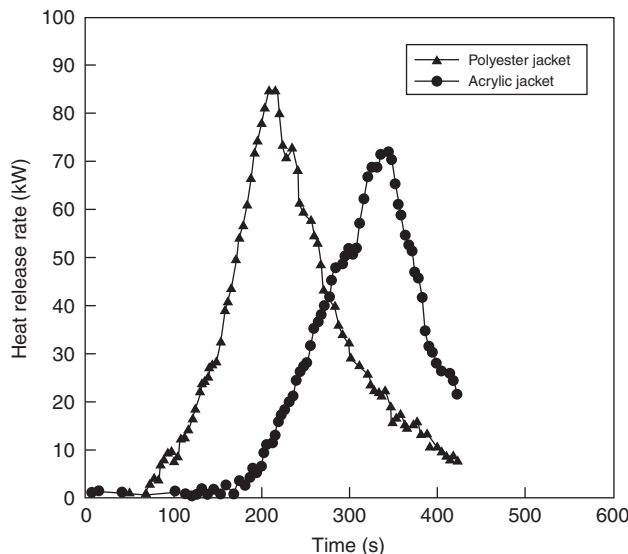


Figure 3-1.19. Two men's jackets.

Cribs (Regular Arrays of Sticks)

Cribs here are taken to mean regular, three-dimensional arrays of sticks. Each stick is of a square cross section and of a length much greater than its thickness. The sticks are placed in alternating rows, with an air space separating horizontally adjacent sticks. (See Figure 3-1.22). Wood crib burning rates have been studied longer than any other product, with early data available from the 1930s.⁷⁶ Different analysis formulas have been presented over the years by numerous authors. Here we present a method of analysis²⁵ based largely on the voluminous experimental data of Nilsson⁷⁷ on wood cribs and the func-

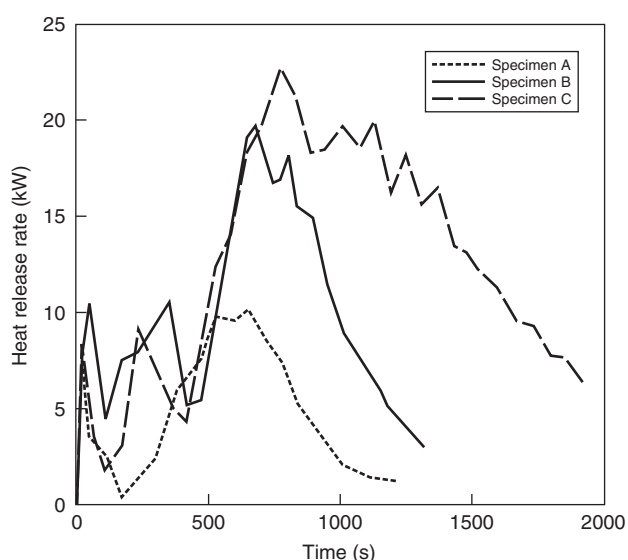


Figure 3-1.20. Coffee makers.

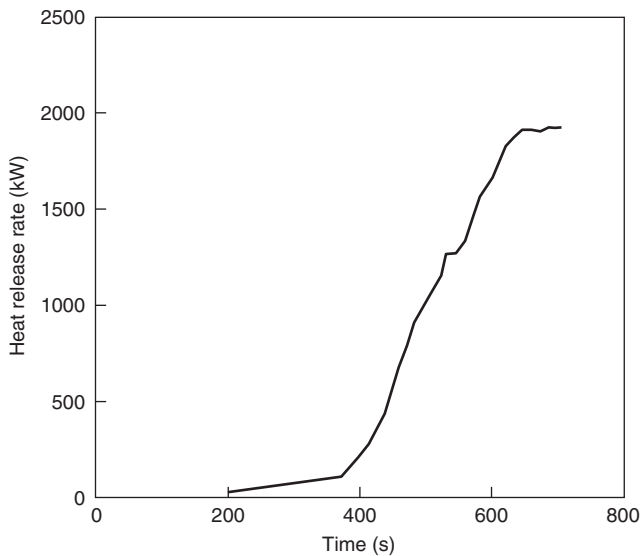


Figure 3-1.21. A rack of computer tapes.

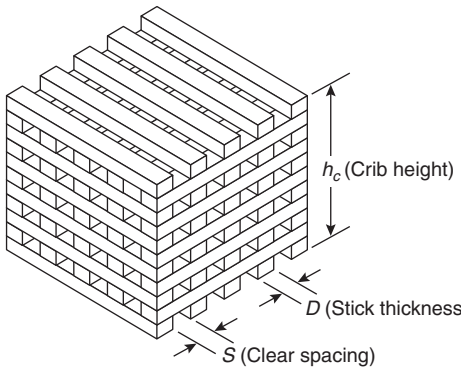


Figure 3-1.22. General arrangement of a wood crib.

tional form suggestions of Yamashika and Kurimoto.⁷⁸ The scant available data on plastic cribs are from Harathy⁷⁹ and Quintiere and McCaffrey.⁸⁰ The conditions of most interest are when cribs are ignited instantaneously, as with the use of a small amount of combustible liquid underneath. The first group of equations below represents this case. There is occasionally an interest in a crib fire where only one end of a crib is ignited, and a slow fire propagation is seen. An analysis for this situation has also been made.⁸¹ A similar analysis is also available for the center-ignited, fire-spreading crib scenario.⁸²

For cribs ignited uniformly overall, it is observed that the burning rate can be governed by one of three conditions: (1) the natural limit of stick surfaces burning freely; this limit applies to cribs with wide interstick spacings; (2) the maximum flow rate of air and combustion products through the air holes in the crib; this governs for tightly packed cribs; and (3) the maximum oxygen that can be supplied to the room; this effect is discussed separately, below. The numerical expressions corresponding to the three conditions are as follows:

(1) Fuel surface control:

$$\dot{m} = \frac{4}{D} m_o v_p \left(1 - \frac{2v_p t}{D} \right) \quad (8a)$$

or

$$\dot{m} = \frac{4}{D} m_o v_p \left(\frac{m}{m_o} \right)^{1/2} \quad (8b)$$

with

$$m = m_o - \sum_i^t \dot{m}_i(t_i) \Delta t \quad (9)$$

(2) Crib porosity control:

$$\dot{m} = 4.4 \times 10^{-4} \left(\frac{S}{h_c} \right) \left(\frac{m_o}{D} \right) \quad (10)$$

(3) Room ventilation control:

$$\dot{m} = 0.12 A_v \sqrt{h_v} \quad (11)$$

The *least* of Equations 8a, 10, or 11 is to be taken as the governing rate (Equation 11 is discussed below). Equation 8b is necessary instead of the simpler Equation 8a when a switch of burning regime occurs during the course of the fire, for example, the burning changes from porosity control to fuel surface control at some point. This can happen since Equation 8a (or 8b) is a time-dependent expression. Thus, a crib may start burning under porosity or room ventilation-controlled conditions, then later switch to fuel surface control.

In the above equations, D is the stick thickness, m_o is the crib initial mass, t is the time since ignition, h_c is crib height, S is the clear spacing between sticks, and room ventilation variables are A_v , the ventilation opening area, and h_v , the ventilation opening height. The fuel surface regression velocity, v_p , is taken as dependent on the stick thickness and on the fuel type, as shown in Table 3-1.2. The experimental data for the plastic materials are extremely scant, however, so the values should be viewed as indicative rather than quantitative.

For the case of the center-ignited crib, the burning regimes are divided according to whether the flame spread has reached the edge of the crib at a particular time. This time is defined as t_0 .

$$t_0 = 15.7n \quad (12)$$

Table 3-1.2 Fuel Type versus Regression Velocity v_p for Cribs

Material	v_p
Wood	$2.2 \times 10^{-6} D^{-0.6}$
Polymethylmethacrylate	$1.4 \times 10^{-6} D^{-0.6}$
Thermosetting polyester	$3.1 \times 10^{-6} D^{-0.6}$
Rigid polyurethane foam	$3.8 \times 10^{-6} D^{-0.6}$

where n = the number of sticks per row. For time $t < t_0$, the following relation holds:⁸²

$$\dot{m} = 0.0254 m_o \frac{v_p t^2}{n^2 D} \quad (13)$$

For $t > t_0$, Equations 8a through 11 are used. The heat release rate is determined from Equation 1. For plastics, the heat of combustion is commonly fairly constant and can be taken from tabulations or from cone calorimeter testing. For wood cribs, commonly the heat of combustion is taken to be $12 \times 10^3 \text{ kJ}\cdot\text{kg}^{-1}$. However, as illustrated in Figure 3-1.1, the heat of combustion of wood is a varying function of time. A better procedure would be either to predict the HRR of wood cribs directly, without going through Equation 1, or else to be able to have recourse to a realistic value of $\Delta h_c(t)$. Neither of these possibilities have currently been developed.

Room fire effects: Experimentally, it has long been observed⁷⁷ that, unlike a pool fire, which can burn in a room in a highly fuel-rich manner, a wood crib does not burn more than approximately 30 to 40 percent fuel rich. Conditions more fuel rich than that are not sustained, presumably, because of the highly vitiated air being supplied to the crib under those conditions. The stoichiometric fuel pyrolysis rate can be estimated as¹¹

$$\dot{m}_p(\text{st}) = \frac{1}{r} \cdot 0.5 A_v \sqrt{h_v} \quad (14)$$

where the stoichiometric air/fuel mass ratio, r , for wood can be taken as $r = 5.7$. Comparing, then, the maximum pyrolysis rate given by Equation 11 with the stoichiometric rate given by Equation 14, it can be seen that a limit of approximately 37 percent fuel rich is reached when Equation 11 becomes the governing limit to the burning rate. Similar limits may possibly exist for other classes of combustibles, but experimental data are only available for wood cribs.

Curtains

The heat content and burning rate of curtains are generally moderate, but they are combustible and can contribute to the severity of fires by quickly propagating fire over large surfaces. Moore has done the most extensive study of curtains and draperies.⁸³ His test specimens were ignited with a match along the bottom. The results are summarized in Table 3-1.3 and Figure 3-1.23. His results show primarily the effect of fabric weight. Lightweight fabrics, of weight around $125 \text{ kg}\cdot\text{m}^{-2}$, can show heat-release-rate peaks almost as high as heavy ones (around $300 \text{ kg}\cdot\text{m}^{-2}$); however, their potential to ignite surrounding objects is much smaller, as demonstrated in Figure 3-1.23. These conclusions hold for both thermoplastic and cellulosic materials, but not for constructions using foam backings, for which insufficient data were available. Whether the curtain was in the closed or in the open position seemed to make little difference. The reason for the more severe fire performance of the heavyweight curtains was largely due to their increased burning time, which was typically about twice that for the lightweight curtains.

Table 3-1.3 Heat Release Rate Data for Curtains

Type of Fiber	Weight (g/m ²)	Configuration	Peak HRR (kW)	Number of Wall and Ceiling Panels Ignited ^a
Cotton	124	Closed	188	1
Cotton	260	Closed	130	7
Cotton	124	Open	157	0
Cotton	260	Open	152	7
Cotton	313	Closed	600	3
Rayon/cotton	126	Closed	214	0
Rayon/cotton	288	Closed	133	6
Rayon/cotton	126	Open	176	0
Rayon/cotton	288	Open	191	2
Rayon/cotton	310	Closed	177	8
Rayon/acetate	296	Closed	105	4
Acetate	116	Closed	155	0
Cotton/polyester	117	Closed	267	1
Cotton/polyester	328	Closed	338	5
Cotton/polyester	117	Open	303	0
Rayon/polyester	367	Closed	658	2
Rayon/polyester	268	Closed	329	7
Rayon/polyester	53	Closed	219	0
Cotton/polyester	328	Open	236	7
Polyester	108	Closed	202	0
Acrylic	99	Closed	231	0
Acrylic	354	Closed	1177	8
Acrylic	99	Open	360	0
Acrylic	354	Open	NA	7
Cotton/polyester/foam	305	Closed	385	1
Rayon/polyester/foam	284	Closed	326	0
Rayon/fiberglass	371	Closed	129	5
Rayon/fiberglass	371	Closed	106	5

Nominal curtain size: two curtains each, 2.13 m high by 1.25 m wide. Wall area covered: 2.13 m high by 1.0 m wide (in closed position).

^aMaximum possible number of panels to ignite = 10.

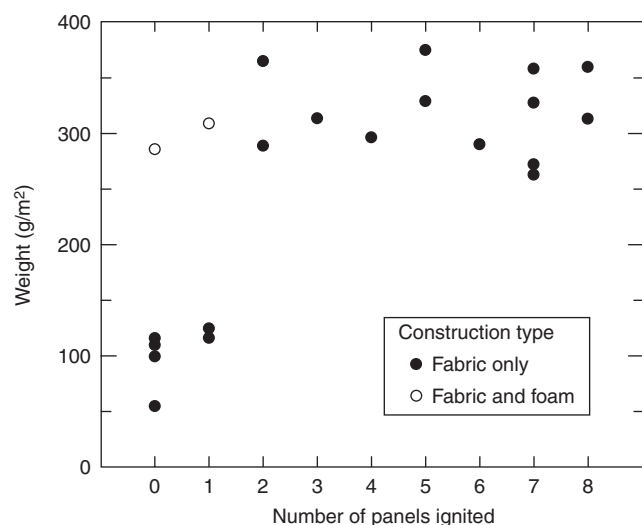


Figure 3-1.23. Effect of fabric weight on number of curtain panels ignited.

Additional data on the HRR of curtains have been published by VTT⁷¹ and by SP.⁸⁴

Dressers

A test of a wooden dresser has been conducted by NIST.⁸⁵ See Figure 3-1.24.

Electric Cable Trays

Cable tray fires present almost an endless plethora of combinations of cable materials, tray construction, stacking, ignition sources, and so forth. Only a very few of these have been explored. The most systematic studies available are those from Tewarson et al.⁸⁶ and Sumitra.⁸⁷ A useful engineering analysis of their data has been prepared by Lee.⁸⁸ Lee provided a basic correlation of Tewarson's and Sumitra's data (see Figure 3-1.25), which shows that the peak full-scale heat-release rate \dot{q}_{fs} ($\text{kW}\cdot\text{m}^{-2}$) can be predicted according to bench-scale heat release rate measurements

$$\dot{q}_{fs} = 0.45 \dot{q}_{bs}'' \cdot A$$

where \dot{q}_{bs}'' is the peak bench-scale HRR ($\text{kW}\cdot\text{m}^{-2}$), measured under $60\text{-kW}\cdot\text{m}^{-2}$ irradiance, and A is the exposed tray area actively pyrolyzing (m^2). The active pyrolysis area, in turn, is estimated from Figure 3-1.26, which gives dA/dt as a function of \dot{q}_{bs}'' . Thus, at any given time, t ,

$$A(t) = A_0 + \frac{dA}{dt} \cdot t$$

Finally, Table 3-1.4 gives a selection of measured values of \dot{q}_{bs}'' for various cable types.

Industrial Stored Commodities

Pallet loads of plastic-based commodities are commonly stored in factories, warehouses, and wholesale es-

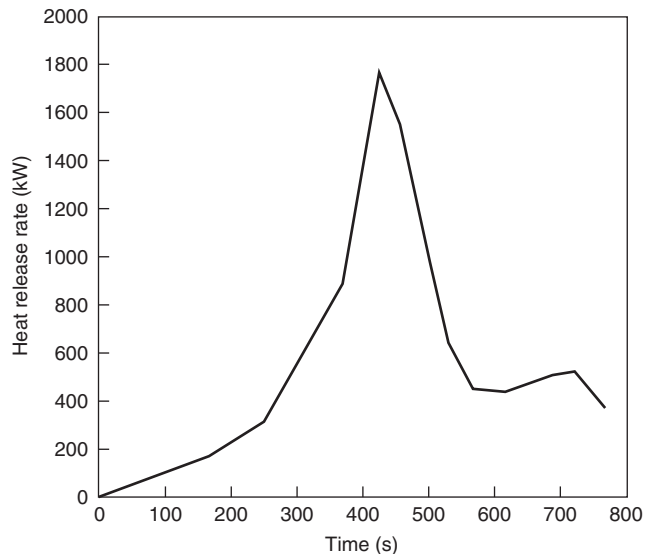


Figure 3-1.24. Wooden dresser.

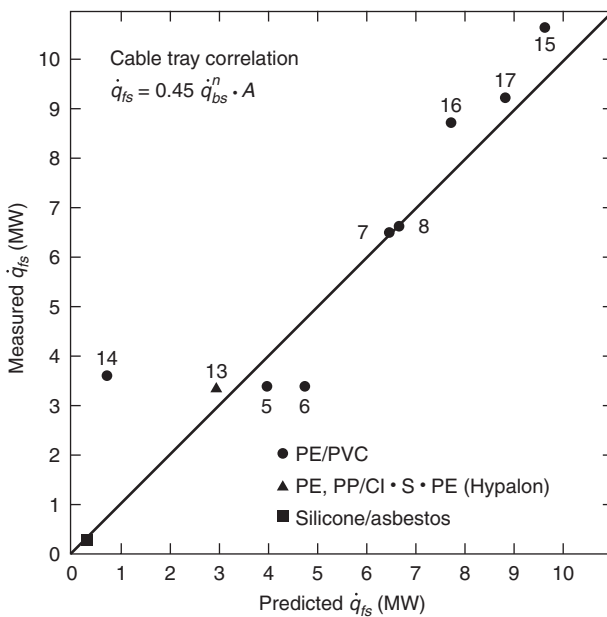


Figure 3-1.25. Heat release rate correlation for cable trays (numbers at data points identify full-scale tests).

tabishments.⁸⁹ Pellets of SBR (styrene-butadiene rubber) were packed in paper bags and loaded on a wooden pallet. The pallet was overwrapped with clear plastic film and spillage did not occur during testing. The full-pallet test was ignited with a propane torch at the bottom. The half-pallet test was ignited with a propane torch at the top. The full-pallet test (Figure 3-1.27) showed an HRR of close to

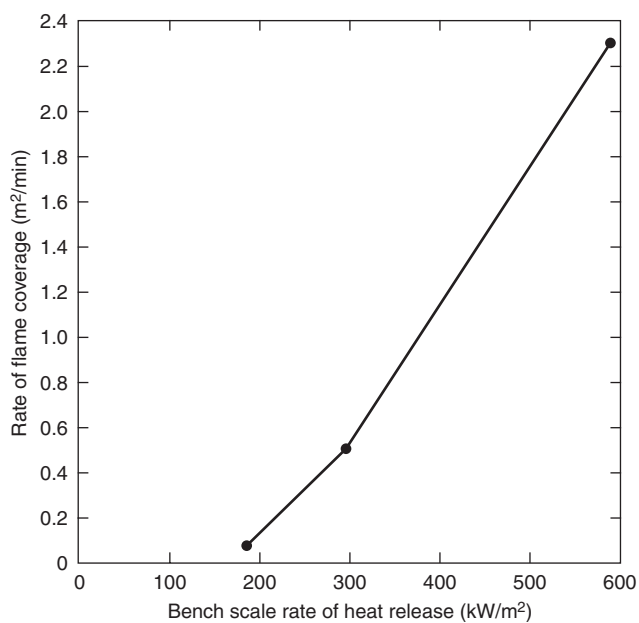
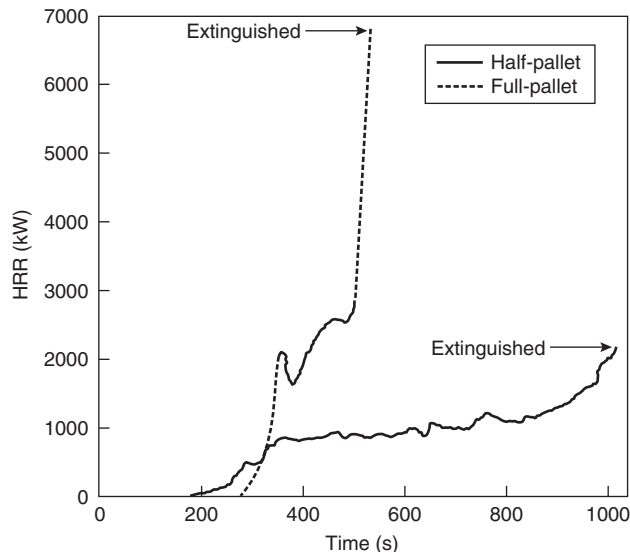


Figure 3-1.26. Effect of bench-scale cable heat release rate on full-scale rate of flame coverage.

Table 3-1.4 Heat Release Rates of Typical Cables in Bench-Scale Tests

Specimen Number	Cable Sample	IEEE 383 Test	\dot{q}_{bs}'' (kW/m ⁻²)
20	Teflon	Pass	98
21	Silicone, glass braid	Pass	128
10	PE, PP/Cl·S·PE	Pass	177
14	XPE/XPE	Pass	178
22	Silicone, glass braid asbestos	Pass	182
16	XPE/Cl·S·PE	Pass	204
18	PE, nylon/PVC, nylon	^a	218
19	PE, nylon/PVC, nylon	^a	231
15	FRXPE/Cl·S·PE	Pass	258
11	PE, PP/Cl·S·PE	Pass	271
8	PE, PP/Cl·S·PE	Pass	299
17	XPE/Neoprene	Pass	302
3	PE/PVC	^a	312
12	PE, PP/Cl·S·PE	Pass	345
2	XPE/Neoprene	^a	354
6	PE/PVC	^a	359
4	PE/PVC	Fail	395
13	XPE/FRXPE	Pass	475
5	PE/PVC	Fail	589
1	IDPE	^a	1071

^aTest not conducted.

**Figure 3-1.27. HRR of bags of SBR pellets on a wooden pallet.**

7 MW when conditions required that the commodity be extinguished; peak HRR conditions had not been reached.

Heskestad^{90,91} analyzed a large series of palletized* storage tests conducted at FRMC in 1975 by Dean.⁹² These

Palletized denotes a storage configuration where pallets are stored directly on top of each other, without use of shelving.

experiments predated the availability of HRR calorimeters, so Heskestad obtained peak HRR values by using mass-loss-rate data and values of effective heat of combustion. The test arrangement was $2 \times 2 \times 3$ pallets high, with a flue space running in only one direction. Heskestad also analyzed a later series of rack storage tests by Yu and Kung.^{93,94} The test arrangement was 2×2 , with heights being 2, 3, or 4 pallets, and with flue spaces running in both directions. Heskestad's tabulated peak HRR values are given in Table 3-1.5. The peak HRR values were obtained by dividing the value in kilowatts by the floor area occupied by the commodity. The cardboard cartons with metal liner are FMRC Standard Class II Commodity, while the PS cups are FMRC Standard Plastic Commodity. Note that there does not exist a scaling rule that would enable HRR values to be computed for stack/rack heights other than those tested. Thus, the reported values could conservatively be applied to shorter heights, but cannot be extrapolated to greater heights. Older data⁹⁵ are given in Table 3-1.6; these have not been reanalyzed by Heskestad.

Additional FMRC data for different commodities loaded onto wooden pallets are shown in Figure 3-1.28. The PET (polyethylene terephthalate) bottle test⁹⁶ used 46 bottles of a 2-L size packed into single-wall corrugated cardboard boxes. Each box contained 2.55 kg of plastic and 1.29 kg of cardboard. Total test arrangement comprised 8 pallet loads arranged in a $2 \times 2 \times 2$ arrangement. Each pallet contained 8 cartons of the size $0.53 \times 0.53 \times 0.53$ m. The newspaper test⁹⁷ comprised 8.2 kg of shredded newsprint placed in a $0.53 \times 0.53 \times 0.51$ m single-wall corrugated cardboard box of 2.73 kg. Eight cartons comprised one pallet load. The pallets were arranged in a $2 \times 2 \times 2$ arrangement. The egg carton test⁹⁸ used foam polystyrene egg cartons of 12-egg capacity. Polyethylene bags were used to hold 200–216 of these egg cartons, open and nested into each other. Each pallet held about 20.4 kg of egg cartons. Each pallet contained about 22.7 kg of wood, and the load also contained about 0.4 kg of polyethylene. In this test, a low density of water extinguishment was applied, but this did not appear to reduce significantly the HRR of the commodity. Only the convective portion of the HRR was measured. Polystyrene shows a very high radiant heat-release fraction; thus, to account for the radiant fraction and for the diminution due to water spraying, the total HRR curve shown in Figure 3-1.28 was estimated by multiplying the measured convective portion by two times.

Packaged computers and computer accessories were tested by Hasegawa et al.^{99,100} They tested pallet loads of packaged goods and also individual items, as packaged and boxed in individual cardboard boxes. The items were ignited using a line burner placed near the bottom edge of the package or stack. Ignition sources in the range of 50–200 kW were used. Table 3-1.7 identifies the specimens tested, while Figure 3-1.29 through Figure 3-1.32 show the results. The monitors were 16.8 kg each, while the desktop computers were 4.9 kg each. The pallet load in test P1 collapsed during testing and the full HRR was not registered; consequently, it was retested with supported sides.

A stack of expanded polystyrene boards was burned by Dahlberg at SP and results are reported by Särdqvist.⁹⁶ The total stack size was $1.2 \times 1.2 \times 1.2$ m, with a mass of

Table 3-1.5 HRR Values of Palletized and Rack Storage Commodities Tested at FMRC

Test	Commodity	Storage Height (m)	Peak HRR ($\text{kW}\cdot\text{m}^{-2}$)	Time of Peak (s)
SP-4	PS jars in compartmented CB cartons	4.11	16,600	439
SP-13	PS foam meat trays, wrapped in PVC film, in CB cartons	4.88	10,900	103
SP-23	PS foam meat trays, wrapped in paper, in CB cartons	4.90	11,700	113
SP-30A	PS toy parts in CB cartons	4.48	5,210	120
SP-35	PS foam insulation	4.21	26,000	373
SP-44	PS tubs in CB cartons	4.17	6,440	447
SP-15	PE bottles in compartmented CB cartons	4.20	5,330	434
SP-22	PE trash barrels in CB cartons	4.51	28,900	578
SP-43	PE bottles in CB cartons	4.41	4,810	190
SP-6	PVC bottles in compartmented CB cartons	4.63	8,510	488
SP-19	PP tubs in compartmented CB cartons	4.26	5,870	314
SP-34	PU rigid foam insulation	4.57	1,320	26
SP-41	Compartmented CB cartons, empty	4.51	2,470	144
RS-1	CB cartons, double triwall, metal liner	2.95	1,680	260
RS-2	" "	2.95	1,490	89
RS-3	" "	2.95	1,680	180
RS-4	" "	4.47	2,520	120
RS-5	" "	4.47	2,250	240
RS-6	" "	5.99	3,260	210
RS-7	PS cups in compartmented CB cartons	2.90	4,420	95
RS-8	" "	2.90	4,420	100
RS-9	" "	2.90	4,420	120
RS-10	" "	4.42	6,580	100
RS-11	" "	5.94	8,030	148

CB, cardboard; PE, polyethylene; PP, polypropylene; PS, polystyrene; PU, polyurethane

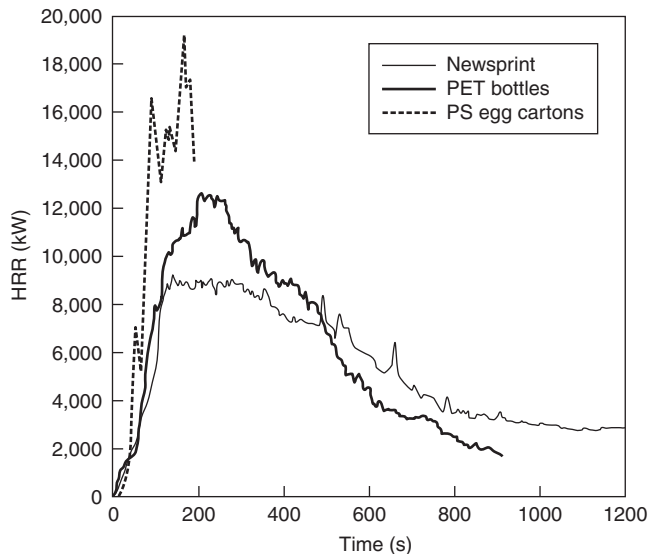
Table 3-1.6 Miscellaneous Stored Commodities Tested by FMRC

Commodity	Storage Height (m)	Peak HRR (kW/m^2)
Fiberglass (polyester) shower stalls, in cartons	4.6	1400
Mail bags, filled	1.52	400
PE letter trays, filled, stacked on cart	1.5	8500
PE and PP film in rolls	4.1	6200

1.4 kg. Ignition was with a 1-MW burner at the side of the stack. The HRR curve is shown in Figure 3-1.33. Numerous other example data are tabulated by Särdqvist.⁹⁶

A study has been reported on burning pallet loads of organic peroxides.¹⁰¹ Liquids were packaged in plastic containers within cardboard boxes, while solids were packaged in cardboard drums. The data are given only for a few packaging configurations with sufficient data not being available to generalize HRR predictions to other configurations.

For all rack storage tests, the times are very strongly affected by the ignition source location. Not enough data exist to make general correlations, but Figure 3-1.34 illustrates the basic effect. The storeroom test¹⁰² comprised a

**Figure 3-1.28. FMRC results for several additional commodities.**

mocked-up small storeroom in a retail shop, with miscellaneous goods boxed in cardboard boxes, placed on shelving 2.4 m high. A small amount of additional shelving was provided across an aisle 1.4 m wide. The FMRC

Table 3-1.7 Boxed Computer Items Tested by Hasegawa et al.

Code	Items	Peak HRR (kW)
P1	Boxed monitors, 1 pallet of 12	4,700
P8	Boxed monitors, 1 pallet of 12, point-source ignition	5,030
P5	Boxed monitors, 1 pallet of 12 (stabilized from collapse)	6,400
P6	Boxed monitors, 2 pallets (side-by-side) of 12 each	17,300
P10	Boxed monitors, stack of 2 pallets high, 10 per pallet	14,100
P3	Boxed desktop computers, 1 pallet of 16	1,400
P7	Boxed desktop computers, pallet of 16 with boxed accessory boxes on top	8,190
P9	Polystyrene foam in boxes	6,730
P11	Monitor boxes, 1 pallet of 12	4,600

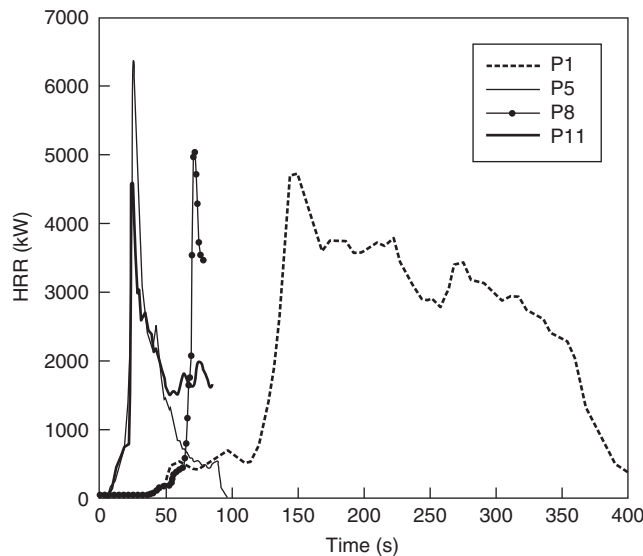


Figure 3-1.30. Pallets of packaged, boxed computer monitors.

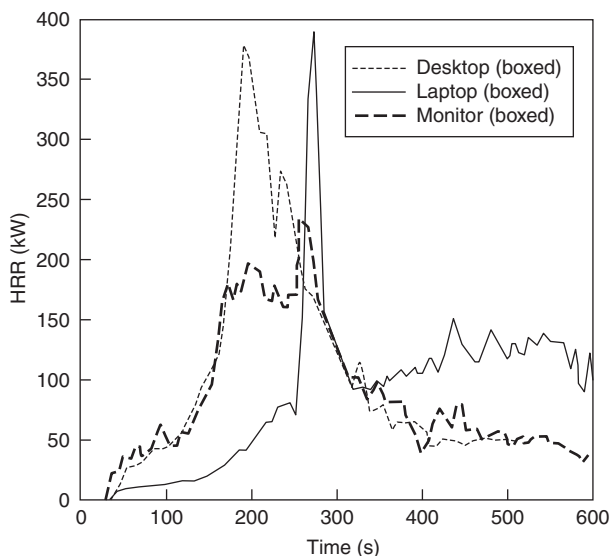


Figure 3-1.29. Single, packaged, and boxed computers and monitors.

test involved pallets in a $2 \times 2 \times 2$ arrangement. In the storeroom test, ignition was at the base of the face of the main storage rack. The FMRC test¹⁰³ used the standard FMRC procedure whereby an ignitor is also placed at the base, but is located internally, at the two-way intersection of flue spaces between piles. The data for the storeroom test are plotted as real time, while the FMRC test data were shifted 470 s to make the steep HRR rise portions coincide. From a comparison of this kind, one can roughly estimate that igniting a rack at the front face causes events to occur 470 s later than would happen if ignition were at the center of the flue spaces.

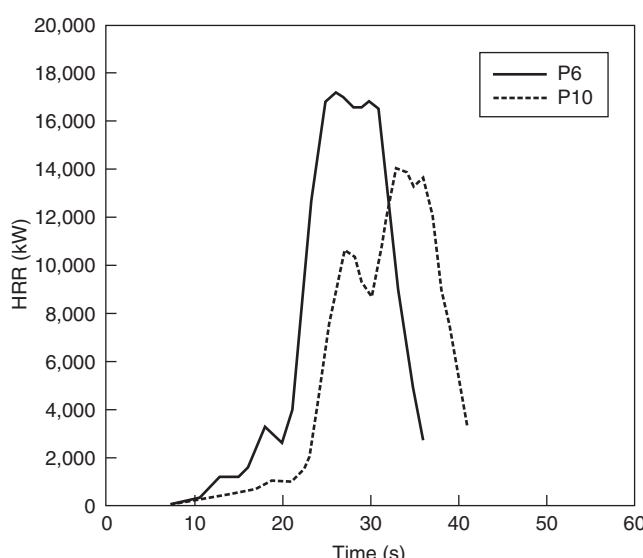


Figure 3-1.31. Pallets of packaged, boxed computer monitors.

Kiosks

NIST has reported¹⁰⁴ some HRR results on full-scale tests of kiosks. These are manned booths used in shopping malls, exhibitions, and other places wherein a small amount of merchandise display or sales occur. Some HRR curves are illustrated in Figure 3-1.35 for a kiosk, built largely of wood, that measured 1.2 m \times 1.2 m \times 2.1 m high. Tests 2–5 are all of the same-sized kiosk, but refer to various configurations of the openable panels. Test 5 appears to have been more severe since all the panels were

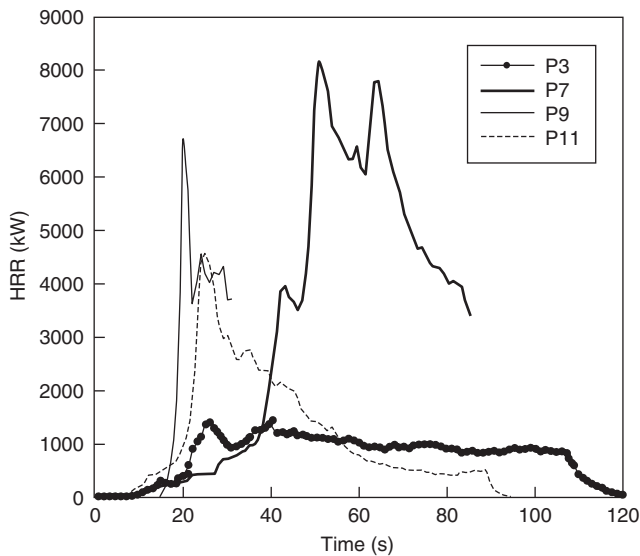


Figure 3-1.32. Pallets of miscellaneous computer items.

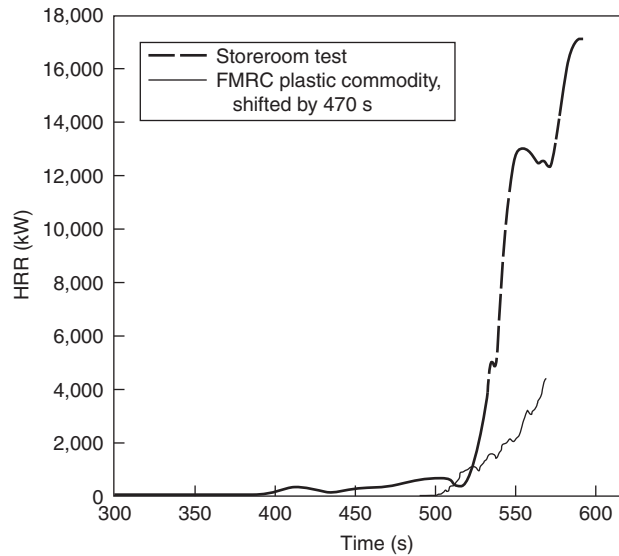


Figure 3-1.34. Effect of ignition source location on fire development.

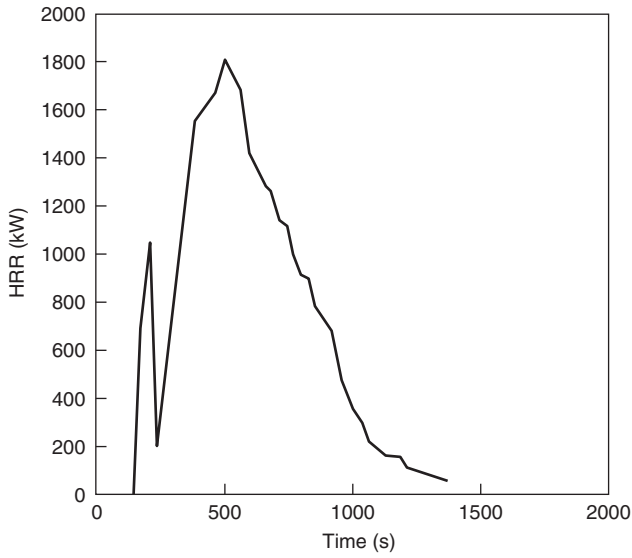


Figure 3-1.33. Stack of foam polystyrene boards.

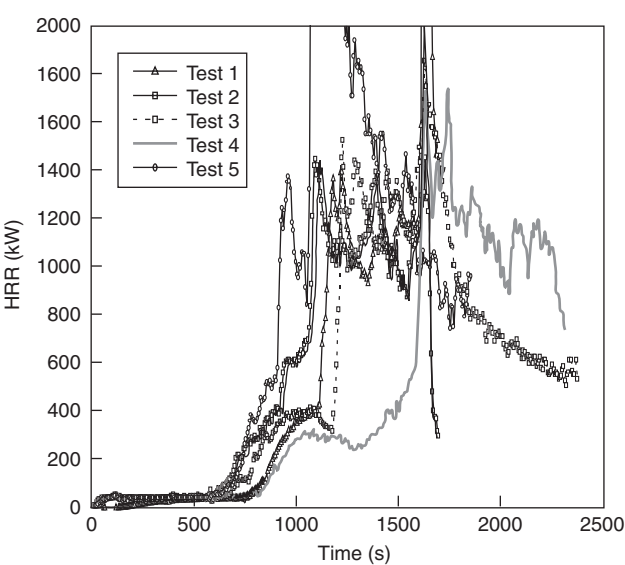


Figure 3-1.35. Display kiosks.

closed. Test 1 involved the same kiosk placed in a room, rather than in the furniture calorimeter.

Mattresses

Despite the relatively simple shape of mattresses, the prediction of mattress HRR from bench-scale data is difficult. Even the use of full-scale HRR data is problematic, due to a peculiarity of mattress fires. Most other combustibles interact only modestly with their environment, until large HRR values are reached or until room flashover is being approached. Liquid pools on the other hand, as discussed below, interact very strongly with a room, if either the room size or the available ventilation are not very

large in comparison to the pool's HRR. The identical phenomenon is observed with mattresses. Thus, there may not be a single value of the HRR of a mattress, because the HRR must be considered in relation to the room itself.

Some example data are compiled in Table 3-1.8 to illustrate the peak full-scale HRR values that are found for common material combinations.³⁸ The full-scale test protocol used a complete set of bedding; ignition was achieved with a wastebasket. Figure 3-1.36 illustrates the relation of bench-scale to full-scale data from the same data set, where full-scale testing was done under conditions not leading to significant room fire effect. Not enough specimens were tested to develop a usable correlation, so the results should be taken only as indicative.

Table 3-1.8 Some Mattress Heat Release Rate Data

Padding Material	Ticking Material	Combustible Mass (kg)	Peak HRR, Full-Scale ^a (kW)	Bench-Scale HRR ^b (kW·m ⁻²)
Latex foam	PVC	19	2720	479
Polyurethane foam	PVC	14	2630	399
Polyurethane foam	PVC	6	1620	138
Polyurethane foam	Rayon	6	1580	179
Polyurethane foam	Rayon	4	760	NA
Neoprene	FR cotton	18	70	89
Cotton/jute	FR cotton	13	40	43

^aFull-scale data are for small or no room effect.^bBench-scale data are peak values taken at 25 kW·m⁻² irradiance.

Some full-scale data obtained under conditions where a strong room interaction effect was seen are shown in Table 3-1.9.^{105,106} The full-scale test setup was different for this data set, in that no bedding was used and ignition was with a burner flame at the edge of the mattress. Thus, some mattresses were able to show essentially zero HRR since bedding was not available to sustain burning, and the ignition source could be evaded by receding specimens. A relation between full-scale and bench-scale results from this study is shown in Figure 3-1.37. The results of the behavior in that study follow:

- Mattresses with a bench-scale HRR (180-s average value) of < 165 kW·m⁻² led to room fires of less than 100 kW.
- Mattresses with a bench-scale HRR (180-s average value) of > 165 kW·m⁻² generally led to room fires on the order of 1 to 2 MW.
- The transition between those extremes was very abrupt.

The sharp transition between trivial fires and room flashover conditions can be attributed to the details of the test room, but also to the use of an ignition source that specimens of intermediate characteristics could evade.

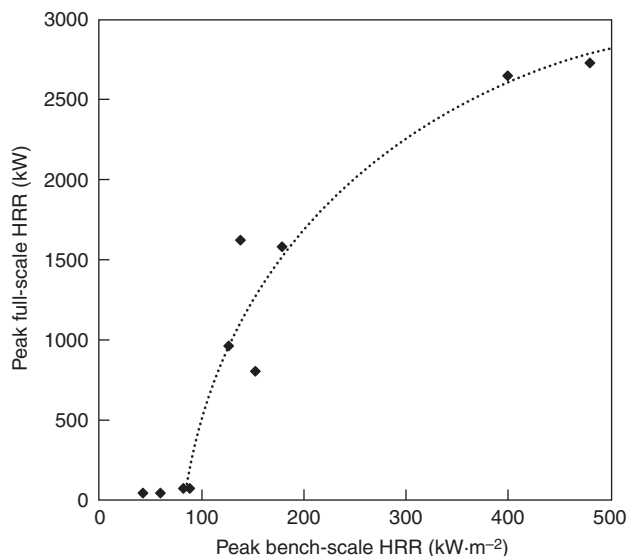


Figure 3-1.36. HRR of mattresses predicted from bench-scale results. Full-scale tests under conditions of negligible room effect; bench-scale HRR measured at 25-kW·m⁻² irradiance.

Additional data on mattress HRR have been published by SP¹⁰⁷ and by Lund University.¹⁰⁸ The latest study on mattress HRR has been the CBUF project.¹⁰ The CBUF study included full-scale room fire tests, open-burning furniture calorimeter tests, and cone calorimeter tests. The mattress results are given in Table 3-1.10. In both of the full-scale test environments, no bedding was used, but a square-head burner was applied to the top surface of the specimen, precluding complications from any receding surface behavior. The bench-scale test data presented were obtained at a 35 kW·m⁻² irradiance. The results indicate that, when tested in the standard ISO 9705 room, a very drastic room effect occurs for open-air HRR values over about 300 kW.

Table 3-1.9 Some Mattress Heat Release Rate Data

Padding Material	Ticking Material	Combustible Mass (kg)	Peak HRR, Full Scale ^a (kW)	180-s Average HRR, Bench Scale (kW·m ⁻²)
Polyurethane foam	Unidentified fabric	8.9	1716	220
Melamine-type PUR/cotton batting/polyester fiber pad	Polyester/polypropylene	NA	547	169
Polyurethane foam/cotton batting/polyester fiber pad	Unidentified fabric	NA	380	172
Polyurethane foam/polyester fiber pad	PVC	NA	335	195
Melamine-type PUR	FR fabric	15.1	39	228
FR cotton batting	PVC	NA	17	36
FR cotton batting	Polyester	15.7	22	45
Neoprene	PVC	14.9	19	31

^aFull-scale data include room effect of small bedroom.

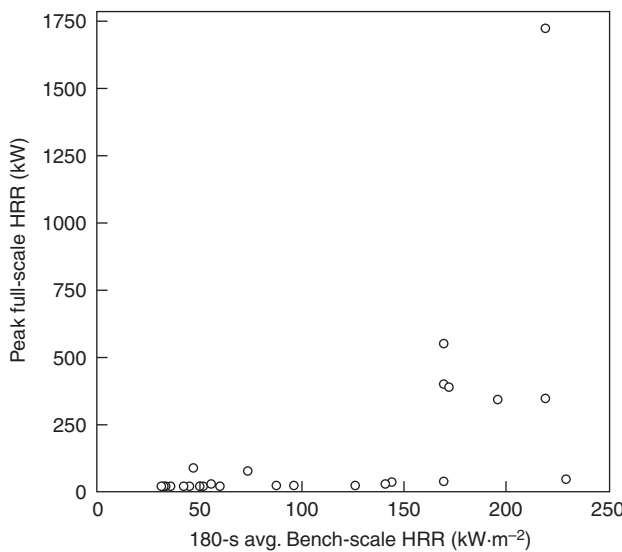


Figure 3-1.37. HRR of mattresses predicted from bench-scale results. Full-scale tests under conditions of significant room effect; bench-scale HRR measured at 35-kW·m⁻² irradiance.

The bench-scale data indicated that when widely varying mattress thicknesses exist, a simple relation of bench-scale to full-scale HRR cannot be sought, even if only predictions of open-burning (furniture calorimeter) results would be desired. As a first cut, it was concluded that mattresses can be grouped into two categories—those leading to propagating fires (the mattress being consumed in flaming combustion during a relatively short time), and those that do not. The former can be considered of the highest hazard, while the latter present only trivial hazard. Since, for practical reasons, all mattress composites must be tested in the cone calorimeter using a 50-mm thickness, to take into account effects due to thin mattresses, a thickness factor is defined:

$$\text{Th. fac.} = \min \left(\frac{\text{thickness (mm)}}{50}, 1.0 \right)$$

For mattresses where the innersprings are used, the thickness is measured from the top of the mattress down

to top of the metal springs; it is not the total thickness. To determine whether the mattress fire will be propagating or not, the following rules were developed:

if $\dot{q}_{180}'' \cdot (\text{Th.Fac.}) < 100 \text{ kW}\cdot\text{m}^{-2}$ and $\dot{q}_{60}'' < 250 \text{ kW}\cdot\text{m}^{-2}$
then $\dot{Q} < 80 \text{ kW}$ (nonpropagating fire)
else, $\dot{Q} > 80 \text{ kW}$ (propagating fire)

The HRR values over 80 kW in fact are flashover values of up to 2.5 MW, but the scheme does not assign a specific HRR number. Qualitatively, this scheme reflects the type of abrupt behavior change found in earlier studies (Figure 3-1.37), but here some more refined rules were developed that avoid nonpredictions that would occur from simple correlation. During the same CBUF project, a greatly more sophisticated mattress fire model has been developed by Baroudi et al.; this model is not easy to use, but details are given by Sundström¹⁰ and Babrauskas et al.¹⁰⁹

Office Workstations

Office worker cubicles (workstations) have been tested in several projects at NIST.^{110–112} Figure 3-1.38 shows that very severe fire conditions can be generated by these arrangements. In some cases, fires of nearly 7 MW were recorded from the burning of a single person's workstation. The identification of the main conditions in these tests is given in Table 3-1.11. In one test series¹¹¹ replicates were tested in an open furniture calorimeter, then the configuration was tested again in a room test; this is illustrated in Figure 3-1.39.

Pallets

Conceptually, a wood pallet is a similar arrangement to a wood crib. The geometry, however, is different. Instead of being composed of identical rows of square-section sticks, pallets are made up of rectangular elements in a traditionally dimensioned configuration, Figure 3-1.40. The fire safety concern with pallets arises when they are idle and stacked many units high. Krasner¹¹³ has reported on a number of tests in which the burning rate of pallets was measured. A typical experimental heat-release-rate curve is shown in Figure 3-1.41. This curve shows that,

Table 3-1.10 Results on Mattress from the CBUF Study

Peak HRR Furniture Calorimeter (kW)	Peak HRR Room (kW)	Springs	Thickness (mm)	Thickness Factor	\dot{q}_{60}''	\dot{q}_{180}''	$\dot{q}_{180}'' \times$ Thickness Factor	\dot{q}_{tot}''	Propagating Fire
26	42	sofabed	22	0.44	162	135	59	50	N
31	45	N	50	1.00	136	82	82	21	N
47	61	Y	10	0.20	225	227	45	43	N
47	NA	Y	20	0.40	111	118	47	45	N
275	NA	N	90	1.00	111	118	118	45	Y
348	471	Y	20	0.40	327	159	64	30	Y
313	1700	N	100	1.00	256	191	191	62	Y
917	2550	N	140	1.00	232	198	198	37	Y

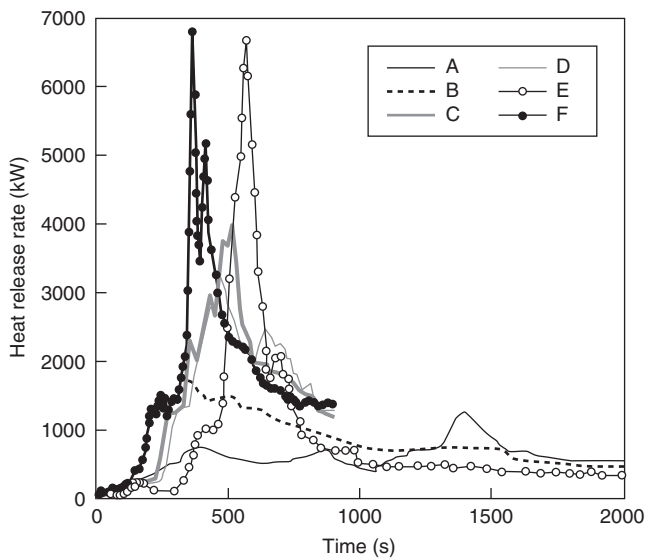


Figure 3-1.38. Office workstations.

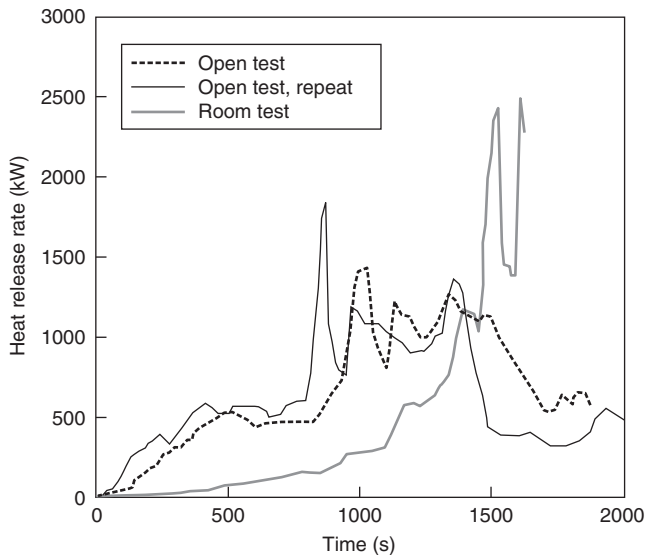


Figure 3-1.39. Identical workstations with old-style wood furniture tested under open burning and under room fire conditions.

much like for a wood crib, a substantially constant plateau burning can be seen if the stack is reasonably high. The results for a standard pallet size of 1.22×1.22 m can be given as a general heat-release-rate expression:

$$\dot{q} = 1368(1 + 2.14h_p)(1 - 0.03M)$$

where h_p is stack height (m), M is moisture (%), and a net heat of combustion of 12×10^3 kJ·kg⁻¹ has been assumed. For convenience in applying to nonstandard pallet sizes, this can be expressed on a per-unit-pallet-floor-area basis as

$$\dot{q}'' = 919(1 + 2.14h_p)(1 - 0.03M)$$

Table 3-1.11 Identification of Workstations in Figure 3.1.38

Code	Combustible Mass (kg)	Description	Number of Sides with Acoustic Panels	Reference
A	291	Mostly old-style wood furniture	0	110
B	291	Semi-modern furniture	1	110
C	335	Modern furniture	2	112
D	—	Modern furniture	3	112
E	291	Modern furniture	4	110
F	—	Modern furniture	4	112

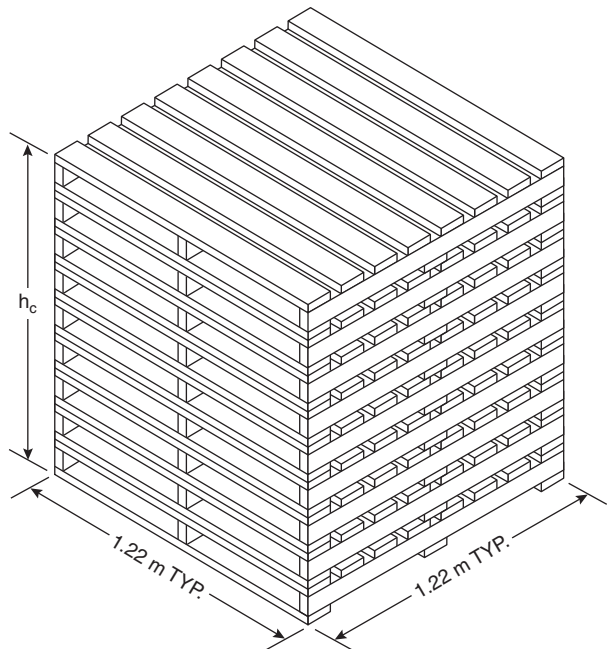


Figure 3-1.40. The geometric arrangement of a stack of wood pallets.

The agreement between the above equations and experimental data is seen to be good over a wide range of pallet heights (Figure 3-1.42), but the expressions do somewhat overpredict the burning rates if applied to short stacks, with stack height $h_p < 0.5$ m.

Pillows

Pillow tests have been reported by NIST¹¹⁴ and SP.¹⁰ The results are given in Figure 3-1.43.

Pipe Insulation

The available data are from a configuration in which pipe insulation is used to cover the entire ceiling of a test

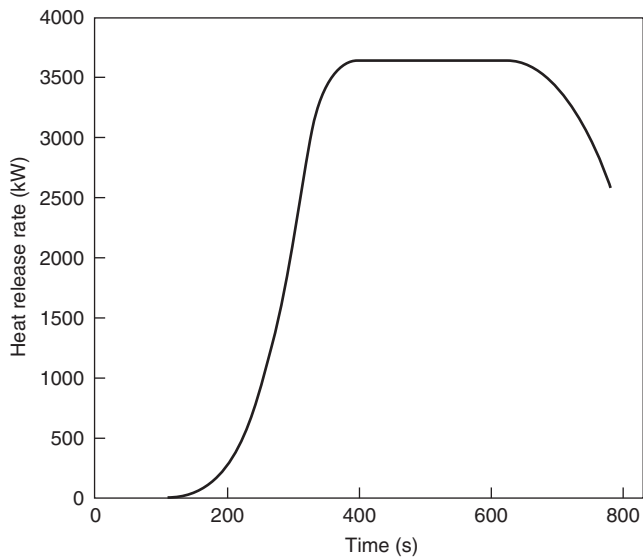


Figure 3-1.41. HRR of a typical wood pallet stack (1.22 × 1.22 × 1.22 m high).

room. The test method used is a variant of ISO 9705, especially configured for pipe insulation testing.¹¹⁵ Data on this configuration have been published by Wetterlund and Göransson¹¹⁶ and by Babrauskas.¹¹⁷

Pools, Liquid or Plastic

Possibly the simplest geometric arrangement of fuel is a liquid (or thermoplastic) pool. Over the last four decades, an enormous number of studies have been conducted in which pool burning was considered theoreti-

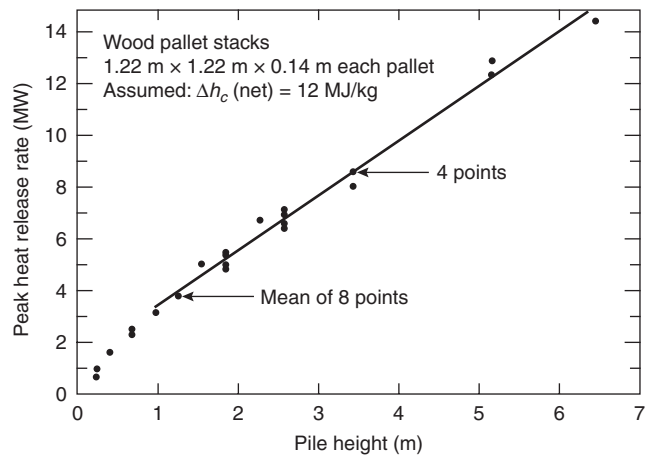


Figure 3-1.42. Dependence of pallet HRR on stack height.

cally or measured empirically. The most systematic early study was by two Russian researchers, Blinov and Khudiaikov.¹¹⁸ Their results were analyzed by Hottel,¹¹⁹ who pointed out that conservation of energy can be applied to the pool:

$$\dot{q} = \dot{q}'' \times A = (\dot{q}_r'' + \dot{q}_c'' - \dot{q}_{rr}'' - \dot{q}_{loss}'') \left(\frac{\Delta h_c}{\Delta h_g} \right) A$$

where

\dot{q} = the heat-release rate of the pool; double-prime denotes per unit area

A = the area of the pool (m^2)

\dot{q}'' = the radiant heat flux absorbed by the pool

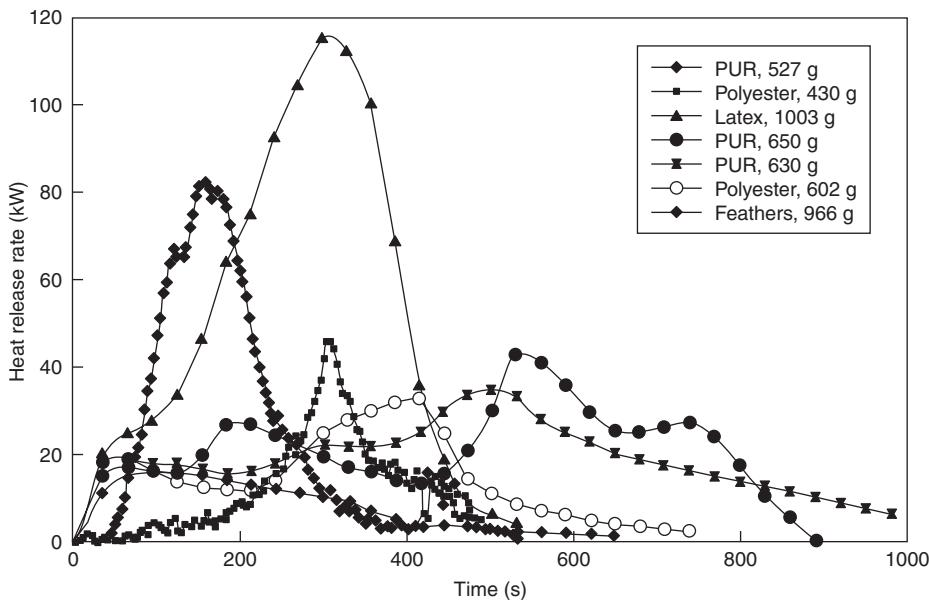


Figure 3-1.43. Pillows.

- \dot{q}_c'' = the convective heat flux to the pool
 \dot{q}_{rr}'' = the heat flux reradiated from the surface of the pool
 \dot{q}_{loss}'' = wall conduction losses and nonsteady terms (lumped together)

The heat of gasification is Δh_g (kJ/kg⁻¹), while the (lower, or net) heat of combustion is $\Delta \dot{h}_c$. Note that some authors use the symbol L for the heat of gasification. The heat of gasification is defined as the enthalpy required to bring a unit of mass of liquid-phase substance at 25°C to the gaseous state at the temperature T_b , its boiling point. It should not be confused with the latent heat of evaporation Δh_v , which is the enthalpy required to change a unit mass of liquid to a gas at 25°C. The relation between these two quantities is

$$\Delta h_g = \Delta h_v + (T_b - 25) \times C_{pv}$$

where we have taken the simplification that C_{pv} , the heat capacity of the vapor (kJ/kg⁻¹·K⁻¹), is a constant. An extensive tabulation of these constants is provided by Babrauskas.¹²⁰

Hottel's analysis of Blinov and Khudiakov's data showed two basic regimes are possible: radiatively dominated burning for large pool diameters, D , and convectively dominated burning for small D . Furthermore, in the convective regime, the flow can be either laminar or turbulent (being always turbulent for radiatively driven pools), while in the radiative regime, the flames can be optically thin or thick. These distinctions can, in the simplest analysis, be made solely on the basis of pool diameter. Such a simple classification is possible if the pool is strictly circular, radiant heating is only from the pool's flames and not augmented by external sources, and there are no interferences to the flow streamlines that could trip the onset of turbulence. In such a simplified case, the regimes can be identified as in Table 3-1.12.

In the convective limit (small pools), one may make the following approximation:

$$\dot{q} = \dot{q}_c'' \cdot \frac{\Delta h_c}{\Delta h_g} \cdot A$$

However, the values of \dot{q}_c'' to be taken are not easily determined. Some additional details are given by Babrauskas.¹²¹ For fire hazard analysis purposes, liquid pool fires will rarely be significantly dangerous if they are smaller than about 0.2 m in diameter. Thus, it will often only be necessary to treat pools burning in the radiative regime. In the radiative regime, it is found that data for most organic liquids can be well correlated by

$$\dot{q} = \Delta h_c \dot{m}_\infty'' (1 - e^{-k\beta D}) \times A$$

Table 3-1.12 The Burning Regimes for Liquid Pools

Diameter (m)	Burning Mode
< 0.05	Convective, laminar
0.05–0.2	Convective, turbulent
0.2–1.0	Radiative, optically thin
> 1.0	Radiative, optically thick

This requires determining two empirical constants: \dot{m}_∞'' and the term $k\beta$. These constants are given in Table 3-1.13 for a number of common fuels. The net heat of combustion, Δh_c , is also listed in the table. In principle, a slightly lower value, the *effective heat of combustion*, should be used instead of the net heat of combustion that is determined with oxygen bomb calorimetry. Some bench-scale values of a combustion efficiency factor to convert oxygen bomb values into experimentally measured values are given in Section 3, Chapter 4. For most liquids, however, the bench-scale values are not greatly below unity and realistic large-scale measurements are not available; thus the improvement in accuracy by extrapolating from bench-scale results may be nil.

Alcohol fuels show minimal radiative flux, in comparison to other fuel types. Thus, the best recommendation previously had been to use constant values of \dot{m}'' , independent of diameter. Based on some newer test results,¹²² it is clear that a diameter effect does exist, although it cannot be expressed in standard form. Thus, it is recommended that for methanol or ethanol the following values be used: $\dot{m}'' = 0.015$ ($D < 0.6$ m); $\dot{m}'' = 0.022$ ($0.6 < D < 3.0$ m); and $\dot{m}'' = 0.029$ ($D > 3.0$ m).

The above discussion implicitly assumed that the pool depth is at least several millimeters. If liquids are spilled on a horizontal surface that has no low spots and no diking, then a liquid layer will form that is less than 1 mm thick. *Thin-layer pools* of this nature (which can occur in arson cases) show a lower HRR than do pools of greater depths. Putorti et al.¹²³ studied gasoline spills on wood parquet, vinyl floor tiles, and carpeting. When a specified volume of liquid is spilled, the problem to be solved can be separated into two components: (1) determining the area of the spill, or, equivalently, the spill thickness; and (2) determining the HRR per unit area. For wood floors, Putorti found the $A = 1.5V$, where A = area (m²) and V = volume (L). For vinyl tile, a similar relation was also found, but with the constant being 1.8. Converted into layer thicknesses, the thickness for wood was 0.67 mm and for vinyl tile it was 0.56 mm.

Earlier work has indicated that a relation of this kind should only be applied to smooth floor surfaces. For rough, absorptive surfaces a constant thickness is not obtained, and larger spill volumes produce, effectively, greater layer thicknesses.¹²⁴ Putorti's study with carpets both indicated large differences between carpet types and also showed that the data could not be represented as a constant layer thickness. The HRR per-unit-area values are shown in Figure 3-1.44. For solid-surface pours, spill areas were in the range 0.4–1.8 m². As presented above, pools of large depths in this size range would show HRR values of 1900–2400 kW·m⁻².

Thus, carpet-surface values are about 70–80 percent of values that would have been computed using the normal pool fire formulas. The smooth-surface values, however, are only about one-fifth of the values that would be found for pools of sizable depths. A similar study by Gotruk et al. (to be published) also describes HRR values for spills on hard surfaces that are, very roughly, about one fifth of those for normal pools. The relationships found by Putorti can only be expected to hold on dead-flat surfaces. If surfaces are crooked, then ponding at low spots will occur and uniform spill depths should never be anticipated.

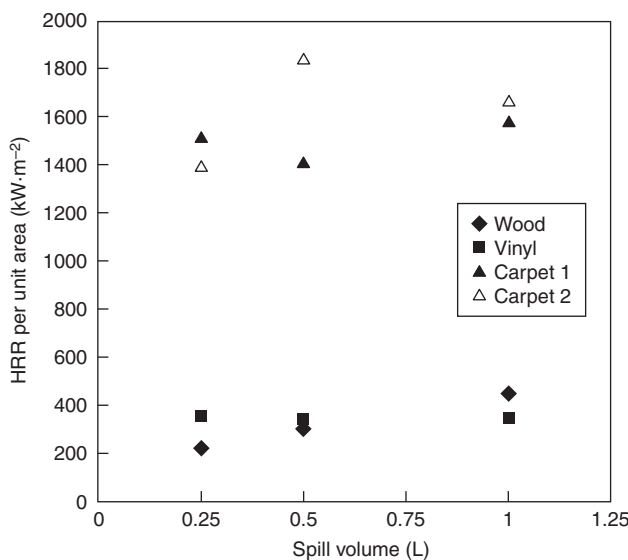


Figure 3-1.44. Thin pools of gasoline over various surfaces.

The discussion above pertains only to *open-burning* fires. Thus, the literature-derived burning rates can be used only in the case of a very large, well-ventilated room (compared to the size of the fire). If calculations show that the free-burning pool would cause a temperature rise of more than, say, 100°C, then it is clear that radiative feedback will start being important and such an approximation cannot be made. No simple formulas exist for computing the enhanced burning rates when a pool receives significant room radiation. If computations under these conditions are necessary, the theoretical study of Babrauskas and Wickström¹¹ should be consulted. The computer program COMPF2¹²⁵ can also be used to treat this case.

The problem of pool burning is interesting from a combustion science point of view, and over the years there has been a very large number of studies that attempted to go beyond empirical predictions.^{50,126–128} In addition, work is going on to provide more detailed experimental measurements for specific fuels.^{129,130}

Television Sets

A limited amount of data are available on the HRR of television sets. Ahonen et al.⁷¹ tested two old televisions with large wood cabinets. Babrauskas et al.⁶³ tested small

Table 3-1.13 Pool Burning: Thermochemical and Empirical Constants for a Number of Common Organic Fuels

Material	Density (kg/m ³)	Δh_g (kJ/kg ⁻¹)	Δh_c (MJ/kg ⁻¹)	\dot{m}'' (kg/m ⁻² s ⁻¹)	k (m ⁻¹)
Cryogenics					
Liquid H ₂	70	442	120.0	0.017 (±0.001)	6.1 (±0.4)
LNG (most CH ₄)	415	619	50.0	0.078 (±0.018)	1.1 (±0.8)
LPG (mostly C ₃ H ₈)	585	426	46.0	0.099 (±0.009)	1.4 (±0.5)
Alcohols					
Methanol (CH ₃ OH)	796	1195	20.0	See text	See text
Ethanol (C ₂ H ₅ OH)	794	891	26.8	See text	See text
Simple organic fuels					
Butane (C ₄ H ₁₀)	573	362	45.7	0.078 (±0.003)	2.7 (±0.3)
Benzene (C ₆ H ₆)	874	484	40.1	0.085 (±0.002)	2.7 (±0.3)
Hexane (C ₆ H ₁₄)	650	433	44.7	0.074 (±0.005)	1.9 (±0.4)
Heptane (C ₇ H ₁₆)	675	448	44.6	0.101 (±0.009)	1.1 (±0.3)
Xylenes (C ₈ H ₁₀)	870	543	40.8	0.090 (±0.007)	1.4 (±0.3)
Acetone (C ₃ H ₆ O)	791	668	25.8	0.041 (±0.003)	1.9 (±0.3)
Dioxane (C ₄ H ₈ O ₂)	1035	552	26.2	0.018	5.4
Diethyl ether (C ₄ H ₁₀ O)	714	382	34.2	0.085 (±0.018)	0.7 (±0.3)
Petroleum products					
Benzine	740	—	44.7	0.048 (±0.002)	3.6 (±0.4)
Gasoline	740	330	43.7	0.055 (±0.002)	2.1 (±0.3)
Kerosene	820	670	43.2	0.039 (±0.003)	3.5 (±0.8)
JP-4	760	—	43.5	0.051 (±0.002)	3.6 (±0.1)
JP-5	810	700	43.0	0.054 (±0.002)	1.6 (±0.3)
Transformer oil, hydrocarbon	760	—	46.4	0.039	0.7
Fuel oil, heavy	940–1,000	—	39.7	0.035 (±0.003)	1.7 (±0.6)
Crude oil	830–880	—	42.5–42.7	0.022–0.045	2.8 (±0.4)
Solids					
Polymethylmethacrylate	1184	1611	24.9	0.020 (±0.002)	3.3 (±0.8)
Polyoxymethylene (CH ₂ O) _n	1425	2430	15.7		
Polypropylene (C ₃ H ₆) _n	905	2030	43.2		
Polystyrene (C ₈ H ₈) _n	1050	1720	39.7		

polystyrene television cabinets of two types, fire-retardant and not. Since the circuit components contribute negligible HRR in comparison to the outer shell, only the cabinets were tested. Two very small (personal size) units were tested side-by-side in each test. This can represent either two appliances or simply the mass of one larger set. The results are given in Figure 3-1.45.

Transport Vehicles and Components

Passenger car HRR was measured at the Fire Research Station¹³¹ and at VTT.¹³² The FRS laboratory examined a 1982 Austin Maestro and a 1986 Citroën BX. VTT

examined a Ford Taunus, a Datsun 160, and a Datsun 180. The dates of manufacture were stated only as late 1970s. In the FRS tests, the Austin measured a peak of 8.5 MW, while the Citroën a peak of 4.5 MW. For the VTT tests, the peak HRR values were all approximately 1.5–2.0 MW. These numbers are rather widely disparate and it is not fully clear why, except that this is not due to the fraction of polymer content onboard. The HRR curves are shown in Figure 3-1.46.

Tests on transport seating (Figure 3-1.47) were also done at SP.¹³³ They measured an array of four double bus seats and a similar arrangement of train seats. The foam was HR polyurethane, while the cover was a viscose/wool/polyester/polyamide blend for the bus seats and 100 percent wool fabric for the train seats.

Vehicle tires can ignite from an overheated axle and can release a substantial amount of heat if they burn. There is one study in the literature that documents such a fire. Hansen¹³⁴ burned a pair of 285/80 R22.5 truck tires mounted in a tandem wheel arrangement. The HRR curve is given in Figure 3-1.47. Vehicle tires are also prone to be ignited and to burn in tire dumps. The HRR will depend directly on the geometry and on the amount of tires involved. Some quantitative HRR experiments have been reported¹³⁵ on experiments done at the Fire Research Station. These experiments were for flaming tires, but most recent tire dump problems have been associated with a smoldering condition and no HRR quantification under these conditions has been reported.

Half a tram car was tested at SP.⁶¹ The most recent HRR data on transport vehicles came from a European research program where nearly two dozen vehicles were tested, including cars, buses, trams, trucks, and rail vehicles. The peak HRR values for many of these tests ranged about 10–35 MW (Figure 3-1.48). However, one test involved a truck loaded with 2 metric tons of modern upholstered furniture. The peak HRR for this vehicle was found

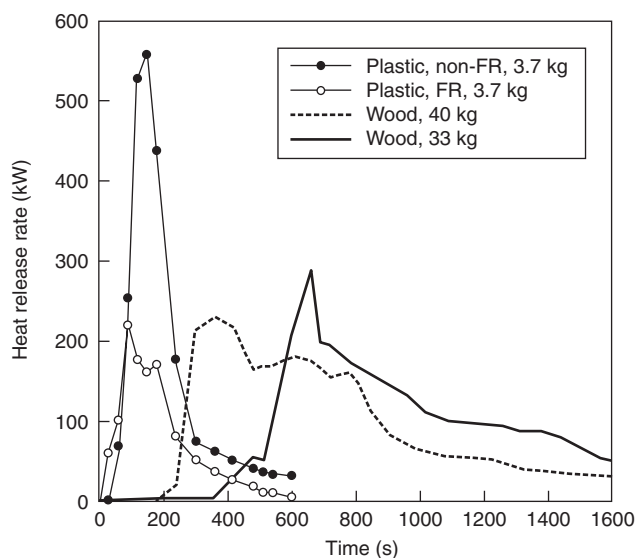


Figure 3-1.45. Television sets.

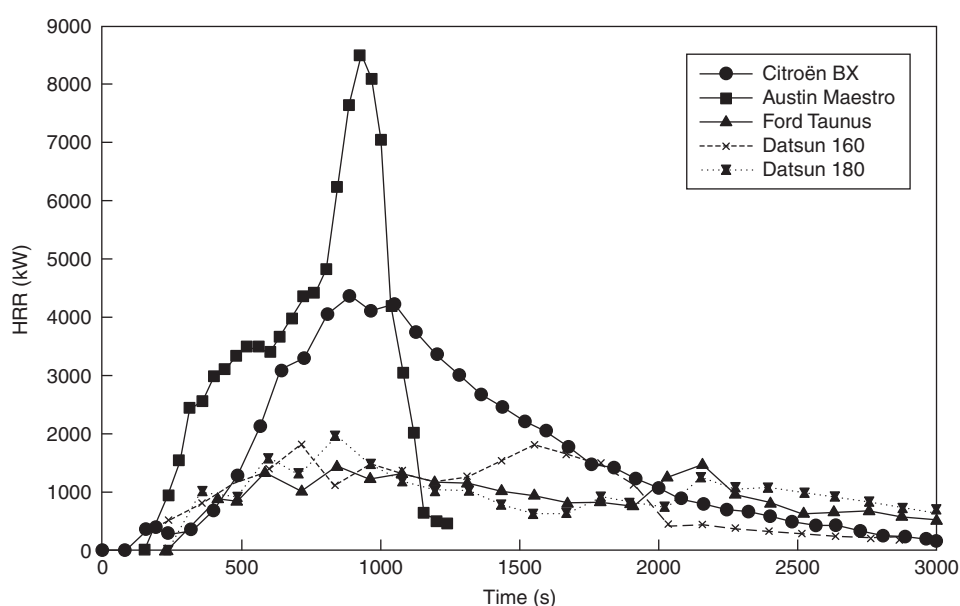


Figure 3-1.46. Passenger cars.

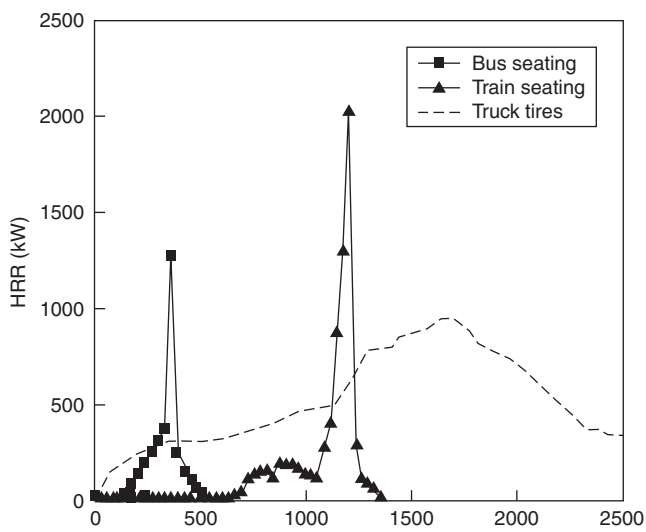


Figure 3-1.47. Vehicle seating and tires.

to be approximately 120 MW. These series of tests have been documented in a book dedicated to the subject of tunnel safety.¹³⁶

Trash Bags and Containers

Bench-scale measurements of trash are not readily feasible, due to the naturally irregular arrangement of these combustibles. There are full-scale test results available, however, that can suggest appropriate values to be used in different circumstances. A small bathroom-size (6.6-L) plastic wastebasket stuffed with 12 milk cartons shows an HRR of about 50 kW, sustained for about 200 s; this has been used extensively as an ignition source in

early HRR testing.³⁸ Some typical trash-bag fires are shown in Figure 3-1.49.⁸⁸ Lee has correlated the peak heat release values according to the effective base diameter and packing density.⁸⁸ Figure 3-1.50 shows that the total burning rate (kW) increases with effective base diameter, but decreases with the tighter packing densities. Figure 3-1.51, conversely, illustrates that when the results are normalized per unit base area, a downward trend can be seen. The correlations according to packing density should only be considered rough observations, and not firm guidelines. Table 3-1.14 shows some additional data,⁷¹ in which, over a certain range, increasing packing density increases the heat release rate. For design purposes, the range of 50 kW to 300 kW appears to cover the bulk of the expected fires from normal residential, office, airplane, or similar occupancy trash bags and trash baskets.

Upholstered Furniture

The HRR of upholstered furniture can be determined in three different ways: (1) by room fire testing; (2) by testing in the furniture calorimeter; (3) by conducting bench-scale tests in the cone calorimeter and then using a mathematical method to predict the full-scale HRR. Of all the occupant goods that can be found in a normal residence, upholstered furniture normally has the highest HRR, thus knowledge of its performance is essential for many applications. Until the 1970s, upholstered furniture used to be made from traditional materials. Thus, in the United States during the 1950s and 1960s, furniture commonly had a wood frame, steel springs, cotton batting padding, and an upholstery fabric of a natural fiber such as wool, silk, or cotton. A fraction of the furniture used latex foam padding instead of cotton batting. In earlier-yet times, furniture was commonly stuffed with rubberized

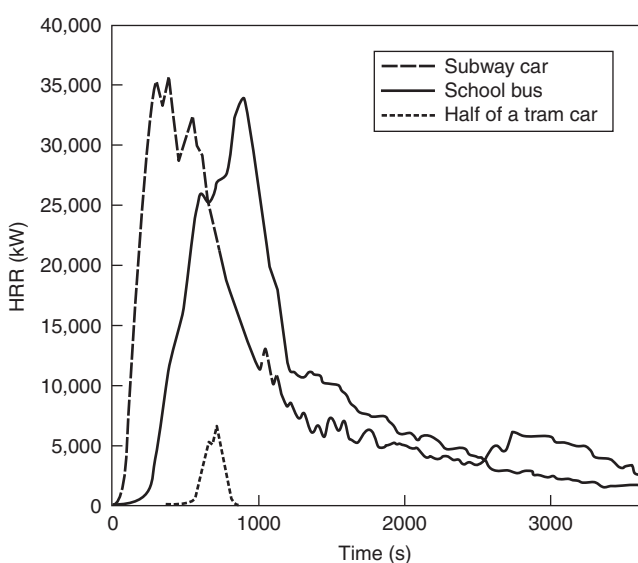


Figure 3-1.48. Transport vehicles.

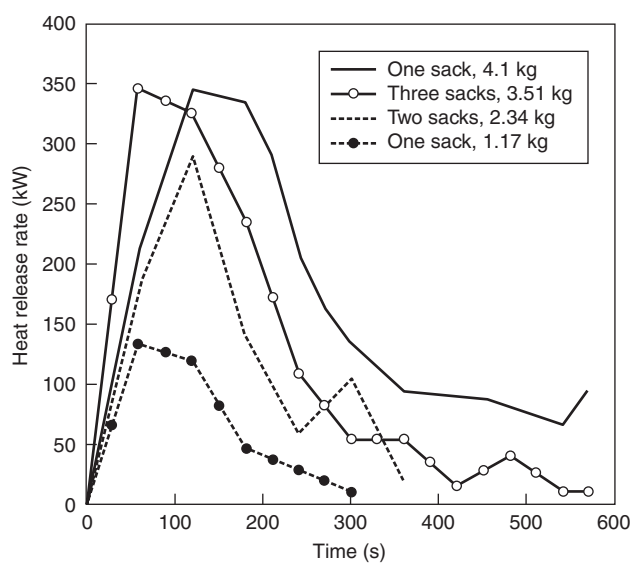
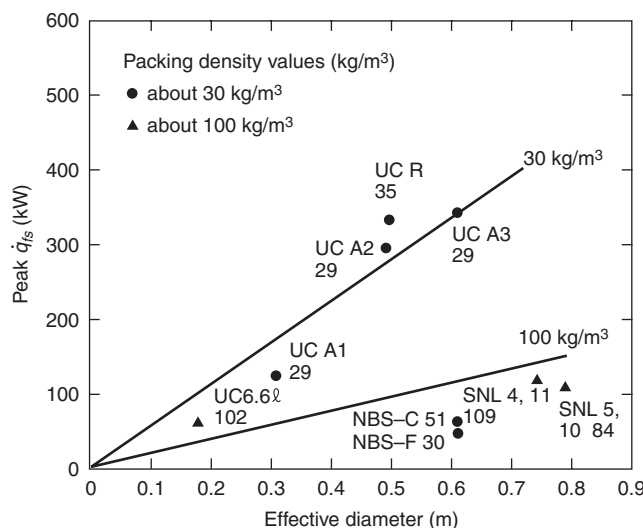
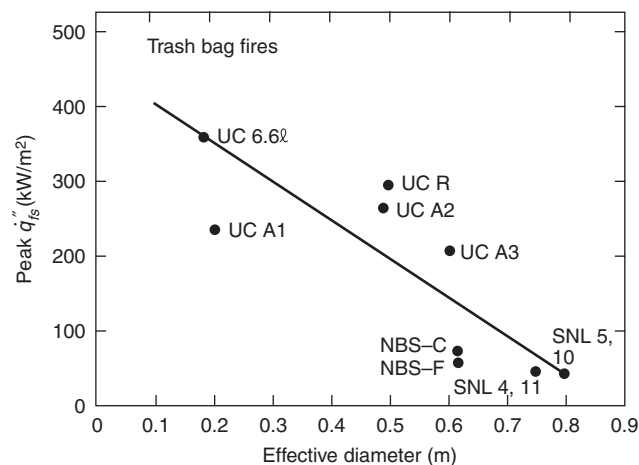


Figure 3-1.49. Trash bags.

Figure 3-1.50. *Trash heat release rates (total HRR).*

horse hair. By the 1970s, however, the predominant padding material became polyurethane foam, and fabric selection became very wide, including both thermoplastic synthetics and natural fibers. The HRRs of the modern furniture were found to be many times those of traditional types,¹³⁷ apart from the special case of latex foam. The latter shows HRR values distinctly higher than for polyurethane foam, but the material has a finite life and few specimens would survive to this day.

Figure 3-1.52 illustrates several furniture items tested at NIST.² Chair F21 used polyurethane foam complying with the California TB 117 standard¹³⁸ and polyolefin fabric. A specimen using ordinary polyurethane foam gave essentially identical results. This level of performance represents a very common but, unfortunately, worst-performance furniture item widely bought by consumers. Specimen F32 is a sofa made from the same materials. Chair F24 illustrates the large improvement in HRR when cotton fabric is substituted for polyolefin fabric. The peak HRR decreases by about one-third, from 2 MW to 700 kW. Further improvements, at present, are not readily available on the retail market. Contract furniture can be procured to advanced specifications, however, notably California TB 133.¹³⁸ The latter limits the peak HRR to val-

Figure 3-1.51. *Trash heat release rates, normalized per unit base area.*

ues less than 80 kW, which will present negligible fire hazard in almost any circumstance.

A cone calorimeter-based prediction method was proposed by Babrauskas and Walton, based on data obtained in 1982.¹³⁹ This was the earliest effort, and was based on a data set comprising materials primarily from the 1970s. Since that time, however, the materials in use by the furniture makers have changed substantially, and, especially, some highly improved materials became available to the contract furniture market. In addition, predictive techniques readily available in the early 1980s were less sophisticated than those developed more recently. Thus, during the course of the European fire research program CBUF, two new predictive models were developed.^{10,109} Model I is a relatively simple model and is described below briefly. A more advanced model was also developed and its details are provided in the above references.

To use the CBUF Model I, cone calorimeter data must first be obtained at an irradiance of 35 kW·m⁻². A well-controlled specimen preparation method is needed, and this is provided in ASTM E1474.¹⁴⁰ Then, one determines if the furniture item is likely to sustain a propagating fire, or whether a moderate external flame source will simply result in limited burning and no propagation. This is determined from the 180-s average of cone calorimeter HRR results. If $\dot{q}_{180}'' < 65 \text{ kW/m}^2$, then no propagation is

Table 3-1.14 *Some Data Obtained at VTT on 14-L Polyethylene Wastebaskets Showing Effect of Packing Density and Basket Construction*

Basket Sides	Basket Mass (kg)	Filling Type	Filling Mass (kg)	Filling Density (kg/m ⁻³)	Peak HRR (kW)	Total Heat Released (MJ)
Solid	0.63	Shredded paper	0.20	14	4	0.7
Netted	0.63	Milk cartons	0.41	29	13	3.0
Solid	0.53	Shredded paper	0.20	14	18	7.3
Netted	0.53	Milk cartons	0.41	29	15	5.8

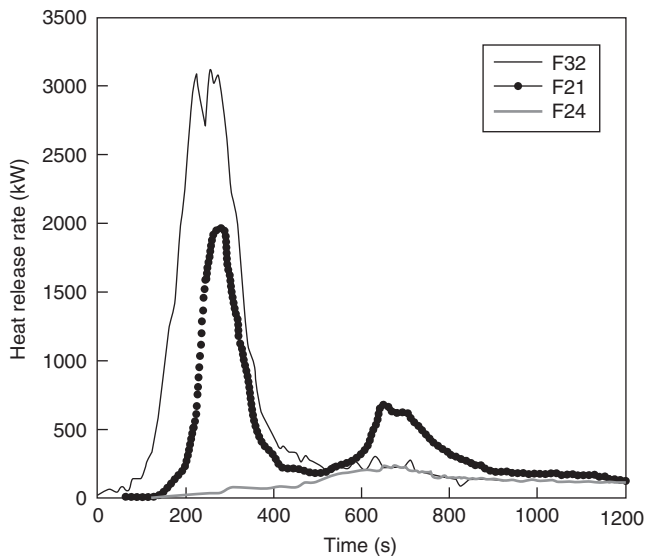


Figure 3-1.52. Several upholstered furniture items tested by NIST.

assumed to occur; otherwise further calculations are made to estimate the peak HRR. The scheme is as follows:

if $(x_1 > 115)$ or $(\dot{q}_{35-\text{tot}}'' > 70)$ and $x_1 > 40$ or
(style = {3,4} and $x_1 > 70$) then $\dot{q}_{fs} = x_2$

Else,

if $x_1 < 56$ then $\dot{q}_{fs} = 14.4x_1$
else, $\dot{q}_{fs} = 600 + 3.77x_1$

where $x_1 = (m_{\text{soft}})^{1.25}$ (style factor A) $(\dot{q}_{35-pk}'' + \dot{q}_{35-300}'')^{0.7}$ $(15 + t_{ig-35})^{-0.7}$ and the subscript 35 denotes that the cone calorimeter HRR tests run at a 35-kW·m⁻² irradiance. The m_{soft} is the mass of the soft, that is, combustible, parts of the item (kg); it includes fabric, foam, interliner, dust cover, and so forth, but does not include the frame nor any rigid support pieces. In addition,

$$x_2 = 880 + 500(m_{\text{soft}})^{0.7} \text{ (style factor A)} \left(\frac{\Delta h_{c,\text{eff}}}{\dot{q}_{35-\text{tot}}''} \right)^{1.4}$$

Here, $\Delta h_{c,\text{eff}}$ is the test-average effective heat of combustion in the cone calorimeter (MJ·kg⁻¹), and $\dot{q}_{35-\text{tot}}''$ is the total heat released at a flux of 35 kW·m⁻². Another correlation predicts the total heat release:

$$q_{\text{tot}} = 0.9m_{\text{soft}} \times \Delta h_{c,\text{eff}} + 2.1(m_{\text{comb,tot}} - m_{\text{soft}})^{1.5}$$

where $m_{\text{comb,tot}}$ denotes the total combustible mass of the item (kg), that is, everything except metal parts.

Finally, the time to peak, t_{pk} (s) for the full-scale item is estimated as

$$t_{pk} = 30 + 4900(\text{style factor B}) \times (m_{\text{soft}})^{0.3} (\dot{q}_{pk\#2}'' - 0.5(\dot{q}_{trough}'')^{-0.5}(t_{pk\#1} + 200))^{0.2}$$

where the peak and trough subscripts refer to the fact that, in the general case, the cone calorimeter HRR of furniture composites shows two main peaks and one trough in between them. The style factors are obtained from Table 3-1.15. With these values computed, a triangular HRR curve can then be constructed. The peak HRR and the time to peak are given directly, while the base width of the triangle is determined from the calculated total heat release of the furniture item.

Wall/Ceiling Lining Materials

Combustible interior finish materials are substantially more difficult to treat than free-standing combustibles. They cannot be measured in a device such as the furniture calorimeter, and require any full-scale study to be a room fire. The materials cover a large area, but the area of active flame involvement is generally not predictable, except after flashover, when in many cases it can be assumed that all surfaces are involved. In the early 1980s, a series of wall materials was studied by Lee at NIST¹⁵ in full-scale, and also in bench-scale, room fires with the cone calorimeter. This work comprised the first attempted correlation between bench scale and full scale for wall lining materials. For several materials in the test series, which included both cellulosics and plastics, it was found that, after flashover, the per-unit-area, full-scale heat-release rates, were approximately the same as the values obtained from the cone calorimeter. Lee's work did not yet lead to a predictive method, since no technique for estimating the flame-covered area, $A(t)$, was found.

At about the same time, Babrauskas found that full-scale fire development on wall/ceiling linings could be

Table 3-1.15 Style Factors Used in the CBUF Model for Predicting Upholstered Furniture Heat Release Rates

Type of Furniture	Style Factor A	Style Factor B
Armchair, fully upholstered, average amount of padding	1.0	1.0
Sofa, 2-seat	1.0	0.8
Sofa, 3-seat	0.8	0.8
Armchair, fully upholstered, highly padded	0.9	0.9
Armchair, small amount of padding	1.2	0.8
Wingback chair	1.0	2.5
Sofa-bed (convertible)	0.6	0.75
Armchair, fully upholstered, metal frame	1.0	0.8
Armless chair, seat and back cushions only	1.0	0.75
Two-seater, armless, seat and back cushions only	1.0	1.0

approximated¹⁴¹ by the expression \dot{q}_{bs-pk}''/t_{ig} , where the HRR value and the ignition time were obtained from the cone calorimeter. The $1/t_{ig}$ factor effectively represented the growth of $A(t)$, but such a scheme was only semi-quantitative.

The first successful quantitative method came with the work of Wickström and Göransson in 1987.¹⁴² The model was based on the premise that the full-scale scenario involves the combustible materials located on the walls and ceiling of the ISO 9705 room. Note that the same material is expected to be placed on both walls and ceiling. The model uses the principle of area convolution and elaborates on Babrauskas' assumption that $1/t_{ig}$ controls the growth of the burning area. The model was later extended and extensively validated in the European research program EUREFIC, EUropean REaction to FIre Classification.¹⁴³ The primary assumptions in the model are

1. The burning area growth rate and the HRR are decoupled.
2. The burning area growth rate is proportional to the ease of ignition, that is, the inverse of the time to ignition in small scale.
3. The history of \dot{q}'' at each location in the full scale is to be the same as in the cone calorimeter test.

The model pays mind to the observation that burning patterns on wall/ceilings can be very different and, especially, that some products stop spreading fire under certain conditions, while others continue. The basic area growth regimes are illustrated in Figure 3-1.53, where the regimes are marked in Roman numerals. The fire spread may follow three different routes. At points A and B fire spread may or may not continue, based on whether a calculated fictitious surface temperature is higher than a critical value. The calculation is based on data from the cone calorimeter. Within the different flame spread regimes, the burning area growth rate depends on ignitability, that is, time to ignition in the cone calorimeter. Once the flame

spread rate is determined, the HRR is calculated assuming that \dot{q}'' is the same in small and large scale. This is understood to be a simplification. The HRR depends on the actual heat flux level received by the product as a function of time. Experience showed, however, that the errors average out and can be included in empirical constants. The method is only moderately difficult to apply, but the description is somewhat lengthy. Details are contained in Babrauskas and Grayson.²² This reference also contains graphs illustrating the kind of agreement that is obtained between predictions and experiments.

While highly successful for its intended purpose, the EUREFIC model does have notable limitations. This model:

- Can only treat the standard ISO 9705 room, with the standard doorway for ventilation
- Only predicts the ISO 9705 100 kW/300 kW burner
- Requires that the material be on both walls and ceiling
- Cannot deal with products that do not ignite in the cone calorimeter at a 25-kW·m⁻² irradiance.

It must be remembered that the primary purpose for developing this model was to predict product performance categories to be obtained in the ISO 9705 test, while only using bench-scale cone calorimeter data. For its intended purpose, it has been an unquestionable success.

The above limitations indicate that the EUREFIC model, while a major breakthrough, was certainly not the final answer to modeling needs for wall/ceiling products. Two extensions have been proposed to generalize the applicability of this model. Göransson, one of the developers of the EUREFIC model, proposed an extension¹⁴⁴ to encompass a huge-scale room. Such a test room was constructed at VTT. Its dimensions were 6.75 m by 9.0 m, with a ceiling height of 4.9 m. The door opening, 0.8 by 2.0 m high, however, was the same as for the ISO 9705 room. The burner operation was at the 100-kW level for 10 min, then at 300 kW for another 10 min, finally at 900 kW for 10 more minutes. An extended model was created for this situation by introducing a new set of regimes to correspond to the 900-kW burner level. In addition, it was found that the constant had to be modified for the 100-kW and 300-kW time periods. The agreement between model and prediction was very good, but only five tests were available for validation at the huge scale.

A second extension was developed by Sumathipala and coworkers.^{145,146} This model extends the applicability to the case of the room fire test studied by Lee.¹⁵ The dimensions of that room are almost identical to the ISO room. The differences arise because (a) the two burner regimes are 40 kW and 160 kW, (b) the burner face size is different, and (c) the product is normally mounted on walls only, rather than walls and ceiling. The authors, however, in their development work included tests of both rooms in both mounting configurations. The success of these extensions confirms that the basic ideas behind the EUREFIC model are sound and can potentially have flexibility. On the other hand, it must be borne in mind that even the extensions are hard-wired configurations and do not yet approach a technique that could be applicable towards user-selected room sizes, burner levels, and product configurations.

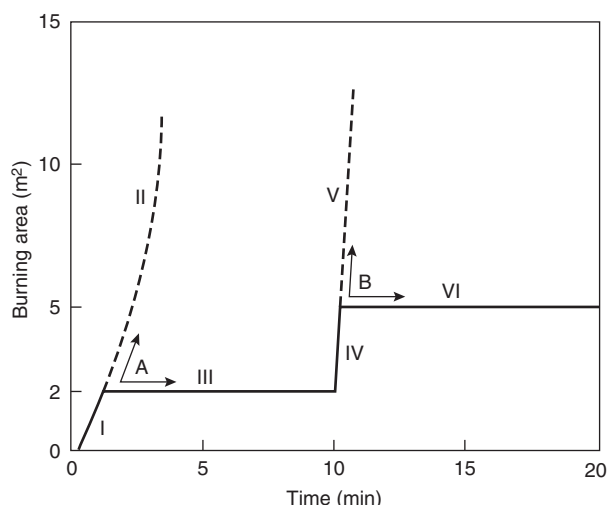


Figure 3-1.53. EUREFIC fire spread regimes.

Perhaps the most ambitious model so far for wall/ceiling products has been one developed by Karlsson and coworkers.^{147,148,149} Karlsson's model incorporates much more of current concepts of plumes, flame length calculations, ceiling jets, and similar constructs than does the EUREFIC model. The model has the same hard-wired limitations that the EUREFIC model has in terms of ignition sources, product configuration, and room size being fixed. Another wall/ceiling model was developed by Quintiere and Cleary^{40,150,151} and extended by Janssens and coworkers.¹⁵²

Wardrobes

Information on the HRR of wardrobes is available from a NIST study.¹⁵³ The test wardrobes are illustrated in Figure 3-1.54; data are given in Table 3-1.16 and Figure 3-1.55. The wardrobes were outfitted with a small amount of clothing, or simulated clothing, and some paper. Tests were not run on the clothes items by themselves. However, since in the case of the steel wardrobe, the only other combustible present was the paint on the metal, it is reasonable to assign a value of about 270-kW peak for the 1.93-kg clothes load. The most important conclusion, however, was that, for combustible constructions, the peak HRR is inversely dependent on wardrobe panel thickness (and, by contrast, no simple connection to combustible specimen mass is seen). Thus, while the total heat content of the 19-mm particleboard specimen is high (see Table 3-1.16), its peak HRR is quite low, since flame spread and fire involvement proceed more slowly over a thick material.

Windows, Plastic

In applications where vandal resistance is needed, polycarbonate windows are sometimes used. This material is combustible, and limited testing was reported by Peacock et al.¹⁵⁴ The tests indicated that it is hard to derive an innate HRR value. The windows do not burn unless a sustained flame or heat source is applied. In that case, the

HRR of the product increases with increasing severity of the ignition source. For a 50-kW exposure source, a test window showed an additional 50-kW HRR, with a burning time of approximately 80 s. For a 200-kW exposure source, the window peak HRR was about an additional 250 kW, but with a longer duration of about 200 s, at progressively diminishing HRR values.

Estimating the HRR for General Combustibles

The previous edition of the Handbook suggested a hypothetical method for estimating the HRR for general combustibles. This was based on some very simplified assumptions, especially that flame spread could, in the first approximation, be ignored. Further experience gained with additional classes of combustibles, as discussed above, suggests that such a condition will only very rarely hold. Furthermore, the user has no way of knowing when it might hold. Thus, prudent design practice should now demand that first recourse be made to the specific sections above that may address the modeler's needs. If they do not, then testing is indicated. For the modeler wishing to start up a major research activity, the schemata outlined for upholstered furniture, mattresses, and wall/ceiling lining should serve as illustrations of appropriate starting points in theory and practice. It must be pointed out, however, that such research programs have proved to be complex and that quick or inexpensive results cannot be expected.

Uncertainty of HRR Measurements

As in any engineering measurement, uncertainty in HRR measurements can be subdivided into (1) bias and (2) random error, sometimes termed *precision uncertainty*. Bias is properly minimized by use of calibration standards; for HRR testing this often comprises a metered flow of a calibration gas of high purity. Another source of bias that can be minimized, when appropriate, is specific to oxygen consumption calorimetry bases measurements. For most testing, a standard oxygen consumption constant value of $13.1 \text{ MJ} \cdot \text{kg}^{-1}$ of oxygen consumed is used. A small number of substances of fire safety interest show oxygen consumption constants substantially different from this standard value. If the molecular composition of the substance is known, a correction can always be made to eliminate this source of bias.

Most of the instruments in which the HRR measurements are made have been subjected to round robins (interlaboratory trials) to quantify the magnitude of random error that can be expected. Comparative values have been compiled by Janssens,¹⁵⁵ as shown in Table 3-1.17. For a number of them, several round robins have been conducted, thus the data shown are identified by year. SBI denotes the European Single Burning Item test,¹⁵⁶ which is a regulatory HRR test for building products that uses two wall panels in a corner configuration, without a ceiling. Observe that the values tabulated refer to the 95 percent confidence intervals; standard deviations can be obtained by dividing the figures shown by 2.8.

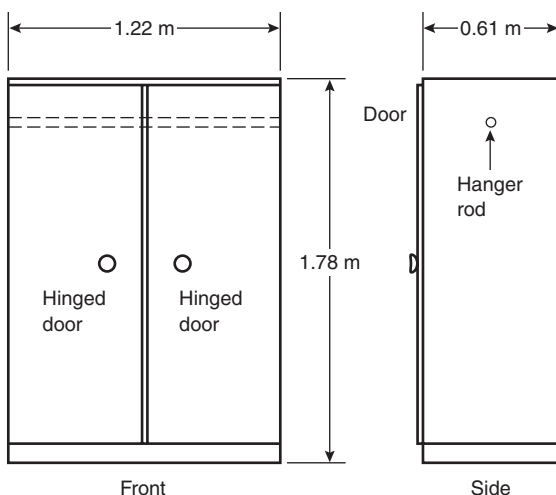


Figure 3-1.54. Configuration of the tested wardrobes.

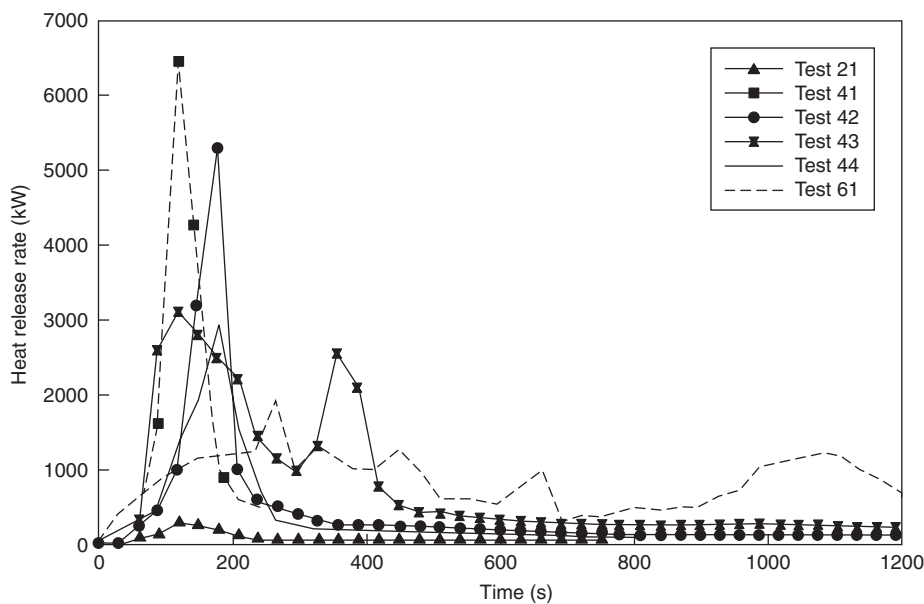


Figure 3-1.55. Various wardrobes.

Table 3-1.16 The Heat Release Rate Properties of Wardrobes

Test Number	Construction	Wardrobe Combustible Mass (kg)	Clothing and Paper (kg)	Peak HRR (kW)	Total Heat Released (MJ)	Average Heat of Combustion (MJ/kg ⁻¹)
21	Steel	0	1.93	270	52	18.8
43	Plywood, 12.7 mm thick	68.3	1.93	3100	1068	14.9
41	Plywood, 3.2 mm thick, unpainted	36.0	1.93	6400	590	16.9
42	Plywood, 3.2 mm thick, 1 coat FR paint	37.3	1.93	5300	486	15.9
44	Plywood, 3.2 mm thick, 2 coats FR paint	37.3	1.93	2900	408	14.2
61	Particleboard, 19 mm thick	120.3	0.81	1900	1349	17.5

Table 3-1.17 The 95 Percent Confidence Limits for Heat Release Rate Test Apparatuses as Determined from Recent Round Robins

Apparatus	Year	Labs	Levels	Peak HRR		Total HRR	
				r (%)	R (%)	r (%)	R (%)
Cone calorimeter	2000	4	16	17	23	8	15
ICAL	1999	3	8	56	67	72	118
SBI	1997	16	30	38	54	47	71
Room calorimeter	1994	12	5	65	79	25	41

Note that *r* denotes the repeatability value whereas *R* denotes the reproducibility value.

References Cited

1. V. Babrauskas, and R.D. Peacock, "Heat Release Rate: The Single Most Important Variable in Fire Hazard," *Fire Safety J.* 18, pp. 255-272 (1992).
2. V. Babrauskas, J.R. Lawson, W.D. Walton, and W.H. Twilley, "Upholstered Furniture Heat Release Rates Measured with a Furniture Calorimeter," *NBSIR 82-2604*, National Bureau of Standards, Washington, DC (1982).
3. G. Heskstad, "A Fire Products Collector for Calorimetry into the MW Range" *FMRC J. I. OC2El.RA*, Factory Mutual Research Corp., Norwood, MA (1981).
4. "Standard Test Method for Fire Testing of Real Scale Upholstered Furniture Items," *ASTM E 1537*, American Society for Testing and Materials, Philadelphia (1993).
5. "Standard Test Method for Fire Testing of Real Scale Mattresses," *ASTM E 1590*, American Society for Testing and Materials, Philadelphia (1994).
6. "Pipe Insulation: Fire Spread and Smoke Production—Full-Scale Test," *NT FIRE 036*, NORDTEST, Espoo, Finland (1988).
7. "Upholstered Furniture: Burning Behaviour—Full-Scale Test," *NT FIRE 032*, 2nd ed., NORDTEST, Espoo, Finland (1991).
8. "Standard Fire Test of Limited-Smoke Cables, UL 1685," Underwriters Laboratories, Northbrook, IL (1991).
9. M.M. Hirschler, "Use of Heat Release Calorimetry in Standards," in *Fire Calorimetry, DOT/FAA/CT-95/46*, Federal Aviation Administration, Atlantic City International Airport, NJ, pp. 69-80 (1995).
10. B. Sundström (ed.), "Fire Safety of Upholstered Furniture—The Final Report on the CBUF Research Programme," *Report EUR 16477 EN*, Directorate-General Science, Research and Development (Measurements and Testing), European Commission, Distributed by Interscience Communications Ltd., London (1995).
11. V. Babrauskas, and U.G. Wickström, "Thermoplastic Pool Compartment Fires," *Combustion and Flame*, 34, pp. 195-201 (1979).
12. M. Dahlberg, "Error Analysis for Heat Release Rate Measurement with the SP Industry Calorimeter," *SP Report 1994:29*, Swedish National Testing and Research Institute, Borås (1994).
13. L.Y. Cooper, "Some Factors Affecting the Design of a Calorimeter Hood and Exhaust," *J. Fire Prot. Engineering*, 6, pp. 99-112 (1994).
14. F.L. Fisher and R.B. Williamson, "Intralaboratory Evaluation of a Room Fire Test Method," *NBS-GCR-83-421*, National Bureau of Standards, Washington, DC (1983).
15. B.T. Lee, "Standard Room Fire Test Development at the National Bureau of Standards," in *Fire Safety: Science and Engineering, ASTM STP 882* (T.Z. Harmathy, ed.), American Society for Testing and Materials, Philadelphia (1985).
16. B. Sundström, "Room Fire Test in Full Scale for Surface Products," *Rapport SP-RAPP 1984:16*, Statens Provningsanstalt, Borås, Sweden (1984).
17. "Surface Products: Room Fire Tests in Full Scale," *NT FIRE 025*, NORDTEST, Espoo, Finland (1986).
18. "International Standard—Fire Tests—Full Scale Room Test for Surface Products," *ISO 9705:1993(E)*, International Organization for Standardization, Geneva (1993).
19. V. Babrauskas, "Development of the Cone Calorimeter—A Bench Scale Heat Release Rate Apparatus Based on Oxygen Consumption," *Fire and Materials*, 8, pp. 81-95 (1984).
20. "Standard Test Method for Heat and Visible Smoke Release Rates for Materials and Products Using an Oxygen Consumption Calorimeter," *ASTM E 1354*, American Society for Testing and Materials, Philadelphia (1997).
21. "International Standard—Fire Tests—Reaction to Fire—Part 1: Rate of Heat Release from Building Products (Cone Calorimeter Method)," *ISO 5660-1:1993(E)*, International Organization for Standardization, Geneva (1993).
22. V. Babrauskas and S.J. Grayson (eds.), *Heat Release in Fires*, Elsevier Applied Science Publishers, London (1992).
23. J. Urbas and G.E. Luebbers, "The Intermediate Scale Calorimeter Development," *Fire and Materials*, 19, pp. 65-70 (1995).
24. "Standard Test Method for Determining of Fire and Thermal Parameters of Materials, Products, and Systems Using an Intermediate Scale Calorimeter (ICAL)," *ASTM E 1623*, American Society for Testing and Materials, Philadelphia.
25. V. Babrauskas, "A Closed-Form Approximation for Post-Flashover Compartment Fire Temperatures," *Fire Safety J.*, 4, pp. 63-73 (1981).
26. M. Kokkala, U. Göransson, and J. Söderbom, "Five Large-Scale Room Fire Experiments. Project 3," *EUREFIC Fire Research Program (VTT Publications 104)*, VTT-Technical Research Center of Finland, Espoo (1992).
27. W.J. Parker, "Prediction of the Heat Release Rate of Wood," Ph.D. Dissertation, George Washington University, Washington, DC (1988).
28. T. Hirata, T. Kashiwagi, and J.E. Brown, "Thermal and Oxidative Degradation of Poly(methylmethacrylate): Weight Loss," *Macromolecules*, 18, pp. 1410-1418 (1984).
29. T. Kashiwagi, T. Hirata, and J.E. Brown, "Thermal and Oxidative Degradation of Poly(methylmethacrylate): Molecular Weight," *Macromolecules*, 18, pp. 131-138 (1985).
30. C. Vovelle, J.L. Delfau, M. Reuillon, J. Bransier, and N. Laraqui, "Experimental and Numerical Study of the Thermal Degradation of PMMA," in *Papers of ITSEMAP International Meeting of Fire Research and Test Centers*, Avila, Spain, pp. 43-66 (1986).
31. K.A. Holland and I.D. Rae, "Thermal Degradation of Polymers, Part 3. Thermal Degradation of a Compound Which Models the Head-to-Head Linkage in Poly(Methyl Methacrylate)," *Australian J. of Chemistry*, 40, pp. 687-692 (1987).
32. L.E. Manring, "Thermal Degradation of Saturated Poly(methylmethacrylate)," *Macromolecules*, 21, pp. 528-530 (1988).
33. A. Inaba, T. Kashiwagi, and J.E. Brown, "Effects of Initial Molecular Weight on Thermal Degradation of Poly(methyl methacrylate), Part 1," *Polymer Degradation and Stability*, 21, pp. 1-20 (1988).
34. K.D. Steckler, T. Kashiwagi, H.R. Baum, and K. Kanemaru, "Analytical Model for Transient Gasification of Noncharring Thermoplastic Materials," in *Fire Safety Science—Proceedings of the Third International Symposium*, Elsevier Applied Science, New York, pp. 895-904 (1991).
35. K. Opstad, "Modelling of Thermal Flame Spread on Solid Surfaces in Large-Scale Fires," Ph.D. Dissertation, Norges Tekniske Høgskole, Trondheim, Norway (1995).
36. V. Babrauskas, "Specimen Heat Fluxes for Bench-Scale Heat Release Rate Testing," *Fire and Materials*, 19, pp. 243-252 (1995).
37. "Basic Considerations in the Combustion of Hydrocarbon Fuels in Air," *NACA Report 1300*, National Advisory Committee for Aeronautics, Washington, DC (1957).
38. V. Babrauskas and J.F. Krasny, "Fire Behavior of Upholstered Furniture," *NBS Monograph 173*, National Bureau of Standards, Washington, DC (1985).
39. M. Kokkala and M. Heinilä, "Flame Height, Temperature, and Heat Flux Measurements on a Flame in an Open Corner of Walls," *Project 5 of the EUREFIC Fire Research Programme*, Valtion Teknillinen Tutkimuskeskus, Espoo, Finland (1991).

40. J.G. Quintiere, "A Simulation Model for Fire Growth on Materials Subject to a Room-Corner Test," *Fire Safety J.*, 20, pp. 313–339 (1993).
41. A.J. Parker, A.B. Wenzel, and T. Al-Hassan, "Evaluation of Passive Fire Protection by Jet Fire Test Procedure," Paper 4-d in Twenty-Ninth Loss Prevention Symposium, American Institute of Chemical Engineers, New York (1995).
42. J. Söderbom, "EUREFIC—Large Scale Tests According to ISO DIS 9705," *Project 4 of the EUREFIC Fire Research Programme, SP Report 1991:27*, Statens Provningsanstalt, Borås, Sweden (1991).
43. Y. Hasemi, "Experimental Wall Flame Heat Transfer Correlations for the Analysis of Upward Wall Flame Spread," *Fire Science and Technology*, 4, pp. 75–90 (1984).
44. J.G. Quintiere, "The Application of Flame Spread Theory to Predict Material Performance," *J. of Research of the National Bureau of Standards*, 93, pp. 61–70 (1988).
45. A.K. Kulkarni, C.I. Kim, and C.H. Kuo, "Turbulent Upward Flame Spread for Burning Vertical Walls Made of Finite Thickness," *NIST-GCR-91-597*, National Institute of Standards and Technology, Gaithersburg, MD (1991).
46. J.B. Fang and J.N. Breese, "Fire Development in Residential Basement Room," *NBSIR 80-2120*, National Bureau of Standards, Gaithersburg, MD (1980).
47. V. Babrauskas and R.B. Williamson, "The Historical Basis of Fire Resistance Testing, Parts I and II," *Fire Technology*, 14, pp. 184–194, 205, 304–316 (1978).
48. B.T. Rhodes, "Burning Rate and Flame Heat Flux for PMMA in the Cone Calorimeter" M.S. Thesis, University of Maryland, *NIST-GCR-95-664*, National Institute of Standards and Technology, Gaithersburg, MD (1994).
49. D. Hopkins, Jr. and J.G. Quintiere, "Material Fire Properties and Predictions for Thermoplastics," *Fire Safety J.*, 26, pp. 241–268 (1996).
50. J. Gore, M. Klassen, A. Hamins, and T. Kashiwagi, "Fuel Property Effects on Burning Rate and Radiative Transfer from Liquid Pool Flames," in *Fire Safety Science—Proceedings of the Third International Symposium*, Elsevier Applied Science, London, pp. 395–404 (1991).
51. M. Janssens, "Cone Calorimeter Measurements of the Heat of Gasification of Wood," in *INTERFLAM '93: Sixth International Fire Conference Proceedings*, Interscience Communications Ltd., London, pp. 549–558 (1993).
52. U. Sorathia, T. Dapp, J. Kerr, and J. Wehrle, "Flammability Characteristics of Composites," *DTRC SME 89/90*, U.S. Navy, David Taylor Research Center, Bethesda, MD (1989).
53. J.W. Rowen and J.W. Lyons, "The Importance of Externally Imposed Heat Flux on the Burning Behavior of Materials," *J. Cellular Plastics*, 14, pp. 25–32 (1978).
54. K. Paul, unpublished data, RAPRA Technology, Shawbury, England.
55. P. Elliot, R.H. Whiteley, and J.E. Staggs, "Steady State Analysis of Cone Calorimeter Data," in *Proceedings of the Fourth International Fire and Materials Conference*, Interscience Communications Ltd., London, pp. 35–42 (1995).
56. T.G. Cleary, and J.G. Quintiere, "Flammability Characterization of Foam Plastics," *NISTIR 4664*, National Institute of Standards and Technology, Gaithersburg, MD (1991).
57. R.M. Nussbaum and B.A.L. Östman, "Larger Specimens for Determining Rate of Heat Release in the Cone Calorimeter," *Fire and Materials*, 10, pp. 151–160 (1986); and 11, p. 205 (1987).
58. M. Janssens and J. Urbas, "Comparison of Small and Intermediate Scale Heat Release Data," in *INTERFLAM '96*, Interscience Communications Ltd., London, pp. 285–294 (1996).
59. L. Orloff, A.T. Modak, and R.L. Alpert, "Burning of Large-Scale Vertical Wall Surfaces," in *Sixteenth International Symposium on Combustion*, The Combustion Institute, Pittsburgh, pp. 1345–1354 (1976).
60. V. Babrauskas, "Cone Calorimeter Annotated Bibliography 1982–1991," *Tech. Note 1296*, National Institute of Standards and Technology, Gaithersburg, MD (1992).
61. S. Särdqvist, "Initial Fires: RHR, Smoke Production and CO Generation from Single Items and Room Fire Tests, *LUTVDG/TVBB-3070-SE*, Lund University, Dept. of Fire Safety Engineering, Lund, Sweden (1993).
62. P.S. Klitgaard and R.B. Williamson, "The Impact of Contents on Building Fires," *J. Fire and Flammability/Consumer Product Flammability Supplement*, 2, pp. 84–113 (1975).
63. V. Babrauskas et al., "Fire Hazard Comparison of Fire-Retarded and Non-Fire-Retarded Products," *NBS Special Publication SP 749*, National Bureau of Standards, Washington, DC (1988).
64. J. Mangs and O. Keski-Rahkonen, "Full Scale Experiments on Electronic Cabinets," *VTT Publications 186*, Valtion Teknillinen Tutkimuskeskus, Espoo, Finland (1994).
65. J. Mangs and O. Keski-Rahkonen, "Full Scale Experiments on Electronic Cabinets II," *VTT Publications 269*, Valtion Teknillinen Tutkimuskeskus, Espoo, Finland (1996).
66. O. Keski-Rahkonen and J. Mangs, "Maximum and Minimum Rate of Heat Release during Flashover in Electronic Cabinets of NPPS," Paper presented at *Fire Safety in Power Plants and Industrial Installations, SMiRT 13 Post Conference Seminar No. 6*, Gramado, Brazil, Valtion Teknillinen Tutkimuskeskus, Espoo, Finland (1995).
67. K.M. Tu and S. Davis, "Flame Spread of Carpet Systems Involved in Room Fires," *NBSIR 76-1013*, National Bureau of Standards, Washington, DC (1976).
68. P. Vandeveld and P. Van Hees, "Wind Aided Flame Spread of Floor Coverings, Development and Evaluation of Small and Large Scale Tests," in *INTERFLAM '96*, Interscience Communications Ltd., London, pp. 57–67 (1996).
69. S. Ames, R. Colwell, and K. Shaw, "The Fire Behaviour and Fire Testing of Carpet Used as a Stair Covering," in *INTERFLAM '96*, Interscience Communications Ltd., London, pp. 69–77 (1996).
70. R.B. Williamson and N.A. Dembsey, "Advances in Assessment Methods for Fire Safety," *Fire Safety J.*, 20, pp. 15–38 (1993).
71. A. Ahonen, M. Kokkala, and H. Weckman, "Burning Characteristics of Potential Ignition Sources of Room Fires," *Research Report 285*, Technical Research Centre, Espoo, Finland (1984).
72. G. Damant and S. Nurbakhsh, "Christmas Trees—What Happens When They Ignite?" *Fire and Materials*, 18, pp. 9–16 (1994).
73. V. Babrauskas and E. Stauss, to be published.
74. D.W. Stroup, L. DeLauter, J. Lee, and G. Roadarmel, "Scotch Pine Christmas Tree Fire Tests," *FR 4010*, National Institute of Standards and Technology, Gaithersburg, MD (1999).
75. J.S. Steel, unpublished data, National Institute of Standards and Technology, Gaithersburg, MD (1985).
76. F. Folke, "Experiments in Fire Extinguishment," *NFPA Quarterly*, 31, p. 115 (1937).
77. L. Nilsson, "The Effect of Porosity and Air Flow on the Rate of Combustion of Fire in an Enclosed Space," *Bulletin 18*, Lund Institute of Technology, Lund, Sweden (1971).
78. S. Yamashika and H. Kurimoto, "Burning Rate of Wood Crib," *Rept. of Fire Res. Inst. Japan*, 41, p. 8 (1976).
79. T.Z. Harmathy, "Experimental Study on the Effect of Ventilation on the Burning of Piles of Solid Fuels," *Comb. and Flame*, 31, p. 259 (1978).
80. J.G. Quintiere and B.J. McCaffrey, "The Burning of Wood and Plastic Cribs in an Enclosure, Vol. 1," *NBSIR 80-2054*, National Bureau of Standards, Washington, DC (1980).

81. W.L. Fons, H.B. Clements, and P.M. George, "Scale Effects on Propagation Rate of Laboratory Crib Fires," in *Ninth International Symposium on Combustion*, The Combustion Institute, Pittsburgh (1962).
82. M.A. Delichatsios, "Fire Growth Rates in Wood Cribs," *Comb. and Flame*, 27, p. 267 (1976).
83. L.D. Moore, "Full-Scale Burning Behavior of Curtains and Drapes," *NBSIR 78-1448*, National Bureau of Standards, Washington, DC (1978).
84. I. Wetterlund and U. Göransson, "A Full-Scale Fire Test Method for Free-Hanging Curtain and Drapery Textiles," *SP Report 1988:45*, Swedish National Testing Institute, Borås (1988).
85. National Institute of Standards and Technology, unpublished data, Gaithersburg, MD.
86. A. Tewarson, J.L. Lee, and R.F. Pion, "Categorization of Cable Flammability, Part 1. Experimental Evaluation of Flammability Parameters of Cables Using Laboratory-Scale Apparatus," *EPRI Project RP 1165-1*, Factory Mutual Research Corp., Norwood, MA (1979).
87. P.S. Sumitra, "Categorization of Cable Flammability. Intermediate-Scale Fire Tests of Cable Tray Installations," *Interim Report NP-1881, Research Project 1165-1*, Factory Mutual Research Corp., Norwood, MA (1982).
88. B.T. Lee, "Heat Release Rate Characteristics of Some Combustible Fuel Sources in Nuclear Power Plants," *NBSIR 85-3195*, National Bureau of Standards, Washington, DC (1985).
89. V. Babrauskas, unpublished test results (1997).
90. G. Heskestad, "Flame Heights of Fuel Arrays with Combustion in Depth," in *Fire Safety Science—Proceedings of the Fifth International Symposium*, International Association for Fire Safety Science, Melbourne, Australia, pp. 427–438 (1997).
91. G. Heskestad, "Flame Heights of Fuel Arrays with Combustion in Depth," *FMRC J.I. 0Y0J3.RU(2)*, Factory Mutual Research Corp., Norwood, MA (1995).
92. R.K. Dean, "Stored Plastics Test Program," *FMRC Serial No. 20269*, Factory Mutual Research Corp., Norwood, MA (1975).
93. H.-Z. Yu and H.-C. Kung, "Strong Buoyant Plumes of Growing Rack Storage Fires," in *Twentieth Symposium (International) on Combustion*, The Combustion Institute, Pittsburgh, pp. 1547–1554 (1984).
94. H.-Z. Yu and H.-C. Kung, "Strong Buoyant Plumes of Growing Rack Storage Fires," *FMRC J.I. 0G2E7.RA(1)*, Factory Mutual Research Corp., Norwood, MA (1984).
95. "Guide for Smoke and Heat Venting," *NFPA 204*, National Fire Protection Association, Quincy, MA (1998).
96. J.L. Lee and R.K. Dean, "Fire Products Collector Tests of Polyethylene Terephthalate (PET) Plastic Bottles in Corrugated Carton," *FMRC J.I. 0N0J6.RA070(A)*, Factory Mutual Research Corp., Norwood, MA (1986).
97. J.L. Lee, "Combustibility Evaluation of Shredded Newsprint Commodity and an Improved Polyurethane Foam Packaging Product Using the Fire Products Collector," *FMRC J.I. 0K0E6.RANS*, Factory Mutual Research Corp., Norwood, MA (1984).
98. H.-Z. Yu, "RDD and Sprinklered Fire Tests for Expanded Polystyrene Egg Crates," *FMRC J.I. 0R2E3.RA(1)*, Factory Mutual Research Corp., Norwood, MA (1990).
99. H. Hasegawa, N.J. Alvares, and J.A. White, "Fire Tests of Packaged and Palletized Computer Products," *Fire Technology*, 35, pp. 294–307 (1999).
100. H. Hasegawa, personal communication (2000).
101. T.A. Roberts, R. Merrifield, and S. Tharmalingam, "Thermal Radiation Hazards from Organic Peroxides," *J. Loss Prev. Process Industries*, 3, pp. 244–252 (1990).
102. V. Babrauskas, unpublished test data (1997).
103. H.-Z. Yu and P. Stavrianidis, "The Transient Ceiling Flows of Growing Rack Storage Fires," *FMRC J.I. 0N1J0.RA(3)*, Factory Mutual Research Corp., Norwood, MA (1989).
104. H.E. Mitler, "Input Data for Fire Modeling," in *Thirteenth Meeting of the UJNR Panel on Fire Research and Safety, NISTIR 6030, vol. 1*, National Institute of Standards and Technology, Gaithersburg, MD, pp. 187–199 (1997).
105. V. Babrauskas, "Bench-Scale Predictions of Mattress and Upholstered Chair Fires," in *Fire and Flammability of Furnishings, ASTM STP 1233*, American Society for Testing and Materials, Philadelphia, pp. 50–62 (1994).
106. G.H. Damant and S. Nurbakhsh, *Heat Release Tests of Mattresses and Bedding Systems*, State of California, Bureau of Home Furnishings and Thermal Insulation, North Highlands, CA (1991).
107. G. Holmstedt and I. Kaiser, "Brand I Vårdbäddar," *SP-RAPP 1983:04* Statens Provningsanstalt, Borås, Sweden (1983).
108. B. Andersson, "Fire Behaviour of Beds and Upholstered Furniture—An Experimental Study," *LUTVDG/ISSN 0282-3756*, Lund University, Dept. of Fire Safety Engineering, Lund, Sweden (1985).
109. V. Babrauskas, D. Baroudi, J. Myllymäki, and M. Kokkala, "The Cone Calorimeter Used for Predictions of the Full-Scale Burning Behaviour of Upholstered Furniture," *Fire and Materials*, 21, pp. 95–105 (1997).
110. W.D. Walton and E.K. Budnick, "Quick Response Sprinklers in Office Configurations: Fire Test Results," *NBSIR 88-3695*, National Bureau of Standards, Gaithersburg, MD (1988).
111. D. Madrzykowski and R.L. Vettori, "Sprinkler Fire Suppression Algorithm for the GSA Engineering Fire Assessment System," *NISTIR 4833*, National Bureau of Standards, Gaithersburg, MD (1992).
112. D. Madrzykowski, "Office Work Station Heat Release Rate Study: Full Scale vs. Bench Scale," in *INTERFLAM '96*, Interscience Communications Ltd., London, pp. 47–55 (1996).
113. L.M. Krasner, "Burning Characteristics of Wooden Pallets as a Test Fuel," *Serial 16437*, Factory Mutual Research Corp., Norwood, MA (1968).
114. V. Babrauskas, "Pillow Burning Rates," *Fire Safety J.*, 8, pp. 199–200 (1984/85).
115. "Pipe Insulation: Fire Spread and Smoke Production—Full-Scale Test," *NT FIRE 036*, NORDTEST, Espoo, Finland (1988).
116. I. Wetterlund and U. Göransson, "A New Test Method for Fire Testing of Pipe Insulation in Full Scale," *SP Report 1986:33*, Swedish National Testing Institute, Borås (1986).
117. V. Babrauskas, "Toxic Fire Hazard Comparison of Pipe Insulations: The Realism of Full-Scale Testing Contrasted with Assessments from Bench-Scale Toxic Potency Data Alone," in *ASIAFLAM '95*, Interscience Communications Ltd., London, pp. 439–452 (1995).
118. V.I. Blinov and G.N. Khudiakov, "Diffusion Burning of Liquids," *NTIS No. AD296762*, U.S. Army Translation (1961).
119. H.C. Hottel, "Review Certain Laws Governing Diffusive Burning of Liquids," by V.I. Blinov and G.N. Khudiakov, *Fire Research Abstracts and Reviews*, 1, pp. 41–44 (1958).
120. V. Babrauskas, tables and charts in *Fire Protection Handbook*, 18th ed., National Fire Protection Assn., Quincy, MA, pp. A-1 to A-17 (1997).

121. V. Babrauskas, "Estimating Large Pool Fire Burning Rates," *Fire Technology*, 19, pp. 251–261 (1983).
122. A. Gosse, personal communication, BG Technologies Ltd. (2000).
123. A.D. Putorti, Jr., J.A. McElroy, and D. Madrzykowski, "Flammable and Combustible Liquid Spill/Burn Patterns" NIJ 604-00, National Institute of Justice, U.S. Department of Justice, Washington, DC (2000).
124. A.T. Modak, "Ignitability of High-Fire-Point Liquid Spills," EPRI NP-1731, Electric Power Research Inst., Palo Alto, CA (1981).
125. V. Babrauskas, "COMPF2: A Program for Calculating Post-Flashover Fire Temperatures," Tech. Note 991, National Bureau of Standards, Washington, DC (1979).
126. A. Hamins, S.J. Fischer, T. Kashiwagi, M.E. Klassen, and J.P. Gore, "Heat Feedback to the Fuel Surface in Pool Fires," *Combustion Science and Technology*, 97, pp. 37–62 (1994).
127. K.C. Adiga, D.E. Ramaker, P.A. Tatem, and F.W. Williams, "Modeling Pool-Like Gas Flames of Propane," *Fire Safety J.*, 14, pp. 241–250 (1989).
128. K.C. Adiga, D.E. Ramaker, P.A. Tatem, and F. Williams, "Modeling Thermal Radiation in Open Liquid Pool Fires," in *Fire Safety Science—Proceedings of the Second International Symposium*, International Association for Fire Safety Science, Hemisphere Publishing Corp., New York, pp. 241–250 (1989).
129. H. Koseki and G.W. Mulholland, "Effect of Diameter on the Burning of Crude Oil Pool Fires," *Fire Technology*, 27, pp. 54–65 (1991).
130. H. Koseki, "Boilover and Crude Oil Fire," *J. Applied Fire Science*, 3, pp. 243–272 (1993/1994).
131. M. Shipp and M. Spearpoint, "Measurements of the Severity of Fires Involving Private Motor Vehicles," *Fire and Materials*, 19, pp. 143–151 (1995).
132. J. Mangs and O. Keski-Rahkonen, "Characterization of the Fire Behaviour of a Burning Passenger Car, Part I: Car Fire Experiments," *Fire Safety J.*, 23, pp. 17–35 (1994).
133. U. Göransson, and A. Lundqvist, "Fires in Buses and Trains: Fire Test Methods," SP Report 1990:45, Swedish National Testing and Research Institute, Borås (1990).
134. P.A. Hansen, "Fire in Tyres: Heat Release Rate and Response of Vehicles," STF25 A95039, SINTEF NBL, Norwegian Fire Research Laboratory, Trondheim, Norway (1995).
135. M.P. Shipp, "Fire Spread in Tyre Dumps," in *INTERFLAM '96*, Interscience Communications Ltd., London, pp. 79–88 (1996).
136. *Proceedings of the International Conference on Fires in Tunnels, SP—Swedish National Testing and Research Institute, Borås*, Interscience Communications Ltd, London (1994).
137. V. Babrauskas, "Upholstered Furniture Heat Release Rates: Measurements and Estimation," *J. Fire Sciences* 1, pp. 9–32 (1983).
138. Flammability Information Package (contains Technical Bulletins 116, 117, 121, 133, 106, and 26). Bureau of Home Furnishings, Dept. of Consumer Affairs, State of California, North Highlands (1987).
139. V. Babrauskas and W.D. Walton, "A Simplified Characterization for Upholstered Furniture Heat Release Rates," *Fire Safety J.*, 11, pp. 181–192 (1986).
140. "Standard Test Method for Determining the Heat Release Rate of Upholstered Furniture and Mattress Components or Composites Using a Bench-Scale Oxygen Consumption Calorimeter," E 1474-96a, American Society for Testing and Materials, Philadelphia (1996).
141. V. Babrauskas, "Bench-Scale Methods for Prediction of Full-Scale Fire Behavior of Furnishings and Wall Linings," SFPE Technical Report 84-10, Society of Fire Protection Engineers, Boston (1984).
142. U. Wickström and U. Göransson, "Prediction of Heat Release Rates of Surface Materials in Large-Scale Fire Tests Based on Cone Calorimeter Results," *J. Testing and Evaluation*, 15, pp. 364–370 (1987).
143. *Proceedings of the International EUREFIC Seminar 1991*, Interscience Communications Ltd, London (1991).
144. U. Göransson, "Model, Based on Cone Calorimeter Results, for Explaining the Heat Release Rate Growth of Tests in a Very Large Room," in *INTERFLAM '93: Sixth Intl. Fire Conf. Proc.*, Interscience Communications Ltd., London, pp. 39–47 (1993).
145. K. Sumathipala, A.K. Kim, and G.D. Lougheed, "A Comparison of ASTM and ISO Full-Scale Room Fire Test Methods," in *Proceedings of Fire and Materials, Second International Conference*, Interscience Communications Ltd., London, pp. 101–110 (1993).
146. K. Sumathipala, A.K. Kim, and G.D. Lougheed, "Configuration Sensitivity of Full-Scale Room Fire Tests," in *Proceedings of Fire and Materials, Third International Conference*, Interscience Communications Ltd., London, pp. 237–246 (1994).
147. B. Karlsson and S.E. Magnusson, "An Example Room Fire Model," in *Heat Release in Fires*, Elsevier Applied Science, London, pp. 159–171 (1992).
148. B. Karlsson, "Models for Calculating Flame Spread on Wall Lining Materials and the Resulting Heat Release Rate in a Room," *Fire Safety J.*, 23, pp. 365–386 (1994).
149. S.E. Magnusson and B. Sundström, "Combustible Linings and Room Fire Growth—A First Analysis," in *Fire Safety: Science and Engineering*, ASTM STP 882, American Society for Testing and Materials, Philadelphia, pp. 45–69 (1985).
150. T.G. Cleary and J.G. Quintiere, "A Framework for Utilizing Fire Property Tests," in *Fire Safety Science—Proceedings of the Third International Symposium*, Elsevier Applied Science, London, pp. 647–656 (1991).
151. J.G. Quintiere, G. Haynes, and B.T. Rhodes, "Applications of a Model to Predict Flame Spread over Interior Finish Materials in a Compartment," *J. Fire Prot. Engineering*, 7, p. 1013 (1995).
152. M. Janssens, O. Grexa, M. Dietenberger, and R. White, "Predictions of ISO 9705 Room/Corner Test Using a Simple Model," in *Proceedings of Fire and Materials Fourth International Conference*, Interscience Communications Ltd., London, pp. 73–83 (1995).
153. J.R. Lawson, W.D. Walton, and W.H. Twilley, "Fire Performance of Furnishings as Measured in the NBS Furniture Calorimeter, Part I," NBSIR 83-2787, National Bureau of Standards, Gaithersburg, MD (1983).
154. R.D. Peacock, P.A. Reneke, J.D. Averill, R.W. Bukowski, and J.H. Klote, "Fire Safety of Passenger Trains, Phase II: Application of Fire Hazard Analysis Techniques," National Institute of Standards and Technology, Gaithersburg, MD (2000).
155. M.L. Janssens, "Heat Release Rate," *FORUM Workshop on Measurement Needs for Fire Safety*, National Institute of Standards and Technology, Gaithersburg, MD (2000).
156. D.A. Smith and K. Shaw, "Single Burning Item (SBI) Test: The Euroclasses and Transitional Arrangements," in *INTERFLAM '99*, Interscience Communications Ltd., London, pp. 1–9 (1999).

SECTION THREE

CHAPTER 2

Calorimetry

Marc Janssens.

Introduction

Heat release rate is the primary variable that determines the contribution to compartment fire hazard from materials. This was clearly demonstrated by Babrauskas and Peacock in a recent sensitivity study using the NIST fire hazard assessment software Hazard I.¹ However, the importance of heat release rate in fire hazard assessment was first recognized three decades ago by Smith at Ohio State University.² Smith and co-workers developed one of the first bench-scale heat release rate test methods.³ They also proposed various procedures to assess compartment fire hazard on the basis of the bench-scale data, ranging from simple calculation methods⁴ to a complex computer model.⁵ This work was initiated at a time when the most accurate measuring techniques for heat release rate were not available, and when computer fire modeling was still in its infancy. Moreover, Smith advocated a practical approach based on engineering judgment and intuition rather than detailed science. Hence, his test and fire hazard assessment methods were far from perfect and received major criticism.^{6,7} Nevertheless, Smith deserves recognition as one of the pioneers of heat release rate calorimetry.

There are several reasons why heat release rate is so important. First, it is directly related to mass loss rate. The toxic fire hazard of a material is a function of the release rate of toxic gases, which is the product of total mass loss rate and yield of these gases. Thus, the fire hazard of material A, which has a high yield of toxic gases, is less than

that of material B with a lower yield, if the mass loss rate of A under identical exposure conditions is significantly lower. For example, many fire retardant treatments increase the yield of toxic gases, but dramatically reduce the mass loss rate, resulting in a lower fire hazard. This was illustrated in the study by Babrauskas and Peacock.¹ Second, the heat released by a material burning in a compartment results in a temperature rise of the hot layer gases and compartment walls and ceiling. Part of the radiation from hot surfaces and gases strikes the fuel surface, resulting in an increase in the mass loss rate over that if the material were to burn outside a compartment. Increased heat release enhances this thermal feedback effect.

With compartment fire hazard assessment as the primary application, there is a need for high quality heat release rate data, and, consequently, for devices and methods to measure it accurately. There are two basic approaches to evaluate the fire hazard of a material. The first option consists of an experimental evaluation in full scale. Typically, this approach requires multiple large scale fire tests covering all relevant fire and end-use conditions. The second option is the use of bench-scale data, primarily heat release rate, in conjunction with a calculation procedure to estimate full-scale fire performance. This second approach is significantly more versatile, and time and cost efficient. With the continuous improvement of the predictive capability and accuracy of fire models and calculation methods, it has become the preferred approach. With this in mind, the emphasis of this chapter is on bench-scale calorimetry.

Many reaction-to-fire test methods include an (often crude) measure of heat release rate.⁸⁻¹² However, with one exception (model box test in Japan¹²), these test methods were developed several decades ago and their measuring techniques are inaccurate and obsolete. Moreover, exposure conditions were not well defined and controlled, therefore it is difficult to relate the results of these early tests to real fire performance. The discussion in this chap-

Dr. Marc Janssens is associate professor in the Fire Safety Engineering Technology program at the Department of Engineering Technology of the University of North Carolina at Charlotte. His research has focused on computer fire modeling, fire hazard and risk assessment, fire test standards development, and the experimental and theoretical evaluation of material flammability with emphasis on heat release calorimetry.

ter does not include these reaction-to-fire tests, and is limited to calorimetric methods that were developed primarily for measuring heat release rate. These heat release test methods vary widely in concept and features. Four measuring techniques have been used and are described in detail below. This is followed by a discussion of the effect of various bench-scale calorimeter features and construction details. Then, a brief description is given of the many bench-scale calorimeters that were developed since the early 1970s. A comparison between these calorimeters is also included. The chapter is concluded with a discussion of some large-scale calorimeters, and a section on the uncertainty of heat release rate measurements. However, it is appropriate to start with a review of different methods for using heat release rate data in fire hazard assessment, illustrating the kind of data a bench-scale calorimeter needs to provide.

Use of Bench-Scale Heat Release Rate Data

Because of the volume of available data, a general discussion of this subject would be either incomplete or very lengthy. Therefore, the focus here is on one particular fire scenario; namely, wall linings in a room/corner test. Such a test consists of a small room with a single ventilation opening in the front narrow wall. Specimens of the material to be evaluated are attached to walls and/or ceiling. A gas burner ignition source is placed in contact with the walls in one of the rear corners. Products of combustion emerging through the ventilation opening are collected in a hood, and extracted through an exhaust duct. Instrumentation is located in the duct to measure the mole fraction of various gas species, total flow rate, smoke obscuration, and so on. Room/corner test methods have become a popular tool to evaluate the fire hazard of linings and have been standardized throughout the world.¹³⁻¹⁶ These tests are discussed in more detail in the section on large-scale calorimeters.

Techniques for using bench-scale data to predict performance in the room/corner test differ widely in degree of complexity and sophistication. Requirements for the calorimeter that provides bench-scale data vary accordingly.

Interpretation of Bench-Scale Data in Terms of Material Properties

The most sophisticated technique to predict room/corner test performance uses heat release rate and other bench-scale measurements to obtain material properties. These properties (ideally) are apparatus-independent, and are used as input for a computer model that predicts full-scale fire performance. The two properties that are related to heat release rate are the effective heat of combustion, $\Delta h_{c,\text{eff}}$ ($\text{kJ}\cdot\text{g}^{-1}$), and the heat of gasification, Δh_g ($\text{kJ}\cdot\text{g}^{-1}$). These properties are described below.

The effective heat of combustion is the ratio of heat release rate to mass loss rate

$$\Delta h_{c,\text{eff}} = \frac{\dot{q}''}{\dot{m}''} \quad (1)$$

where

\dot{q}'' = heat release rate per unit exposed area ($\text{kW}\cdot\text{m}^{-2}$)

\dot{m}'' = mass loss rate per unit exposed area ($\text{g}\cdot\text{m}^{-2}\cdot\text{s}^{-1}$)

The symbol $\Delta h_{c,\text{eff}}$ is used to make a distinction between this property and the lower calorific value measured in an oxygen bomb calorimeter, $\Delta h_{c,\text{net}}$. The latter is measured in a small container under high pressure and in pure oxygen, conditions that are not representative of real fires. The conditions in the new types of bench-scale calorimeters resemble those in real fires much more closely. For some fuels, in particular gases, $\Delta h_{c,\text{eff}}$ is nearly identical to $\Delta h_{c,\text{net}}$. However, for most solid materials $\Delta h_{c,\text{eff}}$ is significantly lower and is the value to be used for fire hazard assessment. The issue is revisited in the next section.

The second material property is heat of gasification, Δh_g , defined as the net heat flow into the material required to convert one mass unit of solid material to volatiles. The net heat flux into the material can be obtained from an energy balance at the surface of the specimen (see Figure 3-2.1). Typically, a sample exposed in a bench-scale calorimeter is heated by external heaters and by its own flame. Heat is lost from the surface in the form of radiation. Due to the small sample size, the flame flux is primarily convective, and flame absorption of external heater and specimen surface radiation can be neglected. Hence, Δh_g can be defined as

$$\Delta h_g = \frac{\dot{q}_{\text{net}}''}{\dot{m}''} = \frac{\dot{q}_e'' + \dot{q}_f'' - \dot{q}_l''}{\dot{m}''} \quad (2)$$

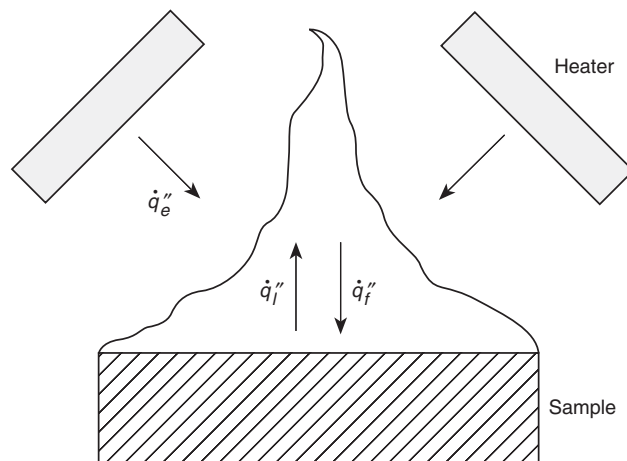


Figure 3-2.1. Surface heat balance.

If the flame is approximated as a homogeneous gray gas volume, the fluxes in the numerator of equation (2) can be written as

$$\dot{q}_f'' = \dot{q}_{f,c}'' + \dot{q}_{f,r}'' = h^*(T_f - T_s) + \sigma \varepsilon_f T_f^4 \approx h^*(T_f - T_s) \quad (3)$$

and

$$\dot{q}_l'' = \sigma \varepsilon_s (T_s^4 - T_\infty^4) \quad (4)$$

where

h^* = convection coefficient, corrected for blowing ($\text{kW} \cdot \text{m}^{-2} \cdot \text{K}^{-1}$)

\dot{q}_e'' = incident heat flux from external heaters ($\text{kW} \cdot \text{m}^{-2}$)

\dot{q}_f'' = flame flux ($\text{kW} \cdot \text{m}^{-2}$)

$\dot{q}_{f,c}''$ = convective fraction of the flame flux ($\text{kW} \cdot \text{m}^{-2}$)

$\dot{q}_{f,r}''$ = radiative fraction of the flame flux ($\text{kW} \cdot \text{m}^{-2}$)

\dot{q}_l'' = radiative losses from the surface ($\text{kW} \cdot \text{m}^{-2}$)

\dot{q}_{net}'' = net heat flux into the sample ($\text{kW} \cdot \text{m}^{-2}$)

T_f = flame temperature (K)

T_s = surface temperature (K)

T_∞ = ambient temperature (K)

ε_f = flame emissivity

ε_s = surface emissivity

σ = Boltzmann constant ($5.67 \cdot 10^{-11} \text{ kW} \cdot \text{m}^{-2} \cdot \text{K}^{-4}$)

Some materials exhibit nearly steady mass loss rates when exposed to a fixed irradiance, \dot{q}_e'' . For these materials, T_s reaches a steady value after a short initial transient period, and all terms in Equations 1–4 are approximately constant. Δh_g can then be obtained by measuring steady mass loss rates over a range of irradiance levels, and by plotting \dot{m}'' as a function of \dot{q}_e'' . Δh_g is calculated as the reciprocal of the slope of a straight line fitted through the data points. $\dot{q}_l'' - \dot{q}_f''$ is obtained as the intercept of this line with the abscissa. Tewarson et al.¹⁷ and Petrella¹⁸ have used this technique to obtain average Δh_g values for a large number of materials. Tewarson et al. also conducted tests in vitiated O₂/N₂ mixtures, and found \dot{q}_f'' to decrease linearly with decreasing oxygen concentration. Analysis of these additional experiments made it possible to separate \dot{q}_f'' and \dot{q}_l'' .

Many materials, in particular those that form an insulating char layer as they burn, take a long time to reach steady burning conditions or may never reach steady conditions. Equations 1–4 are still valid for such materials, but the heat and mass fluxes and resulting $\Delta h_{c,\text{eff}}$ and Δh_g values vary with time. Tewarson and Petrella have used the same techniques to determine average Δh_g values for nonsteady burning materials using average mass loss rates. They found that average \dot{m}'' is still an approximately linear function of \dot{q}_e'' . However, the average heat of gasification values obtained in this manner may not have any physical meaning. Physically meaningful nonsteady values for Δh_g can be obtained from Equation 2, with \dot{q}_f'' and \dot{q}_l'' calculated according to Equations 3 and 4 respectively. In order to do this, ε_s , T_s , ε_f , and T_f need to be measured, calculated or estimated in some way. Surface

temperature is the most important and most difficult to determine. Flame temperature and emissivities are nearly constant over the duration of a test, and can be estimated more easily.^{19–21} Urbas and Parker used thermocouples to measure T_s for wood specimens tested in the cone calorimeter.²² The problem with this technique is maintaining good contact between the thermocouple and the exposed surface. Parker and Urbas designed a special tension system to hold the thermocouple hot junction against the char surface as this surface recedes during a test. The technique worked quite well, but the tension system made testing rather tedious. Urbas used an infrared pyrometer to measure T_s for wood specimens in an intermediate scale calorimeter.²³ This technique is much more practical, but not without problems. First, the pyrometer must operate in a specific wavelength range so that the flame becomes transparent. The sensor used by Urbas responds to infrared radiation between 8 and 12 μm. This is well above the radiation bands of CO₂ and H₂O, and in a region where, given the high flame temperature (compared to the surface temperature), soot radiation is negligible. Second, a pyrometer measures emitted and reflected radiation from a surface. Hence, assuming the surface acts as a gray body radiator, surface emissivity must be known to calculate T_s from this measurement. For wood char, Urbas found $\varepsilon_s \approx 1$ and confirmed this by comparing pyrometer and thermocouple measurements. For many other materials $\varepsilon_s < 1$, so that reflected radiation from the heater might be a problem. An alternative approach to determine T_s is by calculation. Janssens obtained T_s as a function of time for wood specimens exposed in the cone calorimeter by solving the equation for heat conduction through the char layer using an integral technique.²⁴ The resulting values for Δh_g compared well with those by Urbas. A drawback of this approach is that thermal properties of the material or its char are needed.

Another problem with unsteady values of $\Delta h_{c,\text{eff}}$ and Δh_g is the fact that time from ignition in a bench-scale test does not correspond directly to that in a full-scale room/corner fire. Considering a small element of the wall lining that is exposed in a room/corner test, incident heat flux varies with time as the compartment fire grows. In a bench-scale calorimeter, incident heat flux is nearly constant. Hence, the time axis of the unsteady $\Delta h_{c,\text{eff}}$ and $\Delta h_{c,\text{net}}$ curves must be transformed to a variable that also can be used for unsteady exposure conditions. Smith proposed using cumulative heat release rate to scale the time axis.²⁵ Mitler suggested cumulative mass loss.²⁶ Janssens plotted Δh_g curves for wood as a function of char depth.²⁴ Since char depth was defined as being proportional to cumulative mass loss, this approach is analogous to Mitler's.

With $\Delta h_{c,\text{eff}}$ and Δh_g for a material, performance in a room/corner test can be predicted. First, the exposed surface of the material is subdivided into smaller elements so that the incident heat flux to each element is approximately uniform. Then, a model is needed to determine the net heat flux into every element. This requires calculation of radiative and convective heat transfer between the different surfaces, gas volumes, and flames in the compartment coupled with the solution of compartment-wide mass, energy, and species conservation equations.

\dot{m}'' can be calculated for every segment as the ratio of \dot{q}_{net}'' to Δh_g . The heat release rate from every segment is then obtained by multiplying \dot{m}'' with $\Delta h_{c,\text{eff}}$, with adjustment for oxygen vitiation or starvation. Note that, although $\Delta h_{c,\text{eff}}$ and Δh_g are the most important properties, other properties are needed to estimate the time to ignition of every element and the resulting flame spread over the surface. As the fire grows and conditions in the compartment change, the sequence of calculations must be repeated for subsequent time steps. Due to the required spatial subdivision of the exposed surfaces which can be adapted to the gas phase mesh, field models are ideally suited for this kind of application. Nevertheless, only a few attempts to use such models for simulating room/corner tests have been reported.^{27,28} This is probably because field models are very complex. Consequently, the number of field model users is small and most of them are not concerned with modeling the room/corner test. Fortunately, a simple model developed by Quintiere indicates such a level of detail is not needed to obtain reasonable predictions.²⁹ Quintiere assumed the total burning area is exposed to a uniform heat flux, and estimated this flux on the basis of experimental data for flame fluxes and hot layer temperatures as a function of heat release rate. Constant values were used for $\Delta h_{c,\text{eff}}$ and Δh_g , where the latter was determined from a reciprocal of the slope of a straight line fitted through data points of peak \dot{m}'' plotted against \dot{q}_e'' measured in the cone calorimeter.

If heat release measurements are first converted to material properties to use them for fire hazard assessment, the bench-scale calorimeter that is used must have certain features. If unsteady values for $\Delta h_{c,\text{eff}}$ and Δh_g are used, the calorimeter must be capable of measuring \dot{m}'' and the addition of instrumentation to measure T_s must be practical (unless T_s is calculated or estimated in some other way). If average or steady values for $\Delta h_{c,\text{eff}}$ and Δh_g are sufficient, only the total mass loss over the duration of a test is needed, and measuring \dot{m}'' is not required. If the model addresses the effect of oxygen vitiation or starvation on $\Delta h_{c,\text{eff}}$, it must be possible to operate the calorimeter in atmospheres different from ambient. If the model keeps track of the concentration of gas species and soot, the calorimeter must be capable of measuring soot and gas yields. The calorimeter must also be capable of running tests over a wide range of (steady) irradiance levels.

The discussion in this subsection is useful in clarifying a common misconception. Often it is believed that materials which are used in a particular orientation in practice should be tested in that orientation. This is not necessarily correct. Heat release rate as such is independent of specimen orientation. However, the heat release rate in a calorimeter under otherwise identical exposure conditions is higher in the horizontal than in the vertical orientation. This is because the heat feedback from the flame is much greater in the horizontal orientation. In that orientation, the flame is a relatively large volume of hot gas located above the specimen. The flame is only a thin sheet in front of a vertical sample, leading to a much lower heat feedback. Neither of these situations is comparable to that in a real fire, where burning areas are much larger and heat flux from the flame is much greater regardless of orientation of the fuel surface. Hence, the best

approach is to interpret bench-scale measurements in terms of material properties that are independent of the test apparatus. These material properties can then be used to predict full-scale performance using a method which accounts for the effect of the enhanced heat flux from large flames. The above reasoning indicates that bench-scale testing in the vertical orientation is preferable, because the heat feedback to the flame is smaller and errors of flame flux estimates are relatively less important. However, for practical reasons, it is often preferable to run bench-scale tests in the horizontal orientation to avoid problems with, for example, melting and dripping of the specimen.

Direct Use of Heat Release Rate Curves at Multiple Irradiance Levels

If the differences between surface heat losses and flame fluxes in full-scale versus bench-scale are ignored or compensated for by an adjustment to the calculated external full-scale heat flux, heat release curves obtained over a range of irradiance levels can be used without conversion to material properties. This approach was suggested by Smith.⁵ Heat release rate is measured as a function of time at three or four irradiance levels in the range of 20 to 65 $\text{kW}\cdot\text{m}^{-2}$. Then, the time axis is transformed, for reasons discussed in the previous subsection, by using cumulative heat release. Smith also developed a computer model to predict the incident heat flux to the burning area which is subdivided into smaller elements. Heat release from an element at a certain time is based on interpolation between the measured heat release curves, corresponding to the cumulative heat release from that element at that time and to the calculated incident heat flux. Smith and Green demonstrated that this interpolation method is reasonably accurate by running tests in their calorimeter while varying the incident heat flux.³⁰ The heat release rate curves measured under dynamic exposure conditions could be predicted quite accurately from interpolation between measurements of heat release rate under constant irradiance levels. A calorimeter that is to produce data suitable for this use must be capable of exposing specimens over a fairly wide range of constant irradiance levels.

Direct Use of Heat Release Rate Curves at a Single Irradiance Level

The approach outlined in the previous subsection can be simplified even further, if a heat release curve at a single irradiance level is used. This irradiance level is chosen so that it is a representative average (over space and time) of heat flux levels occurring in room/corner tests, typically between 25 and 50 $\text{kW}\cdot\text{m}^{-2}$. Thus, the dynamic effects of the room fire on the exposure level are ignored while the dynamics of the heat release curve are largely maintained. The single heat release curve is used in combination with a flame spread algorithm to predict heat release rate as a function of time in the room/corner test. The flame spread algorithm can be very simple, but needs at least some ignition data for the material. Transformation of the time axis for the heat release curve is not

necessary. As time proceeds, the burning area expands as new sections of the material are ignited. The flame spread algorithm calculates at every time step how large this newly ignited section is. Once ignited, the heat release rate from this section is obtained from the heat release curve for the same time relative to ignition. Thus, the total burning area and heat release at any time is obtained as a convolution integral. The most widely known room/corner test simulation of this nature was developed by Wickström and Göransson.³¹ A calorimeter that is to provide data suitable for this use must be capable of providing heat release data at a single irradiance level, and some ignition data for the flame spread algorithm.

Regression Analysis

A regression analysis is the least sophisticated method. A room/corner test result that is indicative of the fire hazard of a material, for example, time to flashover, is correlated against a heat release parameter in combination with one or several other parameters measured in the calorimeter. This heat release parameter is typically the average heat release rate over a fixed period of time measured at one irradiance level. A (usually linear) statistical model is developed, and a regression analysis is performed to obtain model constants that give the best predictions for a given set of bench-scale and full-scale data. The resulting equation can then be used to predict full-scale performance on the basis of bench-scale data for materials that have not been tested in the room/corner test. Reasonable correlations of this type for the International Standards Organization (ISO) room/corner test were reported by Östman et al.³² and Karlsson.³³ Clearly, with this approach the dynamics of the heat release curve are lost entirely. There is no difference in the prediction of full-scale performance for two materials with heat release curves of very different shape, provided the average heat release rate and other bench-scale measurements used in the correlation are identical. The predictions are valid for one scenario and geometry only. A positive aspect of this method is that the most rudimentary bench-scale calorimeter is sufficient to provide the necessary bench-scale data.

Summation of Bench-Scale Test Data Use

It is thus obvious that there is a wide variety of methods to use bench-scale heat release rate data for predicting real fire hazard of a material. In general, the versatility of the approach varies inversely with its complexity. A method using material properties can usually be applied over a range of conditions and configurations. Simple regression analyses are locked into one specific full-scale fire scenario. As an example, Quintiere's model can be used for different ignition sources (e.g. ASTM vs. ISO burner), specimen configurations (materials on walls only vs. walls and ceiling), and geometries. Östman's correlation only predicts time to flashover for one specific set of room/corner test conditions.

It must be stressed that, although heat release rate is the most important parameter, it is not the only parameter that needs to be included in a hazard analysis. Other

factors related to piloted ignition, smoke release rate, opposed-flow flame spread, and so on, must be considered also. The Babrauskas/Peacock study illustrated that fire hazard is most sensitive to changes in the heat release rate of the burning fuel, but varies with other material characteristics as well.

Techniques for Measuring Heat Release Rate

Sensible Enthalpy Rise Method

Consider the energy balance of a gas-phase control volume enclosing the flame of a burning specimen (see Figure 3-2.2). Air enters the control volume at a flow rate \dot{m}_a and temperature T_a . The enthalpy of this air can be written as

$$h_a = h_a^0 + c_p(T_a - T_0) \quad (5)$$

where

h_a = enthalpy of air at temperature T_a ($\text{kJ}\cdot\text{kg}^{-1}$)

h_a^0 = enthalpy of air at reference temperature T_0 ($\text{kJ}\cdot\text{kg}^{-1}$)

c_p = average specific heat of air between T_0 and T_a ($\text{kJ}\cdot\text{kg}^{-1}\cdot\text{K}^{-1}$)

T_a = temperature of the air entering the combustion zone (K)

T_0 = reference temperature (K)

Part of the heat flux that strikes the exposed surface is conducted into the specimen. This heat flow raises the temperature of the solid, and decomposes some fraction into combustible fuel vapors. These vapors are generated at a rate \dot{m}_v , and enter the control volume at temperature T_v . Under the assumption that specific heat of all gases is

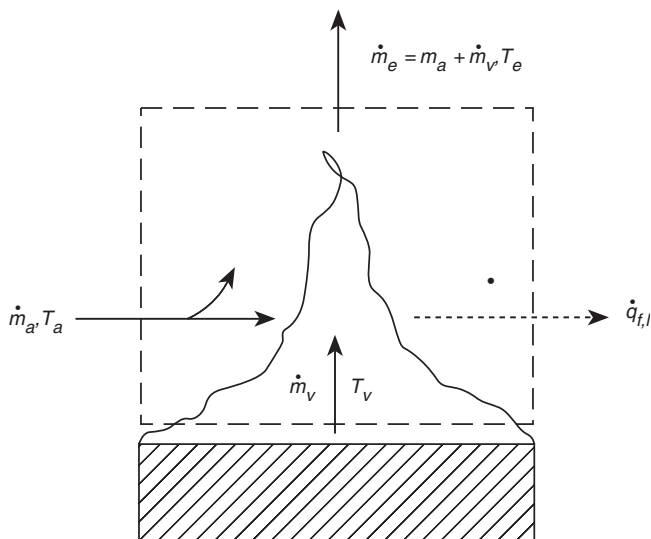


Figure 3-2.2. **Gas-phase energy balance.**

approximately constant and temperature-independent (a reasonable approximation), the enthalpy of the fuel vapors can be written as

$$h_v = h_v^0 + c_p(T_v - T_0) \quad (6)$$

where

h_v = enthalpy of volatiles at temperature T_v ($\text{kJ}\cdot\text{kg}^{-1}$)

h_v^0 = enthalpy of volatiles at reference temperature T_0 ($\text{kJ}\cdot\text{kg}^{-1}$)

T_v = temperature of volatiles entering the combustion zone (K)

The fuel vapors mix with air, and are converted in the flame to products of combustion. The total flow rate, \dot{m}_e , of combustion products, which includes some excess air, has a temperature T_e and enthalpy given by

$$h_e = h_e^0 + c_p(T_e - T_0) \quad (7)$$

where

h_e = enthalpy of combustion products at temperature T_e ($\text{kJ}\cdot\text{kg}^{-1}$)

h_e^0 = enthalpy of combustion products at reference temperature T_0 ($\text{kJ}\cdot\text{kg}^{-1}$)

T_e = temperature of combustion products leaving the control volume (K)

T_e is higher than the mass-weighted average of T_a and T_v , because of the heat released by combustion in the flame, \dot{q} . However, only a fraction of this heat contributes to the temperature rise of the gases. This fraction is referred to as the convective fraction of the heat release rate. The remaining fraction of \dot{q} is lost and is denoted as $\dot{q}_{f,l}$. For the most part, $\dot{q}_{f,l}$ is lost in the form of thermal radiation to the walls of the apparatus (closed configuration) or to the environment (open configuration). A small part of $\dot{q}_{f,l}$ consists of convective and radiative feedback to the fuel surface. Assuming gas phase transients can be neglected, application of the first law of thermodynamics for the control volume in Figure 3-2.2 results in

$$\dot{q}_{f,l} = \dot{m}_a h_a + \dot{m}_v h_v - \dot{m}_e h_e \quad (8)$$

As an example, suppose now that the same flow rates of air and volatiles, both at temperature T_0 , are mixed in a hypothetical combustion chamber. Furthermore, assume the combustion reactions are identical to those in the calorimeter in Figure 3-2.2, and the products of combustion are cooled down to the reference temperature T_0 without condensing water. This hypothetical situation is shown in Figure 3-2.3. Application of the first law of thermodynamics for the combustion chamber control volume in Figure 3-2.3 leads to

$$\dot{q} = \dot{m}_a h_a^0 + \dot{m}_v h_v^0 - \dot{m}_e h_e^0 \quad (9)$$

Here, \dot{q} is equal to the total rate of heat released by combustion in the flame. This heat release rate is identical in Figure 3-2.2 and Figure 3-2.3, but it is distributed in dif-

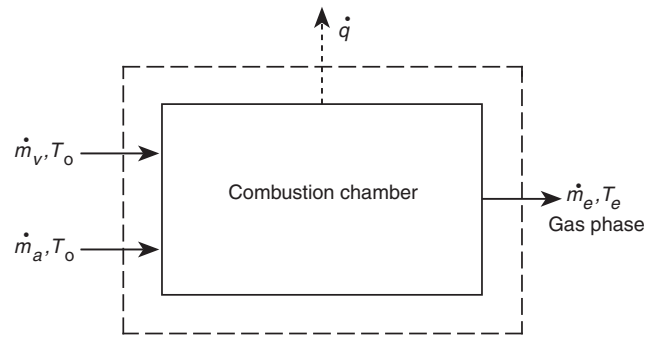


Figure 3-2.3. Hypothetical combustion chamber.

ferent ways. By expressing the heat released per unit mass of volatiles, an effective heat of combustion can be defined as

$$\dot{m}_v \Delta h_{c,\text{eff}} \equiv \dot{q} \quad (10)$$

or per unit exposed area

$$\dot{m}'_v \Delta h_{c,\text{eff}} \equiv \dot{q}'' \quad (11)$$

$\Delta h_{c,\text{eff}}$ is for the combustion reactions as they take place in the calorimeter. As explained in the previous section, $\Delta h_{c,\text{eff}}$ must be distinguished from the net heat of combustion, $\Delta h_{c,\text{net}}$, measured in an oxygen bomb calorimeter. The difference between $\Delta h_{c,\text{eff}}$ and $\Delta h_{c,\text{net}}$ is very significant for charring materials such as wood. In an oxygen bomb calorimeter, nearly all the mass of wood is consumed, leaving a small fraction of noncombustible ash (usually less than 1 percent by mass). The net heat of combustion, $\Delta h_{c,\text{net}}$, of dry wood is in the range of 16–18 $\text{kJ}\cdot\text{g}^{-1}$. When exposed under real fire conditions, only 70–80 percent of the mass is converted to volatiles that burn almost completely. The heat of combustion of the volatiles, $\Delta h_{c,\text{eff}}$, measured in a bench-scale calorimeter is only 12–13 $\text{kJ}\cdot\text{g}^{-1}$. A solid char residue remains, primarily consisting of carbon, with a net heat of combustion of approximately 30 $\text{kJ}\cdot\text{g}^{-1}$. In an oxygen bomb calorimeter, most of this char is also burnt, explaining why $\Delta h_{c,\text{net}}$ exceeds $\Delta h_{c,\text{eff}}$ by 25–50 percent. Even for materials that do not form a char, $\Delta h_{c,\text{eff}}$ can be significantly lower than $\Delta h_{c,\text{net}}$ if combustion of the volatiles in the bench-scale calorimeter is incomplete. In this case, the products of combustion contain measurable amounts of combustible components such as CO, soot, unburnt hydrocarbons, and so forth. The ratio of $\Delta h_{c,\text{eff}}$ to $\Delta h_{c,\text{net}}$ is defined as combustion efficiency, χ . For clean-burning gaseous fuels, such as methane, χ is close to unity. For fuels that produce sooty flames, including gases, χ can be significantly lower. For example, χ for acetylene is approximately 0.75. χ values for a number of gases, liquids and solids are listed in Chapter 4 of Section 3.

Substitution of equations 5, 6, 7, and 9 into 8 leads to

$$\begin{aligned} \dot{q} - \dot{q}_{f,l} &= c_p \dot{m}_e (T_e - T_0) - c_p \dot{m}_a (T_a - T_0) \\ &\quad - c_p \dot{m}_v (T_v - T_0) \end{aligned} \quad (12)$$

For most combustible materials, the stoichiometric air to fuel ratio ranges between 3 and 16. Moreover, bench-scale calorimeters are usually operated with excess air. For example, the standard initial flow rate in the cone calorimeter is $30 \text{ g}\cdot\text{s}^{-1}$. Based on the oxygen consumption method discussed later in this chapter, the stoichiometric flow rate of air for a 10 kW fire (practical upper limit in the cone calorimeter) can be calculated as $[10 \text{ kW}]/[3 \text{ kJ per g of air}] = 3.3 \text{ g}\cdot\text{s}^{-1}$. Thus, the air supply in the cone calorimeter is at least nine times stoichiometric, or at least $9 \times 3 = 27$ times the generation rate of volatiles. Usually, the ratio is much greater. Hence, \dot{m}_o is negligible compared to \dot{m}_a and Equation 12 can be approximated as

$$\dot{q} - \dot{q}_{f,l} \approx \dot{m}_a c_p (T_e - T_a) \quad (13)$$

This equation is the basis for the sensible enthalpy method. Heat release rate is calculated from the temperature rise $T_e - T_a$ of the gases flowing through a calorimeter. A schematic of a calorimeter based on this principle is shown in Figure 3-2-4.

There are a few problems with the practical implementation of this technique. The main concern is that only a fraction of the heat released in the flame is used to raise the sensible enthalpy or temperature of the gases. Therefore, another method is needed to recover or measure the loss term, $\dot{q}_{f,l}$. Some calorimeters have water-cooled walls that trap most of the losses. These losses can be estimated by measuring the enthalpy rise of the cooling water. However, due to the additional hardware and instrumentation, such calorimeters are rather complex and difficult to operate. A more popular method relies on a gas burner

calibration to determine $\dot{q}_{f,l}$, under the assumption that the losses are fuel-independent. Defining the loss fraction, χ_R , by

$$\dot{q} - \dot{q}_{f,l} \equiv (1 - \chi_R)\dot{q} \quad (14)$$

The symbol χ_R is chosen for this fraction, since $\dot{q}_{f,l}$ consists primarily of radiation. If the calorimeter is operated with a constant air flow rate \dot{m}_a , Equation 13 can then be written as

$$\dot{q} \approx \frac{\dot{m}_a c_p}{1 - \chi_R} (T_e - T_a) \equiv k(T_e - T_a) \quad (15)$$

The calibration factor, k , is determined from a gas burner calibration with known \dot{q} . By repeating the calibration over a range of heat release rate levels, k can be determined as a function of \dot{q} or T_e . If the specimen is enclosed with the heater, Equation 15 is still valid, provided a reference temperature T_r is used instead of T_a . The temperature difference $T_r - T_a$ results from the heat transfer between the heater and the air flow through the enclosure. T_r is therefore a function of heater setting, to be determined via calibration.

Smith's rate of heat release test developed at Ohio State University is the most well known and most widely used calorimeter based on the sensible enthalpy rise method.³ The test is described in detail in a following section.

Substitution Method

For practical reasons, calorimeters based on the sensible enthalpy rise method use a closed configuration. The specimen and heater(s) are located inside a metal box, which may be (partly) insulated. The dynamic response of the enclosure to changes in the thermal environment creates major problems in the practical implementation of the sensible enthalpy rise method. After ignition, part of the heat released by a burning sample is transferred by radiation to the enclosure walls. A fraction of this heat is stored in the walls, causing an increase of its temperature, in turn resulting in an enhanced heat transfer with the air flowing through the box. The result is that, for a material which quickly reaches steady burning conditions, there is a delay for T_e to reach the corresponding steady temperature. A similar phenomenon occurs when heat release rate from the specimen decreases, or after the specimen burns out and heat release rate goes back to zero. Under unsteady burning conditions, T_e constantly lags behind the temperature corresponding to the instantaneous heat release rate. Several methods have been suggested to mathematically address this problem, but none are completely satisfactory.³⁴⁻³⁷

The substitution method was developed to eliminate problems associated with thermal lag. The method requires two runs to determine heat release rate of a material under a given set of conditions. The first run uses a similar arrangement as shown in Figure 3-2-4. The temperature difference $T_e - T_a$ is measured as a function of time. The second run uses the same apparatus, air flow rate, and irradiance. However, the specimen is replaced by a noncombustible dummy specimen and a substitution

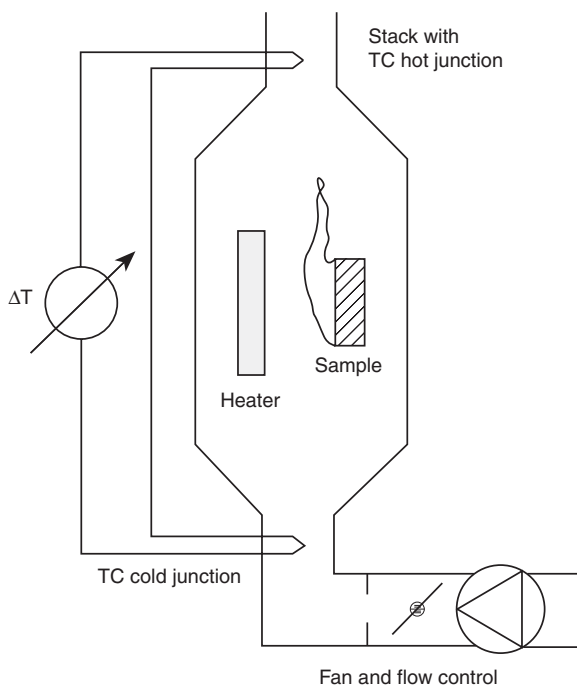


Figure 3-2-4. Sensible enthalpy rise calorimeter.

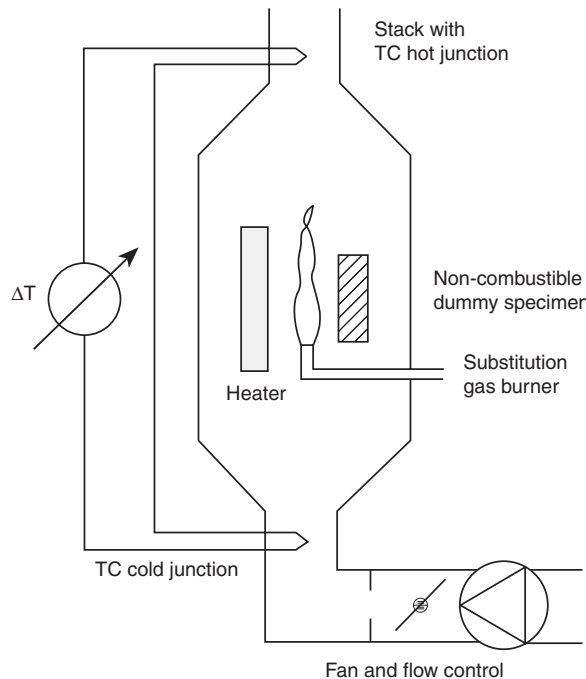


Figure 3-2.5. Second run with substitution calorimeter.

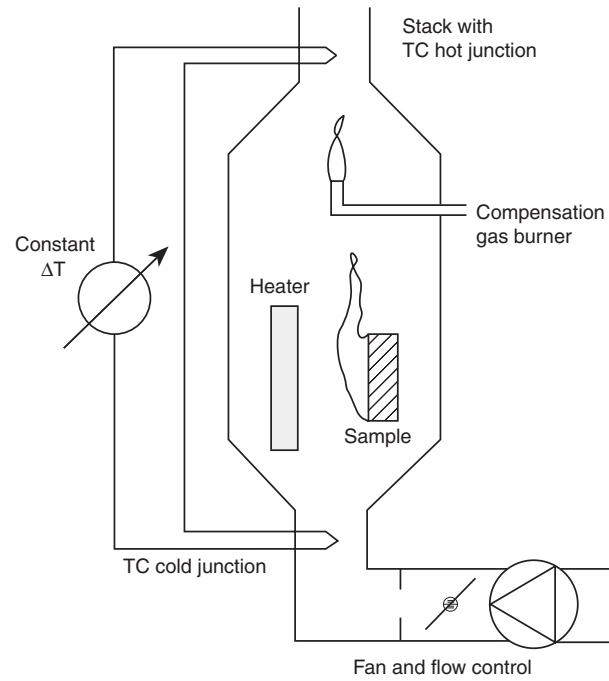


Figure 3-2.6. Compensation calorimeter.

gas burner. The flow of gas to the burner is controlled in such a way that the temperature difference $T_e - T_a$ closely follows the curve measured during the first run. Figure 3-2.5 shows a schematic of the substitution run.

Presumably, the dynamics are identical in both runs. Hence, problems with thermal lag have been eliminated, and the heat release rate of the specimen can be determined from the fuel flow rate to the burner in the second run. Unfortunately, implementation of this method is not trivial, since a sophisticated control system is needed for the second run. Moreover, due to the addition of substitution runs, the number of tests needed to evaluate a material are doubled.

The substitution method was first implemented at Factory Mutual.³⁸ The apparatus was designed to measure the heat release rate from roof assemblies. The test method is briefly discussed in the section on large-scale calorimeters. A bench-scale substitution calorimeter developed at the Forest Products Laboratory³⁹ is described in more detail in the section on bench-scale calorimeters.

Compensation Method

A compensation calorimeter is similar to a substitution calorimeter, except that the burner is operated while a specimen is exposed. A schematic is shown in Figure 3-2.6. Initially, the burner flow rate is chosen so that the corresponding heat release rate exceeds that of any material to be tested. During a test, the gas flow rate to the burner is controlled so that $T_e - T_a$ remains constant. The heat release rate corresponding to the reduction in flow rate to the burner is equal to the heat release rate from the specimen.

The compensation method also eliminates problems with the dynamic response of the calorimeter enclosure. In theory, a compensation calorimeter is operated at a constant temperature. This would resolve another problem associated with the assumption that $\dot{q}_{f,l}$ is fuel independent, while in reality it is not ($\dot{q}_{f,l}$ is a strong function of the sootiness of the flame). In practice, however, the specimen and burner have to be separated to prevent radiation from the burner flame enhancing irradiance to the specimen. Hence, the calorimeter enclosure is not truly isothermal, and the problem remains unresolved. As with substitution calorimeters, the burner flow control system makes compensation calorimeters rather complex and difficult to operate. As a result, they are suitable only for research and not for routine testing.

Compensation calorimeters developed at the National Bureau of Standards^{40,41} and Stanford Research Institute⁴² are described in following sections.

Oxygen Consumption Method

In 1917, Thornton showed that for a large number of organic liquids and gases, a more or less constant net amount of heat is released per unit mass of oxygen consumed for complete combustion.⁴³ Huggett found this also to be true for organic solids and obtained an average value for this constant of $13.1 \text{ kJ}\cdot\text{g}^{-1}$ of oxygen.⁴⁴ His value may be used for practical applications and is accurate, with very few exceptions, to within ± 5 percent. Thornton's rule implies that it is sufficient to measure the oxygen consumed in a combustion system in order to determine the net heat released. This idea is the basis for the oxygen consumption method for measuring heat release rate in fire tests.

Perhaps the first application of the oxygen consumption principle in fire research was performed by Parker on the ASTM E-84 tunnel test.⁴⁵ During the late 1970s and early 1980s, the oxygen consumption technique was refined at the National Bureau of Standards (NBS, currently the National Institute of Standards and Technology or NIST). The oxygen consumption method is now recognized as the most accurate and practical technique for measuring heat release rates from experimental fires. It is widely used throughout the world, both for bench-scale and large-scale applications.

The basic requirement to use the oxygen consumption technique is that all of the combustion products are collected and removed through an exhaust duct. At a distance downstream sufficient for adequate mixing, both flow rate and composition of the gases are measured. A schematic of an oxygen consumption calorimeter is shown in Figure 3-2.7. It is not necessary to measure the inflow of air, provided the flow rate is measured in the exhaust duct. Therefore, oxygen consumption calorimeters are typically open, to avoid that part of $\dot{q}_{f,l}$ is reflected by the calorimeter walls and reaches the specimen surface. This would result in an uncontrolled irradiance, in addition to that from the heater.

The practical implementation of the oxygen consumption method is not straightforward. Application of Thornton's rule to the combustion system shown in Figure 3-2.8 leads to the following equation for the heat release rate

$$\dot{q} = E(\dot{m}_a Y_{O_2}^a - \dot{m}_e Y_{O_2}^e) \quad (16)$$

where

E = heat release per mass unit of oxygen consumed ($\approx 13.1 \text{ kJ}\cdot\text{g}^{-1}$)

$Y_{O_2}^a$ = mass fraction of oxygen in the combustion air ($0.232 \text{ g}\cdot\text{g}^{-1}$ in dry air)

$Y_{O_2}^e$ = mass fraction of oxygen in the combustion products ($\text{g}\cdot\text{g}^{-1}$)

The problems with the use of this equation are threefold. First, oxygen analyzers measure the mole fraction and not

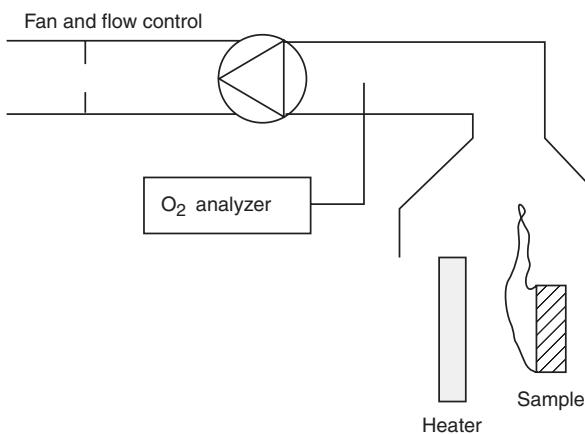


Figure 3-2.7. Oxygen compensation calorimeter.

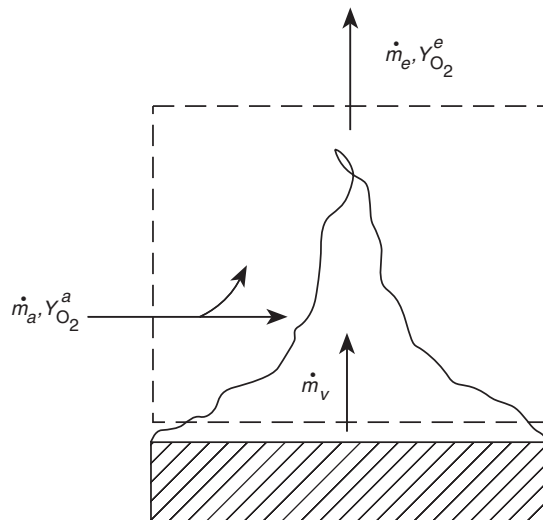


Figure 3-2.8. Gas-phase oxygen balance.

the mass fraction of oxygen in a gas sample. Mole fractions can be converted to mass fractions by multiplying the mole fraction with the ratio between molecular mass of oxygen and molecular mass of the gas sample. The latter is usually close to the molecular mass of air ($\approx 29 \text{ g}\cdot\text{mol}^{-1}$). Second, water vapor is removed from the sample before it passes through a paramagnetic analyzer, so that the resulting mole fraction is on a dry basis. This problem can be avoided by using a zirconium oxide analyzer, which measures oxygen mole fraction in a hot and wet sample. However, the performance of such analyzers is significantly inferior to that of paramagnetic instruments, making them unsuitable for accurate oxygen consumption calorimetry.⁴⁶ Third, flow meters measure volumetric rather than mass flow rates. The volumetric flow rate in the exhaust duct, normalized to the same pressure and temperature, is usually slightly different from the inflow rate of air because of expansion due to the combustion reactions.

Equations for calculating rate of heat release by oxygen consumption for various applications were developed by Parker⁴⁷ and Janssens.⁴⁸ The differences in treatment and equations to be used are mainly due to the extent to which gas analysis is made. As a minimum, the oxygen concentration must be measured. However, accuracy can be improved by adding instrumentation for measuring the concentration of CO_2 , CO and H_2O . Equations for the most common configurations of the gas analysis system are given below. Detailed derivations are not repeated here, and can be found in the aforementioned references. Modified equations to address specific circumstances or problems, such as heat release rate measurements during suppression experiments or from fires with significant soot yields, can also be found in the literature.^{49,50}

Only O_2 is measured: In this case all water vapor (by a cooling unit and a moisture sorbent) and CO_2 (by a chemical sorbent) must be removed from the exhaust gas sam-

ple stream before O_2 is measured. This leads to the assumption that the sample gas only consists of O_2 and N_2 . The resulting equation for calculating heat release rate is

$$\dot{q} = E \frac{\phi}{1 + \phi(a - 1)} \dot{m}_e \frac{M_{O_2}}{M_a} (1 - X_{H_2O}^a - X_{CO_2}^a) X_{O_2}^{Aa} \quad (17)$$

with

$$\phi = \frac{X_{O_2}^{Aa} - X_{O_2}^{Ae}}{(1 - X_{O_2}^{Ae}) X_{O_2}^{Aa}} \quad (18)$$

where

ϕ = oxygen depletion factor

a = volumetric expansion factor

M_{O_2} = molecular mass of oxygen ($28 \text{ g}\cdot\text{mol}^{-1}$)

M_a = molecular mass of the combustion air ($29 \text{ g}\cdot\text{mol}^{-1}$ for dry air)

$X_{H_2O}^a$ = actual mole fraction of water vapor in the combustion air

$X_{CO_2}^a$ = actual mole fraction of carbon dioxide in the combustion air

$X_{O_2}^{Aa}$ = measured mole fraction of oxygen in the combustion air

$X_{O_2}^{Ae}$ = measured mole fraction of oxygen in the exhaust flow

As the composition of the fuel is usually not known, some average value has to be used for a . Complete combustion of carbon in dry air results in $a = 1$. If the fuel is pure hydrogen, a is equal to 1.21. A recommended average value for a is 1.105. $X_{H_2O}^a$ can be calculated from the relative humidity and temperature in the laboratory. Typically it is less than a few percent in a temperature-controlled laboratory. $X_{CO_2}^a$ in dry air is 330 ppm. Note that the symbols for oxygen mole fraction measured in the combustion air (prior to a test) and the exhaust flow include a superscripted *A*. This is to make a distinction between the actual and measured mole fractions of oxygen, with the latter on a dry gas sample basis.

Equation 17 is expected to be accurate to within ± 10 percent, provided combustion is complete (i.e., all of the carbon is converted to CO_2). The error might be larger if CO or soot production is considerable, or if a significant amount of combustion products consist of species other than CO_2 or H_2O (e.g., HCl). The error is partly due to the uncertainty of E and a . If more exact values are available, accuracy can be improved by using those instead of the generic values of $13.1 \text{ kJ}\cdot\text{g}^{-1}$ and 1.105.

O_2 and CO_2 are measured: In this case, only water vapor is trapped before the exhaust gas sample reaches the analyzers. The rate of heat release is given by Equation 17, with the minor modification that $X_{CO_2}^a$ is not included in the expression inside parentheses. In addition, ϕ is slightly different and follows from

$$\phi = \frac{X_{O_2}^{Aa}(1 - X_{CO_2}^{Ae}) - X_{O_2}^{Ae}(1 - X_{CO_2}^{Aa})}{(1 - X_{O_2}^{Ae} - X_{CO_2}^{Ae}) X_{O_2}^{Aa}} \quad (19)$$

where

$X_{CO_2}^{Aa}$ = measured mole fraction of carbon dioxide in the air ($\approx 330 \text{ ppm}$)

$X_{CO_2}^{Ae}$ = measured mole fraction of carbon dioxide in the exhaust flow

Generally, adding CO_2 measurement does not greatly improve accuracy of \dot{q} .

O_2 , CO_2 , and CO are measured: If a significant fraction of carbon in the fuel is converted to CO instead of CO_2 , the equations may have to be corrected to take incomplete combustion into account. Heat release rate is now calculated from

$$\dot{q} = \left[E\phi - (E_{CO} - E) \frac{1 - \phi}{2} \frac{X_{CO}^{Ae}}{X_{O_2}^{Ae}} \right] \cdot \frac{\dot{m}_e}{1 + \phi(a - 1)} \frac{M_{O_2}}{M_a} (1 - X_{H_2O}^a) X_{O_2}^{Aa} \quad (20)$$

with

$$\phi = \frac{X_{O_2}^{Aa}(1 - X_{CO_2}^{Ae} - X_{CO}^{Ae}) - X_{O_2}^{Ae}(1 - X_{CO_2}^{Aa})}{(1 - X_{O_2}^{Ae} - X_{CO_2}^{Aa} - X_{CO}^{Ae}) X_{O_2}^{Aa}} \quad (21)$$

where

E_{CO} = heat release per mass unit of oxygen consumed for combustion of CO to CO_2 ($\approx 17.6 \text{ kJ}\cdot\text{g}^{-1}$)

X_{CO}^{Ae} = measured mole fraction of carbon monoxide in the exhaust flow

One might wonder under what conditions the CO correction becomes significant. Figure 3-2.9 shows the ratio of heat release rate obtained by ignoring CO to the actual heat release rate, as a function of the ratio of measured CO to CO_2 mole fractions in the exhaust flow for

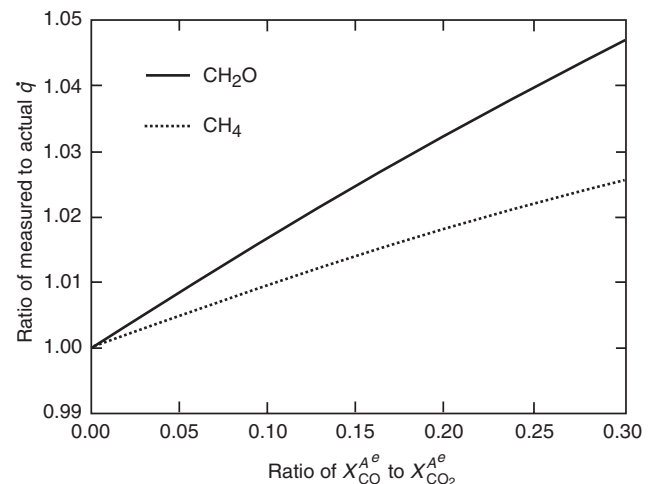


Figure 3-2.9. Effect of ignoring CO production on \dot{q} error.

methane and for a gaseous fuel of composition $(\text{CH}_2\text{O})_n$. According to Roberts,⁵¹ the molecular formula of the latter represents the thermal degradation products of beech wood. For the CO effect examined here, this fuel represents a worst case since it contains enough oxygen for combustion of all hydrogen. Methane gives a practical lower limit for the error, because it is the hydrocarbon with the highest hydrogen to carbon ratio. There is some experimental evidence that the yield of CO in underventilated fires reaches an upper limit approximately equal to 0.2 kg of CO per kg of fuel, when the equivalence ratio exceeds unity.⁵² For the fuels considered here, the limit corresponds to a ratio of $X_{\text{CO}}^{A^e}$ to $X_{\text{CO}_2}^{A^e}$ of 0.27. Figure 3-2-9 indicates that, even under the worst conditions, the error by ignoring CO generation is less than 5 percent.

O₂, CO₂, CO, and H₂O are measured: Often the combustion products comprise only O₂, CO₂, CO, H₂O, and N₂ in significant amounts. In that case the expansion factor no longer has to be estimated, but can be calculated. Heat release rate is calculated from

$$\dot{q} = \left[E\phi - (E_{\text{CO}} - E) \frac{1 - \phi}{2} \frac{X_{\text{CO}}^{A^e}}{X_{\text{O}_2}^{A^e}} \right] \dot{m}_a \frac{M_{\text{O}_2}}{M_a} (1 - X_{\text{H}_2\text{O}}^a) X_{\text{O}_2}^{A^a} \quad (22)$$

with

$$\frac{\dot{m}_a}{M_a} = \frac{(1 - X_{\text{H}_2\text{O}}^c)(1 - X_{\text{O}_2}^{A^e} - X_{\text{CO}_2}^{A^e} - X_{\text{CO}}^{A^e})}{(1 - X_{\text{H}_2\text{O}}^a)(1 - X_{\text{O}_2}^{A^a} - X_{\text{CO}_2}^{A^a})} \cdot \frac{\dot{m}_e}{18 + 4(1 - X_{\text{H}_2\text{O}}^c)(X_{\text{O}_2}^{A^e} + 4X_{\text{CO}_2}^{A^e} + 2.5)} \quad (23)$$

where

$X_{\text{H}_2\text{O}}^c$ = actual mole fraction of water vapor in the exhaust flow

The oxygen depletion factor, ϕ , is still determined according to Equation 21.

The oxygen consumption technique is the most accurate and convenient way to measure net release rate. Problems due to thermal lag are eliminated. Instrumentation delay and response times can be accounted for relatively easily.⁵³ Drawbacks of the technique are the high cost of instrumentation (only the best available oxygen analyzers are adequate), and the need for a rigorous calibration and maintenance schedule. Nevertheless, the benefits outweigh the disadvantages.

Solid or volatile heat release rate? An interesting question is whether the oxygen consumption technique measures heat release rate for the volatiles or the solid fuel. As explained in previous sections, thermal methods approximately measure heat release rate from the volatiles. However, Huggett's constant of 13.1 kJ·g⁻¹, is based on the average net heat of combustion for a large set of materials. Hence, one would expect that oxygen consumption calorimetry gives the heat released by the fuel in its natural state at ambient temperature, since that is how the fuel is supplied in an oxygen bomb calorimeter. The question can be examined in more detail for some synthetic polymers, by comparing the net heat of combustion of the polymer to that of the corresponding monomer. If one were to burn a monomer in an oxygen consumption calorimeter, the products of complete combustion would be the same as for the corresponding polymer, provided test conditions are identical. Therefore, measured heat release rate would be the same in the two cases. However, the net heat of combustion is higher for the monomer. The difference with the net heat of combustion of the polymer is the net heat released in the polymerization process. Table 3-2-1 gives values for the net heat of combustion of 9 polymers and their monomers. The former are taken from Huggett,⁴⁴ the latter are obtained by adding the heat of polymerization as reported in the literature.⁵⁴ Table 3-2-1 confirms that the oxygen consumption technique measures net heat release rate of a solid fuel. The heat release rate from the volatiles is always higher, but not by as much as indicated in the last column of the table, because only a fraction of polymeric fuels decomposes back into the monomer (see Section 1, Chapter 7).

Table 3-2-1 Net Heat of Combustion of Some Polymers and Their Monomers

Polymer	$\Delta h_{c,\text{net}}$ (kJ·g ⁻¹ fuel)	$\Delta h_{c,\text{net}}$ (kJ·g ⁻¹ O ₂)	Monomer (state)	$\Delta h_{c,\text{net}}$ (kJ·g ⁻¹ fuel)	$\Delta h_{c,\text{net}}$ (kJ·g ⁻¹ O ₂)	Diff (%)
Polyethylene	-43.3	-12.65	C ₂ H ₄ (g)	-47.2	-13.78	8.9
Polypropylene	-43.3	-12.66	C ₃ H ₆ (g)	-45.8	-13.39	5.8
Polybutadiene	-42.8	-13.14	C ₄ H ₆ (l)	-44.1	-13.56	3.2
Polystyrene	-39.9	-12.97	C ₆ H ₈ (l)	-40.5	-13.19	1.7
Polyvinylchloride	-16.4	-12.84	C ₂ H ₃ Cl (g)	-18.0	-14.10	9.8
Polyvinylidene chloride	-8.99	-13.61	C ₂ H ₂ Cl ₂ (l)	-9.77	-14.79	8.7
Polyvinylidene fluoride	-13.3	-13.32	C ₂ H ₂ F ₂ (g)	-15.6	-15.61	17.2
Polymethylmethacrylate	-24.9	-12.98	C ₅ H ₈ O ₂	-25.4	-13.26	2.2
Polyacrylonitrile	-30.8	-13.61	C ₃ H ₃ N (l)	-32.2	-14.25	4.7
Average		-13.09			-13.99	6.9

Effects of Bench-Scale Calorimeter Construction Details

In this section, the effects of some calorimeter construction details on quality and accuracy of the measurements are examined. The discussion results in some guidelines for building the "ideal" calorimeter for a certain application.

Open or Closed Configuration

Calorimeters which utilize a measuring technique other than oxygen consumption consist of a closed box configuration. Combustion air is supplied to one side of the box, and combustion products are removed from the opposite side. Sample, heater, and ignition device typically are located inside the box. Advantages of a closed configuration are that air flow rate can be measured at the inlet under clean and soot-free conditions, the combustion air can be heated, and the oxygen concentration in the air can be increased (by adding O₂) or decreased (by adding N₂) over ambient. Disadvantages are the thermal lag due to heating or cooling of the enclosure walls, and uncontrolled radiation feedback from the enclosure walls to the specimen.

To resolve the first problem, various numerical procedures have been proposed for correcting the temperature signal measured with calorimeters based on the sensible enthalpy rise method.³⁴⁻³⁷ These procedures are based on a mathematical model of the calorimeter consisting of two first order systems in series. The first system has a rather small time constant (between 8 and 30 seconds for various calorimeters), which is related to the heat capacity of the gases flowing through the calorimeter. The second system has a large time constant (200 to 930 seconds for various calorimeters), which is associated with the heat capacity of the calorimeter walls. The correction procedures adjust the output signal for thermal lag, using discrete forward and inverse Laplace transform techniques. In spite of the complex calculations, the resulting correction may not always be accurate due to the crude mathematical model for the calorimeter. A more convenient, and perhaps as accurate correction method relies on an electronic compensator.^{55,56} The compensator electronically corrects the output signal of the exhaust thermocouples, based on the negative feedback of a wall temperature signal. The oxygen consumption method also has a time delay, but with properly adjusted sampling flows and oxygen analyzer, this delay consists almost entirely of the transport time for a gas sample from the combustion zone to the analyzer.⁵⁷ Since flow rates in the exhaust duct and sampling lines do not change significantly during a test, this delay time is approximately constant. It can be determined with gas burner calibrations, and can be easily accounted for by shifting the gas analysis data over the appropriate time interval. When an inferior oxygen analyzer is used, its internal response time might become significant. In such a case, the analyzer output signal can be corrected numerically for time delays in a similar way as temperature measurements. Oxygen analyzers behave as a first or second order system, and the appropriate time constants can be

obtained from step response measurements. However, it is highly recommended that only the best and most accurate analyzers for oxygen consumption calorimetry be used, in which case internal delays are not a problem.

The second problem can only be eliminated by using blackened water-cooled calorimeter walls. If the walls are allowed to heat or cool freely, they emit radiation which varies with time. Part of this radiation reaches the specimen surface and enhances the irradiance from the heater in an uncontrolled fashion. Obviously, the need for water-cooled walls makes the apparatus much more complex and costly.

In conclusion, problems with thermal lag and radiation feedback to the specimen can be eliminated by using an open configuration. Solid objects must be water-cooled, or sufficiently remote from heater and specimen so that they do not interfere with the controlled irradiance to the specimen. A closed configuration can only be recommended for specialized applications (e.g., to study the effect of oxygen concentration or temperature of the combustion air on heat release rate and burning behavior).

Type of Heater

Heat release rates must be measured at constant heat flux levels over a range that is relevant for the fire of interest. The heat flux can be provided with a gas burner flame in contact with the specimen, or with a radiant panel remote from the specimen.

Incident heat flux from impinging gas burner flames can only be adjusted over a narrow range. To increase the heat flux from a gas burner, either flame size has to be increased, or a fuel with higher soot yield has to be used. Usually, these parameters can be adjusted only slightly, or not at all. It is very difficult to set and maintain a specific heat flux level since a major fraction of the heat transfer is convective. Moreover, the burner gas and combustion products mix with fuel volatiles, which affects burning behavior. In short, impinging flames are not desirable as the external heat source in heat release rate calorimeters.

It is much easier to create constant and uniform exposure conditions if the incident heat flux is primarily radiative. Porous gas panels as well as electrical heating elements are used for this purpose. The irradiance can be adjusted by changing the power of the heater, or by changing the distance between heater and specimen. If the second method is used, there are practical upper and lower limits to the range of irradiance levels that can be created. If the heater is too close to the specimen, convective heat transfer becomes significant. Therefore, the upper limit corresponds to the minimum distance that has to be maintained in order to ensure predominantly radiative heat transfer. The lower limit is determined by the uniformity of the incident irradiance, which drops with increasing distance between heater and specimen. The exact limits depend on the geometrical configuration, power of the heater, and the degree of nonuniformity of the incident heat flux profile that is deemed acceptable.

Another important aspect is the ability of the heater to maintain the irradiance at a constant level during a test.

If the heater is operated at a constant power level, incident irradiance changes during testing. At the start of a test, a cold sample is inserted. The sample acts as a heat sink, resulting in a decrease of the heater temperature, and consequently a decrease of the incident irradiance. After ignition, the heat released by the specimen results in an increase to the heater temperature and incident irradiance. Therefore, in order to maintain incident irradiance during a test, it is necessary to keep the temperature of the heater constant. This is very difficult with a gas panel, but relatively straightforward for electrical heating elements. With the oxygen consumption method, another drawback of using a gas panel is that its products of combustion result in an oxygen depletion that is usually much larger than the oxygen consumed for combustion of the specimen. Thus, small fluctuations in panel flow can result in significant error of the measured heat release rate. This baseline problem can be avoided by using a separate exhaust system for the heater.

It is clear from the previous discussion that an electrical heater is preferable to a gas panel. High and low temperature electrical heaters are used. The former are commonly Tungsten filament lamps that operate at temperatures close to 2300 K. According to Wien's displacement law, peak irradiance from such lamps is at a much shorter wavelength than for real fires, with temperatures in the range of 600 to 1400 K. Piloted ignition studies on plastics and wood have shown that these materials absorb much less radiation in the visible and near-infrared range, than at higher wavelengths.^{58,59} On the basis of these findings, it can be concluded that high temperature electrical heating elements are not suitable for use in fire testing. It is therefore recommended that commercially available low temperature elements be used. Such elements typically operate between 800 and 1200 K, a range that is representative of real fire exposure conditions.

Type of Ignition Pilot

Heat release rate tests are most often conducted with an ignition pilot. The use of a pilot reduces the variation in time to sustained flaming between multiple tests conducted under identical test conditions. Because the duration of the preheat period prior to ignition affects burning rate after ignition, use of a pilot also improves repeatability of heat release rate measurements. Furthermore, piloted ignition is used because it is representative of most real fires, and conservative in other cases. The ignition pilot in bench-scale fire tests consists of a small gas burner flame, a glowing wire, or an electric spark. An impinging flame should not be used because it locally enhances the incident heat flux to the specimen. Another problem with pilot flames is that they are sometimes extinguished by fire retardants or halogens in the fuel volatiles. A glowing wire is not an efficient method for igniting fuel volatiles, sometimes leading to poor repeatability. An electric spark remains stable when fire retardants or halogens are present. However, it occupies a small volume, so that the positioning of the spark plug is more critical than with other types of ignition pilots. In conclusion, each type of pilot has its drawbacks. Nonetheless, a spark igni-

tor is probably the best type of ignition pilot for heat release rate tests.

Sample Size

The ideal situation would be if small-scale heat release rate data could be used directly to predict burning rate in real scale fires. Unfortunately, the minimum bench-scale sample size that is required to allow for such a straightforward prediction is not practical. As described in previous sections, the burning rate of a specimen is a direct function of the net heat flux transferred to the fuel. The net flux is equal to the total of external heat flux, flame convection and flame radiation, minus radiative heat losses from the fuel surface and heat losses (or gains) at the specimen edges. The Russian work on the effect of diameter on pool fire burning rate by Blinov and Khudakov gives some insight into this problem. A detailed discussion of this work and its implications is given by Drysdale.⁶⁰ If the pool diameter is less than 0.03 m, flame convection is laminar and burning rate increases with decreasing diameter. If the pool diameter exceeds 1 m, flame convection is turbulent and burning rate is independent of diameter. There is a transition region between these two limits, with a minimum burning rate for a pool diameter of approximately 0.1 m. Therefore, the sample size in a heat release rate calorimeter must be at least 1 m for the results to be independent of scale, which is not feasible in practice. The Russian pool fire data also indicate that heat transfer at the edges becomes excessive at diameters below 0.1 m. Therefore, sample size in bench-scale calorimeters should be at least 0.1 m. To predict real scale burning rates, differences in flame heat transfer and heat transfer at the edges have to be accounted for. Nussbaum and Östman reported ignition and heat release data for 13 materials and two sample sizes.⁶¹ Increase in sample size from 0.1×0.1 m to 0.2×0.2 m resulted in a slight reduction of piloted ignition time. Average heat release rate over the first minute after ignition on a per-unit-area basis increased by approximately 12 percent at exposure levels exceeding $25 \text{ kW}\cdot\text{m}^{-2}$. Larger increases were observed at the $25 \text{ kW}\cdot\text{m}^{-2}$ exposure level, and for peak heat release rate. Janssens and Urbas presented a comparison of heat release rate data for nine wood products obtained in the cone and an intermediate-scale calorimeter.⁶² A 100-fold increase in sample size only resulted in a 10 percent increase of the heat release rate. The modest effect can be explained by the fact that the heat feedback from the flame is relatively insensitive to sample area for testing in the vertical orientation, in particular for materials that do not produce very luminous flames, such as wood.

Depending on the specimen size in a bench-scale test, there is a limit on the degree of nonuniformity and irregularity of the product being tested, if the test conditions are to be representative of end-use conditions. Therefore, there might be some merit in choosing a specimen size that exceeds the minimum of 0.1 m. However, the main trade-off is that a larger specimen requires a larger and more powerful heater to ensure uniform incident irradiance to the specimen. It should be recognized that, no matter what the specimen size is, there are assemblies and

composites for which it is not possible to prepare representative bench-scale specimens. Intermediate-scale or full-scale tests are needed to evaluate the fire performance of such assemblies and composites.

An issue that is closely related to specimen size is that of edge effects. These effects have been studied extensively in the cone calorimeter. ASTM⁶³ and ISO⁶⁴ standards of the cone calorimeter prescribe that, except for calibrations with PMMA, the specimen is to be wrapped with aluminum foil on the sides and bottom. The main purpose of the foil is to eliminate mass transfer along all boundaries except the exposed face of the specimen. Furthermore, the ISO standard requires all tests be conducted in the horizontal orientation with the stainless steel edge frame. Further details on the cone calorimeter specimen preparation and test conditions can be found in Section 3, Chapter 3. Toal et al. tested several materials with and without foil wrapping, and with and without the edge frame.^{65,66} They found that the edge frame reduces peak heat release rate and lengthens the burning time. Lengthened burning time is to be expected, because the edge frame is a relatively large mass of steel that acts as a heat sink, reducing the energy transferred to the specimen. Urbas and Sand were also concerned with the heat sink effect of the edge frame.⁶⁷ They designed an alternative edge frame, comprising an insulating collar made of medium-density or high-density refractory material. Their conclusion was that the best edge conditions are obtained using the insulating frame with insulation material that most closely resembles the specimen in thermal properties. Babrauskas et al. conducted a very extensive study of the effects of specimen edge conditions on heat release rate.⁶⁸ The objective of this study was to further examine the issues raised by Toal et al. and by Urbas and Sand, and to develop definitive recommendations. Specimens of 10 materials were tested in the horizontal orientation at 50 kW·m⁻² using three configurations; without edge frame, with edge frame, and with an insulated edge frame akin to that developed by Urbas and Sand. All specimens were wrapped in aluminum foil. The study concluded that the use of an insulated frame gives heat release rate values that are slightly closer to the expected true values. However, the insulated frame makes the test procedure significantly more complicated, so that it is not recommended for routine testing. If the standard edge frame is used, Babrauskas et al. recommend heat release rate data be expressed on the basis of an effective exposure area of 0.0081 m². The standard edge frame reduces the actual exposed area from 0.1 × 0.1 m to 0.094 × 0.094 m, or from 0.01 m² to 0.0088 m². The recommendation by Babrauskas et al. to further reduce the exposed area to an effective value of 0.0081 m² indicates that the heat sink effect of the edge frame reduces heat release rate values by approximately 8 percent. Tsantaridis and Östman tested 11 products in the cone calorimeter in the horizontal orientation at 50 kW·m⁻², with and without the edge frame.⁶⁹ They also found that the use of the edge frame results in a reduction of heat release rate greater than what can be explained by the reduction of the exposed area. For the average heat release over the first three minutes following ignition, they found an average reduction of 8 percent,

identical to Babrauskas et al. However, for maximum heat release rate they found reductions as high as 25 percent. It can be concluded from these studies that the sample holder configuration in a bench-scale heat release rate test may have a significant effect on the measurements, and that this should be accounted for if the test data are used to predict performance in real fires.

Specimen Orientation

As previously explained, products do not necessarily have to be tested in the same orientation as they are used. For practical reasons, the preferred orientation for bench-scale testing is horizontal facing upward. The vertical orientation might be preferable for collecting specialized data for research purposes.

Air Flow

Standard rate of heat release test methods are operated under overventilated conditions. Plenty of excess air is supplied, so that the measurements are not affected by lack of oxygen. However, specialized studies have been conducted to evaluate the effect of ventilation and vitiation.⁷⁰ Such studies require a closed configuration. The original ISO heat release rate apparatus had the capability of heating the combustion air, so that the effect of air temperature on heat release rate could be studied.⁷¹

Other Measurements

Heat release rate calorimeters often include additional instrumentation to measure parameters that are important in characterizing the fire performance of materials. Perhaps the most important additional measurement is that of mass loss rate. Most calorimeters can be provided with a load cell to measure specimen mass loss, but this can be very difficult in a closed configuration. Mass loss rate is obtained from numerical differentiation of the mass loss measurements. Smoke meters are added to measure smoke obscuration in the exhaust duct. Both white light and laser light systems are being used. Toxic gas species can be measured in the exhaust duct with additional gas analysis equipment. Such equipment ranges from standard infrared CO and CO₂ analyzers to complex online Fourier transform infrared (FTIR) instrumentation. Whether instrumentation can be added depends mainly on the design and construction details of the calorimeter.

Survey of Bench-Scale Calorimeters

Numerous bench-scale heat release rate calorimeters have been developed since the early 1970s. Many of these calorimeters are described in detail here.

The Ohio State University (OSU) Apparatus

Originally designed by Smith at Ohio State University,³ the OSU apparatus is one of the most widely used and best known bench-scale calorimeters. The test method

was first published as a proposed ASTM standard in 1980. In 1983 it was adopted as ASTM Standard Test Method E906, and the method has not changed since then.⁵⁵ A schematic view of the apparatus is shown in Figure 3-2.10. The apparatus consists of an insulated metal box. The conical wall section between the combustion chamber and the stack is hollow. Air flows through this cavity and mixes with the combustion products downstream of the thermocouple hot junctions. However, recovery of a significant fraction of wall heat losses is not fully accomplished. Some features of the OSU apparatus are described below.

Measuring technique: Heat release rate is determined by the sensible enthalpy rise method. The temperature of inflowing air, and outflowing gases are measured with a thermopile of three type K thermocouples. The hot junctions are located symmetrically along a diagonal of the stack cross section, above the baffle plate. The cold junctions are located below the air distributor plate. An electrical compensator is used to correct the temperature signals for thermal lag. The factor k in Equation 15 is obtained from line burner calibration runs.

Configuration: Heater and specimen are located inside a box with approximate dimensions of $0.2 \times 0.41 \times 0.64$ m. The side walls of the box are insulated, and the hollow top wall section is cooled with air.

Heater: The vertical radiant heat source measures approximately 0.3×0.3 m, and consists of four silicon carbide heating elements. A steel masking plate is located in front of the elements to improve uniformity of the incident heat flux distribution over the specimen. The maximum incident heat flux to a vertical specimen is approximately $65 \text{ kW}\cdot\text{m}^{-2}$.

Ignitor: The optional ignition source is a pilot flame of $2 \text{ ml}\cdot\text{s}^{-1}$ methane, premixed with $14 \text{ ml}\cdot\text{s}^{-1}$ air. The pilot flame is either impinging on the specimen at the bottom

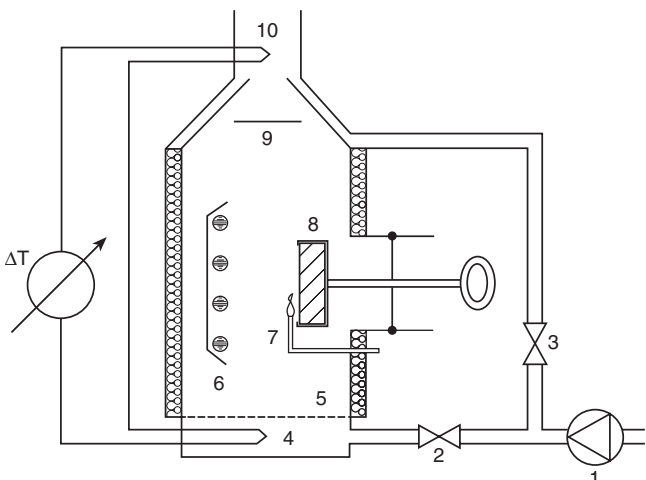
(point ignition), or is located in the gas phase at the top of the specimen (pilot ignition), or is not used.

Specimen size and orientation: For testing in the vertical orientation, specimens with an exposed area of 0.15×0.15 m are positioned parallel to the heating elements. Specimens can be tested in the horizontal orientation with the aid of an aluminum reflector foil, which reflects the radiation from the heating elements to the specimen. In this case, maximum irradiance is reduced to $50 \text{ kW}\cdot\text{m}^{-2}$ and specimen size is 0.11×0.15 m. The use of the reflector plate is awkward and cumbersome, so that testing in the horizontal orientation with the OSU apparatus is not recommended.

Air flow: Total air flow rate is $40 \text{ l}\cdot\text{s}^{-1}$, of which only $10 \text{ l}\cdot\text{s}^{-1}$ passes through the combustion chamber and the remaining $30 \text{ l}\cdot\text{s}^{-1}$ flows through the upper hollow wall section. Nevertheless, the air flow rate through the combustion chamber contains enough oxygen to feed a 36 kW fire. Because, the heat release rate from test specimens rarely exceeds 20 kW , burning conditions in the OSU apparatus are always overventilated. The air flow rates are measured accurately with standard orifices.

Additional measurements: The ASTM E906 standard does not include a mass loss measurement but has a smoke measuring system with a white light source in the stack.

Federal Aviation Administration (FAA) version of the OSU apparatus: In 1978 the FAA established a committee to examine the factors affecting the ability of aircraft cabin occupants to survive in a post-crash environment. The committee recommended research to evaluate the fire performance of cabin materials, and development of a method using radiant heat for testing cabin materials. As a result, the FAA conducted an extensive series of full-scale fire tests and evaluated numerous bench-scale tests for their capability to provide results that correlate well with full-scale performance. The OSU apparatus, standardized as ASTM E906, was found to be the most suitable for material qualification. Improved flammability standards and requirements for airplane cabin interior materials based on ASTM E906 first went into effect in 1986.⁷² The limits for acceptance were based on heat release rate measured at an irradiance level of $35 \text{ kW}\cdot\text{m}^{-2}$. Peak heat release rate could not exceed $100 \text{ kW}\cdot\text{m}^{-2}$, and average heat release rate over the first two minutes following ignition had to be $50 \text{ kW}\cdot\text{m}^{-2}$ or less. Originally, the test method used by the FAA was identical to ASTM E906. Since then, modifications have been made.⁷³ The FAA method now uses a thermopile of five thermocouples, a lighter sample holder, and a modified test procedure to minimize problems associated with thermal lag.⁷⁴ The FAA criteria for acceptance were revised in 1990 to $65 \text{ kW}\cdot\text{m}^{-2}$ for peak heat release rate during the five-minute test, and to $32.5 \text{ kW}\cdot\text{m}^{-2}$ for average heat release rate over the first two minutes following ignition.⁷²



- | | |
|-------------------------|---------------------|
| 1 Air supply fan | 6 Heating elements |
| 2 Main flow control | 7 Gas pilot |
| 3 By-pass flow control | 8 Sample and holder |
| 4 TC cold junctions | 9 Baffle plate |
| 5 Air distributor plate | 10 TC hot junctions |

Figure 3-2.10. Schematic of the OSU apparatus.

OSU Apparatus Modified for Oxygen Consumption

When oxygen consumption calorimetry became the preferred method for measuring rate of heat release, laboratories in the United States, Canada, and Sweden modified their OSU apparatus. These modifications typically

consisted of the elimination of the original thermopile, the addition of a gas sampling probe and gas analysis equipment, and some adjustments to the air flow rates. A brief summary of these investigations follows.

Modified OSU apparatus at NBS: As part of an investigation of combustion of mattresses exposed to flaming ignition sources, a number of mattress materials were tested at NBS in a modified OSU apparatus.^{6,74} The following modifications were made to the standard OSU apparatus:

- The oxygen consumption technique was used instead of the sensible enthalpy rise method.
- The air flow through the hollow upper wall section was cut off to increase sensitivity of the oxygen measurement.
- The air flow rate through the combustion chamber was increased to $12 \text{ l}\cdot\text{s}^{-1}$.
- Specimen size was reduced to $0.1 \times 0.1 \text{ m}$.
- The aluminum reflector foil was replaced by a more durable steel plate.

As a result of this study, good agreement was found between heat release rates measured in the modified OSU apparatus, and a classification of mattresses based on performance in full-scale experiments.

Modified OSU apparatus at the National Research Council of Canada (NRCC): The oxygen consumption method was compared with the three thermal methods, and was found to be preferable.⁷⁵ As a result, the OSU apparatus at NRCC was modified for oxygen consumption calorimetry and for measuring heat release rates at reduced air flow rates. Air regulators and flow meters were replaced so that the flow rates through the combustion chamber and through the upper hollow wall section could be set between 0.8 and $10 \text{ l}\cdot\text{s}^{-1}$, and between 0.8 and $30 \text{ l}\cdot\text{s}^{-1}$, respectively. At lower flow rates, longer flames were observed. The stack of the apparatus was extended to ensure all combustion took place inside the apparatus. For a wood specimen exposed to $25 \text{ kW}\cdot\text{m}^{-2}$, it was found that both air flow rates could be reduced to $2.5 \text{ l}\cdot\text{s}^{-1}$ without significant incomplete combustion or flaming outside the apparatus.

Modified OSU apparatus at Lund University: The OSU apparatus at Lund University in Sweden was also modified for oxygen consumption calorimetry.⁷⁶ The air flow through the upper hollow wall section was cut off, and the stack of the apparatus was extended.

Modified OSU apparatus at the Forest Products Laboratory: Two significant modifications were made to the FPL apparatus, in addition to the inclusion of instrumentation for oxygen consumption calorimetry.⁷⁷ An auxiliary heat flux meter was added beneath the specimen, to monitor incident irradiance during a test. Measurements obtained with this auxiliary meter indicated that the incident irradiance to a burning wood specimen increases significantly during a test. For example, the incident irradiance to a Douglas fir plywood specimen at the end of a 10-minute burning period increased by 20 percent over the $35 \text{ kW}\cdot\text{m}^{-2}$ baseline. The increase is due to the fact that

the heater elements in the OSU calorimeter are supplied with constant power and are not temperature controlled, and that the calorimeter walls are allowed to heat up (or cool down) during testing. The fact that exposure conditions in the OSU calorimeter are not constant is a major weakness of the apparatus. It is nearly impossible to remedy this problem. The addition of an auxiliary heat flux meter is highly recommended. Thus, at least the time-varying exposure conditions are known. The second modification at FPL was the addition of a load cell to measure specimen mass loss during a test. This was a rather difficult task due to the geometry of the apparatus, and the mechanism for inserting specimens. The FPL load cell design seemed to be satisfactory, demonstrating the feasibility of measuring mass loss in the OSU apparatus.

The NBS I Calorimeter

This apparatus was developed by Parker and Long at NBS.⁴⁰ It consists of a combustion chamber at the bottom, a control chamber in the middle, and a mixing chamber at the top. Gases flow through the apparatus from bottom to top. The apparatus has the following features.

Measuring technique: Heat release rate is determined by the compensation method. The flow rate of propane to an auxiliary burner in the control chamber is adjusted to maintain the temperature in the mixing chamber at a constant level between 370 and 470°C . Additional air supplied to the control room greatly eliminates heat losses to the walls of this part of the apparatus.

Configuration: Three heaters and the specimen are located inside the combustion chamber with approximate dimensions of $0.33 \times 0.33 \times 0.36 \text{ m}$.

Heaters: Three walls of the combustion chamber consist of gas panels, capable of producing a heat flux to the specimen of up to $100 \text{ kW}\cdot\text{m}^{-2}$. Incident irradiance to the specimen is checked with a copper disk heat flux meter.

Ignitor: Ignition of the specimen is nonpiloted.

Specimen size and orientation: The vertical specimen measures $0.114 \times 0.15 \text{ m}$ with a maximum thickness of 25 mm . The specimen holder fits into an opening in the remaining combustion chamber wall that faces the three radiant panel walls.

Air flow: Air is supplied to the combustion chamber at a rate of $63 \text{ l}\cdot\text{s}^{-1}$. The products of combustion are further diluted in the control chamber with air at a rate of $69 \text{ l}\cdot\text{s}^{-1}$. The dilution air is induced through the porous walls of the control chamber, and serves to reduce the temperature of the exhaust gases. This reduces measurement errors and thermal stresses in the mixing chamber wall material. The errors result primarily from the assumption that constant temperature of the exhaust gases is equivalent to constant heat content. This is only approximately correct because of differences in specific heat between various gas species in the exhaust stream and air.

Additional measurements: The apparatus does not include any additional instrumentation, and specimen mass loss and smoke obscuration are not measured.

Stanford Research Institute Calorimeter: A scaled-up version of the NBS I calorimeter was constructed at Stanford Research Institute.⁴² The redesigned combustion

chamber measured approximately $0.86 \times 0.68 \times 0.98$ m. Maximum specimen size was increased to 0.46×0.61 m, and the radiant heat flux range was reduced to $15\text{--}70$ $\text{kW}\cdot\text{m}^{-2}$.

The FPL Calorimeter

This apparatus was developed by Brenden at the Forest Products Laboratory in Madison, Wisconsin.³⁹ The apparatus has the following features.

Measuring technique: Heat release rate is determined by the substitution method. The flow rate of propane to the substitution burner in the combustion chamber is adjusted during a second run so that the temperature-time curve of the exhaust gases traces that measured during the experiment with the test specimen. Combustion chamber walls and the unexposed side of the specimen holder are water-cooled. Heat losses through walls and specimen are accounted for by measuring the enthalpy rise of the cooling water.

Configuration: The apparatus consists of a water-cooled combustion chamber with approximate dimensions of $0.76 \times 0.43 \times 1.09$ m.

Heater: The specimen is exposed to the heat flux from a premixed gas burner flame. Experiments were conducted⁷⁸ using approximately $0.5 \text{ l}\cdot\text{s}^{-1}$ natural gas mixed with $5 \text{ l}\cdot\text{s}^{-1}$ air, generating a total heat flux to the specimen between 30 and $40 \text{ kW}\cdot\text{m}^{-2}$.

Ignitor: The burner flame impinges on the specimen and also acts as ignition pilot.

Specimen size and orientation: The vertical specimen measures 0.45×0.45 m with a maximum thickness of 0.1 m.

Air flow: In addition to that supplied to the premixed burner, secondary air is supplied at the bottom of the combustion chamber. Various wood products were tested⁷⁸ with a secondary air flow rate of $14 \text{ l}\cdot\text{s}^{-1}$. The maximum total flow rate of air that can be supplied is $130 \text{ l}\cdot\text{s}^{-1}$.

Additional measurements: The apparatus does not include any additional instrumentation.

The FMRC Fire Propagation Apparatus

The Factory Mutual Research Corporation (FMRC) fire propagation apparatus was initially developed to measure convective heat release rate and generation rates of smoke and combustion products.⁷⁹ Originally, only convective heat release rate was measured on the basis of enthalpy rise of the exhaust gases. Test results reported since the late 1970s also include total heat release rates calculated from oxygen consumption or carbon dioxide generation. In the 1980s, the FMRC apparatus was constructed in industrial laboratories in France, Germany, and the United States. Tewarson used the apparatus to determine fire hazard indices⁸⁰ and material properties for fire modeling.¹⁷ He also investigated the effect of environmental conditions (such as oxygen concentration in the combustion air) on heat release rate and burning behavior. The results of his extensive research are summarized in Section 3, Chapter 4. The FMRC fire propagation apparatus has the following features.

Measuring technique: Total heat release rate is determined by the oxygen consumption method. Tewarson also used carbon dioxide generation to calculate heat release rate. However, the amount of energy generated per mass unit of carbon monoxide generated is much more fuel dependent than the amount of energy produced per mass unit of oxygen consumed. Therefore, this technique is not as universally accepted as the oxygen consumption method.

Configuration: Tests are conducted in a semi-open environment. The specimen is located inside a quartz tube, 0.61 m in length and 0.17 m in diameter. A mixture of oxygen and nitrogen is supplied at the bottom of the tube. A stainless steel funnel and vertical exhaust duct are located at some distance above the tube. Dilution air is entrained in the area between the tube and the exhaust system. The total flow of gases through the exhaust duct is determined by measuring pressure drop across a precalibrated orifice.

Heater: Four heaters, which are located coaxially outside the quartz tube, are used to generate an incident heat flux to the specimen with a maximum of $70 \text{ kW}\cdot\text{m}^{-2}$. The electrical heaters operate at high temperatures, so that the spectral distribution of the emitted radiation is not representative of that present in most fires. This problem is discussed in detail in a previous section.

Ignitor: A small pilot flame is located approximately 10 mm above the center of the specimen.

Specimen size and orientation: The specimen is circular and has a diameter of 0.1 m. Maximum thickness is 50 mm. The specimen is tested in the horizontal orientation.

Air flow: Total gas flow rate supplied to the bottom of the quartz tube can be set between 0 and $8.3 \text{ l}\cdot\text{s}^{-1}$. Oxygen content of the combustion air can vary between 0 and 60 percent. Oxygen concentrations below ambient are used for simulating ventilation-controlled fires. Oxygen concentrations above ambient are used to increase flame radiation simulating larger fires.⁸¹ Pure nitrogen is used to determine the heat of gasification.

Additional measurements: The apparatus includes instrumentation to measure specimen mass loss, smoke obscuration, smoke corrosivity, and soot and gas species concentrations in the exhaust flow.

The First ISO Rate of Heat Release Apparatus

The apparatus discussed here never made it beyond a prototype. In 1984, ISO/TC92/SC1 initiated development of an international standard test method for measuring heat release rate of building products on the basis of the cone calorimeter. The cone calorimeter is discussed in a subsequent section, and more in detail in a separate chapter. The development of an ISO heat release rate test method started more than ten years earlier, in the early 1970s. The original design was based on the British fire propagation test, BS 476 part 6. Much of the development work was conducted by three laboratories; two in England (Fire Research Station, and Timber Research and Development Association) and one in Denmark (Danish National Testing Institute). The prototype apparatus based on the sensible enthalpy rise method was finalized

in 1980. The apparatus was modified for oxygen consumption calorimetry a few years later, and some of the technical problems with the prototype were resolved. The resulting apparatus is described in detail in a report issued by the laboratory that conducted the work between 1980 and 1982.⁷¹ The features of this apparatus are briefly discussed here.

Measuring technique: Heat release rate is determined by the oxygen consumption method.

Configuration: Specimen and heater are located inside an insulated box with approximate dimensions $0.1 \times 0.38 \times 0.38$ m.

Heater: The radiant panel measures 0.3×0.38 m, and consists of nine electrical elements. Maximum irradiance to the specimen is between 60 and 70 $\text{kW}\cdot\text{m}^{-2}$. The power to the heating elements is controlled to keep panel temperature constant during testing.

Ignitor: A small hydrogen pilot flame is located in front of the specimen.

Specimen size and orientation: The exposed area of the specimen is 0.205×0.205 m. Maximum thickness is 125 mm. The specimen can be tested in any orientation by rotating the entire apparatus.

Air flow: Experiments have been conducted at an air flow rate of $8.3 \text{ l}\cdot\text{s}^{-1}$. Air can be preheated to 100°C with heating elements located in the inlet duct. When testing specimens in the vertical orientation, direction of the air flow is from top to bottom. This results in a more uniform heat feedback from the flame to the specimen surface. When testing specimens in the horizontal orientation, air flows from one side to the other.

Additional measurements: The apparatus does not include instrumentation to measure specimen mass loss or other parameters.

The NBS II Calorimeter

This apparatus was derived from the NBS I calorimeter to accommodate larger specimens.⁴¹ It has the following features.

Measuring technique: Heat release rate is determined by the compensation method. Gas flow to the burner is adjusted to maintain the temperature in the stack at a constant value of approximately 400°C. The same apparatus without compensation burner was used to explore its suitability for oxygen consumption calorimetry.

Configuration: Radiant panels, specimen, and compensation burner are located in the same chamber with approximate dimensions of $1.07 \times 1.37 \times 1.07$ m. When testing in the vertical orientation, two specimens are positioned back-to-back to approximate adiabatic rear boundary conditions.

Heaters: Two gas panels are located in front of two of the combustion chamber walls, forming an array of 0.3×0.6 m. Four panels are located in front of the remaining two walls, forming an array of 0.6×0.6 m. The specimen is positioned in the center between all panel arrays. Irradiance to the specimen can be set between 25 and 80 $\text{kW}\cdot\text{m}^{-2}$.

Ignitor: An electric spark is used as the ignition pilot at the top of vertical specimens, and over the edge of hor-

izontal specimens. Various other pilot flame configurations can be used as an option.

Specimen size and orientation: Initially, specimens of 0.3×0.3 m were tested in the vertical orientation. Babrauskas used the apparatus to test mattress samples of 0.15×0.3 m in the horizontal orientation.⁷⁴ A heat flux meter adjacent to the specimen was used to monitor incident irradiance during tests.

Air flow: Air is supplied at the bottom of the combustion chamber and to the premixed gas panel burners. The products are extracted through the stack at the top of the combustion chamber.

Additional measurements: The specimen is mounted on a load cell. Instrumentation is provided in the stack for measuring smoke obscuration and concentration of oxygen, carbon dioxide, and carbon monoxide.

The Cone Calorimeter

The cone calorimeter was developed at NBS by Dr. Vytenis Babrauskas in the early 1980s.⁵⁷ It is presently the most commonly used bench-scale rate of heat release apparatus. The apparatus and test procedure are standardized in the United States⁶³ and internationally.⁶⁴ The cone calorimeter is described in detail in a separate chapter, and its main features are summarized here.

Measuring technique: Heat release rate is determined by the oxygen consumption method. The gas flow rate in the exhaust duct is calculated from the pressure drop across, and temperature at, an orifice plate in the duct.

Configuration: Cone heater, spark ignitor, sample holder, and load cell are located underneath a hood. The standard configuration is open, with free access of air to the combustion zone.

Heater: The heater consists of a 5 kW electrical heating element, wound inside an insulated stainless steel conical shell. Hence, the apparatus is named cone calorimeter. The heater can be oriented horizontally or vertically, to perform tests in either orientation. When tests are performed in the horizontal orientation, the specimen is positioned approximately 25 mm beneath the bottom plate of the cone heater. Flames and products of combustion rise and emerge through a circular opening at the top of the heater. Maximum irradiance to the specimen exceeds 100 $\text{kW}\cdot\text{m}^{-2}$.

Ignitor: An electric spark is used as the ignition pilot at the top of vertical specimens, and over the center of horizontal specimens.

Specimen size and orientation: Specimen size in both orientations is 0.1×0.1 m.

Air flow: Combustion products and dilution air are extracted through the hood and exhaust duct by a high-temperature fan. The initial flow rate can be adjusted between 10 and 32 $\text{l}\cdot\text{s}^{-1}$. Volumetric flow rate remains relatively constant during testing. Some cone calorimeters include additional instrumentation to optionally control and maintain the mass flow rate through the exhaust duct.

Additional measurements: The specimen is mounted on a load cell. Most cone calorimeters include instrumentation for measuring smoke obscuration (using a laser light source, described in ASTM E1354 and ISO 5660-2) and

concentration of soot, carbon dioxide, carbon monoxide, and other gases.

Larger cone heater at Trätek: A conical heater was designed at the Swedish Wood Research Institute (Trätek) double the size of that in cone calorimeter.⁶¹ The larger heater was used to study the effect of specimen size on heat release rate.

The Trätek Calorimeter

The Swedish Wood Research Institute developed an open oxygen consumption calorimeter using the apparatus built by Sensenig at NBS as a model.^{82,83} The apparatus, which now has been replaced by a cone calorimeter, has the following features.

Measuring technique: Heat release rate is determined by the oxygen consumption method. Oxygen concentration is measured with a zirconium oxide cell. This analyzer has the advantage that oxygen concentration is measured in a hot and wet gas sample, which greatly simplifies the calculations. However, the accuracy of zirconium oxide cells is inferior to that of paramagnetic oxygen analyzers. For this reason, the laboratory later changed to a paramagnetic analyzer after it acquired a cone calorimeter.⁴⁶ The gas flow rate in the exhaust duct is calculated from center-line velocity measured with a Pitot tube, and gas temperature.

Configuration: Heater, pilot flame, sample holder, and balance are located underneath a hood. The standard configuration is open, with free access of air to the combustion zone.

Heater: The heater measures approximately 0.3×0.3 m, and consists of tubular medium-wave infrared lamps. Maximum irradiance to the specimen is $50 \text{ kW} \cdot \text{m}^{-2}$. The irradiance level is adjusted by changing the distance between heater and specimen. Various heater operating conditions were examined, and conditions were chosen that result in the closest match with the spectral distribution of radiation from wood and oil flames.

Ignitor: A small pilot flame at the top of the specimen was found to result in the quickest involvement of the entire exposed specimen area.

Specimen size and orientation: Specimen size is 0.15×0.15 m. Specimens are positioned in the vertical orientation, parallel to the heating panel.

Air flow: Combustion products and dilution air are extracted through the hood and exhaust duct. The initial flow rate through the duct can be varied, but tests were conducted with a flow rate of approximately $20 \text{ l} \cdot \text{s}^{-1}$.

Additional measurements: The specimen is mounted on an electronic balance to measure mass loss. A white light source system is used for measuring smoke obscuration in the exhaust duct.

Comparison between Bench-Scale Calorimeters

How do results obtained with different calorimeters for the same material compare? A number of comparisons

are reported in the literature. Sensenig tested particle-board, Type X gypsum board, medium-density fiberboard, and polyurethane foam in his oxygen consumption calorimeter, and according to ASTM E906.⁸³ Specimen holder, orientation, specimen size (0.15×0.15 m), mounting method, ignition pilot, and heat flux were identical to eliminate some of the possible sources of variation. The heat release curves from the two methods agreed quite well. In general, results from the OSU apparatus were slightly higher. Chamberlain compared heat release rates for 10 wood products measured in a slightly modified NBS I calorimeter to results from the NBS II calorimeter.⁸⁴ Poor correlations were found for peak heat release rate and average heat release rate over the first minute. Agreement was much better for 5-minute and 10-minute averages. This indicates that the dynamic response of the two methods is very different. Östman et al. reported on a comparison of heat release data for 13 building materials, obtained with the modified OSU apparatus at Lund, the cone calorimeter, and the Trätek apparatus.⁸⁵ Agreement was remarkably good with a correlation coefficient exceeding 90 percent for average heat release rate over the first minute following ignition. Babrauskas compared peak heat release rate from various calorimeters for five aircraft wall paneling materials.⁸⁶ He found good agreement between the FMRC apparatus and the cone calorimeter. However, he also found that the peak heat release rate from the OSU apparatus was approximately 50 percent of the peak from the cone calorimeter. Whether thermopile or oxygen consumption were employed seemed to have only a minor effect on the results from the OSU apparatus. Unfortunately, correlation of average heat release rate was not reported, so that a comparison with the Swedish work is not possible.

Tran compared heat release rate curves for Douglas fir plywood from the cone calorimeter, and the OSU apparatus at FPL modified for oxygen consumption.⁷⁷ First and second peaks agreed well, but the OSU data exceeded the cone calorimeter data by up to 20 percent between the peaks. The increased burning rate can be explained by the enhanced irradiance to the specimen due to temperature rise of the calorimeter walls and heater during a test. Tran tested the same material in the OSU apparatus with the vertical specimen holder from the cone calorimeter and found no effect.

Finally, two comparative studies were recently conducted involving electrical cables. Gandhi et al. measured shorter ignition times and lower heat release rates in the FMRC combustibility apparatus than in the cone calorimeter for communication cables.⁸⁷ Carman et al. compared oxygen consumption and thermopile measurements for six different types of cables.⁸⁸ Good agreement was obtained between the two measurement techniques under flaming conditions.

Heat release data from bench-scale calorimeters are always apparatus dependent. Differences in geometry, test conditions, and mounting methods explain discrepancies between the results from different calorimeters. Apparatus-specific factors must be considered and accounted for in a comparison between different calorimeters, or when the data are used to predict performance in real scale.

Large-Scale Heat Release Rate Calorimeters

There are two primary reasons for conducting a full-scale fire test: to validate computer fire models that are used for hazard assessment, or to evaluate the fire performance of products and assemblies for which bench-scale tests are not representative. Many types of full scale fire test rigs have been equipped with instrumentation to measure heat release rate. This became even more feasible with the development of the oxygen consumption method. These experimental arrangements can be categorized in the following groups: scaled-up heat release rate calorimeters, furniture calorimeters, room tests, industrial-size calorimeters, and other large scale fire tests equipped with instrumentation for measuring heat release rate.

Scaled-Up Heat Release Rate Calorimeters

These are larger scale versions of the bench-scale calorimeters discussed in previous sections. A sample of one to several square meters is exposed to a constant or preprogrammed thermal exposure.

Perhaps the oldest calorimeter of this type is the Factory Mutual Construction Materials Calorimeter.³⁸ A specimen of 1.22×1.22 m is exposed for 10–30 minutes to the standard ASTM E119 temperature-time curve, compressed into a much shorter time. Maximum heat flux is $150 \text{ kW}\cdot\text{m}^{-2}$. The specimen is horizontal facing downward and is exposed to a furnace operated with premixed heptane burners. Heat release rate is determined with the substitution method.

In recent years, a number of large scale panel tests have been developed. These tests consist of a large radiant gas panel and a flat specimen parallel to the panel. Panel and specimen are located beneath a hood and exhaust system. Heat release rate is measured by oxygen consumption. A calorimeter of this type was developed in Canada for facade systems.⁸⁹ The test is capable of exposing specimens of 1.22×2.08 m to a maximum irradiance of $30 \text{ kW}\cdot\text{m}^{-2}$. An intermediate-scale calorimeter of the same type was developed in the United States, primarily to evaluate the heat release rate from construction assemblies.⁹⁰ Sample size is 1×1 m, with a maximum irradiance of $60 \text{ kW}\cdot\text{m}^{-2}$. The method is now standardized by ASTM under designation E1623.⁹¹

Furniture Calorimeters

Furniture calorimeters have been developed in the United States,⁹² the Nordic countries,⁹³ and England.⁹⁴ These calorimeters measure heat release rate from objects such as chairs, sofas, mattresses, and so on. The primary use of this kind of information is for input into compartment fire models and smoke transport models, which form part of fire hazard assessment. The specimen is placed on a load cell platform, beneath a hood and exhaust system. Instrumentation is provided in the exhaust duct to measure flow rate, oxygen and other gas species concentrations, and smoke obscuration. In the United States, standard methods have been developed by ASTM

for the evaluation of single or stacked chairs and mattresses.^{95–97}

Room Tests

Room fire experiments are routinely conducted throughout the world for various reasons. Since the development of oxygen consumption calorimetry, heat release has become one of the routine measurements. Until a few years ago there was little or no standardization in the way room tests were carried out. In the 1970s it was recognized that there was a need for a standard room fire test procedure, in particular for evaluating wall and ceiling lining materials. On the basis of observations made in earlier tests, it was concluded that a room/corner scenario was the best choice for such a standardized procedure. Two major developments greatly contributed to the standardization of a room/corner fire test. The first development was the use of gas burner ignition sources over wood cribs. Gas burners are repeatable and reproducible. They have the advantage that a wide range of steady or time-varying exposure levels can easily be obtained. The second development was that of oxygen consumption calorimetry.

Most of the work toward the development of a standard room/corner test was done in the late 1970s and early 1980s in the United States. The need for a standard room fire test and some aspects of its design were discussed by Benjamin in 1977.⁹⁸ Subsequent research in North America to arrive at a standard full scale test was conducted primarily by Williamson and co-workers at the University of California (UCB)⁹⁹ and by Lee at NBS.¹⁰⁰

Considerable research has also been conducted in the Nordic countries. A detailed project to construct a full-scale room calorimeter was undertaken in Sweden.^{101,102} No oxygen consumption measurements were made at the time. A heat balance was obtained by comparing the theoretical heat release from combustion of gaseous fuel to the sum of the heat losses. The heat losses consisted of convection through the doorway, conduction through the walls and ceiling, and radiation through the doorway. Heat convection through the doorway was estimated by measuring gas velocity and temperature at many points in the doorway. Heat conduction through the surrounding surfaces was calculated using total heat flux, radiation, and surface temperature data. Heat loss by radiation through the door was calculated from radiometer measurements. Initially, a series of quasi-steady calibration tests were conducted in an inert room. Three different circular propane gas burners were used with a diameter of 0.2, 0.3, and 0.4 m respectively. Heat balance calculations showed reasonable agreement, with convection losses being dominant. In subsequent tests with surface finishes, a heptane pool fire with a heat release rate of about 50 kW was used as the ignition source.

Ahonen et al. at the Technical Research Center of Finland studied the effects of different gas burner ignition sources on room/corner fire growth.¹⁰³ Three different burner sizes ($0.17 \text{ m} \times 0.17 \text{ m}$, $0.305 \text{ m} \times 0.305 \text{ m}$, and $0.5 \text{ m} \times 0.5 \text{ m}$) and three square wave output levels (40 kW, 160 kW, and 300 kW) were used, leading to a total of nine combinations. Oxygen consumption calorimetry was

implemented for measuring heat release rate. The burner was placed in a rear corner of the room. In all tests, the walls and ceiling, except for the front wall, were lined with a 10 mm particle board of fairly high density ($720 \text{ kg}\cdot\text{m}^{-3}$). The following six criteria were used to determine the time to flashover:

- Flames emerging through the door (flameover)
- A total heat release rate of 1 MW
- Total heat flux to the floor of $20 \text{ kW}\cdot\text{m}^{-2}$
- A minimum rate of smoke production
- 600°C at the geometric center of the room
- Total heat flux to the floor of $50 \text{ kW}\cdot\text{m}^{-2}$

With the time to flashover defined as the average of the six criteria, the following remarkable results were obtained:

- At the 40 kW level, the medium-sized burner resulted in flashover first, followed by the smaller burner and then the larger burner.
- At 160 kW, the largest burner resulted in flashover first, quickly followed by the other two configurations.
- At 300 kW, the trend was the same as at 160 kW with an even smaller spread between the three results.

The effect of burner size was most significant at the lowest power level, where the medium sized burner was the most severe. At higher exposure levels, the size of the burner was not important. Radiative and convective heat transfer from the burner flame was shown to depend on burner size and power level and had a significant effect on the performance of the material tested. On the basis of the results, the medium burner size and power level were recommended.

Based on the work at NBS and UCB, ASTM drafted a proposal for a standard room/corner test. The proposal was printed in the gray pages of the Annual Book of Standards in 1982 and 1983,¹³ but was never formally published as an ASTM standard. The draft specifies dimensions and geometry of the test compartment, burner size and exposure level, and basic instrumentation and measurements required. The compartment has a floor area of 2.44 m by 3.66 m, interior room height is 2.44 m. A single door in the middle of a square wall is 0.76 m wide and 2.03 m high. A sand burner ignition source is located in a corner opposite from the door. All combustion products emerging through the door are collected in a hood. Measurements are made in the exhaust duct to calculate heat release rate via oxygen consumption. The National Fire Protection Association recently published room test standard NFPA 286, which is nearly identical to the ASTM proposed standard.¹⁵ The ignition source specified in NFPA 286 is a sand burner with an area of $0.3 \times 0.3 \text{ m}$ at 0.3 m off the floor. The net heat output is 40 kW for 5 min followed by 160 kW for 10 min. A few years prior to publication of NFPA 286 the National Fire Protection Association developed NFPA 265, which is a slightly different room test procedure specifically for the evaluation of textile wallcoverings.¹⁴ The two NFPA room test standards use the same burner, but NFPA 265 requires that it be placed at a 50 mm standoff distance from the back and

side walls and be supplied with propane to result in a net heat output of 40 kW for 5 min followed by 150 kW for 10 min. The protocol described in NFPA 265 has been specified for more than 10 years in the U.S. model building codes to qualify textile wallcoverings and is based on extensive research conducted at UCB.¹⁰⁴

Parallel to the development of the ASTM proposal for a room/corner test, ISO has developed an international room test standard. The ISO standard was published in 1992¹⁶ and is based primarily on the Nordic research described above. The concept is identical to that of the draft ASTM method. The dimensions of the test room and ventilation opening are basically the same, but the ISO standard allows ignition sources and specimen configurations other than those described in the ASTM document. The primary ignition source in ISO 9705 is a sand burner with an area of $0.17 \times 0.17 \text{ m}$ at 0.17 m off the floor. The net heat output is 100 kW for 10 min followed by 300 kW for another 10 min.

Industrial-Size Calorimeters

The first industrial-size calorimeter for fires into the MW range was built at Factory Mutual around 1980.¹⁰⁵ This calorimeter, also referred to as the FM Fire Products Collector, was designed to measure heat and other fire products from test fires up to a size associated with sprinkler activation in commodity warehouse storage and other representative occupancies. Approximately 10 years later, a similar industrial-size calorimeter for heat release rate measurements up to 10 MW was constructed at the National Testing Laboratory (SP) in Sweden.¹⁰⁶ Since then several other laboratories, such as the National Research Council of Canada, the Fire Research Station in the UK, and Underwriters Laboratories and Southwest Research Institute in the United States, developed the capability of measuring heat release rate from large fires into the MW range. Cooper presented useful guidelines to address the special challenges associated with calorimetry of large fires.¹⁰⁷

Other Large-Scale Fire Tests

The oxygen consumption method makes it possible to measure heat release rate on almost any fire test. Measurements are reported in the literature for very small fires (kW range) up to 100 MW. Standard fire endurance tests have been instrumented for oxygen consumption calorimetry.^{108,109} Exhaust systems of entire laboratories have been equipped for the technique. There are virtually no limits.

Uncertainty of Heat Release Rate Measurements

The accuracy of a measured value indicates how well it agrees with the true value. The difference between a measured and the true value is referred to as the measurement error. Measurement errors consist of two components: bias error and precision error.

Bias error is fixed or systematic, that is, it does not vary when experiments are repeated (within a single lab-

oratory) or reproduced (in another laboratory). For example, the E value used to determine heat release rate on the basis of oxygen consumption (Equations 17, 20, and 22) may be a source of bias error. Use of a generic E value for a fuel of unknown composition results in an error that is always the same regardless of when, where, and how many times the experiment is conducted.

Precision errors are random in nature. For example, the turbulent flow in the exhaust duct of an oxygen consumption calorimeter results in fluctuations of the differential pressure across the bidirectional probe. Therefore, single-point velocity measurements are likely to slightly deviate from the mean.

The uncertainty of a measurement is the interval around the measured value within which the true value lies with a certain probability, usually 95 percent. In many cases the measured value is calculated from other independent measurements through a functional relationship. For example, heat release rate measured on the basis of oxygen consumption is calculated from differential pressure, temperature, and oxygen concentration measurements according to Equation 17. Standard mathematical techniques can be used to determine the uncertainty of heat release rate measurements on the basis of the uncertainties associated with all sources of error in the equation. Dahlberg performed such an uncertainty analysis for the industrial-size calorimeter at SP and reported values of ± 7 percent and ± 12 percent depending on the use of the CO correction (i.e., for Equations 20 and 17, respectively).¹¹⁰ Enright and Fleischmann reported an uncertainty of ± 5 percent for the cone calorimeter.¹¹¹ These uncertainties are significantly below the precision obtained from interlaboratory trials involving oxygen consumption calorimeters. For example, the most recent cone calorimeter round robin resulted in estimates for the peak heat release rate repeatability and reproducibility of 17 percent and 23 percent, respectively.¹¹² The discrepancies can be explained by the fact that the uncertainty analyses did not account for dynamic errors and sample, operator, and heat flux variations.

Nomenclature

c_p	specific heat at constant pressure ($\text{kJ}\cdot\text{kg}^{-1}\cdot\text{K}^{-1}$)
E	heat release per mass unit of oxygen consumed ($\text{kJ}\cdot\text{g}^{-1}$)
E_{CO}	heat release per mass unit of oxygen consumed for combustion of CO to CO_2 ($\text{kJ}\cdot\text{g}^{-1}$)
h	convection coefficient ($\text{kW}\cdot\text{m}^{-2}\cdot\text{s}^{-1}$) or enthalpy ($\text{kJ}\cdot\text{kg}^{-1}$)
k	OSU calorimeter calibration factor ($\text{kW}\cdot\text{K}^{-1}$)
M	molecular mass ($\text{g}\cdot\text{mol}^{-1}$)
\dot{m}	mass loss rate or mass flow ($\text{g}\cdot\text{s}^{-1}$)
\dot{q}	heat flow (kW)
T	temperature (K)
X	mole fraction ($\text{mol}\cdot\text{mol}^{-1}$)
Y	mole fraction ($\text{g}\cdot\text{g}^{-1}$)

Greek

α	volumetric expansion factor
χ_R	radiative heat loss fraction
$\Delta h_{c,\text{eff}}$	effective heat of combustion ($\text{kJ}\cdot\text{g}^{-1}$)
Δh_g	heat of gasification ($\text{kJ}\cdot\text{g}^{-1}$)
ϵ	emissivity
ϕ	oxygen depletion factor
σ	Boltzman constant ($5.67 \cdot 10^{-11} \text{ kW}\cdot\text{m}^{-2}\cdot\text{K}^{-4}$)

Subscripts

a	air
c	convective
CO	carbon monoxide
CO_2	carbon dioxide
e	external or exhaust
f	flame
H_2O	water vapor
l	loss
net	net
O_2	oxygen
r	radiative
s	surface
v	volatiles
∞	ambient

Superscripts

A	analyzer
a	air
e	exhaust
$''$	per unit area
$*$	corrected for blowing
0	reference

References Cited

1. V. Babrauskas and R. Peacock, "Heat Release Rate: The Single Most Important Variable in Fire Hazard," *Fire Safety J.*, 18, pp. 255–272 (1992).
2. E. Smith, "An Experimental Determination of Combustibility," *Fire Technology*, 7, pp. 109–119 (1971).
3. E. Smith, "Heat Release Rate of Building Materials," in *Ignition, Heat Release and Noncombustibility of Materials* (A. Robertson, ed.), American Society of Testing and Materials, West Conshohocken, PA, pp. 119–134 (1972).
4. E. Smith, "Application of Release Rate Data to Hazard Load Calculations," *Fire Technology*, 10, pp. 181–186 (1974).
5. E. Smith and S. Satija, "Release Rate Model for Developing Fires," *J. of Heat Transfer*, 105, pp. 282–287 (1983).
6. V. Babrauskas, "Performance of the OSU Rate of Heat Release Apparatus Using PMMA and Gaseous Fuels," *Fire Safety J.*, 5, pp. 9–20 (1982).
7. M. Janssens, "Critical Analysis of the OSU Room Fire Model for Simulating Corner Fires," in *Fire and Flammability of Furnishings and Contents* (A. Fowell, ed.), American Society for

- Testing and Materials, West Conshohocken, PA, pp. 169–185 (1994).
8. BS476, *Fire Tests on Building Materials and Structures. Part 6: Method for Test for Fire Propagation for Products*, British Standards Institution, London, UK (1981).
 9. DIN 4102, *Part 1: Fire Behavior of Building Materials and Building Components; Building Materials; Terminology, Calibration and Test Procedures*, DIN, Berlin, Germany (1984).
 10. NF P 92-501, *Safety against Fire—Building Materials—Reaction to Fire Tests—Radiation Test Used for Rigid Materials or Materials on Rigid Substrate (Flooring and Finishes) of All Thicknesses, and for Flexible Materials Thicker than 5 mm*, AFNOR, Paris, France (1985).
 11. NT Fire 0004, *Building Products: Heat Release and Smoke Generation*, NORDTEST, Helsinki, Finland (1985).
 12. "Designation of Semi-Non-Combustible Materials and Fire Retardant Materials," *Notification No. 1231*, Ministry of Construction, Tokyo, Japan (1986).
 13. "Proposed Method for Room Fire Test of Wall and Ceiling Materials and Assemblies," *ASTM Annual Book of Standards*, American Society for Testing and Materials, Philadelphia, pp. 958–978 (1983).
 14. NFPA 265, *Standard Methods of Fire Tests for Evaluating Room Fire Growth Contribution of Textile Wall Covering*, National Fire Protection Association, Quincy, MA (1998).
 15. NFPA 286, *Standard Methods of Fire Tests for Evaluating Contribution of Wall and Ceiling Interior Finish to Room Fire Growth*, National Fire Protection Association, Quincy, MA (2000).
 16. ISO 9705, *Full-Scale Room Test*, International Standards Organization, Geneva, Switzerland (1992).
 17. A. Tewarson and R. Pion, "Flammability of Plastics, I. Burning Intensity," *Combustion and Flame*, 26, pp. 85–103 (1976).
 18. V. Petrella, "The Mass Burning Rate of Polymers, Wood and Liquids," *J. of Fire and Flammability*, 11, pp. 3–21 (1980).
 19. N. Iqbal and J. Quintiere, "Flame Heat Fluxes in PMMA Pool Fires," *J. of Fire Protection Engineering*, 6, pp. 153–162 (1994).
 20. B. Rhodes and J. Quintiere, "Burning Rate and Heat Flux for PMMA in the Cone Calorimeter," *Fire Safety J.*, 26, pp. 221–240 (1996).
 21. D. Hopkins and J. Quintiere, "Material Fire Properties and Predictions for Thermoplastics," *Fire Safety J.*, 26, pp. 241–268 (1996).
 22. W. Parker and J. Urbas, "Surface Temperature Measurements on Burning Wood Specimens in the Cone Calorimeter and the Effect of Grain Orientation," *J. of Fire and Materials*, 17, 5, pp. 205–208 (1993).
 23. J. Urbas, "Non-Dimensional Heat of Gasification Measurements in the Intermediate Scale Heat Release Apparatus," *J. of Fire and Materials*, 17, pp. 119–123 (1993).
 24. M. Janssens, "Cone Calorimeter Measurements of the Heat of Gasification of Wood," *Proceedings of the Interflam '93 Conference*, Interscience Communications, London, England, pp. 549–558 (1993).
 25. E. Smith, "Math Model of a Fire in a Compartment Having Combustible Walls and Ceiling," in *AIChE Symposium Series* 246, 81, pp. 64–74 (1985).
 26. H. Mitler, "Predicting the Spread Rates of Fires on Vertical Surfaces," in *23rd Symposium (International) on Combustion*, The Combustion Institute, pp. 1715–1721 (1990).
 27. K. Opstad, "Fire Modeling Using Cone Calorimeter Results," in *Proceedings of the Eurefic Seminar*, Interscience Communications, London, England, pp. 65–71 (1991).
 28. Y. Zhenghua and G. Holmstedt, "CFD and Experimental Studies of Room Fire Growth on Wall Lining Materials," *Fire Safety J.*, 27, pp. 201–238 (1996).
 29. J. Quintiere, "A Simulation Model for Fire Growth on Materials Subject to a Room-Corner Test," *Fire Safety J.*, 20, pp. 313–339 (1993).
 30. E. Smith and T. Green, "Release Rate Tests for a Mathematical Model," *Mathematical Modeling of Fires*, (J. Mehaffey, ed.), American Society for Testing and Materials, West Conshohocken, PA, pp. 7–20 (1987).
 31. U. Wickström and U. Göransson, "Full-Scale/Bench-Scale Correlations of Wall and Ceiling Linings," *J. of Fire and Materials*, 16, pp. 15–22 (1992).
 32. B. Östman and R. Nussbaum, "Correlation Between Small-Scale Rate of Heat Release and Full-Scale Room Flashover for Surface Linings," in *Fire Safety Science, Proceedings of the 2nd International Symposium*, Hemisphere Publ. Co., New York, pp. 823–832 (1989).
 33. B. Karlsson, "Modeling Fire Growth on Combustible Lining Materials in Enclosures," Ph.D. Dissertation, University of Lund, Sweden (1992).
 34. D. Evans and L. Breden, "Time Delay Correction for Heat Release Rate Data," *Fire Technology*, 14, pp. 85–96 (1978).
 35. D. Bluhme and R. Getka, "Rate of Heat Release Test - Calibration, Sensitivity and Time Constants of ISO RHR Apparatus," *NORDTEST Project 115-77*, National Institute for Testing of Materials, Copenhagen, Denmark (1979).
 36. P. Vandevelde, "An Evaluation of Heat Release Criteria in Reaction-to-Fire Tests," *J. of Fire and Materials*, 4, pp. 157–162 (1980).
 37. A. Abramowitz and R. Lyon, "Effect of Instrument Response Time on Heat Release Rate Measurements," *J. of Fire and Materials*, 19, pp. 11–17 (1995).
 38. N. Thompson and E. Cousins, "The FM Construction Materials Calorimeter," *NFPA Quarterly*, 52, pp. 186–192 (1959).
 39. J. Brenden, "Apparatus for Measuring Rate of Heat Release from Building Materials," *J. of Fire and Flammability*, 6, pp. 50–64 (1975).
 40. W. Parker and M. Long, "Development of a Heat Release Rate Calorimeter at NBS," in *Ignition, Heat Release and Non-combustibility of Materials*, (A. Robertson, ed.), American Society of Testing and Materials, pp. 135–151 (1972).
 41. J. Tordella and W. Twilley, "Development of a Calorimeter for Simultaneously Measuring Heat Release and Mass Loss Rate," *NBSIR 83-2708*, National Bureau of Standards, Gaithersburg, MD (1983).
 42. S. Martin, "Characterization of the Stanford Research Institute Large-Scale Heat-Release Rate Calorimeter," *NBS-GCR 76-54*, National Bureau of Standards, Gaithersburg, MD (1975).
 43. W. Thornton, "The Relation of Oxygen to the Heat of Combustion of Organic Compounds," *Philosophical Magazine and Journal of Science*, 33 (1917).
 44. C. Huggett, "Estimation of the Rate of Heat Release by Means of Oxygen Consumption," *J. of Fire and Materials*, 12, pp. 61–65 (1980).
 45. W. Parker, "An Investigation of the Fire Environment in the ASTM E-84 Tunnel Test," *NBS Technical Note 945*, National Bureau of Standards, Gaithersburg, MD (1977).
 46. R. Nussbaum, "Oxygen Consumption Measurements in the Cone Calorimeter—A Direct Comparison between a Paramagnetic Cell and a High-Temperature Cell," *J. of Fire and Materials*, 11, pp. 201–203 (1987).
 47. W. Parker, "Calculations of the Heat Release Rate by Oxygen Consumption for Various Applications," *NBSIR 81-2427*, National Bureau of Standards, Gaithersburg, MD (1982).
 48. M. Janssens, "Measuring Rate of Heat Release by Oxygen Consumption," *Fire Technology*, 27, pp. 234–249 (1991).

49. S. Brohez, C. Delvosalle, G. Marlair, and A. Tewarson, "Soot Generation in Fires: An Important Parameter for Accurate Calculation of Heat Release," in *Fire Safety Science, Proceedings, 6th International Symposium*, Poitiers, France, pp. 265–276 (2000).
50. B. Dlugogorski, J. Mawhinney, and V. Duc, "Measurement of Heat Release Rates by Oxygen Consumption Calorimetry in Fires Under Suppression," in *Fire Safety Science, Proceedings, 4th International Symposium*, Ottawa, Canada, pp. 877–888 (1994).
51. A. Roberts, "Ultimate Analysis of Partially Decomposed Wood Samples," *Combustion and Flame*, 8, pp. 345–346 (1964).
52. V. Babrauskas, "The Generation of CO in Bench-Scale Fire Tests and the Prediction for Real-Scale Fires," in *Proceedings of the 1st Fire and Materials Conference*, Interscience Communications, London, England, pp. 155–177 (1992).
53. B. Messerschmidt and P. van Hees, "Influence of Delay Times and Response Times on Heat Release Rate Measurements," *J. of Fire and Materials*, 24, pp. 121–130 (2000).
54. H. Sawada, *Thermodynamics of Polymerization*, Marcel Dekker, New York (1976).
55. ASTM E906, "Test Method for Heat and Visible Smoke Release Rates for Materials and Products," in *Annual Book of ASTM Standards*, American Society for Testing and Materials, West Conshohocken, PA, pp. 658–683 (1999).
56. ASTM E1317, "Standard Test Method for Flammability of Marine Surface Finishes," in *Annual Book of ASTM Standards*, American Society for Testing and Materials, West Conshohocken, PA, pp. 696–713 (1999).
57. V. Babrauskas, "Development of the Cone Calorimeter—A Bench-Scale Heat Release Rate Apparatus Based on Oxygen Consumption," *J. of Fire and Materials*, 8, pp. 81–95 (1984).
58. A. Koohyar, "Ignition of Wood by Flame Radiation," Ph.D. Dissertation, University of Oklahoma, Norman, OK (1967).
59. J. Hallman, "Ignition Characteristics of Plastics and Rubber," Ph.D. Dissertation, University of Oklahoma, Norman, OK (1971).
60. D. Drysdale, *An Introduction to Fire Dynamics*, John Wiley and Sons, Chichester, England, pp. 153–160 (1985).
61. R. Nussbaum and B. Östman, "Larger Specimens for Determining Rate of Heat Release in the Cone Calorimeter," *J. of Fire and Materials*, 10, pp. 151–160 (1986).
62. M. Janssens and J. Urbas, "Comparison of Small and Intermediate Scale Heat Release Rate Data," in *Proceedings of the Interflam '96 Conference*, Interscience Communications, London, England, pp. 285–294 (1996).
63. ASTM E1354, "Test Method for Heat and Visible Smoke Release Rates for Materials and Products Using an Oxygen Consumption Calorimeter," in *Annual Book of ASTM Standards*, American Society for Testing and Materials, West Conshohocken, PA, pp. 750–767 (1999).
64. ISO 5660-1, *Rate of Heat Release of Building Products (Cone Calorimeter)*, International Standards Organization, Geneva, Switzerland (1992).
65. B. Toal, T. Shields, and W. Silcock, "Observations on the Cone Calorimeter," *J. of Fire and Materials*, 14, pp. 73–76 (1989).
66. B. Toal, T. Shields, and W. Silcock, "Suitability and Preparation of Samples for the Cone Calorimeter," *Fire Safety J.*, 16, pp. 85–88 (1990).
67. J. Urbas and H. Sand, "Some Investigations on Ignition and Heat Release of Building Materials Using the Cone Calorimeter," in *Proceedings of the Interflam '90 Conference*, Interscience Communications, London, England, pp. 183–192 (1990).
68. V. Babrauskas, W. Twilley, and W. Parker, "The Effect of Specimen Edge Conditions on Heat Release Rate," *J. of Fire and Materials*, 17, pp. 51–63 (1993).
69. L. Tsantaridis and B. Östman, "Communication: Retainer Frame Effects on Cone Calorimeter Results for Building Products," *J. of Fire and Materials*, 17, pp. 43–46 (1993).
70. V. Babrauskas, W. Twilley, M. Janssens, and S. Yusa, "A Cone Calorimeter for Controlled-Atmosphere Studies," *J. of Fire and Materials*, 16, pp. 37–43 (1992).
71. D. Bluhme, "ISO RHR Test Apparatus with Oxygen Consumption Technique," *NORDTEST Project 115-77, Dantest*, Copenhagen, Denmark (1982).
72. *Federal Register*, 51, pp. 26206–26221 (1986).
73. "Aircraft Material Fire Test Handbook," *DOT/FAA/CT-89/15*, US Department of Transportation, Federal Aviation Administration, Atlantic City, NJ (1990).
74. V. Babrauskas, "Combustion of Mattresses Exposed to Flaming Ignition Sources, Part II: Bench-Scale Tests and Recommended Standard Test," *NBSIR 80-2186*, National Bureau of Standards, Gaithersburg, MD (1981).
75. Y. Tsuchiya, "Methods of Determining Heat Release Rate: State-of-the-Art," *Fire Safety J.*, 5, pp. 49–57 (1982).
76. J. Blomqvist, "Rate of Heat Release of Building Materials, Experiments with an OSU Apparatus Using Oxygen Consumption," *Report LUTVDG/(TVBB-3017)*, Lund University, Sweden (1983).
77. H. Tran, "Modifications to an Ohio State University Apparatus and Comparison with Cone Calorimeter Results," in *Heat and Mass Transfer in Fires, Proceedings of the AIAA/ASME Thermophysics and Heat Transfer Conference*, HTD 141, 1990, American Society of Mechanical Engineers, Seattle, WA, pp. 131–139 (1990).
78. J. Brenden, "Wood-Base Building Materials: Rate of Heat Release," *J. of Fire and Flammability*, 6, pp. 274–293 (1975).
79. A. Tewarson, "Heat Release Rates from Burning Plastic," *J. of Fire and Flammability*, 8, pp. 115–130 (1977).
80. A. Tewarson, "Reliable Small-Scale Fire Testing Apparatus," *Modern Plastics*, pp. 58–62 (1980).
81. A. Tewarson, J. Lee, and R. Pion, "The Influence of Oxygen Concentration on Fuel Parameters for Fire Modeling," *18th Symposium (International) on Combustion*, Combustion Institute, pp. 563–570 (1981).
82. G. Svensson and B. Östman, "Rate of Heat Release by Oxygen Consumption in an Open Test Arrangement," *J. of Fire and Materials*, 8, pp. 206–216 (1984).
83. D. Sensenig, "An Oxygen Consumption Technique for Determining the Contribution of Interior Wall Finishes to Room Fires," *NBS Technical Note 1128*, National Bureau of Standards, Gaithersburg, MD (1980).
84. D. Chamberlain, "Heat Release Rate Properties of Wood-Based Materials," *NBSIR 82-2597*, National Bureau of Standards, Gaithersburg, MD (1983).
85. B. Östman, G. Svensson, and J. Blomqvist, "Comparison of Three Test Methods for Measuring Rate of Heat Release," *J. of Fire and Materials*, 9, pp. 176–184 (1985).
86. V. Babrauskas, "Comparative Rates of Heat Release from Five Different Types of Test Apparatuses," *J. of Fire Sciences*, 4, pp. 148–159 (1986).
87. P. Gandhi, L. Caudill, and T. Chapin, "Comparison of Cone Calorimeter Data with FM3972 for Communication Cables," in *Proceedings of the Fifth Fire and Materials Conference*, Interscience Communications, London, England, pp. 217–227 (1998).
88. J. Caman, D. Price, G. Milnes, and D. Purser, "Comparison of Heat Release Rates as Measured by Oxygen Depletion and Thermopile Techniques," in *Proceedings of the Interflam '99 Conference*, Interscience Communications, London, England, pp. 1367–1371 (1999).

89. I. Oleszkiewicz and G. Crampton, "Heat Release from Combustion of Large-Scale Wall Assemblies," in *Abstracts of the 1st Heat Release and Fire Hazard Symposium*, Interscience Communications, London, England, 1991, pp. 18–22.
90. J. Urbas and J. Shaw, "Testing Wall Assemblies on an Intermediate Scale Calorimeter (ICAL)," *Fire Technology*, 29, pp. 332–349 (1993).
91. ASTM E1623, "Test Method for Determination of Fire and Thermal Parameters of Materials, Products, and Systems Using an Intermediate Scale Calorimeter (ICAL)," in *Annual Book of ASTM Standards*, American Society for Testing and Materials, West Conshohocken, PA, pp. 875–892 (1999).
92. V. Babrauskas, J. Lawson, W. Walton, and W. Twilley, "Upholstered Furniture Heat Release Rates Measured with a Furniture Calorimeter," *NBSIR 82-2604*, National Bureau of Standards, Gaithersburg, MD (1982).
93. NT Fire 032, *Upholstered Furniture: Burning Behavior—Full Scale Test*, NORDTEST, Helsinki, Finland (1987).
94. S. Ames and S. Rogers, "Large and Small Scale Fire Calorimetry Assessment of Upholstered Furniture," in *Proceedings of the Interflam '90 Conference*, Interscience Communications, London, England, pp. 221–232 (1990).
95. ASTM E1537, "Test Method for Fire Testing of Upholstered Furniture," in *Annual Book of ASTM Standards*, American Society for Testing and Materials, West Conshohocken, PA, pp. 807–826 (1999).
96. ASTM E1590, "Test Method for Fire Testing of Mattresses," in *Annual Book of ASTM Standards*, American Society for Testing and Materials, West Conshohocken, PA, pp. 841–861 (1999).
97. ASTM E1822, "Test Method for Fire Testing of Stacked Chairs," in *Annual Book of ASTM Standards*, American Society for Testing and Materials, West Conshohocken, PA, pp. 930–950 (1999).
98. I. Benjamin, "Development of a Room Fire Test," *Fire Standards and Safety*, American Society for Testing and Materials, Philadelphia, PA, pp. 300–311 (1977).
99. F. Fisher and R. Williamson, "Intralaboratory Evaluation of a Room Fire Test Method," *NBS GCR 83-421*, National Bureau of Standards, Gaithersburg, MD (1983).
100. B. Lee, "Standard Room Fire Test Development at the National Bureau of Standards," *Fire Safety Science and Engineering*, American Society for Testing and Materials, Philadelphia, PA, pp. 29–42 (1985).
101. B. Sundström and U. Wickström, "Fire: Full Scale Tests," *Technical Report SP-RAPP 1980:14*, National Testing Institute, Borås, Sweden (1980).
102. B. Sundström and U. Wickström, "Fire: Full Scale Tests, Calibration of Test Room—Part 1," *Technical Report SP-RAPP 1980:48*, National Testing Institute, Borås, Sweden (1981).
103. A. Ahonen, C. Holmlund, and M. Kokkala, "Effects of Ignition Source in Room Fire Tests," *Fire Science and Technology*, 7, pp. 1–13 (1987).
104. D. Belles, F. Fisher, and R. Williamson, "Evaluating the Flammability of Textile Wall Coverings," *Building Standards*, 56, pp. 8–14, 52 (1987).
105. G. Heskstad, "A Fire Products Collector for Calorimetry into the MW Range," *Technical Report FMRC J. I 0C2E1.RA*, Factory Mutual Research Corporation, Norwood, MA (1981).
106. M. Dahlberg, "The SP Industry Calorimeter—For Rate of Heat Release Rate Measurements up to 10 MW," *SP Report 1992:43*, Swedish National Testing and Research Institute, Borås, Sweden (1992).
107. L. Cooper, "Some Factors Affecting the Design of a Calorimeter Hood and Exhaust," *J. of Fire Protection Engineering*, 6, pp. 99–112 (1994).
108. J. Brenden and D. Chamberlain, "Heat Release Rates from Wall Assemblies," *Research Paper FPL-RP-476*, Forest Products Laboratory, Madison, WI (1986).
109. H. Tran and R. White, "Heat Release from Wood Wall Assemblies Using Oxygen Consumption Method," *Fire and Polymers: Hazards, Identification, and Prevention*, ACS Symposium Series 425, American Chemical Society, Washington, DC, pp. 411–428 (1990).
110. M. Dahlberg, "Error Analysis for Heat Release Rate Measurements with the SP Industry Calorimeter," *SP Report 1994:29*, Swedish National Testing and Research Institute, Borås, Sweden (1994).
111. P. Enright and C. Fleischmann, "Uncertainty of Heat Release Rate Calculation of the ISO 5660-1 Cone Calorimeter Standard Test Method," *Fire Technology*, 35, pp. 153–169 (1999).
112. J. Urbas, "BDMC Interlaboratory Cone Calorimeter Test Program," *J. of Fire and Materials*, in press.

SECTION THREE

CHAPTER 3

The Cone Calorimeter

Vytenis Babrauskas

Introduction

Section 3, Chapter 2 describes the history and development of techniques for measuring heat release rate (HRR). This chapter outlines features and details of today's preferred instrument for measuring bench-scale HRR—the cone calorimeter. Other cone calorimeter measuring functions are:

1. Effective heat of combustion
2. Mass loss rate
3. Ignitability
4. Smoke and soot
5. Toxic gases

The cone calorimeter is based on the concept of oxygen consumption calorimetry, which is also presented in Section 3, Chapter 2.

This chapter provides both an introduction to and description of cone calorimeter measurement technology. The cone calorimeter has recently assumed a dominant role in bench-scale fire testing of various products; therefore, an emphasis will be placed on the *why* of various design features. When conducting tests, the cone calorimeter operator needs to consult several other documents. Testing will presumably be in conformance with either ISO 5660¹ or ASTM E1354.² In addition, the "User's Guide for the Cone Calorimeter"³ should be consulted. This chapter, thus, does not emphasize the operational aspects, which are documented in the above references, but provides the reader with an overall feel for the equipment. Space is not available in the Handbook to fully discuss the applications of cone calorimeter data, apart from the review of data given in Section 3, Chapter 1. Extensive guidance on using cone calorimeter data is given in a textbook on this subject.⁴ It also provides example data compilations and information on using cone calorimeter data for predictions of fires.

Summary of Features

A schematic view of the cone calorimeter is shown in Figure 3-3-1. Figure 3-3-2 shows a commercial instrument, while Figure 3-3-3 identifies some of the major components. The more salient operational features and limits of the apparatus are

• Specimen size	100 mm × 100 mm, thickness of 6 to 50 mm
• Specimen orientation	Horizontal, face up (standard testing) or vertical (reserved for exploratory studies)
• Specimen back-face conditions	Very low loss insulating ceramic fibrous material
• Load cell live load capacity	500 g
• Load cell tare capacity	3.5 kg
• Load cell resolution	0.005 g
• Ignition	Electric spark
• Heating flux range	0 to 110 kW·m ⁻²
• Flux uniformity, horizontal	Typically 2 percent
• Flux uniformity, vertical	Typically 7 percent
• Sensing principle	Oxygen consumption, only
• Maximum instantaneous output	In excess of 20 kW
• Normally calibrated range	0 to 12 kW
• Linearity over 0 to 12 kW range	5 percent
• Noise intrinsic to oxygen meter	20 ppm O ₂
• Noise in HRR measurement, over 0 to 12 kW range	2.5 percent
• Smoke meter operating range	0 to 20 m ⁻¹ (linear)
• Smoke meter resolution	0.01 m ⁻¹
• Soot sampler mass fraction range	0 to 1 part in 200 (of exhaust gas flow)

Dr. Vytenis Babrauskas is the president of Fire Science and Technology Inc., a company specializing in fire safety research, fire testing issues, and fire science applications to fire investigations and litigations.

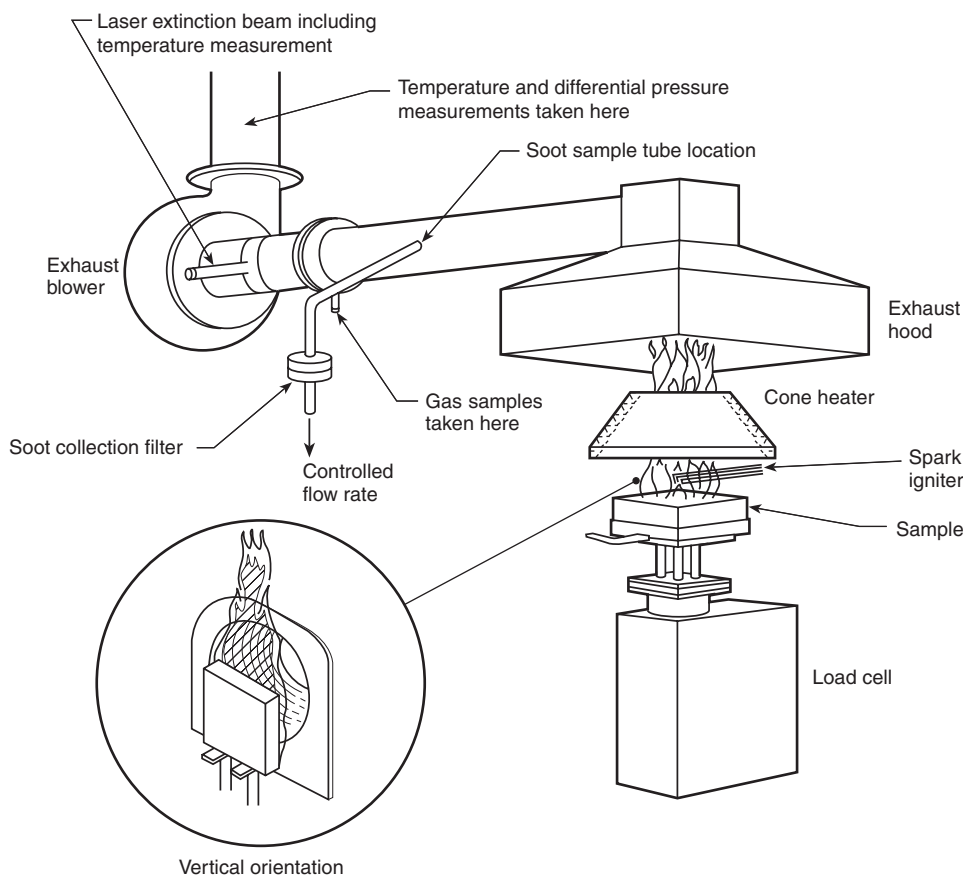


Figure 3-3.1. Schematic view of the cone calorimeter.

Operating Principle

It is emphasized at this point that the cone calorimeter has been designed to use *only* oxygen consumption calorimetry as its measurement principle. Other calorimeters that on occasion use oxygen consumption principles, for example, the Factory Mutual Research Corporation

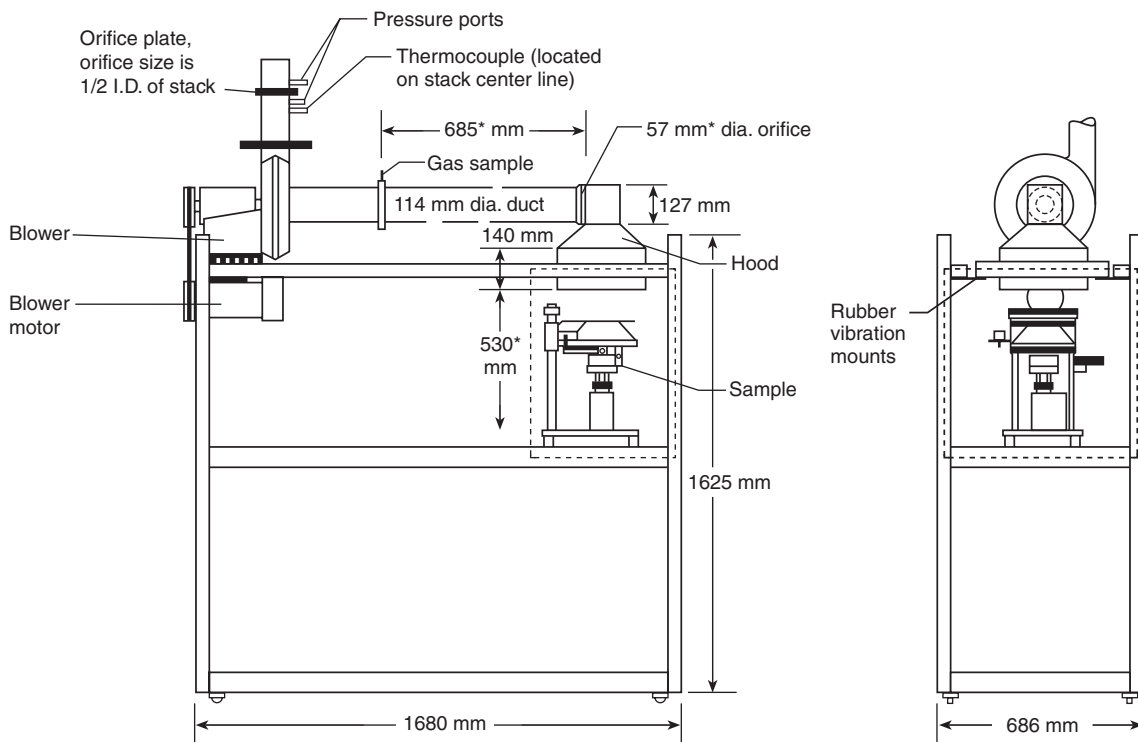
(FMRC) flammability apparatus (see Section 3, Chapter 2), sometimes incorporate a sensible enthalpy flow measurement technique to arrive at the *convective component* of the heat release rate. In the design of the cone calorimeter, such an approach was deemed to be misleading. The implicit assumption behind this type of measurement is that the fraction of the total heat release being manifest as the sensible flow enthalpy is a property of the material being tested. Such is not, in fact, the case. The convective fraction is dependent on details of the apparatus design, and also on the scale of the specimen.⁵

Where high-quality results are required, such as in the cone calorimeter, current-day practice demands that a paramagnetic oxygen analyzer be used. The various manufacturers use measuring schemes that differ in detail, but all rely on the same paramagnetic principle whereby the sensing element is sensitive to the partial pressure of oxygen in the cell. The most significant interferences to this detection principle are NO and NO₂, both of which show a strong paramagnetic response, but not as strong as that of oxygen. Interferents are never a problem in fire testing, however, since O₂ levels measured are 10 to 21 percent, while concentrations of NO_x are rarely above 100 ppm.

Unlike in applications where oxygen levels are monitored as simply one of many indications of fire hazard, in HRR work it is essential that the instrumentation be designed for the highest possible resolution. Thus, both the



Figure 3-3.2. A commercial cone calorimeter. (Photo courtesy Dark Star Research.)



*Indicates a critical dimension

Figure 3-3.3. View of major components of the cone calorimeter.

ASTM and the ISO standards specify that the short-term noise + drift of the oxygen analyzer must be ≤ 50 ppm O₂. The best-grade commercial instruments are able to meet a 20 ppm O₂ limit. In addition, the standards provide a significant amounts of detail on the layout of the gas sampling system, including desiccation, mass flow control, and bypass flows. All of these aspects have to be in conformance with the specifications for good repeatability and reproducibility performance (see Figure 3-3.3) to be achieved.

Because the detection principle responds to oxygen partial pressure, there needs to be a compensation for changes in atmospheric pressure. This can be done with a mechanical back-pressure regulator or by measuring the pressure and correcting electrically. If this compensation is not made, there can be significant error in the calculated heat release rate. Carbon dioxide, the other major component expected to be in the oxygen analyzer, causes less than 0.3 percent error in the oxygen reading. Extensive practice advice on selecting, setting up, and calibrating oxygen analysis systems is given in References 3 and 4.

The Radiant Heater

After establishing the operating principle, the next most important feature is the type of heater. In general, such a heater should be able to achieve adequately high irradiances, have a relatively small convective heating component, present a highly uniform irradiance over the entire exposed face of the specimen, and be designed so as not to change its irradiance when the main voltage

varies, when heater element aging occurs, or when the apparatus retains some residual heat from the exposure given to a prior specimen.

Range of heat fluxes needed for testing: A room fire burning near its maximum rate can show gas temperatures over 1000°C, producing corresponding irradiances to walls and contents of 150 kW·m⁻². Testing under such extreme conditions may not be required; nonetheless, if post-flashover fires are to be stimulated, irradiances of over 75 kW·m⁻² should be available, and preferably closer to 100 kW·m⁻². A significant convective component would negate the purpose of having a radiant ignition test. Rather low convective fluxes can be achieved for specimens oriented horizontally, face up, and with the prevailing airflow being upwards. For vertical specimens, orientation is considered, and it becomes evident that a boundary layer will normally be expected to develop that will add some convective component. The convective boundary layer component is not uniform over the height of a specimen; thus it is seen that better uniformity can also be expected under conditions where the convective component is minimized.

Choice of heater type: In a real fire, the ignition source is, in most cases, in the vicinity of a combustible. The radiation spectrum depends on the size of the fire. A very small fire can show a substantial fraction of its radiation at wavelengths characteristic of H₂O, CO₂, and other combustion products.⁶ For larger fires—certainly for

room fires reaching a hazardous condition—the radiation from the soot tends to dominate. The result is an approximation to a grey-body radiation.⁷ For such a grey-body radiation the temperature is typically in the vicinity of 1000°C.⁸ Experimentally, heater choices for test apparatuses have included gas-fired panels, electric resistance heaters, flames, and high-temperature lamps. Electrical heaters tend to have a near-grey-body characteristic and, assuming a dull or oxidized surface condition, a high emissivity. Gas-fired panels derive a substantial portion of their radiation from the ceramic face; thus, while there are discrete molecular wavelength peaks, overall the radiation shows a grey-body continuum, typically in the range of 700 to 1000°C.⁹ High-temperature lamps, which have been used by several investigators,^{6,10} typically have radiating temperatures of 2200 to 3000°C. The spectral distribution of such a source—further limited by a translucent enclosure—is much different from one operating at 1000°C. Whether this change in spectral characteristics is important depends on the surface of the material to be ignited. For a material with a radiant absorbance independent of wavelength, this source variation would not matter. Hallman, however, has reported data for a large number of plastics and shows that while there are some specimens with negligible wavelength dependence to their absorbance, the majority show strong variations.⁶ Hallman also measured ignition times of plastics with both a flame source and high-temperature lamps. The effect on ignition times ranges from negligible to more than an order of magnitude, depending on the specimen. For a general-purpose test, flames would probably be the least desirable source of heating. For a bench-scale test, flame size has to be kept small. This means that such flames are optically thin, their emissivity is low, and higher heat fluxes cannot be achieved unless a strong convective component is added.

Design details: Once an electrical radiant heater had been decided upon, design details were also influenced by work at NIST with earlier types of calorimeters. One of the primary requirements of the heater is that it not change the irradiance impressed on the specimen when the specimen ignites. This undesired event is, of course, exactly what happens with several of the older types of calorimeters. The specimen's flames directly heat up nearby ironwork, which, in turn, radiates to the specimen. The heater which had been viewing a cold specimen prior to ignition, also starts to view a hot flame afterwards. The result is that its efficiency increases drastically, giving a rise to its radiating temperature. Based on these observations, guidelines were formulated so that the specimen must, as much as possible, view only

1. A temperature-controlled heater
2. A water-cooled plate
3. The open-air, ambient-temperature environment

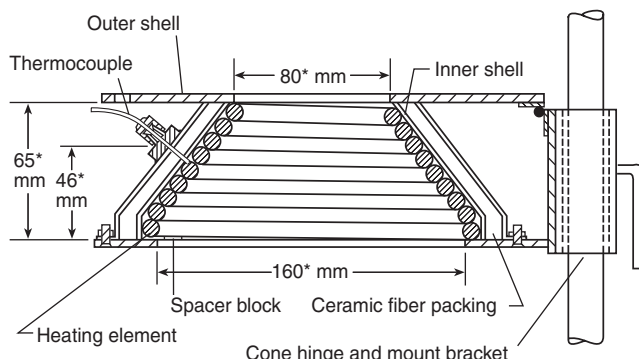
Reliance on item 2 increased costs significantly; thus, it was more desirable to use only items 1 and 3. Prior to the development of the cone calorimeter, fire test apparatuses typically controlled the power (or fuel rate) into the heater, but did not maintain it at a fixed temperature.

The conical shape: The cone calorimeter derives its name from the conical shape of the heater. (See Figure 3-3.4.) The decision had been made to use an electric resistance heater, running at a realistic maximum temperature of about 950°C, but its material and shape still had to be determined. Based on poor experiences with exposed-wire resistance heaters and with silicon carbide rod-type heaters, the tube heater was chosen. The tube heater consists of a resistive wire element inside a protective tube, swaged over a packing of inorganic insulation. The tube is made of Incoloy™ and can be bent to a desired shape.

To determine the best shape, the conical heater used in the ISO 5657 ignitability apparatus¹¹ was examined. This seemed to be a promising shape. The proper shape had to have a hole in the middle, since otherwise a hot spot would occur at the sample center, where the radiation view factor is the highest. The same heater had to serve in both horizontal and vertical orientations. In the horizontal orientation, it was essential that all the products of combustion flow out the hole in the middle, and not "splash" on the heater coil itself, nor escape from the underside. The original ISO 5657 design proved to be unsuitable in the former respect. It also had problems with durability and assembly. Thus a totally new design was created, one that looks, however, superficially similar to the ISO 5657 cone. With the actual cone calorimeter design, the flames from the specimen do not splash on the heater coil. Instead, a sheath of cold air is pulled up, surrounding the flame plume. Thus, there is not a concern that any surface reactions occur on the heater coil.

The space between the inner and outer cones is packed with refractory fiber. This arrangement helps keep the outside of the unit cool and also helps bring the heater up to operating temperature rapidly.

Emissivity of the heater: The emissivity was characterized by Janssens.¹² The heater coil, once installed and fired up a few times, becomes essentially radiatively black. The emissivity itself cannot be directly measured; however, it is possible to compute an approximate view factor, F , for the cone heater. The possibility of measure-



*Indicates a critical dimension

Figure 3-3.4. Cross-sectional view through the cone heater.

ments is based on a simultaneous determination of the heater surface temperature and the heat flux falling on the heat flux meter, with the meter held in place at the same location where a specimen is situated. Over the range of fluxes of 10 to 90 $\text{kW}\cdot\text{m}^{-2}$, Janssens determined the $\varepsilon \times F$ product to be 0.73, with F being computed as 0.78. Then, solving for ε gives $\varepsilon = 0.91$. Since the temperatures of the heater closely resemble those in room fires, and the emissivity approaches 1.0, this means that the spectral distribution is likely to be very close to that expected from room fires (neglecting the molecular radiation contribution from CO_2 and H_2O).

Convective fraction of the heating flux: During the development of the cone calorimeter at NIST, a study was conducted to determine the fraction of the heating flux, which is accounted for by the convective contribution.¹³ When measured with respect to a water-cooled heat flux meter, the results showed that, in the horizontal specimen orientation, the convective contribution was immeasurably small. In the vertical orientation, the fraction was typically 8 to 12 percent. Janssens later remeasured the vertical configuration¹² using a more accurately calibrated heat flux meter and found that, even for the vertical orientation, the convective transfer is immeasurably small. Thus, it can be stated that the objective of having a test method where the heating is primarily radiant was successfully met. For modeling of test results, however, one may be more interested in the possibility of convective heat transfer to a specimen that is heated, or even burning, not to a calibration meter constrained by its water-cooling jacket at near-room temperature. Janssens also made some determinations of such actual specimen heating. The direction of the heat transfer was such as to represent a heat loss from the specimen in all cases. A single convective heat transfer coefficient could not be derived, however, since the value was dependent on the irradiance level from the heater. Janssens' results could be represented by:

Irradiance from Heater ($\text{kW}\cdot\text{m}^{-2}$)	Convective Heat Transfer Coefficient h_c ($\text{W}\cdot\text{m}^{-2}\cdot\text{K}^{-1}$)
20	9.0
40	18.0
60	27.0

For practical work, Janssens recommended that an average value of $h_c = 13.5 \text{ W}\cdot\text{m}^{-2}\cdot\text{K}^{-1}$ should be appropriate for work over the common irradiance range of 20 to 40 $\text{kW}\cdot\text{m}^{-2}$. The actual details of this small amount of convective heat transfer are pertinent only to certain specialized studies. For most work, it is entirely adequate to assume that the specimen heating is entirely radiative.

Uniformity of the heating flux: The uniformity of the heating flux over the face of the specimen in the cone calorimeter has been described.¹³ Over the range of irradiances from 25 to 100 $\text{kW}\cdot\text{m}^{-2}$, the ratio of the flux at the specimen center to average flux varied only from 1.00 to 1.06. The peak deviations from average were typically 2

percent in the horizontal orientation and 7 percent in the vertical. Deviations are higher in the vertical orientation, since the effect of convective fluxes, due to the boundary layer flow, is more pronounced there. Additional measurements have been made in the specimen-depth plane. Control of the surface of the specimen was a special concern to the designers of the ISO apparatus, where a special compressive loading mechanism is provided that attempts to relevel the exposed surface, in case the specimen recedes due to melting. In the cone calorimeter, measurements have been made in the horizontal orientation using a small, 6-mm diameter Gardon-type heat flux gage. A flux mapping was obtained starting at the initial surface, and progressing down to the maximum depth of a specimen, which is 50 mm. A normal aluminum foil rectangular specimen wrap was used for these tests, but without any specimen. The results show that, at heating fluxes of both 25 and 50 $\text{kW}\cdot\text{m}^{-2}$, the deviations over the entire specimen depth are less than 10 percent, and can, therefore, be neglected. (See Figure 3-3.5.) At the lower depths, reflection from the aluminum foil probably assists in maintaining this uniformity.

Orientation of the heater and specimen: It is seen that the normal orientation of the specimen should be horizontal, face up, with the heater being parallel, face down. This allows thermoplastics, liquids, and other melting or dripping samples to be successfully tested. For certain application exploratory studies, it was considered desirable to allow testing in a vertical orientation. Thus, provision was made to swing the heater 90 degrees into a vertical orientation. Vertical orientation testing may be preferable when probing the flame regions, or measuring specimen surface temperatures is desired. Figures 3-3.6 and 3-3.7 show the comparative horizontal and vertical heater orientations, respectively. It is especially emphasized that no standard testing should be specified for the vertical orientation, *even for products that are normally used in a vertical orientation*. The ASTM standard² was amended in 1992 to clarify that the vertical orientation is only for special research studies and not for product testing.

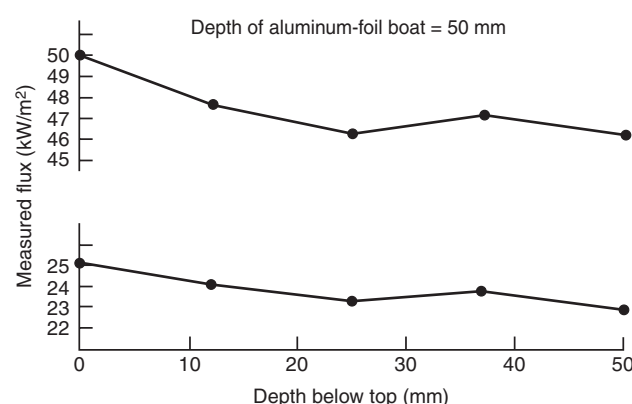


Figure 3-3.5. *Measured flux at various positions below the top surface of a specimen.*

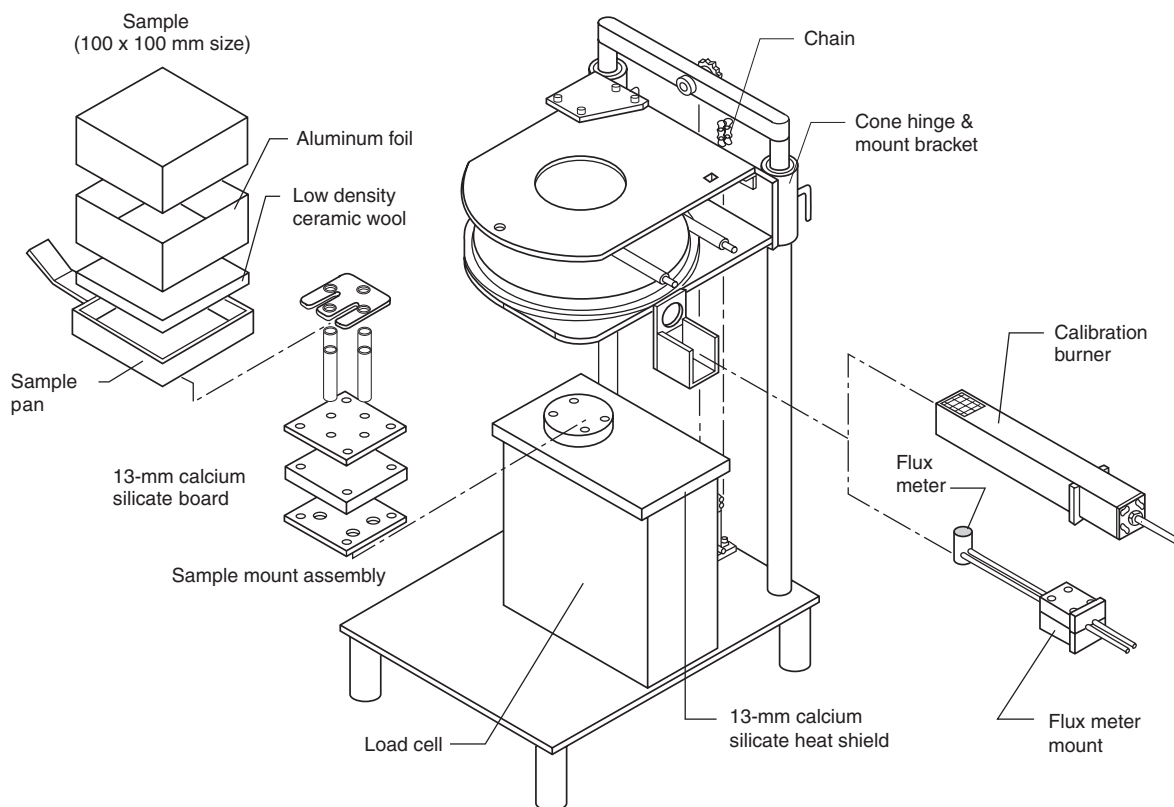


Figure 3-3.6. Heater in the horizontal (standard) orientation.

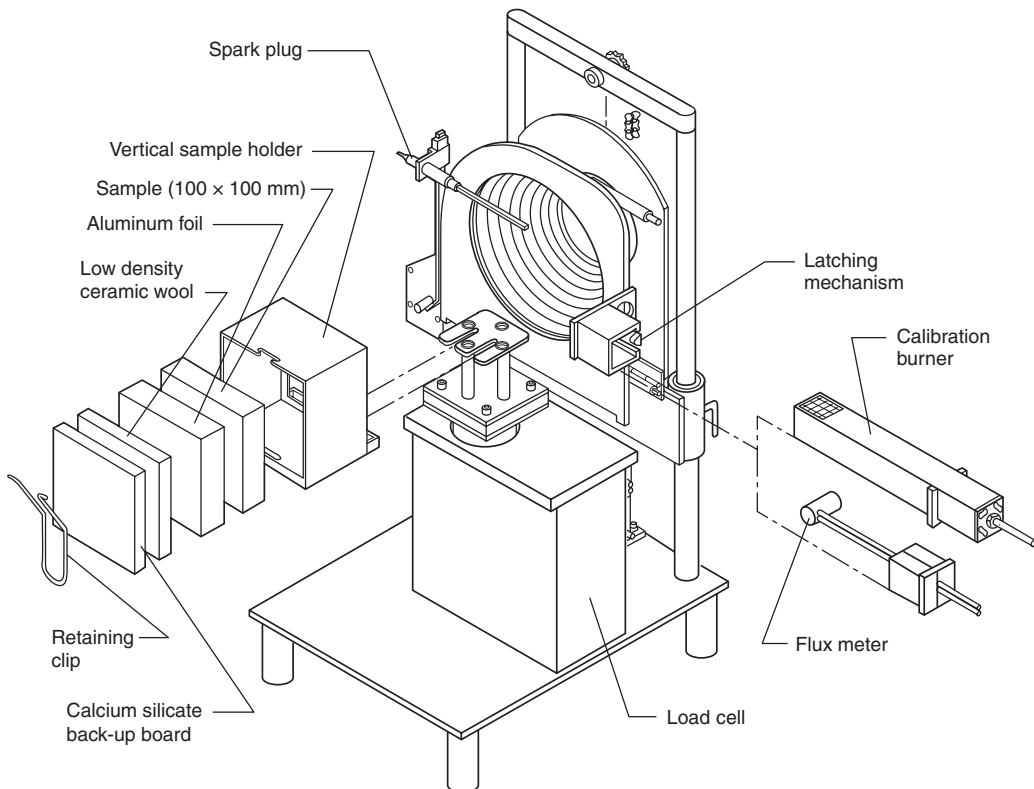


Figure 3-3.7. Heater in the vertical orientation.

Airflow

The feasible airflow rate through the system is bound by certain limits. It must not be so fast that ignition results are improperly affected. It must also not be so slow that products of combustion spill out of the hood. If this were a closed system, one would also be concerned about airflow being so slow that the air/fuel ratio drops into the fuel-rich regime. The standard cone calorimeter, however, has been designed for ambient air testing, and this consideration does not apply.

Systematic guidance in this area was not available. However, as an example of the effect of airflow, measurements were made at NIST using the OSU apparatus. Specimens of black polymethylmethacrylate (PMMA) were exposed in the horizontal orientation to a heating flux of $35 \text{ kW} \cdot \text{m}^{-2}$. With an airflow rate of $12 \ell \cdot \text{s}^{-1}$ through the combustion chamber, the ignition time was 209 s. When the airflow rate was doubled to $24 \ell \cdot \text{s}^{-1}$, the specimen ignition time increased to 403 s. By contrast, Table 3-3.1 shows comparative results with the cone calorimeter; it can be seen a flow rate of $24 \ell \cdot \text{s}^{-1}$ was found to be satisfactory. That flow rate was also about a factor of 2 greater than the minimum at which no spill out of the hood occurs.

The exhaust system uses a high-temperature cast-iron blower to exhaust the gases, and an orifice plate flowmeter. (See Figure 3-3.8.) The orifice plate flowmeter is instrumented with a differential pressure transducer and a thermocouple. For specialized studies, where the entire combustion system is glass enclosed,¹⁴ it is possible to go to flow rates below $12 \ell \cdot \text{s}^{-1}$. With such enclosed systems, accurate measurements can be made down to about $9 \ell \cdot \text{s}^{-1}$ using the standard orifice plate. For lower flow

Table 3-3.1 Effect of Exhaust Hood Airflow on Ignition Times in the Cone Calorimeter^a

Material	Thickness (mm)	Orientation	Fan Setting	Ignition Time ^b (s)
PMMA	13	Horizontal	no fan	71
PMMA	13	Horizontal	$24 \ell \cdot \text{s}^{-1}$	76
PMMA	13	Horizontal	$41 \ell \cdot \text{s}^{-1}$	67
PMMA	13	Vertical	no fan	86
PMMA	13	Vertical	$24 \ell \cdot \text{s}^{-1}$	84
PMMA	13	Vertical	$41 \ell \cdot \text{s}^{-1}$	77
Redwood	13	Horizontal	no fan	23
Redwood	13	Horizontal	$24 \ell \cdot \text{s}^{-1}$	24
Redwood	13	Horizontal	$41 \ell \cdot \text{s}^{-1}$	31
Redwood	13	Vertical	no fan	22
Redwood	13	Vertical	$24 \ell \cdot \text{s}^{-1}$	27
Redwood	13	Vertical	$41 \ell \cdot \text{s}^{-1}$	29

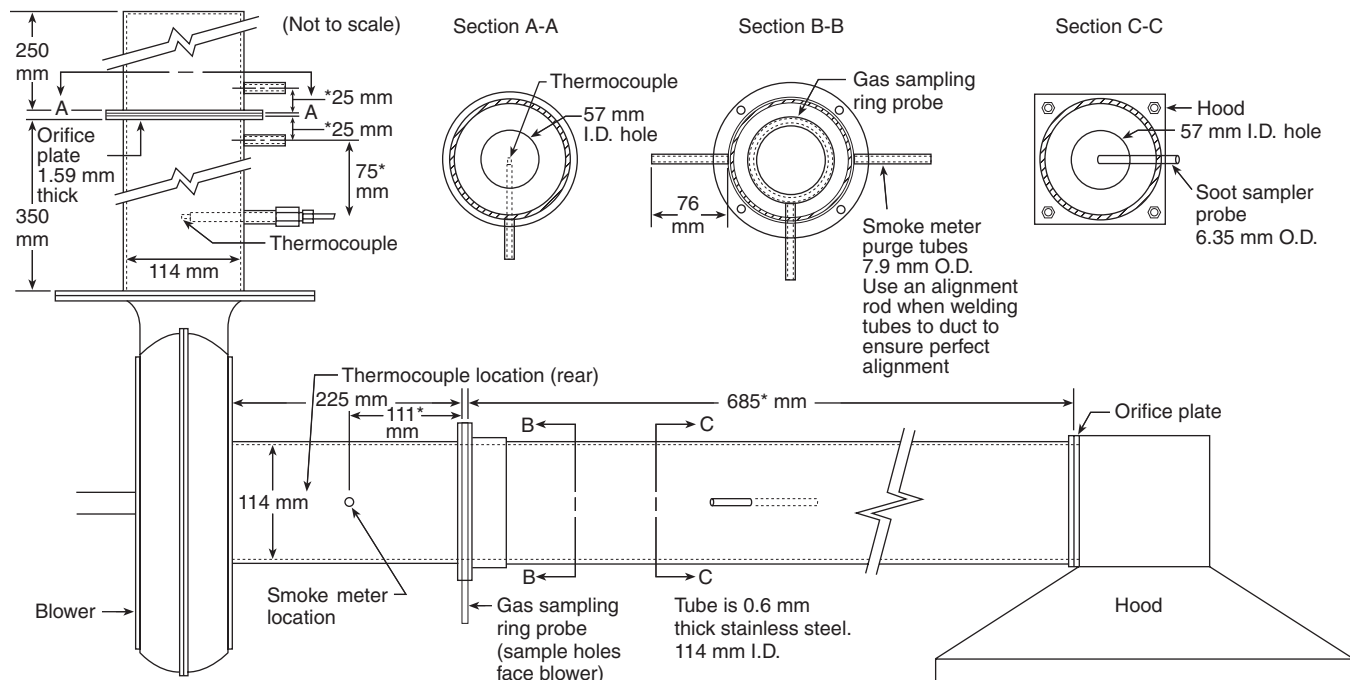
^aAt an irradiance of $35 \text{ kW} \cdot \text{m}^{-2}$

^bTypical ignition time scatter was on the order of $\pm 10\%$ (1σ , $N = 3$)

rates, down to about $5 \ell \cdot \text{s}^{-1}$, the standard orifice plate is replaced by one with a smaller opening.

Means of Ignition

In some cases no external ignition source is desired, and specimen testing is to be done solely on the basis of autoignition. In most cases, however, an external ignition source is desirable. This ignition source should, in general, not impose any additional localized heating flux on the specimen. Apparatus designs have been developed,



*Indicates a critical dimension

Figure 3-3.8. Exhaust duct.

with impinging pilots that can, in some cases, produce such high localized heat fluxes as to burn a hole through the specimen at the point of impingement, yet not ignite it outside of that region. (See Reference 15.) Applications for such devices tend to be specialized, since the general objective of radiant ignition testing is to produce data that can be analyzed in the context of an assumed one-dimensional heat flow. A design using an impinging pilot has an additional difficulty. Since most of the specimen face is not yet heated to the ignition temperature when ignition first begins in the vicinity of the pilot, no unique ignition time can be determined. Instead, there is a significant time spread between when ignition first occurs at the initial location, to when the final portions of the face have been ignited.

The ignitor should reliably ignite a combustible gas mixture in its vicinity. Thus, the location of the ignitor must be chosen so that it is near the place where maximum evolution of pyrolysis gases is expected. Some materials are highly fire-retardant treated, and, when heated, emit vapors that tend to extinguish a pilot flame. The ignitor has to be designed so as not to be extinguished by fire-retardant compounds coming from the specimen, nor by airflows within the test apparatus.

The ISO 5657 apparatus was designed with a "dipping" gas pilot, which is periodically thrust for a short while down close to the specimen face, then retracted. This solution, however, introduces an uncertainty into ignition times and provides further complexity. A gas pilot, based on experience, also requires oxygen premix to be used if a flame that is both small and resistant to blowout is to be achieved.¹⁶ With highly fire-retardant-bearing products, even such precautions are not likely to lead to a reliable pilot; thus, for instance, the ISO 5657 apparatus uses a second pilot to reignite the main pilot. Pilot stability also tends to be crucially dependent on the physical condition of the pilot tube tip, and significant maintenance can be necessary. Finally, if used in a heat release apparatus, a gas pilot can add noise to the baseline of the heat release measurement. Initial experimental results at NBS, using a more tractable alternative (i.e., electric spark ignition) were obtained with the NBS-II calorimeter, where a spark plug arrangement was provided for ignition. This development was successful, and so a similar electric pilot was designed for the cone calorimeter. The location of the ignitor should be at the place where the lower flammable limit is expected to first be reached when the specimen begins its pyrolysis. It should, however, not be so close to the specimen surface that minor swelling of the specimen would interfere with the ignition function. In the cone calorimeter, the ignitor locations were chosen so that, when testing in the horizontal orientation, the spark plug gap is located 13 mm above the center of the specimen; in the vertical orientation, the spark plug gap is located at the specimen plane and 5 mm above the top of the specimen holder.

The actual spark plug arrangement is shown in Figure 3-3-9. The spark plug is provided by a special-purpose 10-kV ignition transformer. The spark plug is moved in and out by remote control, operated by an air motor that rotates the shaft on which the spark plug rests. A reversible lock bar is used to adjust the spark-plug-to-

heater distance when changing from the horizontal to the vertical orientation (the spark gap is 13 mm away from the heater baseplate in the horizontal orientation, but 25 mm away in the vertical).

Specimen Area and Thickness

Both specimen area and thickness may be expected to have some effect on the ignitability and the heat release rate. The main practical size and thickness limitations come from the fact that the specimens to be tested should exhibit primarily one-dimensional heat transfer. Thus, the configuration should be such that excessive edge effects are not seen. If the specimen thickness is such that it is thermally thick (the heat wave penetration depth being less than the physical depth), then further increases in thickness are not expected to change ignitability results. For thinner specimens, however, there can be expected to be a thickness effect, and the backing or substrate material's thermophysical properties can be of importance.

Specimen area: Janssens¹² studied in some detail the general problem of area effect on ignition. The effect is seen to be smaller when irradiances are high rather than low. The exact magnitude of the effect is also dependent on the specimen's thermophysical properties. For specimens of area 0.01 m² or larger, however, his results show an increase in ignition time of only about 10 percent over what would be seen with a specimen of infinite area. Later, Nussbaum and Östman¹⁷ studied specimens in an experimental apparatus somewhat similar to the cone calorimeter, but accommodating 200 × 200 mm specimens. Their comparison of the ignition times of these larger specimens against the standard 100 × 100 mm ones shows that quadrupling the specimen area decreases the ignition time by about 20 percent.

For heat release rate, the specimen size affects the measurement, since flame volume is larger over larger specimens; consequently the flame radiation tends to approach a value of higher emissivity. Nussbaum and Östman also examined the heat release rates from the larger size specimens; the differences were generally of the same order of magnitude as the repeatability of the results. Babrauskas, in commenting on these data,¹⁸ discussed tests on larger size, horizontal PMMA samples, where each doubling of the specimen's area increased the heat release rate, per unit area, by about 10 percent. The more general treatment of the horizontal specimen, of course, is as a liquid pool. Section 3, Chapter 1, Heat Release Rate, gives details on the size effect for burning pools. It can be seen that the diameter has to be greater than about 1 m before the specimen area effect becomes negligible.

The effect of specimen size for vertical samples was examined at Factory Mutual Research Corporation (FMRC) in a series of experiments on PMMA walls.^{19,20} The FMRC studies showed little size effect for specimen heights up to 200 mm; beyond 200 mm there was approximately a linear dependence of q'' on the height. This was true up to the maximum height tested, that is, 3.56 m. Unlike horizontal pools, the rate of heat release was not leveling off at even these sizes, and estimates suggested that

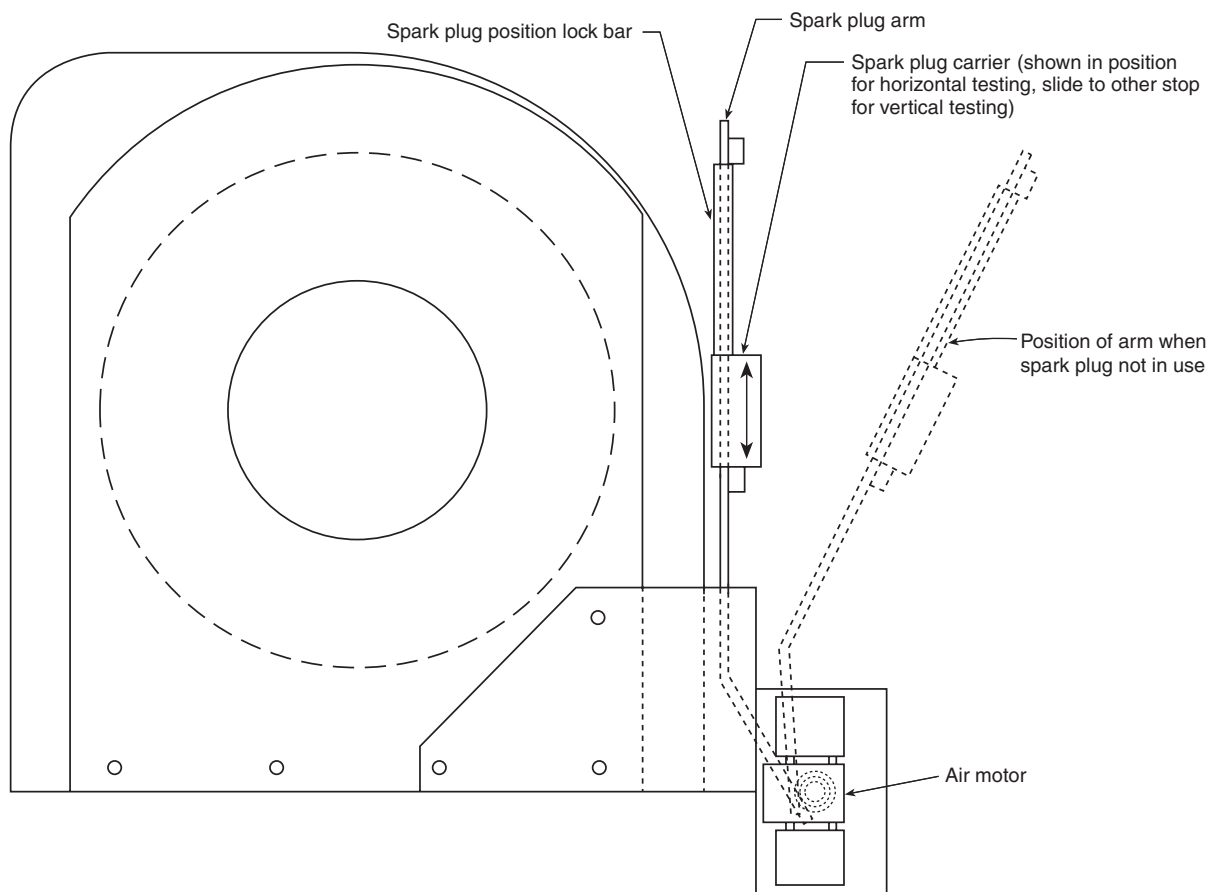


Figure 3-3.9. Spark plug, carrier, and air motor.

the specimen size would have to be increased by another order of magnitude before a leveling off would be seen.

The conclusion from the above studies was that 100 mm × 100 mm was a suitable size for bench-scale testing, but that the bench-scale \dot{q}'' rates will always be somewhat lower than for full-scale fires.

Specimen thickness: The cone calorimeter is intended for testing actual commercial products. Thus the specimen thickness should be, as much as possible, the thickness of the finished product. There are limitations at both ends of the scale, however. The instrument is restricted to testing specimens not thicker than 50 mm. For products that in their finished state are greater than 50 mm thick, it can readily be seen that, for almost any realizable combination of thermophysical properties and incident radiant fluxes, a 50-mm specimen is thermally thick, and increasing thickness would not change the ignition times.^{21,22} By making calculations for various densities and heat fluxes, it was found that for particleboard the minimum thickness required to ensure that the specimen is thermally thick can be represented by

$$\ell = 0.6 \frac{\rho}{\dot{q}''} \quad (1)$$

where

ℓ = thickness (mm)

ρ = density ($\text{kg} \cdot \text{m}^{-3}$)

\dot{q}'' = heat flux ($\text{kW} \cdot \text{m}^{-2}$)

This is probably a reasonable rule of thumb for other materials as well. The proportionality of the required thickness to ρ/\dot{q}'' is derived from classical heat conduction theory by equating the time for the front surface to reach the ignition temperature to the time for the rear surface temperature to begin to rise, assuming that the thermal conductivity is proportional to the density. Numerical calculations were necessary to determine a suitable constant because of the impact of the front surface heat losses.

For materials that are not thermally thick at the time of ignition, the nature of the backing material or substrate can influence the measured value of the ignition time. In the cone calorimeter, the substrate is a blanket of refractory ceramic fiber material, having a nominal density of 65 $\text{kg} \cdot \text{m}^{-3}$. In use, the material assumes a more compacted density of roughly 100 $\text{kg} \cdot \text{m}^{-3}$. Whenever possible, materials whose thicknesses are less than the minimum suggested in the above formula should be mounted on that substrate material over which they will actually be used. As a practical guide for testing unknown commercial

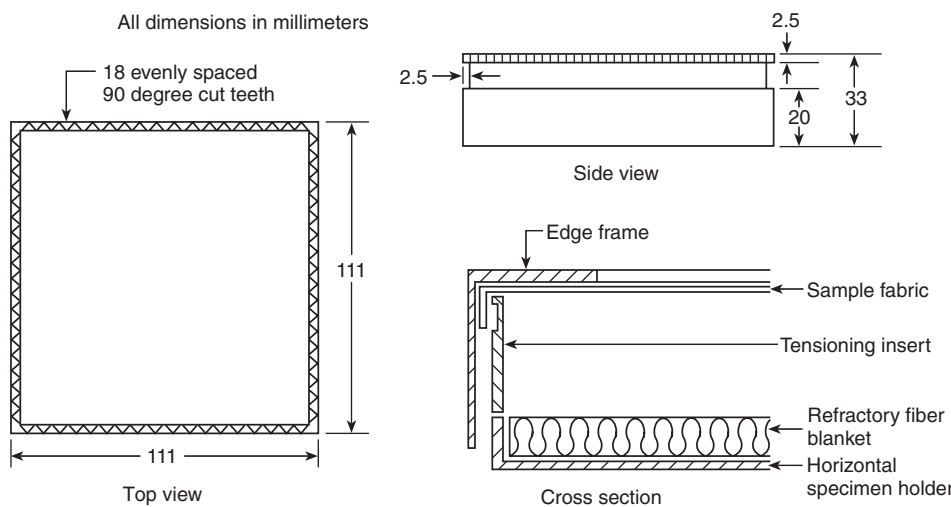


Figure 3-3.10. Special holder for testing fabrics and similar thin materials.

samples, it is desirable to specify that any specimens less than 6 mm thick should always be considered as needing to be tested over their in-use substrate.

Fabrics are a special case. Thin fabrics are sometimes used for constructing air-supported structures; these should be tested with an air space in back, simulating the usage conditions. A special holder has been constructed that allows the fabrics to be pulled taut and held above a dead-air space. (See Figure 3-3.10.)

Sample Testing Specifications

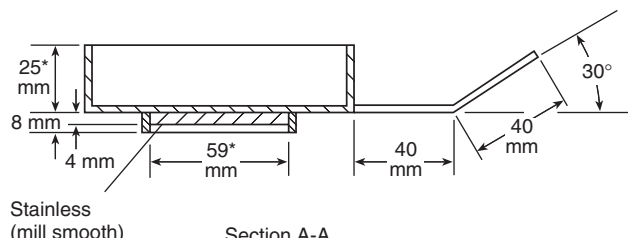
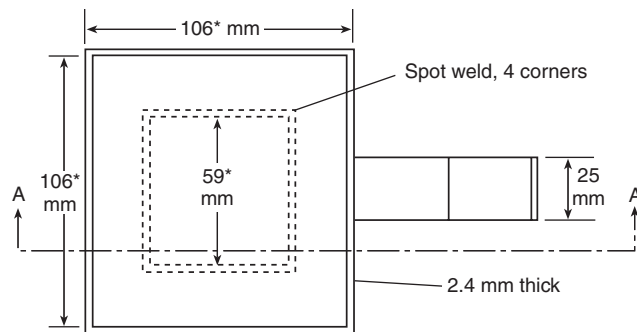
Specimen Orientation and Specimen Holders

As discussed, both a horizontal and vertical specimen orientation are provided. It is considered that the horizontal orientation is standard, while the vertical orientation is reserved for special-purpose testing only. The specimen holders in Figures 3-3.11 and 3-3.12 show the two specimen holders, respectively. With proper precautions, the horizontal orientation can be used for testing liquids and melting materials. The vertical orientation has a small melt trough that can only catch a very small amount of molten material. Also, some specimens, when tested in the vertical orientation, show a tendency to lose physical strength and fall out of the holder. This does not happen in the horizontal orientation.

To present a standardized heat flow boundary condition to the rear face of the specimen, all specimens are backed by a 13-mm layer of low-density (nominal $65 \text{ kg}\cdot\text{m}^{-3}$) ceramic fiber blanket. Such a blanket is the most insulating product readily available for use. In the vertical orientation, there are several layers of rigid millboard behind the blanket, sufficient in thickness to fill out the depth of the specimen holder. The specimen is wrapped in a single sheet of aluminum foil, covering the sides and bottom. The aluminum foil serves to limit the flow of molten material and prevent it from seeping into the refractory blanket.

Load Cell

Many ancillary measurements made in the cone calorimeter (such as yields of various gas species) require the use of a load cell. Transducers had been tried in various earlier apparatuses, but most suffered because they were not designed for purely single-axis linear motion. That is, if the weight of the specimen was not well balanced, or differential heating stresses occurred, it was likely that a mechanical moment (or *torque*) would be applied to the device, with the transducer then being prone to jamming. For the cone calorimeter, a commercial-



*Indicates a critical dimension

Figure 3-3.11. Horizontal orientation specimen holder.

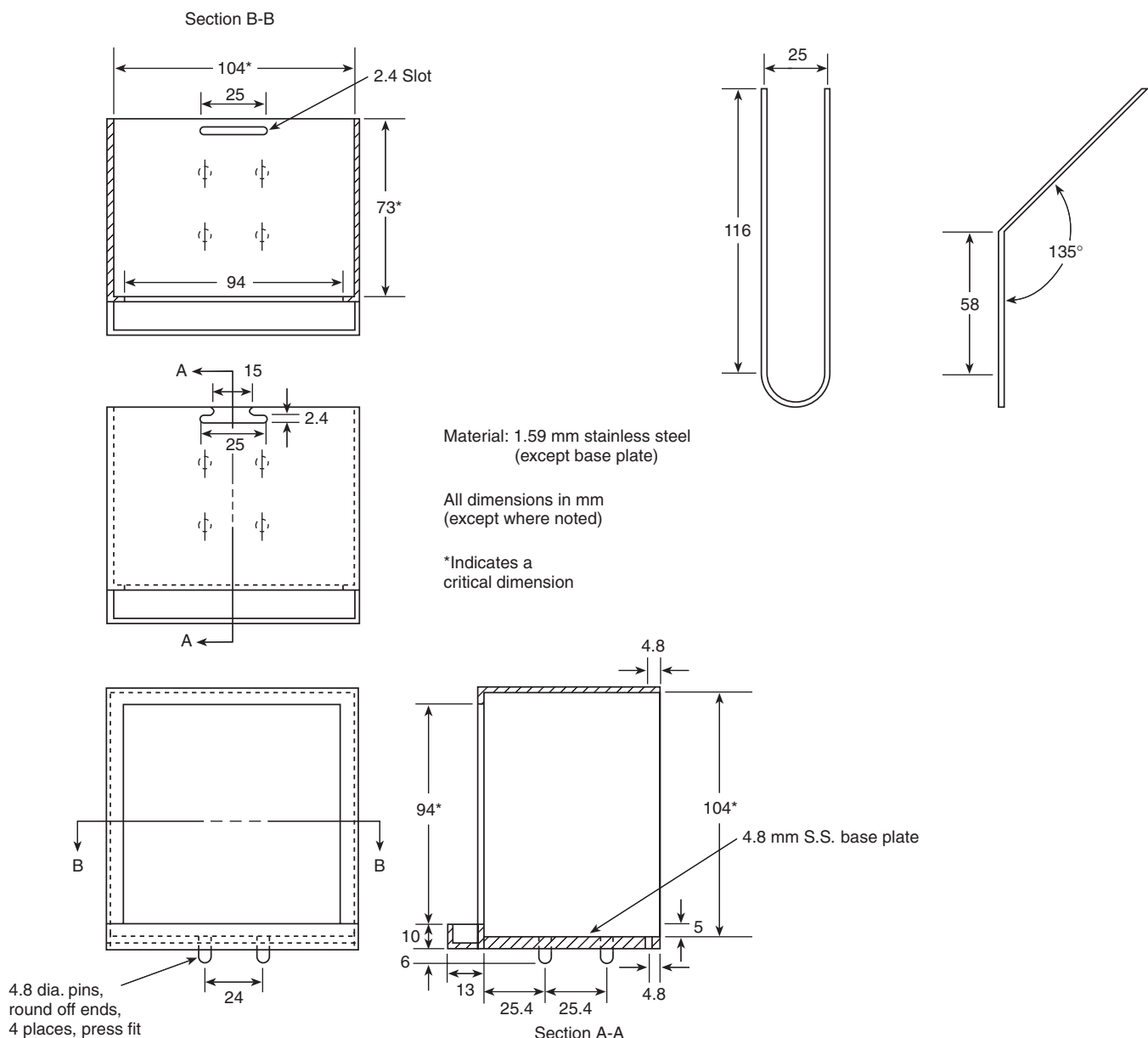


Figure 3-3.12. Vertical orientation specimen holder.

design load cell was found that permits only up-and-down axial motion, while being insensitive to torques or forces from other directions.

The load cell has to accommodate two different orientation specimen holders, and may need to hold additional fixtures. All of these can have substantial—and different—weights, yet must allow accurate mass determination for low-density specimens. The solution adopted was a weighing system that has a large (3.5 kg) mechanical tare adjustment range, along with a sensitive weighing range (500 g). A resolution of 0.005 g is readily achievable.

Figures 3-3.6 and 3-3.7 show, respectively, how the horizontal and vertical orientation specimen holders are accommodated on the load cell. The horizontal holder has

a square recess on the bottom and simply is placed straight down. The vertical holder is more conveniently inserted in a direction of moving toward the heater; thus the specimen is correctly located by four mounting pins on the bottom. In both cases there is a positive specimen location, and the operator does not have to be concerned with how far to insert the holder.

Edge Conditions

Edge effects: In an apparatus such as the cone calorimeter, it is desired that the small-scale test specimen would behave, as much as is possible, like a correspondingly sized element of the full-scale object. If one is dealing with

relatively large, flat, full-scale objects, then heat and mass transfer will occur only in the direction perpendicular to the exposed face. There will be no heat or mass flow along either of the face directions. The guidance to be derived from this conceptual model in designing the bench-scale test environment is clear: there should be a minimum of heat or mass transfer at the specimen edges. The aluminum foil used to wrap the specimen usually serves to minimize any mass transfer that may occur. The heat transfer situation, however, is more complicated.

In the vertical specimen orientation, the specimen has to be restrained against falling out; therefore, the vertical specimen holder incorporates a small lip extending 3 mm along the edges. In the horizontal orientation, no special measures need to be taken against falling out. Thus, for many types of specimens it is satisfactory to simply cover the edges and bottom with aluminum foil, leaving the top exposed in its entirety.

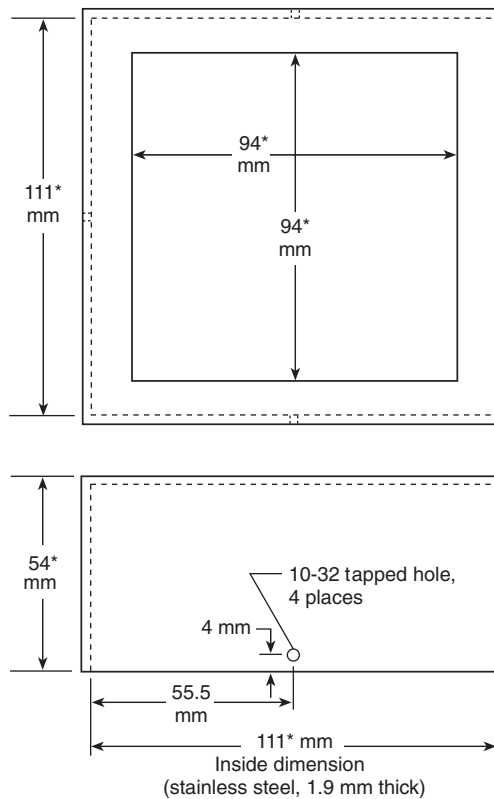
Some categories of specimens, however, present special problems. These are specimens that either have a propensity to ignite first along the outside edge, or ones that, when ignited, burn disproportionately vigorously near the edges. Such behavior is often found with wood specimens and with certain composites. This problem is alleviated by using a stainless steel edge frame for the horizontal orientation, which, in the same way as the vertical holder, provides a 3-mm lip around the edge of the specimen face. (See Figure 3-3.13.)

For specimens showing unrepresentative edge burning, the situation can be viewed as a spurious heat gain along the edges, when compared against a hypothetical ideal situation of exactly zero heat loss/gain at the edges. When an edge frame is applied, the opposite situation can tend to result, that is, a net heat loss from the specimen is observed.²³ The ideal situation, where a specimen is prevented from showing unrepresentative increased edge burning, but is equally not sustaining any losses to an edge frame, may be difficult to approach in practice. This is still a topic of active study at several institutions.

In some cases, an edge frame is needed for thermostructural reasons. Some specimens, especially certain composites, can show pronounced edge warping and curling when subjected to heat. The burning of such a specimen would be highly non-uniform if its edges were not held down with an edge frame. In many cases, an edge frame is all that is required. In some cases, however, additional measures, such as a wire grid (see below), are required.

For the testing of electric cables, there can be a pronounced tendency for pyrolysis gases to flow along the length of the cable interior, and to burn only at the edges, not uniformly over the surface. For such specimens, it has often been found useful to coat the cable ends with a sodium silicate cement, such as Insa-Lute Adhesive Cement Paste No. 1, produced by the Sauereisen Cements Co. When the ends are sealed in such a manner, a knife puncture must be made in the face of each piece of cable to avoid pressure buildup and rupture.

Intumescing samples: A common difficulty with fire test specimens is when they intumesce, either before ignition or during the burning. The simplest solution used in



*Indicates a critical dimension

Figure 3-3.13. Edge frame for the horizontal specimen holder.

the cone calorimeter, which suffices in many, but not all, cases, is the use of a *wire grid* placed on top of the specimen. Figure 3-3.14 shows a medium-weight grid. For minimizing the effect on the measurements, the grid weight should be the smallest possible consistent with providing adequate mechanical restraint to the particular specimen being tested. Mikkola²⁴ demonstrated that the effects on the measurements will be negligible if the average grid mass is $<0.6 \text{ kg}\cdot\text{m}^{-2}$ of specimen face area. This mass corresponds to quite a thin, small grid and will practically be usable only in occasional cases. Additional guidance is given in the NBS "User's Guide for the Cone Calorimeter,"²⁵ but testing laboratories will, on occasion, be required to devise their own special schemes for mounting and restraint.

Smoke Measurement

One of the most essential ancillary measurements performed with the cone calorimeter is smoke obscuration. This system was devised due to widespread dissatisfaction with older, closed-box types of smoke tests.^{26,27} A large number of both practical and theoretical difficulties were found with closed-box systems, and these were successfully resolved by developing a flow-through smoke measuring system, using a helium-neon laser as the light source, and a sophisticated quasi-dual-beam

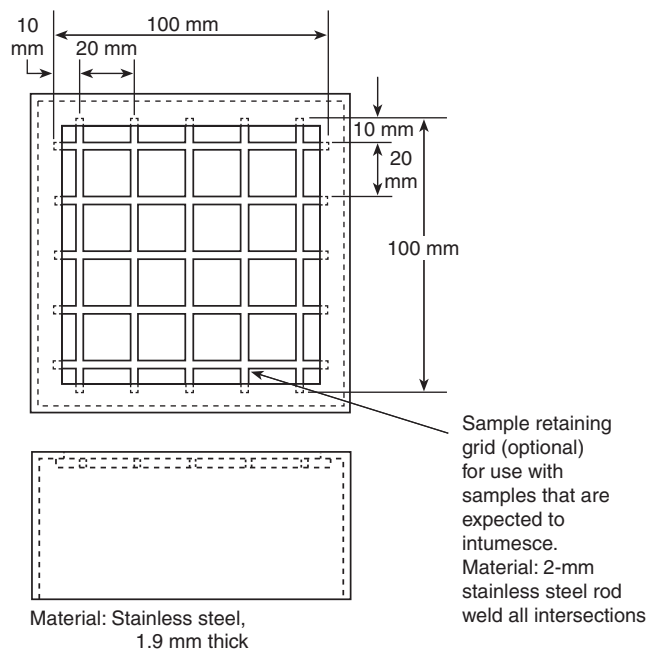


Figure 3-3.14. Wire grid.

measuring arrangement. Figure 3-3.15 shows the overall arrangement of the laser photometer. It is mounted on the exhaust duct at the location shown in Figure 3-3.8. A thermocouple is also mounted nearby, since the calculations require a determination of the actual volume flow rate in the duct at the photometer location. The user should consult Reference 27 for details explaining the operation of the laser photometer. Briefly, the light from the laser goes, via two beam splitters, into two detectors. The light reaching the compensation detector is not attenuated by

smoke; its signal serves as the reference to cancel out fluctuations in laser output power. The main beam detector measures a signal that is attenuated by the smoke. The optical path is purged by a minute flow of room air through a purge system. The flow is maintained by the pressure differential in the exhaust duct.

For certain research purposes, it is advantageous, in addition to obtaining optical smoke obscuration measurement, also to record the gravimetric soot yield. That is, the grams of soot evolved, per gram of specimen burned, can be measured. To do this, a soot mass sampler is connected to the port indicated in section C-C of Figure 3-3.8. A known mass fraction of the exhaust duct flow is passed through a measuring filter, and is weighed before and after the test.

Calibration Equipment

Two basic calibrations are needed: (1) the calibration of the temperature controller for the conical heater, and (2) the actual heat release rate calibration. The temperature controller is calibrated using a Schmidt-Boelter-type heat flux meter. The heat flux meter is equipped with a locating collar and is inserted in place of the specimen, with its face at the same place that the specimen face would be located. No specimen holder is used for this operation. Figures 3-3.6 and 3-3.7 show the insertion of the heat flux meter.

The heat release rate is calibrated by the use of a calibration burner, again inserted into the same bracket as is used for the heat flux meter. (See Figure 3-3.16.) The calibration burner, however, instead of always being inserted facing the heater, is inserted so that the discharge opening faces upward. Calibration is accomplished by controlling the flow of high-purity methane going to the burner and comparing it to a known value and using the net heat of combustion for pure CH_4 as $50 \text{ MJ} \cdot \text{kg}^{-1}$.

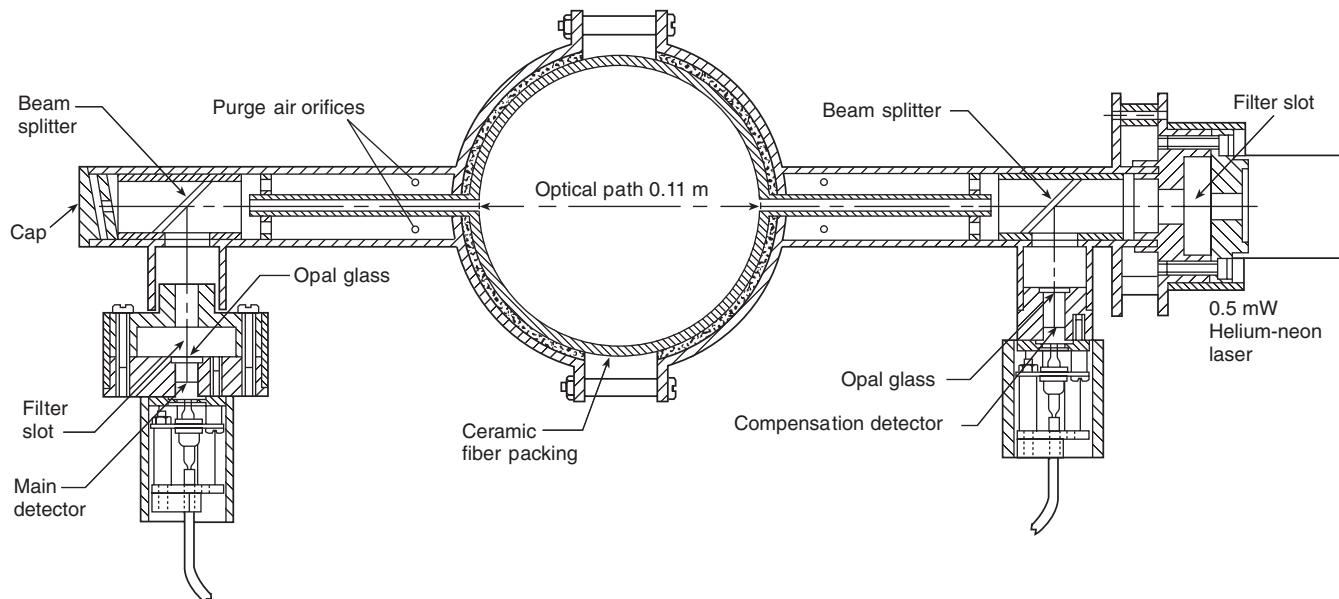


Figure 3-3.15. Laser photometer.

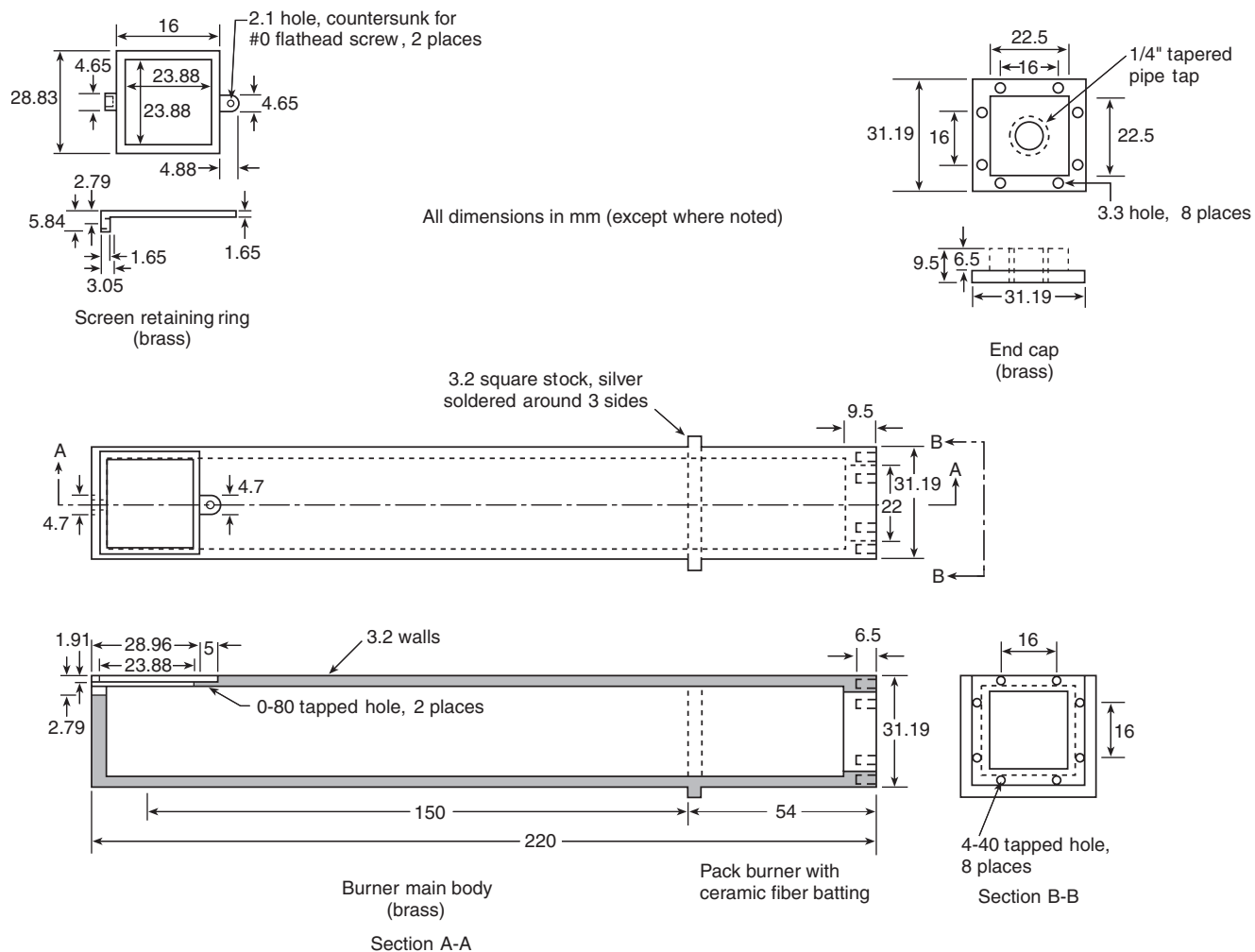


Figure 3-3.16. Calibration burner.

The laser photometer is calibrated by neutral-density glass filters. These are inserted into a filter slot in front of the main beam detector. An auxiliary filter slot is provided in front of the laser. This serves to check the correct balancing of the dual-beam system's common mode rejection ratio.

The NBS "User's Guide to the Cone Calorimeter"²⁵ details how calibrations are performed.

Miscellaneous Details

Ring Sampler

The combustion products flowing through the exhaust system can be heavily laden in soot. Soot would cause rapid clogging of the oxygen measurement system if precautions were not taken. The most important precaution is the specially designed ring sampler. (See Figure 3-3.17.) The sampler is installed in the exhaust duct with the intake holes facing *away* from the direction of airflow. A number of small holes are used so as to provide a certain degree of smoothing with respect to duct flow turbulence.

Additional Gas Analyzers

Many users of cone calorimeters provide not just an oxygen analyzer, but also additional gas analyzers to help in determining the combustion chemistry and toxicity. CO and CO₂ analyzers are simply fitted into the same sampling line serving the oxygen analyzer. Other analyzers, for example, H₂O, HCl, and total unburned hydrocarbons, require a completely separate, heated sampling line system. Such a system also needs to have a heated soot filter at the front.

Measurements Taken with the Cone Calorimeter

The relevant ISO or ASTM standards mandate certain minimum variables to be recorded. In practice, it is normally desired to make the data from the test be as complete as possible. Cone calorimeter data are normally handled as data tables and files standardized according to the FDMS prescription.²⁸ A complete set of data from the

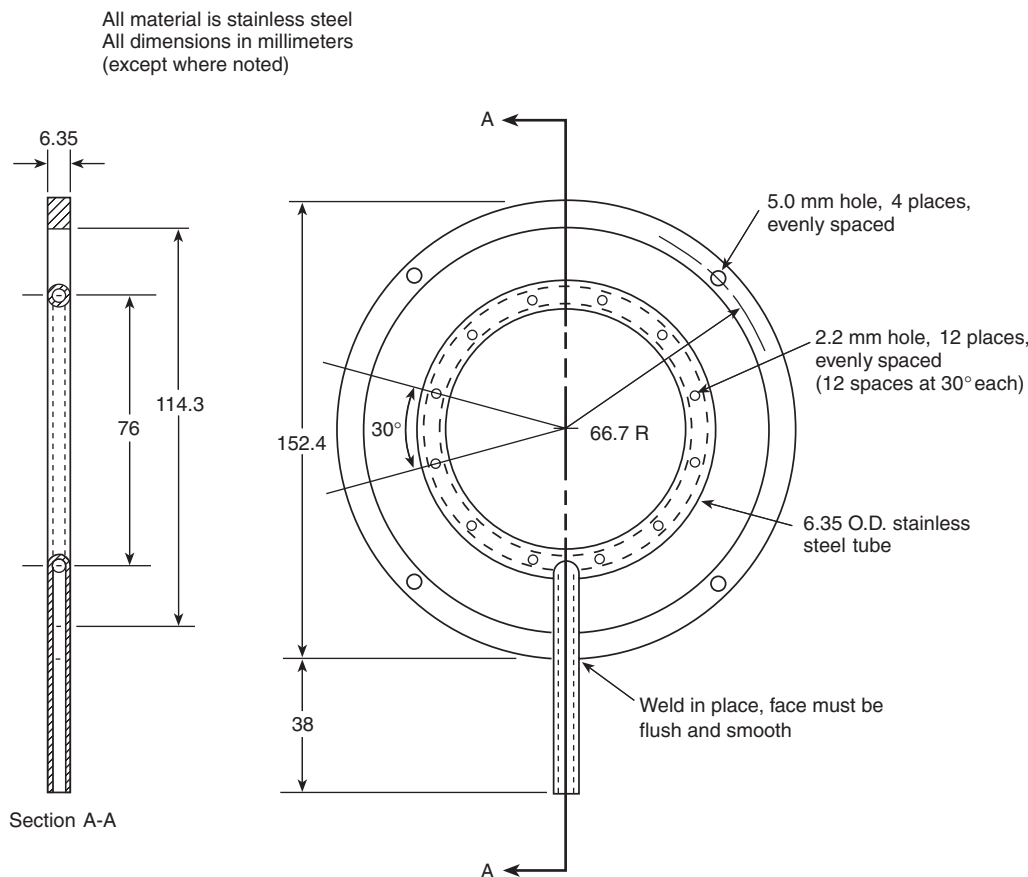


Figure 3-3.17. Ring sampler.

cone calorimeter are illustrated there. Here, the more important ones of these are given, somewhat augmenting the ISO and ASTM set. Note that most of these items must be reported for each test run, but a complete test consists of three runs.

Identification

Various data items must be included here

Preparation

Any non-standard specimen preparation details must be reported

Test no.

Serial number of test; also information on testing laboratory, operator, and so forth.

Irradiance

The heating flux set for the test ($\text{kW}\cdot\text{m}^{-2}$)

Exhaust flow rate

Recorded for completeness, usually the standard value of $24 \text{ l}\cdot\text{s}^{-1}$

Orientation

Horizontal or vertical

Spark ignition

Yes or no

Edge frame

Yes or no

Wire grid

Yes or no

Area of specimen

(m^2), since may be nonstandard in special cases

Specimen initial mass

(g)

Specimen final mass

(g)

Time to ignition

Time to flameout

Peak \dot{q}''

Peak \dot{m}''

Total \dot{q}

O_2 consumption const.

Eff. heat of combustion

Specific extinction rate

Avg. mass loss rate

This, according to the ISO and ASTM standards, is for "sustained flaming" (s)

(s)

($\text{kW}\cdot\text{m}^{-2}$)

($\text{g}\cdot\text{s}^{-1}\cdot\text{m}^{-2}$)

($\text{MJ}\cdot\text{m}^{-2}$)

($\text{kJ}\cdot\text{kg}^{-1}$); this is set to a specific value if known, otherwise to 13100

($\text{MJ}\cdot\text{kg}^{-1}$), reported for period of entire test run

($\text{m}^2\cdot\text{kg}^{-1}$), reported for period of entire test run

Computed over period starting when 10 percent of the ultimate specimen mass loss rate has occurred and ending at the time when 90 percent of the ultimate specimen mass loss has occurred ($\text{g}\cdot\text{s}^{-1}\cdot\text{m}^{-2}$)

Avg. \dot{q}'' (60 s)

Avg. \dot{q}'' (180 s)

Avg. \dot{q}'' (300 s)

Computed for the first 60 s after ignition ($\text{kW}\cdot\text{m}^{-2}$)

Computed for the first 180 s after ignition ($\text{kW}\cdot\text{m}^{-2}$)

Computed for the first 300 s after ignition ($\text{kW}\cdot\text{m}^{-2}$)

Note in the above 60, 180, and 300 s averages that, if the test is ended before having burned, say, 300 s, a proper average can still be correctly computed (i.e., at the end of the averaging period a number of zeroes are used for data points past the end of the test). Since users are often confused by this point, it must be emphasized: *It is not sensible to report an "average heat-release rate" without specifying the time interval.* The reason has to do with the question of what is the *end* of the test. The ISO and ASTM standards specify that the end of the test is considered to be:

1. After all flaming and other signs of combustion cease
2. While there may still be vestigial combustion evidence, but the mass loss rate has become very small (less than 150 g·m⁻² being lost during any 1 min)
3. 60 min have elapsed

These rules are needed for establishing some uniformity among testing laboratories. They do not, however, mean that it is technically sound to compare the average \dot{q}'' of one material that may have burned for 10 min., with another that may have burned for 5 min. It is technically sound, however, to compare their burning over the first one, three, and so forth, minutes of test.

Further information on the form, units, and usage of fire properties measured in the cone calorimeter can be found in Reference 29; specific information on the smoke and soot properties measured in the cone calorimeter is given in Reference 26.

Repeatability and Reproducibility

The repeatability, r , and reproducibility, R , of the cone calorimeter were studied in two sets of interlaboratory trials, one sponsored by ISO and one by ASTM. According to the ISO instructions,³⁰ the definitions of repeatability and reproducibility were taken as

$$r = 2.8 \sigma_r$$

$$R = 2.8 \sigma_R$$

where σ_r is the repeatability standard deviation, σ_R is the reproducibility standard deviation, and the 2.8 factor comes from the fact the probability level of 95 percent is being specified.

From the results of the interlaboratory trials, values for r and R were calculated for six variables. These variables, chosen as being representative for the test results were: t_{ign} , \dot{q}_{max}'' , \dot{q}_{180}'' , \dot{q}_{tot}'' , $\Delta h_{c,\text{eff}}$, and σ_f . A linear regression model was used to describe r and R as a function of the mean overall replicates and overall laboratories for each of the six variables. The regression equations are given below. The range of mean values over which the fit was obtained is also indicated.

The results for time to sustained flaming, t_{ign} , in the range of 5 to 150 s were

$$r = 4.1 + 0.125 t_{\text{ign}}$$

$$R = 7.4 + 0.220 t_{\text{ign}}$$

The results for peak heat release rate, \dot{q}_{max}'' , in the range of 70 to 1120 kW·m⁻² were

$$r = 13.3 + 0.131 \dot{q}_{\text{max}}''$$

$$R = 60.4 + 0.141 \dot{q}_{\text{max}}''$$

The results for 180-s average heat release rate, \dot{q}_{180}'' , in the range of 70 to 870 kW·m⁻² were

$$r = 23.3 + 0.037 \dot{q}_{180}''$$

$$R = 25.5 + 0.151 \dot{q}_{180}''$$

The results for total heat released, \dot{q}_{tot}'' , in the range of 5 to 720 MJ·m⁻² were

$$r = 7.4 + 0.068 \dot{q}_{\text{tot}}''$$

$$R = 11.8 + 0.088 \dot{q}_{\text{tot}}''$$

The results for effective heat of combustion, $\Delta h_{c,\text{eff}}$, in the range of 7 to 40 kJ·g⁻¹ were

$$r = 1.23 + 0.050 \Delta h_{c,\text{eff}}$$

$$R = 2.42 + 0.055 \Delta h_{c,\text{eff}}$$

The results for average specific extinction area, σ_f , in the range of 30 to 2200 m²·kg⁻¹ were

$$r = 59 + 0.076 \sigma_f$$

$$R = 63 + 0.215 \sigma_f$$

A comparison of the cone calorimeter repeatability and reproducibility to the values obtained for the ISO 5657 radiant ignition test showed the cone calorimeter results to be about a factor of 2 better.

Special Cone Calorimeters

The standard cone calorimeter has been designed for using room air for its combustion. All standard testing is done under such conditions. For special combustion studies, however, it can be of interest to explore the burning of materials at oxygen levels other than 21 percent. Such a unit has been constructed at NIST; Reference 14 gives details. This NIST controlled-atmosphere unit has already been used for studies of the burning of materials under conditions where the oxygen in the air supply is <21 percent, with N₂ or CO₂ being mixed into the air stream. (See Figure 3-3.18.) It has also been used for pyrolysis studies under pure nitrogen flow conditions. In principle, it could also be used for studies of enriched-oxygen atmospheres; however, the necessary safety procedures for handling high-concentration oxygen streams are different. A unit for handling O₂ > 21 percent mixtures has been constructed for NASA, but data are not yet available from it. A controlled-atmosphere unit is also appropriate for use when airflow rates of less than 12 ℓ·s⁻¹ are required.



Figure 3-3.18. The NIST controlled-atmosphere cone calorimeter.

All of the present cone calorimeter designs, both standard and otherwise, have been designed for use only under *ambient* pressures. There is interest at this time from at least one research group to design and construct a unit for aerospace studies that would function under *nonambient* pressures.

References Cited

1. ISO 5660, International Standard, "Fire Tests—Reaction to Fire—Rate of Heat Release from Building Products," International Organization for Standardization, Geneva (1993).
2. ASTM E1354, *Standard Test Method for Heat and Visible Smoke Release Rates for Materials and Products Using an Oxygen Consumption Calorimeter*, American Society for Testing and Materials, Philadelphia.
3. W.H. Twilley and V. Babrauskas, "User's Guide for the Cone Calorimeter," NBS Special Publication SP 745, U.S. Natl. Bur. Stand., Gaithersburg, MD (1988).
4. V. Babrauskas and S.J. Grayson, eds., *Heat Release in Fires*, Elsevier, London (1992). Distributed in the U.S. by NFPA.
5. B.J. McCaffrey and G. Cox, "Entrainment and Heat Flux of Buoyant Diffusion Flames," NBSIR 82-2473, U.S. Natl. Bur. Stand. (1982).
6. J.R. Hallman, "Ignition Characteristics of Plastics and Rubber," Ph.D. dissertation, University of Oklahoma, Norman (1971).
7. B. Hägglund and L-E. Persson, "The Heat Radiation from Petroleum Fires," FOA Rapport C 20126-D6(A3), Försvarets Forskningsanstalt, Stockholm (1976).
8. V. Babrauskas, "Estimating Large Pool Fire Burning Rates," *Fire Technology*, 19, pp. 251–261 (Nov. 1983).
9. J.J. Comeford, "The Spectral Distribution of Radiant Energy of a Gas-Fired Radiant Panel and Some Diffusion Flames," *Comb. and Flame*, 18, pp. 125–132 (1972).
10. A. Tewarson, "Physico-Chemical and Combustion/Pyrolysis Properties of Polymeric Materials," NBS-GCR-80-295, U.S. Natl. Bur. Stand., Gaithersburg, MD (1980).
11. ISO 5657, "Fire Tests—Reaction to Fire—Ignitability of Building Products," International Organization for Standardization, Geneva (1986).
12. M.L. Janssens, "Fundamental Thermophysical Characteristics of Wood and Their Role in Enclosure Fire Growth," Ph.D. dissertation, University of Gent, Belgium (1991).
13. V. Babrauskas, "Development of the Cone Calorimeter—A Bench-Scale Heat Release Rate Apparatus Based on Oxygen Consumption," *Fire and Materials*, 8, pp. 81–95 (1984).
14. V. Babrauskas, W.H. Twilley, M. Janssens, and S. Yusa, "A Cone Calorimeter for Controlled-Atmospheres Studies," *Fire and Materials*, 16, pp. 37–43 (1992).
15. ASTM E906, "Standard Test Method for Heat and Visible Smoke Release Rates for Materials and Products," American Society for Testing and Materials, Philadelphia.
16. V. Babrauskas, "Combustion of Mattresses Exposed to Flaming Ignition Sources, Part II. Bench-Scale Tests and Recommended Standard Test," NBSIR 80-2186, U.S. Natl. Bur. Stand. (1981).
17. R.M. Nussbaum and B.A.-L. Östman, "Larger Specimens for Determining Rate of Heat Release in the Cone Calorimeter," *Fire and Materials*, 10, pp. 151–160 (1986).
18. V. Babrauskas, Letter to the editor, *Fire and Materials*, 11, p. 205 (1987).
19. L. Orloff, J. deRis, and G.H. Markstein, "Upward Turbulent Fire Spread and Burning of Fuel Surfaces," in *Fifteenth Symp. (Intl.) on Combustion*, The Combustion Institute, Pittsburgh pp. 183–192 (1974).
20. L. Orloff, A.T. Modak, and R.L. Alpert, "Burning of Large-Scale Vertical Wall Surfaces," in *Sixteenth Symp. (Intl.) on Combustion*, The Combustion Institute, Pittsburgh, pp. 1345–1354 (1976).
21. W.D. Weatherford, Jr. and D.M. Sheppard, "Basic Studies of the Mechanism of Ignition of Cellulosic Materials," *Tenth Symp. (Intl.) on Combustion*, The Combustion Institute, Pittsburgh, pp. 897–910 (1965).
22. H.R. Wesson, J.R. Welker, and C.M. Sliepcevich, "The Piloted Ignition of Wood by Thermal Radiation," *Comb. and Flame*, 16, pp. 303–310 (1971).
23. J. Urbas and H. Sand, "Some Investigations on Ignition and Heat Release of Building Materials Using the Cone Calorimeter," in *Interflam '90, Fifth Intl. Fire Conf. Proc.*, Interscience Communications, Ltd., London, pp. 183–192 (1990).
24. E. Mikkola, unpublished study, VTT, Espoo, Finland (1989).
25. W.H. Twilley and V. Babrauskas, "User's Guide for the Cone Calorimeter," NBS Special Publication SP 745, U.S. Natl. Bur. Stand., Gaithersburg, MD (1988).
26. V. Babrauskas and G. Mulholland, "Smoke and Soot Data Determinations in the Cone Calorimeter," in ASTM STP 983, *Mathematical Modeling of Fires*, American Society for Testing and Materials, Philadelphia, pp. 83–104 (1987).
27. P.J. Geake, "Smoke Characterisation by Laser Diffraction," Ph.D. Dissertation, Polytechnic of the South Bank, London (1988).
28. V. Babrauskas, R.D. Peacock, M. Janssens, and N.E. Batho, "Standardizing the Exchange of Fire Data—The FDMS," *Fire and Materials*, 15, pp. 85–92 (1991).
29. V. Babrauskas, "Effective Measurement Techniques for Heat, Smoke, and Toxic Fire Gases," in *Fire: Control the Heat . . . Reduce the Hazard*, QMC Fire & Materials Centre, London, pp. 4.1–4.10 (1988).
30. ISO 5725, "Precision of Test Methods—Determination of Repeatability and Reproducibility for a Standard Test Method by Inter-Laboratory Tests," International Organization for Standardization, Geneva (1986).

Additional Readings

Apparatus Development

- J.E. Leonard, P.A. Bowditch, and V.P. Dowling, "The Development of a Controlled Atmosphere Cone Calorimeter," *DBCE Doc 98/038*, CSIRO, Highett, Vic., Australia (1998).
- V. Babrauskas and I. Wetterlund, "Choice of Optical Calibration Filters for Laser Photometers," *Fire Safety J.*, 24, pp. 197–199 (1995).
- V. Babrauskas, "The Development and Evolution of the Cone Calorimeter: A Review of 12 Years of Research and Standardization," *Fire Standards in the International Marketplace, ASTM STP 1163* (Arthur F. Grand, ed.), American Society for Testing and Materials, Philadelphia, pp. 3–22 (1995).
- M.R. Christy, R.V. Petrella, and J.J. Penkala, "Controlled-atmosphere Cone Calorimeter," *Fire and Polymers II*, ACS Symp. Series 599, American Chemical Society, Washington, pp. 498–517 (1995).

Building Products

- G. Cowles and P. Collier, "The Safety of Exterior Wall Claddings," *Build*, New Zealand No. 42, pp. 28–30 (1997).
- C. Wade, "Fire Performance of External Wall Claddings under a Performance-based Building Code," *Fire and Materials*, 19, pp. 127–132 (1995).

Composites

- F.-Y. Hsieh and H.D. Beeson, "Flammability Testing of Flame-retarded Epoxy Composites and Phenolic Composites," *Fire and Materials*, 21, pp. 41–49 (1997).
- U. Sorathia, R. Lyon, R.G. Gann, and L. Gritzo, "Materials and Fire Threat," *Fire Technology*, 33, pp. 260–275 (1997).
- A.G. Gibson and J. Hume, "Fire Performance of Composite Panels for Large Marine Structures," *Plastics, Rubber and Composites Processing and Applications*, 23, pp. 175–183 (1995).

Electric Wires and Cables

- Y. Nakagawa, "A Comparative Study of Bench-Scale Flammability Properties of Electric Cables with Different Covering Materials," *J. Fire Sciences*, 16, pp. 179–205 (1998).
- M.A. Barnes, P.J. Briggs, M.M. Hirschler, A.F. Matheson, and T.J. O'Neill, "A Comparative Study of the Fire Performance of Halogenated and Non-halogenated Materials for Cable Applications. Part I, Tests on Materials and Insulated Wires," *Fire and Materials*, 20, pp. 1–16 (1996). "Part II, Tests on Cables," *Fire and Materials*, 20, pp. 17–37 (1996).
- P.J. Elliot and R.H. Whiteley, "A Cone Calorimeter Test for the Measurement of Flammability Properties of Insulated Wire," *Polymer Testing '96*, Rapra Technology Ltd., Shawbury, pp. 3-1–3-9 (1996).

Error Analysis

- P.A. Enright and C.M. Fleischmann, "Uncertainty of Heat Release Rate Calibration of the ISO 5660-1 Cone Calorimeter Test Standard," *Fire Technology*, 35, pp. 153–169 (1999).

Extinguishment

- B. Moghtaderi, B.Z. Dlugogorski, E.M. Kennedy, and D.F. Fletcher, "Effects of the Structural Properties of Solid Fuels

on Their Re-ignition Characteristics," *Fire and Materials*, 22, pp. 165–166 (1998).

- J.C. Yang, C.I. Boyer, and W.L. Grosshandler, "Minimum Mass Flux Requirements to Suppress Burning Surfaces with Water Sprays," *NISTIR 5795*, Natl. Inst. Stand. and Technol., Gaithersburg, MD (1996).

Fabrics

- E. Yanai, T. Suzuki, and T. Yamada, "A Study of the Flammability of Non-flame-retardant and Flame-retardant Materials by Using Cone Calorimeter," *Intl. Symp. on Fire Science and Technology*, Korean Institute of Fire Science & Engineering, Seoul, pp. 85–92 (1997).

Floor Coverings

- P. Van Hees and P. Vandeveldt, "Mathematical Models for Wind-Aided Flame Spread of Floor Coverings," *Fire Safety Science—Proc. 5th Intl. Symp.*, Intl. Assn. for Fire Safety Science, Boston, pp. 321–332 (1997).
- B.A.-L. Östman, "European Fire Tests for Flooring," *Interflam '96*, Interscience Communications Ltd, London, pp. 819–826 (1996).

Furniture

- V. Babrauskas and I. Wetterlund, "Testing of Furniture Composites in the Cone Calorimeter: A New Specimen Preparation Method and Round Robin Results," *Fire Safety J.*, 30, pp. 179–194 (1998).
- V. Babrauskas, D. Baroudi, J. Myllymäki, and M. Kokkala, "The Cone Calorimeter Used for Predictions of the Full-scale Burning Behaviour of Upholstered Furniture," *Fire and Materials*, 21, pp. 95–105 (1997).

Industrial and Agricultural Chemicals

- J. Hietaniemi, R. Kallonen, and E. Mikkola, "Burning Characteristics of Selected Substances: Production of Heat, Smoke and Chemical Species," *Fire and Materials*, 23, pp. 171–185 (1999).
- J. Hietaniemi, R. Kallonen, and E. Mikkola, "Fires at Chemical Warehouses: A Cone Calorimeter Study on the Burning Characteristics and Fire Effluent Composition of Selected Chemical Compounds," VTT Research Note 1810, Valtion Teknillinen Tutkimuskeskus, Espoo, Finland (1997).
- K.-M. Tu, A. Aaronson, and R. Hombek, "A Study of the Combustion Characteristics of Fire Resistant Industrial Fluids Using the Cone Calorimeter," *Proc. 21st Intl. Conf. on Fire Safety*, Product Safety Corp., Sissonville, WV, pp. 42–55 (1996).
- H. Breulet and S. Desmet, "Characterization of Industrial Liquids by Means of the Cone Calorimeter," *Industrial Fires II—Workshop Proceedings*, Report EUR 15967 EN, European Commission, Luxembourg, pp. 223–235 (1995).

Plastics

- F. Gensous and S. Grayson, "Improved Procedure for Testing Intumescent Materials Using the Cone Calorimeter," *Interflam '96*, Interscience Communications Ltd, London, pp. 977–981 (1996).
- A.F. Grand, "The Use of the Cone Calorimeter to Assess the Effectiveness of Fire Retardant Polymers under Simulated Real Fire Test Conditions," *Interflam '96*, Interscience Communications Ltd., London, pp. 143–152 (1996).

- M. Hirschler, "Comparative Analysis of Effectiveness of Fire Retardants Using Heat Release Calorimetry," *Flame Retardants '96*, Interscience Communications Ltd., London, pp. 199–214 (1996).
- D. Hopkins, Jr. and J.G. Quintiere, "Material Fire Properties and Predictions for Thermoplastics," *Fire Safety J.*, 26, pp. 241–268 (1996).
- L. Costa, G. Camino, G. Bertelli, and G. Borsini, "Mechanistic Study of the Combustion Behaviour of Polymeric Materials in Bench-scale Tests. I. Comparison between Cone Calorimeter and Traditional Tests," *Fire and Materials*, 19, pp. 133–142 (1995).
- J. Rychly and L. Costa, "Modelling of Polymer Ignition and Burning Adopted for Cone Calorimeter Measurements: The Correlation between the Rate of Heat Release and Oxygen Index," *Fire and Materials*, 19, pp. 215–220 (1995).

Room Fire Models

- M. Dietenberger and O. Grexa, "Analytical Model of Flame Spread in Full-scale Room/Corner Tests," ISO 9706, *Fire and Materials '99, 6th Intl. Conf.*, Interscience Communications Ltd., London, pp. 211–222 (1999).
- C.A. Wade, D. LeBlanc, J. Ierardi, and J.R. Barnett, "A Room-Corner Fire Growth and Zone Model for Lining Materials," *Proc. 2nd Intl. Conf. on Fire Research and Engineering*, Society of Fire Protection Engineers, Bethesda, MD, pp. 106–117 (1998).
- C.L. Beyler, S.P. Hunt, N. Iqbal, and F.W. Williams, "A Computer Model of Upward Flame Spread on Vertical Surfaces," *Fire Safety Science—Proc. 5th Intl. Symp.*, Intl. Assn. for Fire Safety Science, Boston, pp. 297–308 (1997).
- M. Kokkala, D. Baroudi, and W.J. Parker, "Upward Flame Spread on Wooden Surface Products: Experiments and Numerical Modelling," *Fire Safety Science—Proc. 5th Intl. Symp.*, Intl. Assn. for Fire Safety Science, Boston, pp. 309–320 (1997).
- G. Grant and D. Drysdale, "Numerical Modelling of Early Flame Spread in Warehouse Fires," *Fire Safety J.*, 24, pp. 247–278 (1995).
- M. Janssens, O. Grexa, M. Dietenberger, and R. White, "Predictions of ISO 9705 Room/Corner Test Using a Simple Model," *Proc. Fourth Intl. Fire and Materials Conf.*, Interscience Communications Ltd., London, pp. 73–83 (1995).
- B. Karlsson, "Models for Calculating Flame Spread on Wall Lining Materials and the Resulting Heat Release Rate in a Room," *Fire Safety J.*, 23, pp. 365–386 (1994).

Smoke Production

- A.W. Heskstad and P.J. Hovde, "Empirical Prediction of Smoke Production in the ISO Room Corner Fire Test by Use of ISO Cone Calorimeter Fire Test Data," *Fire and Materials*, 23, pp. 193–199 (1999).

Theoretical Pyrolysis Studies of Materials

- J.E. Staggs, "Modelling Thermal Degradation of Polymers Using Single-step First-order Kinetics," *Fire Safety J.*, 32, pp. 17–34 (1999).
- J.E. Staggs and R.H. Whiteley, "Modelling the Combustion of Solid-phase Fuels in Cone Calorimeter Experiments," *Fire and Materials*, 23, pp. 63–69 (1999).

M.I. Nelson, "A Dynamical Systems Model of Autoignition in the Cone Calorimeter," *Fire Safety Science—Proc. 5th Intl. Symp.*, Intl. Assn. for Fire Safety Science, Boston, pp. 547–558 (1997).

M.I. Nelson, J. Brindley, and A. McIntosh, "A Mathematical Model of Ignition in the Cone Calorimeter," *Combustion Science and Technology*, 104, pp. 33–54 (1995).

Toxicity Studies

- H. Pottel, "The Toxic Potency of the Smoke of Burning Carpets: A Cone Calorimeter and FTIR Study," *UNITEX*, No. 6, pp. 56–65 (1996).
- B. Andersson, G. Holmstedt, and S. Särdqvist, "Production of Toxic Gases—Scaling Effects," *Industrial Fires II—Workshop Proceedings, Report EUR 15967 EN*, European Commission, Luxembourg, pp. 155–166 (1995).
- V. Babrauskas, "Generation of CO in Bench-scale Fire Tests and the Prediction for Real-scale Fires," *Fire and Materials*, 19, pp. 205–213 (1995).
- R. Kakko, V. Christiansen, E. Mikkola, R. Kallonen, L. Smith-Hansen, and K.H. Jørgensen, "Toxic Combustion Products of Three Pesticides," *J. Loss Prevention in the Process Industries*, 8, pp. 127–132 (1995).
- H. Pottel, "The Use of Partial Least Squares (PLS) in Quantitative FTIR: Determination of Gas Concentrations in Smoke Gases of Burning Textiles," *Fire and Materials*, 19, pp. 221–231 (1995).

Transportation

- R.D. Peacock, R.W. Bukowski, and S.H. Markos, "Evaluation of Passenger Train Car Materials in the Cone Calorimeter," *Fire and Materials*, 23, pp. 53–62 (1999).

Wood Materials and Vegetation

- J. Fangrat, Y. Hasemi, M. Yoshida, and T. Hirata, "Surface Temperature at Ignition of Wooden Based Slabs," *Fire Safety J.*, 27, pp. 249–259 (1997).
- O. Grexa, E. Horváthová, and A. Osvald, "Cone Calorimeter Studies of Wood Species," *Intl. Symp. on Fire Science and Technology*, Korean Institute of Fire Science & Engineering, Seoul, pp. 77–84 (1997).
- B. Moghtaderi, V. Novozhilov, D.F. Fletcher, and J.H. Kent, "A New Correlation for Bench-scale Piloted Ignition Data of Wood," *Fire Safety J.*, 29, pp. 41–59 (1997).
- B. Moghtaderi, V. Novozhilov, D.F. Fletcher, and J.H. Kent, "Mathematical Modelling of the Piloted Ignition of Wet Wood Using the Heat-Balance Integral Method," *J. Applied Fire Science*, 6, pp. 91–107 (1996/97).
- R.H. White, D. DeMars, and M. Bishop, "Flammability of Christmas Trees and Other Vegetation," *24th Intl. Conf. on Fire Safety*, Product Safety Corp., Sissonville WV, pp. 99–110 (1997).
- R.H. White, D.R. Weise, and S. Frommer, "Preliminary Evaluation of the Flammability of Native and Ornamental Plants with the Cone Calorimeter," *Proc. 21st Intl. Conf. on Fire Safety*, Product Safety Corp., Sissonville, WV, pp. 256–265 (1996).

CHAPTER 4

Generation of Heat and Chemical Compounds in Fires

Archibald Tewarson

Introduction

Fire hazard is characterized by the generation of calorific energy and products, per unit of time, as a result of the chemical reactions between surfaces and vapors of materials and oxygen from air. If heat is the major contributor to hazard, it is defined as thermal hazard.¹ If fire products (smoke, toxic, corrosive, and odorous compounds) are the major contributors to hazard, it is defined as nonthermal hazard.¹ Various tests are used to determine the generation per unit of time of (1) the calorific energy, defined as the heat release rate, and (2) fire products. The heat release rate and generation rates of fire products normalized by the generation rate of material vapors, airflow, and so forth, defined as fire properties, are used in models to predict (1) heat release rate to assess the thermal hazard and fire protection needs; and (2) generation rates of fire products to assess the nonthermal hazard due to reduced visibility, and smoke damage, toxicity, corrosivity, and protection needs.

The region where vapors are generated is defined as the pyrolysis region and its leading edge as the pyrolysis front. The initiation of flaming fire is defined as ignition. Ignition is a process where vapors generated by heating the surface of a material mix with air, form a combustible mixture, ignite, and a fire is initiated. The region where the ignition process occurs is defined as the *ignition zone*. Minimum heat flux at or below which a material cannot generate the combustible mixture is defined as the *critical heat flux* (CHF).¹⁻⁴ The resistance of a material to generate a combustible mixture is defined as the *thermal response parameter* (TRP).¹⁻⁴ The higher the CHF and TRP values, the longer it takes for the material to heat up, ignite, and initiate a fire, and thus the lower the fire propagation rate.

Depending on the magnitude of the heat flux provided by external sources and the flame of the material

burning in the ignition zone, the pyrolysis front and flame can move beyond the ignition zone. The movement of the pyrolysis front is defined as fire propagation. The rate of movement of the pyrolysis front on the surface is defined as the fire propagation rate.

Heat and chemical compounds are generated as a result of the chemical reactions between (1) pyrolyzing material vapors and oxygen in the gas phase, and (2) pyrolyzing material surface and oxygen in the solid phase. Heat generated in chemical reactions is defined as the *chemical heat*.²⁻⁴ The rate of generation of chemical heat is defined as the *chemical heat release rate*. The chemical heat release rate distributes itself into a convective component, defined as the *convective heat release rate*, and into a radiative component, defined as the *radiative heat release rate*.²⁻⁴ Convective heat release is associated with the flow of a hot products-air mixture, and radiative heat release is associated with the electromagnetic emission from the flame.

In a majority of cases, hazards to life and property are due to fires in enclosed spaces, such as in buildings. In general, fires in enclosed spaces are characterized by an upper and a lower layer. The main constituents of the upper layer are the hot fire products, and the main constituent of the lower layer is fresh air. In early stages, a building fire is well ventilated, and is easy to control and extinguish. However, if the fire is allowed to grow, especially with limited enclosure ventilation and large material surface area, the chemical reactions between oxygen from air and products of incomplete combustion (smoke, CO, hydrocarbons, and other intermediate products) remain incomplete, resulting in an increase in nonthermal hazard. Rapid increase in the generation rates of products of incomplete combustion and growth rate of the fire, due to sudden and dramatic involvement of most of the exposed material surfaces, is termed flashover. Flashover is the most dangerous condition in a fire.

Heat release rate and generation rates of fire products as well as their nature are governed by (1) fire initiation within the ignition zone; (2) fire propagation rate beyond

Dr. Archibald Tewarson is senior research specialist at Factory Mutual Research. His research has focused on chemical aspects of fires.

the ignition zone; (3) fire ventilation; (4) external heat sources; (5) presence or absence of the fire suppression/extinguishing agents; and (6) materials: (a) their shapes, sizes, and arrangements; (b) their chemical natures; (c) types of additives mixed in; and (d) presence of other materials. In this handbook most of these areas have been discussed from a fundamental as well as applied views. For example, the mechanisms of thermal decomposition of polymers, which govern the generation rates of material vapors, is discussed by Beyler in Section 1, Chapter 7; generation rate of heat (or heat release rate) from the viewpoint of thermochemistry is discussed by Drysdale in Section 1, Chapter 5. Flaming ignition of the mixture of material vapors and air is discussed by Kanury in Section 2, Chapter 11; and surface flame spread by Quintiere in Section 2, Chapter 12.

Several other chapters in this handbook relate to the subjects discussed here and should be consulted for complete information. The chapters are as follows: Section 3, Chapter 2 by Janssens on calorimetry; Section 3, Chapter 3 by Babrauskas on the cone calorimeter; Section 2, Chapter 5 by Gottuk and Roby on the effect of combustion conditions on species production; Section 2, Chapter 13 by Mulholland on smoke production and properties. Physical and combustion properties of selected fuels in air, heats of combustion and related properties of pure substances, plastics, and miscellaneous materials listed in Appendix C should be consulted for information that may not be included in this chapter. This chapter presents the applications of the principles discussed in several chapters in this handbook to determine the fire properties of materials. Simple calculations have been included in the chapter to show how the properties can be used for various applications.

Concepts Governing Generation of Heat and Chemical Compounds in Fires

Fire Initiation (Ignition)

The fundamental ignition principles are described in detail by Kanury in Section 2, Chapter 11. The principles suggest that, for fire initiation, a material has to be heated above its CHF value (CHF value is related to the fire point). The CHF value can be determined in one of the several heat release rate apparatuses, for example, Ohio State University's (OSU) heat release rate apparatus,⁵⁻⁸ shown in Figure 3-4.1; the ASTM E2058 fire propagation apparatus (FPA),^{1-4,9-16} shown in Figures 3-4.2, parts (a) and (b); and the cone calorimeter,¹⁷⁻¹⁹ shown in Figure 3-4.3. The design features, test conditions, and types of measurements for the three apparatuses are listed in Table 3-4.1.

Typically the CHF values are determined by exposing the horizontal sample (e.g., about 100-mm diameter or about 100 × 100-mm square and up to about 100-mm in thickness with blackened surface in the flammability apparatus) to various external heat flux values until a value is found at which there is no ignition for about 15 min.

As the surface is exposed to heat flux, initially most of the heat is transferred to the interior of the material. The

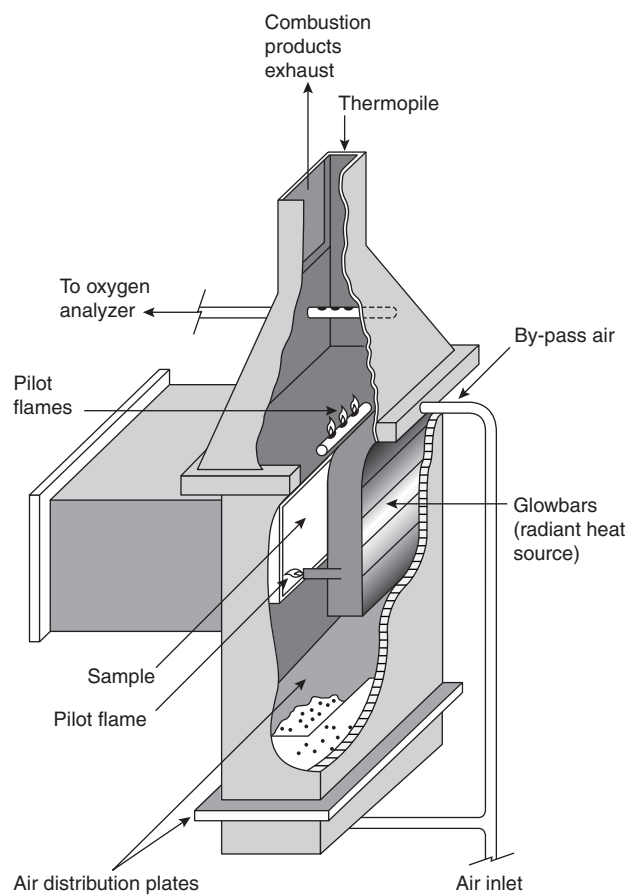


Figure 3-4.1. Ohio State University's (OSU, ASTM E906-83) heat release rate apparatus.⁵⁻⁸

ignition principles suggest that the rate with which heat is transferred depends on the ignition temperature (T_{ig}), ambient temperature (T_a), material thermal conductivity (k), material specific heat (c_p), and the material density (ρ). (See Section 2, Chapter 11.) The combined effects are expressed by a parameter defined as the thermal response parameter (TRP) of the material^{1-4,9-15}

$$\text{TRP} = \Delta T_{ig} \sqrt{kpc_P \left(\frac{\pi}{4} \right)} \quad (1)$$

where ΔT_{ig} ($= T_{ig} - T_a$) is the ignition temperature above ambient (K). The units are as follows: k is in $\text{kW}/\text{m}\cdot\text{K}$, ρ is in g/m^3 , c_p is in $\text{kJ}/\text{g}\cdot\text{K}$, and TRP is in $\text{kW}\cdot\text{s}^{1/2}/\text{m}^2$. TRP is a very useful parameter for the engineering calculations to assess resistance to ignition and fire propagation.

The ignition principles (see Section 2, Chapter 11) suggest that, for thermally thick materials, the inverse of the square root of time to ignition is expected to be a linear function of the external heat flux away from the CHF value:

$$\sqrt{\frac{1}{t_{ig}}} = \frac{(\dot{q}_e'' - \text{CHF})}{\text{TRP}} \quad (2)$$

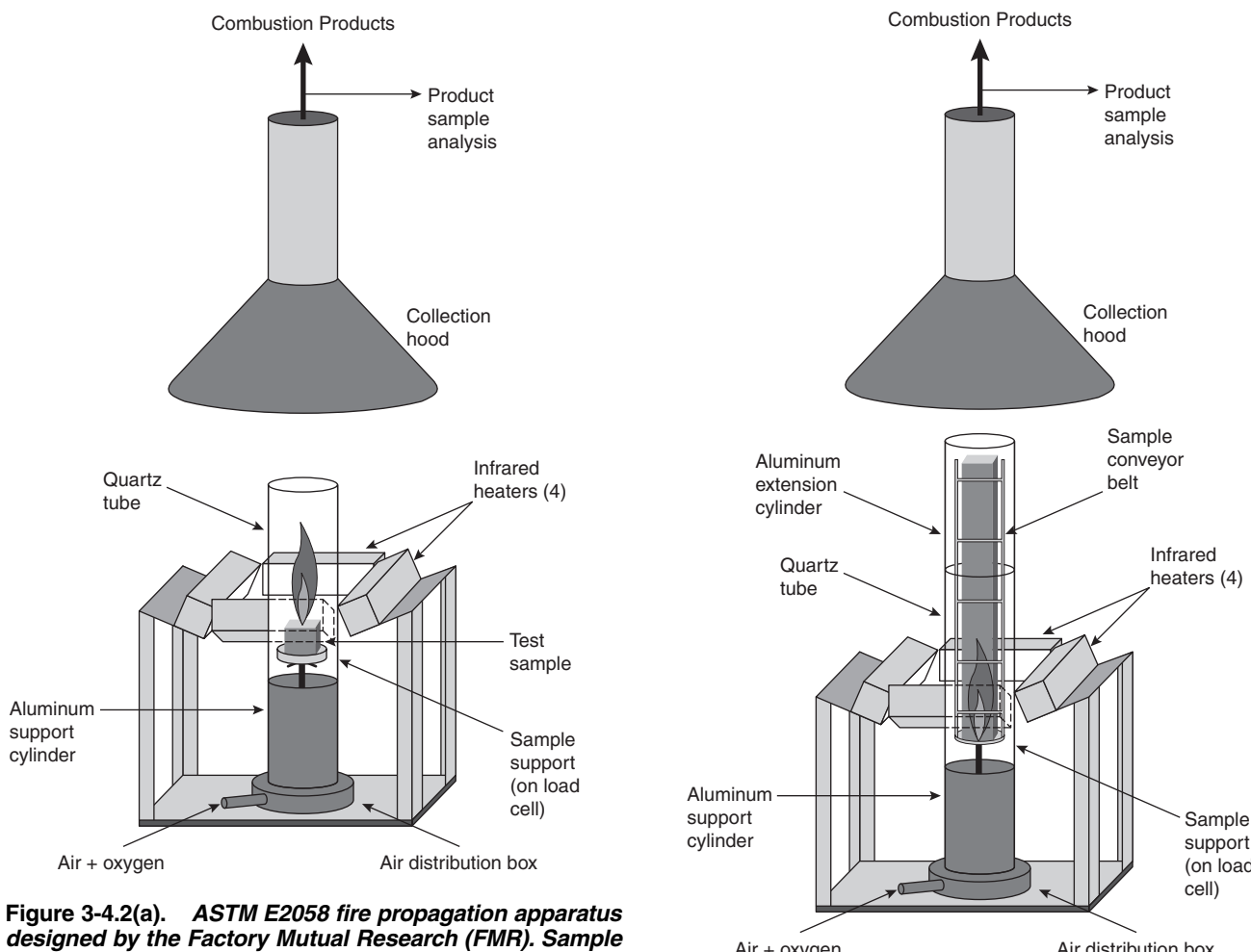


Figure 3-4.2(a). *ASTM E2058 fire propagation apparatus designed by the Factory Mutual Research (FMR). Sample configuration for ignition, pyrolysis, and combustion tests.^{1-4,9-16}*

where t_{ig} is time to ignition (s) and \dot{q}_e'' is the external heat flux (kW/m^2). CHF is in kW/m^2 . Most commonly used materials behave as thermally thick materials and satisfy Equation 2, such as shown by the data in Figure 3-4.4 for polymethylmethacrylate (PMMA); in Figure 3-4.5 for heavy corrugated paper sheets, measured in the ASTM E2058 fire propagation apparatus; and in Figure 3-4.6 for nonblackened samples, measured in the cone calorimeter. The cone calorimeter data are taken from Reference 20.

The value of TRP is determined, for example, in the ASTM E2058 fire propagation apparatus, by (1) measuring the time to ignition for 100×100

The value of TRP for a surface that is not blackened is higher than the value for the blackened surface. For example, for nonblackened and blackened surfaces of polymethylmethacrylate (PMMA), $\text{TRP} = 383$ and 274

Figure 3-4.2(b). *ASTM E2058 fire propagation apparatus designed by the Factory Mutual Research (FMR). Sample configuration for fire propagation tests.^{1-4,9-16} A conveyor belt sample is shown.*

$\text{kW}\cdot\text{s}^{1/2}/\text{m}^2$, respectively, from the ASTM E2058 fire propagation apparatus.² The value for TRP for a blackened surface of PMMA is close to the value calculated from the known T_{ig} , k , ρ , and c_p values for PMMA.²

TRP depends on the chemical as well as the physical properties of materials, such as the chemical structure, fire retardants, and thickness. For example, Figure 3-4.7 shows that TRP increases with sample thickness and increases in the amount of passive fire protection agent used, such as provided by a surface coating to a heavy corrugated paper sheet.

CHF and TRP values for materials derived from the ignition data measured in the ASTM E2058 fire propagation apparatus and the cone calorimeter (as reported in Reference 20) are listed in Table 3-4.2. In the cone calorimeter, the surface was not blackened, and thus the values of TRP may be somewhat higher than expected from the T_{ig} , k , ρ , and c_p values.

Examples of the values of T_{ig} , k , ρ , c_p , and measured and calculated TRP values are listed in Table 3-4.3.

Table 3-4.1 Design Features, Test Conditions, and Types of Measurements for OSU and ASTM E2058 Fire Propagation Apparatuses, and NIST Cone Calorimeter

Design and Test Conditions	OSU ^a	ASTM E2058 Fire Propagation Apparatus ^b	Cone ^c
Inlet gas flow	Co-flow	Co-flow/natural	Natural
Oxygen concentration (%)	21	0 to 60	21
Co-flow gas velocity (m/s)	0.49	0 to 0.146	NA
External heaters	Silicon carbide	Tungsten-quartz	Electrical coils
External heat flux (kW/m ²)	0 to 100	0 to 65	0 to 100
Exhaust product flow (m ³ /s)	0.04	0.035 to 0.364	0.012 to 0.035
Horizontal sample dimensions (mm)	110 × 150	100 × 100	100 × 100
Vertical sample dimensions (mm)	150 × 150	100 × 600	100 × 100
Ignition source	Pilot flame	Pilot flame	Spark plug
Heat release rate capacity (kW)	8	50	8
Measurements			
Time to ignition	Yes	Yes	Yes
Material gasification rate	No	Yes	Yes
Fire propagation rate	No	Yes	No
Generation rates of fire products	Yes	Yes	Yes
Light obscuration by smoke	Yes	Yes	Yes
Optical properties of smoke	No	Yes	No
Electrical properties of smoke	No	Yes	No
Gas-phase corrosion	No	Yes	No
Chemical heat release rate	Yes	Yes	Yes
Convective heat release rate	Yes	Yes	No
Radiative heat release rate	No	Yes	No
Flame extinction			
By water	No	Yes	No
By halon	No	Yes	No
By halon alternates	No	Yes	No

^aAs specified in ASTM E906-83⁷ and by DOT/FAA⁸^bAs specified in ASTM E2058 fire propagation apparatus^cAs specified in ASTM E1354-90¹⁹**EXAMPLE 1:**

In a fire, newspaper and polypropylene are exposed to a heat flux value of 50 kW/m². Estimate which material will ignite first, assuming physical conditions to be very similar for both the materials.

SOLUTION:

From Table 3-4.2, for newspaper and polypropylene, CHF = 10 and 15 kW/m², respectively, and TRP = 108 and 193 kW·s^{1/2}/m², respectively. Substituting these values in Equation 2 with $\dot{q}_e'' = 50 \text{ kW/m}^2$, the times to ignition are calculated to be 6 and 24 sec for newspaper and polypropylene, respectively. Thus, newspaper will ignite first.

EXAMPLE 2:

Halogenated materials are obtained by replacing hydrogen atoms with halogen atoms in the chemical structures of the materials. For example, a unit in polyethylene (PE) consists of C₂H₄. If a hydrogen atom (H) is replaced by a chlorine atom (Cl) in a PE unit, it becomes a unit of rigid polyvinylchloride (PVC), that is, C₂H₃Cl. If two H atoms are replaced by two fluorine atoms (F) in a PE unit, it becomes a unit of Tefzel (ethylene tetrafluoroethylene), that is, C₂H₂F₂. If all the hydrogen atoms are replaced by four F atoms in a PE unit, it becomes a unit of Teflon (polytetrafluoroethylene), that is, C₂F₄. Show how the re-

placement of hydrogen atoms by the halogen atoms affects the ignitability of the materials.

SOLUTION:

From Table 3-4.2, for PE (high density), PVC (rigid), Tefzel, and Teflon, the CHF values are 15, 15, 27, and 38 kW/m², respectively, and the TRP values are 321, 406, 356, and 682 kW·s^{1/2}/m², respectively. In the calculations, it is assumed that these materials are exposed to a uniform heat flux of 60 kW/m² in a fire under very similar physical conditions. From Equation 2, using $\dot{q}_e'' = 60 \text{ kW/m}^2$, the times to ignition for PE (high density), PVC (rigid), Tefzel, and Teflon are calculated to be 40, 64, 91, and 755 sec, respectively. Thus, resistance to ignition increases as the hydrogen atom is replaced by the halogen atom in the chemical structure of PE. The higher the number of hydrogen atoms replaced by the halogen atoms in the structure, the higher the resistance to ignition. When all the hydrogen atoms are replaced by the fluorine atoms, the material becomes highly resistant to ignition.

Fire Propagation

The fundamental surface flame spread principles are described by Quintiere in Section 2, Chapter 12. According to these principles, the fire propagation process, as

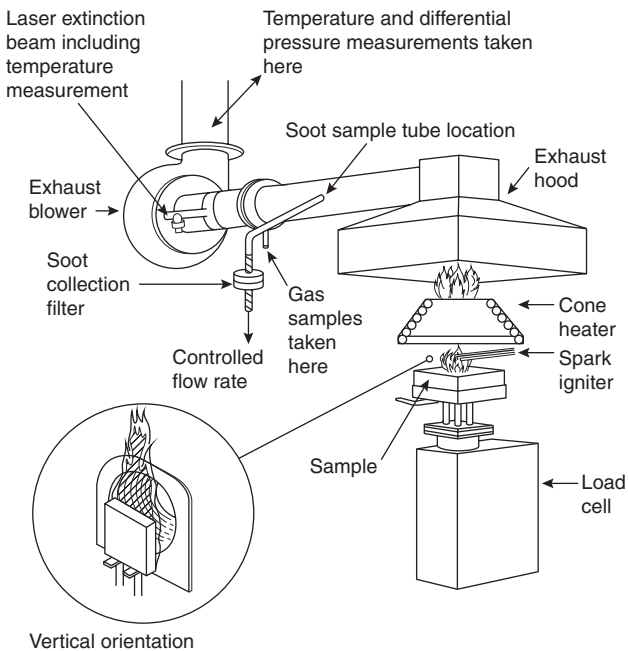


Figure 3-4.3. The cone calorimeter (ASTM E1354-90) designed at the National Institute of Standards and Technology (NIST).¹⁷⁻¹⁹

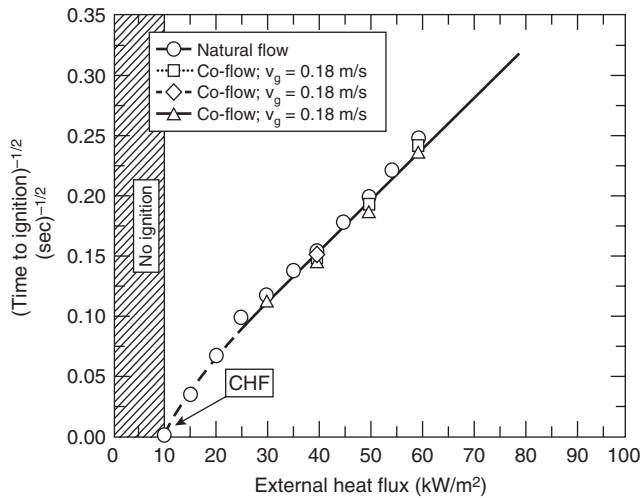


Figure 3-4.4. Square root of the inverse of time to ignition versus external heat flux for $100 \times 100 \times 25\text{-mm-thick}$ polymethylmethacrylate (PMMA) slab with blackened surface. Data measured in the ASTM E2058 fire propagation apparatus and reported in Reference 2 are shown.

indicated by surface flame spread, can be explained as follows.

As a material is exposed to heat flux from internal and/or external heat sources, a combustible mixture is formed that ignites, and a flame anchors itself on the surface in the ignition zone. As the vapors of the material burn in the flame, they release heat with a certain rate, defined

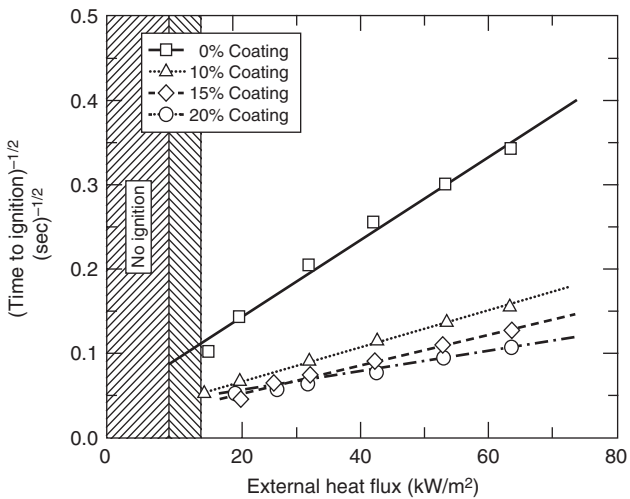


Figure 3-4.5. Square root of the inverse of time to ignition versus external heat flux for two $100 \times 100 \times 11\text{-mm-thick}$ sheets of heavy corrugated paper with blackened surface. Data measured in ASTM E2058 fire propagation apparatus.

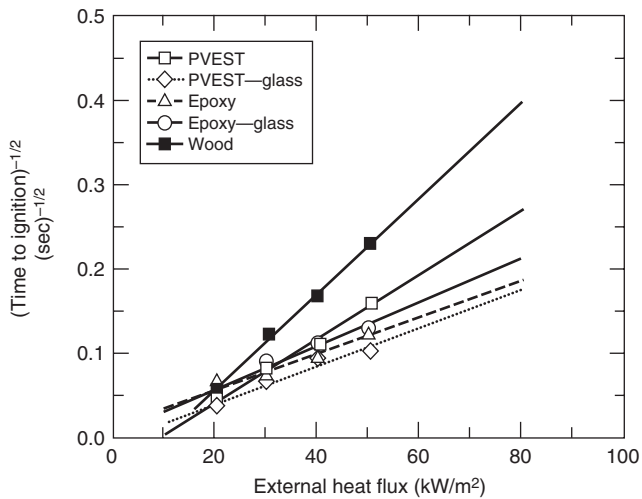


Figure 3-4.6. Square root of the inverse of time to ignition versus external heat flux for $100 \times 100\text{-mm}$ non-blackened surfaces of $10 \times 11\text{-mm-thick}$ polyvinyl ester (PVEST), 11-mm-thick epoxy, and 6-mm-thick wood (hemlock). Data measured in the cone calorimeter as reported in Reference 20 are shown.

as the chemical heat release rate.* Part of the chemical heat release rate is transferred beyond the ignition zone as conductive heat flux through the solid and as convective and radiative heat fluxes from the flame. If the heat flux transferred beyond the ignition zone satisfies CHF, TRP, and gasification requirements of the material, the pyrolysis and

*In earlier papers, it was defined as the actual heat release rate, \dot{Q}_A .

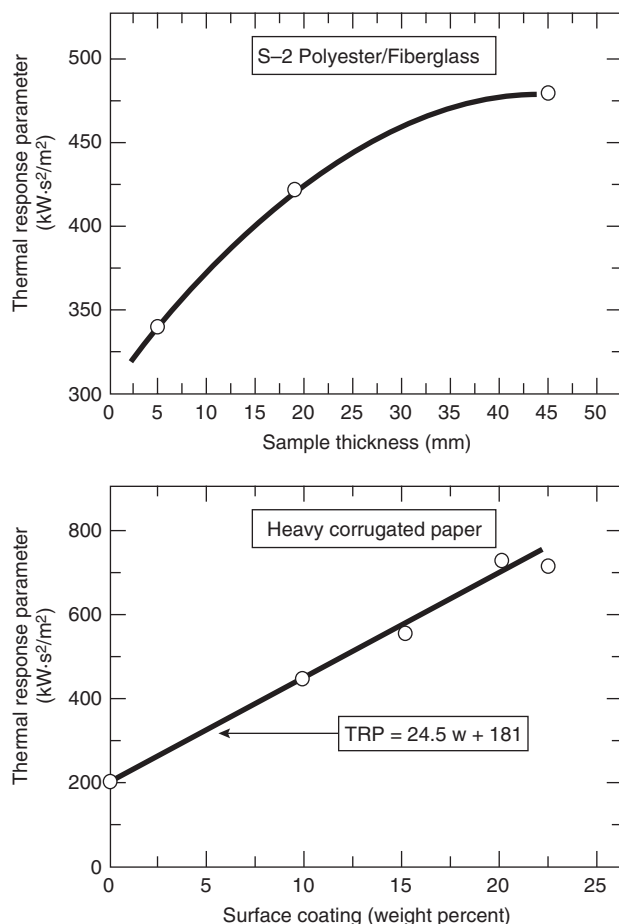


Figure 3-4.7. Thermal response parameter versus thickness for S-2 polyester/fiberglass sample and weight percent of surface coating for the heavy corrugated paper. Data measured in the ASTM E2058 fire propagation apparatus. *w* is weight %.

flame fronts move beyond the ignition zone and the flame anchors itself over additional surface. Due to increase in the burning surface area, flame height, chemical heat release rate, and heat flux transferred ahead of the pyrolysis front all increase. The pyrolysis and flame fronts move again, and the process repeats itself and burning area increases. Fire propagation on the surface continues as long as the heat flux transferred ahead of the pyrolysis front (from the flame or external heat sources) satisfies CHF, TRP, and gasification requirements of the material.

The rate of movement of the pyrolysis front is generally used to define the fire propagation rate:

$$u = \frac{dX_p}{dt} \quad (3)$$

where u is the fire propagation rate (mm/s or m/s), and X_p is the pyrolysis front (mm or m).

The fire propagation rate can be determined in one of the several apparatuses: (1) the LIFT described by Quintiere in Section 2, Chapter 12; (2) the ASTM E2058 fire

Table 3-4.2 Critical Heat Flux and Thermal Response Parameter of Materials

Materials	CHF (kW/m²)	TRP (kW·s¹/²/m²)	ASTM E2058 Fire Propagation Apparatus	ASTM E2058 Fire Propagation Apparatus	ASTM E1354- 90 ^a
	ASTM E2058 Fire Propagation Apparatus	ASTM E2058 Fire Propagation Apparatus			
<i>Natural materials</i>					
Flour	10	218	—	—	—
Sugar	10	255	—	—	—
Tissue paper	10	95	—	—	—
Newspaper	10	108	—	—	—
Wood (red oak)	10	134	—	—	—
Wood (Douglas fir)	10	138	—	—	—
Corrugated paper (light)	10	152	—	—	—
Corrugated paper (heavy)	—	—	—	—	—
No coating	10	189	—	—	—
Coating (10% by weight)	15	435	—	—	—
Coating (15% by weight)	15	526	—	—	—
Coating (20% by weight)	15	714	—	—	—
Wood (hemlock)	—	—	175	—	—
Wool 100%	—	—	—	252	—
Wood (Douglas fir/fire retardant, FR)	10	251	—	—	—
<i>Synthetic materials</i>					
Epoxy resin	—	—	457	—	—
Polystyrene (PS)	13	162	—	—	—
Acrylic fiber 100%	—	—	180	—	—
Polypropylene (PP)	15	193	—	291	—
PP/FR panel	15	315	—	—	—
Styrene-butadiene (SB)	10	198	—	—	—
Crosslinked polyethylenes (XLPE)	15	224–301	—	—	—
Polyvinyl ester	—	—	263	—	—
Polyoxymethylene	13	269	—	—	—
Nylon	15	270	—	—	—
Polyamide-6	—	—	379	—	—
Polymethylmethacrylate (PMMA)	11	274	—	—	—
Isophthalic polyester	—	—	296	—	—
Acrylonitrile-butadiene-styrene (ABS)	—	—	317	—	—
Polyethylene (high density) (PE)	15	321	—	364	—
PE/nonhalogenated fire retardants	15	652–705	—	—	—
Polyvinyl ester panels	13–15	440–700	—	—	—
Modified acrylic (FR)	—	—	526	—	—
Polycarbonate	15	331	—	—	—
Polycarbonate panel	16	420	—	—	—
<i>Halogenated materials</i>					
Isoprene	10	174	—	—	—
Polyvinylchloride (PVC)	10	194	—	—	—
Plasticized PVC, LOI = 0.20	—	—	285	—	—
Plasticized PVC, LOI = 0.25	—	—	401	—	—
Plasticized PVC, LOI = 0.30	—	—	397	—	—
Plasticized PVC, LOI = 0.35	—	—	345	—	—
Rigid PVC, LOI = 0.50	—	—	388	—	—
Rigid PVC1	15	406	—	—	—
Rigid PVC2	15	418	—	—	—
PVC panel	17	321	—	—	—

^aCalculated from the ignition data reported in Reference 20.

(continued)

Table 3-4.2 Critical Heat Flux and Thermal Response Parameter of Materials (Continued)

Materials	CHF (kW/m ²)	TRP (kW·s ^{1/2} /m ²)			Materials	CHF (kW/m ²)	TRP (kW·s ^{1/2} /m ²)		
	ASTM E2058 Fire Propagation Apparatus	ASTM E2058 Fire Propagation Apparatus	ASTM E1354- 90 ^a	ASTM E2058 Fire Propagation Apparatus		ASTM E2058 Fire Propagation Apparatus	ASTM E2058 Fire Propagation Apparatus	ASTM E1354- 90 ^a	
<i>Halogenated materials (cont.)</i>									
PVC fabric	26	217	—		<i>Foams (wall-ceiling insulation materials, etc.)</i>				
PVC sheets	15	446–590	—		Polyurethane foams	13–40	55–221	—	
Ethylene tetrafluoroethylene (ETFE), Tefzel	27	356	—		Polystyrene foams	10–15	111–317	—	
Fluorinated ethylene-propylene (FEP), Teflon	38	682	—		Phenolic	20	610	—	
Teflon fabric	50	299	—		Phenolic laminate—45% glass	—	—	683	
Teflon coated on metal	20	488	—		Latex foams	16	113–172	—	
<i>Composite and fiberglass-reinforced materials</i>									
Polyether ether keton—30% fiberglass	—	—	301		<i>Materials with fiberweb, net-like and multiplex structures</i>				
Isophthalic polyester—77% fiberglass	—	—	426		Polypropylenes	8–15	108–417	—	
Polyethersulfone—30% fiberglass	—	—	256		Polyester-polypropylene	10	139	—	
Polyester 1—fiberglass	—	—	430		Wood pulp-polypropylene	8	90	—	
Polyester 2—fiberglass	10	275	—		Polyester	8–18	94–383	—	
Polyester 3—fiberglass	10	382	—		Rayon	14–17	161–227	—	
Polyester 4—fiberglass	15	406	—		Polyester-rayon	13–17	119–286	—	
Polyester 5—fiberglass	10	338	—		Wool-nylon	15	293	—	
Epoxy Kevlar (thin sheet)	—	—	120		Nylon	15	264	—	
Epoxy fiberglass (thin sheet)	10	156	198		Cellulose	13	159	—	
Epoxy graphite	15	395	—		Cellulose-polyester	13–16	149–217	—	
Epoxy 1—fiberglass	10	420	—		<i>Electrical cables—power</i>				
Epoxy 2—fiberglass	15	540	—		PVC/PVC	13–25	156–341	—	
Epoxy 3—fiberglass	15	500	—		PE/PVC	15	221–244	—	
Epoxy 4—fiberglass	10	388	—		PVC/PE	15	263	—	
Epoxy resin—69% fiberglass	—	—	688		Silicone/PVC	19	212	—	
Epoxy-graphite 1	—	481	—		Silicone/cross linked polyolefin (XLPO)	25–30	435–457	—	
Epoxy-graphite 1/ceramic coating (CC)	—	2273	—		EPR (ethylene-propylene rubber/EPR)	20–23	467–567	—	
Epoxy-graphite 1/intumescant coating (IC)	—	962	—		XLPE/XLPE	20–25	273–386	—	
Epoxy-graphite 1/IC-CC	—	1786	—		XLPE/EVA (ethyl-vinyl acetate)	12–22	442–503	—	
Polyvinyl ester 1—69% fiberglass	—	—	444		XLPE/Neoprene	15	291	—	
Polyvinyl ester 2—fiberglass	—	281	—		XLPO/XLPO	16–25	461–535	—	
Polyvinyl ester 2—fiberglass//CC	—	676	—		XLPO, PVF (polyvinylidene fluoride) XLPO	14–17	413–639	—	
Polyvinyl ester 2—fiberglass/IC	—	1471	—		EPR/Chlorosulfonated PE	14–19	283–416	—	
Polyvinyl ester 2—fiberglass/IC-CC	—	1923	—		EPR, FR	14–28	289–448	—	
Graphite composite	40	400	—		<i>Electrical cables—communications</i>				
Phenolic fiberglass (thin sheet)	33	105	172		PVC/PVC	15	131	—	
Phenolic fiberglass (thick sheet)	20	610	—		PE/PVC	20	183	—	
Phenolic-graphite 1	20	333	—		XLPE/XLPO	20	461–535	—	
Phenolic-graphite 2	—	—	400		Si/XLPO	20	457	—	
Phenolic kevlar (thin sheet)	20	185	258		EPR-FR	19	295	—	
Phenolic kevlar (thick sheet)	15	403	—		Chlorinated PE	12	217	—	
Phenolic-graphite 1/CC	—	807	—		ETFE/EVA	22	454	—	
Phenolic-graphite 1/IC	—	1563	—		PVC/PVF	30	264	—	
					FEP/FEP	36	638–652	—	

^aCalculated from the ignition data reported in Reference 20.

Table 3-4.3 Thermal Properties and Thermal Response Parameter Values of Polymers^a

Polymers	T_g (°C)	$\rho \times 10^{-3}$ (g/m ³)	c_p (kJ/Kg-K)	$k \times 10^{-3}$ (kW/m·K)	TRP Exp	TRP Cal
Polyethylene	443	0.94	2.15	0.42	454	345
Polypropylene-1	443	0.93	2.20	0.20	288	240
Polypropylene-2	443	0.90	2.20	0.20	323	237
Polypropylene-3	443	1.06	2.08	0.20	277	208
Polypropylene-4	443	NM	NM	0.20	310	NM
Polypropylene-5	443	1.04	1.93	0.20	333	238
Polycarbonate-1	497	1.18	1.51	0.20	357	252
Polycarbonate-2	497	1.19	2.06	0.20	434	296
Polycarbonate-3	580	1.20	1.20	0.21	455	273
Polyvinylchloride-1	357	1.20	1.37	0.21	263	176
Polyvinylchloride-2	374	1.95	1.14	0.21	215	214
Nylon 6	497	0.12	2.19	0.24	154	106
Polyethyleneterephthalate	374	0.66	1.32	0.15	174	113
Polymethylmethacrylate	378	1.19	2.09	0.27	274	259
Teflon, PTFE	700	2.18	1.01	0.25	654	444
Teflon, FEP	700	2.15	1.20	0.25	680	484
Tefzel, ETFE	540	1.70	0.90	0.23	481	273
Kel-F, PCTFE	580	2.11	0.90	0.22	460	321
Halar, ECTFE	613	1.69	1.01	0.15	450	265
Polysulfone	580	1.24	1.30	0.28	469	333
Polyetheretherketone	580	1.32	1.82	0.25	550	382

^aData taken from Reference 21.

propagation apparatus (50- and 500-kW scales)—the 50-kW scale apparatus is shown in Figure 3-4.2(b); and (3) the fire products collector (10,000-kW scale ASTM E2058 fire propagation apparatus) shown in Figure 3-4.8. Examples of the type of data obtained from the ASTM E2058 fire propagation apparatus are shown in Figures 3-4.9 through 3-4.12. In Figure 3-4.12, heat release rates increase linearly with time during downward fire propagation, very similar to the pyrolysis front values for the downward fire propagation in Figure 3-4.9.

The slopes of the lines in Figures 3-4.9 through 3-4.12 represent fire propagation rates. The upward fire propagation rate is much faster than the downward fire propagation rate. For downward fire propagation, linear increases in the pyrolysis front and heat release rates indicate decelerating fire propagation behavior. For upward fire propagation, nonlinear increases in the pyrolysis front indicate accelerating fire propagation behavior.

Relationship between fire propagation rate, flame height, pyrolysis front, and heat release rate: Numerous researchers have found the following relationship between the flame height and pyrolysis front (as discussed by Quintiere in Section 2, Chapter 12 and reviewed in References 2 and 22)

$$X_f = a X_p^n \quad (4)$$

where

X_f = flame height (m)

$a = 5.35$

$n = 0.67$ to 0.80

for steady wall fires.² X_p is in m.

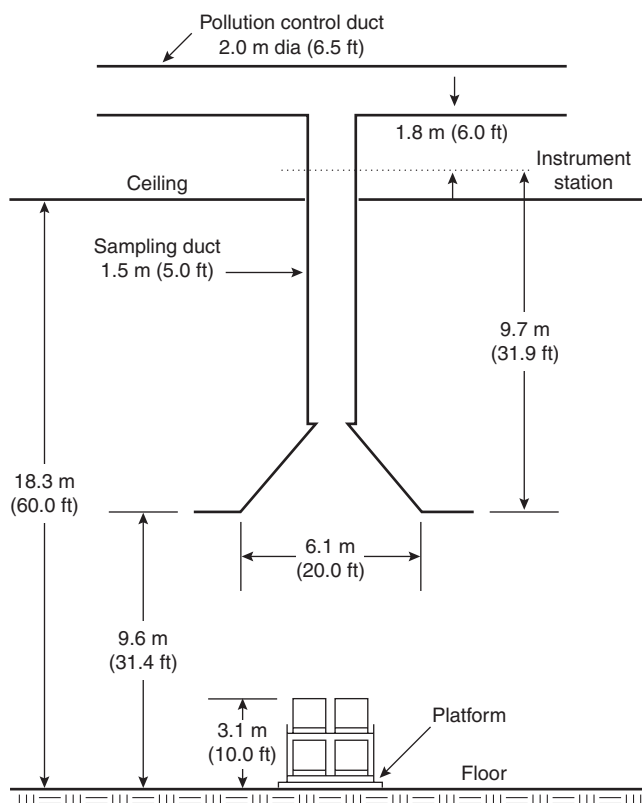


Figure 3-4.8. The fire products collector (10,000-kW scale ASTM E2058 fire propagation apparatus) for large-scale combustion and fire propagation tests. Corrugated boxes with various products, arranged in two-pallet loads × two-pallet loads × two-pallet loads high are shown. The fire products collector is designed by the Factory Mutual Research Corporation.

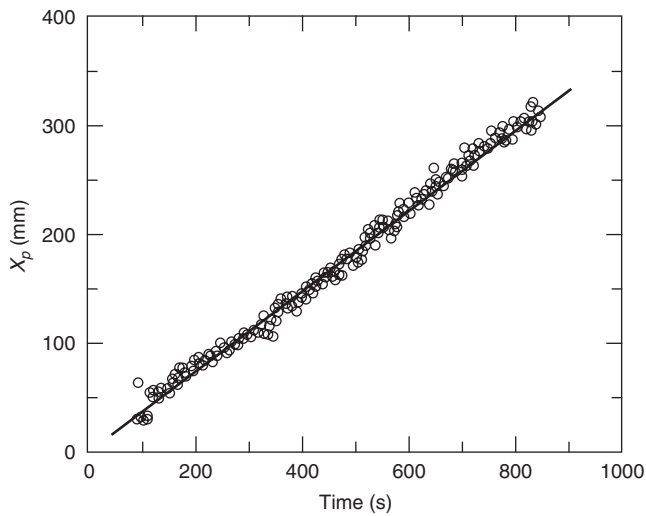


Figure 3-4.9. Pyrolysis front versus time for the downward fire propagation for 300-mm-long, 100-mm-wide, and 25-mm-thick PMMA vertical slab under opposed airflow condition in the ASTM E2058 fire propagation apparatus. Airflow velocity = 0.09 m/s. Oxygen mass fraction = 0.334. (Figure is taken from Reference 2.)

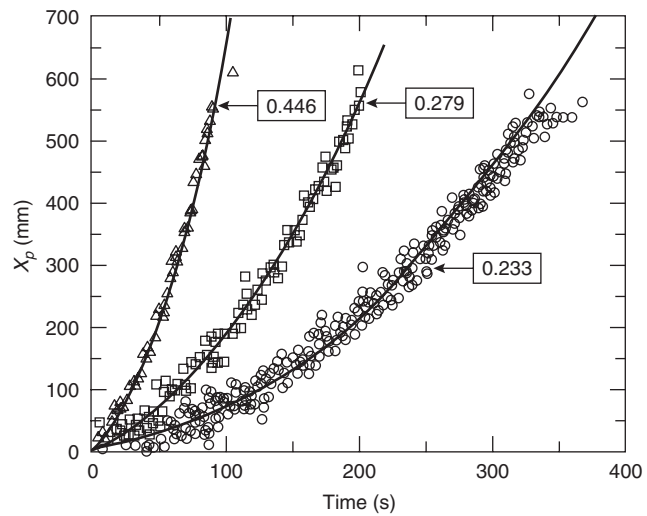


Figure 3-4.11. Pyrolysis front versus time for the upward fire propagation for 600-mm-long and 25-mm-thick diameter PMMA cylinder under co-airflow condition in the ASTM E2058 fire propagation apparatus. Airflow velocity = 0.09 m/s. Numbers inside the frames are the mass fractions of oxygen in air. (Figure is taken from Reference 2.)

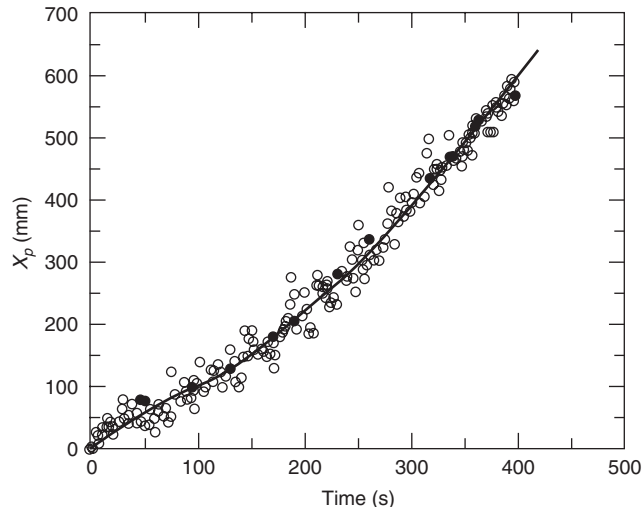


Figure 3-4.10. Pyrolysis front versus time for the upward fire propagation for 600-mm-long, 100-mm-wide, and 25-mm-thick PMMA vertical slab under co-airflow condition in the ASTM E2058 fire propagation apparatus. Airflow velocity = 0.09 m/s. Oxygen mass fraction = 0.233. (Figure is taken from Reference 2.)

Fire propagation data for PMMA from the ASTM E2058 fire propagation apparatus² and for electrical cables from several standard tests for cables (IECA, CSA FT-4, and UL-1581)⁹ satisfy Equation 4, as shown in Figure 3-4.13, with $a = 5.32$ and $n = 0.78$. The visual measurement of the pyrolysis front as damage length is used for the acceptance criterion in many of the standard tests for electrical cables. For example, for upward fire propagation

in the CSA FT-4, damage length less than 60 percent of the total length of the cable tray for 20-min exposure time is used as the acceptance criterion.⁹ For horizontal fire propagation in the UL-1581 test, flame length of less than 40 percent of the total length of the cable tray is used as the acceptance criterion.⁹

The relationship between the flame height and the chemical heat release rate, expressed as the normalized chemical heat release rate (NCHRR) is defined as

$$\text{NCHRR} = \frac{\dot{Q}'_{ch}}{\rho c_p T_a g^{1/2} X_p^{3/2}} \quad (5)$$

where

\dot{Q}'_{ch} = chemical heat release rate per unit width (kW/m)

ρ = density of air (g/m³)

c_p = specific heat of air (kJ/g·K)

T_a = ambient temperature (K)

g = acceleration due to gravity (m²/s)

X_p is in m.

Many researchers have shown that the ratio of the flame height to pyrolysis front is a function of the heat release rate, such as the following relationship (as discussed by Quintiere in Section 2, Chapter 12 and reviewed in References 2 and 22)

$$\frac{X_f}{X_p} = a [\text{NCHRR}]^n \quad (6)$$

where a and n are constants. This relationship reported in the literature (as reviewed in Reference 2) for methane, ethane, and propylene is shown in Figure 3-4.14. The data

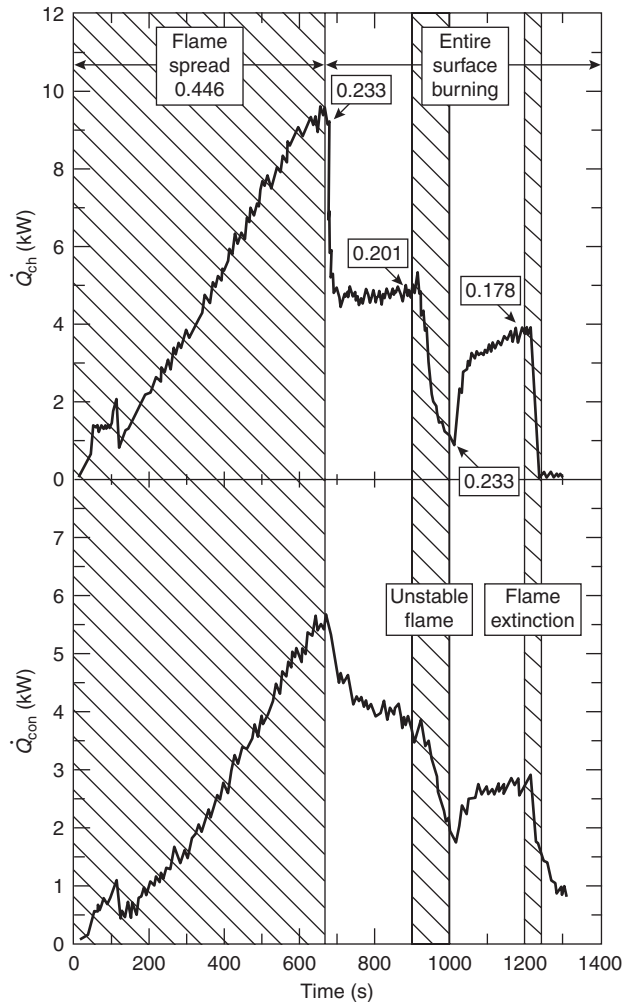


Figure 3-4.12. Chemical and convective heat release rate versus time for the downward fire propagation, combustion, and flame extinction for 300-mm-long, 100-mm-wide, and 25-mm-thick PMMA vertical slab under opposed airflow condition in the ASTM E2058 fire propagation apparatus. Airflow velocity = 0.09 m/s. Numbers inside the frames are the mass fractions of oxygen in air. (Figure is taken from Reference 2.)

for the upward fire propagation for PMMA from the ASTM E2058 fire propagation apparatus² and for the electrical cables from the several standard tests for cables (UL-1581, ICEA, and CSA FT-4) also satisfy this relationship as indicated in Figure 3-4.14.⁹

In Figure 3-4.14, data in the lower left-hand corner are for the low-intensity polyvinylchloride (PVC) electrical cable fire propagation in the standard tests for cables. These data show that for $NCHRR < 0.2$, $X_f/X_p < 1.5$ and $n = 1/10$. This is a characteristic property of materials for which there is either no fire propagation or a limited fire propagation beyond the ignition zone. These materials are defined as Group 1 materials.^{4,9-15} Cables with Group 1 material characteristics pass the standard tests for cables (UL-910, CSA FT-4, UL-1581, and ICEA). The data for higher intensity fire propagation in Figure 3-4.14 show that

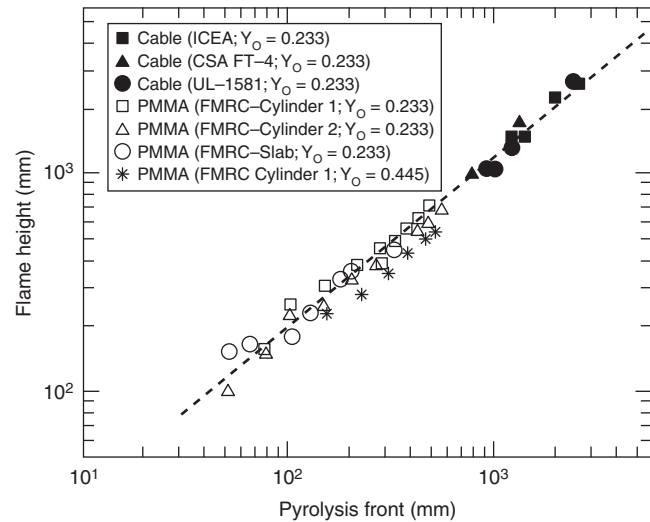


Figure 3-4.13. Flame height versus pyrolysis front for the upward fire propagation in normal air. Data are for the vertical fire propagation for electrical cables contained in 2.44-m-long, 310-mm-wide, and 76-mm-deep trays in standard tests for electrical cables (ICEA, CSA FT-4, and UL-1581) and for 600-mm long PMMA slabs (100-mm-wide and 25-mm-thick) and cylinder (25-mm diameter) in the ASTM E2058 fire propagation apparatus. Data for fire propagation in an oxygen mass fraction of 0.445 are also included. (Figure is taken from References 2 and 9.)

(1) for $0.2 > NCHRR < 5$, $n = 2/3$ and $1.5 > X_f/X_p < 20$ (PMMA fire propagation and methane combustion); and (2) for $NCHRR > 5$, $n = 1/2$ and $X_f/X_p > 20$ (ethane and propylene combustion). Thus, the ratio of the flame height to pyrolysis front is a good indicator of the fire propagation characteristics of the materials. Materials for which flame height is close to the pyrolysis front during fire propagation can be useful indicators of decelerating fire propagation behavior.

Researchers have also developed many correlations between the flame heat flux transferred ahead of the pyrolysis front and heat release rate for downward, upward, and horizontal fire propagation (as discussed by Quintiere in Section 2, Chapter 12 and reviewed in References 2 and 22). For example, small- and large-scale fire propagation test data from the ASTM E2058 fire propagation apparatus [Figure 3-4.2(b)] and fire products collector (Figure 3-4.8) suggest that, for thermally thick materials with highly radiating flames, the following semi-empirical relationship is satisfied:³

$$\dot{q}_f'' \propto \left(\frac{\chi_{\text{rad}}}{\chi_{\text{ch}}} \dot{Q}'_{\text{ch}} \right)^{1/3} \quad (7)$$

where \dot{q}_f'' is the flame heat flux transferred ahead of the pyrolysis front (kW/m^2) and χ_{rad} is the radiative fraction of the combustion efficiency, χ_{ch} . The fire propagation rate is expressed as³

$$\sqrt{u} \propto \frac{[(\chi_{\text{rad}}/\chi_{\text{ch}})(\dot{Q}'_{\text{ch}})]^{1/3}}{\text{TRP}} \quad (8)$$

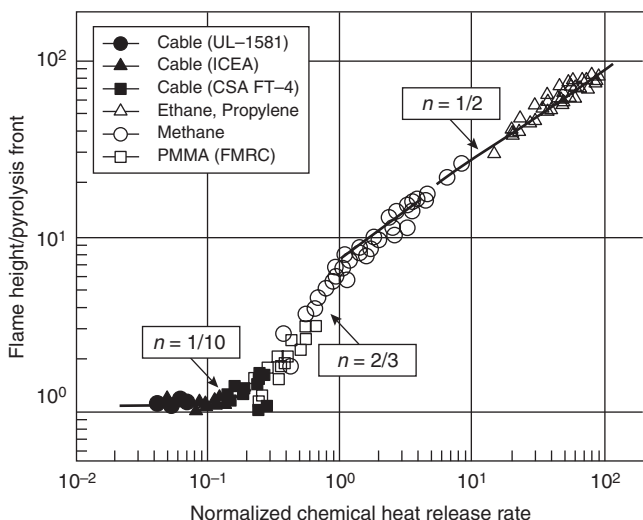


Figure 3-4.14. Ratio of flame height to pyrolysis front versus the normalized chemical heat release rate for the upward fire propagation in normal air. Data for the diffusion flames of methane, ethane, and propylene are from the literature. Data for the cables are from the standard tests for electrical cables (ICEA, CSA FT-4, and UL-1581).⁹ Data for PMMA are from the ASTM E2058 fire propagation apparatus for 600-mm-long vertical PMMA slabs (100-mm-wide, 25-mm-thick) and cylinders (25-mm-diameter).² (Figure is taken from Reference 9.)

In a simplified form of Equation 8, the right-hand side of Equation 8 multiplied by 1000 is defined as the fire propagation index (FPI):^{4,9-15}

$$\text{FPI} = \frac{1000(0.42\dot{Q}'_{ch})^{1/3}}{\text{TRP}} = \frac{750(\dot{Q}'_{ch})^{1/3}}{\text{TRP}} \quad (9)$$

FPI describes the fire propagation behavior of materials under highly flame-radiating conditions prevalent in large-scale fires. The small- and large-scale fire propagation test data and understanding of the fire propagation suggest that the FPI values can be used to classify the materials into four groups:^{2-4,9-15}

1. $\text{FPI} < 7$ (Nonpropagating) Group N-1 Materials—Materials for which there is no fire propagation beyond the ignition zone. Flame is at critical extinction condition.
2. $7 < \text{FPI} < 10$ (Decelerating Propagation): Group D-1 Materials—Materials for which fire propagates beyond the ignition zone although in a decelerating fashion. Fire propagation beyond the ignition zone is limited.
3. $10 < \text{FPI} < 20$ (Nonaccelerating Propagation): Group 2 Materials—Materials for which fire propagates slowly beyond the ignition zone.
4. $\text{FPI} > 20$ (Accelerating Propagation): Group 3 Materials—Materials for which fire propagates rapidly beyond the ignition zone.

The FPI values for the upward fire propagation, under highly flame-radiating conditions, have been determined for numerous materials in the ASTM E2058 fire

propagation apparatus. The highly radiating conditions are created by using a value of 0.40 for the mass fraction of oxygen. Two sets of tests are performed:

1. *Thermal response parameter test.* Ignition tests are performed in the ASTM E2058 fire propagation apparatus [Figure 3-4.2(a)], and TRP value is determined from the time to ignition versus external heat flux as described in the subsection on fire initiation (ignition).
2. *Upward fire propagation test.* Fire propagation tests for vertical slabs, sheets, or cables are performed in the ASTM E2058 fire propagation apparatus [50- and 500-kW scale, Figure 3-4.2(b)]. About 300- to 600-mm-long, up to about 100-mm-wide, and up to about 100-mm-thick samples are used. The bottom 120 to 200 mm of the sample is in the ignition zone, where it is exposed to 50 kW/m² of external heat flux in the presence of a pilot flame. Beyond the ignition zone, fire propagates by itself, under co-airflow condition with an oxygen mass fraction of 0.40. During upward fire propagation, measurement is made for the chemical heat release rate as a function of time in each test.

TRP value and the chemical heat release rate are used in Equation 9 to calculate the FPI as a function of time. The FPI profile is used to classify materials into Group 1, 2, or 3.

Application of the Fire Propagation Index (FPI) to classify materials:

Electrical cables. The FMRC standard for cable fire propagation Class No. 3972¹⁴ is used to classify electrical cables, based on their upward fire propagation behavior, under highly flame-radiating conditions (oxygen mass fraction = 0.40), for protection needs in noncombustible occupancies. A noncombustible occupancy is defined as an occupancy where only specific types of combustibles are present, ignition sources are relatively small, and their contributions toward thermal and nonthermal hazards are negligible compared to the contributions of the combustibles. TRP and upward fire propagation tests are performed, and Equation 9 is used to calculate the FPI, as described above. Figure 3-4.15 shows an example of a typical profile for the FPI versus time for a polyethylene (PE)/polyvinylchloride (PVC) cable. This cable does not pass any of the standard electrical cable tray fire tests, and the FPI profile in Figure 3-4.15 shows that it is a Group 3 cable.

The following fire protection guidelines are recommended by FMRC for grouped cables:^{11,13,14}

1. Group 1 cables do not need additional fire protection in noncombustible occupancies with noncombustible construction.
2. Group 2 cables can be used without additional fire protection in noncombustible occupancies with noncombustible construction under certain conditions.
3. Group 3 cables need fire protection.

Table 3-4.4 lists FPI values for selected electrical cables, composites, and conveyor belts.

EXAMPLE 3:

What type of fire behavior is represented by a 300-mm-wide, 8-m-high, and 25-mm-thick vertical sheet of a

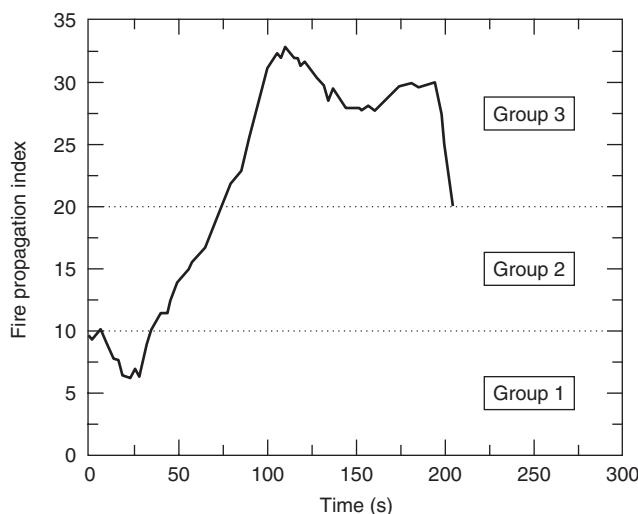


Figure 3-4.15. Fire Propagation Index versus time for a polyethylene (PE)/polyvinylchloride (PVC) Group 3 cable determined in the ASTM E2058 fire propagation apparatus. This cable does not pass any standard tests for electrical cables.

material with a TRP value of $95 \text{ kW}\cdot\text{s}^{1/2}/\text{m}^2$ if the peak chemical heat release during the upward fire propagation is 50 kW ?

SOLUTION:

Fire propagation behavior is assessed by the FPI value. For the material, the chemical heat release rate per unit width, $\dot{Q}'_{ch} = 50/0.3 = 167 \text{ kW/m}$. Substituting this value in Equation 9, with $\text{TRP} = 95 \text{ kW}\cdot\text{s}^{1/2}/\text{m}^2$, $\text{FPI} = 43$. The TRP value is greater than 20, and thus the material is a Group 3 material and represents an accelerating fire propagation behavior.

EXAMPLE 4:

A noncombustible cable spreading room has an old and a new area with a 3-hr-rated solid fire wall between the two. The old area is filled with several trays of polyethylene (PE)/polyvinylchloride (PVC) communications cables, and the new area is filled with several trays of crosslinked polyolefin (XLPO/XLPO) communications cables. In order to determine the fixed fire protection needs for these two areas, cable samples were submitted to a testing laboratory. The laboratory reported the following test data:

1. Ignition data.

	Heat flux (kW/m^2)	30	40	50	60	100
Time to ignition (s)						
PE/PVC	76	27	14	8	2	
XLPO/XLPO	—	716	318	179	45	

2. Peak chemical heat release rate.

During vertical fire propagation for 0.60-m-long cable sample in a highly radiating environment (oxygen mass fraction = 0.40), the following data were measured:

Cable	Peak chemical heat release rate per unit cable circumference (kW/m^2)
PE/PVC	100
XLPO/XLPO	20

The data were used to calculate the FPI values, which suggested that the area with PE/PVC cable trays needed fixed fire protection, whereas the area with XLPO/XLPO cable trays did not need fixed fire protection. Do you agree?

SOLUTION:

The TRP values from the linear regression analysis of the ignition data are 131 and $535 \text{ kW}\cdot\text{s}^{1/2}/\text{m}^2$ for the PE/PVC and the XLPO/XLPO cable samples, respectively. The data for \dot{Q}'_{ch} are given. Thus, from Equation 9, the FPI values for the PE/PVC and the XLPO/XLPO cable samples are 29 and 4 , respectively. The FPI values suggest that the PE/PVC cable is a Group 3 cable and is expected to have an accelerating fire propagation behavior, and the

Table 3-4.4 Fire Propagation Index for Cables, Composites, and Conveyor Belts, Determined in the ASTM E2058 Fire Propagation Apparatus

	Diameter/ Thickness (mm)	FPI	Group	Fire Propagation ^a
Power cables				
PVC/PVC	4–13	11–28	2–3	P
PE/PVC	11	16–23	3	P
PVC/PE	34	13	2	P
Silicone/PVC	16	17	2	P
Silicone/XLPO	55	6–8	1	N-D
EP/EP	10–25	6–8	1	N-D
XLPE/XLPE	10–12	9–17	1–2	D-P
XLPE/EVA	12–22	8–9	1	D
XLPE/Neoprene	15	9	1	D
XLPO/XLPO	16–25	8–9	1	D
XLPO, PVF/XLPO	14–17	6–8	1	N-D
EP/CLP	4–19	8–13	1–2	D-P
EP, FR/None	4–28	9	1	D
Communications cables				
PVC/PVC	4	36	3	P
PE/PVC	4	28	3	P
PXLPE/XLPO	22–23	6–9	1	N-D
Si/XLPO	28	8	1	D
EP-FR/none	28	12	2	P
PECI/none	15	18	2	P
ETFE/EVA	10	8	1	D
PVC/PVF	5	7	1	N
FEP/FEP	8	4	1	N
FEP/FEP	10	5	1	N
Conveyor belts^b				
Styrene-butadiene rubber (SBR)	8–11	1–2	D-P	
Chloroprene rubber (CR)	5	1	P	
CR/SBR	8	1	D	
PVC	4–10	1–2	N-P	

^aP: propagation; D: decelerating propagation; N: no propagation.

^b3 to 25 mm thick.

XLPO/XLPO is a Group 1 cable and fire propagation is expected to be either limited to the ignition zone or decelerating. These calculations support that the cable spreading room area filled with the PE/PVC cable trays would need fixed fire protection, whereas it would not be needed for the area filled with the XLPO/XLPO cable trays.

Conveyor belts. A conveyor belt standard is being developed at the Factory Mutual Research Corporation (FMRC) following the FMRC standard for cable fire propagation Class No. 3972.¹⁴ TRP and upward fire propagation tests are performed, and Equation 9 is used to calculate the FPI as described above.

Conveyor belts are classified as propagating or non-propagating. For an approximately 600-mm-long and 100-mm-wide vertical conveyor belt, the data measured in the ASTM E2058 fire propagation apparatus under highly flame-radiating conditions show that the nonpropagating fire condition is satisfied for $FPI \leq 7.0$ for the belts that show limited fire propagation in the large-scale fire propagation test gallery of the U.S. Bureau of Mines.^{12,23}

Table 3-4.4 lists FPI values for selected conveyor belts taken from References 12 and 23.

EXAMPLE 5:

Conveyor belts are made of solid woven or piles of elastomers, such as styrene-butadiene rubber (SBR), polychloroprene rubber (CR), polyvinylchloride (PVC), reinforced with fibers made of polymers, such as nylon. In large-scale fire propagation tests in a tunnel, fire on the surface of a CR-based conveyor belt was found to be non-propagating, whereas for a CR/SBR-based conveyor belt fire was found to be propagating. Small-scale tests showed that the CR- and CR/SBR-based conveyor belts had the following fire properties, respectively: (1) CHF = 20 and 15 kW/m², (2) TRP = 760 and 400 kW·s^{1/2}/m², and (3) peak \dot{Q}'_{ch} = 114 and 73 kW/m under highly flame-radiating conditions (oxygen mass fraction = 0.40). Show that small-scale test results are consistent with the large-scale fire propagation behaviors of the two conveyor belts, using the criterion that, for nonpropagating fire behavior, the FPI is equal to or less than 7.

SOLUTION:

Substituting the TRP and \dot{Q}'_{ch} values in Equation 9, the FPI values for the CR- and CR/SBR-based conveyor belts are 5 and 8, respectively. Thus, the CR-based conveyor belt is expected to have a nonpropagating fire behavior, whereas the CR/SBR-based conveyor belt is expected to have a propagating fire behavior. The small-scale test results, therefore, are consistent with the large-scale fire propagation behaviors of the two conveyor belts.

Polymeric materials for clean rooms. The microchip devices are manufactured, many at a time, on disks of semiconducting materials called wafers.²⁴ Wafers are manufactured in several stages: material preparation, crystal growth and wafer preparation, wafer fabrication, and packaging. The area where wafer fabrication takes place is called a *clean room*. The cleanliness of the room is highly controlled in order to limit the number of contaminants to which the wafer is exposed. The stringent requirements of the solid-state devices define levels of cleanliness that far

exceeds those of almost any other industry. Contamination in a clean room is defined as anything that interferes with the production of wafers and/or their performance. The overall clean room design principle is to build a sealed room that is supplied with clean air, is built with polymeric materials that are noncontaminating, and includes systems to prevent accidental contamination from outside, from the interactions of the polymeric materials and the wafer cleaning liquids, from operators, and from accidental fires.

In 1997, Factory Mutual Research introduced a new methodology, identified as the 4910 Test Protocol,²⁵ for testing the fire propagation and smoke development behaviors of polymeric materials for use in clean rooms for the semiconductor industry. For the acceptance of polymeric materials, two criteria need to be satisfied: (1) Fire Propagation Index (FPI) ≤ 6 (m/s^{1/2})/(kW/m)^{2/3} and (2) Smoke Development Index (SDI) ≤ 0.4 (g/g) (m/s^{1/2})/(kW/m)^{2/3}.

In the 4910 Test Protocol,²⁵ Fire Propagation Index (FPI) is formulated from (1) the thermal response parameter (TRP), which relates the time to ignition to the net heat flux, and (2) the chemical heat release rate measured during the upward fire propagation in air having a 40 percent oxygen concentration to simulate flame heat transfer at large scale. SDI is related to the smoke release rate and is obtained by multiplying the FPI value by the smoke yield as shown in Figure 3-4.16. The smoke yield is defined as the ratio of the total mass of smoke released per unit mass of the vapors from the polymeric material burned.

The FPI and SDI values for various polymeric materials determined from the tests in the ASTM E2058 fire propagation apparatus are listed in Table 3-4.5, where data are taken from References 4, 10, and 25 to 29.

It can be noted from Table 3-4.5 that specialty polymeric materials (highly halogenated thermoplastics and high temperature thermosets) have low FPI and SDI values and several of them satisfy the 4910 test protocol criteria [FPI ≤ 6 (m/s^{1/2})/(kW/m)^{2/3} and SDI ≤ 0.4

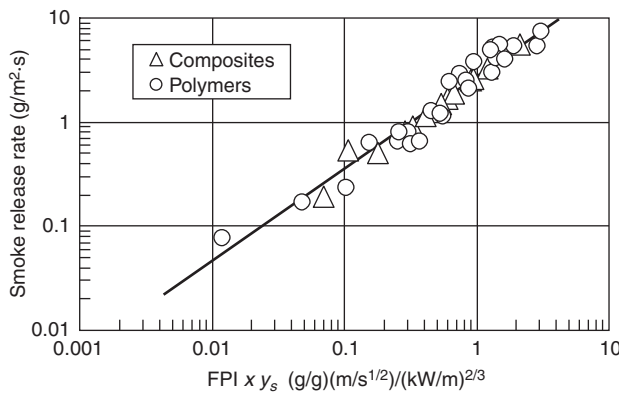


Figure 3-4.16. Peak smoke rates measured in the combustion tests in normal air with imposed external heat flux of 50 kW/m² versus peak FPI values from the propagation tests in air with 40 percent oxygen concentration multiplied by the smoke yields from the combustion tests. Tests were performed in the ASTM E2058 fire propagation apparatus.

Table 3-4.5 Fire Propagation Index and Smoke Development Index for Polymeric Materials^a

Polymeric Material	FPI (m/s ^{1/2})/(kW/m) ^{2/3}	SDI (g/g)(m/s ^{1/2})/(kW/m) ^{2/3}	Polymeric Material	FPI (m/s ^{1/2})/(kW/m) ^{2/3}	SDI (g/g)(m/s ^{1/2})/(kW/m) ^{2/3}			
<i>Fire-retarded or unmodified electrical cables</i>								
Polyvinyl chloride(PVC)/polyvinyl chloride PVC)	36	4.1	Unmodified ethyleneclorotrifluoroethylene (U-ECTFE, Halar)	4	0.15			
Polyethylene (PE)/polyvinyl chloride (PVC)	28	3.8	Unmodified ethylenetetrafluoroethylene (U-ETFE, Tefzel)	7	0.17			
Silicone/polyvinyl chloride (PVC)	17	2.0	Unmodified perfluoroalkoxy (U-PFA, Teflon)	2	0.01			
<i>Modified electrical cables</i>								
Polyvinylchloride (PVC)	8	1.2	<i>High-temperature specialty polymeric materials</i>					
High-temperature polyvinylchloride (PVC)	7	0.69	Phenol formaldehyde	5	0.06			
Polyethylene (PE)/ethylvinylacetate (EVA)	5	0.40	Polyetheretherketone (PEEK)	4	0.03			
<i>Ordinary polymeric materials</i>								
Fire-retarded polystyrene (FR-PS)	34	5.60	Melamine	7	0.24			
Fire-retarded polybutyleneterephthalate (FR-PBT)	32	2.20	Unmodified polycarbonate (U-PC)	14	4.2			
Unmodified polymethylmethacrylate, (U-PMMA)	23	1.1	Modified polycarbonate (M-PC)-1	10	4.2			
Unmodified polyoxymethylene, (U-POM)	15	0.03	Modified polycarbonate (M-PC)-2	7	4.0			
Fire-retarded (FR) vinyl ester	10	2.5	Unmodified polysulfone (U-POS)	18	1.49			
Unmodified wood slab	14	0.20	Modified polysulfone (M-POS)-1	11	1.4			
Unmodified polyethylene (U-PE)	30	1.4	Modified polysulfone (M-POS)-2	11	0.32			
Polyethylene with 25% chlorine	15	1.7	Modified polysulfone (M-POS)-3	7	1.2			
Polyethylene with 36% chlorine	11	1.5	Modified polysulfone (M-POS)-4	7	0.25			
Polyethylene with 48% chlorine	8	1.9	Modified polyetherimide (M-PEI)-1	6	0.24			
Modified polyethylene (M-PE)-1	7	0.64	Modified polyetherimide (M-PEI)-2	6	0.04			
Modified polyethylene (M-PE)-2	6	0.65	Modified polyetherimide (M-PEI)-3	5	0.46			
Unmodified polypropylene (U-PP)	31	1.7	Unmodified polyphenyleneoxide (U-PPO)	9	1.6			
Fire-retarded polypropylene (FR-PP)	30	2.1	<i>Glass fiber-reinforced ordinary polyesters</i>					
Modified polypropylene (M-PP)-1	11	3.0	Glass fiber-reinforced fire-retarded polyester (FR-PES)-1	21	5.4			
Modified polypropylene (M-PP)-2	7	0.95	Glass fiber-reinforced fire-retarded polyester (FR-PES)-1	16	7.4			
Modified polypropylene (M-PP)-3	7	0.35	Glass fiber-reinforced fire-retarded polyester (FR-PES)-1	14	4.0			
Modified polypropylene (M-PP)-4	6	0.41	Glass fiber-reinforced modified polyester (M-PES)-1	11	5.5			
Modified polypropylene (M-PP)-5	5	0.40	Glass fiber-reinforced modified polyester (M-PES)-1	10	5.2			
Modified polypropylene (M-PP)-6	5	0.19	Glass fiber-reinforced modified polyester (M-PES)-1	9	3.1			
Modified polypropylene (M-PP)-7	5	0.21	<i>Composites</i>					
Modified polypropylene (M-PP)-8	4	0.19	Fire-retarded polyester (30%)/glass fibers (70%-1)	13	0.91			
Fire-retarded flexible polyvinylchloride (FR-PVC)	16	1.6	Fire-retarded polyester (30%)/glass fibers (70%-2)	10	0.68			
Unmodified rigid polyvinylchloride (U-PVC)-1	8	0.86	Unmodified phenolic (16%)/Kevlar fibers (84%)	8	0.33			
Unmodified rigid polyvinylchloride (U-PVC)-2	7	1.2	Modified phenolic (20%)/glass fibers (80%)	3	0.07			
Modified rigid polyvinylchloride (M-PVC)-1	6	0.31	Fire-retarded epoxy (35%)/glass fibers (65%-1)	11	2.1			
Modified rigid polyvinylchloride (M-PVC)-2	5	0.64	Fire-retarded epoxy (35%)/glass fibers (65%-2)	10	0.94			
Modified rigid polyvinylchloride (M-PVC)-3	4	0.15	Fire-retarded epoxy (35%)/glass fibers (65%-3)	9	1.2			
Modified rigid polyvinylchloride (M-PVC)-4	3	0.16	Modified epoxy (24%)/glass fibers (76%-1)	5	0.61			
Modified rigid polyvinylchloride (M-PVC)-5	3	0.29	Modified epoxy (29%)/graphite fibers (71%)	5	0.54			
Modified rigid polyvinylchloride (M-PVC)-6	2	0.11	Modified epoxy and phenolic (18%)/glass fibers (82%)	2	0.18			
Modified rigid polyvinylchloride (M-PVC)-7	2	0.04	Modified polyphenylenesulfide (16%)/glass fibers (84%)	3	0.29			
Modified rigid polyvinylchloride (M-PVC)-8	2	0.06	Modified cyanate (27%)/graphite fibers (73%)	4	0.41			
Modified rigid polyvinylchloride (M-PVC)-9	1	0.03						
Chlorinated rigid polyvinylchloride (CPVC, Corzan)	3	0.13						
<i>Highly halogenated specialty polymeric materials</i>								
Unmodified polyvinylidenefluoride (U-PVDF Kynar)-1	5	0.14						
Unmodified polyvinylidenefluoride (U-PVDF)-2	4	0.08						

^aData taken from References 4, 10, and 25 to 29.

$(g/g)(m/s^{1/2})/(kW/m)^{2/3}$] for acceptance as clean room materials. These polymeric materials have high thermal stability with reduced release of carbon, hydrogen, and halogen atoms, as can be noted from their decomposition temperatures listed in Table 3-4.6, where data are taken from Reference 30.

Ordinary thermoplastics (such as PE, PP, and PVC) can also be modified such that they behave similarly to the specialty polymeric materials and have low FPI and SDI values to satisfy the 4910 Test Protocol criteria for acceptance as clean room materials.

Composites and fiberglass-reinforced materials. The use of composites and fiberglass-reinforced materials is increasing very rapidly because of low weight and high strength in applications such as aircraft, submarines, naval ships, military tanks, public transportation vehicles including automobiles, space vehicles, tote boxes, pallets, chutes, and so forth. Fire propagation, however, is one of the major concerns for the composites and fiberglass-reinforced materials; the FPI concept thus is used.^{4,10} For the determination of the FPI for the composites and fiberglass-

reinforced materials, the TRP and upward fire propagation tests are performed and Equation 9 is used, as discussed previously for electrical cables and conveyor belts.

The FPI concept used for the composites and fiber-glass-reinforced materials is based on the knowledge gained during the development of the FMRC standard for cable fire propagation Class No. 3972¹⁴ and FMRC studies on conveyor belts.^{12,23} The nonpropagating fire condition is satisfied in the ASTM E2058 fire propagation apparatus for $FPI \leq 6.0$, for about 600-mm-long and 100-mm-wide vertical composites and fiberglass-reinforced materials, under highly flame-radiating conditions (oxygen mass fraction = 0.40), very similar to the conveyor belts.

Table 3-4.5 lists FPI values for selected composites and fiberglass-reinforced materials taken from References 4 and 10.

Interior finish wall/ceiling materials. Since 1971, Factory Mutual Research Corporation has used the 25-ft corner test as a standard test. The 25-ft corner test is performed in a 7.6-m (25-ft)-high, 15.2-m (50-ft)-long and 11.6-m (38-ft)-wide building corner configuration to evaluate the burning characteristics of interior finish wall and ceiling materials.³¹⁻³⁴ The materials tested are typically panels with a metal skin over an insulation core material. The materials installed in the corner configuration are subjected to a growing exposure fire (peak heat release rate of about 3 MW) comprised of about 340 kg (750 lb) of 1.2-m (4-ft) × 1.2-m (4-ft) wood (oak) pallets stacked 1.5 m (5 ft) high at the base of the corner. The material is considered to have failed the test if within 15 min either (1) fire propagation on the wall or ceiling extends to the limits of the structure, or (2) flame extends outside the limits of the structure through the ceiling smoke layer.

The fire environment within the 25-ft corner test structure has been characterized through heat flux and temperature measurements.^{31,33} It has been shown that the fire propagation boundary (pyrolysis front) measured by visual damage is very close to the critical heat flux (CHF) boundary for the material, as shown in Figure 3-4.17, taken from Reference 32. This relationship is in agreement with the general understanding of the fire propagation process. Through small- and large-scale fire propagation tests for low-density, highly char-forming wall and ceiling insulation materials, using the ASTM E2058 fire propagation apparatus [Figure 3-4.2(a)], fire products collector (Figure 3-4.8), and 25-ft corner test (Figure 3-4.17), a semi-empirical relationship has been developed for fire propagation rate for a 15-min test in the 25-ft corner test³¹⁻³³

$$\frac{X_p}{X_t} = \frac{\dot{Q}_{con}''}{TRP} \quad (10)$$

where

X_p = average fire propagation length along the eaves (Figure 3-4.17) of the 25-ft corner test (pyrolysis front) measured visually (m)

X_t = total available length [11.6-m (38 ft)] in the 25-ft corner test

\dot{Q}_{con}'' = convective heat release rate (kW/m^2)

Table 3-4.6 Decomposition Temperature, Char Yield, and Limiting Oxygen Index for Polymeric Materials^a

Polymeric Material	Decomposition Temperature (°C)	Char Yield (%)	Limiting Oxygen Index (%)
Polybenzobisoxazole (PBO)	789	75	56
Polyparaphenylenne	652	75	55
Polybenzimidazole (PBI)	630	70	42
Polyamideimide (PAI)	628	55	45
Polyaramide (kevlar)	628	43	28
Polyetherketoneketone (PEKK)	619	62	40
Polyetherketone (PEK)	614	56	40
Polytetrafluoroethylene (PTFE)	612	0	95
Polyetheretherketone (PEEK)	606	50	35
Polyphenylsulfone (PPSF)	606	44	38
Polypara(benzoyl)phenylene (PX)	602	66	41
Fluorinated cyanate ester	583	44	40
Polyphenylenesulfide (PPS)	578	45	44
Polyetherimide (PEI)	575	52	47
Polypromellitimide (PI)	567	70	37
Polycarbonate (PC)	546	25	26
Polysulfone (PSF)	537	30	30
Polyethylene (PE)	505	0	18
Polyamide 6 (PA6)-nylon	497	1	21
Polyethyleneterephthalate (PET)	474	13	21
Acrylonitrile-butadiene-styrene (ABS)	470	0	18
Polyurethane elastomer (PU)	422	3	17
Polymethylmethacrylate (PMMA)	398	2	17
Polychlorotrifluoroethylene	380	0	95
Polyvinylchloride (PVC)	370	11	50
Polystyrene (PS)	364	0	18
Polyoxymethylene (POM)	361	0	15
Polyvinylidenefluoride (PVDF)	355	0	44

^aData are taken from Reference 30.

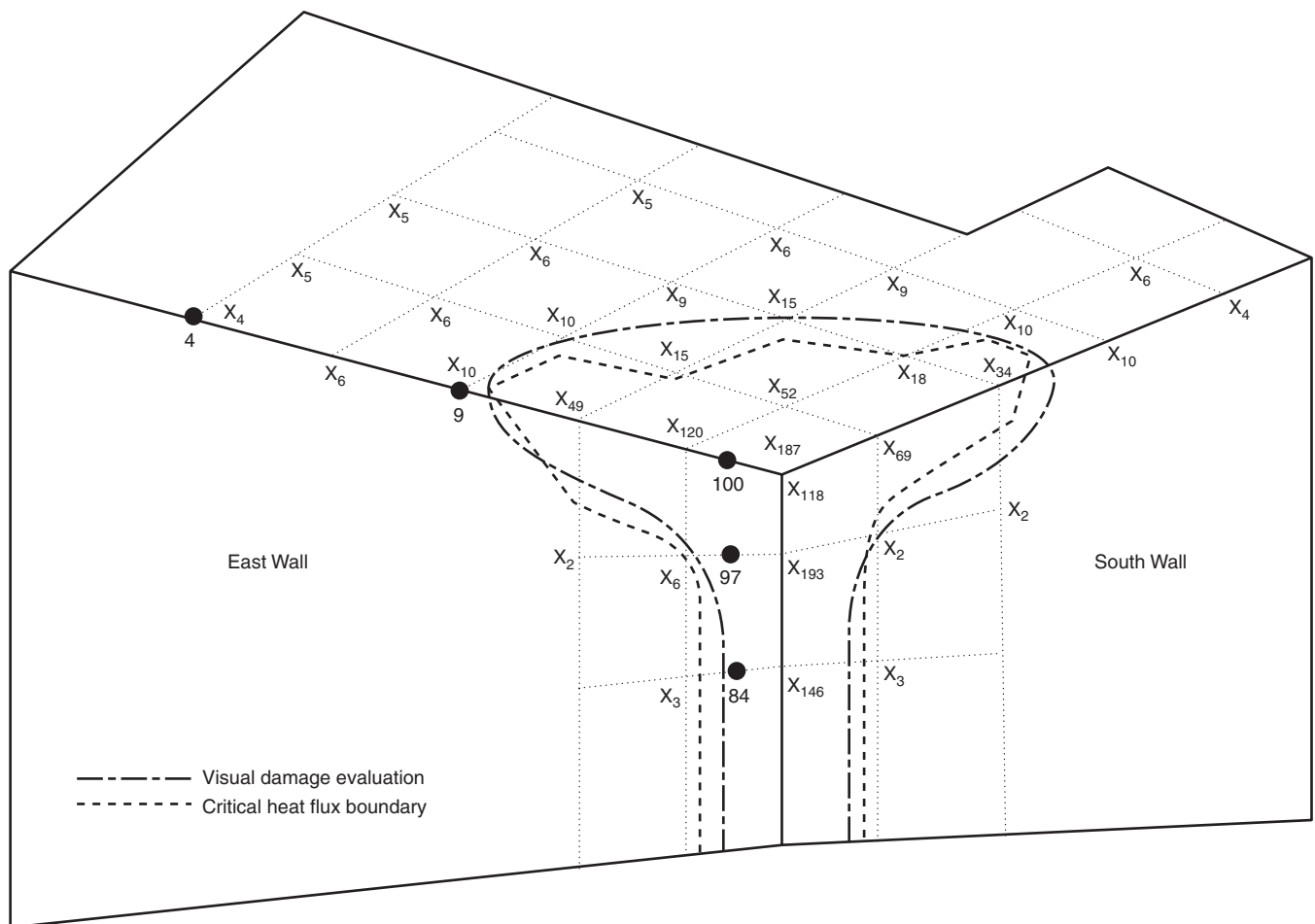


Figure 3-4.17. Critical heat flux boundary and visual observations for the extent of fire propagation in the FMRC 25-ft corner test for a product that passes the tests.³²

The right-hand side of Equation 10 with the convective heat release rate measured at 50 kW/m² of external heat flux is defined as the convective flame spread parameter (FSP_c).^{32,33} Figure 3-4.18 shows a correlation between the convective flame spread parameter obtained from the ASTM E2058 fire propagation apparatus and the normalized fire propagation length in the FMRC 25-ft corner test. Pass/fail regions, as determined from the 25-ft corner test, are indicated in the figure. Materials for which $FSP_c \leq 0.39$ pass the 25-ft corner test, and materials for which $FSP_c \geq 0.47$ are judged to be unacceptable (i.e., fail).³²⁻³⁴ The region where the FSP_c values are greater than 0.39 but less than 0.47 is uncertain.³²⁻³⁴

The correlation and pass/fail criterion shown in Figure 3-4.18 have been adopted in the FMRC Class No. 4880 for insulated wall or wall and ceiling panels.³⁴ In this standard, the 25-ft corner test has been replaced by the ASTM E2058 fire propagation apparatus [Figure 3-4.2(a)] tests. Two sets of tests are performed in the apparatus:³²⁻³⁴

1. *Thermal response parameter test.* Ignition tests are performed using approximately 100-mm × 100-mm and up to 100-mm-thick samples. Times to ignition at vari-

ous external heat flux values are measured to determine the TRP as described earlier.

2. *Convective heat release rate test.* Combustion tests are performed using about 100-mm × 100-mm and up to 100-mm-thick samples. Samples are burned in normal air under an external heat flux exposure of 50 kW/m². During the test, measurement is made for the convective heat release as a function of time.

The data for the TRP and convective heat release rate at 50 kW/m² of external heat flux are used to calculate the flame spread parameter (FSP_c) that accepts or rejects the sample.

Flaming and Nonflaming Fires

During fire propagation, the surface of the material regresses in a transient fashion with a rate slower than the fire propagation rate.² The surface regression becomes steady after fire propagates throughout the available surfaces. The surface regression continues until all the combustible components of the material are exhausted. During fire propagation and surface regression, the material generates

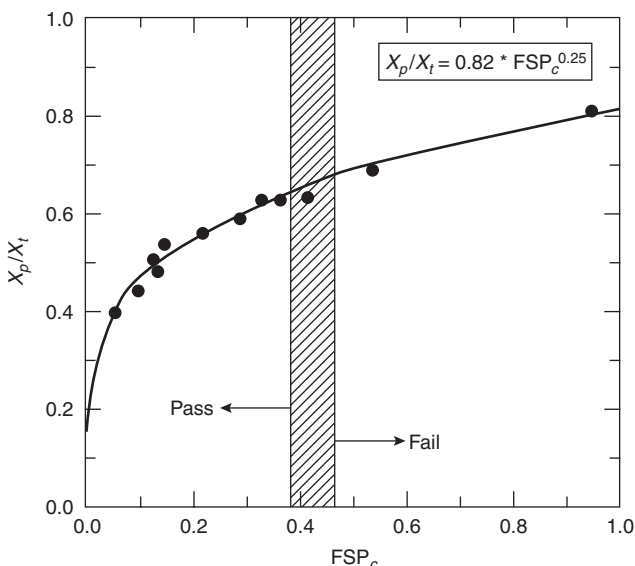


Figure 3-4.18. Normalized fire propagation length measured in the 25-ft corner test versus the convective flame spread parameter obtained from the ASTM E2058 fire propagation apparatus. (Figure is taken from References 32 and 33.)

vapors at a transient or steady rate. The generation rate of the material vapors is measured by the mass loss rate. In the presence of a flame and/or external heat flux, the mass loss rate, under steady state, is expressed as^{2,4,16}

$$\dot{m}'' = \frac{(\dot{q}_e'' + \dot{q}_{fr}'' + \dot{q}_{fc}'' - \dot{q}_{rr}'')}{\Delta H_g} \quad (11)$$

where

\dot{m}'' = mass loss rate ($\text{g}/\text{m}^2 \cdot \text{s}$)

\dot{q}_{fr}'' = flame radiative heat flux transferred to the surface (kW/m^2)

\dot{q}_{fc}'' = flame convective heat flux transferred to the surface (kW/m^2)

\dot{q}_{rr}'' = surface re-radiation loss (kW/m^2)

ΔH_g = heat of gasification (kJ/g)

total flame heat flux to the surface $\dot{q}_f'' = \dot{q}_{fr}'' + \dot{q}_{fc}''$

According to Equation 11, the generation rate of material vapors is governed by the external and flame heat flux, surface re-radiation loss, and the heat of gasification.

Heat of gasification: The heat of gasification for a melting material is expressed as³⁵

$$\Delta H_g = \int_{T_a}^{T_m} c_{p,s} dT + \Delta H_m + \int_{T_m}^{T_v} c_{p,l} dT + \Delta H_v \quad (12)$$

where

ΔH_g = heat of gasification (kJ/g)

$c_{p,s}$ = specific heat of solid in $\text{kJ}/\text{g} \cdot \text{K}$

- $c_{p,l}$ = specific heat of molten solid in $\text{kJ}/\text{g} \cdot \text{K}$
- ΔH_m = heat of melting/vaporization at melting temperature in kJ/g
- ΔH_v = heat of vaporization at vaporization temperature in kJ/g
- T_a = ambient temperature
- T_m = melting temperature
- T_v = vaporization temperature in K

For materials that do not melt, but sublime, decompose, or char, Equation 12 is modified accordingly. The heat of gasification can be determined from (1) the parameters on the right-hand side of Equation 12, which can be quantified by the thermal analysis techniques or calculated from the properties listed in the literature; and (2) nonflaming tests using apparatuses, such as the OSU heat release rate apparatus, the ASTM E2058 fire propagation apparatus, or the cone calorimeter. The following are some examples of the techniques:

1. *Heats of gasification of polymers from the differential scanning calorimetry.* The $c_{p,s}$, $c_{p,l}$, ΔH_m , and ΔH_v values for polymers have been quantified in the FMRC laboratory.³⁵ The techniques involve measurement of the specific heat as a function of temperature, such as shown in Figure 3-4.19 for polymethylmethacrylate, measured in the FMRC Flammability Laboratory. The specific heat increases with temperature; a value close to the vaporization temperature of PMMA is used in Equation 12. Further measurements are made of the heats of melting and vaporization. Some examples of the data measured in our laboratory are listed in Table 3-4.7.
2. *Heat of gasification from the literature data for the heats of gasification for various molecular weight hydrocarbons (alkanes).* The CRC Handbook of Chemistry and Physics³⁶ listing for the heats of gasification for liquid and solid

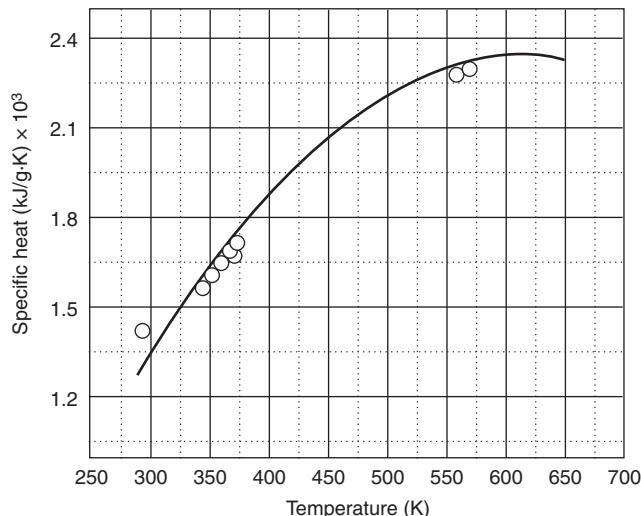


Figure 3-4.19. Specific heat of polymethylmethacrylate versus temperature measured by a differential scanning calorimeter at the flammability laboratory of the Factory Mutual Research Corporation.

Table 3-4.7 Surface Re-Radiation and Heats of Gasification of Various Materials

Materials	Surface Re-radiation (kW/m ²)	Heat of Gasification (kJ/g)			
		Flam. App. ^a	Cone ^b	DSC ^c	Cal ^d
Distilled water	0.63	2.58	—	2.59	2.58
<i>Hydrocarbons (alkanes)</i>					
Hexane	0.50	—	—	—	0.50
Heptane	0.63	—	—	—	0.55
Octane	0.98	—	—	—	0.60
Nonane	1.4	—	—	—	0.64
Decane	1.8	—	—	—	0.69
Undecane	2.3	—	—	—	0.73
Dodecane	2.8	—	—	—	0.77
Tridecane	3.0	—	—	—	0.81
Tetradecane	3.0	—	—	—	0.85
Hexadexane	3.0	—	—	—	0.92
<i>Natural materials</i>					
Filter paper	10	3.6	—	—	—
Corrugated paper	10	2.2	—	—	—
Wood (Douglas fir)	10	1.8	—	—	—
Plywood/FR	10	1.0	—	—	—
Particleboard	—	—	3.9	—	—
<i>Synthetic materials</i>					
Epoxy resin	—	—	2.4	—	—
Polypropylene	15	2.0	1.4	2.0	—
Polyethylene (PE) (low density)	15	1.8	—	1.9	—
PE (high density)	15	2.3	1.9	2.2	—
PE foams	12	1.4–1.7	—	—	—
PE/25% chlorine (Cl)	12	2.1	—	—	—
PE/36% Cl	12	3.0	—	—	—
PE/48% Cl	10	3.1	—	—	—
Rigid polyvinylchloride (PVC)	15	2.5	2.3	—	—
PVC/plasticizer	10	1.7	—	—	—
Plasticized PVC, LOI = 0.20	10	2.5	2.4	—	—
Plasticized PVC, LOI = 0.25	—	—	—	—	—
Plasticized PVC, LOI = 0.30	—	—	2.1	—	—
Plasticized PVC, LOI = 0.35	—	—	2.4	—	—
Rigid PVC, LOI = 0.50	—	—	2.3	—	—
Polyisoprene	10	2.0	—	—	—
PVC panel	17	3.1	—	—	—
Nylon 6/6	15	2.4	—	—	—
Polyoxymethylene (Delrin)	13	2.4	—	2.4	—
Polymethylmethacrylate (Plexiglas)	11	1.6	1.4	1.6	—
Polycarbonate	11	2.1	—	—	—
Polycarbonate panel	16	2.3	—	—	—
Isophthalic polyester	—	—	3.4	—	—
Polyvinyl ester	—	—	1.7	—	—
Acrylonitrile-butadiene-styrene (ABS)	10	3.2	2.6	—	—
Styrene-butadiene	10	2.7	—	—	—
Polystyrene (PS) foams	10–13	1.3–1.9	—	—	—
PS (granular)	13	1.7	2.2	1.8	—
<i>Polyurethane (PU) foams</i>					
Flexible polyurethane (PU) foams	16–19	1.2–2.7	2.4	1.4	—
Rigid polyurethane (PU) foams	14–22	1.2–5.3	5.6	—	—
Polyisocyanurate foams	14–37	1.2–6.4	—	—	—
Phenolic foam	20	1.6	—	—	—
Phenolic foam/FR	20	3.7	—	—	—
Ethylenetetrafluoroethylene (Tefzel)	27	0.9	—	—	—
Fluorinated ethylene propylene, FEP (Teflon)	38	2.4	—	—	—
Tetrafluoroethylene, TFE (Teflon)	48	0.8–1.8	—	—	—
Perfluoroalkoxy, PFA (Teflon)	37	1.0	—	—	—
<i>Composite and fiberglass-reinforced materials</i>					
Polyether ether ketone—30% fiberglass	—	—	7.9	—	—
Polyethersulfone—30% fiberglass	—	1.8	—	—	—
Polyester 1—fiberglass	—	—	2.5	—	—
Polyester 2—fiberglass	10	1.4	—	—	—
Polyester 3—fiberglass	10	6.4	—	—	—
Polyester 4—fiberglass	15	5.1	—	—	—
Polyester 5—fiberglass	10	2.9	—	—	—
Phenolic fiberglass (thick sheet)	20	7.3	—	—	—
Phenolic Kevlar (thick sheet)	15	7.8	—	—	—

^aFrom the ASTM E2058 fire propagation apparatus under nonflaming fire conditions.

^bCalculated from the cone calorimeter data reported in References 20 and 41 for the mass loss rate at various external heat flux values in flaming fires.

^cFrom the flammability laboratory using the differential scanning calorimetry.

^dCalculated from the data reported in the CRC Handbook.³⁶

hydrocarbons (alkanes) satisfies the following relationship in the molecular weight range of 30 to 250 g/mol:

$$\Delta H_g = -3.72 \times 10^{-6}M^2 + 0.0042M + 0.164 \quad (13)$$

where M is the molecular weight of the hydrocarbon (g/mol).

The heats of gasification calculated from Equation 13 for various alkanes are listed in Table 3-4.7.

3. *Heat of gasification from the literature data for the specific heats and heats of vaporization.* Water will be used as an example. The specific heat of liquid water, $c_{p,l}$ is 0.0042 kJ/g-K,³⁷ and the heat of vaporization of water at 373 K is 2.26 kJ/g.³⁷ Assuming the ambient temperature to be 298 K and the vaporization temperature to be 373 K, the heat of gasification of water from Equation 12 is calculated as follows:

$$\int_{298}^{373} c_{p,l} dT = 0.0042(373 - 298) = 0.32 \text{ kJ/g}$$

$$\Delta H_{v,373} = 2.26 \text{ kJ/g}$$

$$\Delta H_g = 0.32 + 2.26 = 2.58 \text{ kJ/g}$$

From the differential scanning calorimetry, the heat of gasification of water determined in the FMRC Flammability Laboratory is 2.59 kJ/g, which is in excellent agreement with the calculated value. These two values for the heat of gasification of water are listed in Table 3-4.7.

4. *Heat of gasification from the nonflaming tests using the ASTM E2058 fire propagation apparatus.* The measurement for the heat of gasification from the nonflaming fire tests in the ASTM E2058 fire propagation apparatus was introduced in 1976.³⁵ In nonflaming fires, $\dot{q}_f'' = 0$, and Equation 11 becomes

$$\dot{m}'' = \frac{\dot{q}_e'' - \dot{q}_{rr}''}{\Delta H_g} \quad (14)$$

where mass loss rate is a linear function of the external heat flux, and the heat of gasification is the inverse of the slope of the straight line. This equation provides a convenient method to determine the heat of gasification in the nonflaming tests, where mass loss rate of the sample is measured at various external heat flux values. The heat of gasification is determined from the linear regression analysis of the average steady-state mass loss rate as a function of the external heat flux. In the ASTM E2058 fire propagation apparatus tests, approximately 100- × 100-mm square and up to 100-mm-thick samples are used with co-flowing nitrogen or air with an oxygen mass fraction of about 0.10.

Figure 3-4.20 shows a plot of the vaporization rate of water in a 0.0072 m² Pyrex glass dish against time at 50 kW/m² of external heat flux, measured in the ASTM E2058 fire propagation apparatus. The figure also includes the predicted mass loss rate using Equation 14, where

$$\dot{q}_{rr}'' = \varepsilon\sigma(T_v^4 - T_a^4) \quad (15)$$

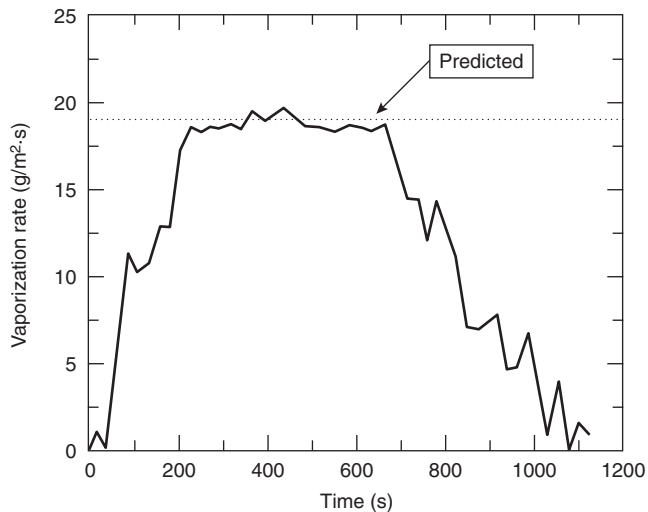


Figure 3-4.20. Vaporization rate of water versus time measured in the ASTM E2058 fire propagation apparatus using 99.69 g of water in a Pyrex dish with an area of 0.0072 m². Water was exposed to an external heat flux of 50 kW/m².

where ε is the emissivity of water (0.95 to 0.963 in the temperature range 298 to 373 K),³⁸ and σ is the Stefan-Boltzmann constant (56.7×10^{-12} kW/m²-deg⁴). For water, $T_v = 373$ K and $T_a = 298$ K, and thus $\dot{q}_{rr}'' = 1$ kW/m². From Equation 14, using $\dot{q}_e'' = 50$ kW/m², $\dot{q}_{rr}'' = 1$ kW/m², and $\Delta H_g = 2.57$ kJ/g, $\dot{m}'' = 19.0$ g/m²·s. There is excellent agreement between the measured and predicted values at the steady state in Figure 3-4.20. Water vaporization tests and calculations are routinely used for the calibration of the ASTM E2058 fire propagation apparatus.

Heats of gasification determined from the mass loss rate as a function of external heat flux in nonflaming fire conditions in the ASTM E2058 fire propagation apparatus are listed in Table 3-4.7 for selected materials. Excellent agreement can be noted between the heats of gasification determined from the ASTM E2058 fire propagation apparatus and those obtained from the differential scanning calorimetry.

Heat of gasification can also be determined from the flaming fires if high external heat flux values are used such that $\dot{q}_e'' \gg \dot{q}_{fr}'' + \dot{q}_{fc}'' - \dot{q}_{rr}''$ in Equation 11. This method has been used to calculate the heat of gasification from the cone calorimeter data for the mass loss rate in flaming fires reported in the literature.^{20,39} The values calculated from the cone calorimeter data are also listed in Table 3-4.7 and show a general agreement with the values from the ASTM E2058 fire propagation apparatus.

EXAMPLE 6:

Estimate the ignition temperature of a material with a CHF of 11 kW/m². Assume its surface emissivity to be unity, ambient temperature to be 20°C, and vaporization temperature to be approximately equal to the ignition temperature.

SOLUTION:

From Equation 15,

$$\begin{aligned} 11(\text{kW/m}^2) &= 56.7 \times 10^{-12}(\text{kW/m}^2 \cdot \text{deg}^4)(T_v^4)(\text{deg})^4 \\ &\quad - 56.7 \times 10^{-12}(\text{kW/m}^2 \cdot \text{deg}^4) \\ &\quad \times (298)^4(\text{deg})^4 \\ T_v &\equiv \left[\frac{11 \times 10^{12}}{56.7} + (298)^4 \right]^{1/4} \\ &\equiv (1940 \times 10^8 + 78.9 \times 10^8)^{1/4} \approx 670 \text{ K} \end{aligned}$$

By assumption, vaporization temperature is equal to the ignition temperature, which is 670 K (397°C).

EXAMPLE 7:

A material with a surface re-radiation loss of 10 kW/m² and heat of gasification of 1.8 kJ/g was found to be involved in a fire with an exposed area of 2 m². The combined flame and external heat flux exposure to the material was estimated to be 70 kW/m². Estimate the peak mass loss rate at which the material may have been burning in the fire in terms of g/m²·s and g/s.

SOLUTION:

From Equation 11,

$$\dot{m}'' = \frac{70 - 10}{1.8} = 33 \text{ g/m}^2 \cdot \text{s}$$

The estimated peak mass loss rate that the material may have been burning in the fire is 33 g/m²·s, or 33 × 2 = 67 g/s.

Flame heat flux: For flaming fires, in the absence of external heat flux, from Equation 11

$$\dot{m}'' = \frac{(\dot{q}_{fr}'' + \dot{q}_{fc}'' - \dot{q}_{rr}'')}{\Delta H_g} \quad (16)$$

The results from numerous small- and large-scale fire tests show that, as the surface area of the material increases, the flame radiative heat flux increases and reaches an asymptotic limit, whereas the flame convective heat flux decreases and becomes much smaller than the flame radiative heat flux at the asymptotic limit in large-scale fires.⁴⁰ It is also known that, in small-scale fires of fixed size with buoyant turbulent diffusion flames, as the oxygen mass fraction is increased, the flame radiative heat flux increases and reaches an asymptotic limit comparable to the asymptotic limit in large-scale fires, whereas the flame convective heat flux decreases and becomes much smaller than the flame radiative heat flux.⁴¹

The effect of the mass fraction of oxygen on the flame radiative and convective heat fluxes in small-scale fires is shown in Figure 3-4.21 for 100- × 100-mm square × 25-mm-thick slabs of polypropylene. The data were measured in the ASTM E2058 fire propagation apparatus.⁴¹ The increase in the flame radiative heat flux with increase in the mass fraction of oxygen is due to the increase in the flame temperature and soot formation and decrease in the residence time in the flame.⁴¹ The oxygen mass fraction

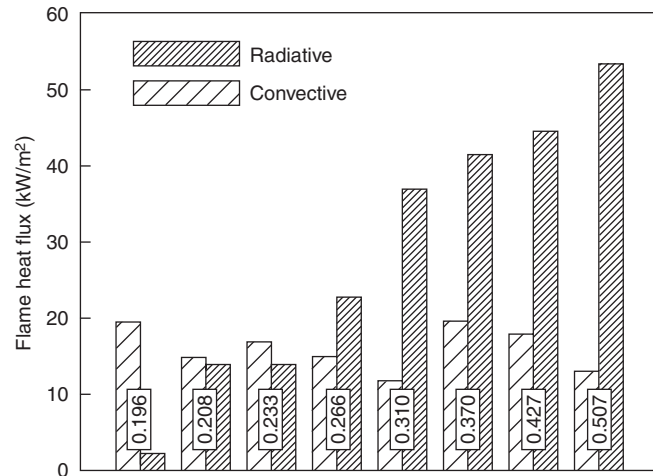


Figure 3-4.21. Flame radiative and convective heat fluxes at various oxygen mass fractions for the steady-state combustion of 100- × 100-mm square × 25-mm-thick slabs of polypropylene in the ASTM E2058 fire propagation apparatus under co-airflow velocity of 0.09 m/s. Data taken from Reference 41. Mass fractions of oxygen are indicated by the numbers inside the frames.

variation technique to simulate large-scale flame-radiative heat flux conditions in small-scale fires is defined as the *flame radiation scaling technique*.⁴

In the flame radiation scaling technique, the flame radiative and convective heat fluxes are determined from (1) the measurements for the mass loss rate at various oxygen mass fractions in the range of 0.12 (close to flame extinction) to about 0.60, under co-airflow conditions; (2) the convective heat transfer coefficient for the ASTM E2058 fire propagation apparatus, derived from the combustion of methanol; (3) the mass transfer number; and (4) Equation 16. In the ASTM E2058 fire propagation apparatus, the asymptotic limit is reached for the oxygen mass fraction ≥ 0.30. At the asymptotic limit, Equation 16 can be expressed as

$$\dot{m}_{asy}'' = \frac{\dot{q}_{f,asy}'' - \dot{q}_{rr}''}{\Delta H_g} \quad (17)$$

where subscript asy represents the asymptotic limit. The asymptotic values for the mass loss rate and flame heat flux determined from the flame radiation scaling technique in the ASTM E2058 fire propagation apparatus are listed in Table 3-4.8. The measured asymptotic values of the mass loss rate reported in the literature and flame heat flux in large-scale fires are also listed in Table 3-4.8. Flame heat flux values for the large-scale fires are derived from the asymptotic values of the mass loss rate and known values of surface re-radiation losses and heats of gasification.

The data in Table 3-4.8 show that the asymptotic flame heat flux values, determined in the ASTM E2058 fire propagation apparatus, using the flame radiation scaling technique, are in good agreement with the values

Table 3-4.8 Asymptotic Values of Mass Loss Rate and Flame Heat Flux^a

Material	\dot{m}'' (g/m ² ·s)		\dot{q}_f'' (kW/m ²)	
	S*	L ^b	S*	L ^b
<i>Aliphatic carbon-hydrogen atoms^c</i>				
Polyethylene	26	—	61	—
Polypropylene	24	—	67	—
Heavy fuel oil (2.6–23 m)	—	36	—	29
Kerosene (30–80 m)	—	65	—	29
Crude oil (6.5–31 m)	—	56	—	44
n-Dodecane (0.94 m)	—	36	—	30
Gasoline (1.5–223 m)	—	62	—	30
JP-4 (1.0–5.3 m)	—	67	—	40
JP-5 (0.60–17 m)	—	55	—	39
n-Heptane (1.2–10 m)	~66	75	32	37
n-Hexane (0.75–10 m)	—	77	—	37
Transformer fluids (2.37 m)	27–30	25–29	23–25	22–25
<i>Aromatic carbon-hydrogen atoms^c</i>				
Polystyrene (0.93 m)	36	34	75	71
Xylene (1.22 m)	—	67	—	37
Benzene (0.75–6.0 m)	—	81	—	44
<i>Aliphatic carbon-hydrogen-oxygen atoms^c</i>				
Polyoxymethylene 16	—	50	—	
Polymethylmethacrylate (2.37 m)	28	30	57	60
Methanol (1.2–2.4 m)	20	25	22	27
Acetone (1.52 m)	—	38	—	24
<i>Aliphatic carbon-hydrogen-oxygen-nitrogen atoms</i>				
Flexible polyurethane foams	21–27	—	64–76	—
Rigid polyurethane foams	22–25	—	49–53	—
<i>Aliphatic carbon-hydrogen-halogen atoms</i>				
Polyvinylchloride	16	—	50	—
Tefzel (ETFE)	14	—	50	—
Teflon (FEP)	7	—	52	—

Mass loss rates are from the data reported in the literature.

^aSmall-scale fires, pool diameter fixed at 0.10 m, flame radiation scaling technique was used in the ASTM E2058 fire propagation apparatus, $Y_0 \geq 0.30$.

^bLarge-scale fires in normal air.

^cNumbers in m in parentheses are the pool diameters used in large-scale fires.

measured in the large-scale fires. The asymptotic flame heat flux values vary from 22 to 77 kW/m², dependent primarily on the mode of decomposition and gasification rather than on the chemical structures of the materials. For example, for the liquids, which vaporize primarily as monomers or as very low molecular weight oligomer, the asymptotic flame heat flux values are in the range of 22 to 44 kW/m², irrespective of their chemical structures. For polymers, which vaporize as high molecular weight oligomer, the asymptotic flame heat flux values increase substantially to the range of 49 to 71 kW/m², irrespective of their chemical structures. The independence of the asymptotic flame heat values from the chemical structures of materials is consistent with the dependence of flame radiation on optical thickness, soot concentration, and flame temperature in large-scale fires.

EXAMPLE 8:

Calculate the peak mass loss rate for polypropylene in large-scale fires, burning in the open, with no external heat sources in the surroundings.

SOLUTION:

In the calculation Equation 16 will be used. From Table 3-4.7, $\dot{q}_{rr}'' = 15$ kW/m² and $\Delta H_g = 2.0$ kJ/g, and from Table 3-4.8, $\dot{q}_{f,asy}'' = 67$ kW/m². Using these values in Equation 16,

$$\dot{m}'' = \frac{67 - 15}{2.0} = 26.0 \text{ g/m}^2\cdot\text{s}$$

EXAMPLE 9:

Calculate the peak mass loss rate for polypropylene in large-scale fires burning in the open in the presence of a burning object, which provides 20 kW/m² of heat flux to the polypropylene surface, in addition to its own flame heat flux of 67 kW/m².

SOLUTION:

In the calculation, Equation 11 will be used with $\dot{q}_e'' = 20$ kW/m². From Table 3-4.7, $\dot{q}_{rr}'' = 15$ kW/m² and $\Delta H_g = 2.0$ kJ/g and from Table 3-4.8, $\dot{q}_{f,asy}'' = 67$ kW/m². Using these values in Equation 11,

$$\dot{m}'' = \frac{67 + 20 - 15}{2.0} = 36.0 \text{ g/m}^2\cdot\text{s}$$

Heat Release Rate

The determination of heat release rate in fires has been influenced by the principles and techniques used for the controlled combustion in the heating and power industries. Heat in the flowing combustion products (convective heat) and thermal radiation are used to generate steam, heat a furnace or space, produce mechanical power in internal combustion engines or gas turbines, and so forth. Heat is generated by injecting fuel (gas, liquid, or solid) into a hot environment, where it undergoes evaporation, gasification, and thermal decomposition or pyrolysis. Fuel vapors react chemically with oxygen and produce heat and products, such as carbon monoxide (CO), carbon dioxide (CO₂), hydrocarbons, water (H₂O), and soot. Theoretical air requirement for complete combustion is estimated from an empirical guide, which suggests that, for every 10.6 kJ of heat in the fuel burned, 3.4 g of air are required for complete combustion.⁴² Equivalently, the heat of combustion per unit mass of oxygen consumed (ΔH_0^*) is 13.4 kJ/g. Using $\Delta H_0^* \approx 13.4$ kJ/g to determine the heat release rate in fires from the mass consumption rate of oxygen is discussed in References 16 and 43. This technique is defined as the *oxygen consumption (OC) calorimetry*.

A combustion process is characterized by its *combustion efficiency*, defined as the fraction of heat of complete combustion released in the chemical reactions, which is the ratio of the chemical heat release rate to the heat release rate for complete combustion or the ratio of the chemical heat of combustion to net heat of complete com-

bustion. The calorific energy generated in chemical reactions leading to complete combustion per unit mass of fuel, water produced being in the vapor state, is defined as the *net heat of complete combustion*. The calorific energy generated in chemical reactions leading to varying degrees of incomplete combustion per unit mass of the fuel consumed is defined as the *chemical heat of combustion*. In the heating and power industries, combustion efficiency is determined routinely from the waste products (flue gas) analysis, especially for CO, CO₂, and O₂, and from the measurements of temperature in the combustion products-air mixture and thermal radiation. For higher combustion efficiency, *mass fuel-to-air ratio* relative to the *stoichiometric mass fuel-to-air ratio* or the *equivalence ratio* is controlled by maintaining desired primary and secondary airflow.

The net heat of complete combustion is measured in the oxygen bomb calorimeter and is calculated from the standard heats of formation of the materials, CO₂ and H₂O (the standard heat of formation of O₂ in its standard state being zero). For example, for polymethylmethacrylate (PMMA) and polystyrene (PS), the net heats of complete combustion measured in the oxygen bomb calorimeter by the FMRC Flammability Laboratory are 25.3 and 39.2 kJ/g, respectively; and from the standard heats of formation, they are 24.9 and 39.8 kJ/g, respectively. For soot generated from the combustion of PMMA and PS, the net heats of complete combustion measured in the oxygen bomb calorimeter by the FMRC Flammability Laboratory are 33.9 and 32.1 kJ/g, respectively, and 32.8 kJ/g from the standard heats of formation of graphite and CO₂.

In fires, complete combustion is rarely achieved and products of incomplete combustion, such as CO and smoke, are quite common. An example of incomplete combustion is given in Table 3-4.9, where chemical heat of combustion and combustion efficiency decrease as CO, carbon, and ethylene are formed at the expense of CO₂ and H₂O with reduced O₂ consumption, a typical condition found in the ventilation-controlled fires.⁴⁴ The chemical heat of combustion is the ratio of the chemical heat release rate to the mass loss rate. The upper limit of the

combustion efficiency is 1.00, corresponding to complete combustion, and the lower limit is 0.46, corresponding to unstable combustion leading to flame extinction for combustion efficiency ≤ 0.40 .^{44,45}

Chemical heat release rate: The chemical heat release rate is determined from the *carbon dioxide generation* (CDG) and *oxygen consumption* (OC) *calorimetry*.

The CDG calorimetry:^{2-4,16,28,29,41,44,46} The chemical heat release rate is determined from the following relationships:

$$\dot{Q}_{ch}'' = \Delta H_{CO_2}^* \dot{G}_{CO_2}'' + \Delta H_{CO}^* \dot{G}_{CO}'' \quad (18)$$

$$\Delta H_{CO_2}^* = \frac{\Delta H_T}{\Psi_{CO_2}} \quad (19)$$

$$\Delta H_{CO}^* = \frac{\Delta H_T - \Delta H_{CO} \Psi_{CO}}{\Psi_{CO}} \quad (20)$$

where

$$\dot{Q}_{ch}'' = \text{chemical heat release rate (kW/m}^2\text{)}$$

$$\Delta H_{CO_2}^* = \text{net heat of complete combustion per unit mass of CO}_2 \text{ generated (kJ/g)}$$

$$\Delta H_{CO}^* = \text{net heat of complete combustion per unit mass of CO generated (kJ/g)}$$

$$\Delta H_T = \text{net heat of complete combustion per unit mass of fuel consumed (kJ/g)}$$

$$\Psi_{CO_2} = \text{stoichiometric yield for the maximum conversion of fuel to CO}_2 (\text{g/g})$$

$$\Psi_{CO} = \text{stoichiometric yield for the maximum conversion of fuel to CO (g/g)}$$

$$\dot{G}_{CO_2}'' = \text{generation rate of CO}_2 (\text{g/m}^2\cdot\text{s})$$

$$\dot{G}_{CO}'' = \text{generation rate of CO (g/m}^2\cdot\text{s})$$

The values for the net heats of complete combustion per unit mass of fuel consumed and CO₂ and CO generated are listed in Tables 3-4.10 through 3-4.13. The values depend on the chemical structures of the materials. With some exceptions, the values remain approximately constant within each generic group of fuels. The average values are also listed in the tables. From the average values, $\Delta H_{CO_2}^* = 13.3 \text{ kJ/g} \pm 11 \text{ percent}$ and $\Delta H_{CO}^* = 11.1 \text{ kJ/g} \pm 18 \text{ percent}$. In the CDG calorimetry, the CO correction for well-ventilated fires is very small because of the small amounts of CO generated. The variations of 11 and 18 percent in the $\Delta H_{CO_2}^*$ and ΔH_{CO}^* values, respectively, would reduce significantly if values for low molecular weight hydrocarbons with small amounts of O, N, and halogen were used in averaging.

For the determination of the chemical heat release rate, generation rates of CO₂ and CO are measured and either the actual values or the average values of the net heat of complete combustion per unit mass of CO₂ and CO generated are used. The measurements for the generation rates of CO₂ and CO are described in the subsection entitled "Generation Rates of Chemical Compounds and Fire Ventilation."

Table 3-4.9 Chemical Heat of Combustion and Combustion Efficiency of Polymethylmethacrylate

Reaction Stoichiometry	ΔH_{ch} (kJ/g) ^a	χ_{ch}
C ₅ H ₈ O ₂ (g) + 6.0 O ₂ (g) = 5CO ₂ (g) + 4H ₂ O (g)	24.9	1.00
C ₅ H ₈ O ₂ (g) + 5.5 O ₂ (g) = 4CO ₂ (g) + 4H ₂ O (g) + CO (g)	22.1	0.89
C ₅ H ₈ O ₂ (g) + 4.5 O ₂ (g) = 3CO ₂ (g) + 4H ₂ O (g) + CO (g) + C (s)	18.2	0.73
C ₅ H ₈ O ₂ (g) + 3.0 O ₂ (g) = 2CO ₂ (g) + 3H ₂ O (g) + CO (g) + C (s) + 0.50 C ₂ H ₄ (g)	11.5	0.46

^aStandard heat of formation in kJ/mol: PMMA (C₅H₈O₂) (g) = -442.7; O₂ (g) = 0; CO₂(g) = 393.5; H₂O (g) = -241.8; CO (g) = -110.5; C (s) = 0; and C₂H₄ (g) = +26.2, where g is the gas and s is the solid.

The OC calorimetry:^{2-4,17-19,28,29,41,43,44,46,47} The chemical heat release rate is determined from the following relationships:

$$\dot{Q}_{\text{ch}}'' = \Delta H_{\text{O}}^* \dot{C}_{\text{O}}'' \quad (21)$$

$$\Delta H_{\text{O}}^* = \frac{\Delta H_T}{\Psi_{\text{O}}} \quad (22)$$

where

ΔH_{O}^* = net heat of complete combustion per unit mass of oxygen consumed (kJ/g)

\dot{C}_{O}'' = mass consumption rate of oxygen (g/m²·s)

Ψ_{O} = stoichiometric mass-oxygen-to-fuel ratio (g/g)

The values for the net heats of complete combustion per unit mass of oxygen consumed are listed in Tables 3-4.10 through 3-4.13 along with the values for the net heats of complete combustion per unit mass of fuel consumed and CO₂ and CO generated. The average values of the net heat of complete combustion per unit mass of oxygen consumed are also listed in the tables. The values depend on the chemical structures of the materials. With some exceptions, the values remain approximately constant within each generic group of fuels. From the average values, $\Delta H_{\text{O}}^* = 12.8 \text{ kJ/g} \pm 7 \text{ percent}$. The ΔH_{O}^* value of 12.8 kJ/g is close to 13.4 kJ/g used in the heating and power industries⁴² and 13.1 kJ/g ± 5 percent reported in Reference 43. The variation of 7 percent would reduce significantly if values for low molecular weight hydrocarbons with small amounts of O, N, and halogen were used in averaging.

For the determination of the chemical heat release rate, mass consumption rate of oxygen is measured, and either the actual values or the average values of the net heats of complete combustion per unit mass of oxygen consumed are used. The measurement for the consumption rate of oxygen is described in the subsection entitled "Generation Rates of Chemical Compounds and Fire Ventilation."

Convective heat release rate: The convective heat release rate is determined from the *gas temperature rise* (GTR) *calorimetry*, where the following relationship is used:^{2-7,16,41,44}

$$\dot{Q}_{\text{con}}'' = \frac{\dot{W} c_p (T_g - T_a)}{A} \quad (23)$$

where

\dot{Q}_{con}'' = convective heat release rate (kW/m²)

c_p = specific heat of the combustion product-air mixture at the gas temperature (kJ/g·K)

T_g = gas temperature (K)

T_a = ambient temperature (K)

\dot{W} = total mass flow rate of the fire product-air mixture (g/s)

A = total exposed surface area of the material (m²)

Radiative heat release rate: Chemical heat release rate consists of a convective and a radiative component. Some fraction of the chemical heat release rate may be lost as conductive heat. In systems where heat losses are negligi-

bly small, the radiative heat release rate can be obtained from the difference between the chemical and convective heat release rates:^{2-4,16,41,44}

$$\dot{Q}_{\text{rad}}'' = \dot{Q}_{\text{ch}}'' - \dot{Q}_{\text{con}}'' \quad (24)$$

where \dot{Q}_{rad}'' is the radiative heat release rate (kW/m²).

Use of GTR, CDG, and OC calorimetries: In 1972 the GTR calorimetry was used for the first time by the Ohio State University (OSU) to determine the heat release rate.^{5,6} The apparatus used is now known as the OSU heat release rate apparatus; it is shown in Figure 3-4.1. The OSU apparatus is an ASTM⁷ and an FAA standard test apparatus.⁸ In the GTR calorimetry, it is assumed that almost all the thermal radiation from the flame is transferred to the flowing fire products-air mixture, as the flames are inside an enclosed space and heat loss by conductive heat transfer is negligibly small. The OC calorimetry has now been adapted to the OSU apparatus.⁵¹

The CDG, OC, and GTR calorimetries were used for the first time during the mid-1970s by the Factory Mutual Research Corporation (FMRC) to determine the chemical, convective, and radiative heat release rates.^{35,52-54} The apparatus used is now known as the ASTM E2058 fire propagation apparatus (50-kW scale); it is shown in Figure 3-4.2(a). Heat release rate from the CDG and OC calorimetries in the ASTM E2058 fire propagation apparatus was defined as the actual heat release rate until 1986,^{16,41,48,52-55} but after 1986 it was changed to the chemical heat release rate to account for the effects of (1) the chemical structures of the materials and additives; (2) fire ventilation; (3) the two dominant modes of heat release, that is, convective and radiative; and (4) the effects of the flame extinguishing and suppressing agents.

The ASTM E2058 fire propagation apparatus is a standard test apparatus for electrical cables¹⁴ and for wall and ceiling insulation materials, replacing the 25-ft corner test;³⁴ and is expected to be adopted as a standard test apparatus for conveyor belts, composites, sample storage commodities, and other applications related to the commercial and industrial fire protection needs in the future.

In 1982 the National Institute of Standards and Technology (NIST) used the OC calorimetry,^{17,18} following the methodology described in Reference 43. The apparatus developed to use this methodology, known as the cone calorimeter, is shown in Figure 3-4.3. The cone calorimeter became an ASTM standard test apparatus in 1990.¹⁹

Sampling ducts have been designed for the ASTM E2058 fire propagation apparatus and the cone calorimeter to measure the mass generation rates of CO₂ and CO and mass consumption rate of oxygen for use in the CDG and OC calorimetries. (See Equations 18 and 21.) The CDG and OC calorimetries are used in the ASTM E2058 fire propagation apparatus (50-, 500-, and 10,000-kW scale). In the OSU apparatus and the cone calorimeter, only the OC calorimetry is used.

The CDG and OC calorimetries are also used in numerous large-scale fire tests, such as the CDG calorimetry in the wind-aided turbulent horizontal flame spread in large-scale fire test galleries at the Londonderry Occupa-

Table 3-4.10 Net Heats of Complete Combustion per Unit Mass of Fuel and Oxygen Consumed and Carbon Dioxide and Carbon Monoxide Generated for Carbon- and Hydrogen-Containing Fuels^a

Fuel	Formula	ΔH_T (kJ/g)	ΔH_O^* (kJ/g)	ΔH_{CO_2} (kJ/g)	ΔH_{CO}^* (kJ/g)	Fuel	Formula	ΔH_T (kJ/g)	ΔH_O^* (kJ/g)	ΔH_{CO_2} (kJ/g)	ΔH_{CO}^* (kJ/g)					
Normal alkanes																
Methane	CH ₄	50.1	12.5	(18.2)	(18.6)	Heptene	C ₇ H ₁₄	44.6	12.9	14.1	12.2					
Ethane	C ₂ H ₆	47.1	12.7	16.2	15.4	Octene	C ₈ H ₁₆	44.5	12.9	14.1	12.1					
Propane	C ₃ H ₈	46.0	12.9	15.3	14.0	Nonene	C ₉ H ₁₈	44.3	12.9	14.1	12.1					
Butane	C ₄ H ₁₀	45.4	12.7	15.1	13.7	Decene	C ₁₀ H ₂₀	44.2	12.9	14.1	12.2					
Pentane	C ₅ H ₁₂	45.0	12.6	14.7	13.2	Dodecene	C ₁₂ H ₂₄	44.1	12.9	14.1	12.2					
Hexane	C ₆ H ₁₄	44.8	12.7	14.6	12.9	Tridecene	C ₁₃ H ₂₆	44.0	12.9	14.1	12.2					
Heptane	C ₇ H ₁₆	44.6	12.7	14.5	12.8	Tetradecene	C ₁₄ H ₂₈	44.0	12.9	14.1	12.2					
Octane	C ₈ H ₁₈	44.5	12.6	14.4	12.7	Hexadecene	C ₁₆ H ₃₂	43.9	12.9	14.1	12.1					
Nonane	C ₉ H ₂₀	44.3	12.7	14.3	12.5	Octadecene	C ₁₈ H ₃₆	43.8	12.9	14.1	12.1					
Decane	C ₁₀ H ₂₂	44.4	12.7	14.3	12.4			Average	13.2	14.2	12.4					
Undecane	C ₁₁ H ₂₄	44.3	12.7	14.3	12.4											
Dodecane	C ₁₂ H ₂₆	44.2	12.7	14.2	12.3	Cyclic alkenes										
Tridecane	C ₁₃ H ₂₈	44.2	12.7	14.2	12.3	Cyclohexene	C ₆ H ₁₀	43.0	13.0	13.4	11.0					
Kerosene	C ₁₄ H ₃₀	44.1	12.7	14.1	12.2	Methylcyclohexene	C ₇ H ₁₂	43.1	12.9	13.4	11.1					
Hexadecane	C ₁₆ H ₃₄	44.1	12.7	14.2	12.3			Average	13.0	13.4	11.1					
		Average	12.7	14.6	12.9											
Substituted alkanes																
Methylbutane	C ₅ H ₁₂	45.0	12.6	14.7	13.1	Dienes										
Dimethylbutane	C ₆ H ₁₄	44.8	12.7	14.6	13.0	1-3 Butadiene	C ₄ H ₆	44.6	13.7	13.7	11.5					
Methylpentane	C ₆ H ₁₄	44.8	12.7	14.6	12.9	Cyclooctadiene	C ₈ H ₁₂	43.2	13.3	13.3	10.9					
Dimethylpentane	C ₇ H ₁₆	44.6	12.7	14.5	12.9			Average	13.5	13.5	11.2					
Methylhexane	C ₇ H ₁₆	44.6	12.6	14.4	12.7	Normal alkynes										
Isooctane	C ₈ H ₁₈	44.5	12.6	14.4	12.7	Acetylene	C ₂ H ₂	47.8	(15.6)	14.3	12.4					
Methylethylpentane	C ₈ H ₁₈	44.5	12.6	14.4	12.7	Heptyne	C ₇ H ₁₂	44.8	13.4	13.9	11.8					
Ethylhexane	C ₈ H ₁₈	44.5	12.6	14.4	12.7	Octyne	C ₈ H ₁₄	44.7	13.3	14.0	11.9					
Dimethylhexane	C ₈ H ₁₈	44.5	12.7	14.5	12.8	Decyne	C ₁₀ H ₁₈	44.5	13.2	13.9	11.9					
Methylheptane	C ₈ H ₁₈	44.5	12.6	14.4	12.7	Dodecyne	C ₁₂ H ₂₂	44.3	13.2	14.0	12.0					
		Average	12.6	14.6	12.8			Average	13.3	14.0	12.0					
Cyclic alkanes																
Cyclopentane	C ₅ H ₁₀	44.3	12.8	13.9	11.9	Arenes										
Methylcyclopentane	C ₆ H ₁₂	43.8	12.7	13.9	11.9	Benzene	C ₆ H ₆	40.1	13.0	11.9	8.7					
Cyclohexane	C ₆ H ₁₂	43.8	12.7	13.8	11.7	Toluene	C ₇ H ₈	39.7	12.9	12.1	9.0					
Methylcyclohexane	C ₇ H ₁₄	43.4	12.7	13.8	11.7	Styrene	C ₈ H ₈	39.4	13.1	12.0	8.8					
Ethylcyclohexane	C ₈ H ₁₆	43.2	12.7	13.8	11.7	Ethylbenzene	C ₈ H ₁₀	39.4	12.9	12.3	9.4					
Dimethylcyclohexane	C ₈ H ₁₆	43.2	12.7	13.8	11.7	Xylene	C ₈ H ₁₀	39.4	13.0	12.4	9.5					
Cyclooctane	C ₈ H ₁₆	43.2	12.7	13.9	11.9	Propylbenzene	C ₉ H ₁₂	39.4	12.9	12.5	9.6					
Decalin	C ₁₀ H ₁₈	42.8	12.7	13.4	11.0	Trimethylbenzene	C ₉ H ₁₂	39.2	12.9	12.5	9.7					
Bicyclohexyl	C ₁₂ H ₂₂	42.6	12.6	13.3	11.0	Cumene	C ₉ H ₁₂	39.2	12.9	12.9	9.6					
		Average	12.7	13.8	11.6	Naphthalene	C ₁₀ H ₈	39.0	12.9	11.3	7.7					
Normal alkenes																
Ethylene	C ₂ H ₄	48.0	13.8	15.0	13.6	Tetralin	C ₁₀ H ₁₂	39.0	12.9	12.2	9.2					
Propylene	C ₃ H ₆	46.4	13.4	14.6	12.9	Butylbenzene	C ₁₀ H ₁₄	39.0	12.9	12.7	9.9					
Butylene	C ₄ H ₈	45.6	14.3	14.3	12.5	Diethylbenzene	C ₁₀ H ₁₄	39.0	13.7	13.5	11.1					
Pentene	C ₅ H ₁₀	45.2	14.3	14.3	12.5	p-Cymene	C ₁₀ H ₁₄	39.0	13.0	12.5	9.6					
Hexene	C ₆ H ₁₂	44.9	12.9	14.1	12.2	Methylnaphthalene	C ₁₁ H ₁₀	38.9	12.9	11.5	8.1					
						Pentylbenzene	C ₁₁ H ₁₆	38.8	13.0	12.8	10.2					
						Triethylbenzene	C ₁₂ H ₁₈	38.7	12.7	12.7	10.0					
								Average	13.0	12.4	9.4					

^aData from References 48 and 49. Numbers in parentheses not used for averaging.

tional Safety Centre in Australia and Pittsburgh Research Center, U.S. Bureau of Mines.^{56,57}

In the GTR calorimetry, a thermopile located in the flue gas chimney is used in the OSU apparatus, and a thermocouple located in the sampling duct is used in the ASTM E2058 fire propagation apparatus, where heat

losses by conduction are negligibly small. The cone calorimeter has not been designed for the GTR calorimetry.

The radiative heat release rate is determined from the difference between the chemical and convective heat release rates only in the ASTM E2058 fire propagation apparatus.

Table 3-4.11 Net Heats of Complete Combustion per Unit Mass of Fuel and Oxygen Consumed and Carbon Dioxide and Carbon Monoxide Generated for Carbon-, Hydrogen-, and Oxygen-Containing Fuels^a

Fuel	Formula	ΔH_T (kJ/g)	ΔH_O^* (kJ/g)	ΔH_{CO_2} (kJ/g)	ΔH_{CO}^* (kJ/g)	Fuel	Formula	ΔH_T (kJ/g)	ΔH_O^* (kJ/g)	ΔH_{CO_2} (kJ/g)	ΔH_{CO}^* (kJ/g)
Alcohols											
Methyl alcohol	CH_3O	20.0	13.4	14.5	12.9	Formic acid	CH_2O_2	5.7	16.4	5.96	0
Ethyl alcohol	C_2H_5O	27.7	13.2	14.5	12.7	Acetic acid	$C_2H_4O_2$	14.6	13.7	9.95	5.65
<i>n</i> -Propyl alcohol	C_3H_8O	31.8	13.3	14.5	12.7	Benzoic acid	$C_7H_6O_2$	24.4	12.4	9.66	5.18
Isopropyl alcohol	C_3H_8O	31.8	13.3	14.5	12.7	Cresylic acid	$C_8H_8O_2$	34.0	(16.0)	13.1	10.6
Allyl alcohol	C_3H_6O	31.4	14.2	13.8	11.7	Acids					
<i>n</i> -Butyl alcohol	$C_4H_{10}O$	34.4	13.3	14.5	12.8	Formic acid	CH_2O_2	20.2	13.3	11.3	7.8
Isobutyl alcohol	$C_4H_{10}O$	34.4	13.3	14.5	12.8	Acetic acid	$C_2H_4O_2$	23.9	13.2	12.0	8.8
Sec-butyl alcohol	$C_4H_{10}O$	34.4	13.3	14.5	12.8	Benzoic acid	$C_5H_{10}O_2$	26.6	13.0	12.3	9.4
Ter-butyl alcohol	$C_4H_{10}O$	34.4	13.3	14.5	12.8	Cresylic acid	$C_6H_8O_2$	20.2	13.3	11.3	7.8
<i>n</i> -Amyl alcohol	$C_5H_{12}O$	36.2	13.3	14.5	12.8	Esters					
Isobutyl carbinol	$C_5H_{12}O$	36.2	13.3	14.5	12.8	Ethyl formate	$C_2H_6O_2$	28.7	13.0	12.6	9.8
Sec-butyl carbinol	$C_5H_{12}O$	36.2	13.3	14.5	12.8	<i>n</i> -Propyl formate	$C_4H_8O_2$	26.6	13.0	12.3	9.4
Methylpropylcarbinol	$C_5H_{12}O$	36.2	13.3	14.5	12.8	<i>n</i> -Butyl formate	$C_5H_{10}O_2$	23.9	13.2	12.0	8.8
Dimethylethylcarbinol	$C_5H_{12}O$	36.2	13.3	14.5	12.8	Methyl acetate	$C_3H_6O_2$	20.2	13.3	11.3	7.8
<i>n</i> -Hexyl alcohol	$C_6H_{14}O$	37.4	13.3	14.5	12.7	Ethyl acetate	$C_4H_8O_2$	23.9	13.2	12.0	8.8
Dimethylbutylalcohol	$C_6H_{14}O$	37.4	13.3	14.5	12.7	<i>n</i> -Propyl acetate	$C_5H_{10}O_2$	26.6	13.0	12.3	9.4
Ethylbutyl alcohol	$C_6H_{14}O$	37.4	13.3	14.5	12.7	<i>n</i> -Butyl acetate	$C_6H_{12}O_2$	28.7	13.0	12.6	9.8
Cyclohexanol	$C_6H_{12}O$	37.3	13.7	14.1	12.2	Isobutyl acetate	$C_6H_{12}O_2$	30.3	13.0	12.6	9.8
Benzyl alcohol	C_7H_8O	32.4	13.0	11.4	8.0	Amyl acetate	$C_7H_{14}O_2$	30.3	13.0	12.8	10.1
<i>n</i> -Heptyl alcohol	$C_7H_{16}O$	39.8	13.7	15.0	13.6	Cyclohexyl acetate	$C_8H_{14}O_2$	31.5	13.3	12.7	10.0
<i>n</i> -Octyl alcohol	$C_8H_{18}O$	40.6	13.7	15.0	13.6	Octyl acetate	$C_{10}H_{20}O_2$	33.6	12.9	13.1	10.6
<i>n</i> -Nonyl alcohol	$C_9H_{20}O$	40.3	13.4	14.7	13.0	Ethylacetooacetate	$C_6H_{10}O_3$	30.3	(17.6)	(14.9)	(13.5)
		Average	13.3	14.5	12.8	Methyl propionate	$C_4H_8O_2$	23.9	13.2	12.0	7.4
Aldehydes											
Formaldehyde	CH_2O	18.7	(17.5)	12.7	10.1	Ethyl propionate	$C_5H_{10}O_2$	26.6	13.0	12.3	9.4
Acetaldehyde	C_2H_4O	25.1	13.8	12.6	9.7	<i>n</i> -Butyl propionate	$C_7H_{14}O_2$	30.3	13.0	12.8	10.1
Butyraldehyde	C_4H_8O	33.8	13.9	13.9	11.7	Isobutyl propionate	$C_6H_{16}O_2$	31.6	12.9	12.9	10.3
Crotonaldehyde	C_4H_6O	34.8	15.2	13.8	11.8	Ethyl laurate	$C_14H_{28}O_2$	37.2	13.3	13.8	11.6
Benzaldehyde	C_7H_6O	32.4	13.4	11.2	7.5	Ethyl lactate	$C_5H_{10}O_3$	30.8	(18.9)	(16.5)	(16.0)
Ethyl hexaldehyde	$C_8H_{16}O$	39.4	13.7	12.7	9.9	Butyl lactate	$C_7H_{14}O_3$	33.3	(16.8)	(15.8)	(14.8)
		Average	14.2	13.3	10.6	Amyl lactate	$C_8H_{16}O_3$	34.3	(16.4)	(15.6)	(14.5)
Ketones											
Acetone	C_3H_6O	29.7	13.4	13.1	10.5	Ethyl benzoate	$C_9H_{10}O_2$	34.5	(15.4)	13.1	10.5
Methylethyl ketone	C_4H_8O	32.7	13.4	13.4	11.0	Ethyl carbonate	$C_5H_{10}O_3$	30.8	(18.9)	(16.5)	(16.0)
Diethyl ketone	$C_5H_{10}O$	33.7	12.9	13.2	10.7	Ethyl oxalate	$C_4H_6O_4$	28.7	(20.2)	(16.6)	(20.2)
Cyclohexanone	$C_6H_{10}O$	35.9	13.8	13.3	11.0	Ethyl malonate	$C_5H_8O_4$	32.2	(17.9)	(19.3)	(20.4)
Methyl butyl ketone	$C_6H_{12}O$	35.2	12.9	13.3	11.0			Average	13.0	12.5	9.7
Di-acetone alcohol	$C_6H_{12}O_2$	37.3	(16.9)	(16.4)	(15.7)	Others					
Dipropyl ketone	$C_8H_{14}O$	38.6	13.8	14.3	12.5	Camphor	$C_{10}H_{16}O$	38.8	13.7	13.4	11.1
Phenylbutyl ketone	$C_{11}H_{14}O$	34.8	12.6	11.6	(8.4)	Cresol	C_7H_8O	34.6	13.7	12.1	9.1
		Average	13.2	13.2	11.1	Resorcinol	$C_6H_6O_2$	26.0	13.7	10.8	5.9
						Acrolein	C_3H_4O	29.1	14.6	12.3	9.4

^aData from References 48 and 49. Numbers in parentheses not used for averaging.

Figure 3-4.22 shows a typical example of the heat release rate profile. The profile is for the chemical heat release rate of polypropylene, determined from the CDG and OC calorimetries in the ASTM E2058 fire propagation apparatus (500-kW scale). The polypropylene sample was 100 mm in diameter and 25 mm in thickness. It was exposed to an external heat flux of 50 kW/m² under co-flowing normal air. In the figure, solid, molten, and boiling-liquid zones are indicated.

In the solid zone in Figure 3-4.22, combustion is at the steady state between about 400 and 900 sec. During the

steady-state combustion, a very thin liquid film is present at the surface. In the molten zone, the thickness of the liquid film and chemical heat release rate increase rapidly during combustion. At the end of the zone, the entire sample is present as a liquid. In the boiling-liquid zone, the liquid boils vigorously, chemical heat release rate increases exponentially until the sample is consumed, the base diameter of the flame is considerably larger than the diameter of the sample dish (100 mm), and the flames are as high as 1.5 m (5 ft). This zone is the most dangerous zone.

Table 3-4.12 Net Heats of Complete Combustion per Unit Mass of Fuel and Oxygen Consumed and Carbon Dioxide and Carbon Monoxide Generated for Carbon-, Hydrogen-, Nitrogen-, and Sulfur-Containing Fuels^a

Fuel	Formula	ΔH_T (kJ/g)	ΔH_O^* (kJ/g)	$\Delta H_{CO_2}^*$ (kJ/g)	ΔH_{CO}^* (kJ/g)
C-H-N fuels					
Acrylonitrile	C_3H_3N	24.5	8.5	9.8	5.4
Diethylamine	$C_4H_{11}N$	38.0	11.2	15.8	14.8
n-Butylamine	$C_4H_{11}N$	38.0	11.2	15.8	14.8
sec-Butylamine	$C_4H_{11}N$	38.0	11.2	15.8	14.8
Pyridine	C_5H_9N	32.2	11.0	11.6	8.2
Aniline	C_6H_7N	33.8	11.2	11.9	8.7
Picoline	C_6H_7N	33.8	11.2	11.9	8.7
Triethylamine	$C_6H_{15}N$	39.6	11.6	15.2	13.8
Toluidine	C_7H_9N	34.9	11.3	12.1	9.1
Dimethylaniline	$C_8H_{11}N$	35.7	11.5	12.3	9.3
Di-n-butylamine	$C_8H_{19}N$	40.6	11.9	14.9	13.4
Quinoline	C_9H_7N	36.1	12.4	11.8	8.5
Quinaldine	$C_{10}H_9N$	36.7	12.4	11.9	8.7
Butylaniline	$C_{10}H_{15}N$	37.0	11.7	12.5	9.7
Tri-n-butylamine	$C_{12}H_{27}N$	41.6	12.1	14.6	12.9
		Average	11.5	15.4	14.1
C-H-S fuels					
Carbon disulfide	CS_2	13.6	10.8	(23.5)	(27.0)
Thiophene	C_4H_4S	31.9	14.0	15.2	14.0
Methylthiophene	C_5H_6S	33.2	13.6	14.8	13.2
Thiophenol	C_6H_6S	34.1	13.8	14.2	12.3
Hexyl mercaptan	$C_6H_{14}S$	33.0	11.6	14.8	13.2
Thiocresol	C_7H_8S	34.9	13.5	14.1	12.1
Heptyl mercaptan	$C_7H_{16}S$	33.7	11.6	14.4	12.7
Cresolmethylsulfide	$C_8H_{11}S$	36.2	13.4	15.9	15.0
Decylmercaptan	$C_{10}H_{22}S$	34.9	11.5	13.8	11.7
Dodecyl mercaptan	$C_{12}H_{26}S$	35.5	11.5	13.6	11.4
Hexyl sulfide	$C_{12}H_{26}S$	35.5	11.5	13.6	11.4
Heptyl sulfide	$C_{14}H_{30}S$	35.9	11.5	13.4	11.1
Octyl sulfide	$C_{16}H_{34}S$	36.3	11.5	13.3	10.9
Decyl sulfide	$C_{20}H_{42}S$	36.8	11.4	13.1	10.7
		Average	11.3	13.1	11.5

^aData from References 48 and 49. Numbers in parentheses not used for averaging.

The chemical heat release rate profiles from the CDG and OC calorimetries are very similar, as expected.

Energy released in a fire: The total amount of heat generated as a result of chemical reactions in the combustion of a material is defined as the chemical energy. The chemical energy has a convective and a radiative component:

$$E_{ch} = E_{con} + E_{rad} \quad (25)$$

where

E_{ch} = chemical energy (kJ)

E_{con} = convective energy (kJ)

E_{rad} = radiative energy (kJ)

The chemical energy and its convective and radiative components are calculated by the summation of the respective heat release rates:

$$E_i = A \sum_{n=t_{ig}}^{n=t_{ex}} \dot{Q}_i''(t_n) \Delta t_n \quad (26)$$

where

E_i = chemical, convective, or radiative energy (kJ)

A = total surface area of the material burning (m^2)

t_{ig} = the ignition time (s)

t_{ex} = flame extinction time (s)

The total mass of the material lost during combustion is measured directly from the initial and final mass and is calculated by the summation of the mass loss rate:

$$W_f = A \sum_{n=t_{ig}}^{n=t_{ex}} \dot{m}''(t_n) \Delta t_n \quad (27)$$

where W_f is the total mass of the material lost in the combustion (g).

Heat release rate can also be expressed as the product of the mass loss rate and the heat of combustion:

$$\dot{Q}_i'' = \Delta H_i \dot{m}'' \quad (28)$$

where ΔH_i is the chemical, convective, or radiative heat of combustion (kJ/g). The average chemical, convective, or radiative heats of combustion are calculated from the relationship based on Equations 26 and 27:

$$\bar{\Delta H}_i = \frac{E_i}{W_f} \quad (29)$$

where $\bar{\Delta H}_i$ is the average chemical, convective, or radiative heat of combustion (kJ/g). The average chemical heat of combustion determined in the cone calorimeter is defined as the effective heat of combustion.¹⁷⁻¹⁹

Heat release parameter (HRP): Heat release parameter (HRP) is defined as the amount of energy generated per unit amount of energy absorbed. From Equations 11 and 28,

$$\dot{Q}_i'' = \left(\frac{\Delta H_i}{\Delta H_g} \right) (\dot{q}_e'' + \dot{q}_f'' - \dot{q}_{rr}'') \quad (30)$$

where $\Delta H_i/\Delta H_g$ is defined as the chemical, convective, or radiative HRP, $(HRP)_{ch}$, $(HRP)_{con}$, or $(HRP)_{rad}$, respectively.⁴ The HRP values are characteristic fire properties of materials, but depend on fire ventilation. The chemical HRP is independent of fire size.

In Figure 3-4.22, the theoretical prediction is from Equation 30, with chemical $HRP = 19$, external heat flux = 50 kW/m², and surface re-radiation = 18 kW/m² with negligibly small flame heat flux. The theoretical prediction is very close to the measured value in the solid zone.

Experimental data support Equation 30, as shown in Figures 3-4.23 through 3-4.25, where the average peak or steady-state chemical heat release rates are plotted against

Table 3-4.13 Net Heats of Complete Combustion per Unit Mass of Fuel and Oxygen Consumed and Carbon Dioxide and Carbon Monoxide Generated for Polymeric Materials^a

Fuel	Formula ^b	ΔH_T^c (kJ/g)	ΔH_O^* (kJ/g)	$\Delta H_{CO_2}^*$ (kJ/g)	ΔH_{CO}^* (kJ/g)	Fuel	Formula ^b	ΔH_T^c (kJ/g)	ΔH_O^* (kJ/g)	$\Delta H_{CO_2}^*$ (kJ/g)	ΔH_{CO}^* (kJ/g)						
Carbon-hydrogen atoms in the structure																	
Polyethylene	CH ₂	43.6	12.8	13.9	11.8	Carbon-hydrogen-oxygen-nitrogen atoms in the structure (continued)											
Polypropylene	CH	43.4	12.7	13.8	11.7	<i>Rigid polyurethane foams</i>											
Polyisobutylene	CH ₂	43.7	12.7	13.9	11.9	GM29	CH _{1.1} O _{0.23} N _{0.10}	26.0	12.6	10.7	6.8						
Polybutadiene	CH _{1.5}	42.8	13.1	13.1	10.7	GM31	CH _{1.2} O _{0.22} N _{0.10}	25.0	11.9	10.2	6.1						
Polystyrene	CH	39.2	12.7	12.2	9.2	GM37	CH _{1.2} O _{0.20} N _{0.08}	28.0	12.7	11.2	7.5						
<i>Expanded polystyrene</i>																	
GM47	CH _{1.1}	38.1	12.4	11.3	7.7	<i>Rigid polyisocyanurate foams</i>											
GM49	CH _{1.1}	38.1	12.4	11.3	7.7	GM41	CH _{1.0} O _{0.19} N _{0.11}	26.2	12.5	10.4	6.4						
GM51	CH	35.6	11.6	10.8	7.0	GM43	CH _{0.93} O _{0.20} N _{0.11}	22.2	10.8	8.9	(4.0)						
GM53	CH _{1.1}	37.6	12.4	11.3	7.7	Average											
		Average	12.5	12.4	9.5												7.2
Carbon-hydrogen-oxygen-nitrogen atoms in the structure																	
Polyoxy-						Carbon-hydrogen-chlorine atoms in the structure											
methylene	CH ₂ O	15.4	14.4	10.5	6.6	<i>Polyethylene with</i>											
Polymethyl-						25% chlorine	CH _{1.9} Cl _{0.13}	31.6	12.7	13.4	10.8						
methacrylate	CH _{1.6} O _{0.4}	25.2	13.1	11.5	8.0	36% chlorine	CH _{1.8} Cl _{0.22}	26.3	12.8	12.9	10.2						
Polyester	CH _{1.4} O _{0.22}	32.5	13.9	12.5	9.6	48% chlorine	CH _{1.7} Cl _{0.36}	20.6	12.8	12.3	9.4						
Epoxy	CH _{1.3} O _{0.20}	28.8	12.1	10.8	6.9	Polychloroprene	CH _{1.3} Cl _{0.30}	25.3	13.3	12.7	9.5						
Polycarbonate	CH _{0.88} O _{0.19}	29.7	13.1	10.7	6.9	Polyvinylchloride	CH _{1.5} Cl _{0.50}	16.4	11.7	11.7	8.2						
Cellulose						Polyvinyl-	idenechloride	CHCl	9.0	13.5	9.8	(5.5)					
triacetate	CH _{1.3} O _{0.67}	17.6	13.3	9.6	5.1	Average											
Polyethylene-						Carbon-hydrogen-fluorine atoms in the structure^d											
terephthalate	CH _{0.80} O _{0.40}	22.0	13.2	9.6	5.1	Teflon TFE	CF ₂	6.2	9.7	(7.1)	(1.1)						
Rigid phenolic						Teflon FEP	CF _{1.8}	4.8	(6.9)	(5.0)	(0)						
foam	CH _{1.1} O _{0.24}	36.4	(16.8)	(14.0)	(12.0)	Tefzel ETFE	CHF	12.6	12.6	9.2	(4.4)						
Polyacrylonitrile						Teflon PFA	CF _{1.7} O _{0.01}	5.0	(8.0)	(5.3)	(0)						
(PAN)	CHN _{0.33}	30.8	10.7	12.3	9.4	Kel-F (CTFE)	CF _{1.5} Cl _{0.50}	6.5	11.8	8.6	(3.5)						
Red Oak	CH _{1.7} O _{0.72} N _{0.001}	17.1	13.2	10.2	5.0	Halar (E-CTFE)	CHF _{0.75} Cl _{0.25}	12.0	9.8	9.8	(5.4)						
Douglas Fir	CH _{1.7} O _{0.74} N _{0.002}	16.4	12.4	9.5	5.0	Kynar (PVF ₂)	CHF	13.3	12.4	9.1	(4.2)						
Nylon	CH _{1.8} O _{0.17} N _{0.17}	30.8	11.9	13.3	10.8	Tedlar (PVF)	CH _{1.5} F _{0.50}	13.5	(6.5)	(7.1)	(1.1)						
<i>Flexible polyurethane foams</i>																	
GM21	CH _{1.8} O _{0.30} N _{0.05}	26.2	12.1	11.5	8.0	Carbon-hydrogen-oxygen-silicone atoms in the structure											
GM23	CH _{1.8} O _{0.35} N _{0.06}	27.2	13.7	12.5	9.7	Silicone-1	CH _{1.3} O _{0.25} Si _{0.18}	21.7	12.6	11.0	7.4						
GM25	CH _{1.7} O _{0.32} N _{0.07}	24.6	12.0	11.1	7.5	Silicone-2	CH _{1.5} O _{0.30} Si _{0.26}	21.3	13.9	12.4	9.4						
GM27	CH _{1.7} O _{0.03} N _{0.08}	23.2	11.2	10.4	6.2	Silicone-3	CH ₃ O _{0.50} Si _{0.50}	25.1	14.5	21.0	23.0						

^aFrom the data measured in the FMRC Flammability Laboratory.^bFrom the data for the elemental composition of the polymeric materials measured in the FMRC Flammability Laboratory.^cFrom the data measured by the FMRC Flammability Laboratory in the oxygen bomb calorimeter and corrected for water as a gas and for the residue.^dTrade names from Reference 50.

the net heat flux. Linear relationship between the chemical heat release rate and net heat flux is satisfied. For the condition $\dot{q}_e'' \gg \dot{q}_f'' - \dot{q}_{rr}''$, the average value of the HRP is calculated from the summation of the heat release rate and the external heat flux:

$$\overline{(HRP)}_i = \frac{E_i}{A \sum_{n=t_{ig}}^{n=t_{ex}} \dot{q}_e'' \Delta t_n} \quad (31)$$

Complete and incomplete combustion: In fires, combustion is never complete. Thus, the chemical heat release rate or the chemical heat of combustion is less than the heat release rate for complete combustion or the net heat of complete combustion. The ratio of the chemical heat re-

lease rate to the heat release rate for complete combustion or the ratio of the chemical heat of combustion to net heat of complete combustion is defined as combustion efficiency:^{2-4,16,41,44}

$$\chi_{ch} = \frac{\dot{Q}_{ch}''}{\dot{Q}_T''} = \frac{\dot{m}'' \Delta H_{ch}}{\dot{m}'' \Delta H_T} = \frac{\Delta H_{ch}}{\Delta H_T} \quad (32)$$

where χ_{ch} is the combustion efficiency and \dot{Q}_T'' is the heat release rate for complete combustion (kW/m²). The convective and radiative components of the combustion efficiency are defined in a similar fashion:^{2-4,16,41,44}

$$\chi_{con} = \frac{\dot{Q}_{con}''}{\dot{Q}_T''} = \frac{\dot{m}'' \Delta H_{con}}{\dot{m}'' \Delta H_T} = \frac{\Delta H_{con}}{\Delta H_T} \quad (33)$$

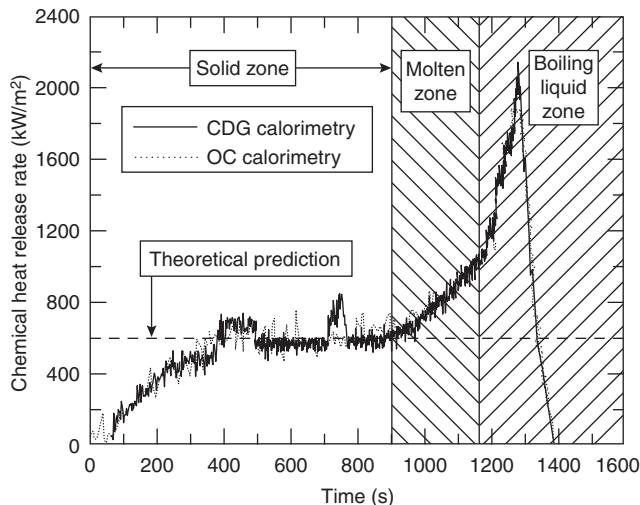


Figure 3-4.22. Chemical heat release rate for 100-mm diameter and 25-mm-thick slab of polypropylene exposed to an external heat flux of 50 kW/m² and 0.09 m/s co-flowing normal air in the ASTM E2058 fire propagation apparatus. The theoretical prediction is based on the heat release parameter for polypropylene listed in Table 3-4.15.

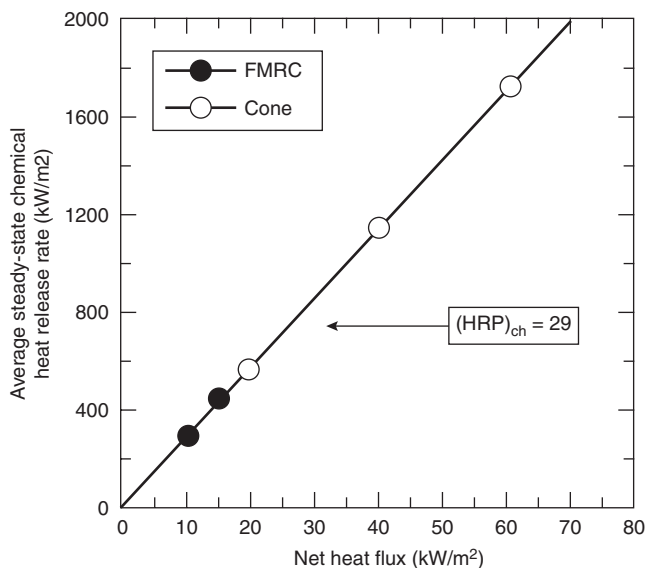


Figure 3-4.23. Average steady-state chemical heat release rate versus net heat flux for polystyrene slab. Net heat flux is the sum of the external and flame heat flux minus the surface re-radiation.

$$\chi_{\text{rad}} = \frac{\dot{Q}_{\text{rad}}''}{\dot{Q}_T''} = \frac{\dot{m}'' \Delta H_{\text{rad}}}{\dot{m}'' \Delta H_T} = \frac{\Delta H_{\text{rad}}}{\Delta H_T} \quad (34)$$

where χ_{con} is the convective component of the combustion efficiency and χ_{rad} is the radiative component of the combustion efficiency. From the definitions,

$$\Delta H_{\text{ch}} = \Delta H_{\text{con}} + \Delta H_{\text{rad}} \quad (35)$$

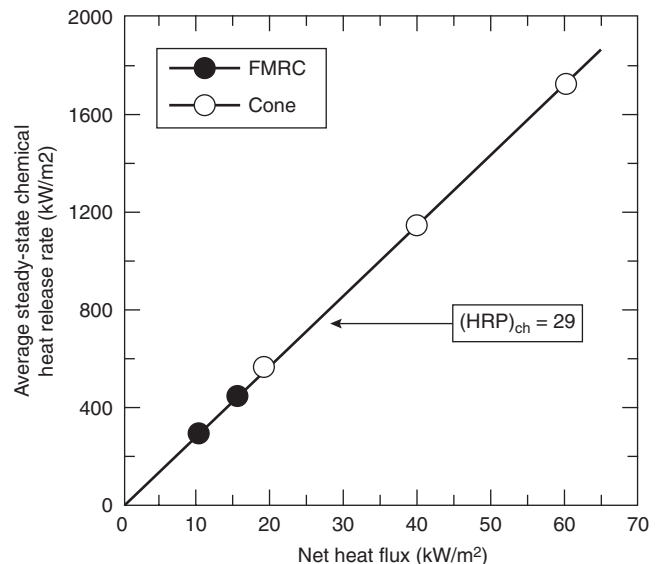


Figure 3-4.24. Average steady-state chemical heat release rate versus the net heat flux for high molecular weight hydrocarbon liquid burning in a 100-mm-diameter dish. The cone calorimeter data were measured at the research laboratory of the Dow-Corning Corporation, Midland, Michigan. Net heat flux is the sum of the external and flame heat flux minus the surface re-radiation.

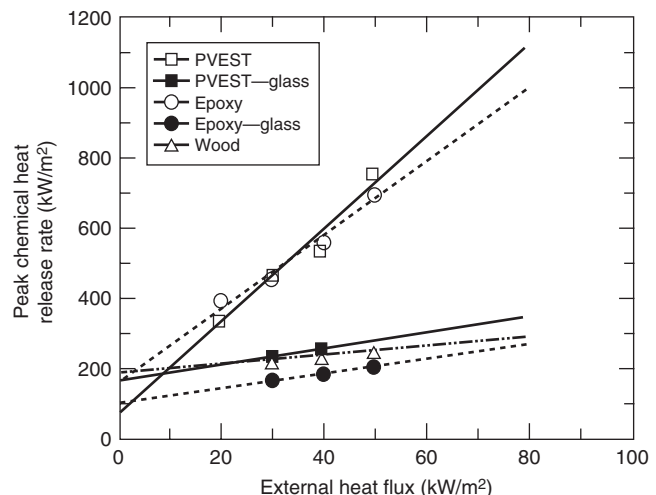


Figure 3-4.25. Peak chemical heat release rate versus the external heat flux for 100- x 100-mm x 3- to 11-mm-thick slab of polyvinyl ester (PVEST), PVEST/fiberglass, epoxy, epoxy/fiberglass, and wood (hemlock). Data measured in the cone calorimeter as reported in Reference 20 are shown.

$$\chi_{\text{ch}} = \chi_{\text{con}} + \chi_{\text{rad}} \quad (36)$$

The chemical, convective, and radiative heat release rates, heats of combustion, and combustion efficiencies depend on the chemical structures of the materials and fire ventilation. The distribution of the chemical heat into convec-

tive and radiative components changes with fire size. The larger the fire size, the larger the fraction of the chemical heat distributed into the radiative component.

The chemical, convective, and radiative heats of combustion and the HRP values for the well-ventilated fires are listed in Tables 3-4.14 and 3-4.15, respectively. Comparisons between the limited data from the OSU apparatus, ASTM E2058 fire propagation apparatus, and cone calorimeter are satisfactory.

EXAMPLE 10:

Heptane was burned in a 2-m-diameter pan, and measurements were made for the mass loss rate, mass generation rates of CO and CO₂, and mass consumption rate of O₂. The average values in g/m²·s for the mass loss rate, mass generation rates of CO and CO₂, and mass consumption rate of O₂ were 66, 9, 181, and 216 respectively. For large-scale fires of heptane, the literature values are $\chi_{ch} = 0.93$, $\chi_{con} = 0.59$, and $\chi_{rad} = 0.34$. The net heat of complete combustion for heptane reported in the literature is 44.6 kJ/g. Calculate the chemical heat release rate and show that it is consistent with the rate based on the literature value of the combustion efficiency. Also calculate the convective and radiative heat release rates.

SOLUTION:

From Table 3-4.10, the net heat of complete combustion per unit mass of oxygen consumed is 12.7 kJ/g; the net heat of complete combustion per unit mass of CO₂ generated is 14.5 kJ/g; and the net heat of complete combustion per unit mass of CO generated is 12.8 kJ/g. From the CDG calorimetry (Equation 18),

$$\begin{aligned}\dot{Q}_{ch}'' &= 14.5 \times 181 + 12.8 \times 9 \\ &= 2625 + 115 = 2740 \text{ kW/m}^2\end{aligned}$$

From OC calorimetry (Equation 21),

$$\dot{Q}_{ch}'' = 12.7 \times 216 = 2743 \text{ kW/m}^2$$

The chemical heat release rate from the CDG and OC calorimetries are in excellent agreement, the average being 2742 kW/m².

The chemical heat of combustion is the product of net heat of complete combustion (44.6 kJ/g) and the combustion efficiency (0.93), which is 41.5 kJ/g.

The chemical heat release is the product of the mass loss rate (66 g/m²·s) and chemical heat of combustion (41.5 kJ/g), which is 2739 kW/m², compared to the averaged value 2742 kW/m² from the CDG and OC calorimetries. Thus, the chemical heat release determined from the measurements is consistent with the rate from the literature value of the combustion efficiency.

The convective heat release rate is equal to the convective heat of combustion and the mass loss rate. The convective heat of combustion is equal to the convective component of the combustion efficiency ($\chi_{con} = 0.59$) times the net of complete combustion (44.6 kJ/g). Thus, the convective heat release rate for heptane is $66 \times 0.59 \times 44.6 = 1737 \text{ kW/m}^2$. In a similar fashion, the radiative heat release rate is $66 \times 0.34 \times 44.6 = 1001 \text{ kW/m}^2$.

EXAMPLE 11:

From the flame radiation scaling technique, the asymptotic mass loss rate values in g/m²·s expected in large-scale fires, as listed in Table 3-4.8, for polyethylene, polystyrene, polyvinylchloride, and Teflon are 26, 36, 16, and 7, respectively. The chemical heats of combustion in kJ/g listed in Table 3-4.14 for these materials are 38.4, 27.0, 5.7, and 4.1, respectively. Estimate the chemical heat release rates expected in large-scale fires of polyethylene, polystyrene, polyvinylchloride, and Teflon. (In this chapter Teflon refers mainly to FEP, except in cases where it is identified otherwise.)

SOLUTION:

The chemical heat release rate is calculated from Equation 28. The chemical heat release rates estimated in the large-scale fires are (1) polyethylene: $26 \times 38.4 = 998 \text{ kW/m}^2$; (2) polystyrene: $36 \times 27.0 = 972 \text{ kW/m}^2$; (3) polyvinylchloride: $16 \times 5.7 = 91 \text{ kW/m}^2$; and (4) Teflon: $7 \times 4.1 = 28 \text{ kW/m}^2$.

EXAMPLE 12:

Heat release rate is the product of the HRP and the net heat flux absorbed by the material, as indicated in Equation 30. This concept is used in various models to predict fire propagation and heat release rates, whereas values for the HRP are taken from a handbook such as this handbook, and net heat flux is estimated through correlations. The lower the value of the HRP for a fixed value of the net heat flux, the lower the heat release rate.

The values for the surface re-radiation, flame heat flux for large-scale fires, and chemical HRP are listed in Tables 3-4.7, 3-4.8, and 3-4.15, respectively. Calculate the chemical heat release rates expected in large-scale fires of heptane, kerosene, polyethylene, polypropylene, polystyrene, polymethylmethacrylate, polyvinylchloride, and Teflon.

SOLUTION:

The chemical heat release rates are calculated from the relationship $[(HRP)_{ch} \times (\dot{q}_f'' - \dot{q}_{rr}'')]$, which is Equation 30:

1. heptane: $(75)(37 - 1) = 2700 \text{ kW/m}^2$
2. kerosene: $(47)(29 - 1) = 1316 \text{ kW/m}^2$
3. polyethylene: $(17)(61 - 15) = 782 \text{ kW/m}^2$
4. polypropylene: $(19)(67 - 15) = 988 \text{ kW/m}^2$
5. polystyrene: $(16)(75 - 13) = 992 \text{ kW/m}^2$
6. polymethylmethacrylate: $(15)(57 - 11) = 690 \text{ kW/m}^2$
7. polyvinylchloride: $(2)(50 - 15) = 70 \text{ kW/m}^2$
8. Teflon: $(2)(52 - 38) = 28 \text{ kW/m}^2$

The example shows the importance of the chemical HRP, flame heat flux, and surface re-radiation.

Heat release rate and fire ventilation: In the majority of fires, hazards are due to fires occurring in enclosed spaces. In early stages, a building fire is well-ventilated and is easy to control and extinguish. However, if the fire is allowed to grow, especially with limited enclosure ventilation and large material surface area, it becomes a ventilation-controlled fire and can lead to flashover, a very dangerous condition. In ventilation-controlled fires, the chemical reactions between oxygen from air and products of incomplete combustion from the decomposed and

Table 3-4.14 Yields of Fire Products and Chemical, Convective, and Radiative Heats of Combustion for Well-Ventilated Fires^a

Material	ΔH_T (kJ/g)	y_{CO_2}	y_{CO}	y_{ch}	y_s	ΔH_{ch}	ΔH_{con}	ΔH_{rad}
				(g/g)			(kJ/g)	
<i>Common gases</i>								
Methane	50.1	2.72	—	—	—	49.6	42.6	7.0
Ethane	47.1	2.85	0.001	0.001	0.013	45.7	34.1	11.6
Propane	46.0	2.85	0.005	0.001	0.024	43.7	31.2	12.5
Butane	45.4	2.85	0.007	0.003	0.029	42.6	29.6	13.0
Ethylene	48.0	2.72	0.013	0.005	0.043	41.5	27.3	14.2
Propylene	46.4	2.74	0.017	0.006	0.095	40.5	25.6	14.9
1,3-Butadiene	44.6	2.46	0.048	0.014	0.125	33.6	15.4	18.2
Acetylene	47.8	2.60	0.042	0.013	0.096	36.7	18.7	18.0
<i>Common liquids</i>								
Methyl alcohol	20.0	1.31	0.001	—	—	19.1	16.1	3.0
Ethyl alcohol	27.7	1.77	0.001	0.001	0.008	25.6	19.0	6.5
Isopropyl alcohol	31.8	2.01	0.003	0.001	0.015	29.0	20.6	8.5
Acetone	29.7	2.14	0.003	0.001	0.014	27.9	20.3	7.6
Methylethyl ketone	32.7	2.29	0.004	0.001	0.018	30.6	22.1	8.6
Heptane	44.6	2.85	0.010	0.004	0.037	41.2	27.6	13.6
Octane	44.5	2.84	0.011	0.004	0.038	41.0	27.3	13.7
Kerosene	44.1	2.83	0.012	0.004	0.042	40.3	26.2	14.1
Benzene	40.1	2.33	0.067	0.018	0.181	27.6	11.0	16.5
Toluene	39.7	2.34	0.066	0.018	0.178	27.7	11.2	16.5
Styrene	39.4	2.35	0.065	0.019	0.177	27.8	11.2	16.6
Hydrocarbon	43.9	2.64	0.019	0.007	0.059	36.9	24.5	12.4
Mineral oil	41.5	2.37	0.041	0.012	0.097	31.7	—	—
Polydimethyl siloxane	25.1	0.93	0.004	0.032	0.232	19.6	—	—
Silicone	25.1	0.72	0.006	0.008	—	15.2	12.7	2.5
<i>Chemicals and solvents</i>								
Tetrahydrofuran (C_4H_8O)	32.2	2.29	0.021	—	—	30.3	—	—
Phenol (C_6H_6O)	31.0	2.63	0.057	—	0.099	27.6	13.3	14.3
Acetonitrile (C_2H_3N)	29.6	2.04	0.025	—	0.026	29.0	23.0	6.0
Ethylisonicotate ($C_8H_9O_2N$)	26.3	2.37	0.029	—	0.142	24.3	12.8	11.5
Adiponitrile ($C_6H_8N_2$)	33.1	2.35	0.045	—	0.045	31.1	22.1	9.0
Hexamethylenediamine ($C_6H_{16}N_2$)	35.3	2.28	0.029	—	0.045	32.6	15.7	16.9
Toluenediisocyanate ($C_9H_6O_2N_2$)	23.6	1.77	0.052	—	0.141	19.3	11.1	8.2
Diphenylmethanediisocyanate MDI ($C_{15}H_{10}O_2N_2$)	27.1	0.95	0.042	—	0.154	19.6	13.7	5.9
Polymeric MDI ($C_{23}H_{19}O_3N_3$)	29.6	1.22	0.032	—	0.165	23.3	15.0	8.3
Isoproturon ($C_{12}H_{18}ON_2$)	32.8	1.70	0.056	—	0.115	23.9	14.0	9.9
3 Chloropropene (C_3H_5Cl)	23.0	0.75	0.076	—	0.179	10.8	6.9	3.9
Monochlorobenzene (C_6H_5Cl)	26.4	0.86	0.083	—	0.232	11.2	—	—
Dichloromethane (CH_2Cl_2)	6.0	0.11	0.088	—	0.081	2.0	—	—
1,3 Dichloropropene ($C_3H_4Cl_2$)	14.2	0.35	0.090	—	0.169	5.6	—	—
Ethylmonochloroacetate ($C_4H_7O_2Cl$)	15.7	1.24	0.019	—	0.138	14.1	10.1	4.0
Chloronitrobenzoic acid ($C_7H_4O_4NCl$)	15.9	0.39	0.057	—	—	4.4	—	—
Aclonifen ($C_{12}H_9O_3N_2Cl$)	19.7	0.68	0.063	—	0.186	7.0	—	—
2,6 Dichlorobenzonitrile (dichlobenil) ($C_7H_3NCl_2$)	17.8	0.39	0.068	—	—	4.3	—	—
Diuron ($C_9H_{10}ON_2Cl_2$)	20.3	0.76	0.080	—	0.159	10.2	7.7	2.5
Trifluoromethylbenzene ($C_6H_5CF_3$)	18.7	1.19	0.069	—	0.185	10.8	5.1	5.7
Metatrifluoromethylphenylacetonitrile ($C_9H_6NF_3$)	16.0	0.89	0.058	—	0.168	7.3	4.0	3.3
Tetramethylthiurammonosulfide ($C_6H_{12}N_2S_3$)	22.6	1.06	0.041	—	—	19.6	—	—
Methylthiopropionaldehyde (C_4H_8OS)	25.0	1.62	0.001	—	0.005	23.8	18.8	5.0
<i>Pesticides</i>								
2,4 D acid (Herbicide, $C_8H_6O_3Cl_2$)	11.5	0.50	0.074	—	0.163	4.5	3.0	1.5
Mancozeb ($C_4H_6N_2S_4Mn_1Zn_0.4$)	14.0	0.50	—	—	—	9.5	—	—
Folpel ($C_9H_4O_2NSCl_3$)	9.1	0.37	0.072	—	0.205	3.6	—	—
Chlорfenvinphos ($C_{12}H_{24}O_4Cl_3P$)	18.0	0.43	0.011	—	0.288	7.7	—	—
Chlormephos ($C_5H_{12}O_2S_2ClP$)	19.1	0.51	0.075	—	0.055	13.9	—	—

(continued)

Table 3-4.14 Yields of Fire Products and Chemical, Convective, and Radiative Heats of Combustion for Well-Ventilated Fires^a (Continued)

Material	ΔH_T (kJ/g)	y_{CO_2}	y_{CO}	y_{ch} (g/g)	y_s	ΔH_{ch}	ΔH_{con}	ΔH_{rad}
<i>Natural materials</i>								
Tissue paper	—	—	—	—	—	11.4	6.7	4.7
Newspaper	—	—	—	—	—	14.4	—	—
Wood (red oak)	17.1	1.27	0.004	0.001	0.015	12.4	7.8	4.6
Wood (Douglas fir)	16.4	1.31	0.004	0.001	—	13.0	8.1	4.9
Wood (pine)	17.9	1.33	0.005	0.001	—	12.4	8.7	3.7
Corrugated paper	—	—	—	—	—	13.2	—	—
Wood (hemlock) ^b	—	—	—	—	0.015	13.3	—	—
Wool 100% ^b	—	—	—	—	0.008	19.5	—	—
<i>Synthetic materials—solids</i> (abbreviations/names in the nomenclature)								
ABS ^b	—	—	—	—	0.105	30.0	—	—
POM	15.4	1.40	0.001	0.001	—	14.4	11.2	3.2
PMMA	25.2	2.12	0.010	0.001	0.022	24.2	16.6	7.6
PE	43.6	2.76	0.024	0.007	0.060	38.4	21.8	16.6
PP	43.4	2.79	0.024	0.006	0.059	38.6	22.6	0
PS	39.2	2.33	0.060	0.014	0.164	27.0	11.0	16.0
Silicone	21.7	0.96	0.021	0.006	0.065	10.6	7.3	3.3
Polyester-1	32.5	1.65	0.070	0.020	0.091	20.6	10.8	9.8
Polyester-2	32.5	1.56	0.080	0.029	0.089	19.5	—	—
Epoxy-1	28.8	1.59	0.080	0.030	—	17.1	8.5	8.6
Epoxy-2	28.8	1.16	0.086	0.026	0.098	12.3	—	—
Nylon	30.8	2.06	0.038	0.016	0.075	27.1	16.3	10.8
Polyamide-6 ^b	—	—	—	—	0.011	28.8	—	—
IPST ^b	—	—	—	—	0.080	23.3	—	—
PVEST ^b	—	—	—	—	0.076	22.0	—	—
Silicone rubber	21.7	0.96	0.021	0.005	0.078	10.9	—	—
Polyetheretherketone (PEEK-CH _{0.63} O _{0.16})	31.3	1.6	0.029	—	0.008	17.5	—	—
Polysulfone (PSO-CH _{0.81} O _{0.15} S _{0.04})	29.0	1.8	0.034	—	0.020	24.3	—	—
Polyethersulfone (PES-CH _{0.67} O _{0.21} S _{0.08})	25.2	1.5	0.040	—	0.021	20.4	—	—
Polyetherimide (PEI-CH _{0.68} N _{0.05} O _{0.14})	30.1	2.0	0.026	—	0.014	27.2	—	—
Polycarbonate (PC-CH _{0.88} O _{0.13})	31.6	1.5	0.054	—	0.112	18.4	—	—
<i>Polyurethane (flexible) foams</i>								
GM21	26.2	1.55	0.010	0.002	0.131	17.8	8.6	9.2
GM23	27.2	1.51	0.031	0.005	0.227	19.0	10.3	8.7
GM25	24.6	1.50	0.028	0.005	0.194	17.0	7.2	9.8
GM27	23.2	1.57	0.042	0.004	0.198	16.4	7.6	8.8
<i>Polyurethane (rigid) foams</i>								
GM29	26.0	1.52	0.031	0.003	0.130	16.4	6.8	9.6
GM31	25.0	1.53	0.038	0.002	0.125	15.8	7.1	8.8
GM35	28.0	1.58	0.025	0.001	0.104	17.6	7.8	9.8
GM37	28.0	1.63	0.024	0.001	0.113	17.9	8.7	9.2
GM41	26.2	1.18	0.046	0.004	—	15.7	5.7	10.0
GM43	22.2	1.11	0.051	0.004	—	14.8	6.4	8.4
<i>Polystyrene foams</i>								
GM47	38.1	2.30	0.060	0.014	0.180	25.9	11.4	14.5
GM49	38.2	2.30	0.065	0.016	0.210	25.6	9.9	15.7
GM51	35.6	2.34	0.058	0.013	0.185	24.6	10.4	14.2
GM53	37.6	2.34	0.060	0.015	0.200	25.9	11.2	14.7
<i>Polyethylene foams</i>								
1	41.2	2.62	0.020	0.004	0.056	34.4	20.2	14.2
2	40.8	2.78	0.026	0.008	0.102	36.1	20.6	15.5
3	40.8	2.60	0.020	0.004	0.076	33.8	18.2	15.6
4	40.8	2.51	0.015	0.005	0.071	32.6	19.1	13.5

Table 3-4.14 Yields of Fire Products and Chemical, Convective, and Radiative Heats of Combustion for Well-Ventilated Fires^a (Continued)

Material	ΔH_T (kJ/g)	y_{CO_2}	y_{CO}	y_{ch}	y_s	ΔH_{ch}	ΔH_{con}	ΔH_{rad}
				(g/g)			(kJ/g)	
<i>Phenolic foams</i>								
1 ^b	—	—	—	—	0.002	10.0	—	—
2 ^b	—	—	—	—	—	10.0	—	—
<i>Halogenated materials (abbreviations/names in the nomenclature)</i>								
Polyethylene with								
25% chlorine	31.6	1.71	0.042	0.016	0.115	22.6	10.0	12.6
36% chlorine	26.3	0.83	0.051	0.017	0.139	10.6	6.4	4.2
48% chlorine	20.6	0.59	0.049	0.015	0.134	7.2	3.9	3.3
PVC	16.4	0.46	0.063	0.023	0.172	5.7	3.1	2.6
PVC-1 ^b (LOI = 0.50)	—	—	—	—	0.098	7.7	—	—
PVC-2 ^b (LOI = 0.50)	—	—	—	—	0.076	8.3	—	—
PVC ^b (LOI = 0.20)	—	—	—	—	9.099	11.3	—	—
PVC ^b (LOI = 0.25)	—	—	—	—	0.078	9.8	—	—
PVC ^b (LOI = 0.30)	—	—	—	—	0.098	10.3	—	—
PVC (LOI = 0.35)	—	—	—	—	0.088	10.8	—	—
PVC panel	—	—	—	—	—	7.3	—	—
CPVC (CH _{1.3} Cl _{0.70})	12.8	0.48	0.052	—	0.043	4.4	—	—
PVDF (CHF)	13.3	0.53	0.055	—	0.037	3.8	—	—
ECTFE (CHF _{0.75} Cl _{0.25})	12.0	0.41	0.095	—	0.038	4.6	—	—
ETFE (Tefzel, CHF)	12.6	0.78	0.035	—	0.028	7.3	—	—
PFA (Teflon, CF _{1.6} O _{0.01})	5.0	0.42	0.099	—	0.002	2.2	—	—
FEP (Teflon, CF _{1.8})	4.8	0.25	0.116	—	0.003	1.3	—	—
TFE (Teflon, CF _{1.8})	6.2	0.38	0.092	—	0.003	2.0	—	—
<i>Building products^c</i>								
Particleboard (PB)	—	1.2	0.004	—	—	14.0	—	—
Fiberboard (FB)	—	1.4	0.015	—	—	14.0	—	—
Medium-density FB	—	1.2	0.002	—	—	14.0	—	—
Wood panel	—	1.2	0.002	—	—	15.0	—	—
Melamine-faced PB	—	0.8	0.025	—	—	10.7	—	—
Gypsumboard (GB)	—	0.3	0.027	—	—	4.3	—	—
Paper on GB	—	0.4	0.028	—	—	5.6	—	—
Plastic on GB	—	0.4	0.028	—	—	14.3	—	—
Textile on GB	—	0.4	0.025	—	—	13.0	—	—
Textile on rock wool	—	1.8	0.091	—	—	25.0	—	—
Paper on PB	—	1.2	0.003	—	—	12.5	—	—
Rigid PU	—	1.1	0.200	—	—	13.0	—	—
EPS	—	1.9	0.054	—	—	28.0	—	—
<i>Composite and fiberglass-reinforced materials (FGR) (abbreviations/names in the nomenclature)</i>								
PEEK/FGR ^b	—	—	—	—	0.042	20.5	—	—
IPST/FGR ^b	—	—	—	—	0.032	27.0	—	—
PES/FGR ^b	—	—	—	—	0.049	27.5	—	—
PEST1/FGR ^b	—	—	—	—	—	16.0	—	—
PEST2/FGR ^b	—	—	—	—	—	12.9	—	—
PEST1/FGR	—	—	—	—	—	19.0	—	—
PEST2/FGR	—	—	—	—	—	13.9	—	—
PEST3/FGR	—	1.47	0.055	0.007	0.070	17.9	10.7	7.2
PEST4/FGR	—	1.24	0.039	0.004	0.054	16.0	9.9	6.1
PEST5/FGR	—	0.71	0.102	0.019	0.068	9.3	6.5	2.8
Epoxy/FG ^b	—	—	—	—	0.056	27.5	—	—
PVEST/FGR	—	—	—	—	0.079	26.0	—	—
Kevlar/Phenolic	—	1.27	0.025	0.002	0.041	14.8	11.1	3.7
Phenolic-1/FGR	—	0.98	0.066	0.003	0.023	11.9	8.9	3.0
Phenolic-2/FGR ^b	—	—	—	—	0.016	22.0	—	—

(continued)

Table 3-4.14 Yields of Fire Products and Chemical, Convective, and Radiative Heats of Combustion for Well-Ventilated Fires^a (Continued)

Material	ΔH_T (kJ/g)	y_{CO_2}	y_{CO}	y_{ch}	y_s	ΔH_{ch}	ΔH_{con}	ΔH_{rad}
		(g/g)					(kJ/g)	
<i>Aircraft panel materials</i>								
Epoxy/FGR/paint	—	0.828	0.114	0.016	0.166	11.3	6.2	5.1
Epoxy/Kevlar/paint	—	0.873	0.091	0.016	0.126	11.4	6.3	5.1
Phenolic/FGR/paint	—	1.49	0.027	0.002	0.059	22.9	11.5	11.4
Phenolic/Kevlar/paint	—	1.23	0.088	0.011	0.094	18.6	8.9	9.7
Phenolic/graphite/paint	—	1.67	0.026	0.003	0.062	24.6	14.0	10.6
Polycarbonate	—	—	—	—	—	20.5	—	—
<i>Electric cables (abbreviations/names in the nomenclature)</i>								
<i>Polyethylene/Polyvinylchloride</i>								
1	—	2.08	0.100	0.021	0.076	31.3	11.6	19.7
2	—	1.75	0.050	0.013	0.115	25.1	11.1	14.0
3	—	1.67	0.048	0.012	—	24.0	13.0	11.0
4	—	1.39	0.166	0.038	—	22.0	14.0	8.1
5	—	1.29	0.147	0.042	0.136	20.9	10.7	10.2
<i>EPR/Hypalon</i>								
1	—	1.95	0.072	0.014	—	29.6	15.8	13.9
2	—	1.74	0.076	0.022	—	26.8	17.0	9.8
3	—	1.21	0.072	0.014	—	19.0	12.3	6.7
4	—	0.99	0.090	0.085	0.082	17.4	6.6	10.8
5	—	0.95	0.122	0.024	—	17.3	7.5	9.8
6	—	0.89	0.121	0.022	0.164	13.9	9.2	4.7
<i>Silicone</i>								
1	—	1.65	0.011	0.001	—	25.0	17.5	7.3
2	—	1.47	0.029	0.001	—	24.0	20.0	4.0
<i>XLPE/XLPE</i>								
1	—	1.78	0.114	0.029	0.120	28.3	12.3	16.0
2	—	0.83	0.110	0.024	0.120	12.5	7.5	5.0
<i>XLPE/Neoprene</i>								
1	—	0.68	0.122	0.031	—	12.6	5.9	6.7
2	—	0.63	0.082	0.014	0.175	10.3	4.9	5.5
<i>Silicone/PVC</i>								
1	16.4	0.76	0.110	0.015	0.111	10.0	—	—
2	16.4	1.19	0.065	0.005	0.119	15.6	—	—
<i>PVC/Nylon/PVC-Nylon</i>								
1	—	0.63	0.084	0.024	—	10.2	5.0	5.2
2	—	0.49	0.082	0.032	0.115	9.2	4.8	4.4
<i>PTFE</i>								
1	—	0.180	0.091	0.012	0.011	3.2	2.7	0.4
2	6.2	0.383	0.103	—	0.005	5.7	—	—
<i>Materials with fiberweb, netlike, and multiplex structure (abbreviations/names in the nomenclature)</i>								
Olefin	—	1.49	0.006	—	—	16.5	13.3	3.2
PP-1	—	1.25	0.0029	—	—	14.0	10.8	3.2
PP-2	—	1.56	0.0048	—	—	17.2	10.5	6.7
Polyester-1	—	2.21	0.015	—	—	24.6	8.9	15.7
Polyester-2	—	1.51	0.0079	—	—	16.8	9.1	7.7
Polyester-3	—	2.55	0.020	—	—	28.5	22.6	5.9
Polyester-4	—	1.92	0.014	—	—	21.4	12.4	9.0
Rayon-1	—	1.80	0.043	—	—	20.3	14.1	6.2
Rayon-2	—	1.91	0.043	0.002	—	21.5	13.3	8.2
Rayon-3	—	1.18	0.047	—	—	13.5	8.3	5.2
Polyester-Rayon	—	1.52	0.005	—	—	16.8	9.1	7.7
Polyester-polyamide	—	1.82	0.008	—	—	20.2	10.4	9.8
Rayon-PE	—	1.50	0.027	—	—	16.9	8.72	8.2

Table 3-4.14 Yields of Fire Products and Chemical, Convective, and Radiative Heats of Combustion for Well-Ventilated Fires^a (Continued)

Material	ΔH_T (kJ/g)	y_{CO_2}	y_{CO}	y_{ch}	y_s	ΔH_{ch}	ΔH_{con}	ΔH_{rad}
		(g/g)					(kJ/g)	
<i>Two to eight 100- × 100- × 100-mm corrugated paper boxes with and without the polymers with three-dimensional arrangement (abbreviations/names in the nomenclature)^d</i>								
Empty	—	1.53	0.023	0.001	—	14.2	10.7	3.5
With PVC (62%-thick)	—	1.01	0.073	0.007	0.119	10.7	9.5	1.2
With PC (59%-thick)	—	1.73	0.047	0.002	0.061	18.4	13.5	4.9
With PS (58%-thick)	—	1.40	0.138	0.026	0.285	16.2	12.5	3.7
With PS (60%-thin)	—	1.88	0.068	0.020	0.140	19.4	10.1	9.3
With PS (40%-thin)	—	1.74	0.042	0.005	0.167	18.0	11.7	6.7
With ABS (59%-thick)	—	1.53	0.089	0.006	0.143	16.1	12.7	3.4
With PET (41%-thin)	—	1.87	0.050	0.006	0.053	19.9	11.8	8.1
With PU (40%-foam)	—	1.56	0.024	—	—	14.4	8.6	5.8
<i>High-pressure liquid spray combustion^e</i>								
<i>Hydraulic fluids</i>								
Organic polyol esters								
1	36.6	—	—	—	—	35.5	—	—
2	35.7	—	—	—	—	35.1	—	—
3	40.3	—	—	—	—	37.2	—	—
4	37.0	—	—	—	—	35.7	—	—
Phosphate esters								
1	31.8	—	—	—	—	29.3	—	—
2	32.0	—	—	—	—	29.6	—	—
Water-in-oil emulsions								
1	27.6	—	—	—	—	2.5	—	—
Polyglycol-in-water								
1	11.0	—	—	—	—	10.4	—	—
2	11.9	—	—	—	—	11.1	—	—
3	14.7	—	—	—	—	12.2	—	—
4	12.1	—	—	—	—	10.6	—	—
<i>Liquid fuels</i>								
Mineral oil	46.0	—	—	—	—	44.3	—	—
Methanol	20.0	—	—	—	—	19.8	—	—
Ethanol	27.7	—	—	—	—	26.2	—	—
Heptane	44.4	—	—	—	—	40.3	—	—

^aData measured in the ASTM E2058 fire propagation apparatus. Data measured in the cone calorimeter are identified by superscripts ^b and ^c. Some of the data are corrected to reflect well-ventilated fire conditions. All the data are reported for turbulent fires, that is, materials exposed to higher external heat flux values.

Dashes: either not measured or are less than 0.001.

^bCalculated from the data measured in the cone calorimeter as reported in References 20 and 39.

^cCalculated from the data measured in the cone calorimeter as reported in Reference 58.

^d100- × 100- × 100-mm corrugated paper boxes with and without the 99- × 99- × 99-mm polymer boxes or pieces on corrugated paper compartments. The boxes are arranged in one and two layers, about 12 mm apart, with one to four boxes in each layer, separated by about 12 mm. All the boxes are placed on a very light metal frame made of rods with screen base. Measurements made in the ASTM E2058 fire propagation apparatus; numbers in parentheses are the weight percents.

^eData from Reference 59 measured in high-pressure liquid spray combustion in the fire products collector (10,000-kW scale apparatus in Figure 3-4.8).

gasified material (e.g., smoke, CO, hydrocarbons, and other intermediate products) remain incomplete and heat release rate decreases.⁴⁴

In ventilation-controlled fires, heat release rate depends on the air supply rate and the mass loss rate, in addition to other factors. For ventilation-controlled fires, the effects of the mass flow rate of air and fuel mass loss rate are characterized, most commonly, by the local equivalence ratio:

$$\Phi = \frac{S\dot{m}'A}{\dot{m}_{air}} \quad (37)$$

where

Φ = equivalence ratio

S = stoichiometric mass air-to-fuel ratio (g/g)

\dot{m}' = mass loss rate (g/m²·s)

A = exposed area of the material burning (m²)

\dot{m}_{air} = mass flow rate of air (g/s)

Generalized-state relationships between mass fractions of major species (O₂, fuel, CO₂, H₂O, CO, and H₂) and temperature as functions of local equivalence ratios

Table 3-4.15 Chemical and Convective Heat Release Parameters

Materials	(HRP) _{ch}			(HRP) _{con}		
	ASTM E2058 Fire Propagation Apparatus	ASTM E1354 ^a	Cal ^b	ASTM E2058 Fire Propagation Apparatus	ASTM E906 ^c	Cal ^b
<i>Liquids and gases (hydrocarbons, alkanes)</i>						
Hexane	—	—	83	—	—	56
Heptane	—	—	75	—	—	50
Octane	—	—	68	—	—	46
Nonane	—	—	64	—	—	42
Decane	—	—	59	—	—	39
Undecane	—	—	55	—	—	36
Dodecane	—	—	52	—	—	34
Tridecane	—	—	50	—	—	32
Kerosene	—	—	47	—	—	17
Hexadexane	—	—	44	—	—	28
<i>Solids (abbreviations/names in the nomenclature)</i>						
ABS	—	14	—	—	—	—
Acrylic sheet	—	6	—	—	—	—
Epoxy	—	11	—	—	—	—
IPST	—	6	—	—	—	—
Polyamide	21	—	—	—	—	—
Polypropylene	19	—	—	11	—	—
Polyethylene	17	21	—	12	—	—
Polystyrene	16	19	—	6	—	—
Polymethylmethacrylate	15	14	—	10	—	—
Nylon	12	—	—	7	—	—
Polyamide-6	—	21	—	—	—	—
Filled phenolic foam—50% inert	—	1	—	—	—	—
Polycarbonate	9	—	—	—	—	—
Polyoxymethylene	6	—	—	5	—	—
Polyethylene/25% Cl	11	—	—	5	—	—
Plasticized-PVC-3, LOI 0.25	—	5	—	—	—	—
Plasticized-PVC-4, LOI 0.30	—	5	—	—	—	—
Plasticized-PVC-5, LOI 0.35	—	5	—	—	—	—
Polyethylene/35% Cl	4	—	—	2	—	—
Rigid PVC-1, LOI 0.50	—	3	—	—	—	—
Rigid PVC-2	2	3	—	1	—	—
PVC panel	2	—	—	—	—	—
Polyethylene/48% Cl	2	—	—	—	—	—
PVEST	—	13	—	—	—	—
ETFE (Tefzel)	6	—	—	—	—	—
PFA (Teflon)	5	—	—	—	—	—
FEP (Teflon)	2	—	—	—	—	—
TFE (Teflon)	2	—	—	—	—	—
Wood (hemlock)	—	1	—	—	—	—
Wood (Douglas fir)	7	—	—	5	—	—
Wool	—	5	—	—	—	—
<i>Composites and fiberglass-reinforced materials (FGR) (abbreviations/names in the nomenclature)</i>						
Bismaleimide/graphite/ceramic (CC)	—	1	—	—	—	—
Epoxy/FGR	—	2	—	—	—	—
Epoxy/graphite	2	—	—	—	—	—
Epoxy/graphite/CC	2	—	—	—	—	—
Epoxy/graphite/intumescent (IC)	2	—	—	—	—	—
IPST/FGR	—	1	—	—	—	—
PEEK/FGR	—	3	—	—	—	—
PES/FGR	—	1	—	—	—	—
PEST-1/FGR	3	—	—	—	—	—
PEST-2/FGR	8	—	—	—	—	—
PEST-3/FGR	10	—	—	—	—	—
PEST-4/FGR	3	—	—	—	—	—
PEST-5/FGR	3	—	—	—	—	—
PEST-6/FGR	3	—	—	—	—	—

Table 3-4.15 Chemical and Convective Heat Release Parameters (Continued)

Materials	(HRP) _{ch}			(HRP) _{con}		
	ASTM E2058 Fire Propagation Apparatus	ASTM E1354 ^a	Cal ^b	ASTM E2058 Fire Propagation Apparatus	ASTM E906 ^c	Cal ^b
<i>Composites and fiberglass-reinforced materials (FGR) (continued)</i>						
Phenol/FGR	—	1	—	—	—	—
Phenolic/Kevlar	2	—	—	—	—	—
Phenol/graphite	1	—	—	—	—	—
PVEST-1/FGR	3	—	—	—	—	—
PVEST-1/FGR/CC	3	—	—	—	—	—
PVEST-1/FGR/IC	1	—	—	—	—	—
PVEST-2/FGR	7	—	—	—	—	—
PVEST-3/FGR	2	—	—	—	—	—
<i>Aircraft panel materials</i>						
Epoxy fiberglass	4	4	—	2	1	—
Epoxy Kevlar	4	4	—	2	2	—
Phenolic Kevlar	5	4	—	2	—	—
Phenolic graphite	4	3	—	1	—	—
Phenolic fiberglass	4	3	—	2	1	—
Polycarbonate panel	9	—	—	—	—	—
<i>Foams</i>						
Polystyrene						
GM53	20	—	—	6	—	—
GM49	19	—	—	8	—	—
GM51	18	—	—	9	—	—
<i>Flexible polyurethane</i>						
GM 21	7	—	—	3	3	—
GM 23	9	—	—	5	6	—
GM 25	14	—	—	6	4	—
GM 27	9	—	—	4	2	—
Phenolic	—	1	—	—	—	—
<i>Electrical cables (abbreviations/names in the nomenclature)</i>						
PVC/PVC-1 (Group 3)	15	—	—	—	—	—
PE/PVC (Group 3)	19	—	—	—	—	—
PP,PEST/PVC (Group 3)	11	—	—	—	—	—
PVC/PVC-2 (Group 3)	14	—	—	—	—	—
Chlorinated PE (Group 2)	5	—	—	—	—	—
PVC/PVC-3 (Group 2)	4	—	—	—	—	—
EPR/PVC (Group 2)	6	—	—	—	—	—
PVC/EPR (Group 2)	4	—	—	—	—	—
XLPE/XLPE (Group 2)	6	—	—	—	—	—
EPR/hypalon-1 (Group 2)	6	—	—	—	—	—
EPR/hypalon-2 (Group 2)	4	—	—	—	—	—
EPR/hypalon-3 (Group 1)	3	—	—	—	—	—
EPR/hypalon-4 (Group 1)	3	—	—	—	—	—
EPR/EPR-1 (Group 1)	3	—	—	—	—	—
EPR/EPR-2 (Group 1)	3	—	—	—	—	—
EPR/EPR-3 (Group 1)	2	—	—	—	—	—
XLPE-EVA-1 (Group 1)	3	—	—	—	—	—
XLPE-EVA-2 (Group 1)	3	—	—	—	—	—
ETFA (Group 1)	3	—	—	—	—	—
PVC/PVF ₂ (Group 1)	1	—	—	—	—	—
FEP/FEP-1 (Group 1)	2	—	—	—	—	—
FEP/FEP-2 (Group 2)	2	—	—	—	—	—

^aCalculated from the data reported in References 20 and 39.^bCalculated from the data in References 48 and 49.^cFrom Reference 60.

for hydrocarbon-air diffusion flames are available.⁶¹ The relationships suggest that the generation efficiencies of CO, fuel vapors, water, CO₂, and H and the consumption efficiency of O₂ are in approximate thermodynamic equilibrium for well-ventilated combustion, but deviate from equilibrium for ventilation-controlled combustion. This concept has been used for fires of polymeric materials.⁴⁴ In the tests, chemical and convective heat release rates, mass loss rate, and generation rates of fire products have been measured for various equivalence ratios in the ASTM E2058 fire propagation apparatus [Figure 3-4.2(a)] and in the Fire Research Institute's (FRI) 0.022-m³ enclosure in Tokyo, Japan, described in Reference 44. The combustion efficiency and its convective component are found to decrease as fires become fuel rich, due to increase in the equivalence ratio. The ratio of the combustion efficiency and its convective component or chemical and convective heats of combustion for ventilation-controlled to well-ventilated combustion is expressed as⁴⁴

$$\zeta_{ch} = \frac{(\chi_{ch})_{vc}}{(\chi_{ch})_{wv}} = \frac{(\Delta H_{ch}/\Delta H_T)_{vc}}{(\Delta H_{ch}/\Delta H_T)_{wv}} = \frac{(\Delta H_{ch})_{vc}}{(\Delta H_{ch})_{wv}} \quad (38)$$

$$\zeta_{con} = \frac{(\chi_{con})_{vc}}{(\chi_{con})_{wv}} = \frac{(\Delta H_{con}/\Delta H_T)_{vc}}{(\Delta H_{con}/\Delta H_T)_{wv}} = \frac{(\Delta H_{con})_{vc}}{(\Delta H_{con})_{wv}} \quad (39)$$

where ζ_{ch} and ζ_{con} are the ratio of the combustion efficiency to its convective component, or chemical and convective heats of combustion for ventilation-controlled to well-ventilated combustion. Subscript *vc* represents ventilation-controlled fire, and *wv* represents well-ventilated fire.

The experimental data for the ratios of the chemical and convective heats of combustion for ventilation-controlled to well-ventilated fires at various equivalence ratios are shown in Figures 3-4.26 and 3-4.27. The data are measured in the ASTM E2058 fire propagation apparatus and the FRI's 0.022-m³ enclosure, details of which are described in Reference 44. The data for the polymers indicated in the figures satisfy the following general correlations, irrespective of their chemical structures:⁴⁴

$$\frac{(\Delta H_{ch})_{vc}}{(\Delta H_{ch})_{wv}} = 1 - \frac{0.97}{\exp(\Phi/2.15)^{-1.2}} \quad (40)$$

$$\frac{(\Delta H_{con})_{vc}}{(\Delta H_{con})_{wv}} = 1 - \frac{1.0}{\exp(\Phi/1.38)^{-2.8}} \quad (41)$$

The effects of ventilation on the chemical and convective heats of combustion are reflected by the magnitudes of the expressions within the parentheses on the right-hand sides of Equations 40 and 41. For a well-ventilated fire, $\Phi \ll 1.0$, $(\Delta H_{ch})_{vc} = (\Delta H_{ch})_{wv}$, and $(\Delta H_{con})_{vc} = (\Delta H_{con})_{wv}$.

As a fire changes from well ventilated to ventilation controlled, equivalence ratio increases and the magnitudes of the expressions within the parentheses on the right-hand sides of Equations 40 and 41 increase. Thus with increase in the equivalence ratio, the chemical and convective heats of combustion decrease. The decrease in the convective heat of combustion is higher than it is for the chemical heat of combustion, because the coefficients for the equivalence ratios are different. The correlation suggests that a higher fraction of the chemical heat of combustion is expected to be converted to the radiative heat of combustion as fires change from well ventilated to venti-

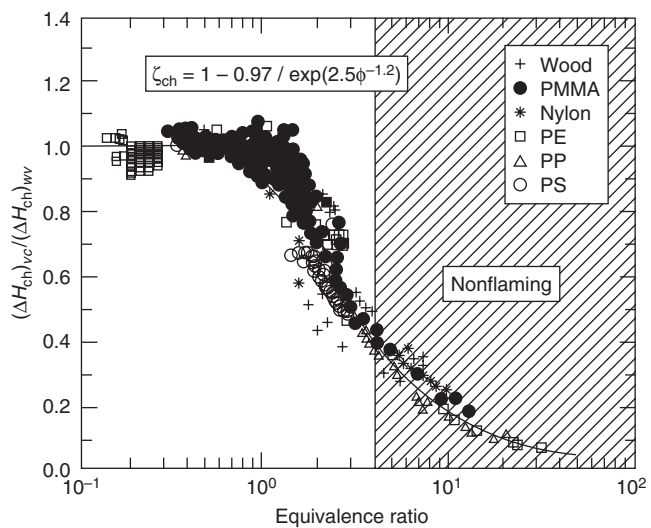


Figure 3-4.26. Ratio of the ventilation-controlled to well-ventilated chemical heat of combustion versus the equivalence ratio. Data are measured in the ASTM E2058 fire propagation apparatus and in the Fire Research Institute's enclosure.⁴⁴ Subscript *vc* represents ventilation-controlled fires, and subscript *wv* represents well-ventilated fires.

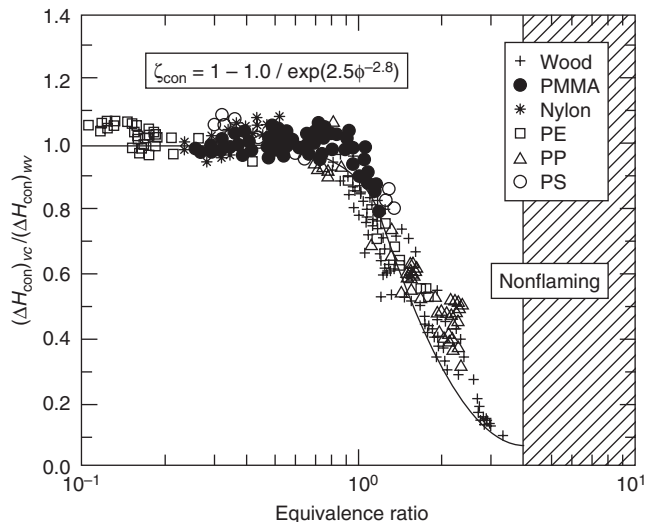


Figure 3-4.27. Ratio of the ventilation-controlled to well-ventilated convective heat of combustion versus the equivalence ratio. Data are measured in the ASTM E2058 fire propagation apparatus and in the Fire Research Institute's enclosure.⁴⁴ Subscript *vc* represents ventilation-controlled fires, and subscript *wv* represents well-ventilated fires.

lation controlled. This is in general agreement with the observations for the ventilation-controlled fires in buildings.

Equations 40 and 41 can be used in models for the assessment of the ventilation-controlled fire behavior of materials, using chemical and convective heats of combustion for well-ventilated fires such as from Table 3-4.14.

EXAMPLE 13:

Calculate the chemical heats of combustion at equivalence ratios of 1, 2, and 3 for red oak, polyethylene, polystyrene, and nylon using Equation 40 and data from Table 3-4.14 for well-ventilated fires.

SOLUTION:

Material	Chemical Heats of Combustion (kJ/g)			
	$\Phi \ll 1.0$	$\Phi = 1.0$	$\Phi = 2.0$	$\Phi = 3.0$
Red oak	12.4	11.4	8.3	6.2
Polyethylene	38.4	35.3	25.9	19.3
Polystyrene	27.0	24.9	18.2	13.6
Nylon	27.1	24.9	18.2	13.6

Generation of Chemical Compounds and Consumption of Oxygen

Chemical compounds (smoke, toxic, corrosive, and odorous compounds) are the main contributors to non-thermal hazard and thus the assessments of their chemical natures and generation rates, relative to the airflow rate, are of critical importance for the protection of life and property.

In fires, compounds are generated as a result of gasification and decomposition of the material and burning of the species in the gas phase with air in the form of a diffusion flame. In general, generation of the fire products and consumption of oxygen in diffusion flames occur in two zones.⁴⁴

1. *Reduction zone.* In this zone, the material melts, decomposes, gasifies, and/or generates species that react to form smoke, CO, hydrocarbons, and other intermediate products. Very little oxygen is consumed in this region. The extent of conversion of the material to smoke, CO, hydrocarbons, and other products depends on the chemical nature of the material.
2. *Oxidation zone.* In this zone, the reduction zone products (smoke, CO, hydrocarbons, and other intermediates) react with varying degrees of efficiency with the oxygen from air and generate chemical heat and varying amounts of products of complete combustion, such as CO₂ and H₂O. The lower the reaction efficiency, the higher the amounts of reduction zone products emitted from a fire. The reaction efficiency of the reduction zone products with oxygen depends on the concentrations of the products relative to the oxygen concentration, temperature, and mixing of the products and air. For example, in laminar diffusion flames, smoke is emitted when the temperature of the oxidation zone falls below about 1300 K.

The hot ceiling layer in a building fire may be considered in terms of oxidation and reduction zone products. In building fires with plenty of ventilation, the concentrations of the reduction zone products are higher in the central region of the ceiling layer, whereas the concentrations of the oxidation zone products are higher closer to the room opening. As the air supply rate, or oxygen concentration available to the fire, decreases due to restrictions in the ventilation, the ceiling layer expands and starts occupying greater room volume with increase in the concentrations of

the reduction zone products. Under these conditions, large amounts of the reduction zone products are released within the building increasing the nonthermal hazard.

The generation rate of a fire product is directly proportional to the mass loss rate, the proportionality constant being defined as the yield of the product:^{1-4,9-16,41,44,45,48,49,52-55}

$$\dot{G}_j'' = y_j \dot{m}'' \quad (42)$$

where \dot{G}_j'' is the mass generation rate of product j (g/m²·s), and y_j is the yield of product j (g/g). The total mass of the product generated is obtained by the summation of the generation rate:

$$W_j = A \sum_{n=t_0}^{n=t_f} \dot{G}_j''(t_n) \Delta t_n \quad (43)$$

where

W_j = total mass of product j generated from the flaming and/or nonflaming fire of the material (g)

t_0 = time when the sample is exposed to heat (s)

t_f = time when there is no more vapor formation (s)

From Equations 27, 42, and 43, the average value of the yield of product j is

$$\bar{y}_j = \frac{W_j}{W_f} \quad (44)$$

The mass consumption rate of oxygen is also directly proportional to the mass loss rate:^{1-4,9-16,33,36-39,42-45}

$$\dot{C}_O'' = c_O \dot{m}'' \quad (45)$$

where \dot{C}_O'' is the mass consumption rate of oxygen (g/m²·s), and c_O is the mass of oxygen consumed per unit mass of fuel (g/g).

The mass generation rates of fire products and mass consumption rate of oxygen are determined by measuring the volume fractions of the products and oxygen and the total volumetric or mass flow rate of the fire products-air mixture:^{2,3,44}

$$\dot{G}_j'' = \frac{f_j \dot{V} \rho_j}{A} = f_j \dot{W} \left(\frac{\rho_j}{\rho_g A} \right) \quad (46)$$

$$\dot{C}_O'' = \frac{f_O \dot{V} \rho_O}{A} = f_O \dot{W} \left(\frac{\rho_O}{\rho_g A} \right) \quad (47)$$

where

f_j = volume fraction of product j

f_O = volume fraction of oxygen

\dot{V} = total volumetric flow rate of the fire product-air mixture (m³/s)

\dot{W} = total mass flow rate of the fire product-air mixture (g/s)

ρ_j = density of product j at the temperature of the fire product-air mixture (g/m³)

ρ_g = density of the hot fire product-air mixture (g/m³)

ρ_O = density of oxygen at the temperature of the fire product-air mixture (g/m³)

A = total area of the material burning (m²)

For volume fraction measurements, sampling ducts are used where fire products and air are well mixed, such as in the ASTM E2058 fire propagation apparatuses [Figure 3-4.2, parts (a) and (b) and 3-4.8] and in the cone calorimeter (Figure 3-4.3). Figure 3-4.28 shows the measurement locations in the sampling duct of the ASTM E2058 fire propagation apparatus. The volume fractions are measured by various types of instruments; for example, in the ASTM E2058 fire propagation apparatuses, they are measured continuously by (1) commercial infrared analyzers for CO and CO₂; (2) a high-sensitivity commercial paramagnetic analyzer for oxygen; (3) a commercial flame ionization analyzer for the mixture of low molecular weight gaseous hydrocarbons; and (4) by a turbidimeter, designed by the FMRC Flammability Laboratory,⁶² for smoke. The turbidimeter measures the optical density defined as

$$D = \frac{\ln(I_0/I)}{\ell} \quad (48)$$

where

D = optical density (1/m)

I/I_0 = fraction of light transmitted through smoke

ℓ = optical path length (m)

The volume fraction of smoke is obtained from the following relationship:⁶²

$$f_s = \frac{D\lambda \times 10^{-6}}{\Omega} \quad (49)$$

where

f_s = volume fraction of smoke

λ = wavelength of the light source (μm)

Ω = coefficient of particulate extinction taken as 7.0.⁶²

In the ASTM E2058 fire propagation apparatuses, optical density is measured at wavelengths of 0.4579 μm (blue), 0.6328 μm (red), and 1.06 μm (IR). In the cone calorimeter, optical density is measured by using a helium-neon laser with a wavelength of 0.6328 μm (red).

From Equations 46 and 49,

$$\begin{aligned} \dot{G}_s'' &= \frac{f_s \dot{V} \rho_s \times 10^{-6}}{A} = \left(\frac{D\lambda}{7} \right) \left(\frac{\rho_s \dot{V} \times 10^{-6}}{A} \right) \\ &= \left(\frac{D\lambda}{7} \right) \left(\frac{\rho_s}{\rho_a} \right) \left(\frac{\dot{W} \times 10^{-6}}{A} \right) \end{aligned} \quad (50)$$

In the ASTM E2058 fire propagation apparatuses and the cone calorimeter, the fire products in the sampling duct are diluted about 20 times and thus the density of air, $\rho_a = 1.2 \times 10^3$ g/m³, and the density of smoke, $\rho_s = 1.1 \times 10^6$ g/m³, as suggested in Reference 62, are used:

$$\begin{aligned} \dot{G}_s'' &= \left(\frac{1.1 \times 10^6 \times 10^{-6}}{7} \right) \left(\frac{\dot{V}}{A} \right) D\lambda \\ &= \left(\frac{1.1 \times 10^6 \times 10^{-6}}{7 \times 1.2 \times 10^3} \right) \left(\frac{\dot{W}}{A} \right) D\lambda \end{aligned} \quad (51)$$

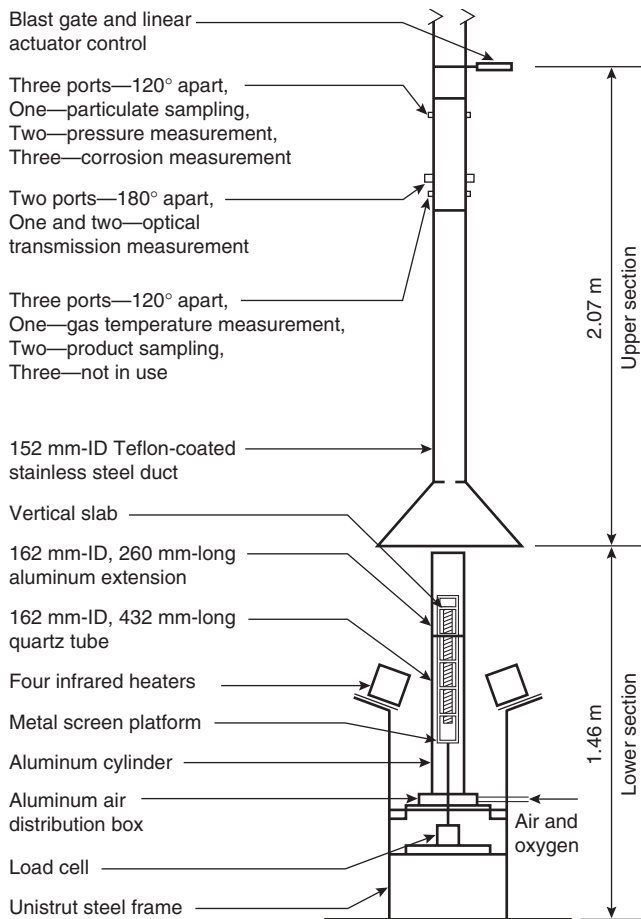


Figure 3-4.28. Sketch of the ASTM E2058 fire propagation apparatus showing locations where measurements are made for the product concentration, optical transmission, particulate concentration, and corrosion.

For blue wavelength of light ($\lambda = 0.4579$ μm),

$$\dot{G}_s'' = 0.0720 \left(\frac{D_{\text{blue}} \dot{V}}{A} \right) = 0.0600 \times 10^{-3} \left(\frac{D_{\text{blue}} \dot{W}}{A} \right) \quad (52)$$

For red wavelength of light ($\lambda = 0.6328$ μm),

$$\dot{G}_s'' = 0.0994 \left(\frac{D_{\text{red}} \dot{V}}{A} \right) = 0.0829 \times 10^{-3} \left(\frac{D_{\text{red}} \dot{W}}{A} \right) \quad (53)$$

For infrared wavelength of light ($\lambda = 1.06$ μm),

$$\dot{G}_s'' = 0.1666 \left(\frac{D_{\text{IR}} \dot{V}}{A} \right) = 0.1388 \times 10^{-3} \left(\frac{D_{\text{IR}} \dot{W}}{A} \right) \quad (54)$$

where D_{blue} , D_{red} , and D_{IR} are the optical densities measured at wavelengths of 0.4579, 0.6328, and 1.06 μm, respectively. These optical densities and total mass flow rate of the fire products-air mixture, \dot{W} , are measured continuously in the ASTM E2058 fire propagation apparatuses and the cone calorimeter, and A is known. The generation rates of smoke obtained from the optical densities at three wavelengths in the ASTM E2058 fire propagation appara-

tus are averaged. The smoke mass generated in the test is also measured continuously in the ASTM E2058 fire propagation apparatus by a commercial smoke mass monitoring instrument. The data are used to calculate the mass generation rate of smoke. The smoke generation rates obtained from the optical density and smoke mass monitor show very good agreement.

In the cone calorimeter, the smoke data are reported in terms of the average specific extinction area: (m^2/kg)¹⁹

$$\bar{\tau} = \frac{\sum_i \dot{V}_i D_i \Delta t_i}{W_f} \quad (55)$$

where $\bar{\tau}$ is the average specific extinction area determined in the cone calorimeter (m^2/g). Multiplying both sides of Equation 55 by $\rho_s \lambda \times 10^{-6}/7$ and rearranging

$$\begin{aligned} \bar{\tau}(\rho_s \lambda / 7) \times 10^{-6} &= \frac{\sum_i [(D\lambda \times 10^{-6}/7)\rho_s \dot{V}_i] \Delta t_i}{W_f} \\ &= \frac{W_s}{W_f} = \bar{y}_s \end{aligned} \quad (56)$$

In the cone calorimeter, $\lambda = 0.6328 \mu\text{m}$ for red wavelength and using $\rho_s = 1.1 \times 10^6 \text{ g/m}^3$, as suggested in Reference 62, the average yield of smoke from the average specific extinction area determined in the cone calorimeter can be calculated from the following expression:

$$\bar{y}_s = 0.0994 \times 10^{-3} \bar{\tau} \quad (57)$$

where \bar{y}_s is the average yield of smoke (g/g).

The smoking characteristics of a material are also reported in terms of *mass optical density* (MOD):^{1,4,16,60}

$$\text{MOD} = \left[\frac{\log_{10}(I_0/I)}{\ell} \right] \left[\frac{\dot{V}}{A\dot{m}''} \right] = \left[\frac{D}{2.303} \right] \left[\frac{\dot{V}}{A\dot{m}''} \right] \quad (58)$$

From Equations 42 and 50, with $\rho_s = 1.1 \times 10^6 \text{ g/m}^3$ and $\lambda = 0.6328 \mu\text{m}$,

$$y_s = \left(\frac{\lambda \rho_s}{7.0} \right) \left(\frac{D\dot{V} \times 10^{-6}}{A\dot{m}''} \right) = 0.0994 \left(\frac{\text{MOD}}{2.303} \right) \quad (59)$$

MOD is generally reported with \log_{10} , however if it is changed to \log_e and m^2/kg by multiplying it by 2.303 and dividing it by 1000, it becomes the specific extinction area, a terminology used in reporting the cone calorimeter data.

The average data for the yields of CO, CO_2 , mixture of gaseous hydrocarbons, and smoke for well-ventilated fires are listed in Table 3-4.14.

EXAMPLE 14:

For a fiberglass-reinforced material, the following data were measured for combustion in normal air at an external heat flux value of 50 kW/m^2 :

Total mass of the sample lost (g)	229
Total mass generated (g)	
CO	0.478
CO_2	290
Hydrocarbons	0.378
Smoke	6.31
Total energy generated (kJ)	3221

Calculate the average yields of CO, CO_2 , hydrocarbons, and smoke and the average chemical heat of combustion.

SOLUTION:

The average yields are calculated from Equation 44, and the average chemical heats of combustion are calculated from Equation 29.

Average yields (g/g)	
CO	0.0021
CO_2	1.27
Hydrocarbons	0.002
Smoke	0.028
Average chemical heats of combustion (kJ/g)	14.1

EXAMPLE 15:

A circular sample of polystyrene, about 0.007 m^2 in area and 25 mm in thickness, was burned in normal air in the presence of external heat flux. In the test, measurements were made for the mass loss rate and light obscuration by smoke in the sampling duct with an optical path length of 0.149 m. The total volumetric flow rate of the mixture of fire products and air through the sampling duct was $0.311 \text{ m}^3/\text{s}$, and the wavelength of light source used was $0.6328 \mu\text{m}$. At the steady-state combustion of polystyrene, the measured mass loss rate was $33 \text{ g/m}^2\cdot\text{s}$ with smoke obscuring 83.5 percent of the light. Calculate the yield of smoke from the data using a value of $1.1 \times 10^6 \text{ g/m}^3$ for the density of smoke.

SOLUTION:

The optical density from Equation 48 is

$$D = \frac{\ln(I_0/I)}{\ell} = \frac{\ln(100/83.5)}{0.149} = 121 \left(\frac{1}{\text{m}} \right)$$

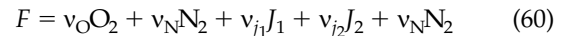
The smoke generation rate from Equation 51 is

$$\dot{G}'_s = \frac{1.1 \dot{V} D \lambda}{7 \times A} = \frac{1.1 \times 0.311 \times 1.21 \times 0.6328}{7 \times 0.007} = 5.35 \text{ g/m}^2\cdot\text{s}$$

The smoke yield from Equation 42 is

$$y_s = \frac{5.35 \text{ g/m}^2\cdot\text{s}}{33 \text{ g/m}^2\cdot\text{s}} = 0.162 \text{ g/g}$$

Efficiencies of oxygen mass consumption and mass generation of products: A chemical reaction between oxygen and a fuel monomer of a material can be expressed as



where

F = fuel monomer of a material

v_O = stoichiometric coefficient for oxygen

v_N = stoichiometric coefficient and nitrogen

v_{j_1}, v_{j_2} = stoichiometric coefficients for the maximum possible conversion of the fuel monomer to products J_1 and J_2 , respectively

The stoichiometric mass oxygen-to-fuel ratio for the maximum possible conversion of the fuel monomer is expressed as

$$\Psi_O = \frac{v_O M_O}{M_f} \quad (61)$$

where

Ψ_O = stoichiometric mass oxygen-to-fuel ratio for the maximum possible conversion of the fuel monomer to products

M_O = molecular weight of oxygen (32 g/mol)

M_f = molecular weight of the fuel monomer of the material (g/mol)

M_f is calculated from its elemental composition. For the elemental composition measurements, microanalytical techniques are used.

The stoichiometric yield for the maximum possible conversion of the fuel monomer of the material to a product is expressed as

$$\Psi_j = \frac{v_j M_j}{M_f} \quad (62)$$

where Ψ_j is the stoichiometric yield for the maximum possible conversion of the fuel monomer of the material to product j , and M_j is the molecular weight of product (g/mol).

The stoichiometric yields for some selected materials, calculated from the elemental composition data from the flammability laboratory, are listed in Table 3-4.16 for fuel monomer conversion to CO, CO_2 , hydrocarbons, smoke, HCl, and HF. The stoichiometric yields depend on the number of atoms relative to the carbon atom. The yields provide an insight into the nature of products and the amounts of products expected to be generated in flaming and nonflaming fires, when expressed as the stoichiometric oxygen mass consumption rate and stoichiometric mass generation rates of products:

$$\dot{C}_{\text{stoich},O}'' = \Psi_O \dot{m}'' \quad (63)$$

$$\dot{G}_{\text{stoich},j}'' = \Psi_j \dot{m}'' \quad (64)$$

where $\dot{C}_{\text{stoich},O}''$ and $\dot{G}_{\text{stoich},j}''$ are the stoichiometric oxygen mass consumption rate and stoichiometric mass generation rate of product j for the maximum possible conversion of the fuel monomer to the product, respectively ($\text{g}/(\text{m}^2 \cdot \text{s})$).

In fires, the actual oxygen mass consumption rate and the mass generation rates of products are significantly less than the stoichiometric rates. The ratio of the actual oxygen mass consumption rate to stoichiometric rates is thus defined as the efficiency of oxygen mass consumption or product mass generation:^{2-4,16,44}

$$\eta_O = \frac{\dot{C}_{\text{actual},O}''}{\dot{C}_{\text{stoich},O}''} = \frac{c_O \dot{m}''}{\Psi_O \dot{m}''} = \frac{c_O}{\Psi_O} \quad (65)$$

$$\eta_j = \frac{\dot{G}_{\text{actual},j}''}{\dot{G}_{\text{stoich},j}''} = \frac{y_j \dot{m}''}{\Psi_j \dot{m}''} = \frac{y_j}{\Psi_j} \quad (66)$$

where η_O is efficiency of oxygen mass consumption and η_j is the generation efficiency of product j . Subscript repre-

sents the actual oxygen mass consumption rate or the actual mass generation rate of a product.

EXAMPLE 16:

A material is made up of carbon, hydrogen, and oxygen. The weight of the material is distributed as follows: 54 percent as carbon, 6 percent as hydrogen, and 40 percent as oxygen. Calculate the chemical formula of the fuel monomer of the material.

SOLUTION:

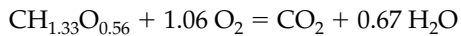
From the atomic weights and the weight percent of the atoms, the number of atoms are as follows: carbon (C): $54/12 = 4.5$; hydrogen (H): $6/1 = 6.0$; and oxygen (O): $40/16 = 2.5$. Thus the chemical formula of the fuel monomer of the material is $\text{C}_{4.5}\text{H}_{6.0}\text{O}_{2.5}$ or, dividing by 4.5, $\text{CH}_{1.33}\text{O}_{0.56}$.

EXAMPLE 17:

For the material in Example 16, calculate the stoichiometric mass oxygen-to-fuel ratio, stoichiometric mass air-to-fuel ratio, and stoichiometric yields for maximum possible conversion of the fuel monomer of the material to CO, CO_2 , hydrocarbons, water, and smoke. Assume smoke to be pure carbon, and hydrocarbons as having the same carbon-atom-to-hydrogen-atom ratio as the original fuel monomer.

SOLUTION:

1. For stoichiometric yields of CO_2 and water and the stoichiometric mass oxygen and air-to-fuel ratio for the maximum possible conversion of the fuel monomer of the material to CO_2 and H_2O , the following expression represents the maximum possible conversion of the fuel monomer of the material to CO_2 and H_2O :



The molecular weight of the fuel monomer of the material is $1 \times 12 + 1.33 \times 1 + 0.56 \times 16 = 22.3$, the molecular weight of oxygen is 32, the molecular weight of CO_2 is 44, and the molecular weight of H_2O is 18. Thus,

$$\Psi_{\text{CO}_2} = \frac{44}{22.3} = 1.97$$

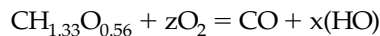
$$\Psi_{\text{H}_2\text{O}} = \frac{0.67 \times 18}{22.3} = 0.54$$

$$\Psi_O = \frac{1.06 \times 32}{22.3} = 1.52$$

The stoichiometric mass air-to-fuel ratio can be obtained by dividing Ψ_O by 0.233; that is, $1.52/0.233 = 6.52$.

2. For stoichiometric yields of CO, hydrocarbons, and smoke for the maximum possible conversion of the fuel monomer of the material to these products, the following expressions represent the maximum possible conversion of the fuel monomer of the material to these products:

For CO,



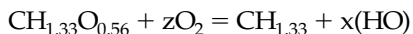
$$\Psi_{\text{CO}} = \frac{28}{22.3} = 1.26$$

Table 3-4.16 Stoichiometric Yields of Major Products^a

Carbon-Hydrogen Atoms in the Structure								
Material	Formula	Ψ_O	Ψ_{CO_2}	Ψ_{CO}	Ψ_s	Ψ_{hc}	Ψ_{HCl}	Ψ_{HF}
PE	CH ₂	3.43	3.14	2.00	0.857	1.00	0	0
PP	CH ₂	3.43	3.14	2.00	0.857	1.00	0	0
PS	CH	3.08	3.38	2.15	0.923	1.00	0	0
<i>Expanded polystyrene</i>								
GM47	CH _{1.1}	3.10	3.36	2.14	0.916	1.00	0	0
GM49	CH _{1.1}	3.10	3.36	2.14	0.916	1.00	0	0
GM51	CH	3.08	3.38	2.15	0.923	1.00	0	0
GM53	CH _{1.1}	3.10	3.36	2.14	0.916	1.00	0	0
Carbon-hydrogen-oxygen-nitrogen atoms in the structure								
POM	CH ₂ O	1.07	1.47	0.933	0.400	0.467	0	0
PMMA	CH _{1.6} O _{0.40}	1.92	2.20	1.40	0.600	0.680	0	0
Nylon	CH _{1.8} O _{0.17} N _{0.17}	2.61	2.32	1.48	0.634	0.731	0	0
Wood (pine)	CH _{1.7} O _{0.83}	1.21	1.67	1.06	0.444	0.506	0	0
Wood (oak)	CH _{1.7} O _{0.72} N _{0.001}	1.35	1.74	1.11	0.476	0.543	0	0
Wood (Douglas fir)	CH _{1.7} O _{0.74} N _{0.002}	1.32	1.72	1.10	0.469	0.536	0	0
Polyester	CH _{1.4} O _{0.22}	2.35	2.60	1.65	0.709	0.792	0	0
Epoxy	CH _{1.3} O _{0.20}	2.38	2.67	1.70	0.727	0.806	0	0
Polycarbonate	CH _{0.88} O _{0.19}	2.26	2.76	1.76	0.754	0.872	0	0
PET	CH _{0.80} O _{0.40}	1.67	2.29	1.46	0.625	0.667	0	0
Phenolic foam	CH _{1.1} O _{0.24}	2.18	2.60	1.65	0.708	0.773	0	0
PAN	CHN _{0.33}	2.87	2.50	1.59	0.681	0.681	0	0
<i>Flexible polyurethane foams</i>								
GM21	CH _{1.8} O _{0.30} N _{0.05}	2.24	2.28	1.45	0.622	0.715	0	0
GM23	CH _{1.8} O _{0.35} N _{0.06}	2.11	2.17	1.38	0.593	0.682	0	0
GM25	CH _{1.7} O _{0.32} N _{0.07}	2.16	2.22	1.41	0.606	0.692	0	0
GM27	CH _{1.7} O _{0.30} N _{0.08}	2.21	2.24	1.43	0.612	0.698	0	0
<i>Rigid polyurethane foams</i>								
GM29	CH _{1.1} O _{0.23} N _{0.10}	2.22	2.42	1.54	0.660	0.721	0	0
GM31	CH _{1.2} O _{0.22} N _{0.10}	2.28	2.43	1.55	0.662	0.729	0	0
GM37	CH _{1.2} O _{0.20} N _{0.08}	2.34	2.51	1.60	0.685	0.753	0	0
<i>Rigid polyisocyanurate foams</i>								
GM41	CH _{1.0} O _{0.19} N _{0.11}	2.30	2.50	1.59	0.683	0.740	0	0
GM43	CH _{0.93} O _{0.20} N _{0.11}	2.25	2.49	1.58	0.679	0.732	0	0
Carbon-hydrogen-oxygen-silicone atoms in the structure								
Silicone-1 ^b	CH _{1.3} O _{0.25} SiO _{1.18}	1.98	1.97	1.25	0.537	0.595	0	0
Silicone-2 ^c	CH _{1.5} O _{0.30} SiO _{1.26}	1.86	1.72	1.09	0.469	0.528	0	0
Silicone-3 ^d	CH ₃ O _{0.50} SiO _{1.50}	1.73	1.19	0.757	0.324	0.405	0	0
Carbon-hydrogen-oxygen-chlorine-fluorine atoms in the structure								
<i>Fluoropolymers</i>								
PVF (Tedlar)	CH _{1.5} F _{0.50}	1.74	1.91	1.22	0.522	0.587	0	0.435
PVF2 (Kynar)	CHF	1.00	1.38	0.875	0.375	0.406	0	0.594
ETFE (Tefzel)	CH _{1.0} F _{0.99}	1.01	1.38	0.880	0.377	0.409	0	0.622
E-CTFE (Halar)	CHF _{0.75} Cl _{0.25}	0.889	1.22	0.778	0.333	0.361	0.257	0.417
PFA (Teflon)	CF _{1.7} O _{0.01}	0.716	1.00	0.630	0.270	0	0	0.765
FEP (Teflon)	CF _{1.8}	0.693	0.952	0.606	0.260	0	0	0.779
TFE (Teflon)	CF ₂	0.640	0.880	0.560	0.240	0	0	0.800
CTFE (Kel-F)	CF _{1.5} Cl _{0.50}	0.552	0.759	0.483	0.207	0	0.310	0.517
<i>Chloropolymers</i>								
PE-25% Cl	CH _{1.9} Cl _{0.13}	2.56	2.38	1.52	0.650	0.753	0.254	0
PE-36% Cl	CH _{1.8} Cl _{0.22}	2.16	2.05	1.30	0.558	0.642	0.368	0
Neoprene	CH _{1.25} Cl _{0.25}	1.91	2.00	1.27	0.546	0.602	0.409	0
PE-42% Cl	CH _{1.8} Cl _{0.29}	1.94	1.84	1.17	0.501	0.576	0.424	0
PE-48% Cl	CH _{1.7} Cl _{0.36}	1.73	1.67	1.06	0.456	0.521	0.493	0
PVC	CH _{1.5} Cl _{0.50}	1.42	1.42	0.903	0.387	0.436	0.581	0
PVCl ₂	CHCl	0.833	0.917	0.583	0.250	0.271	0.750	0

^aCalculated from the data for the elemental compositions of the materials in the FMRC Flammability Laboratory; subscript hc is total gaseous hydrocarbons; s is soot.^b $\eta SiO_2 = 0.483$.^c $\eta SiO_2 = 0.610$.^d $\eta SiO_2 = 0.811$.

For hydrocarbons,



$$\Psi_{\text{hc}} = \frac{13.3}{22.3} = 0.60$$

For smoke,



$$\Psi_s = \frac{12}{22.3} = 0.54$$

EXAMPLE 18:

For the material in Examples 16 and 17, the generation efficiencies of CO_2 , CO , hydrocarbons, and smoke are 0.90, 0.004, 0.002, and 0.036, respectively. The heat of gasification is 1.63 kJ/g, the surface re-radiation loss is 11 kW/m², and the predicted asymptotic flame heat flux value for large-scale fires is 60 kW/m². Calculate the yields and asymptotic values for the generation rates of CO_2 , CO , hydrocarbons, and smoke expected in large-scale fires.

SOLUTION:

- Yields from Equation 66 and data from Example 17:

$$y_{\text{CO}_2} = 0.90 \times 1.97 = 1.77 \text{ g/g}$$

$$y_{\text{CO}} = 0.004 \times 1.26 = 0.005 \text{ g/g}$$

$$y_{\text{hc}} = 0.002 \times 0.60 = 0.001 \text{ g/g}$$

$$y_s = 0.036 \times 0.54 = 0.019 \text{ g/g}$$

- Asymptotic values for the mass loss rate from Equation 11:

$$\dot{m}'' = \frac{60 - 11}{1.63} = 30 \text{ g/m}^2\cdot\text{s}$$

- Asymptotic values for the mass generation rates of products from Equation 42 and the above data:

$$\dot{G}_{\text{CO}_2}'' = 1.77 \times 30 = 53 \text{ g/m}^2\cdot\text{s}$$

$$\dot{G}_{\text{CO}}'' = 0.005 \times 30 = 0.159 \text{ g/m}^2\cdot\text{s}$$

$$\dot{G}_{\text{hc}}'' = 0.001 \times 30 = 0.036 \text{ g/m}^2\cdot\text{s}$$

$$\dot{G}_s'' = 0.019 \times 30 = 0.584 \text{ g/m}^2\cdot\text{s}$$

Generation rates of fire products and fire ventilation:

As discussed previously, the effects of decrease in fire ventilation, as characterized by the increase in the local equivalence ratio, are reflected in the increase in the generation rates of the reduction zone products (smoke, CO , hydrocarbons, and others). For example, for flaming wood crib enclosure fires, as the equivalence ratio increases, the combustion efficiency decreases, flame becomes unstable, and the generation efficiency of CO reaches its peak for the equivalence ratio between about 2.5 and 4.0.⁴⁴

The ventilation-controlled building fires are generally characterized by two layers: (1) a ceiling vitiated layer, identified as *upper layer*, and (2) an uncontaminated layer below, identified as *lower layer*. Incorporation of

these two layers is the classical two-zone modeling of fires in enclosed spaces. Under many conditions, the depth of the upper layer occupies a significant fraction of the volume of the enclosed space. Eventually, the interface between the upper layer and the lower layer positions itself so that it is very close to the floor, very little oxygen is available for combustion, and most of the fuel is converted to the reduction zone products, that is, smoke, CO , hydrocarbons, and others.

Ventilation-controlled large- and small-enclosure and laboratory-scale fires and fires in the vitiated upper layer under the experimental hoods have been studied in detail, and are discussed or reviewed in References 44 and 63 through 66. The results from these types of fires are very similar. Detailed studies⁴⁴ performed for the generation rates of fire products for various fire ventilation conditions in the ASTM E2058 fire propagation apparatus [Figure 3-4.2(a)], and in the Fire Research Institute's (FRI) enclosure, show that with increase in the equivalence ratio (1) generation efficiencies of oxidation zone products, such as CO_2 , and reactant consumption efficiency (i.e., oxygen) decrease, and (2) generation efficiencies of the reduction zone products, such as smoke, CO , and hydrocarbons increase.

Generalized correlations have been established between the generation efficiencies and the equivalence ratio for the oxidation and reduction zone products. The changes in the consumption or generation efficiencies of the products are expressed as ratios of the efficiencies for the ventilation-controlled (*vc*) to well-ventilated (*wv*) fires:

Reactants (oxygen)

$$\zeta_O = \frac{(n_O)_{\text{vc}}}{(n_O)_{\text{wv}}} = \frac{(c_O/\Psi_O)_{\text{vc}}}{(c_O/\Psi_O)_{\text{wv}}} = \frac{(c_O)_{\text{vc}}}{(c_O)_{\text{wv}}} \quad (67)$$

Oxidation zone products (carbon dioxide, water, etc.)

$$\zeta_{\text{oxid}} = \frac{(\eta_j)_{\text{vc}}}{(\eta_j)_{\text{wv}}} = \frac{(y_j/\Psi_j)_{\text{vc}}}{(y_j/\Psi_j)_{\text{wv}}} = \frac{(y_j)_{\text{vc}}}{(y_j)_{\text{wv}}} \quad (68)$$

where ζ_{oxid} is the oxidation zone product generation efficiency ratio.

Reduction zone products (smoke, carbon monoxide, hydrocarbons, etc.)

$$\zeta_{\text{red}} = \frac{(\eta_j)_{\text{vc}}}{(\eta_j)_{\text{wv}}} = \frac{(y_j/\Psi_j)_{\text{vc}}}{(y_j/\Psi_j)_{\text{wv}}} = \frac{(y_j)_{\text{vc}}}{(y_j)_{\text{wv}}} \quad (69)$$

where ζ_{red} is the reduction zone product generation efficiency ratio.

The relationships between the ratios of the mass of oxygen consumed per unit mass of fuel, the yields of the products for the ventilation-controlled to well-ventilated fires, and the equivalence ratio are shown in Figures 3-4.29 through 3-4.33. The ratios for oxygen and CO_2 (an oxidation zone product) do not depend on the chemical structures of the materials, whereas the ratios for the reduction zone products do depend on the chemical structures of the materials.

Oxygen and CO_2 . The relationships for oxygen consumed and carbon dioxide generated are shown in Figures 3-4.29 and 3-4.30, respectively. The relationships are

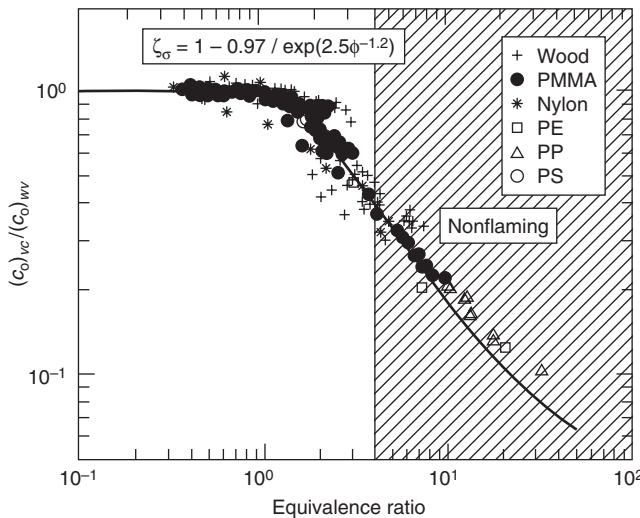


Figure 3-4.29. Ratio of the mass of oxygen consumed per unit mass of the fuel for ventilation-controlled to well-ventilated fires. Data are measured in the ASTM E2058 fire propagation apparatus and in the Fire Research Institute's enclosure.⁴⁴ Subscript vc represents ventilation-controlled fires, and subscript wv represents well-ventilated fires.

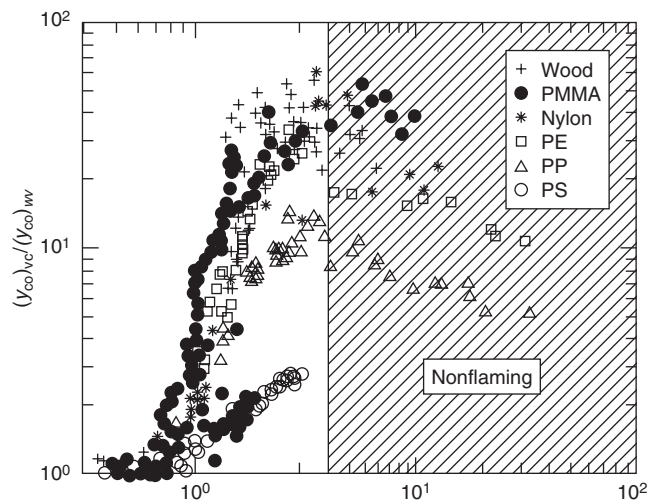


Figure 3-4.31. Ratio of the mass of carbon monoxide generated per unit mass of the fuel for ventilation-controlled to well-ventilated fires. Data are measured in the ASTM E2058 fire propagation apparatus and in the Fire Research Institute's enclosure.⁴⁴ Subscript vc represents ventilation-controlled fires, and subscript wv represents well-ventilated fires.

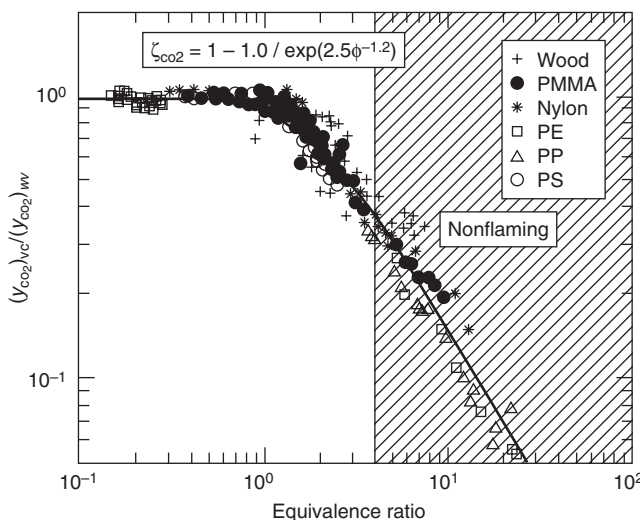


Figure 3-4.30. Ratio of the mass of carbon dioxide generated per unit mass of the fuel for ventilation-controlled to well-ventilated fires. Data are measured in the ASTM E2058 fire propagation apparatus and in the Fire Research Institute's enclosure.⁴⁴ Subscript vc represents ventilation-controlled fires, and subscript wv represents well-ventilated fires.

very similar to the relationships for the chemical and convective heats of combustion ratios (Equations 40 and 41), as expected:

$$\frac{(c_O)_{vc}}{(c_O)_{wv}} = 1 - \frac{0.97}{\exp(\Phi/2.14)^{-1.2}} \quad (70)$$

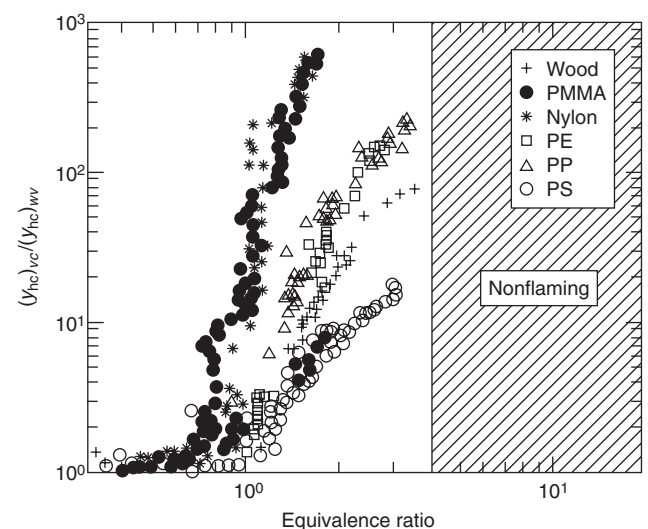


Figure 3-4.32. Ratio of the mass of hydrocarbons generated per unit mass of the fuel for ventilation-controlled to well-ventilated fires. Data are measured in the ASTM E2058 fire propagation apparatus and in the Fire Research Institute's enclosure.⁴⁴ Subscript vc represents ventilation-controlled fires, and subscript wv represents well-ventilated fires.

$$\frac{(y_{CO_2})_{vc}}{(y_{CO_2})_{wv}} = 1 - \frac{1.00}{\exp(\Phi/2.15)^{-1.2}} \quad (71)$$

Carbon monoxide. The relationship between the ratio of the CO yields for ventilation-controlled to well-ventilated

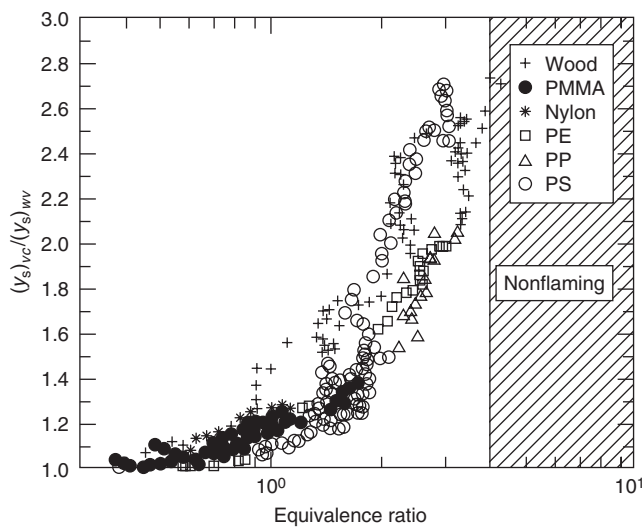


Figure 3-4.33. Ratio of the mass of smoke generated per unit mass of the fuel for ventilation-controlled to well-ventilated fires. Data are measured in the ASTM E2058 fire propagation apparatus and in the Fire Research Institute's enclosure.⁴⁴ Subscript vc represents ventilation-controlled fires, and subscript wv represents well-ventilated fires.

fires and the equivalence ratio is shown in Figure 3-4.30. The data suggest the following relationship:⁴⁴

$$\frac{(y_{CO})_{vc}}{(y_{CO})_{wv}} = 1 + \frac{\alpha}{\exp(2.5\Phi^{-\xi})} \quad (72)$$

where α and ξ are the correlation coefficients, which depend on the chemical structures of the materials. The values for the correlation coefficients for CO are listed in Table 3-4.17.

The increase in the ratio of the carbon monoxide yields for the ventilation-controlled to well-ventilated fires with the equivalence ratio is due to the preferential conversion of the fuel carbon atoms to CO. The experimental data show the following order for the preferential conversion: wood (C-H-O aliphatic structure) > PMMA

(C-H-O aliphatic structure) > nylon (C-H-O-N aliphatic structure) > PE (C-H aliphatic linear unsaturated structure) > PP (C-H aliphatic branched unsaturated structure) > PS (C-H aromatic structure). A similar trend is found for the liquid and gaseous fuels, such as shown in Table 3-4.18.⁴⁴ The presence of O and N atoms in the fuels with aliphatic C-H structure appears to enhance preferential fuel carbon atom conversion to CO.

Hydrocarbons. The relationship between the ratio of the hydrocarbon yields for ventilation-controlled to well-ventilated fires and the equivalence ratio is shown in Figure 3-4.32. The data suggest the following relationship:⁴⁴

$$\frac{(y_{hc})_{vc}}{(y_{hc})_{wv}} = 1 + \frac{\alpha}{\exp(5.0\Phi^{-\xi})} \quad (73)$$

The correlation coefficient values for hydrocarbons are listed in Table 3-4.17. The numerator in the second term on the right-hand side of Equation 73 is 10 to 40 times that of CO, whereas the denominator is twice that for CO. This relationship suggests that there is a significantly higher preferential fuel conversion to hydrocarbons than to CO, with increase in the equivalence ratio. The order for the preferential fuel conversion to hydrocarbons is very similar to CO, except for wood; that is, PMMA > nylon > PE = PP > wood > PS. The exception for wood may be due to char-forming tendency of the fuel, which lowers the C-to-H ratio in the gas phase.

Smoke. The relationship between the ratio of the smoke yields for ventilation-controlled to well-ventilated fires and the equivalence ratio is shown in Figure 3-4.33. The data suggest the following relationship:⁴⁴

$$\frac{(y_s)_{vc}}{(y_s)_{wv}} = 1 + \frac{\alpha}{\exp(2.5\Phi^{-\xi})} \quad (74)$$

The correlation coefficient values for smoke are listed in Table 3-4.17. The values of the correlation coefficients in

Table 3-4.18 Carbon Monoxide Generation Efficiency for Ventilation-Controlled and Well-Ventilated Combustion^a

Fuel	Well-Ventilated (wv) ^b $\Phi < 0.05$	Ventilation- Controlled (vc) $\Phi \approx 4.0$		$\frac{(y_{CO})_{vc}}{(y_{CO})_{wv}}$
		Ref. 64	Ref. 65	
Methane	0.001	0.10	—	100
Propane	0.001	—	0.12	120
Propylene	0.004	0.10	—	25
Hexane	0.002	0.10	0.52 ^c	50 (260 ^c)
Methanol	0.001	0.27	1.00 ^c	270 (1000 ^c)
Ethanol	0.001	0.18	0.66 ^c	180 (660 ^c)
Isopropanol	0.002	0.21	—	105
Acetone	0.002	0.21	0.63 ^c	105 (315 ^c)

^aTable taken from Reference 44.

^bFrom ASTM E2058 fire propagation apparatus.

^cNonflaming.

Table 3-4.17 Correlation Coefficients to Account for the Effects of Ventilation on the Generation Rates of CO, Hydrocarbons, and Smoke

Material	CO		Hydrocarbons		Smoke	
	α	ξ	α	ξ	α	ξ
PS	2	2.5	25	1.8	2.8	1.3
PP	10	2.8	220	2.5	2.2	1.0
PE	10	2.8	220	2.5	2.2	1.0
Nylon	36	3.0	1200	3.2	1.7	0.8
PMMA	43	3.2	1800	3.5	1.6	0.6
Wood	44	3.5	200	1.9	2.5	1.2
PVC	7	8.0	25	1.8	0.38	8.0

the second term on the right-hand side of Equation 74 suggest that, with the increase in the equivalence ratio, the preferential fuel conversion to smoke is lower than it is to hydrocarbons and CO. Also, the order for the preferential conversion of the fuel carbon atom to smoke is opposite to the order for the conversion to CO and hydrocarbons, except for wood. The order is PS > wood > PE = PP > nylon > PMMA, suggesting that the order is probably due to decrease in the preference for the reactions between OH and CO compared to the reactions between OH and soot.

Other reduction zone products. Since the sum of the generation efficiencies of all the products for a material cannot exceed unity, the generation efficiency of products other than CO, CO₂, hydrocarbons, and smoke is

$$\eta_{\text{other}} = 1 - (\eta_{\text{CO}} + \eta_{\text{CO}_2} + \eta_{\text{hc}} + \eta_s) \quad (75)$$

where η_{other} is the generation efficiency of products other than CO, CO₂, hydrocarbons, and smoke. The generation efficiency of other products can be calculated from Equations 71 through 75 using correlation coefficients from Table 3-4.17. The generation efficiency values for other products calculated in this fashion for various equivalence ratios are shown in Figure 3-4.34. The figure shows that, for equivalence ratios greater than 4, where fires are nonflaming, about 10 to 60 percent of fuel carbon is converted to products other than CO, CO₂, soot, and hydrocarbons.

The order for the preferential conversion of fuel carbon to other products in the nonflaming zone is PS (C-H aromatic structure) < PE & PP (C-H aliphatic structure) < wood (C-H-O aliphatic structure) < nylon (C-H-O-N aliphatic structure) < PMMA (C-H-O aliphatic structure). It thus appears that, in nonflaming fire, fuels with C-H structures are converted mainly to CO, smoke, and hydro-

carbons, rather than to other products, whereas fuels with C-H-O and C-H-O-N structures are converted mainly to products other than CO, CO₂, smoke, and hydrocarbons. Some of the products include formaldehyde (HCHO) and hydrogen cyanide (HCN).⁴⁴

Generation efficiencies of formaldehyde, hydrogen cyanide, and nitrogen dioxide. The experimental data for the generation efficiencies of formaldehyde, hydrogen cyanide, and nitrogen dioxide versus the equivalence ratio are shown in Figures 3-4.35 and 3-4.36.

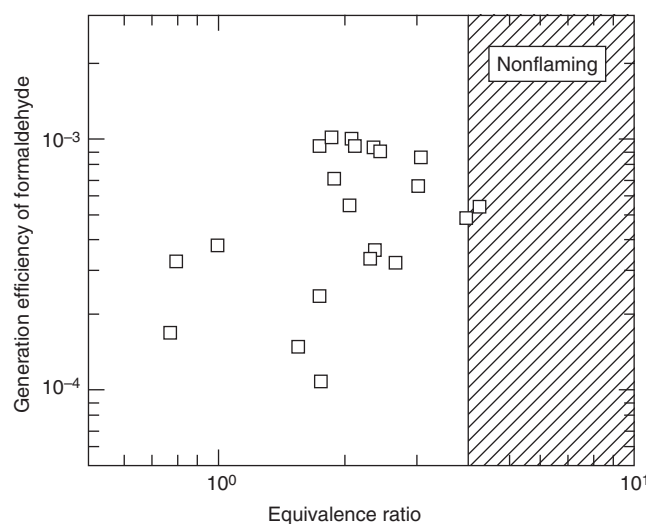


Figure 3-4.35. Generation efficiency of formaldehyde generated from wood versus the equivalence ratio.

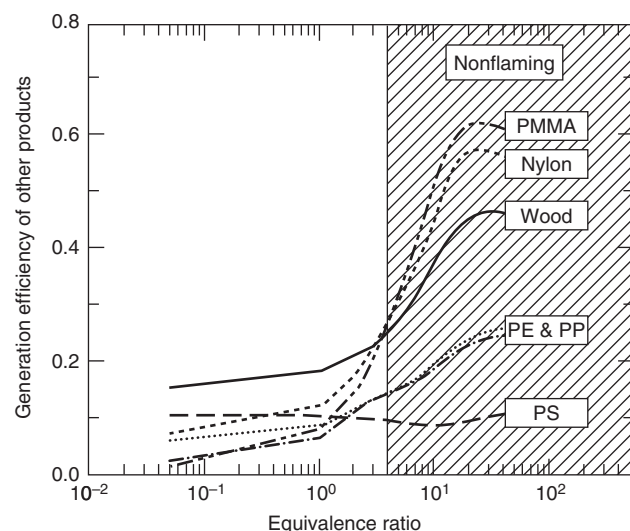


Figure 3-4.34. Generation efficiency of products other than CO, CO₂, hydrocarbons, and smoke versus the equivalence ratio.

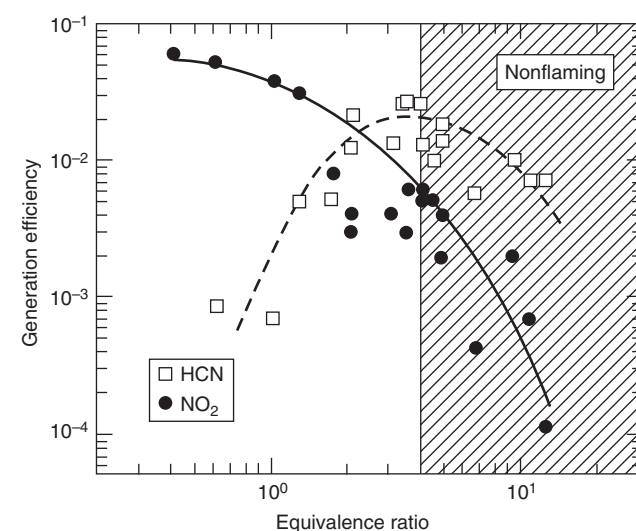


Figure 3-4.36. Generation efficiencies of hydrogen cyanide and nitrogen dioxide generated from nylon versus the equivalence ratio.

Formaldehyde is generated in the pyrolysis of wood (C-H-O structure). It is attacked rapidly by oxygen (O) and hydroxyl (OH) radicals in the flame, if unlimited supply of oxygen is available. Thus, only traces of formaldehyde are found in well-ventilated fires. The generation efficiency of formaldehyde, however, increases with the equivalence ratio, indicating reduced concentrations of O and OH radicals and gas temperature due to lack of oxygen available for combustion.

In fires, hydrogen cyanide is formed in the reduction zone from materials with hydrogen and nitrogen atoms in the structure, such as nylon (C-H-O-N structure). Nitrogen dioxide (NO_2), on the other hand, is formed in the oxidation zone, as a result of the oxidation of hydrogen cyanide. The data in Figure 3-4.36 show that the generation efficiency of hydrogen cyanide increases and the generation efficiency of NO_2 decreases with the equivalence ratio. This observation supports that O and OH radical concentrations decrease with increase in the equivalence ratio. The decrease in the generation efficiency of hydrogen cyanide in the nonflaming fire suggests decrease in the fuel mass transfer rate.

Relationship between the generation efficiencies of CO_2 and CO. The relationship between the generation efficiencies of CO_2 and CO is shown in Figure 3-4.37, where the data are taken from Reference 44. CO is generated in the reduction zone of the flame as a result of the oxidative pyrolysis of the fuel, and is oxidized to CO_2 in the oxidation zone of the flame. The generation efficiency of CO_2 is independent of the chemical structure of the fuel (Figure 3-4.30), whereas the generation efficiency of CO depends on the chemical structure of the fuel (Figure 3-4.31). In Figure 3-4.37, the curves represent approximate predictions based on the correlation coefficients from Table 3-4.17 and Equations 71 and 72.

The relationship between the generation efficiencies of CO_2 and CO is quite complex. The boundary of the shaded region marked *air* in Figure 3-4.37 is drawn using

the data for the well-ventilated combustion for equivalence ratios less than 0.05. The boundary of the *air* region may be considered as equivalent to the lower flammability limit. No flaming combustion is expected to occur in this region, as the fuel-air mixture is below the lower flammability limit; however, nonflaming combustion, generally identified as smoldering, may continue. The boundary of the shaded region marked *fuel* is drawn using the data for the ventilation-controlled combustion for equivalence ratio of 4.0, and may be considered as equivalent to the upper flammability limit. In the *fuel* region, no flaming combustion is expected to occur, as the fuel-air mixture is above the upper flammability limit; however, nonflaming processes may continue. The shaded region marked *chemical structure* and drawn to the right of the methanol curve is an imaginary region as it is not expected to exist, because there are no stable carbon-containing fuel structures below the formaldehyde with a structure of HCHO. For the stable fuels with C-H-O structures, formaldehyde (HCHO) and methanol (CH_3OH) have the lowest molecular weights (30 and 32, respectively). Thus, data for HCHO and CH_3OH probably would be comparable.

The curves in Figure 3-4.37 show that, in flaming combustion, with increase in the equivalence ratio, the preference for fuel carbon atom conversion to CO, relative to the conversion to CO_2 , follows this order: methanol (C-H-O structure) > ethanol (C-H-O structure) > wood (C-H-O structure) > PMMA (C-H-O structure) > nylon (C-H-O-N structure) > PP (C-H aliphatic unsaturated branched structure) \geq (CH_4 , C_3H_6 , C_3H_8 , C_6H_{14}) \geq PE (C-H aliphatic unsaturated linear structure) > PS (C-H aromatic unsaturated structure). Thus for fires in enclosed spaces, generation of higher amounts of CO relative to CO_2 at high local equivalence ratios is expected for fuels with C-H-O structures compared to the fuels with C-H structures. The reason for higher amounts of CO relative to CO_2 for fuels with C-H-O structures is that CO is easily generated in fuel pyrolysis, but is oxidized only partially to CO_2 due to limited amounts of oxidant available.

Relationship between the generation efficiencies of CO and smoke: The relationship between the generation efficiencies of CO and smoke is shown in Figure 3-4.38, where data are taken from Reference 44. CO and smoke are both generated in the reduction zone of the flame as a result of the oxidative pyrolysis of the fuel, and their generation efficiencies depend on the chemical structure of the fuel (Figures 3-4.31 and 3-4.33). In Figure 3-4.38, the curves represent approximate predictions based on the correlation coefficients from Table 3-4.17 and Equations 72 and 74.

The relationship in Figure 3-4.38 is quite complicated. The boundary of the shaded region marked *air* is drawn using the data for the well-ventilated combustion for equivalence ratios less than 0.05. The boundary of the shaded region marked *fuel* is drawn using the data for the ventilation-controlled combustion for equivalence ratio of 4.0. The boundary for the region marked *air* may be considered as equivalent to the lower flammability limit, and the boundary for the region marked *fuel* may be considered as equivalent to the upper flammability limit.

In Figure 3-4.38, the order for the preference for fuel carbon atom conversion to smoke relative to conversion

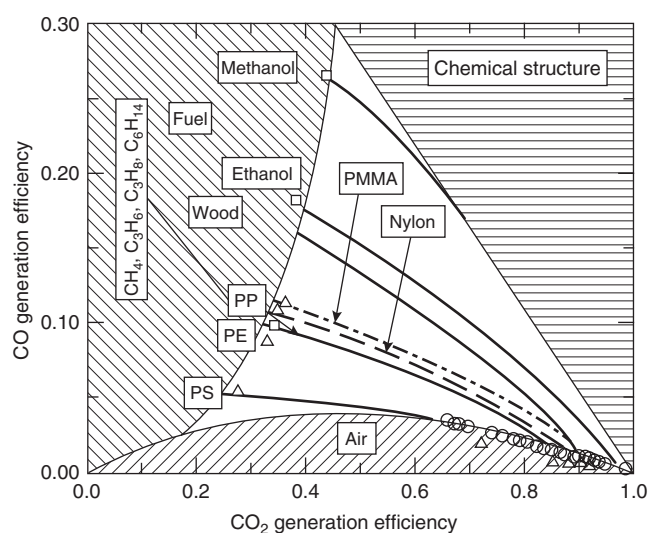


Figure 3-4.37. Relationship between the generation efficiencies of CO_2 and CO. Data taken from Reference 44.

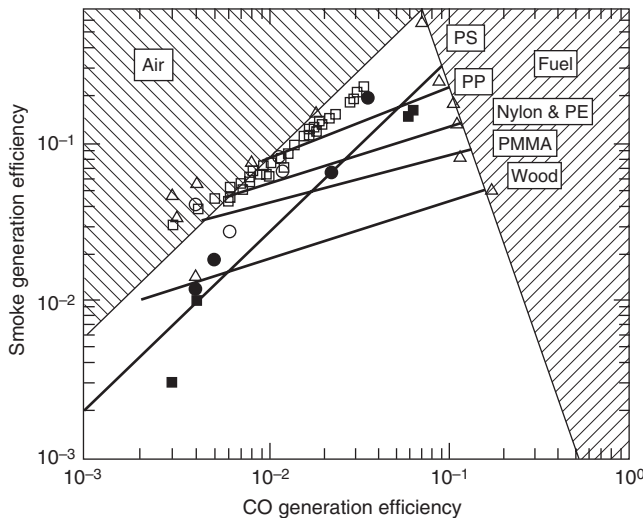


Figure 3-4.38. Relationship between the generation efficiencies of CO and smoke. Data taken from Reference 44.

to CO is wood (C-H-O structure) < PMMA (C-H-O structure) < nylon (C-H-O-N structure) < PP (C-H aliphatic unsaturated branched structure) \approx PE (C-H aliphatic unsaturated linear structure) < PS (C-H aromatic structure). The generation efficiency of smoke for PS, which is a polymer with aromatic C-H structure, is the highest. The generation efficiency of smoke for wood, which is a polymer with aliphatic C-H-O structure, is the lowest.

Generalized Relationships to Calculate Chemical, Convective, and Radiative Heats of Combustion and Yields of Products at Various Equivalence Ratios

The following relationship is the generalized form of Equations 40, 41, and 70 through 74:

$$fp = fp_{\infty} \left[1 + \frac{\alpha}{\exp(\Phi/\beta)^{-\xi}} \right] \quad (76)$$

where

fp = fire property

α , β , and ξ = correlation coefficients characteristic of the chemical structures of the polymers

subscript ∞ = infinite amount of air

fp = constant for each polymer when determined under turbulent flame conditions

The fire properties are heat of combustion (or combustion efficiency) and yields (or generation efficiencies) of products. Three conditions can be identified: (1) for $\Phi \gg \beta$, $fp = fp_{\infty}(1 + \alpha)$; (2) for $\Phi \ll \beta$, $fp = fp_{\infty}$; and (3) $\Phi \approx \beta$, $fp \approx fp_{\infty}(1 + \alpha/2.7)$. Thus, the parameter α is associated primarily with the magnitude of the fire properties in nonflaming fires (high Φ values). The parameter β is associated with the fire properties in the transition region be-

tween the fires with an infinite amount of air and the fires with a very restricted amount of air. The parameter ξ is associated with the range of Φ values for the transition region. A high value of α is indicative of a strong effect of ventilation on the fire and its properties and vice versa. High values of β and ξ are indicative of rapid change of fire from flaming to nonflaming by a small change in the equivalence ratio, such as for the highly fire-retarded or halogenated materials for which flaming combustion in normal air itself is unstable.

Chemical heat of combustion versus equivalence ratio for the nonhalogenated polymers: From Equation 76,

$$\Delta H_{ch} = \Delta H_{ch,\infty} \left[1 - \frac{0.97}{\exp(\Phi/2.15)^{-1.2}} \right] \quad (77)$$

The values of $\Delta H_{ch,\infty}$ for several polymers are listed in Table 3-4.14.

Chemical heat of combustion versus equivalence ratio for the halogenated polymers (polyvinylchloride):

$$\Delta H_{ch} = \Delta H_{ch,\infty} \left[1 - \frac{0.30}{\exp(\Phi/0.53)^{-11}} \right] \quad (78)$$

As can be noted from the terms inside the brackets in Equations 77 and 78, the effect of ventilation on the chemical heat of combustion is much stronger for PVC than it is for the nonhalogenated polymers. The effect for PVC occurs at $\Phi \geq 0.4$, which is significantly lower than $\Phi \geq 2.0$ found for the nonhalogenated polymers.^{44,68} For PVC homopolymer, the flaming combustion changes to nonflaming combustion for $\Phi \geq 0.70$, which is also significantly lower than $\Phi \geq 4.0$ found for the nonhalogenated polymers. This attribute is consistent with the highly halogenated nature of PVC and its mode of decomposition. The decomposition of PVC is characterized by the release of HCl, which is initiated at temperatures as low as about 100°C. At temperatures of up to 200 to 220°C, HCl is the major effluent. Presence of oxygen in the air enhances HCl release. The generation of HCl from PVC leads to the formation of double bonds and release of various aromatic/unsaturated hydrocarbons (benzene, ethylene, propylene, butylene, etc.).

Convective heats of combustion versus equivalence ratio for the nonhalogenated polymers: From Equation 76,

$$\Delta H_{con} = \Delta H_{con,\infty} \left[1 - \frac{1.0}{\exp(\Phi/1.38)^{-2.8}} \right] \quad (79)$$

The values of $\Delta H_{con,\infty}$ for several polymers are listed in Table 3-4.14.

Radiative heats of combustion versus equivalence ratio for the nonhalogenated polymers: Radiative heats of combustion are obtained from the difference between the chemical and the convective heats of combustion:

$$\Delta H_{rad} = \Delta H_{ch} - \Delta H_{con} \quad (80)$$

Consumption of oxygen for the nonhalogenated polymers: From Equation 76,

$$c_O = c_{O,\infty} \left[1 - \frac{0.97}{\exp(\Phi/2.14)^{-1.2}} \right] \quad (81)$$

Yield of carbon dioxide for the nonhalogenated polymers: From Equation 76,

$$y_{CO_2} = y_{CO_2,\infty} \left[1 - \frac{1.0}{\exp(\Phi/2.15)^{-1.2}} \right] \quad (82)$$

$y_{CO_2,\infty}$ values are listed in Table 3-4.14.

Yield of carbon dioxide for the halogenated polymers (PVC): From Equation 76,

$$y_{CO_2} = y_{CO_2,\infty} \left[1 - \frac{0.30}{\exp(\Phi/0.53)^{-11}} \right] \quad (83)$$

From the terms inside the brackets in Equations 82 and 83, a stronger effect of ventilation on the yield of CO_2 for PVC than for the nonhalogenated polymers can be noted. $y_{CO_2,\infty}$ values are listed in Table 3-4.14.

Yields of carbon monoxide, hydrocarbons, and smoke for the nonhalogenated polymers: From Equation 76,

Polystyrene

$$y_{CO} = y_{CO,\infty} \left[1 + \frac{2.0}{\exp(\Phi/1.44)^{-2.5}} \right] \quad (84)$$

$$y_{hc} = y_{hc,\infty} \left[1 + \frac{25}{\exp(\Phi/2.45)^{-1.8}} \right] \quad (85)$$

$$y_s = y_{s,\infty} \left[1 + \frac{2.8}{\exp(\Phi/2.02)^{-1.3}} \right] \quad (86)$$

The $y_{CO,\infty}$, $y_{hc,\infty}$, and $y_{s,\infty}$ values are listed in Table 3-4.14.

Polyethylene and Polypropylene

$$y_{CO} = y_{CO,\infty} \left[1 + \frac{10}{\exp(\Phi/1.39)^{-2.8}} \right] \quad (87)$$

$$y_{hc} = y_{hc,\infty} \left[1 + \frac{220}{\exp(\Phi/1.90)^{-2.5}} \right] \quad (88)$$

$$y_s = y_{s,\infty} \left[1 + \frac{2.2}{\exp(\Phi/2.50)^{-1.0}} \right] \quad (89)$$

The $y_{CO,\infty}$, $y_{hc,\infty}$, and $y_{s,\infty}$ values are listed in Table 3-4.14.

Polymethylmethacrylate

$$y_{CO} = y_{CO,\infty} \left[1 + \frac{43}{\exp(\Phi/1.33)^{-3.2}} \right] \quad (90)$$

$$y_{hc} = y_{hc,\infty} \left[1 + \frac{1800}{\exp(\Phi/1.58)^{-3.5}} \right] \quad (91)$$

$$y_s = y_{s,\infty} \left[1 + \frac{1.6}{\exp(\Phi/4.61)^{-0.60}} \right] \quad (92)$$

The $y_{CO,\infty}$, $y_{hc,\infty}$, and $y_{s,\infty}$ values are listed in Table 3-4.14.
Wood

$$y_{CO} = y_{CO,\infty} \left[1 + \frac{44}{\exp(\Phi/1.30)^{-3.5}} \right] \quad (93)$$

$$y_{hc} = y_{hc,\infty} \left[1 + \frac{200}{\exp(\Phi/2.33)^{-1.9}} \right] \quad (94)$$

$$y_s = y_{s,\infty} \left[1 + \frac{2.5}{\exp(\Phi/2.15)^{-1.2}} \right] \quad (95)$$

The $y_{CO,\infty}$, $y_{hc,\infty}$, and $y_{s,\infty}$ values are listed in Table 3-4.14.
Nylon

$$y_{CO} = y_{CO,\infty} \left[1 + \frac{36}{\exp(\Phi/1.36)^{-3.0}} \right] \quad (96)$$

$$y_{hc} = y_{hc,\infty} \left[1 + \frac{1200}{\exp(\Phi/1.65)^{-3.2}} \right] \quad (97)$$

$$y_s = y_{s,\infty} \left[1 + \frac{1.7}{\exp(\Phi/3.14)^{-0.8}} \right] \quad (98)$$

The $y_{CO,\infty}$, $y_{hc,\infty}$, and $y_{s,\infty}$ values are listed in Table 3-4.14.

Yields of Carbon Monoxide, Hydrocarbons, and Smoke for the Halogenated Polymers (Polyvinylchloride)

From Equation 76,

$$y_{CO} = y_{CO,\infty} \left[1 + \frac{7}{\exp(\Phi/0.42)^{-8.0}} \right] \quad (99)$$

$$y_{hc} = y_{hc,\infty} \left[1 + \frac{25}{\exp(\Phi/0.42)^{-1.8}} \right] \quad (100)$$

$$y_s = y_{s,\infty} \left[1 + \frac{0.38}{\exp(\Phi/2.02)^{-8.0}} \right] \quad (101)$$

From the above relationships for PVC, for $0.40 \geq \Phi \geq 1.0$, the maximum CO and smoke yields reach about 60 percent of the stoichiometric yields, listed in Table 3-4.16. For nonhalogenated polymers, the maximum CO and smoke yields reach ≤ 30 percent of the stoichiometric yields for $\Phi \geq 2.0$. Polystyrene is the only polymer, within the above group of polymers, for which the smoke yield exceeds that of PVC. These trends suggest that CO and smoke are generated much easier from PVC than from the nonhalo-

generated polymers, possibly due to the formation of double bonds, as HCl is eliminated at temperatures as low as 100°C from the PVC structure, and formation of various compounds occurs with aromatic/unsaturated bonds.

For nonhalogenated polymers considered with $\Phi \geq 4.0$, the CO yield is lowest and the smoke yield is highest for polystyrene, an aromatic ring-containing polymer; whereas, for polymethylmethacrylate, an aliphatic carbon-hydrogen-oxygen-atom-containing polymer, the CO yield is highest and smoke yield is lowest. This result suggests that aromatic ring structure promotes smoke formation, whereas the strong C-O bond in the structure remains intact as ventilation is reduced.

EXAMPLE 19:

Following Example 13, calculate the yields of CO and smoke at equivalence ratios of 1, 2, and 3 for polystyrene, polyethylene, wood, and nylon using Equations 84 and 86, 87 and 89, 93 and 95, and 96 and 98, respectively.

SOLUTION:

Material	Yield (g/g)							
	$\Phi \ll 1.0$		$\Phi = 1.0$		$\Phi = 2.0$		$\Phi = 3.0$	
	CO	Smoke	CO	Smoke	CO	Smoke	CO	Smoke
Polystyrene	0.060	0.164	0.070	0.202	0.137	0.331	0.162	0.417
Polyethylene	0.024	0.060	0.043	0.071	0.191	0.098	0.238	0.117
Wood	0.004	0.015	0.018	0.018	0.145	0.028	0.171	0.034
Nylon	0.038	0.075	0.149	0.086	1.04	0.105	1.28	0.120

Prediction of Fire Properties Using Smoke Point

Smoke emission characteristics of fuels have been expressed for decades by smoke point, defined as a minimum laminar axisymmetric diffusion flame height (or fuel volumetric or mass flow rate) at which smoke just escapes from the flame tip.^{48,49,69–84} Smoke-point values have been measured for numerous gases, liquids, and solids.^{48,49,69–74}

Almost all the knowledge on smoke formation, oxidation, and emission from diffusion flames is based on the combustion of fuels containing carbon and hydrogen atoms (hydrocarbons).^{71,76–79} On the basis of the chemical structure, hydrocarbons are divided into two main classes: (1) aliphatic and (2) aromatic. Fuels containing both aliphatic and aromatic units are known as arenes. Aliphatic fuels have open-chain structure, and aromatic fuel structures consist of benzene rings. Aliphatic hydrocarbons are divided into three families: (1) alkanes (C_nH_{2n+2}), where n is an integer—the suffix *ane* indicates a single bond; (2) alkenes (C_nH_{2n})—the suffix *ene* indicates a double bond, and *diene*, two double bonds between carbon-carbon atoms; and (3) alkynes ($C_{2n}H_{2n-2}$)—the suffix *yne* indicates a triple bond. The integer n can vary from one in a gas, such as methane, to several thousands in solid polymers, such as polyethylene. In cyclic aliphatic fuels, carbon atoms are also arranged as rings. Dienes are classified as (1) conjugated—double bonds alternate with

single bonds, (2) isolated—double bonds separated by more than one single bond, and (3) allens—double bonds with no separation. Conjugated dienes are more stable than other dienes.

Solid carbon particles present in smoke are defined as soot.^{71,76} Soot is generally formed in the fuel-rich regions of the flame and grows in size through gas-solid reactions, followed by oxidation (burnout) to produce gaseous products, such as CO and CO_2 . Time that is available for soot formation in the flame is a few milliseconds. Soot particle inception occurs from the fuel molecule via oxidation and/or pyrolysis products, which typically includes unsaturated hydrocarbons, especially acetylene, polyacetylenes, and polycyclic aromatic hydrocarbons (PAH). Acetylene, polyacetylenes, and PAH are relatively stable with respect to decomposition. Acetylene and PAH are often considered the most likely precursors for soot formation in flames. PAH have the same role in diffusion flames for both aliphatic and aromatic fuels. In all flames, irrespective of the fuel, initial detection of soot particles takes place on the centerline when a temperature of 1350 K is encountered. Thus, even though the extent of conversion of a fuel into soot may significantly change from fuel to fuel, a common mechanism of soot formation is suggested.

Soot production in the flame depends on the chemical structure, concentration, and temperature of the fuel and flame temperature, pressure, and oxygen concentration.^{71,76–79} The diffusion-controlled flame ends when fuel and oxidant are in stoichiometric ratio on the flame axis. The flame is followed by a soot after-burning zone, which is partially chemically controlled. The soot oxidation zone increases from about 10 to 50 percent of the visible flame length as the soot concentration increases. Flame luminosity and smoke emission in the plume depend on overall soot production and oxidation. Flames emit soot when soot temperature in the oxidation zone falls below 1300 K. The soot temperature decreases downstream because of radiation losses and diffusion of fresh cold air, both of which quench soot oxidation. At high soot concentrations, flame emissivity approaches unity, and flame luminosity becomes independent of the amount of soot.

Smoke point, carbon-to-hydrogen ratio, aromaticity, and flame temperature have been suggested as useful parameters to assess relative smoke emission characteristics of fuels in laminar diffusion flames.^{48,49,69–74} The soot-forming tendency of fuels is inversely proportional to smoke point. General trends observed for smoke points for hydrocarbon fuels in laminar diffusion flames are aromatics < alkynes < alkenes < alkanes. Smoke-point values have been correlated with flame radiation, combustion efficiency and its convective and radiative components, and generation efficiencies of products.^{48,49,69–74} Figures 3-4.39 through 3-4.41 show the relationships between the smoke point and the combustion efficiency and its convective and radiative components, and generation efficiencies of CO and smoke. The data were measured in the ASTM E2058 fire propagation apparatus [Figure 3-4.2(a)], and reported in References 48 and 49. The following relationships have been found from the data:^{48,49}

$$\chi_{ch} = 1.15L_{sp}^{0.10} \quad (102)$$

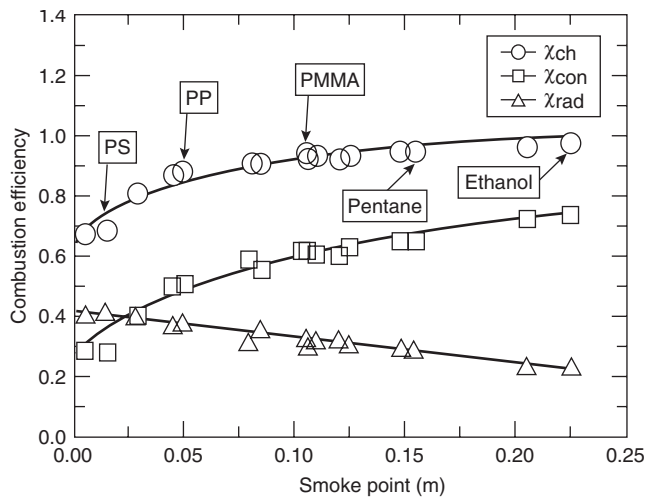


Figure 3-4.39. Relationships between the combustion efficiency and its convective and radiative components, and the smoke point. Data were measured in the ASTM E2058 fire propagation apparatus, and reported in References 48 and 49.

where χ_{ch} is the combustion efficiency (–), and L_{sp} is the smoke point (m) as measured in the ASTM E2058 fire propagation apparatus.

$$\chi_{rad} = 0.41 - 0.85L_{sp} \quad (103)$$

where χ_{rad} is the radiative component of the combustion efficiency (–). This correlation is very similar to the one reported in the literature.⁷²

$$\chi_{con} = \chi_{ch} - \chi_{rad} \quad (104)$$

where χ_{con} is the convective component of the combustion efficiency (–).

$$\eta_{CO} = -[0.0086 \ln(L_{sp}) + 0.0131] \quad (105)$$

where η_{CO} is the generation efficiency of CO (–).

$$\eta_s = -[0.0515 \ln(L_{sp}) + 0.0700] \quad (106)$$

where η_s is the generation efficiency of smoke (–).

The highest value of L_{sp} that has been measured is 0.240 m for ethane. Although methane and methanol would be expected to have smoke points higher than 0.240 m, they have not been measured experimentally. Since the combustion efficiency cannot exceed unity and the generation efficiencies of CO and smoke cannot be negative, the relationships in Equations 102 through 106 are valid for $0 > L_{sp} \leq 0.240$ m.

Smoke point decreases with increase in the molecular weight. The smoke-point values for monomers and polymers, however, show different types of dependencies: (1) the smoke-point values for ethylene and polyethylene

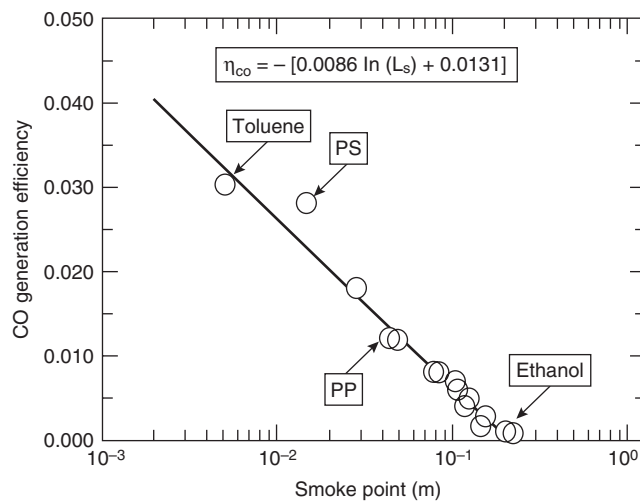


Figure 3-4.40. Relationships between the CO generation efficiency and the smoke point. Data were measured in the ASTM E2058 fire propagation apparatus, and reported in References 48 and 49.

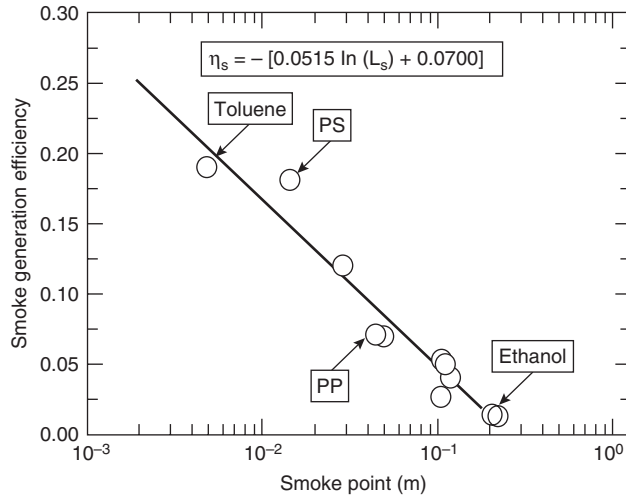


Figure 3-4.41. Relationships between the smoke generation efficiency and the smoke point. Data were measured in the ASTM E2058 fire propagation apparatus, and reported in References 48 and 49.

are 0.097 and 0.045 m, respectively; (2) the smoke-point values for propylene and polypropylene are 0.030 and 0.050 m, respectively; and (3) the smoke-point values for styrene and polystyrene are 0.006 and 0.015 m, respectively. The smoke-point data for polymers support the accepted vaporization mechanisms of polymers;⁸⁵ that is, polyethylene, polypropylene, and polystyrene vaporize as higher molecular weight oligomers rather than as monomers, and thus, their smoke-point values are different than the values for the monomers. The smoke-point

values suggest that polyethylene is expected to have higher smoke emission than ethylene, whereas polypropylene and polystyrene are expected to have lower smoke emissions than propylene and styrene.

The correlations show that emissions of CO and smoke are very sensitive to changes in the smoke-point values compared to combustion efficiency and its convective and radiative components. This condition is expected from the understanding of the relationship between the smoke point and chemical structures of fuels. For example, a decrease of 33 percent in the smoke-point value of 0.15 m to 0.10 m produces a decrease of 4 and 12 percent in the combustion efficiency and its convective component, respectively, and an increase of 14 percent in the radiative component of the combustion efficiency; however, the generation efficiencies of CO and smoke increase by 89 and 67 percent, respectively.

Equations 102 through 106 can be used to estimate the fire properties of gases, liquids, and solids from their smoke-point values. The smoke-point values, however, depend strongly on the apparatus and cannot be used as reported. One of the approaches is to establish correlations between the smoke-point values measured in different apparatuses and a single apparatus for which relationships such as given in Equations 102 through 106 are available. This type of approach has been described in References 38 and 39 for the ASTM E2058 fire propagation apparatus, where smoke-point values for 165 fuels, reported in the literature, were translated to the values for the ASTM E2058 fire propagation apparatus. The fire properties (chemical, convective, and radiative heats of combustion and yields of CO and smoke) estimated in this fashion, from Equations 102 through 106, are listed in Tables 3-4.19 through 3-4.21. In the tables, molecular formula and weight, stoichiometric mass air-to-fuel ratio, and net heat of complete combustion have also been tabulated. The estimated data in the tables have been validated by direct measurements in the small- and large-scale fires using several fuels.^{48,49}

The data in Tables 3-4.19 through 3-4.21 show linear dependencies on the molecular weight of the fuel monomer within each group:^{48,49}

$$\Delta H_i = h_i + \frac{m_i}{M} \quad (107)$$

$$y_j = a_j \pm \frac{b_j}{M} \quad (108)$$

where

ΔH_i = net heat of complete combustion or chemical, convective, or radiative heat of combustion (kJ/g)

y_j = yield of product j (g/g)

M = molecular weight of fuel monomer (g/mol)

h_i = mass coefficient for the heat of combustion (kJ/g)

m_i = molar coefficient for the heat of combustion (kJ/mol)

a_j = mass coefficient for the product yield (g/g)

b_j = molar coefficient for the product yield (g/mol)

The coefficients depend on the chemical structures of the fuel; m_i and b_j become negative with the introduction of oxygen, nitrogen, and sulfur atoms into the chemical structure. Relationships in Equations 107 and 108 support the suggestion⁷⁹ that generally smaller molecules offer greater resistance to smoke formation and emission. The relationships suggest that for gases, liquids, and solids gasifying as high molecular weight fuels, $\Delta H_i \approx h_i$ and $y_j \approx a_j$.

The variations of chemical, convective, and radiative heats of combustion and yields of CO and smoke with the chemical structures of the fuels are similar to the smoke-point variations.

EXAMPLE 20:

The following smoke-point values have been reported in the literature:

Polymer	PE	PP	PMMA	PS
Smoke point (m)	0.045	0.050	0.105	0.015

For well-ventilated conditions, estimate (1) the chemical, convective, and radiative heats of combustion using Equations 102 through 104 and data for the net heat of complete combustion from Table 3-4.14; and (2) yields of CO and smoke using Equations 105 and 106 and stoichiometric yields from Table 3-4.16.

SOLUTION:

- From Equations 102 through 104 and Table 3-4.14,

Polymer	PE	PP	PMMA	PS
ΔH_T (kJ/g)	43.6	43.4	25.2	39.2
ΔH_{ch} (kJ/g)	36.8	37.0	23.1	29.6
ΔH_{con} (kJ/g)	20.6	21.1	15.0	14.0
ΔH_{rad} (kJ/g)	16.2	15.9	8.1	15.6

- From Equations 105 and 107 and Table 3-4.16,

Polymer	PE	PP	PMMA	PS
Ψ_{CO}	2.00	2.00	1.40	2.15
Ψ_s	0.857	0.857	0.600	0.923
y_{CO} (g/g)	0.027	0.025	0.009	0.050
y_s (g/g)	0.077	0.072	0.028	0.135

Nonthermal Damage Due to Fire Products

Damage due to heat is defined as thermal damage, and damage due to smoke, toxic, and corrosive products is defined as nonthermal damage. Nonthermal damage depends on the chemical nature and deposition of products on the walls, ceilings, building furnishings, equipment, components, and so forth, and the environmental conditions. The severity of the nonthermal damage increases with time. Examples of nonthermal damage to property are corrosion, electrical malfunctions, discoloration, and odors.

Most commercial and industrial occupancies are susceptible to nonthermal fire damage. Examples of typical commercial and industrial occupancies are telephone

Table 3-4.19 Combustion Properties of Fuels with Carbon and Hydrogen Atoms in the Chemical Structure

Hydrocarbon	Formula	M (g/mol)	S	Heat of Combustion (kJ/g)				Yield (g/g)	
				ΔH_T	ΔH_{ch}	ΔH_{con}	ΔH_{rad}	CO	Smoke
<i>Normal alkanes</i>									
Ethane	C ₂ H ₆	30	16.0	47.1	45.7	34.1	11.6	0.001	0.013
n-Propane	C ₃ H ₈	44	15.6	46.0	43.7	31.2	12.5	0.005	0.024
n-Butane	C ₄ H ₁₀	58	15.4	45.4	42.6	29.6	13.0	0.007	0.029
n-Pentane	C ₅ H ₁₂	72	15.3	45.0	42.0	28.7	13.3	0.008	0.033
n-Hexane	C ₆ H ₁₄	86	15.2	44.8	41.5	28.1	13.5	0.009	0.035
n-Heptane	C ₇ H ₁₆	100	15.1	44.6	41.2	27.6	13.6	0.010	0.037
n-Octane	C ₈ H ₁₈	114	15.1	44.5	41.0	27.3	13.7	0.010	0.038
n-Nonane	C ₉ H ₂₀	128	15.0	44.4	40.8	27.0	13.8	0.011	0.039
n-Decane	C ₁₀ H ₂₂	142	15.0	44.3	40.7	26.8	13.9	0.011	0.040
n-Undecane	C ₁₁ H ₂₄	156	15.0	44.3	40.5	26.6	13.9	0.011	0.040
n-Dodecane	C ₁₂ H ₂₆	170	14.9	44.2	40.4	26.4	14.0	0.011	0.041
n-Tridecane	C ₁₃ H ₂₈	184	14.9	44.2	40.3	26.3	14.0	0.012	0.041
n-Tetradecane	C ₁₄ H ₃₀	198	14.9	44.1	40.3	26.2	14.1	0.012	0.042
Hexadecane	C ₁₆ H ₃₄	226	14.9	44.1	40.1	26.0	14.1	0.012	0.042
<i>Branched alkanes</i>									
Methylbutane	C ₅ H ₁₂	72	15.3	45.0	40.9	27.2	13.8	0.012	0.042
Dimethylbutane	C ₆ H ₁₄	86	15.2	44.8	40.3	26.3	14.0	0.014	0.046
Methylpentane	C ₆ H ₁₄	86	15.2	44.8	40.3	26.3	14.0	0.014	0.046
Dimethylpentane	C ₇ H ₁₆	100	15.1	44.6	39.9	25.7	14.1	0.015	0.049
Methylhexane	C ₇ H ₁₆	100	15.1	44.6	39.9	25.7	14.1	0.015	0.049
Trimethylpentane	C ₈ H ₁₈	114	15.1	44.5	39.6	25.3	14.3	0.016	0.052
Methylethylpentane	C ₈ H ₁₈	114	15.1	44.5	39.6	25.3	14.3	0.016	0.052
Ethylhexane	C ₈ H ₁₈	114	15.1	44.5	39.6	25.3	14.3	0.016	0.052
Dimethylhexane	C ₈ H ₁₈	114	15.1	44.5	39.6	25.3	14.3	0.016	0.052
Methylheptane	C ₈ H ₁₈	114	15.1	44.5	39.6	25.3	14.3	0.016	0.052
<i>Cyclic alkanes</i>									
Cyclo-Pentane	C ₅ H ₁₀	70	14.7	44.3	39.2	24.1	15.1	0.018	0.055
Methylcyclopentane	C ₆ H ₁₂	84	14.7	43.8	38.2	23.0	15.2	0.019	0.061
Cyclohexane	C ₆ H ₁₂	84	14.7	43.8	38.2	23.0	15.2	0.019	0.061
Methylcyclohexane	C ₇ H ₁₄	98	14.7	43.4	37.5	22.3	15.2	0.021	0.066
Ethylcyclohexane	C ₈ H ₁₆	112	14.7	43.2	36.9	21.7	15.3	0.021	0.069
Dimethylcyclohexane	C ₈ H ₁₆	112	14.7	43.2	36.9	21.7	15.3	0.021	0.069
Cyclooctane	C ₈ H ₁₆	112	14.7	43.2	36.9	21.7	15.3	0.021	0.069
Decalin	C ₁₀ H ₁₈	138	14.4	42.8	36.2	20.9	15.3	0.023	0.073
Bicyclohexyl	C ₁₂ H ₂₂	166	14.5	42.6	35.7	20.4	15.3	0.023	0.076
<i>Alkenes</i>									
Ethylene	C ₂ H ₄	28	14.7	48.0	41.5	27.3	14.2	0.013	0.043
Propylene	C ₃ H ₆	42	14.7	46.4	40.5	25.6	14.9	0.017	0.095
Butylene	C ₄ H ₈	56	14.7	45.6	40.0	24.8	15.2	0.019	0.067
Pentene	C ₅ H ₁₀	70	14.7	45.2	39.7	24.2	15.4	0.020	0.065
Hexene	C ₆ H ₁₂	84	14.7	44.9	39.4	23.9	15.5	0.021	0.064
Heptene	C ₇ H ₁₄	98	14.7	44.6	39.3	23.7	15.6	0.021	0.063
Octene	C ₈ H ₁₆	112	14.7	44.5	39.2	23.5	15.7	0.022	0.062
Nonene	C ₉ H ₁₈	126	14.7	44.3	39.1	23.3	15.8	0.022	0.062
Decene	C ₁₀ H ₂₀	140	14.7	44.2	39.0	23.2	15.8	0.022	0.061
Dodecene	C ₁₂ H ₂₄	168	14.7	44.1	38.9	23.1	15.9	0.023	0.061
Tridecene	C ₁₃ H ₂₆	182	14.7	44.0	38.9	23.0	15.9	0.023	0.061
Tetradecene	C ₁₄ H ₂₈	196	14.7	44.0	38.8	22.9	15.9	0.023	0.060
Hexadecene	C ₁₆ H ₃₂	224	14.7	43.9	38.8	22.8	16.0	0.023	0.060
Octadecene	C ₁₈ H ₃₆	252	14.7	43.8	38.7	22.8	16.0	0.023	0.060
Polyethylene	(C ₂ H ₄) _n	601	14.7	43.6	36.8	20.6	16.2	0.027	0.077
Polypropylene	(C ₃ H ₆) _n	720	14.7	43.4	37.0	21.1	15.9	0.025	0.072
<i>Cyclic alkenes</i>									
Cyclohexene	C ₆ H ₁₀	82	14.2	43.0	35.7	20.2	15.5	0.029	0.085
Methylcyclohexene	C ₇ H ₁₂	96	14.3	43.1	35.8	19.8	16.0	0.029	0.085
Pinene	C ₁₀ H ₁₆	136	14.1	36.0	33.5	18.9	14.6	0.039	0.114

Table 3-4.19 Combustion Properties of Fuels with Carbon and Hydrogen Atoms in the Chemical Structure (Continued)

Hydrocarbon	Formula	M (g/mol)	S	Heat of Combustion (kJ/g)				Yield (g/g)	
				ΔH_T	ΔH_{ch}	ΔH_{con}	ΔH_{rad}	CO	Smoke
<i>Alkynes and Butadiene</i>									
Acetylene	C ₂ H ₂	26	13.2	47.8	36.7	18.7	18.0	0.042	0.096
Heptyne	C ₇ H ₁₂	96	14.3	44.8	36.0	18.8	17.1	0.036	0.094
Octyne	C ₈ H ₁₄	110	14.4	44.7	35.9	18.9	17.1	0.036	0.094
Decyne	C ₁₀ H ₁₈	138	14.4	44.5	35.9	18.9	17.0	0.035	0.094
Dodecyne	C ₁₂ H ₂₂	166	14.5	44.3	35.9	18.9	17.0	0.035	0.094
1, 3-Butadiene	C ₄ H ₆	54	14.0	44.6	33.6	15.4	18.2	0.048	0.125
<i>Arenes</i>									
Benzene	C ₆ H ₆	78	13.2	40.1	27.6	11.0	16.5	0.067	0.181
Toluene	C ₇ H ₈	92	13.4	39.7	27.7	11.2	16.5	0.066	0.178
Styrene	C ₈ H ₈	104	13.2	39.4	27.8	11.2	16.6	0.065	0.177
Ethylbenzene	C ₈ H ₁₀	106	13.6	39.4	27.8	11.2	16.6	0.065	0.177
Xylene	C ₈ H ₁₀	106	13.6	39.4	27.8	11.2	16.6	0.065	0.177
Indene	C ₉ H ₈	116	13.0	39.2	27.9	11.3	16.6	0.065	0.176
Propylbenzene	C ₉ H ₁₂	120	13.7	39.2	27.9	11.3	16.6	0.065	0.175
Trimethylbenzene	C ₉ H ₁₂	120	13.7	39.2	27.9	11.3	16.6	0.065	0.175
Cumene	C ₉ H ₁₂	120	13.7	39.2	27.9	11.3	16.6	0.065	0.175
Naphthalene	C ₁₀ H ₈	128	12.9	39.0	27.9	11.3	16.6	0.065	0.175
Tetralin	C ₁₀ H ₁₂	132	13.5	39.0	27.9	11.4	16.6	0.064	0.174
Butylbenzene	C ₁₀ H ₁₄	134	13.8	39.0	27.9	11.4	16.6	0.064	0.174
Diethylbenzene	C ₁₀ H ₁₄	134	13.8	39.0	27.9	11.4	16.6	0.064	0.174
p-Cymene	C ₁₀ H ₁₄	134	13.8	39.0	27.9	11.4	16.6	0.064	0.174
Methylnaphthalene	C ₁₁ H ₁₀	142	13.0	38.9	28.0	11.4	16.6	0.064	0.174
Pentylbenzene	C ₁₁ H ₁₆	148	13.9	38.8	28.0	11.4	16.6	0.064	0.173
Dimethylnaphthalene	C ₁₂ H ₁₂	156	13.2	38.8	28.0	11.4	16.6	0.064	0.173
Cyclohexylbenzene	C ₁₂ H ₁₆	160	13.7	38.7	28.0	11.4	16.6	0.064	0.173
Diisopropylbenzene	C ₁₂ H ₁₈	162	14.0	38.7	28.0	11.4	16.6	0.064	0.173
Triethylbenzene	C ₁₂ H ₁₈	162	14.0	38.7	28.0	11.4	16.6	0.064	0.173
Triamylbenzene	C ₂₁ H ₃₆	288	14.3	38.1	28.2	11.6	16.6	0.063	0.169
Polystyrene	(C ₈ H ₈) _n	200	13.2	39.2	29.6	14.0	15.6	0.050	0.135

Table 3-4.20 Combustion Properties of Fuels with Carbon, Hydrogen, and Oxygen Atoms in the Chemical Structure

Hydrocarbon	Formula	M (g/mol)	S	Heat of Combustion (kJ/g)				Yield (g/g)	
				ΔH_T	ΔH_{ch}	ΔH_{con}	ΔH_{rad}	CO	Smoke
<i>Aliphatic esters</i>									
Ethyl formate	C ₃ H ₆ O ₂	74	6.5	20.2	19.9	13.5	6.3	0.003	0.011
n-Propyl formate	C ₄ H ₈ O ₂	88	7.8	23.9	23.4	15.4	8.0	0.005	0.019
n-Butyl formate	C ₅ H ₁₀ O ₂	102	8.8	26.6	26.0	16.7	9.3	0.007	0.025
Methyl acetate	C ₃ H ₆ O ₂	74	6.5	20.2	19.9	13.5	6.3	0.003	0.011
Ethyl acetate	C ₄ H ₈ O ₂	88	7.8	23.9	23.4	15.4	8.0	0.005	0.019
n-Propyl acetate	C ₅ H ₁₀ O ₂	102	8.8	26.6	26.0	16.7	9.3	0.007	0.025
n-Butyl acetate	C ₆ H ₁₂ O ₂	116	9.5	28.7	28.0	17.8	10.2	0.008	0.029
Isobutyl acetate	C ₆ H ₁₂ O ₂	116	9.5	28.7	28.0	17.8	10.2	0.008	0.029
Amyl acetate	C ₇ H ₁₄ O ₂	130	10.0	30.3	29.5	18.6	11.0	0.009	0.033
Cyclohexyl acetate	C ₈ H ₁₄ O ₂	142	10.2	31.5	30.6	19.1	11.5	0.010	0.035
Octyl acetate	C ₁₀ H ₂₀ O	172	11.2	33.6	32.6	20.2	12.5	0.012	0.039
Ethyl acetoacetate	C ₆ H ₁₀ O ₃	130	7.4	30.3	29.5	18.6	11.0	0.009	0.033
Methyl propionate	C ₄ H ₈ O ₃	88	7.8	23.9	23.4	15.4	8.0	0.005	0.019
Ethyl propionate	C ₅ H ₁₀ O ₂	102	8.8	26.6	26.0	16.7	9.3	0.007	0.025
n-Butyl propionate	C ₇ H ₁₄ O ₂	130	10.0	30.3	29.5	18.6	11.0	0.009	0.033
Isobutyl propionate	C ₇ H ₁₄ O ₂	130	10.0	30.3	29.5	18.6	11.0	0.009	0.033
Amyl propionate	C ₈ H ₁₆ O ₂	144	10.5	31.6	30.8	19.2	11.6	0.010	0.035
Methyl butyrate	C ₅ H ₁₀ O ₂	102	8.8	26.6	26.0	16.7	9.3	0.007	0.025
Ethyl butyrate	C ₆ H ₁₂ O ₂	116	9.5	28.7	28.0	17.8	10.2	0.008	0.029
Propyl butyrate	C ₇ H ₁₄ O ₂	130	10.0	30.3	29.5	18.6	11.0	0.009	0.033

(continued)

Table 3-4.20 Combustion Properties of Fuels with Carbon, Hydrogen, and Oxygen Atoms in the Chemical Structure (Continued)

Hydrocarbon	Formula	<i>M</i> (g/mol)	S	Heat of Combustion (kJ/g)				Yield (g/g)	
				ΔH_T	ΔH_{ch}	ΔH_{con}	ΔH_{rad}	CO	Smoke
<i>Aliphatic esters</i>									
<i>n</i> -Butyl butyrate	C ₈ H ₁₆ O ₂	144	10.5	31.6	30.8	19.2	11.6	0.010	0.035
Isobutyl butyrate	C ₈ H ₁₆ O ₂	144	10.5	31.6	30.8	19.2	11.6	0.010	0.035
Ethyl laurate	C ₁₄ H ₂₈ O	228	12.0	37.2	35.6	26.5	9.1	0.008	0.031
Ethyl oxalate	C ₄ H ₆ O ₄	102	6.1	28.7	27.7	21.3	6.4	0.001	0.003
Ethyl malonate	C ₅ H ₈ O ₄	132	7.7	32.2	31.0	23.4	7.5	0.003	0.015
Ethyl lactate	C ₅ H ₁₀ O ₃	118	7.0	30.8	29.6	22.5	7.1	0.001	0.010
Butyl lactate	C ₇ H ₁₄ O ₃	146	8.5	33.3	32.0	24.1	7.9	0.004	0.018
Amyl lactate	C ₈ H ₁₆ O ₃	160	9.0	34.3	32.9	24.7	8.2	0.005	0.021
Ethyl carbonate	C ₅ H ₁₀ O ₃	118	7.0	30.8	29.6	22.5	7.1	0.001	0.010
<i>Aliphatic alcohols</i>									
Methyl alcohol	CH ₄ O	32	6.4	20.0	19.1	16.1	3.0	0.001	0.001
Ethyl alcohol	C ₂ H ₆ O	46	9.0	27.7	25.6	19.0	6.5	0.001	0.008
<i>n</i> -Propyl alcohol	C ₃ H ₈ O	60	10.3	31.8	29.0	20.6	8.5	0.003	0.015
Isopropyl alcohol	C ₃ H ₈ O	60	10.3	31.8	29.0	20.6	8.5	0.003	0.015
<i>n</i> -Butyl alcohol	C ₄ H ₁₀ O	74	11.1	34.4	31.2	21.6	9.6	0.004	0.019
Isobutyl alcohol	C ₄ H ₁₀ O	74	11.1	34.4	31.2	21.6	9.6	0.004	0.019
Sec butyl alcohol	C ₄ H ₁₀ O	74	11.1	34.4	31.2	21.6	9.6	0.004	0.019
Ter butyl alcohol	C ₄ H ₁₀ O	74	11.1	34.4	31.2	21.6	9.6	0.004	0.019
<i>n</i> -Amyl alcohol	C ₅ H ₁₂ O	88	11.7	36.2	32.7	22.2	10.4	0.005	0.022
Isobutyl carbinol	C ₅ H ₁₂ O	88	11.7	36.2	32.7	22.2	10.4	0.005	0.022
Sec butyl carbinol	C ₅ H ₁₂ O	88	11.7	36.2	32.7	22.2	10.4	0.005	0.022
Methylpropyl carbinol	C ₅ H ₁₂ O	88	11.7	36.2	32.7	22.2	10.4	0.005	0.022
Dimethylethyl carbinol	C ₅ H ₁₂ O	88	11.7	36.2	32.7	22.2	10.4	0.005	0.022
<i>n</i> -Hexyl alcohol	C ₆ H ₁₄ O	102	12.1	37.4	33.7	22.7	11.0	0.006	0.024
Dimethylbutyl alcohol	C ₆ H ₁₄ O	102	12.1	37.4	33.7	22.7	11.0	0.006	0.024
Ethylbutyl alcohol	C ₆ H ₁₄ O	102	12.1	37.4	33.7	22.7	11.0	0.006	0.024
Allyl alcohol	C ₃ H ₆ O	58	9.5	31.4	28.6	20.4	8.2	0.003	0.014
Cyclohexanol	C ₆ H ₁₂ O	100	11.7	37.3	33.6	22.6	11.0	0.005	0.024
<i>Aliphatic ketones</i>									
Acetone	C ₃ H ₆ O	58	9.5	29.7	27.9	20.3	7.6	0.003	0.014
Methyl ethyl ketone	C ₄ H ₈ O	72	10.5	32.7	30.6	22.1	8.6	0.004	0.018
Cyclohexanone	C ₆ H ₁₀ O	98	11.2	35.9	33.7	24.1	9.6	0.005	0.023
Di-acetone alcohol	C ₆ H ₁₂ O ₂	116	9.5	37.3	35.0	24.9	10.1	0.006	0.026
<i>Other aliphatic fuels</i>									
Monoethyl ether	C ₆ H ₁₀ O ₂	90	8.4	26.7	25.8	20.0	5.8	0.001	0.007
Monoethylether acetate	C ₇ H ₁₂ O ₃	132	7.8	32.2	31.0	23.2	7.7	0.001	0.011
Monoethylether diacetate	C ₆ H ₁₀ O ₄	146	6.1	33.3	32.0	24.2	7.9	0.001	0.009
Glycerol triacetate	C ₉ H ₁₄ O ₆	218	6.0	36.9	35.4	26.3	9.1	0.002	0.011
<i>Other aromatic fuels</i>									
Benzaldehyde	C ₇ H ₆ O	106	10.4	32.4	21.2	8.1	13.2	0.062	0.166
Benzyl alcohol	C ₇ H ₈ O	108	10.8	32.6	22.9	9.8	13.1	0.050	0.137
Cresylic acid	C ₈ H ₈ O	136	9.1	34.0	25.1	11.6	13.5	0.039	0.107
Ethyl benzoate	C ₉ H ₁₀ O ₂	150	9.6	34.5	27.4	14.1	13.3	0.030	0.084
Phenylbutyl ketone	C ₁₁ H ₁₄ O	162	11.9	34.8	26.3	12.6	13.7	0.041	0.115

central offices, computer rooms, power-plant control rooms, space satellites in operation, under construction or in storage, department and grocery stores, hotels, restaurants, various manufacturing facilities, and transportation vehicles such as aircraft, ships, trains, and buses.

For this chapter, the subject of corrosion for commercial and industrial occupancies has been reviewed based on the knowledge derived from the telephone central office (TCO) experience for the deposition of atmospheric

pollutants and fire products on equipment, severity of corrosion damage, and ease of cleaning the equipment.⁸⁶⁻⁸⁹ Galvanized zinc or zinc-chromated finishes represent a major portion of the structural components of the TCO equipment and the HVAC ductwork.⁸⁷⁻⁸⁹ Unfortunately all zinc surfaces are sensitive to corrosion attack by corrosive products. For example, on exposure to HCl gas, zinc forms zinc chloride, which is very hygroscopic and picks up moisture from air with relative humidity as

Table 3-4.21 Combustion Properties of Fuels with Carbon, Hydrogen, Nitrogen, and Sulfur Atoms in the Chemical Structure

Hydrocarbon	Formula	M (g/mol)	S	Heat of Combustion (kJ/g)				Yield (g/g)	
				ΔH_f	ΔH_{ch}	ΔH_{con}	ΔH_{rad}	CO	Smoke
<i>Aliphatic fuels with carbon, hydrogen, and nitrogen</i>									
Diethylamine	C ₄ H ₁₁ N	73	14.6	38.0	34.0	21.3	12.6	0.012	0.039
n-Butylamine	C ₄ H ₁₁ N	73	14.6	38.0	34.0	21.3	12.6	0.012	0.039
Sec-Butylamine	C ₄ H ₁₁ N	73	14.6	38.0	34.0	21.3	12.6	0.012	0.039
Triethylamine	C ₆ H ₁₅ N	101	14.6	39.6	35.3	22.0	13.3	0.014	0.044
Di-n-butylamine	C ₈ H ₁₉ N	129	14.6	40.6	36.1	22.4	13.7	0.014	0.047
Tri-n-butylamine	C ₁₂ H ₂₇ N	185	14.7	41.6	37.0	22.9	14.1	0.015	0.049
<i>Aromatic fuels with carbon, hydrogen, and nitrogen</i>									
Pyridine	C ₅ H ₅ N	79	12.6	32.2	24.0	11.5	12.5	0.037	0.104
Aniline	C ₆ H ₅ N	93	12.9	33.8	25.0	11.7	13.3	0.043	0.119
Picoline	C ₆ H ₅ N	93	12.9	33.8	25.0	11.7	13.3	0.043	0.119
Toluidine	C ₇ H ₉ N	107	13.2	34.9	25.8	11.9	13.9	0.048	0.130
Dimethylaniline	C ₈ H ₁₁ N	121	13.3	35.7	26.4	12.1	14.3	0.051	0.139
Quinoline	C ₉ H ₇ N	129	12.5	36.1	26.7	12.1	14.5	0.052	0.143
Quinaldine	C ₁₀ H ₉ N	143	12.7	36.7	27.1	12.2	14.8	0.055	0.149
Butylaniline	C ₁₀ H ₁₅ N	149	13.6	37.0	27.2	12.2	15.0	0.056	0.151
<i>Aliphatic fuels with carbon, hydrogen, and sulfur</i>									
Hexyl mercaptan	C ₆ H ₁₄ S	118	12.2	33.0	30.1	17.9	12.2	0.012	0.040
Heptyl mercaptan	C ₇ H ₁₆ S	132	12.5	33.7	30.4	18.1	12.3	0.013	0.044
Decyl mercaptan	C ₁₀ H ₂₂ S	174	13.0	34.9	31.1	18.4	12.7	0.016	0.051
Dodecyl mercaptan	C ₁₂ H ₂₆ S	202	13.3	35.5	31.4	18.6	12.8	0.017	0.054
Hexyl sulfide	C ₁₂ H ₂₆ S	202	13.3	35.5	31.4	18.6	12.8	0.017	0.054
Heptyl sulfide	C ₁₄ H ₃₀ S	230	13.4	35.9	31.6	18.7	13.0	0.018	0.057
Octyl sulfide	C ₁₆ H ₃₄ S	258	13.6	36.3	31.8	18.8	13.1	0.019	0.059
Decyl sulfide	C ₂₀ H ₄₂ S	314	13.8	36.8	32.1	18.9	13.2	0.020	0.061
<i>Aromatic fuels with carbon, hydrogen, and sulfur</i>									
Thiophene	C ₄ H ₄ S	84	9.8	31.9	23.4	10.8	12.6	0.031	0.086
Methylthiophene	C ₅ H ₆ S	98	10.5	33.2	24.1	10.9	13.2	0.039	0.107
Thiophenol	C ₆ H ₆ S	110	10.6	34.1	24.6	11.0	13.6	0.045	0.122
Thiocresol	C ₇ H ₈ S	124	11.1	34.9	25.0	11.0	14.0	0.050	0.135
Cresolmethyl sulfide	C ₈ H ₁₁ S	155	11.6	36.2	25.7	11.1	14.5	0.058	0.155

low as 10 percent to form electrically conductive liquid zinc chloride solution. The solution flows on the surfaces, drips down or runs onto equipment, resulting in very serious electrical shorting problems. In two major TCO losses, zinc chloride played a key role in both the rate of restoration as well as the ability to salvage equipment.

In TCO fires involving PVC-based cables, contamination levels in the range of about 5 to 900 microgram/cm² have been observed.⁸⁷⁻⁸⁹ In general, an electronic switch would be expected to accumulate zinc chloride levels in the range of about 5 to 9 microgram/cm² from the interaction with the environment over its expected lifetime of over 20 years. Clean equipment is expected to have less than 2 microgram/cm² of chloride contamination, whereas contaminated equipment can have as high as 900 microgram/cm². Thus, equipment contamination levels and ease of restoration have been classified into four levels,⁸⁷⁻⁸⁹ as listed in Table 3-4.22.

Corrosion

Corrosion is defined as an unwanted chemical reaction and/or destruction or deterioration of a material be-

cause of reaction with its environment. Factors that are considered to be important for the extent of corrosion damage are (1) oxygen, (2) nature and concentrations of the fire products, (3) relative humidity, (4) temperature, (5) nature of the target and its orientation relative to the flow of the fire products-air mixture, (6) flow velocity of the fire products-air mixture, (7) presence of extinguishing agents, (8) techniques used for cleaning the exposed surface and their implementation time after the fire, and others.

Most of the knowledge on corrosion damage has been based on air pollution, for example, due to acid rain. Acid deposition is generally described as *acid rain*.⁹⁰ Rain usually includes all forms of precipitation (rain, snow, sleet, hail, etc.). Acid deposition is a broader term and includes the uptake of gases by surfaces, impact of fog, and settling of dust and small particles.⁹⁰ Precipitation is one of the principal removal mechanisms by which the atmosphere cleanses itself. Acids in rain precipitation result mainly from sulfuric, nitric, and hydrochloric acids, either absorbed directly into precipitation or formed in the aqueous phase from precursor compounds.

In general, all forms of pollution deposition not involving precipitation are referred to as dry, including dew

Table 3-4.22 Contamination Levels for the Surface Deposition of Chloride Ions for Electronic Equipment^a

Chloride Ion (microgram/cm ²)	Level	Damage/Cleaning/Restoration
2	One	No damage expected. No cleaning and restoration required.
<30	Two	Equipment can be easily restored to service by cleaning, with little impact on long-term reliability.
30 to 90	Three	Equipment can also be restored to service by cleaning, as long as no unusual corrosion problem arise, and the environment is strictly controlled soon after the fire.
>90	Four	The effectiveness of cleaning the equipment dwindles, and the cost of cleaning quickly approaches the replacement cost. Equipment contaminated with high chloride levels may require severe environmental controls even after cleaning, in order to provide potentially long-term reliable operation.

^aData taken from Reference 87.

and fog processes.⁹⁰ With the exception of nitric acid vapors, most gases do not readily deposit on dry, inert surfaces. However, if the gas is soluble in water, the presence of a liquid film (e.g., resulting from condensation) will generally accelerate dry deposition. In these cases, the amount deposited on the surfaces will depend not only on the concentration of the pollutant, but also on the relative frequency of encountering a wet surface.

Data in Figure 3-4.42, taken from Reference 91, show that the deposition of HCl on wet filter paper is almost four times as high as the deposition on dry paper, in agreement with Reference 90. HCl was generated by exposing PVC to an external heat flux of 20 kW/m² in an inert environment in the ASTM E2058 fire propagation apparatus. The chloride ion deposition is high in the initial stages and decreases with time, which is consistent with the decomposition mechanism of PVC. The decomposition of PVC is characterized by the release of HCl, which is initiated at a temperature as low as about 100°C. At a temperature of up to about 200 to 220°C, HCl is the major effluent. Presence of oxygen in the air enhances

HCl release. The generation of HCl from PVC leads to the formation of double bonds and release of CO and various aromatic/unsaturated hydrocarbons (benzene, toluene, ethylene, propylene, butylene, etc). The yields of some of these products from the combustion and pyrolysis of PVC are listed in Table 3-4.23, taken from Reference 92.

Deposition of HCl on walls of enclosures has also been quantified in larger-scale fire tests. For example, in the fire tests with PVC floor covering performed in a 2.8- × 2.8- × 2.4-m-high unventilated room, about 50 percent of the original chloride ions in PVC were deposited on the walls.⁹³ With the exception of vinyl film (wallpaper) and super-gloss enamel paint on polyethylene, the chloride ion deposition on all other surfaces was in the range of 30 to 90 microgram/cm². The differences in the chloride ion deposition on various materials on the wall appear to be related to the hydrophilic (water-attracting) and hydrophobic (water-repelling) nature of the surfaces, that is, filter paper is hydrophilic and vinyl film is hydrophobic, in agreement with Reference 90. This deposition corresponds to the third level of contamination for TCOs. (See Table 3-4.22.)

The corrosion damage in fires follows the basic corrosion relationship,

$$D_{\text{corr}} = \mu c^m t^n \quad (109)$$

where

D_{corr} = metal corrosion (penetration depth or metal loss in microns, angstroms, mils)

t = exposure time (min, day)

c = concentration of the corrosive product (g/m³)

μ, m, n = empirical constants

The constant μ may be defined as a corrosion parameter characteristic of the corrosive nature of the product. The constant n is a function of the corrosion resistance characteristics of the film at the surface. When the film on the surface protects the surface and inhibits further corrosion by diffusion, $n = 1/2$.⁹⁰ When the film is permeable to corrosive gases and offers no protection, $n = 1$.⁹⁰

For short-term exposure of metal surfaces to aqueous solutions of corrosive fire products, $n = 1$, and from Equation 109,

$$\dot{R}_{\text{corr}} = \mu c^m \quad (110)$$

where \dot{R}_{corr} is corrosion rate (Å/min).

For long-term exposure of metal surfaces to aqueous solutions of corrosive fire products, as a protective layer

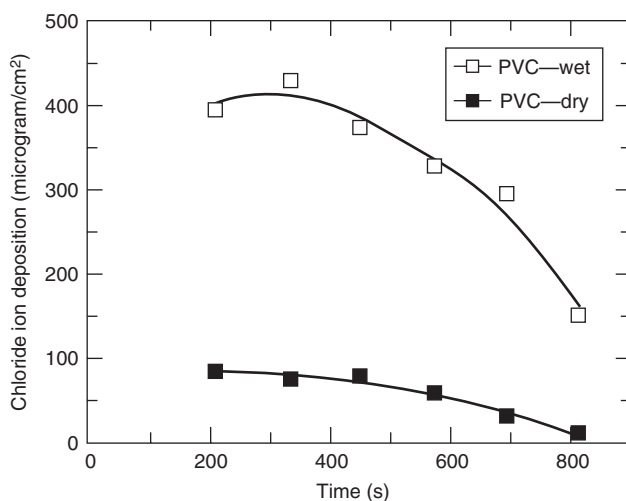


Figure 3-4.42. Deposition of HCl on wet and dry cellulosic filter paper during the pyrolysis of PVC at an external heat flux of 20 kW/m² under co-airflow with 10 percent of oxygen concentration in the ASTM E2058 fire propagation apparatus. Flow velocity 0.09 m/s with filter paper at right angle to the flow. Data used in figure are taken from Reference 91.

Table 3-4.23 Yield of CO, HCl, Benzene, and Toluene from the Combustion/Pyrolysis of Polyvinylchloride^a

Combustible ^b	Air/Inert	Yield (g/g)			
		CO	HCl	Benzene	Toluene
<i>PVC homopolymer</i>					
Rigid PVC sheet (49.3% Cl)	inert	—	0.480	0.022	0.002
	air	—	0.479	0.022	0.001
Rigid PVC-1	inert	—	0.555	0.058	0.008
	air	—	0.472	0.044	0.004
Rigid PVC-2	air	0.356	0.513	—	—
PVC resin	air	—	0.486	0.048	0.001
PVC homopolymer-1	air	0.422	0.583	0.031	0.001
PVC homopolymer-2	air	0.413	0.584	0.036	0.001
PVC homopolymer-3	air	0.299	0.500	0.029	0.001
PVC homopolymer-4	air	0.429	0.580	0.043	0.004
<i>PVC + plasticizer</i>					
PVC (33% Cl) + dioctylphthalate (67%)	air	0.275	0.269	—	—
PVC (31% Cl) + tricresylphosphate	air	0.248	0.269	—	—
<i>PVC + plasticizer + acid neutralizer</i>					
PVC (%) + dioctylphthalate (%) + K ₂ CO ₃ (%)					
42.4 + 42.4 + 15.2	N ₂	—	0.171	—	—
38.2 + 38.2 + 23.6	N ₂	—	0.111	—	—
32.5 + 32.5 + 35.0	N ₂	—	0.029	—	—
PVC (%) + dioctylphthalate (%) + CaCO ₃ (%)					
45.5 + 45.5 + 9.0	N ₂	—	0.221	—	—
41.7 + 41.7 + 16.0	N ₂	—	0.171	—	—
35.7 + 35.7 + 28.6	N ₂	—	0.117	—	—
<i>Electrical cables</i>					
PVC jacket	air	—	0.277–0.408	—	—
FR PVC insulation	air	—	0.204–0.285	—	—
Insulation (51% PVC + 49% Plasticizer + additives)	air	0.067	0.273	0.010	0.001
Insulation (57% PVC + 43% Plasticizer + additives)	air	0.090	0.333	0.011	0.001
PVC cable	air	—	0.263	0.033	0.001
<i>General products</i>					
Floor tile (33% PVC + 70% CaCO ₃ + inert)	air	0.031	0.073	0.001	—
PVC-nylon brattice cloth	air	—	0.174	0.048	0.001
PVC-nylon fabric	air	—	0.254	0.051	0.001
FR PVC-nylon product	air	—	0.206	0.025	0.001
FR PVC	air	—	0.300	0.020	0.001

^aFrom Reference 92.^bFR—fire retarded, K₂CO₃—potassium carbonate; CaCO₃—calcium carbonate.

of corrosion byproducts is formed at the surface, $n = 1/2$, and from Equation 109,

$$\dot{R}_{\text{corr}} = \frac{\mu c^m}{t^{1/2}} \quad (111)$$

showing that corrosion rate decreases with time.

Figure 3-4.43 shows a plot of the corrosion rate of a mild steel probe exposed to aqueous solutions of hydrochloric and nitric acid of varying concentrations for 24 hrs. The data used in the figure are taken from Reference 81. No protective layer is formed for 24 hrs, and thus Equation 110 is followed. From linear regression analysis, $\mu = 2.08 (\text{\AA}/\text{min})(\text{g}/\text{m}^3)^{-1/2}$ and $m = 1/2$. This relationship suggests that the corrosion rate does not increase rapidly with the concentration of the corrosive products. For example, if the concentration of the corrosive product is increased ten times, the corrosion rate would increase only by a factor of three.

For corrosion in the gas phase, the presence of water is essential or the volume fraction of water $\neq 0$. The experimental data for corrosion in the gas phase suggest that $m = 1$ in Equation 110, which can be expressed in the following modified form:

$$\dot{R}_{\text{corr}} = \frac{\mu y_{\text{corr}} \dot{m}' A}{f_{\text{water}} \dot{V}} \quad (112)$$

where

y_{corr} = yield of the corrosive product (g/g)

\dot{m}' = mass loss rate of the material (g/m²·s)

A = total exposed surface area of the material (m²)

f_{water} = volume fraction of water generated in the combustion of the material and present in the humid air

\dot{V} = total volumetric flow rate of fire product-air mixture (m³/s)

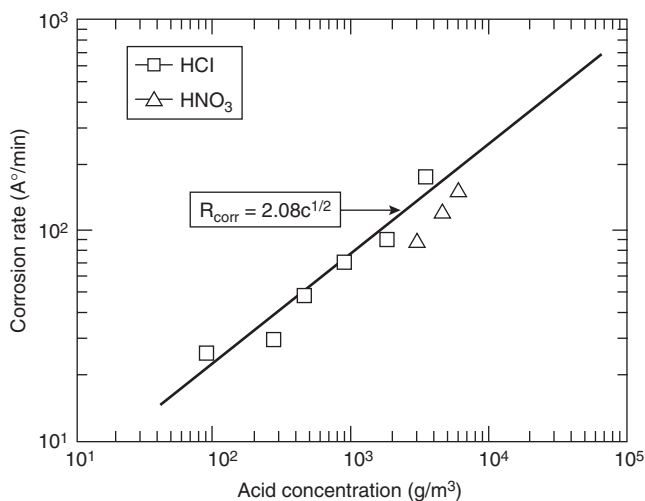


Figure 3-4.43. Corrosion rate of a mild steel probe versus hydrochloric and nitric acid concentrations. Data used in figure are taken from Reference 91.

All the terms in Equation 112 can be measured, and thus the corrosion parameter, μ , can be calculated for the generalized application of the corrosion data.

Corrosion measurements: For corrosion measurements, fire products are generated in small-scale tests and the corrosion is measured by exposing metal probes to the products in the gas phase at various relative humidities or in the aqueous solutions of the products. The common test methods are as follows:

1. The ASTM E2058 fire propagation apparatus test method [Figures 3-4.2(a), 3-4.2(b), and 3-4.27]^{1,68,91,94-96}
2. The cone calorimeter test method (Figure 3-4.3)^{97,98}
3. The radiant combustion/exposure test method^{97,98}
4. The CNET (Centre National d'Etudes des Telecommunications) corrosion test method^{97,100,101}
5. The DIN 57472 test method^{97,102}
6. The DIN 53436 with metal sheets and CNET corrosion probe test method¹⁰³

Corrosion measurements in the gas phase. The measurements are made in the ASTM E2058 fire propagation apparatus, the cone calorimeter, the CNET, and the radiant combustion/exposure test methods. For the measurements, either high-sensitivity Rohrback Cosasco (RC) atmospheric metal corrosion probes or CNET metal corrosion probes are used.

The RC corrosion probes are manufactured by a vacuum deposition technique to obtain an open matrix with little resistance to in-depth diffusion of products, resulting in rapid corrosion. It is designed to monitor short-term corrosion (16 to 24 hr) for environments with small concentrations of corrosive products. The RC probe consists of two metal strips (5,000 to 90,000 Å) embedded in an epoxy-fiberglass plate. One metal strip is coated and acts as a reference, and the other noncoated metal strip acts as a sensor. As the sensor strip corrodes and loses its thickness, its resistance changes. The change in resistance,

which represents the extent of corrosion of the metal, is measured as a function of time, by the difference in the resistance between the two strips. The probe readings remain reliable up to about half the thickness of the metal strip (probes are identified as 2500 to 45,000 Å probes).

The CNET probe consists of an epoxy-fiberglass plate embedded with about 170,000 Å thick copper conductors. The change in the resistance of the probe is recorded at the beginning and at the end of the test to determine the extent of corrosion.

The corrosion in the gas phase is measured during the tests every min and every hr after the test for 16 to 24 hr. The corrosion rate is calculated as a function of time, using the following type of relationship:

$$\dot{R}_c = \frac{D_{c1} - D_{c2}}{t_2 - t_1} \quad (113)$$

where

\dot{R}_c = corrosion rate in Å/min

D_{c1} = metal thickness in angstroms at time t_1 (s)

D_{c2} = metal thickness in angstroms at time t_2 (s)

Data have been reported in the literature for the gas-phase corrosion, mass loss rate, and total volumetric rate of fire products-air mixture with relative humidity maintained approximately constant. From Equation 112,

$$\frac{\dot{R}_{corr}}{(\dot{m}'A/\dot{V})} = \frac{\mu\gamma_{corr}}{f_{water}} \quad (114)$$

where f_{water} is approximately constant, and thus the values of $\dot{R}_{corr}/(\dot{m}'A/\dot{V})$ can be used to assess the relative corrosion nature of the fire products generated from various materials. Tables 3-4.24 and 3-4.25 list the values of the corrosion rate per unit fuel vapor concentration, $\dot{R}_{corr}/(\dot{m}'A/\dot{V})$. The data show the following:

1. For significant gas-phase corrosion, it is necessary to have hydrogen atoms in the structure of the halogenated materials as suggested by the stoichiometric yields listed in Table 3-4.16. For example, the corrosion rates per unit fuel vapor concentration for PVC (hydrogen atoms in the structure) and Teflon (no hydrogen atoms in the structure) differ by a factor of 7. The difference is probably due to (a) the inefficiency of the hydrolysis process during the conversion of fluorocarbon products generated from Teflon to HF, and (b) the high water solubility of HCl generated from PVC.
2. The corrosion rates per unit fuel vapor concentration for halogenated materials with hydrogen atoms in the structure are high [greater than 0.14 (Å/min)/(g/m³)], whereas they are negligibly small for fires of nonhalogenated materials [less than 0.007 (Å/min)/(g/m³)], as expected.
3. Fire retardation of nonhalogenated materials by halogenated materials increases the corrosion rate per unit fuel vapor concentration for the nonhalogenated materials from less than 0.007 to 0.011 to 0.046 (Å/min)/(g/m³). These values, however, are still about 1/10 the values for the halogenated materials.

Table 3-4.24 Corrosion Rate per Unit Fuel Vapor Concentration in the Gas Phase for Flaming and Nonflaming Fires with Variable Oxygen Concentration in the ASTM E2058 Fire Propagation Apparatus and the Radiant Combustion/Exposure Chamber

Polymer ^a	O ₂ (%)	F/NF ^b	Water Present ^c	Corrosion Rate ^d	
				FLAM ^e	RC/E ^f
EVA	21	F	no	nd	0.001
EVA-FR1	21	F	no	nd	0.021
PE	21	F	no	nd	0.002
PE-FR1	21	F	no	nd	0.024
PE-FR1	21	F	yes	nd	0.036
PE-FR2	21	F	no	nd	0.022
PE-FR2	21	F	yes	nd	0.024
PE-FR2	21	F	no	nd	0.014
PE-FR2	21	F	yes	nd	0.016
PE/25% Cl	10	N	yes	0.14	nd
PE/36% Cl	10	NF	yes	0.15	nd
PE/48% Cl	10	NF	yes	0.19	nd
PVC	10	NF	yes	0.15	nd
	21	NF	no	nd	0.027
	21	NF	yes	0.12	0.087
	21	F	yes	1.0	nd
TFE	0	NF	yes	0.0036	nd
	10	NF	yes	0.011	nd
	40	NF	yes	0.035	nd
	21	F	yes	0.42	nd

FR-1, red phosphorus fire retardant; FR-2, bromine fire retardant; EVA, ethylene-vinyl acetate copolymer; PE, polyethylene; Cl, chlorine; TFE, tetrafluoroethylene (Teflon); and nd, not determined.

^aSee nomenclature.

^bF: flaming, NF: nonflaming.

^cIncreased humidity in the gas phase with water.

^dPer unit fuel vapor concentration (Å/min)/(g/m³)

^eThe ASTM E2058 fire propagation apparatus test method.^{1,68,91,94–97}

^fThe radiant combustion/exposure test method,^{98,100} 1500-min average.

4. Increase in the corrosion rate per unit fuel vapor concentration due to the presence of water is not significant for halogenated materials with hydrogen atoms in the structure, as expected, as water is generated in the combustion process.
5. Increase in the oxygen concentration in the environment increases the corrosion rate per unit fuel vapor concentration.

Corrosion measurements in the aqueous solution. The measurements are made in the ASTM E2058 fire propagation apparatus and the DIN 57472 test methods. For the measurements, Rohrback Cosasco (RC) loop-type metal corrosion probes are used. The probes are exposed to the aqueous solutions of the fire products. The probe consists of a metal loop attached to an epoxy-fiberglass rod, with a built-in reference. The metal loop acts as a sensor. As the sensor loop corrodes and loses its thickness, its resistance changes. The extent of corrosion is measured by the difference in the resistance between the loop and the reference. The corrosion rate is determined from Equation 113.

Table 3-4.25 Corrosion Rate per Unit Fuel Vapor Concentration in the Gas Phase for Flaming Fires in Air in the Radiant Combustion/Exposure Chamber⁹⁷

Sample Description	Corrosion Rate ^a
Crosslinked polyolefin (XLPO) + metal hydrate	0.007
HD polyethylene (PE) + chlorinated PE blend	>0.098
Chlorinated PE + fillers	>0.098
Ethylvinylacetate (EVA) PO + ATH filler	0.012
Polyphenylene oxide/polystyrene (PS) blend	0.005
Polyetherimide	0.002
Polyetherimide/siloxane copolymer	0.005
Intumescent polypropylene (PP)	0.025
Polyolefin copolymer + mineral filler	0.046
XLPO + mineral filler	0.011
XLPO + ATH	0.003
EVA-PO + mineral filler	0.007
PO + mineral filler	0.013
CLPE + chlorinated additive	>0.098
Polyvinylidene fluoride	>0.098
Polytetrafluoroethylene	>0.098
Polyvinylchloride (PVC)	>0.098
PVC wire	>0.098
PE homopolymer	0.006
Douglas fir	0.006
EVA-PO copolymer	0.003
Nylon 6,6	0.008
XLPE copolymer + brominated additives	0.091

^aPer unit fuel vapor concentration (Å/min)/(g/m³); average gas-phase concentration ≈ 17.0 g/m³.

The fire products are either bubbled directly into known volumes of water or are collected in the gas phase on cellulose-based filter papers of known area. After the test, the color, odor, and mass of the products deposited on the filter papers are determined. The fire products are extracted with a known volume of deionized water.

The corrosion in the aqueous solution is measured every hour for 16 to 24 hr. In some cases, concentrations of corrosive ions, such as chloride, bromide, and fluoride, are also determined using selective ion electrodes in the ASTM E2058 fire propagation apparatus test method. In the DIN 57472 test standard, pH and conductivity of the solution are measured.

The solution-phase corrosion parameters measured by the ASTM E2058 fire propagation apparatus test method show that they are comparable for all the halogenated materials and are significantly higher than the values for the gas phase.

Smoke Damage

Smoke is a mixture of black carbon and aerosol.^{104,105} Smoke is generated by many sources and is released to the environment, causing pollution, reduction in visibility, and nonthermal damage (discoloration, odor, electrical shorting and conduction, corrosion, etc.). The estimated influx of black carbon to the environment from burning is

0.5 to 2×10^{15} g/yr.¹⁰⁴ Black carbon is often called charcoal, soot, elemental carbon, and so forth.¹⁰⁴ The particulate organic matter (POM) in aerosols consists of¹⁰⁴ (1) hydrocarbons—these are the alkanes, alkenes, and some aromatics, with aliphatics constituting the greatest fraction, and range from C₁₇ to C₃₇; (2) polycyclic aromatic hydrocarbons; (3) oxidized hydrocarbons—these classes include acids, aldehydes, ketones, quinones, phenols, and esters, as well as the less stable epoxides and peroxides, and may be produced directly in combustion processes or through oxidations in the atmosphere; (4) organo-nitrogen compounds—the aza-arenes are the only types of this class that have been so far analyzed, and they are one or two orders of magnitude less than the polycyclic aromatic hydrocarbons; and (5) organosulfur compounds—heterocyclic sulfur compounds, such as benzothiazole, have been reported in urban aerosols.

The environmental behavior of black carbon introduced by combustion processes depends on the characteristics of the source, aerosol properties, chemical composition of black carbon, and meteorology.¹⁰⁴ The yield of black carbon depends on the material and combustion conditions, as discussed in previous sections. Table 3-4.26 lists data, taken from Reference 104, for the yield of black carbon from some industrial combustion processes.

Multimodal distributions of black carbon issuing from flames, diesel engines, and freeway traffic show that the *nuclei mode* has a geometric mean radius between 0.0025 and 0.020 microns and probably results from the condensation of gaseous carbon moieties.¹⁰⁴ The *accumulation mode* encompasses particles in the size range 0.075 to 0.25 microns and apparently results from the coagulation and condensation of the nuclei mode particles.¹⁰⁴ Finally in the case of vehicular emissions there is a *coarse mode* at several microns that is attributed to the precipitation of fine particles on the walls of exhaust systems and a subsequent entrainment in the issuing gases.¹⁰⁴ The coal-fired utility boilers produce soot with peaks at particle radius of about 0.05 microns.¹⁰⁴ Long-range transport of particles shows that about 60 percent of the soot is less than 0.05 microns radius size class.¹⁰⁴ The larger particles are probably removed preferentially from the air during its travel.

In fires, large variations in smoke particle size, due to coagulation and condensation, have been found. As the smoke moves away from the fire origin, large particles

Table 3-4.26 Yield of Black Carbon from Some Industrial Combustion Processes¹⁰⁴

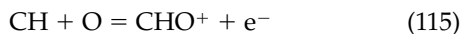
Fuel	Source	Yield (g/kg)
Natural gas	Steam generator	3×10^{-4}
	Domestic water heater	0.1
	Heating boiler	0.01–0.07
Gasoline	Automobile engine	0.1
	Truck/bus engine	0.6–1
Diesel	Automobile engine	2–4
Jet A	Aircraft turbine	0.5–3
	Utility turbine	0.08

settle down to the floor, leaving small particles in the gas phase,¹⁰⁶ similar to the long-range transport in the atmosphere discussed in Reference 104. The data from various fires show that initially the smoke particles are in the coarse mode. The particle size decreases slowly with time, suggesting that large particles settle down from the hot layer at the ceiling.

Relationships between transport of heat and smoke generated in large enclosure fires and for smoke characterization have been developed and data have been reported for the most frequently occurring smoke particle radius.¹⁰⁷ These data are listed in Table 3-4.27, which shows that radii of the smoke particles vary between 0.062 to 0.09 microns, belonging to the lower end of the accumulation mode.

It thus appears that, in fires, smoke damage in the room of fire origin is expected to be due to particles of several microns in radius in the coarse mode, whereas smoke damage downstream of the fire is expected to be due to particles with radius less than 0.1 micron in the lower end of the accumulation mode.

Although concentration, size, physical, and optical properties, and chemical composition of smoke particles have been studied in detail, very little is known about the charges on the particles.¹⁰⁸ It has been suggested that soot nucleation and growth occur near the highly ionized regions of the flames in combustion processes, possibly suggesting that some of the charges are transferred to smoke particles. In hydrocarbon-oxygen flames, the following reaction is considered to be the dominant reaction for the charge separation:¹⁰⁸



Charges on smoke particles generated in flaming and nonflaming fires of wood, cotton wick, polyurethane, heptane with 3 percent toluene, and an alcohol have been examined.¹⁰⁸ The results show that, in nonflaming fires,

Table 3-4.27 Most Frequently Occurring Smoke Particle Radii in Fires of Some Materials¹⁰⁷

Material	Smoke Particle Radius (microns)
Coal	0.078
Polystyrene	0.078
Kerosene	0.079
Polypropylene	0.079
Polyethylene	0.077
Propylene	0.076
Ethylene	0.072
Heptane	0.077
Propane	0.068
Nylon	0.075
PMMA	0.068
Douglas fir	0.062
Polyethylene with chlorine	0.090
Polychloroprene	0.090
PVC	0.083
Styrene-butadiene rubber with chlorine	0.073

initially a very small fraction of particles is charged. During aging, the charge increases slowly. For flaming polyurethane fires, where large amounts of black carbon are generated, smoke carries a high initial charge; 70 percent of the particles in the size interval from 0.018 to 0.032 microns are charged. Similar results are found for heptane. Flaming wood fires, however, show particle charges between that of nonflaming fires of wood and cotton wick and that of flaming fires of polyurethane. In the flaming fire of alcohol, there is no smoke.

Char and black carbon are efficient absorbers of HCl. In the combustion of plasticized PVC wire, about 25 percent of the original chloride ions are retained in the char, and the ions are predominantly inorganic in nature.¹⁰⁹ In the combustion of PE-PVC cables in rooms, smoke particles that settle down in the room contain about 33 percent by weight of inorganic chloride ions, and less than 2 percent of the theoretically expected mass of the chloride ions leaves the enclosure.¹⁰⁶ In the combustion of 79.5 percent PVC-20.5 percent PE, 19 mg of HCl/g of smoke is loosely bound and 27 mg of HCl/g of smoke is tightly bound to carbon.¹¹⁰

It thus appears that, for nonthermal fire damage, the important factors are (1) concentrations of fire products and their deposition on surfaces, (2) chemical and physical nature of the products, (3) nature of the surfaces, (4) presence of moisture, and other factors. These factors depend on (1) fire initiation and spread, (2) generation rates of fire products and their chemical and physical natures, (3) relative humidity and temperature, (4) in-flow rate of air and its mixing with the products and the flow velocity of the mixture, (5) nature and orientation of the target relative to the flow of the products, (6) exposure duration, (7) presence or absence of fire extinguishing agents, and so forth.

Fire Control, Suppression, and Extinguishment

For the prevention of loss of life and property in fires, both active and passive fire protection techniques are used.¹¹¹ Passive fire protection is provided by (1) modifying the chemical structures of the materials for high resistance to ignition and fire propagation, (2) incorporating fire retardants within the materials, (3) coating and wrapping the surfaces, (4) separating materials by inert fire barriers, (5) modifying configuration and arrangement of materials, and so forth. Active fire protection is provided by the application of agents to control, suppress, and/or extinguish fires. The most commonly used liquid and gaseous agents at the present time are water, CO₂, N₂, and halons* 1211 (CBrClF₂), 1301 (CBrF₃), and 2402 (CBrF₂CBrF₂). Because of the contribution of halons to depletion of the stratospheric ozone layer, they will not be used in the future. There is

thus an intense effort underway to develop alternative fire suppressants to replace ozone-layer-depleting halons.

The mechanisms of passive and active fire protection are generally known.^{45,111-118} Flame extinction by liquid and gaseous agents is mainly due to physical processes (such as removal of heat from the flame and burning surface and creation of nonflammable mixtures) and/or chemical processes (such as termination of chemical reactions). The effectiveness of water is mainly due to removal of heat from the burning surface as a result of vaporization. The effectiveness of halons is mainly due to termination of chemical reactions. N₂ and CO₂ are effective mainly due to creation of nonflammable mixtures by reducing mass fraction of oxygen.

Passive Fire Protection

Passive fire protection is provided by various chemical and physical means, as follows.

Increasing the resistance to ignition and fire propagation by increasing the critical heat flux (CHF) and thermal response parameter (TRP) values: The critical heat flux is expressed as

$$\text{CHF} \approx \sigma(T_{ig}^4 - T_a^4) \quad (116)$$

where

σ = Stefan-Boltzmann constant (56.7×10^{-12} kW/m²·K⁴)

T_{ig} = ignition temperature (K)

T_a = ambient temperature (K)

TRP is defined in Equations 1 and 2, and its relationship to fire propagation in Equations 8 and 9.

The relationships between time to ignition, fire propagation rate, fire propagation index, and TRP (Equations 2, 8, and 9) show that the time to ignition is directly proportional to the TRP value to the power 2; and the fire propagation rate and the fire propagation index are inversely proportional to the TRP value to the power 2 and 1, respectively. Thus the higher the TRP value, the longer the time to ignition, the slower the fire propagation rate, and the lower the FPI value. For high TRP values with FPI < 7, there is no fire propagation beyond the ignition zone, defined as the nonfire-propagating behavior. Also, for materials with high CHF values, higher heat flux exposure is required to initiate a fire.

The CHF and TRP values can be increased by modifying the pertinent parameters, such as increase in the chemical bond dissociation energy and decrease in thermal diffusion (combination of the density, specific heat, and thermal conductivity). Figures 3-4.44 and 3-4.45 show the CHF and TRP values for a tri-wall corrugated paper sheet containing various amounts of a passive fire protection agent (identified as agent A here); the data were obtained from the ignition experiments in the ASTM E2058 fire propagation apparatus. Figure 3-4.46 shows the TRP value for a single-wall corrugated paper sheet containing various amounts of the passive fire protection agent A; the data were obtained from the ignition experiments in

*The numbers represent: first, number of carbon atoms; second, number of fluorine atoms; third, number of chlorine atoms; fourth, number of bromine atoms.

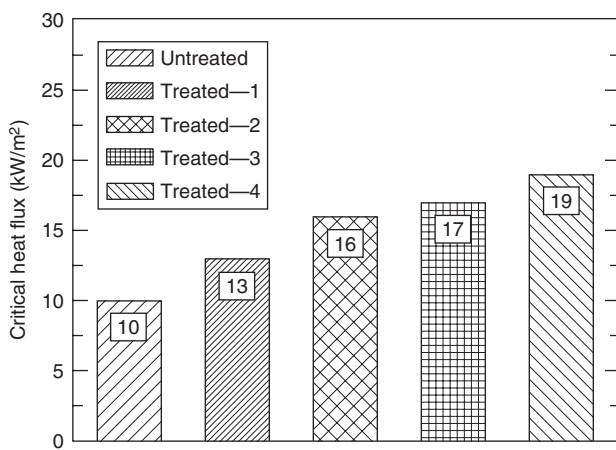


Figure 3-4.44. Critical heat flux for untreated and treated tri-wall corrugated paper sheet. The amount of passive fire protection agent is increasing from Treated 1 to 4. Data obtained from the ignition experiments in the ASTM E2058 fire propagation apparatus. Numbers indicated on top of each bar are the critical heat flux values.

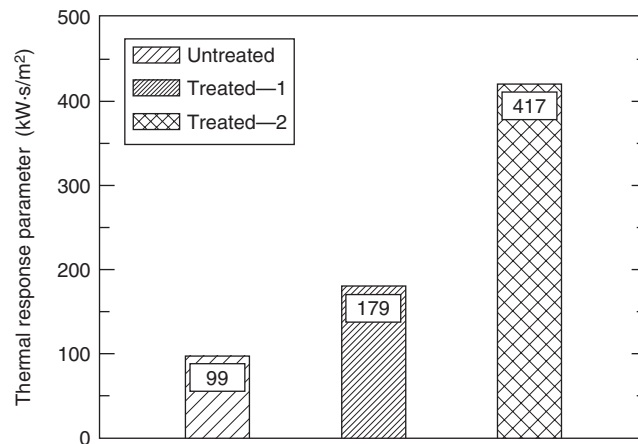


Figure 3-4.46. Thermal response parameter for untreated and treated single-wall corrugated paper sheet. The amount of passive fire protection agent is increasing from Treated 1 to 2. Data obtained from the ignition experiments in the ASTM E2058 fire propagation apparatus. Numbers indicated on top of each bar are the TRP values.

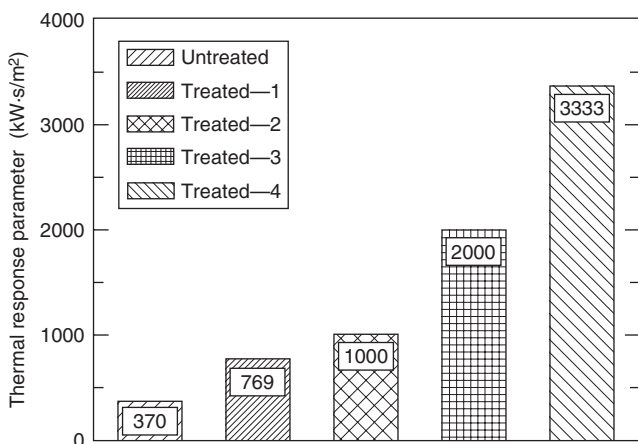


Figure 3-4.45. Thermal response parameter for untreated and treated tri-wall corrugated paper sheet. The amount of passive fire protection agent is increasing from Treated 1 to 4. Data obtained from the ignition experiments in the ASTM E2058 fire propagation apparatus. Numbers indicated on top of each bar are the TRP values.

the ASTM E2058 fire propagation apparatus. The CHF and TRP values increase with increase in the amount of agent; thus, the passive fire protection agent would complement the active fire protection agents. Corrugated paper boxes treated with higher amounts of the passive fire protection agent are expected to require reduced amounts of the active fire protection agents for fire control, suppression, or extinguishment compared to the amounts of the active fire protection agents required for the untreated boxes.

The passive fire protection requirements for various materials can be assessed from the data for CHF and TRP listed in Table 3-4.2.

Decreasing the values of the heat release parameter (HRP) and the flame heat flux: Heat release rate is equal to the heat release parameter (HRP) times the net heat flux (Equation 30). HRP is the ratio of the heat of combustion to heat of gasification, and thus the HRP value can be decreased by decreasing the heat of combustion and/or increasing the heat of gasification by various chemical and physical means. An examination of data in Table 3-4.14 for heats of combustion shows that introduction of oxygen, nitrogen, sulfur, halogen, and other atoms into the chemical structures of the materials reduces the heat of combustion. For example, the heat of combustion decreases when the hydrogen atoms attached to carbon atoms in polyethylene are replaced by the halogen atoms, such as by fluorine in Teflon. The chemical heat of combustion decreases from 38.4 kJ/g to 4.2 kJ/g (Table 3-4.14), and the chemical HRP value decreases from 17 to 2 (Table 3-4.15).

The HRP values can also be reduced by increasing the heat of gasification and decreasing the heat of combustion by retaining the major fraction of the carbon atoms in the solid phase, a process defined as charring. Several passive fire protection agents are available commercially to enhance the charring characteristics of materials.

Figure 3-4.47 shows the reduction in the chemical heat release rate as a result of increase in charring of a tri-wall corrugated paper sheet by the passive fire protection agent A; the data were obtained from the combustion experiments in the ASTM E2058 fire propagation apparatus. The amount of the agent A is increasing from Treated 1 to 3. There is a very significant decrease in the chemical heat

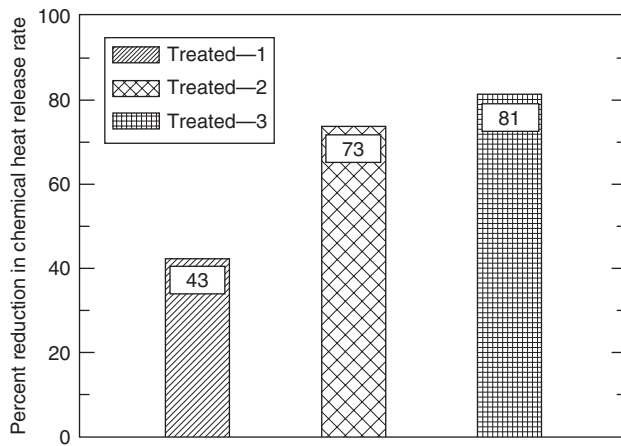


Figure 3-4.47. Percent reduction in the chemical heat release rate of untreated tri-wall corrugated paper sheet by a passive fire protection agent. The amount of the passive fire protection agent is increasing from Treated 1 to 3. Data from the combustion experiments in the ASTM E2058 fire propagation apparatus. Numbers indicated on top of each bar are the percent reductions in the chemical heat release rate.

release rate of the tri-wall corrugated paper sheet by the passive fire protection agent A, which will complement the active fire protection agents. Corrugated paper boxes treated with higher amounts of the passive fire protection agent are expected to require reduced amounts of the active fire protection agents for fire control, suppression, or extinguishment compared to the one required for the untreated boxes.

The effect on flame heat flux by passive fire protection is determined by using the radiation scaling technique, where combustion experiments are performed in oxygen concentration higher than the ambient values. Very little is known about this subject. Table 3-4.8 lists some of the flame heat flux values derived from the radiation scaling technique, but no systematic study has been performed for the effectiveness of passive fire protection. For liquids that vaporize primarily as monomers or as very low molecular weight oligomers, the flame heat flux values are in the range of 22 to 44 kW/m², irrespective of their chemical structures. For solid materials, which vaporize as high molecular weight oligomers, the flame heat flux values increase substantially to the range of 49 to 71 kW/m², irrespective of their chemical structures. The independence of the asymptotic flame heat values from the chemical structures of materials is consistent with the dependence of flame radiation on optical thickness, soot concentration, and flame temperature in large-scale fires. Passive fire protection agents, which can reduce the molecular weight of the vaporized materials, would be effective in reducing the flame heat flux and complement the active fire protection agents.

Changing the molten behavior of materials: Figure 3-4.22 shows the chemical heat release rate versus time for the well-ventilated combustion of a 90-mm-diameter and

25-mm-thick slab of polypropylene exposed to an external heat flux of 50 kW/m². The data were measured in the ASTM E2058 fire propagation apparatus. For about 900 sec, the polypropylene slab burns as a solid with a thin liquid layer at the surface. The measured and calculated values of the heat release rate under this condition agree very well. The heat release rate was calculated from Equation 30 with $\dot{q}_e'' \gg \dot{q}_f'' - \dot{q}_{rr}''$.

Between about 900 and 1150 sec, the polypropylene slab melts rapidly. At about 1150 sec, the entire sample changes to a liquid and burns as a boiling-liquid pool fire. The chemical heat release rate triples at this stage. This stage is the most dangerous in a fire and presents a serious challenge to the active fire protection agents, such as water applied as a spray from sprinklers. Inert passive fire protection agents that eliminate the boiling-liquid pool fire stage will be effective in complementing the active fire protection agents, such as water.

Changing the nature of the fire products: Nonhalogenated passive fire protection agents or agents that reduce or eliminate the release of halogenated and highly aromatic products and enhance release of aliphatic products, rich in hydrogen and oxygen atoms but poor in carbon atoms, are effective in reducing the nonthermal damage due to smoke and corrosion. Some of the passive fire protection agents, available commercially, interact with the materials in the solid as well as in the gas phase during pyrolysis and combustion.

The critical parameter that needs to be examined in the presence and absence of the passive fire protection agents is the ratio of the generation rate of products [such as for smoke, CO, corrosive products (HCl), and others] to heat release rate. The effectiveness of the passive fire protection agent is reflected in the small values of the ratios at fire control, suppression, and/or extinguishment stages.

Active Fire Protection

Active fire protection is provided by applying agents to the flame and/or to the surface of the burning material. The fire control, suppression, and extinguishment have been described by the fire point equation.^{114,116} According to the fire point theory, the convective heat flux from the flame to surface as flame extinction condition is reached is expressed as^{114,116}

$$\dot{q}_{fc}'' = \phi \Delta H_T \dot{m}_{cr}'' \quad (117)$$

where

\dot{q}_{fc}'' = convective flame heat flux from the flame to the surface as the extinction condition is reached (kW/m²)

ϕ = maximum fraction of combustion energy that the flame reactions may lose to the sample surface by convection without flame extinction and is defined as the kinetic parameter for flame extinction

ΔH_T = net heat of complete combustion (kJ/g)

\dot{m}_{cr}'' = critical mass loss rate for flame extinction (g/m²·s)

The kinetic parameter is defined as^{114,116}

$$\phi = \frac{\Delta H_{g,\text{con}}}{\Delta H_T} \quad (118)$$

where $\Delta H_{g,\text{con}}$ is the flame convective energy transfer to the fuel per unit mass of fuel gasified (kJ/g). The kinetic parameter is expected to be higher for fast-burning material vapors and lower for slower burning material vapors, such as materials containing halogens, sulfur, and nitrogen. It is suggested that, at flame extinction, combustion is controlled primarily by the convective heat transfer, and thus the critical mass loss rate would follow Spalding's mass transfer number theory:¹¹³

$$\dot{m}_{\text{cr}}'' = \frac{h}{c_p} \ln(B_{\text{cr}} + 1) \quad (119)$$

where

h = convective heat transfer coefficient (kW/m²·K)

c_p = specific heat of air (kJ/g·K)

B_{cr} = critical mass transfer number

The critical mass transfer number is defined as

$$B_{\text{cr}} = \frac{Y_O \Delta H_O^* - c_p(T_s - T_a)}{\Delta H_{g,\text{con}}} \quad (120)$$

where

Y_O = oxygen mass fraction

ΔH_O^* = net heat of complete combustion per unit mass of oxygen consumed (kJ/g), which is approximately constant (Tables 3-4.10 through 3-4.13)

T_s = surface temperature (K)

T_a = ambient temperature (K)

For ambient conditions, $Y_O \Delta H_T \gg c_p(T_s - T_a)$. From equations 118 through 120,

$$\phi = \frac{Y_O \Delta H_O^*}{\Delta H_T \exp(\dot{m}_{\text{cr}}'' c_p/h) - 1} \quad (121)$$

The fire point theory^{114,116} and experimental data show that the critical mass loss rate for flame extinction is similar to the critical mass loss rate for ignition;^{16,63,115,117,119} the critical mass loss rate for ignition, however, has to be measured at the time period where the sustained flame is just being established. The data for the critical mass loss rate for ignition and flame extinction and the kinetic parameter for flame extinction are listed in Table 3-4.28. The values for the critical mass loss rate for ignition from the ASTM E2058 fire propagation apparatus (Reference 16) are measured at the time period where the sustained flame is just being established, and thus are higher than the values from the University of Edinburgh (Reference 119). The University of Edinburgh data are probably measured just before the sustained flame is established. For polymethylmethacrylate, the critical mass loss rate for ignition from the ASTM E2058 fire propagation apparatus (Reference 16)

Table 3-4.28 Critical Mass Loss Rate for Ignition and Kinetic Parameter for Flame Extinction

Material	Critical Mass Loss Rate (g/m ² ·s)		Kinetic Parameter	
	Ref. 16 ^a	Ref. 119 ^b	Ref. 16 ^a	Ref. 119 ^b
Polyoxymethylene	4.5	1.7	0.43	1.05
Polymethylmethacrylate	3.2	1.9	0.28	0.53
Polyethylene	2.5	1.3	0.27	—
Polypropylene	2.7	1.1	0.24	0.50
Polyethylene foams				
1	2.6	—	0.24	—
2	2.6	—	0.25	—
3	2.5	—	0.25	—
4	2.6	—	0.25	—
Chlorinated polyethylenes				
25% chlorine	6.6	—	0.15	—
36% chlorine	7.5	—	0.09	—
48% chlorine	7.6	—	0.08	—
Polystyrene	4.0	0.80	0.21	0.78
Polystyrene foams				
GM47	6.3	—	0.11	—
GM49	4.9	—	0.14	—
GM51	6.3	—	0.10	—
GM53	5.7	—	0.11	—
Polyurethane foams (flexible)				
GM21	5.6	—	0.16	—
GM23	5.3	—	0.17	—
GM25	5.7	—	0.15	—
GM27	6.5	—	0.12	—
1/CaCO ₃	7.2	—	0.19	—
Polyurethane foams (rigid)				
GM29	7.9	—	0.10	—
GM31	8.4	—	0.09	—
GM35	6.9	—	0.11	—
Polyisocyanurate foams (rigid)				
GM41	6.8	—	0.12	—
GM43	5.5	—	0.15	—
Phenolic foam	5.5	—	0.17	—

^aIgnition data measured in the ASTM E2058 fire propagation apparatus.

^bIgnition data measured at the University of Edinburgh, U.K.

agrees with the critical mass loss rate for flame extinction from Reference 117.

The data in Table 3-4.28 show that the values of the kinetic parameter are higher for the aliphatic materials than the values for the aromatic and chlorinated materials, which is opposite to the trend for the heat of combustion. The data suggest that the materials can be arranged in the following decreasing order of the kinetic parameter values (using FMRC values): polyoxymethylene ($\phi = 0.43 >$ polymethylmethacrylate $\phi = 0.28 >$ polyethylene, polypropylene, and polyethylene foams ($\phi = 0.27$ to $0.25 >$ polystyrene ($\phi = 0.21 >$ polyurethane, polystyrene, and polyisocyanurate foams and chlorinated polyethylenes

($\phi = 0.09$ to 0.19). As expected from the fire point theory,^{114,116} the reactivity of the vapors in the gas phase follows the kinetic parameter.

The combustion efficiency and product generation efficiencies follow the reactivity of the vapors in the gas phase, such as shown in Figure 3-4.48 for the combustion efficiency. The lower the value of the kinetic parameter (Equation 121), the lower the reactivity of the material vapors, which is reflected in the (1) reduced values of the combustion efficiency (Equations 32 through 34), (2) reduced values of the generation efficiencies (Equation 66) of the oxidation zone products (such as CO_2), and (3) increased values of the generation efficiencies of the reduction zone products (such as smoke, CO , and hydrocarbons).

The flame extinction can also be expressed in terms of the critical heat release rate:

$$\dot{Q}_{\text{cr},i}'' = \Delta H_i \dot{m}_{\text{cr}}'' \quad (122)$$

where $\dot{Q}_{\text{cr},i}''$ is the critical heat release rate (chemical, convective, or radiative in kW/m^2), and ΔH_i is the heat of combustion (chemical, convective, and radiative in kJ/g). Table 3-4.29 lists the critical chemical, convective, and radiative heat release rates for flame extinction, where critical mass loss rate values are taken from Table 3-4.28 and heats of combustion from Table 3-4.14.

The data in Table 3-4.29 suggest that the critical heat release rate for flame extinction is weakly dependent on the chemical nature of the material, contrary to the critical mass loss rate. The critical heat release rates thus can be averaged, which are 100 ± 7 , 53 ± 9 , and $47 \pm 10 \text{ kW}/\text{m}^2$ for the chemical, convective, and radiative heat release rates, respectively. For materials with highly reactive vapors, such as polyethylene, large amounts of extinguishing agent are needed to reduce the heat release rate to the criti-

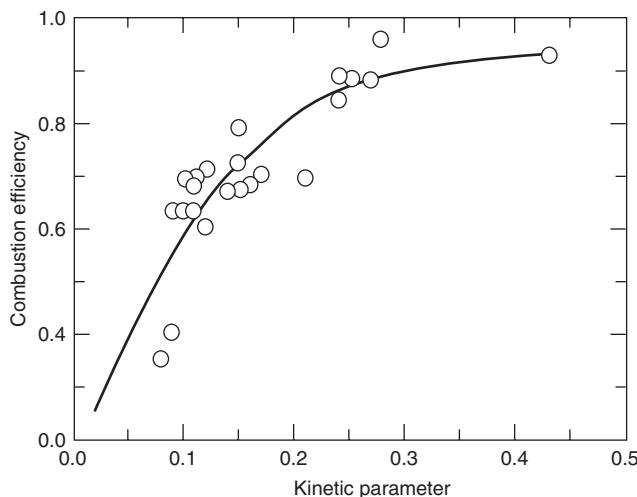


Figure 3-4.48. Kinetic parameter for flame extinction versus the combustion efficiency and production generation efficiencies. Data are measured in the ASTM E2058 fire propagation apparatus.

Table 3-4.29 Critical Chemical, Convective, and Radiative Heat Release Rates for Flame Extinction^a

Material	Critical Heat Release Rate (kW/m^2)		
	Chemical	Convective	Radiative
Polyoxymethylene	(65)	50	(14)
Polymethylmethacrylate	77	53	24
Polyethylene	96	55	42
Polypropylene	104	61	43
Polyethylene foams	88	51	38
Chlorinated polyethylenes	95	48	47
Polystyrenes	108	44	64
Polyurethane foams (flexible)	101	48	53
Polyurethane foams (rigid)	102	44	58
Average	96 ± 10	51 ± 6	46 ± 12

^aCritical mass loss rates from the ASTM E2058 fire propagation apparatus, and heats of combustion from Table 3-4.14.

cal value. For materials with highly nonreactive vapors, such as Teflon, it is difficult to reach the critical heat release rate values unless high external heat flux is applied.

The energy balance at the surface as the flame extinction condition is reached is¹¹³

$$\dot{m}'' = \frac{\phi \Delta H_T \dot{m}_{\text{cr}}'' + \dot{q}_e'' - \dot{q}_{rr}'' - \dot{q}_{\text{agent}}''}{\Delta H_g} \quad (123)$$

$$\dot{Q}_i'' = \frac{\Delta H_i}{\Delta H_g} (\phi \Delta H_T \dot{m}_{\text{cr}}'' + \dot{q}_e'' - \dot{q}_{rr}'' - \dot{q}_{\text{agent}}'') \quad (124)$$

where

\dot{q}_e'' = external heat flux (kW/m^2)

\dot{q}_{rr}'' = surface re-radiation loss (kW/m^2)

\dot{q}_{agent}'' = heat flux removed from the surface or from the flame by the agent as the flame extinction condition is reached (kW/m^2)

ΔH_i = chemical, convective, or radiative heat of combustion (kJ/g)

ΔH_g = heat of gasification (kJ/g)

$\Delta H_i/\Delta H_g$ is defined as the heat release parameter (HRP).

Flame suppression/extinguishment by water: The heat flux removed from the surface of a burning material by water, as a result of vaporization, is expressed as¹¹³

$$\dot{q}_w'' = \varepsilon_w \dot{m}_w \Delta H_w \quad (125)$$

where

ε_w = water application efficiency

\dot{m}_w'' = water application rate per unit surface area of the material ($\text{g}/\text{m}^2\text{s}$)

ΔH_w = heat of gasification of water (2.58 kJ/g)

If only part of the water applied to a hot surface evaporates and the other part forms a puddle, such as on a horizontal surface, blockage of flame heat flux to the surface and escape of the fuel from the material surface are expected. Equation 125 thus is modified as

$$\dot{q}_w'' = \dot{m}_w'' (\varepsilon_w \Delta H_w + \delta_w) \quad (126)$$

where δ_w is the energy associated with the blockage of flame heat flux to the surface and escape of the fuel vapors per unit mass of the fuel gasified (kJ/g).

From Equations 123 and 126,

$$\dot{m}_w'' = \frac{\dot{q}_e''}{\varepsilon_w \Delta H_w + \delta_w} + \frac{\phi \Delta H_T \dot{m}_{cr}'' - \dot{q}_{rr}'' - \dot{m}'' \Delta H_g}{\varepsilon_w \Delta H_w + \delta_w} \quad (127)$$

At flame extinction, $\dot{m}'' = \dot{m}_{cr}''$ and from Equation 127

$$\dot{m}_{w,ex}'' = \frac{\dot{q}_e''}{\varepsilon_w \Delta H_w + \delta_w} + \frac{\dot{m}_{cr}'' (\phi \Delta H_T - \Delta H_g) - \dot{q}_{rr}''}{\varepsilon_w \Delta H_w + \delta_w} \quad (128)$$

where $\dot{m}_{w,ex}''$ is the water application rate per unit surface area of the material for flame extinction (g/m²·s). As discussed in Reference 113, in the absence of the external heat flux with no water puddle formation at the surface, the critical water application rate for flame extinction is

$$\dot{m}_{w,cr}'' = \frac{\dot{m}_{cr}'' (\phi \Delta H_T - \Delta H_g) - \dot{q}_{rr}''}{\varepsilon_w \Delta H_w} \quad (129)$$

where $\dot{m}_{w,cr}''$ is the critical water application rate (g/m²·s), which is related to the fundamental fire property of the material. The calculated values of the critical water application rate for materials are listed in Table 3-4.30, where efficiency of water application was taken as unity. The values were calculated from Equation 128, using data from Table 3-4.14 for the net heats of complete combustion, from Table 3-4.28 for the critical mass loss rate and the kinetic parameter, from Table 3-4.7 for the heats of

gasification and surface re-radiation loss, and using a value of 2.59 kJ/g for the heat of gasification of water.

All the materials listed in Table 3-4.30 burn in normal air without the external heat flux, except polyethylene with 36 and 48 percent chlorine by weight. The critical water application rate for flame extinction for materials that do not burn in normal air without the external heat flux is zero. The materials in Table 3-4.30 that burn without the external heat flux can be arranged in the following order of increased water application rate required for flame extinction: polyoxymethylene, polymethylmethacrylate, and polyethylene with 25 percent chlorine (2.1 to 2.5 g/m²·s) < polyethylene and polypropylene (3.5 to 4.1 g/m²·s) < polystyrene (5.1 g/m²·s).

The data in Table 3-4.30 suggest that the critical water application rate required for flame extinction, with no water puddle at the surface, can be calculated to support the experimental data. The input data for the calculation can be obtained from the measurements for the fire properties in the small-scale apparatuses, such as the oxygen bomb calorimetry, the ASTM E2058 fire propagation apparatus, the OSU apparatus, and the cone calorimeter. The properties and respective tests are (1) surface re-radiation loss (from the CHF and critical mass loss rate, using ignition tests), (2) heat of gasification using the non-flaming tests, (3) net heat of complete combustion from the oxygen bomb calorimeter, and (4) kinetic parameter (Equation 121) where the ratio of the convective heat transfer coefficient to specific heat is needed. The ratio can be obtained from the methanol combustion at variable oxygen mass fractions and external heat flux for known inlet airflow rates, a procedure that has been used in the ASTM E2058 fire propagation apparatus for such applications.⁴¹

The first term on the right-hand side of Equation 128 can be considered as the term to account for the effects of fire size as well as the shapes and arrangements of the materials. As the fire intensity increases due to changes in the shape, size, and arrangements of the material, heat flux to the surface of the material increases, and water application

Table 3-4.30 Critical Water Application Rates for Flame Extinction

Material	\dot{q}_{rr}'' (kW/m ²)	ΔH_T (kJ/g)	ΔH_g (kJ/g)	\dot{m}_{cr}'' (g/m ² ·s)	ϕ (g/m ² ·s)	Critical Water Appl. Rate (g/m ² ·s)
Polyoxymethylene	13	15.4	2.4	4.5	0.43	2.3
Polymethylmethacrylate	11	25.2	1.6	3.2	0.28	2.5
Polyethylene	15	43.6	1.8	2.5	0.27	3.8
Polypropylene	15	43.4	2.0	2.7	0.24	3.0
Polyethylene foams						
1	12	41.2	1.7	2.6	0.24	3.6
2	13	40.8	1.4	2.6	0.25	3.8
3	12	40.8	1.8	2.5	0.25	3.5
4	12	40.8	1.5	2.6	0.25	4.1
Chlorinated polyethylenes						
25% chlorine	12	31.6	2.1	6.6	0.15	2.1
36% chlorine	12	26.3	3.0	7.5	0.12	0
48% chlorine	10	20.6	3.1	7.6	0.13	0
Polystyrene	13	39.2	1.7	4.0	0.21	5.1

rates above and beyond the critical water application rate for flame extinction thus would be required. For example, water application rate for extinguishment of fires burning at the asymptotic limits can be calculated from (1) the values of the flame heat flux to the surface listed in Table 3-4.8, in place of the external heat flux in Equation 128; and (2) the data for the critical water application rate for flame extinction listed in Table 3-4.30. The calculated water application rates for extinguishment of fires burning at the asymptotic limits are listed in Table 3-4.31. The data show that the first term of Equation 128 becomes very dominant at the asymptotic limit compared to the second term, which is the critical water application rate. In Table 3-4.31, the water application rates at the asymptotic limits are thus calculated on the basis of flame heat flux alone.

Numerous small- and large-scale tests have been performed to assess the extinguishment of fires by water sprays.^{113–118,120–123} For example, small-scale fire suppression/extinguishment tests are performed in the ASTM

E2058 fire propagation apparatus [Figures 3-4.2(a) and (b)], and large-scale fire suppression/extinguishment tests are performed in the fire products collector (Figure 3-4.8) and at the FMRC Test Center, mostly at the 30-ft site (Figure 3-4.49).^{35,45,111,112,115,120–124}

Small-scale fire suppression/extinguishment tests using water and materials with two- and three-dimensional configurations burning in co- and natural-airflow conditions: Several studies have been performed for these types of configurations and airflow conditions.^{111–118} For example, small-scale fire suppression/extinguishment tests using water are performed in the ASTM E2058 fire propagation apparatus, under co- and natural airflow conditions. In the tests, measurements are made, in the presence and absence of water, for the critical heat flux (CHF); thermal response parameter (TRP); mass loss rate; chemical, convective, and radiative heat release rates; generation rates of CO and CO₂; hydrocarbons; smoke; optical transmission through smoke; corrosion in the gas phase; and other products (depending on the need).

The test samples used, with and without the external heat flux, consist of (1) two-dimensional samples: 100 × 100 mm square and 100-mm-diameter circular samples up to 50 mm in thickness; and (2) three-dimensional samples identified as *sample commodities*: (a) cross piles of sticks, defined as the *crib*—single crib is used in the test; and (b) 50-, 75-, and 100-mm cubic boxes—one to eight boxes are arranged in one to four layers with a separation of about 12 mm between the boxes and the layers. The designation used for the arrangement of the boxes is as follows: number of boxes along the length × number of boxes along the width × number of layers, that is,

1. One box with a single layer:
1 × 1 × 1 sample commodity,
2. Two boxes with a single layer:
2 × 1 × 1 sample commodity,
3. Two boxes with two layers:
1 × 1 × 2 sample commodity,
4. Three boxes with three layers:
1 × 1 × 3 sample commodity,
5. Four boxes with four layers:
1 × 1 × 4 sample commodity,
6. Four boxes with a single layer:
2 × 2 × 1 sample commodity,
7. Eight boxes with two layers:
2 × 2 × 2 sample commodity.

There are provisions to use more than eight boxes and four layers. The arrangements have strong effect on the fire intensity as shown in Figure 3-4.50, where chemical heat release rate is plotted against time for 100-mm cubic box with one box to a layer for a total of four layers. Visual flame heights from the bottom of the first box are indicated for two arrangements. The data were measured in the ASTM E2058 fire propagation apparatus. The data show that the increase in the chemical heat release rate is more than expected from the increase in the surface area. For example, the surface area increases by a factor of 4 from one to four boxes, whereas the peak chemical heat release rate increases by a factor of 5, even though all the surface areas are not burning. This relationship is indica-

Table 3-4.31 Water Application Rate for the Extinguishment of Fires at the Asymptotic Limits^a

Material	$\dot{m}_{w,cr}''$ (g/m ² ·s)	\dot{q}_f'' (kW/m ²)	Water Appl. Rate (g/m ² ·s)
<i>Aliphatic carbon-hydrogen atoms</i>			
Polyethylene	3.8	61	27
Polypropylene	3.0	67	29
Heavy fuel oil (2.6–23 m)	?	29	11 ^b
Kerosene (30–80 m)	?	29	11 ^b
Crude oil (6.5–31 m)	?	44	17 ^b
n-Dodecane (0.94 m)	?	30	12 ^b
Gasoline (1.5–223 m)	?	30	12 ^b
JP-4 (1.0–5.3 m)	?	40	16 ^b
JP-5 (0.60–17 m)	?	39	15 ^b
n-Heptane (1.2–10 m)	?	37	14 ^b
n-Hexane (0.75–10 m)	?	37	14 ^b
Transformer fluids (2.37 m)			
<i>Aromatic carbon-hydrogen atoms</i>			
Polystyrene (0.93 m)	5.1	75	34
Xylene (1.22 m)	?	37	14 ^b
Benzene (0.75–6.0 m)	?	44	17 ^b
<i>Aliphatic carbon-hydrogen-oxygen atoms</i>			
Polyoxymethylene	2.3	50	22
Polymethylmethacrylate (2.37 m)	2.5	60	26
Methanol (1.2–2.4 m)	?	27	10 ^b
Acetone (1.52 m)	?	24	9 ^b
<i>Aliphatic carbon-hydrogen-halogen atoms</i>			
Polyvinylchloride	0	50	19
Tefzel (ETFE)	0	50	19
Teflon (FEP)	0	52	20

^aFor water application efficiency of unity with no water puddle at the surface.

^bCalculated from the flame heat flux alone. Because water does not stay at the surface, the flame extinction of liquid pool fires with water is not an efficient process. The efficiency of unity used in the calculations thus may not be correct and actual water application rates would probably be higher than calculated.

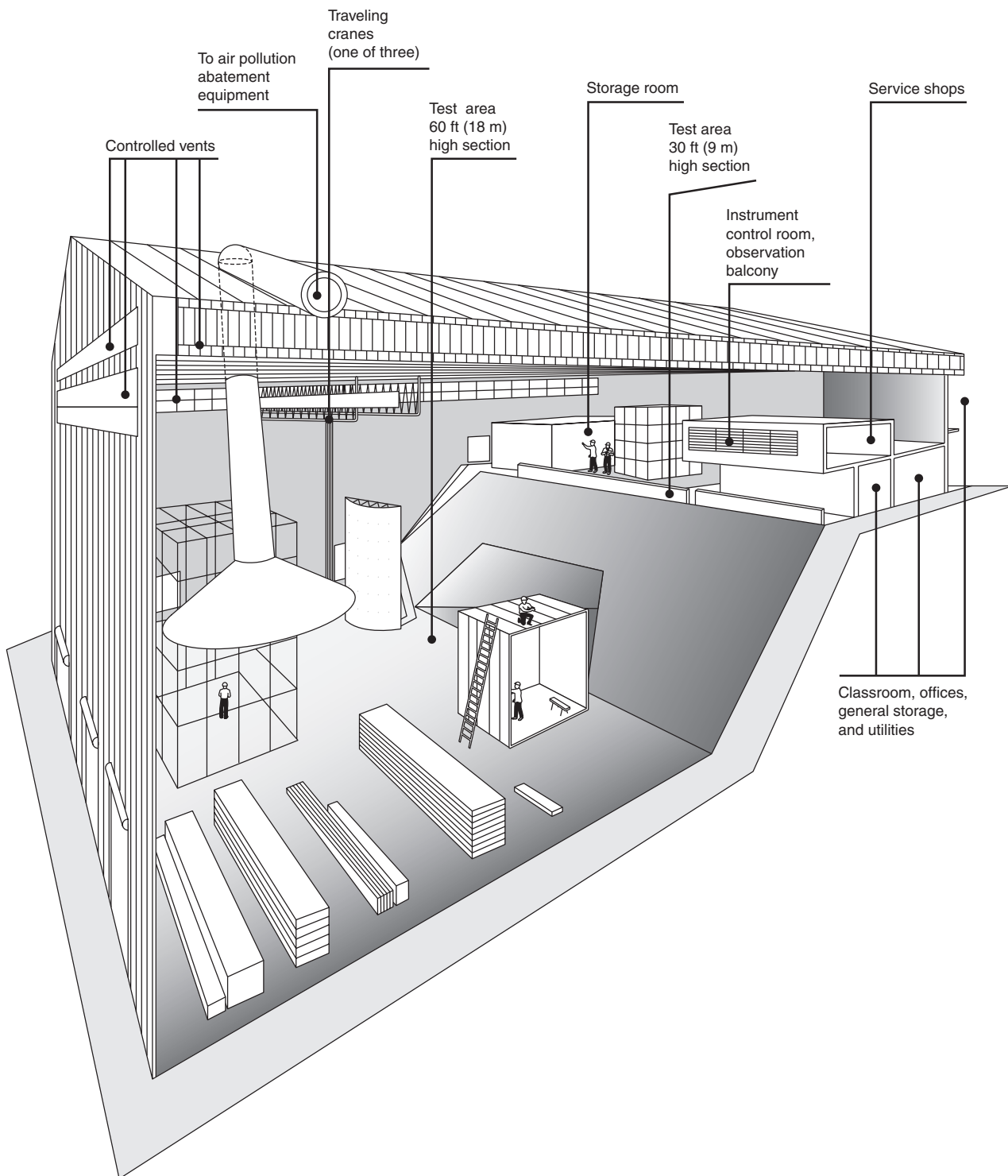


Figure 3-4.49. The Factory Mutual Research Corporation's Test Center at West Gloucester, Rhode Island, where large-scale fire tests are performed.

tive of the enhancement of the flame heat flux in a three-dimensional arrangement.

In the three-dimensional arrangement of the sample commodities, the water application rate for fire suppression/extinguishment is expected to be governed by the first term rather than by the second term in Equation 128 (see Table 3-4.31), due to the enhancement of the flame heat flux. With water application efficiency of unity and

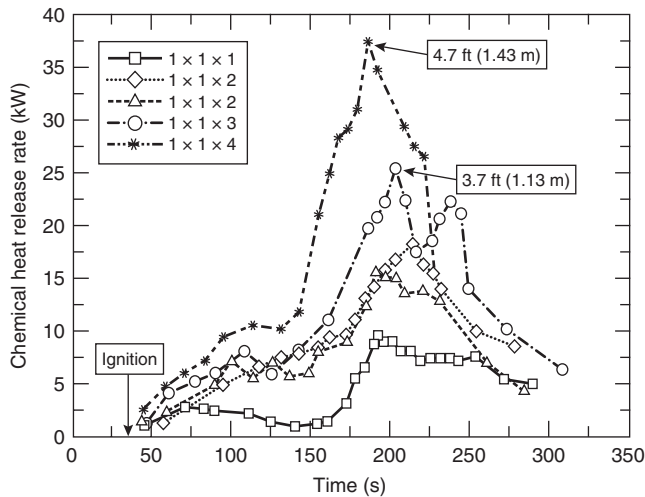


Figure 3-4.50. Free-burning chemical heat release rate versus time for 100-mm cubic empty corrugated paper boxes arranged as one box per layer for a total of four layers. Each layer is about 12 mm apart. Visual flame heights are indicated for two arrangements. Data were measured in the ASTM E2058 fire propagation apparatus.

no water puddle at the surface, the water application rate required for flame suppression/extinguishment for the three-dimensional arrangement of sample commodities, from Table 3-4.31 for solids, is expected to be in the range of 19 to 34 g/m²s. These rates are about ten times the critical water application rates for flame extinction (Table 3-4.30).

Figures 3-4.51 through 3-4.53 show examples of the fire extinguishment test data from the ASTM E2058 fire propagation apparatus for 100-mm-diameter and 13-mm-thick circular Whatman No. 3 cellulosic filter paper slabs.¹²⁴ Figure 3-4.51 is a plot of the average heat flux removed from the surface of wet filter paper by the gasification of water versus the average heat flux required to gasify the water. The average heat flux removed from the surface, during the test time period, is calculated from Equation 123 using the measured values of the mass loss rate with and without the water on the surface, and the values from Table 3-4.7 for the heats of gasification and surface re-radiation loss of filter paper. The average heat flux required to gasify the water, during the test time period, is calculated from Equation 125 using the measured values of the mass of water applied to the surface, where efficiency of application is unity. As expected from the published literature on this subject,^{111-118,128} there is excellent agreement between the heat flux removed from the surface by water and heat flux required to gasify it.

The data in Figure 3-4.52 show that the time to sustained autoignition for the filter paper increases with increase in the amount of water at the surface, as expected due to removal of energy by (1) the gasification of water and (2) blockage of flame heat flux to the surface and escape of the fuel vapors. It is well known that the wetting action of water delivered from sprinklers is effective in resisting the fire jump across the aisles of stored com-

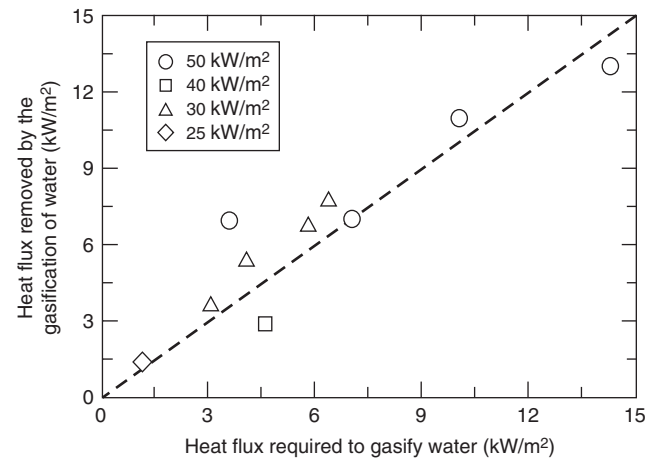


Figure 3-4.51. Average heat flux removed from the surface by the gasification of water versus the average heat flux required for the gasification of water. The data are for 100-mm-diameter and 13-mm-thick horizontal wetted slabs of the Whatman No. 3 cellulosic filter paper. The slabs were exposed to external heat fluxes in the range of 25 to 50 kW/m² in the ASTM E2058 fire propagation apparatus under co-flow conditions in normal air. The slabs were wetted with different amounts of water until saturation. Data are taken from Reference 124.

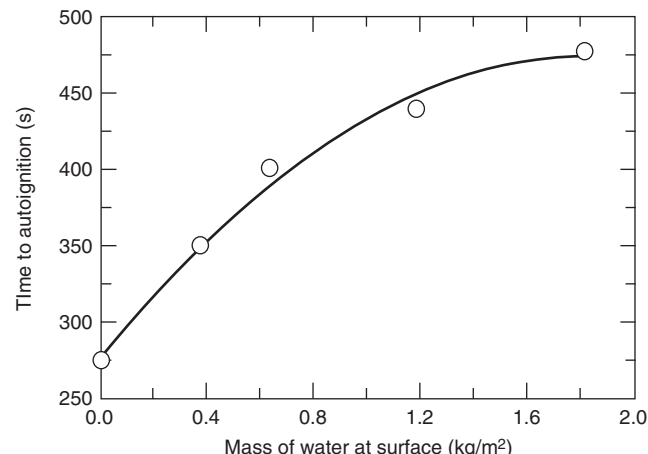


Figure 3-4.52. Time to autoignition versus the total amount of water used to wet the 100-mm-diameter and 13-mm-thick horizontal wetted slabs of the Whatman No. 3 cellulosic filter paper. The slabs were exposed to external heat fluxes in the range of 25 to 50 kW/m² in the ASTM E2058 fire propagation apparatus under co-flow conditions in normal air. The slabs were wetted with different amounts of water until saturation. Data are taken from Reference 124.

modities in warehouses. The wetting action of water is considered to be one of the major advantages of the sprinkler fire protection.

Figure 3-4.53 shows the percent reduction in the chemical heat release rate versus the water application

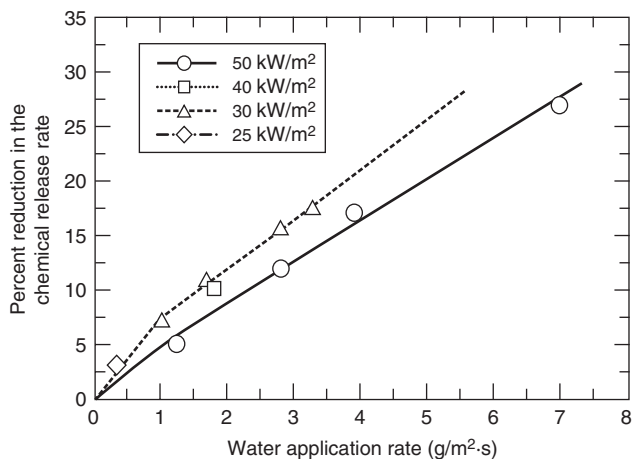


Figure 3-4.53. Percent reduction in the chemical heat release rate versus the water application rate for the combustion of 100-mm-diameter and 13-mm-thick horizontal wetted slabs of the Whatman No. 3 cellulosic filter paper. The slabs were exposed to external heat fluxes in the range of 25 to 50 kW/m² in the ASTM E2058 fire propagation apparatus under co-flow conditions in normal air. Data are taken from Reference 124.

rate for the cellulosic filter paper sample exposed to various heat fluxes. From Equation 124, the reduction in the chemical heat release rate for a fixed external heat flux value can be expressed as follows:

$$\dot{Q}_{ch}'' - \dot{Q}_{ch,w}'' = \frac{\Delta H_{ch}}{\Delta H_g} \dot{q}_w'' \quad (130)$$

where $\dot{Q}_{ch,w}''$ is the chemical heat release rate in the presence of water (kW/m²). $\Delta H_{ch}/\Delta H_g$ is the HRP. From Equations 126 and 130,

$$\dot{Q}_{ch}'' - \dot{Q}_{ch,w}'' = \text{HRP}(\varepsilon_w \Delta H_w + \delta_w) \dot{m}_w'' \quad (131)$$

In the tests, the water was applied directly to the surface and there was no puddle formation on the surface, thus $\varepsilon_w = 1$ and $\delta_w = 0$. For cellulosic filter paper, HRP = 3.6 and the heat of gasification of water is 2.6 kJ/g. Using these values in Equation 131,

$$\frac{\dot{Q}_{ch}'' - \dot{Q}_{ch,w}''}{\dot{Q}_{ch}''} \times 100 = \left[\frac{100 \times 3.6 \times 2.6}{\dot{Q}_{ch}''} \right] \dot{m}_w'' \quad (132)$$

or, the percent reduction in the chemical heat release rate is

$$\frac{\dot{Q}_{ch}'' - \dot{Q}_{ch,w}''}{\dot{Q}_{ch}''} \times 100 = \frac{936}{\dot{Q}_{ch}''} \dot{m}_w'' \quad (133)$$

Equation 133 suggests that a plot of the percentage reduction in the chemical heat release rate versus the water application rate should be a straight line with a slope of $936/\dot{Q}_{ch}''$. For the external heat flux values of 25, 30, 40, and 50 kW/m², the free-burning chemical heat release rates are 120, 190, 210, and 235 kW/m², respectively. Thus, the slopes at these fluxes are 7.8, 4.9, 4.5, and 4.0 (g/m²·s)⁻¹,

respectively. The slopes of the lines from the experimental data for 30 and 50 kW/m² in Figure 3-4.53 are 4.7 and 3.9 (g/m²·s)⁻¹, respectively, in excellent agreement with the expected slopes from Equation 133. Thus, the experimental data support the heat balance mechanism for flame extinction by the gasification of water, as long as there is no water puddle at the surface.

Small-scale fire suppression/extinguishment tests using water with horizontal and vertical slabs burning under natural airflow condition. Several studies have been performed in this type of configuration.¹¹³⁻¹¹⁸ For example, fire extinguishment tests have been performed with water applied to the burning vertical and horizontal slabs of polymethylmethacrylate (PMMA), polyoxymethylene (POM), polyethylene (PE), and polystyrene (PS).¹¹⁷ The horizontal slabs were 0.18-m squares and the vertical slabs were 0.18 m wide and 0.37 m high.¹¹⁷ The slabs were exposed to external heat flux values in the range 0 to 17 kW/m² in normal air in the presence of water applied at a rate of 0 to 7.8 g/m²·s.¹¹⁷ The water application efficiency was close to unity.

Figure 3-4.54 shows the time to flame extinction and mass loss rate for various external heat fluxes applied to the surface of the vertical PMMA slab burning in normal air with a water application rate of 5.2 g/m²·s; the data in the figure are taken from the study reported in Reference 117. With increase in the external heat flux, the time to flame extinction increases until, close to the critical heat flux (CHF) value of 11 kW/m² (Table 3-4.2), it goes to infinity (no flame extinction). The mass loss rate data in Figure 3-4.54 show that, close to the CHF value, the mass loss rate approaches the critical rate of 3.2 g/m²·s, determined from the ignition experiments (Table 3-4.29). These data support the fire point theory.^{114,116}

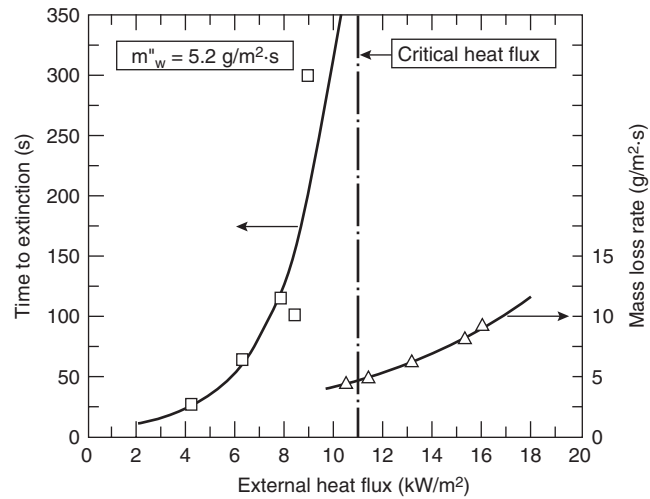


Figure 3-4.54. Time to flame extinction and mass loss rate at various external heat fluxes for the combustion of a 0.18-m-wide, 0.37-m-high, and 50-mm-thick vertical slab of polymethylmethacrylate in the presence of water with an application rate of 5.2 g/m²·s. Data are taken from the study reported in Reference 117.

Figure 3-4.55 shows water application rates required for flame extinction for vertical slabs of polymethylmethacrylate (PMMA), polyoxymethylene (POM), polystyrene (PS), and polyethylene (PE) burning in normal air with various external heat flux exposure. The data satisfy Equation 127:

Polymethylmethacrylate

Vertical

$$\dot{m}_w'' = 0.37\dot{q}_e'' + 1.67 \quad (R^2 = 0.99) \quad (134)$$

Horizontal

$$\dot{m}_w'' = 0.22\dot{q}_e'' + 1.56 \quad (R^2 = 0.99) \quad (135)$$

Polyoxymethylene

Vertical

$$\dot{m}_w'' = 0.42\dot{q}_e'' + 1.97 \quad (R^2 = 0.98) \quad (136)$$

Horizontal

$$\dot{m}_w'' = 0.24\dot{q}_e'' + 2.08 \quad (R^2 = 0.99) \quad (137)$$

Polystyrene

Horizontal

$$\dot{m}_w'' = 0.22\dot{q}_e'' + 3.1 \quad (R^2 = 0.98) \quad (138)$$

Equations 134 and 136 show that, for vertical slabs, the inverse of the slope is equal to 2.7 and 2.3 kJ/g for PMMA and POM, respectively, which are close to the heat

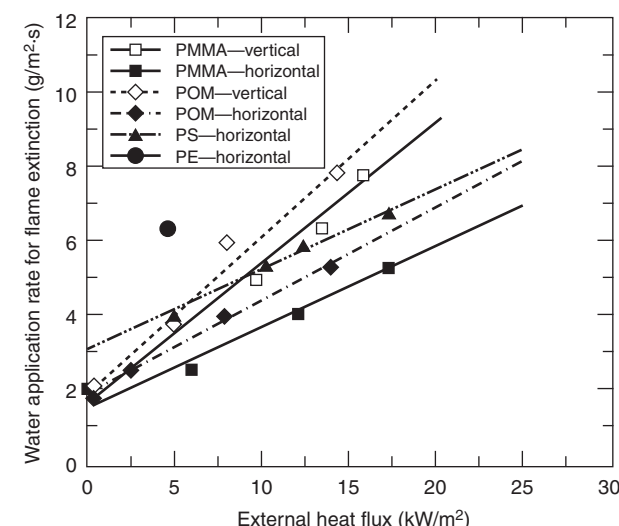


Figure 3-4.55. Water application rate required for flame extinction of horizontal and vertical slabs of polymethylmethacrylate (PMMA), polyoxymethylene (POM), polystyrene (PS), and polyethylene (PE) burning in normal air at various external heat fluxes. Data are taken from the study reported in Reference 117.

of gasification of water (2.6 kJ/g). Thus, the effect of a water puddle at the surface is negligible as expected for the vertical surfaces. Equations 135, 137, and 138 show that, for horizontal surfaces, the inverse of the slopes for PMMA, POM, and PS are 4.6, 4.1, and 4.6 kJ/g, respectively, which are almost twice the value for the heat of gasification of water. The data for the horizontal slabs thus suggest that the blockage of flame heat flux and escape of the fuel from the surface are as important as the gasification of water. The energy associated with the blockage is about the same magnitude as the energy associated with the gasification of water.

Large-scale fire suppression/extinguishment tests using water. Numerous large-scale fire suppression/extinguishment tests have been performed.^{111–118,121–124} In almost all cases, the materials are heterogeneous and the configurations are three dimensional, identified as *commodities*. Tests are performed under natural airflow conditions with water applied from a series of sprinklers. The sprinklers are either at the ceiling or close to the top surface of the commodities. At FMRC, large-scale fire suppression/extinguishment tests are performed in the fire products collector (Figure 3-4.8) and at the FMRC Test Center, mostly at the 30-ft site (Figure 3-4.50).^{35,45,111,112,115,120–124}

FMRC classifies a stored commodity by its potential fire protection challenge, which is essentially dependent on the commodity's ability to release heat in a fire in the presence of water.¹²⁰ Most stored commodities are classified into one of the six classes, such as the following examples.¹²⁰

Noncombustible: Do not burn and do not, by themselves, require sprinkler protection.

Combustibles: *Class I:* Example—noncombustible products on wood pallets or noncombustible products packaged in ordinary corrugated paper boxes or wrapped in ordinary paper on wood pallets. Class I commodity is simulated by glass jars in compartmented corrugated paper boxes.

Class II: Example—Class I products in more combustible packaging, such as wood crates or multiple-thickness corrugated boxes. Class II commodity is simulated by metal-lined double tri-wall corrugated paper boxes.

Class III: Example—packaged or unpackaged wood, paper, or natural-fiber cloth, or products made from them, on wood pallets. Class III commodity is simulated by using paper cups in compartmented corrugated paper boxes.

Class IV: Class I, II, and III commodities containing no more than 25 percent (by volume) or 15 percent by weight of high-heat-release-rate synthetic materials. Class IV commodity is simulated by polystyrene (15 percent by weight) and paper cups in compartmented corrugated paper boxes.

Group A plastics: Simulated by polystyrene cups in compartmented corrugated paper boxes.

For the tests in the fire products collector, the commodities are used in a 2 × 2 × 2 arrangement (two pallet

loads along the length \times two pallet loads along the width \times two layers).^{111,112,120,123} Each pallet load consists of a wood pallet with eight 0.53-cubic corrugated paper boxes, containing products under test, in a $2 \times 2 \times 2$ arrangement (two boxes along the length \times two boxes along the width in two layers, with boxes touching each other). Each pallet load is a 1-m (42-in.) cube of product and separated by about 150 mm. This arrangement leads to the test commodity consisting of eight pallet loads with 64 corrugated paper boxes containing products with overall dimensions of 2.3 m (7.5 ft) \times 2.3 m (7.5 ft) \times 2.9 m (9.7 ft) high.

In the fire products collector (10,000-kW-scale ASTM E2058 fire propagation apparatus) fire suppression/extinguishment tests, water is applied at the top of the commodity, in a uniform fashion, with application rates in the range of 0 to 407 g/m²·s (0 to 0.6 gpm per sq ft). The range of the water application rates is about ten times the predicted range for the three-dimensional arrangements (Table 3-4.31 with water application efficiency of unity and no water puddles at the surfaces). It thus appears that blockage of flame heat flux to the surface and escape of fuel vapors are as important as gasification of water for the fire suppression/extinguishment of the commodities, similar to the flame extinction for horizontal slabs (Equations 135, 137, and 138) in small-scale tests, discussed previously.

Figure 3-4.56 shows the calculated values of the free-burning average peak heat release rate for the simulated Class I through Group A plastic commodities. In the calculations data measured in the fire products collector (10,000-kW-scale ASTM E2058 fire propagation apparatus) were used.¹²⁴ The Class I through Class III commodities were made of cellulosic materials and had lower heat

release rates. This behavior is expected on the basis of the values of (1) surface re-radiation loss and heat of gasification (Table 3-4.7), (2) flame heat flux (close to polyoxymethylene, Table 3-4.8), (3) heat of combustion (Table 3-4.14), and (4) heat release parameter (Table 3-4.15) for wood and paper. The heat release rates for Class I through Class III commodities increase gradually from Class I through Class III.

Introduction of polystyrene from about 15 percent (Class IV) to 100 percent (plastics Group A) inside the corrugated paper boxes results in an exponential increase in the chemical and radiative heat release rates as indicated in Figure 3-4.56. This behavior is expected on the basis of the higher values of (1) heat of gasification (Table 3-4.7), (2) flame heat flux (Table 3-4.8), (3) heat of combustion (Table 3-4.14), and (4) heat release parameter (Table 3-4.15) for polystyrene compared to the values for the cellulosic materials in Class I through III commodities. The higher intensity fire due to the introduction of polystyrene is also indicated by the higher water applications rates required for fire suppression/extinguishment in Figure 3-4.57. The higher water requirement for fire suppression/extinguishment for Class IV and plastics Group A commodities is expected from Equation 128, due to higher value of the flame heat flux which dominates the water application rate requirements.

Flame Extinction by the Processes in the Gas Phase

The process of flame extinction by gaseous, powdered, and foaming agents and by increase in the local equivalence ratio is predominantly a gas-phase process and thus is different from the process of flame extinction by water,

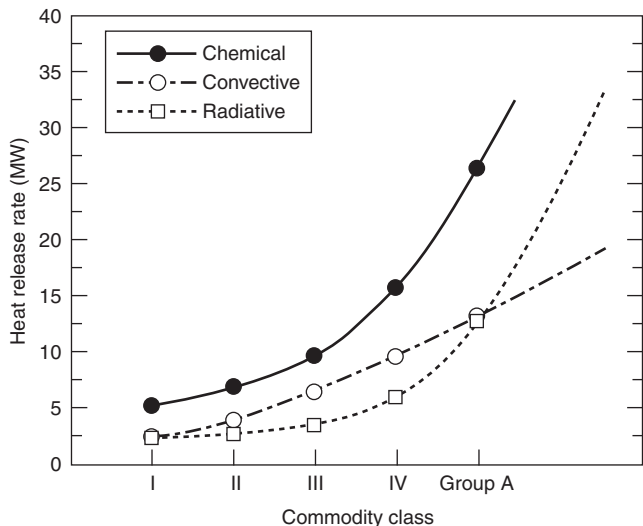


Figure 3-4.56. Calculated average peak heat release rates for free-burning fires of simulated commodities from the data measured in the fire products collector (10,000-kW-scale ASTM E2058 fire propagation apparatus). Data are taken from References 111, 112, 120, 123, and 124.

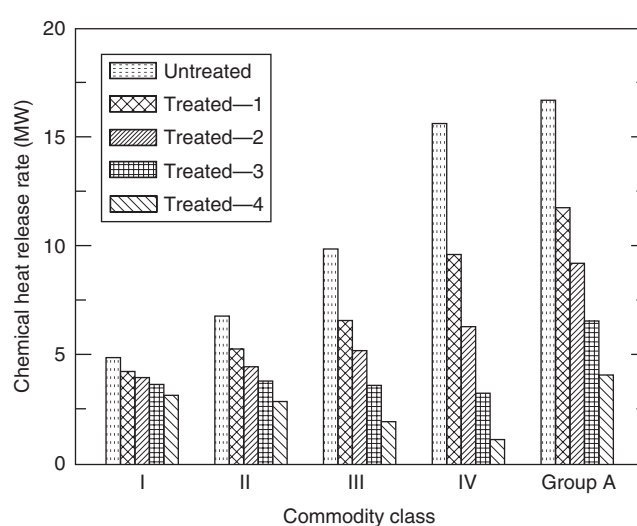


Figure 3-4.57. Calculated average peak chemical heat release rates at various water application rates for fires of simulated commodities from the data measured in the fire products collector (10,000-kW-scale ASTM E2058 fire propagation apparatus). Data are taken from References 111, 112, 120, 123, and 124. One gpm/ft² = 769 g/m²·s.

which occurs predominantly in the solid phase at the surface of the material. The kinetic parameter for flame extinction defined in Equation 118, however, is still applicable:¹¹³

$$\phi = \frac{\phi_0 - \kappa Y_{j,\text{ex}} \left[\frac{1 + \Delta c_p(T_{\text{ad}} - T_a) + \Delta H_D}{\Delta H_{\text{O}}^* Y_{\text{O}}} \right]}{1 - Y_{j,\text{ex}}} \quad (139)$$

where

ϕ = kinetic parameter in the presence of the extinguishing agent

ϕ_0 = kinetic parameter in the absence of the extinguishing agent

κ = ratio between the kinetic parameters at the flame temperature and at the adiabatic flame temperature

$Y_{j,\text{ex}}$ = mass fraction of the extinguishing agent

Δc_p = difference between the heat capacities of the extinguishing agent and the fire products (kJ/g·K)

T_{ad} = adiabatic flame temperature at the stoichiometric limit (K)

T_0 = initial temperature of the reactants (K)

ΔH_D = heat of dissociation (kJ/g)

Equation 139 shows that the addition of an extinguishing agent reduces the kinetic parameter from its normal value and includes the effects of four flame extinction mechanisms:¹¹³ (1) dilution, effects are included in the $\kappa Y_{j,\text{ex}}$ term; (2) added thermal capacity, effects are included in Δc_p ; (3) chemical inhibition, effects are included through increases in T_{ad} value; for most fuels the adiabatic flame temperature at the stoichiometric limit is about 1700 K;¹¹³ more reactive fuels, such as hydrogen, have lower adiabatic flame temperature at the stoichiometric limit, and less reactive or retarded materials have higher values of the adiabatic flame temperature at the stoichiometric limit; and (4) kinetic chain breaking and endothermic dissociation through Δc_p and ΔH_D terms.

From Equation 123, in the presence of an extinguishing agent that works in the gas phase,

$$\dot{m}'' = \frac{\phi \Delta H_T \dot{m}_{\text{cr}}'' + \dot{q}_e'' - \dot{q}_{rr}''}{\Delta H_g} \quad (140)$$

For a fixed value of the external heat flux, the addition of an extinguishing agent reduces the normal value of the kinetic parameter by one or more of the four mechanisms expressed by Equation 139; the mass loss rate decreases and approaches the critical value at which the flame is extinguished. Increase in the external heat flux would increase the mass loss rate, and further addition of the extinguishing agent would be needed to reduce the mass loss to its critical value and to reestablish the flame extinction condition. Continued increase in the extinguishing agent with external heat flux will result in the first term in the denominator on the right-hand side of Equation 140 to become zero, and the equation will represent a nonflaming fire.

For a fixed airflow rate, as is generally the case in enclosure fires where the extinguishing agent working in

the gas phase is used, increase in the mass loss rate due to external heat flux results in an increase in the equivalence ratio, defined in Equation 36. As the equivalence ratio increases and approaches values of 4.0 and higher, the combustion efficiency approaches values less than or equal to 0.40, flames are extinguished, and nonflaming conditions become important.^{44,45} Thus, the upper limit for the application of the extinguishing agent working in the gas phase is dictated by the equivalence ratio ≥ 4.0 and/or the combustion efficiency ≤ 0.40 . Under nonflaming conditions, increase in the external heat flux increases the generation rate of the fuel vapors and the reduction-zone products.

Flame Extinction by Reduced Mass Fraction of Oxygen

Flame extinction by reduced mass fraction of oxygen can be the result of (1) dilution and heat capacity effects due to the addition of inert gases, such as N₂ and CO₂; and (2) chemical effects due to the retardation of chemical reactions and reduction in the flame heat flux to the surface, especially the radiative component.

Theoretical and experimental analyses have been performed for flame extinction by reduced oxygen mass fractions. For example, for polymethylmethacrylate (PMMA), an oxygen mass fraction value of 0.180 is predicted for flame extinction¹²⁵ compared to the experimental values of 0.181 for a 70-mm-wide, 190-mm-high, and 19-mm-thick vertical PMMA slab¹²⁶ and 0.178 for a 100-mm-wide, 25-mm-thick, and 300- and 610-mm-high vertical slabs of PMMA, and 25-mm-diameter and 610-mm-high vertical cylinder of PMMA.² The critical values of the chemical, convective, and radiative heat release for PMMA are 106, 73, and 33 kW/m², respectively,² showing a trend similar to one reported in Table 3-4.29. At oxygen mass fractions equal to or less than 0.201, flames are unstable and faint blue in color.²

The effect of increased external heat flux on flame extinction due to reduced oxygen mass fraction has been examined for the buoyant turbulent diffusion flames. For example, for rectangular and circular horizontal PMMA slabs, 0.06 to 0.10 m² in area and 0.03 to 0.05 m in thickness, exposed to external heat flux values of 0, 40, 60, and 65 kW/m², flame extinction is found at oxygen mass fractions of 0.178, 0.145, 0.134, and 0.128, respectively.³⁵ The data support Equation 140 and show that, for buoyant turbulent diffusion flames, flaming can occur up to relatively low oxygen mass fraction values. The only condition is that, in the gas phase, the reactant-oxidizer mixture is within the flammability limit.

The effect of reduced oxygen mass fraction on flame extinction of materials in the three-dimensional arrangement, where flame heat flux is enhanced, has been examined. Figure 3-4.59 shows an example where chemical heat release rates at oxygen mass fractions of 0.233, 0.190, and 0.167 versus time are shown for the combustion of 50-mm cubes of empty corrugated paper boxes in a 2 × 2 × 2 arrangement. The weight of each box is about 13 g (839 g/m²). The measurements are from the ASTM E2058 fire propagation apparatus.

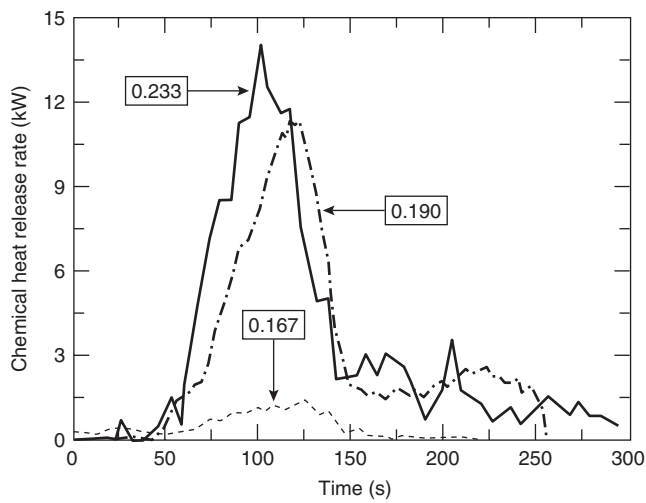


Figure 3-4.58. *Chemical heat release rate versus time for 50-mm empty corrugated paper boxes in a 2 × 2 × 2 arrangement (two boxes along the length × two boxes along the width × two layers, for a total of eight boxes separated by about 12 mm). Measurements were made in the ASTM E2058 fire propagation apparatus with no external heat flux under the co-flow condition at various oxygen mass fractions, which are indicated in the figure.*

In Figure 3-4.58, at oxygen mass fraction of 0.167, the flame is close to the extinction condition, only 10.5 percent of the initial weight of the boxes is consumed, which is equivalent to consumption of a single box with a surface area of about 0.0155 m^2 . The peak chemical heat release rate close to flame extinction, in Figure 3-4.59, is about 1.5 kW or 97 kW/m^2 , using a surface area of 0.0155 m^2 . This value is in excellent agreement with the average value in Table 3-4.29, derived from the critical mass loss rates for ignition. The data in Figure 3-4.59 for the three-dimensional arrangement of the corrugated boxes thus support the fire point theory,^{114,116} independence of the critical heat release rate for flame extinction from the geometrical arrangement and surface areas of the materials, and Equations 139 and 140 as originally formulated in Reference 113.

Nomenclature

A	total exposed surface area of the material (m^2)
a_j	mass coefficient for the product yield (g/g)
b_j	molar coefficient for the product yield (g/mol)
B_{cr}	critical mass transfer number ($Y_O \Delta H_O^*/\Delta H_{g,\text{con}}$)
CHF	critical heat flux (kW/m^2)
\dot{C}_O''	mass consumption rate of oxygen ($\text{g/m}^2\text{s}$)
$\dot{C}_{\text{stoich},O}''$	stoichiometric mass consumption rate of oxygen ($\text{g/m}^2\text{s}$)
c_O	mass of oxygen consumed per unit mass of fuel (g/g)
c_P	specific heat ($\text{kJ/g}\cdot\text{K}$)
Δc_P	difference between the heat capacities of the extinguishing agent and the fire products ($\text{kJ/g}\cdot\text{K}$)
CDG	carbon dioxide generation calorimetry
D	optical density $\{[\ln(I_0/I)]/\ell\}$ (1/m)
D_{corr}	metal corrosion (penetration depth or metal loss in microns, angstroms, mils)
E_i	total amount of heat generated in the combustion of a material (kJ)
f_j	volume fraction of a product
f_p	fire property
FPI	Fire Propagation Index 1000 $(0.42\dot{Q}_{\text{ch}}'')^{1/3}/\text{TRP}$
FSP_c	convective flame spread parameter
\dot{G}_j''	mass generation rate of product j ($\text{g/m}^2\text{s}$)
$\dot{G}_{\text{stoich},j}''$	stoichiometric mass generation rate of product j ($\text{g/m}^2\text{s}$)
GTR	gas temperature rise calorimetry
ΔH_i	heat of combustion per unit mass of fuel vaporized (kJ/g)
ΔH_{CO}	heat of complete combustion of CO (10 kJ/g)
ΔH_D	heat of dissociation (kJ/g)
ΔH_g	heat of gasification at ambient temperature (kJ/g)
$\Delta H_{g,\text{con}}$	flame convective energy transfer to the fuel per unit mass of fuel gasified (kJ/g)
ΔH_m	heat of melting at the melting temperature (kJ/g)
ΔH_T	net heat of complete combustion per unit of fuel vaporized (kJ/g)
ΔH_v	heat of vaporization at the vaporization temperature (kJ/g)
ΔH_w	heat of gasification of water (2.58 kJ/g)
ΔH_{CO}^*	net heat of complete combustion per unit mass of CO generated (kJ/g)
$\Delta H_{\text{CO}_2}^*$	net heat of complete combustion per unit mass of CO_2 generated (kJ/g)
ΔH_O^*	net heat of complete combustion per unit mass of oxygen consumed (kJ/g)
HRP	heat release parameter ($\Delta H_i/\Delta H_g$)
h_i	mass coefficient for the heat of combustion (kJ/g)
I/I_0	fraction of light transmitted through smoke
j	fire product
k	thermal conductivity ($\text{kW/m}\cdot\text{K}$)
L_{sp}	smoke point (m)
ℓ	optical path length (m)
\dot{m}''	mass loss rate ($\text{g/m}^2\text{s}$)
\dot{m}_w''	water application rate per unit surface area of the material ($\text{g/m}^2\text{s}$)
M	molecular weight (g/mol)
m_i	molar coefficient for the heat of combustion (kJ/mol)
MOD	mass optical density ($D\dot{V}/A\dot{m}''$) (m^2/g)
\dot{m}_{air}	mass flow rate of air (g/s)
OC	oxygen consumption calorimetry
\dot{q}_e''	external heat flux (kW/m^2)
\dot{q}_f''	flame heat flux (kW/m^2)

\dot{Q}_i''	heat release rate per unit sample surface area ($\dot{m}''\Delta H_{ch}$) (kW/m ²)	v_j	stoichiometric coefficient of product j
\dot{Q}_i'	heat release rate per unit sample width (kW/m)	v_O	stoichiometric coefficient of oxygen
\dot{R}_{corr}	corrosion rate (Å/min)	Ψ_j	stoichiometric yield for the maximum conversion of fuel to product j
S	stoichiometric mass air-to-fuel ratio (g/g)	Ψ_O	stoichiometric mass oxygen-to-fuel ratio (g/g)
t	time (s)	ζ	ratio of fire properties for ventilation-controlled to well-ventilated combustion
t_f	time at which there is no more vapor formation (s)	ζ_{oxid}	oxidation zone product generation efficiency ratio
t_0	time at which the sample is exposed to heat (s)	ζ_{red}	reduction zone product generation efficiency ratio
T	temperature (K)		
ΔT_{ig}	ignition temperature above ambient (K)		
TRP	thermal response parameter [$\Delta T_{ig}(kpc_p)^{1/2}$] (kW·s ^{1/2} /m ²)		
u	fire propagation rate (dX_p/dt) (mm/s or m/s)	<i>a</i>	air or ambient
v_g	co-flow air velocity (m/s)	<i>ad</i>	adiabatic
\dot{V}	total volumetric flow rate of fire product-air mixture (m ³ /s)	<i>asy</i>	asymptotic
\dot{W}	total mass flow rate of the fire product-air mixture (g/s)	<i>ch</i>	chemical
W_f	total mass of the material lost in the flaming and nonflaming fire (g)	<i>con</i>	convective
W_j	total mass of product j generated in the flaming and nonflaming fire (g)	<i>corr</i>	corrosion
X_f	flame height (m or mm)	<i>cr</i>	critical
X_p	pyrolysis front (m or mm)	<i>e</i>	external
X_t	total length available for fire propagation (m or mm)	<i>ex</i>	extinguishment
y_j	yield of product j (\dot{G}_j''/\dot{m}'')	<i>f</i>	flame or fuel
$Y_{j,ex}$	mass fraction of the extinguishing agent	<i>fc</i>	flame convective
Y_O	mass fraction of oxygen	<i>fr</i>	flame radiative
		<i>g</i>	gas
		<i>g, con</i>	flame convective energy for fuel gasification
		<i>i</i>	chemical, convective, radiative
		<i>ig</i>	ignition
		<i>j</i>	fire product
		<i>n</i>	net
		<i>0</i>	initial
		<i>oxid</i>	oxidation zone of a flame
		<i>rad</i>	radiation
		<i>red</i>	reduction zone of a flame
		<i>stoich</i>	stoichiometric for the maximum possible conversion of fuel monomer to a product
		<i>rr</i>	surface re-radiation
		<i>s</i>	surface
		<i>vc</i>	ventilation-controlled fire
		<i>w</i>	water
		<i>wv</i>	well-ventilated fire
		∞	infinite amount of air

Greek

α	correlation coefficient (nonflaming fire)
β	correlation coefficient (transition region)
δ_w	energy associated with the blockage of flame heat flux to the surface and escape of fuel vapors per unit mass of the fuel gasified (kJ/g)
ε_w	water application efficiency
ϕ	kinetic parameter for flame extinction
ξ	correlation coefficient (transition region)
Φ	equivalence ratio ($\dot{S}\dot{m}''/\dot{m}_{air}$)
χ_{ch}	combustion efficiency $\dot{Q}_{ch}''/\dot{m}''\Delta H_T$)
χ_{con}	convective component of the combustion efficiency $\dot{Q}_{con}''/\dot{m}''\Delta H_T$)
χ_{rad}	radiative component of the combustion efficiency $\dot{Q}_{rad}''/\dot{m}''\Delta H_T$)
η_j	generation efficiency ($\dot{G}_j''/\dot{m}''\Psi_j$)
κ	ratio between the kinetic parameters for the flame temperature and adiabatic flame temperature
λ	wavelength of light (μm)
σ	Stefan-Boltzmann constant (56.7×10^{-12} kW/m ² ·K ⁴)
τ	average specific extinction area (m ² /g)
μ	corrosion parameter (Å·min·ml)
ρ	density (g/m ³)

v_j	stoichiometric coefficient of product j
v_O	stoichiometric coefficient of oxygen
Ψ_j	stoichiometric yield for the maximum conversion of fuel to product j
Ψ_O	stoichiometric mass oxygen-to-fuel ratio (g/g)
ζ	ratio of fire properties for ventilation-controlled to well-ventilated combustion
ζ_{oxid}	oxidation zone product generation efficiency ratio
ζ_{red}	reduction zone product generation efficiency ratio

Subscripts

<i>a</i>	air or ambient
<i>ad</i>	adiabatic
<i>asy</i>	asymptotic
<i>ch</i>	chemical
<i>con</i>	convective
<i>corr</i>	corrosion
<i>cr</i>	critical
<i>e</i>	external
<i>ex</i>	extinguishment
<i>f</i>	flame or fuel
<i>fc</i>	flame convective
<i>fr</i>	flame radiative
<i>g</i>	gas
<i>g, con</i>	flame convective energy for fuel gasification
<i>i</i>	chemical, convective, radiative
<i>ig</i>	ignition
<i>j</i>	fire product
<i>n</i>	net
<i>0</i>	initial
<i>oxid</i>	oxidation zone of a flame
<i>rad</i>	radiation
<i>red</i>	reduction zone of a flame
<i>stoich</i>	stoichiometric for the maximum possible conversion of fuel monomer to a product
<i>rr</i>	surface re-radiation
<i>s</i>	surface
<i>vc</i>	ventilation-controlled fire
<i>w</i>	water
<i>wv</i>	well-ventilated fire
∞	infinite amount of air

Superscripts

\cdot	per unit time (s ⁻¹)
$'$	per unit width (m ⁻¹)
$''$	per unit area (m ⁻²)

Definitions

Chemical heat of combustion	calorific energy generated in chemical reactions leading to varying degrees of incomplete combustion per unit fuel mass consumed
-----------------------------	--

Convective heat of combustion	calorific energy carried away from the flame by the fire products-air mixture per unit fuel mass consumed
Heat of gasification	energy absorbed to vaporize a unit mass of fuel originally at ambient temperature
Heat release parameter	calorific energy generated per unit amount of calorific energy by the fuel
Kinetic parameter for flame extinction	maximum fraction of combustion energy that the flame reactions may lose to the sample surface by convection without flame extinction
Net heat of complete combustion	calorific energy generated in chemical reactions leading to complete combustion, with water as a gas, per unit fuel mass consumed
Radiative heat of combustion	calorific energy emitted as thermal radiation from the flame per unit fuel mass consumed

Abbreviations

ABS	acrylonitrile-butadiene-styrene
CPVC	chlorinated polyvinylchloride
CR	neoprene or chloroprene rubber
CSP (or CSM)	chlorosulfonated polyethylene rubber (Hypalon)
CTFE	chlorotrifluoroethylene (Kel-F)
E-CTFE	ethylene-chlorotrifluoroethylene (Halar)
EPR	ethylene propylene rubber
ETFE	ethylenetetrafluoroethylene (Tefzel)
EVA	ethylvinyl acetate
FEP	fluorinated polyethylene-polypropylene (Teflon)
IPST	isophthalic polyester
PAH	polyaromatic hydrocarbons
PAN	polyacrylonitrile
PC	polycarbonate
PE	Polyethylene
PEEK	Polyether ether ketone
PES	Polyethersulphone
PEST	Polyester
PET	Polyethyleneterephthalate (Melinex, Mylar)
PFA	perfluoroalkoxy (Teflon)
PMMA	polymethylmethacrylate
PO	Polyolefin
POM	Polyoxymethylene
PP	Polypropylene
PS	Polystyrene
PTFE	Polytetrafluoroethylene (Teflon)
PU	Polyurethane
PVCl ₂	Polyvinylidene chloride (Saran)
PVDF	Polyvinylidene fluoride (Kynar)
PVEST	Polyvinylester
PVF	Polyvinyl fluoride (Tedlar)
PVF ₂	Polyvinylidene fluoride (Kynar, Dyflor)
PVC	Polyvinylchloride
SBR	styrene-butadiene rubber
TFE	tetrafluoroethylene (Teflon)
XLPE	crosslinked polyethylene

References Cited

- ASTM E2058, *Standard Methods of Test for Measurement of Synthetic Polymer Material Flammability Using a Fire Propagation Apparatus (FPA)*, American Society for Testing and Materials, Philadelphia (in press).
- A. Tewarson and S.D. Ogden, "Fire Behavior of Polymethylmethacrylate," *Combustion and Flame*, 89, pp. 237-259 (1992).
- A. Tewarson and M.M. Khan, "Flame Propagation for Polymers in Cylindrical Configuration and Vertical Orientation," in *Twenty-Second Symposium (International) on Combustion*, Combustion Institute, Pittsburgh, PA, pp. 1231-1240 (1988).
- A. Tewarson, "Flammability Parameters of Materials: Ignition, Combustion, and Fire Propagation," *J. Fire Science*, 10, pp. 188-241 (1994).
- E.E. Smith, "Measuring Rate of Heat, Smoke, and Toxic Gas Release," *Fire Technology*, 8, pp. 237-245 (1972).
- E.E. Smith, "Heat Release Rate of Building Materials," *Ignition, Heat Release, and Non-combustibility of Materials*, ASTM STP 502, American Society for Testing and Materials, Philadelphia, pp. 119-134 (1972).
- ASTM E906-83, "Standard Test Method for Heat and Visible Smoke Release Rates for Materials and Products," The American Society for Testing and Materials, Philadelphia (1984).
- C.P. Sarkos, R.A. Filipczak, and A. Abramowitz, "Preliminary Evaluation of an Improved Flammability Test Method for Aircraft Materials," *Technical Report DOT/FAA/CT-84/22*, Federal Aviation Administration, Atlantic City, NJ.
- A. Tewarson, "Flame Spread in Standard Tests for Electrical Cables," *Technical Report J.I.OMO2E1.RC-2*, Factory Mutual Research, Norwood, MA (1993).
- A. Tewarson and D. Macaione, "Polymers and Composites—An Examination of Fire Spread and Generation of Heat and Fire Products," *J. Fire Sciences*, 11, pp. 421-441 (1993).
- A. Tewarson and M.M. Khan, "A New Standard Test Method for the Quantification of Fire Propagation Behavior of Electrical Cables Using Factory Mutual Research Corporation's Small-Scale Flammability Apparatus," *Fire Technology*, 28, pp. 215-227 (1992).
- M.M. Khan, "Classification of Conveyor Belts Using Fire Propagation Index," *Technical Report J.I.OT1E2.RC*, Factory Mutual Research, Norwood, MA (1991).
- A. Tewarson and M.M. Khan, "Electrical Cables—Evaluation of Fire Propagation Behavior and Development of Small-Scale Test Protocol," *Technical Report J.I.OM2E1.RC*, Factory Mutual Research, Norwood, MA (1989).
- Specification Standard for Cable Fire Propagation, Class No. 3972*, Factory Mutual Research, Norwood, MA (1989).
- A. Tewarson, "A Study of Fire Propagation and Generation of Fire Products for Selected Cables Used by the United States Navy," *Technical Report J.I.OP3N3.RC/OP1N3.RC*, Factory Mutual Research, Norwood, MA (1988).
- A. Tewarson, "Experimental Evaluation of Flammability Parameters of Polymeric Materials," *Flame Retardant Polymeric Materials* (M. Lewin, S.M. Atlas, and E.M. Pearce, eds.), pp. 97-153, Plenum Press, New York (1982).
- V. Babrauskas, "Development of the Cone Calorimeter—A Bench-Scale Heat Release Rate Apparatus Based on Oxygen Consumption," *Technical Report NBSIR 82-2611*, National Institute of Standards and Technology, Gaithersburg, MD (1982).
- Heat Release and Fires* (V. Babrauskas and S.J. Grayson, eds.), Elsevier Publishing Company, London (1992).
- ASTM E1354-90, *Standard Test Method for Heat and Visible Smoke Release Rates for Materials and Products Using Oxygen*

- Consumption Calorimeter*, American Society for Testing and Materials, Philadelphia, PA (1990).
20. M.J. Scudamore, P.J. Briggs, and F.H. Prager, "Cone Calorimetry—A Review of Tests Carried Out on Plastics for the Association of Plastics Manufacturers in Europe," *Fire and Materials*, 15, pp. 65–84 (1991).
 21. A. Tewarson, I.A. Abu-Isa, D.R. Cummings, and D.E. LaDue, "Characterization of the Ignition Behavior of Polymers Commonly Used in the Automotive Industry," *Fire Safety Science—Proceedings of the Sixth International Symposium*, University of Poitiers, France (in press).
 22. A.C. Fernandez-Pello and T. Hirano, "Controlling Mechanisms of Flame Spread," *Combustion Science and Technology*, 32, pp. 1–31 (1983).
 23. V. Apte, R. Bilget, and A. Tewarson, "Replacing a Regulatory Large-Scale Flammability Test for Conveyor Belts with a Small-Scale Test," *Interflam 2001*, 9th International Conference, Edinburgh, UK (2001).
 24. P.V. Zant, *Microchip Fabrication: A Practical Guide to Semiconductor Processing*, McGraw-Hill Inc., New York, 2nd ed. (1990).
 25. *Test Standard, Factory Mutual Research Corporation, FMRC Clean Room Materials Flammability Test Protocol, Class Number FMRC 4910*, Factory Mutual Research, Norwood, MA (1997).
 26. A. Tewarson, M.M. Khan, P.K. Wu, and R.G. Bill, "Flammability of Clean Room Polymeric Materials for the Semiconductor Industry," *Fire and Materials*, 25, pp. 31–42 (2001).
 27. A. Tewarson, R.G. Bill, R.L. Alpert, A. Braga, V. DeGiorgio, and G. Smith, "Flammability of Clean Room Materials," *J.I. OYOE6.RC*, Factory Mutual Research, Norwood, MA (1999).
 28. A. Tewarson and D. Macaione, "Polymers and Composites—An Examination of Fire Spread and Generation of Heat and Fire Products," *J. Fire Sciences*, 11, pp. 421–441 (1993).
 29. A. Tewarson, "Fire Hardening Assessment (FHA) Technology for Composite Systems," *Technical Report ARL-CR-178*, Army Research Laboratory, Aberdeen Proving Ground, MD (1994).
 30. R.E. Lyon, "Solid-State Thermochemistry of Flaming Combustion," *Final Report DOT/FAA/AR-99/56*, Federal Aviation Administration, Atlantic City, NJ (1999).
 31. J.S. Newman and A. Tewarson, "Flame Spread Behavior of Char-Forming Wall/Ceiling Insulations," *Fire Safety Science—Proceedings of the Third International Symposium*, Elsevier Applied Science, New York, pp. 679–688 (1991).
 32. J.S. Newman, "Integrated Approach to Flammability Evaluation of Polyurethane Wall/Ceiling Materials," *Polyurethanes World Congress Oct. 10–13*, Society of the Plastics Industry, Washington, DC (1993).
 33. J.S. Newman, "Cost-Effective Method for Flammability Characterization of Alternate Polyols and Blowing Agents," in *Proceedings of the SPI 32nd Annual Technical/Marketing Conference*, Society of the Plastics Industry, Washington, DC (1989).
 34. *Approval Standard for Class I A) Insulated Wall or Wall and Roof/Ceiling Panels, B) Plastic Interior Finish Materials, C) Plastic Exterior Building Panels, D) Wall/Ceiling Coating Systems, E) Interior or Exterior Finish Systems, Class No. 4880*, Factory Mutual Research, Norwood, MA (1993).
 35. A. Tewarson and R.F. Pion, "Flammability of Plastics. I. Burning Intensity," *Combustion and Flame*, 26, pp. 85–103 (1976).
 36. *CRC Handbook of Chemistry and Physics*, 61st ed. (R.C. Weast and M.J. Astle, eds.), CRC Press, Inc., Boca Raton, FL (1980).
 37. M.A. Paul, *Physical Chemistry*, D.C. Heath and Company, Boston, MA, p. 46 (1962).
 38. D.Q. Kern, *Process Heat Transfer*, McGraw-Hill Book Company, New York, p. 72 (1950).
 39. M.M. Hirschler, "Fire Hazard and Toxic Potency of the Smoke from Burning Materials," *J. Fire Sciences*, 5, pp. 289–307 (1987).
 40. H.C. Hottel, "Review: Certain Laws Governing the Diffusive Burning of Liquids by Blinov and Khudiakov (1957) Dokl Akad Nauk SSSR, Vol. 113, 1094, 1957," *Fire Research Abstract and Reviews*, 1, pp. 41–45 (1959).
 41. A. Tewarson, J.L. Lee, and R.F. Pion, "The Influence of Oxygen Concentration on Fuel Parameters for Fire Modeling," *Eighteenth Symposium (International) on Combustion*, Combustion Institute, Pittsburgh, PA, pp. 563–570 (1981).
 42. J.C. Macrae, *An Introduction to the Study of Fuel*, Elsevier Publishing Company, London (1966).
 43. C. Hugget, "Estimation of Rate of Heat Release by Means of Oxygen Consumption Measurements," *Fire & Materials*, 4, pp. 61–65 (1980).
 44. A. Tewarson, F.H. Jiang, and T. Morikawa, "Ventilation-Controlled Combustion of Polymers," *Combustion and Flame*, 95, pp. 151–169 (1993).
 45. A. Tewarson and M.M. Khan, "Extinguishment of Diffusion Flames of Polymeric Materials by Halon 1301," *J. Fire Sciences*, 11, pp. 407–420 (1993).
 46. C. Costa, G. Treand, F. Moineault, and J.L. Gustin, "Assessment of the Thermal and Toxic Effects if Chemical and Pesticide Pool Fires Based on Experimental Data Obtained Using the Tewarson Apparatus," *Transactions IChemE*, Institution of Chemical Engineers, 77, B, pp. 154–164 (1999).
 47. A. Tewarson, "Flammability Properties of Engine Compartment Fluids, Part 1: Combustion Properties of Fluids Containing Carbon, Hydrogen and Oxygen," *Technical Report OBIR7.RC*, Factory Mutual Research, Norwood, MA (1998).
 48. A. Tewarson, "Prediction of Fire Properties of Materials Part 1: Aliphatic and Aromatic Hydrocarbons and Related Polymers," *Technical Report NBS-GCR-86-521*, National Institute of Standards and Technology, Gaithersburg, MD (1986).
 49. A. Tewarson, "Smoke Point Height and Fire Properties of Materials," *Technical Report NBS-GCR-88-555*, National Institute of Standards and Technology, Gaithersburg, MD (1988).
 50. *Handbook of Plastics and Elastomers* (C.A. Harper, ed.), McGraw-Hill Book Company, New York (1975).
 51. Y. Tsuchiya and J.F. Mathieu, "Measuring Degrees of Combustibility Using an OSU Apparatus and Oxygen Depletion Principle," *Fire Safety Journal*, 17, pp. 291–299 (1991).
 52. A. Tewarson, "Heat Release Rates from Samples of Polymethylmethacrylate and Polystyrene Burning in Normal Air," *Fire & Materials*, 1, pp. 90–96 (1976).
 53. A. Tewarson and F. Tamanini, "Research and Development for a Laboratory-Scale Flammability Test Method for Cellular Plastics," *Technical Report No. 22524, RC76-T-64*, National Institute of Standards and Technology, Gaithersburg, MD (1976).
 54. A. Tewarson, "Heat Release Rate in Fires," *J. Fire & Materials*, 8, pp. 115–121 (1977).
 55. A. Tewarson, "Physico-Chemical and Combustion/Pyrolysis Properties of Polymeric Materials," *Technical Report NBS-GCR-80-295*, National Institute of Standards and Technology, Gaithersburg, MD (1980).
 56. A.R. Apte, R.W. Bilger, A.R. Green, and J.G. Quintiere, "Wind-Aided Turbulent Flame Spread and Burning over Large-Scale Horizontal PMMA Surfaces," *Combustion and Flame*, 85, pp. 169–184 (1991).
 57. F.J. Perzak and C.P. Lazzara, "Flame Spread over Horizontal Surfaces of Polymethylmethacrylate," in *Twenty-Fourth Symposium (International) on Combustion*, Combustion Institute, Pittsburgh, PA, pp. 1661–1667 (1992).
 58. L. Tsantarides and B. Ostman, "Smoke, Gas, and Heat Release Data for Building Products in the Cone Calorimeter,"

- Technical Report I 8903013, Swedish Institute for Wood Technology Research, Stockholm, Sweden (1989).*
59. M.M. Khan, "Characterization of Liquid Fuel Spray Fires," *Heat and Mass Transfer in Fire and Combustion Systems*, 223, American Society of Mechanical Engineers, New York (1992).
 60. A. Tewarson and R.G. Zalosh, "Flammability Testing of Aircraft Cabin Materials," in *73rd Symposium AGARD Conference Proceedings*, No. 467, *Aircraft Fire Safety*, National Technical Information Service, Springfield, VA, pp. 33-1 to 33-12 (1989).
 61. Y.R. Sivathanu and G.M. Faeth, "Generalized State Relationships for Scalar Properties in Nonpremixed Hydrocarbon/Air Flames," *Combustion and Flame*, 82, pp. 211-230 (1990).
 62. J.S. Newman and J. Steciak, "Characterization of Particulates from Diffusion Flames," *Combustion and Flame*, 67, pp. 55-64 (1987).
 63. D. Drysdale, *An Introduction to Fire Dynamics*, Wiley, New York, pp. 278-400 (1985).
 64. C.L. Beyler, "Major Species Production by Diffusion Flames in a Two-Layer Compartment Fire Environment," *Fire Safety J.*, 10, pp. 47-56 (1986).
 65. C.L. Beyler, in *Fire Safety Science—Proceedings of the Third International Symposium*, Elsevier Applied Science, New York, pp. 431-440 (1986).
 66. E.E. Zukowski, in *Fire Safety Science—Proceedings of the Third International Symposium*, Elsevier Applied Science, New York, pp. 1-30 (1986).
 67. T. Morikawa, "Effects of Supply Rate and Concentration of Oxygen and Fuel Location on CO Evolution in Combustion," *J. Fire Science*, 1, pp. 364-378 (1983).
 68. A. Tewarson, F. Chu, and F.H. Jiang, "Combustion of Halogenated Polymers," in *Fire Safety Science Fourth International Symposium*, Elsevier Applied Science, New York, pp. 563-574 (1994).
 69. ASTM D 1322-80, *Standard Test Method for Smoke Points of Aviation Turbine Fuels*, American Society for Testing and Materials, Philadelphia (1980).
 70. J. deRis and X. Cheng, "The Role of Smoke-Point in Material Flammability Testing," in *Fire Safety Science—Proceedings of the Fourth International Symposium*, Elsevier Applied Science, New York, pp. 301-312 (1994).
 71. I. Glassman, "Soot Formation in Combustion Processes," in *Twenty-Second Symposium (International) on Combustion*, Combustion Institute, Pittsburgh, pp. 295-311 (1986).
 72. G.H. Markstein, "Correlations for Smoke Points and Radiant Emission of Laminar Hydrocarbon Diffusion Flames," in *Twenty-Second Symposium (International) on Combustion*, Combustion Institute, Pittsburgh, pp. 363-370 (1986).
 73. L. Orloff, J. deRis, and M.A. Delichatsios, "Radiation from Buoyant Turbulent Diffusion Flames," *Combustion and Flame*, 69, pp. 177-186 (1992).
 74. J.H. Kent, "Turbulent Diffusion Flame Sooting—Relationship to Smoke-Point Tests," *Combustion and Flame*, 67, pp. 223-233 (1987).
 75. J.H. Kent, "A Quantitative Relationship Between Soot Yield and Smoke Point Measurements," *Combustion and Flame*, 63, pp. 349-358 (1986).
 76. J.H. Kent and Gg. Wagner, "Why Do Diffusion Flames Emit Soot," *Combustion Science and Technology*, 41, pp. 245-269 (1984).
 77. O.L. Gulder, "Influence of Hydrocarbon Fuel Structure Constitution and Flame Temperature on Soot Formation in Laminar Diffusion Flames," *Combustion and Flame*, 78, pp. 179-194 (1989).
 78. O.L. Gulder, "Soot Formation in Laminar Diffusion Flames at Elevated Temperatures," *Combustion and Flame*, 88, pp. 74-82 (1992).
 79. B.S. Haynes and H.Gg. Wagner, "Soot Formation," *Progress in Energy and Combustion Sciences*, 7, pp. 229-273 (1981).
 80. U.O. Koyle and G.M. Faeth, "Structure of Overfire Soot in Buoyant Turbulent Diffusion Flames at Long Residence Times," *Combustion and Flame*, 89, pp. 140-156 (1992).
 81. U.O. Koyle, Y.R. Sivathanu, and G.M. Faeth, "Carbon Monoxide and Soot Emissions from Buoyant Turbulent Diffusion Flames," in *Fire Safety Science—Proceedings of the Third International Symposium*, Hemisphere Publishing Co., New York, pp. 625-634 (1991).
 82. U.O. Koyle and G.M. Faeth, "Carbon Monoxide and Soot Emissions from Liquid-Fueled Buoyant Turbulent Diffusion Flames," *Combustion and Flame*, 87, pp. 61-76 (1991).
 83. Y.R. Sivathanu and G.M. Faeth, "Soot Volume Fractions in the Overfire Region of Turbulent Diffusion Flames," *Combustion and Flame*, 81, pp. 133-149 (1990).
 84. D.B. Olson, J.C. Pickens, and Gill, "The Effects of Molecular Structure on Soot Formation, II. Diffusion Flames," *Combust. and Flame*, 62, pp. 43-60 (1985).
 85. S.L. Madorsky, *Thermal Degradation of Organic Polymers*, Interscience Publishers, John Wiley & Sons, Inc., New York, p. 192 (1964).
 86. "Network Reliability: A Report to the Nation, Compendium of Technical Papers," Federal Communications Commission's Network Reliability Council, National Engineering Consortium, Chicago (1993).
 87. B.T. Reagor, "Smoke Corrosivity: Generation, Impact, Detection, and Protection," *J. Fire Sciences*, 10, pp. 169-179 (1992).
 88. B.T. Reagor and C.A. Russell, "A Survey of Problems in Telecommunications Equipment Resulting from Chemical Contamination," *IEEE Transactions*, CHMT-9, 2, p. 209 (1986).
 89. B.T. Reagor and C.A. Russell, "A Survey of Manufacturing Problems in Telecommunications Equipment," *Proceedings of the International Conference on Electrical Contacts, Electromechanical Components, and Their Applications*, Nagoya, Japan (1986).
 90. F.W. Lipfert, "Effects of Acidic Deposition on the Atmospheric Deterioration of Materials," in *Material Performance*, pp. 12-19 (1987).
 91. F.L. Chu, "Development and Application of Nonthermal Damage Assessment Techniques," *Technical Report J.I. OV1J1.RC*, Factory Mutual Research, Norwood, MA (1992).
 92. A. Tewarson, "The Effects of Fire-Exposed Electrical Wiring Systems on Escape Potential from Buildings, Part I: A Literature Review of Pyrolysis/Combustion Products and Toxicities—Poly(Vinyl Chloride)," *Technical Report No. 22491, RC75-T-47*, Factory Mutual Research, Norwood, MA (1975).
 93. K.G. Martin and D.A. Powell, "Toxic Gas and Smoke Assessment Studies on Vinyl Floor Coverings with the Fire Propagation Tests," *Fire and Materials*, 3, pp. 132-139 (1979).
 94. A. Tewarson, "Non-Thermal Damage," *J. Fire Sciences*, 10, pp. 188-241 (1992).
 95. A. Tewarson and M.M. Khan, "Generation of Smoke from Electrical Cables," *Proceedings of the ASTM Symposium on Characterization and Toxicity of Smoke* (H.K. Hasegawa, ed.), ASTM STP 1082, American Society for Testing and Materials, Philadelphia, pp. 100-117 (1988).
 96. A. Tewarson, M.M. Khan, and J.S. Steciak, "Combustibility of Electrical Wire and Cable for Rail Rapid Transit Systems, Vol. 1. Flammability," *Technical Report DOT-TSC-UMTA-83*

- 4.1, National Technical Information Service, Springfield, VA (1982).
97. S.L. Kessel, C.E. Rogers, and J.G. Bennett, "Corrosive Test Methods for Polymeric Materials, Part 5—A Comparison of Four Test Methods," *J. Fire Sciences*, 12, pp. 196–233 (1994).
 98. P.A. Dickinson, "Evolving Fire Retardant Materials Issues: A Cable Manufacturer's Perspective," *Fire Technology*, 4, pp. 345–368 (1992).
 99. A.F. Grand, "Evaluation of the Corrosivity of Smoke Using a Laboratory Radiant Combustion Exposure Apparatus," *J. Fire Sciences*, 10, pp. 72–93 (1992).
 100. P. Rio, "Présentation de l'essai Corrosivite mis au point au CNET-Lab-SER/ENV," *Centre National d'Etudes des Télécommunications* (1983).
 101. M.F. Bottin, "The ISO Static Test Method for Measuring Smoke Corrosivity," *J. Fire Science*, 10, pp. 160–168 (1992).
 102. "Testing of Cables, Wires, and Flexible Cords, Corrosivity of Combustion Gases," DIN 57472, Part 813 Standard, Verband Deutscher Elektrotechniker (VDE) Specification 0472 (1983).
 103. E. Barth, B. Muller, F.H. Prager, and F. Wittbecker, "Corrosive Effects of Smoke: Decomposition with the DIN Tube According to DIN 53436," *J. Fire Sciences*, 10, pp. 432–454 (1992).
 104. E.D. Goldberg, *Black Carbon in the Environment: Properties and Distribution*, John Wiley & Sons, New York (1985).
 105. *Particulate Carbon Formation During Combustion* (D.C. Siegla and G.W. Smith, eds.), Plenum Press, New York (1981).
 106. S.P. Nolan, "A Review of Research at Sandia National Laboratories Associated with the Problem of Smoke Corrosivity," *Fire Safety Journal*, 15, pp. 403–413 (1989).
 107. J.S. Newman, "Smoke Characterization in Enclosure Environments," in *Proceedings of the ASTM Symposium on Characterization and Toxicity of Smoke* (H.K. Hasegawa, ed.), ASTM STP 1082, American Society for Testing and Materials, Philadelphia, pp. 123–134 (1988).
 108. H. Burtscher, A. Reiss, and A. Schmidt-Ott, "Particle Charge in Combustion Aerosols," *J. Aerosol Science*, 17, p. 47 (1986).
 109. J.J. Beitel, C.A. Bertelo, W.F. Carroll, R.O. Gardner, A.F. Grand, M.M. Hirschler, and G.F. Smith, "HCl Transport and Decay in a Large Apparatus, II. Variables Affecting Hydrogen Chloride Decay," *J. Fire Sciences*, 5, pp. 105–145 (1987).
 110. J.P. Stone, R.N. Hazlett, J.E. Johnson, and H.W. Carhart, "The Transmission of HCl by Soot from Burning PVC," *J. Fire and Flammability*, 4, pp. 42–57 (1973).
 111. A. Tewarson, and M.M. Khan, "The Role of Active and Passive Fire Protection Techniques in Fire Control, Suppression, and Extinguishment," in *Fire Safety Science—Proceedings of the Third International Symposium*, Hemisphere Publishing Co., New York, pp. 1007–1017 (1991).
 112. "Small-Scale Testing: The Role of Passive Fire Protection in Commodity Classification," *FMRC Update*, 4, 3, Factory Mutual Research, Norwood, MA (1990).
 113. C. Beyler, "A Unified Model of Fire Suppression," *Journal of Fire Protection Engineering*, 4, pp. 5–16 (1992).
 114. D.J. Rashbash, "The Extinction of Fire with Plain Water: A Review," in *Fire Safety Science—Proceedings of the First International Symposium*, Hemisphere Publishing Co., New York, pp. 1145–1163 (1986).
 115. G. Hesketh, "The Role of Water in Suppression of Fire: A Review," *J. Fire and Flammability*, 11, pp. 254–262 (1980).
 116. D.J. Rashbash, "A Flame Extinction Criterion for Fire Spread," *Combustion and Flame*, 26, pp. 411–412 (1976).
 117. R.S. Magee and R.D. Reitz, "Extinguishment of Radiation-Augmented Plastics Fires by Water Sprays," in *Fifteenth Symposium (International) on Combustion*, Combustion Institute, Pittsburgh, pp. 337–347 (1975).
 118. D.J. Rashbash, "The Extinction of Fires by Water Sprays," *Fire Research Abstracts and Reviews*, 4, pp. 28–52 (1962).
 119. H.E. Thomson, and D.D. Drysdale, "Critical Mass Flow Rate at the Firepoint of Plastics," in *Fire Safety Science—Proceedings of the Second International Symposium*, Hemisphere Publishing Co., New York, pp. 67–76 (1989).
 120. "Advances in Commodity Classification, A Progress Report," *FMRC Update*, 4, 1, Factory Mutual Research, Norwood, MA (1990).
 121. C. Yao, "The Development of the ESFR Sprinkler System," *Fire Safety Journal*, 14, pp. 65–73 (1988).
 122. H.C. Kung, H. You, W.R. Brown, and B.G. Vincent, "Four-Tier Array Rack Storage Fire Tests with Fast-Response Prototype Sprinklers," in *Fire Safety Science—Proceedings of the Second International Symposium*, Hemisphere Publishing Co., New York, pp. 633–642 (1989).
 123. J.L. Lee, "Extinguishment of Rack Storage Fires of Corrugated Cartons Using Water," in *Fire Safety Science—Proceedings of the First International Symposium*, Hemisphere Publishing Co., New York, pp. 1177–1186 (1986).
 124. M.M. Khan and A. Tewarson, "Passive Fire Protection for Materials and Storage Commodities," in *Flame Retardancy, Educational Symposium No. 28, Rubber Division, American Chemical Society, Fall 1992*, Paper J, The University of Akron, Akron, OH, pp. 1–30 (1992).
 125. H. Kodama, K. Miyasaka, and A.C. Fernandez-Pello, "Extinguition and Stabilization of a Diffusion Flame on a Flat Combustible Surface with Emphasis on Thermal Controlling Mechanisms," *Combustion Science and Technology*, 54, pp. 37–50 (1987).
 126. A.K. Kulkarni and M. Sibulkin, "Burning Rate Measurements on Vertical Fuel Surfaces," *Combustion and Flame*, 44, pp. 185–186 (1982).

SECTION THREE

CHAPTER 5

Compartment Fire Modeling

James G. Quintiere

Introduction

An approach for predicting various aspects of fire phenomena in compartments has been called *zone modeling*. It is based on a conceptual representation for the compartment fire process, and is an approximation to reality. Any radical departure by the fire system from the basic concept of the zone model can seriously affect the accuracy and validity of the approach. The zone model simply represents the system as two distinct compartment gas zones: an upper volume and a lower volume resulting from thermal stratification due to buoyancy. Conservation equations are applied to each zone and serve to embrace the various transport and combustion processes that apply. The fire is represented as a source of energy and mass, and manifests itself as a plume, which acts as a pump for the mass from the lower zone to the upper zone through a process called *entrainment*.

The zone modeling approach emerged in the mid-1970s when the effort to study the developing fire in a compartment intensified. Careful measurements and observations revealed characteristics of the compartment fire system. The upper and lower layers (zones) were deemed relatively uniform in temperature and composition. Distinct phenomena were discerned that could be studied in isolation, enabling better predictions of their roles in the compartment fire system.

Fowkes,¹ in his work with Emmons on the Home Fire Project, was the first to publish a basis for the zone model approach in his description of the "Bedroom Fire" series conducted at Factory Mutual Research Corporation. Almost simultaneously, computer models based on the zone model approach were produced by Quintiere,² Pape and Waterman,³ and Mitler⁴ working with Emmons. Since then the development of such computer models has been prolific. They have extended the early efforts from a single

room to computer codes that can address a number of interconnected rooms, using a number of new fire phenomena and computer features. These advances in fire science, together with the development of the personal computer, have given the engineer a convenient tool for investigating the hazard of fire in buildings. A notable illustration of this tool is the software "Hazard I," developed by the National Institute of Standards and Technology (NIST).⁵ At this time, numerous computer codes and software packages exist based on the zone model approach. In a recent survey, Friedman⁶ cited 21 zone models in use around the world.

This chapter outlines the basic conservation equations for the gas zones, and describes the various transport and combustion processes that make up the system. These processes are referred to as the submodels of the system. As such, they can contribute subroutines to computer codes, which implement the mathematical solution. Discussion of submodels will be limited, but the reader will be referred to appropriate references. In most cases, other chapters of *The SFPE Handbook of Fire Protection Engineering* will be cited. No discussion of a computer code or its numerical solution algorithm will be addressed, since these are issues more of style and mathematics. The presentation will elucidate the mathematical basis of the zone model, its assumptions, its features, and its scope of application. Each user of this approach must sufficiently understand its basis to assess its accuracy and validity. When used correctly, zone models predict the average macroscopic features of compartment fires. There are many examples of comparisons to data that illustrate their level of accuracy, and these will not be repeated here. The user must be skilled in assessing the quality of the data and submodels that directly influence the variables of the problem of interest. It is hoped that the discussion that follows will make the user more knowledgeable or sensitive in making these quality assessments.

Conservation Equations

The building block of the zone model is the conservation equations for the upper and lower gas zones. These

Dr. J. G. Quintiere is the John L. Bryan Professor of Fire Protection Engineering at the University of Maryland. His research has focused on fire growth and flame spread.

equations are developed either (1) by using fundamental equations of energy, mass, and momentum transport in control volume form as applied to the zones, or (2) by using differential equations that represent the conservation laws and integrating them over the zones. However, the momentum equation will not be explicitly applied, since information needed to compute velocities and pressures is based on assumptions and specific applications of momentum principles at vent boundaries of the compartment. An extensive review of control volume equations for mass, species, and energy conservation in a combustion system has been presented by Quintiere⁷ and serves as reference for the equations that follow.

Figure 3-5.1 illustrates a typical zone model for a compartment fire process. It shows a fire plume and a door vent. The hot combustion gases that collect in the upper space of the room and spill out of the vent constitute the upper-layer zone. A control volume, CV_1 , is defined to enclose the gas in this upper layer and the fire plume. The lower interface of the upper layer moves with the control volume such that no mass is transferred across this thermally stratified region. The velocity of the control volume along this interface, \bar{w} , is equal to the fluid velocity, \bar{v} . The temperature of the upper layer is greater than that in the lower layer (zone) which includes all the remaining gas in the room, and is delineated by a second control volume, CV_2 . It has been assumed in zone modeling that the volume of the fire plume is small relative to the gas layer or zone volumes, and therefore its effect has been ignored. In general, multiple fire plumes can occur at any height in the room, and multiple vents or mass transport can take place between the zones (CV_1 and CV_2) and the surroundings. In each case mass transport must be appropriately described in terms of the system variables; however, this may not always be easy or known. The properties of the upper and lower zones are assumed to be spatially uniform, but can vary with time. Thus, temperature, T , and species mass concentration, Y_i , are

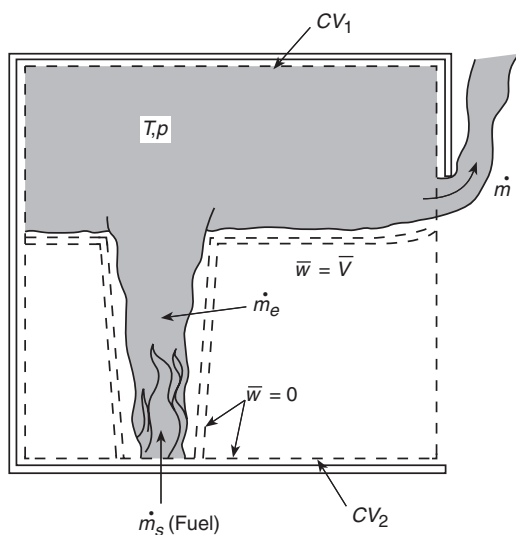


Figure 3-5.1. Control volumes selected in zone modeling.

properties associated with ideal upper and lower homogeneous gas layers. Other assumptions in the application of the conservation laws to the zones are listed below:

1. The gas is treated as an ideal gas with a constant molecular weight and constant specific heats: c_p and c_v .
2. Exchange of mass at free boundaries is due to pressure differences or shear mixing effects. Generally these are caused by natural or forced convection, or by entrainment processes.
3. Combustion is treated as a source of mass and energy. No mechanism from first principles is included to resolve the extent of the combustion zone.
4. The plume instantly arrives at the ceiling. No attempt is made to account for the time required to transport mass vertically or horizontally in the compartment. Hence, transport times are not explicitly accounted for in zone modeling.
5. The mass or heat capacity of room contents is ignored compared to the enclosure wall, ceiling, and floor elements; that is, heat is considered lost to the structure, but not to the contents. Where room contents shield boundary structural surfaces, some compensations can occur in the analysis, but for cluttered rooms this assumption may be poor.
6. The horizontal cross section of the enclosure is a constant area, A . In most cases of zone modeling, rectilinear compartments have been considered. However, this is not a necessary assumption, and enclosures in which A varies with height can easily be handled.
7. The pressure in the enclosure is considered uniform in the energy equation, but hydrostatic variations account for pressure differences at free boundaries of the enclosure; that is, $p \geq pgH$. In general, the enclosure pressure, p , is much greater than the variations due to hydrostatics. For example, for $p = 1 \text{ atm} = 14.7 \text{ psi} = 10^2 \text{ kPa (kN/m}^2\text{)} = 10^5 \text{ Pa}$, the hydrostatic variation for a height, $H = 1 \text{ m}$, gives a pressure difference of $pgH = 1.2 \text{ kg/m}^3 \times 9.8 \text{ m/s}^2 \times 1 \text{ m} = 10 \text{ kg/m}\cdot\text{s}^2 = 10 \text{ Pa (N/m}^2\text{)}$.
8. Mass flow into the fire plume is due to turbulent entrainment. Entrainment is the process by which the surrounding gas flows into the fire plume as a result of buoyancy. Empirically, the inflow velocity linearly depends on the vertical velocity in the plume.
9. Fluid frictional effects at solid boundaries are ignored in the current models.

Conservation of Mass

The conservation of mass for a control volume states that the rate of change of mass in the volume plus the sum of the net mass flow rates out is zero for J flow streams

$$A \frac{d}{dt} (\rho z_l) + \sum_{j=1}^J \dot{m}_j = 0 \quad (1)$$

(net out)

where

ρ = density of the gas in the control volume (or zone)

z_l = the height of the zone

For the illustration in Figure 3-5.1, applying Equation 1 to the upper layer (CV_1) would give

$$\sum_{j=1}^3 \dot{m}_j = \dot{m} - \dot{m}_e - \dot{m}_s \quad (2)$$

where

\dot{m} = mass flow rate out of the door

\dot{m}_e = mass rate of entrainment into the fire plume

\dot{m}_s = mass rate of gaseous fuel supplied

Mass flows at the boundaries can occur due to many phenomena. Therefore, the user or designer of a zone model must include the appropriate mass flow phenomena. For example, in addition to the mass rates in Equation 2, mass flows can occur due to forced convection from wind or ventilation effects, from shear entrainment as flows affect layer interfaces, or from cold plumes that could plunge through hot layers.

Conservation of Species

The mass conservation of species i is given by Y_i . By using Equation 1 and applying the conservation of mass for species i to a control volume, it follows that

$$\rho z_l A \frac{dY_i}{dt} + \sum_{j=1}^J \dot{m}_j (Y_{ij} - Y_i) = \dot{\omega}_i \quad (3)$$

where

Y_{ij} = mass concentration of species i leaving the control volume through the j flow stream

$\dot{\omega}_i$ = mass production rate of species due to combustion

The production term, $\dot{\omega}_i$, in principle, can be described through a knowledge of the chemical equation of the reaction or its particular stoichiometry. Thus, stoichiometric coefficients can be used to represent the production of species and the consumption of oxygen in terms of the mass rate of fuel *reacted*. Stoichiometry is not easily determined, and the fuel gases as they emerge from the pyrolysis of solids can take many chemical forms that differ from the solid fuel's original molecular composition. A partial way to overcome these complications has been to represent the mass production of species for fire in terms of the rate of mass *loss* for the pyrolyzing fuel. Hence, one must be careful to distinguish between the mass of fuel lost and that reacted, and to relate available species yield data to the particular fire conditions of the application. Yield is defined as the mass ratio of species to fuel lost. The yields or production rates may change with fire conditions, and therefore, in general, will not be consistent with data from small-scale tests. For example, the production rate of CO changes markedly with air-to-fuel ratio.

Conservation of Energy

The conservation of energy for the control volume is applied along with Equation 1 and the equation of state, $p = \rho RT$, to give

$$\begin{aligned} \rho c_p z_l A \frac{dT}{dt} - z_l A \frac{dp}{dt} + cp \sum_{j=1}^J \dot{m}_j (T_j - T) \\ = \dot{\omega}_F \Delta H - \dot{Q}_{\text{net loss}} \end{aligned} \quad (4)$$

where

T = temperature of the gases within the control volume

T_j = temperature of the gases in the j flow stream crossing the control volume boundary

$\dot{Q}_{\text{net loss}}$ = net rate of heat transfer lost at the boundary

ΔH = the heat of combustion (taken as a positive quantity)

$\dot{\omega}_F$ = the rate at which the fuel supplied is *reacted*

Usually in zone models it is assumed that all of the fuel supplied can react, provided there is sufficient oxygen available. One assumption on the sufficiency of oxygen is to consider that all the fuel supplied is reacted as long as the oxygen concentration in that control volume is greater or equal to zero, that is,

$$\dot{\omega}_F = \dot{m}_s \quad \text{if} \quad Y_o \geq 0 \quad (5)$$

Thereafter, an excess rate of fuel can exist that can be transported into adjoining zones or control volumes where a decision must be made about whether it can continue to react. At this condition, all of the net oxygen supplied to the control volume is reacted, so that, as long as $Y_o = 0$

$$\dot{\omega}_F = r \times (\text{net mass rate of oxygen supplied}) \quad (6)$$

where r is the stoichiometric fuel-to-oxygen mass ratio. This condition when $Y_o = 0$ in compartment fires is termed the ventilation-limited condition. At this moment, significant changes take place in the nature of the chemical reaction. Notably, incomplete combustion is more likely, and for hydrocarbon fuels this leads to a significant increase in the yield of carbon monoxide and soot. Thus, care must be used in interpreting the results of zone models once ventilation-limited conditions arise, particularly with respect to the prediction of species concentrations and the extent of burning. Material data used for well-ventilated conditions will no longer apply. The issue of what constitutes a flammable mixture in a compartment gas layer and combustion in a vitiated layer has not yet been resolved satisfactorily. Thus, combustion under ventilation-limited conditions has not been adequately addressed for a zone model, and needs more study.

The first term on the left side of Equation 4 arises due to the change of internal energy with the control volume. If the temperature is not changing rapidly with time, this term can be small and its elimination gives rise to a quasi-steady approximation for growing fires that allows a more simple analysis. The second term arises from the rate of work done by pressure as the gas layer expands or contracts due to the motion of the thermal stratification interface. Having been rearranged, this term now is expressed as rate of pressure, p , increase for the compartment and is essentially caused by net heat or mass additions to the compartment gases. Except for the rapid accumulation of

mass or energy, for compartments with small openings to the surroundings, this pressure rise is small, and the pressure nominally remains at nearly the ambient pressure. For example, an addition of 100 kW to a 40 m³ gas volume in a room with a 0.1 m² vent area gives rise to roughly an increase of 10 Pa in less than 10⁻² s over normal ambient pressure of 10⁵ Pa.⁷ Any increase in pressure within the compartment could give rise to a flow of mass through a vent, and this term in Equation 4 may be associated with a *volumetric expansion* effect, as referred to by some. Conversely, a reduction in energy release rate will cause the pressure to drop relative to the ambient. This phenomenon, when cycling between heating and cooling, explains the *breathing effect* for fires in closed buildings.

The third term of Equation 4 accounts for the enthalpy flow rates and only applies to j flow streams that enter the control volume, since $T_j = T$ for all flow streams leaving, as long as the uniform temperature assumption still applies.

Summary

The zone model for the compartment fire system consists of two zones: the upper and lower gas layers. The solution process for the layer properties can be visualized by considering the conservation Equations 1, 3, and 4 applied to each zone. The species equation can yield the Y_i for each layer. The mass and energy equations comprise four equations that permit the determination of the two layer temperatures, one layer height (since the height of the other layer is directly found by difference from the total height of the compartment), and the compartment pressure (which is assumed uniform by Equation 7). The densities are found from the ideal gas equation of state in which approximately ρT is a constant. To complete this solution process, each source or transport term in the equations must be given in terms of the above layer properties, or auxiliary relationships must be included for each new variable introduced. The source terms are associated with the $\dot{\omega}_i$ terms, and the transport terms include the j mass flow rates and the boundary heat transfer rates. The extent to which source and transport relationships are included reflects the sophistication and scope of the zone model. Some source and transport terms are essential to a basic zone model, others can be specified as approximations to reality, and others can be ignored when physically irrelevant. These source and transport relationships can be termed *submodels* and can comprise subroutines of a zone model computer code. The nature of these submodels is discussed below.

Source Term Submodels

The principal source term is the rate of fuel supplied. In an experimental fire this can be known if the fire source is simulated by a gas burner. In the other extreme, the mass of fuel supply can be a result of a spreading fire over an array of different solid fuels. In general,

$$\dot{m}_s = f(\text{fuel properties, heat transfer}) \quad (7)$$

in which the heat transfer to the fuel results from the flame configuration and the heated compartment. The fuel properties are still not completely defined or conventionally accepted for fire applications, since no general theory exists for pyrolysis, and theories of flame spread and ignition are couched in terms of effective fire properties, which are modeling parameters. Nevertheless, data exist for fuel fire properties and can enable approximate models for \dot{m}_s of reasonable accuracy. For example, Tewarson describes how the mass supply and energy release can be determined from fuel properties, and tabulates properties for a number of solid fuels. (See Section 3, Chapter 4.) For realistic items under well-ventilated conditions, Babrauskas has compiled results that could serve as initial estimates for \dot{m}_s in compartment fires. (See Section 3, Chapter 1.)

The rate of energy release, $\dot{\omega}_F \Delta H$, required by Equation 4 has already been discussed through Equations 5 and 6. The point should be made that the heat of combustion, ΔH , employed must be with respect to the mass of fuel gases pyrolyzed, given by such data as Tewarson's, and is not the theoretical oxygen bomb value for the solid fuel. (See Section 3, Chapter 4.) Due to incomplete combustion, ΔH will be less than the theoretical value, in general.

The production of species can be described in terms of species yield, γ_i , such that

$$\dot{\omega}_i = \gamma_i \dot{m}_s \quad (8)$$

For well-ventilated fires, γ_i may be reasonably constant for a given fuel, as tabulated by Tewarson. (See Section 3, Chapter 4.) In general, it can vary with time and can significantly vary as ventilation-limited conditions are approached and achieved. For example, Tewarson shows that γ_i for CO can vary with equivalence ratio, Φ , where

$$\Phi = \frac{\text{mass of fuel available / mass of oxygen available}}{r} \quad (9)$$

where r is the stoichiometric value for complete combustion. Zukoski et al.⁸ have shown how this relationship may be applied to compartment fires. The equivalence ratio, Φ , may be computed in a zone (or upper layer) where combustion has occurred by computing the mass concentrations of the "available" fuel and oxygen in the zone. This is done by Equation 3 in which $\dot{\omega}_i$ is set equal to zero for both the fuel and oxygen, since this yields the available Y_F and Y_o values, not their actual concentrations in the layer following combustion. The generality of considering $\gamma_i = \gamma_i(\Phi)$ for zone models is still under study, and its use must be considered as exploratory. Nevertheless, it currently offers the only practical approach for estimating species, such as CO, under ventilation-limited conditions in compartment fires.

Mass and Heat Transport Submodels

Entrainment

An essential feature of a zone model is the mass rate of entrainment, \dot{m}_e , relationship for the fire plume. This relationship allows the principal mechanism for flow

between the lower and upper stratified gas layers. Considerable work has been performed to develop entrainment relationships for pool fires or axisymmetric gas burner fires. Unfortunately both the ideal theoretical plume models and correlations based on data vary widely, and no consensus exists among zone models in practice for the optimum pool fire entrainment model. Rockett⁹ illustrates the variations in results he found using different fire entrainment models in the Harvard/NIST Mark VI compartment fire zone model. He found that the layer height, entrainment rate, and layer gas temperature varied by roughly a factor of two among the various models. More useful data rather than ideal mathematical models are clearly needed to resolve this issue of accuracy for a simple pool fire. Yet even a perfect entrainment relationship for an axisymmetric pool fire would not necessarily be perfect in a zone model, because a plume in a compartment can be subject to nonsymmetric airflows that can bend the plume and thus affect its entrainment rate. Usually wind effects will increase the entrainment rate.

Rockett⁹ has shown that the effect of the entrainment model is crucial to predictions for the developing fire. This research suggests that the entrainment model must be representative of the actual object burning. However, no entrainment models exist for a wall, corner, or item of furniture; this dramatizes the lack of much-needed research in this area. Yet, this does not mean that the zone model has a fatal flaw; it simply means much more systematic data are necessary to expand the versatility of the zone model and its accuracy. Moreover, if a zone model with its selected entrainment relationship tracks well with data from an experimental fire scenario, it can be assumed accurate for simulating the process and can be used with some assurance for that scenario. A catalogue of empirical entrainment relationships for various object fires developed from specialized entrainment apparatus would help resolve the entrainment issue. This apparatus could be developed from the large calorimeter intended to measure energy release rate in which the fire plume is collected in a hood-duct system and the total flow rate is recorded.

Vent Flows through Openings in Vertical Partitions

Classic models of fire in a room or building represent the structure with an opening, such as a door or window, to the ambient surroundings. Fire-induced flows through such openings have been well studied, and a widely accepted model exists to compute these flows based on the temperature distribution of the gases on either side of the opening. The theoretical basis of the computation is orifice flow utilizing Bernoulli's equation along a streamline, as illustrated in Figure 3-5.2. The velocity at station two is given by

$$v_2 = \sqrt{\frac{2(\rho_1 - \rho_2)}{\rho_1}} \quad (10)$$

where v_1 is assumed to be zero. The mass flow rate is computed by integration over the flow area, A , adjusted by a flow coefficient, C :

$$\dot{m} = C \int \rho_1 v_2 dA \quad (11)$$

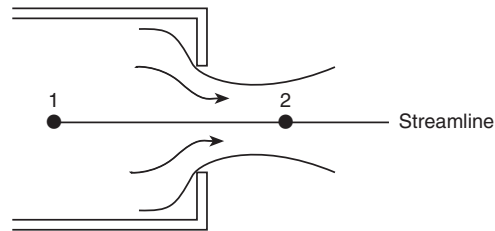


Figure 3-5.2. *Orifice flow.*

Emmons suggests that a value of 0.68 for C has an accuracy of ± 10 percent, except at very low flow rates at the beginning of a fire. (See Section 2, Chapter 3.) In general, C will depend on the Reynolds number. Figure 3-5.3 depicts examples of typical vent flows through an opening in a vertical partition. In both cases Equations 10 and 11 apply, but the pressure distribution must be described appropriately. For example, in the pure natural convection case shown in Figure 3-5.3 (a), the pressure is determined by the static pressure with respect to the floor pressure, $p(0)$. Actually it is the floor pressure that applies in Equation 4 and in the perfect gas equation of state.

The assumption is that the flow velocities are small compared to the vent flow velocities, justifying the static pressure computation. Thus, the vertical pressure distribution on either side of the opening is computed as

$$p(z) = p(0) - \int_0^z \rho g dz \quad (12)$$

McCaffrey and Rockett¹⁰ illustrate the accuracy of the hydrostatic assumption in Figure 3-5.4. The sign of the pressure difference across the opening determines the flow direction. Emmons presents the general equations that enable this computation to be included in a zone model. (See Section 2, Chapter 3.) It is by far the most accurate of the submodels, and provides the basis for linking rooms together in a zone model, which allows smoke and fire growth computations for a large building.

The flow through an opening in a horizontal partition can be compared to that for the vertical partition, provided the pressure difference is large enough. If there is only a single vent from the fire compartment through a horizontal partition, such as a ceiling, the flow must be oscillatory or bi-directional. The latter case implies a zero pressure

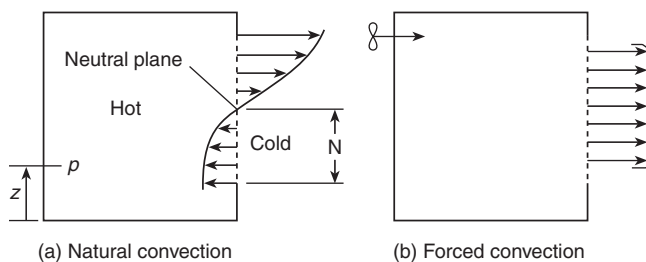


Figure 3-5.3. *Typical vent flows.*

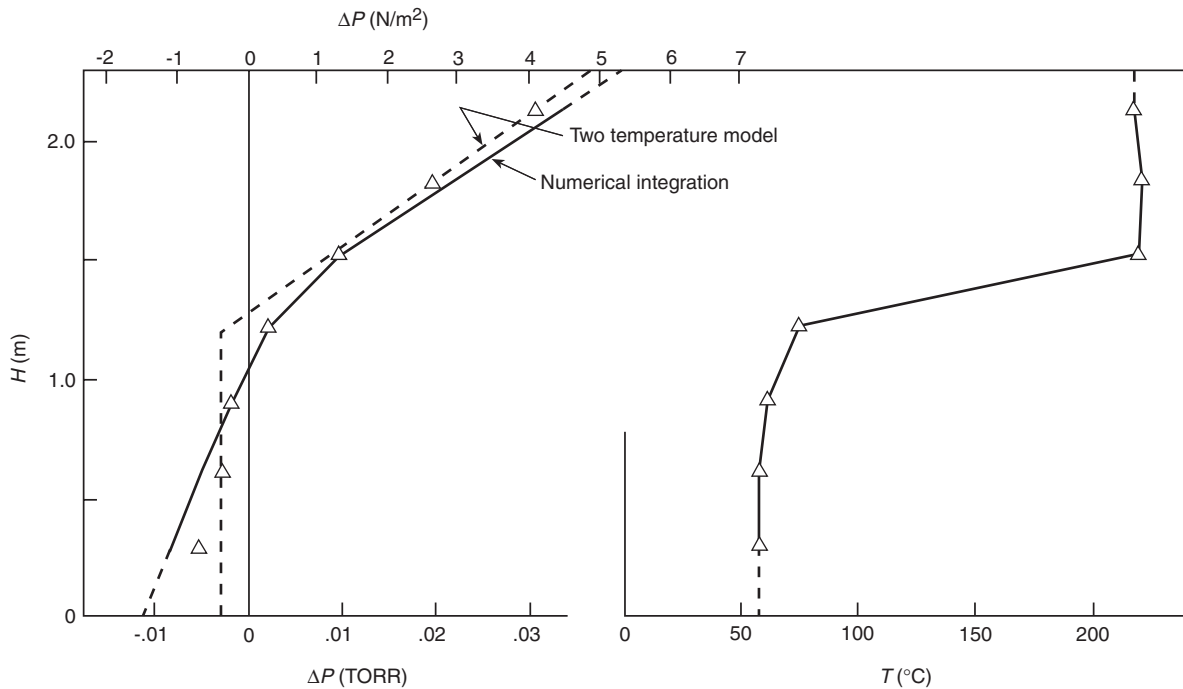


Figure 3-5.4. Vertical pressure difference across a room vertical partition compared to a computation based on room fire temperature distribution and a two-temperature zone model approximation using the hydrostatic pressure assumption.¹⁰

difference, with gravity solely determining the flow. A theory for this case has been developed by Epstein¹¹ and has been implemented by Cooper.¹² For orifice-like vents with zero pressure difference, the volumetric exchange flow rate, \dot{V} , given by Epstein,¹¹ is approximately

$$\dot{V} = 0.055 \left[D^5 g (\rho_1 - \rho_2) \left(\frac{\rho_1 + \rho_2}{2} \right) \right]^{1/2} \quad (13)$$

where D is the diameter of the vent and ρ_1 and ρ_2 are the corresponding fluid densities on either side of the vent. For vents of significant depth, L , the coefficient in Equation 13 depends on L/D .

Convective Heat Transfer to Surfaces

The $\dot{Q}_{\text{net loss}}$ term in Equation 4 is composed of the convective and radiative heat loss to the boundary surfaces of the layer control volumes. This involves both heat transfer from the gas layers at their bulk temperatures and the heat transfer from the flame. Consistent treatment of the flame and layer gas heat transfer must be carried out for the zone model. If the flame becomes large and fills the upper layer, one cannot count the flame and gas heat transfer without being redundant.

Convective heat transfer to a ceiling by a fire plume has been widely studied at modest scales, such that flame radiation may have been insignificant. Alpert¹³ specifically examined only convective heating in contrast to studies by You and Faeth¹⁴ and Kokkala¹⁵ who included flame effects.

In general, convective effects will vary along the ceiling, walls, and floor, and depend on the nature and position of the fire. In some cases an *adiabatic wall temperature* has been appropriately introduced since the driving force for convective heat transfer locally is not the bulk gas layer temperature, but the local boundary layer temperature, which is not explicitly computed. Convective heat transfer data for the walls and floor of a fire compartment or for rooms beyond the fire compartment have not been developed. Hence, most zone models use estimates from natural convection correlations.

Radiative Heat Transfer

The theory of radiative heat transfer is adequate to develop the needed components for the zone model. However, the theory is not sufficiently developed to predict flame radiation from first principles without very sophisticated modeling of the soot and temperature distributions. Hence, flame radiation is relegated to empirical practices. Radiation from a smoke layer is easier to deal with within the context of a uniform property gas layer for the zone model. One difficulty still is the availability of property data to determine the contribution of smoke particulates to the layer radiation properties. The discussion presented by Tien et al. can be used to begin a development of the radiative equations needed by the zone model. (See Section 1, Chapter 4.) Also, the presentation by Mudan and Croce gives empirical approaches to dealing with flame radiation. (See Section 3, Chapter 11.) The report by Forney¹⁶ lays out the theory and equations

describing radiation exchange between the gas layers and boundary surfaces.

Conduction Heat Transfer

The radiative and convective heat transfer from the gas must be balanced by conduction heat transfer through the boundary surfaces. This balancing requires a numerical solution to a partial differential equation in conjunction with the ordinary differential equations in time describing the conservation of energy and mass for the gas layers. Usually zone models have considered only one-dimensional conduction, which should be adequate for most applications. Most multiple-compartment models do not consider communication by conduction into the next compartment, treating the structural elements as thermally thick instead. In principle, there is no difficulty with developing an accurate algorithm for conduction through the boundary elements for any conditions. For more information, the reader is referred to the discussion by Rockett and Milke. (See Section 1, Chapter 2.)

Mixing between the Layers

The primary exchange of fluid between the lower and upper gas layers is due to the buoyant effect of the fire plume. Secondary, but significant, mixing processes can occur due to the other effects. These are shown in Figure 3-5.5 and include three phenomena:

1. Exchange due to a cold flow injected into the hot layer
2. Exchange due to shear mixing associated with vent flows
3. Exchange due to wall flows

Phenomenon 1 is the inverse of the hot fire plume penetrating the upper layer. In both cases the fluid at the edge of the plume may not be buoyant enough to penetrate the respective layer. A comparable situation is a cold forced jet introduced vertically into the lower layer. Depending on the relative temperatures, it may not escape the lower layer and, therefore, may not penetrate into the upper layer. These are issues that can be resolved to some extent by research available in the literature on buoyant plumes and jets.

Phenomenon 2 has not been sufficiently studied. Data suggest that the flow rate of the mixed stream can be significant relative to the vent flow rate, especially for small vents.¹⁷ A correlation for the mixing rate has been developed from saltwater simulation experiments.¹⁸

Phenomenon 3 has been discussed by Jaluria.¹⁹ He presents relationships that allow the estimation of the rate of transfer of cold fluid adjacent to the wall in the hot upper gas layer into the cold lower gas layer or vice versa.

All of these flows tend to blur the sharp distinction between the upper and lower gas layers, reducing their degree of stratification. Obviously, if sufficient mixing occurs, the layer may appear to become well-mixed or destratified. Destratification should occur naturally in the context of the zone model, and one should not have to switch to a well-mixed compartment model under these conditions.

Relationships for all of these secondary flows have not been developed with confidence nor with full accep-

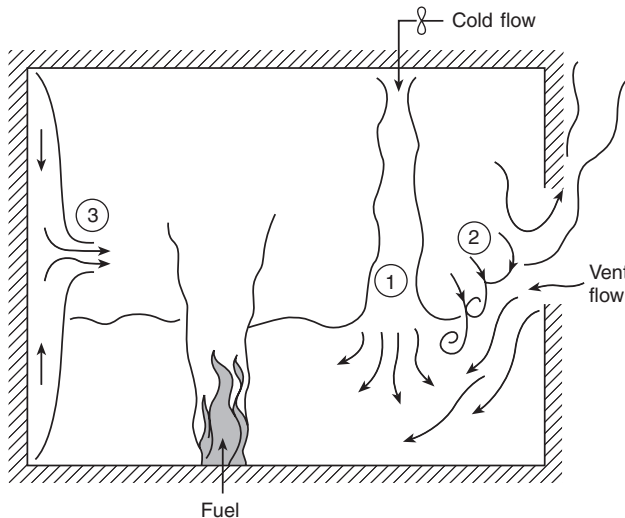


Figure 3-5.5. Secondary flows—mixing phenomena. 1. A cold plume descending from the upper layer into the lower layer; 2. Shear mixing of an entering vent flow stream; 3. Wall flows due to local buoyancy effects.

tance. Although they are important for improving the accuracy of a zone fire model, little work has gone forward to establish their validity.

Forced Flow Effects

The effect of forced airflow on the fire conditions and smoke spread due to mechanical or natural wind forces has always been an issue in large building fires. Wind effects and the resultant pressure distribution around a tall building has become a standard element of design data for structural design, but this has not been utilized for fire safety design. The movement of smoke through a building due to the mechanical ventilation system has been simulated by network models that treat the compartment volume as uniform in properties, and include the pressure losses due to vents and duct friction. A two-layer zone model has not been linked to the mechanical ventilation system in a building. To create a link, one must include the full-pressure-flow characteristics of fans in both directions to allow for the possibility of the backflow of smoke against the direction of airflow in the ducts. An attempt at this linkage has been presented by Klotz and Cooper,²⁰ who hypothesize a fan characteristic relationship. Ultimately an experimental study will be needed to lay a foundation for this analysis.

Fire Growth Rate

In most all zone models, the fire source is considered an input quantity, based on some experimental or empirical data. This limits the simulation capability of a zone model, since fire growth and spread is not modeled. Also the effects of compartment feedback due to thermal and vitiation (oxygen depletion) effects are not taken into account. The versatility and utility of a zone model can only

be improved by developing techniques for accommodating the fire growth of realistic building contents and architectural elements. This process will have an impact on the use and development of flammability tests for hazard analysis and product acceptability.

Embedded Submodels

The detailed physics that one can include in a zone model are only limited by current research and imagination. The zone model can be versatile in accommodating new phenomena, even if they appear inconsistent with the uniform property layer assumption. By analogy to the relationship between inviscid flow and boundary layer flow in the analysis of aerodynamic bodies, the layer properties can be regarded as first-order approximation for higher order analysis. Flame and boundary layer phenomena within the compartment can be computed by regarding the layer properties as infinite reservoirs. These phenomena can be computed after the primary layer properties are computed. Examples of embedded phenomena are shown in Figure 3-5.6. Although the combustion region is assumed to be of negligible volume at the zone model for mutation, the flame height can be computed along with the velocity and temperature distributions in an axisymmetric fire plume.²¹ Other embedded phenomenon are: (1) the ceiling jet, (2) the computation of temperature distributions over the ceiling, (3) the deposition of soot and other products of combustion on surfaces, and (4) the heating and degradation of structural elements.

Unresolved Phenomena

Some significant phenomena are not addressed by the zone-modeling approach for fire, such as vent flames, transient flow in corridors, and shaft flows. (See Figure 3-5.7.) These phenomena require more research and new strategies to enable them to be included into a zone

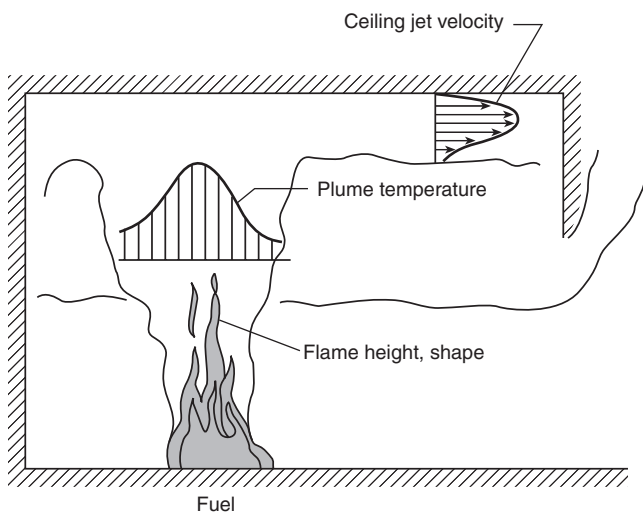


Figure 3-5.6. Examples of embedded phenomena.

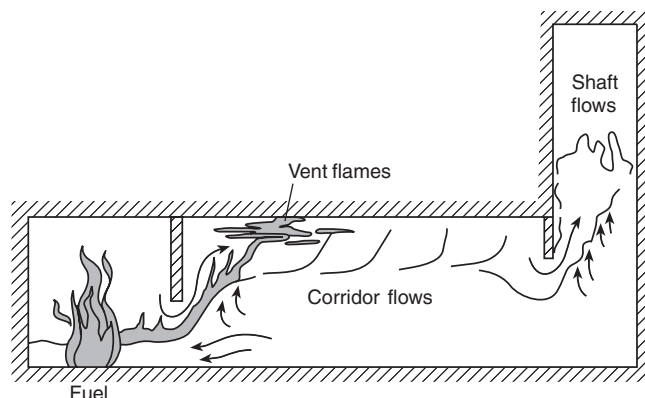


Figure 3-5.7. Examples of significant phenomena absent from zone models.

model. Vent flames are significant for fire growth into the next compartment and usually follow flashover. Information about their rate of heat transfer and extent needs to be computed. Transient corridor flows are important in the analysis of smoke transport through long corridors. The current zone model methodology yields an instantaneous layer, which would descend, but the actual process produces a transient ceiling jet. Flows in vertical shafts involve the interaction of plumes with walls, pressure-driven effects, and turbulent mixing.

Selected Reading and Comments

Zone models provide the integrating framework for the phenomena of fire and its fire protection engineering components. Many zone models have been constructed for fire predictions in compartments. They involve the basic conservation equations, submodels describing the particular phenomena included, and the mathematical algorithm for solution. Some have developed user-friendly interfaces. Most provide documentation on the model and its use. The interested reader is referred to some published models for more detailed information.²²⁻²⁴ Many zone-model computer models exist, similar both in substance and the ability to analyze fire effects in buildings. They can stimulate needed research. However, more effort appears to have gone into the computer code developments rather than the experimental research needed for improvement in the model.

Nomenclature

<i>A</i>	area compartment floor
<i>C</i>	flow coefficient
<i>c_p</i>	specific heat at constant pressure
<i>c_v</i>	specific heat at constant volume
<i>g</i>	acceleration due to gravity
<i>H</i>	compartment height
<i>J</i>	number of flow streams in control volume
<i>m</i>	mass

p	pressure
Q	heat transfer
r	stoichiometric fuel-to-oxygen mass ratio
R	ideal gas constant
t	time
T	temperature
v	fluid velocity
V	volume
w	control volume velocity
Y	mass fraction
z_l	height of control volume or zone
ΔH	heat of combustion
γ_i	yield of species i
ρ	density
Φ	equivalence ratio
$\dot{\omega}_F$	consumption rate of fuel
$\dot{\omega}_i$	production rate of species

Subscripts

e	entrained
F	fuel
i	species
j	flow stream
s	supplied

Superscripts

(\cdot) per unit time

References Cited

1. N.D. Fowkes, "A Mechanistic Model of the 1973 and 1974 Bedroom Test Fires," in *A Study of Room Fire Development: The Second Full-Scale Bedroom Fire Test of the Home Fire Project* (P.A. Croce, ed.), (July 24, 1974), Vol. II, FMRC Tech. Rept. No. 21011.4, pp. 8–50 (1975).
2. J. Quintiere, "Growth of Fire in Building Compartments," in *Fire Standards and Safety* (A.F. Robertson, ed.), ASTM STP614, American Soc. for Testing and Materials, pp. 131–167 (1977).
3. R. Pape and T. Waterman, "Modification to the FIRES Pre-Flashover Room Fire Computer Model," IITRI Project J6400, IIT Res. Inst., Chicago, IL (1977).
4. H.E. Mitler, "The Physical Basis for the Harvard Computer Fire Code," *Home Fire Proj. Tech. Rept.* No. 34, Harvard Univ., Cambridge, MA (1978).
5. R.W. Bukowski, R.D. Peacock, W.W. Jones, and C.L. Forney, "HAZARD I: Technical Reference Guide," *NIST Handbook 146*, Vol. II (1989).
6. R. Friedman, *Survey of Computer Models for Fire and Smoke*, 2nd ed., Factory Mutual Research Corp., Norwood, MA (1991).
7. J.G. Quintiere, "Fundamentals of Enclosure Fire Zone Models," *J. of Fire Protection Engr.*, 1, 3 (1989).
8. E.E. Zukoski, S.J. Toner, J.H. Morehart, and T. Kubota, "Combustion Processes in Two-Layered Configurations," *Fire Safety Science—Proc. 2nd Int. Symp.*, Hemisphere Publishing Corp., New York, pp. 255–304 (1989).
9. J.A. Rockett, "Using the Harvard/NIST Mark VI Fire Simulation," *NISTIR 4464*, Nat. Inst. of Standards and Technology (1990).
10. B.J. McCaffrey and J.A. Rockett, "Static Pressure Measurements of Enclosure Fires," *J. of Fire Research*, Nat. Bur. Stand. (1977).
11. M. Epstein, "Buoyant-Driven Exchange Flow Through Small Openings in Horizontal Partitions," *Jour. of Heat Transfer*, American Soc. for Testing and Materials, 110 (1988).
12. L.Y. Cooper, "An Algorithm and Associated Computer Subordinate for Calculating Flow Through a Horizontal Ceiling Flow Vent in a Zone-Type Compartment Fire Model," *NISTIR 4402*, Nat. Inst. of Stand. and Technology (1990).
13. R.L. Alpert, "Convective Heat Transfer in the Impingement Region of a Buoyant Plume," *Jour. of Heat Transfer*, American Soc. for Testing and Materials, 109 (1987).
14. H.Z. You and G.M. Faeth, "Ceiling Heat Transfer During Fire Plume and Fire Impingement," *Fire and Materials*, 3, 3 (1979).
15. M.A. Kokkala, "Experimental Study of Heat Transfer to Ceiling from an Impinging Diffusion Flame," *Fire Safety Science—Proc. of 3rd Inter. Symp.*, G. Cox and B. Langford, ed., Elsevier Applied Science, London (1991).
16. G.P. Forney, "Computing Radiative Heat Transfer Occurring in a Zone Model," *NISTIR 4709*, Nat. Inst. of Stand. and Technology (1991).
17. B.J. McCaffrey and J.G. Quintiere, "Buoyancy-Driven Countercurrent Flows Generated by a Fire Source," *Heat Transfer and Turbulent Buoyant Convection*, Vol. II (D.B. Spalding and N. Afgan, ed.), Hemisphere Pub. Co., pp. 457–472 (1977).
18. C.S. Lim, E.E. Zukoski, and T. Kubota, "Mixing in Doorway Flows and Entrainment in Fire Flames," Cal. Inst. of Technology, NBS Grant No. NB82NADA3033 (1984).
19. Y. Jaluria, "National Convection Wall Flows," in *SFPE Handbook of Fire Protection Engineering* (P.J. DiNenno, et al., eds.), National Fire Protection Association, Quincy, MA, pp. 2-50–2-63 (1995).
20. J.H. Klote and L.Y. Cooper, "Model of a Simple Fan-Resistance Ventilation System and Its Application to Fire Modeling," *NISTIR 89-4141*, Nat. Inst. of Stand. and Technology (1989).
21. B. McCaffrey, "Flame Height," in *SFPE Handbook of Fire Protection Engineering* (P.J. DiNenno, et al., eds.), National Fire Protection Association, Quincy, MA, pp. 2-1–2-8 (1995).
22. H.W. Emmons, H.E. Mitler, and L.N. Trefethen, "Computer Fire Code III," *Home Fire Proj. Tech Rept.* No. 25, Harvard Univ. Cambridge, MA (1978).
23. T. Tanaka, "A Model of Multicompartment Fire Spread," *NBSIR 83-2718*, Nat. Bur. Stand. (1983).
24. R.D. Peacock, W.W. Jones, R.W. Bukowski, and C.L. Forney, "Technical Reference Guide for the HAZARD I Fire Hazard Assessment Method," Ver. 1.1, *NIST Hdbk 146*, Nat. Inst. of Stand. and Tech. (1991).

CHAPTER 6

Estimating Temperatures in Compartment Fires

William D. Walton and Philip H. Thomas

Introduction

The ability to predict temperatures developed in compartment fires is of great significance to the fire protection professional. There are many uses for a knowledge of compartment fire temperatures, including the prediction of (1) the onset of hazardous conditions, (2) property and structural damage, (3) changes in burning rate, (4) ignition of objects, and (5) the onset of flashover.

The fundamental principles underlying compartment fires are presented in Section 3, Chapter 5. This chapter gives a number of simplified solution techniques.

Fire Stages

In this chapter, compartment fires are defined as fires in enclosed spaces, which are commonly thought of as rooms in buildings, but may include other spaces such as those found in transportation vehicles such as ships, planes, trains, and the like.

Compartment fires are often discussed in terms of growth stages.¹ Figure 3-6.1 shows an idealized variation of temperature with time along with the growth stages. The growth stages are

1. Ignition
2. Growth
3. Flashover
4. Fully developed fire
5. Decay

While many fires will not follow this idealization, it provides a useful framework for the discussion of com-

partment fires. All fires include an ignition stage but, beyond that, may fail to grow, or they may be affected by manual or automatic suppression activities before going through all of the stages listed above.

Growth Stage Definitions

Ignition stage: The period during which the fire begins.

Growth stage: Following ignition, the fire initially grows primarily as a function of the fuel itself, with little or no influence from the compartment. The fire can be described in terms of its rate of energy and combustion product generation. A discussion of energy generation or burning rate can be found in Section 3, Chapter 1. If sufficient fuel and oxygen are available, the fire will continue to grow, causing the temperature in the compartment to rise. Fires with sufficient oxygen for combustion are said to be fuel controlled.

Flashover: Flashover is generally defined as the transition from a growing fire to a fully developed fire in which all combustible items in the compartment are involved in fire. During this transition there are rapid changes in the compartment environment. Flashover is not a precise term, and several variations in definition can be found in the literature. Most have criteria based on the temperature at which the radiation from the hot gases in the compartment will ignite all of the combustible contents. Gas temperatures of 300 to 650°C have been associated with the onset of flashover, although temperatures of 500 to 600°C are more widely used.² The ignition of unburnt fuel in the hot fire gases, the appearance of flames from openings in a compartment, or the ignition of all of the combustible contents may actually be different phenomena.

Fully developed fire: During this stage, the heat release rate of the fire is the greatest. Frequently during this stage

Mr. William D. Walton is a research fire protection engineer with the Building and Fire Research Laboratory, National Institute of Standards and Technology.

Dr. Philip H. Thomas is retired from the Fire Research Station, Borehamwood, England.

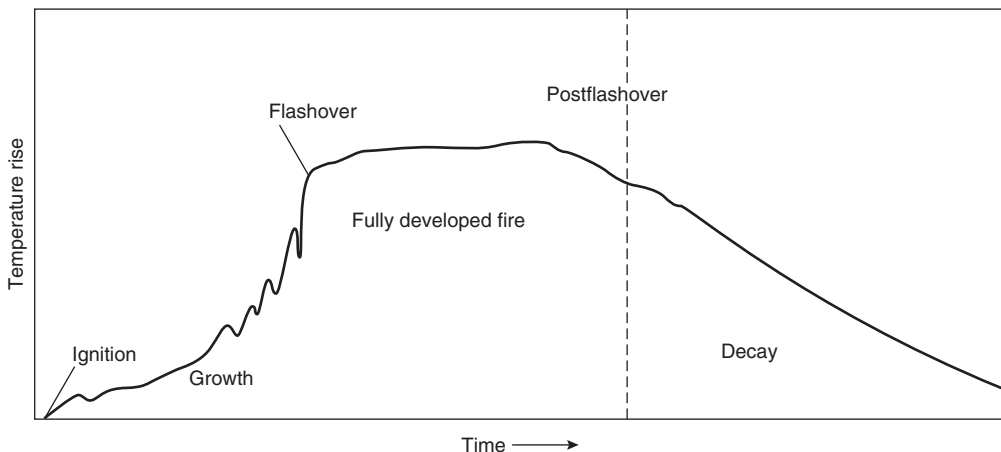


Figure 3-6.1. General description of room fire in absence of fire control.

more fuel is pyrolyzed than can be burned with the oxygen available in the compartment. In this case, the fire is said to be ventilation controlled. If there are openings in the compartment, the unburned fuel will leave the compartment in the gas flow and may burn outside of the compartment. During the fully developed stage, the environment within the compartment has a significant effect on the pyrolysis rate of the burning objects.

Decay stage: Decay occurs as the fuel becomes consumed, and the heat release rate declines. The fire may change from ventilation to fuel controlled during this period.

the compartment walls (e.g., doors and windows), hot gas will flow out the openings and outside air will flow into the openings. This description of compartment fire phenomena is referred to as a two-layer or zone model. The basic compartment fire phenomena are shown schematically in Figure 3-6.2.

The two-layer-model concept assumes that the compositions of the layers are uniform, that is, that the temperature and other properties are the same throughout each layer. Although the temperature of the lower layer will rise during the course of the fire, the temperature of the upper layer will remain greater and is the most important factor in compartment fires. The assumptions may be less valid for very large spaces or for long, narrow spaces such as corridors and shafts.

Compartment Fire Phenomena

Compartment Fire Model

In order to calculate or predict the temperatures generated in a compartment fire, a description or model of the fire phenomena must be created. This model will be described in terms of physical equations which can be solved to predict the temperature in the compartment. Such a model is, therefore, an idealization of the compartment fire phenomena. Consider a fire which starts at some point below the ceiling and releases energy and products of combustion. The rate at which energy and products of combustion are released may change with time. The hot products of combustion form a plume, which, due to buoyancy, rises toward the ceiling. As the plume rises, it draws in cool air from within the compartment, decreasing the plume's temperature and increasing its volume flow rate. When the plume reaches the ceiling, it spreads out and forms a hot gas layer which descends with time as the plume's gases continue to flow into it. There is a relatively sharp interface between the hot upper layer and the air in the lower part of the compartment. The only interchange between the air in the lower part of the room and the hot upper layer assumed is through the plume. As the hot layer descends and reaches openings in

Calculation of Compartment Fire Temperatures

The basic principle used to calculate the temperature in a compartment fire is the conservation of energy. As applied to the hot upper layer, the conservation of energy can be simply stated as follows: the energy added to the hot upper layer by the fire equals the energy lost from the hot layer plus the time rate of change of energy within the hot upper layer. From the time rate of change of en-

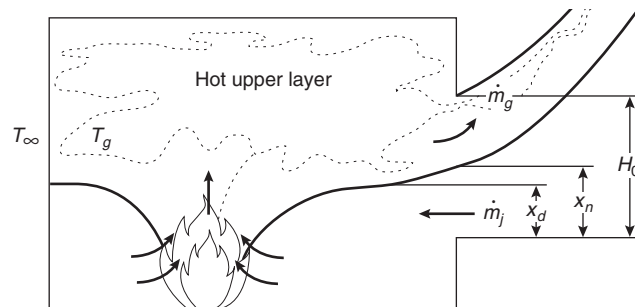


Figure 3-6.2. Two-layer model with no exchange between layers except the plume.

ergy within the hot layer, the temperature of the layer can be computed. Conservation of energy can also be applied to the lower layer. Since the volume of the upper layer changes with time, and mass flows in and out of the upper layer, conservation of mass must be used along with the conservation of energy. Because the energy generated by the fire and the temperatures in the compartment vary as a function of time, the application of conservation of energy will result in a series of differential equations. For the purposes of examining the components of the conservation of energy, the steady-state expressions for the conservation of energy for the hot upper layer will be used.

The transport of energy in a compartment fire is a very complex process. In order to formulate expressions for the conservation of energy in a practical way, a number of assumptions must be made. It is possible to formulate the equations for the conservation of energy in a number of ways, based on the level of detail desired. The expressions and assumptions used in this chapter are based on those commonly found in the fire research literature and represent a somewhat simplified description of the phenomena. Additional details may be found in the references cited.

The steady-state conservation of energy for the hot upper gas layer in a compartment can be simply stated as follows: the energy generated by the fire and added to the hot layer equals the energy lost from the hot layer through radiation and convection plus the energy convected out the compartment openings.

Energy Generated by the Fire

The energy generated by the fire is the primary influence on the temperature in a compartment fire, and much research has been conducted in predicting the energy release rate of many fuels under a variety of conditions. This discussion will focus on flaming combustion, as it is most important in generating a significant temperature rise in a compartment. A discussion of smoldering combustion is found in Section 2, Chapter 9. As a fuel is heated and releases pyrolysis products, these products react with oxygen, generating heat and producing flames. The rate of energy release is equal to the mass loss rate of the fuel times the heat of combustion of the fuel:

$$\dot{Q} = \dot{m}_f \Delta h_c \quad (1)$$

where

\dot{Q} = energy release rate of the fire (kW)

\dot{m}_f = mass burning rate of the fuel (kg/s)

Δh_c = effective heat of combustion of the fuel (kJ/kg)

The effective heat of combustion is the heat of combustion which would be expected in a fire where incomplete combustion takes place. This amount is less than the theoretical heat of combustion as measured in the oxygen bomb calorimeter. The effective heat of combustion is often described as a fraction of the theoretical heat of combustion. The effect of fluctuations is largely neglected.

In fuel-controlled fires, there is sufficient air to react with all the fuel within the compartment. In ventilation-controlled fires, there is insufficient air within the compartment, and some of the pyrolysis products will leave the compartment, possibly to react outside the compartment. For calculating the temperatures produced in compartment fires, the primary interest is the energy released within the compartment.

The pyrolysis rate of the fuel depends on the fuel type, its geometry, and the fire-induced environment. The energy generated in the compartment by the burning pyrolysis products then depends on the conditions (temperature, oxygen concentration, etc.) within the compartment. While the processes involved are complex, and some are not well understood, there are two cases where some simplifying assumptions can lead to useful methods for approximation of the energy released by the fire.

Free-burning fires are defined as those in which the pyrolysis rate and the energy release rate are affected only by the burning of the fuel itself and not by the room environment. This definition is analogous to a fire burning out of doors on a calm day. Babrauskas has provided a collection of data on free-burning fires in Section 3, Chapter 1. This data is most useful for estimating burning rates of primarily horizontal fuels in preflashover fires, where the primary heating of the fuel is from the flames of the burning item itself. Vertical fuels, such as wall linings and fuels located in the upper hot gas layer, will likely be influenced by the preflashover room environment.

Ventilation-controlled fires are defined as those in which the energy release rate in the room is limited by the amount of available oxygen. The mass flow rate of air or oxygen into the room through a door or window can be calculated from the expressions described below and in Section 2, Chapter 3. For most fuels, the heat released per mass of air consumed is a constant approximately equal to 3000 KJ/kg.³ Therefore, the rate of energy release of the fire can be approximated from the air inflow rate.

The amount of energy released by the fire which enters the hot upper layer is a function of the fire, layer conditions, and geometry. For most fires, approximately 35 percent of the energy released by the fire leaves the fire plume as radiation.⁴ (A discussion of flame radiation can be found in Section 2, Chapter 12.) In a compartment fire, a fraction of the radiated energy reaches the upper layer. The majority of the remaining energy released by the fire is convected into the upper layer by the plume. As the plume rises, it entrains air from the lower layer, thus reducing its temperature and increasing the mass flow rate. For a first approximation, it can be assumed that all of the energy generated by the fire is transported to the upper layer. For a complete discussion of fire plumes see Section 2, Chapter 1.

Conservation of Mass

The mass flow into the compartment and the flow out are related by

$$\dot{m}_g = \dot{m}_a + \dot{m}_f \quad (2)$$

where \dot{m}_f is the mass burning rate of the fuel (kg/s).

The mass flow rate of hot gas out of a window or door is given by Rockett:⁵

$$\dot{m}_g = \frac{2}{3} C_d W_0 \rho_\infty \left[2g \frac{T_\infty}{T_g} \left(1 - \frac{T_\infty}{T_g} \right) \right]^{1/2} (H_0 - X_N)^{3/2} \quad (3)$$

where

\dot{m}_g = mass flow rate of hot gas out an opening (kg/s)

C_d = orifice constriction coefficient (typically ≈ 0.7)

W_0 = opening width (m)

H_0 = opening height (m)

ρ_∞ = ambient air density (kg/m³)

g = acceleration due to gravity, 9.8 m/s²

X_N = height of neutral plane (m)

T_g = temperature of the hot upper gas layer (K)

T_∞ = ambient temperature (K)

The mass flow rate of air into a door or window is given by

$$\dot{m}_a = \frac{2}{3} C_d W_0 \rho_\infty \left[2g \left(1 - \frac{T_\infty}{T_g} \right) \right]^{1/2} (X_N - X_d)^{1/2} (X_N + X_d / 2) \quad (4)$$

where X_d = height of the interface (m).

The expressions for mass flow in and mass flow out cannot be solved directly for T_g since the height to the neutral plane and interface are unknown. The complete solution of these equations requires expressions for plume entrainment and additional energy equations and is normally carried out only in computer fire models. If the mass burning rate of the fuel is small compared with the mass flow rate of air into the compartment, the mass flow out of the opening may be approximated as equal to the mass inflow rate. Flows out of vents in the ceiling are discussed in Section 3, Chapter 11.

For preflashover fires in compartments with typical doors or windows, the neutral plane and interface can be approximated at the midlevel of the opening. This approximation can only be made after the initial smoke filling of the compartment is complete, and flow in and out of the opening is established.

For fires nearing flashover and post-flashover fires, the interface between the upper and lower layers is located near the floor, and the flow reaches a maximum for a given upper gas temperature. Rockett has shown the temperature dependence on the flow becomes small above 150°C, and the flow into the compartment can be approximated as a constant multiplied by⁵ $A_0 \sqrt{H_0}$.

Rockett calculated values for this constant of 0.40 to 0.61 kg/s·m^{5/2}, depending on the discharge coefficient of the opening. Thomas and Heselden estimate the value of this constant at 0.5 kg/s·m^{5/2}, which is the value most commonly found in the literature.⁶ The resulting approximation is then

$$\dot{m}_a = 0.5 A_0 \sqrt{H_0} \quad (5)$$

where

A_0 = area of opening (m²)

H_0 = height of opening (m)

The term $A_0 \sqrt{H_0}$ is commonly known as the ventilation factor. The first use of this type of opening flow analysis for evaluating postflashover-fire test data is attributed to Kawagoe.⁷ From early work analyzing such data, the empirical observation was made that wood fires in rooms with small windows appeared to burn at a rate approximately stoichiometric. Although flames emerging from the windows implied that some fuel was burning outside, calculations often suggested that enough air was entering the fire for stoichiometric burning. Empirical observations on wood fires⁷ led to

$$\dot{m}_f = 0.09 A_0 \sqrt{H_0} \quad (6)$$

There is now a body of data⁸ that modifies this simple proportionality between \dot{m}_f and $A_0 \sqrt{H_0}$.

The Conseil International du Bâtiment (CIB) experiments upon which Law⁹ has based her method shows a dependance on A_T . It seems possible that the wide use of Equation 6 is a result of a concentration of experimental fires in rooms of a limited range of

$$\frac{A_T}{A_0 \sqrt{H_0}}$$

where

A_T = total area of the compartment enclosing surfaces (m²)

Traditionally, energy balances were often stated in terms of the energy produced by the burning fuel and, thereby, led to an effective heat of combustion of the fuel. However, this practice in principle leads to the same result—the energy produced is related to the air flow for ventilation-controlled fires. Kawagoe⁷ and Magnusson and Thelandersson¹⁰ used 10.75 MJ/kg for the effective heat of combustion of wood in the flaming phase for fully developed compartment fires. With 16.4 MJ/kg for the heat of combustion of wood volatiles, this setup corresponds to a combustion efficiency of 10.75/16.4, which is virtually identical to the 0.65 used in several computer models.

By far the majority of data is based on experiments in which the fuel was cellulosic, and much of the experimental data are based on wood in the form of cribs. For the postflashover burning of a different fuel with a different chemistry, the burning rate expressions may still be used, as long as the fuel is a hydrocarbon producing approximately 3000 kJ for each kg of air consumed in the combustion process. Because different fuels react differently to the thermal environment and will pyrolyze at different rates according to the energy requirements to produce volatiles, one can only estimate temperatures by evaluating the differences, or obtain maximum temperatures by using stoichiometry. Fuels more volatile than wood will probably produce lower temperatures inside a compartment, even if the excess fuel produces a greater hazard outside the compartment. The assumptions that the energy is related to the air flow and that the fuel is in stoichiometric proportion will give an upper estimate of temperatures for ventilation-controlled fires. Since Equation 6 is close to stoichiometric, it could, coupled with the

Table 3-6.1 Heat Balance Measured in Experimental Fires in a Compartment of 29 m² Floor Area with a Fire Load of Wood Cribs

Fire Load (kg)	Window Area (m ²)	Heat Release (kcal/s)	Heat Loss from Hot Gases (%)			
			Effluent Gas	Structural Surfaces	Feedback to Fuel	Window Radiation
877	11.2	1900	65	15	11	9
	5.6	1900	52	26	11	11
1744	11.2	3200	61	15	11	13
	5.6	2300	53	26	12	9
	2.6	1600	47	30	16	7

effective heat of combustion of wood, give results close to an upper temperature limit for other fuels.

Conservation of Energy

The heat generated by burning materials within a compartment is absorbed by the enclosing surfaces of the compartment and any other structural surfaces, by the surfaces of the fuel, and by the incoming air and any excess fuel. Heat is lost to the exterior in the flames and hot gases that exit from the openings in the compartment enclosing surfaces and by radiation through the openings. An example of an experimental heat balance measured in a small compartment is given in Table 3-6.1. For this compartment, unglazed windows provided ventilation from the start of the fire.

Table 3-6.1 illustrates the significant amount of heat loss in the effluent gases and shows that, with decreasing window area, a larger proportion of the heat released will be absorbed by the enclosing surfaces. The total heat released, assuming a complete burnout, is directly proportional to the amount of the fire load, but the rate of heat release may also be controlled by the ventilation. In this example, with the lower fire load, both window areas give sufficient ventilation for the fuel to burn at its maximum (free-burning) rate but, with the doubled fire load, the burning rate is not doubled, because the window area restricts the ventilation needed.

Methods for Predicting Preflashover Compartment Fire Temperatures

The solution of a relatively complete set of equations for the conservation of energy requires the solution of a large number of equations which vary with time. Although individual energy transport equations may be solved, in general there is not an explicit solution for a set of these equations. As a result, one of two approaches can be taken. The first is an approximate solution which can be accomplished by hand using a limiting set of assumptions. The second is a more complete solution utilizing a computer program. In either case, a number of methods have been developed. The methods presented are those which appear most widely accepted in the fire protection

community. Each method employs assumptions and limitations which should be understood before employing the method. The methods presented in this chapter predict average temperatures and are not applicable to cases where prediction of local temperatures are desired. For example, these methods should not be used to predict detector or sprinkler actuation or the temperatures of materials as a result of direct flame impingement.

Method of McCaffrey, Quintiere, and Harkleroad

McCaffrey, Quintiere, and Harkleroad have used a simple conservation of energy expression and a correlation with data to develop an approximation of the upper layer temperature in a compartment.¹¹ Applying the conservation of energy to the upper layer yields

$$\dot{Q} = \dot{m}_g c_p (T_g - T_\infty) + q_{\text{loss}} \quad (7)$$

where

\dot{Q} = energy (heat) release rate of the fire (kW)

\dot{m}_g = gas flow rate out the opening (kg/s)

c_p = specific heat of gas (kJ/kg·K)

T_g = temperature of the upper gas layer (K)

T_∞ = ambient temperature (K)

q_{loss} = net radiative and convective heat transfer from the upper gas layer (kW)

The left-hand side of Equation 7 is the energy generated by the fire. On the right-hand side, the first term is the heat transported from the upper layer in the gas flow out an opening. The second term is the net rate of radiative and convective heat transfer from the upper layer, which is approximately equal to rate of heat conduction into the compartment surfaces. The rate of heat transfer to the surfaces is approximated by

$$q_{\text{loss}} = h_k A_T (T_g - T_\infty) \quad (8)$$

where

h_k = effective heat transfer coefficient (kW/m·K)

A_T = total area of the compartment enclosing surfaces (m²)

Substituting Equation 8 into Equation 7 yields the nondimensional temperature rise in terms of two dimensionless groups:

$$\frac{\Delta T_g}{T_\infty} = \frac{\dot{Q}/(c_p T_\infty \dot{m}_g)}{1 + h_k A_T / (c_p \dot{m}_g)} \quad (9)$$

where ΔT_g is the upper gas temperature rise above ambient ($T_g - T_\infty$) (K).

The mass flow rate of hot gas out of a window or door can be rewritten from Equation 3:

$$\dot{m}_g = \frac{2}{3} C_d W_0 H_0^{3/2} \rho_\infty \left[2g \frac{T_\infty}{T_g} \left(1 - \frac{T_\infty}{T_g} \right) \right]^{1/2} \left(1 - \frac{X_N}{H_0} \right)^{3/2} \quad (10)$$

where

C_d = orifice constriction coefficient

W_0 = opening width (m)

H_0 = opening height (m)

ρ_∞ = ambient air density (kg/m³)

g = acceleration due to gravity, 9.8 m/s²

X_N = height of neutral plane (m)

Since X_N primarily depends on T_g , \dot{Q} , and geometric factors (H_0 and W_0), \dot{m}_g may be replaced by $\sqrt{g} \rho_\infty A_0 \sqrt{H_0}$ in the two dimensionless variables in Equation 10, without any loss in generality. The effects of T_g and \dot{Q} are incorporated into the correlation via other terms. Based on an analysis of test data, Equation 9 was written as a power-law relationship:

$$\Delta T_g = 480 \left(\frac{\dot{Q}}{\sqrt{g c_p \rho_\infty T_\infty A_0 \sqrt{H_0}}} \right)^{2/3} \left(\frac{h_k A_T}{\sqrt{g c_p \rho_\infty A_0 \sqrt{H_0}}} \right)^{-1/3} \quad (11)$$

where

A_0 = area of opening (m²)

H_0 = height of opening (m)

The numbers 480, 2/3, and -1/3 were determined by correlating the expression with the data from over 100 experimental fires. These data included both steady-state and transient fires in cellulosic and synthetic polymeric materials and gaseous hydrocarbon fuels. Compartment height ranged from 0.3 m to 2.7 m and floor areas from 0.14 m² to 12.0 m². The compartments contained a variety of window and door sizes. The term raised to the 2/3 power in Equation 11 represents the ratio of the energy released to the energy convected, and the term raised to the -1/3 power represents the energy lost divided by the energy convected.

Substituting the values for ambient conditions of

$g = 9.8 \text{ m/s}^2$

$c_p = 1.05 \text{ kJ/kg}\cdot\text{K}$

$\rho_\infty = 1.2 \text{ kg/m}^3$

$T_\infty = 295 \text{ K}$

into Equation 11 yields^{12,13}

$$\Delta T_g = 6.85 \left(\frac{\dot{Q}^2}{A_0 \sqrt{H_0} h_k A_T} \right)^{1/3} \quad (12)$$

The heat transfer coefficient can be determined using a steady-state approximation when the time of exposure, t , is greater than the thermal penetration time, t_p , by

$$h_k = k/\delta \quad \text{for } t > t_p \quad (13)$$

The thermal penetration time is defined as

$$t_p = \left(\frac{\rho c}{k} \right) \left(\frac{\delta}{2} \right)^2 \quad (14)$$

where

ρ = density of the compartment surface (kg/m³)

c = specific heat of the compartment surface material (kJ/kg·K)

k = thermal conductivity of compartment surface (kW/m·K)

δ = thickness of compartment surface (m)

t = exposure time (s)

t_p = thermal penetration time (s)

When the time of exposure is less than the penetration time, an approximation based on conduction in a semi-infinite solid is

$$h_k = \left(\frac{k \rho c}{t} \right)^{1/2} \quad \text{for } t \leq t_p \quad (15)$$

If there are several wall and/or ceiling materials in the compartment, an area-weighted average for h_k should be used.

The limitations as stated by McCaffrey et al. on the use of this method for estimating temperatures are as follows:

1. The correlation holds for compartment upper layer gas temperatures up to approximately 600°C.
2. It applies to steady-state as well as time-dependent fires, provided the primary transient response is the wall conduction phenomenon.
3. It is not applicable to rapidly developing fires in large enclosures in which significant fire growth has occurred before the combustion products have exited the compartment.
4. The energy release rate of the fire must be determined from data or other correlations.
5. The characteristic fire growth time and thermal penetration time of the room-lining materials must be determined in order to evaluate the effective heat transfer coefficient.
6. The correlation is based on data from a limited number of experiments and does not contain extensive data on ventilation-controlled fires nor data on combustible walls or ceilings. Most of the fuel in the test fires was near the center of the room.

Example of McCaffrey et al. method: Calculate the upper layer temperature of a room 3 × 3 m in floor area and

2.4 m high with a door opening 1.8 m high and 0.6 m wide. The fire source is a steady 750 kW fire. The wall-lining material is 0.016 m (5/8 in.) gypsum plaster on metal lath. Perform the calculation at times of 10, 60, and 600 s after ignition. Using Equation 11,

$$\Delta T_g = 480 \left(\frac{\dot{Q}}{\sqrt{g} c_p \rho_\infty T_\infty A_0 \sqrt{H_0}} \right)^{2/3} \left(\frac{h_k A_T}{\sqrt{g} c_p \rho_\infty A_0 \sqrt{H_0}} \right)^{-1/3}$$

where

$$c_p = 1 \text{ kJ/kg}\cdot\text{K}$$

$$T_\infty = 27^\circ\text{C} (300 \text{ K})$$

$$\rho_\infty = 1.18 \text{ kg/m}^3$$

$$A_0 = 1.8 \text{ m} \times 0.6 \text{ m} = 1.08 \text{ m}^2$$

$$g = 9.8 \text{ m/s}^2$$

$$H_0 = 1.8 \text{ m}$$

$$\dot{Q} = 750 \text{ kW}$$

$$\begin{aligned} A_T &= A_{\text{walls}} + A_{\text{floor}} + A_{\text{ceiling}} - A_{\text{openings}} \\ &= 4 \times (3 \times 2.4) + (3 \times 3) + (3 \times 3) - 1.08 \\ &= 28.8 \text{ m}^2 + 9 \text{ m}^2 + 9 \text{ m}^2 - 1.08 \\ &= 45.72 \text{ m}^2 \end{aligned}$$

The wall heat loss coefficient, h_k , is a function of time.

a. Calculate the thermal penetration time, t_p .

$$t_p = \left(\frac{\rho c}{k} \right) \left(\frac{\delta}{2} \right)^2$$

where

$$\rho = \text{wall material density (1440 kg/m}^3)$$

$$k = 0.48 \times 10^{-3} \text{ kW/m}\cdot\text{c}$$

$$c = 0.84 \text{ kJ/kg}\cdot^\circ\text{C}$$

$$\delta = 0.016 \text{ m}$$

$$t_p = 161.3 \text{ s}$$

b. Calculate h_k at 10, 60, and 600 s.

For $t < t_p$ (10, 60 s),

$$h_k = \left(\frac{k_p c}{t} \right)^{1/2} \quad k_p c = 0.581$$

1. At $t = 10 \text{ s}$,

$$h_k = \left(\frac{0.581}{10} \right)^{1/2} = 0.24 \text{ kW/m}\cdot\text{K}$$

2. At $t = 60 \text{ s}$,

$$h_k = \left(\frac{0.581}{60} \right)^{1/2} = 0.098 \text{ kW/m}\cdot\text{K}$$

3. For $t > t_p$ (600 s) at $t = 600 \text{ s}$,

$$h_k = \frac{k}{\delta} = \frac{0.48 \times 10^{-3}}{0.016} = 0.03 \text{ kW/m}\cdot\text{K}$$

c. Calculate the compartment temperature at the three times using Equation 11.

1. At $t = 10 \text{ s}$,

$$\begin{aligned} \Delta T_g &= 480 \left[\frac{750}{(\sqrt{9.8})(1)(1.18)(300)(1.08)(\sqrt{1.8})} \right]^{2/3} \\ &\quad \cdot \left[\frac{(0.24)(45.72)}{(\sqrt{9.8})(1)(1.18)(1.08)(\sqrt{1.8})} \right]^{-1/3} \\ &= 480(0.47)^{2/3}(2.05)^{-1/3} \\ &= 227 \text{ K} \end{aligned}$$

2. At $t = 60 \text{ s}$,

$$\begin{aligned} \Delta T_g &= 480(0.47)^{2/3}(0.837)^{-1/3} \\ &= 307 \text{ K} \end{aligned}$$

3. At $t = 600 \text{ s}$,

$$\begin{aligned} \Delta T_g &= 480(0.47)^{2/3}(0.26)^{-1/3} \\ &= 453 \text{ K} \end{aligned}$$

Method of Foote, Pagni, and Alvares

The Foote, Pagni, and Alvares method follows the basic correlations of McCaffrey, Quintiere, and Harkleroad and adds data for forced-ventilation fires. Using Equation 9 and not introducing an expression for doorway flow results in the expression¹⁴

$$\frac{\Delta T_g}{T_\infty} = 0.63 \left(\frac{\dot{Q}}{\dot{m}_g c_p T_\infty} \right)^{0.72} \left(\frac{h_k A_T}{\dot{m}_g c_p} \right)^{-0.36} \quad (16)$$

where

$$\Delta T_g = \text{upper gas temperature rise above ambient (K)}$$

$$T_\infty = \text{ambient air temperature (K)}$$

$$\dot{Q} = \text{energy (heat) release rate of the fire (kW)}$$

$$\dot{m}_g = \text{compartment mass ventilation rate (kg/s)}$$

$$c_p = \text{specific heat of gas (kJ/kg}\cdot\text{K)}$$

$$h_k = \text{effective heat transfer coefficient (kW/m}\cdot\text{K)}$$

$$A_T = \text{total area of the compartment-enclosing surfaces (m}^2)$$

The coefficient and exponents are based on data from well-ventilated tests in a compartment with a $6 \times 4 \text{ m}$ floor area and a height of 4.5 m with ventilation rates of 110 to 325 g/s. The compartment exhaust was through a $0.65 \times 0.65 \text{ m}$ duct located 3.6 m above the floor. Four air inlet openings were $0.5 \times 0.12 \text{ m}$ high, with centerlines 0.1 m above the floor. A methane gas burner fire in the center of the floor with heat release rates of 150 to 490 kW resulted in upper gas temperatures of approximately 100 to 300°C.

Foote et al. have shown that the correlation for forced-ventilation fires agrees well with the data presented by McCaffrey et al. for free ventilation fires with

$$\dot{m} \approx 0.1 (\rho_\infty \sqrt{g} A_0 \sqrt{H_0})$$

Example of Foote et al. method: Estimate the temperature in a 5×5 m floor area $\times 4$ m high compartment having 0.025-m-(1-in.)-thick concrete walls. The forced-ventilation rate is $2.4 \text{ m}^3/\text{s}$ of air (5000 cfm). Perform the calculation for $t > t_p$. The fire size is given as 1000 kW; ambient air conditions at 300 K. Using Equation 16,

$$\frac{\Delta T_g}{T_\infty} = 0.63 \left(\frac{\dot{Q}}{\dot{m}_g c_p T_\infty} \right)^{0.72} \left(\frac{h_k A_T}{\dot{m}_g c_p} \right)^{-0.36}$$

where

$$\dot{Q} = 1000 \text{ kW}$$

$$T_\infty = 300 \text{ K}$$

$$c_p = 1.0 \text{ kJ/kg}\cdot\text{K}$$

$$A_T = 4 \times (5 \times 4) + 2(5 \times 5) = 105 \text{ m}^2$$

$$\dot{m}_g = (2.4 \text{ m}^3/\text{s}) (1.18 \text{ kg/m}^3) = 2.8 \text{ kg/s}$$

Calculate h_k for $t > t_p$. For 0.025-m-thick concrete,

$$\delta = 0.025 \text{ m}$$

$$\rho = 2000 \text{ kg/m}^3$$

$$k = 1.4 \times 10^{-3} \text{ kW/m}\cdot\text{K}$$

$$c_p = 0.88 \text{ kJ/kg}\cdot\text{K}$$

$$\begin{aligned} t_p &= \left(\frac{\rho c}{k} \right) \left(\frac{\delta}{2} \right)^2 \\ &= \left[\frac{(2000) \cdot (0.88)}{1.4 \times 10^{-3}} \right] \left(\frac{0.025}{2} \right)^2 \\ &= 196 \text{ s} \quad \text{for } t > t_p \end{aligned}$$

$$\begin{aligned} h_k &= \frac{k}{\delta} \\ &= \frac{1.4 \times 10^{-3}}{0.025} \\ &= 0.056 \text{ kW/m}^2\cdot\text{K} \end{aligned}$$

$$\frac{\Delta T_g}{T_\infty} = (0.63) \left[\frac{1000}{(2.8)(1)(300)} \right]^{0.72} \left[\frac{(0.056)(105)}{(2.8)(1)} \right]^{-0.36}$$

$$\begin{aligned} \Delta T_g &= (0.14)(T_\infty) \\ &= 164 \text{ K} \\ T_g &= 164 + 300 \text{ K} = 464 \text{ K} \end{aligned}$$

Method of Beyler and Deal

Beyler and Deal compared a number of methods for naturally ventilated compartments to test data and recommend the method of McCaffrey, Quintiere, and Harkleroad for naturally ventilated compartments. Beyler offers an improved correlation for compartments where the forced-ventilation flow rate is known.^{15,16} This method begins by applying the conservation of energy in the upper layer of a compartment. Combining Equations 7 and 8 yields

$$\dot{Q} = \dot{m}_g c_p (T_g - T_\infty) + h_k A_T (T_g - T_\infty) \quad (17)$$

where:

\dot{Q} = energy (heat) release rate of the fire (kw)

\dot{m}_g = gas flow rate out the opening (kg/s)

c_p = specific heat of gas (kJ/kg·K)

T_g = temperature of the upper gas layer (K)

T_∞ = ambient temperature (K)

h_k = effective heat transfer coefficient (kW/m·K)

A_T = total area of the compartment enclosing surfaces (m²)

Rearranging Equation 17a yields

$$\Delta T_g = \frac{\dot{Q}}{\dot{m}_g c_p + h_k A_T} \quad (17a)$$

or

$$\frac{\Delta T_g \dot{m}_g c_p}{\dot{Q}} = \frac{1}{1 + (h_k A_T) / \dot{m}_g c_p} \quad (17b)$$

where $\Delta T_g = T_g - T_\infty$.

A nondimensional temperature rise is defined as

$$\Delta T^* \equiv \frac{\Delta T_g \dot{m}_g c_p}{\dot{Q}} \quad (18)$$

and the ratio of the bounding surface loss to the ventilation losses is defined as

$$Y^* \equiv 1 + \frac{h_k A_T}{\dot{m}_g c_p} \quad (19)$$

By plotting ΔT^* as a function of ΔY^* for data with experiments with known ventilation rates Beyler and Deal developed a correlation for the effective heat transfer coefficient of

$$h_k = 0.4 \max \left(\sqrt{\frac{k \rho c}{t}}, \frac{k}{\delta} \right) \quad (20)$$

where

k = thermal conductivity of the compartment surface (kW/m·K)

ρ = density of the compartment surface (kg/m³)

c = specific heat of the compartment surface material (kJ/kg·K)

δ = thickness of the compartment surface (m)

t = exposure time (s)

The expression switches from transient to steady state at a thermal penetration time of $t_p = (\rho c / k) \delta^2$ rather than $t_p = (\rho c / k) (\delta / 2)^2$ used by McCaffery et al. and Foote et al. For the data set Beyler and Deal evaluated, the standard error for their method was 29 K as compared to 51 K for the method of Foote et al., even though the equation uses only one fitting constant.

Beyler and Deal demonstrated that this method works for ventilation to the lower part of the compartment (with or without a plenum) as well as for ventilation to the upper part of the compartment. The Beyler and

Deal method was based on data up to 2000 s into fire tests. At longer times, the heat loss model breaks down.

Example of Beyler and Deal method: Estimate the temperature in a 5 m × 5 m floor area and 4 m high compartment with 0.025 m (1 in.)-thick concrete walls. The forced-ventilation rate is 2.4 m³/s of air (5000 cfm). Perform the calculation for $t > t_p$. The fire size is given as 1000 kW; ambient air conditions at 300 K. Using Equation 17a,

$$T_g - T_\infty = \frac{\dot{Q}}{\dot{m}_g c_p + h_k A_T}$$

where

$$\begin{aligned}\dot{Q} &= 1000 \text{ kW} \\ \dot{m}_g &= (2.4 \text{ m}^3/\text{s}) (1.18 \text{ kg/m}^3) = 2.8 \text{ kg/s} \\ c_p &= 1.0 \text{ kJ/kg·K} \\ T_\infty &= 300 \text{ K} \\ A_T &= 4(5 \times 4) + 2(5 \times 5) = 105 \text{ m}^2\end{aligned}$$

a. Calculate h_k for $t > t_p$. For 0.25-m-thick concrete,

$$\begin{aligned}\delta &= 0.25 \text{ m} \\ \rho &= 2000 \text{ kg/m}^3 \\ k &= 1.4 \times 10^{-3} \text{ kW/m·K} \\ c &= 0.88 \text{ kJ/kg·K} \\ h_k &= 0.4 \left(\frac{k}{\delta} \right) = 0.4 \left(\frac{1.4 \times 10^{-3}}{0.25} \right) = 0.0224 \text{ kW/m}^2\cdot\text{K}\end{aligned}$$

b. Calculate the compartment temperature using Equation 17a.

$$\begin{aligned}T_g - 300 &= \frac{1000}{(2.8)(1.0) + (0.0224)(105)} \\ T_g &= 494 \text{ K}\end{aligned}$$

Method of Peatross and Beyler

The correlations used in the McCaffrey, Quintiere, and Harkleroad method and the Beyler and Deal method are based on the assumption of normal insulating-wall materials. For highly conductive walls such as steel, Peatross and Beyler suggest the use of an alternative heat transfer coefficient.¹⁷ Using a lumped mass analysis for heat transfer through the wall which is appropriate for a highly conductive wall yields

$$m''_w c \frac{dT_w}{dt} = h_g(T_g - T_w) - h_\infty T_w \quad (21)$$

where

$$m''_w = \text{mass per unit area of the wall (kg/m}^2\text{)}$$

$$c = \text{specific heat of the wall (kJ/kg·K)}$$

$$T_w = \text{wall temperature (K)}$$

$$t = \text{time (s)}$$

$$h_g = \text{heat transfer coefficient on the hot side of the wall (kW/m·K)}$$

$$T_g = \text{upper layer temperature (K)}$$

$$h_\infty = \text{heat transfer coefficient on the ambient side of the wall (kW/m·K)}$$

Solving for the wall temperature with the initial condition of the wall at ambient temperature yields

$$T_w = \frac{h_g T_g}{h_g + h_\infty} \left[1 - \exp \left(- \frac{h_g - h_\infty}{m''_w c} t \right) \right] \quad (22)$$

The heat transfer through the wall, \dot{q}'' , may be expressed in terms of the heat transfer to the hot side of the wall or in terms of an overall effective heat transfer coefficient, h_k .

$$\dot{q}'' = h_g(T_g - T_w) = h_k(T_g - T_\infty) \quad (23)$$

Solving for h_k yields

$$h_k = h_g - \frac{h_g^2}{h_g + h_\infty} \left[1 - \exp \left(- \frac{h_g - h_\infty}{\rho \delta c} t \right) \right] \quad (24)$$

where

$$\rho = \text{density of the wall (kg/m}^3\text{)}$$

$$\delta = \text{thickness of the wall (m)}$$

From the above equations it can be seen that

$$\begin{aligned}h_k &= \frac{h_g h_\infty}{h_g + h_\infty} \quad \text{at } t = \infty \\ h_k &= h_g \quad \text{at } t = 0\end{aligned}$$

From a number of experiments, Peatross and Beyler found the heat transfer coefficients of 30 W/m²·K for h_g and 20 W/m²·K for h_∞ . Substituting these values yields

$$h_k = 30 - 18 \left[1 - \exp \left(- \frac{50}{\rho \delta c} t \right) \right] \quad (25)$$

The h_k calculated with this method can be used directly in the Beyler and Deal method. It must be multiplied by 2.5 for use in the McCaffery, Quintiere, and Harkleroad method to account for the 0.4 fitting constant in the h_k in the Beyler and Deal method.

Example of Peatross and Beyler method for forced ventilation: Estimate the temperature in a 5 m × 5 m floor area and 4 m-high compartment having 0.00635 m- (0.25 in.)-thick, 0.5 percent carbon steel walls. The forced-ventilation rate is 2.4 m³/s of air (5000 cfm). Perform the calculation for $t = 200$ s. The fire size is given as 1000 kW; ambient air conditions at 300 K. Using equation 17a,

$$T_g - T_\infty = \frac{\dot{Q}}{\dot{m}_g c_p + h_k A_T}$$

where

$$\dot{Q} = 1000 \text{ kW}$$

$$\dot{m}_g = (2.4 \text{ m}^3/\text{s}) (1.18 \text{ kg/m}^3) = 2.8 \text{ kg/s}$$

$$c_p = 1.0 \text{ kJ/kg·K}$$

$$T_\infty = 300 \text{ K}$$

$$A_T = 4(5 \times 4) + 2(5 \times 5) = 105 \text{ m}^2$$

- a. Using equation 25, calculate h_k for $t = 200$ s. For 0.25-m-thick, 0.5 percent carbon steel,

$$\delta = 0.00635 \text{ m}$$

$$\rho = 7833 \text{ kg/m}^3$$

$$c = 0.465 \text{ kJ/kg}\cdot\text{K}$$

$$\begin{aligned} h_k &= 30 - 18 \left[1 - \exp \left(-\frac{50}{\rho \delta c} t \right) \right] \\ &= 30 - 18 \left\{ 1 - \exp \left[-\frac{50}{(7833)(0.00635)(0.465)} 200 \right] \right\} \\ &= 12 \text{ kW/m}^2\cdot\text{K} \end{aligned}$$

- b. Calculate the compartment temperature using Equation 17a.

$$\begin{aligned} T_g - 300 &= \frac{1000}{(2.8)(1.0) + (12)(105)} \\ T_g &= 301 \text{ K} \end{aligned}$$

Method of Beyler

For compartments with no ventilation the quasi-steady approximation used in many of the methods is not appropriate since the conditions in the compartment will not reach steady state. Beyler applied a nonsteady energy balance to the closed compartment expressed by the differential equation¹⁵

$$mc_p \frac{dT}{dt} = \dot{Q} = h_k A_T \Delta T_g \quad (26)$$

where

\dot{Q} = energy (heat) release rate of the fire (kw)

m = mass of the gas in the compartment (kg/s)

c_p = specific heat of gas (kJ/kg·K)

$\Delta T_g = T_g - T_\infty$

T_g = temperature of the upper gas layer (k)

T_∞ = ambient temperature (K)

h_k = effective heat transfer coefficient (kW/m·K)

A_T = total area of the compartment enclosing surfaces (m²)

ρ = density of the compartment surface (kg/m³)

δ = thickness of the compartment surface (m)

t = exposure time (s)

In this case a "closed" compartment has sufficient leaks to prevent pressure buildup, but the leakage is ignored. The mass of the fuel is ignored, and the initial temperature is assumed to be ambient temperature. For constant heat release rate, the solution to Equation 26 is

$$\Delta T_g = \frac{2K_2}{K_1^2} (K_1 \sqrt{t} - 1 + e^{-K_1 \sqrt{t}}) \quad (27)$$

where

$$K_1 = \frac{2(0.4\sqrt{kpc})}{mc_p} \quad (28)$$

$$K_2 = \frac{\dot{Q}}{mc_p} \quad (29)$$

where

k = thermal conductivity of the compartment surface (kW/m·K)

c = specific heat of the compartment surface material (kJ/kg·K)

which include the fitting coefficient. Beyler used data with a maximum temperature rise of 150°C to develop this correlation.

Example of Beyler method: Estimate the temperature in a 5 m × 5 m in floor area and 4-m-high "closed" compartment having 0.025 m-(1 in.)-thick concrete walls. Perform the calculation for $t = 120$ s. The fire size is given as 100 kW; ambient air conditions at 300 K. Using Equation 27,

$$\Delta T = \frac{2K_2}{K_1^2} (K_1 \sqrt{t} - 1 + e^{-K_1 \sqrt{t}})$$

where

$$T_\infty = 300 \text{ K}$$

$$t = 120 \text{ s}$$

- a. Calculate K_1 using Equation 28.

$$\begin{aligned} K_1 &= \frac{2(0.4\sqrt{kpc})}{mc_p} \\ &= \frac{2(0.4\sqrt{(1.4 \times 10^{-3})(2000)(0.88)})}{(118)(1.0)} \\ &= 0.01064 \end{aligned}$$

where

$$m = (100 \text{ m}^3)(1.18 \text{ kg/m}^3) = 118 \text{ kg}$$

$$c_p = 1.0 \text{ kJ/kg}\cdot\text{K}$$

$$\rho = 2000 \text{ kg/m}^3$$

$$k = 1.4 \times 10^{-3} \text{ kW/m}\cdot\text{K}$$

$$c = 0.88 \text{ kJ/kg}\cdot\text{K}$$

- b. Calculate K_2 using Equation 29.

$$\begin{aligned} K_2 &= \frac{\dot{Q}}{mc_p} \\ &= \frac{100}{(118)(1.0)} \\ &= 0.84746 \end{aligned}$$

where

$$m = (100 \text{ m}^3)(1.18 \text{ kg/m}^3) = 118 \text{ kg}$$

$$c_p = 1.0 \text{ kJ/kg}\cdot\text{K}$$

- c. Calculate the compartment temperature using Equation 27.

$$\begin{aligned} T_g - 300 &= \frac{(2)(0.84746)}{(0.01064)^2} ((0.01064)\sqrt{120} - 1 + e^{-(0.01064)\sqrt{120}}) \\ T_g &= 397.8 \text{ K} \end{aligned}$$

Methods for Predicting Postflashover Compartment Fire Temperatures

Method of Babrauskas

The following method is based on the work of Babrauskas.^{18,19} The upper gas temperature, T_g , is expressed according to a series of factors, each one accounting for a different physical phenomenon:

$$T_g = T_\infty + (T^* - T_\infty) \cdot \theta_1 \cdot \theta_2 \cdot \theta_3 \cdot \theta_4 \cdot \theta_5 \quad (30)$$

where T^* is an empirical constant = 1725 K, and the factors θ are in Equations 36, 41, 43, 44, 46, and 47.

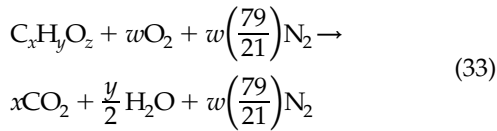
Burning rate stoichiometry, θ_1 : The dimensionless stoichiometric coefficient ϕ is defined as

$$\phi = \frac{\dot{m}_f}{\dot{m}_{f,st}} \quad (31)$$

where \dot{m} is the fuel mass pyrolysis rate (kg/s), and $\dot{m}_{f,st}$ is the stoichiometric mass burning rate (i.e., no excess fuel and no excess oxygen).

$$\dot{m}_{f,st} = \frac{0.5A_0\sqrt{H_0}}{r} \quad (32)$$

where the ratio r is such that 1 kg fuel + r kg air \rightarrow (1 + r) kg products. The value of r is readily computable for fuels containing carbon, hydrogen, and/or oxygen from the chemical formula of the fuel, taking the products to be CO_2 , H_2O , and N_2 .



where

$$w = \frac{2x + y/2 - z}{2} \quad (34)$$

and

$$r = \frac{[w + w(3.76)]28.97}{12.01x + 1.00y + 16.00z} \quad (35)$$

At stoichiometry $\phi = 1$, and it is greater than 1 for fuel-rich burning and less than 1 for fuel-lean conditions.

The effect of ϕ on gas temperatures was evaluated by numerical computations using the COMPF2 computer program.²⁰ The efficiency factor, θ_1 , accounts for deviation from stoichiometry and is shown in Figure 3-6.3. It is seen that the fuel-lean and the fuel-rich regimes exhibit a very different dependence. For the fuel-lean regime, the results can be approximated by

$$\theta_1 = 1.0 + 0.51 \ln \phi \quad \text{for } \phi < 1 \quad (36)$$

Similarly, in the fuel-rich regime a suitable approximation is

$$\theta_1 = 1.0 - 0.05(\ln \phi)^{5/3} \quad \text{for } \phi > 1 \quad (37)$$

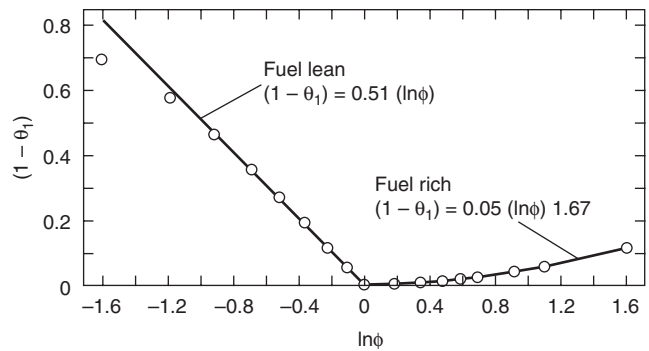


Figure 3-6.3. Effect of equivalence ratio.

If heat release rate, \dot{Q} , rather than mass loss rate, \dot{m} , is used, then

$$\phi = \frac{\dot{Q}}{\dot{Q}_{\text{stoich}}} \quad (38)$$

And, since the stoichiometric heat release rate is

$$\dot{Q} = 1500A_0\sqrt{H_0} \quad (39)$$

then

$$\phi = \frac{\dot{Q}}{1500A_0\sqrt{H_0}} \quad (40)$$

The value of \dot{Q} can be determined from Section 3, Chapter 1.

A separate procedure is necessary for pool fires, due to the strong radiative coupling. Here

$$\theta_1 = 1.0 - 0.092(-\ln \eta)^{1.25} \quad (41)$$

where

$$\eta = \left(\frac{A_0\sqrt{H_0}}{A_f} \right) \frac{0.5\Delta h_p}{r\sigma(T_g^4 - T_b^4)} \quad (42)$$

where

Δh_p = heat of vaporization of liquid (kJ/kg)

A_f = pool area (m^2)

σ = Stefan-Boltzmann constant ($5.67 \times 10^{-11} \text{ kW/m}^2\text{K}^4$)

T_b = liquid boiling point temperature (K)

This expression unfortunately requires an estimate for T_g to be made, so for the pool fire case, a certain amount of iteration is necessary. The relationship above is plotted in Figure 3-6.4.

Wall steady-state losses, θ_2 : The next efficiency factor, θ_2 , accounts for variable groups of importance involving the wall surface (which is defined to include the ceiling) properties: area $A_T(\text{m}^2)$, thickness L (m), density ρ (kg/m^3), thermal conductivity k ($\text{kW/m}\cdot\text{K}$), and heat capacity $c_p(\text{kJ/kg}\cdot\text{K})$. This factor is given as

$$\theta_2 = 1.0 - 0.94 \exp \left[-54 \left(\frac{A_0\sqrt{H_0}}{A_T} \right)^{2/3} \left(\frac{L}{k} \right)^{1/3} \right] \quad (43)$$

and is shown in Figure 3-6.5.

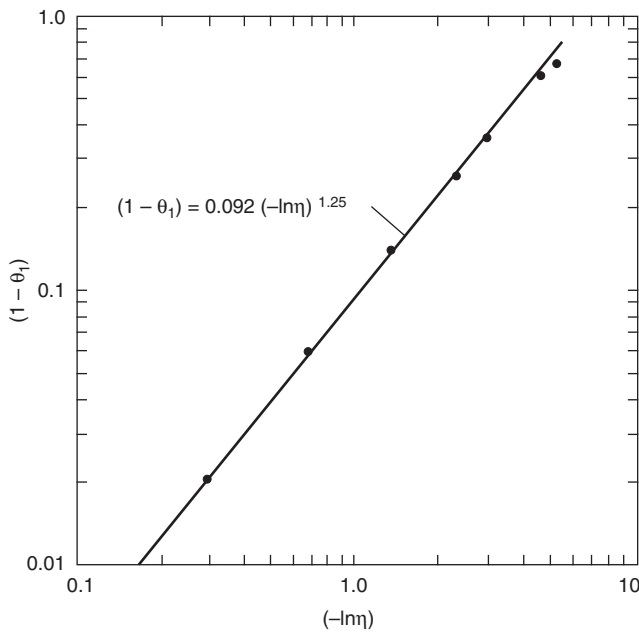


Figure 3-6.4. Effect of pool diameter.

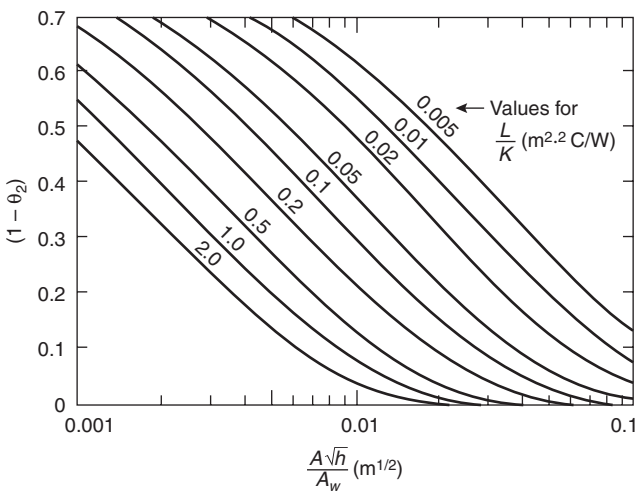


Figure 3-6.5. Effect of wall steady-state losses.

Wall transient losses, θ_3 : For the transient case, the above relationship predicts the asymptotic temperature value. An additional time-dependent factor, however, is needed. See Figure 3-6.6.

$$\theta_3 = 1.0 - 0.92 \exp \left[-150 \left(\frac{A_0\sqrt{H_0}}{A_T} \right)^{0.6} \left(\frac{t}{kpc_p} \right)^{0.4} \right] \quad (44)$$

If only steady-state temperatures need to be evaluated, then $\theta_3 = 1.0$.

Wall effects for t just slightly greater than zero are not well modeled with the above relationships for $\theta_2 \times \theta_3$; however, this condition is not a serious limitation, since the method is only designed for postflashover fires.

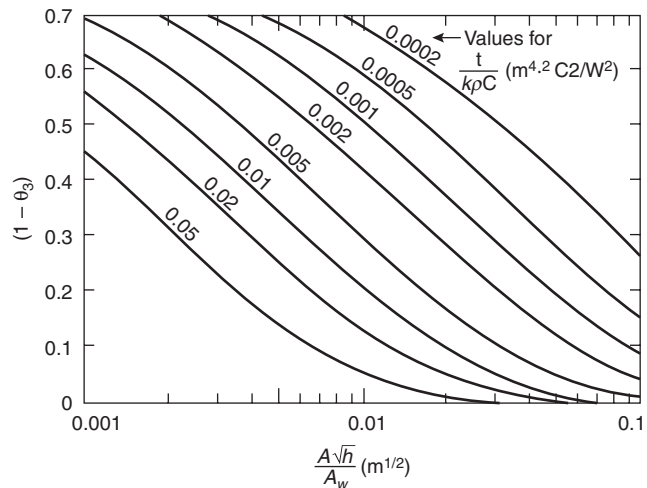


Figure 3-6.6. Effect of wall transient losses.

For transient fires, the possibility of two separate effects must be considered. First, the wall loss effect, represented by Equation 44, in all fires, exhibits a nonsteady character. Second, the fuel release rate may not be constant. Since in the calculational procedure the previous results are not stored, it is appropriate to restrict consideration to fires where \dot{m}_f does not change drastically over the time scale established by θ_3 . This "natural" time scale can be determined as the time when the response has risen to 63 percent of its ultimate value, that is, at $\theta_3 = 0.63$, and is

$$t = 2.92 \times 10^{-6} (kpc_p) \left(\frac{A_T}{A_0\sqrt{H_0}} \right)^{1.5} \quad (45)$$

Opening height effect, θ_4 : The normalization of burning rate and wall loss quantities with the ventilation factor $A_0\sqrt{H_0}$ does not completely determine the total heat balance. An opening of a given $A_0\sqrt{H_0}$ can be tall and narrow or short and squat. For the shorter opening, the area will have to be larger. Radiation losses are proportional to the opening area and will, therefore, be higher for the shorter opening. By slight simplification, a representation for θ_4 can be made as

$$\theta_4 = 1.0 - 0.205 H_0^{-0.3} \quad (46)$$

as shown in Figure 3-6.7.

Combustion efficiency, θ_5 : The fire compartment is viewed as a well, but not perfectly, stirred reactor. Thus a certain "unmixedness" is present. A maximum combustion efficiency, b_p , can be used to characterize this state. Since the model assumes infinitely fast kinetics, any limitations can also be included here. Data have not been available to characterize b_p in real fires, but agreement with measured fires can generally be obtained with b_p values in the range 0.5 to 0.9. The effect of b_p variation can be described by

$$\theta_5 = 1.0 + 0.5 \ln b_p \quad (47)$$

as shown in Figure 3-6.8.

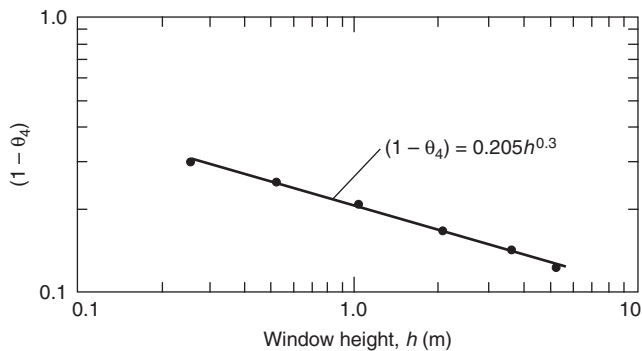


Figure 3-6.7. Effect of window height.

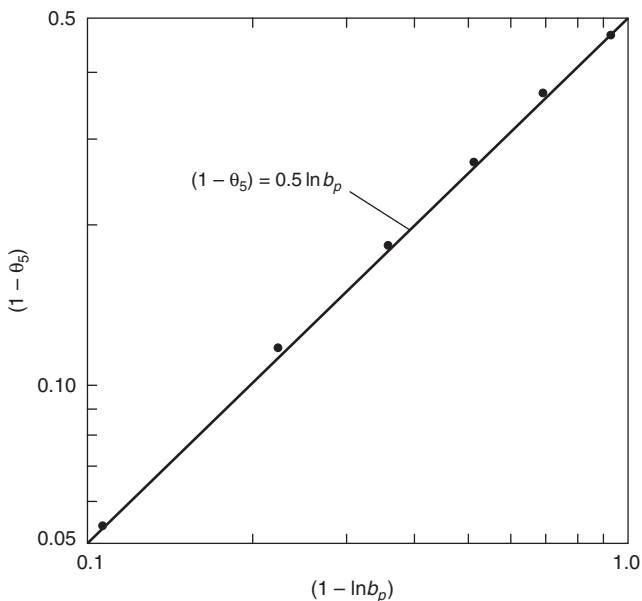


Figure 3-6.8. Effect of b_p , the maximum combustion efficiency.

Method of Law

The area of structural surface to which heat is lost is expressed by $(A_T - A_0)$. For a given fire load, compartments with different values of A_T , A_0 , and height H_0 will have a different heat balance, and thus the temperatures in the compartments will differ. This is illustrated in Figure 3-6.9 which shows how temperature varies with

$$\Omega = \frac{(A_T - A_0)}{A_0 \sqrt{H_0}}$$

For low values of Ω (i.e., high ventilation), the rate of heat release is at a maximum, but the heat loss from the window is also large and the resultant temperature is low. For high values of Ω (i.e., low-ventilation areas), there is little heat loss to the outside, but the rate of heat release is also small and the resultant temperature is, again, low.

The curve in Figure 3-6.10 has been derived from many experimental fires conducted internationally by CIB.⁸ For design purposes, Law has defined it as follows:

$$T_{g(\max)} = 6000 \frac{(1 - e^{-0.1\Omega})}{\sqrt{\Omega}} \quad (48)$$

where

$$\Omega = \frac{(A_T - A_0)}{A_0 \sqrt{H_0}}$$

and

A_T = total area of the compartment enclosing surfaces (m^2)

A_0 = area of opening (m^2)

H_0 = height of opening (m)

This equation represents an upper limit of fire temperature rise for a given Ω . However, if the fire load is low, this value may not be obtained. The importance of the effect of fire load also depends on A_0 and A_T , and can be expressed as

$$T_g = T_{g(\max)}(1 - e^{-0.05\psi}) \quad (49)$$

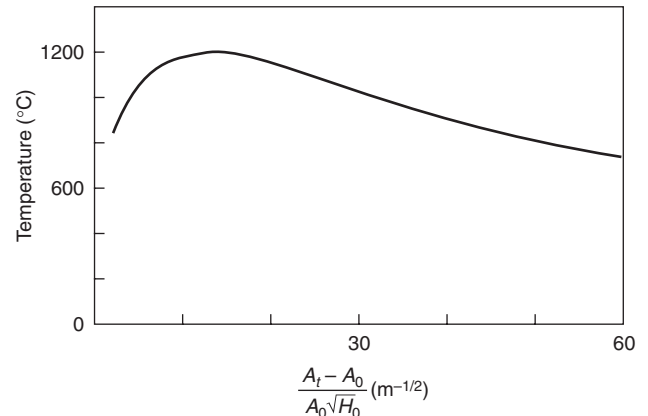


Figure 3-6.9. Average temperature during fully developed period measured in experimental fires in compartments.

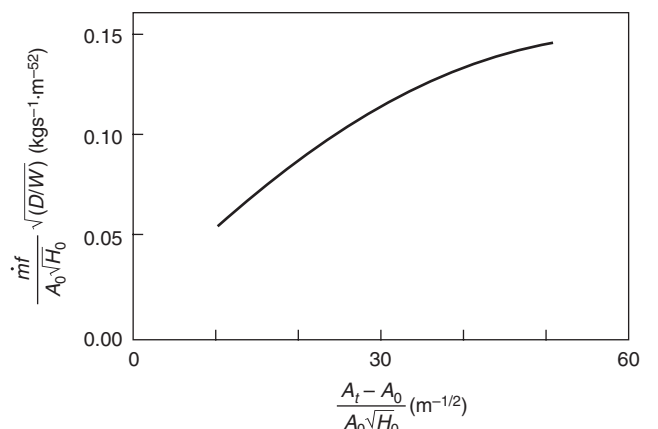


Figure 3-6.10. Variation of a rate of burning during fully developed period measured in experimental fires in compartments.

where

$$\psi = \frac{L}{[A_0(A_T - A_0)]^{0.5}}$$

where L is the fire load (wood) in kg.

The effect of the fire on the structure depends not only on the value of T_g but also on the duration of heating. The effective fire duration, τ , in seconds, is given by

$$\tau = \frac{L}{\dot{m}_f} \quad (50)$$

where \dot{m}_f is the rate of burning measured in kg/s.

Equation 6 implies that the smaller the value of $A_0\sqrt{H_0}$ the lower the rate of burning and the longer the duration. Assuming a complete burnout, therefore, the effect on the structure tends to be more severe for large values of Ω given for small $A_0\sqrt{H_0}$.

For design purposes the following equation has been developed to express the correlation of experimental results:⁹

$$\dot{m}_f = 0.18A_0\sqrt{H_0}(W/D)1 - e^{-0.036\Omega}\xi < 60 \quad (51)$$

where

W = compartment width (m)

D = compartment depth (m)

$$\xi = \frac{\dot{m}_f}{A_0\sqrt{H_0}} \left(\frac{D}{W} \right)^{1/2}$$

Equation 51 is shown in Figure 3-6.10 over the range where the data lie. Both equations are for ventilation-controlled fires. When there is ample ventilation, so that the fuel is free burning, the value of \dot{m}_f depends on L and the type of fuel. For example, domestic furniture has a free-burning fire duration of about 20 min, giving $\tau = 1200$ s and $\dot{m}_f = L/1200$.

The temperatures discussed above are averages measured during the fully developed period of the fire. It is assumed that all fires are ventilation controlled, with the simple relationship for rate of burning given by Equation 51, which is near stoichiometric burning, and it is assumed that combustion of 1 kg of wood releases 18.8 MJ in total.

Swedish Method

The Swedish method, developed by Magnusson and Thelandersson,¹⁰ is based on the conventional mass and energy balance equations. The fire itself is not modeled; heat release rate curves are provided as input and, in all instances, the energy release must be less than stoichiometric. The method does not take into account that the actual mass loss rate may be greater than stoichiometric, with the excess fuel burning outside the compartment. A computer program SFIRE (versions 1 through 3) is available to perform this method. The results from the computer program have been compared with a large number of full-scale fire experiments, both in the fuel- and ventilation controlled regimes, with good agreement between theory and experiment. It should be added, however, that most of the experiments involved wood crib fires, which inherently burn slower and produce less excess fuel load than furnishings and other combustibles found in practi-

cal fire loads. In the Swedish method, the fire load is expressed in relation to A_T as $\dot{Q} 18.8 L/A_T$ MJ/m².

The design curves approved by the Swedish authorities were computed on the basis of systemized ventilation-controlled heat-release curves taken from Reference 10. Figure 3-6.11 shows some typical curves. The curves are calculated for wall, floor, and ceiling materials with "normal" thermal properties from an energy balance which assumes a uniform temperature in the compartment.

Predicting Flashover

One of the uses of predicted compartment fire temperatures is the estimation of the likelihood of flashover. The methods used are similar to those used in the prediction of temperature. In one case, that of McCaffrey et al., the method is simply an extension of the temperature calculation.

Method of Babrauskas

Babrauskas uses the energy balance for the upper layer given in Equation 7, where the gas flow rate out of the opening is approximated by²¹

$$\dot{m}_g \approx 0.5A_0\sqrt{H_0} \quad (52)$$

The primary energy loss is assumed to be radiation to 40 percent of the wall area which is at approximately ambient temperature:

$$q_{\text{loss}} = \varepsilon\sigma(T_g^4 - T_\infty^4)(0.40A_T) \quad (53)$$

where

ε = emissivity of the hot gas

σ = Stefan-Boltzmann constant 5.67×10^{11} kW/m²K⁴

Combining Equations 7, 52, and 53, using a gas temperature for flashover of 873 K, a specific heat of air of 1.0 kJ/kg·K, an emissivity of 0.5, and assuming the correlation between compartment wall and opening area of

$$\frac{A_T}{A_0\sqrt{H_0}} \approx 50$$

yields a minimum \dot{Q} required for flashover,

$$\dot{Q} = 600A_0\sqrt{H_0} \quad (54)$$

The air flow into the compartment has been approximated as

$$0.5A_0\sqrt{H_0}$$

The maximum amount of fuel which can be burned completely with this air is known as the stoichiometric amount. For most fuels, the heat released per mass of air consumed is a constant approximately equal to 3000 kJ/kg. Therefore, the stoichiometric heat release rate \dot{Q}_{stoich} can be calculated

$$\begin{aligned} \dot{Q}_{\text{stoich}} &= 3000\dot{m}_g = 3000(0.5A_0\sqrt{H_0}) \\ &= 1500A_0\sqrt{H_0} \end{aligned} \quad (55)$$

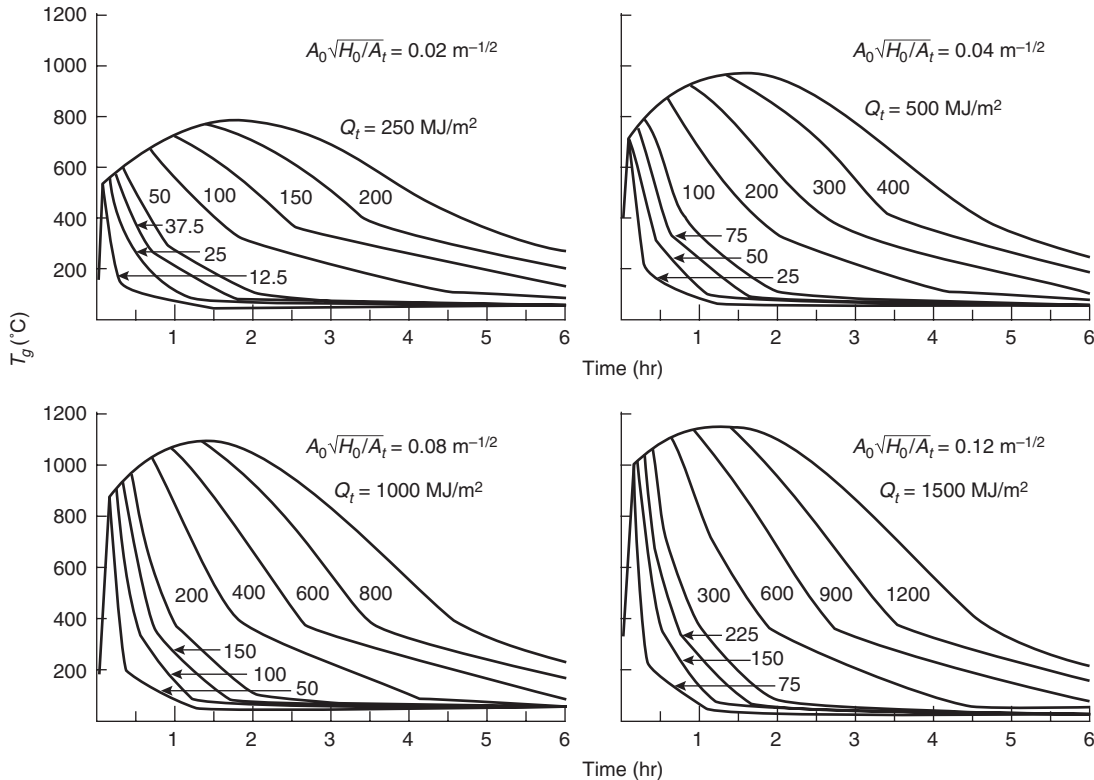


Figure 3-6.11. Examples of gas temperature-time curves of postflashover compartment fires for different values of the fire load density \dot{Q}_t , MJ per unit of total internal surface area, A_t , and the opening factor $A_0\sqrt{H_0/A_t}$. Fire compartment, type A—from authorized Swedish standard specifications.¹⁰

From this derivation, it is shown that the minimum \dot{Q} required for flashover equals $0.4 \dot{Q}_{\text{stoich}}$. Comparing these results with fire tests, Babrauskas found that the data falls within a range of $\dot{Q} = 0.3\dot{Q}_{\text{stoich}}$ to $\dot{Q} = 0.7\dot{Q}_{\text{stoich}}$. A best fit of the data suggests

$$\dot{Q} = 0.5\dot{Q}_{\text{stoich}}$$

which, substituting into Equation 55 yields

$$\dot{Q} = 750A_0\sqrt{H_0} \quad (56)$$

The 33 test fires used had energy release rates from 11 to 3840 kW, with fuels primarily of wood and polyurethane. Ventilation factors $A_0\sqrt{H_0}$ ranged from 0.03 to 7.51 $\text{m}^{5/2}$, and surface area to ventilation factor ratios

$$\frac{A_T}{A_0\sqrt{H_0}}$$

ranged from 9 to 65 $\text{m}^{-1/2}$.

Example of Babrauskas' method: Calculate the heat release rate necessary to cause flashover, using the method of Babrauskas. Assume the same room as in the McCaffrey et al. method example for predicting compartment fire temperatures. From Equation 56

$$\dot{Q} = 750A_0\sqrt{H_0}$$

where

$$A_0 = 1.08 \text{ m}^2$$

$$H_0 = 1.8 \text{ m}$$

$$\dot{Q} = (750)(1.08)(1.8)^{1/2} = 1087 \text{ kW}$$

Method of McCaffrey, Quintiere, and Harkleroad

The method of McCaffrey, Quintiere, and Harkleroad for predicting compartment fire temperatures may be extended to predict the energy release rate of the fire required to result in flashover in the compartment.

Equation 11 can be rewritten as

$$\dot{Q} = \left[\sqrt{g}c_p\rho_\infty T_\infty^2 \left(\frac{\Delta T_g}{480} \right)^3 \right]^{1/2} (h_k A_T A_0 \sqrt{H_0}) \quad (57)$$

Selecting an upper gas temperature of 522°C and ambient temperature of 295 K or $\Delta T_g = 500^\circ\text{C}$ for flashover, and substituting values for the gravitational constant ($g = 9.8 \text{ m/s}^2$), the specific heat of air ($c_p = 1.0 \text{ kJ/kg}\cdot\text{K}$), and the density of air ($\rho_\infty = 1.18 \text{ kg/m}^3$), and rounding 607.8 to 610 yields

$$\dot{Q} = 610(h_k A_T A_0 \sqrt{H_0})^{1/2} \quad (58)$$

where

$$h_k = \text{effective heat transfer coefficient } [(\text{kW/m})/\text{K}]$$

$$A_T = \text{total area of the compartment surfaces } (\text{m}^2)$$

$$A_0 = \text{area of opening } (\text{m}^2)$$

$$H_0 = \text{height of opening } (\text{m})$$

Using Equation 12 yields a slightly different value, 623.6 rounded to 620, of the leading coefficient because of the difference in the value used for the specific heat of air

$$\dot{Q} = 620(h_k A_T A_0 \sqrt{H_0})^{1/2} \quad (59)$$

The use of either 610 or 620 is acceptable within the accuracy of the expression.

Example of McCaffrey et al. method: Estimate the energy release rate required for flashover of a compartment. Assume the same room as in the McCaffrey et al. method example for predicting compartment fire temperatures. Assuming $\Delta T_g = 500^\circ\text{C}$ as a condition for flashover, and air properties at 295 K, use Equation 45

$$\dot{Q} = 610(h_k A_T A_0 \sqrt{H_0})^{1/2}$$

where

$$h_k = \frac{k}{\delta} = \frac{0.48 \times 10^{-3}}{0.016} = 0.03 \text{ kW/m}\cdot\text{K}$$

$$A_T = 45.72 \text{ m}^2$$

$$A_0 = 1.08 \text{ m}^2$$

$$H_0 = 1.8 \text{ m}$$

Therefore,

$$\begin{aligned} \dot{Q} &= 610[(0.03)(45.72)(1.08)(\sqrt{1.8})]^{1/2} \\ &= 860 \text{ kW} \end{aligned}$$

Method of Thomas

Thomas uses the energy balance for the upper layer shown in Equation 7, where the gas flow rate out of the opening is approximated by²

$$\dot{m}_g \approx 0.5 A_0 \sqrt{H_0} \quad (60)$$

Thomas develops an expression for \dot{q}_{loss} which assumes the area for the source of radiation for roughly cubical compartments is $A_T/6$:

$$\dot{q}_{\text{loss}} \approx h_c(T_g - T_w) \frac{A_T}{2} + \varepsilon \sigma (2T_g^4 - T_w^4 - T_{\text{flr}}^4) \frac{A_T}{6} \quad (61)$$

where

$$A_T = \text{total area of the compartment-enclosing surfaces (m}^2\text{)}$$

$$h_c = \text{convective heat transfer coefficient (kW/m}^2\text{K)}$$

$$T_w = \text{temperature of the upper walls (K)}$$

$$T_{\text{floor}} = \text{temperature of the floor (K)}$$

From experimental data, Thomas developed an average for \dot{q}_{loss} of $7.8 A_T$. Using an upper layer temperature of 577°C or a ΔT_g of 600°C for flashover criterion and $c_p = 1.26 \text{ kJ/kg}\cdot\text{K}$ yields an expression for the minimum rate of energy release for flashover:

$$\dot{Q} = 7.8 A_T + 378 A_0 \sqrt{H_0} \quad (62)$$

Comparison of Methods for Predicting Flashover

Babrauskas has compared the effect of room wall area on the energy release required for flashover, using the above methods.²² The results of his comparisons, along with some experimental data for rooms with gypsum board walls, are shown in Figure 3-6.12. The graph shows the energy required for flashover as a function of compartment wall area, both normalized by the ventilation factor $A_0 \sqrt{H_0}$. Babrauskas observes that over the range of compartment sizes of most interest, all of the methods produce similar results. The method of McCaffrey et al. diverges from the others for small room sizes. Babrauskas notes that all of the methods are a conservative representation of the data.

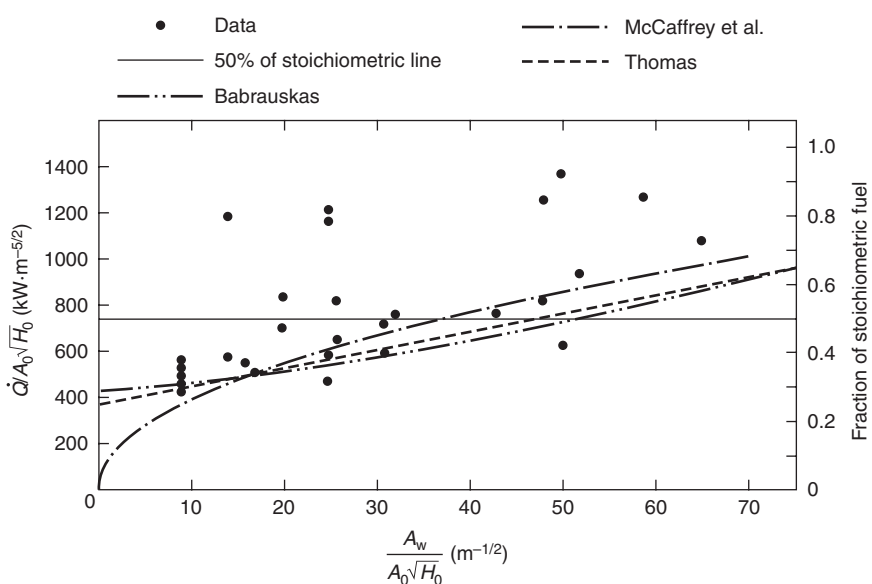


Figure 3-6.12. The effect of room wall area (gypsum walls) on the heat required for flashover.

Nomenclature

A_T	total area of the compartment enclosing surfaces (m^2)
A_{ceiling}	area of compartment ceiling (m^2)
A_f	pool fire area (m^2)
A_{floor}	area of compartment floor (m^2)
A_{openings}	area of compartment openings (m^2)
A_{walls}	area of compartment walls (m^2)
c	specific heat of the wall ($\text{kJ/kg}\cdot\text{K}$)
C_d	orifice constriction coefficient
c_p	specific heat of gas ($\text{kJ/kg}\cdot\text{K}$)
D	compartment depth (m)
g	acceleration due to gravity, 9.8 m/s^2
h_c	convective heat transfer coefficient
Δh_c	effective heat of combustion of the fuel (kJ/kg)
h_g	heat transfer coefficient on the hot side of the wall ($\text{kW/m}\cdot\text{K}$)
h_k	effective heat transfer coefficient ($\text{kW/m}\cdot\text{K}$)
h_∞	heat transfer coefficient on the ambient side of the wall ($\text{kW/m}\cdot\text{K}$)
H_o	opening height (m)
k	thermal conductivity of the wall ($\text{kW/m}\cdot\text{K}$)
L	fire load, wood (kg)
m	mass of the gas in the compartment (kg/s)
\dot{m}_a	mass flow rate of air into an opening (kg/s)
\dot{m}_g	gas flow rate out the opening (kg/s)
\dot{m}_f	mass burning rate of fuel (kg/s)
$\dot{m}_{f,\text{st}}$	stoichiometric mass burning rate of fuel (kg/s)
\dot{m}_w''	mass per unit area of the wall (kg/m^2)
q_{loss}	net radiative and convective heat transfer from the upper gas layer (kW)
\dot{Q}	energy (heat) release rate of the fire (kW)
\dot{Q}_{stoich}	stoichiometric heat release rate (kW)
t	time (s)
t_p	thermal penetration time (s)
T_b	liquid boiling point (K)
T_{flr}	temperature of the floor (K)
T_g	temperature of the upper gas layer (K)
T_w	wall temperature (K)
T_∞	ambient temperature (K)
W	compartment width (m)
W_o	opening width (m)
X_d	height of the interface (m)
X_N	height of neutral plane (m)

Greek characters

δ	thickness of the wall (m)
ε	emissivity of the hot gas
ρ	density of the wall (kg/m^3)
ρ_∞	ambient air density (kg/m^3)
σ	Stefan-Boltzmann constant, $5.67 \times 10^{-11} \text{ kW/m}^2 \cdot \text{K}^4$

Subscripts

a	air
b	boiling
ceiling	ceiling
d	thermal discontinuity
f	fuel
g	gas
floor	floor
loss	loss
N	neutral plane
o	opening
openings	openings
p	penetration
stoich	stoichiometric
T	total
w	wall
walls	walls
∞	ambient

Superscripts

\cdot	per unit time (s^{-1})
$"$	per unit area (m^{-1})

References Cited

1. D. Drysdale, "The Pre-Flashover Compartment Fire," *An Introduction to Fire Dynamics*, John Wiley and Sons, Chichester, England, pp. 278–303 (1985).
2. P.H. Thomas, "Testing Products and Materials for Their Contribution to Flashover in Rooms," *F. and Matls.*, 5, 3, pp. 103–111 (1981).
3. C. Huggett, "Estimation of Rate of Heat Release by Means of Oxygen Consumption Measurements," *F. and Matls.*, 4, 2, pp. 61–65 (1980).
4. J. de Ris, *Fire Radiation—A Review*, Tech. Report FMRC, RC78-BT-27, Factory Mutual Research Corporation, Norwood, pp. 1–41 (1978).
5. J.A. Rockett, "Fire Induced Gas Flow in an Enclosure," *Comb. Sci. and Tech.*, 12, pp. 165–175 (1976).
6. P.H. Thomas and A.J.M. Heselden, "Fully Developed Fires in Single Compartments," *Fire Research Note No. 923*, Fire Research Station, Borehamwood, England (1972).
7. K. Kawagoe, "Fire Behaviour in Rooms," Report of the Building Research Institute, Ibaraki-ken, Japan, No. 27 (1958).
8. P.H. Thomas and A.J.M. Heselden, "Fully Developed Fires in Single Compartments," *CIB Report No. 20*, A Co-operating Research Programme of the Conseil International du Batiment, Joint Fire Research Organization Fire Research Note 923/197.
9. M. Law, *Structural Engr.*, 61A, 1, p. 25 (1983).
10. S.E. Magnusson and S. Thelandersson, "Temperature-Time Curves of Complete Process of Fire Development. Theoretical Study of Wood Fuel Fires in Enclosed Spaces," *Civil Engineering and Building Construction Series No. 65*, Acta Polytechnica Scandinavica, Stockholm, Sweden (1970).
11. B.J. McCaffrey, J.G. Quintiere, and M.F. Harkleroad, "Estimating Room Fire Temperatures and the Likelihood of Flashover Using Fire Test Data Correlations," *Fire Tech.*, 17, 2, pp. 98–119 (1981).

12. J.G. Quintiere, "A Simple Correlation for Predicting Temperature in a Room Fire," *NBSIR 83-2712*, National Bureau of Standards, Washington, D.C. (June 1983).
13. J.R. Lawson and J.G. Quintiere, "Slide-Rule Estimates of Fire Growth," *NBSIR 85-3196*, National Bureau of Standards, Washington, D.C. (June 1985).
14. K.L. Foote, P.J. Pagni, and N.J. Alvares, "Temperature Correlations for Forced-Ventilated Compartment Fires," in *Proceedings of the First International Symposium*, International Association for Fire Safety Science, Hemisphere Publishing, pp. 139-148 (1986).
15. C. Beyler, "Analysis of Compartment Fires with Forced Ventilation," *Fire Safety Science—Proceedings of the Third International Symposium*, Elsevier Science, New York, pp. 291-300 (1991).
16. S. Deal and C. Beyler, "Correlating Preflashover Room Fire Temperatures," *J. of Fire Prot. Engr.*, 2, 2, pp. 33-88 (1990).
17. M. J. Peatross and C.L. Beyler, "Thermal Environmental Prediction in Steel-bounded Preflashover Compartment Fires," in *Fire Safety Science—Proceedings of the Fourth International Symposium*, International Association for Fire Safety Science, Boston, pp. 205-216 (1994).
18. V. Babrauskas, "A Closed-form Approximation for Post-Flashover Compartment Fire Temperatures," *F. Safety J.*, 4, pp. 63-73 (1981).
19. V. Babrauskas and R. B. Williamson, "Post-Flashover Compartment Fires: Basis of a Theoretical Model," *Fire and Matls.*, 2, 2, pp. 39-53 (1978).
20. V. Babrauskas, "COMPF2—A Program for Calculating Post-Flashover Fire Temperatures," *NBS TN 991*, National Bureau of Standards, Washington, D.C. (1979).
21. V. Babrauskas, "Estimating Room Flashover Potential," *Fire Tech.*, 16, 2, pp. 94-104 (1980).
22. V. Babrauskas, "Upholstered Furniture Room Fires—Measurements, Comparison with Furniture Calorimeter Data, and Flashover Predictions," *J. of F. Sci.*, 2, pp. 5-19 (1984).

CHAPTER 7

Zone Computer Fire Models for Enclosures

William D. Walton.

Introduction

Computer programs are used in many areas of fire protection design, including suppression system design, smoke control system design, and egress analysis. The emphasis in this chapter is on zone computer fire models for enclosures. Zone fire models are computer programs designed to predict the conditions resulting from a fire in an enclosure. These models solve the equations based on the zone assumptions describing the fire-induced conditions within an enclosure.

Computer fire models can provide a faster and more accurate estimate of the impact of a fire and the measures used to prevent or control the fire than many of the methods previously used. While manual calculation methods provide good estimates of specific fire effects (e.g., prediction of time to flashover), they are not well suited for comprehensive analyses involving the time-dependent interactions of multiple physical and chemical processes present in developing fires.

The state of the art in computer fire modeling is changing rapidly. Understanding of the processes involved in fire growth is improving, and, thus, the technical basis for the models is improving. The capabilities, documentation, and support for a given model can change dramatically over a short period of time. In addition, computer technology itself (both hardware and software) is advancing rapidly. A few years ago, a large mainframe computer was required to use most of the computer fire models. Today, all of the zone fire models can be run on personal computers. Therefore, rather than provide an exhaustive review of rapidly changing state-of-the-art available computer models, the following discussion will focus on a representative selection. The reader is guided to References 1 and 2 for a comprehensive review of computer fire models.

Mr. William D. Walton is a research fire protection engineer with the Building and Fire Research Laboratory, National Institute of Standards and Technology.

Enclosure Fire Models

There are two major classes of computer models for analyzing enclosure fire development. *Stochastic* or *probabilistic* models generally treat fire growth as a series of sequential events or states. These models are sometimes referred to as *states transition models*. Mathematical rules are established to govern the transition from one event to another (e.g., from ignition to established burning). Probabilities are assigned to each transfer point based on analysis of relevant experimental data, historical fire incident data, and computer model results. For a complete discussion of stochastic models, see Section 3, Chapter 16.

In contrast, *deterministic* models represent the processes encountered in a compartment fire by interrelated mathematical expressions based on physics and chemistry. These models may also be referred to as *room fire models*, *computer fire models*, or *mathematical fire models*. Ideally, such models represent the ultimate capability: discrete changes in any physical parameter could be evaluated in terms of the effect on fire hazard. While the state of the art in understanding fire processes will not yet support the *ultimate* model, a number of computer models are available that provide reasonable estimates of selected fire effects.

The newest type of deterministic fire model is the *field* model. This type of model solves the fundamental equations of mass, momentum, and energy for each element in an enclosure space that has been divided into a grid of smaller units. A complete discussion of field modeling can be found in Section 3, Chapter 8. Although field model technology and use have advanced rapidly in recent years, it should be noted that field models require substantial computer resources and are relatively complex to use.

The most common type of physically based fire model is the *zone* or *control volume* model, which solves the conservation equations for distinct and relatively large regions (control volumes). A complete discussion of the fundamental principles behind the zone fire model formulation can be found in Section 3, Chapter 5. A number of

zone models exist, varying to some degree in the detailed treatment of the fire phenomena. The dominant characteristic of this type of model is that it divides the room(s) into a hot, upper layer and a cooler, lower layer. (See Figure 3-7.1.) The model calculations provide estimates of key conditions for each of the layers as a function of time. Zone modeling has proved to be a practical method for providing estimates of fire processes in enclosures.

The beginnings of pre-flashover zone fire modeling can be traced to the mid-1970s with the publication of a description of the fundamental equations by Quintiere.³ Based on these equations, the first zone fire model published was RFIRE_S by Pape and Waterman,⁴ followed shortly by the HARVARD model by Emmons and Mitler.⁵ The development of zone fire models was facilitated both by the advancement in the understanding of the basic physics of fire growth in a compartment and advances in, and the availability of, mainframe computers. Following the publication of these two models a number of zone fire models for mainframe computers were introduced. In 1985 the first zone model, ASET-B, written specifically for the newly available IBM-compatible personal computers, was introduced by Walton.⁶ Since that time additional models have been introduced, and most of the models written for mainframe computers have been converted for use in personal computers.

No zone fire model is *best* for all applications. The selection of a zone fire model for a particular application depends on a number of factors. While most of the zone fire models are based on the same fundamental principles, there is significant variation in features among the different models. The decision to use a model should be based on an understanding of the assumptions and limitations for the particular model. In general the more detailed the model outputs, the more extensive the model inputs, and the greater the computer execution time required. When using any computer fire model, it is always a good idea to test the sensitivity of the model outputs to changes in model inputs. If small changes in model inputs result in large changes in model outputs, the user must exercise great care in selecting the input values.

A key issue in selecting a model is model validation. Comparison of model results with experimental data is valuable for determining the applicability of a model to a

particular situation. Comparisons of model results with experimental data are limited, and the number of comparisons varies widely among the models. The model user should carefully examine model validation comparisons before selecting a model. Frequently, experienced model users will use more than one model to evaluate a particular situation. If several models provide similar results this can increase the confidence in the results. Similar results do not, however, guarantee that the results accurately represent the physical conditions being modeled, since most of the zone fire models are based on the same basic assumptions.

Overview of Representative Zone Fire Models

ASET Computer Program

ASET (available safe egress time) is a program for calculating the temperature and position of the hot upper smoke layer in a single room with closed doors and windows. ASET can be used to determine the time to the onset of hazardous conditions for both people and property. The required program inputs are the heat-loss fractions, the height of the fuel above the floor, criteria for hazard and detection, the room ceiling height, the room floor area, a heat release rate, and (optional) species generation rate of the fire. The program outputs are the temperature, thickness, and (optional) species concentration of the hot upper smoke layer as a function of time, and the time to hazard and detection. ASET can examine multiple cases in a single run. ASET was written in FORTRAN by Cooper and Stroup.⁶

ASET-B Computer Program

ASET-B is a program for calculating the temperature and position of the hot upper smoke layer in a single room with closed doors and windows. ASET-B is a compact version of ASET, designed to run on personal computers. The required program inputs are a heat-loss fraction, the height of the fire, the room ceiling height, the room floor area, the maximum time for the simulation, and the rate of heat release of the fire. The program outputs are the temperature and thickness of the hot upper smoke layer as a function of time. Species concentrations and time to hazard and detection, calculated by ASET, are not calculated in the compact ASET-B version. ASET-B was written in BASIC by Walton.⁶

COMPBRN III Computer Program

COMPBRN III is primarily used in conjunction with probabilistic analysis for the assessment of risk in the nuclear power industry. The model is based on the assumption of a relatively small fire in a large space, or a fire involving large fuel loads early during the pre-flashover fire growth period. The model's strengths are (1) emphasis on the thermal response of elements within the enclosure to a fire within the enclosure, and (2) model simplicity. The temperature profile within each element is computed,

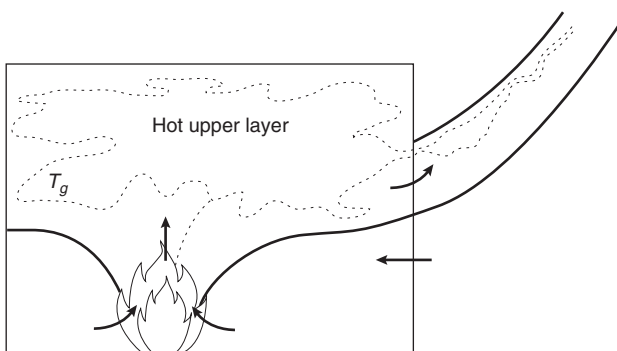


Figure 3-7.1. Two-layer model with no exchange between layers except the plume.

and an element is considered ignited or damaged when its surface temperature exceeds the user-specified ignition or damage temperature. The model outputs include the total heat release rate of the fire, the temperature and depth of the hot gas layer, the mass burning rate for individual fuel elements, the surface temperatures, and the heat flux at user-specified locations. COMPBRN III was written by Siu et al.⁷

COMP2 Computer Program

COMP2 is a computer program for calculating the characteristics of a post-flashover fire in a single building compartment, based on fire-induced ventilation through a single door or window. It is intended both for performing design calculations and for the analysis of experimental burn data. Wood, thermoplastics, and liquid fuels can be evaluated. A comprehensive output format is provided that gives gas temperatures, heat-flow terms, and flow variables. The documentation includes input instructions, sample problems, and a listing of the program. The program was written in FORTRAN by Babrauskas.⁸

CSTBZ1 Computer Program

CSTBZ1 is a computer program for post-flashover fires, based on similar basic assumptions as those of COMP2. The equations of mass and energy conservation are written without neglecting the fuel source term, and several vertical openings in a room can be considered. The equation of heat diffusion into the walls is solved either by a classical explicit finite difference method, or by a new modal approach that offers the capability of storing in a file a few numbers characterizing a given wall, leading to a rapid calculation of the superficial wall temperatures. A sophisticated numerical algorithm was used to solve the equations through uncoupling. The program was written by Curtat and Bodart.⁹

CFAST Computer Program

The CFAST (consolidated model of fire growth and smoke transport) is an upgrade of the FAST program¹⁰ and incorporates numerical solution techniques originally implemented in CCFM program.¹¹ FAST is now the graphical user interface program for CFAST. CFAST is a multi-room model that predicts within a structure resulting from a user-specified fire. CFAST version 4.0.1 can accommodate up to 30 compartments with multiple openings between compartments and to the outside. The required program inputs are the geometrical data describing the compartments and connections; the thermophysical properties of the ceiling, walls, and floors; the fire as a rate of mass loss; and the generation rates of the products of combustion. The programs outputs are the temperature and thickness of, and species concentrations in, the hot, upper layer and the cooler, lower layer in each compartment. Also given are the surface temperatures and heat transfer and mass flow rates. CFAST also includes mechanical ventilation, a ceiling jet algorithm, capability of multiple fires (up to 30), heat transfer to targets, detection and suppression systems, and a flame spread model. CFAST was written in FORTRAN by Jones, et al.^{12,13}

BRANZFIRE Computer Program

BRANZFIRE is a zone fire model for predicting the fire environment in an enclosure, resulting from a room-corner fire involving walls and ceilings. The zone fire model uses conservation equations based on those found in CFAST.¹² BRANZFIRE predicts ignition, flame spread, and the resultant heat released by the wall and ceiling lining material subjected to a burner fire. The model considers upward flame spread on the walls and beneath the ceiling, lateral flame spread on the walls, and downward flame spread from the ceiling jet. Wall and ceiling flame spread properties are computed from cone calorimeter data. Program outputs include layer height, species concentrations, gas temperatures, visibility, wall temperatures, and heat release rate. BRANZFIRE was written in Visual Basic by C. Wade.^{14,15,16}

JET Computer Program

JET is a two-zone single compartment model where the compartment is enclosed by a combination of draft curtains and walls. The ceiling may contain fusible links and vents where the vents operate in response to the fusing of the links. The ceiling vents remove hot, upper layer gas from the compartment. The fire is characterized by a time-dependent heat release rate, a time-dependent radiative fraction, and either a constant or variable fire diameter, which is determined using a heat release rate per unit area for the burning material. Inputs also include the thermal properties of the ceiling. Program outputs include the ceiling jet temperature and velocity, link temperature, and activation times. JET was written in FORTRAN by W. D. Davis.¹⁷

FIRST Computer Program

FIRST is the direct descendant of the HARVARD V⁵ program developed by Emmons and Mitler. The program predicts the development of a fire and the resulting conditions within a room given a user-specified fire or user-specified ignition. It predicts the heating and possible ignition of up to three targets. The required program inputs are the geometrical data describing the rooms and openings, and the thermophysical properties of the ceiling, walls, burning fuel, and targets. The generation rate of soot must be specified, and the generation rates of other species may be specified. The fire may be entered either as a mass loss rate or in terms of fundamental properties of the fuel. Among the program outputs are the temperature and thickness of, and species concentrations in, the hot, upper layer and the cooler, lower layer in each compartment. Also given are surface temperatures and heat transfer and mass flow rates. The FIRST program was written in FORTRAN by Mitler and Rockett.¹⁸

FPETOOL Computer Program

FPETOOL is the descendent of the FIREFORM program.¹⁹ It contains a computerized selection of relatively simple engineering equations and models useful in estimating the potential fire hazard in buildings. The calculations in FPETOOL are based on established engineering

relationships. The FPETOOL package addresses problems related to fire development in buildings and the resulting conditions and response of fire protection systems. The subjects covered include smoke filling in a room, sprinkler/detector activation, smoke flow through (small) openings, temperatures and pressures developed by fires, flashover and fire severity predictions, fire propagation (in special cases), and simple egress estimation. The largest element in FPETOOL is a zone fire model called FIRE SIMULATOR. FIRE SIMULATOR is designed to estimate conditions in both pre- and post-flashover enclosure fires. The inputs include the geometry and material of the enclosure, a description of the initiating fire, and the parameters for sprinklers and detectors being tracked. The outputs include the temperature and volume of the hot smoke layer; the flow of smoke from openings; the response of heat-actuated detection devices, sprinklers, and smoke detectors; oxygen, carbon monoxide, and carbon dioxide concentrations in the smoke; and the effects of available oxygen on combustion. FPETOOL was written in BASIC by Nelson.²⁰

LAVENT Computer Program

LAVENT is a program developed to simulate the environment and the response of sprinkler elements in compartment fires with draft curtains and fusible-link-actuated ceiling vents. The zone model used to calculate the heating of the fusible links includes the effects of the ceiling jet and the upper layer of hot gases beneath the ceiling. The required program inputs are the geometrical data describing the compartment, the thermophysical properties of the ceiling, the fire elevation, the time-dependent heat release rate of the fire, the fire diameter or the heat release rate per unit area of the fire, the ceiling vent area, the fusible-link response time index (RTI) and activation temperature, the fusible-link positions along the ceiling, the link assignment to each vent, and the ambient temperature. A maximum of 5 ceiling vents and 10 fusible links are permitted in the compartment. The program outputs are the temperature and height of the hot layer, the temperature of each link, the ceiling jet temperature and velocity at each link, the radial temperature distribution along the interior surface of the ceiling, the activation tie of each link, and the area opened. LAVENT was written in FORTRAN.²¹

WPI/FIRE Computer Program

WPI/FIRE is a direct descendant of the HARVARD V⁵ and FIRST¹⁸ programs. It includes all of the features of the HARVARD program version 5.3 and many of the features of the FIRST program. WPI/FIRE also includes the following additional features: improved input routine, momentum-driven flows through ceiling vents, two different ceiling jet models for use in detector activation, forced ventilation for ceiling and floor vents, and an interface to a finite difference computer model for the calculation of boundary surface isotherms and hot spots. The WPI/FIRE program was written in FORTRAN by Satterfield and Barnett,²² and additions to the program continue

to be developed by graduate students at the Center for Fire Safety Studies, Worcester Polytechnic Institute.

References Cited

1. R. Friedman, *An International Survey of Computer Models for Fire and Smoke*, 2nd ed. (Dec. 1991). Available from Library, Factory Mutual Research Corporation, 1151 Boston-Providence Turnpike, Norwood, MA 02062.
2. R. Friedman, "An International Survey of Computer Models for Fire and Smoke," *Jour. of Fire Prot. Engr.*, 4, 3, pp. 83-92 (1992).
3. J. Quintiere, "Growth of Fires in Building Compartments," ASTM STP 614, American Society for Testing and Materials, Philadelphia, PA (1977).
4. R. Pape, T.E. Waterman, and T.V. Eichler, "Development of a Fire in a Room from Ignition to Full Room Involvement—RFIRES," NBS-GCR-81-301, National Bureau of Standards, Washington (1981).
5. H.E. Mitler, "The Harvard Fire Model," *F. Safety J.*, 9, pp. 7-16 (1985).
6. W.D. Walton, "ASET-B A Room Fire Program for Personal Computers," NBSIR 85-3144, National Bureau of Standards, Washington, DC (1985).
7. V. Ho, N. Siu, and Apostolakis, "COMPBRN III—A Fire Hazard Model for Risk Analysis," *Fire Safety J.*, 13, 2-3, pp. 137-154 (1988).
8. V. Babrauskas, "COMPF2—A Program for Calculating Post-Flashover Fire Temperatures," NBS TN 991, National Bureau of Standards, Washington, DC (1979).
9. M.R. Curtat and X.E. Bodart, *1st Symposium International Association for Fire Safety Science*, Hemisphere Publications, Gaithersburg, MD, p. 637 (1986).
10. W.W. Jones, "A Multicompartment Model for the Spread of Fire, Smoke and Toxic Gases," *F. Safety J.*, 9, pp. 55-79 (1985).
11. G.P. Forney and L.Y. Cooper, "The Consolidated Compartment Fire Model (CCFM) Computer Application. VENTS, Parts I, II, III, IV," NISTIR, National Institute of Standards and Technology, Gaithersburg, MD (1990).
12. W.W. Jones, G.P. Forney, R.D. Peacock, and P.A. Reneke, "A Technical Reference for CFAST: An Engineering for Estimating Fire and Smoke Transport," TN-1431, National Institute of Standards and Technology, Gaithersburg, MD (2000).
13. R.D. Peacock, P.A. Reneke, W.W. Jones, R.W. Bukowski, and G.P. Forney, "A User's Guide for FAST: Engineering Tools for Estimating Fire Growth and Smoke Transport," SP-921, 2000 Edition, National Institute of Standards and Technology, Gaithersburg, MD (2000).
14. C.A. Wade, D. LeBlanc, J. Ierardi, and J.R. Barnett, "A Room-Corner Fire Growth & Zone Model for Lining Materials," Second International Conference on Fire Research and Engineering (ICFRE2), National Institute of Standards and Technology and Society of Fire Protection Engineers, Gaithersburg, MD, pp. 106-117 (1998).
15. C. Wade and J. Barnett, "A Room-Corner Fire Model Including Fire Growth on Linings and Enclosure Smoke-Filling," *J. of Fire Prot. Engr.*, 8(4), pp. 183-193 (1997).
16. C. Wade, "Branzfire-Engineering Software for Evaluating Hazard of Room Lining Materials," in *Conference Proceedings on the Eight International Interflam Conference*, Interscience Communications Limited, London, pp. 1147-1152 (1999).
17. W.D. Davis, "The Zone Fire Model Jet: A Model for the Prediction of Detector Activation and Gas Temperature in the

- Presence of a Smoke Layer," *NISTIR 6324*, National Institute of Standards and Technology, Gaithersburg, MD (1999).
- 18. H.E. Mitler and J.A. Rockett, "User's Guide to FIRST, A Comprehensive Single-Room Fire Model," *CIB W14/88/22*, National Bureau of Standards, Gaithersburg, MD (1987).
 - 19. H.E. Nelson, "FIREFORM—A Computerized Collection of Convenient Fire Safety Computations," *NBSIR 86-3308*, National Bureau of Standards, Gaithersburg, MD (1986).
 - 20. H.E. Nelson, "FPETOOL: Fire Protection Engineering Tools for Hazard Estimation," *NISTIR 4380*, National Institute of Standards and Technology, Gaithersburg, MD (1990).
 - 21. Y.L. Cooper, "Estimating the Environment and the Response of Sprinkler Links in Compartment Fires with Draft Curtains and Fusible-Link-Actuated Ceiling Vents Theory," *F. Safety J.*, 16, pp. 137–163 (1990).
 - 22. D.B. Satterfield and J.R. Barnett, "User's Guide to WPI-FIRE Version 2 (WPI-2)—A Compartment Fire Model," Worcester Polytechnic Institute, Center for Fire Safety Studies, Worcester, MA (Aug. 1990).

Additional Readings

- L.Y. Cooper and D.W. Stroup, "ASSET—A Computer Program for Calculating Available Safe Egress Time," *F. Safety J.*, 9, pp. 29–45 (1985).
- B. Hagglund, "A Room Fire Simulation Model," *FOA C 20501-D6*, National Defense Research Institute, Sweden (June 1983).
- B. Hagglund, "Simulating the Smoke Filling in Single Enclosures," *FOA C 20513-D6*, National Defense Research Institute, Sweden (October 1983).
- J.A. Swartz et al., *Final Technical Report on Building Fire Simulation Model*, Vols. I and II, National Fire Protection Association, Quincy (1983).
- T. Tanaka, "A Model of Multiroom Fire Spread," *NBSIR 83-2718*, National Bureau of Standards, Washington (1983).
- E.E. Zukoski and T. Kubota, "Two-Layer Modeling of Smoke Movement in Building Fires," *F. and Matls.*, 4, 1, p. 17 (1980).

CHAPTER 8

Modeling Enclosure Fires Using CFD

Geoff Cox and Suresh Kumar

Introduction

It was in the early 1920s, that Lewis Richardson first demonstrated the feasibility of solving, using numerical methods, the governing equations of fluid flow.¹ His purpose was weather prediction, but it was not for another 50 years that the technology we now know as *computational fluid dynamics* (or CFD) began to emerge as a general tool for the analysis of the full breadth of fluid flow problems, including those associated with fire.

Solution of the Reynolds-averaged Navier-Stokes equations using numerical simulation tools has now become commonplace in the design and analysis of many practical engineering problems. This advance has been driven by the availability of commercial CFD software together with massive increases in computer speed accompanied by ever-reducing hardware costs.

This technology evolved outside the fire community and has been imported into it, in contrast to zonal models (Section 3, Chapter 7), which were developed within this discipline. This has far-reaching implications since the same basic CFD technology is also being exploited, developed, tested, and verified for an extremely wide range of applications. Problems and successes demonstrated elsewhere can often be exploited in the fire context, although as we will see, many issues are unique to fire and can only be the responsibility of the fire community. But the same tools that are used to study, for example, heat transfer in an internal combustion engine can also be used to ex-

plore, for example, indoor air movement, early detection of smoke, and the dispersion of combustion products within the atmospheric boundary layer.

The study of fire spread inside buildings and indeed other enclosures such as ships and aircraft is another such application. CFD provides the potential to study these extremely complicated problems that are only partially amenable to reduced-scale physical modeling because of the very large number of nondimensional groups that need to be preserved to simulate full-scale behavior.

The starting point for CFD models is the “exact” system of coupled partial differential equations that describe the balance between the competing influences on the transport of mass, momentum, chemical species, and energy within the fire and throughout the enclosure containing it. However, rigorous solution of the “exact” equations, resolving fully the length and time scales that occur in the flows associated with the turbulent combustion characteristic of fire, is still beyond the capabilities of even the largest computers currently available. To capture the details of the chemical reaction zone in a fire would require a characteristic mesh size below 1 mm. As a consequence it is necessary to simplify the system of exact equations by some form of modeling.

Most practical approaches (see Reference 2, for example) solve the so-called Reynolds-averaged Navier-Stokes (RANS) equations.* These are obtained from the exact equations by first time-averaging them and then solving the resulting continuous equations in discretized form over the domain of interest. The full rigor of the initial balance equations is now lost because of problems associated with the terms that result from averaging the turbu-

Geoff Cox is technical director of the U.K. Fire Research Station where he has been conducting research since 1973. He is visiting professor at Cranfield University and chairman of the International Standards Technical Committee on Fire Safety.

Dr. Suresh Kumar joined the U.K. Fire Research Station in 1980, and heads the CFD fire-modeling team. His major research interests are in fire science, fire modeling, and fire safety engineering. He has pioneered the development of the CFD models JASMINE and TUN-FIRE for fire safety design and hazard assessment.

*A density-weighted variant of Reynolds averaging (Favre averaging) is often necessary for the treatment of regions where density fluctuations have a significant effect. This is not usually a serious issue in smoke movement studies but can be close to the fire source. This treatment is not presented here but will be found, for example, in Cox.¹

lent transport processes. These terms, which describe the contributions of turbulent mixing and its influences on chemical kinetics and radiant heat transfer, need to be modeled. In most practical computer models this is achieved by use of the two-equation $k \sim \varepsilon$ turbulence model (k is the kinetic energy of the turbulence and ε is its rate of dissipation), and it is here where full rigor is lost.

An alternative approach is to exploit large-eddy simulation techniques,^{3,4} where the larger turbulent vortices are simulated rigorously but the finer-scale turbulent motions are either modeled in a similar fashion to RANS modeling⁴ or perhaps ignored entirely.³ It is important to realize that neither of these approaches capture the length and times scales associated with the details of the combustion processes involved. These can only be described by the submodels employed.

A full, direct numerical simulation that solves the exact equations rigorously currently remains beyond the scope of problems of practical interest although research with this approach is growing apace,⁵ certainly improving our understanding of fine-scale behavior.

In addition to the uncertainties associated with the modeling of turbulent flow, others are also introduced as a result of the numerical methods used to solve the continuous equations no matter which strategy is adopted. Recognition of the limitations in each of these departures from rigor is essential for the successful practical exploitation of CFD to solve fire problems.

It should be recognized that this topic, like most involving computation, is rapidly evolving and that this chapter can represent only a snapshot in time of current capability. Where 1000 mesh points represented the upper limit of capability for discretization in the early 1980s, one or two thousand times that number would, as we write, be quite routine! However the principles will be largely unchanged although their outreach will grow with time. While treatment of smoke movement problems is more mature, there is considerable research in progress at the time of writing on some of the more detailed issues relating to the combustion science involved (e.g., flame spread, oxygen vitiation) where the challenges are prodigious indeed.

This chapter does not dwell on the theoretical underpinning to CFD. This is too large a topic to be dealt with in this brief and hopefully practical chapter. Such detail will be found in very many textbooks and reviews on the topic. Cox,^{2,6} for example, specifically addresses these issues in the fire context, while many (Patankar,⁷ and Versteeg and Malalasekera,⁸ for example) discuss them in a more general sense. Kumar⁹ provides a full review of turbulence modeling and its application to fire problems. The chapter here places more emphasis on the use of CFD in a practical environment and on fire-specific issues that are essential for proper exploitation of the CFD methodology.

Currently CFD is being used by the practicing fire protection engineer primarily for the assessment of smoke control problems. Most of what is presented here is directed toward assisting in the proper use of the methodology for that purpose. However, some information is also provided on more advanced applications so that the potential of the methodology can be appreciated.

The Principles

The simplifications and assumptions that are essential in the synthesis of zone fire modeling as exemplified in Section 3, Chapter 7 are unnecessary when using the very different philosophy of field (or CFD) modeling. Instead, the full, partial differential equation set, expressing the principles of local conservation of mass, momentum, energy, and species, the *field equations*, are solved using numerical methods subject only to the boundary conditions of the problem.

Solutions are obtained on a numerical grid of typically hundreds of thousands or millions, if they can be afforded, of elementary control volumes filling the domain of interest.

The numerical mesh is chosen to provide acceptably accurate approximations to the field equations. Unlike the few large, physically contrived control volumes of the zonal models, field models ensure local conservation of the governing equations in the many thousands or millions of relatively small control volumes situated for the convenience of numerical approximation.

Whether a fire plume is deflected from the vertical by a door jet through an enclosure opening and as a consequence entrains extra air or, perhaps, rises only part way to the ceiling before losing its buoyancy should be determined by the solution of the equations and not by prior assumption.

This chapter concentrates on the Reynolds-averaged approach to CFD modeling. This engineering approach, pioneered in the wider context by Spalding and his coworkers,¹⁰ has made particular use of the two-equation $k \sim \varepsilon$ turbulence model to provide a predictive capability for the treatment of practical problems. This is the approach adopted by all commercial packages to date, although some offer alternatives; the $k \sim \varepsilon$ model still remains the industry workhorse. Here the physical and chemical processes occurring at length scales less than that of the numerical grid are replaced by approximate models that attempt to describe their subgrid behavior.

The Modeling of Turbulent Flow

Before we go on to describe CFD modeling any further, it is important to understand the choices available for the treatment of turbulence in these problems. Turbulence is generated at large scale, typically of the order of a few meters and representative of physical lengths associated with the generation of shear layers in the flow—maybe a room or doorway dimension or a fire width. Without any further stimulus, this turbulent energy decays, and with it turbulent eddy sizes become smaller and smaller until they are small enough for the energy to be dissipated by viscous forces. It is at these finest length scales that fuel/air mixing takes place and at which chemical reaction occurs.

A schematic spectral plot (Figure 3-8.1) of turbulent energy with inverse eddy dimension illustrates these different scales. A notional fine-wire thermocouple trace from within the fire, as shown in Figure 3-8.2, presents this same information in a different form.

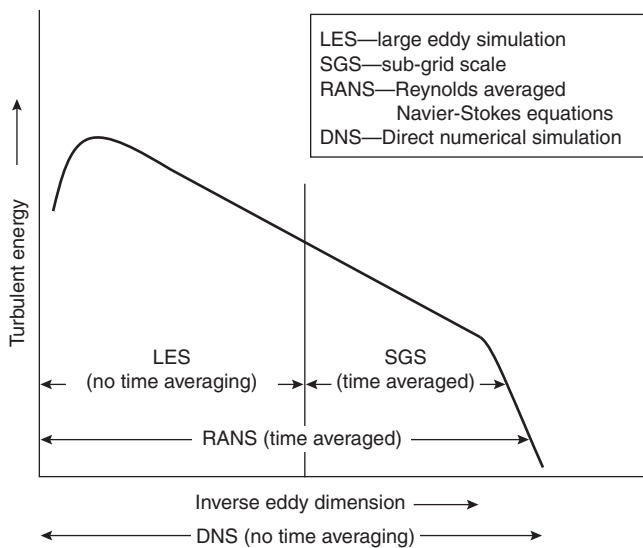


Figure 3-8.1. Schematic representation of turbulent energy spectrum showing different modeling treatments.

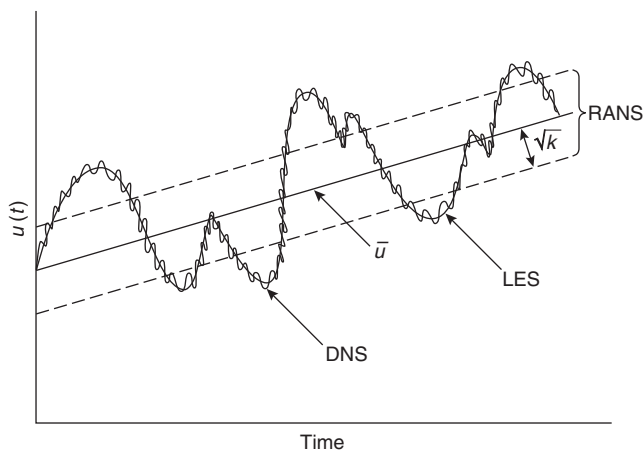


Figure 3-8.2. Schematic representation of different treatments for turbulence.

We can use these illustrations to explain different treatments that the CFD methodology can employ for fire simulation purposes. The RANS model solves only for time-averaged properties. The very important influences of turbulent fluctuations are dealt with by turbulence models, which encompass influences over the whole length-scale range by replacing the very complex correlations between fluctuating variables, using modeled equations. Although turbulent fluctuations are time averaged, the time evolution of the averages is followed in much the same way as a thermocouple of a relatively long time constant measures an experimental average.

The large-eddy simulation (LES) avoids time averaging of fluctuations at scales larger than the mesh size. Thus the larger eddy influences are rigorously represented. However, below the mesh size, certainly at length

scales associated with the chemical reaction, fluctuations are either totally ignored³ or perhaps time averaged in a similar way to that used in the RANS approach.⁴ The thermocouple analogue here is of a much shorter time constant than previously, able to follow some larger fluctuations but not the small-scale detail.

Finally and not yet possible at practical scale, because of computing limitations, is for the simulation to follow fluctuations at all length scales right down to those associated with viscous dissipation and without any time averaging. The thermocouple analogue here is of a thermocouple of zero time constant. This technique, generally referred to as direct numerical simulation (DNS), will remain the preoccupation of the research community for many years to come.

The Governing Equations for the RANS Approach

The governing equations for the RANS models start with the set of time-mean, turbulence-modeled conservation equations for mass, momentum, energy, and species together with transport equations for the turbulence variables k and ε . These equations (eight and more) can be conveniently written in terms of a general time-mean variable, ϕ :

$$\frac{\partial}{\partial t}(\rho\phi) + \frac{\partial}{\partial x_j}(\rho u_j\phi) = \frac{\partial}{\partial x_j}\left(\Gamma_\phi \frac{\partial \phi}{\partial x_j}\right) + S_\phi \quad (1)$$

This equation "simply" describes the principles of conservation for each of the many elementary control volumes filling the domain of interest. The first term represents the time rate of change of the property within the volume; the second, the influences of convection on the volume; the third, the influences of diffusion; and the last term, any generation or destruction involved. This last term might, for example, in the case of enthalpy conservation, describe radiant heat exchanges with adjacent volumes and surfaces. It is also this term that describes the buoyancy forces in the momentum equations and the effects of buoyancy on turbulent mixing in the k and ε equations.

Equation 1 describes momentum conservation when ϕ stands for u_i , energy conservation when ϕ stands for h , and mass continuity when $\phi = 1$. It also describes the transport of turbulence kinetic energy, when $\phi = k$, and its dissipation rate, when $\phi = \varepsilon$, in addition to the conservation of the mixture fraction when $\phi = f$, and the conservation of the species i when $\phi = Y_i$. The Γ_ϕ term is an effective exchange coefficient appropriate to ϕ , which includes the effects of both molecular and turbulent diffusion. S_ϕ is a source term.

With the conservation equations written in this form, the meaning of Γ_ϕ and S_ϕ for each property is given in Table 3-8.1. Each variable is a time average of the true fluctuating variable.

The values of the empirical constants C_1 , C_2 , C_μ , σ_k , and σ_t are those recommended by Jones and Whitelaw¹¹ and obtained from detailed studies of nonbuoyant shear flows. It has been common practice to use these in application to enclosure fire problems. Some discussion of these constants in the fire context will be found in Cox.²

Table 3-8.1 Effective Exchange Coefficients and Source Terms in Generic Transport Equation for ϕ (Equation 1).

Transport of	ϕ	Γ_ϕ	S_ϕ
Mass	1	0	0
Momentum	u_i	μ_{eff}	$-\frac{\partial p}{\partial x_i} + \frac{\partial}{\partial x_j} \left[\mu_{\text{eff}} \frac{\partial u_j}{\partial x_i} \right] + g_i$
Enthalpy	h	$\frac{\mu_{\text{eff}}}{\sigma_h}$	$\frac{\partial p}{\partial t} + S_{h,\text{rad}}$
Kinetic energy of turbulence	k	$\frac{\mu_{\text{eff}}}{\sigma_k}$	$G_k + G_B - \rho \varepsilon$
Rate of dissipation of turbulent energy	ε	$\frac{\mu_{\text{eff}}}{\sigma_\varepsilon}$	$\frac{\varepsilon}{k} [(G_k + G_B)C_1 - C_2 \rho_\varepsilon]$
Mixture fraction	f	$\frac{\mu_{\text{eff}}}{\sigma_f}$	0
Mass fraction of fuel	γ_f	$\frac{\mu_{\text{eff}}}{\sigma_Y}$	S_f

where $G_k = \mu_t \left(\frac{\partial u_i}{\partial x_j} + \frac{\partial u_j}{\partial x_i} \right) \frac{\partial u_i}{\partial x_j}$

$$G_B = -\beta g \frac{\mu_t}{\sigma_t} \frac{\partial T}{\partial x_i}$$

$$\mu_{\text{eff}} = \mu_t + \mu_f$$

$$\mu_t = C_\mu \rho \frac{k^2}{\varepsilon}$$

and

$$C_1 = 1.44, C_2 = 1.92, C_\mu = 0.09, \sigma_k = 1.0, \sigma_\varepsilon = 1.3, \sigma_t = \sigma_h = \sigma_f = \sigma_Y = 0.7.$$

We will return later to the issues associated with the influence of buoyancy on turbulent mixing.

Many fire engineers will exploit one of the general-purpose commercial CFD packages currently available in which all the above detail has been coded for them and they may feel that they have no need for this detail. However, extremely important for the fire application is the G_B term. It is this that describes the influences of fire-generated density gradients on turbulent mixing.

In the bulk flow, buoyancy forces disturb the simple picture of isotropic turbulence assumed by the traditional $k \sim \varepsilon$ model. Turbulent mixing in a rising plume is enhanced by buoyancy while in a stably stratified ceiling layer it will be inhibited. In this respect the modeling of turbulent mixing in compartment fires requires particular attention. The production term in the k equation associated with the buoyancy forces,

$$G_B = -\beta g \frac{\mu_t}{\sigma_t} \frac{\partial T}{\partial x_i} \quad (2)$$

takes on opposite signs in regions of stable and unstable stratification. This term, which describes the exchange of

turbulent kinetic energy with potential energy, represents a source in the unstable situation of the fire plume, where heated gases emerge beneath cool gases, but it becomes a sink in the hot gas ceiling layer, where the opposite occurs.

It is important that the fire-engineering practitioner ensures that this term is either activated or is coded for when using commercial codes. An illustration of the consequence of omitting this term is graphically illustrated by Figure 3-8.3, taken from Markatos et al.¹²

This treatment for turbulent buoyant mixing has proved its worth in many comparisons of predictions with experimental data and its success can be measured particularly by, for example, the "blind" simulations of Miles et al.¹³ These will be discussed in the section on validation below.

Special Treatment for Flow Close to Walls

The CFD model solves discretized forms of the continuous Equation set 1 throughout the domain of study subject to the boundary conditions for the problem. To cope with regions very close to solid surfaces such as walls or obstructions where the flow changes from turbulent to laminar, the RANS models use universal wall laws to describe this transition. This is necessary because very close gridding in these regions would be required to capture this behavior numerically thus substantially increasing computational cost and effort.

Generally, the turbulent boundary layer can be split into a laminar, viscous sublayer closest to the wall ($y^+ < 5$), an inertial log-law sublayer ($30 < y^+ < 400$) where the flow is fully turbulent but where the shear stress can be considered uniform, and between them ($5 < y^+ < 30$) a region of transition between laminar and turbulent flow.

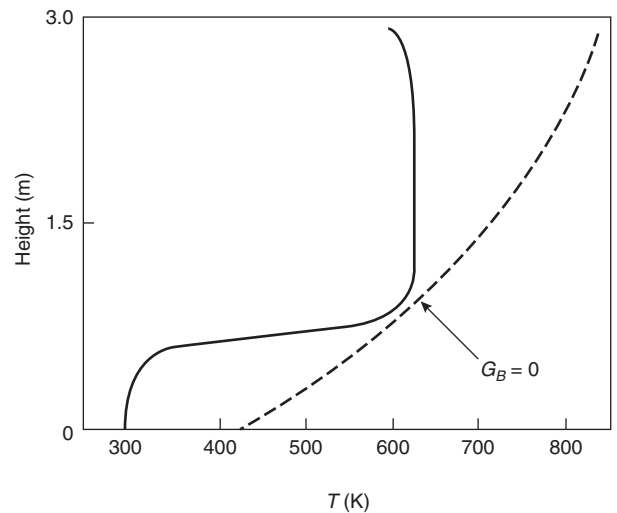


Figure 3-8.3. Predicted gas temperature profile with and without including buoyancy in $k \sim \varepsilon$ turbulence model.

It is general practice to locate the near-wall node point close enough to the wall to be in the inertial sublayer. Then the velocity and enthalpy profiles between the near-wall node and the wall are

$$u^+ = \frac{1}{\kappa} \ln(Ey^+) \quad (3)$$

$$h^+ = \sigma_t(u^+ + P_j) \quad (4)$$

where

$$y^+ = \frac{\rho k_p^{1/2} C_\mu^{1/4} y_p}{\mu} \quad (5)$$

and

$$h^+ = \frac{\rho^{1/2} \tau_w^{1/2} (h_w - h_p)}{\dot{q}_w''} \quad (6)$$

κ is the von Karman constant relating mixing length to distance from the wall. E is a parameter that lumps together the effects of the viscous sublayer. Its value depends upon the surface roughness of the wall as does P_j , which represents the resistance of the laminar sublayer to the transport of enthalpy. For smooth surfaces E is often taken as 9.0 and P_j is given by the function

$$P_j = 9.24 \left[\left(\frac{\sigma}{\sigma_t} \right)^{3/4} - 1 \right] \left[1 + 0.28 \exp(-0.007 \left(\frac{\sigma}{\sigma_t} \right)) \right] \quad (7)$$

which is -2.77 for $\sigma/\sigma_t = 0.7$, or is zero for $\sigma/\sigma_t = 1.0$. For general finish brick, E could be as low as 0.064 and P_j should then be 6.56.

Where there is a requirement to provide a very fine mesh close to the wall—perhaps for faithful representation of a ceiling jet, then the near-wall node will most likely need to be in the laminar or transitional regions. For $y^+ < 11$, a linear velocity profile,

$$u^+ = y^+ \quad (8)$$

should be used instead of Equation 3. Strictly speaking, Equation 3 is valid for $y^+ < 5$ (laminar sublayer), but it can be used up to $y^+ = 11$, which corresponds to the intersection point of the linear (Equation 8) and the logarithmic (Equation 3) velocity profiles.

For $11 < y^+ < 30$ (bridging the laminar and inertial sublayers), the log-law Equation 3 can still be used. However, for $y^+ < 30$, Equations 3 and 8 should ideally be coupled with a low Reynolds number $k-\epsilon$ turbulence model.¹⁴ Otherwise, the boundary values of k and ϵ obtained from the standard high Reynolds number $k-\epsilon$ turbulence model will not be accurate.

Combustion Models

With the material described so far, supplemented by a prescription of the appropriate boundary conditions, we are in a position to examine buoyant flows that

emerge from fires—a significant aspect of the smoke movement problem. It is often tempting simply to represent the fire source in such simulations as a volumetric heat source \dot{q}'' .

Such a simplified treatment of the fire source cannot properly capture the effects of distributed combustion that can play such an important part in fire problems. For more realistic simulations, models need to be incorporated to describe the influences of combustion and radiative heat exchange.

The purpose of incorporating a combustion model in smoke movement simulations is two-fold. First, it allows the process of fuel-air mixing, and therefore of distributed heat release, an essential feature of fire, to be determined by both flow conditions and by the shortage of one or other reactant. Prejudgment of heat-releasing control volumes is avoided, thus admitting natural treatments for wind-blown flames and of flame extension due to under-ventilation. Second, predictions of chemical species yield and transport become possible both to provide estimates of, for example, local toxic species concentrations and of thermal radiation absorption/emission properties of fire gases.

Most models assume for engineering purposes that the combustion process can be represented as a single, one-step reaction:



where F , O , and P simply represent the masses of fuel, oxidant, and product. At this stage it is not necessary to consider their detailed chemical compositions—this is only manifest by the stoichiometric air requirement of the fuel. In principle the task now involves solution of the species conservation equation (Equation 1, when $\phi = Y_i$) for each of the components in the reaction. However, the influences of turbulence on the source terms in these equations causes considerable further complexity.

By recasting the species conservation equations in terms of a conserved scalar, the mixture fraction

$$f = \frac{\beta - \beta_O}{\beta_F - \beta_O} \quad (10)$$

where $\beta = Y_f - (Y_o/s)$ is a conserved variable and the F and O refer to fuel and oxidant streams, respectively, and making the assumption that component diffusivities are equal, it is then possible to eliminate the source term in determining the degree of mixing between fuel and oxidant.

Spalding's eddy break-up model¹⁵ allows for the influences of turbulence on chemical reaction. This assumes that the rates of chemical reaction are infinitely fast and that the mean rate of consumption of fuel at the molecular level is controlled by the rate of molecular mixing of reactants, in turn proportional to the rate of dissipation of turbulent eddies.

Magnussen and Hjertager¹⁶ modified Spalding's original model such that this rate was controlled by the "deficient" reactant, air or fuel. Thus in the case of fire in the open, it is the local fuel concentration that controls the reaction, except of course immediately above the fuel bed. In

ventilation-controlled enclosure fires, the air is deficient and it is then the oxygen concentration that controls the reaction. A third controlling term based on mean property kinetics is sometimes added to limit the rate of reaction of cold mixtures:

$$S_f = -C \rho \frac{\varepsilon}{k} \min \left\{ Y_f, \frac{Y_{ox}}{s}, Y_f Y_{ox} B \exp \left(\frac{-E}{RT} \right) \right\} \quad (11)$$

Magnussen et al.¹⁷ with an assumption of isotropic turbulence suggests for C a functional form,

$$C = 23.6 \left(\frac{ve}{k^2} \right)^{1/4} \quad (12)$$

but it is common practice to assume C to be a dimensionless constant of the order of 4.¹⁶

This assumption for source term closure permits the transport equation for fuel mass fraction to be solved in addition to that for the mixture fraction to provide predictions of mass fraction of each component of the simplified chemical reaction. Application of this type of treatment to fire problems has been reasonably successful,^{13,18,19} as it has been in other areas of combustion engineering.

The model has the merit of simplicity and permits the enthalpy to be released over a distributed volume determined by the enclosure geometry and availability of air. The phenomenon of flame lengthening as a consequence of ventilation control is incorporated by this modeling approach.

Concentrations of the stable species, CO_2 and H_2O , can then be deduced by assuming that they occupy the products of combustion in their stoichiometric proportions. An assumption of local thermodynamic equilibrium will allow detailed chemical species concentrations to be determined using procedures such as those embodied within the NASA-Lewis series of computer programs.²⁰

The effects of finite-rate chemical kinetics and non-equilibrium kinetics are, however, not treated by such a scheme. For the realistic prediction of partially oxidized species, such as CO, and soot, more sophistication is needed. These will not be discussed here but the reader can consult Cox² and Moss²¹ for more complex strategies. These are still primarily in the research domain and are unlikely, at the time of writing, to be used by the fire engineer. An estimate of CO concentration can be established by exploiting the equilibrium assumption. Although this can produce considerable overprediction of CO compared to the measured data,²² such information can, as long as the limitations are recognized, be useful in obtaining engineering estimates of upper bounds of toxic hazard.

Radiant Heat Transfer

Two quite distinct difficulties need to be addressed for the realistic modeling of radiant heat transfer in enclosure fires. The first concerns the geometric problem associated with the exchange of radiant energy between remote emitters and receivers, solid surfaces, and the soot

particulate/gas phase mixtures of flames and smoke aerosols. The second difficulty concerns the calculation of local emissive powers and absorptivities. The relative contributions from soot and gaseous emissions vary substantially between flame and smoke products. A successful model must be able to cope with not only these differences, but also those between relatively dense smoke layers and the almost transparent layers of the incoming air. In addition, as with fluid flow and combustion chemistry, the effect of turbulent fluctuations in temperature and composition must be considered particularly at the fire source itself. In most practical treatments of far-field conditions in enclosure fires, these effects are ignored. Recent work on this issue is presented in References 2, 21, and 23.

The influences of radiant heat transfer on the governing equations are exerted through the source term in the enthalpy conservation equation.

Exact solutions are not possible for most practical applications; instead, several approximate methods have been developed and have been applied to compartment fire problems.

Flux Methods

A substantial simplification becomes possible if the spatial and angular distributions of radiation intensity can be separated. This is the approach of the flux methods. If the spectral intensity is assumed uniform on given intervals of solid angle, then the radiative transfer equation reduces to a series of coupled, linear, ordinary differential equations in terms of spatially averaged radiation intensities or fluxes.

The solid angles are assumed to coincide with the faces of a control volume in Cartesian space and the radiant flux across each face is assumed uniform (Figure 3-8.4). Then, when F_i^+ is the flux passing through the

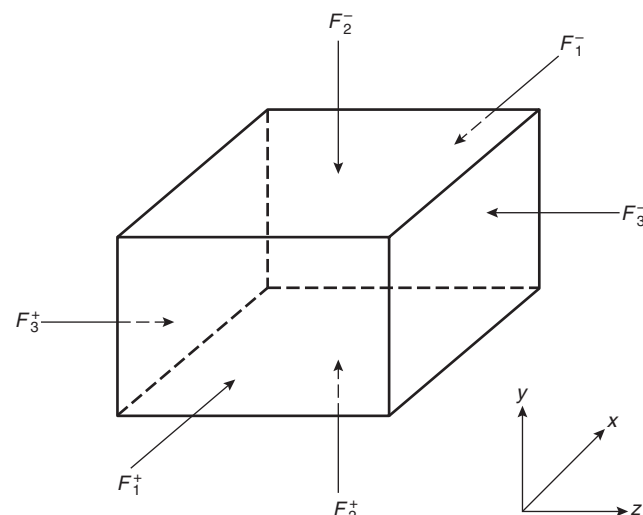


Figure 3-8.4. Six-flux distribution of a radiating control volume.

control volume in the positive i direction and F_i^- is the flux in the negative i direction,

$$\frac{dF_i^+}{dx_i} = -(a + s)F_i^+ + aE_b + \frac{s}{6} \sum_{i=1}^3 (F_i^+ + F_i^-) \quad (13)$$

$$\frac{dF_i^-}{dx_i} = (a + s)F_i^- - aE_b - \frac{s}{6} \sum_{i=1}^3 (F_i^+ + F_i^-) \quad (14)$$

where a and s are local absorption and scattering coefficients and E_b is the blackbody emissive power of the control volume.

By combining these and differentiating with respect to x_i , we obtain

$$\begin{aligned} \frac{d}{dx_i} \left[\Gamma_R \frac{d}{dx_i} (F_i^+ + F_i^-) \right] &= -S_i \\ &= (a + s)(F_i^+ + F_i^-) - 2aE_b - \frac{s}{3} \sum_{i=1}^3 (F_i^+ + F_i^-) \end{aligned} \quad (15)$$

where

$$\Gamma_R = \frac{1}{a + s} \quad (16)$$

This equation has the same form as the generic conservation Equation 1 and can be solved using the same numerical algorithm. The radiative contribution to the source term in the enthalpy equation for each control volume is then

$$S_{h,\text{rad}} = - \sum_{i=1}^3 S_i = a \sum_{i=1}^3 (F_i^+ + F_i^-) - 6aE_b \quad (17)$$

This model is attractive for CFD using the Cartesian grid since it computes the fluxes in Cartesian coordinate directions and exploits the same numerical techniques as employed to solve the hydrodynamic equations. It is often sufficient for the treatment of smoke movement problems. However, it does have a number of serious limitations, the most important of which, for application to fire, is its inability to model radiant transfer accurately at angles oblique to the Cartesian grid.

Discrete Transfer Method

The discrete transfer (DT) method developed by Lockwood and Shah²⁴ overcomes many of these difficulties, combining computational economy with greater realism. It utilizes features of the zone, flux, and Monte Carlo methods by tracing rays of electromagnetic radiation through the computational domain between boundaries. However, rather than their directions being generated at random, they are instead chosen in advance in a similar way to choosing the location of the hydrodynamic mesh. The technique involves solving the radiative transfer equation along the paths of these rays chosen to emanate usually from the centers of the bounding, hydrodynamic control volume faces (Figure 3-8.5).

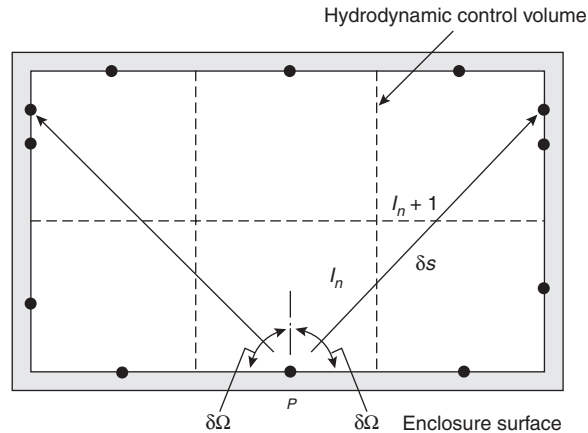


Figure 3-8.5. Schematic of discrete transfer method showing two representative rays.

The number and direction of rays from each such point are chosen, a priori, to provide the desired level of accuracy in the same way as the finite-difference grid is selected for undertaking the hydrodynamic calculation. The hemisphere around each point is divided into segments of equal circumferential area over which the intensity is assumed uniform.

A simple recurrence relationship is solved for each ray as it traverses from one bounding surface to another:

$$I_{n+1} = I_n \exp [-(a + s)\delta s] + \frac{E^*}{\pi} \{1 - \exp [-(a + s)\delta s]\} \quad (18)$$

where

I_{n+1} = the intensity leaving the n th hydrodynamic control volume

I_n = the intensity entering the n th control volume

δs = the pathlength through the control volume

and

$$E^* = \frac{a}{a + s} \cdot E_b + \frac{s}{4(a + s)} \int_{\Omega'=0}^{4\pi} I d\Omega' \quad (19)$$

It has been assumed that temperatures, absorption, and scattering coefficients are uniform within the hydrodynamic control volume.

The net gain or loss of radiant energy in each control volume is then deduced from the numbers of rays crossing it and this can be introduced into the enthalpy conservation equation as before, for the n th control volume:

$$S_{h,\text{rad}} = \sum_{\text{all rays through } n} (I_{n+1} - I_n) \Omega \delta\Omega \delta A \quad (20)$$

where δA is the area of the cell surface.

Accuracy clearly improves with increased numbers of rays, but Bressloff²⁵ demonstrates that between 16 and 32 rays emitted from each boundary control surface should be adequate for the prediction of heat transfer in

the gas phase for smoke movement problems. The method can, though, create erroneous "fingers" of high heat flux and "hot spots" on boundaries in the directions of high ray density. These errors are reduced, the greater the number of rays used and, of course, the finer the hydrodynamic grid. More information on the accuracy of the DT treatment in application to fire problems will be found in References 26–28.

Radiative Properties of the Combustion Products

For each of these methods, computations for local absorptance and emittance are required. In an enclosure fire, conditions vary considerably from the comparatively transparent entrained air close to the floor to the highly emissive, luminous flames of the fire source and the optically dense ceiling smoke layer.

The simplest treatment for the smoke layer assumes it to be a gray gas of prescribed absorption coefficient.²⁹ More realistic treatments allow absorptance and emittance to be determined from the local predictions within each hydrodynamic control volume of concentration of CO₂, H₂O, and soot. There exist a hierarchy of models for the computation of these local properties.

Lockwood and Malalasekera³⁰ used the mixed gray gas model developed by Truelove³¹ in conjunction with the discrete transfer model to model room fire growth. This is particularly attractive because it links the physical realism of Beer's law with the simplicity of the gray gas approximation. By assuming that the combustion product mixture is composed of a number of gray gases (CO₂, H₂O) and soot, the model defines total emissivity/absorptivity of the gas/soot mixture as

$$\varepsilon_m = \sum_{j,j'} b_{m,j,j'}(T) [1 - \exp\{[-a_{g,j}(p_w + p_c) - a_{s,j'}c]\delta_s\}] \quad (21)$$

where the temperature-dependent weighting coefficient, $b_{m,j,j'}(T)$, represents the fraction of blackbody energy in the wavelength region where the absorption coefficient is $a_{g,j}$ for the gas mixture and $a_{s,j'}$ for the soot mixture, and should satisfy the sum rules:

$$\begin{aligned} \sum_{j'} b_{m,j,j'}(T) &= b_{g,j}(T) \\ \sum_j b_{m,j,j'}(T) &= b_{s,j'}(T) \end{aligned} \quad (22)$$

The weighting coefficients $b_{m,j,j'}(T)$ are obtained by a least-squares fit of Equation 21 to the mixture of the total emittance data evaluated from the measured gas and soot spectral properties.

Recently, Bressloff et al.²⁶ have demonstrated the benefits of the computational efficiency of this relatively simple model compared to more accurate but relatively expensive wide- and narrow-band models.^{32–35}

Modak³³ developed a relatively simple wide-band model based on a curve-fitting method for the spectral data for homogeneous, isothermal mixtures of soot, CO₂, and H₂O that does not involve spectral calculations. He determined mixture absorptivity from

$$a = a_s + a_g - a_s a_g \quad (23)$$

where a_s is the soot absorptivity, given by

$$a_s \equiv 1 - \exp(1 - 12b_0 f_v \delta s T_s) \quad (24)$$

and a_g is the absorptivity of the molecular species CO₂ and H₂O, given by

$$a_g = \varepsilon_g \left(\frac{T}{T_s} \right)^{0.65 - 0.2\xi} \quad \xi = \frac{p_w}{(p_w + p_c)} \quad (25)$$

where

T = the temperature of the local gas mixture

T_s = the blackbody temperature of the soot

f_v = the soot volume fraction

p_w and p_c = the partial pressures of water and carbon dioxide

ε_g = the emissivity of the CO₂-H₂O mixture that is determined by curve fitting to detailed spectral calculations using the method of Felske and Tien³⁵

An application of this treatment can be found in Reference 29.

Yan and Holmstedt³⁶ have recently developed a very efficient narrow-band model for fire applications that they claim is twenty times faster than existing narrow-band models.

In flaming regions where fluctuations in species concentration and temperature are large, the time-mean treatments described here are likely to underpredict radiative transfer.^{37,38} To capture these effects, more sophistication is required than is presented here. References 21 and 38 discuss these treatments in some detail.

Boundary Conditions

The boundary conditions to be used will clearly be dependent on the problem of concern. Those for the momentum equations at solid boundaries have been outlined above. Naturally ventilated fires, though, entrain air from the surrounding environment driven by pressure differences caused by the fire's buoyant acceleration. It is thus necessary to represent an infinite physical region in the finite computational domain. This is generally achieved by taking the computational boundary a long way from the region of the primary flow. The pressure is fixed at this plane while velocity derivatives normal to the boundary are set to zero. At this free boundary, at points of outflow, the derivatives of the scalar fields are set to zero while at points of inflow, ambient conditions are specified.

Heat will be lost from the fire into the structure at a rate determined by both the thermal properties of the bounding walls and time. Early in the fire the walls will be cold and heat-transfer rates, all other things being equal, will be at their highest. Later as the walls get heated, the rate will reduce. Convective and radiative

energy exchanges with control volume faces at the bounding walls must balance conductive loss into the bulk of the solid.

This can be achieved by coupling the solution to a time-dependent, heat conduction equation for the walls. There are a number of ways of treating this. The simplest is to assume that the process can be described by a series of quasi-steady, one-dimensional approximations to the heat conduction equation,

$$\dot{q}_{\text{tot}}'' = -k_s \frac{\partial T}{\partial x} \quad (26)$$

By assuming that the thermal wave penetrates a distance $\delta(t)$ into the solid boundary of thickness d (see Figure 3-8.6), the quasi-steady approximation gives³⁹

$$\delta(t) = \frac{2}{\sqrt{\pi}} \left(\frac{k_s t}{\rho_s c_s} \right)^{1/2} \quad (27)$$

where t is the elapsed time from ignition, and k_s , ρ_s , and c_s are respectively the thermal conductivity, density, and specific heat of the solid.

This simple approximation appears to be reasonably acceptable for use in smoke movement applications where the transience of the gas phase is much shorter than that of the solid walls. Since it underestimates heat flux in the bounding walls, it is not sufficiently accurate for application to surface heat-transfer problems (see the Validation section below). Here the quasi-steady approximation will be inadequate and a more accurate solution of Equation 26 is required.

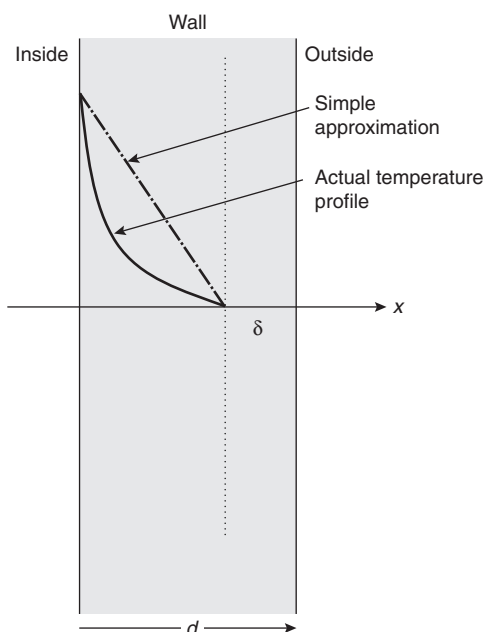


Figure 3-8.6. Simple illustration of one-dimensional conduction.

Numerical Solution Method

Equation 1 describes the local conservation principles for the continuous behavior of ϕ within the domain of interest. The objective of the numerical method is to discretize these nonlinear partial differential equations in space and time and then to solve the resulting set of simultaneous algebraic equations. The discretized form of the generic Equation 1 can be written as

$$A_P^\phi \phi_P = \sum_{nb} A_i^\phi \phi_i + b^\phi \quad (28)$$

where nb stands for all neighboring nodes surrounding the node P . A_i^ϕ and A_P^ϕ are the influence coefficients that comprise convection and diffusion of the property ϕ .

Details of the procedures involved are very complex and cannot be discussed in detail here. They will be found elsewhere (e.g., References 2, 7, and 40).

Ideally, fire-engineering practitioners would prefer not to concern themselves with solution details but with CFD. It is essential to understand the various pitfalls and possible sources of error that may occur. Of course, in numerical approximation, a measure of success of the solution is whether it has converged, meaning, literally, is the numerical solution approaching that of the continuous equations? Converged solutions will be approached by a series of fit-and-try techniques. Successive guesses for the variables are substituted into the equations until each side balances to within acceptable errors. This is repeated over and over many times in a process known as iteration. On any given grid, when the difference between right and left sides—the residuals of the discretized equations—are low for every variable and when examined over the whole field, then the solution might be considered to be converged. However, as we see below, it is essential to demonstrate that the solution is also grid independent before we can be content that we have a reasonably accurate solution to the coupled, continuous equation set.

Some insight can be obtained by considering a discretized form of a continuous spatial derivative at the node point P ,

$$\left(\frac{\partial \phi}{\partial x} \right)_P = \frac{\phi_w - \phi_P}{\Delta x} - \left[\frac{1}{2} \Delta x \left(\frac{\partial^2 \phi}{\partial x^2} \right)_P + \text{H.O.T.} \right] \quad (29)$$

where H.O.T. stands for higher-order terms.

This form of the equation uses an upwind differencing approximation based on only two node points on the numerical mesh—the central node, P , and upwind, west node, W , in this case. This is quite common practice in practical CFD modeling where unconditionally stable solutions are required.

As Δx becomes vanishingly small, it is clear that the terms in the brackets become insignificant. Of course, in reality Δx is finite, and sometimes larger than would be ideal, and thus omission of these terms represents a truncation error in the numerical derivative. Since the largest of these terms, the first in the squared brackets, has the same physical form as does the diffusion equation for ϕ , this is often referred to as *numerical diffusion*. More accurate, higher-order schemes based on additional node points are also

available in most CFD software but tend to give rise to numerical stability problems. However, this simple illustration explains why it is important to use as fine a grid as can be afforded and not to be content with a solution until reasonable grid independence can be demonstrated.

Since an iterative method is used for obtaining the final converged solution, it is desirable to restrict variations in the field values of the solution variable ϕ from one iteration to the next as this reduces the chance of divergence. This process, known as relaxation can be applied in two different ways. A direct way of applying this, the so-called underrelaxation of field variables, is where the “new” solution resulting from the next step of the iterative process does not completely replace its predecessor but only has a weighted influence on it, for example,

$$\phi_p^{\text{new}} = K_\phi \phi_p^{\text{new}} + (1 - K_\phi) \phi_p^{\text{old}}, \quad 0 < K_\phi < 1 \quad (30)$$

where the superscripts “old” and “new” represent the values of ϕ before and after iteration and K_ϕ is a relaxation factor for the variable ϕ . This relaxation factor can differ for the particular equation being solved. The smaller K_ϕ is, the smaller the change in the field variables and heavier the underrelaxation.

The choice of K_ϕ is crucial for achieving a stable and rapid solution. For larger K_ϕ , the solution may experience oscillations that can lead to solution divergence. For smaller K_ϕ , although the solution follows a stable route to convergence, the speed of convergence may be so slow that it becomes effectively “frozen” (when K_ϕ approaches zero).

It is normal practice to use heavy underrelaxation in CFD (for stability of the solution), but it is important to realize that the solution may only change very slowly as a consequence. It is therefore not safe to assume that simply because the residuals or differences, between the left and right side of an equation do not change, convergence has been achieved. This may occur because the equation has been too heavily underrelaxed.

Another way of achieving relaxation is based on inertial relaxation or the method of “false” time steps.⁷ Here, instead of applying relaxation to the field variable, the discretized control volume equations are modified by incorporating an inertial relaxation term, K_{in} :

$$(A_p^\phi + K_{\text{in}})\phi_p = \sum_{nb} A_i^\phi \phi_i + b^\phi + K_{\text{in}} \phi_p^{\text{old}}; \quad K_{\text{in}} \geq 0 \quad (31)$$

where

$$K_{\text{in}} = \frac{\rho_p \text{Vol}_p}{\delta_{\text{ft}}} \quad (32)$$

Here ρ_p is the fluid density at P , Vol_p is the volume of grid cell P and δ_{ft} is a relaxation factor called the false time step (applicable to both steady-state and transient solutions). The larger K_{in} , or the smaller δ_{ft} , the greater the underrelaxation. Similar caution as for the above must be exercised in assessing the convergence of the solution.

When examining a numerical solution, it is also necessary to demonstrate that global mass and enthalpy balances have been achieved. Global mass inflow rates at

enclosure openings together with fuel mass release rates must balance mass outflow rates to within acceptable accuracy. Heat lost by conduction into the enclosing structure together with convected and radiated loss through openings must balance the heat released by the fire source.

Validation

The foregoing text has outlined the basic principles involved in the use of CFD. Here some consideration is given to issues associated with the validation and verification of these models in the fire context. Every commercial CFD code includes a series of test cases to demonstrate the capabilities of the software in application to some classic fluid flow problems. It is important to recognize that while these do validate the technology in general terms, the responsibility for ensuring validity for the application resides with the fire community.

Why is this necessary? The turbulence models used in RANS software have tended to be developed for turbulent shear flow rather than for buoyant convective flow. Thus the assumptions that are made of isotropic turbulence in the standard $k \sim \varepsilon$ model are not strictly valid. The treatments available to describe the influences of buoyancy on turbulent mixing (Equation 2) need to be explored for their validity, as do, of course, many of the other submodels (e.g., for combustion, radiation, etc.) used to describe the whole process.

The general issue of the validity of CFD model simulations is something that the American Association for Aeronautics and Astronautics have addressed in a recent guide.⁴¹ They use the following definitions of validation and verification:

Validation. The process of determining the degree to which a model is an accurate representation of the real world from the perspective of the intended users of the model

Verification. The process of determining that a model implementation accurately represents the developer’s conceptual description of the model and the solution of the model

In the fire context, for example, the turbulence, combustion, and radiation models need to be validated to test their representation of reality. Whether the model equations are then solved to adequate accuracy is then the issue of verification.

The fire literature contains many comparisons of CFD predictions with experimental data (e.g., 42–51). These studies contain elements of both validation and verification. Most, however, have been conducted with a prior knowledge of the experimental results. One of the most important model validation studies has involved a recent series of blind simulation tests conducted under the auspices of Conseil International du Batiment’s Fire Commission CIB W14.⁵² Both zonal and CFD models were applied by various users to round robin test problems for which experimental data were available but not released to users until after their simulations had been submitted.

The experiment used for the model evaluation illustrated here was one of a series performed in the 1980s in the VTT testing hall in Finland, but the results were not published. Two wooden cribs were located inside an enclosure containing a single high-level slot opening (Figure 3-8.7). One of these cribs was ignited and fire was allowed to spread from the first to the second crib. This is a particularly severe test of the modeling methodology since the fire reaches flashover after 20 min or so and continues to burn for approximately 2 hours. This is a severe challenge to both the combustion model and also to the computer hardware requirements needing to compute transient predictions for such a long period.

Other than the geometry and the thermal properties of the wall materials, the only information supplied for the blind simulations was the measured, individual mass loss rates for each crib together with an effective heat of combustion. Mass loss rates were determined from the raw weight loss data through which a smooth curve had been fitted and time derivatives determined. Figure 3-8.8 shows the resultant mass loss rates for the two cribs. A measurement of the effective heat of combustion from oxygen depletion calorimetry throughout the duration of the fire was also supplied (Figure 3-8.9).

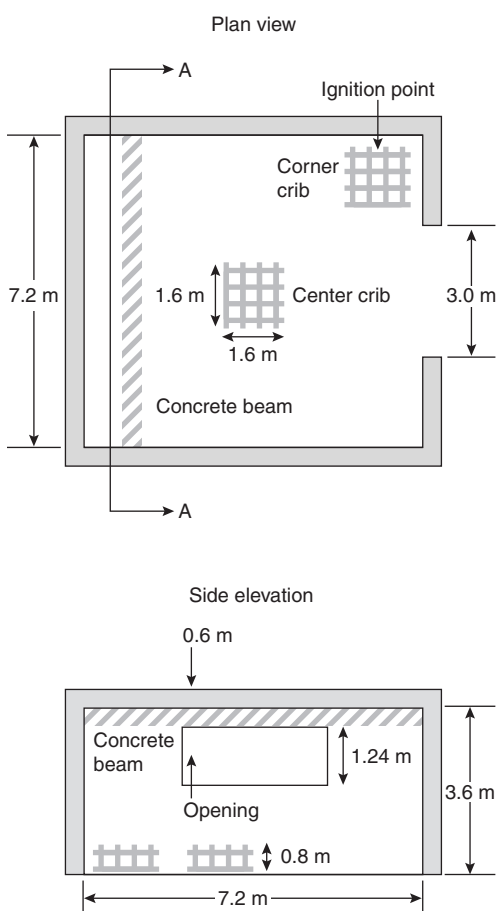


Figure 3-8.7. Geometry of the experiment.

A selection of the results from the JASMINE CFD model is illustrated here (Figures 3-8.10–3-8.13).¹³ It will be seen that gas temperatures and major gas species concentrations have been reasonably well reproduced. Although not perfect, agreement can be seen to be generally acceptable for many practical purposes. The discrepancy evident in the minimum oxygen concentrations is almost certainly due to instrumentation sensitivity limitations at low concentrations.

The poorest performance of the model was in its predicted total heat flux to the bounding surfaces (Figure 3-8.13). Although reasonably acceptable in terms of its impact on local gas temperatures (see Figure 3-8.12), this is not sufficiently accurate for use in the study of heat transfer to structural elements or to new fuel about to ignite as a consequence of the initial fire.

It is likely that this performance results from the crude one-dimensional heat conduction approximation, Equation 26 assumed here, where the linear approximation to the surface temperature gradient underestimates actual heat fluxes at the surface. This is yet to be proved,

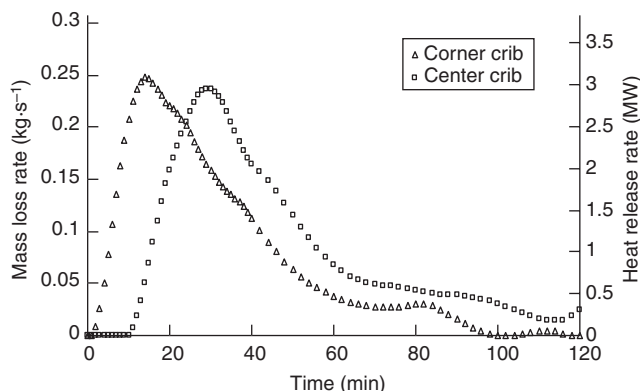


Figure 3-8.8. Mass loss and heat release rates of the two wooden cribs.

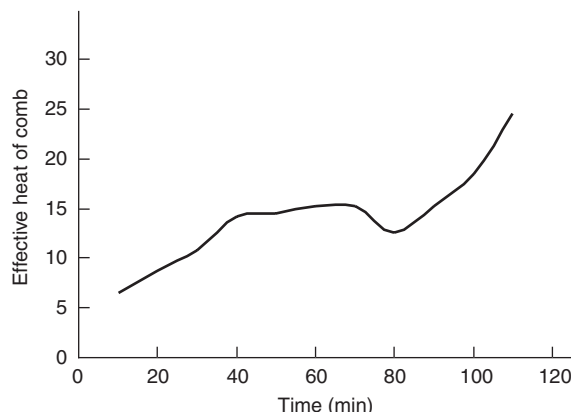


Figure 3-8.9. Measured heat of combustion as a function of time.

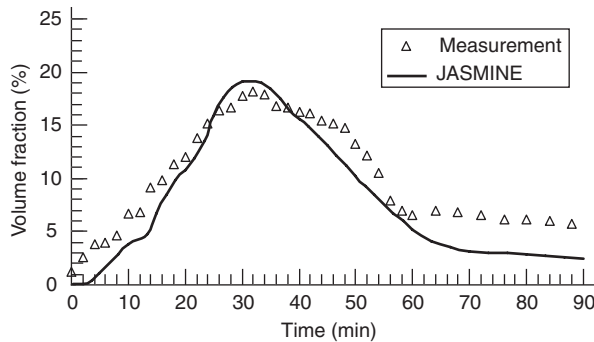


Figure 3-8.10. Comparison of predicted and measured CO_2 volume fraction near the center of the ceiling.

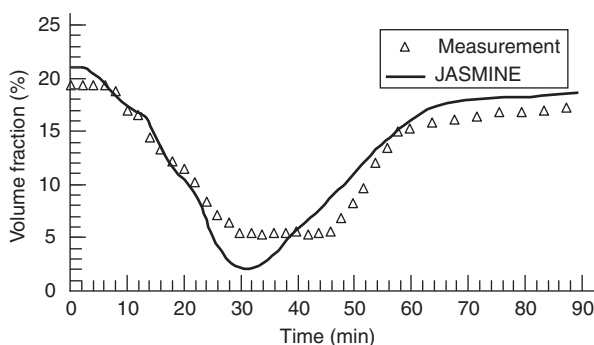


Figure 3-8.11. Comparison of predicted and measured O_2 volume fraction near the center of the ceiling.

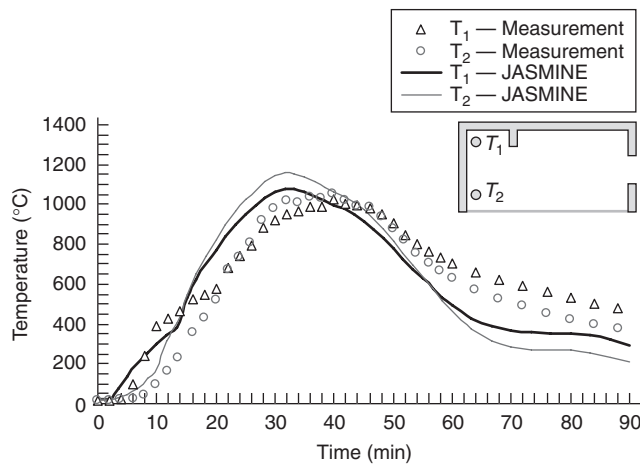


Figure 3-8.12. Predicted and measured gas temperatures close to the back wall.

but these results suggest that the combinations of assumptions adopted together with the CFD methodology are fit for purpose for the exploration of gas phase calculations but that the simple conduction treatment adopted

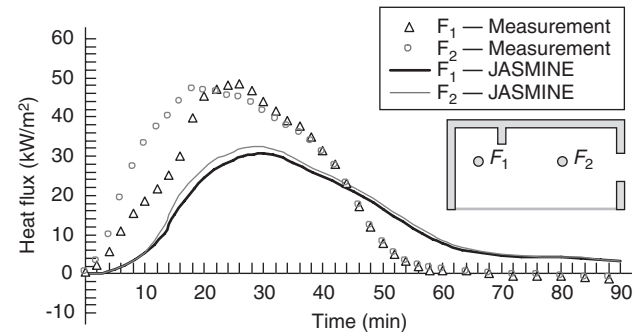


Figure 3-8.13. Predicted and measured surface fluxes from gas to normal density concrete bores.

in this study is not appropriate for examination of solid phase questions.

Ensuring Proper Use

So far we have discussed in outline the principles and content of CFD models. We now need to turn to the issues surrounding their proper use. The performance of the model depends on the proper description of physical and chemical processes for the particular problem, combined with appropriate initial and boundary conditions.

There are two essential components to this process—the first concerning the treatment of fire science and the second concerning establishment of a good numerical solution.

An example of the possible misuse of the modeling methodology as a result of incorrect prescription of the fire itself might be to characterize the fire source by a known or prescribed heat-release rate but then to associate that heat-release rate with an inappropriate fuel area. Close attention needs to be paid, for example, to the relative influences of momentum and buoyancy at the fire source. They are represented by the nondimensional heat-release rate (or source Froude number), Q^* :

$$Q^* = \frac{Q}{\rho_a c_p T_a D^2 \sqrt{gD}} \quad (33)$$

where

Q = heat release rate of the fire

D = characteristic fuel dimension (say, diameter of the fuel base)

g = acceleration due to gravity

The value of Q^* above anything around 2.5 is not representative of buoyant fires but is more appropriate for higher-momentum jet fires. If the problem concerns the normal unwanted fire, then it is likely that too small a fuel area has been associated with the heat release rate. Of course, if the hazard being modeled is a high-pressure gas-pipe leakage, then a higher Q^* is perfectly reasonable.

Another problem can occur when no combustion model is employed and instead a volumetric heat source is used to describe the fire. Too small a volume will yield gas temperatures in the source that are much too high. The authors have seen examples of peak gas temperature predictions of over 5000°C in such sources when the adiabatic flame temperature—an absolute limit on gas temperature—is unlikely to exceed, say 2000°C. Clearly this kind of erroneous source description grossly misrepresents buoyant acceleration and indeed buoyant turbulent mixing at the source. Such errors are easy to avoid with proper attention to the characteristics of buoyant fires.

Measured time-averaged gas temperatures in a fire seldom exceed around 1300°C. Since the CFD code spatially averages these temperatures over the mesh spacing, it is unlikely that model will predict temperatures as high as this. Anything above this temperature should be treated with caution and anything above the adiabatic flame temperature must be incorrect.

Other key features that need to be scrutinized closely when studying a numerical solution are, in addition to the fire source itself, the thermal plume above the flame tip, the resulting ceiling jet and upper hot gas layer, together with wall and vent flows. Simple calculations can be undertaken to check these components of the overall solution.

Concerning the numerical description of the problem an extremely important requirement is that the free boundary conditions outside a compartment opening, for example, or surrounding an unbounded fire, are far enough away as not to influence the solution in the region of interest. Providing a constant-pressure boundary condition across a doorway opening will not, for example, allow the proper inflow and outflow characteristics to be established.

It is comparatively easy to produce impressive-looking visual images of the fluid flow with modern software, but it is essential to demonstrate that the solution is reasonably well converged, by checking for sensitivity to further numerical iteration and further mesh refinement.

A checklist of some of the more important considerations that need to be taken concerning the problem set-up and examination of the solution is listed here.

Considerations of Numerical Aspects

1. Resist the temptation to undertake two-dimensional simulations. These can provide physically misleading solutions. Think where the air entrained into the fire would come from if the problem were really two-dimensional.
2. Choose the mesh to capture the main physical features of the flow ensuring that the near-wall nodes satisfy the criterion $y^+ < 400$ (see Equation 5). Ensure an adequately fine mesh resolution for the fire source and at enclosure openings.
3. Ensure that the aspect ratio of cells is not too large—typically not larger than 50.

4. Analyze the accuracy of the solution by a grid refinement study preferably using at least three different grid resolutions—ideally by doubling the grid cells in all directions. For these buoyant flows, special attention should be given to the vertical mesh spacing.
5. It is likely that a first-order numerical differencing scheme will be used at least initially since it is stable, but, if possible, as convergence is approached use a second- or higher-order scheme.
6. It is not advisable to change too many relaxation parameters at once, as it then becomes difficult to analyze which of the changes has influenced the solution.
7. In transient simulations, be sure that the time step is adapted to the choice of the grid and check the influence of the time step on the results. For a rapidly developing fire, more iterations per time step are generally needed.
8. Normalized mass and momentum continuity errors, and residual errors for all the solved variables, should be less than about 0.01, preferably less than 0.001. In an ideal simulation, the residuals will decrease steadily. However, in practice some equations may oscillate for a while but should eventually decrease (in a damped oscillatory manner).
9. Examine convergence by following monitor data, especially pressure, at critical locations (e.g., in the plume, in the hot gas layer, and in ventilation openings). Monitor values should gradually settle down to their converged levels.
10. Global mass and heat balances should be better than 95 percent in one or more analysis regions. One of these regions should encompass the entire enclosure or building. Generally, global mass balance is achieved quite easily—regardless of the quality of the solution. Global heat balance is often more difficult and a good indicator of how well a solution is converged.
11. Be careful when exploiting an assumed axis of symmetry. When a simulation is run on half a domain for economy, undertake a simulation on the full domain using the half-domain results as the initial condition.
12. Explore difficulties in achieving a steady-state solution by utilizing transient simulations. There may be no steady solution if physical oscillation is present.

Considerations of Fire Science

1. Use a combustion model to allow a proper coupling between local air flow and distributed heat release.
2. Check that Q^* is representative of the fire of concern, for buoyant fires $Q^* < 2.5$.
3. It is important to incorporate radiative loss from the flaming region. The fire plume can lose up to 50 percent of its heat by radiation.
4. Ensure that boundary heat losses are accounted for. These can cause ceiling layers to lose their buoyancy and cool wall currents to fall through a buoyant layer.
5. Check ventilation conditions:

- What is the role of compartment leakages?—See Reference 53 for a discussion of this issue.
 - Has the HVAC been modeled if it is important?
 - Are underventilated conditions likely, and, if so, have they been accounted for in the combustion modeling?
6. Check whether modeling of fire protection measure (e.g., detector, sprinkler, etc.) is required. Realistic reproduction of the ceiling jet characteristics, and therefore a reasonably fine underceiling mesh resolution, will be needed to predict the likelihood of detector or sprinkler activation. Impingement point details, if important, will not be accurately captured by the standard $k \sim \epsilon$ model.
7. For smoke movement problems, a six-flux radiation model is normally adequate. However, for boundary heat transfer predictions, a more sophisticated method such as the discrete transfer method should be considered.
8. Ensure that free boundaries are chosen carefully. A free-pressure boundary should be far enough from any ventilation openings not to affect flows through them (for example, with the ISO room, this should at least be equal to the length of the room). Avoid steep pressure gradients near the free-pressure boundary and ensure that simulations are reasonably insensitive to the boundary position.
9. Do the predictions of the fire source make sense? For example, flame temperature should not exceed 1300°C. Anything higher than 2000°C must be incorrect due to an erroneous source specification; anything higher than 1300°C should be examined closely.
10. Compare flame temperature, flame height, plume entrainment, upper-layer temperature, ceiling jet properties, and so on with empirical correlations.

There will be occasions when the model may suggest unexpected behavior. In a physical model, although presenting a surprise for the engineer, such behavior would nonetheless be believable. However, with a numerical simulation, such an outcome is disturbing because it can have one of two explanations. Either it is genuine as in the physical simulation, or it is the result of some misleading numerical artifact. The possibility of the latter cannot be completely discounted with such complex simulations. It is therefore essential that simple calculations be used to "shadow" the numerical simulations.

During the official enquiry⁵⁴ into the King's Cross underground fire in London, such an unexpected outcome was predicted by the CFD analysis.^{55,56} The flames on a wooden passenger escalator were predicted not to rise in a vertical plume as might at first sight be expected but to lay down in the trench of the escalator. It was only with a study of sensitivity of the results to fire source conditions as well as subsequent physical testing that these numerical predictions were demonstrated to be correct. And indeed, *with hindsight*, not unexpected!

The flames were shown to lay down only when the air required for entrainment into the fire could be provided from above and below the fire, but not from the sides, that is, after the fire had spread across the width of

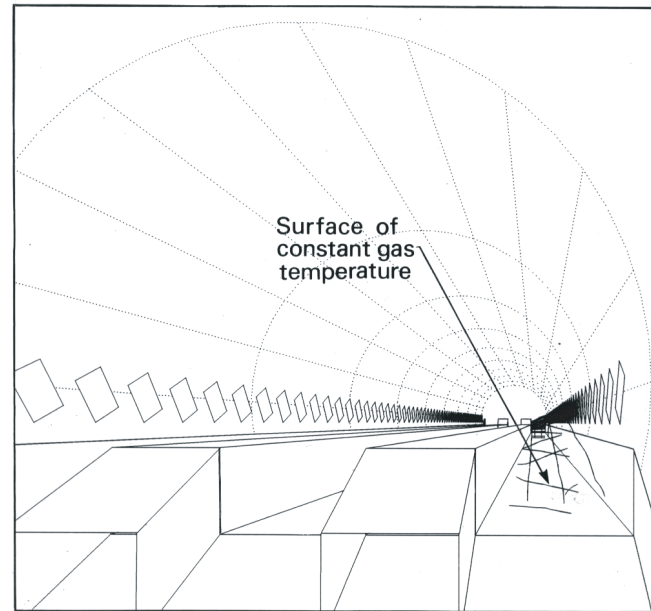


Figure 3-8.14(a). A 1.6-MW fire across the whole width of the channel.

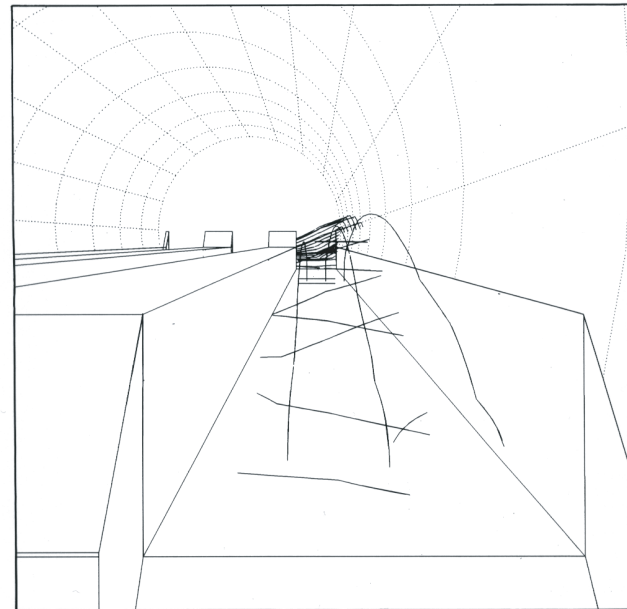


Figure 3-8.14(b). Enlargement of (a) with advertisements removed.

the escalator (Figure 3-8.14).⁵⁶ The fluid mechanics here were locally, essentially two-dimensional. With the fire confined to one side of the escalator, and with local flow three-dimensional, the flames did indeed rise vertically (Figure 3-8.15). This phenomenon with hindsight was already well known from experiences of forest fires accelerating up slopes due to flame leaning.

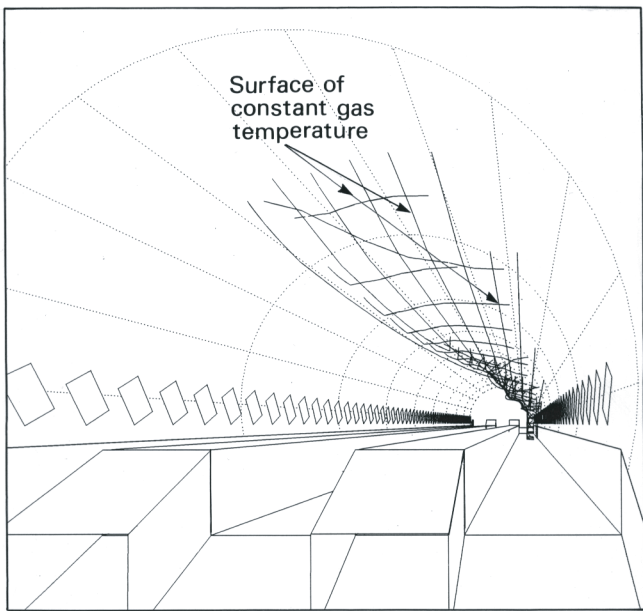


Figure 3-8.15. A 0.5-MW fire across one-third of the channel width.

Some Practical Applications

Most commercial applications of CFD have been restricted to the assessment of smoke control design strategies particularly in large buildings. It is in these kinds of

structures where the traditional building regulations are often not readily applicable and an engineered solution is, of necessity, required. Covered shopping malls, atrium hotels, leisure complexes, airport and railway terminals are just some examples of where the technology is finding its utility for the practicing engineer. Often these structures are unique in nature (e.g., the Millennium Dome in London), but increasingly the codes are being used for more routine problems. An example of the use of CFD for a very large atrium leisure complex is outlined in the Appendix at the end of this chapter. An illustration of the use of CFD to model smoke movement in conjunction with a passenger egress model is provided in Figure 3-8.16. The illustration shows the progress of the combustion products 3 min from ignition of a luggage fire in the terminal building of Brussels International Airport. In this example, the heat release history of the luggage fire source has been taken from experimental data and used as input to the CFD model. The occupants are making their escape based on assumed detection of this fire at one minute.

Figure 3-8.17 illustrates another application of the CFD methodology to an exploration of heat transfer within a fire-resistant furnace.⁵⁷ The figure shows predicted gas and furnace surface temperature contours in addition to gas flow streamlines and some gas temperature contours for a commercial fire-resistance wall furnace powered by natural gas and following the standard ISO 834 time-temperature curve. The DT model was used for the treatment of radiant heat transfer but assumed a constant absorption coefficient throughout the furnace. Thermocouple temperatures by which the furnace was controlled were simulated by use of *virtual thermocouples*

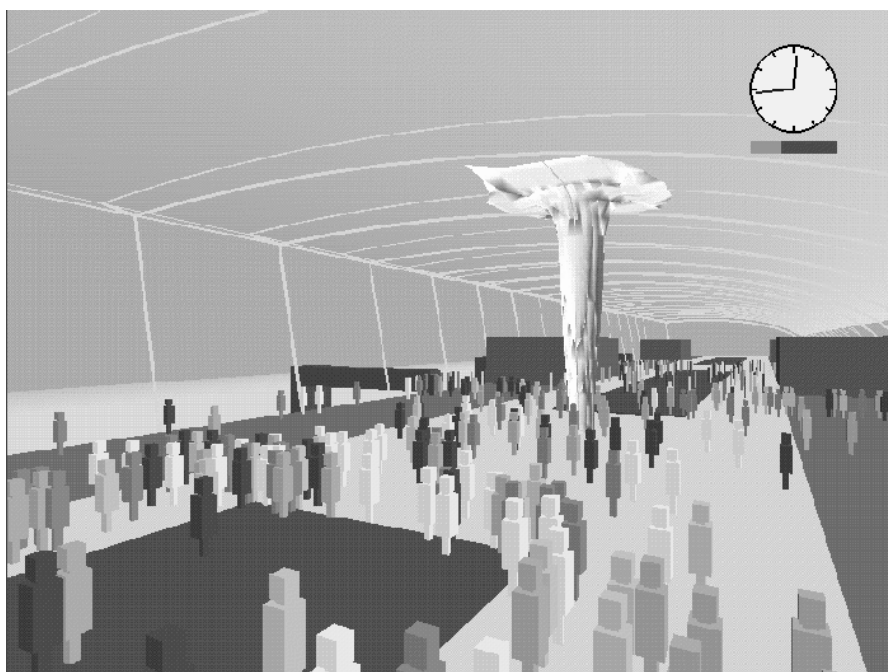


Figure 3-8.16. Simulation of smoke spread and human egress in the design for the Brussels airport passenger terminal.



Figure 3-8.17. Predicted gas and furnace surface temperature contours and flow streamlines.

to account for thermocouple heat transfer and thermal inertia.

More Advanced Application

The CFD methodology has the potential to be used for more complex problems than those associated with smoke movement. The interaction of water sprinklers with the smoke layer is one such example. Another is the issue of flame spread. Both these problems are, though, extremely complex. A brief outline is provided of the approaches that are being applied by the research community that may be of practical utility in the future.

Solid Phase Combustion

The behavior of solid combustibles can be described by applying the conservation principles within the bulk

of the solid subject to the boundary conditions set by the gas phase. For a porous solid, the mass continuity and energy conservation equations will often be sufficient if the solid can be assumed to offer no resistance to the flow of the gaseous pyrolysates from within its bulk. Then the mass continuity equation is

$$\frac{\partial \rho_s}{\partial t} + \frac{\partial}{\partial x_j} (\rho u_j) = 0 \quad (34)$$

where ρ_s is the instantaneous local density of the solid, and the energy conservation equation is

$$\frac{\partial}{\partial t} (\rho_s c_s T_s) + \frac{\partial}{\partial x_j} (\rho u_j c_p T_s) = \frac{\partial}{\partial x_j} \left(k_s \frac{\partial T_s}{\partial x_j} - \dot{q}_R \right) - H_p \frac{\partial \rho_s}{\partial t} \quad (35)$$

where H_p is the heat of pyrolysis. The terms on the left side of Equation 35 represent the unsteady accumulation of energy in the solid together with the energy carried by the gas pyrolysates through the elementary control volume. The right side comprises terms describing thermal conduction, the influence of in-depth absorption of thermal radiation, and the energy lost in the phase change. An Arrhenius pyrolysis rate equation closes the system of equations:

$$\frac{\partial \rho_s}{\partial t} = -B \rho_s \exp \left(-\frac{E_s}{RT_s} \right) \quad (36)$$

These equations can now be solved subject to the boundary condition at the solid surface that

$$\dot{q}_{\text{net}}'' = -k_s \frac{\partial T}{\partial x_j} \quad (37)$$

where \dot{q}_{net}'' represents the net heat transfer to the solid from the gas phase. As has been discussed earlier, the accurate prediction of surface heat transfer is an extremely complex issue and further research is required before robust predictions can be made.

Extensive studies of this kind have been conducted by di Blasi et al.⁵⁸ for the study of flame spread over well-behaved materials such as polymethylmethacrylate and to a lesser degree wood. Others have adopted a similar methodology for the study of both flame spread and pyrolysis from these materials.^{59,60}

Figure 3-8.18 illustrates the application of such an approach to the modeling of flame spread over samples of polymethylmethacrylate within an experimental wind tunnel. These predictions are compared with the measurements of Chao and Fernandez-Pello⁶¹ who varied wind speed, oxygen concentration, and turbulence intensity in the approach flow. The figure shows conditions at a time 25 s after ignition from the front edge of the PMMA slabs over both floor and ceiling samples for an oxygen mass fraction of 0.5, a wind speed of 2 m/s and a turbulence intensity of 10 percent. The predictions clearly show the greater progress of the flame in the floor-mounted case. This, perhaps surprising, result is also shown in the experiment and appears to be the result of the lower flame thickness under the ceiling, resulting from the influences of buoyancy.

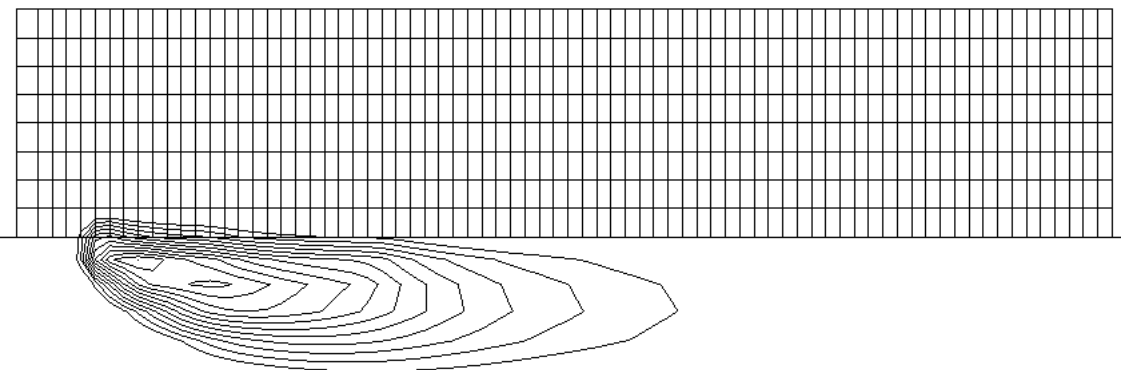


Figure 3-8.18(a). Flame spread over a ceiling-mounted sample of PMMA in a wind tunnel as illustrated by isotherm contours 25 s from ignition (wind speed 2 m/s, oxygen concentration 0.5, and turbulence intensity 10%).

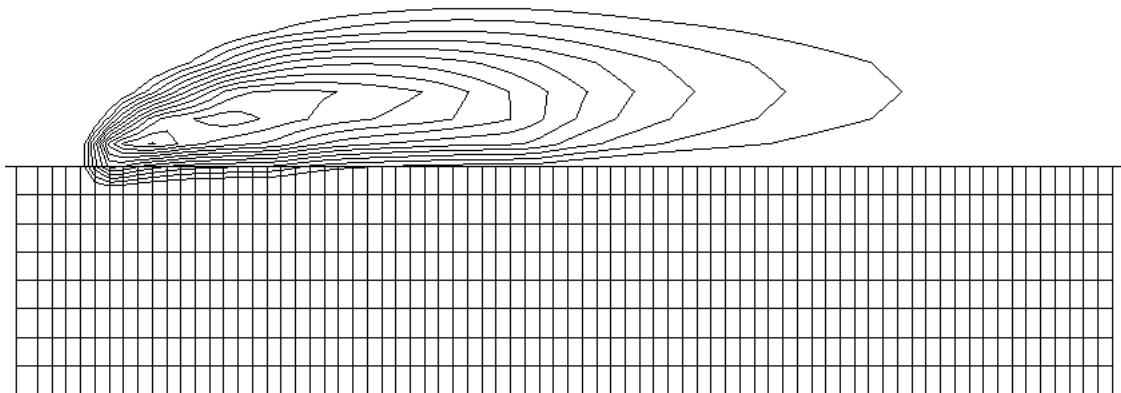


Figure 3-8.18(b). Flame spread over a floor-mounted sample of PMMA in a wind tunnel as illustrated by isotherm contours for the same conditions as in Figure 3-8.18(a).

However, for the full range of products to be found in building structures, a rigorous analysis such as this is not a practical proposition. Physical effects such as delamination, cracking, and bubbling are not readily amenable to such a treatment, and a more pragmatic approach needs to be adopted.

Here a coupling between gas and solid phases exploiting standardized fire test data is likely to be the most successful. Some modeling, exploiting this more pragmatic approach, has been described, for example, by Opstad⁶² and Yan and Holmstedt.⁵⁹

The Influence of Water Sprays on Combustion Products

Naturally, if the solid phase combustion processes are difficult to model, the further complexity of added water at the fire source makes the task even more complex. However, some studies have been undertaken of the interactions of water sprays on fire gases remote from the source to explore the likelihood of smoke being drawn down to floor level by sprinkler sprays.

To model these processes, extra contributions to the gas phase source terms are added in the enthalpy and momentum equations to describe heat and momentum exchange between phases. Furthermore, a mass source term is also needed to account for mass addition from the spray to the gas by evaporation.

These can be obtained by using Lagrangian particle-tracking techniques to trace the trajectories of the droplets through the flow field.⁶³ For a water droplet of diameter D , subject to gravitational acceleration and viscous drag forces, its equation of motion can be written (e.g., see Reference 64) as

$$\frac{dv_i}{dt} = -\left(\frac{18\mu}{\rho_d D^2}\right)\left(\frac{C_D \text{Re}}{24}\right)(v_i - u_i) + g \quad (38)$$

where

v_i = droplet velocity in the i direction

u_i = gas velocity in the i direction

ρ_d = liquid density

C_D = drag coefficient

Re = Reynolds number based on the droplet diameter

$$Re = \frac{\rho D}{\mu} |v_i - u_i| \quad (39)$$

The diameter of the evaporating droplet can be determined from the expression

$$\frac{dD}{dt} = \frac{C_b}{2D} (1 + 0.23 Re^{1/2}) \quad (40)$$

and a vaporization rate constant can be expressed as

$$C_b = \frac{8k}{\rho c_p} \ln \left[1 + \frac{c_p}{L} (T_g - T_d) \right] \quad (41)$$

where k , ρ , and c_p are for the surrounding gas and L is the latent heat of vaporization of the droplet. The droplet temperature as it traverses the flow field can be determined from

$$\frac{dT}{dt} = 6k(2 + 0.6 Re^{1/2} \sigma^{1/3}) \frac{(T_g - T_d)}{\rho_d D^2 c_{p,d}} \quad (42)$$

where $c_{p,d}$ is the specific heat of the liquid.

These ordinary differential equations permit the location, velocity, size, and temperature of each droplet or each size range of droplets to be determined as functions of time.

The contributions that the droplets make to the source terms in the gas phase equations are evaluated by summing the contributions to each gas phase control volume of each size range as it enters and leaves the volume element.

The boundary conditions for the gas phase calculation will be as has already been discussed, but for the droplet calculation will depend upon initial values of velocity, size, and temperature of the droplets. Such information is not readily available although there has been some recent effort to obtain such data for typical sprinkler heads (e.g., see Reference 65).

Figure 3-8.19 illustrates a simple calculation of spray-fire interactions in a forced ventilated enclosure fire. Immediately above a 400-kW pool fire is an imaginary sprinkler injecting, at a velocity of $10 \text{ m}\cdot\text{s}^{-1}$ a line of droplets of 0.5-mm diameter. Their progress through the fire plume is shown with the stars representing the point at which complete evaporation has occurred. Only very few of the droplets reach the floor of the compartment, most being lifted by the buoyant plume to evaporate at a high level. Work of this kind is in its infancy, but calculations such as these demonstrate the potential.

Software and Hardware Issues

Software tends to be divided between the fire-specific computer programs that have been developed by fire research laboratories and general-purpose programs available from commercial software vendors. The latter contain much of the same fundamental treatments for turbulence and thermal radiation but often not the fire-specific components. In essence, all are alike although they do differ in detail. Each has its strengths and weaknesses. Usually the commercial programs are more highly developed in terms

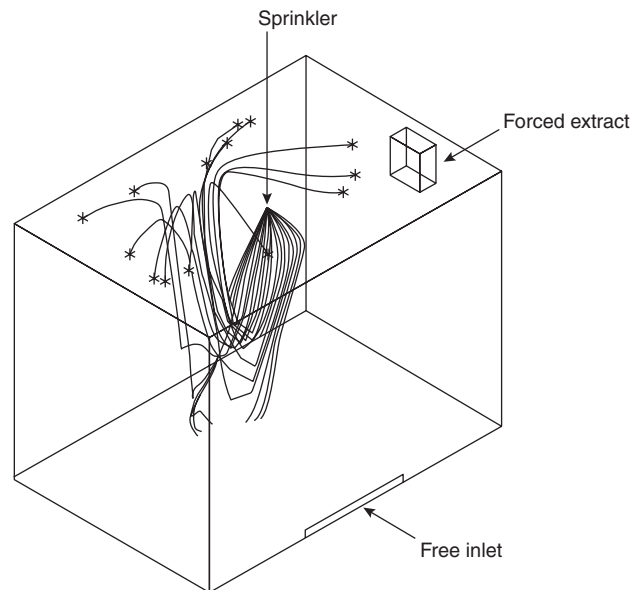


Figure 3-8.19. Predicted trajectories of water droplets.

of their numerical efficiency and incorporation of a broader range of treatments for some of the more general physical aspects but do not have the same pedigree of validation as the fire-specific codes.

The RANS fire-specific programs include JASMINE,¹⁸ SOFIE,⁴⁶ SMARTFIRE,⁵⁰ and KAMELEON.¹⁹ In the general-purpose category are PHOENICS,⁶⁶ CFX,⁶⁷ FLUENT,⁶⁸ and STAR-CD.⁶⁹ The NIST LES model³ is unique in the sense that it is the only LES fire model that has so far been used for practical three-dimensional fire applications.

Workstations and top-end PCs are quite suitable for calculation of smoke movement problems. Hardware costs continue to drop, and while, as always, the fastest machine available will always be preferable, a \$5,000 machine should be enough to allow three-dimensional smoke movement simulations to be conducted on a 100,000 node mesh. Steady-state simulations should be completed overnight with transient simulations up to around 10-min real time over a couple of days.

Annual licenses on commercial software range from around \$10,000 to \$20,000. For fire-specific software, license costs are lower. The higher prices of the commercial software tend to reflect the greater degree of software support, documentation, and maintenance available, although this tends, of course, to be of a general nature, with naturally less support available from commercial vendors for fire problems.

Conclusion

The use of CFD fire modeling in fire safety design is growing rapidly. Such models are no longer restricted to just the academic developers and research institutions. Many building design offices now have access to CFD codes offering the ability to design smoke control systems with the same tools as can be used to assess building

ventilation. The possibility of simulating ambient air movements both before and after the outbreak of fire also offers a powerful new capability for examination of early fire detection strategies. With the increasing trend toward performance-based regulation, such simulation tools will inevitably become increasingly attractive, particularly now that they can be used on personal computers. The relatively low license and hardware costs now ensure much greater accessibility than ever before.

However, education and training costs to ensure proper use cannot be ignored. It is relatively easy to run modern CFD software to produce impressive color images that may look plausible, but without proper consideration of the issues we have raised in this chapter, there are serious risks that the models will be misused. Hopefully this contribution will go some way to guide fire safety engineers on the proper use of this extremely powerful technology.

Appendix: An Exemplification of the Use of CFD for Smoke Control in a Large Atrium Building

This study was undertaken on behalf of local building control authorities to assess the effectiveness of a smoke control design based on traditional calculation methods. CFD was used because of the unique size of the building (regulations and traditional design approaches outside their normal expected range of validity).

The Building

The particular building of concern here was a large, six-story atrium complex designed for use as an indoor leisure park. An outline of the atrium design is shown in Figure 3-8.A1. The atrium building was a single envelope of overall dimensions 150 m long, 62 m wide, and 52 m high. Inside, the proposed design consisted of a central

atrium approximately 104 m long, 27 m wide, and 40 m high, with five floors of galleries, each approximately 17.5 m in width and 6 m high, open to the central atrium. The side elevation of the gallery on the first floor is shown in Figure 3-8.A2.

Main doorways, 6 m wide by 5 m high, were situated at either end of the main atrium, providing both means of escape for occupants on the atrium floor and for the provision of replacement air for the high-level powered extraction systems.

Ventilation

Fans capable of handling six air changes per hour— $165 \text{ m}^3/\text{s}$ (the recommendation of the local building control authority) were proposed to be installed at the top of the atrium void. These were to be activated on fire detection by beam detector at first floor level. On each gallery the fresh air supply at ceiling level of $1.7 \text{ m}^3/\text{s}$ in each partitioned smoke zone switched to an extraction of $29 \text{ m}^3/\text{s}$ on fire detection. The fan capacities had been calculated based on traditional methods and for a steady 5-MW fire.

Fire Safety Objectives

The purpose of the study was to assess the validity of the smoke control strategy based on traditional calculation methods. The occupants of a gallery were assumed to be able to escape to a place of safety within 10 min of fire detection—no egress calculations were performed.

Fire Scenarios

Three main fire scenarios were considered for the galleries. The first scenario corresponded to a growing fire situated centrally at the front part of the first gallery floor. The second examined that same fire now at the back of

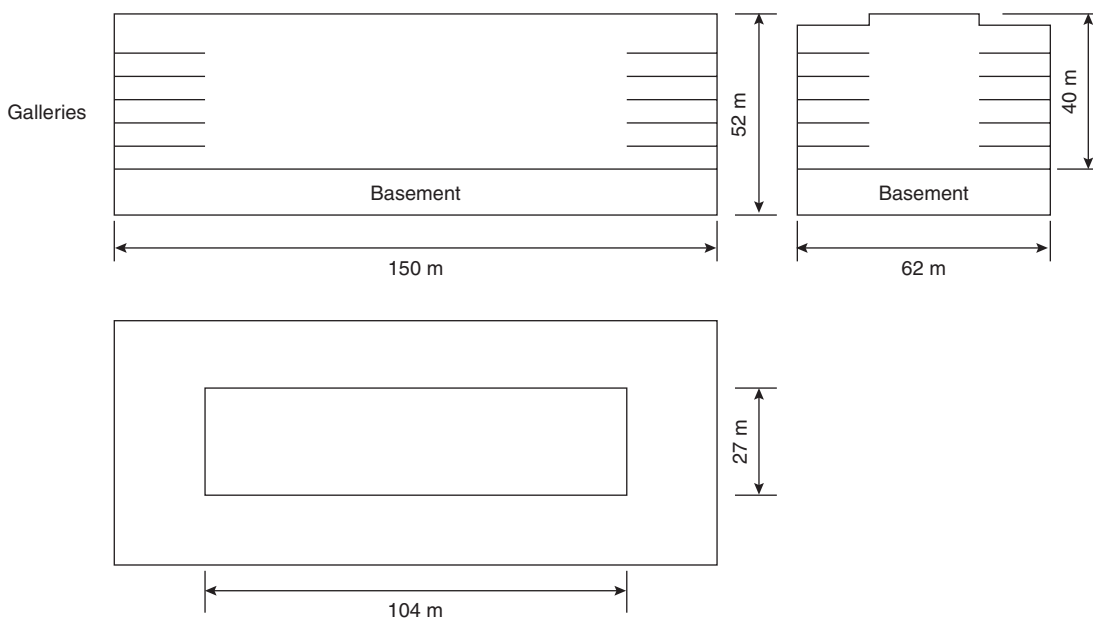


Figure 3-8.A1. Outline of large atrium surrounded by open galleries.

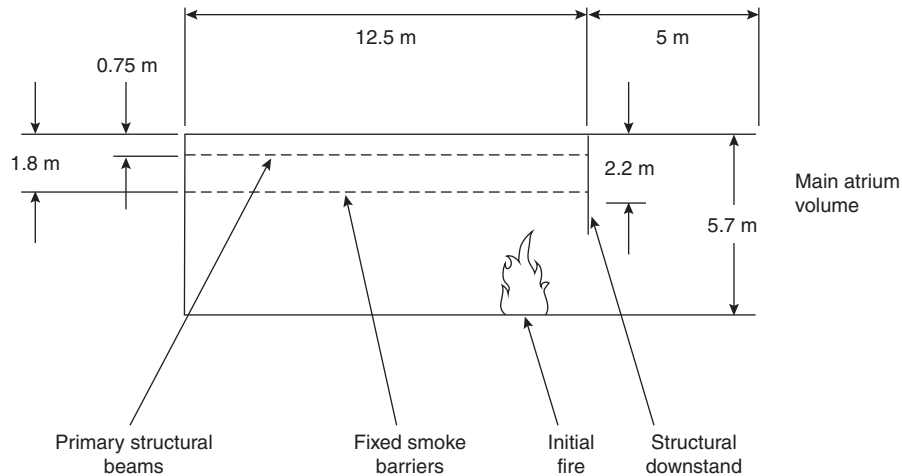


Figure 3-8.A2. Gallery—side elevation.

the gallery. The concern here was to explore the likely effects of a fire close to a reservoir screen. The third scenario corresponded to a fire on the floor of the atrium, situated along the centerline and 25 m from one end.

Design Fire Sizes

Design fires were chosen after discussions with representatives of designers and local building control and fire service representatives. Exponentially growing fires, with an initial rate of heat release of 100 kW, were assumed for each fire scenario. For the gallery cases, the fire was assumed to grow exponentially, with a doubling time of 1 min until the calculated operation of the first sprinkler head. The rate of heat release was then assumed to drop suddenly to one-half of its value at that time and then to continue to grow exponentially, but more slowly, with a doubling time of 3 min. The area of the fire source was also allowed to increase such that the local rate of heat release per unit area did not exceed 0.5 MW/m².

For the atrium fire, the rate of heat release was allowed to grow exponentially, doubling every minute until it reached 3.2 MW (at 5 min), at which level it was assumed constant.

Detection and Fire Suppression Activation Criteria

Fire detection was assumed to occur when the product mass fraction exceeded 1.4×10^{-3} at the detector head locations. This empirical value was taken to be equivalent to 20-m visibility through the smoke from polyurethane mattress fires. Sprinkler activation was determined from the rate of rise of gas temperature in the control volumes occupied by sprinkler heads and by assuming a response time index for each sprinkler head to be $210 \text{ m}^{1/2} \cdot \text{s}^{1/2}$.

Prefire Conditions

For the gallery fire, an ambient air temperature of 20°C has been assumed throughout the computational domain. For the atrium fire, the air temperature has been assumed to increase linearly from 20°C at floor level to 45°C just under the ceiling.

Results and Discussion

Gallery fire: Figure 3-8.A3(a) shows the times for the operation of detectors D1 and D2 in the fire zone, detector

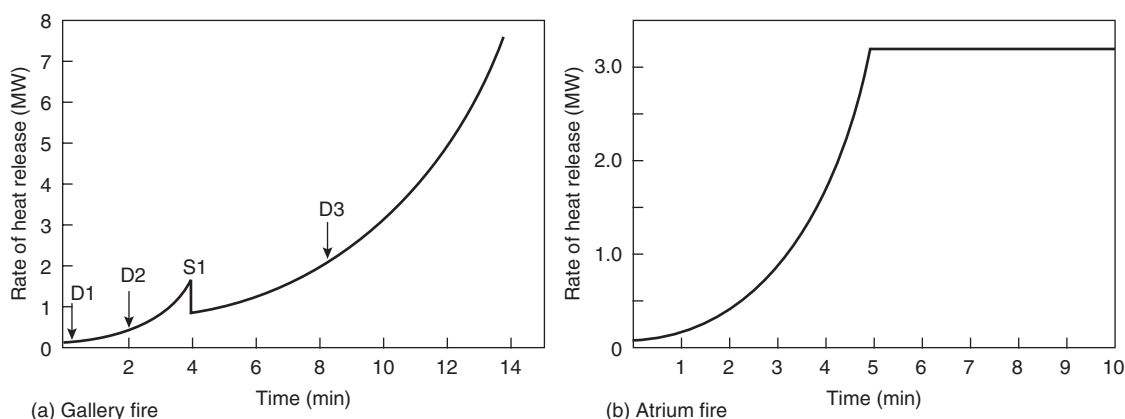


Figure 3-8.A3. Design fires for atrium complex.

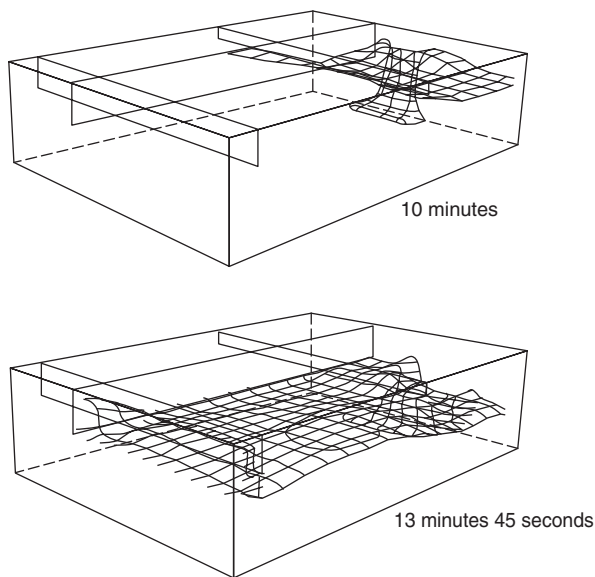


Figure 3-8.A4. Evolution of hazardous gas temperature of 80°C from above, looking toward main atrium volume.

D3 in the adjacent zone, and the operation time for the first sprinkler nearest to the fire. It can be seen that the detector adjacent to the fire operated almost immediately. Figure 3-8.A4 shows the evolution of the contour of a hazardous, breathable gas temperature (80°C).

It can be seen that this hazardous contour takes about 10 min to reach the structural beam and crosses the smoke barrier (toward the adjacent smoke zone) in 11 min (not shown) and then starts spilling into the atrium as well as

to the adjacent zone. This suggests that for the growing fire considered, the proposed extraction system would be able to cope with the smoke produced until 11 min have elapsed from the start of the fire.

The sprinkler operation pattern is shown in Figure 3-8.A5. By the time the rate of heat release had reached 5 MW (at 12 min), 14 sprinkler heads were predicted to have operated. This is well within the maximum operating area of the ordinary hazard group III sprinkler system specified under LPC rules for automatic sprinkler installations.⁷⁰

Should the fire continue to grow in the way assumed, however, then by the time 7.5 MW was reached, 40 heads would have operated, well in excess of the LPC rules for assumed maximum area. The system would, therefore, "overrun" in these circumstances.

Atrium fire: The progress of a number of predicted visibility contours on a vertical slice through the center of the atrium is illustrated in Figure 3-8.A6. The model predicts that a beam detector, at the first gallery floor level, detects the fire at 65 s when its heat output has reached 200 kW. On detection, the mechanical extract system operates and the escape doors at both ends of the atrium open to admit replacement air. The sudden opening of the doors causes the rising smoke plume to be deflected sideways, so much so that the dense smoke extends across the floor of the atrium, threatening occupants over a distance of 20 m to 30 m. As the fire continues to grow, producing greater buoyancy, the plume slowly recovers. However, smoke at floor level does remain a problem until around 8 min. Smoke also enters the galleries at a high level, but since its temperature, optical density, and toxic gas concentration are below significant levels, this does not cause serious concern.

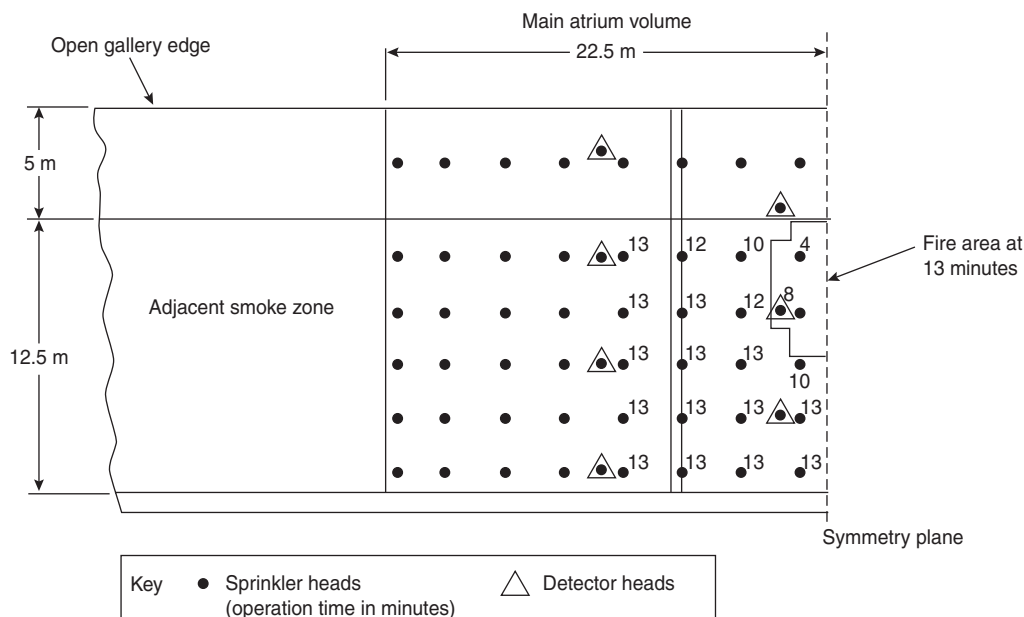


Figure 3-8.A5. Sprinkler operation pattern in gallery smoke zone.

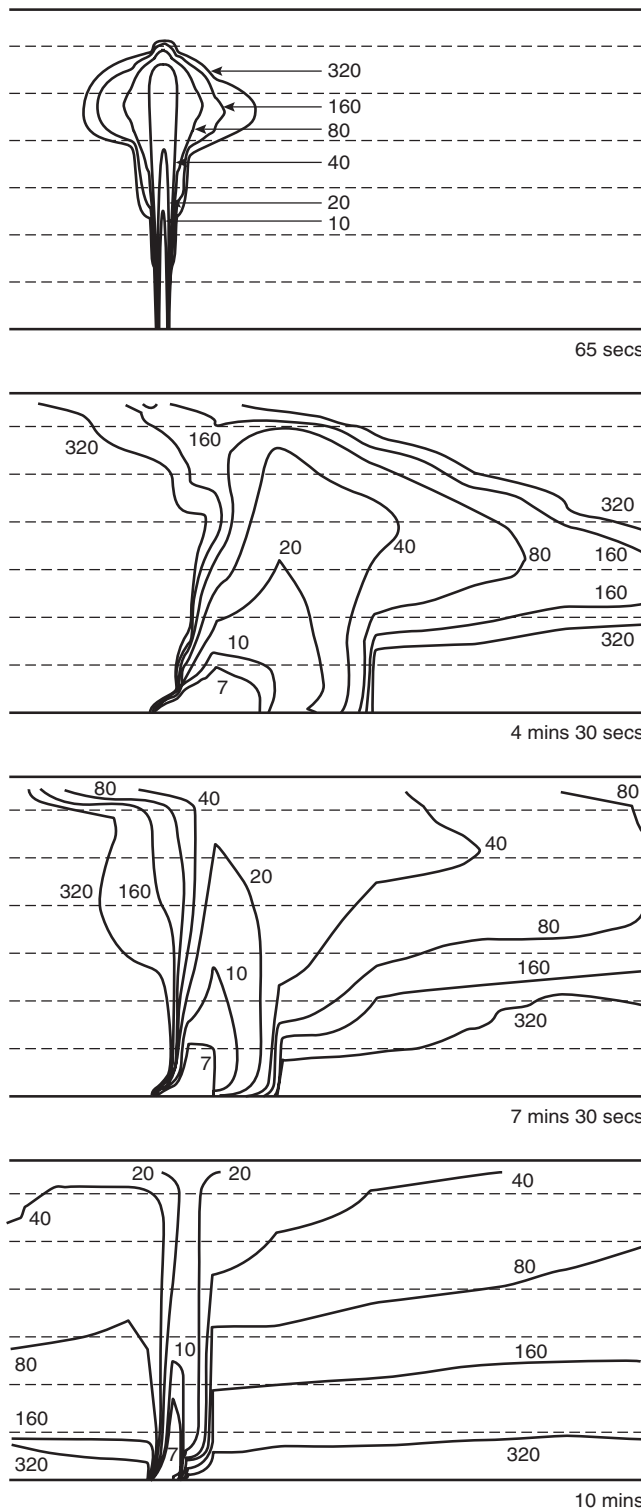


Figure 3-8.A6. *Evolution of predicted visibility contours (m) on a vertical slice through the center of the atrium.*

Conclusion

The model predictions suggest that management of the smoke extraction system required attention in the main atrium. A progressive increase of the extraction rate

would be one solution to the deflection of the smoke along the atrium, as would a redesign of the air inlets to prevent jetting.

Nomenclature

a	radiation absorption coefficient (Equations 13–21)
A_i^ϕ	influence coefficients (Equations 28, 31)
b^ϕ	source and time-dependent terms (Equations 28, 31)
b	weighting coefficient (Equations 21, 22)
B	pre-exponential factor (Equations 11, 36)
c	soot concentration (Equation 21)
c_p	specific heat
C_1, C_2	constants in $k \sim \varepsilon$ model (Table 3-8.1)
C_μ	
C_D	drag coefficient (Equation 38)
C_b	evaporation constant (Equations 40, 41)
d	wall thickness (Figure 3-8.6)
D	fuel base diameter (Equation 33); droplet diameter (Equations 38–40, 42)
E	constant in log-law of wall (Equation 3), activation energy (Equation 11)
E_b	blackbody emissive power (Equations 13–21)
f	mixture fraction (Table 3-8.1, Equation 10)
f_v	soot volume fraction (Equation 24)
F	Fuel (Equation 9)
F_i	radiative flux in i th direction (Equations 13–17)
G	turbulent generation term (Table 3-8.1)
g	acceleration due to gravity
H.O.T.	higher-order terms (Equation 29)
h	enthalpy
I	radiation intensity (Equation 18)
k	thermal conductivity (Equations 26, 35), turbulent kinetic energy (Table 3-8.1, Equations 11, 12)
K_ϕ, K_{in}	underrelaxation and inertial relaxation factors (Equations 30–32)
l	pathlength (Equation 21)
L	latent heat of vaporization
O	oxidant (Equation 9)
p	pressure
p_w, p_c	partial pressures for water vapor and CO_2 (Equations 21, 25)
P_j	constant in Equation 4 representing resistance of laminar sublayer
P	product (Equation 9)
\dot{q}''	flux
\dot{Q}	heat release rate
Q^*	nondimensional heat release rate (or source Froude number)
R	gas constant (Equation 11)
Re	Reynolds number
s	stoichiometric requirement of fuel (Equations 9, 11), scattering coefficient
S	source term (Table 3-8.1)

<i>t</i>	time
<i>T</i>	temperature
<i>u</i>	gas velocity
<i>v</i>	droplet velocity
Vol	cell volume
<i>x</i>	spatial coordinate
<i>y</i>	distance from wall (Equation 5)
<i>Y</i>	mass fraction (Table 3-8.1; Equation 11)

Greek

α	radiation absorptivity (Equations 23–25)
β	conserved scalar (Equation 10)
γ	coefficient of thermal expansion (Equation 2)
Γ	exchange coefficient (Table 3-8.1)
ε	rate of dissipation of turbulent kinetic energy (Table 3-8.1, Equation 11)
κ	von Karman constant (Equation 3)
λ	radiation wavelength (Equation 24)
μ	absolute viscosity (Table 3-8.1; Equation 5)
ν	kinematic viscosity
ρ	density
σ	Prandtl/Schmidt numbers (Table 3-8.1)
ϕ	general fluid property variable (Table 3-8.1)
Ω	solid angle (Equations 19, 20)
ξ	normalized partial pressure (Equation 25)

Superscripts

$+$	dimensionless property in wall functions
$-$	time average
$'$	fluctuating property, correction
$"$	per unit area
$'''$	per unit volume
$*$	guessed value; derived expression; nondimensional parameter
t	near wall value

Subscripts

i,j,k	three Cartesian coordinate directions
a	ambient
b	blackbody
B	buoyancy
c	convective
d	liquid drop
f	fuel
k	shear
l	laminar
nb	neighboring node
o	oxidant
ox	oxygen
P	nodal point
R	radiation

<i>s</i>	solid, soot
st	stoichiometric value
<i>t</i>	turbulent
tot	total
<i>w</i>	wall

References Cited

1. L.F. Richardson, "Volume 1: Meteorogy and Numerical Analysis," Collected Papers, Cambridge University Press (1993).
2. G. Cox, *Combustion Fundamentals of Fire*, Academic Press, London (1995).
3. K.B. McGrattan, H.R. Baum, and R.G. Rehm, "Large Eddy Simulations of Smoke Movement," *F. Safety J.*, 30, p. 161 (1998).
4. X. Zhou, K.H. Luo, and J.J.R. Williams, "Dynamic Behaviour in Reacting Plumes," in *Proceedings of the Twenty-Eighth Symposium (International) on Combustion*, Combustion Institute, Pittsburgh (2000).
5. L. Vervisch and T. Poinsot, "Direct Numerical Simulation of Non-Premixed Turbulent Flames," *Ann. Rev. Fluid Mech.*, 30, p. 655 (1998).
6. G. Cox, *Turbulent Closure and the Modelling of Fire Using CFD*, Phil. Trans. Roy. Soc., London, A 356, p. 2835 (1998).
7. S.V. Patankar, *Numerical Heat Transfer and Fluid Flow*, Hemisphere, Washington, DC (1980).
8. H.K. Versteeg and W.M.G. Malalasekera, *An Introduction to Computational Fluid Dynamics*, Longman, London (1995).
9. S. Kumar, "Mathematical Modelling of Natural Convection in Fire—A State of the Art Review of the Field Modelling of Variable Density Turbulent Flow," *Fire Materials*, 7, pp. 1–24 (1983).
10. S.V. Patankar and D.B. Spalding, "A Computer Model for Three-Dimensional Flow in Furnaces," in *Fourteenth Symposium (International) on Combustion*, Combustion Institute, Pittsburgh, pp. 605–614 (1973).
11. W.P. Jones and J.H. Whitelaw, "Calculation Methods for Reacting Turbulent Flows: A Review," *Combustion & Flame*, 48, p. 1 (1982).
12. N.C. Markatos, M.R. Malin, and G. Cox, "Mathematical Modelling of Buoyancy Induced Smoke Flow in Enclosures," *Int. J. Heat Mass Transfer*, 25, pp. 63–75 (1982).
13. S.D. Miles, S. Kumar, and G. Cox, "Comparison of 'Blind Predictions' of a CFD Model with Experimental Data," in *Proceedings of the Sixth International Symposium on Fire Safety Science*, IAFSS, Boston, pp. 543–554 (2000).
14. B.E. Launder and B.I. Sharma, "Application of the Energy Dissipation Model of Turbulence to the Calculation of Flow Near a Spinning Disc," *Lett. Heat and Mass Transf.*, 1, pp. 131–138 (1974).
15. D.B. Spalding, "Mixing and Chemical Reaction in Steady State Confined Turbulent Flames," in *Thirteenth Symposium (International) on Combustion*, Combustion Institute, Pittsburgh, pp. 649–657 (1971).
16. B.F. Magnussen and B.H. Hjertager, "On Mathematical Modelling of Turbulent Combustion with Special Emphasis on Soot Formation and Combustion," in *Sixteenth Symposium (International) on Combustion*, Combustion Institute, Pittsburgh, pp. 719–729 (1976).
17. B.F. Magnussen, B.H. Hjertager, J.G. Olsen, and D. Bhaduri, "Effects of Turbulent Structure and Local Concentrations on Soot Formation and Combustion in Acetylene Diffusion Flames," in *Seventeenth Symposium (International) on Combustion*, Combustion Institute, Pittsburgh, pp. 1383–1393 (1978).

18. G. Cox and S. Kumar, "Field Modelling of Fire in Forced Ventilated Enclosures," *Combust. Sci. Technol.*, 52, pp. 7–23 (1987).
19. J. Holen, M. Brostrom, and B.F. Magnussen, "Finite Difference Calculation of Pool Fires," *Twenty-Third Symposium (International) on Combustion*, Combustion Institute, Pittsburgh, pp. 1677–1683 (1990).
20. S. Gordon and B.J. McBride, "Computer Program for Calculation of Complex Chemical Equilibrium Compositions, Rocket Performance, Incident and Reflected Shocks and Chapman-Jouguet Detonations," *NASA SP-273* (1971).
21. J.B. Moss, "Turbulent Diffusion Flames," *Combustion Fundamentals of Fire*, Academic Press, London (1995).
22. S.K. Liew, K.N.C. Bray, and J.B. Moss, "A Flamelet Model of Turbulent Non-Premixed Combustion," *Combust. Sci. Technol.*, 27, pp. 69–73 (1981).
23. G.M. Faeth, S.M. Jeng, and J. Gore, "Radiation from Fires," in *Heat Transfer in Fire and Combustion Systems*, 45, p. 137 (1985).
24. F.C. Lockwood and N.G. Shah, "A New Radiation Solution Method for Incorporation in General Combustion Prediction Procedures," in *Proceedings of the Eighteenth Symposium (International) on Combustion*, Combustion Institute, Pittsburgh, pp. 1405–1414 (1981).
25. N.W. Bressloff, "CFD Prediction of Coupled Radiation Heat Transfer and Soot Production in Turbulent Flames," Ph.D. Thesis, Cranfield University, UK (1996–1997).
26. N.W. Bressloff, J.B. Moss, and P.A. Rubini, "Application of a New Weighting Set for the Discrete Transfer Radiation Model," in *Proceedings of the Third European Conference on Industrial Furnaces and Boilers*, Lisbon, Portugal (1995).
27. P.S. Cumber, "Ray Effect Mitigation in Jet Fire Radiation Modelling," *Int. J. Heat Mass Transf.*, 43, pp. 935–943 (2000).
28. M. Aksit, P. Mackie, and P.A. Rubini, "Coupled Radiative Heat Transfer and Flame Spread Simulation in a Compartment," in *Proceedings of the Third International Seminar on Fire and Explosion Hazards*, Lake Windermere, UK, pp. 343–354 (2000).
29. S. Kumar, A.K. Gupta, and G. Cox, "Effects of Thermal Radiation on the Fluid Dynamics of Compartment Fires," in *Proceedings of the Third International Symposium on Fire Safety Science*, Elsevier, London, p. 345 (1991).
30. F.C. Lockwood and W.M.G. Malalasekera, "Fire Computation: the Flashover Phenomenon," in *Proceedings of the Twenty-Second Symposium (International) on Combustion*, Combustion Institute, Pittsburgh, pp. 1319–1328 (1988).
31. J.S. Truelove, "Mixed Grey Gas Model for Flame Radiation," Harwell, UK Atomic Energy Authority Report AERE HL 76/3448, (1976).
32. W.L. Grosshandler, "Radiative Heat Transfer in Non-Homogeneous Gases: A Simplified Approach," *Intl. J. Heat Mass Transfer*, 23, p. 1447 (1980).
33. A.T. Modak, "Radiation from the Products of Combustion," *Fire Res.*, 1, pp. 339–361 (1978–79).
34. B. Leckner, "Spectral and Total Emissivity of Water Vapour and Carbon Dioxide," *Combust. Flame*, 19, pp. 33–48 (1972).
35. J.D. Felske and C.L. Tien, "Calculation of the Emissivity of Luminous Flames," *Combust. Sci. Technol.*, 7, pp. 25–31 (1973).
36. Z. Yan and G. Holmstedt, "Fast, Narrow-Band Computer Model for Radiation Calculations," *Numerical Heat Transfer*, 31B, p. 61 (1997).
37. G. Cox, "On Radian Heat Transfer from Turbulent Flames," *Combust. Sci. Technol.*, 17, pp. 75–78 (1977).
38. J.P. Gore and G.M. Faeth, "Structure and Spectral Radiation Properties of Turbulent Ethylene/Air Diffusion Flames," in *Twenty-First Symposium (International) on Combustion*, Combustion Institute, Pittsburgh, pp. 1521–1531 (1987).
39. H.S. Carslaw and J.C. Jaeger, *Conduction of Heat in Solids*, Oxford University Press, England (1959).
40. C.T. Shaw, *Using Computational Fluid Dynamics*, Prentice Hall, London (1992).
41. Guide for the Verification & Validation of CFD Simulations, American Institute of Aeronautics & Astronautics, Guide G-077-1998, AIAA, Reston, VA (1998).
42. S. Kumar and G. Cox, "The Application of a Numerical Field Model of Smoke Movement to the Physical Scaling Compartment Fires," in *Numerical Methods in Thermal Problems*, pp. 837–848 (1983).
43. S. Kumar and G. Cox, "Mathematical Modelling of Fire in Road Tunnels," in *Proceedings of the Fifth International Symposium on Aerodynamics and Ventilation of Vehicle Tunnels*, BHRA, Cranfield, UK, p. 61 (1985).
44. W.H. Ayres, "Fundamental Studies of the Extinguishment of Pool Fires in a Cross Wind," Ph.D. Thesis, University of Sheffield, UK (1988).
45. F.C. Lockwood and W.M.G. Malalasekera, "Fire Computation: the Flashover Phenomenon," in *Twenty-Second Symposium (International) on Combustion*, Combustion Institute, Pittsburgh, pp. 1319–1328 (1988).
46. M.J. Lewis, J.B. Moss, and P.A. Rubini, "CFD Modelling of Combustion and Heat Transfer in Compartment Fires," in *Proceedings of the Fifth International Symposium on Fire Safety Science*, International Association for Fire Safety Science, Melbourne, Australia, pp. 463–474 (1997).
47. N.L. Crawford, S.K. Liew, and J.B. Moss, "Experimental and Numerical Simulation of a Buoyant Fire," in *Comb. Flame*, 61, p. 63 (1985).
48. G. Cox, S. Kumar, and N.C. Markatos, "Some Field Model Validation Studies," in *Proceedings of the First International Symposium on Fire Safety Science*, Hemisphere, Washington, DC, pp. 159–171 (1986).
49. Y.L. Sinai, "Validation of CFD Modelling of Unconfined Pool Fires with Cross Wind: Flame Geometry," *Fire Safety J.*, 24, p. 1 (1995).
50. L. Kerrison, N. Mawhinney, E.R. Galeas, N. Hoffmann, and M.K. Patel, "A Comparison of Two Fire Field Models with Experimental Room Fire Data," in *Proceedings of the Fourth International Symposium on Fire Safety Science*, IAFSS, Ottawa, Canada, pp. 161–172 (1994).
51. S. Nam, "Numerical Simulation of Smoke Movement in Clean Room Environments," *Fire Safety J.*, 34, p. 169 (2000).
52. S. Hostikka and O. Keski-Rahkonen, "Design and Simulation Reports of CIB W14 Round Robin for Code Assessment, Scenario B," *VTT Building Technology Internal report RTE119-IR-2*, Espoo, Finland (1998).
53. Y. Sinai, "Comments on the Role of Leakages in Field Modelling of Under-Ventilated Compartment Fires," *Fire Safety J.*, 33, p. 11 (1999).
54. D. Fennel, "Investigation into the King's Cross Underground Fire," Her Majesty's Stationery Office, London (1988).
55. S. Simcox, N.S. Wilkes, and I.P. Jones, "Computer Simulation of the Flows of Hot Gases from the Fire at the King's Cross Underground Station," *Fire Safety J.*, 18, p. 49 (1992).
56. G. Cox, R. Chitty, and S. Kumar, "Fire Modelling and the King's Cross Fire Investigation," *Fire Safety J.*, 15, p. 7 (1989).
57. S. Welch and P. Rubini, "Three Dimensional Simulation of a Fire Resistance Furnace," in *Proceedings of the Fifth International Symposium on Fire Safety Science*, IAFSS, Melbourne, Australia, pp. 1009–1020 (1997).
58. C. di Blasi, S. Crescitelli, G. Russo, and A.C. Fernandez-Pello, "Model of the Flow Assisted Spread of Flames over a Thin Charring Combustible," in *Proceedings of the Twenty-Second*

- Symposium (International) on Combustion*, Combustion Institute, Pittsburgh, pp. 1205–1212 (1988).
- 59. Z. Yan and G. Holmstedt, "CFD and Experimental Studies of Room Fire Growth on Wall Lining Materials," *Fire Safety J.*, 27, p. 201 (1996).
 - 60. V. Novozhilov, B. Moghtaderi, D.F. Fletcher, and J.H. Kent, "Computational Fluid Dynamics Modelling of Wood Combustion," *Fire Safety J.*, 27, p. 69 (1996).
 - 61. Y.H.C. Chao and A.C. Fernandez-Pello, "Concurrent Horizontal Flame Spread: The Combined Effect of Oxidiser Flow Velocity, Turbulence and Oxygen Concentration," *Comb. Sci. Tech.*, 19, pp. 110–111 (1995).
 - 62. K. Opstad, "Modelling of Thermal Flame Spread on Solid Surfaces in Large Scale Fires," Doctoral Thesis, University of Trondheim, Norway (1995).
 - 63. C.T. Crowe, M.P. Sharma, and D.E. Stock, "The Particle-Source-in-Cell Model for Gas Droplet Flows," *ASME Journal of Fluids Engineering*, 99, p. 325 (1977).
 - 64. F. Boysan, W.H. Ayres, J. Swithenbank, and Z. Pan, "Three Dimensional Model of Spray Combustion in Gas Turbine Combustors," *J. Energy*, 6, p. 368 (1982).
 - 65. S. Kumar, G.M. Heywood, and S.K. Liew, "Superdrop Modelling of a Sprinkler Spray in a Two-Phase CFD-Particle Tracking Model," in *Proceedings of the Fifth International Symposium on Fire Safety Science*, Melbourne, Australia, p. 889 (1997).
 - 66. <http://www.cham.co.uk>
 - 67. <http://www.aeat.com/cfx>
 - 68. <http://www.fluent.com>
 - 69. <http://www.cd.co.uk>
 - 70. *Rules for Automatic Sprinkler Installations*, Loss Prevention Council, UK (1996).

SECTION THREE

CHAPTER 9

Smoke and Heat Venting

Leonard Y. Cooper

Introduction

Objectives of Venting by Design

Smoke and heat venting is the removal of hot smoky gases from the upper parts of one or more rooms of a fire-containing facility and the introduction of relatively cool and uncontaminated air into the lower parts of the rooms from adjacent spaces or from the outside environment. Smoke removal by venting may be driven by (1) natural convection (i.e., buoyancy-driven forces), occurring either fortuitously (e.g., natural venting of smoke through broken windows near the top of a room of fire origin) or by design (e.g., a well-designed system of fusible-link-actuated ceiling vents); by (2) mechanical ventilation (i.e., fan-driven smoke removal); or by (3) a combination of these.

The main objectives of venting by design are (1) to facilitate escape of people from fire environments by restricting spread of smoke and hot gases into escape routes; (2) to facilitate fire fighting by enabling fire fighters to enter the building and to see the seat of the fire; and (3) to reduce property damage from fires due to exposure to smoke and hot gases.

The Focus of This Chapter

The focus of this chapter is on fire safety problems involving smoke venting of single spaces of fire origin and/or freely connected (i.e., via relatively large connecting

Dr. Leonard Y. Cooper was a research engineer in the Building and Fire Research Laboratory of the National Institute of Standards and Technology from 1978 to 1998. Since 1998 he has been senior scientist/engineer at Hughes Associates Inc., a fire protection engineering research and development firm. Since 1978 he has focused on applying a broad range of the physical and mechanical engineering sciences to develop and transfer research results into technically sound engineering practices in the field of applied fire safety. His research has included the development of mathematical models of fire phenomena and on the assembly of these into compartment fire models and associated computer programs for practical and research-oriented compartment fire simulations.

openings) adjacent spaces by designed use of ceiling- or near-ceiling-mounted vents. Typical, relevant compartment geometries are (1) large, open, ceiling vent-deployed warehouse-type spaces (see Figure 3-9.1), possibly divided by ceiling-mounted screens or draft curtains into separate, freely-connected, curtained spaces; and (2) multiple-space, atrium-like facilities (see Figure 3-9.2) involving fire near the floor of a ceiling-vented atrium (Space 1) or fire in a ground- or mezzanine-level shop (Space 2A or Space 2B) adjacent and freely connected to a ceiling-vented atrium.

This chapter is concerned with basic engineering concepts underlying the design of complete venting systems

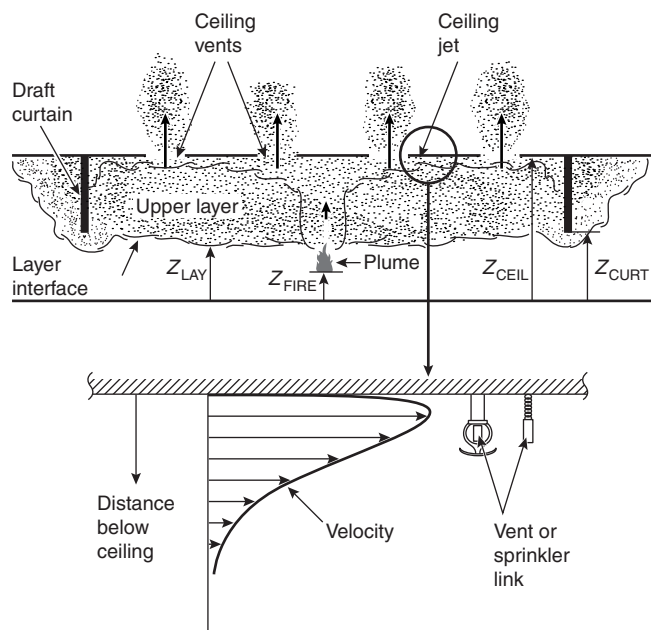


Figure 3-9.1. Fire in a building space with draft curtains and ceiling vents.

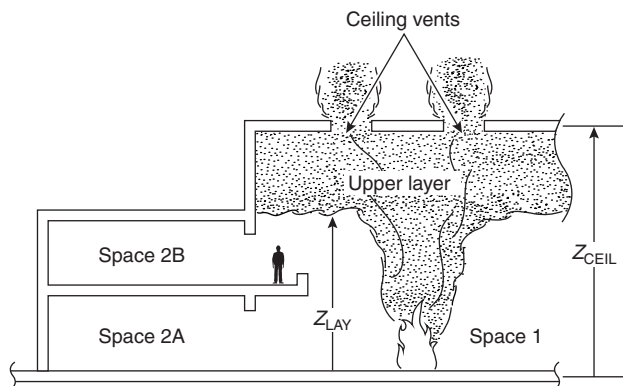


Figure 3-9.2. Fire near the floor of a ceiling-vented atrium with ground- and mezzanine-level shops.

for the above types of facility. These include the provision of vents and inlets, fans, and allied features, such as ceiling-mounted screens or draft curtains, where the latter would be deployed to divide a space into separate curtained compartments to limit the smoke from spreading outside an arbitrary, curtained compartment of fire origin.

Venting phenomena become significantly more complex when venting is used in conjunction with active sprinkler systems. The first part of the chapter deals with the traditional aspects of venting in the absence of operating sprinklers. The extent of current knowledge on the interaction of vents and sprinklers and the design of combined vent/sprinkler systems is discussed at the end of the chapter.

It is beyond the scope of this chapter to be exhaustive on all aspects of the subject of smoke and heat venting. In this regard, the reader is particularly encouraged to complement the material presented here with that provided in References 1–4, each of which provides design-type guidance on aspects of smoke and heat venting, and in Section 4, Chapter 13, "Smoke Management in Covered Malls and Atria."

A major feature of this chapter is the presentation of the actual equations required for the design of successful smoke- and heat-venting systems. Many of these equations can be found in References Cited. When introducing these equations, it is an important objective of the presentation here to include their physical bases and their logical context. This is done to enhance the reader's understanding of basic concepts and, to the extent possible, to avoid their inappropriate use.

Simulating Fire-Generated Environments and the Action of Venting

Criteria for Successful Vent Design

A ceiling-vent design is successful to the extent that it controls the fire-generated environment of fire origin according to any of a variety of possible specified criteria. For example, if the likely growth rate of a fire in a particular burning commodity is known, a vent system with

large enough vent area, designed to provide for timely opening of the vents, should be expected to lead to rates of smoke removal consistent with a fire-safe environment. Regarding life safety objectives, the design should allow occupants of the space enough time to exit safely. Regarding property protection, fire fighters arriving at the fire at a specified time subsequent to fire detection should be able to approach and attack the fire successfully and protect commodities in adjacent spaces from being damaged.

Evaluating the Success of a Particular Vent Design

To evaluate the success of a particular vent design and/or design strategy it is necessary to predict the development of the fire environment in the fire compartment as a function of any of a number of physical characteristics that define, and may have a significant effect on, the fire environment. Examples of such characteristics are floor-to-ceiling height and area of the compartment spaces and thermal properties of its ceilings, walls, and floors; type of barriers that separate the space of fire origin and adjacent spaces (e.g., full walls with vertical door-like vents or ceiling-mounted draft curtains); material type and arrangement of burning commodities (in the case of warehouse configurations, e.g., wood pallets in $3\text{ m} \times 3\text{ m}$ arrays and stacked 2 m high); type, location, and method of deployment of devices that detect the fire and actuate the opening of deployed ceiling vents, or initiate the operation of sprinklers [e.g., fusible links of specified Response Time Index (RTI) that are distributed at a specified spacing and mounted at a specified distance below the ceiling]; and size of the open area of deployed ceiling vents themselves.

Fire environments can involve substantially steady-state phenomena, but it is more typical for time-dependent phenomena to play a prominent role in real fire safety problems of interest. In most cases, the best way to predict the fire environment and to evaluate the likely effectiveness of a vent design is to use a reliable mathematical model that simulates the various, relevant physical phenomena that come into play during the fire scenario. Such a tool of analysis would be designed to solve well-formulated mathematical problems, based on relevant principles of physics and fundamentally sound, well-established empirical relationships. In this regard, venting phenomena are part of the general phenomena of fire and smoke spread through single- or multiroom compartments. Indeed, any compartment fire model that can simulate the development of fire-generated conditions in enclosed facilities can typically also be used as an engineering tool for the design and analysis of venting.

Even for a particular class of problem, like the engineering problem associated with successful vent design, there is a good deal of variation among applicable mathematical models that are available or among those that could be developed to carry out the task. Such models would differ from one another by the number and detail of individual physical phenomena taken into account. Thus, the above list of physical characteristics that define and may have a significant effect on the fire scenario does not include outside wind conditions, which could have an important influence on the fire-generated environment. A

model may or may not include the effect of wind. One that included this effect would be more difficult to develop and validate and more complicated to use, but, if well developed, it would be significantly more reliable than a model that assumes a quiescent outside environment.

In the next section a group of phenomena is described that, taken together, represents a physical basis for estimating the fire-generated environment and the response of fusible vent or sprinkler links in well-ventilated compartment fires with draft curtains and fusible-link-actuated ceiling vents. The phenomena include growth of the smoke layer in the curtained compartment; flow dynamics of the buoyant fire plume; flow of smoke through open ceiling vents; flow of smoke below draft curtains; continuation of the fire plume in the upper layer; heat transfer to the ceiling surface and thermal response of the ceiling; velocity and temperature distribution of the plume-driven, near-ceiling flow (called the *ceiling jet*) and response of near-ceiling-deployed fusible links. An understanding of and capability of accounting quantitatively for these phenomena is a basic requirement for understanding and simulating their simultaneous action.

The Physical Basis for Simulating Fire-Venting Phenomena

The Basic Fire Scenario

Unless noted otherwise, the discussion of basic phenomena is couched in terms of a generic Figure 3-9.1-type of fire scenario and facility. As will be mentioned, these considerations are also directly applicable to Figure 3-9.2-type scenarios.

The reader is referred to the first part of Section 3, Chapter 10, "Compartment Fire-Generated Environment and Smoke Filling," for a complementary and somewhat more general qualitative discussion of phenomena for generic two-room compartment fire scenarios. The discussion there is applicable to all configurations of Figures 3-9.1 and 3-9.2.

Refer to Figure 3-9.1. Consider the space of fire origin defined by ceiling-mounted draft curtains and with near-ceiling, fusible-link-actuated ceiling vents and sprinklers. The curtained area can be considered one of several such spaces in a large building compartment. Also, by specifying that the curtains be deep enough, they can be thought of as simulating the walls of a single uncurtained compartment. The first part of this chapter identifies and discusses critical physical phenomena that determine the overall environment in the curtained space up to the time of actuation of sprinklers, if they are deployed. The objective is to identify and describe the phenomena in a manner that captures the essential features of this generic class of fire scenario, and allows for a complete and general, but appropriately concise and simple, simulation.

The overall building compartment is assumed to have near-floor inlet vents that are large enough to maintain the inside environment, below any near-ceiling smoke layers which may form, at outside-ambient conditions. It is assumed that a two-layer zone-type model describes adequately the phenomena under investigation.

The characteristics of the lower layer, from the floor, at $z = 0 = z_{\text{FLOOR}}$, to the bottom of the upper smoke layer, at $z = z_{\text{LAY}}$, are assumed to be well described by those of the outside ambient. In general, the upper smoke-layer thickness changes with time, but at any instant it is assumed to be uniform in space, with absolute temperature, T_{LAY} , and density, ρ_{LAY} .

Mass and energy are transferred continuously to and from the upper and lower layers by a variety of mechanisms to be discussed. Conservation of energy and mass along with the perfect gas law is applied to the layers. This leads to equations that require estimates of components of heat transfer, enthalpy flow, and mass flow to the layers. Qualitative and some key quantitative features of these phenomena are described and presented below.

Hydrostatic Pressure Variation as a Function of Elevation within the Fire Space and in the Outside Environment

The hydrostatic pressure of a standard ambient atmosphere at sea level is $P_{\text{AMB}} = 101325 \text{ Pa}$. Also, air at nearly standard atmospheric conditions can be well approximated as a perfect gas with equation of state

$$P = \rho RT \quad (1)$$

where P , T , and ρ are absolute pressure, temperature, and density, respectively, and $R = 286.8 \text{ J}/(\text{kg}\cdot\text{K})$ is the gas constant for air. For an ambient temperature, assumed here to be $T_{\text{AMB}} = 293 \text{ K}$, it follows from Equation 1 that, for a quiescent standard atmosphere, $\rho_{\text{AMB}} = 1.2 \text{ kg}/\text{m}^3$.

It is generally accepted that for the accuracy required in fire model simulations, the equation of state of fire-heated and -contaminated air, that is, smoke, can be taken to be that of air. Therefore, Equation 1 represents the equation of state for ambient air and for smoke at arbitrary temperatures that are realizable in fires.

The momentum equation, that is, hydrostatics, leads to

$$P(z) = P(z_0) - \int_{z_0}^z \rho(\eta)gd\eta \equiv P(z_0) + \Delta P(z) \quad (2)$$

where z_0 is a datum elevation and $g = 9.8 \text{ m}/\text{s}^2$ is the acceleration of gravity.

Using Equation 1 in Equation 2, it can be shown⁵ that relative variations in $P(z)$ are negligible throughout typical buildings, even when a building includes a fire environment, and throughout the "nearby" outside environment. In particular, throughout buildings and local outside environments

$$P(z) = P(z_0)[1 + O(\delta)] \approx P(z_0) \quad (3)$$

where

$$\delta = \frac{\rho g(z - z_0)}{P(z_0)} \ll 1 \quad (4)$$

The fact that δ is generally small can be shown for the outside environment, for example, by considering changes in

elevation from a z_0 datum of the order of 100 m and by adopting the estimate, $\rho = \rho_{\text{OUT}}(z) \approx \rho_{\text{AMB}}$. Then, assuming that $P_{\text{OUT}}(z_0) \approx P_{\text{AMB}}$, it follows from Equation 4 that

$$\begin{aligned}\delta_{\text{OUT}} &= \frac{\rho_{\text{OUT}}g(z - z_0)}{P_{\text{OUT}}(z_0)} \\ &\approx \frac{(1.2 \text{ kg/m}^3)(9.8 \text{ m/s}^2)(100 \text{ m})}{[10^5 \text{ kg/(ms}^2)]} \\ &= 0.012\end{aligned}$$

and, from Equation 3, that changes in $P_{\text{OUT}}(z)$ throughout the 100-m elevation range will generally (only) be of the order of 1 percent.

It is concluded from Equations 3 and 4 that throughout all practical fire environment-related spaces, including the nearby outside ambient,

$$\rho T \approx \rho_{\text{AMB}} T_{\text{AMB}} = \frac{P_{\text{AMB}}}{R} = \text{constant} \quad (5)$$

Although Equation 5 is a generally valid approximation, and $\Delta P(z)$ of Equation 2 is typically relatively small throughout fire environment-related spaces, these latter variations in pressure as a function of elevation will be seen to play an important role in determining the rate of buoyancy-driven flows through vents. Using again the approximation $\rho = \rho_{\text{OUT}}(z) \approx \rho_{\text{AMB}} = \text{constant}$ in Equation 2 leads to the following estimate for the elevation-dependent variation of the outside environment

$$\begin{aligned}\Delta P_{\text{OUT}}(z) \equiv P_{\text{OUT}}(z) - P_{\text{OUT}}(z_0) &= - \int_{z_0}^z \rho_{\text{OUT}}(\eta) g d\eta \\ &\approx -\rho_{\text{AMB}} g(z - z_0) \quad (6)\end{aligned}$$

Flow through Vents

General theory: The reader is referred to Section 2, Chapter 3, "Vent Flows," for a general discussion on the topic of flow through vents.

Consider a vent (i.e., an opening) in a wall-, ceiling-, or floorlike partition, and, for purpose of discussion, designate the two sides/spaces that are connected by the vent as sides/spaces 1 and 2. In most cases of practical interest here, flow is driven through such a vent mainly by cross-vent hydrostatic pressure differences from the high- to the low-pressure side of the vent, where the traditional means of calculating vent-flow rates is by using an orifice-type flow calculation.

At a particular elevation, somewhat removed from the vent opening, that is, on either side of the partition where velocities of the vent flow are relatively small, assume that the environment is relatively quiescent in the sense that the pressure there is well represented by the hydrostatic pressure. Relative to a common datum elevation, the hydrostatic pressure distributions, $P_1(z)$ and $P_2(z)$, associated with side/space 1 and 2, respectively, on both sides of the vent are calculated from Equation 2. Then, ΔP_{1-2} , the cross-vent difference of these distributions is constructed from

$$\Delta P_{1-2}(z) \equiv P_1(z) - P_2(z) \quad (7)$$

At any particular elevation, the average velocity of the vent flow at a vent opening, V_{VENT} , assumed to be in the direction normal to the plane of the vent opening and from the high- to the low-pressure side of the vent, can typically be well estimated from Bernoulli's equation as applied to flow through orifices

$$|V_{\text{VENT}}(z)| = C \left[\frac{2|\Delta P_{1-2}(z)|}{\rho_{\text{VENT}}(z)} \right]^{1/2} \quad (8)$$

where $\rho_{\text{VENT}}(z)$ is the density of the vent flow (i.e., the density at elevation z in the space, 1 or 2, from which the vent flow originates) and C is the flow coefficient, or coefficient of contraction of the flow subsequent to its passage through the vent opening.

Where the Equation 8 formulation is valid, then for relatively narrow vents (e.g., the characteristic horizontal or vertical span of the vent is relatively small compared to the horizontal or vertical span, respectively, of the partition in which it is contained), C is typically taken to be

$$C \approx 0.61 \quad (9)$$

This is the value associated with relatively high Reynolds-number flows through sharp-edged, circular orifices.

For relatively wide vents (e.g., the width and height of the vent are of the order of the width and height, respectively, of the space from which the vent flow originates), there is no significant contraction of the vent flow subsequent to its passage through the vent, and

$$C \approx 1.0 \quad (10)$$

Equations 8 and 10 will be used below in estimating the rate of smoke flow below draft curtains.

Once $V_{\text{VENT}}(z)$ is obtained from Equation 8, the mass flow rate through the vent is finally calculated by integrating the mass-flow-rate flux across the entire area of the vent. For example, in the case of vents located in vertical wall partitions, the intergral would be from the bottom to the top elevations of the vent opening, z_{BOT} and z_{TOP} , respectively. (Note that an important feature of flows through vents in vertical wall partitions, e.g., flows through open doors or windows or under draft curtains, is that the direction of the flow, i.e., the velocity of the flow, can change direction as a function of elevation because of changes in sign with elevation of ΔP_{1-2} .)

The orientation of a vent; horizontal and vertical vents: Define α as the angle that the normal to the plane of a vent opening makes with the vertical. Throughout this chapter, vents with $\alpha = 0$ will be designated as *horizontal* vents in the sense that the planes of the openings of such vents define horizontal planes. Similarly, vents with $\alpha = 90^\circ$ will be designated as *vertical* vents.

Flow through nonhorizontal vents or through horizontal strips of nonhorizontal vents where ΔP_{1-2} does not change sign: For flow configurations where ΔP_{1-2} does not change signs across the area of a nonhorizontal vent, or across the area of a horizontal strip of a nonhorizontal vent

(a horizontal strip of a vent is defined as a portion of the vent between two horizontal planes), the above-indicated mass-flow-rate-flux integral leads to the following final representation for the total flow rate, \dot{m}_{VENT} , through the vent or through the vent strip:

$$\dot{m}_{VENT} = \left(\frac{1}{\sin \alpha} \right) \int_{z_{BOT}}^{z_{TOP}} W_{VENT}(\eta) \rho_{VENT}(\eta) |V_{VENT}(\eta)| d\eta, \quad (11)$$

$\alpha > 0$

where $W_{VENT}(z)$ is the width of the vent at elevation z ; z_{TOP} and z_{BOT} are the elevations at the top and bottom of the vent or of the strip, respectively; and $|V_{VENT}(z)|$ and $\rho_{VENT}(z)$ are determined from Equation 8 and from the direction of the flow.

Flow through horizontal vents: For horizontal vents, ΔP_{1-2} is uniform in sign and magnitude, V_{VENT} is uniform in direction and magnitude across the entire vent area, and

$$\dot{m}_{VENT} = A_{VENT} \rho_{VENT} |V_{VENT}(z_{VENT})| \quad (12)$$

where A_{VENT} is the area of the vent, z_{VENT} is the uniform elevation of the vent, and $|V_{VENT}(z_{VENT})|$ is obtained from Equations 7 and 8.

Flow through Ceiling Vents in a Figure 3-9.1-Type Fire Scenario

Cross-vent pressure, velocity, and mass-flow rate: Consider Figure 3-9.1-type fire scenarios. For well-designed smoke vent systems, it will be seen from considerations of Equation 2 that the buoyancy of the high-temperature smoke in the fire-containing curtained space will lead to an inside pressure at the ceiling that is larger than the outside pressure. Open ceiling vents there will lead to the desired outflow of smoke through the open vents according to Equations 8 and 12.

For a well-designed smoke vent system, it is assumed that there are always low-elevation (below any inside smoke layer that would have developed), open, inlet-/makeup-air vents connecting the inside space to the outside environment. The flow of outside air into the lower levels of the enclosed space is assumed to maintain the inside environment, outside any smoke layer, at a pressure, temperature, and density that is well approximated by that of the outside environment.

For the above assumptions to be valid, it is necessary that at any particular time during a fire scenario, the total area of the open inlet vents, A_{INLET} , is relatively large compared to A_{VENT} , large enough so that the pressure drop across the inlet vents is negligible compared to the pressure drop across any open ceiling vents. As will be seen, the latter assumption will typically be valid if the total area of the inlet vents is at least 1.5–2 times the total area of open ceiling vents.

Using Equation 6, the assumptions of negligible, below-smoke-layer, inside-to-outside pressure, temperature, and density differences *inside the facility but outside or below the smoke layer* lead to the result:

$$P_{IN}(z) = P_{OUT}(z) = P_{OUT}(z_0) - \rho_{AMB}g(z - z_0), \quad (13)$$

$z \leq z_{LAY}$

where P_{IN} is the hydrostatic pressure inside the facility. A continuation of $P_{IN}(z)$ upward and *into the smoke layer in the curtained space of fire origin* is determined from Equations 2 and 13 as

$$P_{IN}(z) = P_{IN}(z_{LAY}) - \rho_{LAY}g(z - z_{LAY}), \quad (14)$$

$z_{LAY} < z \leq z_{CEIL}$

and ΔP_{IN-OUT} , the inside-to-outside pressure difference *inside the curtained space of fire origin* according to Equation 7, is found from Equations 6, 13, and 14 as

$$\Delta P_{IN-OUT}(z) = \begin{cases} 0, z \leq z_{LAY} \\ (\rho_{AMB} - \rho_{LAY})g(z - z_{LAY}) > 0, \\ z_{LAY} < z \leq z_{CEIL} \end{cases} \quad (15)$$

From Equation 15, the *inside-to-outside pressure difference across horizontal ceiling vents* is

$$\begin{aligned} \Delta P_{IN-OUT}(z_{CEIL}) &= (\rho_{AMB} - \rho_{LAY})g(z_{CEIL} - z_{LAY}) \\ &= \rho_{AMB}g(z_{CEIL} - z_{LAY}) \frac{(T_{LAY} - T_{AMB})}{T_{LAY}} > 0 \end{aligned} \quad (16)$$

Within the smoke layer, in general, and at $z = z_{CEIL}$ in particular, it is seen from Equations 15 and 16 that the inside pressure is always greater than the outside pressure. Thus, as expected, the flow through ceiling vents is from the smoke layer in the inside space to the outside space. Therefore, $\rho_{VENT} = \rho_{LAY}$. Using this last result with Equations 5, 8, 9, and 12 leads to the following estimate for $V_{VENT}(z)$, and \dot{m}_{VENT} for *horizontal ceiling vents*:

$$\begin{aligned} V_{VENT} &= 0.61 \left[2 \frac{\Delta P_{IN-OUT}(z_{CEIL})}{\rho_{LAY}} \right]^{1/2} \\ &= 0.61 \left[2 \frac{\Delta P_{IN-OUT}(z_{CEIL}) T_{LAY}}{(\rho_{AMB} T_{AMB})} \right]^{1/2} \end{aligned} \quad (17)$$

$$\begin{aligned} \dot{m}_{VENT} &= A_{VENT} \rho_{LAY} V_{VENT} \\ &= 0.61 A_{VENT} \left[2 \rho_{AMB} T_{AMB} \frac{\Delta P_{IN-OUT}(z_{CEIL})}{T_{LAY}} \right]^{1/2} \end{aligned} \quad (18)$$

Using Equations 16 and 18, the following final and particularly interesting representation for \dot{m}_{VENT} for *horizontal ceiling vents* is obtained:

$$\begin{aligned} \frac{(\dot{m}_{VENT}/A_{VENT})}{\{0.61 \rho_{AMB} [g(z_{CEIL} - z_{LAY})/2]\}^{1/2}} &= \left[4 \left(1 - \frac{T_{AMB}}{T_{LAY}} \right) \frac{T_{AMB}}{T_{LAY}} \right]^{1/2} \end{aligned} \quad (19)$$

From the above it is seen that the left side of Equation 19 is a function only of T_{LAY}/T_{AMB} . Also, it is easily shown that this dimensionless vent flow-rate variable has a maximum value of 1 when $T_{LAY} = 2T_{AMB}$. For example, for the currently adopted value of $T_{AMB} = 293$ K, the maximum possible flow rate from a ceiling vent above an arbitrary depth of smoke layer will occur when the temperature of the layer is $T_{LAY} = 2(293$ K) = 586 K. If T_{LAY} is larger or smaller than T_{AMB} then there will be a reduction in the vent flow rate from the maximum possible value. (Although larger layer temperatures would lead to greater buoyancy of the layer and larger cross-vent pressure drops, these increased pressure drops, which are proportional to V_{VENT}^2 , would not be great enough to sustain the earlier mass flow rate. This is the case because, with the now-reduced layer density, a larger flow velocity would be required to maintain the previous mass flow rate.)

All the above are well illustrated in Figure 3-9.3 where the left side of Equation 19 is plotted as a function of T_{LAY}/T_{AMB} . From this plot it is seen that if $T_{LAY}/T_{AMB} > 1.3$, that is, $T_{LAY} - T_{AMB} > 90$ K for $T_{AMB} = 293$ K, the effect of T_{LAY} on \dot{m}_{VENT} is minimal and \dot{m}_{VENT} will always be within 80 percent of its maximum possible value. The plot also indicates that T_{LAY} values much smaller than $1.3T_{AMB}$ will lead to significant reductions in \dot{m}_{VENT} .

Generic plots of $P_{IN}(z)$, $P_{OUT}(z)$, and $\Delta P_{IN-OUT}(z)$ and an illustration of the flow through a ceiling vent are presented in Figure 3-9.4.

EXAMPLE 1:

Flow through a horizontal ceiling vent: As an example of the above, consider horizontal ceiling vents above a 3-m-thick smoke layer that is 100 K greater than $T_{AMB} = 293$ K. From Equations 16 and 17 the cross-vent pressure difference and the velocity will be

$$\begin{aligned}\Delta P_{IN-OUT}(z_{LAY}) &= 1.2(\text{kg/m}^3)(9.8)(\text{m/s}^2)(3 \text{ m}) \frac{(100)}{(393)} \\ &= 9.0 \text{ kg/(m}\cdot\text{s}^2) = 9.0 \text{ Pa}\end{aligned}$$

$$\begin{aligned}V_{VENT} &= 0.61 \left[2(9.0 \text{ kg/m}\cdot\text{s}) \frac{(393/293)}{(1.2 \text{ kg/m}^2)} \right]^{1/2} \\ &= 2.7 \text{ m/s}\end{aligned}$$

and, from Equations 5 and 18 and the latter result for V_{VENT} , the mass flow rate of smoke flow per unit area of vent will be

$$\begin{aligned}\dot{m}_{VENT}/A_{VENT} &= 1.2 (\text{kg/m}^3) \left(\frac{293}{393} \right) (2.7) \text{ m/s} \\ &= 2.4 (\text{kg/s})/\text{m}^2\end{aligned}$$

Flow through Shallow Vents on a Sloping Roof

Consider flow through a vent on a sloping roof as depicted in Figure 3-9.5. Here, the cross-vent pressure difference, $\Delta P_{IN-OUT}(z)$, would again be obtained from Equation 15. Designate z_{MID} as the elevation of the middle of the vent and, as depicted in the figure, consider scenarios where the entire vent is above the bottom of the smoke

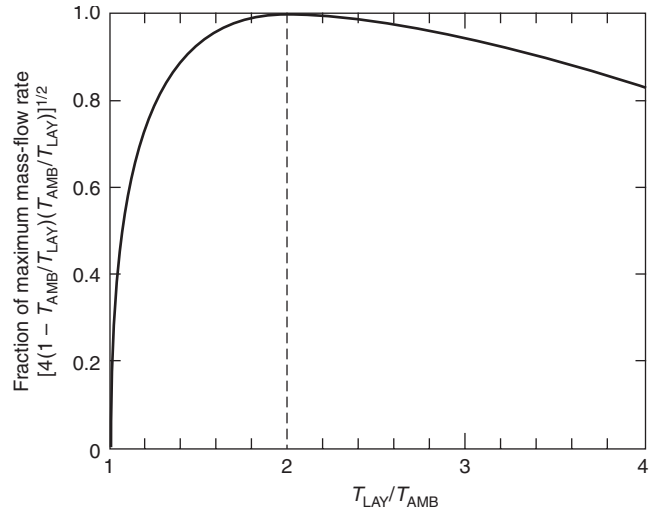


Figure 3-9.3. Plot of $(\dot{m}_{VENT}/A_{VENT})/[0.61\rho_{AMB}[g(z_{CEIL} - z_{LAY})/2]^{1/2}]$ as a function of T_{LAY}/T_{AMB} according to Equation 19.

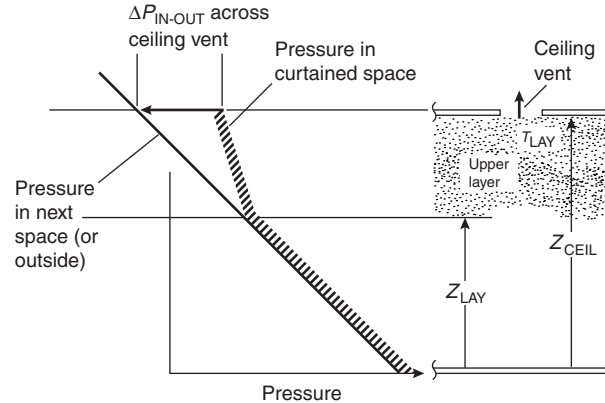


Figure 3-9.4. Flow through a ceiling vent.

layer, that is, $z_{BOT} - z_{LAY} > 0$ and $\rho_{VENT}(z) = \rho_{LAY}$. Then, for the entire surface defined by the vent opening, $\Delta P_{IN-OUT}(z)$ will be uniformly well approximated by $\Delta P_{IN-OUT}(z_{MID})$ if the vent is shallow in the sense that half the height of the vent, $(z_{TOP} - z_{BOT})/2$, is small compared to the depth of the portion of the smoke layer below z_{MID} , that is,

$$\begin{aligned}\Delta P_{IN-OUT}(z) &= \Delta P_{IN-OUT}(z_{MID}) \left[1 - \frac{(z_{MID} - z)}{(z_{MID} - z_{LAY})} \right] \\ &\approx \Delta P_{IN-OUT}(z_{MID})\end{aligned}\quad (20)$$

if (criterion for a "shallow" vent):

$$0 < \frac{(z_{TOP} - z_{BOT})/2}{(z_{MID} - z_{LAY})} \ll 1 \quad (21)$$

When Equation 21 is satisfied, Equation 20 and the constant value, ρ_{LAY} , for $\rho_{VENT}(z)$ can be used in Equation 8.

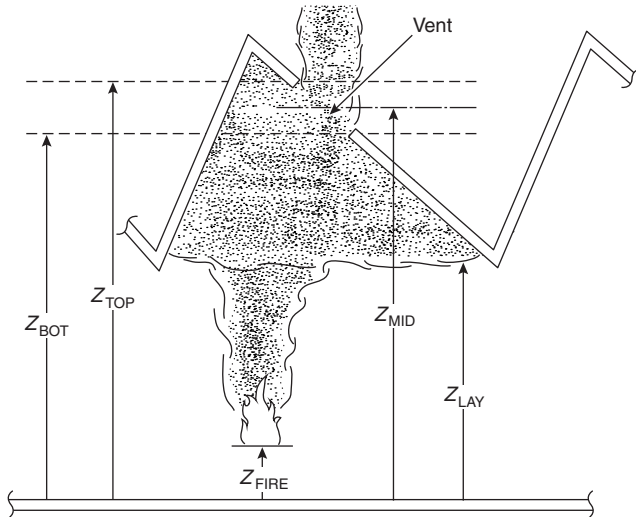


Figure 3-9.5. Flow through a vent in a sloping roof.

Then Equation 11 is well approximated by Equation 12 with z_{VENT} replaced by z_{MID} , and the results of Equations 17–19 for flow through horizontal vents is valid for flow through shallow sloped vents if z_{CEIL} is replaced by z_{MID} .

The Effect of Limited Inlet-Vent Area on the Flow through Ceiling Vents in Figure 3-9.1-Type Fire Scenarios

The above results depend on the assumption that A_{INLET} , the total area of the inlet vents, is large enough compared to the total area of open ceiling vents (in the curtained space of fire origin) that the inside-to-outside cross-inlet-vent pressure drop is small compared to the cross-ceiling-vent pressure drop of Equation 16. If the inlet-vent area is *not* large enough, then, based on the $\Delta P_{IN-OUT}(z_{LAY})$ and V_{VENT} estimates of Equations 16 and 17, respectively, Equations 18 and 19 can still be used to estimate \dot{m}_{VENT} provided the *actual* A_{VENT} in these latter equations is replaced by an *effective* vent area, $A_{VENT,EFF}$, according to⁶

$$\frac{A_{VENT,EFF}}{A_{VENT}} = \left[1 + \left(\frac{A_{VENT}}{A_{INLET}} \right)^2 \left(\frac{T_{AMB}}{T_{LAY}} \right) \right]^{-1/2} \quad (22)$$

$A_{VENT,EFF}/A_{VENT}$ as a function of A_{INLET}/A_{VENT} is plotted in Figure 3-9.6 for fixed values $T_{LAY}/T_{AMB} = 1, 1.3$, and 2 . As can be seen from Equation 22 and from the plot, the larger the value of T_{LAY}/T_{AMB} , the smaller the impact of reduced A_{INLET}/A_{VENT} on reductions below 1 of $A_{VENT,EFF}/A_{VENT}$. It can also be seen in the plot that for $T_{LAY}/T_{AMB} > 1.3$, where the 1.3 value corresponds to the above-identified lowest T_{LAY} for effective venting, $A_{VENT,EFF}/A_{VENT}$ will exceed 0.9, that is, the ceiling vents will be more than 90 percent effective, if $A_{INLET}/A_{VENT} > 1.8$.

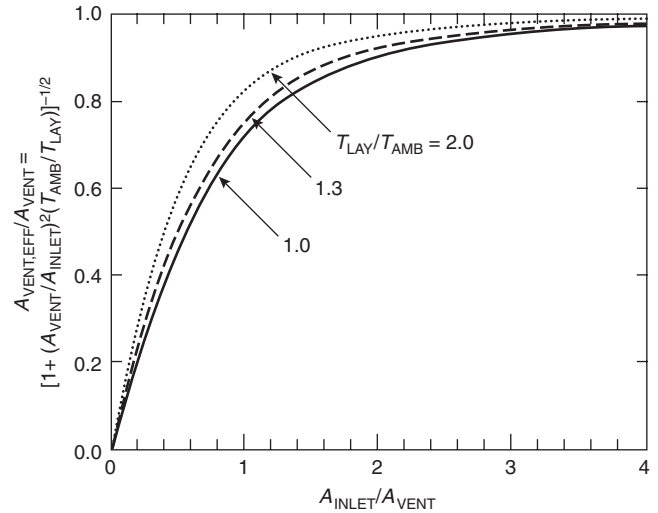


Figure 3-9.6. Plot of $A_{VENT,EFF}/A_{VENT}$ as a function of A_{INLET}/A_{VENT} for fixed values $T_{LAY}/T_{AMB} = 1, 1.3$, and 2 according to Equation 22.

The Effect of Outside Wind Conditions on the Flow through Ceiling Vents in Figure 3-9.1-Type Fire Scenarios

General considerations: Assume that there is a prevailing wind condition in the outside environment. Depending on the wind speed, V_{WIND} , and the wind direction relative to the outside building geometry and relative to the geometry of possible nearby buildings, and assuming that all vents on the outside surface of the building are closed, the aerodynamic flow around the building will lead to the establishment of a location-dependent pressure distribution along the outside building surface

$$P_{SURF}(\text{position}) = P_{OUT}(z) + \frac{C_{PRES}(\text{position})\rho_{ATM}V_{WIND}^2}{2} \quad (23)$$

where C_{PRES} is the local pressure coefficient. Example values of C_{PRES} for flow around an isolated, low, square building are shown in Figure 3-9.7.

If the building vents are open and if vent areas are relatively small compared to the building surface areas, then pressures near the vent openings, but away from any local

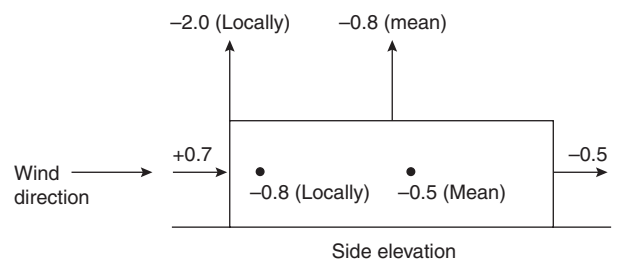


Figure 3-9.7. Pressure coefficients for an isolated, low, square building.

through-vent flows that may develop, will be substantially unchanged from the above-mentioned, closed-vent pressure distribution. Also, while the near-vent pressure distributions generally vary from vent to vent, they will be relatively uniform for any particular vent. Under these conditions, a determination of flow rates into and/or out of vents and through the interior of the building would be based on an interior building flow analysis, with pressure-specified boundary conditions at the open vents.

A single, open inlet vent or multiple openings at the same P_{SURF} : If there is only one open inlet vent, say in the upwind side of the building leading to a relatively high pressure differential there *above* the local hydrostatic pressure [the upwind $C_{\text{PRES}} = 0.7$ value of Figure 3-9.7 indicates, e.g., that for $V_{\text{WIND}} = 10 \text{ m/s}$, P_{SURF} at the vent would be $0.7\rho_{\text{ATM}}V_{\text{VENT}}^2/2 \approx 0.7(1.2)(10)^2/2 \text{ kg}/(\text{ms}^2) = 42 \text{ Pa}$ greater than P_{OUT}], or if there are several open vents, all at locations on the outside surface of the building where pressures are substantially identical, then, *independent* of the magnitude of V_{WIND} , the wind will have no effect on the inflow or outflow through the vents. Thus, if the air inside the building is uniformly at the outside air temperature (assumed to be uniform) and if there is no mechanical ventilation, then the effect of the wind will be simply to bring the interior hydrostatic pressure at the location of the vent(s) to the aerodynamic-flow-specified value, P_{SURF} ; the interior of the building will be "pressurized" as a result of the open vent(s), but there will be no wind-induced interior flows. If there is a fire in the room with the open vent (e.g., the vent is a broken window), then, in the usual way, there will be fresh air inflow into the room toward the bottom of the vent and buoyant smoke outflow toward the top of the vent, all this taking place at an aerodynamic-flow-specified, elevated hydrostatic pressure within the room.

If the open vent is in a side of the building facing downwind, that is, exposed to the wake of the flow, then, as in Figure 3-9.7, C_{PRES} typically will be negative. The pressure at the vent will be relatively low, at the outside, local hydrostatic pressure *reduced* by an amount on the order of $\rho_{\text{ATM}}V_{\text{VENT}}^2/2$. There will again be no wind-induced flow at the vent.

Two inlet vents, one on the upwind side and one on the downwind side of the building: If there are two inlet vents in the walls of the building, one upwind and one downwind (again, no heating and no mechanical ventilation), then there *will* be wind-induced flow through the vents and within the building. There will be inlet air at the high-pressure upwind vent and outlet air at the low-pressure downwind vent, with levels of through-vent flows and of interior hydrostatic pressures determined by an appropriate analysis that accounts for conservation of momentum (i.e., Bernoulli's equation) and mass at the exterior vents and at room-to-room vents within the interior of the building. The changes in hydrostatic pressures within the rooms of the building, over and above the hydrostatic pressures that would be in evidence in a quiescent environment, would be somewhere between the wind-induced pressures at the locations of the high-pressure vent and the low-pressure vent.

Wind-modified pressures at roof surfaces and wind-modified action of ceiling vents: As in the Figure 3-9.7 example (also see Figure 1-1.34 of Section 1, Chapter 1, "Introduction to the Mechanics of Fluids"), independent of wind direction, roof surfaces of flat-roofed buildings tend to have negative, wind-induced pressure coefficients. (This is not the case for sloping roofs, for which pressure coefficients can be positive or negative, depending on wind direction.) Therefore, if the interior, wind-induced hydrostatic pressures are higher than those associated with a quiescent environment, say, the result of open vents in the upwind side of the building, then the flow of smoke through ceiling vents can be enhanced significantly by virtue of increased, favorable, cross-vent pressures. However, for reduced interior pressures, say, the result of open vents on the downwind side of the building, the effect of wind conditions can disrupt completely the desired smoke-removing action of ceiling vents, even reducing the *direction* of the cross-vent pressures and, as a result, the direction of the flow through the vents, that is, from outside to inside.

For a square, low, flat-roofed building configuration like that of Figure 3-9.7, it seems that the latter problem would not exist if, say, identical open inlets are provided on all four sides. Thus, the figure indicates that the smallest of the pressure coefficients at such side vents would be greater than -0.8 and the pressure coefficients on the roof surface would typically be less than -0.8 . As a result, wind-modified, cross-ceiling-vent pressure differentials would always exceed a design value that was based on a windless outside environment. All this would lead to enhanced wind-induced performance of roof vents. (Note: The reader is referred to the end of Section 1, Chapter 1, "Introduction to the Mechanics of Fluids," for additional discussion on the effect of wind on the action of ceiling vents.)

The Effect of Combined Buoyancy- and Pressure-Driven Flow through Horizontal Ceiling Vents

Flow through horizontal vents when $\Delta P_{\text{IN-OUT}} = 0$: At the beginning of the section Flow through Vents, it was stated that "flow is driven through vents... mainly by cross-vent hydrostatic pressure differences" (italics added). In the case of horizontal vents, there is another phenomenon that can affect significantly the validity and the accuracy of the present flow estimates, which were based solely on hydrostatic pressure differences and on use of the traditional Bernoulli equation flow model, referred to below as the *standard flow model*. The phenomenon involves a buoyancy-driven instability, the basic feature of which is explained here by considering an example two-layer scenario with horizontal ceiling vents where $\Delta P_{\text{IN-OUT}}(z_{\text{CEIL}}) = 0$.

Analysis of the Figure 3-9.1 scenario, which assumed a quiescent outside environment, led to the Equation 16 estimate of $\Delta P_{\text{IN-OUT}}(z_{\text{CEIL}})$. As indicated, for a non-zero-thickness smoke layer, the latter is always positive. However, as discussed in the previous section, wind conditions and poorly positioned inlet vents can lead to scenarios where, even in the case of a relatively high-temperature,

low-density, upper smoke layer, $\Delta P_{\text{IN-OUT}}(z_{\text{CEIL}})$ can be brought to zero (and even to negative values). For $P_{\text{IN-OUT}}(z_{\text{CEIL}}) = 0$, the standard flow model equation of Equations 8 or 17 and then Equation 18 leads to the estimate, $V_{\text{VENT}} = \dot{m}_{\text{VENT}} = 0$. However, under these circumstances it is clear that the standard flow model does not describe either quantitatively or qualitatively the real state of the vent flow.

The fundamental problem⁷⁻⁹ here involves a "heavy" fluid (the relatively low-temperature and high-density outside air) positioned above an open vent, below which is a "light" fluid (the relatively buoyant, high-temperature, and low-density smoke). This is an unstable configuration (i.e., a zero-flow configuration cannot be sustained), and it will lead to an unsteady and purely buoyancy-driven, exchange-type flow through the vent; the relatively buoyant smoke inside the facility will flow up through the vent to the outside, and the more dense, cool, outside air will flow down through the vent into the inside space. (The flow phenomenon is analogous to the exchange flow that is observed during the emptying of an open upside-down bottle, initially filled with liquid, where the bottle opening is analogous to the vent, and where the liquid above and the air below are analogous to the "heavy" outside air and the "light" smoke, respectively.)

Flow through horizontal vents for positive, moderate $\Delta P_{\text{IN-OUT}}$: Assume now that $\Delta P_{\text{IN-OUT}}(z_{\text{CEIL}})$ is increased from zero through positive values (with or without a quiescent outside environment). The above exchange flow will persist, but there will be a *reduction* in the above-described outside-to-inside flow component and an *increase* in the inside-to-outside flow component. As $\Delta P_{\text{IN-OUT}}(z_{\text{CEIL}})$ is increased further, flow through the vent will eventually become unidirectional, from inside to outside, that is, the flow will be qualitatively similar to that predicted by the standard flow model. When unidirectional flow is first achieved, the flow condition is referred to as the *flooding-flow condition*⁷; the corresponding value of $\Delta P_{\text{IN-OUT}}(z_{\text{CEIL}})$ is designated as ΔP_{FLOOD} , the flooding-flow cross-vent pressure; and the corresponding vent flow velocity is designated V_{FLOOD} , the *flooding-flow velocity*.

For vent areas with moderate aspect ratios, for example, circular or square vents or moderate-aspect-ratio rectangular vents, with length of sides, L_1 and L_2 , satisfying $0.5 \leq L_1/L_2 \leq 2.0$, ΔP_{FLOOD} and V_{FLOOD} can be estimated from⁷

$$\begin{aligned} \Delta P_{\text{FLOOD}} &= 0.97 \left(1 + \frac{\varepsilon}{2} \right) \exp(1.1\varepsilon) g \rho_{\text{AMB}} \left(1 - \frac{T_{\text{AMB}}}{T_{\text{LAY}}} \right) D_{\text{VENT}} \\ V_{\text{FLOOD}} &= 0.195 (g D_{\text{VENT}}^5 \varepsilon)^{1/2} \exp(0.55\varepsilon) \end{aligned} \quad (24)$$

$$\varepsilon = \frac{(1 - T_{\text{AMB}}/T_{\text{LAY}})}{(1 + T_{\text{AMB}}/T_{\text{LAY}})};$$

$$D_{\text{VENT}} = (4A_{\text{VENT}}/\pi)^{1/2}$$

where D_{VENT} is the equivalent diameter of a single vent of interest (i.e., A_{VENT} of Equation 24 is the area of a *single* vent, as distinguished from the previous usage, where it denoted the total area of *all* open vents).

A plot of $V_{\text{VENT}}/V_{\text{FLOOD}}$ vs. $\Delta P_{\text{IN-OUT}}(z_{\text{CEIL}})/\Delta P_{\text{FLOOD}} > 1$, that takes into account the effect of combined buoyancy- and pressure-driven flow, is presented in Figure 3-9.8. Included in the figure is a plot of relevant data¹⁰ acquired in a reduced-scale experimental facility involving fan-specified cross-vent pressure differentials with a cold-air over hot-air configuration. The figure also includes a second plot of the same variables, but where V_{VENT} is the vent flow velocity predicted with the standard flow model, for example, using Equation 19 in the present application under conditions of a quiescent outside environment.

As seen in the Figure 3-9.8 plots,⁷ the value of V_{VENT} at the flooding-flow condition is estimated to be less than one-third of the value obtained from the standard flow model. In particular, at the flooding-flow condition the effective value for the flow coefficient, $C_{\text{EFF},\text{FLOOD}}$, is estimated to be⁷

$$C_{\text{EFF},\text{FLOOD}} = 0.178 \quad \text{instead of } C = 0.61 \quad (25)$$

As $\Delta P_{\text{IN-OUT}}(z_{\text{CEIL}})$ is increased beyond ΔP_{FLOOD} , it eventually would become large enough for the Equation 19 standard-flow-model result to provide good estimates for V_{VENT} . In this regard, it is seen in the plots of Figure 3-9.8 that, for example, the standard flow model will overpredict V_{VENT} by no more than 20 percent of actual values once $\Delta P_{\text{IN-OUT}}(z_{\text{CEIL}})/\Delta P_{\text{FLOOD}}$ exceeds 3.

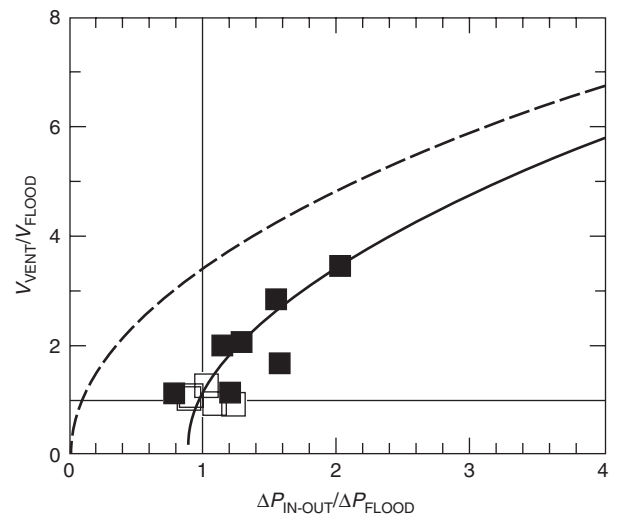


Figure 3-9.8. Plot of $V_{\text{VENT}}/V_{\text{FLOOD}}$ vs. $\Delta P_{\text{IN-OUT}}(z_{\text{CEIL}})/\Delta P_{\text{FLOOD}}$; a result⁷ that accounts for the combined effects of buoyancy- and pressure-driven flows through a ceiling vent (—); experimental data⁹ flooding-flow conditions (□) and nonflooding-flow conditions (■); and Bernoulli's equation, which ignores the effect of buoyancy-driven instability (- - -).

EXAMPLE 2:

Flow through a ceiling vent: As in Example 1, consider horizontal ceiling vents above a 3-m-thick smoke layer that is 100 K greater than $T_{AMB} = 293$ K. As determined there, for large inlet vents and a zero-wind condition $P_{IN-OUT}(z_{CEIL}) = 9.0$ Pa. From Equation 24 it is now determined that $\varepsilon \equiv (1 - 293/393)/(1 + 293/393) = 0.14$ and $\Delta P_{FLOOD} = 0.97(1 + 0.14/2)\exp[1.1(0.14)/2](9.8)(1.2)(1 - 293/393)(4/\pi)^{1/2}(A_{VENT}/m^2)^{1/2}$ Pa = $3.7(A_{VENT}/m^2)^{1/2}$ Pa. Based on the above, it is therefore estimated that the Example 1 result (from standard-flow-model considerations) of $\dot{m}_{VENT}/A_{VENT} = 2.4$ (kg/s)/m² will overpredict the correct vent-flow rate, but by no more than 20 percent of the expected value if $\Delta\dot{P}_{IN-OUT}(z_{CEIL})/P_{FLOOD} = 9.0/[3.7(A_{VENT}/m^2)^{1/2}] > 3$, that is, provided $A_{VENT} < 0.65$ m².

In practical terms it is noted that 0.65 m² is a small area for a single vent unit. (U.S. vent-system designs typically use single-vent units with dimensions ranging from 1.2 m × 1.2 m = 1.5 m² to 1.8 m × 2.6 m = 4.7 m².) In practical full-scale venting systems, a 0.65-m² maximum-allowable limit on the area of single-vent units would represent a problematic design constraint with a relatively large number of vent units required for a specified total vent area and corresponding to relatively high costs of implementation. It is also noteworthy that the results of Equation 24 and of Figure 3-9.8 have only been validated for a limited number of reduced-scale tests, involving vents with areas less than 0.65 m². There do not appear to be any available, reliable flow-rate vs. pressure data for flow-through vent units with areas in the range 1.5 m² to 4.7 m² or greater.

Plug-Holing

The phenomenon of plug-holing: Refer to Figure 3-9.9. This depicts the phenomenon of flow being extracted from an upper layer through a ceiling vent, where extraction at a specified volumetric flow rate leads to the average flow velocity, V_{VENT} . For this configuration, define the Froude number, F , and the layer thickness, h , as

$$F \equiv \frac{V_{VENT} A_{VENT}}{\{[g(\rho_{AMB} - \rho_{LAY})/\rho_{AMB}]^{1/2} h^{5/2}\}}; \quad (26)$$

$$h = z_{CEIL} - z_{LAY}$$

For large enough F , the interface of the layer, as indicated in the figure, will be depressed a distance h_{DEP} that is comparable to h . Results presented in the literature^{11,12} lead to the following conclusions for circular vents:

1. If $F > F_{CRITICAL} = 1.6$, then $h_{DEP}/h = 1$ and flow through the vent will include some fluid from the lower-layer environment, that is, $\dot{m}_{VENT} > \rho_{LAY} V_{VENT} A_{VENT}$.
2. The condition $F/F_{CRITICAL} = 1$ represents a scenario where $h_{DEP}/h = 1$, but where, for this critical value of F and for all smaller values, flow through the vent is entirely from the upper-layer environment, that is, $\dot{m}_{VENT} = \rho_{LAY} V_{VENT} A_{VENT}$.
3. If $F/F_{CRITICAL} = 1 - \delta_1$ where $0 < \delta_1 \ll 1$, then $h_{DEP}/h = 1 - \varepsilon_1(\delta_1)$ where $\lim_{\delta_1 \downarrow 0} \varepsilon_1(\delta_1) \downarrow 0$.

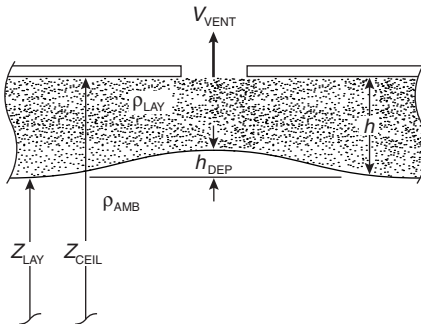


Figure 3-9.9. The phenomenon of plug-holing.

4. If $0 < F/F_{CRITICAL} = \delta_2 \ll 1$, then $h_{DEP}/h = \varepsilon_2(\delta_2)$ where $\lim_{\delta_2 \downarrow 0} \varepsilon_2(\delta_2) \downarrow 0$. (27)

(In the list above, the meaning of the limits in items 3 and 4 is if δ_1 or δ_2 approach zero through positive values, then ε_1 or ε_2 will approach zero through positive values.)

Note that there are no results available in the literature that provide a quantitative estimate of the relationship between h_{DEP}/h and $0 < F/F_{CRITICAL} < 1$. Nevertheless, it is reasonable to expect that

$$\lim_{F/F_{CRITICAL} \rightarrow 0} \frac{h_{DEP}}{h} = \beta \frac{F}{F_{CRITICAL}} \quad (28)$$

where $0 < \beta = \text{constant} = 0(1)$

It is also reasonable to expect that the above conclusions can be extended to moderate-aspect-ratio vents other than circular vents, for example, square vents or moderate-aspect-ratio rectangular vents.

The phenomenon of Figure 3-9.9, where the layer interface is depressed to the elevation of the ceiling as a result of $F/F_{CRITICAL} > 1$, that is, where flow through the vent is extracted partially from the ambient lower layer, is known as plug-holing. (Note: The reader is referred to References 4, 13, and 14 for additional discussion on the topic of plug-holing.)

Plug-holing and natural venting: It is possible to apply the above result to the natural vent flow problems of current interest. Thus, if $F/F_{CRITICAL}$ is small, say,

$$\text{if } F/F_{CRITICAL} < 0.2, \quad \text{then, } h_{DEP}/h \text{ will be small,} \\ \text{on the order of } F/F_{CRITICAL} \quad (29)$$

according to Equation 28; that is, if $F/F_{CRITICAL}$ is small, then the layer-interface depression of Figure 3-9.9 will be small. Now, if the vent flow leading to the F value is the result of natural ventilation and not forced mechanical ventilation, then the traditional results of Equations 16–19 associated with natural venting will be relevant. From these latter equations and from the definition of Equation 26, it follows that in natural venting, when there is no plug-holing and $h_{DEP}/h \approx 1$,

$$\frac{F}{F_{\text{CRITICAL}}} = 0.54 \left(\frac{\rho_{\text{AMB}}}{\rho_{\text{LAY}}} \right)^{1/2} \frac{A_{\text{VENT}}}{h^2} \quad (30)$$

The requirement of internal consistency between the conditions of Equation 28 and those of 29 and 30 leads to the following final result: in natural venting through moderate-aspect-ratio vents, if

$$\left(\frac{\rho_{\text{AMB}}}{\rho_{\text{LAY}}} \right)^{1/2} \frac{A_{\text{VENT}}}{(z_{\text{CEIL}} - z_{\text{LAY}})^2} < 0.4 \quad (31)$$

then the plug-holing phenomenon will be insignificant; if Equation 31 is not satisfied, then plug-holing can be significant.

Therefore, if Equation 31 is satisfied, then all earlier results for flow through ceiling vents will be relevant. If Equation 31 is not satisfied, then, because of possible plug-holing, the earlier results can be unreliable.

EXAMPLE 3:

Maximum vent area for avoiding plug-holing in the Example 1 venting scenario: As in Example 1, consider horizontal ceiling vents above a 3-m-thick smoke layer that is 100 K greater than $T_{\text{AMB}} = 293$ K. Applying the criterion of Equation 31, it is determined that plug-holing will be avoided in the Example 1 venting scenario if moderate-aspect-ratio vents are used and if the area of individual vents satisfy

$$\begin{aligned} A_{\text{VENT}} &< 0.4 \frac{(z_{\text{CEIL}} - z_{\text{LAY}})^2}{(\rho_{\text{AMB}}/\rho_{\text{LAY}})^{1/2}} \\ &= 0.4 \frac{(3 \text{ m})^2}{(293/393)^{1/2}} \\ &= 4.2 \text{ m}^2 \end{aligned}$$

Smoke Flow under Draft Curtains

Velocity of flow under draft curtains: Refer to Figure 3-9.10. If and when the layer interface drops below the bottom of the draft curtains, smoke will start to flow out of this space and into adjacent spaces. Here, the "vent" consists of the open area in the plane of and below the draft curtain, at $z < z_{\text{CURT}}$. As with ceiling vents, the flow rate here is determined by the cross-vent hydrostatic pressure difference, which now varies with z . Here the flow is from within the curtained space to the adjacent curtained space, where it is assumed that the outside environment conditions still persist in the adjacent spaces, from z_{FLOOR} up to z_{CEIL} , that is, it is assumed that any smoke that may have already "spilled into" the adjacent space has not yet modified significantly the initial outside-ambient environment. Thus, the pressure in the adjacent space, P_{ADJ} , is estimated from Equation 6 as

$$\begin{aligned} P_{\text{ADJ}}(z) &\approx P_{\text{OUT}}(z) = P_{\text{OUT}}(z_0) - \rho_{\text{AMB}}g(z - z_0), \\ z_{\text{FLOOR}} &< z \leq z_{\text{CEIL}} \end{aligned} \quad (32)$$

$P_{\text{IN}}(z)$ is again given by Equations 13 and 14, and the cross-vent pressure difference, $\Delta P_{\text{IN-ADJ}}(z)$, which is again (essentially) always positive, is estimated from

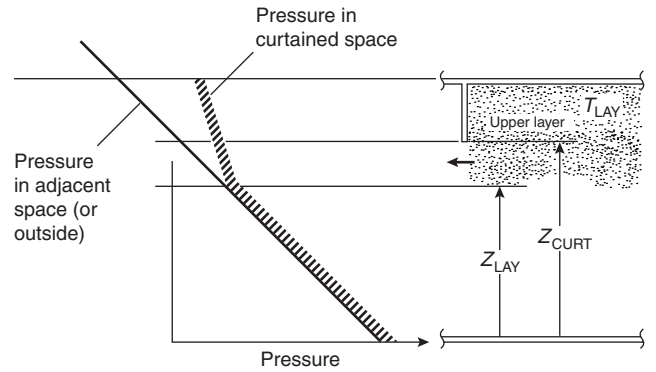


Figure 3-9.10. Flow below a draft curtain.

$$\Delta P_{\text{IN-ADJ}}(z) \equiv P_{\text{IN}}(z) - P_{\text{ADJ}}(z) \approx \Delta P_{\text{IN-OUT}}(z) > 0 \quad (33)$$

according to Equation 15. Also, since the pressure is again higher in the curtained space of fire origin than the adjacent space, once again, $\rho_{\text{VENT}} = \rho_{\text{LAY}}$.

In the present configuration, the velocity at the below-curtain vent will vary with z , where this variation is determined from Equations 8, 15, and 33:

$$\begin{aligned} V_{\text{VENT}}(z) &= \left[\frac{2\Delta P_{\text{IN-ADJ}}(z)}{\rho_{\text{LAY}}} \right]^{1/2} \\ &= \left[\frac{2\Delta P_{\text{IN-ADJ}}(z)T_{\text{LAY}}}{(\rho_{\text{AMB}}T_{\text{AMB}})} \right]^{1/2} \end{aligned} \quad (34)$$

where, for the present vent configuration, Equation 10 was used to provide the appropriate choice for C .

Mass-flow rate under draft curtains: Let L_{CURT} be the total length of the draft curtains that separate the curtained space of fire origin from all adjacent spaces, that is,

$$W_{\text{VENT}}(z) = L_{\text{CURT}} = \text{constant} \quad (35)$$

Then, Equations 15, and 33–35 in Equation 11, with $\alpha = 90^\circ$, lead to the following estimate for \dot{m}_{CURT} , the total mass flow rate under the draft curtains from the curtained space of fire origin to all adjacent spaces,

$$\begin{aligned} \dot{m}_{\text{CURT}} &= \\ &0 \quad \text{if } z_{\text{LAY}} \geq z_{\text{CURT}} \\ &\left(\frac{L_{\text{CURT}}}{3} \right) [8(z_{\text{CURT}} - z_{\text{LAY}})^3 \rho_{\text{LAY}} (\rho_{\text{AMB}} - \rho_{\text{LAY}}) g]^{1/2} \\ &= \left(\frac{L_{\text{CURT}}}{3} \right) \rho_{\text{AMB}} \left(\frac{T_{\text{AMB}}}{T_{\text{LAY}}} \right) \\ &\times \left[\frac{8(z_{\text{CURT}} - z_{\text{LAY}})^3 g (T_{\text{LAY}} - T_{\text{AMB}})}{T_{\text{AMB}}} \right]^{1/2} \\ &\quad \text{if } z_{\text{LAY}} < z_{\text{CURT}} \end{aligned} \quad (36)$$

EXAMPLE 4:

Smoke flow under draft curtains: As an example of the above, consider a 3.5-m-thick smoke layer where, as in Examples 1, 2, and 3, T_{LAY} is 100 K greater than $T_{AMB} = 293$ K. Here, let z_{LAY} be 0.5 m below z_{CURT} (i.e., the depth of the draft curtains are 3.0 m), and let the curtained space of fire origin be away from any walls, with a square plan area of $30 \text{ m} \times 30 \text{ m}$, that is, with $L_{CURT} = 4(30 \text{ m}) = 120 \text{ m}$. Then, from Equation 36 it is determined that

$$\begin{aligned}\dot{m}_{CURT} &= (120 \text{ m}/3)(1.2 \text{ kg}/\text{m}^3) \left(\frac{293}{393} \right) \\ &\quad \left[8(0.5 \text{ m})^3(9.8 \text{ m}/\text{s}^2) \left(\frac{100}{293} \right) \right]^{1/2} \\ &= 66 \text{ kg/s}\end{aligned}$$

Based on Example 1, it is seen from Figure 3-9.1 that if the fire in the curtained area is nearly steady and if the mass flow rate of smoke in the fire plume, at an elevation 3 m below the ceiling, is approximately 66 kg/s, then smoke spilling below the curtains will be avoided if there are approximately $(66 \text{ kg/s})/[2.4 (\text{kg/s})/\text{m}^2] = 28 \text{ m}^2$ of open ceiling vents in the ceiling of the curtained space of fire origin. If no open ceiling vents are provided, then there will be spilling below the curtains to an approximate depth of 0.5 m. In the latter case, smoke spilling into, and smoke filling of, the adjacent spaces will continue until all adjacent spaces are filled with smoke from the ceiling to a depth of approximately 3.5 m, after which the depth of the smoke layer will continue to develop uniformly throughout the entire building space, always increasing in thickness.

Convection Mass and Enthalpy to the Smoke Layer from the Fire Plume

Different plume models: The major contributor of convected mass and enthalpy to the smoke layer is from the fire plume. This is depicted in Figure 3-9.11. If the plume is unobstructed at least to the top of its combustion zone, it is assumed that the rate of energy release of the fire's combustion zone, \dot{Q}_{TOTAL} , does not vary significantly from free-burn values. It is also assumed that a fixed fraction, λ_{RAD} , of this energy is radiated from the combustion zone and that above the combustion zone the rest of \dot{Q}_{TOTAL} ,

$$\dot{Q}_{CONV} \equiv (1 - \lambda_{RAD})\dot{Q}_{TOTAL} \quad (37)$$

is convected upward in the plume. Generally applicable estimates of λ_{RAD} and \dot{Q}_{CONV} for full-scale hazardous fires (see Section 3, Chapter 10, "Compartment Fire-Generated Environment and Smoke Filling") are

$$\lambda_{RAD} = 0.35; \quad \dot{Q}_{CONV} = 0.65\dot{Q}_{TOTAL} \quad (38)$$

Regarding the radiation transfer, for relatively early times in the fire development, for example, prior to the activation of sprinklers when they are deployed, it is reasonable to assume that the smoke layer is relatively trans-

Convective heating:

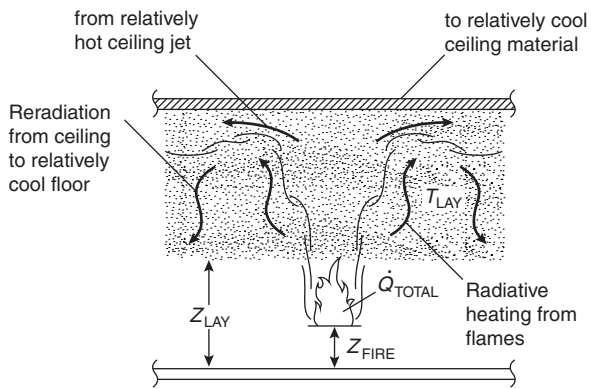


Figure 3-9.11. The fire, the fire plume, and heat transfer to the ceiling.

parent, that is, that all radiation heat transfer from the fire, at the rate $\lambda_{RAD}\dot{Q}_{TOTAL} \approx 0.35\dot{Q}_{TOTAL}$, is incident on the bounding surfaces of the compartment.

A plume model is selected from the several available in the literature,¹⁵ and it is used to determine the rate of mass and enthalpy flow in the plume at the elevation of the layer interface, $z = z_{LAY}$. It is assumed that all this flow penetrates the layer interface and enters the upper layer.

In general, the mass-flow rate in the plume, \dot{m}_{PLUME} , increases with elevation above the base of the fire, $z - z_{FIRE}$, as a result of lateral entrainment into the rising hot and buoyant plume gases. Estimates of \dot{m}_{PLUME} for four different plume models are presented here: *pool fire*, *large fire*, *free line fire*, and *near-wall line fire*. The first two of these are for a plume above a fire with effective circular base of diameter, D_{FIRE} , where A_{FIRE} is the effective plan area of the fire and

$$D_{FIRE} = \left(\frac{4A_{FIRE}}{\pi} \right)^{1/2} \quad (39)$$

The other two models are for plumes above a linelike fire of effective length, L_{FIRE} . For such fires, \dot{Q}_{CONV} and \dot{m}_{PLUME} can be specified in terms of the convected energy-release rate per unit length, \dot{Q}'_{CONV} , and mass-flow rate per unit length, \dot{m}'_{LINE} , respectively,

$$\dot{Q}'_{CONV} \equiv \frac{\dot{Q}_{CONV}}{L_{FIRE}} \quad (40)$$

$$\dot{m}'_{LINE} \equiv \frac{\dot{m}_{PLUME}}{L_{FIRE}} \quad (41)$$

Pool fire; \dot{m}_{PLUME} at arbitrary elevations: The following is one of the several available estimates for \dot{m}'_{PLUME} above a pool fire.¹⁶ It is valid at arbitrary elevation above the base of the fire. For a pool fire at arbitrary elevation, with \dot{m}_{PLUME} measured in kg/s; \dot{Q} and \dot{Q}_{CONV} in kW; and z , z_{FIRE} , L_{FLAME} , and D_{FIRE} in m:

$$\dot{m}_{\text{PLUME}}(z) = \begin{cases} 0.0054 \dot{Q}_{\text{CONV}}(z - z_{\text{FIRE}})/L_{\text{FLAME}} & \text{if } 0 < (z - z_{\text{FIRE}})/L_{\text{FLAME}} < 1; \\ 0.071 \dot{Q}_{\text{CONV}}^{1/3} (z - z_{\text{FIRE}} - L_{\text{FLAME}} + 0.166 \dot{Q}_{\text{CONV}}^{2/5})^{5/3} & \\ \times [1 + \varepsilon \dot{Q}_{\text{CONV}}^{2/3} (z - z_{\text{FIRE}} - L_{\text{FLAME}} + 0.166 \dot{Q}_{\text{CONV}}^{2/5})^{-5/3}] & \text{if } (z - z_{\text{FIRE}})/L_{\text{FLAME}} \geq 1 \end{cases} \quad (42)$$

where L_{FLAME} , the length of the reacting flaming region of the fire, and ε are

$$\varepsilon = 0.0054/0.071 - (0.166)^{5/3} = 0.0259168209... \approx 0.026 \quad (43)$$

$$L_{\text{FLAME}}/D_{\text{FIRE}} = \begin{cases} 0 & \text{if } \Lambda < 0; \\ \Lambda & \text{if } \Lambda \geq 0 \end{cases} \quad (44)$$

and where $\Lambda = [0.083/(1 - \lambda_{\text{RAD}})^{2/5} + 0.166] \dot{Q}_{\text{CONV}}^{2/5}/D_{\text{FIRE}} - 1.02$

Large fire: The following is an estimate⁶ for \dot{m}_{PLUME} above large fires of perimeter P . Use of the model is restricted to elevations above the base of the fire that are so small compared to D_{FIRE} , for example, $z_{\text{LAY}} - z_{\text{FIRE}} < 2D_{\text{FIRE}}$, that the entire temperature of the plume volume to that height can be reasonably estimated as $T_{\text{AMB}} + 900$ K. The model is applicable to large fires in the sense that the maximum elevation considered, that is, the maximum elevation of the smoke-layer interface, is expected to be close enough to the base of the fire that the lateral bounds of the plume there still mostly coincide with the lateral bounds of the lower, continuously flaming region of the fire, where temperatures are relatively uniform at the maximum value of approximately 900 K above the inlet air at T_{AMB} (see Figure 2-1.3 of Section 2, Chapter 1, "Fire Plumes"), that is, approximately 1200 K. For a large fire, where $z - z_{\text{FIRE}} < 2D_{\text{FIRE}}$:

$$\dot{m}_{\text{PLUME}}(z)/(\text{kg/s}) = 0.18(P/\text{m})[(z - z_{\text{FIRE}})/\text{m}]^{3/2} \quad (45)$$

or, alternatively,

$$\dot{m}_{\text{PLUME}}(z) = 0.18P(z - z_{\text{FIRE}})^{3/2};$$

with $\dot{m}_{\text{PLUME}}(z)$ in kg/s and P , z , and z_{FIRE} in m. (When other equations "like" Equation 45 are presented below, they will *not* be presented with their "alternative" forms. The reader that prefers the alternative-type form is advised to construct it by analogy to the Equation 45 example.)

Note that an unusual feature of the Equation 45 estimate for \dot{m}_{PLUME} is that it is independent of \dot{Q}_{TOTAL} .

Free line fire: The following is an estimate for \dot{m}'_{PLUME} above a free line fire:¹⁷

$$\begin{aligned} \dot{m}'_{\text{LINE}}(z)/[\text{kg}/(\text{m}\cdot\text{s})] &= 0.18[(z - z_{\text{FIRE}})/\text{m}][\dot{Q}'_{\text{CONV}}/(\text{kW/m})]^{1/3} \end{aligned} \quad (46)$$

where the above result is for a wedgelike plume that rises above a line fire (or a linelike source of high-temperature smoke) that is removed enough from walls so that the plume can entrain "freely" from both its sides, and where the estimate of Equation 46 is expected to be useful for $z - z_{\text{FIRE}} < O(L_{\text{FIRE}})$, that is, for elevations above the fire base of the order of the length of the line fire. Note that the line fire plume cannot be expected to maintain its two-dimensional, wedgelike character much beyond $z = z_{\text{FIRE}} + L_{\text{FIRE}}$. For higher elevations, the plume flow rate would perhaps be best estimated with the pool-fire estimate of Equations 42–44, using an appropriate, effective base diameter, D_{FIRE} .

Near-wall line fire: If the line fire is immediately adjacent to a wall, so that it can only entrain on one side of the wedgelike plume (or, if the buoyant source of the plume is smoke from a fire in an adjacent room that enters the space of interest through a wide vent opening, where the smoke is unobstructed in its ascent along the wall immediately above the vent opening), then it will be referred to here as a *near-wall line fire*. Using a plume reflection-type principle, an estimate of \dot{m}'_{LINE} for this case can be obtained with the use of Equation 46 by "doubling" \dot{Q}'_{CONV} and halving the resulting \dot{m}'_{LINE} that is, for a near-wall line fire:

$$\begin{aligned} \dot{m}'_{\text{LINE}}(z)/[\text{kg}/(\text{m}\cdot\text{s})] &= (0.18/2)(z - z_{\text{FIRE}})/\text{m}[\dot{Q}'_{\text{CONV}}/(\text{kW/m})]^{1/3} \end{aligned} \quad (47)$$

where, as was the case for Equation 46, it is again reasonable to expect that Equation 47 cannot be used with confidence much beyond $z = z_{\text{FIRE}} + L_{\text{FIRE}}$. The estimate of Equation 47 is consistent with the assumption that below a z -elevation of interest the integrated heat transfer losses from the plume to the adjacent wall are small compared to the convected enthalpy in the plume at that elevation.

EXAMPLE 5:

\dot{m}'_{LINE} in a balcony spill plume: The plume flow estimate of Equation 46 for a free line fire would be applicable in determining \dot{m}'_{LINE} in so-called balcony spill plumes² (see Figure 3-9.12). Consider the following example problem.

PROBLEM:

Referring to Figure 3-9.12, consider a $\dot{Q}_{\text{TOTAL}} = 5$ MW pool-like fire of $A_{\text{FIRE}} = 4 \text{ m}^2$ (i.e., from Equation 39, $D_{\text{FIRE}}/\text{m} = [4(4)/\pi]^{1/2} = 2.3$) below a balcony of width $W = 3 \text{ m}$. Let $H = 3 \text{ m}$ be the elevation of the balcony above the base of the fire, that is, $H = z_{\text{BALCONY}} - z_{\text{FIRE}} = 3 \text{ m}$. Assume that $\dot{Q}_{\text{CONV}} = 0.65 \dot{Q}_{\text{TOTAL}} = 3.25$ MW. After impinging on the lower surface of the balcony, assume that the smoke from the pool-fire plume flows below and (eventually and mostly) toward the edge of the balcony, without significant additional entrainment and without significant heat transfer losses. The smoke then spills upward from below the balcony, continuing upward as a free line fire-generated spill plume. Whatever the actual position of the pool fire relative to the edge of the balcony,

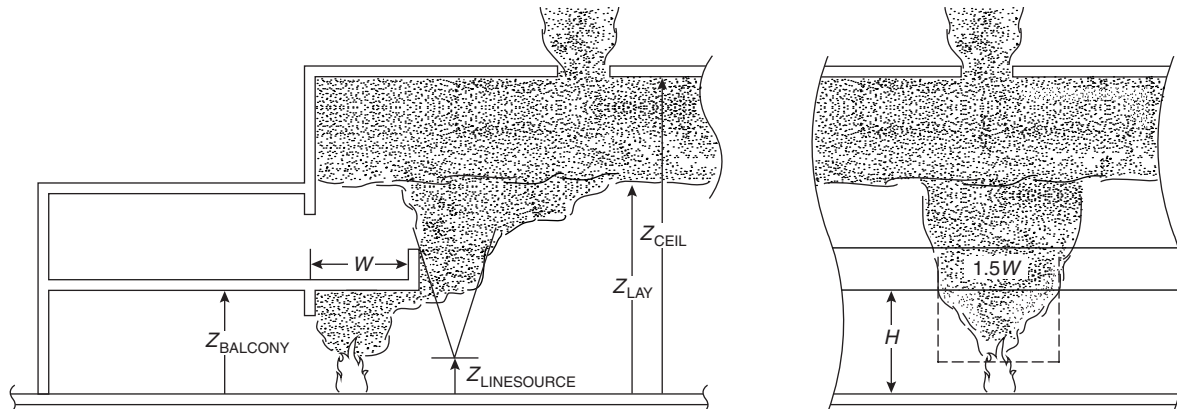


Figure 3-9.12. Scenario of Example 5 involving a balcony spill plume.

it is expected that the effective lengths of the spill plume and of its free line-fire source, L_{PLUME} and $L_{\text{FIRE}} = L_{\text{PLUME}}$, respectively, will be of the order of W , say, between W and $2W$. Therefore, estimate $L_{\text{FIRE}} = L_{\text{PLUME}} \approx 1.5W = 4.5$ m.

Designate the elevation of the unknown, equivalent, free line-fire source for the spill plume as $z_{\text{LINESOURCE}}$ and the mass-flow rate of the pool-fire plume at the elevation of balcony impingement as $\dot{m}_{\text{PLUME}}(z_{\text{BALCONY}})$. Then, at the edge of the balcony, the criterion of equivalency between mass-flow rate in the spill plume, $\dot{m}'_{\text{LINE}}(z_{\text{BALCONY}})$, and in the pool-fire plume is

$$\dot{m}'_{\text{LINE}}(z_{\text{BALCONY}}) = \dot{m}_{\text{PLUME}}(z_{\text{BALCONY}})/L_{\text{FIRE}}$$

Consider the problem of determining the total mass-flow rate in the spill plume at an elevation of 3 m above the balcony, that is, 6 m above the base of the fire, where, for life safety considerations, it is desired to ensure that z_{LAY} of the smoke layer that would fill the upper parts of the space would never fall below this elevation, that is, $z_{\text{LAY}} - z_{\text{FIRE}} = 6$ m.

SOLUTION:

From the above-specified information it can be estimated from Equations 42–44 that $L_{\text{FLAME}} = 4.4$ m and

$$\dot{m}_{\text{PLUME}}(z_{\text{BALCONY}}) = 12.0 \text{ kg/s}$$

Also, from Equation 40, \dot{Q}'_{CONV} for the equivalent free line-fire source is

$$\dot{Q}'_{\text{CONV}} = \frac{\dot{Q}_{\text{CONV}}}{L_{\text{FIRE}}} = \left(\frac{3250}{4.5} \right) \text{ kW/m} = 722 \text{ kW/m}$$

Using the latter two results, Equation 46, and the above criterion of equivalency leads to

$$\begin{aligned} \dot{m}'_{\text{LINE}}(z_{\text{BALCONY}})/[\text{kg}/(\text{m}\cdot\text{s})] \\ = 0.18[(z_{\text{BALCONY}} - z_{\text{LINESOURCE}})/\text{m}](722)^{1/3} \\ = (12.0)/(4.5) = 2.7 \end{aligned}$$

from which it is determined that

$$(z_{\text{BALCONY}} - z_{\text{LINESOURCE}})/\text{m} = 2.7/[0.18(722)^{1/3}] = 1.7$$

that is, the equivalent free line-fire source is 1.7 m below the elevation of the balcony and $(3 + 1.7)$ m = 4.7 m below the elevation of interest. Using Equation 46 again, it is finally determined that

$$\begin{aligned} \dot{m}'_{\text{LINE}}(z - z_{\text{LINESOURCE}}) &= 4.7 \text{ m} \\ &= 0.18(4.7)(722)^{1/3} \text{ kg}/(\text{m}\cdot\text{s}) \\ &= 7.6 \text{ kg}/(\text{m}\cdot\text{s}) \end{aligned}$$

For the continuation free line-fire plume at $z = z_{\text{FIRE}} + 6$ m = $z_{\text{BALCONY}} + 3$ m,

$$\dot{m}_{\text{PLUME}} = \dot{m}'_{\text{LINE}}L_{\text{FIRE}} = (7.6)(4.5) \text{ kg/s} = 34.2 \text{ kg/s}$$

For comparison with the latter result, it has also been estimated from Equations 42–44 that for the pool fire “in the open,” away from under the balcony at $z = z_{\text{FIRE}} + 6$ m = $z_{\text{BALCONY}} + 3$ m:

$$\dot{m}_{\text{PLUME}} = 26.0 \text{ kg/s}$$

Therefore, with the fire located under the balcony rather than “in the open,” it is estimated that there will be a 31 percent increase of the mass-flow rate of smoke that flows into the upper layer, an increase from 26 kg/s to 34 kg/s.

ALTERNATIVE SOLUTION:

Reference 2 provides the following estimate for $\dot{m}_{\text{SPILLPLUME}}(z_B \equiv z - z_{\text{BALCONY}} > 0)$, the mass flux in spill plumes like the one of the present problem. For balcony spill plumes² at elevation z ,

$$\begin{aligned} \dot{m}_{\text{SPILLPLUME}}(z_B \equiv z - z_{\text{BALCONY}} > 0) &/(\text{kg/s}) \quad (48a) \\ &= 0.39[(\dot{Q}_{\text{TOTAL}}/\text{kW})(L_{\text{PLUME}}/\text{m})^2]^{1/3}(z_B + 0.25H)/\text{m} \end{aligned}$$

or

$$\begin{aligned} \dot{m}_{\text{SPILLPLUME}}(z_B \equiv z - z_{\text{BALCONY}} > 0) &/(\text{lb/s}) = \quad (48b) \\ &0.12[(\dot{Q}_{\text{TOTAL}}/\text{BTU/s})[L_{\text{PLUME}}/\text{ft}]^2]^{1/3}(z_B + 0.25H)/\text{ft} \end{aligned}$$

where $z_B \equiv z - z_{\text{BALCONY}}$ is the elevation above the balcony, \dot{Q}_{TOTAL} is the total heat release rate of the fire below the balcony, and H and L_{PLUME} , as before, are the elevation of the balcony above the base of the fire and the effective length of the spill plume at the edge of the balcony, respectively.

In the present problem, $\dot{Q}_{\text{TOTAL}} = 5 \text{ MW}$, L_{PLUME} is estimated to be $L_{\text{PLUME}} \approx 1.5$; $W = 4.5 \text{ m}$, where $W = 3 \text{ m}$ is the width of the balcony; $z_B = 3 \text{ m}$; and $H = 3 \text{ m}$. Using these values in Equation 48a leads to

$$\begin{aligned}\dot{m}_{\text{SPILLPLUME}} &= 0.39[5(10^3)(4.5)^2]^{1/3}[3 + 0.25(3)] \text{ kg/s} \\ &= 68 \text{ kg/s}\end{aligned}$$

The latter result for mass flow rate in the spill plume is seen to be approximately 2.0 times the flow rate estimate of the earlier free line-fire plume analysis (68 kg/s here vs. 34 kg/s there) and approximately 2.6 times the earlier estimate for flow rate above the pool fire if it were "in the open" (68 kg/s here vs. 26 kg/s there).

Continuation of the Plume's Rise in the Smoke Layer

Refer again to Figure 3-9.11. As the plume flow enters the upper layer, the forces of buoyancy, which act to drive the plume toward the ceiling, are reduced immediately because of the temperature increase of the upper-layer environment over that of the lower ambient. As a result, the continued ascent of the plume gases will be less vigorous, that is, at reduced velocity, than it would have been in the absence of the layer. Also, as they continue their ascent within the layer, the temperature of the plume gases will now be higher than they would have been in the absence of the layer. Such higher temperatures are a result of the modified plume entrainment, which is now from the relatively high-temperature upper layer rather than the ambient-temperature lower layer. Methods of predicting the characteristics of the modified upper-layer plume flow are available.^{18,19}

The Ceiling Jet and Convective Heat Transfer to the Ceiling

Having penetrated the interface, the plume continues to rise toward the ceiling of the curtained compartment. As it impinges on the ceiling surface, the plume flow turns and forms a relatively high-temperature, high-velocity, turbulent ceiling jet that flows radially outward along the ceiling and transfers heat to the relatively cool ceiling surface.¹⁸⁻²² The ceiling jet is cooled by convection and the ceiling material is heated in-depth by conduction. Eventually, the now-cooled ceiling jet reaches the extremities of the curtained space, where it turns and is deposited into and mixed with the upper layer.^{23,24} The convective heat-transfer rate and the ceiling surface temperature on which it depends are both strong functions of the radial distance from the point of plume/ceiling impingement, decreasing rapidly with increasing radius.

Thermal Response of the Ceiling

The thermal response of the ceiling is driven by transient heat conduction. For times of interest here, radial

gradients in ceiling surface conditions are small enough so that the conduction heat transfer is quasi-one-dimensional in space. Thus, the thermal response of the ceiling can be obtained from the solution to a set of one-dimensional conduction problems at a few discrete radial positions. These would be solved subject to net convection and radiation heat-flux boundary conditions. Interpolation in the radial direction between the solutions would lead to a sufficiently smooth representation of the distributions of ceiling surface temperature and convective heat transfer rate. The latter of these would be integrated over the ceiling surface to obtain the net instantaneous rate of convective heat transfer losses from the ceiling jet.²²

The Ceiling Jet and the Response of Fusible Links and Other Thermal Sensor Devices

Convective heating and thermal response of near-ceiling-deployed fusible links or other near-ceiling thermal sensor devices (e.g., liquid-filled glass bulbs that burst at their design temperatures and actuate a sprinkler or thermoplastic vent covers designed to soften and "drop out" at specified actuation design temperatures, thereby opening "initially covered" vents) are determined from the local time-dependent distributions of ceiling jet velocity and temperature. These distributions will depend on vertical distance below the ceiling and radial distance from the fire-plume axis. If and when the link-fuse temperature or temperature that otherwise actuates a particular device is reached, the device or devices operated by the link, for example, a single vent, a group of vents ganged together, or a sprinkler, will be actuated.

For radial distances of interest, relatively near to the plume, the ceiling jet is an inertially dominated flow, that is, only initial velocity, and not initial temperature or buoyancy, plays a significant role in the development of ceiling jet velocity distribution. This velocity distribution, depicted in Figure 3-9.13, can be estimated from the characteristics of the plume, upstream of ceiling impingement. The ceiling jet temperature distribution, depicted in Figure 3-9.14 for either a relatively "hot" or relatively "cool" ceiling surface, is then estimated from the now-known velocity, upper-layer temperature, ceiling surface temperature, and ceiling surface heat flux distributions.

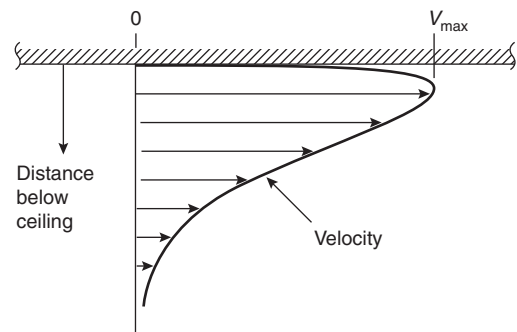


Figure 3-9.13. Ceiling jet velocity.

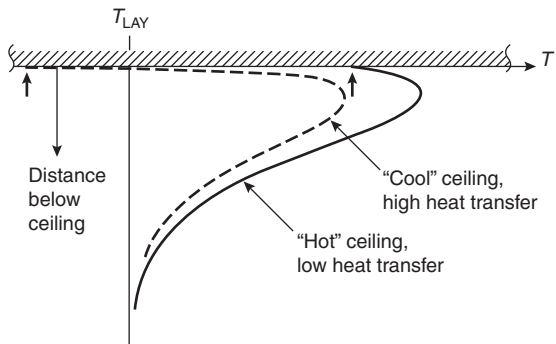


Figure 3-9.14. Ceiling jet temperature.

The LAVENT Model and Computer Code

The mathematical fire model and associated computer program LAVENT (fusible-Link-Actuated VENTS)²⁵⁻²⁷ was developed and is available to simulate most of the phenomena described above. (LAVENT uses the plume model of Equations 43–44. In its current form, it does not take into account wind effects, the reduced effectiveness of vents as a result of limited-area inlet vents, that is, Equation 22, or the buoyancy-driven vent-flow modification discussed in the context of Equations 24 and 25.) All phenomena simulated in LAVENT, some of which were described above with supporting equations and others were presented here only qualitatively, have been presented with detailed model equations.²⁵ The LAVENT model can be used to simulate on a time-dependent basis and to study parametrically a wide range of Figure 3-9.1-type fires.

Full documentation for LAVENT, including its theoretical basis,²⁵ a user guide for the computer code,²⁶ and sample problems using the code, is also included in Appendices A, B, and C, respectively, of NFPA 204.¹

The Minimum Depth of Draft Curtains

The ceiling jet in the curtained space of fire origin will have a depth²⁵ of the order of $0.1(z_{CEIL} - z_{FIRE})$. Consistent with the modeling concepts used throughout this chapter, the effects of the upper layer can only be expected to be generally reliable once the upper layer submerges (i.e., is thicker than) the ceiling jet. In this regard, when draft curtains are used, it is recommended¹ that they have a minimum depth of $0.2(z_{CEIL} - z_{FIRE})$, that is,

$$\text{depth of curtains} \equiv z_{CEIL} - z_{CURT} \geq 0.2(z_{CEIL} - z_{FIRE}) \quad (49)$$

Required Vent Areas

Time-Dependent and Steady-State Design Problems

As mentioned above, it is typical for time-dependent phenomena to play a prominent role in fire safety problems of real interest. This is certainly the case with problems involving fire venting, where the characteristics of

hazardous fires and their corresponding plume dynamics, the thicknesses of smoke layers and their temperature, the number (i.e., the area) of active (i.e., open) vents (e.g., in a system involving individual fusible-link-actuated vents), and so on all change with time during the course of fire development. An analysis that accounts for such interacting phenomena on a time-dependent basis must inevitably involve use of a computer fire model (i.e., rather than "hand" calculations), like LAVENT. Nevertheless, for design purposes it often possible, and it has been traditional to formulate such problems as involving substantially steady-state phenomena.

A steady-state vent-design problem formulation would typically involve (1) a specified steady-state design fire threat, including, for example, the elevation and area of the fire (possibly the fuel type and the configuration of the fuel array) and its characteristic energy-release rate, (2) a minimum acceptable value for z_{LAY} , and (3) relevant building design features, for example, the elevation of deployed ceiling vents, $z = z_{CEIL}$. The actual design problem would be to determine total area of open vents required to maintain the smoke-layer interface at $z = z_{LAY}$.

Solving the Steady-State Design Problem

Smoke-flow rate from the plume to the layer: The steady-state problem solution first requires a determination of $\dot{m}_{PLUME}(z_{LAY})$. This would be obtained from the description of the specified fire and with the use of a relevant plume model equation. To achieve the design objective, that is, to ensure that the elevation of the layer will be maintained at $z = z_{LAY}$, the flow rate out of the vents will have to match $\dot{m}_{PLUME}(z_{LAY})$.

The average temperature of the smoke layer: As the plume gases rise from the base of the fire toward z_{LAY} , they entrain and mix with the lower-layer environment at temperature T_{AMB} . For free plumes that are not bound by or in contact with solid surfaces, the convected energy in the plume gases is conserved at \dot{Q}_{CONV} . (There will be convective heat transfer losses from a plume along portions of its length where it is in contact with wall surfaces, e.g., along the length of a plume above a near-wall-type line fire.) Therefore an estimate for $T_{PLUME}(z_{LAY})$, the average temperature of plume gases as they enter the smoke layer, is

$$T_{PLUME}(z_{LAY}) - T_{AMB} = \frac{\dot{Q}_{CONV}}{[\dot{m}_{PLUME}(z_{LAY})C_p]} \quad (50)$$

where C_p is the specific heat at constant pressure of air.

A fraction, K , of \dot{Q}_{CONV} will be transferred from the smoke layer to bounding surfaces of the enclosure.¹ As a result of this, the temperature of the smoke-layer gases, T_{LAY} , will be less than $T_{PLUME}(z_{LAY})$

$$T_{LAY} - T_{AMB} = \frac{K\dot{Q}_{CONV}}{[\dot{m}_{PLUME}(z_{LAY})C_p]} \quad (51)$$

A reasonably accurate determination of K would involve a generally difficult analysis of the net rate of heat transfer from the upper-layer gases to upper-layer-exposed and -bounding surfaces of the facility. For example, to es-

timate convection heat transfer rates, the analysis would require appropriate predictions of the characteristics of fire plume–driven boundary flows adjacent to the ceiling and wall surfaces that bound the smoke layers.

It has been recommended that $K = 0.5$ can be generally used as a representative value in Equation 51.¹ However, no value for K should be used that leads to a $T_{LAY} - T_{AMB}$ estimate that exceeds 900 K, where the latter value represents the maximum temperature within flames/plumes above free-burning pool fires, that is, the maximum temperature near the base of the fire, within the continuous flaming region (see Section 2, Chapter 1, "Fire Plumes").

In view of the typical significant uncertainty in the value of K , there will be a corresponding significant uncertainty in the value determined for T_{LAY} in Equation 51. Therefore, from the earlier result presented below Equation 19 and in Figure 3-9.3, it is a fortunate circumstance that, for T_{LAY} values that are at least 90 K greater than T_{AMB} , vent mass flow rates are relatively insensitive to T_{LAY} .

Determining the required total vent area: For the design problem at hand, the above results provide estimates for $\dot{m}_{PLUME}(z_{LAY})$ (Equation 42–44 for pool fires, Equation 45 for large fires, Equation 46 for free line fires, and Equation 47 for near-wall line fires) and T_{LAY} (Equation 51). From these and from the specified values for the design smoke-layer depth, $z_{CEIL} - z_{LAY}$, the required total area for all vents would be determined by requiring $\dot{m}_{VENT} = \dot{m}_{PLUME}(z_{LAY})$ and by using the \dot{m}_{VENT}/A_{VENT} estimate of Equation 19. This leads to the following general result for required total vent area:

$$A_{VENT} = \frac{1.16[\dot{m}_{PLUME}(z_{LAY})/\rho_{AMB}]}{[(z_{CEIL} - z_{LAY})(1 - T_{AMB}/T_{LAY})T_{AMB}/T_{LAY}]^{1/2}} \quad (52)$$

EXAMPLE 6:

Required total vent area for large fires; a general result and an example application: Consider relatively steady burning of a 5-m × 5-m square array of combustibles on the floor of a warehouse facility with ceiling elevation of 9 m. The warehouse is subdivided with ceiling-mounted draft curtains where the bottom of the draft curtains are at an elevation of 6 m. It is desired to provide enough ceiling vent area in each curtained space so that, for an arbitrary curtained space of fire origin, the smoke layer that is established will not fall below the bottom of the curtains and will not flow into and threaten commodities stored in adjacent compartments.

For this example problem, $z_{FIRE} = 0$, $z_{LAY} = 6$ m, and $z_{CEIL} = 9$ m and, from Equation 39, $D_{FIRE} = [4(5)(5)/\pi]^{1/2}$ m = 5.64. Therefore, the fire and problem constraints satisfy the condition of Equation 45, that is, $z_{LAY} - z_{FIRE} = 6$ m < $2D_{FIRE} = 11.3$ m, and the fire can be considered to be a large fire with $P = 4(5)$ m = 20 m. As noted earlier, a large fire is one where the gas temperature throughout the entire volume of the plume at and below the relevant, relatively low elevations are uniformly at a characteristic temperature of 1200 K. For plume temperatures of such magnitude and for upper-layer heat-transfer losses asso-

ciated with any reasonable value of K , it is clear from Equation 18 and from Figure 3-9.3 that for large fires,

$$\left[4\left(1 - \frac{T_{AMB}}{T_{LAY}}\right) \frac{T_{AMB}}{T_{LAY}} \right]^{1/2} \approx 1$$

Using this last observation and Equation 45 in Equation 52 leads to the following *general* result for the total required vent area for large fires where $z - z_{FIRE} < 2D_{FIRE}$:

$$A_{VENT}/m^2 = 0.11(P/m)[(z_{LAY} - z_{FIRE})/m]^{3/2}/[(z_{CEIL} - z_{LAY})/m]^{1/2} \quad (53)$$

where the latter result is equivalent to the result in Reference 6 for the required vent area for large fires. (Note that in contrast to $\dot{m}_{PLUME}(z)$ of Equation 45 and the required vent area of Equation 53 for large fires, neither of which depend on \dot{Q}_{CONV} , the plume models and the required vent area for all other types of design fires *will* depend on \dot{Q}_{CONV} .)

Applying the Equation 53 result to the Example 6 problem at hand leads to the result

$$A_{VENT}/m^2 = 0.11(20)(6)^{3/2}/(3)^{1/2} = 18.6$$

The Design Fire

The required vent area for a facility is the minimum vent area that leads to the fire-safe design of the facility (successful removal of smoke according to some adopted design-venting objective) when it is threatened by a particular design fire. The design fire would be an appropriate characterization of a fire associated with the burning of a likely assembly of combustibles expected to be found in the particular facility of interest.

As an example of guidance on constructing an analytic estimate of an appropriate design fire for a particular facility, the reader is referred to Tables 5-5.2(b) and 6-1.4.6.3 of Reference 1. Each of these tables is a catalogue of burning characteristics for a wide range of practical arrays of combustibles, where table entries are based on measurements from full-scale experimental fires. Table 5-5.2(b), "Unit Heat Release Rate for Commodities," lists parameters (energy release rate per unit plan area of the combustible array) that allow a description of steady burning of different kinds of combustibles. Table 6-1.4.6.3, "Continuous Growth Fires," lists parameters (t_g , time for the fire to grow from the effective initiation of flaming ignition to 1000 kW) that allow a description of fire growth in different combustibles that is approximated as being proportional to time-squared, that is, t^2 fire growth:

$$\dot{Q}_{TOTAL} \approx 1000 \left(\frac{t}{t_g} \right)^2 \quad (54)$$

Mechanical Ventilation

There are a variety of situations where smoke vent designs should appropriately rely partially or totally on mechanical ventilation. Examples include situations

where (1) there is a concern that wind-modified cross-vent pressures may reduce seriously the efficiency of a natural vent system; (2) the temperature of the smoke is likely to be so low that, according to the considerations of Equation 19 and Figure 3-9.3, natural venting would not be economical, for example, the total, required natural vent area is excessive; and (3) natural venting would be impractical, for example, a smoke-venting capability is desired at intermediate floors of a multifloor facility or there are other building design constraints that preclude the use of ceiling vents.

The design concept for a system that involves mechanical ventilation is the same as one that relies entirely on natural vents. The design fire plume inflow to the smoke layer at its desired minimum elevation is established, and suitable ventilation fans are chosen that will provide the necessary extraction of smoke at some elevation within the smoke layer.

The operating characteristics of the fans used in a design must take into account the temperature of the smoke that is being extracted.

It is possible to use mechanical ventilation with natural vents to remove the generic requirement of large, open inlet vents. Thus, if most doors and windows at elevations below z_{LAY} are closed and leakage there to the outside is limited, then mechanical ventilation can be used to force fresh air into the facility below z_{LAY} . The idea would be to use fans to pressurize the interior of the facility, and to push the smoke out through open vents located above z_{LAY} , for example, through fusible-link-actuated ceiling vents within a curtained space of fire origin. In this way the difficult problem of designing fans to operate under unfavorable and typically unknown, high-temperature conditions is avoided.

The issue of plug-holing can be a particular concern when using mechanical ventilation for smoke removal.

The reader is referred to Chapter 4 of Reference 2 for a discussion on issues related to equipment and controls of mechanical ventilation systems used for smoke venting.

Designing Systems That Successfully Combine Smoke Vents with Sprinklers

The Difficulty and Controversy of Combining Vent and Sprinkler Systems

The fire safety benefits of vents and sprinklers are different. In appropriate applications, it is evident that fire safety would be enhanced if both sets of benefits could be achieved simultaneously. However, it is not at all clear that a simple combining of the two technologies will lead to a combining of their respective benefits. (Here, *simple combining* of the technologies means deploying the technologies according to design rules that apply for each, in the absence of the other.) Indeed, the varied physical phenomena, that are the basis for the success of the two technologies when deployed independently, to a greater or lesser extent can be expected to be interactive when deployed together. Thus, design features of the smoke and

heat vents can modify sprinkler performance and the design features of the sprinklers can be expected to modify smoke and heat vent performance. As an example of the latter, consider the following.

The water spray associated with sprinkler systems will inherently lead to some cooling of the smoke that rises from the fire's combustion zone and begins to fill the protected space. This is cooling that would not have occurred in the absence of the sprinklers and that would not have been taken into account in a deployed smoke and heat vent design that was based solely on the considerations presented earlier in this chapter. Because the sprinkler spray cools the smoke, the designed effectiveness of the vents to remove the smoke will have been reduced; the mass rate of smoke flowing out of the vents will be less than the design value.

If the extent of the interactions of sprinklers and smoke vents can be shown to be small, or always leading to enhanced benefits, than the idea of a simple combining of the two technologies will succeed. However, if the interaction is significant in the sense that a benefit is modified greatly, and negatively so, then appropriate design modifications to the combined system would have to be identified and implemented. (Thus, in the above example, if sprinkler cooling of the smoke is shown to lead to significant reduction in vent flow rate, then the vent design would have to be appropriately modified, i.e., a larger vent area would be required for a successful design.)

The task of obtaining a clear understanding of the above-mentioned interaction phenomena and the task of developing methods for identifying appropriate design modifications, when required, have been shown to involve difficult and controversial issues. At the time this chapter was prepared no generally accepted technical guidelines existed on the effective design of combined venting/sprinkler systems.

Resolving Claims and Counterclaims on the Benefits of Combined Vent/Sprinkler Systems

Past studies of combined vent/sprinkler systems: Published and unpublished reports of the results of combined sprinkler/vent studies typically conclude that certain enhanced and/or reduced benefits accrue from combining the two technologies, that is, positive and/or negative claims. Also, over the years, many analyses of the results of these studies by people not directly involved in the work have also been published. These analyses invariably conclude with positive or negative claims of the benefits of combining venting and sprinkler technologies, opinions that are partly, and at times entirely, different from the opinions espoused in the corresponding original report of the work in question. Finally, published opinions on the effects of combining vents with sprinklers are often based on simple logical arguments. In some cases even these latter opinions can appear to be contradictory.

There is one study²⁸ that identified and reviewed 34 position papers on the subject and that evaluated the validity of generic claims and counterclaims on the benefits of combined vent/sprinkler systems. A listing of the

claims and counterclaims so identified and a summary of conclusions on their validity follow.

Claims and counterclaims:²⁸ In the literature, claims that have been made *in favor* of vent/sprinkler systems can be reduced to the following three:

1. Smoke and heat vents limit the distribution of products of combustion in the facility whether deployed sprinklers are operative or inoperative.
2. Smoke and heat vents decrease the number of activated sprinklers.
3. Smoke and heat vents assist the fire department in identifying the location of the fire within the facility and in reducing the need for manual roof venting.

In the literature, claims that have been made *against* vent/sprinkler systems can be reduced to the following four:

1. Smoke and heat vents will cause enhanced burning rates.
2. Smoke and heat vents will delay sprinkler activation.
3. Smoke and heat vents increase the number of activated sprinklers.
4. Smoke and heat vent flow rates are insufficient to realize any benefit.

Validity of claims for and against combined vent/sprinkler systems: After evaluating reports of studies of combined vent/sprinkler systems, it has been concluded based on the evidence that²⁸

- Venting does not have a negative effect on sprinkler performance.
- Successful performance of sprinklers does not rely upon reduced oxygen concentrations.
- Venting has no effect on the activation times of early sprinklers and does not affect the total number of sprinklers activated.
- If a fire is directly beneath a vent, activations of the first sprinklers may be delayed slightly, but there is no evidence that this will have a significant impact on sprinkler performance.
- Venting does limit the spread of products of combustion by releasing them from the building (within the curtained compartment of fire origin) near the source of the fire; this improves visibility for building occupants, whose concern is for rapid egress, and for fire fighters, whose concern is to find the seat of the fire to complete fire extinguishment.
- By limiting the spread of smoke and heat, venting also reduces smoke and heat damage to the building.
- In the event that sprinklers do not operate, venting remains a valuable aid in controlling the fire manually.
- Early vent activation has no detrimental effects on sprinkler performance.
- In many fires, current vent design practices, for example, those of NFPA 204,¹ are likely to limit the number of vents operated to one, and, in successful sprinkler operations, vents may not operate at all.
- Design practices should use methods which ensure early operation of vents; vent operation should be ganged so that the benefit of roof vents is fully realized.

- When deployed with vents and draft curtains, a sprinkler design needs to take full account of draft curtains as obstructions.
- Draft curtains should be placed in aisles rather than over storage.

Toward a Methodology for the Design of Combined Vent/Sprinkler Systems

General criteria for successful vent design: Taking the above conclusions into account and drawing on current knowledge of basic physical phenomena involved in vent/sprinkler interactions, it would appear that a consensus on the design of combined sprinkler/vent systems would result by meeting the following general criteria for successful vent design:

1. A *successful vent design, whether deployed with or without sprinklers, is one that leads to the benefits of improved visibility and safety during a fire to the extent that venting removes from a protected facility the highest temperature and most hazardous smoke and slows to an acceptable rate or stops, say, above eye elevation, the growth of the upper smoke layer.*
2. *When draft-curtain compartmentation is included in the vent design, a significant, additional possible benefit comes about to the extent that the smoke is contained successfully within the curtained compartment of fire origin by action of the venting there. Then the losses to building contents will be correspondingly confined to the contents found in the curtained compartment of fire origin.*

The design question is, Without reducing the designed effectiveness of sprinklers to control a fire, how can these criteria on vent design be met when taking proper account of the cooling and mixing actions of discharging sprinklers? To answer this question is to achieve a full-consensus design for combined vent/sprinkler systems.

Interaction of sprinkler spray and smoke layer: The action of sprinkler sprays on the smoke layer includes a combination of evaporative cooling and dilution of the smoke, where the latter is by virtue of spray-driven mixing, via entrainment dynamics, of the relatively cool and uncontaminated lower-layer gases and the upper layer.²⁹⁻⁴¹ Provided sprinkler spray-reduced smoke temperature and associated loss of buoyancy is not too great, it would appear that the effect of evaporative cooling of the smoke, even if accompanied by moderate sprinkler spray-driven mixing, can be offset by additional vent capacity. However, it seems that even without significant evaporative cooling, sprinkler spray-driven mixing action can be so effective that it leads to a precipitous increase in the volume of smoke (i.e., in the depth of the smoke layer) and to a corresponding precipitous decrease from an originally high-temperature concentrated smoke to a much lower-temperature and now-voluminous and -diluted smoke. If and when the latter vigorous mixing occurs, then even impractically large increases in vent capacity would not likely lead to any significant measure of the benefits of

venting. The latter phenomenon is commonly referred to as *smoke-logging*. A vent design that is developed to meet the above general criteria must be based on a credible analysis that accounts for and avoids the phenomena of smoke logging.

There is experimental evidence that smoke logging can be controlled by venting,⁴² and a preliminary analysis to explain the phenomenon has been provided.^{29,30} Thus, it has been reported that "preliminary tests in [a] . . . large-scale mall . . . showed that, under some conditions, [a] . . . smoke layer could be brought down by a manually operated sprinkler spray, [and that] smoke logging then occurred rapidly, with a high smoke density at low level. However, under some conditions, the smoke layer was not disturbed by a sprinkler spray."³⁰

To summarize the above, the major benefits of venting can be achieved, even when used in combination with sprinklers, by identifying and adopting a technically sound design that can be shown to meet the above general criteria for successful vent design. Such criteria can be met only up to the time that smoke logging occurs, or provided that smoke logging does not occur. To determine that the benefits *are* achievable, and that they are in fact achieved in any particular design, requires an analysis and resolution of underlying issues of sprinkler/smoke-layer interaction.

Sprinkler spray-driven cooling, mixing, and smoke logging can be resolved with computer fire-model simulations: From the simplest modeling concepts and through evidence of measurements, it is clear that the action of sprinklers reduce the temperature of the fire environment. However, in terms of past experimental studies, there has been no attempt to deal with the very difficult task of isolating and understanding these effects of temperature reduction in the context of the complex phenomena of sprinkler spray cooling (by heat-transfer and mass-transfer exchanges between spray droplets and the gases that fill the space) and sprinkler spray-driven smoke transport and mixing (transport of room gases by spray-generated pressure distributions and gas/spray-droplet momentum exchanges). What is known through visual measurements, but only anecdotally so, is that spray-driven mixing and transport of an initially stable and growing upper smoke layer can and often does lead to onset of smoke logging, whereby the mixing actions of sprinkler sprays are so vigorous as to effectively and continuously mix the continuous supply of newly generated smoke from the fire plume with all the rest of the (smokey) gas that fills the space. As indicated above, it is not reasonable to expect to achieve the desired benefits of venting subsequent to the initiation of smoke logging.

Given a *design fire* and a reliable means of predicting the corresponding sequencing of sprinkler actuation, resolution of the issue of sprinkler spray-driven cooling, mixing, and smoke logging would be based on a fire-model simulation that takes appropriate account of interactions of the sprinkler sprays and the fire environment and that predicts that vent design objectives have been achieved.

There is some indication that analytic fire-modeling methods can be used to resolve the above issues.⁴¹ Ref-

erence here is to a mathematical model of the generic interaction of a downward-directed sprinkler spray and a two-layer fire environment. The model simulates the action of the sprinkler spray, including the effects of evaporative cooling and the spray-driven mixing of the elevated-temperature, upper smoke layer and the relatively cool and uncontaminated lower layer. The analysis led to the identification of six possible generic configurations of sprinkler/layer interaction.^{40,41} Of the possible configurations, the one that will prevail at a given time during the development of a particular fire was found to depend mainly on the thickness and temperature of the upper smoke layer and on the momentum, spread angle, and characteristic droplet size of the sprinkler spray. In any particular fire scenario, the action of open vents and/or draft-curtain compartmentation could provide some control of the thickness and temperature of the layer, and, therefore, of sprinkler/layer interactions that would prevail.

Of the six above-referenced configurations of sprinkler/vent interaction, four were found to be particularly favorable in the present context, in the sense that they would *maximize* the success of a combined sprinkler/vent design. The idea is that with proper vent design the favorable configurations could lead to the desired control of the smoke-layer depth while minimizing smoke mixing to the lower layer to the point that any smoke there is only in a highly dilute state. Thus, for a given set of sprinkler spray characteristics, if the smoke layer is kept relatively thin and/or not too buoyant (i.e., its temperature is not too high), then the rates of both mass and enthalpy flow entrained into the upper-layer part of the sprinkler's "spray cone of influence" would be relatively insignificant (compared to the corresponding rates associated with the fire-plume flow to the upper layer). As a result, the combined action of cooling and momentum-exchange in the spray cone would be strong enough to transport all of the limited amounts of upper-entrained smoke through the layer interface, and well into the depth of the lower layer, there to be mixed eventually, with negligible consequences, into the rest of the lower-layer gases.

For the above configurations, the overall impact on undesirable mixing of the smoke in the protected space would be minimal. In particular, if it were possible and practical to design a vent system that would keep the smoke layer thin enough to maintain any of the above-referenced configurations of sprinkler/vent interaction for a significant length of time (i.e., by deploying a vent system that would remove from the upper layer most of the continuously in-flowing smoke from the fire plume), then, in the context of the above criteria, the resulting, combined sprinkler/vent system would achieve desired system objectives.

In contrast to the above, of the six possible configurations of sprinkler/vent interaction there were two that are particularly *unfavorable* in the sense that they would *minimize* the likely success of a combined sprinkler/vent design. These configurations could lead to relatively vigorous mixing between the smoke layer and the lower layer, leading to a rapid growth of the upper smoke layer and, possibly, to smoke logging.

Note that at least for the early part of a typical fire scenario, immediately subsequent to one or more rapid-

response sprinkler discharges, the condition of a relatively thin and not-too-high-temperature upper smoke layer will *always* prevail. These are exactly the basic conditions of the first and favorable of the above-mentioned flow configurations. Consistent with experience, smoke logging at such times is never observed.

Resolving the problem of sprinkler skipping and vent skipping: In terms of achieving vent/sprinkler design objectives, it is important to introduce, discuss, and identify a possible means of resolving problems associated with the phenomena known as *sprinkler skipping* and *vent skipping*.

The first sprinkler discharge introduces sprinkler-spray flows to the developing fire environment. This initial spray and the ones to follow are made up of ensembles of droplets of various sizes and velocities that flow from the respective sprinkler nozzles. Although the spray characteristic of a given sprinkler head design will have certain measurable overall characteristics, it is well beyond the scope of current technology to describe all aspects of the spray, which will, in any event, vary from one nominally identical manufactured sprinkler head to another. Furthermore, even a perfect knowledge of the initial conditions of the droplet trajectories would be of little use in the practical estimate of the precise subsequent droplet trajectories. One reason for this is that the droplet trajectories, especially those of the early discharging sprinklers, will be influenced significantly, by interaction with the relatively unpredictable (because of uncertainties of fire location, growth, etc.) and vigorous upward-moving plume flow. For example, some of the droplets, the ones that leave the vicinity of the sprinkler head with relatively small initial speed, will be accelerated rapidly, by droplet/plume-gas momentum exchanges, to the point where they closely track the trajectories of, and are convected along with, the plume flow. Furthermore, for the larger of these droplets, this close plume tracking will occur well before they evaporate and reach thermodynamic equilibrium with the surrounding plume flow. In the usual way, the plume flow, which now transports random and unpredictable numbers of water droplets, forms the ceiling jet which flows past the downstream sprinkler heads. This is the ceiling jet, which is supposed to heat, fuse the links (or break the bulbs) of, and initiate discharge of these downstream sprinkler heads, the water sprays from which are critical for controlling the fire.

In the above scenario, if ceiling jet-convected water droplets strike a sprinkler link or bulb, then, because of effects of evaporative cooling, there will be a significant reduction of its rate of heating. This can lead to a significant delay in sprinkler discharge. It is the resulting, unpredictable, and deleterious delay in sprinkler discharge that is referred to as *sprinkler skipping*.

The basic principles of traditional automatic vent actuation (i.e., by the melting action of fusible links heated by the high-temperature, high-velocity, ceiling-jet flow) are identical to the principles of fusible-link-actuated, automatic sprinkler discharge. Therefore, the above discussion on the phenomenon of sprinkler skipping is totally relevant and identical to a corresponding phenomenon involving vents, designated as *vent skipping*. Thus, as in the

case of sprinklers, the otherwise predictable automatic opening of fusible-link-actuated vents is subject to random and unpredictable water droplet-cooling delays in vent opening.

Accounting for sprinkler skipping and vent skipping in design: In traditional sprinkler design (i.e., assuming the absence of vents), the effects of sprinkler skipping on the ability of a sprinkler design to control a fire are taken into account empirically via the empirical experimental design process. In this regard, the relatively large numbers of sprinkler heads involved in a typical sprinkler installation and the relatively small number of expected skipped sprinklers, apparently leads to a natural robustness of sprinkler systems relative to the deleterious effects of sprinkler skipping.

In contrast to traditional sprinkler design, when vents and sprinklers are used *together*, the random and unpredictable effects of vent skipping are *not* now taken into account in the design of automatic vent systems. Also, the numbers of installed vent units per unit area of protected space, the *installed vent density*, is typically much smaller than the corresponding *installed sprinkler-head density*. Therefore, when using traditional automatic vent design methods, an appropriate correction for vent skipping would appear to be warranted, for example, by increasing the total design vent area in a compartment by some appropriate safety factor.

In terms of combined vent/draft-curtain designs, and as an alternative to traditional automatic, fusible-link-actuated vents, which involve inevitably the problem of vent skipping, it would appear that more controllable and more reliable means of ensuring timely and effective vent action are available. One generic possibility would involve *ganging*, that is, opening together at an appropriate controlled time all or most vent units in the compartment of fire origin, for example, by signals from smoke detectors or by appropriate indicators of sprinkler discharge.⁴³ A ganging strategy that could be well integrated into a reliable, consensus sprinkler/vent design is one where all vents of the fire compartment are ganged to open together immediately following first sprinkler discharge. Alternatively, by using achievable, "smart" vent-opening control, it should be possible to develop more sophisticated vent actuation strategies, for example, immediately following first sprinkler discharge, open all vents beyond the first or second ring of sprinklers (as identified, say, by the sprinkler of first discharge), and open all other vents after sprinkler control is indicated. The latter strategy would be augmented by an appropriate increase in vent area, over that of the design value, to account for the associated reduced number of early-opened vents.

A Consensus Approach to the Design of Combined Sprinkler/Vent Systems

Using mathematical fire models to achieve design objectives: The above discussion indicates that effective sprinkler/vent systems are feasible, and that mathematical fire models with a proven capability for simulating sprinkler/smoke interactions can be used as the basis for a consensus

approach to identify and establish effective sprinkler/vent system designs.

The capabilities of mathematical models to simulate sprinkler/smoke interactions have been reviewed.^{44,45} The models considered were those that are complete in the sense that they can be used to simulate successfully both isolated sprinkler/smoke interactions and full fire scenarios, where the latter would be used to establish the success of sprinkler/vent designs. Both zone-type and field model-type simulation approaches were found to offer excellent possibilities for addressing the problem. In the usual way, the two approaches are complementary in the sense that the zone model approach would be most applicable and appropriate for parametric studies and as a practical design tool, while the field model approach would be most applicable for simulating and studying the details of specific scenarios that are of particular interest and concern, for example, the discharge sequence of sprinklers and the effectiveness of a vent design in specific fire scenarios where draft curtains are almost directly above the fire.

A sprinkler/vent design approach that uses zone-type fire model simulations might involve application of an advanced version of LAVENT that would include the sprinkler/smoke-interaction simulation model⁴¹ discussed earlier. A successful preliminary implementation of this approach, with a revised prototype model called LAVENTS (fusible Link-Actuated VENTS and Sprinklers), has already been presented.⁴⁶ Relevant successes using the field model approach have also been reported. Examples of these include applications of the LES (Large Eddy Simulation) model,^{47–50} the JASMINE model,^{51,52} and others.^{53,54}

A set of example guidelines for design of a consensus sprinkler/vent system: To fix ideas that are consistent with the above discussion, the following example guidelines for design of a consensus sprinkler/vent system are provided.

1. Establish sprinkler design in the traditional way, that is, develop design parameters using full-scale testing involving effective, rapid, sprinkler-activation strategies in the absence of vents (rapid in the sense that the test/design problem solved is one involving an effectively unconfined ceiling where smoke-layer buildup is negligible in that it does not effect the timing or sequence of early sprinkler discharge).
2. Establish a vent design objective. In cases where sprinkler action is expected to control the fire (i.e., the fire will not exceed a specified, maximum energy-release rate), the design objective for Figure 3-9.1-type scenarios might be for the vents to maintain indefinitely the smoke from spreading beyond the curtained compartment of fire origin (i.e., the smoke-layer interface does not descend below the bottom of the draft curtains). If the latter design objective is shown to be too ambitious, or, in cases where sprinkler action is expected only to slow, but not to stop the growth of the fire, the design objective would be for the vents to maintain the smoke from spreading beyond the curtained compartment of fire origin for a specified time interval, for ex-

ample, the time expected for the fire department to respond and initiate an attack on the fire.

3. Adopt a practical/achievable strategy of early opening of all vents in the compartment of fire origin, for example, ganged operation of all vents in the curtained compartment of fire origin based on and subsequent to first sprinkler activation.
4. Using an appropriate consensus compartment fire model, one with a proven capability of simulating the time-dependent interaction of sprinklers, vents, and draft curtains, develop a vent design that meets the established design objectives.

Nomenclature

A_{FIRE}	effective plan area of fire
A_{INLET}	total area of open inlet vents
A_{VENT}	total area of ceiling vents or area of a single unit vent
$A_{\text{VENT,EFF}}$	effective area of vent
C	flow coefficient, (Equation 8)
$C_{\text{EFF,FLOOD}}$	effective value of C for flooding-flow condition
C_p	specific heat at constant pressure of air
C_{PRES}	local pressure coefficient
D_{VENT}	equivalent diameter of a single vent, (Equation 24)
D_{FIRE}	effective diameter of base of fire, (Equation 39)
F	Froude number, (Equation 26)
F_{CRITICAL}	critical value of F
g	acceleration of gravity, $9.8 \text{ m}^2/\text{s}$
h	
h_{DEP}	$z_{\text{CEIL}} - z_{\text{LAY}}$ depressed distance of layer interface
K	fraction of \dot{Q}_{CONV} (Equation 51)
L_{CURT}	length of draft curtains
L_{FIRE}	effective length of line fire
L_{FLAME}	mean flame height (Equation 43)
L_1, L_2	length of sides of rectangular vent
\dot{m}_{CURT}	mass flow rate under a draft curtain
\dot{m}'_{LINE}	mass flow rate per unit length for plume from line fire (Equation 41)
\dot{m}_{PLUME}	mass flow rate in the plume
$\dot{m}_{\text{SPILLPLUME}}$	mass flow rate in a spill plume (Equation 48)
\dot{m}_{VENT}	mass flow rate through vent
P	absolute pressure
P_{ADJ}	P in space adjacent to curtained space
P_{AMB}	P of standard ambient environment, 101325 Pa
P_{IN}	P inside the facility
P_{OUT}	P of outside environment
P_{SURF}	P along outside building surface
P_1, P_2	P in space 1, 2

\dot{Q}_{CONV}	portion of \dot{Q}_{TOTAL} convected in plume (Equation 37)
\dot{Q}'_{CONV}	convected energy release rate per unit length for line fire (Equation 40)
\dot{Q}_{TOTAL}	total rate of fire energy release
R	gas constant for air, 286.8 (J/kg·K)
T	absolute temperature
T_{AMB}	characteristic T of ambient environment, 293 K
T_{LAY}	T of smoke layer
T_{OUT}	T of outside environment
t_g	time for t -squared fire to grow to 1000 kW
V_{FLOOD}	V_{VENT} for flooding-flow condition
V_{VENT}	average velocity of vent flow at the vent opening
V_{WIND}	wind speed
W_{VENT}	width of vent
z	elevation
z_{BALCONY}	z at bottom of balcony
z_{BOT}	z at bottom of vent
z_{CEIL}	z at ceiling
z_{CURT}	z at bottom of curtain
z_{FIRE}	z at base of fire
z_{FLOOR}	z at floor
z_{LAY}	z at bottom of upper smoke layer
$z_{\text{LINESOURCE}}$	z of line-fire source
z_{MID}	z at middle of nonhorizontal vent
z_{TOP}	z at top of vent
z_{VENT}	z of horizontal vent
z_0	z at datum

Greek

α	angle between normal to vent area and the vertical
β	a constant (Equation 28)
ϵ	defined in Equation 24
ε	defined in Equation 44
$\Delta P(z)$	$P(z) - P(z_0)$
$\Delta P_{\text{IN-ADJ}}(z)$	$P_{\text{IN}}(z) - P_{\text{ADJ}}(z)$
ΔP_{FLOOD}	$\Delta P_{\text{IN-OUT}}(z_{\text{CEIL}})$ for flooding-flow condition
$\Delta P_{\text{IN-OUT}}(z)$	$P_{\text{IN}}(z) - P_{\text{OUT}}(z)$
$\Delta P_{1-2}(z)$	$P_1(z) - P_2(z)$
δ	a measure of normalized P (Equation 4)
η	dummy variable of integration
Λ	dimensionless flame length (Equation 44)
λ_{RAD}	fraction of \dot{Q}_{TOTAL} radiated to far field
ρ	density
ρ_{AMB}	characteristic ρ of ambient environment, 1.2 kg/m ³
ρ_{LAY}	ρ of smoke layer
ρ_{OUT}	ρ of outside environment
ρ_{VENT}	ρ of vent flow

References Cited

- NFPA 204, *Guide for Smoke and Heat Venting*, NFPA, Quincy, MA (1998 edition).
- NFPA 92B, *Guide for Smoke Management Systems in Malls, Atria, and Large Areas*, NFPA, Quincy, MA (2000).
- H.P. Morgan, et al. "Design Methodologies for Smoke and Heat Exhaust Ventilation," *Fire Research Station*, Watford, United Kingdom (1999).
- T. Butcher, ed., *CIBSE Relationships for Smoke Control Calculations, Technical Memoranda TM:1995*, Chartered Institution of Building Services Engineers, London (1995).
- L.Y. Cooper and G.P. Forney, "The Consolidated Compartment Fire Model (CCFM) Computer Code Application CCFM. VENTS—Part I: Physical Basis," *NISTIR 90-4342*, National Institute of Standards and Technology, Gaithersburg, MD (1990).
- P.H. Thomas, et al. "Investigations into the Flow of Hot Gases in Roof Venting," *Fire Research Technical Paper No. 7*, HMSO, London (1963).
- L.Y. Cooper, "Combined Buoyancy- and Pressure-Driven Flow through a Horizontal, Circular Vent," *Journal of Heat Transfer*, 117, pp. 659–667 (1995).
- L.Y. Cooper, "Calculating Combined Buoyancy- and Pressure-Driven Flow through a Horizontal, Circular Vent; Application to a Problem of Steady Burning in a Ceiling-Ventilated Enclosure," *Fire Safety Journal*, 27, pp. 23–35 (1996).
- L.Y. Cooper, "VENTCF2: An Algorithm and Associated Computer Subroutine for Calculating Flow through a Horizontal Ceiling/Floor Vent in a Zone-Type Compartment Fire Model," *Fire Safety Journal*, 28, pp. 253–287 (1997).
- G. Heskestad and R.D. Spalding, "Inflow of Air Required at Wall and Ceiling Appertures to Prevent Escape of Fire Smoke," FMRCJ.I.OQ4E4.RU, Factory Mutual Research Corporation, Norwood, MA (1991).
- J.S. Turner, *Buoyancy Effects in Fluids*, Cambridge Press (1973).
- I.R. Wood, "Selective Withdrawal from a Stably Stratified Fluid," *Journal of Fluid Mechanics*, 32, pp. 209–223 (1968).
- D. Spratt and A. Heselden, "Efficient Extraction of Smoke from a Thin Layer under a Ceiling," *Fire Research Note No. 1001*, Fire Research Station, Department of the Environment and Fire Offices' Committee, Joint Fire Research Organization, Watford, UK (1974).
- J.H. Shanley and C.L. Beyler, "Horizontal Vent Flow Modeling with Helium and Air," *Fire Safety Science—Proceedings of the Second International Symposium*, (T. Wakamatsu, et al. eds.), Hemisphere, New York, pp. 305–313 (1989).
- C.L. Beyler, "Fire Plumes and Ceiling Jets," *Fire Safety Journal*, 11, pp. 53–75 (1986).
- G. Heskestad, "Engineering Relations for Fire Plumes," *Fire Safety Journal*, 7, pp. 25–32 (1984).
- E.E. Zukoski, "Development of a Stratified Ceiling Layer in the Early Stages of a Closed-Room Fire," *Fire and Materials*, 2, 2, pp. 54–62 (1978).
- L.Y. Cooper, "A Buoyant Source in the Lower of Two Homogeneous, Stably Stratified Layers," *20th International Symposium on Combustion*, Combustion Institute, Pittsburgh, pp. 1567–1573 (1984).
- L.Y. Cooper, "Convective Heat Transfer to Ceilings above Enclosure Fires," *19th Symposium (International) on Combustion*, Combustion Institute, Pittsburgh, pp. 933–939 (1982).
- L.Y. Cooper, "Heat Transfer from a Buoyant Plume to an Unconfined Ceiling," *Journal of Heat Transfer*, 104, pp. 446–451 (1982).

21. L.Y. Cooper and A. Woodhouse, "The Buoyant Plume-Driven Adiabatic Ceiling Temperature Revisited," *Journal of Heat Transfer*, 108, pp. 822–826 (1986).
22. L.Y. Cooper and D.W. Stroup, "Thermal Response of Unconfined Ceilings above Growing Fires and the Importance of Convective Heat Transfer," *Journal of Heat Transfer*, 109, pp. 172–178 (1987).
23. L.Y. Cooper, "Ceiling Jet-Driven Wall Flows in Compartment Fires," *Combustion Science and Technology*, 62, pp. 285–296 (1988).
24. L.Y. Cooper, "Fire-Plume Generated Ceiling Jet Characteristics and Convective Heat Transfer to Ceiling and Wall Surfaces in a Two-Layer Zone-Type Fire Environment: Uniform Temperature Ceiling and Walls," *Fire Science and Technology*, 13, 1 and 2, pp. 1–17 (1993).
25. L.Y. Cooper, "Estimating the Environment and the Response of Sprinkler Links in Compartment Fires with Draft Curtains and Fusible Link-Actuated Ceiling Vents," *Fire Safety Journal*, 16, pp. 137–163 (1990).
26. W.D. Davis and L.Y. Cooper, "Estimating the Environment and the Response of Sprinkler Links in Compartment Fires with Draft Curtains and Fusible Link-Actuated Ceiling Vents—Part II: User Guide for the Computer Code LAVENT," *NISTIR 89-4122*, National Institute of Standards and Technology, Gaithersburg, MD (1989).
27. National Institute of Standards and Technology, LAVENT software, Gaithersburg, MD.
28. C.L. Beyler and L.Y. Cooper, "Interaction of Sprinklers With Smoke Vents," in press *Fire Technology*.
29. M.L. Bullen, "The Effect of a Sprinkler on the Stability of a Smoke Layer beneath a Ceiling," *Fire Research Note No. 1016*, Department of the Environment and Fire Officers' Committee, Joint Fire Research Organization, Watford, England (1974).
30. M.L. Bullen, "The Effect of a Sprinkler on the Stability of a Smoke Layer beneath a Ceiling," *Fire Technology*, 13, 1, pp. 21–34 (1977).
31. R.L. Alpert, "Calculated Interaction of Sprays with Large-Scale Buoyant Flows," *Journal of Heat Transfer*, 106, pp. 310–317 (1984).
32. A.J. Gardiner, *First Report on the Interaction between Sprinkler Sprays and the Thermally Buoyant Layers of Gases from Fires*, South Bank Polytechnic, London (1985).
33. A.J. Gardiner, *Second Report on the Interaction between Sprinkler Sprays and the Thermally Buoyant Layers of Gases from Fires*, South Bank Polytechnic, London (1986).
34. A.J. Gardiner, *Third Report on the Interaction between Sprinkler Sprays and the Thermally Buoyant Layers of Gases from Fires*, South Bank Polytechnic, London (1988).
35. A.J. Gardiner, *Fourth Report on the Interaction between Sprinkler Sprays and the Thermally Buoyant Layers of Gases from Fires*, South Bank Polytechnic, London (1988).
36. L.A. Jackman, *Second Report on the Interaction between Sprinkler Sprays and the Thermally Buoyant Layers of Gases from Fires*, South Bank Polytechnic, London (1990).
37. L.A. Jackman, *Third Report on the Interaction between Sprinkler Sprays and the Thermally Buoyant Layers of Gases from Fires*, South Bank Polytechnic, London (1991).
38. L.A. Jackman, P.F. Nolan, A.J. Gardiner, and H.P. Morgan, *Mathematical Model of the Interaction of Sprinkler Spray Drops with Fire Gases*, South Bank University, London, Swedish Fire Research Board, and National Institute of Standards and Technology (NIST), Fire Suppression Research, First International Conference on Fire Suppression Research, May 5–8, 1992, Stockholm, Sweden, (V. Sjolin, D.D. Evans, and N.H. Jason, eds.), pp. 209–227 (1992).
39. G. Heskestad, "Sprinkler/Hot Layer Interaction," *NIST-GCR-91-590*, National Institute of Standards and Technology (NIST), Gaithersburg, MD (1991).
40. L.Y. Cooper, "The Interaction of an Isolated Sprinkler Spray and a Two-Layer Compartment Fire Environment. Phenomena and Model Simulations," *Fire Safety Journal*, 25, 2, pp. 89–107 (1995).
41. L.Y. Cooper, "The Interaction of an Isolated Sprinkler Spray and a Two-Layer Compartment Fire Environment," *International Journal Heat and Mass Transfer*, 38, 4, pp. 679–690 (1995).
42. P.L. Hinkley, "Work by the Fire Research Station on the Control of Smoke in Covered Shopping Centers," *BRE Paper CP 83/75*, Building Research Establishment (BRE), Fire Research Station (FRS), London (1975).
43. A.J.M. Heselden, "The Interaction of Sprinklers and Fire Venting," *Fire Surveyor*, 11, 5, pp. 13–28 (1982).
44. G. Holmstedt, "Sprinkler and Fire Venting Interaction," *Literature Survey on Modeling Approaches and Experiments Available and Recommendations for Further Studies*, 92178 AR GH/AB, Swedish Fire Research Board, Stockholm, Sweden (1992).
45. B. Persson and H. Ingason, "Modeling of Interaction between Sprinklers and Fire Vents," *SP Report 1996:32*, Swedish National Testing and Research Institute, Sweden (1996).
46. L.Y. Cooper, "LAVENTS—A Computer Program to Model the Interaction between Sprinklers, Smoke Layers, and Smoke Vents," presented at the *International Conference on Smoke Ventilation and Sprinklers—Aspects of Combined Use*, Fire Research Station, Borehamwood, England (1992).
47. K.B. McGrattan, A. Hamins, D.W. Stroup, "Sprinkler, Smoke and Heat Vent, Draft Curtain Interaction—Large-Scale Experiments and Model Development," *NISTIR 6196*, National Institute of Standards and Technology (NIST), Gaithersburg, MD (1998).
48. K.B. McGrattan, H.R. Baum, and R.G. Rehm, "Large Eddy Simulations of Smoke Movement," *Fire Safety Journal*, 30, pp. 161–178 (1998).
49. K.B. McGrattan and D.W. Stroup, "Sprinkler, Vent and Draft Curtain Interaction: Experiment and Computer Simulation," *National Institute of Standards and Technology (NIST)*, Gaithersburg, MD (1997).
50. K.B. McGrattan and D.W. Stroup, "Large Eddy Simulations of Sprinkler, Vent and Draft Curtain Performance," *Fire Suppression and Detection Research Application, Symposium, Research and Practice: Bridging the Gap*, Proceedings, National Fire Protection Research Foundation, February 12–14, 1997, Orlando, FL, pp. 59–68 (1997).
51. H. Touvinen, "Validation of Ceiling Jet Flows in a Large Corridor with Vents Using the CFD Code JASMINE," *Fire Technology*, 32, 1, pp. 25–49 (1996).
52. H. Touvinen and L.Y. Cooper, "Validation of Ceiling Jet Flows in a Large Corridor with Vents Using the CFD Code JASMINE: Errata and Additional Remarks," *Fire Technology*, 33, 2, pp. 183–186 (1997).
53. R.N. Mawhinney, E.R. Galea, and M.K. Patel, "Euler-Lagrange Modeling of Fire/Sprinkler Interactions," *Fire Safety Science—Proceedings of the Fifth International Symposium*, International Association of Fire Safety Science (IAFSS), Australia, p. 1336 (1997).
54. W.K. Chow and A.C. Tang, "Experimental Studies on Sprinkler Water Spray Smoke Layer Interaction," *Journal of Applied Fire Science*, 4, 3, pp. 171–184 (1994–95).

CHAPTER 10

Compartment Fire-Generated Environment and Smoke Filling

Leonard Y. Cooper

Fire Safety of Building Designs

Introduction

The following generic problem must be solved if one is to be able to establish the fire safety of building designs:

- Given: Initiation of a fire in a compartment or enclosed space.
- Predict: The environment that develops at likely locations of occupancy, at likely locations of fire/smoke sensor hardware (e.g., detectors and sprinkler links), and in locations of safe refuge and along likely egress paths.
- Compute: The time of fire/smoke sensor hardware response and the time of onset of conditions untenable to life and/or property. This computation would be carried out from the above predictions, using known response characteristics of people, hardware, and materials.

The above is only a simple sketch of the overall problem that is likely to be associated with the interesting details of many real fire scenarios. A long-term challenge of fire science and technology is to solve the above type of problem, even when it is formulated in elaborate detail. Compartment fire modeling is the branch of fire science

and technology which develops the necessary tools to address this generic problem.

This chapter will describe some of the key phenomena that occur in compartment fires, and it will focus on smoke filling which is one of the simplest quantitative global descriptions of these phenomena. A specific smoke-filling model will be presented, and solutions to its model equations will be discussed along with example applications.

Compartment Fire-Generated Environment

Figures 3-10.1 through 3-10.8 depict the various phenomena that make up the compartment fire-generated environment to be predicted when compartment fire modeling is adopted. These figures are intended to illustrate the representative conditions at different instants of time in two generic compartment spaces: (1) an almost-fully enclosed single-room compartment of fire origin and (2) an almost-fully enclosed, freely connected, two-room compartment made up of the room of fire origin and an adjacent space. A description of the phenomena depicted in these figures follows. The physical bases of assumption that can be used to simplify descriptions of some of these phenomena are included in the discussion. Some of these will be important in placing the simple smoke-filling model into the perspective of the overall complex dynamic fire environment.

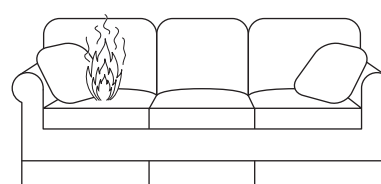


Figure 3-10.1. Events immediately after ignition.

Dr. Leonard Y. Cooper was a research engineer in the Building and Fire Research Laboratory of the National Institute of Standards and Technology from 1978-1998. Since 1998 he has been a senior scientist/engineer at Hughes Associates Inc., a fire protection engineering research and development firm. Since 1978 he has focused on applying a broad range of the physical and mechanical engineering sciences to develop and transfer research results into technically sound engineering practices in the field of applied fire safety. His research included the development of mathematical models of fire phenomena and on the assembly of these into compartment fire models and associated computer programs for practical and research-oriented compartment fire simulations.

Room of Fire Involvement

Fire growth in the combustible of fire origin: An unwanted ignition leading rapidly to flaming is assumed to occur within an enclosed space. This ignition is depicted in Figure 3-10.1 as occurring on the cushion of a couch in, say, a residential type of occupancy. It is, however, important to realize that all of the discussion to follow, and Figure 3-10.1 itself, is also relevant to fire scenarios which may develop in other kinds of occupancies, for example, as a result of ignitions in stacked commodity warehouse enclosures, places of assembly, and so forth.

Within a few seconds of ignition, early flame spread quickly leads to a flaming fire with a power output of the order of a few tens of kW (a power level characteristic of a small wastepaper basket fire). The fire continues to grow. Besides releasing energy, the combustion process also yields a variety of other products, including toxic and nontoxic gases and solids. Together, all of these products are referred to as the "smoke" produced by the fire.

With an adequate description of the ignition source and the involved combustible (e.g., ignited paper match on the corner of a couch whose frame, cushioning and finishing materials, and construction were well defined), one would hope that fire science and technology would provide methods to predict the fire spread and growth process from onset of ignition. Toward this end, ongoing research on flame spread and combustion is under way in a variety of fire research institutions throughout the world. (Examples of such research include boundary layer analyses and experiments with flame spread on idealized materials and geometries; and flame spread tests and rate of heat release tests on small samples of real material composites.) However, for the present and the foreseeable future, it is beyond the state-of-the-art of fire technology to make the required fire growth prediction with any generality. This situation leads to a dilemma for the modeler of compartment fire environments, because the physical and chemical mechanisms which govern the dynamics of the combustion zone actually drive the basic intra-compartment smoke migration phenomena whose simulations are being sought.

A practical engineering solution to the above dilemma, proposed and supported by Cooper,^{1,2} lies in the following compromise in simulation accuracy:

Prior to the time of potential flashover, it is reasonable to neglect the effect of the enclosure on flame spread and to assume that, from the time of ignition to the time shortly before potential flashover, the combustion zone in a particular grouping of combustibles develops as it would in a free-burn situation.

[Free burn here is defined as a burn of the combustibles in a large (compared to the combustion zone), ventilated space with relatively quiescent atmosphere.] To implement these ideas, one simply uses empirical, free-burn test data (which may or may not be presently available) to describe the combustion physics of a fire whose hazard is being evaluated. This compromise would, in the course of time, be supplanted by analytic models of flame spread and fire growth to the extent the future results of research lead to satisfactory methods for predicting such phenomena.

The implementation of the above compromise is, in principle, relatively simple. But for general use, it must be supported by an extensive data base acquired from a series of actual full-scale free-burn tests. This kind of data is being acquired with some regularity at fire test laboratories such as those of the National Institute of Standards and Technology and the Factory Mutual Research Corporation.³⁻⁵

Development of the plume: As depicted in Figure 3-10.2, a large fraction, λ_r , of the rate of energy released in the high-temperature combustion zone is transferred away by radiation. The transferred energy, $\lambda_r \dot{Q}(t)$, irradiates nearby surfaces of the combustible and faraway wall, ceiling, etc., surfaces which are in the line-of-sight of the combustion zone. The actual value of λ_r associated with the free-burn of a specific array of combustibles is often deduced from data acquired during the aforementioned type of free-burn tests. For typical hazardous flaming fires, λ_r is usually of the order of 0.35.

Because of the elevated temperature of the products of combustion, buoyancy forces drive them out of the growing combustion zone and up toward the ceiling. In this way, a plume of upward-moving elevated-temperature gases and particulates is formed above the fire. For the full height of the plume and at its periphery, relatively quiescent and cool gases are entrained laterally and mixed with the plume as it continues its ascent to the ceiling. As a result of this entrainment, the total mass flow in the plume continuously increases, and the average temperature and average concentration of products of combustion in the plume continuously decrease with increasing height. With reasonable accuracy, the plume dynamics at any instant of time can be quantitatively described as a function of the rate of energy, $(1 - \lambda_r)\dot{Q}(t)$, convected up from the combustion zone. A description of the concentration of combustion products in the plume would require, in addition, the combustion zone's rate of product generation. With regard to predictions of the dynamics of the plume, results can be provided at a variety of different levels of detail.⁶⁻⁸ For example, Zukoski et al.

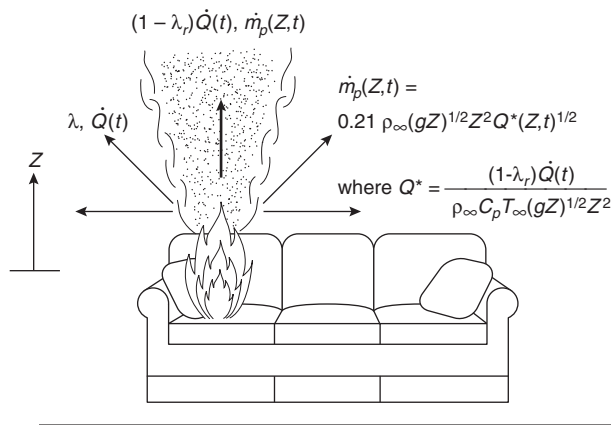


Figure 3-10.2. Development of the plume.

provide the formula in Figure 3-10.2 as an estimate of the mass flux in the plume, \dot{m}_p , at a distance Z above the combustion zone.⁷

Plume-ceiling interaction: As depicted in Figure 3-10.3, when the hot plume gases impinge on the ceiling, they spread across it forming a relatively thin radial jet. This jet of hot gases contains all of the smoke generated from the combustion zone, and all the ambient air which was entrained along the length of the plume.

As the hot jet moves outward under the ceiling surface, it entrains ambient air from below. It transfers energy by conduction to the relatively cool adjacent ceiling surface, and by convection to the entrained air. It is retarded by frictional forces from the ceiling surface above, and by turbulent momentum transfer to the entrained air from below. As a result of all this flow and heat transfer activity, the ceiling jet continuously decreases in temperature, smoke concentration, and velocity, and increases in thickness with increasing radius.

Research reported in the literature has led to results for predicting the quantitative aspects of ceiling-jet dynamics that can be used for selecting and locating smoke detectors and fusible link sprinkler head actuators, and for the mathematical modeling of overall compartment fire environments.⁹⁻¹⁸

With regard to detectors and fusible links, knowledge of the properties of the ceiling jet is the key to the prediction of the response of properly deployed devices in real fire scenarios. With regard to the overall modeling of compartment fire environments, the basic information that must be extracted from the ceiling-jet properties is the rate of heat transfer to the ceiling surface. Experiments have shown that this heat transfer can be significant, of the order of several tens of percent of the total energy released by the combustion zone, and, as a result, it is key to predicting the temperature of the smoke which ultimately spreads throughout the enclosure. Also, a reasonable estimate of this rate of heat transfer is required for estimating temperatures of the ceiling surface material itself.

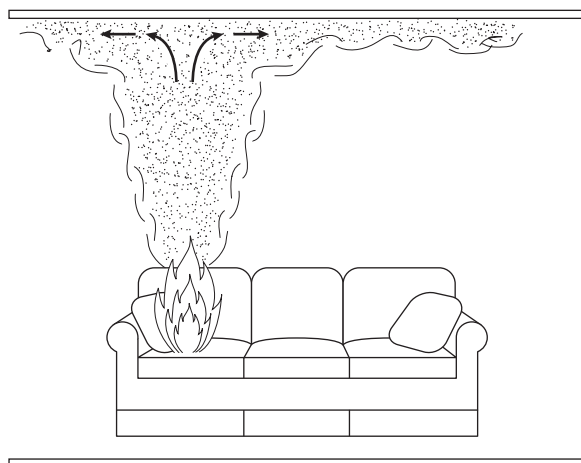


Figure 3-10.3. *The plume-ceiling interaction.*

Ceiling jet-wall interaction: The ceiling jet continues to move radially outward under the ceiling surface, and it eventually reaches the bounding walls of the enclosure. As depicted in Figure 3-10.4, the ceiling jet (now somewhat reduced in temperature from its highest levels near the plume) impinges and turns downward at the ceiling-wall juncture, thereby initiating a downward-directed wall jet.

The downward wall jet is of higher temperature and lower density than the ambient air into which it is being driven. The jet is, therefore, retarded by buoyancy in its downward descent, and at some distance below the ceiling the downward motion of the smoky jet is eventually halted. The wall jet is also retarded (probably to a lesser degree) by frictional forces at the wall surface, and it is cooled by conductive/convective heat transfer to relatively cool wall surfaces. Momentum and heat transfer from the jet occur away from the wall as the jet's outer flow is sheared off and driven back upward on account of buoyancy. In its turn, the now upward-moving flow entrains ambient air in a manner which is reminiscent of entrainment into the original fire plume. Eventually a relatively quiescent upper gas layer is formed below the continuing ceiling-jet flow activity.

The strength of the wall-jet flow activity will be determined by the characteristics of the ceiling jet at the position of its impingement with the wall. For fire scenarios where the proximity of the walls to the fire is no greater than a room height or so, it is reasonable to speculate that, based on test results,^{19,20} rates of conductive/convective heat transfer to wall surfaces can be significant, of the order of tens of percent of the fire's energy release, and that entrainment to the upward moving, reverse portion of the wall flow can lead to significant variations of the early rate of thickening of the upper gas layer. On the other hand, if walls are several room heights from the fire, then it is possible that the ceiling jet will be relatively weak by the time it reaches the walls, in the sense that ceiling jet-wall interactions may not play an important role in the dynamics of the overall fire environment.

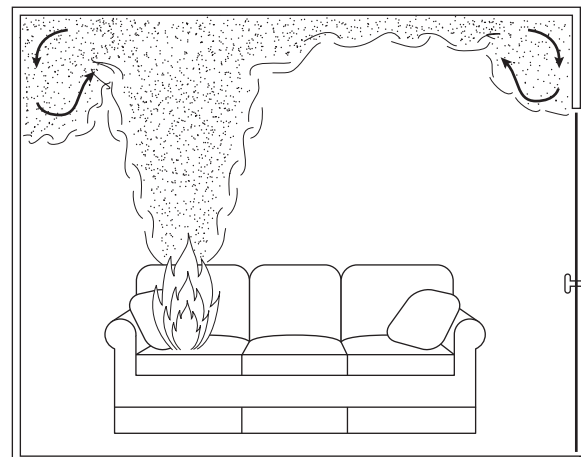


Figure 3-10.4. *Ceiling jet-wall interaction.*

Besides being important in the prediction of the overall fire environment, knowledge of the flow and temperature environments local to vigorous ceiling jet-wall interaction zones would be the key to predicting the response of wall-mounted smoke detectors, fusible links, and so forth.

Development and growth of the upper layer—“smoke filling”: The gases in the ceiling and wall jets redistribute themselves across the upper volume of the room. Eventually, a relatively quiescent, elevated temperature upper smoke layer of uniform thickness is formed below the continuing ceiling-jet flow activity. As the thickness of this layer grows, it eventually submerges the flows generated by the ceiling jet-wall interactions. The bottom of the layer is defined by a distinctive material interface which separates the lower ambient air from the upper, heated, smoke-laden gases. With increasing time the level of the smoke layer interface continues to drop, and the temperature and smoke concentration of the upper layer continue to rise.

In general, one would hope that fire detection, successful occupant alarm, and, if appropriate, successful intervention hardware response would occur during the state of fire growth described above. As suggested earlier, rationally engineered design in this regard would be possible with predictions of the dynamic fire environments local to deployed devices, and with predictions of the resulting response of such devices.

For reasons already mentioned, some detail in the description of plume, ceiling-jet, and ceiling jet-wall flow dynamics is required. However, for the purpose of understanding the impact of the overall fire environment on life and property safety, simplified descriptions compatible with the aforementioned detail would suffice and, for a variety of practical reasons, would actually be preferable. For this reason, available predictive models of compartment fire environments commonly describe the bulk of upper layer environment in terms of its spatially averaged properties. Thus, at any instant of time, it is typically assumed that the portion of the room which contains the fire-generated products of combustion, that is, the smoke, is confined to an upper layer of the room. This upper layer is described as having changing thickness and changing, but spatially uniform, temperature and concentration of combustion products. Actual full-scale testing of compartment fire environments has indicated that such a simple means of describing the distribution of products of combustion represents a reasonable compromise between accuracy in simulation and practicability in implementation.

Figure 3-10.5 is a generic depiction of the compartment fire environment at the stage of fire development under discussion. At this stage, whether or not the space of fire involvement is fully enclosed (i.e., all doors and windows are closed and only limited leakage occurs at bounding partitions) or is freely communicating with adjacent space(s) (e.g., open or broken windows, open doors to the outside environment or to an adjacent enclosed space of limited or virtually unlimited extent) becomes very important in the subsequent development of the fire environment. In the sense that the upper layer thickness and temperature would grow most rapidly, the fully en-

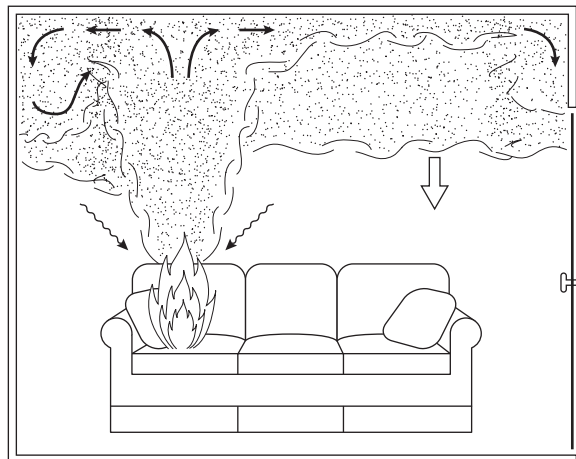


Figure 3-10.5. Fully enclosed space with developed growing upper layer.

closed space with most leakage near the floor would lead to the most rapid development of potentially life and property threatening conditions.

Referring again to the depiction in Figure 3-10.5, the fire plume below the smoke layer interface continues to entrain air as it rises to the ceiling. However, as the hot plume gases penetrate the layer interface and continue their ascent, additional entrainment is from an elevated temperature, smoke-laden environment. Also, once the plume gases enter the smoke layer, they are less buoyant relative to this layer than they were relative to the cool lower layer of ambient air. Thus, the continued ascent of plume gases is less vigorous than it would otherwise be in the absence of the upper layer.

The new and more complex two-layer state of the enclosure environment requires that some modification of the earlier referenced quantitative descriptions of the plume, ceiling-jet, and ceiling jet-wall flow dynamics be introduced. Modifications along these lines are proposed by Cooper.^{21,22}

As depicted in Figure 3-10.6, potentially significant wall flow can develop during the descent of the layer interface. This flow is expected to occur away from regions of vigorous ceiling jet-wall interactions. It is distinct from the previously described upper wall jet and develops because of relatively cool upper wall surfaces which bound the elevated-temperature upper smoke layer. The smoke which is adjacent to these wall surfaces is relatively cool and, therefore, more dense than its surroundings. As a result of this density difference, a continuous, downward-directed wall flow develops which is injected at the smoke interface into the lower, relatively smoke-free layer. Once in the lower layer, the smoke-laden wall flow, now of higher temperature than its surroundings, will be buoyed back upward to either mix with and contaminate the lower layer or to entrain additional (i.e., in addition to the fire plume) lower layer air into the upper layer.

It is noteworthy that the wall effect just described has been observed in full- and reduced-scale fire tests, and that it appears to be particularly significant in enclosures

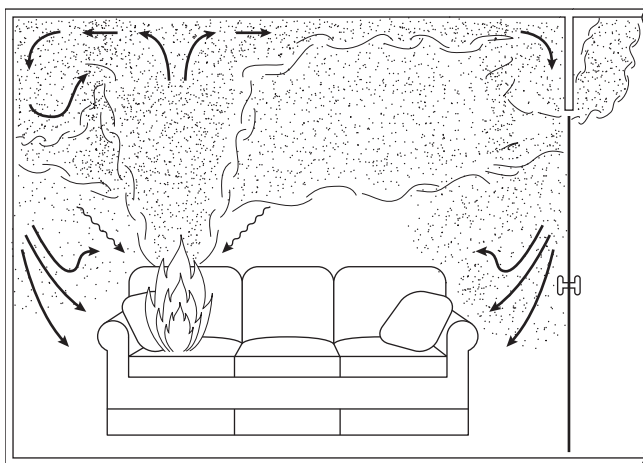


Figure 3-10.6. Further “smoke filling.”

with relatively large ratios of perimeter-to-ceiling height (e.g., in corridors).²³

As a result of its elevated temperature, the smoky upper layer transfers energy by radiation to the ceiling and upper wall surfaces which contain it. As depicted in Figures 3-10.4 and 3-10.5 by the downward-directed arrows, the layer also radiates to the lower surfaces of the enclosure and its contents. Initially, the only significant role of this downward radiation is its effect on human tissue. Indeed, only for downward-directed radiation fluxes significantly in excess of life-threatening levels (characterized by smoke layer temperature levels of the order of 200°C, or by flux levels of the order of 2.5 kW/m²) would the radiant energy feedback to enclosure surfaces and combustibles have a significant impact on fire growth and spread, and on the overall fire environment.^{1,24}

Once radiation feedback becomes of general significance, for example, when the average upper layer temperature reaches 300 to 400°C, it is likely that the potential for flashover will develop within a relatively short time interval (compared to the time interval between ignition and the onset of a life-threatening environment). The events which develop during this time interval will be referred to here as the “transition stage” of fire development.

The onset of life-threatening conditions, which could be caused by any one of a number of reasons, would occur prior to the transition stage of fire development. Before this event can be predicted, quantitative criteria defining a “life-threatening environment” must be established. These criteria must be defined in terms of those physical parameters for which predictive models of compartment fire environments can provide reasonable estimates. Consistent with the earlier discussion, such parameters include the smoke layer thickness (or vertical position of its interface) and temperature. The concentration of potentially hazardous components of the smoke in the upper layer would also be of basic importance. Criteria for the onset of a life-threatening environment could, for example, be based on the following consideration (which would neglect the effect of lower layer contamination due to wall flows):

When the smoke layer interface is above some specified, characteristic face-elevation, an untenable environment would occur if and when a hazardous radiation exposure from the upper layer is attained. Such an exposure could be defined by a specified upper layer critical temperature. If the interface is below face-elevation, then untenability would occur if and when a second critical smoke layer temperature is attained. However, the latter temperature would be lower than the former one, and untenable conditions would result from burns or the inhalation of hot gases. Once the interface dropped below face elevation, untenability would also occur if and when a specified critical concentration (or a specified exposure dosage) of some hazardous product of combustion was attained.²

Transition stage of fire development: Any detailed analysis and prediction of the fire environment during the transition stage of fire development must, of necessity, take account of the effects of upper layer and upper surface reradiation, in general, and of the complex effects of radiation-enhanced fire growth, in particular. Such an analysis would require a mathematical model of compartment fire phenomena which would be significantly more sophisticated than that which would be required to predict the fire environment prior to, and possibly even following, the transition stage.

Regarding the potential difficulty, uncertainty, inconvenience, and/or cost of carrying out transition stage analysis, it is noteworthy that conservative designs for life and property safety may be possible by implementing a strategy of fire environment analysis which avoided the details of the transition stage entirely. This is done by conservatively assuming that the relatively brief time interval associated with the transition stage shrinks to a flashover jump condition at a relatively early time in the fire scenario.¹

Smoke Spread from the Room of Fire Involvement to Adjacent Spaces

Smoke and fresh air exchange between a room of fire involvement and an adjacent space: Under this and the following subheading, smoke spread phenomena associated with a fire-involved room and a communicating adjacent space will be discussed. Reference here will be made to a fully enclosed, two-room space with relatively large common penetrations (e.g., open doors or windows) through which smoke and ambient air exchange will be so significant as to render inadequate an analysis which treats the room of fire involvement as an isolated enclosure. Regarding the two-room spacial configuration, Figures 3-10.1 through 3-10.5 are still relevant to the early development of conditions within the fire room. As the smoke layer interface drops to the level of the soffit of the communicating doorway(s) or window(s), significant amounts of smoke start to move into the adjacent space from above, while significant amounts of ambient air are driven out of the adjacent space (and into the fire room) from below. From that time on, as depicted in Figure 3-10.7, an interdependent smoke-filling process in each of

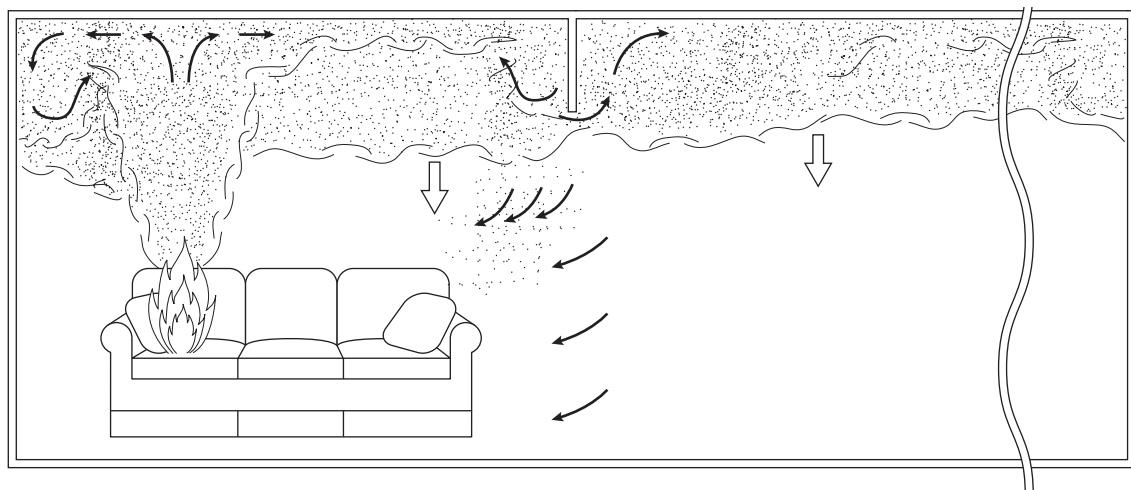


Figure 3-10.7. Smoke and fresh air exchange between a room of fire involvement and an adjacent space.

the two spaces is initiated, and the adjacent space starts to develop a two-layer type of environment.

Throughout the course of typical real-fire scenarios, changes in the absolute pressures of facility spaces are, at the most, of the order of one percent. Yet, dynamic elevation-dependent pressure differences that exist between the rooms of fire involvement and adjacent spaces are large enough to drive a significant cross-door exchange of smoke and ambient air.

Toward the left side of Figure 3-10.8 is a sketch of the vertical static pressure distribution, $P_{\text{fire}}(Z)$, of the room of fire involvement. This is the pressure distribution that is measured in the bulk of the relatively quiescent-environment room, away from vigorous door and plume flows. Notice that the rate of change of pressure with ele-

vation is uniform and relatively large between the floor and the smoke interface, and is uniform and relatively small within the smoke layer. The reason for this is that the temperature-dependent density throughout each of the two layers is assumed to be uniform, and the lower layer is more dense (i.e., of lower temperature) than the upper one. The pressure at the floor is designed as $P_{\text{fire}}(Z = 0) = P_{\text{fire},0}$.

Toward the right side of Figure 3-10.8 is a sketch of the vertical static pressure, $P_{\text{adj}}(Z)$, in the adjacent space. There, the change of slope occurs at the elevation of the adjacent space's smoke interface, which is above the smoke interface in the fire room. Also, the slope of the pressure distribution above the interface is consistent with a smoke layer somewhat more dense or cooler than the smoke

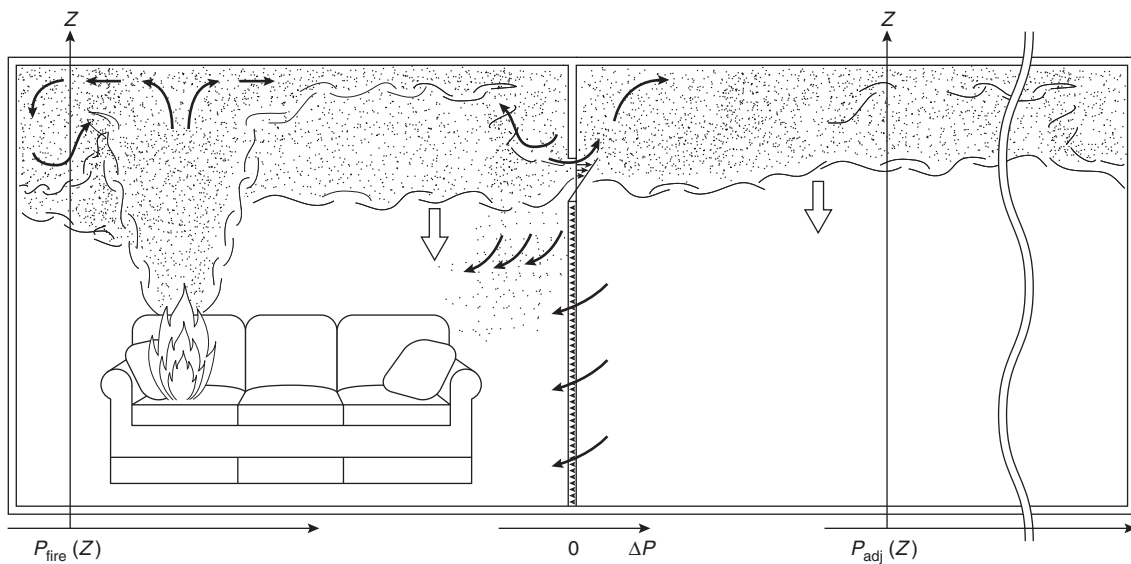


Figure 3-10.8. Figure 3-10.7 with sketches of pressure distributions.

layer in the fire room. Finally, the pressure at the floor is designated as $P_{adj}(Z) = P_{adj,0}$. The two pressure distributions can be compared by the plot of the pressure difference, $\Delta P(Z) = P_{fire}(Z) - P_{adj}(Z)$, which is sketched in the doorway of Figure 3-10.8. At Z elevations below the soffit where ΔP is positive, gases are driven from the fire room into the adjacent space. At elevations where ΔP is negative, gases are driven from the adjacent space into the fire room. At the unique elevation, called the neutral plane, where ΔP is zero, the gases tend to remain stagnant in both spaces. This is the elevation in the doorway which divides outgoing fire room smoke above from inflowing adjacent space air below.

At any given elevation, it is typical in the modeling of fire-generated doorway/window flows to use Bernoulli's equation to estimate the velocity, $V(Z)$, of the flow coming out of or into the fire room. The flow is assumed to be accelerated from rest to a dynamic pressure, $\rho V^2(Z)/2 = \Delta P(Z)$, where ρ is the density of the gas from which the streamlines originate. Also, at any elevation, the flow is assumed to be constricted at the *vena contracta* of the inlet/outlet jet, as with an orifice, to a fraction, C , of the width $W(Z)$ of the doorway. Then the total rate of mass flow across the doorway per unit height at any elevation would be

$$\rho C V(Z) W(Z) = C W(Z) \sqrt{2\rho \Delta P(Z)}$$

Imposing conservation principles at any instant of time when the layer thicknesses and densities (temperatures) in the two rooms are known, leads to the instantaneous values of $\Delta P(Z = 0)$ and neutral plane elevation.

An in-depth presentation of results for calculating total inlet and outlet mass flows and for general application of the above considerations is presented by Zukoski and Kubota.²⁵ Results on most appropriate values to use for C have been obtained from full-scale fire experiments.²⁶

Door plume, ceiling jet, and smoke filling of the adjacent space: Having been driven into the adjacent space by the cross-door pressure differential, the doorway smoke jet is buoyed upward toward the ceiling due to its relatively low density (high temperature). The upward buoyant flow, depicted in Figure 3-10.7, is analogous to the previously discussed fire plume and, with minor modifications, can be quantitatively described by the same kinds of equations. In using these equations, the enthalpy flow rate of the inflowing smoke jet replaces the strength, $\dot{Q}(t)$, of the fire plume, and the smoke jet buoyancy source elevation, taken to be at or near the neutral plane elevation, replaces the elevation of the fire's combustion zone. Further quantitative details on one possible set of door-plume flow calculations are available.²⁵

Just as the doorway smoke jet rises up in the adjacent space, is diluted by entrained fresh ambient air, and is mixed with the upper layer in the manner of a fire plume, so the relatively cool and dense ambient doorway jet enters the fire room, drops down past the upper layer, is contaminated by entrained smoke, and is mixed with the lower layer. This mechanism of lower layer smoke contamination in the room of fire involvement is in addition to

the previously described wall flow mechanism which was depicted in Figure 3-10.6.

Figure 3-10.7 depicts the fire environment after the adjacent space upper layer is already well established. At earlier times, adjacent space smoke movement phenomena are closely related to those effects described above (i.e., Figures 3-10.3 and 3-10.4 and associated text) for the room of fire involvement. Thus, the doorway smoke jet plume impinges on the adjacent space ceiling, leads to the development of a ceiling jet which interacts with wall surfaces, and eventually redistributes itself to form a growing, upper layer of uniform thickness.

As was the case for the room of fire involvement, knowledge of adjacent space ceiling and upper wall properties is of fundamental importance in predicting the response of adjacent-space-deployed fire detection/intervention hardware, and the temperature of the adjacent space environment. Also, contamination of the lower layer by smoke injection from downward-directed wall flows can play a relatively more important role in adjacent spaces than in the fire room itself.²³

All the above adjacent room effects must be predicted quantitatively with reasonable accuracy, since the fire-generated environments in the fire room and in adjacent spaces are strongly coupled by cross-door mass and energy exchanges. Also, of key importance is the ability to predict the onset of adjacent space environmental conditions which are untenable for life or property.

Multiroom and multilevel fire/smoke compartments: The discussion in the last two subparagraphs was related to the two-room illustration of Figure 3-10.7. However, the general principles of smoke migration are no different in fire/smoke compartments of more than two connected spaces.

In multiroom or even multilevel compartments, smoke migration occurs as smoke in successive rooms fills to the door/window soffits, and then starts to "spill out" into the adjacent spaces. At the same time, in each room where filling has been initiated, the phenomena related to plumes, ceiling jets, different wall flows, and upper layer/lower layer mixing are also taking place. In each of the spaces, these various phenomena are generally coupled together through the connecting door/window flows. For this reason, all effects must be analyzed simultaneously. For example, in a multiroom fire/smoke compartment one needs to satisfy the principle of conservation of mass when it is applied not just to a single doorway but to all envelopes which completely bound each compartment. To do so, one needs to solve for the pressure difference distributions and the resulting inflows and outflows across all intercompartment penetrations.

Some Special Classes of Multiroom Fire Scenarios

Single room vented to the outside: One practical, special class of the multiroom fire scenario is the single room of fire involvement which is vented to the outside ambient environment. One can carry out an analysis of the fire environment in such vented spaces by bringing to bear all considerations relevant to the Figure 3-10.7 discussion

and by assuming the adjacent space to be arbitrarily large, that is, large enough so that it would never be filled with smoke to the point where such smoke would interact with the fire room itself. The pressure distribution of the adjacent space from the floor to the top of the door/window would be specified to be the same as that of an outside ambient environment. Dynamics of the plume, which is driven by the smoke flow entering the adjacent space from the fire room, would not be affected by the adjacent space ceiling or far wall surfaces. All inflow to the fire room would be uncontaminated ambient air.

Treating the adjacent space in the above manner leads to considerable simplification in modeling mathematically the room fire environment. It is noteworthy in this regard that the only mathematical models developed specifically to predict post-flashover fire environments are related to this configuration of a single room of fire involvement vented to the outside ambient environment.

Single room vented to large space: Another important class of fire scenario, which is directly related to the last one, is the single room of fire involvement which is actually vented to a very large space. Such is the configuration, for example, when a room of fire involvement is vented to a large atrium.

Under these circumstances one could analyze the fire environment which develops in the large containing space (the atrium) as one would analyze the environment in a space with a single isolated fire (e.g., see Figures 3-10.4 through 3-10.6). Here, the energy and products of combustion release rates of the fire would be taken to be the enthalpy and combustion products' flow rates of the effluent from the doorway/window jet of the fire room. As before (i.e., independent of changes in the large, but finite, adjacent space), and at least for some significant time into the fire, the development of the environment in the fire room itself and the resulting door/window smoke flow could hopefully be predicted analytically. Short of analytic predictions, however, actual measurements of the door/window effluent acquired in full-scale free-burn tests of the fire room, up to and even beyond flashover, could be used as data input in the analysis of the large adjacent space problem.

The combined experimental/analytic approach has been used to predict the environment which develops in large prison cell blocks during fires in single cells of different design.²⁷

Single room and freely connected multiroom fire compartments: For those times of fire development when the compartment of fire involvement consists of a single enclosed space, analysis of the fire environment is considerably simplified. This is because an accounting of inflow and outflow at windows and doors (which are presumably closed) is not required.

When the fire compartment is partitioned into separate but freely connected spaces, the relatively simple, single-enclosed-space analysis, where the area of the single space is taken to be the total area of the fire compartment, can continue to be relevant. Here, "freely connected" refers to fire scenarios and spacial configurations where common openings between rooms are large

enough, and/or the energy release rate of the fire is small enough, so that smoke layers remain reasonably uniform in thickness, temperature, and product concentration through the bulk of the compartment area.

Quantitative criteria for establishing whether a specific fire compartment is freely connected relative to a specified fire threat are not yet available. However, the concept of the freely connected, multiroom fire/smoke compartment has been shown to be valid during full-scale multiroom fire experiments²⁸

Smoke Spread Outside the Smoke Compartment of Fire Involvement

The above paragraphs addressed the development of the fire-generated environment by describing fire/smoke compartments of fire involvement. Yet, the original outline of the generic fire safety problem is also relevant to the general problem of predicting smoke environments throughout an entire facility.

Figure 3-10.9 illustrates a practical concept for modeling the development of smoke environments both inside and outside the smoke compartment of fire involvement. Facility spaces that would be included in the smoke compartment (on the left of the figure) are distinguished from those included in the rest of the building or facility (on the right) by the detail which is required to describe or model mathematically the fire-generated environments within them. In the smoke compartment of fire involvement, smoke would spread within a room, and would be driven from room to room by strong buoyancy forces which lead to layered smoke environments. These environments must be analyzed in the context of (at least) a two-layer model with associated phenomena of plume flow, surface flows, and so forth. In the rest of the building, it is reasonable to describe the smoke in each space as being uniformly dispersed. Here, dynamic changes in the smoke distribution in the environment come about from room-

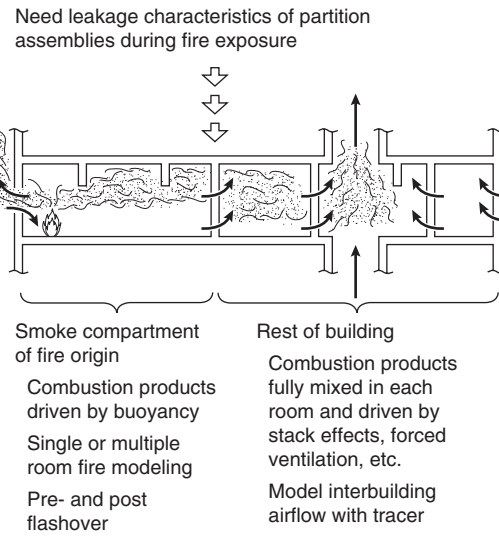


Figure 3-10.9. A concept for modeling smoke spread throughout complex facilities.

to-room pressure differences which are generated by stack effects, wind effects, and forced ventilation, leading to smoke movement, mixing, and dilution.

The fire compartment is the source of smoke to the rest of the building. The rate of introduction of this smoke depends on the pressure differences across common partition assemblies, and on their leakage characteristics.²⁹ Once the rate of smoke leakage across common portions can be expressed quantitatively, the rest of the building problem can be analyzed with a model of smoke movement similar to those presented by Wakamatsu³⁰ and Evers and Waterhouse.³¹

Mathematical Models and Computer Codes for Predicting the Compartment Fire Environment

In recent years, many mathematical models and associated computer codes for predicting dynamic compartment fire environments have been developed. These can be divided into two types: field models and zone models.

Incorporating global partial differential equations which describe the relevant combustion, flow, and heat transfer processes, field models formulate and solve initial/boundary value problems for the unknown variables in compartment fire scenarios. Zone models, however, describe the compartment fire phenomena in terms of coupled submodel algorithms or sets of equations. Each equation set describes a single fire-generated process associated with an actual physical zone of the compartment space. The processes and corresponding zones typically correspond to the ones identified in Figures 3-10.1 through 3-10.8, and as discussed above.

There is a good deal of variation between all types of compartment fire models. Significant differences tend to be in (1) the number and detail of the individual physical phenomena that are taken into account (2) the number and complexity of interconnected fire compartment spaces that can be analyzed and (3) in the most common situation, when a computer is required to solve the model equations, the capability of the computer hardware that is required to carry out the calculations, the user-friendliness of the computer program, and its available documentation.

The intended use for which a given model was developed is probably the most important feature leading to its uniqueness. Such uses can differ widely: for example, at one extreme; to understand and predict coupled, compartment fire-generated processes with the greatest possible accuracy and generality; and at the other, to provide a common-use, firesafety-practitioner's tool for analysis and design. As will be seen, a set of equations which describes the dynamic smoke filling phenomenon in and of itself would constitute a compartment fire model of the simplest variety whose use could fall squarely at the latter extreme of the spectrum.

ASET—A Model for Predicting the Smoke Filling Process in a Room of Fire Origin

The smoke filling process is an essential feature of any zone-type compartment fire model. It basically involves three zones: the fire's combustion zone, the plume,

and the upper smoke layer. The last section presented a relatively detailed qualitative description of many of the processes which make up the overall dynamic compartment fire environment. This section will formulate a mathematical model of the smoke filling process.

The model to be presented was originally developed within the context of life safety in fires.^{1,2,24} In particular it was developed to provide estimates of the Available Safe Egress Time (ASET) in compartments of fire origin, where the available safe egress time is defined as the length of the time interval between fire detection/successful alarm and the onset of life safety hazard. Accordingly, the model has been given the name ASET.

Since life safety considerations are primary, the model focuses attention on phenomena which develop between the times of fire ignition and the onset of hazardous conditions. This allows significant simplifications in the modeling which would not be otherwise justified, vis-à-vis the use of the simplest possible smoke filling process to describe the fire-generated environments of interest.

The basic phenomena of the smoke filling process are outlined as follows:

The fire starts at some position below the ceiling of the enclosure and releases energy and products of combustion in some time-dependent manner. As the fire develops from ignition, buoyancy forces drive the high-temperature products of combustion upward toward the ceiling. In this way, a plume of upward-moving elevated temperature gases is formed above the fire. All along the axis of the plume relatively quiescent and cool ambient air is laterally entrained and mixed with the plume gases as they continue their ascent to the ceiling. As a result of this entrainment, the total mass flow rate in the plume continuously increases, and the average temperature and average concentration of products of combustion in the plume continuously decrease with increasing height. When the plume gases impinge on the ceiling they spread across it, forming a relatively thin, stably stratified upper layer. As the plume gas upward-filling process continues, the upper gas layer grows in depth, and the relatively sharp interface between it and the cool ambient air layer below continuously drops.

In this section, a simple mathematical model of these phenomena, which captures the essential features of the dynamic fire environment, is constructed. The major elements of the model include the turbulent buoyant plume theory³² together with experimental plume results,³³ the theory of the dynamics of such plumes in confined spaces,³⁴ and the application of the plume dynamics theory to the fire problem as presented.³⁵ Figure 3-10.10 presents a simple illustration of the model's smoke filling flow dynamics. The variables introduced there will be defined in this section.

Initial Value Problem for the Temperature of the Upper Layer and the Position of the Interface

To take a conservative approach, the partitions of the room of fire origin are assumed to have all major penetrations (e.g., doors, windows, and vents) closed. Any leakage from the room resulting from fire-driven gas expansion is assumed to occur near the floor level. The

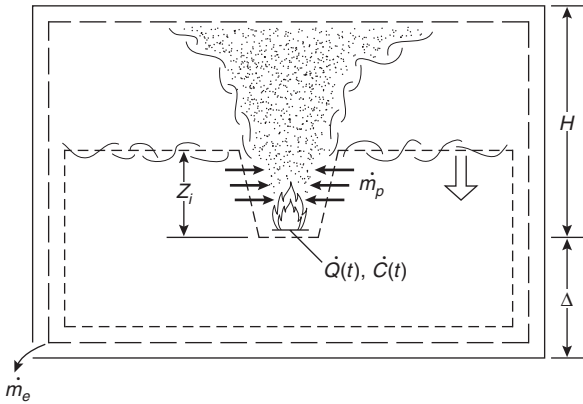


Figure 3-10.10. Simple illustration of fire-in-enclosure flow dynamics.

sketch of Figure 3-10.7 is compatible with these assumptions, both of which lead to some conservatism in the eventual prediction of the time for onset of untenability.

The fire's combustion zone is modeled as a point source of energy release which is effectively located at or above the floor level. The mass flow rate of fuel introduced from this zone into the plume is neglected compared with the mass flow rate of entrained air. Except for the buoyancy forces that they produce, density variations in the flow field are neglected (i.e., the Boussinesq approximation is invoked). Using the fact that the absolute pressure throughout the space varies only insignificantly from a constant uniform value, the density, ρ , can be related to the absolute temperature, T , at any time and spatial position through the perfect gas law according to

$$\rho T = \text{constant} = \rho_a T_a \quad (1)$$

where ρ_a and T_a are the density and absolute temperature, respectively, of the ambient air.

The time-varying total energy release rate of the combustion zone is defined by $\dot{Q}(t)$. It is assumed that $\dot{Q}(t)$ can be approximated by the free-burn energy release rate of the characteristic fuel assembly whose hazard-producing characteristics are under investigation and for which $\dot{Q}(t)$ is known. This assumption is consistent with the fact that onset of hazardous conditions within the enclosure will occur at temperature and depleted-oxygen levels which are low compared with those levels at which variations from free-burn will begin to be significant.

The fraction of \dot{Q} which effectively acts to heat the plume gases and to ultimately drive the plume's upward momentum is $(1 - \lambda_r)$, where λ_r is approximately the fraction of \dot{Q} lost by radiation from the combustion zone and plume.

The total mass flow in the plume, \dot{m}_p , and the mass mixing cup temperature of the plume, \bar{T}_p , at a distance Z above the fire (but below the layer interface) can be estimated by^{7,35}

$$\frac{\bar{T}_p}{T_a} - 1 = \frac{(\dot{Q}^*)^{2/3}}{0.210}, \quad 0 < Z \leq Z_i(t) \quad (2)$$

$$\dot{m}_p = 0.210 \rho_a (gZ)^{1/2} Z^2 (\dot{Q}^*)^{1/3}, \quad 0 < Z \leq Z_i(t) \quad (3)$$

where \dot{Q}^* is defined as

$$\dot{Q}^* = \frac{(1 - \lambda_r) \dot{Q}}{\rho_a C_p T_a (gZ)^{1/2} Z^2}$$

and where g is the acceleration of gravity, C_p is the specific heat at constant pressure, assumed to be constant and uniform throughout the space, and $Z_i(t)$ is the time-varying distance above the fire of the interface which separates a growing upper layer of elevated-temperature (product of combustion-laden gas) and a lower shrinking layer of ambient air. The mass flow rate of gas, \dot{m}_e , leaking out of the room's floor-level leakage paths can be estimated from³⁵

$$\dot{m}_e = \begin{cases} \frac{(1 - \lambda_c) \dot{Q}}{C_p T_a}, & -\Delta < Z_i(t) \\ \frac{(1 - \lambda_c) \dot{Q}}{C_p \bar{T}_h}, & -\Delta = Z_i(t) \end{cases} \quad (4)$$

where Δ is the height of the fire above the floor, and λ_c is the instantaneous fraction of \dot{Q} lost to the bounding surfaces of the room and its contents (i.e., $\lambda_c = \dot{Q}_{\text{loss}}/\dot{Q}$). Also, assuming that the upper layer is well mixed, \bar{T}_h is taken to be its absolute temperature. By using Equation 2, \bar{T}_h can be related to the average upper layer density, $\bar{\rho}_h$, which is defined by

$$\bar{\rho}_h = \frac{1}{(H - Z_i)} \int_{Z_i}^H \rho dZ \quad (5)$$

The total rate of energy loss characterized by λ_c occurs as a result of a variety of convective and radiative heat transfer exchanges between the room's gases and the above-mentioned surfaces. Equation 6 brings attention to the fact that, by the time the layer interface drops to the floor, that is, when $Z_i = -\Delta$, all ambient air has been pushed out of the room. At all subsequent times, the entire room is filled with, and defines the bounds of, the upper layer, and the room's leakage gases are at upper layer rather than ambient conditions.

A mass balance for the lower, shrinking volume of ambient air results in

$$\rho_a A \frac{dZ_i}{dt} = \begin{cases} -\dot{m}_e - \dot{m}_p(Z = Z), & 0 < Z_i(t) \leq H \\ -\dot{m}_e, & -\Delta < Z_i(y) \leq 0 \\ 0, & -\Delta = Z_i(t) \end{cases} \quad (6)$$

where A is the area and H is the height of room of fire origin, and where estimates for \dot{m}_e and \dot{m}_p are provided in Equations 3 and 4.

Using Equations 2 and 7 in an energy balance for the upper layer results in

$$1 - \frac{\bar{\rho}_h}{\rho_a} = 1 - \frac{T_a}{\bar{T}_h} = \frac{\int_0^t (1 - \lambda_c) \dot{Q} d\xi}{\rho_a C_p T_a A (H - Z_i)}, \quad -\Delta < Z_i < H \quad (7)$$

$$(1 - \lambda_c) \dot{Q} = (\Delta + H) \rho_a C_p T_a A \left(\frac{1}{\bar{T}_h} \right) \frac{d\bar{T}_h}{dt}, \quad Z_i = -\Delta \quad (8)$$

Equations 4 and 6 are now used in Equation 6, and Equation 7 is recast into differential form. After some manipulation, the following pair of governing equations for Z_i and \bar{T}_h result

$$\frac{dZ_i}{dt} = \begin{cases} -C_1\dot{Q} - C_2\dot{Q}^{1/3}Z_i^{5/3}, & 0 < Z_i \leq H \\ -C_1\dot{Q}, & -\Delta < Z_i \leq 0 \\ 0, & Z_i = -\Delta \end{cases} \quad (9)$$

$$\frac{d\bar{T}_h}{dt} = \begin{cases} \frac{\bar{T}_h[C_1\dot{Q} - (\bar{T}_h/T_a - 1)C_2\dot{Q}^{1/3}Z_i^{5/3}]}{H - Z_i}, & 0 < Z_i \leq H \\ \frac{\bar{T}_hC_1\dot{Q}}{H - Z_i}, & -\Delta \leq Z_i \leq 0 \end{cases} \quad (10)$$

$$\left. \begin{aligned} C_1 &= \frac{1 - \lambda_c}{\rho_a C_p T_a A} \\ C_2 &= \left(\frac{0.21}{A} \right) \left[\frac{(1 - \lambda_r)g}{(\rho_a C_p T_a)} \right]^{1/3} \end{aligned} \right\} \quad (11)$$

The problem now becomes one of simultaneously solving Equations 9 and 10 subject to the appropriate initial conditions. For the present purpose, these initial conditions can be taken as those relating to one of two different cases.

Case 1: $\dot{Q}(t = 0) \equiv \dot{Q}_0 \neq 0$.

Here assume

$$\lim_{t \rightarrow 0} \dot{Q} \approx \dot{Q}_0 + \dot{Q}'_0 t \quad (12)$$

where

$$\dot{Q}'_0 = \frac{d\dot{Q}}{dt} \quad \text{at } t = 0$$

Then, solve Equations 9 and 10 subject to the initial conditions

$$\begin{aligned} Z_i(t = 0) &= H \\ \bar{T}_h(t = 0) &= T_a \left(1 + \frac{C_1 \dot{Q}_0^{2/3}}{C_2 H^{5/3}} \right) \\ &= T_a + \left(\frac{1 - \lambda_c}{1 - \lambda_r} \right) [\bar{T}_p(t = 0) - T_a] \end{aligned} \quad (13)$$

where the value for $\bar{T}_h(t = 0)$ was obtained with the use of Equation 7. Using Equation 7 further, an analysis of the apparent singularity of Equation 10 at $t = 0$ leads to the result

$$\begin{aligned} \lim_{t \rightarrow 0} \frac{d\bar{T}_h}{dt} &= \\ T_a \left(\frac{C_1}{C_2} \right) \left(\frac{\dot{Q}_0^{2/3}}{6H^{5/3}} \right) &\cdot \left(\frac{2\dot{Q}_0 H}{\dot{Q}_0} + 5(C_1\dot{Q}_0 + C_2 H^{2/3}\dot{Q}_0^{1/3}) \right) \end{aligned} \quad (14)$$

Case 2: $\dot{Q}(t = 0) = 0$

Here assume

$$\lim_{t \rightarrow 0} \dot{Q} \approx \dot{Q}'_0 t \quad (15)$$

Then solve Equations 9 and 10 subject to the initial conditions

$$Z_i(t = 0) = H, \bar{T}_h(t = 0) = T_a \quad (16)$$

In this case, analysis of the problem leads to the following small time estimates:

$$\lim_{t \rightarrow 0} Z_i \approx H - \left(\frac{3}{4} \right) C_2 \dot{Q}'_0^{1/3} H^{5/3} t^{4/3} \quad (17)$$

$$\lim_{t \rightarrow 0} \bar{T}_h \approx T_a + \left(\frac{2}{3} \right) T_a \left(\frac{\dot{Q}'_0^{2/3}}{H^{5/3}} \right) \left(\frac{C_1}{C_2} \right) t^{2/3} \quad (18)$$

Safe Available Egress Time from the Solution to the Initial Value Problem for Upper Layer Thickness and Temperature

The above initial value problem for Z_i and \bar{T}_h would be solved by a numerical integration procedure. For the purpose of using the equations to determine onset of hazardous conditions, the solution would be terminated in a given problem at the time, t_{HAZ} , when

$$\bar{T}_h \geq \bar{T}_{h(HAZ)} \quad (19)$$

(layer temperature reaches a hazardous value associated with an untenable flux of thermal radiation)

or

$$Z_i \leq Z_{i(HAZ)} \quad (20)$$

(interface reaches a characteristic face elevation, $Z_{i(HAZ)}$, and the upper layer gases are assumed to be hazardous for human ingestion or significantly impairing to human vision).

From the computed history of Z_i and \bar{T}_h , and compatible with the detection criterion which is invoked, the time of detection could also be obtained. This would be defined as that time, t_{DET} , when, for example

$$\bar{T}_h \geq \bar{T}_{h(DET)} \quad (21)$$

(layer temperature detection criterion)

and/or

$$\frac{d\bar{T}_h}{dt} \geq \left(\frac{d\bar{T}_h}{dt} \right)_{DET} \quad (22)$$

(layer rate of temperature rise detection criterion)

The time of detection corresponding to other detection criteria which were similarly related to Z_i and \bar{T}_h , and so forth, could also be obtained. Finally, the time of detection could be explicitly specified, for example, "immediate" detection, $t_{DET} = 0$, as a result of the guaranteed presence of alert occupants.

From all the above, the desired value for ASET is computed from

$$ASET = t_{HAZ} - t_{DET}$$

The computer program ASET has been developed to carry out the solution to the above problem for arbitrarily specified $\dot{Q}(t)$. The program is written in American National Standards Institute (ANSI) FORTRAN and it is supported by a user's manual.²⁴

A simplified version of the program, ASET-B, written in BASIC and containing all necessary equation-solving software, has also been developed, and it is supported by its own user's manual.³⁶

Initial Value Problem for the Concentration of Products of Combustion

In this subsection, equations for estimating the concentration of products of combustion in the upper layer are developed.

The time-varying rate at which a combustion product of interest is generated within the combustion zone is designated by $C(t)$. The dimensions of $C(t)$ are u_c per unit time, where u_c is a dimensional unit appropriate for the particular product. For example, u_c could have the dimensions of mass, number of particles, number of particles with mass between m and $(m + dm)$, and so forth.

Just as $\dot{Q}(t)$ is approximated by free-burn energy release rate data, so it is assumed that $C(t)$ can be approximated by the free-burn product generation rate of the fuel assembly under investigation. As is the case with \dot{Q} , C is assumed to be known, say, from experimental free-burn measurements.

The average concentration of product in the upper layer is defined as the average amount of product (dimension u_c) per unit mass of upper layer mixture. The concentration is designated by $M(t)$. It is assumed that the mass fraction of the product in the upper layer is always small compared to 1.

Conservation of the product results in

$$\frac{d}{dt} [\bar{\rho}_h M A (H - Z_i)] = \dot{C}, \quad -\Delta < Z_i \leq H \quad (23)$$

$$\frac{d}{dt} [\bar{\rho}_h M A (H + \Delta)] = \dot{C} - \dot{m}_e M, \quad Z_i = -\Delta \quad (24)$$

Manipulation of Equations 23 and 24 with the use of Equations 9 and 10 leads to the following equation for M :

$$\frac{dM}{dt} = \begin{cases} \left(\frac{\bar{T}_h}{T_a \rho_a A} \right) \frac{\dot{C} - \rho_a A C_2 \dot{Q}^{1/3} Z^{5/3} M}{H - Z_i}, & 0 < Z_i < H \\ \frac{[\bar{T}_h / (T_a \rho_a A)] \dot{C}}{H - Z_i}, & -\Delta \leq Z_i \leq 0 \end{cases} \quad (25)$$

With solutions for Z_i and \bar{T}_h from earlier considerations, Equation 25 can be solved for M once appropriate initial conditions are established. For this purpose, the two cases must be considered again.

Case 1(a): $\dot{Q}(t = 0) \equiv \dot{Q}_0 \neq 0; \dot{C}(t = 0) \equiv \dot{C}_0 \neq 0$.

Here assume

$$\lim_{t \rightarrow 0} \dot{C} \approx \dot{C}_0 + \dot{C}'_0 t \quad (26)$$

where

$$\dot{C}'_0 = \frac{d\dot{C}}{dt} \quad \text{at } t = 0$$

Then, solve Equation 25 subject to

$$M(t = 0) = \frac{\dot{C}_0}{C_2 A H^{5/3} \rho_a \dot{Q}_0^{1/3}} = \frac{\dot{C}_0}{\dot{m}_p(t = 0)} \quad (27)$$

Here, an analysis of the apparent zero time singularity of Equation 25 leads to the result that

$$\lim_{t \rightarrow 0} \frac{dM}{dt} = \left(\frac{5}{6} \right) \left(\frac{C_1}{C_2} \right) \left(\frac{\dot{Q}_0^{2/3} \dot{C}_0}{\rho_a A H^{8/3}} \right) \cdot \frac{1 + H(3\dot{C}'_0/\dot{C} - \dot{Q}'_0/\dot{Q}_0)}{5\dot{Q}_0 \dot{C}_1} + (C_2/C_1)(H^{5/3}/\dot{Q}_0^{2/3})] \quad (28)$$

Case 1(b): $\dot{Q}(t = 0) \equiv \dot{Q}_0 \neq 0; C(t = 0) \equiv C_0 \neq 0$.

Here assume

$$\lim_{t \rightarrow 0} \dot{C} \approx \dot{C}'_0 t \quad (29)$$

Then, solve Equation 25 subject to

$$M(t = 0) = 0 \quad (30)$$

In this case, analysis of Equation 25 leads to the following small time estimate

$$\lim_{t \rightarrow 0} M = \frac{\dot{C}'_0 t}{2\rho_a A^{5/3} Q^{1/3} C_2} = \frac{\dot{C}'_0 t}{2\dot{m}_p(t = 0)} \quad (31)$$

Case 2(b): $\dot{Q}(t = 0) = 0; \dot{C}(t = 0) = 0$.

(Note that the condition $\dot{Q}(t = 0) = 0, C(t = 0) \neq 0$, i.e., nonzero product generation rate with a zero heat release rate, is not allowed.) Here assume Equation 29. Then solve Equation 25 subject to Equation 30. In this case, analysis of Equation 25 leads to

$$\lim_{t \rightarrow 0} M = \frac{2\dot{C}'_0 t^{2/3}}{3\rho_a A C_2 H^{5/2} \dot{Q}_0^{1/3}} \quad (32)$$

Using Combustion Product Concentrations to Establish the Time of Detection and the Onset of Untenability

When a fire's rate of generation of products of combustion is known, the upper layer concentrations can be

estimated from the considerations of the previous section. Under such circumstances, it would be possible to apply detection and hazard criteria which are more detailed than those discussed earlier.

In the case of detection, the response of a detection device which is sensitive to the presence of the predictable combustion product can be simulated. For example, the time of detection, t_{DET} , would be predicted to be the time when the upper layer concentration of the product attained a detectable level, M_{DET} .

In the case of hazard, a criterion for the onset of untenability could depend on a variety of possible conditions involving all of the environmental parameters, Z_i , \bar{T}_h , and M . For example, assume that estimates of the fire's generation rate of water and CO are available. Then, the time-varying values for Z_i , \bar{T}_h , M_{water} , and M_{CO} could be computed, and the time of onset of untenability could be estimated to be the earliest time when (1) the interface was still above a characteristic elevation, Z_F , and \bar{T}_h exceeded a specified hazardous overhead value (associated with an untenable flux of thermal radiation), or (2) the interface was below Z_F , and the upper layer CO concentration or temperature and humidity conditions were such as to be hazardous for human ingestion.

All of the above considerations are taken into account in the ASET computer program. Predictions of product of combustion concentration are not yet included in ASET-B.

Available Safe Egress Time from Rooms of Fire Origin—Some Example Calculations

Assumptions on the Disposition of Energy Release and Their Implications

In order to use the proposed fire model for a specified free-burn fire, values of λ_r and λ_c are required. While appropriately chosen constant- λ values should prove to be adequate for most engineering applications, the model described can, through specified dynamic variations in these λ s, readily accept more detailed characterizations of the gas-to-room surface heat transfer phenomena.

Depending on the fuel and its configuration, the total radiant power output in fire combustion zones is in the range of 15 to 40 percent of the total rate of heat release.^{38,39} Based on this and, for example, on data presented by Cooper,⁴⁰ it appears that $\lambda_r = 0.35$ is a reasonable choice for the type of growing hazardous fires under consideration. Except where noted otherwise, this value will be used in all calculations described in this chapter.

Using the 0.35 value for λ_r , and taking account of convective heat transfer considerations, an appropriate value for λ_c was developed.⁴¹ It was found to lie in the approximate range 0.6 to 0.9. The lower value, 0.6, would relate to high aspect ratio spaces (ratio of ceiling span to room height) with smooth ceilings and with fires positioned far away from walls. The intermediate values and the high, 0.9, value for λ_c would relate to low aspect ratio spaces, fire scenarios where the fire position is within a room height or so from walls and/or spaces with highly irregu-

lar ceiling surfaces. In the latter types of situations, which are representative of most realistic fire scenarios, it is not presently possible to provide general rules to accurately estimate λ_c within this 0.6 to 0.9 range. This fact has strong implications on the capability for establishing accurate estimates for the average upper layer temperature. This can be seen from Equation 10, where, early in the fire and at times of relatively cool upper layer temperatures (\bar{T}_h/T_a close to 1), $d\bar{T}_h/dt$ and, ultimately, $\bar{T}_h - T_a = \Delta\bar{T}_h$ are seen to be proportional (through the factor C_1) to $(1 - \lambda_c)$. In contrast to the upper layer temperature estimate and at times of relatively small values of $\Delta\bar{T}_h/T_a = \bar{T}_h/(T_a - 1)$, the upper layer-lower layer interface position history is not nearly as sensitive to inaccuracies in λ_c . At such times, the second term on the right-hand side of the first line of Equation 9, which is independent of λ_c , will dominate the first term, the two terms being in the ratio of m_p to m_e (compare to the first line of Equation 6).

The above discussion leads to the following guidelines for selection and use of a value for λ_c , when a reliable estimate of its actual value is not otherwise available:

1. For the purpose of computing a conservative estimate of the time when a hazardous temperature or a hazardous interface elevation will be attained (i.e., the predicted t_{HAZ} will be less than the observed t_{HAZ}), one should select $\lambda_c = 0.6$.
2. For the purpose of a conservative estimate of detection time when detection is by temperature or rate of temperature rise of the upper layer (i.e., the predicted t_{DET} will be greater than the actual t_{DET}), one should select $\lambda_c = 0.9$.
3. When fire detection is by temperature or rate of temperature rise, a reasonably accurate (as compared with a conservative) estimate of detection time is achievable only (1) in large aspect ratio, smooth ceiling spaces where detection is based on a $\lambda_c = 0.6$ computation of average upper layer temperature, and (2) in other configurations where detectors are deployed near the ceiling in some regular grid array, and where the time of detection is based on estimates of actual maximum ceiling-jet temperature (i.e., predictions of average upper layer temperature are not the basis for determining likely time of detection). For such estimates, the reader is referred to Section 4, Chapter 1 of this handbook.

Available Safe Egress Time in a Semi-Universal Fire

For the smoke filling model to have utility to practitioners of fire safety, it is necessary that the significant elements of potentially threatening fire scenarios be identified. It is also necessary for the results of fire hazard analyses to be presented in a concise and practical manner. This subsection provides an example of how the whole concept might proceed in practice.

First, one must identify quantitative characteristics of a particular, potentially threatening, free-burn fire of concern. Cooper deals with some practical considerations that would be useful in deducing such characteristics.¹ For the present, a composite, semi-universal-type fire has been constructed from the data of Friedman.⁴¹ The fire's energy release history is plotted in Figure 3-10.11. The fire is

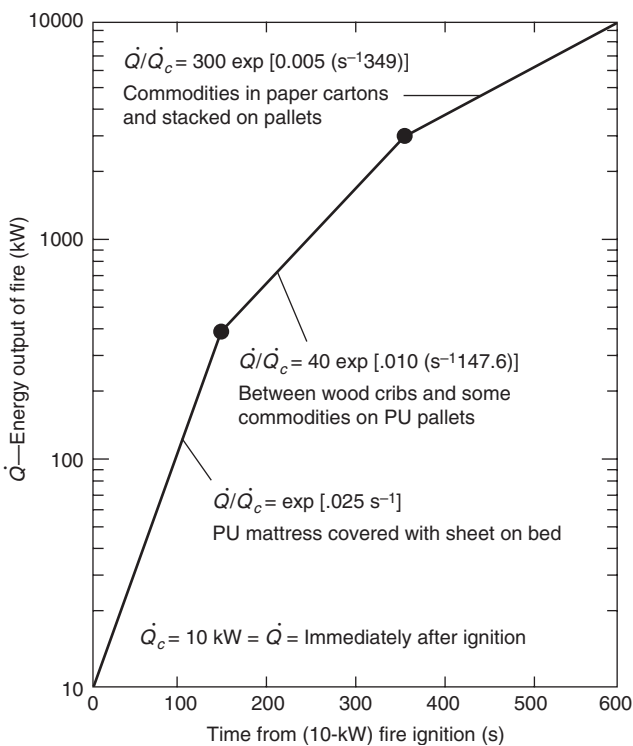


Figure 3-10.11. Free-burn energy release rate from a semi-universal fire. A fictitious construction from the data of O'Neill and Hayes.⁴⁴

assumed to be initiated from a 10 kW ignition source. Initially, it grows exponentially at a rate which is characteristic of a fire initiated in a polyurethane mattress with bedding. This early growth rate would be characteristic of the early growth of fires in a variety of occupancies which typically contain upholstered polyurethane cushioning, for example, hospital patient and lobby rooms, residential spaces, and auditoriums. It is also consistent with the (unreported) early growth state of fires in large assemblies of commodities stacked on pallets. Beyond 400 kW, the fire of Figure 3-10.11 is assumed to grow at a rate which is similar to and/or which bounds the anticipated growth of fires initiated in a variety of different types of commodities stacked on pallets. The portion of the semi-universal fire beyond 400 kW is no doubt also representative of other threatening fires in large mercantile and/or business occupancies.

The fire of Figure 3-10.11 was assumed to be initiated in a variety of different-size spaces. The geometries of these spaces are characterized by areas ranging from 28 to 929 m² and by heights ranging from 2.4 to 6.1 m.

Two possible criteria for fire detection are considered in the analysis of available safe egress time. These include using ASET to calculate instantaneous detection (by whatever means) and detection when the upper gas layer reaches an average temperature of 57°C. The utility of the latter detection criterion is at present strictly speculative. It is included here only to illustrate the type of results which one might hope to generate by solution of the model equations and use of the ASET computer program. (The results could also be obtained with ASET-B.)

The criterion adopted for the onset of hazardous conditions is an upper layer interface position 0.91 m above the floor, or an average upper layer temperature of 183°C (corresponding to a heat flux of 0.25 W cm⁻² at the floor), whichever comes first.

It is assumed that 35 percent of the fire's instantaneous energy release rate is radiated from the combustion zone ($\lambda_r = 0.35$) and that a total of 60 percent of this energy release rate is transferred to the interior surfaces of the room and its contents, that is, 40 percent of this energy is retained in the upper layer products of combustion ($\lambda_c = 0.60$). Recall that the latter choice of λ_c would be appropriate for large aspect ratio spaces with smooth ceiling, but, in any event, the choice of λ_c would have a minor impact on estimated egress times in cases where criteria of detection or hazard are not dependent on upper layer gas temperature.

With the above range of parameters, the quantitative details of the last section were used to estimate available safe egress times with the ASET program. The results of these computations are presented in Figure 3-10.12. In this figure, $ASET = t_{HAZ} - t_{DET}$ is plotted as a function of room area for different parametric values of room height and for different detection criteria.

As an example of the utility of Figure 3-10.12, consider a scenario where a fire is initiated in an occupied, 500 m², nominal, 6.1 m-high ceiling auditorium outfitted with polyurethane cushion seats (which are assumed to be the most significant fuel load). Then, from Figure 3-10.12 one would estimate an available safe egress time of approximately 450 s. This assumes immediate detection as a result of occupant recognition and verbal alarm to fellow occupants at the time of fire initiation. If the auditorium is to be considered safe relative to successful egress, then a further study would have to reveal that the time required for a capacity crowd to evacuate the auditorium is less than 450 s.

The following general features of the results of Figure 3-10.12 are worth noting:

1. As is well known, for life safety as it relates to safe egress, temperature detectors are not particularly effective.

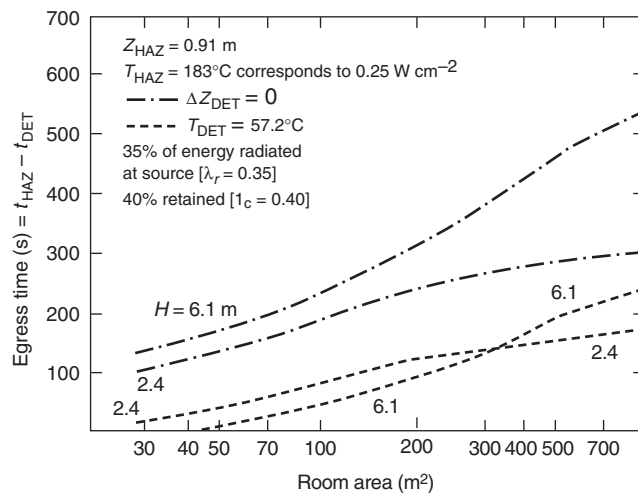


Figure 3-10.12. Estimates of available egress times from the semi-universal fire of Figure 3-10.11.

2. For a given curve, increasing room area eventually leads to an abrupt reduction in the curve's slope. This is the result of a shift in the triggering mechanism for onset of hazardous conditions. On the left side of the change in slope (smaller areas), untenability occurs as a result of the layer interface dropping to the 0.91 m level. On the right side (larger areas), untenability occurs as a result of thermal radiation from a hot upper layer.

Based on the previously developed model equations, the calculation procedure described in this section has been generalized and incorporated with other example calculations into the ASET computer program user's manual.²⁴ For a fire scenario of interest, this computer program carries out ASET calculations corresponding to user-supplied inputs which describe the fire threat, room size, and appropriate user-specified detection and hazard criteria.

A Possible Extension in the Model's Utility

An Experimental, Full-Scale, Multi-Room Fire Scenario

This section compares the results of a full-scale, multi-room fire experiment with calculations based on ASET. The experiment was one of a series of tests in a mockup hospital patient room/corridor building space.⁴⁴

A plan view of the building space is presented in Figure 3-10.13. The space is made up of a room of area 14.4 m² connected by an open doorway to a corridor-lobby configuration of area 74.3 m².

A fire is initiated in a wastepaper basket next to the corner of a polyurethane mattress covered with bedding. The burn characteristics of this assembly were studied prior to the room burns of this series.⁵ The wastepaper basket/mattress fuel energy release rate, as derived from weight loss measurements, is plotted in Figure 3-10.14. For the purpose of the present analysis, it is assumed that this energy release rate was reproduced in the actual test run under review.

The model, which has been quantitatively described so far, is a single-room or room-of-fire-origin model. Thus,

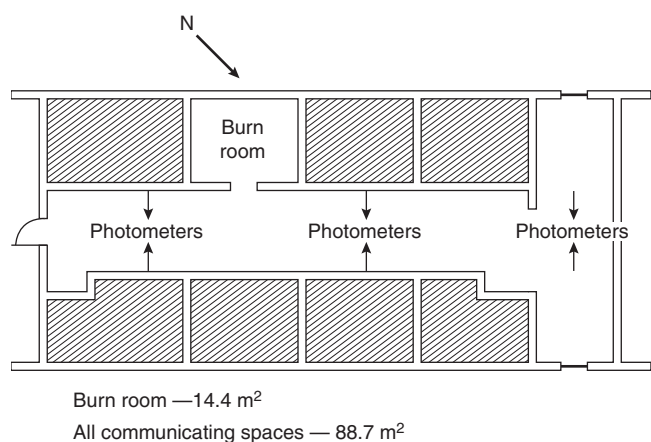


Figure 3-10.13. Plan view of hospital room/corridor mockup space.

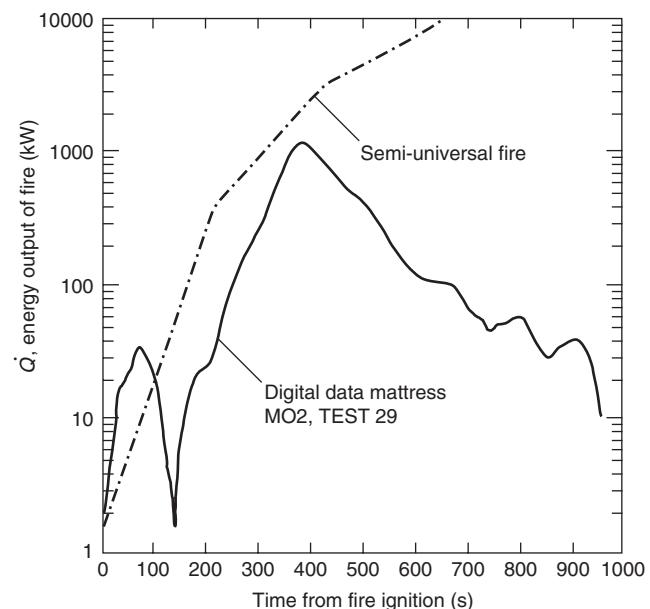


Figure 3-10.14. Energy release rate of wastepaper basket/mattress fuel assembly.

it may not be immediately obvious at what point, if any, it will have relevance to the present fire scenario. It would appear that a two-room or multi-room flow dynamics model would generally be required to study the room-corridor-lobby scenario under consideration. (For example, a two-room example flow calculation for a set of fire and room size parameters which somewhat corresponds to the present scenario has been considered²⁵). Nevertheless, it is possible that a simple, single-room modeling approach to fire scenarios involving relatively free-flowing multi-space configurations can be adequate for the purpose of obtaining engineering estimates of available egress times in the range of conditions that occurred in the referenced hospital patient room/corridor test.

Model Predictions Compared with Experimental Results

Room of fire origin: For early times into the fire, prior to the time when the upper layer interface drops to the level of the connecting doorway soffit, the single-room model is completely relevant. Up to that moment, the open doorway acts as the lower leakage path referred to earlier. Using the energy release data of Figure 3-10.14, and taking the fire source to be effectively at the floor, the model was used to compute the product of combustion-filling history of a 14.4 m² room up to the time that the upper layer thickness exceeded the existing ceiling-to-soffit dimension of 0.41 m. λ_c was estimated at 0.72.⁴⁰ The time for the interface to reach the soffit was computed to be 21 s following ignition.

Adjacent space: Once the smoke flows under the soffit and starts to fill the large corridor-lobby space, a two-room model is required to describe the gas migration and

exchange between the two spaces. This would continue to be true for at least some intermediate time interval. Following this, the single-room model can again be relevant.

If the fire is small enough or the doorway is large enough so that flows through the doorway remain relatively weak, the adjacent space will eventually attain and maintain a smoke layer thickness essentially identical to that of the room of fire origin. After some time interval, the histories of the elevations of the layer interfaces in both the corridor/lobby and room of fire origin spaces will be similar and can be computed from a single-room model, where the single room has an area equal to the combined area of both spaces. Time intervals when the upper layer thickness of the two rooms is not similar would encompass (1) the initial time when the room of fire origin fills up with smoke to the level of the doorway soffit and (2) the subsequent time interval when the upper layer thickness of the adjacent space grows from zero to a value close to that of the room of fire origin.

For fire scenarios where the above is applicable, significant simplifications occur in that the relatively simple single room of fire origin model can be used to study the effects of fire growth when far more complicated multi-room models would, at first hand, appear to be required.

To test the above ideas, the single-room model was used to predict the history of a single interface elevation and the average upper layer temperature within the combined patient room/corridor space. Using the energy release rate of Figure 3-10.14 and a total room area of 88.7 m², the history of the interface elevation and of the average upper layer temperature was computed. An effective λ_c for this combined space scenario is expected to be greater than the above $\lambda_c = 0.72$ value used for the single room of fire origin because of the additional heat transfer to the corridor surfaces. A value of $\lambda_c = 0.85$ was selected for the calculation. This was done with the anticipation that comparisons between computed and experimental average upper layer temperatures would reveal an appropriate correction to this λ_c value. (Recall that the upper layer temperature difference, $\Delta\bar{T}_h$, is approximately proportional to $1 - \lambda_c$.) The results of the computation for interface position and upper layer temperature are presented in Figures 3-10.15 and 3-10.16, respectively.

For the purpose of comparing results for the analytic and experimental interface position, an operational definition of the experimental interface position was required. This definition was based on the outputs of a total of six photometers placed at three different elevations and at one to three different positions (see Figure 3-10.13) in the corridor and lobby. The measured optical density (OD) outputs of these photometers are indicated in Figure 3-10.17. From these outputs, and for the purpose of defining a time when the smoke layer interface position passes the elevations of these photometers, there is still ambiguity as to what value of OD should constitute the presence of a smoke layer. Four different OD values, 0.01, 0.02, 0.03, and 0.04, were used as possible definitions for a minimum upper layer OD. Using the photometer outputs, the result of these four possible interface definitions leads to four possible sets of experimental data points for the interface elevation versus time. These are plotted in Figure 3-10.15 together with the theoretical results of the interface motion.

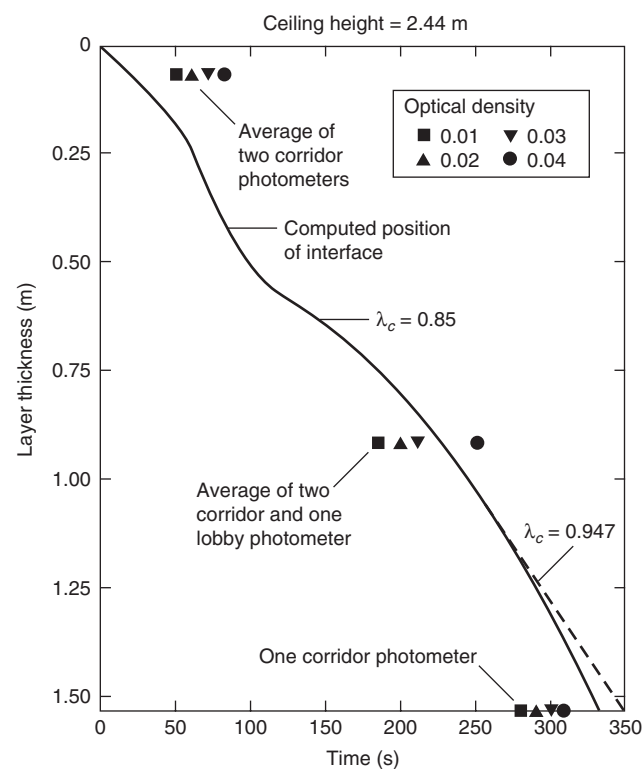


Figure 3-10.15. History of interface position.

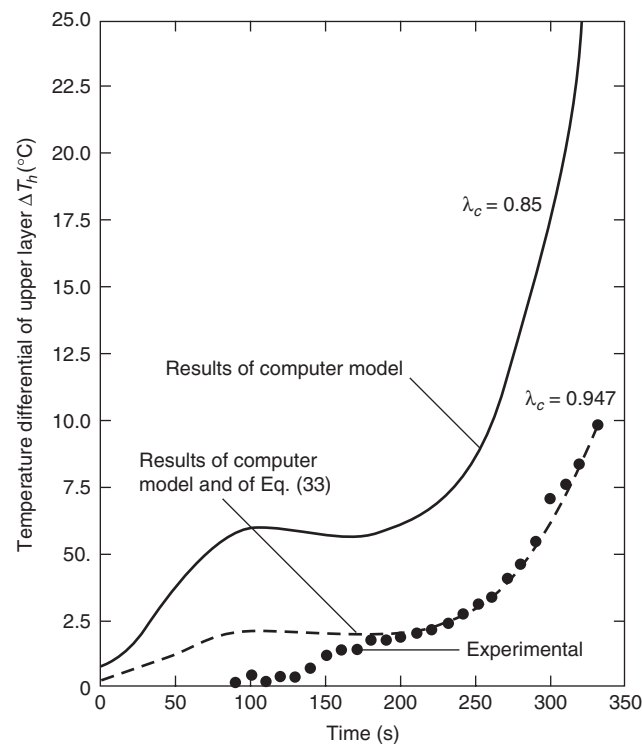


Figure 3-10.16. History of average upper layer temperature.

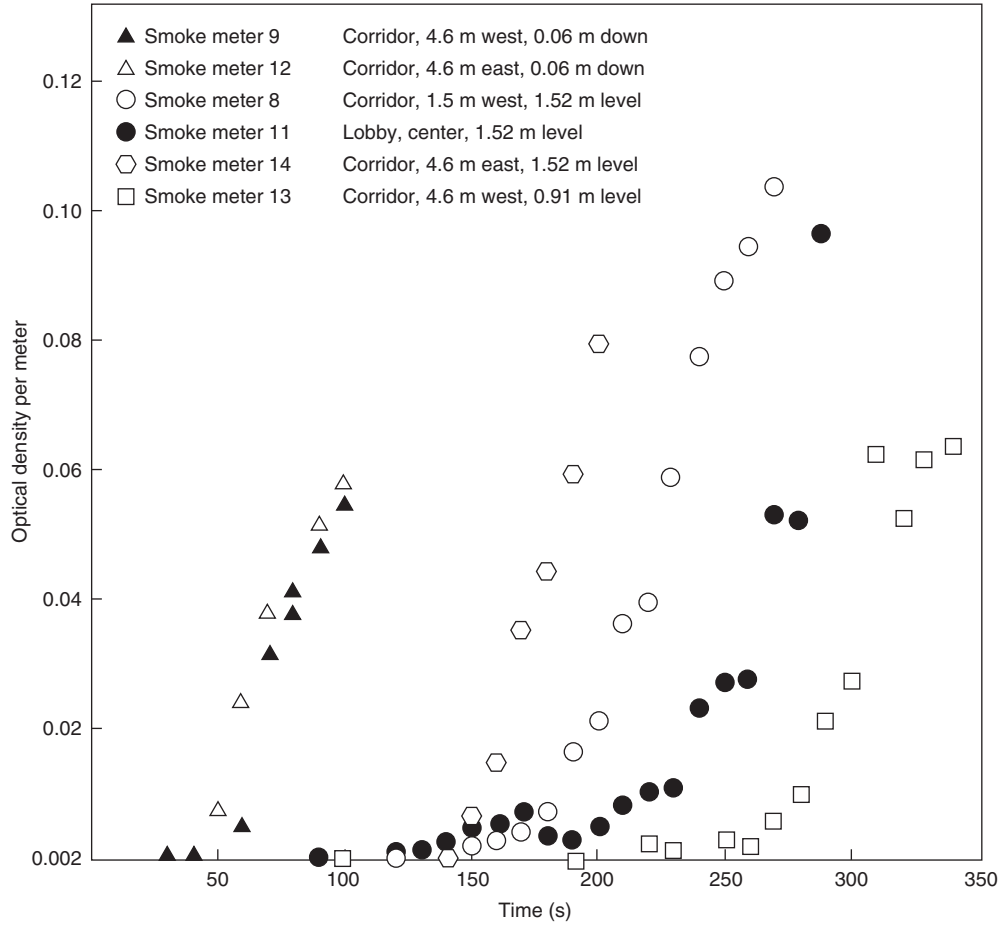


Figure 3-10.17. Optical densities measured by the photometers.

The favorable agreement between the results of theoretical and experimental interface position at the lower two of the three photometer locations illustrates the capability of the single-room model, in the present multi-room fire scenario, to predict the growth of the potentially hazardous upper smoke layer thickness. A favorable comparison at the uppermost photometer elevation located 0.06 m from the ceiling was not to be expected. This is because of the fact that, in the present multi-space configuration, the single-room model implemented in the manner described is clearly not adequate to predict the early growth in the corridor-lobby portion of the test space. Subsequent testing in the Figure 3-10.13 test space has corroborated the potential utility of the model in providing practical simulations of multi-room fire environments.²⁸

Gas temperatures were measured by two thermocouple trees located in the center of the corridor 4.6 m on either side of the room of fire origin doorway. No temperature data were acquired in the lobby space. At any given time, the equi-elevation thermocouples of these two trees measured temperature differences, $(T - T_a)$, which agreed to within 20 percent of one another. For the purpose of comparing analytic and experimental average upper layer temperature histories, an appropriate instantaneous weighting of the measured temperatures of the

limited number of these corridor thermocouples was required. At a given instant of time, this weighing has to be consistent with the estimate/measurement of the interface position as well as with the relative position of the thermocouples in question. A plot of the measured average upper layer temperature history deduced from such a data reduction scheme is presented along with the plot of the computed temperature history in Figure 3-10.16. As noted earlier, if a different λ_c has been used in the computation then, to a first approximation (i.e., using the principle of proportionality between $\Delta\bar{T}_h$ and $1 - \lambda_c$), one would anticipate a shift from the originally computed $\Delta\bar{T}_h(t)$ (with $\lambda_c = 0.85$) to a new temperature history $\Delta\bar{T}_h^{(new)}(t)$ [with $\lambda_c = \lambda_c^{(new)}$], where

$$\Delta\bar{T}_h^{(new)}(t) = [(1 - \lambda_c^{(new)}) / (1 - 0.85)] \Delta\bar{T}_h(t) \quad (33)$$

In view of the above, it is possible to bring the predicted analytic \bar{T}_h plot into coincidence with the experimental \bar{T}_h plot for at least one instant of time by a new choice, $\lambda_c^{(new)}$, for λ_c . Such coincidence is attained at $t = 330$ s (when the computed layer interface is at the potentially hazardous position 0.91 m from the corridor floor) by the specific choice of $\lambda_c^{(new)} = 0.947$. Using this latter value of $\lambda_c^{(new)}$ in Equation 33, an adjusted average upper

layer temperature history was computed and plotted. (See Figure 3-10.16.)

The single-room model was also used to recompute the interface position and temperature histories corresponding to $\lambda_c = 0.947$. These are plotted in Figures 3-10.15 and 3-10.16, respectively. For the parameters of the present scenario, the proximity of the $\lambda_c = 0.85$ and $\lambda_c = 0.947$ plots of Figure 3-10.15 illustrates the relative insensitivity of the interface position history to changes in λ_c . The variations between the two $\lambda_c = 0.947$ temperature history estimates are so small that they cannot be discerned in most of the Figure 3-10.15 plot. For this scenario, this illustrates the insensitivity of interface position on λ_c .

As can be noted in Figure 3-10.16, the experimental and newly calculated estimates for the upper layer temperature history are in good agreement in the time interval 175–330 s but in poor agreement at earlier times. Besides the fact that earlier times are likely to require analysis by a multi-room model, it is worth noting that the relatively complicated nature of the energy transfers which are being simulated may preclude sharper estimates of T_h with a single, constant value of λ_c . In this regard, results indicate that for fires in the present test space, λ_c can vary in time over a wide range of values.²⁸

Solutions to the Model Equations for a Special Class of Growing Fires

As was indicated in the last two sections, the ASET smoke filling model equations are easily solved with the use of the ASET or ASET-B computer programs for any particular fire specified by $\dot{Q}(t)$, $\dot{C}(t)$, and parameters H , A , Δ , λ_r , and λ_c . However, the approach of solving the equations for one set of conditions at a time does not lead readily to insight into solutions of generic problems of interest. For example, to obtain the results of Figure 3-10.12, solutions to the equations were required over a range of input values of A for each of the two input values of H . If more H values were of interest, and if, for example, one wished to study the effect of varying λ_c and/or Δ , then the volume of computer output would quickly become massive and unwieldy. In general, insight into the environment generated by a class of fire scenario (e.g., the semi-universal fire of Figure 3-10.11 in a room of arbitrary H , A , Δ , λ_r , and λ_c) is most clear when solutions can be obtained and displayed by means of limited numbers of graphs, charts, or tables. In this section, features of such a solution for an important, practical class of fire scenario will be displayed graphically, and explanation on how to extract practical results from this will be presented by way of examples. Some very useful and surprising time-of-smoke-filling estimates are obtained from this solution, and these will also be presented.

$Q \propto t^n$ Fire and Its Governing Equations

This subsection will present and solve Equations 9 through 11 and 25 for the broad class of fires whose $\dot{Q}(t)$ can be reasonably approximated by growth rates proportional to t^n for arbitrary $n \geq 0$ and whose product of combustion generation rates, $C(t)$, are approximately proportional to $\dot{Q}(t)$. This class of fire includes the constant

fire, $n = 0$, and the t^2 growing fires, $n = 2$, both of which have been used in a variety of different references to describe the burning of many practical assemblies of combustibles. To be definite, it is assumed that \dot{Q} and C can be approximated by

$$\dot{Q}(t) = \dot{Q}_0 \left(\frac{t H^{3/2} g^{1/2}}{A} \right)^n; \quad C(t) = \beta Q(t) \quad (34)$$

where \dot{Q}_0 represents a characteristic energy release rate, n is any non-negative integer, and β is a constant of proportionality of appropriate dimension.

Notice that for the constant fire problem, $n = 0$ in Equation 34 and \dot{Q}_0 is simply the specified constant energy release rate of the fire. Also, the energy release rate in many practical fires is simulated by $n = 2$ -type fires and is approximated by⁴

$$\dot{Q}(t) = \left(\frac{1000}{t_g^2} \right) t^2 \text{ kW} \quad (35)$$

where t_g , the growth time of the fire, is defined as the time for the fire to grow in a t^2 -type manner from a small flaming fire to a fire of approximately 1000 kW. Equation 34 for $n = 2$ and Equation 35 lead to the result that for these “ t -squared” fires, \dot{Q}_0 should be chosen as⁴

$$\dot{Q}_0 = \frac{1000 A^2}{(t_g^2 g H^3)} \text{ kW for } \dot{Q} \sim t^2 \text{ fires} \quad (36)$$

It is convenient to introduce the following dimensionless variables and parameters:

$$\begin{aligned} \zeta &= \frac{Z_i}{H} && \text{(interface elevation)} \\ \phi &= \frac{T}{T_a} && \text{(upper layer temperature)} \\ \mu &= \frac{(1 - \lambda_c)M}{\beta C_p T_a} && \text{(upper layer product concentration)} \\ \tau &= \frac{3[(1 - \lambda_r)\dot{Q}_0^*]^{1/3}(t H^{3/2} g^{1/2}/A)^{(n+3)/3}}{n + 3} && \text{(time)} \\ \varepsilon &= \frac{(1 - \lambda_c)[(n + 3)/3]^{2n^*(n+3)}\dot{Q}_0^{*2/(n+3)}}{(1 - \lambda_r)^{(n+1)/(n+3)}} && \text{(fire strength)} \\ \dot{Q}_0^* &= \frac{\dot{Q}_0}{\rho_a C_p T_a g^{1/2} H^{5/2}} && \text{(characteristic energy release rate)} \\ \delta &= \frac{\Delta}{H} && \text{(fire elevation)} \end{aligned} \quad (37)$$

Using the above definitions in the model Equations 7, 9, 10, 13, and 16 through 18, eventually leads to the following equations for τ , ϕ , and μ :

$$\frac{d\zeta}{d\tau} = \begin{cases} -\varepsilon \tau^{2n^*(n+3)} - 0.210 \zeta^{5/3}; & 0 < \zeta \leq 1 \\ -\varepsilon \tau^{2n^*(n+3)}; & -\delta < \zeta \leq 0 \\ 0; & \zeta = -\delta \end{cases} \quad (38)$$

$$\phi = \left\{ 1 - \frac{(n+3)\varepsilon\tau^{3(n+1)/(n+3)}}{3(n+1)(1-\zeta)} \right\}^{-1}; \quad -\delta < \zeta \leq 1 \quad (39)$$

$$\frac{d\phi}{d\tau} = \frac{\varepsilon\phi\tau^{2n/(n+3)}}{(1+\delta)}; \quad \zeta = -\delta$$

$$\mu = \phi - 1; \quad -\delta \leq \zeta \leq 1 \quad (40)$$

where Equation 38 must be solved subject to

$$\zeta(\tau = 0) = 1 \quad (41)$$

and where early time estimates for ζ , ϕ , and μ are

for $n = 0$:

$$\begin{aligned} \lim_{\tau \rightarrow 0} \frac{\zeta - 1}{1 + \varepsilon/0.210} &= -0.210\tau + \text{higher order terms in } \tau \\ \lim_{\tau \rightarrow 0} \frac{\phi}{(1 + \varepsilon/0.210)} &= \lim_{\tau \rightarrow 0} \frac{\mu + 1}{1 + \varepsilon/0.210} = 1 + \frac{5\varepsilon\tau}{6} \\ &\quad + \text{higher order terms in } \tau \end{aligned} \quad \left. \right\} (42)$$

for $n > 0$:

$$\begin{aligned} \lim_{\tau \rightarrow 0} (\zeta - 1) &= -0.210\tau + \text{higher order terms in } \tau \\ \lim_{\tau \rightarrow 0} (\phi - 1) &= \lim_{\tau \rightarrow 0} \mu \\ &= \frac{(n+3)\varepsilon\tau^{2n/(n+3)}}{3(n+1)(0.210)} + \text{higher order terms in } \tau \end{aligned} \quad \left. \right\} (43)$$

Equation 38 describes the rate of descent of the interface as it passes through the regions above the fire ($0 < \zeta < 1$), below the fire ($-\delta < \zeta < 0$), and at the floor ($\zeta = -\delta$). Equations 39 and 40 describe the corresponding upper layer temperature and product concentration. Equations 42 and 43 are useful in starting a numerical solution to Equations 38 and 39.

Discussion of the Equations

The last subsection presented the equations which govern the dynamics of the interface, ζ , the upper layer temperature, ϕ , and the upper layer product concentration, μ . From Equation 40, the solution for μ would follow directly from the solution for ϕ . From the time of ignition to the time that the interface drops to the floor of the enclosure, a solution for ϕ could be obtained from Equations 39, 42, and 43, provided a solution for ζ was available. Beyond that time, the solution for ϕ could be determined by a direct integration of the second line of Equation 39.

With the above observations, attention is drawn to the solution for ζ . From ignition at $\tau = 0$ until $\tau = \tau_0 \equiv \tau(\zeta = 0)$, corresponding to the time when the interface drops to $\zeta = 0$, ζ is governed by Equation 41 and the first line of Equation 38. No general closed form solution is possible, and a numerical solution for $\zeta(\tau; \varepsilon, n)$ is in order. Once this has been obtained, the solution can be extended beyond τ_0 by direct integration of the second and third lines of Equation 38.

Solutions from Ignition to τ_0

In general, there is no particular problem in using a computer to integrate Equation 38 numerically and obtain

ζ . However, in terms of generating a display of working graphical solutions which include times when ζ is small and positive, a problem does arise in the limit as ε approaches 0 (e.g., for small, dimensionless fire strength, \dot{Q}^*). Applying such a limit to the first line of Equation 38 leads, in a first approximation, to the total neglect of the earlier referenced (left-hand) expansion term in comparison to the (right-hand) entrainment term. This corresponds, physically, to the situation of an interface that approaches the elevation of the fire, $\zeta = 0$, asymptotically in time. In the present nomenclature, and for a source whose strength grows as t^n , the solution for $\varepsilon = 0$ is found to be

$$\zeta(\tau; \varepsilon = 0, n) = \zeta^{(0)}(\tau) = \left[1 + 0.210 \left(\frac{2}{3} \right) \tau \right]^{-3/2} \quad (44)$$

This result is plotted in Figure 3-10.18 along with numerically obtained, non-zero ε solutions for ζ .

From Equation 44 it is clear that for $\varepsilon = 0$, $\zeta \rightarrow 0$ as $\tau \rightarrow \infty$. But, for a fixed n and an arbitrarily small but non-zero ε , a $\zeta = 0$ position of the interface will, in fact, be attained at some finite, large $\tau = \tau_0$.

This small ε behavior of ζ and its proximity to the $\varepsilon = 0$ solution can be observed in Figure 3-10.18. As can be seen, the smaller the value of ε and the closer the value of n to 0, the longer in time the actual solution is accurately approximated by the $\varepsilon = 0$ solution.

The small ε limit is very important in problems of physical interest. As an example, consider a constant ($n = 0$) smolder source of 0.5 kW, located a distance of 2 m below a ceiling with $\lambda_r = 0.1$ and $\lambda_c = 0.75$. This leads to $\varepsilon = 5.3 (10^{-4})$. As an example of a relatively strong fire, consider a constant flaming fire of 5,000 kW (e.g., a burning gasoline spill approximately 1 m in radius) located 5 m below a ceiling, with $\lambda_r = 0.35$ and $\lambda_c = 0.75$. This leads to $\varepsilon = 6.0 (10^{-2})$. In terms of a "small ε " criterion, the latter fire is still relatively weak.

Time, Temperature, and Concentration When the Smoke Drops to the Fire Elevation

Numerically computed τ_0, ε pairs were obtained and plotted by Cooper⁴³ for a variety of different n values. The corresponding values for $\phi_0 = \phi(\tau_0; \varepsilon, n)$ were also obtained and plotted. All these results are reproduced here in Figure 3-10.19. From these plots and for arbitrary ε and n , it is possible to find the time, t_0 , which corresponds to τ_0 , for the smoke layer to drop to the fire elevation at $Z = 0$. The plots also provide an estimate for $\phi_0 = \phi(t_0)$, from which it is possible to obtain the $t = t_0$ upper layer temperature, T_0 , and (if applicable) the product of combustion concentration, M_0 . The most interesting general feature of Figure 3-10.19 is that, for a given n , the value of the ordinate

$$\varepsilon^{2(n+3)/[3(n+5)]}\tau_0(\varepsilon; n) = f(\varepsilon; n) \quad (45)$$

is relatively uniform over a broad ε range of interest. For example, for $n = 0, 1$, and 2

$$\varepsilon^{2/5}\tau_0(\varepsilon; n = 0) = f(\varepsilon; n = 0) = 4.3(1 \pm 0.15) \quad (46)$$

$$\varepsilon^{1/3}\tau_0(\varepsilon; n = 1) = f(\varepsilon; n = 1) = 3.4(1 \pm 0.16) \quad (46)$$

$$\varepsilon^{10/33}\tau_0(\varepsilon; n = 2) = f(\varepsilon; n = 2) = 3.0(1 \pm 0.17) \quad (46)$$

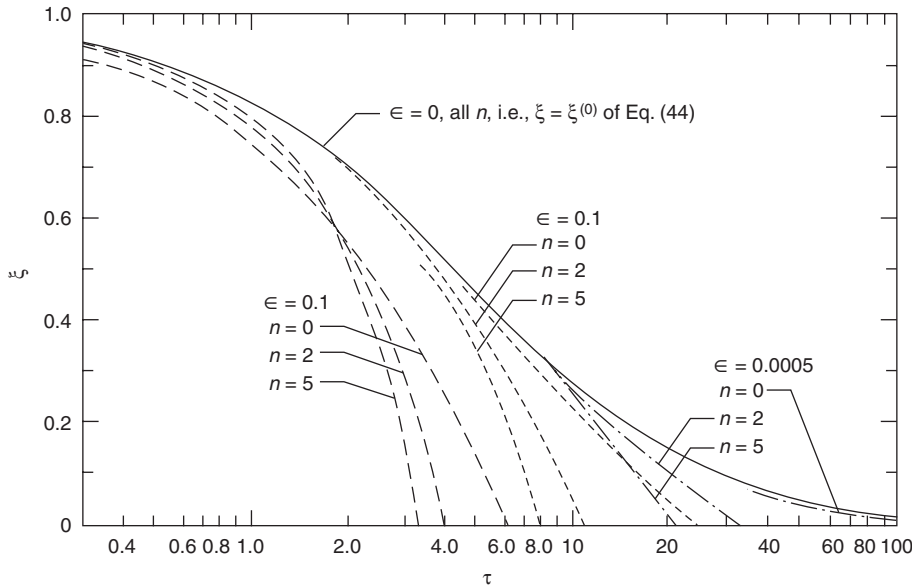


Figure 3-10.18. Plots of $\zeta(\tau)$ for different values of n and ϵ , $0 < \tau \leq \tau_0$.

for ϵ in the range

$$0.2(10^{-4}) < \epsilon < 0.2(10^{-1}) \quad (47)$$

[With somewhat larger errors, Figure 3-10.19 indicates that estimates of τ_0 coming from Equation 46 would remain valid even for ϵ significantly smaller than $0.2(10^{-4})$.] This result can be expressed in practical terms as a general solution for t_0

$$t_0 = [f(\epsilon; n)]^{3/(n+3)} \left\{ \frac{[A(n+3)/3]^5 [\rho_a C_p T_a t_0^n / Q(t_0)]^3}{(1 - \lambda_c)^2 (1 - \lambda_r) g} \right\}^{1/(3n+5)} \quad (48)$$

where the $f(\epsilon; n)$ are provided in Equation 46, or can be found from Figure 3-10.19. Also,

$$\epsilon = (1 - \lambda_c) \left\{ \frac{[A(n+3)/3]^{2n} [Q(t_0) / t_0^n]^2}{(1 - \lambda_r)^{(n+1)} (\rho_a C_p T_a)^2 g^{(n+1)} H^{(3n+5)}} \right\}^{1/(n+3)} \quad (49)$$

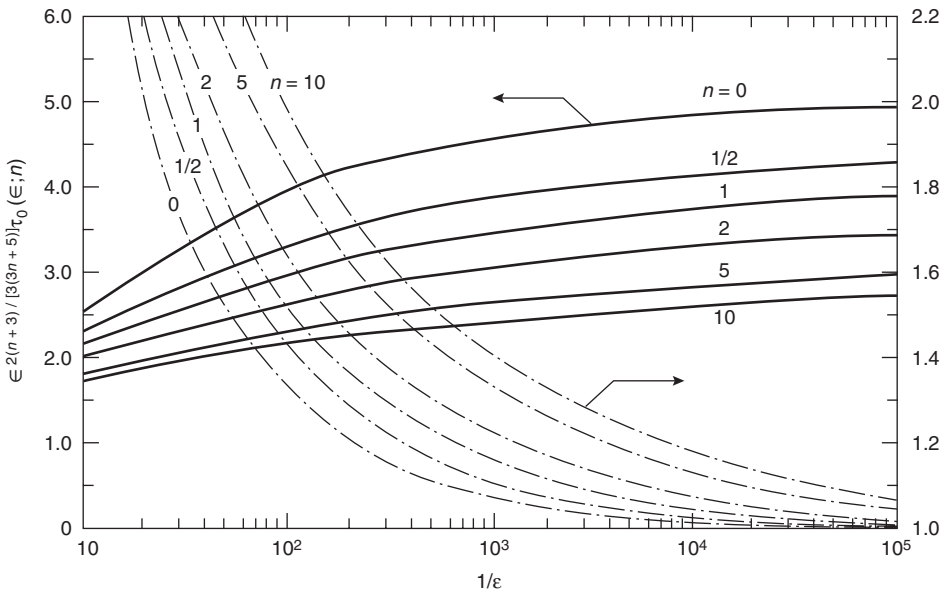


Figure 3-10.19. Plots of $\epsilon^{2(n+3)/(3(n+5))} \tau_0$ and φ_0 as functions of $1/\epsilon$ for different values of n .

Thus, the analysis has led to a remarkable practical result, namely, for fires which grow at rates which are approximately proportional to t^n and for a wide range of fire elevations and room heights of practical interest, the time for a smoke layer to drop from the ceiling to the elevation of the fire is relatively independent of H .

Taking ρ_a , T_a , C_p , and g to be

$$\begin{aligned}\rho_a &= 1.18 \text{ kg/m}^3, \quad T_a = 294 \text{ K}, \quad g = 9.8 \text{ m/s}^2 \\ C_p &= 240 \text{ cal/(kgK)} = 1.005 \text{ Ws/m}^3\end{aligned}\quad (50)$$

Equations 48 and 49 for $n = 0, 1$, and 2 become

$n = 0:$

$$t_0 = 91.4(1 \pm 0.15) \frac{A/Q^{3/5}}{[(1 - \lambda_c)^2(1 - \lambda_r)]^{1/5}}$$

$$\varepsilon = 9.43(10^{-3}) \left(\frac{Q^2}{H^5} \right)^{1/3} \left(\frac{1 - \lambda_c}{1 - \lambda_r} \right)^{1/3} \quad (51)$$

(A in m^2 , Q in kW , t_0 in sec, H in m)

$n = 1:$

$$t_0 = 20.2(1 \pm 0.12) \left[A^5 \frac{[t_0/Q(t_0)]^3}{[(1 - \lambda_c)^2(1 - \lambda_r)]} \right]^{1/8}$$

$$\varepsilon = 1.98(10^{-2}) \left(A \frac{Q(t_0)/t_0}{1 - \lambda_r} \right)^{1/2} \frac{1 - \lambda_c}{H^2} \quad (52)$$

(A in m^2 , Q in kW , t_0 in sec, H in m)

$n = 2:$

$$t_0 = 10.5(1 \pm 0.10) \left[A^5 \frac{[t_0^2/Q(t_0)]^3}{[(1 - \lambda_c)^2(1 - \lambda_r)]} \right]^{1/11} \quad (53)$$

$$\varepsilon = 3.68(10^{-2})(1 - \lambda_c) \left[A^4 \frac{[Q(t_0)/t_0^2]^2}{H^{11}(1 - \lambda_r)^3} \right]^{1/5} \quad (53)$$

(A in m^2 , Q in kW , t_0 in sec, H in m)

or, in terms of t_g of Equation 35⁴

$n = 2:$

$$t_0 = 1.60(1 \pm 0.10) \left[\frac{A^5 t_g^6}{(1 - \lambda_c)^2(1 - \lambda_r)} \right]^{1/11}$$

$$\varepsilon = 0.583(1 - \lambda_c) \left[\frac{(A/t_g)^4}{H^{11}(1 - \lambda_r)^3} \right]^{1/5} \quad (54)$$

(A in m^2 , Q in kW , t_0 and t_g in sec, H in m)

where all the above t_0 estimates are subject to the ε range of Equation 47.

Some Solution Results for $Z_i(t)$, $T(t)$, and $\mu(t)$

Plots of general solutions for $Z_i(t)$, $T(t)$, and $\mu(t)$ are presented in Figure 3-10.20 for $n = 0, 1$, and 2. These plots are useful up to the times when the interface either drops to the floor or to an elevation $0.2 H$ below the fire, whichever event occurs first.

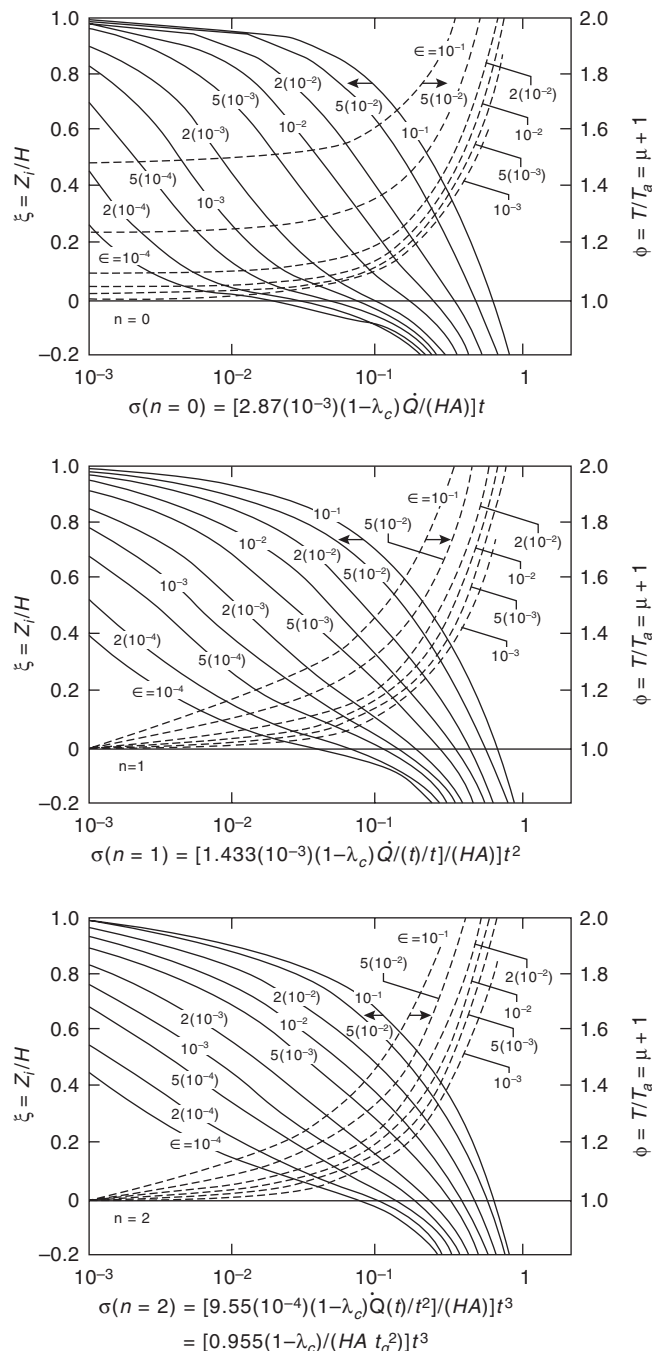


Figure 3-10.20. Plots of $Z_i(t)$, $T(t)$, and $\mu(t)$ up to the time when $Z_i = -0.2 H$ or $Z_i = Z_{\text{floor}}$, whichever comes first, for different values of ε and for $n = 0, 1$, and 2. (Q in kW ; t and t_g in s ; H in m ; and A in m^2 .)

As can be noted, the abscissa of the Figure 3-10.20 plots, which have been taken from Cooper,⁴³ are in the form

$$\sigma = \{\text{constant}\}t^{n+1}$$

The σ of Figure 3-10.20 corresponds to

$$\sigma = \left[\frac{n+3}{3(n+1)} \right] \varepsilon t^{3(n+1)/(n+3)} \quad (55)$$

under the ambient property assumptions of Equation 50. Cooper found σ to be a convenient variable for describing the upper layer environment after the interface had dropped below the fire elevation, $Z_i = 0$, and even subsequent to the time that the interface drops to the compartment floor, that is, when $Z_i = -\Delta$.⁴³ A description of solutions to our problem at these latter times is beyond the scope of this chapter, and the reader is referred to Cooper's work for a full discussion of the relevant results.⁴³

Using the $\dot{Q} \sim t^n$ Solution Plots of Figures 3-10.19 and 3-10.20 to Predict Characteristics of Compartment Fire-Generated Environments

To illustrate the use of the solution plots of Figures 3-10.19 and 3-10.20, they will now be applied to two example problems. The first example will involve a problem of smoldering combustion. The second example illustrates the use of the theory in predicting the environment produced in an enclosure which contains a specific large-scale flaming fire hazard.

EXAMPLE 1:

Smoldering combustion: Smoldering experiments reported by Quintiere et al. were carried out in a single-room compartment of height 2.44 m and floor area 8.83 m².⁴⁵ The opening to the enclosure was formed by a closed undercut door, where the undercut formed a 0.76 m × 0.025 m open horizontal slit at floor level. A smoldering ignition source was placed in the enclosure with the top surface of the source at an elevation of 0.33 m. Gas analysis was carried out at four equidistant elevations, the inlets of sampling tubes extending horizontally approximately 0.5 m from the walls.

The tests evaluated two different smolder sources: a loosely packed bed of cotton, and blocks of flexible polyurethane foam. Mass loss rates, \dot{m} , were found to be approximately linear in time throughout the first hour of the two tests, that is,

$$\dot{m} = at \quad 0 < t < 60 \text{ min} \quad (56)$$

where

$$a = \begin{cases} 0.21 \text{ g/min}^2 & \text{for polyurethane} \\ 0.33 \text{ g/min}^2 & \text{for cotton} \end{cases}$$

The heats of combustion, H_c , of the materials as well as the ratios, γ , of mass-of-CO produced to mass of material lost were obtained in a separate small-scale apparatus. These were found to be

$$H_c = \begin{cases} (11 \pm) \text{ kJ/g}_\text{cotton} \\ (15 \pm 8) \text{ kJ/g}_\text{polyurethane} \end{cases} \quad (57)$$

$$\gamma = \begin{cases} 0.11g_\text{CO}/g_\text{cotton} \\ (0.10 \pm 0.01)g_\text{CO}/g_\text{polyurethane} \\ (-0.04) \end{cases} \quad (58)$$

The results of the previous section will be used to predict the environment which developed in the enclosure during the course of the two different material evaluations.

Comparing Equations 56 through 58 to Equation 34 leads to

$$\dot{Q} = aH_c t = \dot{Q}_0 \left[\frac{t H^{3/2} g^{1/2}}{A} \right]^n \quad (59)$$

where \dot{C}_{CO} is measured in g_{CO} per unit time. From the above, it is concluded that

$$n = 1; \quad \frac{\dot{Q}(t)}{t} = aH_c; \quad \beta = \frac{\gamma}{H_c} \quad (60)$$

Also

$$H = 2.11 \text{ m}, \quad \Delta = 0.33 \text{ m}, \quad A = 8.83 \text{ m}^2 \quad (61)$$

Radiant losses from the combustion zone are neglected, that is, $\lambda_r = 0$. Considerations by Cooper,⁴⁰ together with the experimental results of Mulholland et al. and Veldman et al.,^{46,13} indicate that for a $\lambda_r = 0$ combustion zone in an enclosure with proportions similar to the present one, $\lambda_c \approx 0.6$. This λ_c will be used here.

Using the λ_c value 0.6 and Equations 50, 57, 58, and 60 in the μ definition of Equation 37 and the result of Equation 40 leads to

$$\phi = 1 + 135M_\text{cotton} = 1 + 204M_\text{polyurethane} \quad (62)$$

where, for example, M_cotton is the upper layer concentration of CO ($g_{CO}/g_\text{upper layer}$) during smoldering of the cotton source.

From Equations 56 and 57

$$\frac{\dot{Q}(t)}{t} = aH_c \approx \begin{cases} 0.21(15) \text{ kJ/min}^2 = 9(10^{-4}) \text{ kW/s for polyurethane} \\ 0.33(11) \text{ kJ/min}^2 = 9(10^{-4}) \text{ kW/s for cotton} \end{cases} \quad (63)$$

All parameters of the problem required to estimate t_0 and ε from Equation 52 are now available. These are found to be

$$t_0 = 1400 \text{ sec}; \quad \varepsilon = 1.6(10^{-4}) \quad (64)$$

The value of ε satisfies the ε range of Equation 47 thereby establishing the validity of the t_0 estimate.

From the value of ε , it is now possible to use Figure 3-10.19 to obtain ϕ_0 . Thus, for $1/\varepsilon = 0.61(10^4)$ and for $n = 1$ it is found from the Equation 36 definition of ϕ that

$$\phi_0 = 1.07 \rightarrow T(t_0) = 1.07T_a = 315 \text{ K} = 42^\circ\text{C} \quad (65)$$

Also, from Equation 62, this result for ϕ_0 yields

$$\left. \begin{aligned} M_{\text{cotton}}(t_0) &= \frac{1.07 - 1}{135} \\ &= 5(10^{-4}) \frac{g_{\text{CO}}}{g_{\text{upper layer}}} \\ &= 5(10^2) \text{ ppm CO} \\ M_{\text{polyurethane}}(t_0) &= \frac{1.07 - 1}{204} \\ &= 3(10^{-4}) \frac{g_{\text{CO}}}{g_{\text{upper layer}}} \\ &= 3(10^2) \text{ ppm CO} \end{aligned} \right\} \quad (66)$$

The smoke interface reaches the floor at the time, t_f , corresponding to

$$\zeta_f = \frac{Z_i(t_f)}{H} = -\frac{\Delta}{H} = \delta = -0.16 \quad (67)$$

From the $n = 1$ plots of Figure 3-10.20, it is found that this occurs at t_f corresponding to

$$\begin{aligned} \sigma &= 0.3 = \sigma_f(\zeta = \zeta_f; n = 1) \\ &= \left\{ 1.4(10^{-3})(1 - \lambda_c) \left[\frac{\dot{Q}(t)/t}{HA} \right] \right\} t_f^2 \\ &\quad (\dot{Q} \text{ in kW; } t \text{ in s; } H \text{ in m; } A \text{ in m}^2) \\ &= \left\{ 1.4(10^{-3})(1 - 0.6) \left[\frac{9(10^{-4})}{(2.1)(8.8)} \right] \right\} t_f^2 \\ &= 0.3(10^{-7})t_f^2 \end{aligned} \quad (68)$$

(for both the cotton and polyurethane) at which time

$$\phi(t_f) = \phi_f \approx 1.25 \quad (69)$$

The following results are obtained from Equations 68 and 69 and with the use of Equation 62:

$$\begin{aligned} t_f &= 3(10^3) \text{ sec} \\ M_{\text{cotton}}(t_f) &= \frac{1.25 - 1}{135} = 1.9(10^3) \text{ ppm CO} \\ M_{\text{polyurethane}}(t_f) &= \frac{1.25 - 1}{204} = 1.2(10^3) \text{ ppm CO} \end{aligned} \quad (70)$$

Thus, the above estimate indicates that the interface reached the floor elevation somewhat prior to the 60-min duration of the tests. The reader is referred to Cooper's studies for further discussion of comparisons between calculated and experimental results.⁴³

EXAMPLE 2:

Hazard development in enclosures containing some larger scale fires: NFPA 204M, *Guide for Smoke and Heat Venting*, provides a catalogue of experimentally determined energy release rates for the growth stages of flaming fires in practical fuel assemblies.⁴ The \dot{Q} of all items in this listing is proportional to t_2 . For example, the \dot{Q} of many items can be estimated by

$$t_g = 100 \text{ sec} \quad (71)$$

Using Equation 35, this corresponds to

$$\dot{Q} = 0.10t^2 \text{ kW/s}^2 \quad (72)$$

The latter items include wood pallets stacked 3.0 to 4.6 m high, many different types of polyethylene, polypropylene, polystyrene and PVC commodities in cartons stacked 4.6 m high, and a horizontal polyurethane mattress.

The results of Figures 3-10.19 and 3-10.20 will be used to characterize the hazard development in enclosures which contain Equation 71-type fires.

From Equations 54 and 71 and the abscissa for $n = 2$ of Figure 3-10.20

$$\begin{aligned} t_0 &\approx 20 \left[\frac{A^5}{(1 - \lambda_c)^2(1 - \lambda_r)} \right]^{1/11} \\ \varepsilon &= 1.5(10^{-2}) \left[\frac{(1 - \lambda_c)A^{4/5}}{(1 - \lambda_r)^{3/5}H^{11/5}} \right] \\ \sigma(n = 2) &= 0.96(10^{-4}) \left(\frac{1 - \lambda_c}{HA} \right) t^3 \end{aligned} \quad (73)$$

(t in sec; H in m; A in m²)

With Equation 73, Figures 3-10.19 and 3-10.20 can now be used to answer a wide variety of hazard-related questions. For illustrative purposes, two such questions will be addressed here.

QUESTION 1:

Flaming ignition is initiated in stacked commodities of the "tg = 100 s variety" which are contained in a warehouse of height 6 m and floor area 1500 m². At what time does the upper layer attain the potentially untenable temperature (due to downward radiation) of 183°C, and what is the elevation of the layer interface at this time?¹ At what time does the upper layer completely fill the warehouse?

ANSWER:

Consistent with recommendations by Cooper,² assume $\lambda_r = 0.35$, and, for the purpose of a hazard analysis of this type, conservatively assume that $\lambda_c = 0.6$. Take H to be the floor-to-ceiling dimension, 6 m, and Δ to be zero. Then, for $A = 1500 \text{ m}^2$, Equation 73 leads to

$$\begin{aligned} t_0 &= 680 \text{ sec} \\ \varepsilon &= 5.2(10^{-2}) \\ \sigma(n = 2) &= 4.7(10^{-9})t^3 \end{aligned} \quad (74)$$

Notice that the above value for $\varepsilon = 5.2 (10^{-2}) > 0.2 (10^{-1})$ is somewhat outside the Equation 47 range. As a result, the above $t_0 = 680$ s estimate is not reliable. A better value for t_0 , estimated from Equation 48 and Figure 3-10.19, is found to be $t_0 \approx 600$ s.

The $\varepsilon = 5.2 (10^{-2})$ value corresponds to $1/\varepsilon = 19$ which, for $n = 2$ in Figure 3-10.19, is found to correspond (somewhat off-scale) to

$$\phi_0 \approx 2.4 \rightarrow T(t_0) = 2.4T_a = 710 \text{ K} = 433^\circ\text{C} \quad (75)$$

At the time, t_u , of potential untenability, $T_u = T(t_u)$ is assumed to be 183°C (456 K). Thus

$$\phi_u = \phi(t_u) = \frac{T_u}{T_a} = \frac{456}{294} = 1.55 \quad (76)$$

For $\varepsilon = 5.2 (10^{-2})$, the $n = 2$ plots of Figure 3-10.20 can be interpolated at $\phi = \phi_u = 1.55$ to yield

$$\sigma_u = \sigma(t_u) \approx 0.2 = 4.7(10^{-9})t_u^3 \rightarrow t_u = 350 \text{ sec} \quad (77)$$

which, in turn, is seen to correspond to

$$\zeta_u = \zeta(t_u) = \frac{Z_i(t_u)}{H} = 0.45 \quad (78)$$

Using this last value for ζ_u along with $H = 6$ m leads to

$$Z_i(t_u) = 0.45(6) \text{ m} = 2.7 \text{ m} \quad (79)$$

The above results are summarized as follows: the upper smoke layer will fill the compartment at $t_0 = 600$ s, at which time its average temperature will be approximately 430°C . The potentially untenable condition of $T = 183^\circ\text{C}$ will occur at $t_u = 350$ s, at which time the layer interface is 2.7 m above the floor.

QUESTION 2:

Flaming ignition is initiated in a polyurethane mattress 0.6 m above the floor of a hospital ward with floor-to-ceiling dimension of 3 m and floor area 100 m^2 . At what time, t_u , does the upper layer interface reach the potentially untenable elevation, $Z_u = 1.5$ m, and what is the upper layer temperature, T_u , at this time?

ANSWER:

Take $\lambda_c = 0.8$, and $\lambda_r = 0.35$. Also, $H = 2.4$ m, $\Delta = 0.6$ m, $Z_u = 0.9$ m, and $A = 100 \text{ m}^2$. Then, Equation 73 leads to

$$\begin{aligned} t_0 &= 230 \text{ sec} \\ \varepsilon &= 2.3(10^{-2}) \\ \sigma(n=2) &= 8.0(10^{-8})t^3 \end{aligned} \quad (80)$$

Also, at the time of untenability

$$Z_i(t_u)H = \frac{Z_u}{H} = \frac{0.9}{2.4} = 0.38 \quad (81)$$

For $\varepsilon = 2.3(10^{-2})$, the $n = 2$ plots of Figure 3-10.20 can be interpolated to obtain the desired values of $\sigma(t_u)$, and then $\phi(t_u)$ corresponding to $Z_i/H = 0.38$. Thus

$$\begin{aligned} \sigma(t_u) &= 0.18 = 80(10^{-9})t_u^3 \rightarrow t_u = 130 \text{ sec} \\ \phi(t_u) &= 1.33 \rightarrow T(t_u) = 1.33T_a = 391 \text{ K} = 118^\circ\text{C} \end{aligned} \quad (82)$$

In Equation 80, t_0 is the time for the smoke interface to drop to the level of the mattress which is 0.6 m above the floor. As an additional point of information, for $\varepsilon = 2.3(10^{-2})$, corresponding to $1/\varepsilon = 44$, and for $n = 2$, Figure 3-10.19 provides the result

$$\phi_0 = 1.94 \rightarrow T(t_0) = 1.94T_a = 570 \text{ K} = 297^\circ\text{C} \quad (83)$$

Notice that this result can also be obtained approximately from Figure 3-10.20. To do so, select the value of $\sigma = \sigma(t_0)$ when $\zeta = Z_i/H = 0$, and find the corresponding value for $\phi = \phi(t_0)$, all on the $\varepsilon = 2(10^{-2})$ curves. This leads to $\phi(t_0) = 1.88 \approx 1.94$.

The above results are summarized as follows: the smoke layer interface will drop to the 1.5-m elevation at $t = 130$ s, at which time its average temperature will be approximately 118°C . Also, the interface will reach the mattress elevation at $t = 230$ s and have an average temperature of 297°C .

References Cited

1. L.Y. Cooper, "A Concept for Estimating Available Safe Egress Time in Fire," *F. Safety J.*, 5, pp. 135–144 (1983).
2. L.Y. Cooper, "A Mathematical Model for Estimating Available Safe Egress Time in Fires," *F. and Matls.*, 6, pp. 135–144 (1982).
3. E.G. Butcher and A.C. Parnell, *Smoke Control and Fire Safety Design*, Spon, London (1979).
4. G. Heskstad, "Appendix A," in *NFPA 204M, Guide for Smoke and Heat Venting*, National Fire Protection Association, Quincy, MA (1991).
5. V. Babrauskas, "Combustion of Mattresses Exposed to Flaming Ignition Sources, Part I, Full-Scale Tests and Hazard Analysis," in *NBSIR 77-1290*, National Bureau of Standards, Gaithersburg, MD (1977).
6. G. Heskstad, "Engineering Relations for Fire Plumes," *F. Safety J.*, 7, pp. 25–32 (1984).
7. E.E. Zukoski, T. Kubota, and B. Cetegen, "Entrainment in Fire Plumes," *F. Safety J.*, 3, pp. 107–121 (1980/81).
8. B.J. McCaffrey, "Purely Buoyant Diffusion Flames: Some Experimental Results," in *NBSIR 79-1910*, National Bureau of Standards, Gaithersburg, MD (1979).
9. R.L. Alpert, "Turbulent Ceiling-Jet Induced by Large-Scale Fires," *Comb. Science Tech.*, 11, pp. 197–213 (1975).
10. G. Heskstad, "Similarity Relations for the Initial Convective Flow Generated by Fire," *Paper 72-WA-HT-17*, Winter Annual Meeting, ASME (1972).
11. G. Heskstad and M.A. Delichatsios, "Environments of Fire Detectors—I: Effect of Fire Size, Ceiling Heights, and Material," 1: "Measurements," *FMRC Report NBS-GCR-77-86*, 2: "Analysis," *FMRC Report NBS-GCR-77-95*, National Bureau of Standards, Gaithersburg, MD (1977).
12. G. Heskstad and M.A. Delichatsios, "Environments of Fire Detectors—II: Effect of Ceiling Configuration," 1: "Measure-

- ments," *FMRC Report NBS-GCR-78-128*, 2: "Analysis," *FMRC Report NBS-GCR-78-129*, National Bureau of Standards, Gaithersburg, MD (1978).
13. C.C. Veldman, T. Kubota, and E.E. Zukoski, "An Experimental Investigation of Heat Transfer from a Buoyant Plume to a Horizontal Ceiling—Part I: Unobstructed Ceiling," *C.I.T. Report NBS-GCR-77-97*, National Bureau of Standards, Gaithersburg, MD (1975).
 14. L.Y. Cooper, "Heat Transfer from a Buoyant Plume to an Unconfined Ceiling," *J. of Heat Transfer*, 104, pp. 446–451 (1982).
 15. L.Y. Cooper and A. Woodhouse, "The Buoyant Plume-Driven Adiabatic Ceiling Temperature Revisited," *J. of Heat Transfer*, 108, pp. 822–826 (1986).
 16. L.Y. Cooper and D.W. Stroup, "The Thermal Response of Unconfined Ceilings above Growing Fires and the Importance of Convective Heat Transfer," *J. of Heat Transfer*, 109, pp. 172–178 (1987).
 17. R.L. Alpert, "Calculation of Response Time of Ceiling Mounted Fire Detectors," *Fire Tech.*, 3, pp. 181–195 (1972).
 18. I. Benjamin, G. Hesketh, R. Bright, and T. Mayes, *An Analysis of the Report on Environments of Fire Detectors*, Fire Detection Institute (1979).
 19. D. Goldman and Y. Jaluria, "Effect of Opposing Buoyancy on the Flow in Free and Wall Jets," *J. of Fluid Mech.*, 166, pp. 41–56 (1986).
 20. L.Y. Cooper, "Ceiling Jet Properties and Wall Heat Transfer Near Regions of Ceiling Jet-Wall Impingement," in *NBSIR 86-3307*, National Bureau of Standards, Gaithersburg, MD (1986).
 21. L.Y. Cooper, "Convective Heat Transfer to Ceilings above Enclosure Fires," in *Proceedings of 19th Symposium (International) on Combustion*, Combustion Institute, Haifa, Israel (1982).
 22. L.Y. Cooper, "A Buoyant Source in the Lower of Two, Homogeneous, Stably Stratified Layers—A Problem of Fire in an Enclosure," in *Proceedings of 20th Symposium (International) on Combustion*, Combustion Institute, Pittsburgh, pp. 1567–1573 (1984).
 23. L.Y. Cooper, "On the Significance of a Wall Effect in Enclosures with Growing Fires," *Comb. Science Tech.*, 40, pp. 19–39 (1984).
 24. L.Y. Cooper and D.W. Stroup, "Calculating Available Safe Egress Time (ASET)—A Computer Program and User's Guide," *NBSIR 82-2578*, National Bureau of Standards, (1982). Also, a condensed version: "ASET—A Computer Program for Calculating Available Safe Egress Time," *F. Safety Jour.*, 9, pp. 29–45 (1985).
 25. E.E. Zukoski and T. Kubota, "Two-Layer Modeling of Smoke Movement in Building Fires," *F. and Matls.*, 4, 1, pp. 17–27 (1980).
 26. K. Steckler, J. Quintiere, and W. Rinkinen, "Flow Induced by Fire in a Compartment," in *Proceedings of 19th Symposium (International) on Combustion*, Combustion Institute, Pittsburgh (1982).
 27. NFPA 101, *Life Safety Code*, (A-15-3.1.3), National Fire Protection Association, Quincy, MA (1994).
 28. L.Y. Cooper, M. Harkelroad, J. Quintiere, and W. Rinkinen, "An Experimental Study of Upper Hot Layer Stratification in Full-Scale Multiroom Fire Scenarios," *J. of Heat Transfer*, 104, pp. 741–749 (1982).
 29. L.Y. Cooper, "The Need and Availability of Test Methods for Measuring the Smoke Leakage Characteristics of Door Assemblies," in *Fire Safety: Science and Engineering*, ASTM STP 882, ASTM, Philadelphia, pp. 310–329 (1985).
 30. T. Wakamatsu, "Calculation of Smoke Movement in Buildings," in *Res. Paper 34*, Building Research Institute, Tokyo (1968).
 31. E. Evers and A. Waterhouse, "A Computer Model for Analyzing Smoke Movement in Buildings," in *SCS Ltd. Report CP 68/78* for Fire Research Station, Borehamwood, UK (1978).
 32. B.R. Morton, G.I. Taylor, and J.S. Turner, "Turbulent Gravitational Convection from Maintained and Instantaneous Sources," in *Proceedings of Royal Society (London)*, Ser. A, 234, pp. 1–23 (1956).
 33. S. Yokoi, "On the Heights of Flames from Burning Cribs," *BRI Report 12*, Ministry of Construction, Japanese Government (1963).
 34. W.D. Baines and J.S. Turner, "Turbulent Buoyant Convection from a Source in a Confined Region," *J. of Fluid Mech.*, 37, Part 1, pp. 51–80 (1969).
 35. E.E. Zukoski, "Development of a Stratified Ceiling Layer in the Early Stages of a Closed-Room Fire," *F. and Matls.*, 2, pp. 54–62 (1978).
 36. W.D. Walton, "ASET-B: A Room Fire Program for Personal Computers," in *NBSIR 85-3144-1*, National Bureau of Standards, Gaithersburg, MD (1985).
 37. D. Burgess and M. Hertzberg, "Radiation from Pool Fires" in *Heat Transfer in Flames*, ed. By N.H. Afgan and J.M. Beer, Chap. 27, Wiley and Sons, New York (1974).
 38. J. DeRis, "Fire Radiation—A Review," *Tech. Report FMRC RC 78-BT-27*, Factory Mutual Research Corp., Norwood, MA (1978).
 39. A.T. Modok and P.A. Croce, "Plastic Pool Fires," *Comb. Flame*, 30 (1977).
 40. L.Y. Cooper, "Estimating Safe Available Egress Time from Fires," *NBSIR 80-2172*, National Bureau of Standards, Gaithersburg, MD (1981).
 41. R. Friedman, "Quantification of Threat from a Rapidly Growing Fire in Terms of Relative Material Properties," *F. and Matls.*, 2, pp. 27–33 (1978).
 42. T. Tanaka, "A Model on Fire Spread in Small-Scale Building," in *Third Joint Meeting US-Japan Panel on Fire Research and Safety*, UJNR, Washington, DC (1978).
 43. L.Y. Cooper, "The Development of Hazardous Conditions in Enclosures with Growing Fires," *Comb. Science and Tech.*, 22, pp. 279–297 (1983).
 44. J.G. O'Neill and W.D. Hayes, "Full-Scale Fire Tests with Automatic Sprinklers in a Patient Room" *NBSIR 79-1749*, National Bureau of Standards, Gaithersburg, MD (1979).
 45. J. Quintiere, M. Birky, and G. Smith, "An Analysis of Smoldering Fires in Closed Compartments and Their Hazard Due to Carbon Monoxide," *F. and Matls.*, 6, p. 99 (1982).
 46. G. Mulholland, T. Handa, O. Sugawa, and H. Yamamoto, "Smoke Filling in an Enclosure," *20th National Heat Transfer Conference*, Milwaukee (1981).

CHAPTER 11

Fire Hazard Calculations for Large, Open Hydrocarbon Fires

Craig L. Beyler

Introduction

A major challenge in industrial fire protection is controlling the impact from large, open hydrocarbon fires. The primary mechanism for injury or damage from such fires is thermal radiation. Depending upon the circumstances and conditions leading to such an event, a different type of open fire may result. For example, ignited releases can produce pool fires, jet flames, vapor cloud fires, or fireballs, all of which behave differently and exhibit markedly different radiation characteristics. This chapter presents detailed techniques for calculating impacts from large, open hydrocarbon fires. Examples are included throughout this chapter to illustrate the application of these expressions.

The first section of this chapter discusses hydrocarbon pool fires, an area in which considerable work has been done, including various important geometric parameters (e.g., flame height), thermal radiation models, and atmospheric absorption of radiation. The second section deals with turbulent jet flames and flares, first presenting significant geometric effects and thermal radiation models, then discussing aerodynamic effects on radiant energy and flame stability.

While the above cases involve primarily steady-state thermal radiation, the third section considers two very important cases that involve unsteady radiant effects—burning vapor clouds and fireballs. Although developmental work in both of these areas is still ongoing, limited data are available to lend some confidence to the use of these models.

The following part of this introduction presents an event tree for the release of a flammable material to guide

the user's selection of appropriate potential impacts and model application. It cannot be overstressed that prudent judgment should be exercised in the application of any of these calculation schemes to yield a safe and fair evaluation of scenarios of interest.

Event Tree for Flammable Material Release

Figure 3-11.1 depicts a typical event tree for the release of a flammable material, showing the pathways that lead to the various types of open fires. For this purpose, assume the release occurs from a pressurized container since all types of open fires may be realized from a pressurized release. In this example, the pressurized container may be either a large vessel (for storage, reaction, batch-ing, etc.) or a pipeline (for transfer, fittings, instruments, etc.). The pressure may be the result of either normal operations or abnormal external events. For example, a tank may be pressurized because it contains a compressed liquid or because it has been exposed to an external fire; a pipeline may be pressurized because of a pumping operation or because of steam tracing on a blocked-in segment. Finally, the release may be due to a major failure (e.g., spontaneous tank failure) or a minor accident (e.g., breakage of a fitting).

While tracing the pathways in the event tree, note that a release may or may not be accompanied by immediate ignition. With immediate ignition, that is, following the left branch of the tree, a jet flame will result if the release is from a relatively small opening. Such a release could be either vapor or liquid and, if liquid, could also involve flashing of liquid into vapor and/or accumulation of liquid. If the release is the result of a major spill and there is immediate ignition, the result is usually a fireball, the size of which is strongly affected by the amount of flash vaporization and liquid entrainment that occurs upon release.

If ignition does not occur immediately upon release, the right branch of the event tree is followed. Releases through relief valves, either accidental or intentional, may

Dr. Craig L. Beyler is the technical director of Hughes Associates, Fire Science and Engineering. He was the founding editor of the *Journal of Fire Protection Engineering* and serves on a wide range of committees in the fire safety community. This chapter is based on the chapter written by Krishna Mudan and Paul Croce for the first and second editions of the SFPE Handbook of Fire Protection Engineering.

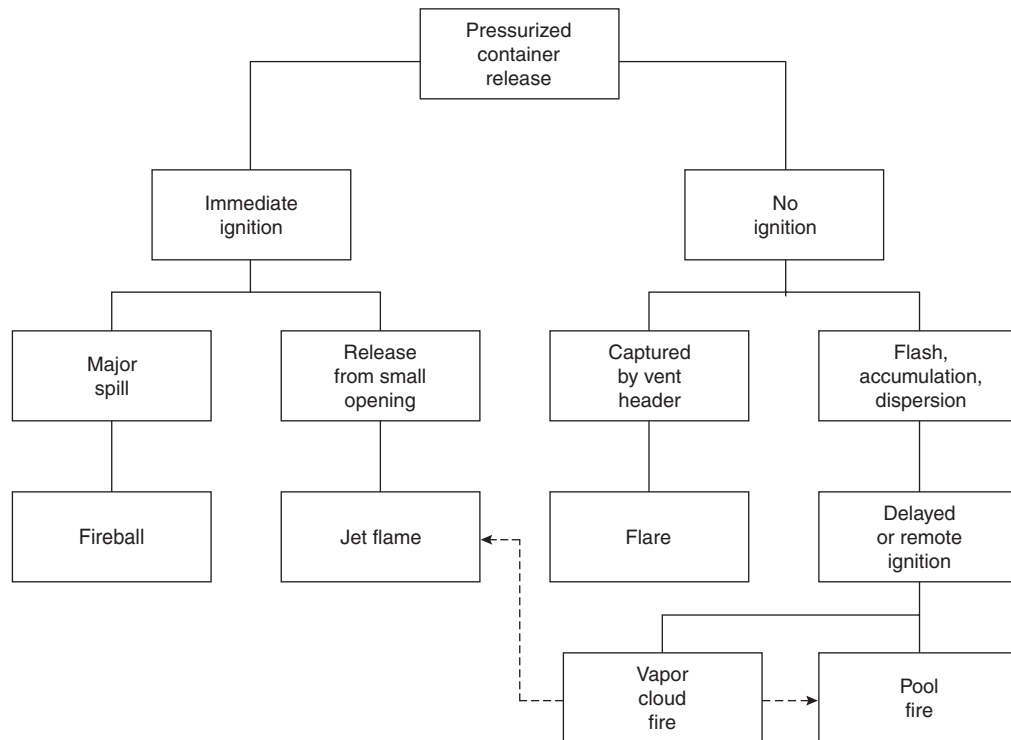


Figure 3-11.1. Example event tree for release of flammable material.

be captured by a vent header system and directed to a flare. Flares must accordingly be designed for expected accident or operational flow capacities, and the design should include consideration of resulting hazard zones.

If the unignited release is to the atmosphere, the spill will be accompanied by flash vaporization, liquid entrainment, accumulation, and/or vapor dispersion. A delayed local ignition following accumulation results in a pool fire whose characteristics are strongly influenced by the geometry of containment (or lack thereof).

Absence of a local ignition source, either immediate or delayed, allows a vapor cloud to form as the vapors disperse downwind. A portion of this vapor cloud will be flammable, and depending upon the size of the release, the flammable region could extend significantly downwind. A remote ignition source can ignite the cloud, resulting in a vapor cloud fire that burns from the point of ignition back toward the source of the cloud, that is, the release point. Note also that the event tree shows dashed pathways from the vapor cloud fire to a pool fire or a jet flame. This is intended to show that the transient burning of the vapor cloud fire back to the release point can initiate a subsequent steady burning jet flame or pool fire, and consideration must be given to potential impacts from both types of fire.

Finally, this event tree represents an example of potential pathways leading to hazardous open fires. Scenarios will be encountered that will be similar to the event tree depicted in Figure 3-11.1 or to parts thereof, but it is important to recognize that in all cases, the event tree

must be structured to reflect the actual scenario under consideration.

Hydrocarbon Pool Fires

The thermal radiation hazards from hydrocarbon pool fires depend on a number of parameters, including the composition of the hydrocarbon, the size and shape of the pool, the duration of the fire, its proximity to the object at risk, and the thermal characteristics of the object exposed to the fire. The objectives of this section of the chapter are to review available techniques for determining the thermal radiation hazards from liquid hydrocarbon pool fires under various credible spill conditions.

The state of the art of predicting the thermal environment of hydrocarbon pool fires consists essentially of semiempirical methods, some of which are based on experimental data. Needless to say, such semiempirical methods are always subject to uncertainties.

Estimating the thermal radiation field surrounding a fire involves the following three major steps:

1. Geometric characterization of the pool fire; that is, the determination of burning rate and the physical dimensions of the fire. In calculating thermal radiation, the size of the fire implies the time-averaged size of the visible envelope.
2. Characterization of the radiative properties of the fire; that is, the determination of the average emissive power of the flames. The intensity of thermal radiation

emitted by pool fires depends upon a number of parameters, including fuel type, fire size, flame temperature, and composition. The major sources of emission in large hydrocarbon fires are the water vapor, carbon dioxide, and soot.

3. Calculation of radiant flux at a given location. This can be accomplished once the geometry of the fire, its radiation characteristics, and the location, geometry, and orientation of the receiver are known. For large distances (hundreds of meters), the absorption of thermal radiation in the intervening atmosphere becomes appreciable. This is dependent on the pathlength, flame temperature, and the relative humidity in the atmosphere.

References 1–7 provide general information concerning radiation heat transfer relevant to pool fires, and References 8–39 are specific studies of pool fire radiation heat transfer underpinning the methods of analysis.

Pool Fire Geometry

The flame geometry for the solid flame model is generally determined by assuming that the flame is a solid, gray emitter having a regular well-defined shape such as a circular or a tilted cylinder. The dimension of the flame area characterized by the flame base diameter, visible flame height, and the flame tilt. The flame diameter is dependent on the pool size (spill volume and/or spill rate). The flame height appears to depend on the flame diameter and the burning rate. These factors, which influence the flame geometry, are discussed in this chapter.

The pool fire geometry is determined by the manner and location of the fuel release. Section 2, Chapter 7 provides detailed means for predictions of the extent of the spill or pool, the spread of flame over the fuel surface, and the resulting burning rate. This information will be required for determination of the flame height and the radiation analyses that follow.

The height or length of a flame is a significant indicator of hazard since it directly relates to flame heat transfer and the propensity to impact surrounding objects. A plume of hot gases rises above a flame, the temperature, velocity and width of this plume change as it rises due to the mixing of the plume with the surrounding. The height and temperature of the flame are important in estimating the ignition of adjacent combustibles. Above the fuel source, the flaming region is characterized by high temperature and is generally luminous. Flame from the pool fires fluctuate periodically so that the tip of the flame will be significantly different from the length of the continuous combustion (or luminous) region. Consequently, flame height has been defined by various criteria in order to correlate data. Investigators have used the degree of luminous flame intermittency, flame temperature, or visible estimations. Hence, correlations for flame height could have inherent variation with the instantaneous flame length due to factors involving flame fluctuation and flame definition. For additional information, see Section 2, Chapter 1, "Fire Plumes."

Flame length: Many investigators have developed correlations for turbulent flame lengths in a quiescent air en-

vironment. Most are based on the dimensional analysis of experimental data; some are based on approximate theoretical models involving some empirical factors.

Thomas⁴⁰ has developed a correlation for the mean visible height of turbulent diffusion flames (in the absence of wind), based on the experimental data of laboratory-scale wood crib fires and dimensional analysis considerations. The correlation for a circular fire is

$$\frac{H}{D} = 42 \left(\frac{\dot{m}''}{\rho_a \sqrt{gD}} \right)^{0.61} \quad (1)$$

where \dot{m}'' = mass burning rate per unit pool area (in kg/m²·s) and ρ_a = ambient air density (kg/m³). For rectangular fires of small aspect ratios, an area equivalent to a circular fire diameter may be used.

The presence of wind may also alter the visible length of flames. The correlation developed by Thomas,⁴⁰ based on wood crib fires, is

$$\frac{H}{D} = 55 \left(\frac{\dot{m}''}{\rho_a \sqrt{gD}} \right)^{0.67} u^{*-0.21} \quad (2)$$

where u^* is the nondimensional wind velocity given by

$$u^* = \frac{u_w}{(g\dot{m}'' D / \rho_v)^{1/3}} \quad (3)$$

Moorhouse³⁴ conducted several large-scale tests of liquified natural gas (LNG) pool fires. The crosswind and downwind motion picture data were analyzed to determine the flame length. The correlation given by Moorhouse is

$$\frac{H}{D} = 62 \left(\frac{\dot{m}''}{\rho_a \sqrt{gD}} \right)^{0.254} u_{10}^{*-0.044} \quad (4)$$

where u_{10}^* is the nondimensional wind speed determined using Equation 3 with measured wind speed at a height of 10 m. In both Equations 14 and 16, u_{10}^* is assigned a value of unity if it is less than 1.

Heskestad^{41,42} has correlated data from a wide variety of sources including pool fires and buoyant jets using the following equation:

$$\frac{H}{D} = 0.235 \frac{\dot{Q}^{2/5}}{D} - 1.02 \quad (5)$$

where \dot{Q} is measured in kW. It can be shown that $\dot{Q}^{2/5}/D$ is proportional to the nondimensional burning rate, $\dot{m}''/(\rho_a \sqrt{gD})$, raised to the 2/5 power.

Figure 3-11.2 shows the flame height to diameter ratio, H/D , as a function of the nondimensional burning rate, $\dot{m}''/(\rho_a \sqrt{gD})$, for a range of pool fire data assembled by Mudan.¹⁴ In addition, the Thomas, Moorhouse, and Heskestad flame heights are shown.

Flame tilt angle: Flame length under wind conditions have been studied by several investigators. Figure 3-11.3 illustrates a general schematic for the windblown flame. The pool fire flame follows a curved trajectory, and the angle, θ , approximates the trajectory. The vertical and hor-

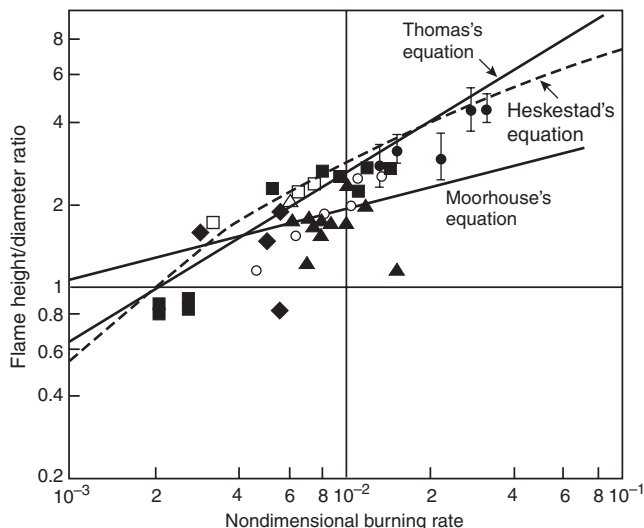


Figure 3-11.2. Flame heights for various hydrocarbon pool fires on land and water.¹⁴

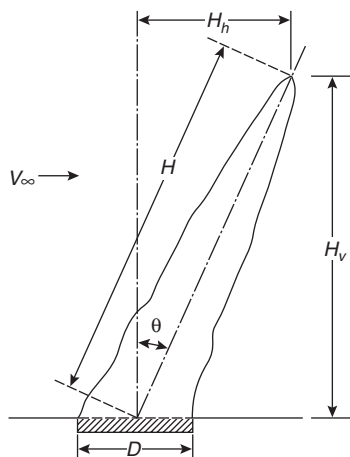


Figure 3-11.3. Flame inclinations due to wind.

horizontal components of the flame length measured along the angle are also shown in the figure.

Walker and Sliepcwick⁴³ and Emori and Saito⁴⁴ derived correlations from small-scale experiments. They correlated the angle of inclination as a function of cross-wind velocity, v_∞ , but the results do not compare well with larger-scale data.

Thomas⁴⁰ developed the following correlation for flame tilt angle, θ , based on the data from two-dimensional wood cribs:

$$\cos \theta = 0.7 \left[\frac{u_w}{(gmr'D/\rho_a)^{1/3}} \right]^{-0.49} \quad (6)$$

Based on the measured values, the American Gas Association (AGA)³⁹ proposed the following correlation to determine the flame tilt angle, θ :

$$\cos \theta = \begin{cases} 1 & \text{for } u^* \leq 1 \\ 1/\sqrt{u^*} & \text{for } u^* \geq 1 \end{cases} \quad (7)$$

where u^* is the nondimensional wind velocity given by Equation 3 with a wind velocity measured at a height of 1.6 m. In Figure 3-11.4, a comparison of observed flame tilt angle is shown for various hydrocarbons pool fires with correlations given by Equations 6 and 7. Although there is considerable scatter in the measured flame tilt, the correlation given by Equation 7 represents the flame tilt most accurately. Defaveri et al.⁴⁵ have studied the effects of wind on high-momentum flames.

Geometry of trench fires: Trench fires have received little attention to date. Small laboratory-scale *n*-hexane and heptane fires have been conducted under wind-free conditions. Moorhouse¹⁶ conducted limited large-scale LNG trench fires with aspect ratios ranging from 1.5 to 2.5. More recently, Mudan and Croce¹⁷ reported on large-scale tests with LNG trenches having aspect ratios of up to 30.0. All the data seem to indicate that flame geometry of trench fires is more sensitive to wind conditions than is flame geometry of conventional pool fires. Flame height was found to be a strong function of trench width rather than length. Indeed, for large aspect ratios, the trench fire seemed to break up into small flamelets having a typical base dimension of the trench width, W .

Based on an extensive analysis of the motion picture data of LNG trench fires, Mudan and Croce¹⁷ suggested that the trench fire geometry can be represented by a modified Froude number. The definition of the modified Froude number is

$$Fr' = \frac{u_w}{2\sqrt{gW}} \quad (8)$$

where

u_w = wind speed, m/s

W = trench width, m

g = acceleration due to gravity, m/s²

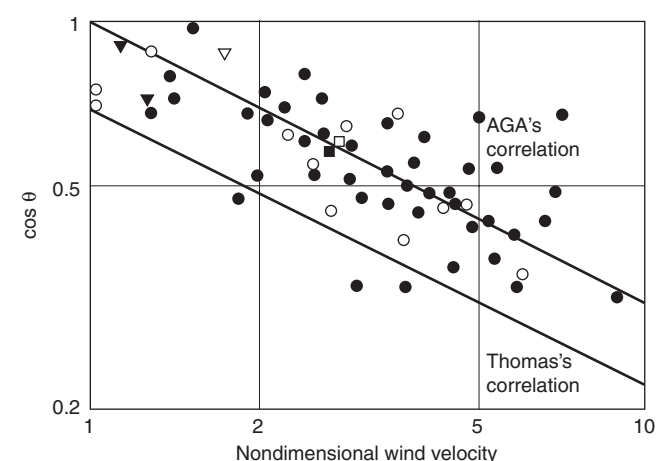


Figure 3-11.4. Relationship between nondimensional wind velocity and flame tilt angle.¹⁴

The measured flame length as a function of the modified Froude number is shown in Figure 3-11.5. The flame length correlation is

$$\frac{H}{W} = \begin{cases} 2.2 & Fr' \geq 0.25 \\ 0.88(Fr')^{-0.65} & 0.25 < Fr' \leq 0.1 \\ 4.0 & Fr' \leq 0.1 \end{cases} \quad (9)$$

The flame drag and flame tilt are given by the following expressions.

Flame drag:

$$\frac{W'}{W} = \begin{cases} 3.5 & Fr' \geq 0.25 \\ 23.3(Fr')^{1.37} & 0.25 < Fr' \leq 0.1 \\ 1 & Fr' \leq 0.1 \end{cases} \quad (10)$$

Flame tilt:

$$\cos \theta = \begin{cases} 0.56 & Fr' \geq 0.25 \\ 0.36(Fr')^{-0.32} & 0.25 \leq Fr' \leq 0.042 \\ 1 & Fr' \leq 0.042 \end{cases} \quad (11)$$

The essential features of the suggested correlations defined by Equations 9, 10, and 11 are

1. The flame geometry (length, drag, and tilt) is independent of the ambient conditions for Froude numbers greater than about 0.25. For example, the critical wind speed for a 4-m-wide trench will be about 3 m/s. For wind speeds greater than 3 m/s, the trench fire geometry does not change significantly.
2. For very low Froude numbers (extremely low-wind to no-wind cases), the flame geometry parameters are dependent on the trench width.
3. For in-between Froude numbers, the flame length decreases with increasing wind speed and the flame drag and tilt increase.

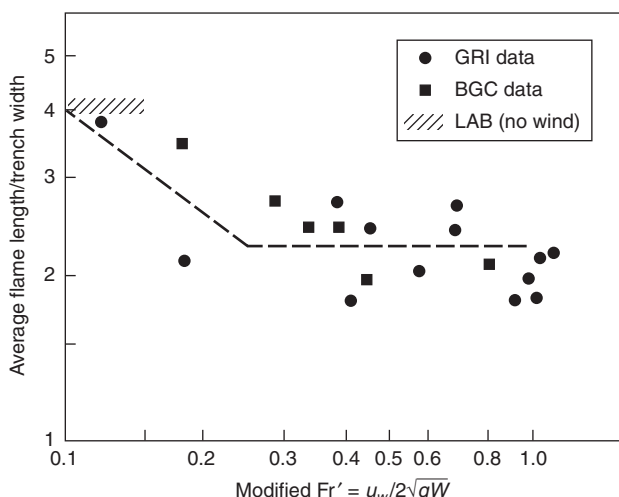


Figure 3-11.5. Nondimensional flame height as a function of the Froude number.¹⁷

Caution must be exercised in using the correlations given by Equations 9, 10, and 11 since they are based only on LNG fire data.

Thermal Radiation Hazards from Liquid Hydrocarbon Pool Fires

Calculation Procedure—Flame Radiation to External Target

This section provides methods for assessing the impact of radiation from pool fires to potential targets. The goal is to provide methods for calculating safe separation distances between fire sources and potential targets that would be damaged or adversely affected by radiation from the fire. The methods in this section include a range of levels of detail and rigor. Some methods are most appropriate for very crude initial hazard assessments, while the more detailed methods are capable of better predictions though requiring more engineering effort. Where separations exist and a simple method demonstrates that the separation is far more than required for safety, it may not be necessary to perform a more rigorous analysis. In other more critical applications, the highest accuracy methods available are required.

The methods presented in this section have been evaluated and included by the Society of Fire Protection Engineers (SFPE) in *Engineering Guide on Pool Fire Radiation*.⁴⁶ In that reference, the methods are described fully, the assumptions inherent in the methods are identified, limits of applicability are assessed, and available input data and data sources are identified. The accuracy of the methods are examined through comparisons of the methods with available experimental data.

Calculation Methods

Estimating the thermal radiation incident upon an object involves the following three major steps:

- (1) Determine the geometric characteristics of the pool fire, that is, determine the burning rate and physical dimensions of the fire.
- (2) Determine thermal radiation characteristics of the fire.
- (3) Calculate the incident radiant flux at the target location.

It is extremely important that a single methodology be used for all three steps of this process. The available methods include empirical elements that, if indiscriminately used, can lead to unpredictable results. Because of this fact, each method is described fully and independently from other methods, even when some elements of the analysis appear similar.

Four methods for estimating radiation from pool fires were identified and evaluated.⁴⁶ Two methods are generally classifiable as simple screening methods and two are more detailed procedures. The screening methods include a very simple correlation developed by Shokri and Beyler,⁴⁷ and the classical point source model. The more detailed procedures are those developed by Shokri and Beyler⁴⁷ and by Mudan.¹⁴

Screening Methods

Shokri and Beyler correlation: Based on experimental data from large-scale pool fire experiments, Shokri and Beyler⁴⁷ developed a simple correlation of radiant heat flux at ground level as a function of the radial position of a vertical target. The incident heat-flux correlation (in kW/m^2) is given by

$$\dot{q}'' = 15.4 \left(\frac{L}{D} \right)^{-1.59} \quad (12)$$

where D is the diameter of the pool fire and L is the distance from the center of the pool fire to the target edge. Note that the edge of the circular pool has a value of L/D of 0.5. While this correlation was determined from circular pool fires, an equivalent-area circular source can be used for noncircular pools with an aspect ratio of approximately one. The equivalent diameter is given by

$$D = \sqrt{\frac{4A}{\pi}} \quad (13)$$

where A is the surface area of the noncircular pool.

This method assumes that the pool is circular or nearly circular. It assumes that the target is vertical and located at ground level. It is known that the radiant heat flux is maximized near the midheight of the radiating source and that a target facing the center of radiation will give the maximum heat flux at a given location. As such, at heights above ground level the radiant flux is expected to exceed that given by Equation 12.

Figure 3-11.6 shows a semilogarithmic plot of the data from Hugglund and Persson,¹⁸ Yamaguchi and

Wakasa,¹⁹ Seeger,²⁰ Yumoto,²¹ Dayan and Tien,²² and May and McQueen²³ with the correlation given by Equation 12. Figure 3-11.7 shows a comparison of the measured and predicted heat fluxes for the original data included in Figure 3-11.6 as well as additional data from the literature that were not used to develop the correlation.

A safety factor of 2 is recommended for use with Equation 12.⁴⁶ Figure 3-11.8 shows a comparison of all the available data to the predictions using Equation 12 with a safety factor of 2. Figure 3-11.8 clearly shows that essentially all the data is overpredicted by Equation 12 with a safety factor of 2 applied. The safety factor of 2 is a recommendation for use in design applications. Where a realistic result is required, no safety factor should be applied.

Point source model: To predict the thermal radiation field of flames, it is customary to model the flame by a point source located at the center of real flame. The point source model is the simplest configurational model of a radiant source. Whereas more realistic radiator shapes give rise to very complex configuration factor equations, the point source model provides a simple relationship that varies with the inverse square of the distance, R . For an actual point source of radiation or a spherical source of radiation, the distance R is just the distance from the point or from the center of the sphere to the target. See Figure 3-11.9 for a graphic representation of relevant nomenclature.

The point source model is widely used (see Drysdale⁴⁸ for example), though it has really never been developed as a rigorous methodology. The method as presented and evaluated here follows the development as given by Drysdale.⁴⁸

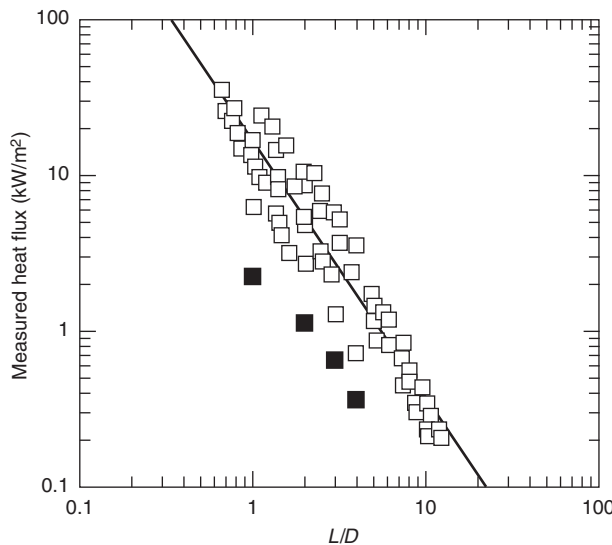


Figure 3-11.6. Measured incident radiant heat flux at ground level to a vertical target as a function of the distance from the pool center to the target normalized by the pool diameter. Solid symbols are 50-m-diameter kerosene data. The solid line is Equation 12.⁴⁷

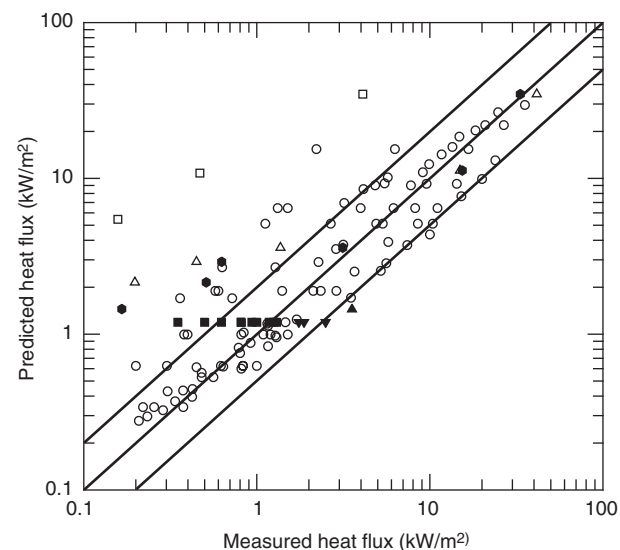


Figure 3-11.7. Comparison of measured and calculated radiative heat flux from large pool fires using the Shokri and Beyler correlation (Equation 12). Solid lines indicate equality of measured and predicted heat fluxes based on the correlation developed by Shokri and Beyler.⁴⁷

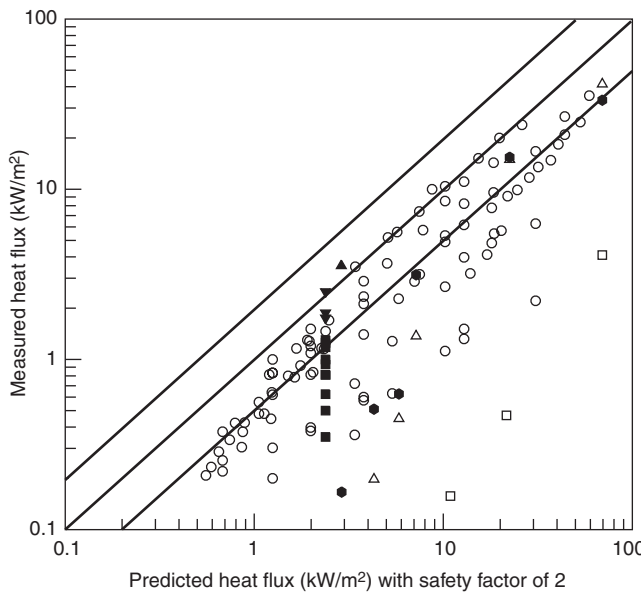


Figure 3-11.8. Comparison of measured and calculated radiative heat flux from large pool fires using the Shokri and Beyler correlation (Equation 12) and a safety factor of 2. Solid lines indicate equality of measured and predicted heat fluxes based on the correlation developed by Shokri and Beyler⁴⁷ with a safety factor of 2.

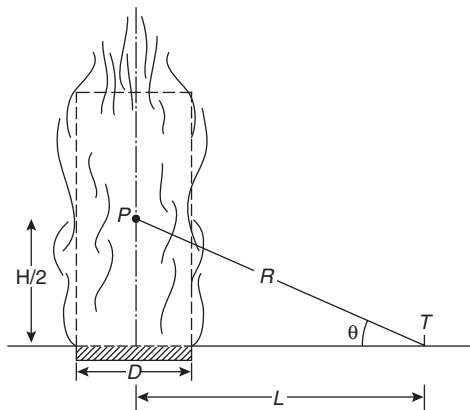


Figure 3-11.9. Nomenclature for use with the point source model.

The incident radiative heat flux is given by

$$\dot{q}'' = \frac{\dot{Q}_r \cos \theta}{4\pi R^2} \quad (14)$$

where

\dot{Q}_r = the total radiative energy output of the fire

θ = the angle between the normal to the target and the line of sight from the target to the point source location

R = the distance from the point source to the target

The location of the equivalent point source, P , is at the center of the pool fire and at the midheight of the flame. The flame height in meters is given by the Heskstad⁴¹ correlation, Equation 5:

$$H = 0.235\dot{Q}^{2/5} - 1.02D \quad (5)$$

where \dot{Q} is the heat release of the pool fire in kW and D is the diameter of the pool fire in meters.

If the pool has a length-to-width ratio near one, an equivalent diameter can be used for noncircular pools in the determination of the flame height. The equivalent diameter is given by Equation 13:

$$D = \sqrt{\frac{4A}{\pi}} \quad (13)$$

where A is the surface area of the noncircular pool.

The distance from the point source location to the target location is given by the Pythagorean theorem:

$$R = \sqrt{L^2 + H_T^2} \quad (15)$$

where H_T is the height of the target relative to the height of the equivalent point source at $H/2$, and L is the horizontal distance from center of the pool to the target.

For a target on the ground, $H_T = H/2$. For a target at the midheight of the flame, $H_T = 0$.

The radiative energy output is given by the radiative fraction, χ_r , multiplied by the total heat release rate:

$$\dot{Q}_r = \chi_r \dot{Q} = (0.21 - 0.0034D)\dot{Q} \quad (16)$$

where the radiative fraction is a function of both the fuel and the pool area and D is the pool diameter in meters.

The radiative fraction deduced from the experiments⁴⁶ is plotted in Figure 3-11.10 as a function of pool diameter, D . The radiative fractions were determined using the point source method for the most remote data point for each experiment. The curve fit used in Equation 16 above is also shown in Figure 3-11.10. At pool diameters above 50 m, the radiative fraction for 50 m should be used.

Estimating the thermal radiation from a pool fire to a target involves the following steps based on the point source model:

1. Determine the heat release rate, \dot{Q} .
2. Determine the diameter of the pool fire, or use Equation 13 for noncircular pools.
3. Determine the location of the equivalent point source, P . The equivalent point source is on the centerline of the pool at a height equal to one-half the flame height given by Equation 5.
4. Calculate the distance, R , from the equivalent point source location to the target location using Equation 15.
5. Determine the radiative output of the flame from Equation 16.
6. Calculate the radiative heat flux to the target using Equation 14.

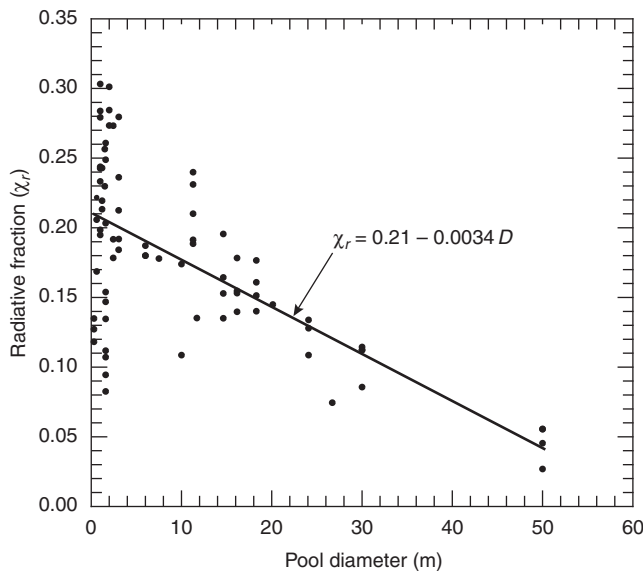


Figure 3-11.10. Radiative fraction (χ_r) as a function of pool diameter. The solid line is a curve fit to the data.⁴⁶

Figure 3-11.11 shows a comparison of all the available data with the prediction of the point source model.⁴⁶ The lines shown on the plot reflect predictions that are one-half and twice those of the measured data. At heat fluxes above about 5 kW/m², there are systematic, nonconservative results.

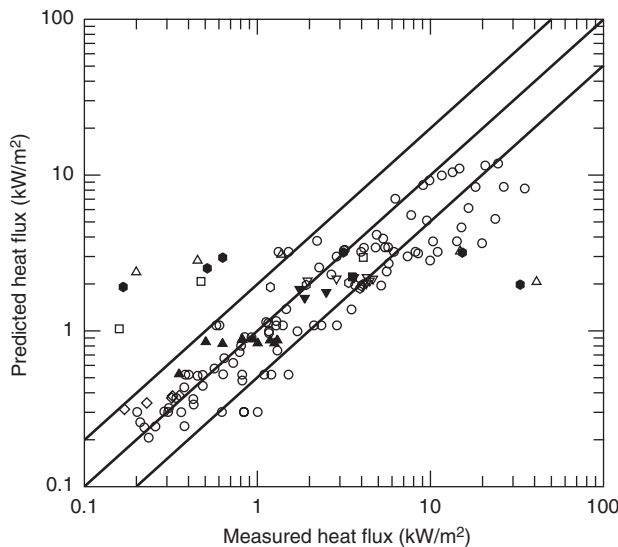


Figure 3-11.11. Comparison of measured and calculated radiative heat flux from large pool fires using the point source model. Solid lines indicate equality of measured and predicted heat fluxes based on the point source model.

The point source configuration factor is known to be a very simplistic representation of a pool fire. It is a correct assumption at large distances from the fire. A theoretical analysis of radiation from a small pool fire by Modak⁴⁹ indicated that the point source model is within 5 percent of the correct incident heat flux when $L/D > 2.5$. This result is, however, dependent upon the specific flame modeled and was not derived from experimental data. The method is known to underpredict incident heat fluxes at closer locations (e.g., see Drysdale⁴⁸). The poor performance at heat fluxes above 5 kW/m² indicate that the point source model is not a good choice under conditions where ignition of combustibles is to be considered.

A safety factor of 2 is recommended for use with the point source model at heat fluxes less than 5 kW/m². Figure 3-11.12 is a comparison of predicted and measured heat fluxes with the inclusion of the recommended factor of safety. The vertical line is located at the maximum heat flux for which the point source model is recommended for use. Figure 3-11.12 clearly shows that essentially all the data is overpredicted by the point source model with a safety factor of 2 applied for heat fluxes less than 5 kW/m². The safety factor of 2 is a recommendation for use in design applications. Where a realistic result is required, no safety factor should be applied.

Detailed Methods

Shokri and Beyler: Shokri and Beyler⁴⁷ have described a method for prediction of radiation from pool fires based on the pool fire radiation data available in the open literature. They correlated experimental data of flame radia-

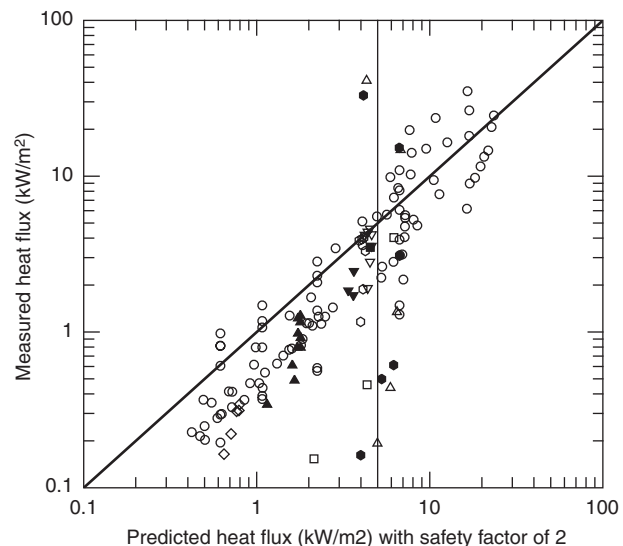


Figure 3-11.12. Comparison of measured and calculated radiative heat flux from large pool fires using the point source model and a safety factor of 2. Solid lines indicate equality of measured and predicted heat fluxes based on the point source model.

tion to external targets in terms of an average effective emissive power of the flame. The flame is assumed to be a cylindrical, blackbody, homogeneous radiator with an average emissive power.

Shokri and Beyler⁴⁷ have treated radiant heat transfer from a source to a target based on the concept of the angle factor, also variously known as the shape, geometrical, configuration, or view factors, including those given by many authors.^{1,3,50-57} and the incident radiative flux (in kW/m^2) to a target outside the flame, \dot{q}'' , is given by

$$\dot{q}'' = EF_{12} \quad (17)$$

where E is the emissive power of the pool fire flame, kW/m^2 , and F_{12} is the view or configuration factor between the target and the flame.

The configuration factor is a function of the target location, the flame height and diameter, and lies between zero and one. When a target is very close to a flame, the configuration factor approaches one since everything viewed by the target is the flame. The flame is idealized as a cylinder with a diameter equal to the pool diameter, D , and a height equal to the flame height, H_f . If the pool has a length-to-width ratio near one, an equivalent-area circular source can be used for noncircular pools in the determination of flame height. For noncircular pools, the effective diameter will be defined as the diameter of a circular pool with an area equal to the actual pool area given by Equation 13:

$$D = \sqrt{\frac{4A}{\pi}} \quad (13)$$

where A is the surface area of the noncircular pool.

Flame height of the pool fire flame is determined using the Heskstad⁴¹ correlation given by Equation 17:

$$H = 0.235\dot{Q}^{2/5} - 1.02D \quad (5)$$

where

H = flame height,

\dot{Q} = heat release of the pool fire, kW

D = diameter of the pool fire, m

Given the diameter and height of the flame, the view factor, F_{12} , is determined using Equation 18 applicable to cylindrical radiation sources. For horizontal and vertical target orientations, expressions for estimating the configuration factor are found in Equations 18a and 18b, respectively.

$$F_{12,H} = \frac{(B - 1/S)}{\pi\sqrt{B^2 - 1}} \tan^{-1} \sqrt{\frac{(B + 1)(S - 1)}{(B - 1)(S + 1)}} - \frac{(A - 1/S)}{\pi\sqrt{A^2 - 1}} \tan^{-1} \sqrt{\frac{(A + 1)(S - 1)}{(A - 1)(S + 1)}} \quad (18a)$$

$$F_{12,V} = \frac{1}{\pi S} \tan^{-1} \left(\frac{h}{\sqrt{S^2 - 1}} \right) - \frac{h}{\pi S} \tan^{-1} \sqrt{\frac{(S - 1)}{(S + 1)}} + \frac{Ah}{\pi S \sqrt{A^2 - 1}} \tan^{-1} \sqrt{\frac{(A + 1)(S - 1)}{(A - 1)(S + 1)}} \quad (18b)$$

where

$$A = \frac{h^2 + S^2 + 1}{2S}, \quad B = \frac{1 + S^2}{2S}$$

$$S = \frac{2L}{D}, \quad h = \frac{2H}{D}$$

and

L = distance between the center of the cylinder to the target

H = height of the cylinder

D = cylinder diameter

See Figure 3-11.13, parts (a) and (b) for an illustration of the nomenclature.

The maximum configuration or shape factor at a point is given by the vectorial sum of the horizontal and vertical view factors:

$$F_{12,\max} = \sqrt{F_{12,H}^2 + F_{12,V}^2} \quad (19)$$

Precalculated maximum view factors are shown in Figures 3-11.14(a) to 3-11.14(e). Each figure gives the maximum view factor for a flame of a particular flame height to pool radius ratio (H/R_p): 2, 3, 4, 5, and 6, respectively.

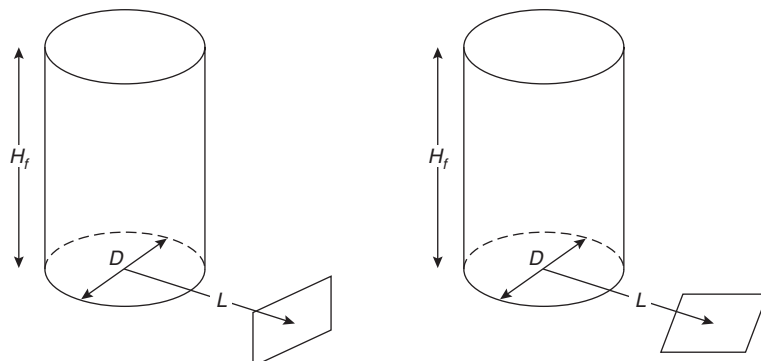


Figure 3-11.13(a). Cylindrical flame-shape configuration factor geometry for vertical and horizontal targets at ground level.

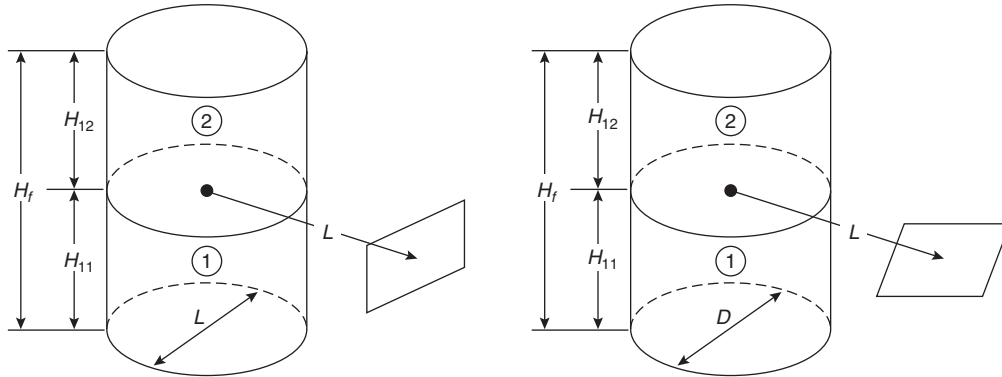


Figure 3-11.13(b). Two-cylinder representations of the configuration factor for target above ground level.

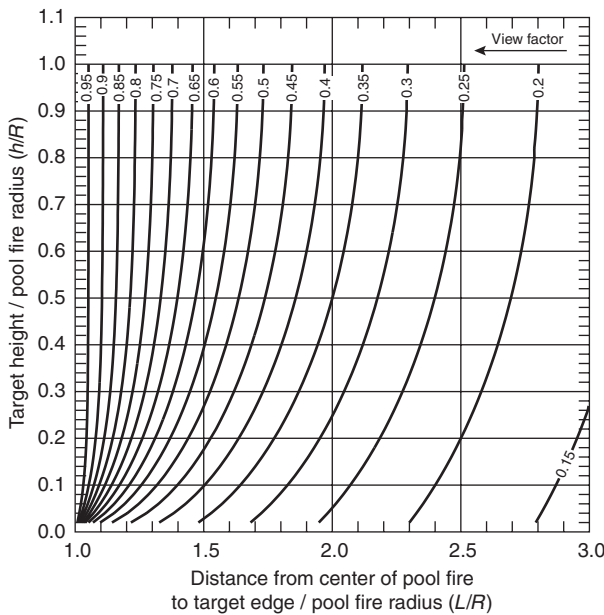


Figure 3-11.14(a). Maximum configuration factor for a flame height to pool fire radius ratio $H/R_p = 2$.

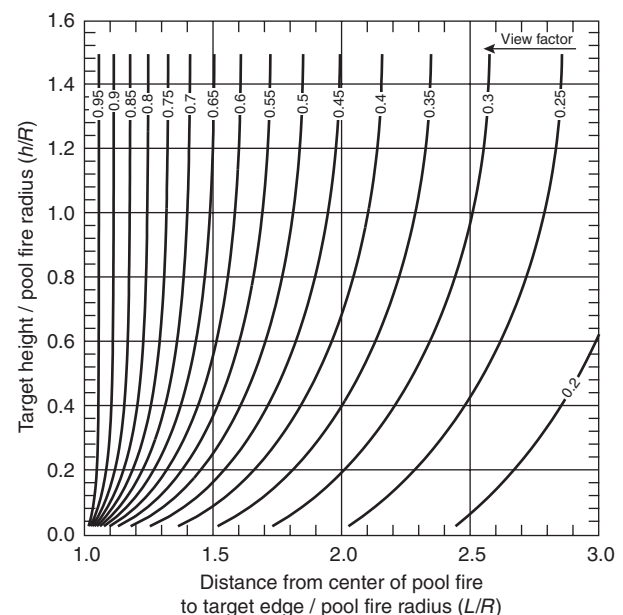


Figure 3-11.14(b). Maximum configuration factor for flame height to pool fire radius of ratio $H/R_p = 3$.

The target location is defined in each figure by the ratio of the target height to the pool radius, and the ratio of the distance of the target from the pool center to the pool radius. The view factors are represented as contours. The figures only include target locations up to one-half the flame height. The curves for target heights above one-half the flame height are symmetric about the half-height and as such need not be included. For example, the view factor for a target at one-fourth of the flame height and three-fourths of the flame height are identical.

Shokri and Beyler⁴⁷ determined the effective emissive power of the flame by fitting experimental measurements of radiant heat flux from pool fires to external targets. The effective emissive power of the pool fire in terms of effective pool diameter is given by the following correlation:

$$E = 58(10^{-0.00823D}) \quad (20)$$

This represents the average emissive power over the whole of the flame and is significantly less than the emissive powers that can be attained locally. The emissive power is reduced with increasing pool diameter due to the increasing prominence of black smoke outside the flame that obscures the radiation from the luminous flame. Figure 3-11.15 is a comparison of Equation 20 with the data used by Shokri and Beyler⁴⁷ to develop Equation 20.

Figure 3-11.16 shows a comparison of the predicted and measured heat fluxes, using the best fit emissive power for each experiment (the value plotted in Figure 3-11.15). Figure 3-11.16 shows that the cylindrical model is an excellent representation of the view factor over a wide range of conditions. Figures 3-11.15 and 3-11.16 together illustrate that the major uncertainty is in the definition of the emissive power and not in the view factor model. Figure 3-11.17 shows the overall performance of the model.

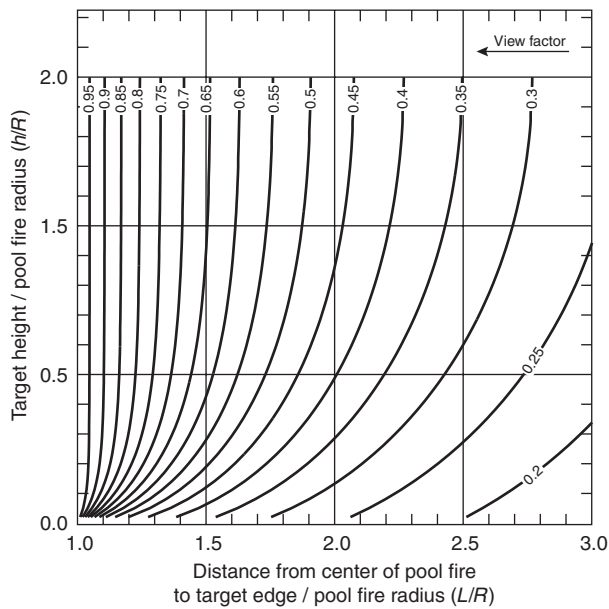


Figure 3-11.14(c). Maximum view factor for a flame height to pool fire radius ratio $H_f/R_p = 4$.

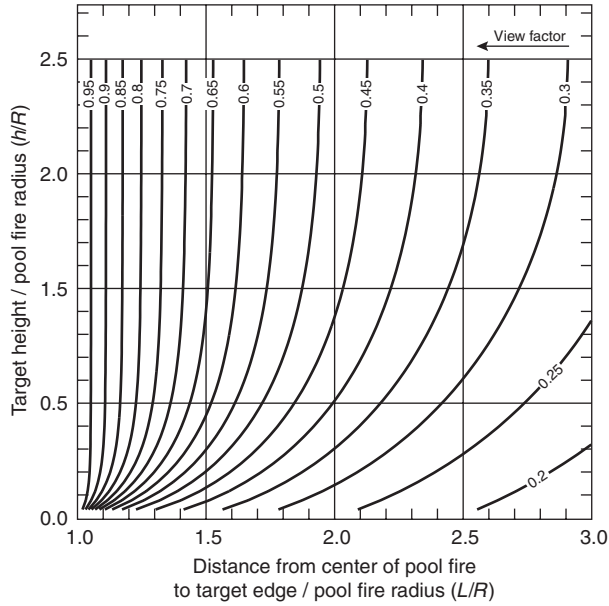


Figure 3-11.14(d). Maximum configuration factor for a flame height to pool fire radius ratio $H/R_p = 5$.

Summary of the procedure for the Shokri and Beyler pool fire radiation method: Estimating the thermal radiation field surrounding a fire involves the following steps based on the method developed by Shokri and Beyler.⁴⁷

1. Determine the heat release rate, \dot{Q} .
2. Determine the height of the pool fire flame from Equation 15.
3. Calculate the view factor from Equation 18 (and Equation 19 if needed). If the target is above ground level, then a two-cylinder representation is required. Alter-

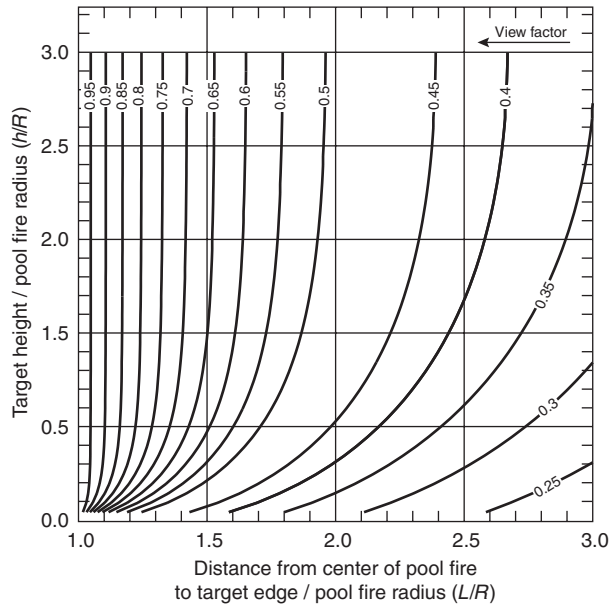


Figure 3-11.14(e). Maximum configuration factor for a flame height to pool fire radius ratio $H/R_p = 6$.

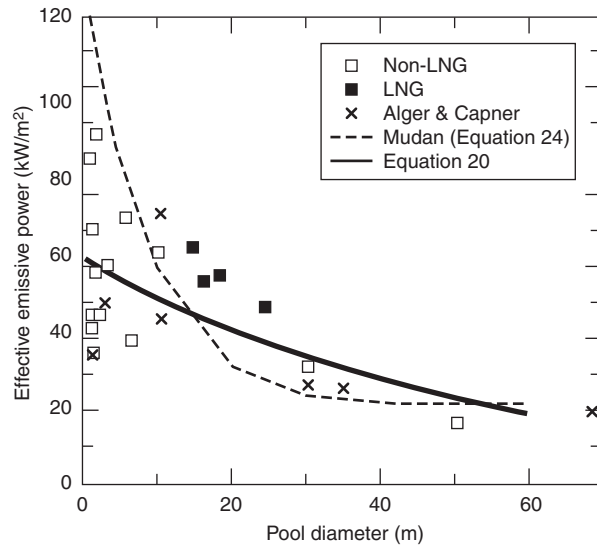


Figure 3-11.15. Effective emissive power as a function of the pool diameter determined by Shokri and Beyler.⁴⁷ The solid line is Equation 20 and the dashed line is Equation 24.

natively, the precalculated view factors in Figure 3-11.14 may be used.

4. Determine the effective emissive power of the flame from Equation 20.
5. Calculate the radiative heat flux to the target using Equation 17.

Factor of safety: A safety factor of 2 is recommended for use with the Shokri and Beyler method.⁴⁶ Since this method is most applicable at heat fluxes greater than 5 kW/m², the recommended factor of safety is only applicable for heat fluxes above this level. Figure 3-11.18 is a

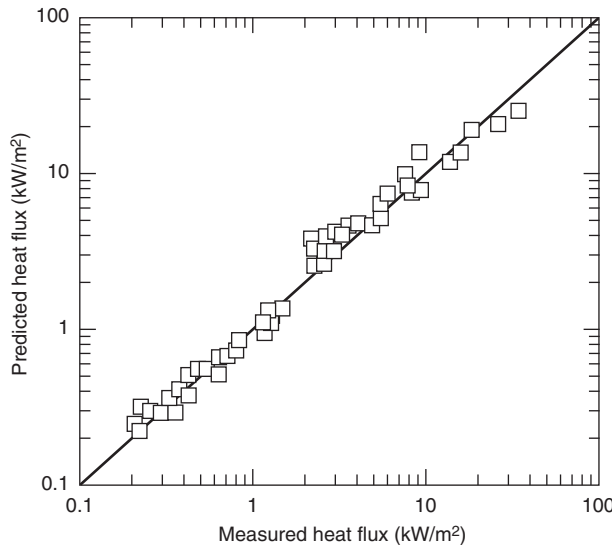


Figure 3-11.16. Comparison of measured and calculated incident radiant heat flux using effective emissive powers. The solid line indicates equality of the measured and predicted heat fluxes based on the method developed by Shokri and Beyler.⁴⁷

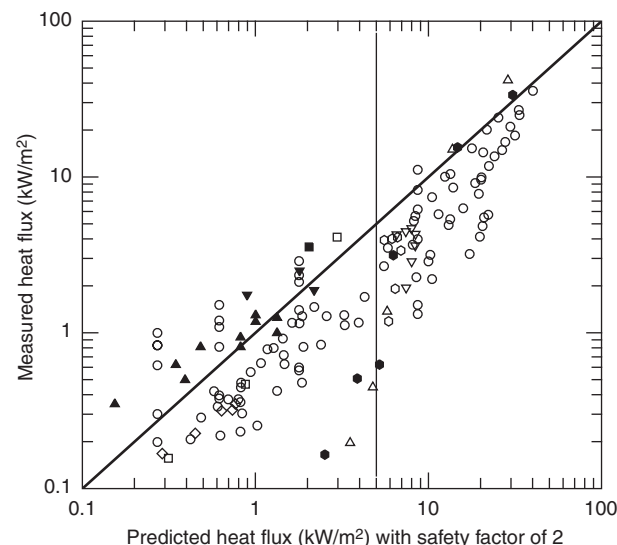


Figure 3-11.18. Comparison of measured and calculated radiative heat flux from large pool fires using the detailed method developed by Shokri and Beyler and a safety factor of 2. Solid lines indicate equality of measured and predicted heat fluxes based on the detailed method developed by Shokri and Beyler⁴⁷ with a safety factor of 2.

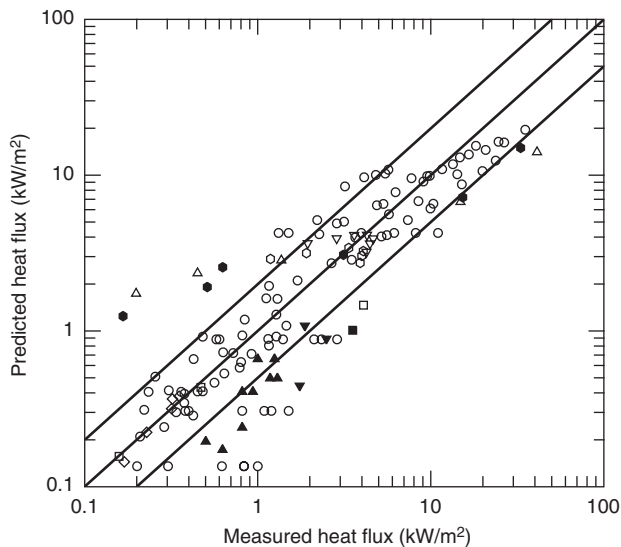


Figure 3-11.17. Comparison of measured and calculated radiative heat flux from large pool fires using the detailed method developed by Shokri and Beyler.⁴⁷ Solid lines indicate equality of measured and predicted heat fluxes based on the detailed method developed by Shokri and Beyler.⁴⁷

comparison of predicted and measured heat fluxes with the inclusion of the recommended factor of safety. The vertical line is located at the minimum heat flux for which the Shokri and Beyler model is recommended for use. Figure 3-11.18 clearly shows that essentially all of the data are overpredicted by the Shokri and Beyler model with a safety factor of 2 applied for heat fluxes greater than 5 kW/m². The safety factor of 2 is a recommendation for use in design applications. Where a realistic result is required, no safety factor should be applied.

Mudan method: Mudan¹⁴ has presented a method for estimating thermal radiation from pool fires for no-wind conditions and for windblown flames. The thermal radiation intensity to an element outside the flame envelope is given by the following equation:

$$\dot{q}'' = EF_{12}\tau \quad (21)$$

where

E = average emissive power at flame surface, kW/m²

F_{12} = view factor

τ = atmospheric transmissivity

Equation 21 is used with the assumption that the flame is a vertical or tilted cylinder. This requires the flame diameter and height to be determined. The flame diameter is taken to be the pool diameter, D . See Figure 3-11.19 for general nomenclature.

The flame height correlation used in this method is based on the correlation of mean visible height, H_f , of turbulent diffusion flames (in absence of wind) developed by Thomas.⁴⁰ The correlation for a circular fire is given by Equation 1:

$$\frac{H}{D} = 42 \left(\frac{\dot{m}''_\infty}{\rho_a \sqrt{gD}} \right)^{0.61} \quad (1)$$

where

D = pool diameter

\dot{m}''_∞ = mass burning rate per unit pool area, kg/m²·s

ρ_a = ambient air density, kg/m³

g = gravitational acceleration, 9.8 m/s²

If the pool has a length-to-width ratio near one, an equivalent-area circular source can be used for noncircular

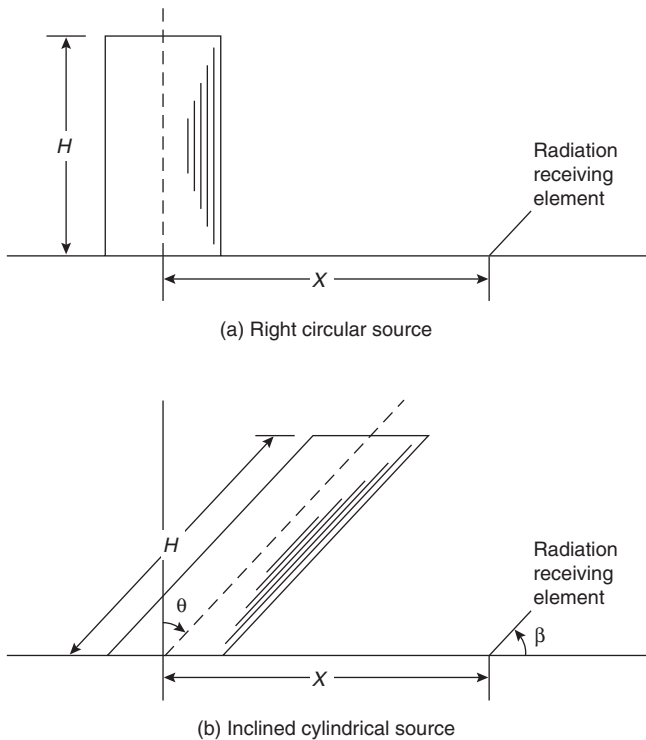


Figure 3-11.19. Configuration factor calculation geometries for right and inclined cylinders.

pools in the determination of the flame height. For noncircular pools, the effective diameter will be defined as the diameter of a circular pool with an area equal to the actual pool area, given by Equation 13 as

$$D = \sqrt{\frac{4A}{\pi}} \quad (13)$$

In the presence of wind, the flame length is given by the following correlation developed by Thomas⁴⁰ (Equation 2):

$$\frac{H}{D} = 55 \left(\frac{\dot{m}_{\infty}''}{\rho_a \sqrt{gD}} \right)^{0.67} (u^*)^{-0.21} \quad (2)$$

where u^* is the nondimensional wind velocity given by Equation 2:

$$u^* = \frac{u_w}{(\dot{m}_{\infty}'' D / \rho_v)^{1/3}} \quad (3)$$

where u_w is the wind speed, m/s, and ρ_v is the fuel vapor density, kg/m³.

In the presence of a significant wind, the flame may not remain vertical, and a flame tilt angle due to the wind is relevant to the assessment of radiation. The American Gas Association (AGA)³⁹ proposed the following correlation to determine the flame tilt (Equation 7):

$$\cos \theta = \begin{cases} 1 & \text{for } u^* \leq 1 \\ 1/\sqrt{u^*} & \text{for } u^* \geq 1 \end{cases} \quad (7)$$

where u^* is the nondimensional wind velocity given by Equation 20 with the wind velocity measured at a height of 1.6 m above the ground.

The turbulent flame is approximated by a cylinder. Under wind-free conditions, the cylinder is vertical (Figure 3-11.19(a)). Under the influence of wind, the cylinder is assumed to be tilted (Figure 3-11.19(b)). View factors for horizontal and vertical targets of a vertical cylinder for no-wind conditions are as follows:

$$F_{12,V} = \frac{1}{\pi S} \tan^{-1} \left(\frac{h}{\sqrt{S^2 - 1}} \right) - \frac{h}{\pi S} \tan^{-1} \sqrt{\frac{(S-1)}{(S+1)}} + \frac{Ah}{\pi S \sqrt{A^2 - 1}} \tan^{-1} \sqrt{\frac{(A+1)(S-1)}{(A-1)(S+1)}} \quad (22a)$$

$$F_{12,H} = \frac{(B-1/S)}{\pi \sqrt{B^2 - 1}} \tan^{-1} \sqrt{\frac{(B+1)(S-1)}{(B-1)(S+1)}} - \frac{(A-1/S)}{\pi \sqrt{A^2 - 1}} \tan^{-1} \sqrt{\frac{(A+1)(S-1)}{(A-1)(S+1)}} \quad (22b)$$

where

$$S = \frac{2L}{D} \quad h = \frac{2H}{D}$$

$$A = \frac{h^2 + S^2 + 1}{2S} \quad B = \frac{1 + S^2}{2S}$$

and

L = distance between the center of the pool fire and the target

H = height of the pool fire

D = pool fire diameter

If the target is either at ground level or at the flame height, then a single cylinder can represent the flame. If the target is above the ground, then two cylinders must be used to represent the flame. One cylinder represents the flame below the height of the target, and the other represents the flame above the height of the target. See Figure 3-11.13b for an illustration of the nomenclature. The overall view factor is the sum of the two component view factors.

The maximum configuration factor at a point is given by the vectorial sum of the horizontal and vertical target configuration factors given by Equation 19:

$$F_{12,\max} = \sqrt{F_{12,H}^2 + F_{12,V}^2} \quad (19)$$

The configuration exchange factor for windblown flame has been given by Mudan,⁵⁴ who employed a contour integral approach developed by Sparrow⁵⁵ to determine closed-form equations for view factors from a tilted cylinder.

The view factor for a tilted cylindrical flame with a circular base is as follows:

$$\pi F_V = \frac{a \cos \theta}{b - a \sin \theta} \frac{a^2 + (b+1)^2 - 2b(1+\sin \theta)}{\sqrt{AB}} \tan^{-1} \sqrt{\frac{A}{B}} \left(\frac{b-1}{b+1} \right)^{1/2} + \frac{\cos \theta}{\sqrt{C}} \times \left[\tan^{-1} \frac{ab - (b^2-1)\sin \theta}{\sqrt{b^2-1}\sqrt{C}} + \tan^{-1} \frac{(b^2-1)\sin \theta}{\sqrt{b^2-1}\sqrt{C}} \right] - \frac{a \cos \theta}{(b - a \sin \theta)} \tan^{-1} \sqrt{\frac{b-1}{b+1}} \quad (23a)$$

$$\begin{aligned} \pi F_H &= \tan^{-1} \sqrt{\frac{b+1}{b-1}} \\ &- \frac{a^2 + (b+1)^2 - 2(b+1 + ab \sin \theta)}{\sqrt{AB}} \times \tan^{-1} \sqrt{\frac{A}{B} \left(\frac{b-1}{b+1} \right)^{1/2}} \\ &+ \frac{\sin \theta}{\sqrt{C}} \times \left[\tan^{-1} \frac{ab - (b^2-1) \sin \theta}{\sqrt{b^2-1} \sqrt{C}} + \tan^{-1} \frac{(b^2-1)^{1/2} \sin \theta}{\sqrt{C}} \right] \end{aligned} \quad (23b)$$

where

$$a = H/R$$

$$b = L/R$$

$$A = a^2 + (b+1)^2 - 2a(b+1) \sin \theta$$

$$B = a^2 + (b-1)^2 - 2a(b-1) \sin \theta$$

$$C = 1 + (b^2-1) \cos^2 \theta$$

When the angle of tilt is zero, Equations 23a and 23b reduce to Equations 22a and 22b, respectively. The maximum configuration factors at the target location are determined using Equation 19. Figures 3-11.20 and 3-11.21 show the calculated configuration factor for no-wind conditions and underwind conditions for a target at ground level. For the no-wind condition, Figure 3-11.14 can also be used to determine the view factor for a more general set of target locations.

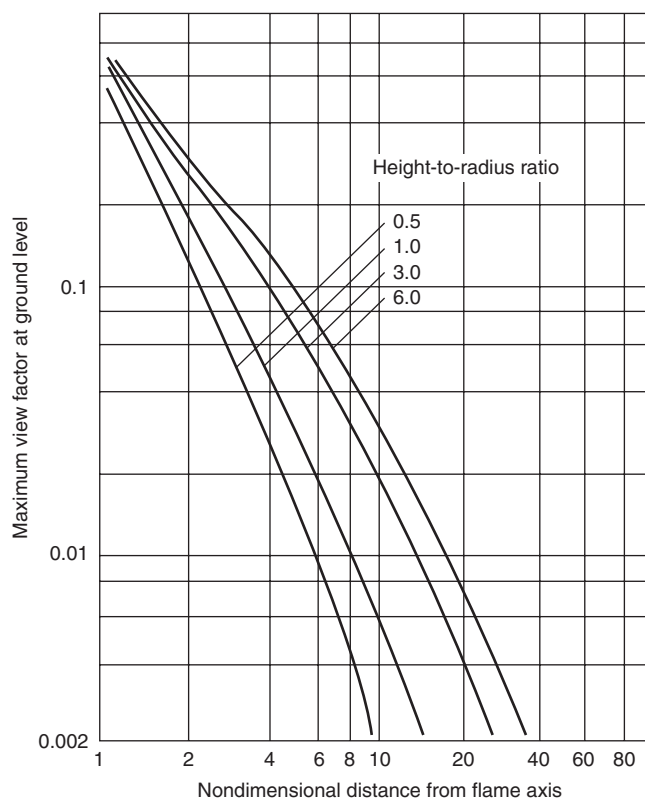


Figure 3-11.20. Maximum configuration factors for a ground-level object from a right circular cylinder. The nondimensional distance from the flame is L/R .

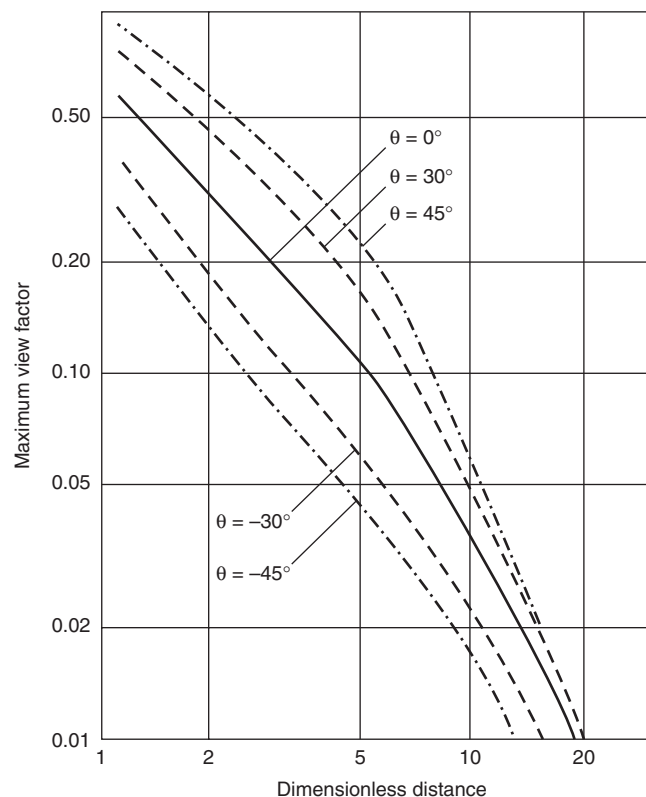


Figure 3-11.21. Maximum configuration factors for tilted circular cylinders with targets at ground level. The dimensionless distance is L/R .

The emissive power, E , of the flame is given by the following correlation:

$$E = E_{\max} e^{-sD} + E_s [1 - e^{-sD}] \quad (24)$$

where

$$E = \text{equivalent blackbody emissive power, } 140 \text{ kW/m}^2$$

$$s = \text{extinction coefficient, } 0.12 \text{ m}^{-1}$$

$$D = \text{equivalent pool diameter, m}$$

$$E_s = \text{emissive power of smoke, } 20 \text{ kW/m}^2$$

Atmospheric Absorption

The radiation from the fire to surrounding objects will be partially attenuated by absorption and scattering along the intervening path. The principal constituents of the atmosphere that absorb thermal radiation are water vapor (H_2O) and carbon dioxide (CO_2). Table 3-11.1 indicates the composition of various gases in the atmosphere. The CO_2 content in the atmosphere is generally constant at about 330 ppm by volume. The water vapor content varies strongly with temperature and humidity. Figure 3-11.22 indicates the relationship between atmospheric temperature, relative humidity, and the amount of precipitable water vapor in a given pathlength.

The principal absorption bands for water vapor are at 1.8, 2.7, and 6.27 μm . Minor absorption bands also exist at 0.94, 1.1, 1.38, and 3.2 μm . Strong absorption by CO_2 existing in the 2.7- μm region, the 4.3- μm region, and the

Table 3-11.1 Composition of Constituent Gases in the Atmosphere and Their Concentrations

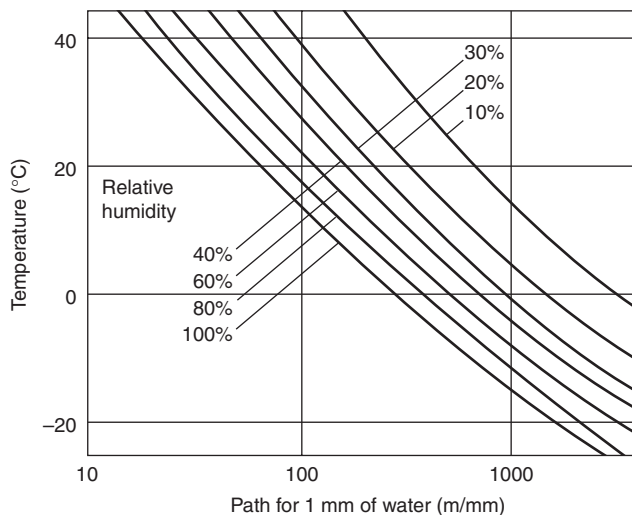
Constituent Gas	Concentration in Atmosphere (% by volume)
Nitrogen	78.088
Oxygen	20.949
Argon	0.93
Carbon dioxide	0.033
Neon	1.8×10^{-3}
Helium	5.24×10^{-4}
Methane	1.4×10^{-4}
Krypton	1.14×10^{-4}
Nitrous oxide	5.0×10^{-5}
Carbon monoxide	2.0×10^{-5}
Xenon	8.6×10^{-6}
Hydrogen	5.0×10^{-6}
Ozone	Variable
Water vapor	Variable (depends on temperature and relative humidity)

region between 11.4 and 20 μm . Weaker absorption bands are present at 1.4, 1.6, 2.0, 4.8, 5.2, 9.4, and 10.4 μm . As the temperature of the emitting or absorbing species increases, the bands tend to broaden.

A useful concept for the quick estimation of atmospheric absorption of continuum radiation is the "equivalent bandwidth of complete absorption." One calculates the integral of absorption over an absorption band and interprets the result as the width of a "rectangular," *complete* absorption band equivalent to the real band profile. For a continuum source, the effect of such opaque bands is then easy to estimate. Three absorption bands in the range of interest (1.5 through 5.5 μm) can be described in this way. These are the water vapor bands at 1.87 and 2.7 μm and the 4.3- μm , CO_2 band. The water absorption beyond about 4.7 μm is not as readily dealt with, since the band structure is not narrow compared to the range of interest. However, the fraction of total energy from a 1300-K blackbody that lies beyond 4.7 μm is about 25 percent and that beyond 5.5 μm is only 19 percent. The results of total absorption bandwidth calculations for the above three bands of interest are given in Tables 3-11.2 and 3-11.3. These calculations are based on the data available in the *Infrared Handbook*.⁵⁶ Also given in the tables are the fractions of a 1300-K blackbody energy that will be absorbed in each of these bands.

Table 3-11.2 Total Absorption Bandwidth for 1.87- μm and 2.7- μm Bands at 300 K

Precipitable Water (mm)	1.87- μm Band		2.7- μm Band	
	Total Absorption Bandwidth, $\Delta\lambda$ (μm)	Fraction of 1300-K Blackbody Energy Absorbed	Total Absorption Bandwidth, $\Delta\lambda$ (μm)	Fraction of 1300-K Blackbody Energy Absorbed
5	0.16	0.04	0.58	0.16
2	0.12	0.03	0.51	0.14
1	0.1	0.03	0.45	0.12
0.1	0.033	0.01	0.22	0.06
0.01	0.01	0.003	0.07	0.02

**Figure 3-11.22. Variation of precipitable water content of the atmosphere with temperature, humidity, and path-length.**

The absorption by the water vapor and carbon dioxide in a certain length of the atmosphere of blackbody radiation from a source can also be calculated using the emissivity charts published by Hottel and Sarofim.⁵⁷ The procedure to calculate the absorption in the water vapor band is as follows:

1. Determine the partial pressure of water vapor, in atmospheres, based on

$$p'_w = \frac{RH}{100} \exp \left(14.4114 - \frac{5328}{T_a} \right) \quad (25)$$

where RH is the relative humidity and T_a is the ambient temperature in Kelvin.

2. Define a pathlength, L (in m), from the flame surface to observer. Determine the partial pressure-pathlength parameter:

$$p_w L = p'_w L (T_s/T_a) \quad (26)$$

where

T_s = source surface temperature (K)

T_a = ambient temperature (K)

3. For the source temperature, and $p_w L$, determine the water vapor emissivity, ε_w , using emissivity plots given in Figure 3-11.23.

Table 3-11.3 Total Absorption Bandwidth for 4.3- μm CO₂ Band at 300 K

Pathlength through the Atmosphere (m)	Total Absorption Bandwidth $\Delta\lambda$ (μm)	Fraction of 1300-K Blackbody Energy Absorbed
1000	0.28	0.04
100	0.22	0.03
10	0.17	0.02
1	0.065	0.01
0.3	0.033	0.004

4. Calculate the water vapor absorption coefficient.

$$a_w = \varepsilon_w (T_a/T_s)^{0.45} \quad (27)$$

The procedure to determine the absorption by carbon dioxide is very similar. The partial pressure of CO₂ re-

mains relatively constant at about 3×10^{-4} atm. The absorption coefficient is given by

$$a_c = \varepsilon_c (T_a/T_s)^{0.65} \quad (28)$$

The emissivity of the carbon dioxide band is shown in Figure 3-11.24. There is also a correction factor due to spectral overlap for the calculation of emissivity of a CO₂-H₂O mixture. This effect, however, accounts for a change in emissivity of about 5 percent at 1200 K and even less at higher temperatures.⁵⁷

The transmissivity is given by

$$\tau = 1 - a_w - a_c \quad (29)$$

and is used in determining the thermal radiation hazard. The procedure outlined in this section may be simplified further if it is assumed that the flame temperature and the ambient temperature remain constant. For most hydrogen fuels, the flame temperature is approximately

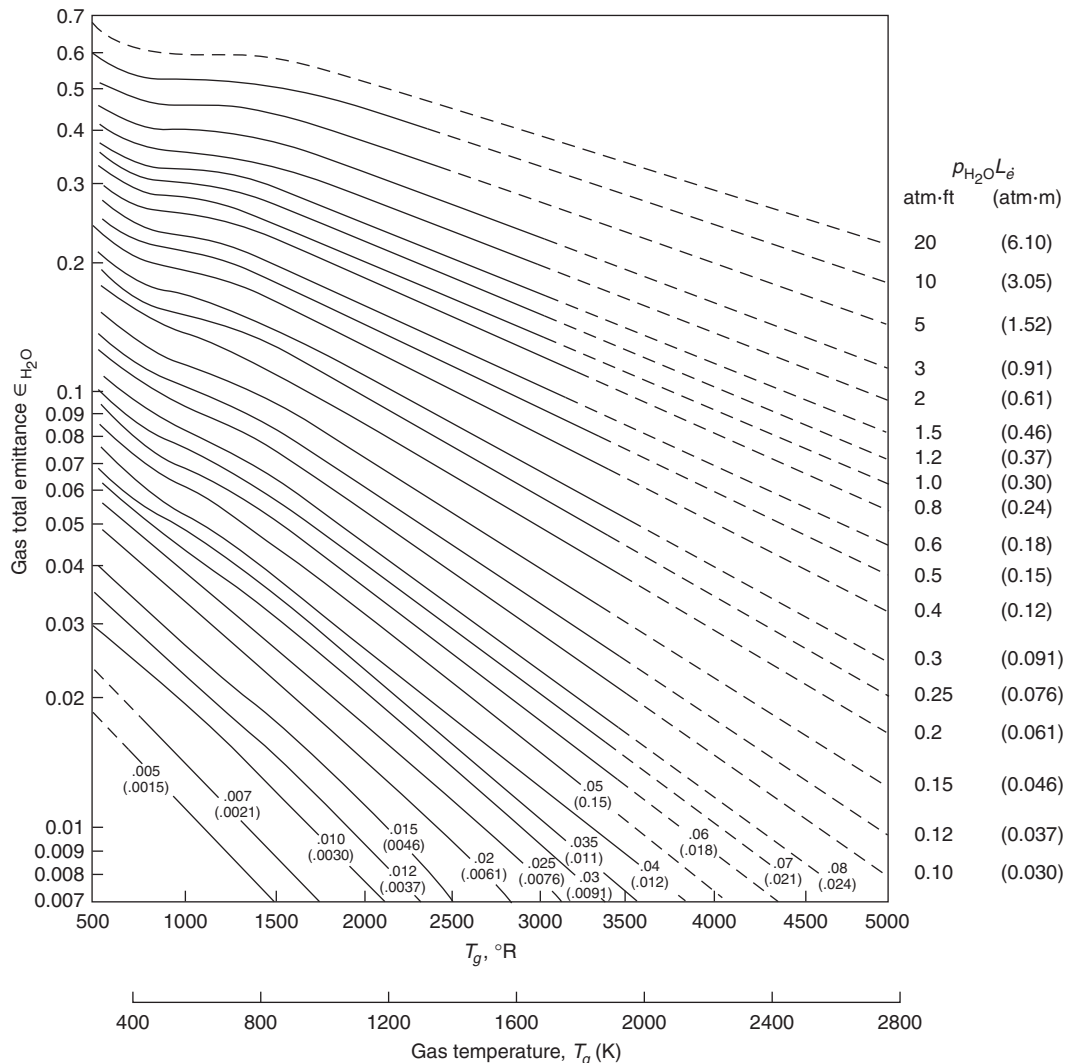


Figure 3-11.23. Total emissivity of water-vapor in a mixture of total pressure of 1 atm.⁵⁷

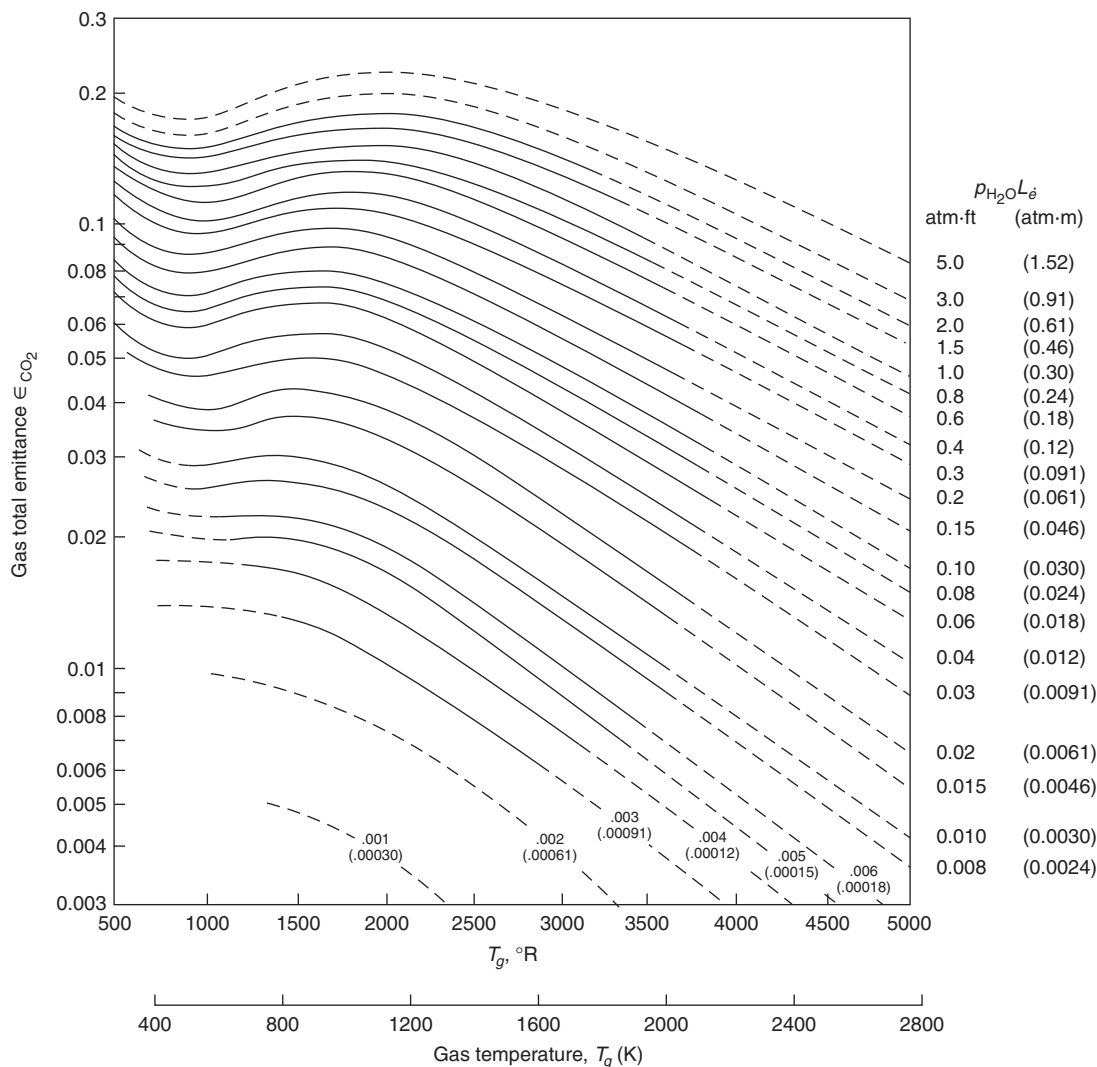


Figure 3-11.24. Total emissivity of carbon dioxide in a mixture of total pressure of 1 atm⁵⁷ where p_{CO_2} is the partial pressure of carbon dioxide and L_e is the equivalent pathlength.

1400 K. If it is assumed that the typical ambient temperature is 293 K (20°C), the transmissivity may be plotted as a function of pathlength. In Figure 3-11.25 the transmissivity is shown as a function of pathlength for various relative humidities. Figure 3-11.25 provides a quick estimate of atmospheric absorption of thermal radiation.

Summary of the procedure for the Mudan pool fire radiation method: Estimating the thermal radiation field surrounding a fire involves the following steps based on the method developed by Mudan:⁴⁴

1. Determine the height of the pool fire flame and tilt angle from Equations 1, 2, 3, and 7.
2. Calculate the configuration factor from Equations 19, 22, and 20. Figures 3-11.14, 3-11.20, or 3-11.21 may be used where appropriate.
3. Determine the effective emissive power of the flame from Equation 24.
4. Calculate the radiative heat flux to target using Equation 21.

Figure 3-11.26 shows a comparison of data with the predictions of this method.⁴⁶ The predictions tend to be conservative, and the differences between measured and predicted values are relatively uniform over the full range of heat fluxes. No validation data are available for wind-tilted conditions.

A safety factor of 2 is recommended for use with the Mudan method.⁴⁶ Figure 3-11.27 is a comparison of predicted and measured heat fluxes with the inclusion of the recommended factor of safety. Figure 3-11.22 clearly shows that essentially all the data are overpredicted by the Mudan model with a safety factor of 2. The safety factor of 2 is a recommendation for use in design applications. Where a realistic result is required, no safety factor should be applied.

Summary and General Recommendations

Table 3-11.4 summarizes the methods included in this section and their ranges of applicability. All the methods

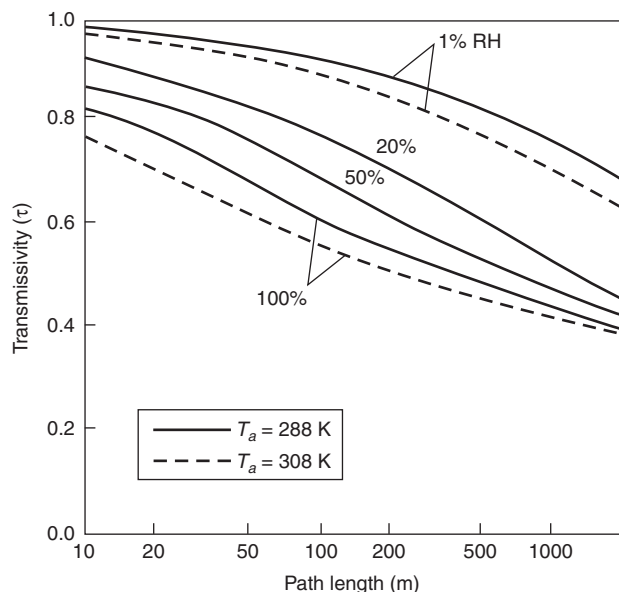


Figure 3-11.25. Transmissivity as a function of path-lengths; source temperature 1400 K.

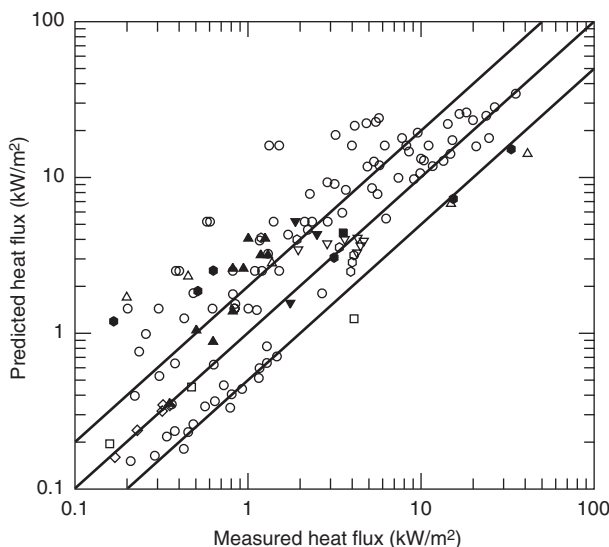


Figure 3-11.26. Comparison of measured and calculated radiative heat flux from large pool fires using the detailed method developed by Mudan.¹⁴ Solid lines indicate equality of measured and predicted heat fluxes based on the detailed method developed by Mudan.¹⁴

used with the indicated safety factors provide conservative results. However, the variations in the predicted versus measured heat fluxes (i.e., the goodness of fit) vary considerably between methods. Methods that minimize these variations are inherently more reliable in that the method better explains the experimental data. The methods that minimize the variation are the point source model and the Shokri and Beyler method, when used in their applicable ranges. Table 3-11.5 shows the correlation coefficient of each method over the indicated ranges of ap-

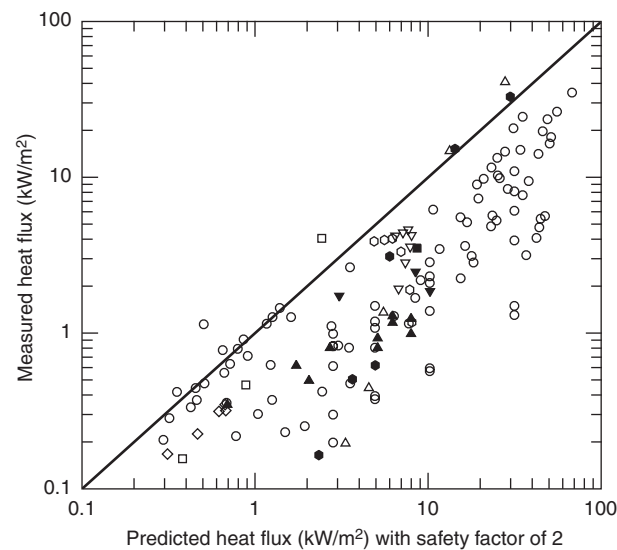


Figure 3-11.27. Comparison of measured and calculated radiative heat flux from large pool fires using the detailed method developed by Mudan with a safety factor of 2. Solid lines indicate equality of measured and predicted heat fluxes based on the detailed method developed by Mudan with a safety factor of 2.¹⁴

Table 3-11.4 Summary of the Methods

Method	Range of Use (kW/m ²)	Recommended Safety Factor	Preferred Methods
Shokri and Beyler correlation	All heat fluxes, ground level only	2	—
Point source model	0–5 kW/m ²	2	< 5 kW/m ²
Shokri and Beyler model	> 5 kW/m ²	2	> 5 kW/m ²
Mudan model	All heat fluxes	2	—

Table 3-11.5 Correlation Coefficients for the Methods

Heat-Flux Calculation Method	Correlation Coefficient	Correlation Coefficient with Safety Factor
Point source model (below 5 kW/m ²)	0.51	0.38
Mudan model (below 5 kW/m ²)	0.53	0.34
Shokri and Beyler model (above 5 kW/m ²)	0.52	0.66
Mudan model (above 5 kW/m ²)	0.35	0.57

plication. The methods with the greatest correlation coefficient better explain the variations observed in the database. While at less than 5 kW/m² there is little difference between the performance of the point source model and the Mudan¹⁴ model, the simplicity of the point source model argues for its use.

The point source model and the Shokri and Beyler model are the preferred models based on both the conservative nature of these methods and the minimization of the variations between the data and the experiments.

Because heat fluxes below 5 kW/m² cannot lead to ignition of combustibles, any analysis involving a combustible target should be performed using the Shokri and Beyler model. Since pain and second-degree burns can occur at 5 kW/m², many analyses involving human exposure can be performed using the simple point source model. If exposure is less than 1 min, it may be necessary to use the more complex Shokri and Beyler model for human exposure.

Illustration of the calculation procedure: In this section two sample calculations are presented to illustrate the calculation procedure for the thermal radiation from pool fires.

EXAMPLE 1:

Toluene from a tank is assumed to spill to form a pool in a diked area of 12-m diameter. The distance from the center of the pool fire to the target edge is assumed to be 30 m.

Calculate flame radiative heat flux to the target at ground level with no wind (Figure 3-11.28) using:

- (a) Shokri and Beyler correlation
- (b) Point source model
- (c) Shokri and Beyler detailed method using shape factor algebra
- (d) Mudan detailed method using shape factor algebra

CALCULATION PROCEDURE:

Properties of toluene (Babrauskas, Section 3, Chapter 1)

Heat of combustion, $\Delta H_c = 40550 \text{ kJ/kg}$

Mass burning rate, $\dot{m}''_\infty = 0.1126 \text{ kg/m}^2\cdot\text{s}$

Properties of air at 20°C, $\rho_a = 1.2 \text{ kg/m}^3$

- (a) Heat flux from the Shokri and Beyler correlation, Equation 12:

$$\dot{q}'' = 15.4 \left(\frac{L}{D} \right)^{-1.59}$$

where $L = 30 \text{ m}$ and $D = 12 \text{ m}$. Therefore, heat flux to the target is

$$\dot{q}'' = 15.4 \left(\frac{30}{12} \right)^{-1.59} = 3.6 \text{ kW/m}^2$$

- (b) Heat flux from point source model, Equation 14:

$$\dot{q}'' = \frac{\dot{Q}_r \cos \theta}{4\pi R^2}$$

The radiative energy output, \dot{Q}_r , is given by the radiative fraction, χ_r , multiplied by the total heat-release rate, \dot{Q} , from Equation 16:

$$\dot{Q}_r = \chi_r \dot{Q}$$

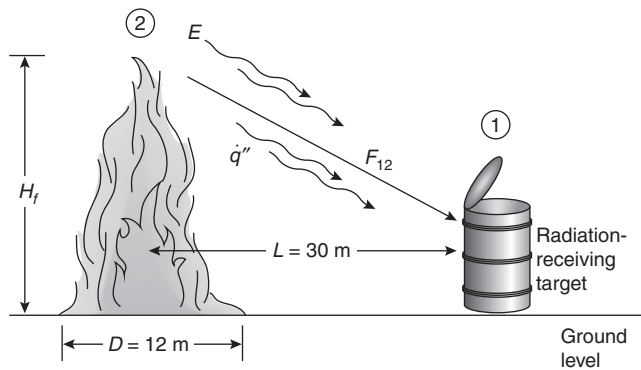


Figure 3-11.28. Toluene pool fire with target at ground level.

Figure 3-11.12 can be used to determine χ_r from curve fit to the experimental data as

$$\chi_r = 0.21 - 0.0034D$$

and \dot{Q} , total heat release rate, is given by

$$\dot{Q} = \dot{m}''_\infty \Delta H_c A$$

and A , area of the pool, can be expressed from Equation 13:

$$A = \frac{\pi}{4} D^2$$

Combining the above equations yields

$$\dot{Q}_r = (0.21 - 0.0034D) \left(\dot{m}''_\infty \Delta H_c \frac{\pi}{4} D^2 \right) = 87,371 \text{ kW}$$

The distance, R , from the point source location to the target location is given by the Pythagorean theorem, Equation 15:

$$R = \sqrt{L^2 + H_T^2}$$

where $L = 30 \text{ m}$ and H_T is given by

$$H_T = \frac{H}{2}$$

H is the height of the flame from Equation 5:

$$H = 0.23 \dot{Q}^{2/5} - 1.02D = 32.11 \text{ m}$$

$$H_T = \frac{0.23(\dot{m}''_\infty \Delta H_c (\pi/4) D^2)^{2/5} - 1.02D}{2} = 16 \text{ m}$$

$$R = \sqrt{30^2 + 16^2} = 34 \text{ m}$$

The angle, θ , between the normal to the target and the line of sight from the point source location can be estimated as

$$\theta = \tan^{-1} \left(\frac{1}{2} \frac{H}{L} \right) = 0.49 \text{ rad}$$

The heat flux from the point source model is

$$\dot{q}'' = \frac{\dot{Q}_r \cos \theta}{4\pi R^2} = \frac{87371 \times \cos(0.49)}{4 \times \pi \times 34^2} = 5.3 \text{ kW/m}^2$$

- (c) Heat flux from the Shokri and Beyler detailed method using shape factor algebra with target at ground level and no wind, Equation 17:

$$\dot{q}'' = EF_{12}$$

The emissive power of the flame, E , is given by Equation 20:

$$E = 58(10^{-0.00823D})$$

$$E = 58(10^{-0.00823 \times 12}) = 46.2 \text{ kW/m}^2$$

Equation 18a can be used to determine the shape factor in the horizontal direction:

$$F_{12,H} = \frac{[B - (1/S)]}{\pi\sqrt{B^2 - 1}} \tan^{-1} \sqrt{\frac{(B + 1)(S - 1)}{(B - 1)(S + 1)}} - \frac{[A - (1/S)]}{\pi\sqrt{A^2 - 1}} \tan^{-1} \sqrt{\frac{(A + 1)(S - 1)}{(A - 1)(S + 1)}}$$

Equation 18b can be used to determine the shape factor in vertical direction:

$$F_{12,V} = \frac{1}{\pi S} \tan^{-1} \left(\frac{h}{\sqrt{S^2 - 1}} \right) - \frac{h}{\pi S} \tan^{-1} \sqrt{\frac{(S - 1)}{(S + 1)}} + \frac{Ah}{\pi S \sqrt{A^2 - 1}} \tan^{-1} \sqrt{\frac{(A + 1)(S - 1)}{(A - 1)(S + 1)}}$$

where

$$S = \frac{2L}{D} = \frac{2 \times 30}{12} = 5$$

$$H_f = 0.23\dot{Q}^{2/5} - 1.02D = 32.11 \text{ m}$$

$$h = \frac{2H_f}{D} = \frac{2 \times 32.11}{12} = 5.35$$

$$A = \frac{h^2 + S^2 + 1}{2S} = \frac{5.35^2 + 5^2 + 1}{2 \times 5} = 5.46$$

$$B = \frac{(1 + S^2)}{2S} = 2.6$$

Substituting values of A , B , S , and h in the shape factor equation to determine $F_{12,H}$ and $F_{12,V}$, the $F_{12,H}$ is equal to 0.039, and $F_{12,V}$ is equal to 0.088.

The maximum shape factor at a point is given by the vectorial sum of the horizontal and vertical shape factors:

$$F_{12,\max} = \sqrt{F_{12,H}^2 + F_{12,V}^2}$$

Therefore, the maximum shape factor at a point is equal to 0.097. Therefore, heat flux to the target is

$$\dot{q}'' = EF_{12,\max} = 48 \times 0.097 = 4.5 \text{ kW/m}^2$$

- (d) Heat flux from the Mudan detailed method using shape factor algebra with target at ground level and no wind, Equation 21:

$$\dot{q}'' = EF_{12}\tau$$

The emissive power of the flame, E is given by Equation 24:

$$E = E_{\max} e^{-sD} + E_s(1 - e^{-sD})$$

$$E = 140e^{-0.12 \times 12} + 20(1 - e^{-0.21 \times 12}) = 48.43 \text{ kW/m}^2$$

Equation 22a can be used to determine the shape factor in the horizontal direction:

$$F_{12,H} = \frac{[B - (1/S)]}{\pi\sqrt{B^2 - 1}} \tan^{-1} \sqrt{\frac{(B + 1)(S - 1)}{(B - 1)(S + 1)}} - \frac{[A - (1/S)]}{\pi\sqrt{A^2 - 1}} \tan^{-1} \sqrt{\frac{(A + 1)(S - 1)}{(A - 1)(S + 1)}}$$

and Equation 22b can be used to determine the shape factor in vertical direction:

$$F_{12,V} = \frac{1}{\pi S} \tan^{-1} \left(\frac{h}{\sqrt{S^2 - 1}} \right) - \frac{h}{\pi S} \tan^{-1} \sqrt{\frac{(S - 1)}{(S + 1)}} + \frac{Ah}{\pi S \sqrt{A^2 - 1}} \tan^{-1} \sqrt{\frac{(A + 1)(S - 1)}{(A - 1)(S + 1)}}$$

$$H_f = 42D \left(\frac{\dot{m}''_\infty}{\rho_a \sqrt{gD}} \right)^{0.61} = 27.79 \text{ m}$$

$$h = \frac{2H_f}{D} = \frac{2 \times 27.79}{12} = 4.63$$

$$S = \frac{2L}{D} = \frac{2 \times 30}{12} = 5$$

$$A = \frac{h^2 + S^2 + 1}{2S} = \frac{4.63^2 + 5^2 + 1}{2 \times 5} = 4.74$$

$$B = \frac{(1 + S^2)}{2S} = 2.6$$

Substituting values of A , B , S , and h in the shape factor equation to determine $F_{12,H}$ and $F_{12,V}$, $F_{12,H}$ is equal to 0.035, and $F_{12,V}$ is equal to 0.084.

The maximum shape factor at a point is given by the vectorial sum of the horizontal and vertical shape factors:

$$F_{12,\max} = \sqrt{F_{12,H}^2 + F_{12,V}^2}$$

Therefore, the maximum shape factor at a point is equal to 0.091.

Therefore, heat flux to the target is

$$\dot{q}'' = EF_{12,V}\tau = 48.43 \times 0.091 \times 1 = 4.45 \text{ kW/m}^2$$

Table 3-11.6 summarizes the results for each of the methods.

EXAMPLE 2:

Calculate flame radiative heat flux from a 10-m-diameter toluene pool fire to a vertical target 2 m above the ground at 12 m from the center of the pool (Figure 3-11.29) with no wind, using:

- (a) Shokri and Beyler method using shape factor algebra
- (b) Mudan method using shape factor algebra

CALCULATION PROCEDURE:

- (a) Heat flux from the Shokri and Beyler detailed method using shape factor algebra with target height 2 m above ground level and no wind

Table 3-11.6 Summary of the Heat Flux from 12-m-Diameter Toluene Pool Fire to 30-m Target at Ground Level with No Wind

Heat Flux Calculation Method	Heat Flux (kW/m ²)
(a) Shokri and Beyler correlation	3.6
(b) Point source model	5.3
(c) Shokri and Beyler method using shape factor algebra	4.5
(d) Mudan method using shape factor algebra	4.45

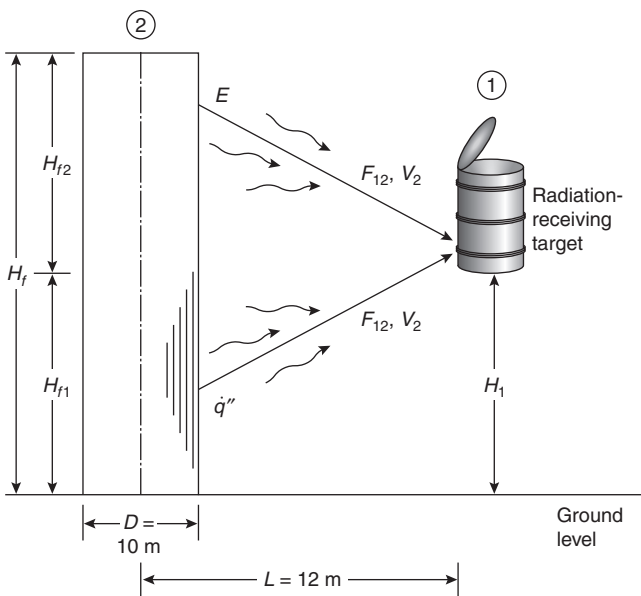


Figure 3-11.29. Toluene pool fire with target above ground level.

Properties of toluene (Babrauskas, Section 3, Chapter 1)

Heat of combustion, $\Delta H_c = 40550 \text{ kJ/kg}$

Mass burning rate, $\dot{m}_\infty'' = 0.1126 \text{ kg/m}^2 \cdot \text{s}$

Properties of air at 20°C $\rho_a = 1.2 \text{ kg/m}^3$

Heat flux is given by Equation 17:

$$\dot{q}'' = EF_{12}$$

The emissive power of the flame, E , is given by Equation 20:

$$E = 58(10^{-0.00823D})$$

$$E = 58(10^{-0.00823 \times 10}) = 48 \text{ kW/m}^2$$

The flame height, H , is given by Equation 17:

$$H = 0.23\dot{Q}^{2/5} - 1.02D$$

where

$$\dot{Q} = \dot{m}_\infty'' \Delta H_c A \text{ kW}$$

$$\dot{Q} = 360,000 \text{ kW}$$

$$H = 28 \text{ m}$$

Since the target is above the ground, but it is not at the flame height, two cylinders must be used to represent the flame. Since the target is strictly vertical, it is not necessary to calculate the horizontal shape factor.

The shape factor for the target located above ground level can be calculated from Figures 3-11.14(a) to 3-11.14(e) or by the following method. For the vertical target, Equation 18b can be used to determine the shape factor at location H_{f1} :

$$F_{12,V1} = \frac{1}{\pi S} \tan^{-1} \left(\frac{h_1}{\sqrt{S^2 - 1}} \right) - \frac{h_1}{\pi S} \tan^{-1} \sqrt{\frac{(S - 1)}{(S + 1)}}$$

$$+ \frac{A_1 h_1}{\pi S \sqrt{A_1^2 - 1}} \tan^{-1} \sqrt{\frac{(A_1 + 1)(S - 1)}{(A_1 - 1)(S + 1)}}$$

$$S = \frac{2L}{D} = \frac{2 \times 12}{10} = 2.4$$

$$H_{f1} = \frac{2H_{f1}}{D} = \frac{2 \times 2}{10} = 0.4$$

$$A_1 = \frac{H_{f1}^2 + S^2 + 1}{2S} = \frac{0.4^2 + 2.4^2 + 1}{2 \times 2.4} = 1.44$$

Substituting values of A_1 , S , and H_{f1} in the shape factor equation to determine $F_{12,V1}$, the $F_{12,V1}$ is equal to 0.066. Shape factor at location H_{f2} is given by

$$F_{12,V2} = \frac{1}{\pi S} \tan^{-1} \left(\frac{H_{f2}}{\sqrt{S^2 - 1}} \right) - \frac{H_{f2}}{\pi S} \tan^{-1} \sqrt{\frac{(S - 1)}{(S + 1)}}$$

$$+ \frac{A_2 H_{f2}}{\pi S \sqrt{A_2^2 - 1}} \tan^{-1} \sqrt{\frac{(A_2 + 1)(S - 1)}{(A_2 - 1)(S + 1)}}$$

$$S = \frac{2L}{D} = \frac{2 \times 12}{10} = 2.4$$

$$H_{f2} = \frac{2H_{f1}}{D} = \frac{2(H_f - H_{f1})}{D} = \frac{2(28 - 2)}{10} = 5.2$$

$$A_2 = \frac{H_{f2}^2 + S^2 + 1}{2S} = \frac{5.2^2 + 2.4^2 + 1}{2 \times 2.4} = 7.04$$

Substituting values of A_2 , S , and H_{f2} in the shape factor equation to determine $F_{12,V2}$, $F_{12,V2}$ is equal to 0.206. Therefore, total shape factor is given by

$$F_{12,V} = F_{12,V1} + F_{12,V2} = 0.066 + 0.206 = 0.27$$

Therefore, heat flux to the target at 2 m above ground is

$$\dot{q}'' = EF_{12,V} = 48 \times 0.27 = 13.0 \text{ kW/m}^2$$

- (b) Heat flux from Mudan¹⁴ method using shape factor algebra with target height 2 m above ground level and no wind

Heat flux is given by Equation 21:

$$\dot{q}'' = EF_{12}\tau$$

The emissive power of the flame, E , is given by Equation 21:

$$E = E_{\max}e^{-sD} + E_s(1 - e^{-sD})$$

$$E = 140e^{-0.12 \times 10} + 20(1 - e^{-0.21 \times 10}) = 56.14 \text{ kW/m}^2$$

The flame height, H , is given by Equation 1:

$$H_f = 42D \left(\frac{\dot{m}_\infty''}{\rho_a \sqrt{gD}} \right)^{0.61} = 25.4 \text{ m}$$

Since the target is above the ground, but it is not at the flame height, two cylinders must be used to represent the flame. Since the target is strictly vertical, it is not necessary to calculate the horizontal shape factor.

The shape factor for the target located above ground level can be calculated from the Figures 3-11.16(a) to 3-11.16(e) or by the following method. For the vertical target, Equation 22b can be used to determine the shape factor at location H_1 :

$$F_{12,V1} = \frac{1}{\pi S} \tan^{-1} \left(\frac{H_1}{\sqrt{S^2 - 1}} \right) - \frac{H_1}{\pi S} \tan^{-1} \sqrt{\frac{(S - 1)}{(S + 1)}} + \frac{A_1 H_1}{\pi S \sqrt{A_1^2 - 1}} \tan^{-1} \sqrt{\frac{(A_1 + 1)(S - 1)}{(A_1 - 1)(S + 1)}}$$

$$S = \frac{2L}{D} = \frac{2 \times 12}{10} = 2.4$$

$$H_1 = \frac{2H_{f1}}{D} = \frac{2 \times 2}{10} = 0.4$$

$$A_1 = \frac{H_1^2 + S^2 + 1}{2S} = \frac{0.4^2 + 2.4^2 + 1}{2 \times 2.4} = 1.44$$

Substituting values of A_1 , S , and h_1 in the shape factor equation to determine $F_{12,V1}$, $F_{12,V1}$ is equal to 0.066.

Shape factor at location H_2 is given by

$$F_{12,V2} = \frac{1}{\pi S} \tan^{-1} \left(\frac{H_2}{\sqrt{S^2 - 1}} \right) - \frac{H_2}{\pi S} \tan^{-1} \sqrt{\frac{(S - 1)}{(S + 1)}} + \frac{A_2 H_2}{\pi S \sqrt{A_2^2 - 1}} \tan^{-1} \sqrt{\frac{(A_2 + 1)(S - 1)}{(A_2 - 1)(S + 1)}}$$

$$S = \frac{2L}{D} = \frac{2 \times 12}{10} = 2.4$$

$$h_2 = \frac{2H_{f2}}{D} = \frac{2(H_f - H_{f1})}{D} = \frac{2(24.5 - 2)}{10} = 4.5$$

$$A_2 = \frac{H_2^2 + S^2 + 1}{2S} = \frac{4.5^2 + 2.4^2 + 1}{2 \times 2.4} = 5.62$$

Substituting values of A_2 , S , and h_2 in the shape factor equation to determine $F_{12,V2}$, $F_{12,V2}$ is equal to 0.206. Therefore, total shape factor is given by

$$F_{12,V} = F_{12,V1} + F_{12,V2} = 0.066 + 0.188 = 0.27$$

Therefore, heat flux to the target at 2 m above ground is

$$\dot{q}'' = EF_{12,V} = 56.14 \times 0.25 = 15.2 \text{ kW/m}^2$$

Heat Transfer to Targets within Pool Fires

Temperatures within pool fires have been widely measured and reported.⁵⁸ Over a very wide range of pool sizes (0.1–50-m diameter), the maximum time-averaged flame temperatures are generally observed to be approximately 900–1100°C. Table 3-11.8 shows measured maximum average temperatures reported in the literature. This maximum has been found to be remarkably independent of the fuel. The maximum time-averaged temperature is observed on the pool centerline over approximately the lower 40 percent of the flame height.

Effective radiation temperatures can be measured with optical pyrometers, narrow angle radiometers, or scanning spectrometers. These measurements tend to

Table 3-11.7 Summary of the Heat Flux from 10-m-Diameter Toluene Pool Fire to 12-m Target at 2 m High above Ground Level with No Wind

Heat Flux Calculation Method	Heat Flux (kW/m ²)
(a) Shokri and Beyler method using shape factor algebra	13.0
(b) Mudan method using shape factor algebra	15.2

Table 3-11.8 Maximum Time-Averaged Temperatures of Pool Fires

	°C
Cox and Chitty ⁵⁹	1000
McCaffrey ⁶⁰	820
Terai and Nitta ⁶¹	770
Kung and Stavrianidis ⁶²	920
Hägglund and Persson ¹⁸	1000
Russell and Canfield ⁶³	1100
Gregory, Keltner, and Mata ⁶⁴	1000
Johnson, Linley, and Mansfield ³²	1200
Anderson et al. ⁶⁵	1000

yield maximum, average, effective radiation temperatures somewhat larger than the actual maximum temperatures, up to 1200°C (see Wayne and Kinsella,⁶⁶ Hägglund and Persson¹⁸), which is a reflection of the fourth-power dependence of radiation on temperature. The radiation is affected by the maximum temperature excursions rather than simply the average. Effective radiation temperatures measured outside the flame can be significantly lower than this due to obscuration by smoke outside the flame.

Average fluxes to objects immersed in flames have been widely measured. Most of the work that has been reported was performed to assess the energy input to liquid tanks for the purpose of determining venting requirements while the remainder of the work has been performed to assess the heating of weapons and nuclear fuel containers. Most of this work has focused on objects located in the lower portions of the flame where the maximum temperatures and fluxes are expected. Table 3-11.9 summarizes the results of a number of investigations and assessments of existing data. Based on the available data, a maximum time-averaged heat flux of 120 kW/m² is a reasonable, conservative representation of the available data. These investigations include data in which the size of the object was small relative to the size of the flame, but the objects were sized to represent tanks and/or weapons. The object was fully immersed in optically thick flames on all sides.

Measurements made with objects comparable inside to the pool fire are far less common (Taylor et al.,⁶⁷ McLain⁶⁸). Heat fluxes in this situation are less than those observed when the object is much smaller than the pool fire. This results from the reduced flame pathlengths observed. The flames are not uniformly optically thick as seen by the object. Measurements of heating rates to objects on the order of 1–3 m in size heated by comparably sized pool fires result in average heat fluxes in the range 75–85 kW/m² (see Table 3-11.9). These heat fluxes were deduced from measured rates of the temperature of tank contents.

The extinction coefficient, k , of pool fires has been measured by several investigators. Typically, pool fires are found to have average extinction coefficients of about 2 1/m. An extinction coefficient of 2 1/m is consistent with the observation that pool fires reach their asymptotic, radiatively dominated burning rate at pool diameters of 1 m.

Table 3-11.9 Large-Scale Pool Fire Maximum Average Heat-Flux Measurements

Large Calorimeters	kW/m ²
Gregory, Keltner, and Mata ⁶⁹	120
Wachtell and Langhaar ⁷⁰	85
Anderson et al. ⁶⁵	100
National Academy of Science ⁷¹ (average of data in the literature pre-1970)	110
Moodie ⁷²	100
Tunc and Venart ⁷³	105
McLain ⁶⁸	85 ^a
Taylor et al. ⁶⁷	75 ^a

Small Calorimeters	kW/m ²
Russell and Cansfield ⁶³	170
Gregory, Keltner, and Mata ⁶⁹	160

^aObject site comparable to pool fire.

The effect of the object size on flame heat fluxes has not been systematically studied. However, it has been observed that larger objects, even if significantly smaller than the flame, do yield smaller heat fluxes than smaller objects. Gregory, Keltner, and Mata⁶⁹ have observed this effect in 9-m × 18-m pool fires with objects up to 1.4 m in diameter. They found fluxes to 1.4-m-diameter calorimeters were 30–40 percent less than for 0.1–0.2-m-diameter calorimeters. Similarly, measurements using conventional heat-flux transducers (Gardon or Schmidt/Boelter) tend to yield higher fluxes than observed with calorimeters, which are sized to represent normal tanks or weapons. Table 3-11.9 summarizes available heat flux data as measured with small calorimeters. It is thought that these effects result from two phenomena. First, the larger calorimeters effectively average the fluxes over the size of the calorimeter. This spacial averaging process tends to reduce the measured fluxes. Second, the larger calorimeters can significantly perturb the flame in the region surrounding the calorimeter, yielding reduced temperatures surrounding the calorimeter. The size of the region affected scales with the diameter of the calorimeter. With small calorimeters, this length is small compared to 1/k so that the radiant fluxes are not much affected. For large calorimeters, the reduction in local flame temperature may be significant over radiative length scales, and radiant fluxes are reduced.

Most measurements that have been performed have been made in the center of the flame where the highest fluxes are expected. Relatively few measurements have been made within the flame near the flame edge. Temperature profiles have been measured by Russell and Canfield⁶³ and Johnson, Linley, and Mansfield.³² Their temperature results indicate that temperatures are reduced to about half the centerline value at one-half the pool radius. Russell and Canfield⁶³ made small-scale calorimeter measurements about 0.3 m from the visible flame edge. Measurements made facing the flame edge were less than 20 kW/m² while measurements made facing the body of the flame were about 135 kW/m². This

value should be compared to fluxes measured on the centerline of the fire of 160 kW/m^2 made with Gardon gages. This indicates that fluxes within the flame are relatively constant until and unless the radiative pathlengths are small enough to reduce the flame emissivity as discussed previously.

Thermal Radiation from Jet Flames

Large turbulent diffusion flames are encountered in a processing environment as a result of an accidental release of hydrocarbon vapors or the intentional disposal of unwanted gases in a flare. Flaring is the combustion process that has been the traditional method for safe disposal of large quantities of unwanted flammable gases and vapors in the petroleum industry. With the advent of air quality standards, flaring has also taken on an added importance as a method of industrial environmental control, since most gases that could previously be vented to the atmosphere must now be burned in a flare. The flaring of gases in the petroleum industry occurs in three ways:

1. *Production flaring.* In a production oil field where no provision exists for collecting and processing of gas, there is a requirement for safe disposal of flammable gases. There was a time when almost all gas released was flared, but the great value now placed on natural gas has made gas recovery economical for some fields. Nevertheless, if gas occurs in small quantities that are uneconomical to process or if the gas is so sour that processing is expensive, it can still be flared.
2. *Process flaring.* Flaring also takes place in petrochemical plants, oil refineries, and gas processing plants where the flare system is one of the off-site facilities. In process flaring, the gas that leaks past safety valves protecting various process units is brought to the flare and burned. This gas feeds the small flames that burn almost continuously on refinery stacks. Process flaring can occur at much greater rates when process units are evacuated during a shutdown or when off-specification products are produced during start-up.
3. *Emergency flaring.* This occurs when large volumes of volatile liquids or flammable gases have to be disposed of safely in an emergency such as fire, power failure, or overpressure in a process vessel.

The flaring process involves the release of a tremendous amount of energy. Since a portion of this energy release is in the form of thermal radiation, it represents a substantial hazard to personnel, equipment, and the environment. The sizing of flare system, both in diameter and height, is of major importance to ensure personnel safety during flaring operations. The ability to predict the thermal radiation field from flares is essential in the design of a reasonably sized, safe operating flare. Experimental data on thermal radiation from full-scale flares are rare, and when available at all, the flow rate and composition of the flared gases are usually unknown. However, several scale-model studies have been conducted to examine the geometric and radiative characteristics of flares.

The geometric characteristics of hydrocarbon flares are similar to turbulent jet flames. In fact, many of the

geometric descriptions of flares are based on small-scale turbulent jet flame experiments. The base diameter of a flare stack, height of the stack, and composition of the burning substance are often known to the user. In modeling accidental releases of hydrocarbon gases, these relevant data may have to be estimated.

The analytical models describing the geometric characteristics of turbulent jet diffusion flames are described in the following section. The models describe parameters such as the flame height, flame width, and flame tilt. Thermal radiation models, the aerodynamic effects on radiation heat transfer, and blowout stability of jet flames, as well as calculation procedures are also described in this section.

Geometry of Turbulent Jet Flames

Combustion in a flare or jet fire occurring in the form of a strong turbulent flame may be buoyancy or momentum dominated. Such a flame presents a number of challenging phenomena for study, including the effect of crosswind on flame shape and size; radiation and formation; and dispersion of smoke and other gaseous pollutants. While applying these models to industrial flares, it is also important to recognize the effects of steam in suppressing smoke formation and thermal radiation. The fundamentals of combustion in flares have been studied by Brzustowski,⁷⁴⁻⁷⁶ Brzustowski and Sommer,⁷⁷ and Brzustowski et al.^{78,79}

Turbulent Jet Flame Height in Stagnant Surroundings

A reasonable measure of progress of burning of a diffusion flame is its height or length. At low velocities the flame is generally attached to the point of release, but at higher velocities it becomes detached, may become unstable, and extinguish. If, however, the flame impinges on an obstruction, this may serve to stabilize it. Predicting the height or length of the diffusion flame of gas jet burning in still air has long been considered one of the classical solved problems in combustion science. State of the art papers on this subject were published by Hottel and Hawthorne,⁸⁰ and Hawthorne et al.⁸¹ Hottel and Hawthorne⁸⁰ considered the case of a primary fuel jet of higher velocity issuing into an infinite atmosphere of air with allowance for primary air in the fuel jet. They observed the progressive change in the flame shape and size as the nozzle velocity is increased. This is illustrated in Figure 3-11.30, which is based on the work of Hottel and Hawthorne⁸⁰ and further interpretation by Gugan.⁸² In the laminar regime the flame length is approximately proportional to the velocity, while in the turbulent regime it is independent of velocity. Turbulence spreads from the flame tip downwards. As velocity increases there are successively a region where the flame may be on the port or lifted, a region where only a lifted flame occurs, and a point beyond which there is blow-off.

Hawthorne et al.,⁸¹ in the earliest attempts, have developed a set of experimental data and a theoretical model for flame length for turbulent flame jets. They envisage the flame as an inverted cone with the apex on the

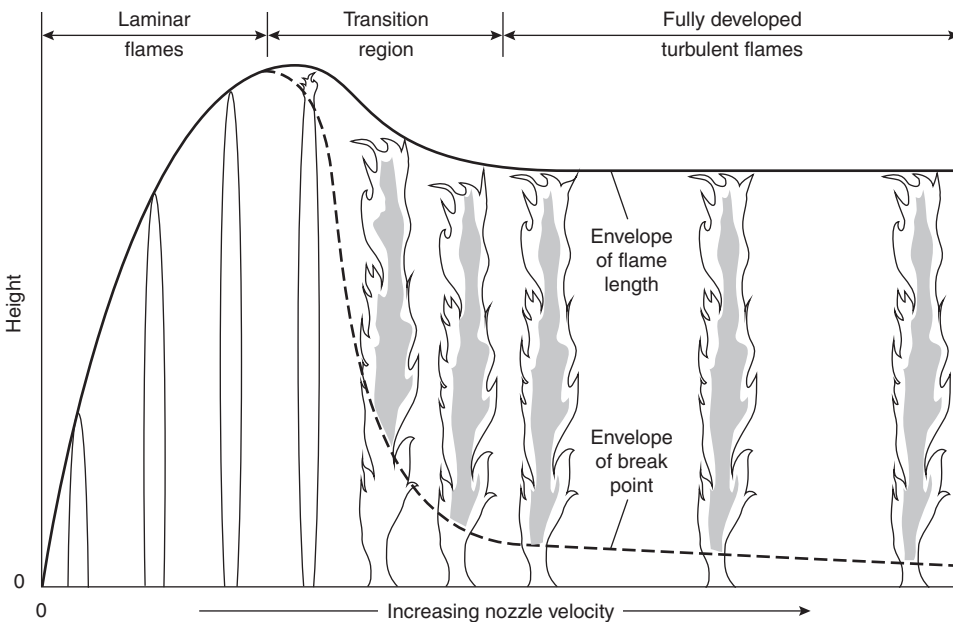


Figure 3-11.30. Progressive change in flame type with increasing jet velocity.

orifice. The equation for the length of the flame was shown to be expressible, largely from momentum consideration, in the form

$$L = \frac{5.3d_j}{C_T} \left\{ \frac{T_F}{a_T T_j} \left[C_T + (1 - C_T) \frac{M_a}{M_f} \right] \right\}^{1/2} \quad (30)$$

where

L = length of visible turbulent flame measured from the break point, m

d_j = jet diameter, m

C_T = fuel concentration in stoichiometric fuel-air mixture

a_T = Mole of reactant per mole of product for stoichiometric fuel-air mixture

M_a, M_f = molecular weight of air and fuel

T_F, T_j = adiabatic flame temperature and temperature of jet fluid (absolute)

The factor 5.3 appearing in Equation 30 is the ratio of visible length to the width of the flame at the point where stoichiometric air has been entrained. This factor was determined from experimental data.

Equation 30, for determining the flame length, reduces to a much simpler expression for most hydrocar-

bon gases. The value of parameters C_T , a_T , and T_F/T_j for various hydrocarbons are given in Table 3-11.10.

Since C_T is typically much less than unity, a_T is approximately unity and T_F/T_j varies between 7 and 9. Equation 30 may be approximated by the following equation:

$$L = \frac{15d_j}{C_T} \left(\frac{M_a}{M_f} \right)^{1/2} \quad (31)$$

Momentum-controlled flame lengths as discussed above are generally 200 to 300 times the jet nozzle diameter. While these are the tallest possible jet flames, over a wide range of conditions, jet flames are buoyancy controlled.

A number of investigators have measured jet flame lengths.^{74,77,83-86} All their flame height results are in the form of a power law of the Froude number, u^2/gD , where u is the nozzle velocity and d is the nozzle diameter. Flame heights, L , are correlated as

$$\frac{L}{D} \approx (\text{Fr})^{1/5} \sim \left(\frac{u^2}{gD} \right)^{1/5} \sim \frac{Q^{2/5}}{D}$$

where Q is the heat release rate. All the available results can satisfactorily be described by

$$L = 0.2Q^{2/5}$$

Figure 3-11.31 from McCaffrey⁸⁶ shows L/D as a function of u/\sqrt{gD} , $\sqrt{\text{Fr}}$. The correlation is seen to hold over a range of about five decades in $\sqrt{\text{Fr}}$. The low end of the correlation corresponds to pool fires and the high end corresponds to momentum-dominated flames.

Kalghatgi⁸⁷ and McCaffrey and Evans⁸⁸ have studied the stability and lift-off characteristics of momentum jet flames. These phenomena have a profound effect on flame radiation as indicated in Figure 3-11.31.

Table 3-11.10 Constant for Equation 41

Hydrocarbon Fuel	C_T	a_T	T_F/T_j
Methane	0.091	1.0	7.4
Ethane	0.074	1.04	9.0
Propane	0.038	0.96	7.6

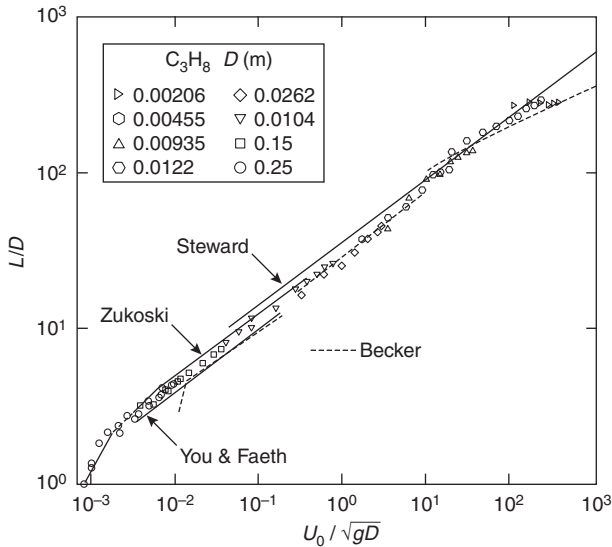


Figure 3-11.31. Flame height per nozzle diameter as a function of u/\sqrt{gD} .

Brzustowski⁷⁴ and Brzustowski and Sommer⁷⁷ proposed that the end of a turbulent diffusion flame at very high Reynolds number occurs at that point on the axis of maximum fuel concentrations where the fuel concentration equals the lean limit. In theory, this criterion can be applied to any flow configuration for which cold-flow concentration data at sufficiently high Reynolds number are available. Brzustowski⁷⁴ has also used some full-scale flare test data to support the lean limit criterion. With this criterion, the flame length for momentum-dominated jets is given by the following equation:

$$\frac{L}{d_j} = \frac{\gamma_{fj}}{0.32} \left(\frac{\rho_j}{\rho_a} \right)^{1/2} \left[1 + \frac{M_a}{M_f} \left(\frac{1}{0.297C_L} - 1 \right) \right] \quad (33)$$

For a flame where buoyancy is the dominating force, the flame length is given by

$$\frac{L}{d_j} = 2.96 \left(\frac{\rho_j}{\rho_a} \right)^{1/2} Fr^{1/5} \gamma_{fj}^{3/5} \times \left[1 + \frac{M_a}{M_f} \left(\frac{1}{0.297C_L} - 1 \right) \right]^{3/5} \quad (34)$$

where, C_L = fuel concentration at the lean flammability limit, by volume. Fr is the Froude number. Since C_L is about 5 percent or less for most hydrocarbons and M_a/M_f is approximately unity, Equations 33 and 34 may be simplified to the following two equations for momentum- and buoyancy-dominated flames, respectively.

$$\frac{L}{d_j} = \frac{10.5}{C_L} \left(\frac{M_a}{M_f} \right)^{1/2} \quad (35)$$

$$\frac{L}{d_j} = 6.1 \left(\frac{u_j^2}{d_j g} \right)^{1/5} \left(\frac{1}{C_L} \right)^{3/5} \left(\frac{\bar{C}_a T_a}{\Delta H} \right)^{1/5} \quad (36)$$

where \bar{C}_a = molar heat capacity of air and ΔH = molar heat of combustion.

Equations 35 and 36 are functionally very similar to the expressions obtained by Hawthorne et al.⁸¹ and Putnam and Speich.⁸⁴ These expressions indicate the similarity in three independent experiments.

Turbulent Jet Flame Length in Crosswind Conditions

A series of controlled experiments have been conducted by Brzustowski et al.⁸⁹ and Gollahalli et al.⁹⁰ in wind tunnels involving hydrogen and propane flames in the presence of wind. The work indicates that in such fires the initial effect of cross flow was to shorten the flame, after which increases in a cross-flow velocity caused increases in the flame length. Shortly before blowoff conditions were reached, flame length was observed to decrease with an increase in crosswind.

The results obtained by Brzustowski et al.⁸⁹ and Gollahalli et al.⁹⁰ with zero-wind condition are consistent with the model equations given in the previous section. Based on wind tunnel data and limited comparison with full-scale data, Brzustowski⁷⁶ has proposed the following procedure to determine the flame shape in the presence of crosswind for a jet flame.

1. Calculate the dimensionless lean limit concentration:

$$\bar{C}_L = C_L \left(\frac{u_j}{u_w} \right) \left(\frac{M_f}{M_a} \right) \quad (37)$$

2. If $\bar{C}_L \leq 0.5$, then $\bar{S}_L = 2.04 (\bar{C}_L)^{-1.03}$
If $\bar{C}_L > 0.5$, then $\bar{S}_L = 2.71 (\bar{C}_L)^{-0.625}$
3. If $\bar{S}_L > 2.35$, then $\bar{X}_L = \bar{S}_L - 1.65$.
If $\bar{S}_L \leq 2.35$, then determine \bar{X}_L by following the equation

$$\bar{S}_L = 1.04 \bar{X}_L^2 + 2.05 \bar{X}_L^{0.28} \quad (38)$$

4. Determine the dimensionless rise, \bar{Z}_L , of the flame tip above flame tip:

$$\bar{Z}_L = 2.04 \bar{X}_L^{0.28} \quad (39)$$

5. Calculate dimensional coordinates of the flame tip using the following equation:

$$X = \bar{X}_L d_j \left(\frac{\rho_j}{\rho_a} \right)^{1/2} \left(\frac{u_j}{u_w} \right) \quad (40)$$

$$Z = \bar{Z}_L d_j \left(\frac{\rho_j}{\rho_a} \right)^{1/2} \left(\frac{u_j}{u_w} \right)$$

Kalghatki⁹¹ conducted a series of 103 small-scale wind tunnel experiments to determine the size and shape of turbulent hydrocarbon jet diffusion flames in the presence of crosswind. The tests were conducted with methane, propane, ethylene, and commercial butane. The

burner diameter ranged from 6 to 22 mm, and the range of velocities were between 13 and 200 m/s. The crosswind velocities were varied from 2.6 to 8.1 m/s. Based on these tests, Kalghatgi⁹¹ concluded that the turbulent jet flame can be described by a frustum of a cone and the geometry of a jet flame under influence of wind can be represented by five geometric parameters:

1. Angle α_B , subtended by the burner tip and the tip of the flame with respect to vertical
2. Angle α , subtended by the flame with respect to vertical
3. Vertical length, L_{BV} , of the flame tip from the plane of the burner
4. The flame base width, W_1
5. The flame tip width, W_2

These parameters are expressed in terms of a dimensional variable called *effective source diameter* and a nondimensional velocity, R . The definitions of these two parameters are

$$D_s = D \left(\frac{\rho_j}{\rho_a} \right) \quad (41)$$

where

D = source diameter, m

ρ_j = density of jet fuel, kg/m³

ρ_a = density of ambient air, kg/m³

$$R = \frac{U}{U_j} \quad (42)$$

where

U = crosswind speed, m/s

U_j = jet velocity, m/s

In Figure 3-11.32 the variation of the vertical flame length parameter is shown as a function of the nondimensional velocity, R . Also shown in Figure 3-11.32 are the correlations suggested by Brzustowski for propane, methane, and ethylene. In order to predict the actual flame length, the flame tilt with respect to the burner axis must be known. Figure 3-11.33 shows the data on flame tilt and the comparison with Brzustowski's calculation procedure. It is seen that the calculation procedure underestimates the flame tilt. Therefore, the measured flame

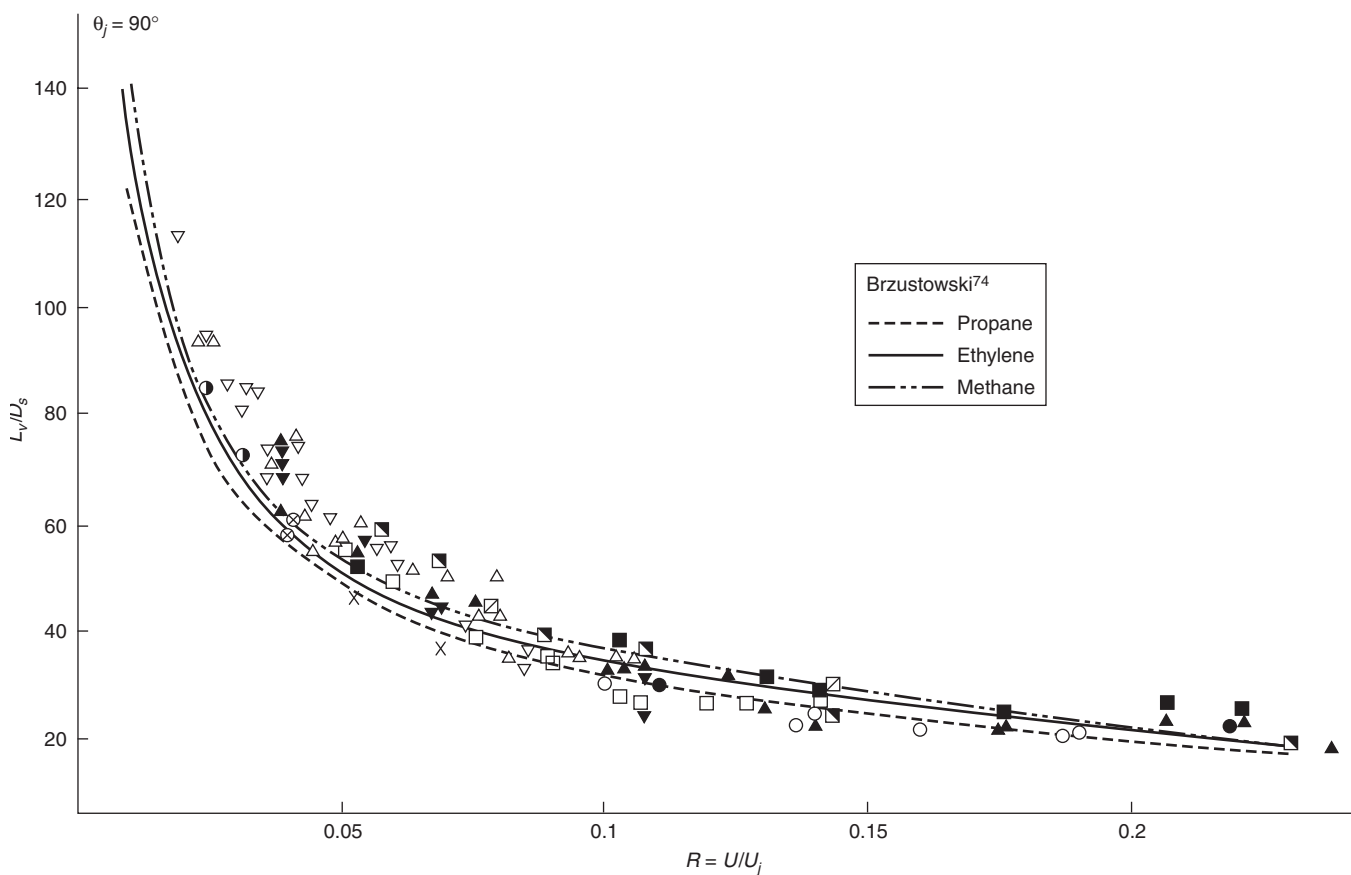


Figure 3-11.32. Variation of the flame length above burner tip with velocity ratio, R .⁹¹

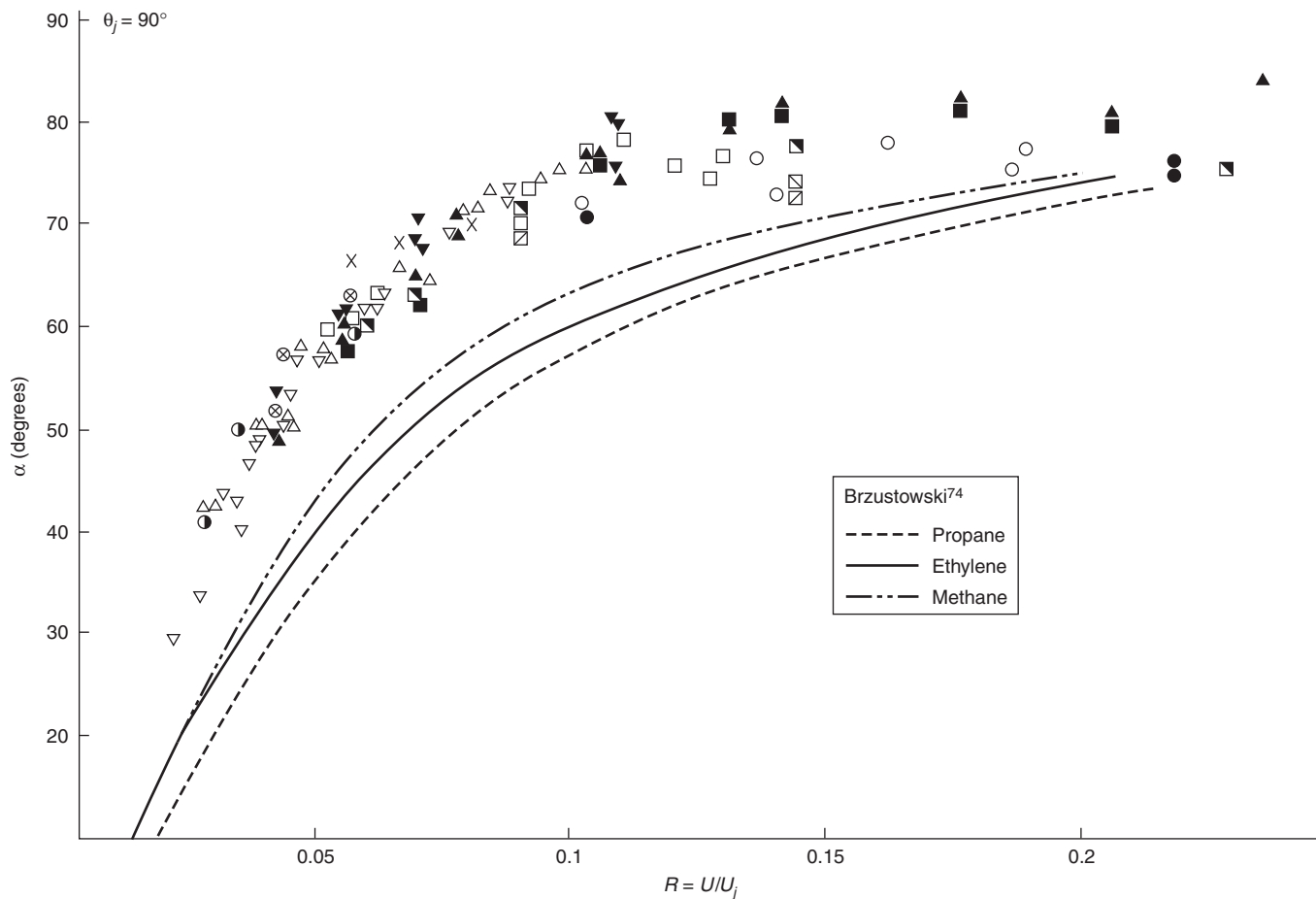


Figure 3-11.33. Variation of angle of tilt with velocity ratio, R .⁹¹

lengths are slightly larger than the ones predicted using Brzustowski's model. Based on these results, Kalghatki⁹¹ suggests the following correlations to determine the flame length and flame tilt parameters.

$$\alpha_B = 94 - \frac{1.6}{R} - 35R \quad (43)$$

$$\alpha = 94 - \frac{1.1}{R} - 30R \quad (44)$$

$$\frac{L_{BV}}{D_s} = 6 + \frac{2.35}{R} + 20R \quad (45)$$

Here the angles α are in degrees. The range of validity of these correlations are for the values of R greater than 0.02 and less than 0.25. The upper limit for R is not a serious limitation to the applicability of the model. For values of R less than 0.02, the wind-free data may be used to determine the flame lengths and the tilt may be assumed to be zero. It should be noted that the flame length given by Equation 45 determines only the vertical component. Actual inclined flame height is given by dividing Equation 45 by the cosine of the angle of tilt given by Equation 43.

It is worth noting that the actual inclined flame length ratio is independent of the velocity ratio and is relatively constant at a value of about 120. This indicates that the majority of the tests conducted in this program were momentum-dominated turbulent jets. Recently, Sonju and Hustad⁹² conducted an experimental study on turbulent diffusion flames. The flare diameters ranged from 2.3 to 80 mm and the velocities ranged from 5 to 250 m/s. Their data indicate that the flame length is proportional to the one-fifth power of the Froude number. For Froude numbers greater than 100,000, the flame lengths appear to be independent of the Froude number. These results are consistent with the data of Putnam and Speich.⁸⁴

Turbulent Jet Flame Diameter in Crosswind Conditions

The work of Hawthorne et al.⁸¹ described above also includes jet flame diameter calculation. They observed that the jet diameter increases as a function of distance. The measured spreading angles were in the range of 3 to 8 degrees (one-half angle). The equivalent diameter for

thermal radiation calculations can be calculated from the following equation:

$$\frac{D_c}{d_j} = \sec \theta + \frac{L}{d_j} \sin \theta \sec^2 \theta \quad (46)$$

The data of Kalghatki⁹¹ for the base and tip widths of the flames indicate the spreading angle is a function of the nondimensional velocity ratio, R . For a jet flame in wind-blown surroundings, Kalghatki⁹¹ gives the following correlation of jet diameter:

$$\frac{W_2}{D_s} = 80 - \frac{0.57}{R} - 570R + 1470R^2 \quad (47)$$

$$\frac{W_1}{D_s} = 49 - \frac{0.22}{R} - 380R + 950R^2 \quad (48)$$

From these calculations, it can also be deduced that the cone half-angle for the frustum decreases from a value of about 5 degrees at $R = 0.025$ to a value of about 2.8 degrees at $R = 0.2$. Therefore, at large, relative wind speeds, a diffusion flame takes an almost cylindrical shape. The data of Sonju and Hustad,⁹² indicates that the flame diameter increases as one-fifth power of the flame Froude number. The suggested constants, proportionally, for methane and propane flames are 2.5 and 4.0, respectively.

Kalghatki⁹¹ also conducted some limited tests with nonorthogonal jet flames and concluded that the flame lengths are dependent on wind direction. These tests were conducted with relative wind angles varying from 45° to 135° (with 90° representing orthogonal cross flow). The value of the nondimensional velocity was greater than 0.025. The data indicate that for a given angle of tilt, the flame length remains relatively constant; however, the flame length decreases with increasing angle of tilt. The data of flame length and wind direction over the entire velocity ratios are shown in Figure 3-11.34. As can be seen from Figure 3-11.34, there appears to be a linear relationship between flame length and wind direction. The correlation suggested by Kalghatki⁹¹ is

$$\frac{L_B}{D_s} = 163 - 0.640\theta_i \quad (64)$$

where θ_i is the angle between wind and jet (degrees).

Aerodynamic effects on flame stability: A jet diffusion flame in still air will lift off the tip of the burner and form a stable lifted flame when the flow velocity through the burner is increased beyond a limiting value known as the lift-off stability limit. If the flow velocity is increased further, the flame is extinguished at some limiting rate known as the *blowout stability* limit.

At the base of a lifted diffusion flame, the local turbulent burning velocity will be equal to the local flow velocity. If the flow rate through the burner is increased, the flow velocity will also increase and the base of the flame will be blown downstream to a new position where the turbulent burning velocity equals local flow velocity. The flame will blow out when the change in the burning velocity cannot keep up with the flow velocity anywhere in the jet as one moves downstream from the base of the jet flame.

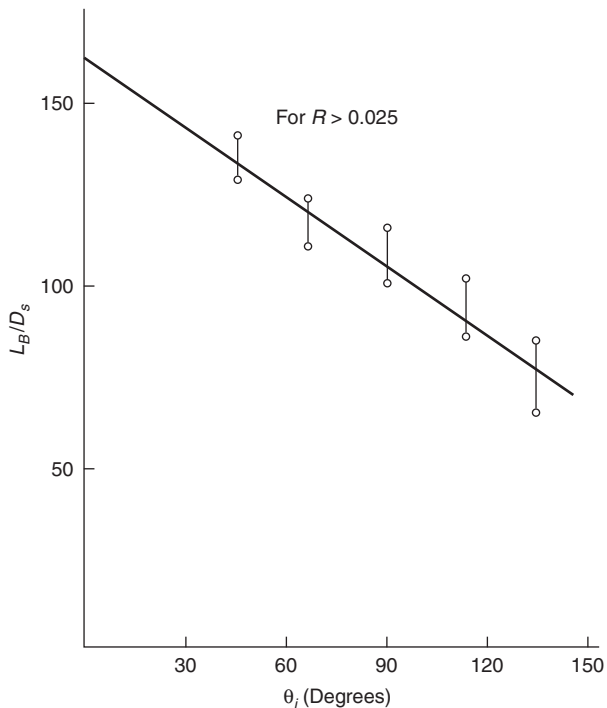


Figure 3-11.34. Variation of flame length with jet axis orientation.⁹¹

The distance along the burner axis where the mean concentration equals the stoichiometric level is independent of the flow velocity and is given by the following equation:

$$\frac{H}{d_e} = 4 \frac{\tilde{\theta}_e}{\tilde{\theta}_s} \left(\frac{\rho_e}{\rho_a} \right)^{1/2} + 5.8 \quad (49)$$

where

H = height along the jet axis, m

d_e = effective jet diameter, m

$\tilde{\theta}_e$ = fuel mass fraction at jet exit

$\tilde{\theta}_s$ = stoichiometric fuel mass fraction

ρ_e = jet mixture density, kg/m³

ρ_a = ambient air density, kg/m³

The effective jet diameter is defined as follows.

For subsonic jets:

$$d_e = d_j \quad \text{for } M < 1$$

For choked flow:

$$d_e = d_j \left[\frac{2 + (\gamma - 1)M^2}{\gamma + 1} \right]^{(\gamma+1)/(\gamma-1)} \frac{1}{\sqrt{M}} \quad (50)$$

where

d_j = jet diameter, m

M = Mach number after expansion to ambient pressure

γ = ratio of specific heats

All things being equal, the larger of the value of H , the more scope there will be for the base of the flame to seek a new stable position as the flow velocity is increased, and therefore it will be more difficult to blow out the flame. Similarly, larger values of burning velocity will lead to larger flow velocities to blow out the flame. The critical velocity at the burner exit for blowout will depend upon the burning velocity, density ratio, and the Reynolds number based on H .

$$\frac{U_e}{S_u} = f\left(R_H, \frac{\rho_e}{\rho_a}\right) \quad (51)$$

where

U_e = critical velocity at jet exit, m/s

S_u = maximum burning velocity, m/s

R_H = Reynolds number given by

$$R_H = HS_u \frac{\mu_e}{\mu_a} \quad (52)$$

where μ_e = dynamic viscosity.

The typical values of the relevant parameters for typical fuels are given in Table 3-11.11.

Kalghatki⁸⁷ conducted a systematic study of the blowout stability of jet diffusion flames in still air. The fuel gases used were methane, propane, ethylene, acetylene, and commercial butane. The burner diameters ranged from 0.2 to 12 mm. The universal stability limit is given by the following equation:

$$\bar{U}_e = 0.017 R_H (1 - 3.5 \times 10^{-6} R_H) \quad (53)$$

where

$$\bar{U}_e = \frac{U_e}{S_u} \left(\frac{\rho_e}{\rho_a} \right)^{1.5} \quad (54)$$

The validity of Equation 53 is shown in Figure 3-11.35. It should be noted that Equation 53 is valid only up to a Reynolds number of 100,000.

Table 3-11.11 Relevant Properties of Hydrocarbon Gases to Determine Blowout Stability

Gas	Molecular Weight	Dynamic Viscosity at 0°C (micropoises)	Maximum Burning Rate S_u (m/s)	Ratio of Specific Heats	Stoichiometric Air-Fuel Ratio
Methane	16	102.7	0.39	1.31	17.2
Propane	44	74	0.45	1.13	15.7
Ethylene	28	91	0.75	1.255	14.9
Acetylene	26	93.5	1.63	1.25	13.3
Butane	54	80	0.44	1.1	15.7
Hydrogen	2	84	3.06	1.33	34.7

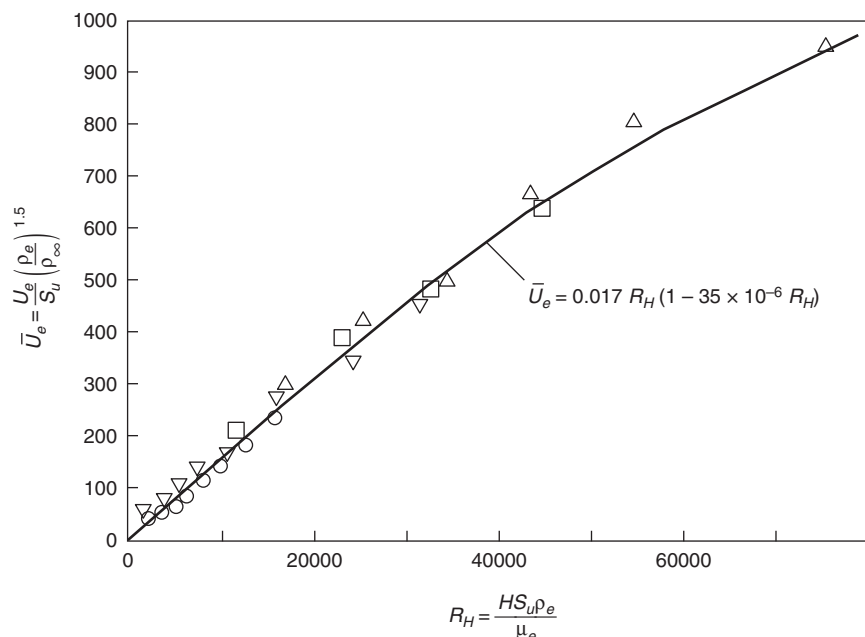


Figure 3-11.35. Universal blowout stability curve for diffusion flames.⁸⁷

Thermal Radiation Hazards from Hydrocarbon Jet Flames

Point Source Model for Jet Flame Radiation

For incident heat flux from a jet flame to a target outside the flame, it is customary to model the flame by a point located at the center of the real flame, as mentioned earlier in the pool fire section. The radiant heat flux per unit area and per unit time received by a target at a distance R from the point source is given by

$$\dot{q}'' = \frac{\dot{Q}_r \cos \theta}{4\pi R^2} \quad (55)$$

where \dot{Q}_r is the radiative output given by the radiation fraction, χ_r , multiplied by the total heat release rate:

$$\dot{Q}_r = \chi_r Q$$

The geometrical aspects of the representation of thermal radiation field given by the point source model are surprisingly accurate for flare stacks, even in the case of long windblown flames. Many of the early experimental investigations relevant to jet flames were concerned with flares. The work covers a variety of jet flames, including flames of natural gas and of liquified petroleum gas (LPG). Representative accounts of work using natural gas are those by Chamberlain,⁹³ Johnson, Brightwell, and Carsley⁹⁴ at Shell, and by Cook, Fairweather, Hammonds, and Hughes⁹⁵ at British Gas. Accounts of work on jet flames of LPG at Shell and British Gas have been given by Hirst⁹⁶ and Tam and Cowley.⁹⁷ The work on flames formed part of a study of emission and gas dispersion of jets as well as of combustion.

Hirst⁹⁸ describes experiments using liquefied propane. Tests were carried out using orifices ranging from 9 to 52 mm in diameter and pressures from about 6 to 20 bar. Both horizontal and vertical releases were studied. A series of tests were done with vertical releases. The liquid rose in a strongly divergent cone bending with the wind. The cone angle was typically 30° for the plume but up to 90° in the flash region. The releases usually reached a steady state before ignition. The visible clouds at ignition were large, extending up to 45 m vertically and 70 m downwind. In most cases fireballs formed and in several tests rose to 100 m; the most fully developed fireballs occurred at low wind speeds. The overpressure generated by the flames were also measured. The maximum observed fell from some 3 bar at 20 m from the release point to about 0.8 bar at 100 m.

Other tests were done with horizontal releases. One of the features measured in these trials was the distance reached by the flame. Figure 3-11.36 gives the relation between the mass flow and the impingement distance of the flame for a 50-mm-diameter pipe. In one of the trials in which a 35-m-long jet flame from a full bore release of 7.9 kg/s from a 50-mm pipe at pressure of 13 bar. The combustion energy was 365 MW. The maximum surface emissive power was 250 kW/m² and occurred 25 m from the release point and just before the flame underwent transition from the momentum-dominated to the buoyancy-dominated condition. However, for such full-scale bore

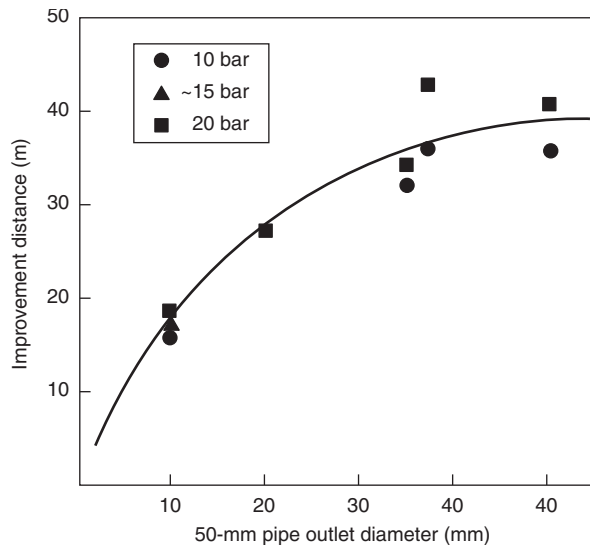


Figure 3-11.36. Jet flames: flame impingement distance versus mass flow for propane.⁵⁷

discharges the heat radiation within the flame was complex, and steady heat fluxes were mainly in the range 50–220 kW/m² and depended on the discharge conditions and the target distance. The maximum temperature occurred at a distance of 4 m and had a value of 1570 K.

Brzustowski⁹⁸ considered a flare (in the presence of high crosswind) as a uniformly radiating cylinder. He observed that the thermal radiation flux given by point source model is similar to those predicted using a cylindrical source model except at distances very close to the source. Brzustowski⁹⁸ also computed radiation heat flux for vertical elements parallel and perpendicular to the wind direction and has concluded that the corrected point source model and the uniform cylinder radiation model essentially yield very similar results.

Brzustowski, Gollahalli, and Sullivan⁸⁹ carried out small- and pilot-scale experiments to study the radiative characteristics of turbulent flares using commercial-grade methane and propane. Small-scale test data were taken at jet velocities from 6.8 to 70 m/s with jet Reynolds numbers from 7500 to 94,000, and ratios of crosswind velocity to jet velocity from 0 to 0.113. Pilot-scale experiments were conducted on an outdoor site with the flare modeled by a vertical 25-mm inner-diameter pipe 1.5 m high. In these tests, provisions were made for injecting steam into the gas below the tip of the flare. The incident heat flux at various distances was measured with and without steam.

Oenbring and Sifferman⁹⁹ compared the point source model predictions with full-scale measurements. The full-scale data consisted of radiation measurements in the Oenbring and Sifferman⁹⁹ studies that were conducted at the oil refinery facility in Conoco's Ponca City, Oklahoma, and in the Gillis gas plant facility in Los Angeles, California. The Gillis flare stack was 40 cm (16 in.) in diameter and 23 m high. The gas velocity ranged from a Mach number of 0.2 to 0.49. All test data indicate that the inverse square law predicts the thermal radiation accurately.

Radiative Fraction for Jet Flames

In order to predict the incident heat flux accurately, it is necessary to determine the fraction of total combustion energy resulting in thermal radiation. In general, the fraction of heat radiated depends on the efficiency of combustion and soot formation and on the heat lost by convection to the entrained air.

Most thermal radiation prediction models tends to ignore the details of the combustion process and concentrate on the overall combustion efficiency, or fraction of the energy that is radiated to the environment. Markstein⁷ conducted a series of radiation measurements on propane turbulent diffusion flames. The total radiative powers of the flames were determined using wide-angle radiometer. The flow rates varied from 44 to 412 cm³/s. A collimated beam radiometer was used to measure the radiation characteristics of different parts of the flames. Based on these measurements, Markstein⁷ concluded that the thermal radiation from diffusion flames is at a maximum at approximately the center of the flame and tapers off on either side, forming a Gaussian distribution. The total radiative power of the flame was observed to be directly proportional to the total heat-release rate. Figure 3-11.37 shows that the fraction of combustion energy released in the form of radiation is approximately 20 percent for the propane diffusion flames. Burgess and Hertzberg³⁷ measured the fraction of combustion energy radiated to the surroundings for several gaseous fuels. Tan¹⁰⁰ and Kent¹⁰¹ have also suggested values for the radiated energy for a variety of fuels.

Table 3-11.12 compares the values of radiative fraction, χ_r , suggested by various investigators. The parameter f_s in Table 3-11.12 represents the fuel mass fraction at which carbon particles begin to form. For any hydrocarbon fuel, C_nH_m burning in air, the fraction f_s is given by

$$f_s = \frac{12n + m}{12n + m + [n/2(137.3)]} \quad (56)$$

For the same entrainment/mixing history, a gas with a higher value of f_s has less tendency to form solid carbon particles than a gas with a lower value of f_s . Higher values of f_s , therefore, correspond to lower radiation levels.

Examination of Table 3-11.12 shows good qualitative agreement. Propane and butane have similar values of f_s , and their χ_r values are comparable. Methane and hydrogen have lower values of χ_r and higher f_s values. But ethylene has a lower value of f_s and, except in one study by Burgess and Hertzberg,³⁷ the χ_r values are also lower. This

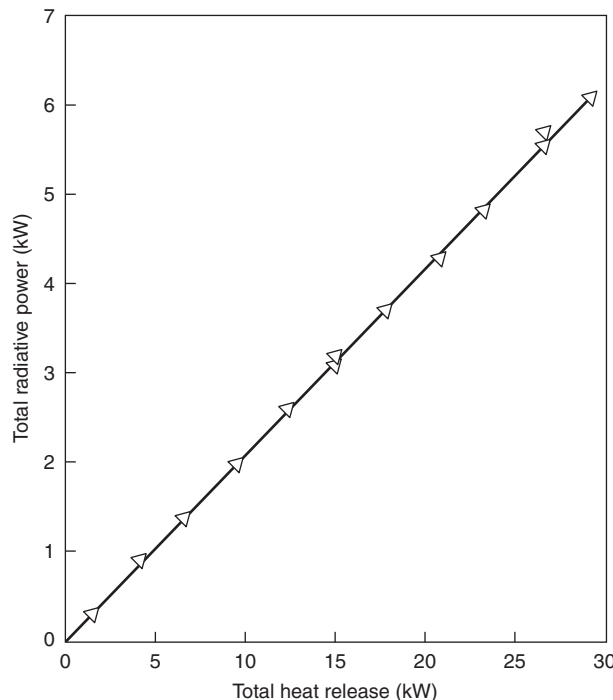


Figure 3-11.37. Radiative power for propane diffusion flames.⁷

may be partially due to straight molecular weight corrections applied by Tan¹⁰⁰ and Kent.¹⁰¹

The intensity of flame radiation may be affected by the medium through which it passes. An appreciable attenuation may occur when radiation is transmitted from a source to a target through the atmosphere. The values of radiative fraction χ_r in Table 3-11.12 are properties of the fuel only. They do not take into account the variation of the operating parameters such as stack exit velocity, cross-wind velocity, and the presence of air steam. However, these parameters have a profound influence on the temperature profiles and affect the fraction of combustion energy radiated, χ_r .

Figure 3-11.38 shows the radiative fraction measured by McCaffrey over six decades: u/\sqrt{gD} . Comparing this figure with Figure 3-11.31 shows that the radiative fraction is constant in the buoyancy-controlled regime, but for momentum-controlled jet flames, the radiative fraction decreases until blowoff occurs.

Table 3-11.12 Comparison of Radiative Fraction, χ_r , of Various Fuels

Fuel	f_s	χ_r Brzustowski ⁹⁸	χ_r Burgess and Hertzberg ³⁷	χ_r Tan ¹⁰⁰	χ_r Kent ¹⁰¹	χ_r McCaffrey ⁸⁶
Hydrogen	1.0	0.2	0.17	—	—	—
Methane (C ₁)	0.189	0.2	0.23	0.20	0.19	0.22
Ethylene (C ₂)	0.170	0.25	0.36	0.26	0.25	0.38
Propane (C ₃)	0.176	0.30	—	0.32	0.32	0.302
Butane (C ₄)	0.175	0.30	0.30	0.37	0.37	—
C ₅ and higher	—	0.40	—	—	—	—

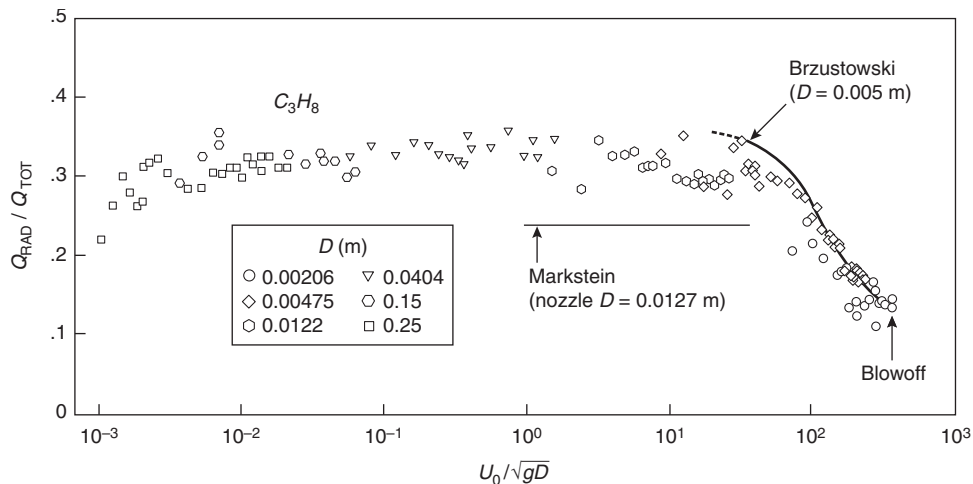


Figure 3-11.38. Radiative fraction measured by McCaffrey.⁸⁶

Evans and Pfenning¹⁰² and McCaffrey^{103,104} have studied jet flame extinction via water spray. They also document significant reductions in flame radiation at subsuppression water spray addition rates of up to 50 percent.

Brzustowski, Gollahalli, Gupta, Kaptein, and Sullivan⁷⁹ conducted a series of laboratory-scale tests on the effects of jet velocity and free stream velocity on the fraction of energy radiated, χ_r , from the turbulent flames. Figure 3-11.39 shows the effect of jet velocity on radiation in the absence of crosswind for methane and propane flames. Also drawn in Figure 3-11.39 are the suggested values of radiative fraction χ_r from Tan¹⁰⁰ and Kent¹⁰¹. As can be seen from Figure 3-11.39 the fraction of energy radiated, χ_r , is strongly dependent on jet velocity and decreases with increasing jet velocity. Figure 3-11.40 shows the effects of crosswind velocity on the radiant energy. In general, increasing crosswind velocity appears to increase the fraction of energy radiated, χ_r .

The significant departures of measured values of χ_r from the values previously published (which do not take into account the aerodynamic effects) can be understood in relation to variation of the detailed temperature profiles in the flames. The underlying explanation deals with the competing processes by which the products of hydrocarbon pyrolysis near the flare stack oxidize directly or form soot that burns in the downstream portion of the flames. Quite obviously, predictions based on the traditional values of χ_r would have overestimated the thermal radiation in all these laboratory-scale experiments. Brzustowski, Gollahalli, Gupta, Kaptein, and Sullivan⁷⁹ also measured thermal radiation from a full-scale flare. The 0.406-m-diameter flare was operating at about 25 percent of the design flaring rate. The best estimates of jet velocity and wind velocity were 28 and 4 m/s, respectively. The flame length was measured to be 25 m and flame tip was about 10 m above the flare tip level. The value of χ_r , calculated from the radiation measurements at two ground sections 0.223 was about 30 percent lower than the values predicted using the Tan¹⁰⁰ and Kent¹⁰¹ approaches.

Figure 3-11.41 shows the fraction of net heat release radiated as a function of the flare Reynolds number for a 5-cm (2-in.) natural gas flare from Straiz, O'Leary, Brennan, and Kardan.¹⁰⁵ The Reynolds numbers in these tests are comparable to full-scale Reynolds numbers (of the order of 10^5 to 10^6). The fraction of energy radiated, χ_r , shows a significant departure at higher Reynolds numbers from its traditionally assumed value of 0.2.

It is quite evident that the aerodynamics of the flow have a significant effect on the radiation from a large

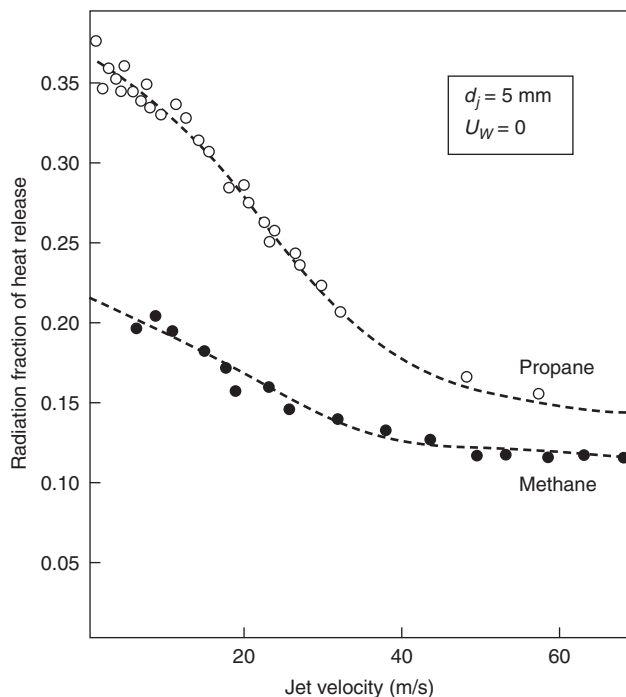


Figure 3-11.39. Effect of jet velocity on radiated fraction of combustion energy.

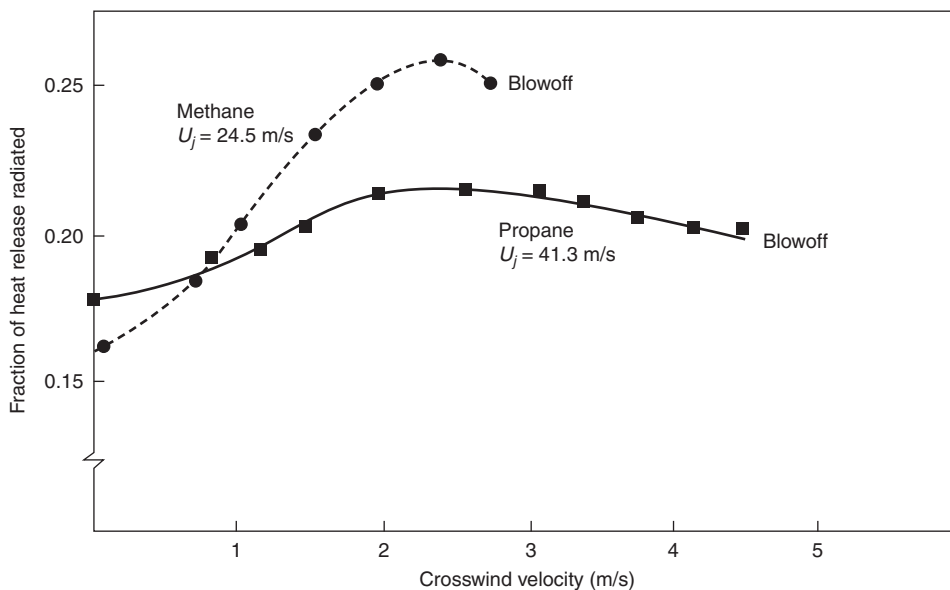


Figure 3-11.40. Effect of crosswind velocity on radiated fraction of combustion energy.

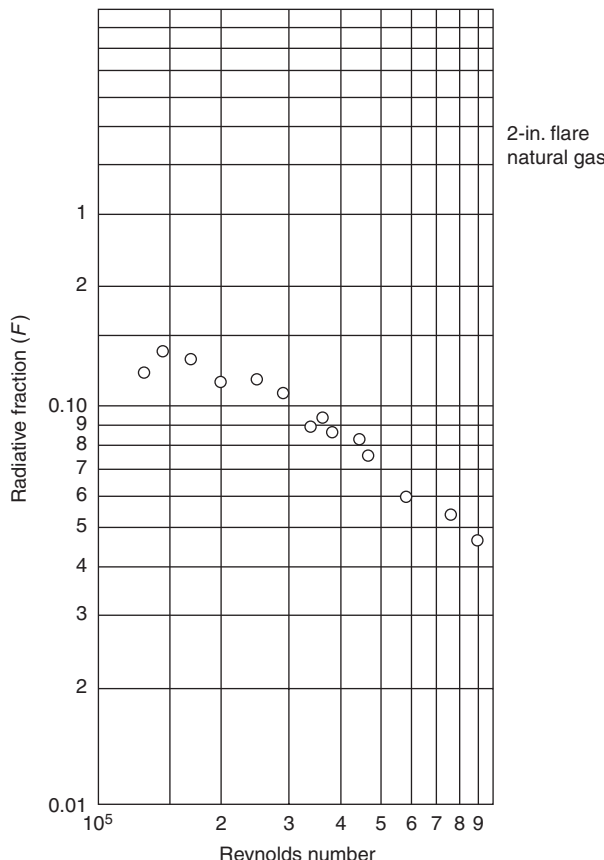


Figure 3-11.41. Radiative fraction for natural gas flames full-scale tests.¹⁰⁵

turbulent diffusion flame. However, the radiation data described above were obtained on the laboratory-scale experiments, and their validity for large flames encountered in an offshore environment cannot be taken for granted.

Line and Cylinder Models for Jet Flame Radiation

As mentioned in the previous section, a point source model is a simple representation of a jet flame and applies only at large distance from the fire. The point source model can be inaccurate for target positions close to the fire. This is particularly important when one is evaluating safe separation distances for storage of hydrocarbon fuels.

The tilted cylinder model discussed in the pool fire section can be used to overcome the inaccuracy of the point source model to determine the thermal radiation from large diffusion flames. This model assumes that the fire can be represented by a solid body of a simple geometrical shape, and all thermal radiation is emitted from its surface.

The incident radiation per unit area per unit time is given by

$$\dot{q}'' = FE\tau \quad (57)$$

where

E = surface emissive power of flame, kW/m^2

F = configuration factor

τ = atmospheric attenuation factor (transmissivity)

The configuration factor is the fraction of the radiation falling directly on the receiving target. The shape or configuration factor depends on the shapes of the fire and receiving target, and on the distance between them.

The surface emissive power is the total radiative power leaving the surface of the fire approximated by the following equation:¹⁰⁶

$$E = E_{bb}(1 - e^{-\kappa L}) \quad (58)$$

where

E_{bb} = equivalent blackbody emissive power, kW/m²

κ = extinction coefficient, m⁻¹

L = effective pathlength, m

The blackbody emissive power E_{bb} can be calculated by

$$E_{bb} = \sigma T_f^4 \quad (59)$$

where σ is the Stefan-Boltzmann constant (5.67×10^{-11} kW/m²·K⁴) and T_f is the flame temperature (K).

Fumarola, de Faveri, Pastorino, and Ferraiolo¹⁰⁷ suggested a line source model to compute radiation from jet flames. An elemental length of the flame is assumed to radiate similar to a point source model. The total incident heat flux at any observer location is computed by integrating the heat flux due to an elemental source over the flame length. They compare their results with Brzustowski⁹⁸ and the Oenbring and Sifferman model and observed that their model predicted lower-incident heat fluxes at ground level.

Galant, Grouset, Martinez, Micheau, and Allemand¹⁰⁹ proposed a three-dimensional numerical model to estimate the flame geometry and thermal radiation from large diffusion flames. The model considers the variation in flow conditions based on a pseudo-streamfunction formulation and includes effects of turbulence, combustion, and soot concentration. The model has been validated with field experiments of up to 254-mm (10-in.) diameter methane jets and agreement between predicted and measured heat flux is within 15 percent.

Jet Fire Impingement Exposure

The severity of the thermal exposure from impinging jet flames far exceeds that observed for pool fire exposures. Heat fluxes of up to 250 and 300 kW/m² for two-phase LPG and sonic natural gas jets, respectively, have been measured in large-scale jet flame tests (e.g., Cowley and Prichard¹¹⁰). In these tests where the flame fully engulfed a cylindrical target, heat fluxes averaged over the impingement area were 200 kW/m² for sonic natural gas jets and were 150 kW/m² for two-phase LPG jets.

The severity of jet flame impingement exposures results from highly radiative, optically thick flames with high convective heat fluxes. The radiative and convective components of the total heat flux tend to be roughly equal in the high heat flux regions of the target (Parker¹¹¹). Wighus and Dransgsholt¹¹² report temperatures as high as 1200°C and impingement velocities of up to 80 m/s in gaseous propane jet flames. They also found that the temperatures observed at the location of peak velocity were lower for higher gas velocities. For instance, they measured 1150°C at 30 m/s and 650°C at 80 m/s. They measured heat fluxes as high as 340 kW/m² in some tests, and the radia-

tive fraction of the total heat flux tended to be about 2/3. Their results would indicate that differences found by Cowley and Prichard¹¹⁰ for natural gas and two-phase LPG flames were primarily the result of the two-phase nature of the LPG release rather than differences between natural gas and propane gaseous flame properties.

Unsteady Thermal Radiation Analysis

Liquefied fuel gases having boiling points below normal ambient temperatures have come to be stored and transported in large quantities. Liquefied natural gas (LNG) is stored for peak demand use. It is also transported by sea in bulk carriers designed for cryogenic cargos. Liquefied petroleum gas (LPG) is stored under pressure and is transported by trucks, railroad tank cars, and by sea in bulk carriers. While liquefied hydrogen has been used in limited quantities as a rocket fuel, serious consideration is being given to its use as a fuel for aircraft and possibly highway vehicles. Because volatile fuels are being transported in rapidly increasing volumes, speculation is being devoted to the kinds of accidents that could result from the release of these fuels.

The failure of a container carrying a pressurized cargo will result in the flash evaporation of a portion of the released liquid and the sudden formation of a vapor cloud from the evolved vapors. Upon contact with an ignition source, one of two situations may occur: the generation of a propagating plume flame, or the formation of a fireball. If the vapor puff is ignited immediately after its formation, it may burn as a rising sphere, usually referred to as a *fireball*. The rapid combustion of vapor clouds in the form of fireballs has been observed in several accidents involving vehicles carrying liquid propane. Here some of the accidents where a fireball has been reported to be observed are reviewed.

In the General Accounting Office report to the U.S. Congress regarding liquefied energy gases safety, an accident is cited involving a tractor-semitrailer carrying 34 m³ (9000 gal) of LPG. About 2 min after the accident, a fireball of about 123 m (135 yd) in diameter was observed. The radiant heat from the fireball burned several people, a house, several other buildings, and some 12 acres of woods.

The National Fire Protection Association has maintained descriptions of several accidents involving LPG where a rising fireball was observed. One such accident happened in Oneonta, New York, where a freight train derailed involving 27 cars, 7 of which contained 120 m³ (33,000 gal) of liquid propane. Seconds after the derailment, a huge fireball erupted from the area where the tank cars were piled up. It is believed that this fireball was the result of ignition of LPG when one of the tank cars split open. The fireball heated other tanks carrying LPG, which resulted in several BLEVEs (boiling liquid expanding vapor explosions).

One of the most cited fireballs occurred in Crescent City, Illinois, when a freight train carrying 15 cars derailed, 10 of them containing 130 m³ (34,000 gal) of LPG each. One of the derailed tank cars rode up and over the pile and tore a hole in another tank car containing propane, causing the release of gas that produced the first

fireball. There were several subsequent explosions that lasted for hours and destroyed 24 individual living quarters and 18 businesses.

The fireballs resulting from such accidents are large—usually of the order of about 100 m in diameter. The duration of the fireball is on the order of a few seconds because of rapid mixing with the surrounding air. During this brief period, a fraction of the combustion energy present in the initial mass of vapor is radiated as thermal energy to the surroundings. The adverse effect of this thermal radiation to population and property depends on the intensity and the duration of the radiation.

If, however, the vapor cloud is allowed to travel with the wind and is ignited at a location away from the source, the resulting vapor fire assumes the form of a propagating plume flame. In both cases, an unsteady diffusion flame is produced. However, the flame geometry is defined by the particular mode of burning. Accordingly, the levels of resulting thermal radiation differ significantly for each mechanism. The unique behavior of these vapor cloud fires is discussed in this chapter. The following sections present an analysis of burning vapor clouds that define a plume fire; a discussion of the formation and burning of a hydrocarbon fireball; and a sample calculation procedure for burning of a vapor cloud in the form of a fireball.

Thermal Radiation from Burning Vapor Clouds

Estimating the thermal radiation field surrounding a burning vapor cloud involves geometric characterization of the cloud, that is, the time-averaged size of the visible envelope. It also requires estimation of the radiative properties of the fire, that is, the average emissive power, and so forth. Finally, the radiant intensity at a given location must be determined. Since the burning behavior of a moving vapor cloud can be best described as unsteady, the standard equations for pool fires do not apply. In the discussion that follows, the flame geometry and effective thermal radiation parameters that characterize a burning vapor cloud are identified.

Given a spill of a volatile, flammable chemical, initially a pool is formed. As the pool vaporizes due to heat transfer from the medium surface (land or water), a vapor cloud is formed above the pool. These vapors are entrained by the ambient wind, and are dispersed in the downwind direction. Two conditions must be met for a burning cloud to be produced; first, there must be an ignition source located away from the spill point; second, the concentration within the vapor cloud must be within the flammability limit range for that material. Assuming these conditions exist, the fire that results is in the form of a propagating plume flame.

Based on experiments with spills of LNG on water, Mudan¹¹³ and Raj et al.³⁸ identified three stages of vapor fire development. First, a transient turbulent flame spreads through the cloud. The flame propagates in both upwind and downwind directions. The second stage in the development of a vapor fire is the steady-state propagation toward the liquid pool. At this location, there appears to be a stationary diffusion flame. The third and final stage of burning results in a small pool fire at the source location. Based on limited experimental data on

vapor cloud fires, the burning behavior and resultant flame geometry can be analyzed.

Flame propagation velocity: Within a few seconds after ignition, flames tend to spread quickly both upwind and downwind of the ignition source. Flame travel in both directions is consistent if the ignition occurs after the flammable vapor cloud travels over it. The flames are initially contained within the cloud, but subsequently extend in the form of a flame plume above the cloud. This is consistent with premixed burning of the regions in the cloud that are within flammable limits prior to flame arrival, followed by diffusive burning of the richer regions in the cloud. After consuming the flammable vapors downwind of the ignition source, the downwind edge of the flame starts moving toward the spill point. Generally, the flame zone is normal to the wind direction.

During this transient flame growth, an *average* flame propagation velocity with respect to the ground can be determined by noting the location of the upwind edge of the flame at various time intervals. The flame speed with respect to gases may be obtained by adding the wind speed to the flame speed with respect to the ground. The initial, rapid propagation of the flame in the premixed vapor cloud can also be measured by the same technique.

Wind speed plays a significant role in the vapor cloud propagation. The flame velocity tends to increase with wind speed. Also, an increase in wind velocity increases the dispersion process. The ignition delay is also affected by the wind speed. Clearly, for a fuel-rich vapor cloud, an increase in mixedness will increase the flame propagation velocity. However, if the fuel concentration is well below stoichiometry, a further increase in ignition delay may, in fact, cause a decrease in flame propagation speed.

Mizner and Eyre³⁶ conducted vapor fire tests with propane spilled on water. The spill rates of propane varied from 2.1 to 5.6 m³/min and the ignition source was located approximately 130 m from the spill point. The wind speeds varied between 6 and 7 m/s. The flame propagation velocities measured by locating the upwind edge of the flame as a function of time. Their analysis indicates that the flame propagation velocity (with respect to the ground) varies between 3.75 and 4.8 m/s.

In Figure 3-11.42 the measured flame propagation velocities (with respect to unburnt gases) are shown for various wind speeds. The data indicate that there is no significant variation in the flame propagation velocities for methane (LNG) and propane (LPG). The maximum laminar burning velocity for methane is 0.45 m/s; laminar flame speed is 3.5 m/s; and the typical expansion ratio is 7.4. The corresponding properties for propane are 0.52, 4.0, and 7.6 m/s, respectively. Since these properties are somewhat similar for methane and propane, it is reasonable to expect the turbulent flame propagation velocities to be similar.

Flame geometry model: Fay and Lewis¹¹⁴ proposed a model for unsteady burning of unconfined fuel vapor clouds. Based on small-scale experiments with methane, ethane, and propane, and a simple entrainment model, they gave expressions to compute the maximum diameter, height, and duration for complete combustion. The model

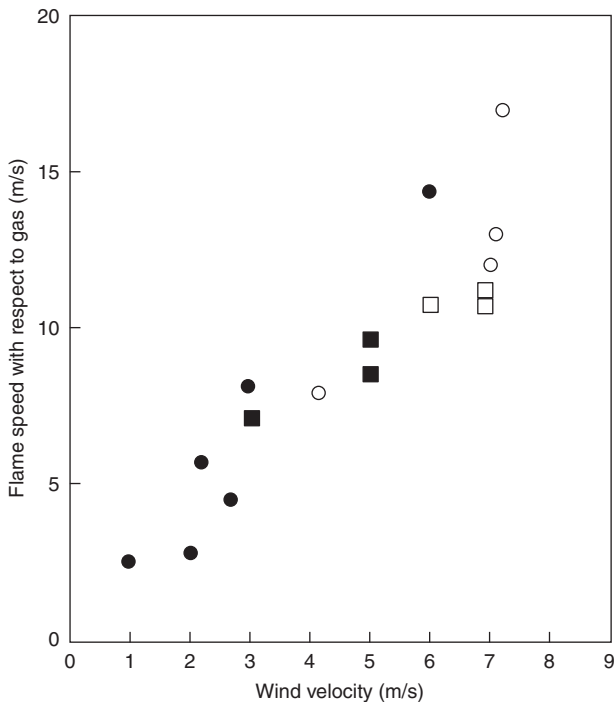


Figure 3-11.42. Flame propagation velocities for LPG and LNG vapor fires.¹¹³

suggested by Fay and Lewis¹¹⁴ assumes that the unsteady, turbulent diffusion flame is in the form of a fireball. The correlations given by the authors are validated over a range of small-scale experimental data (up to 200 cm³) with methane, ethane, and propane gases at room temperature. However, experiments conducted with cold propane vapors ignited in an open environment do not show evidence of a fireball. In fact, the experiments performed by Shell³⁶ with LNG and LPG, and earlier tests involving LNG vapor fires, fail to confirm Fay and Lewis's¹¹⁴ proposition that diffusive burning in unconfined vapor clouds takes place only in the form of a fireball.

Raj and Emmons¹¹⁵ presented a theoretical analysis to estimate the ground level width of a large combustible vapor cloud. The model is based on the principle that the plume above a heat source is characterized by the strength of the heat source. In the case of a burning vapor plume, the rate of burning controls the plume characteristics, and the rate of burning itself is a function of the gas velocity within the plume.

The essential features of the Raj and Emmons¹¹⁵ model are illustrated in Figure 3-11.43. The assumptions made in the model development are as follows:

1. The geometry of the burning vapor cloud is two dimensional.
2. The burning is controlled by natural convection (buoyancy).
3. The flame propagation velocity with respect to unburnt gases is relatively constant.
4. The depth of the vapor cloud is uniform and is not affected by the flame.
5. The variation of the depth of vapor in the preburning zone is linear.

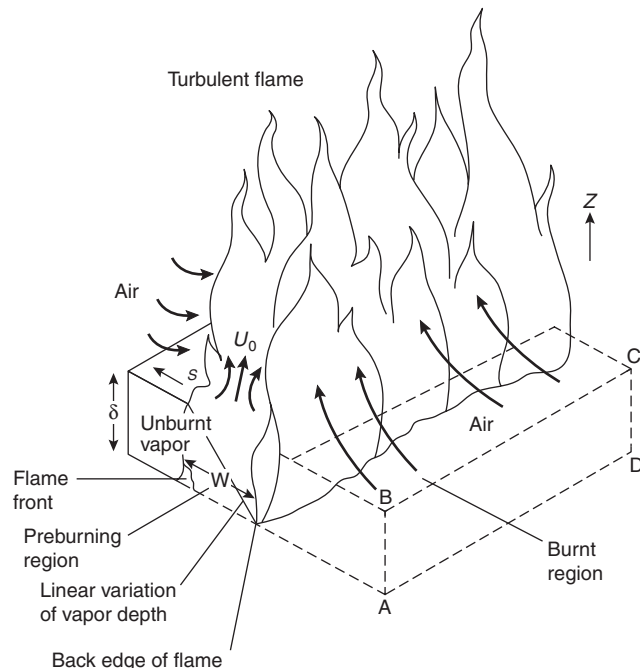


Figure 3-11.43. Schematic diagram showing the unconfined burning of a pure flammable vapor cloud.

6. The steady-state turbulent flame correlation for the ratio of visible flame height to base width is valid.

Using experimentally derived values for flame height-to-width ratio and flame propagation velocity, Raj and Emmons¹¹⁵ gave the following equation to determine the flame width as a function of time:

$$\tau = \left(\frac{Fr_f}{Fr} \right)^{1/3} \left\{ \frac{\pi}{3\sqrt{3}} + \frac{2}{3} \ln \left[\frac{\sqrt{\chi^2 + \chi + 1}}{(1 - \chi)} \right] - \frac{2}{\sqrt{3}} \tan^{-1} \left[\frac{2}{\sqrt{3}} \left(\chi + \frac{1}{2} \right) \right] \right\} \quad (60)$$

and

$$\chi = \left[\left(\frac{Fr}{Fr_f} \right)^{1/3} \xi \right]^{1/2}$$

where

$$\xi = W/\delta$$

$$\tau = 2 St/\delta$$

$$Fr_f = S^2/g\delta = \text{flame Froude number}$$

$$Fr = \text{Froude number} = U_0^2/gW$$

$$S = \text{flame propagation velocity, m/s}$$

$$g = \text{acceleration due to gravity, m/s}^2$$

$$\delta = \text{unburnt vapor cloud thickness, m}$$

$$U_0 = \text{upward velocity at flame base, m/s}$$

$$W = \text{flame width, m}$$

Raj and Emmons¹¹⁵ estimated the Froude number based on Steward's³⁹ data on flame heights for hydrocarbon diffusion flames. The analysis indicates the following relationship for the flame height in a linear heat source.

$$\left(\frac{H}{W}\right)_{\text{stoichiometric}} = 4.98 N_{\text{co}}^{1/3} \quad (61)$$

where N_{co} is the combustion number defined as follows:

$$N_{\text{co}} = \text{Fr} \frac{\rho_0'^2 \omega [r + \omega/\rho_0']^2}{(1 - \omega)^3} \quad (62)$$

where

ρ_0' = density ratio = density of vapor at flame base/density of air.

r = stoichiometric air/fuel mass ratio

ω = inverse volumetric expansion ratio and is defined as follows:

$$\omega = \frac{1}{(1 + Q_c/rC_p T_a)} \quad (63)$$

where

Q_c = heat of combustion, J/kg

C_p = specific heat, J/kg·K

T_a = ambient temperature, K

The maximum width of the vapor fire is given by the following equation:

$$\xi_\infty = \frac{W_\infty}{\delta} = \left(\frac{\text{Fr}}{\text{Fr}_f} \right)^{-1/3} \quad (64)$$

Steward's⁸⁵ data indicates that nearly 400 percent excess air is entrained in the fire plume. The typical height-to-width ratios measured in Steward's⁸⁵ data range between 5 and 50. Raj and Emmons assumed a height-to-width ratio of 2 for LNG vapor fires and demonstrated that Equation 64 predicts the observed behavior of flame width.

Experimental data on methane and propane vapor fires indicate that the flame width varies as the cloud propagates back to the spill point. Typically, it has been observed that the flame width increases as a function of time until all the flammable vapor is consumed. The width of the fire reduces to the dimension of the pool. That rate of increase in flame width appears to be slightly less than the flame propagation velocity (with respect to the ground).

The flame length variation can also be estimated as a function of flame width. It is interesting to note that flame length also increases slightly with time, but the ratio of the flame length to flame width is relatively constant. A plot of flame length-to-width ratios for propane vapor flames is shown in Figure 3-11.44.¹¹³ In general, flame length is about 40 percent of the flame width. The data of Mizner and Eyre³⁶ show that the typical flame length-to-width ratio varies between 20 and 40 percent. It is worth noting that vapor fire flame length-to-width ratios are significantly less than flame height-to-diameter ratios for pool fires.

The time-dependent flame width may be calculated using Equation 64. Figure 3-11.45 compares the computed

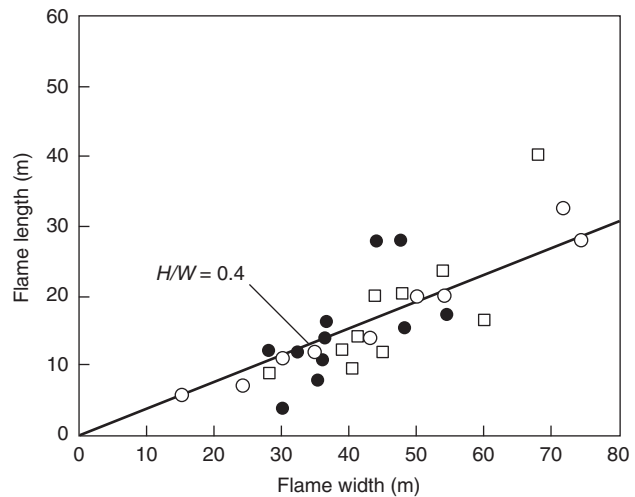


Figure 3-11.44. Flame length as a function of flame width.¹¹³

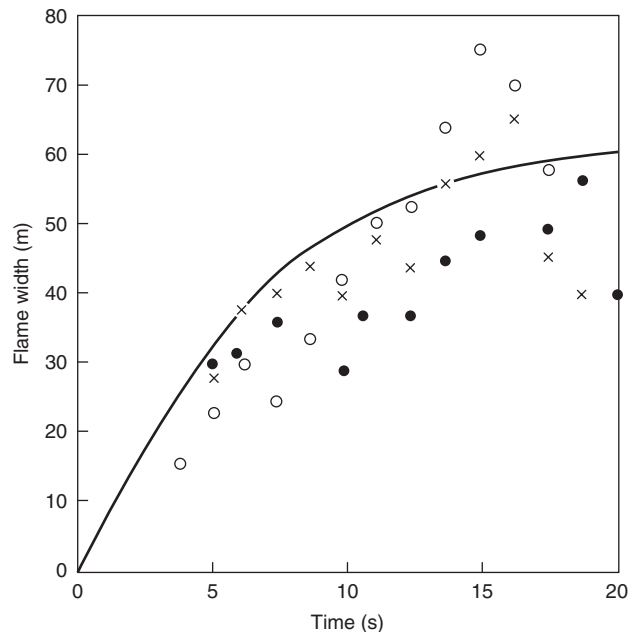


Figure 3-11.45. Comparison of predicted and measured flame widths for LPG vapor fires.¹¹³

flame width to measured flame widths as a function of time. Although there is considerable scatter in the data, the overall agreement between predicted and observed growth rates is good.

Thermal radiation: The incident flux received by a stationary observer from a propagating vapor is a complex function of several factors. First, the emissive power, which defines the radiative properties of the fire, should be determined. Since the duration of a vapor fire is short, and the steady burning period is even shorter, it is difficult to assign an averaging time for determining emissive powers and average incident fluxes. There is, however, a

short period over which the thermal radiation appears to have less fluctuation. This duration can be used in determining average incident fluxes and corresponding emissive powers.

Another important geometrical parameter influencing the thermal radiation from vapor fires is the area of the visible flame. If the flame is optically thick, the thermal radiation increases with an increase in the flame surface area. The area increases rapidly immediately following ignition because both the flame width and flame height increase with time. Therefore, the flame area increases approximately like the square of time. Once the flammable vapors are consumed, the flame area decreases rapidly. The incident flux also increases rapidly due to increasing flame area and drops off as the burnout process begins. The distance to the flame surface is also a key parameter. Since the flame is in motion, the distance varies continuously until the cloud approaches the spill points where a pool fire is formed. Coupled with the variation in distance is the changing effect of absorption by the water vapor and carbon dioxide in the atmosphere. And finally, the geometry of the flame relative to the observer influences the view factor, that is, that portion of flame "seen" by the observer. Therefore, it is evident that the transient nature of the burning process, effected by the changing geometry, severely limits a detailed characterization of thermal radiation from a vapor cloud fire.

For a simple rectangular flame geometry, the centerline horizontal and vertical view factors can be determined using the following equations:²

$$F_h = \frac{1}{2\pi} \left(\tan^{-1} \gamma + \frac{X}{\sqrt{1+X^2}} \tan^{-1} \frac{Y}{\sqrt{1+X^2}} \right) \quad (65)$$

$$F_v =$$

$$\frac{1}{2\pi} \left(\frac{X}{\sqrt{1+X^2}} \tan^{-1} \frac{Y}{\sqrt{1+X^2}} + \frac{Y}{\sqrt{1+Y^2}} \tan^{-1} \frac{X}{\sqrt{1+Y^2}} \right) \quad (66)$$

where X = flame length divided by observer distance, and Y = flame width divided by observer distance.

For asymmetric configurations, trigonometric variations of Equations 65 and 66 can be used to determine the appropriate view factors. The leading edge of the flame (with respect to the observer) may be calculated using the ignition location and the flame propagation velocity. The time dependent flame width may be calculated using Equation 64. Since flame height is related to flame width, the crosswind radiation may be calculated using appropriate view factors. The incident thermal flux is given by the following equation:

$$\dot{q}_{\text{crosswind}}'' = EF_{V,H}\tau \quad (67)$$

where τ represents the atmospheric transmissivity.

A similar procedure may be adopted to calculate incident thermal radiation in the downwind direction. Here the flame is moving away from the observer at flame propagation speed. Therefore, the downwind incident

flux will be at its maximum at the time of ignition (assuming ignition occurs at the downwind edge of the cloud) and will decrease rapidly.

Because of the complex phenomena of a vapor fire, a simple calculation procedure cannot be developed to determine the incident thermal flux. A numerical program based on equations described in this section may be used to determine the time-dependent thermal flux.

Thermal Radiation from Hydrocarbon Fireballs

Fireball combustion occurs when volatile hydrocarbons are released and rapidly ignited. In order to characterize the radiation from fireballs, it is necessary to define the size and dynamics of the fireball and then to assess the radiation based on these results.

Fireball Size and Dynamics

The maximum size of a fireball is governed primarily by the mass of the fuel released and vaporized. While the fireballs are rarely spherical, an equivalent spherical volume is widely used to characterize the size of a fireball. The maximum diameter of the equivalent spherical fireball is given by

$$D = 5.8 m^{1/3} \quad (68)$$

where D is the maximum diameter in meters and m is the mass of fuel in kilograms. This expression was synthesized by Roberts¹¹⁶ from prior work and has been adopted by others since that time (see CPSS¹¹⁷). The maximum fireball diameter is independent of the initial pressure of the fuel so long as the pressure and temperature are sufficient to vaporize the fuel. Hasegawa and Sato^{118,119} suggest that for propane at or above normal ambient temperature (20°C) complete vaporization will occur.

While the maximum size of the fireball is independent of the release pressure, the dynamics of the fireball are dependent upon the momentum of the release, which results from the flash evaporation of the fuel. For momentum-dominated fireballs, the burning duration is given by

$$t_d = 0.45m^{1/3} \quad (69)$$

(see CPSS¹¹⁷), where t_d is in seconds and m is in kilograms. For buoyancy-dominated fireballs, such as would be expected for atmospheric pressure releases, the burning duration is given by

$$t_d = 2.6m^{1/6} \quad (70)$$

(see CPSS¹¹⁷) where t_d is in seconds and m is in kilograms. Not only do burning durations differ for momentum-dominated and buoyancy-dominated fireballs, but the growth histories of the fireballs over their lifetime also differ. For momentum-dominated fireballs, the maximum fireball diameter is reached quickly with the fireball diameter growing initially as the one-fourth power of time

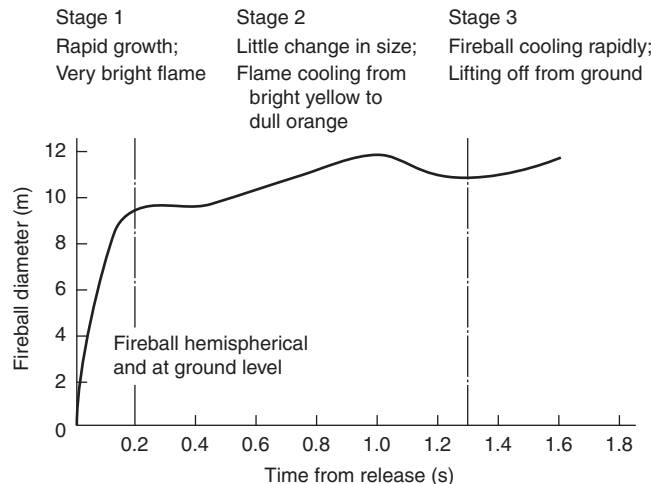


Figure 3-11.46. Fireball development as a function of time; 7.5 kg LPG released from cylinder bursting.¹¹⁶

(see Figure 3-11.46). The fireball diameter remains approximately constant over its lifetime. Conversely, the size of a buoyancy-dominated fireball initially grows as the square of time, controlled by buoyant entrainment processes (Fay and Lewis¹¹⁴).

Comparing the above fireball duration equations, it becomes clear that for large fuel masses, the momentum-dominated duration exceeds the buoyancy-dominated duration. Since buoyancy is ever present, the duration should never exceed the buoyancy-dominated duration. As such, even pressurized releases will be dominated by buoyancy for very large masses (greater than about 30,000 kg), and the buoyancy-dominated expression should be used.

For buoyancy-dominated fireballs, not only is the entrainment rate lower, but the fireball rises during its lifetime. As such, during its lifetime the fireball lifts off from the ground. Roberts¹¹⁶ adopts the correlation of Hardee and Lee¹²⁰ for the time to fireball liftoff:

$$t_e = 1.1m^{1/6} \quad (71)$$

where t_e is in seconds and m is in kilograms. As one would expect, the liftoff time scales in the same manner as the buoyant fireball duration, with the liftoff time being about 40 percent of the burning duration. Based on the work of Fay and Lewis,¹¹⁴ the maximum rise height of a buoyancy-dominated fireball is approximately five-thirds of the maximum fireball diameter. As such, the maximum rise heights range from one to five-thirds of the maximum fireball diameter for both momentum- and buoyancy-dominated fireballs.

Fireball Radiation

Radiation models for fireballs use either the point source or spherical source model. The expressions are essentially equivalent under the simplest conditions but

vary with geometric conditions where the target cannot view the entire fireball.

Point Source Fireball Model

For the point source model, the incident radiant flux, q , is given by

$$q = \tau \chi_R \cdot \frac{\dot{Q}}{4\pi L^2} \cos \theta \quad (72)$$

where

τ = atmospheric transmissivity

χ_R = radiative fraction

\dot{Q} = heat release rate

L = distance from the target to the point source location

θ = angle of the target relative to the line of sight connecting the source and target

The heat release rate is normally estimated by assuming that the total heat content of the fireball, Q , is released uniformly over the fireball duration.

$$\dot{Q} = \frac{Q}{t_d} \quad (73)$$

The radiative fraction is generally in the range 0.1 to 0.4. Roberts¹¹⁶ correlated the data of Hawegawa and Sato^{118,119} to obtain the following correlation for the radiative fraction as a function of the fuel vapor pressure:

$$\chi_R = 0.27P^{0.32} \quad (74)$$

where P is the storage pressure (in MPa), and the original data included vapor pressures from 0.2 to 1.4 MPa.

The distance from the point source to the target is given by simple geometry as

$$L = \sqrt{R_T^2 + (Z_p - H_T)^2} \quad (75)$$

where

R_T = horizontal distance from the release to the target

H_T = target height

Z_p = height of the point source

The appropriate selection of Z_p is the average height of the center of the fireball. This can range from $D/2$ for high-momentum releases with no buoyancy effects to $5/6 D$ for buoyancy-dominated releases.

Spherical Fireball Model

The spherical fireball model assumes that the fireball can be characterized as having an average fireball surface emissive power, E , and a diameter, D . The incident radiant flux to a target outside the fireball is given by

$$q = \tau E F \quad (76)$$

where τ is the transmissivity of the atmosphere between the fireball and the target and F is the configuration factor.

The configuration factor is strictly a geometric factor. Figure 3-11.47 shows the relevant geometric details required for the determination of the configuration factor where ϕ is the half-angle subtended by the fireball; θ is the angle of the normal to the target relative to the axis to the fireball; L is the separation of the target from the fireball center; and r is the fireball radius ($r = D/2$).¹¹⁷ When $\theta < \pi/2 - \phi$, the configuration factor is simply

$$F = \left(\frac{r^2}{L^2} \right) (\cos \theta) \quad \text{for } \theta < \frac{\pi}{2} - \phi \quad (77)$$

When $\theta > \pi/2 - \phi$, portions of the fireball are not visible to the target and the configuration factor is more complex.

$$\begin{aligned} F = & \frac{1}{2} - \frac{1}{\pi} \sin^{-1} \left[\frac{(L^2 - r^2)^{1/2}}{L \sin \Theta} \right] \\ & + \frac{r^2}{\pi L^2} \cos \Theta \cos^{-1} \left[-\frac{(L^2 - r^2)^{1/2}}{r} \cos \Theta \right] \\ & - \frac{1}{\pi L^2} (L^2 - r^2)^{1/2} (r^2 - L^2 \cos^2 \Theta)^{1/2} \end{aligned} \quad (78)$$

for $\Theta > \frac{\pi}{2} - \Phi$

where

r = radius of fireball ($r = D/2$), m

D = diameter of fireball, m

L = distance to center of sphere, m

Θ = angle between normal to surface and connection of point to center of sphere, rad

2Φ = view angle, rad

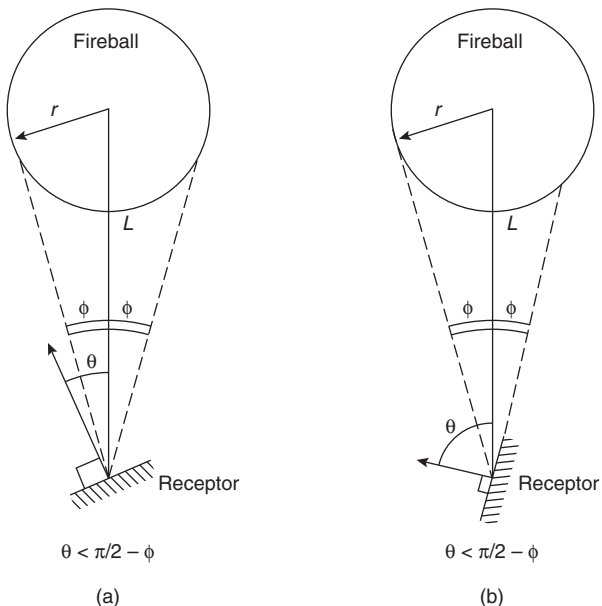


Figure 3-11.47. Geometry of a radiative sphere (fireball). (a) Receptor "sees" the whole fireball. (b) Receptor "sees" part of the fireball.

The appropriate selection of Z_p is the average height of the center of the fireball. This can range from $D/2$ for high-momentum releases with no buoyancy effects to $5/6D$ for buoyancy-dominated releases.

The emissive power of the fireball surfaces have been measured by several investigators and have been found to be in the range of 100–450 kW/m². Pape et al.¹²¹ have correlated the data of Hasegawa and Sato in a form similar to the radiative fraction correlation by Roberts.¹¹⁶

$$E = 235P^{0.39} \quad (79)$$

where E is the emissive power in kW/m² and P is the vapor pressure in MPa. Measurements by Johnson et al.¹²² for 1000 and 2000 kg butane and propane releases at 0.75 and 1.6 MPa yielded surface emissive powers in the range of 320–370 kW/m². An emissive power for large-scale releases of 350 kW/m² is widely used.

Thermal Radiation Hazards

Thermal radiation from hydrocarbon fires may pose significant hazards to both personnel and property. Hazards to personnel result from exposure to intense thermal radiation, causing severe burn injury. In the following subsection the criteria for thermal radiation hazard assessment for determining safe separation distances for personnel are discussed. Discussions of the effects on combustibles and structures can be found elsewhere in the handbook.

Criteria for Thermal Radiation Hazard Assessment

The thermal radiation from a fire may cause burns on bare skin if the intensity of radiation is sufficiently large and if the exposure is of sufficient duration. A more comprehensive treatment of skin burn injury calculations is provided by the SFPE engineering guide.¹²³ Skin burns occur over a continuous range of severity, starting from a burn so minor that the skin is barely damaged and extending through complete destruction of all skin layers to the underlying tissues or bone. Several classifications of skin burn severity have been proposed, each depending on the degree of skin damage. The most familiar classification is to divide skin burns into three degrees. Even with these three degrees, there are several recognized sublevels. For present purposes, the following levels of burn severity can be used, with the attached simple descriptions:

1. *First degree.* The mildest level of skin burn, characterized by erythema (reddening), but no formation of blisters. The mildest of first-degree burns are not particularly painful and commonly present no medical problem. They may, in fact, not even cause symptoms other than a mild impression of warmth. More severe first-degree burns will produce some pain, but no permanent damage. Flaking or scaling of the skin will occur several days after exposure because of damage to the outer skin layer.
2. *Second degree.* An intermediate level of skin burn, characterized by formation of blisters. Blister depth may be shallow, with only the surface layers of the skin

damaged, resulting in a moderate second-degree burn, or with nearly the full depth of the skin destroyed, that is, a severe second-degree burn.

3. *Third degree.* Deep burns, characterized by destruction of all skin layers. The underlying tissue may also be destroyed.

The medical problems of burns covering large areas of the body include the severe loss of fluid and the extreme potential for infection following the loss of a large portion of the protective layers of the skin. Survival of healthy adults and teenagers can normally be expected if less than 20 percent of the body surface has second- and third-degree burns (percent body areas: head 7 percent, arms 14 percent, and hands 5 percent). Survivability decreases rapidly for persons who have more than 50 percent of body surface covered by full-thickness burns, and even with intensive medical care, it is unlikely to find survivors.

Pain and tissue damage are both related to heating of the skin. The skin consists of two main layers: the epidermis, which is a thin (0.05 to 0.1 mm) outer layer, and the derma, which is an inner layer (1 to 2 mm thick). Since the skin is a complex system, there is no perfect mathematical model available for describing its response to heating under all conditions. However, simplified models can be used as an aid in predicting skin response to heating. The simplest analysis begins with the assumption that the skin and underlying tissue behave as a one-dimensional medium with constant thermal properties. Heat transfer is due to conduction only, and the temperature field anywhere in the medium is given by the following equation:¹²⁴

$$\frac{\delta T}{\delta t} = \alpha^2 \frac{\delta^2 T}{\delta x^2} \quad (80)$$

where

T = temperature at time t and distance x below the skin surface

$\alpha^2 = k/pc$ = thermal diffusivity, m^2/s

k = thermal conductivity, $\text{W}/\text{m}\cdot\text{K}$

ρ = density, kg/m^3

c = specific heat, $\text{J}/\text{kg}\cdot\text{K}$

The solution to Equation 80 depends on the initial and boundary conditions. If it is assumed that the skin and the underlying tissue are at a uniform temperature, T_0 , and that at time zero a constant heat flux of \dot{q}'' is applied, the initial and boundary conditions are as follows:

$$\left. \begin{array}{lll} t \leq 0 & x \geq 0 & T = T_0 \\ t > 0 & x = 0 & \frac{\delta T}{\delta x} = -\frac{\dot{q}''}{k} \end{array} \right\} \quad (81)$$

Equation 81 indicates that the heat flux, \dot{q}'' , produces a temperature gradient in the epidermis that is inversely proportional to the value of thermal conductivity. The solution to Equation 80 with the initial and boundary conditions indicated in Equation 81 is as follows:

$$T = \frac{\dot{q}''}{k} \left[\frac{2a\sqrt{t}}{\sqrt{\pi}} \exp\left(-\frac{x^2}{4a^2t}\right) - x \operatorname{erfc}\left(\frac{x}{2a\sqrt{t}}\right) \right] \quad (82)$$

The erfc is the complementary error function. The increase in skin surface temperature ($x = 0$) is given by the following equation:

$$T_s - T_0 = \frac{2\dot{q}''\sqrt{t}}{\sqrt{\pi kpc}} \quad (83)$$

The data of Buettner¹²⁴ obtained by having volunteers expose their forearms to varying degrees of thermal radiation indicate that the threshold pain is felt by human beings when the average temperature of 0.1-mm depth of skin is increased to about 45°C. The data indicate that the time required for pain can be correlated with the intensity of radiation by the following equation:

$$t_p = \left[\frac{35}{\dot{q}''} \right]^{1.33} \quad (84)$$

where

t_p = time required for pain, s

\dot{q}'' = incident thermal radiation, kW/m^2

The deviation of Equation 84 from Equation 83 is attributed to slightly higher surface temperature for higher thermal flux for pain threshold.

In Figure 3-11.48 the time required to cause pain is shown as a function of the incident thermal flux. The sources of data used in Figure 3-11.48 include "pricking" and "threshold" pain.¹²⁴⁻¹²⁷ All the sources of data show general agreement on the time required for pain at low fluxes. No pain was shown, regardless of the exposure duration, for thermal fluxes below 1.7 kW/m^2 (the solar constant is about 1 kW/m^2 on a clear summer day). At higher fluxes, the time required for pain diverges for the several studies. However, Equation 84 appears to predict the time required for pain with reasonable accuracy.

When the skin surface temperature reaches about 55°C, blistering of the skin occurs. Mehta et al.¹²⁸ determined that the severity of the burn depends on the energy absorbed after the skin temperature has reached a temperature of 55°C. If the amount of energy absorbed is 41.8 kJ/m^2 , pain or mild second-degree burns will be experienced. For an additional exposure of 83.6 kJ/m^2 , a blister or severe second-degree burn will become evident. Finally, for an exposure of greater than 162.2 kJ/m^2 , severe third-degree burns will result and the skin tissue will be permanently damaged. Figure 3-11.49 shows the time required for blister formation for human skin as measured by Stoll and Greene¹²⁷ and Mehta et al.¹²⁸ The times required are quite similar for threshold blisters and full blisters, showing that there is little practical difference between the two. Mixter^{129,130} has compared the degree of burns to human skin with that of pigs and found a good correlation. Mixter's¹²⁹ data for second-degree burns to white pigs are also shown in Figure 3-11.49. The difference in Mixter's data and other sources of data is attributed primarily to the source of thermal radiation. Stoll and Greene used a 1000-W projection lamp and Mixter used a carbon arc source.

The data shown in Figures 3-11.48 and 3-11.49 are useful for estimating the time for threshold pain and how rapidly human skin burns will result at various levels of

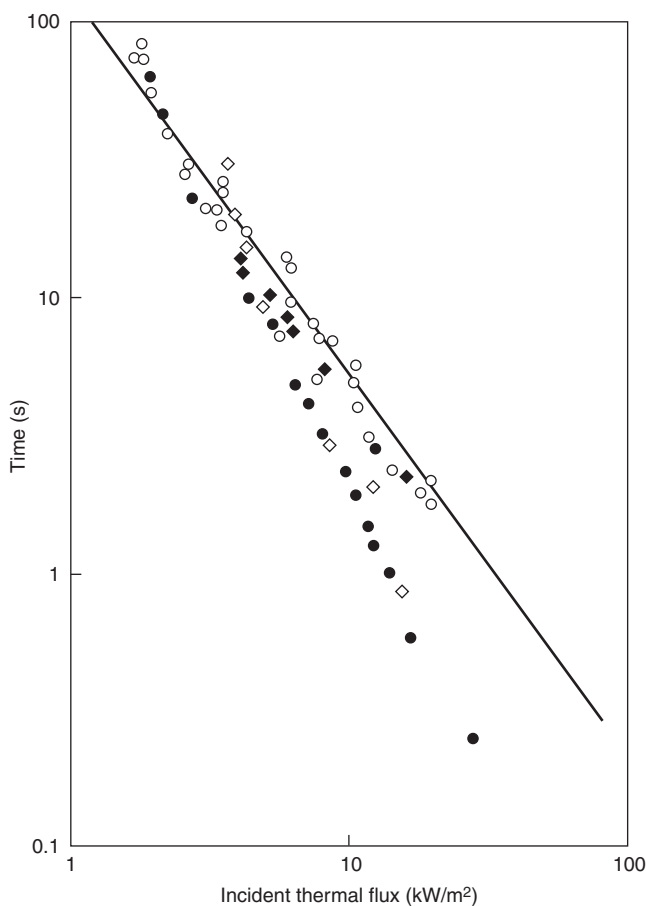


Figure 3-11.48. Time required for pain due to exposure to thermal radiation.¹¹⁴

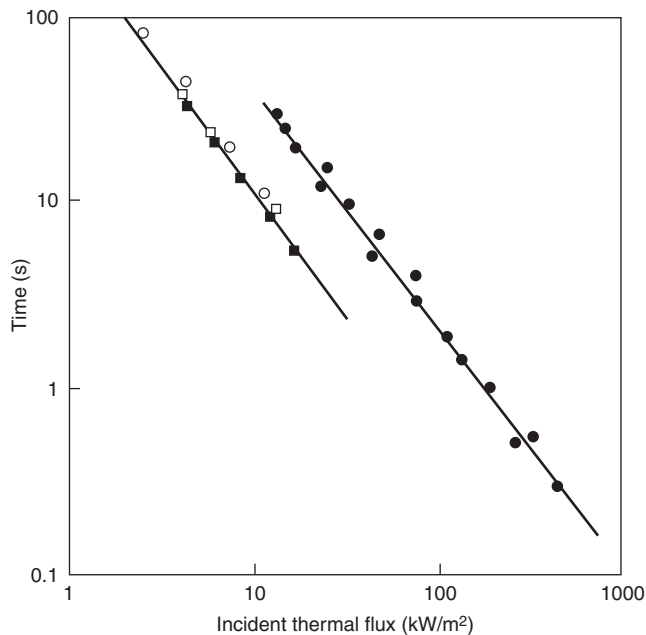


Figure 3-11.49. Time required for skin burns by thermal radiation; data sources.¹¹⁴

radiant exposure. These data, however, do not aid in determining the radiant flux levels at which fatalities may be expected. The only source of data on large-scale deaths from thermal radiation are analyses of fatalities from nuclear weapons. Since the exposure times are typically very short, interpretation of these data is somewhat subjective.

Eisenberg et al.¹³¹ analyzed the data on the relation between thermal radiation intensity and burn injury for nuclear explosions at different yields. The results of their analysis are shown in Figure 3-11.50 for significant injury threshold, 1 percent lethality, near 50 percent lethality, and near 100 percent lethality for various incident radiation intensities. Also shown in Figure 3-11.50 are the second-degree burn data collected by Mixter.¹²⁹ These data correspond very closely to the significant injury threshold.

The *United States Federal Safety Standards for Liquefied Natural Gas Facilities* (49 CFR, Part 193, 1980) suggest an acceptable level of 5 kW/m² for direct exposure of human beings. At this incident flux, exposure time on bare skin before unbearable pain is about 13 s and second-degree burns may occur in about 40 s. This level can, therefore, be used as a criterion for injury. The level at which fatality is likely to occur is more difficult to define. If we assume the duration of exposure to be the same, at about 40 s, Figure 3-11.50 can be used to determine a fatality threshold of about 10 kW/m². This level may, therefore, be used in determining the hazard zone for fatality.

Summary

In the previous sections, we have given detailed techniques for computing impacts of large, open hydrocarbon fires. In particular, we have addressed steady-state thermal radiation from pool fires and flame jets and unsteady-state thermal radiation from vapor fires and fireballs.

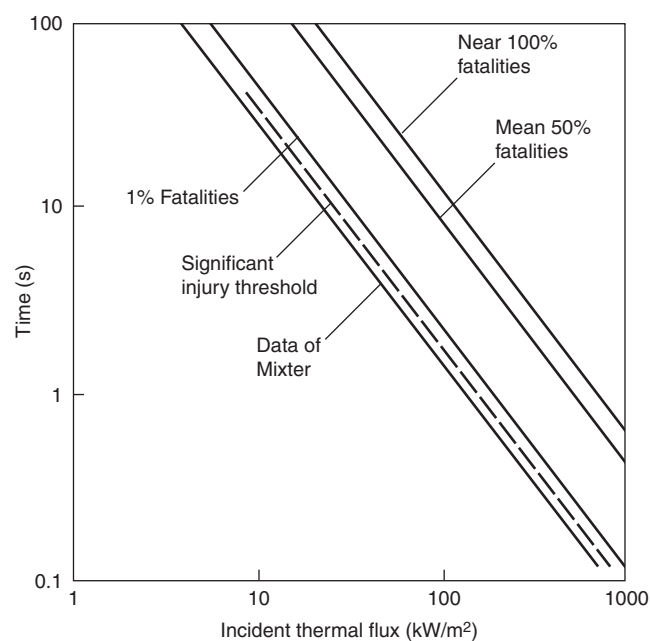


Figure 3-11.50. Fatality levels for thermal radiation.¹³¹

Particular emphasis has been placed on supporting the assessment methodology with available experimental data. These models can be used to appropriate impact criteria to evaluate the fire and flammability hazards associated with hydrocarbon releases.

References Cited

1. E.M. Sparrow and R.D. Cess, *Radiation Heat Transfer*, Brooks Publication Company, Belmont, CA (1966).
2. E.M. Sparrow and R.D. Cess, *Radiation Heat Transfer*, Revised Edition, McGraw-Hill, New York (1978).
3. R. Siegel and J.R. Howell, *Thermal Radiation Heat Transfer*, Third Edition, Hemisphere Publishing Corporation, Washington, DC (1992).
4. M.F. Modest, *Radiation Heat Transfer*, McGraw-Hill, New York (1993).
5. W.H. McAdams, *Heat Transmission*, Third Edition, McGraw-Hill, New York (1954).
6. D.Q. Kern, *Process Heat Transfer*, McGraw-Hill, New York (1950).
7. G.H. Markestein, "Radiative Energy Transfer from Turbulent Diffusion Flames," *Combustion and Flame*, 27, pp. 51–53 (1976).
8. V.I. Blinov and G.N. Khudiakov, "Certain Laws Governing Diffusive Burning of Liquids," *SSSR Doklady*, Academiia Nauk, pp. 1094–1098 (1957).
9. H.C. Hottel, "Certain Laws Governing Diffusive Burning of Liquids," *Fire Research Abstract and Revision*, 1, p. 41 (1959).
10. J. DeRis and L. Orloff, "A Dimensionless Correlation of Pool Burning Data," *Combustion and Flame*, 10, pp. 381–388 (1972).
11. D.S. Burgess, A. Strasser, and J. Grumer, "Diffusive Burning of Liquid Fuels in Open Trays," *Fire Research Abstract and Revision*, 3, p. 177 (1961).
12. J. Grumer, A. Strasser, T.A. Kubala, and D.S. Burgess, "Uncontrolled Diffusive Burning of Some New Liquid Propellants," *Fire Research Abstract and Revision*, 3, p. 159 (1961).
13. M.G. Zabetakis and D.S. Burgess, "Research in Hazards Associated with the Production and Handling of Liquid Hydrogen," *U.S. Bureau of Mines Report*, RI 5707, Pittsburgh, PA (1961).
14. K.S. Mudan, "Thermal Radiation Hazards from Hydrocarbon Pool Fires," *Progress Energy Combustion Science*, 10, pp. 59–80 (1984).
15. S.R. Gollahalli and H.F. Sullivan, "Liquid Pool Fires—A Review," *Research Report #23*, University of Waterloo, Canada (1973).
16. J. Moorhouse, "Scaling Criteria for Pool Fires Derived from Large-Scale Experiments," *I. Chem. Sym.*, 71, pp. 165–179 (1982).
17. K.S. Mudan and P.A. Croce, "Thermal Radiation Model for LNG Trench Fires," *ASME Winter Annual Meeting*, New Orleans (1984).
18. B. Hagglund and L. Persson, "The Heat Radiation from Petroleum Fires," *FOA Report C 20126-D6* (A3), Stockholm, Sweden (1976).
19. T. Yamaguchi and K. Wakasa, "Oil Pool Fire Experiments," *Fire Safety Science—Proceedings of the First International Symposium* (Grant and Pagni, eds.), Hemisphere Publishing Corporation, Washington, DC, pp. 911–918 (1986).
20. P.G. Seeger, "On the Combustion and Heat Transfer in Fires of Liquid Fuels in Tanks," in *Heat Transfer in Fires* (P.L. Blackshear, ed.), Scripta Book Company, Washington, DC, pp. 95–126 (1974).
21. T. Yumoto, "Fire Spread between Two Oil Tanks," *Journal of Fire and Flammability*, 8, p. 494 (1977).
22. T. Dayan and V.L. Tien, "Radiant Heating from a Cylindrical Column," *Combustion Science and Technology*, 9, pp. 51–56 (1974).
23. W.G. May and W. McQueen, "Radiation from Large Liquefied Natural Gas Fires," *Combustion Science and Technology*, 7, pp. 51–56 (1973).
24. M. Klassen and J.P. Gore, "Structure and Radiation Properties of Pool Fires," *NIST-GCR-94-651*, U.S. Department of Commerce, Building and Fire Research Laboratory, National Institute of Standards and Technology, Gaithersburg, MD (1994).
25. H. Koseki and G.W. Mulholland, "The Effect of Diameter on the Burning of Crude Oil Pool Fire," *Fire Technology*, 27, 1, pp. 54–65 (1991).
26. H. Koseki and T. Yumoto, "Air Entrainment and Thermal Radiation from Heptane Pool Fires," *Fire Technology*, 24, 1, pp. 33–47 (1988).
27. H. Koseki and T. Yumoto, "Burning Characteristics of Heptane in 2.7-m Square Dike Fires," *Fire Safety Science—Proceedings of the Second International Symposium* (Wakamatsu et al., eds.), Hemisphere Publishing Corporation, Washington, DC, pp. 231–240 (1989).
28. T. Yumoto, "An Experimental Study on Heat Radiation from Oil Tank Fire," *Fire Research Institute, Report No. 33—Report of Oil Tank Fire*, Fire Research Institute, Tokyo, p. 23 (1971).
29. "Report of Oil Tank Fire Experiment," Japan Society of Safety Engineering (1979).
30. "Report of Oil Tank Fire Extinguishment," Technical Report No. 8, Fire Research Institute (FRI), Tokyo (1976).
31. T.T. Fu, "Heat Radiation from Fires of Aviation Fuels," *Fire Technology*, 10, 1, pp. 54–67 (1973).
32. H.T. Johnson, L.J. Linley, and J.A. Mansfield, "Measurement of the Spatial Dependence of Temperature and Gas and Soot Concentrations within Large Open Hydrocarbon Fuel Fires," *NASA Technical Memorandum 58230*, Lyndon B. Johnson Space Center, Houston (1982).
33. P.K. Raj, K.S. Mudan, and A.N. Moussa, "Experiments Involving Pool and Vapour Fires from Spills of LNG on Water," *Report No. CG-D-55-79*, NTIS AD7707, U.S. Coast Guard, Washington, DC (1979).
34. J. Moorhouse, "Scaling Criteria for Pool Fires Derived from Large-Scale Experiments," *I. Chemical Symposium*, pp. 165–179 (1982).
35. R.S. Alger, R.C. Corlett, A.S. Gordon, and F.A. Williams, "Some Aspects of Turbulent Pool Fires," *Fire Technology*, 15, 2, pp. 142–156 (1979).
36. G.A. Mizner and J.A. Eyre, "Radiation from Liquefied Gas Fire on Water," *Combustion Science and Technology*, 35, pp. 33–57 (1983).
37. D.S. Burgess and M. Hertzberg, "Radiation from Pool Fires," in *Heat Transfer in Fire* (N.H. Afgan and J.R. Beer, eds.), Scripta Book Company, Washington, DC, pp. 413–430 (1974).
38. P.K. Raj, K.S. Mudan, and A.N. Moussa, "Experiments Involving Pool and Vapour Fires from Spills of LNG on Water," *Report No. CG-D-55-79*, NTIS AD77073, U.S. Coast Guard, Washington, DC (1979).
39. "LNG Safety Research Program," *Report IS 3-1*, American Gas Association (1974).
40. P.H. Thomas, "The Size of Flames from Natural Fires," *Ninth Symposium (International) on Combustion*, Combustion Institute, Pittsburgh, pp. 844–859 (1962).
41. G. Heskestad, "Luminous Height of Turbulent Diffusion Flames," *Fire Safety Journal*, 5, 2, pp. 103–108 (1983).
42. G. Heskestad, "Peak Gas Velocities and Flame Heights of Buoyancy-Controlled Turbulent Diffusion Flames," *Eighteenth*

- Symposium (International) on Combustion*, Combustion Institute, Pittsburgh, pp. 951–960 (1981).
43. J.R. Welker and C.M. Sliepcovich, "Bending of Wind-Blown Flames from Liquid Pools," *Fire Technology*, 2, 2, pp. 127–135 (1966).
 44. I. Emori and K. Saito, "Scaling Correlation and Smoke Observations of Oil Tank Fires Under Wind-blown Conditions," *Chemical and Physical Process in Combustion, Fall Technical Meeting, Combustion Institute/Eastern States Section*, Providence, RI, Vol. 67, pp. 1–4 November (1983).
 45. D.M. Defaveri, A. Vidili, R. Pastorino, and G. Ferraiolo, "Wind Effects on Diffusion Flames of Fires of High Source Momentum," *Journal of Hazardous Materials*, 22, pp. 86–100 (1989).
 46. "Assessing Flame Radiation to External Targets from Pool Fires," *SFPE Engineering Guide*, Society of Fire Protection Engineers (SFPE), Bethesda, MD (1999).
 47. M. Shokri and C.L. Beyler, "Radiation from Larger Pool Fires," *SFPE Journal of Fire Protection Engineering*, 4, 1, pp. 141–150 (1989).
 48. D. Drysdale, *An Introduction to Fire Dynamics*, Second Edition, John Wiley and Sons, New York, p. 148 (1999).
 49. A. Modak, "Thermal Radiation from Pool Fires," *Combustion and Flame*, 29, pp. 177–192 (1977).
 50. J.R. Howell, *A Catalog of Radiation Configuration Factors*, McGraw-Hill, New York (1982).
 51. H.C. Hottel, "Radiant Heat Transmission," in W.H. McAdams, McGraw-Hill, New York (1954).
 52. J.H. McGurie, "Heat Transfer by Radiation," *Fire Research Special Report* 2, HM Stationery Office, London (1953).
 53. D.C. Hamilton and W.R. Morgan, "Radiant-Interchange Configuration Factors," *National Advisory Committee for Aeronautic (NACA), Technical Note* 2836, Washington, DC (1952).
 54. K.S. Mudan, "Geometric View Factors for Thermal Radiation Hazard Assessment," *Fire Safety Journal*, 12, 2, pp. 89–96 (1987).
 55. E.M. Sparrow, "A New Simpler Formulation for Radiative Angler Factors," *Journal of Heat Transfer*, ASME, 85, pp. 81–88 (1963).
 56. *Handbook of Military Infrared Technology* (W.L. Wolfe, ed.), Office of National Research, Washington, DC (1965).
 57. H.C. Hottel and A.F. Sarofim, *Radiative Transfer*, McGraw-Hill, New York (1967).
 58. C.L. Beyler, "Fire Plumes and Ceiling Jets," *Fire Safety Journal*, 11, pp. 53–75 (1986).
 59. G. Cox and R. Chitty, *Combust. Flame*, 60, p. 219 (1985).
 60. B. McCaffrey, *NBSIR 79-1910*, National Bureau of Standards, Washington, DC (1979).
 61. T. Terai and K. Nitta, *Symposium of Architectural Institute of Japan*, Nagoya (1976).
 62. H.C. Kung and P. Stavrianidis, *Nineteenth International Symposium on Combustion*, Combustion Institute, Pittsburgh, p. 905 (1982).
 63. L.H. Russell and J.A. Canfield, "Experimental Measurement of Heat Transfer to a Cylinder Immersed in a Large Aviation Fuel Fire," *Journal of Heat Transfer* (1973).
 64. J.J. Gregory, N.R. Keltner, and R. Mata, Jr., "Thermal Measurements in Large Pool Fires," *Journal of Heat Transfer*, 111, (1989).
 65. C. Anderson et al., "Effects of a Fire Environment on a Rail Tank Car Filled with LPG," *Report No. FRA-OR&D 75-31*, U.S. Department of Transportation, Federal Railroad Administration, Washington, DC (1974).
 66. F.D. Wayne and K. Kinsella, "Spectral Emission Characteristics of Large Hydrocarbon Pool Fires," 84-WA/HT-74, The American Society of Mechanical Engineers, New York (1984).
 67. A.J. Taylor et al., "Engulfment Fire Tests on Road Tanker Sections," *Rarde Technical Report 7/75*, Controller HMSO, London (1975).
 68. W.H. McLain, "Investigation of the Fire Safety Characteristics of Portable Tanks Polyethylene Tanks Containing Flammable Liquids," *Report No. CG-M-1-88*, U.S. Coast Guard, Washington, DC (1988).
 69. J.J. Gregory, N.R. Keltner, and R. Mata, Jr., "Thermal Measurements in Large Pool Fires," *SAND-87-0094C*, Sandia National Laboratories, Albuquerque (1987).
 70. G.P. Wachtell and J.W. Langhaar, "Fire Test and Thermal Behavior of 150-Ton Lead-Shielded Cask," *DP 1070, Engineering and Equipment*, TID-4500, E.I. DuPont De Nemours and Co., Wilmington, DE (1966).
 71. National Academy of Science Committee on Hazardous Materials, Division of Chemistry and Chemical Technology (National Research Council, ed.), *Pressure-Relieving Systems for Marine Cargo Bulk Liquid Containers*, National Academy of Sciences, Washington, DC (1973).
 72. K. Moodie et al., "Total Pool Fire Engulfment Trials on a 5-Tonne LPG Tank," *HSE Internal Report No. IR/L/FR/87/27*, London (1987).
 73. M. Tunc and J.E.S. Venart, "Incident Radiation from an Engulfing Pool Fire to a Horizontal Cylinder, Part I & II" *Fire Safety Journal*, 8, pp. 81–95 (1984/1985).
 74. T.A. Brzustowski, "A New Criterion for the Length of a Gaseous Turbulent Diffusion Flame," *Combustion Science and Technology* 6, pp. 313–319 (1973).
 75. T.A. Brzustowski, "Flaring in the Energy Industry," *Progress Energy Combustion Science*, 2, pp. 129–141 (1976).
 76. T.A. Brzustowski, "Flaring: State of the Art," *Loss Prevention*, 11, p. 15 (1977).
 77. T.A. Brzustowski and E.C. Sommer, "Predicting Radiant Heating from Flares," *Proceedings of the API Division of Refining*, 53, p. 865 (1973).
 78. T.A. Brzustowski, S.R. Gollahalli, M.P. Gupta, M. Kaptein, and H.F. Sullivan, "The Turbulent Hydrogen Diffusion Flame in a Cross Wind," *Combustion Science and Technology*, 11, pp. 29–33 (1975).
 79. T.A. Brzustowski, S.R. Gollahalli, M.P. Gupta, M. Kaptein, and H.F. Sullivan, "Radiant Heating from Flares," *ASME Paper 75-HT-4*, American Society of Mechanical Engineers (ASME), New York (1975).
 80. H.C. Hottel and W.R. Hawthorne, "Diffusion in Laminar Flame Jets," *Third Symposium (International) on Combustion*, Combustion Institute, Pittsburgh, pp. 254–266 (1949).
 81. W.R. Hawthorne, D.S. Weddell, and H.C. Hottell, "Mixing and Combustion on Turbulent Gas Jet," *Third Symposium (International) on Combustion*, Combustion Institute, Pittsburgh, pp. 266–288 (1949).
 82. K. Gugan, "Flixborough—A Combustion Specialist's Viewpoint," *Chemical Engineering*, 309, London (1976).
 83. F.P. Ricou and D.B. Spalding, "Measurements of Entrainment by Axisymmetrical Turbulent Jets," *Journal of Fluid Mechanics*, II, p. 21 (1961).
 84. A.A. Putnam and C.F. Speich, "A Model Study of the Interaction of Multiple Turbulent Diffusion Flames," *Ninth Symposium (International) on Combustion*, Combustion Institute, Pittsburgh, pp. 867–877 (1963).
 85. F.R. Steward, "Prediction of the Height of Turbulent Diffusion Buoyant Flames," *Combustion Science and Technology*, 2, pp. 203–212 (1970).

86. B. McCaffrey, "Some Measurements of the Radiative Power Output of Diffusion Flames," *WSS/CI 81-15, Western States Section, Combustion Institute, Pittsburgh* (1981).
87. B. Kalghatgi, "Blow-Out Stability of Gaseous Jet Diffusion Flames, Parts I and II," *Comb. Sci. Tech.*, 26, p. 233–250 (1981).
88. B. McCaffrey and D. Evans, "Very Large Methane Jet Diffusion Flames," *Twenty-First Symposium (International) on Combustion, Combustion Institute, Pittsburgh*, pp. 25–31 (1986).
89. T.A. Brzustowski, S.R. Gollahalli, and H.F. Sullivan, "The Turbulent Hydrogen Diffusion Flames in a Cross-Wind," *Combustion Science and Technology*, II, pp. 29–33 (1975).
90. S.R. Gollahalli, T.A. Brzustowski, and H.F. Sullivan, "Characteristics of a Turbulent Propane Diffusion Flame in a Cross-Wind," *Transactions of CSMC*, 3, pp. 205–214 (1975).
91. G.T. Kalghatki, "The Visible Shape and Size of a Turbulent Jet Diffusion Flame in a Crosswind," *Combustion and Flame*, 52, pp. 91–106 (1983).
92. O.K. Sonju and J. Hustad, "An Experimental Study of Turbulent Jet Diffusion Flame in a Crosswind," *Norwegian Maritime Research*, pp. 2–11 (1984).
93. G.A. Chamberlain, "Developments in Design Methods for Predicting Thermal Radiation from Flares," *Chemical Engineering Research Des.*, 65, p. 299 (1987).
94. A.D. Johnson, H.M. Brightwell, and A.J. Carsley, "A Model for Predicting the Thermal Radiation Hazards from Large-Scale Horizontally Released Nature Gas Jet Fires," *Hazards*, XII, p. 123 (1994).
95. D.K. Cook, M. Fairweather, J. Hammonds, and D.J. Hughes, "Size and Radiative Characteristics of Natural Gas Flares," *Chemical Engineering Research Des.*, 65, pp. 310, 318 (1987).
96. W.J.S. Hirst, "Combustion of Large Scale Jet-Releases of Pressurised Liquid Propane," *Comm. 1241* (London: Institution of Gas Engineers) (1984).
97. V.H.Y. Tam and L.T. Cowley, "Consequence of Pressurised LPG Release—A Full-Scale Experiment," *Gastect 88, Paper 4.3* (1989).
98. T.A. Brzustowski, "Predicting Radiant Heating from Flares," *Esso Engineering Research and Development Report, EE 15ER.71* (1971).
99. P.R. Oenbring and T.R. Sifferman, "Flare Design—Are Current Methods Too Conservative?" *Hydrocarbon Processing*, pp. 124–129 (1980).
100. S.H. Tan, "Flare System Design Simplified," *Hydrocarbon Processing*, 46, pp. 172–176 (1967).
101. G.R. Kent, "Practical Design of Flare Stacks," *Hydrocarbon Processing*, 43, pp. 121–125 (1964).
102. D. Evans and D. Pfennig, "Water Sprays Suppress Gas-Well Blowout Fires," *Oil and Gas Journal*, 83, pp. 80–86 (1985).
103. B. McCaffrey, "Jet Diffusion Flame Suppression Using Water Sprays, An Interim Report," *Comb. Sci. Tech.*, 40, pp. 107–136 (1984).
104. B. McCaffrey, "Momentum Diffusion Flame Characteristics and the Effects of Water Spray," *Comb. Sci. Tech.*, 63, pp. 315–335 (1989).
105. J.F. Straitz III, J.A. O'Leary, J.E. Brennan, and C.J. Kardan, "Flare Testing and Safety," *Loss Prevention*, II, pp. 23–30 (1977).
106. W.W. Yuen and C.L. Tien, "Simple Calculation Scheme for the Luminous Flame Emissivity," *Sixteenth Symposium (International) on Combustion, Combustion Institute, Pittsburgh*, pp. 1481–1487 (1976).
107. G. Fumarola, D.M. de Faveri, R. Pastorino, and G. Ferraiolo, "Determining Safety Zones for Exposure to Flare Radiation," *Institute of Chemical Engineering Symposium, Series 82, Loss Prevention and Safety Promotion*, pp. G23–G30 (1983).
108. P.R. Oenbring and T.R. Sifferman, "Flare Design Based on Full-Scale Plant Data," *Forty-Fifth Midyear Meeting, API Refining Department Proceedings*, 59, Houston (1980).
109. S. Galant, D. Grouset, G. Martinez, P. Micheau, and J.B. Allemand, "Three-Dimensional Steady Parabolic Calculations of Large Scale Methane Turbulent Diffusion Flames to Predict Flare Radiation Under Cross-Wind Conditions," *Twentieth Symposium (International) on Combustion, Combustion Institute, Pittsburgh*, pp. 531–540 (1984).
110. L. Cowley and M. Prichard, "Large-Scale Natural Gas and LPG Jet Fires and Thermal Impact on Structures," *GASTECH 90 Conference*, Amsterdam (1990).
111. A. Parker, "Evaluating High-Temperature Intumescent Insulation Materials Under Fire and Blast Conditions," *Insulation Materials: Testing and Applications: Third Volume, ASTM STP 1320* (Graves and Zarr, eds.), American Society for Testing and Materials, Philadelphia (1997).
112. Wighus and Dransgsholt, "Impinging Jet Fire Experiments—Propane 14 MW Laboratory Tests," *Report STF25 A92026, SINTEF NB*, Norwegian Fire Research Laboratory (1993).
113. K.S. Mudan, "Hydrocarbon Pool and Vapor Fire Data Analysis," *U.S. DOT Report DE-AC01-83EP16008*, U.S. Department of Transportation, Washington, DC (1984).
114. J.A. Fay and D.H. Lewis, "Unsteady Burning of Unconfined Fuel Vapor Clouds," *Sixteenth Symposium (International) on Combustion, Combustion Institute, Pittsburgh*, pp. 1397–1405 (1976).
115. P.K. Raj and H.W. Emmons, "On the Burning of a Large Flammable Vapor Cloud," *Combustion Institute/Central and Western States Sections (Joint Meeting): Flammability and Burning Characteristics of Materials and Fuels*, San Antonio, Combustion Institute, Pittsburgh, pp. 1–23 (1975).
116. A.F. Roberts, "Thermal Radiation Hazards from Releases of LPG from Pressurized Storage," *Fire Safety Journal*, 4, pp. 197–212 (1982).
117. Center for Chemical Process Safety, *Guidelines for Evaluating the Characteristics of Vapor Cloud Explosions, Flash Fires, and BLEVE's*, American Institute for Chemical Engineers, New York, pp. 157–180 (1994).
118. K. Hasegawa and K. Sata, "Study of Fireball Following Steam Explosion of n-Pentane," *Loss Prevention and Safety Promotion*, 2, p. 297 (1977).
119. K. Hasegawa and K. Sata, "Experimental Investigation of the Unconfined Vapor Cloud Explosions of Hydrocarbons," *Technical Memorandum 12*, Fire Research Institute, Tokyo (1978).
120. H.C. Hardee and D.O. Lee, "Thermal Hazard from Propane Fireballs," *Trans. Plan. Tech.*, 2, pp. 121–128 (1973).
121. R.P. Pape et al., "Calculation of the Intensity of Thermal Radiation from Large Fires," *Loss Prevention Bulletin*, 82, pp. 1–11 (1988).
122. D.M. Johnson, M.J. Pritchard, and M.J. Wickens, "Large Scale Catastrophic Releases of Flammable Liquids," *Commission of the European Communities Report, Contract No. EV4T.0014.UK(H)*, Brussels (1990).
123. SFPE, *Predicting 1st and 2nd Degree Skin Burns from Thermal Radiation*, Society of Fire Protection Engineers, Bethesda, MD (2000).
124. K. Buettner, "Effects of Extreme Heat and Cold on Human Skin, II. Surface Temperature, Pain and Heat Conductivity in Experiments with Radiant Heat," *J. Ap. Phys.*, 3, p. 703 (1951).
125. J.D. Hardy, I. Jacobs, and M.D. Meizner, "Thresholds of Pain and Reflex Contraction as Related to Noxious Stimulation," *J. Ap. Phys.*, 5, pp. 725–739 (year?).

126. N. Bigelow, I. Harrison, H. Goodell, and H.G. Wolf, "Studies on Pain: Quantitative Measurements of Two Pain Sensations of the Skin, with Reference to the Nature of Hyperalgesia of Peripheral Neuritis," *J. of Clinical Invest.*, 24, pp. 503-512 (1945).
127. A.M. Stoll and L.C. Greene, "Relationship between Pain and Tissue Damage Due to Thermal Radiation," *J. Ap. Phys.*, 14, pp. 373-382 (1959).
128. A.K. Mehta, F. Wong, and G.C. Williams, "Measurement of Flammability and Burn Potential of Fabrics," *Summary Report to NSF—Grant #GI-31881*, Fuels Research Laboratory, Massachusetts Institute of Technology, Cambridge (1973).
129. G. Mixter, "The Empirical Relation between Time and Intensity of Applied Thermal Energy in Production of 2+ Burns in Pigs," *University of Rochester Report No. UR-316, Contract W-7044 eng49*, New York (1954).
130. G. Mixter, "Thermal Radiation Burns beneath Fabric Systems," *Annals of the New York Academy of Sciences*, 82, pp. 701-713 (1959).
131. N.A. Eisenberg, et al., "Vulnerability Model. A Simulation System for Assessing Damage Resulting from Marine Spills," *NTIS AD-AD015-245*, Springfield, VA (1975).